

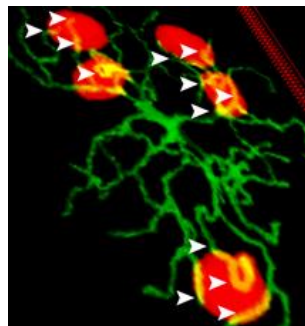
MTA doctoral dissertation
(short dissertation)

Role of microglia in neuronal health, inflammation and brain injury

Ádám Dénes

Institute of Experimental Medicine

Budapest, Hungary



.....To my beloved mother,
who planted the trees that must now flourish without her

Table of Contents

List of abbreviations.....	4
Introduction.....	6
The emerging role of non-neuronal cells in shaping neuronal activity and fate.....	7
Microglia: the main immune cells of the CNS with unique origin and roles beyond immunity	8
The role of microglia in CNS development.....	9
Phenotypes, interactions and function of microglia in the adult brain	11
Housekeeping roles of microglia in the adult brain – implications for brain diseases	13
Mechanisms through which inflammation, brain-immune interactions and microglial dysfunction contribute to pathology in common brain diseases.....	14
Targeting microglia: impact on neuronal function and brain injury	17
Impact of systemic inflammation on central inflammatory actions, microglial states and brain injury	20
Summary of research and specific aims	24
Results.....	25
<i>Chapter 1:</i> Inflammation and microglial actions modulate injury in the brain	25
<i>Chapter 2:</i> Systemic inflammation promotes CNS inflammation, alters microglial function and augments brain injury.....	30
<i>Chapter 3.</i> The role of compartment-specific microglia-neuron interactions in shaping neuronal activity and injury.....	35
Conclusions	42
Lessons from neuroprotection trials and clinical studies.....	43
Microglia emerge as main integrators and modulators of inflammatory processes in the CNS – relevance for neurological disorders	44
Emerging role of compartment-specific interactions between microglia, neurons and other cells in the CNS	46
Future prospects and challenges	51
Publications	53
Acknowledgements.....	57
References	58

List of abbreviations

A β	Amyloid β
AD	Alzheimer's disease
ALS	Amyotrophic Lateral Sclerosis
ALSP	Adult-onset leukoencephalopathy with axonal spheroids and pigmented glia
AMPA	α -amino-3-hydroxy-5-methyl-4-isoxazole propionic acid
APP/PS1 mice	Double transgenic mice expressing a chimeric mouse/human amyloid precursor protein and a mutant human presenilin 1
BBB	Blood-brain barrier
CBF	Cerebral Blood Flow
CD11b	Cluster of differentiation molecule 11b (CD11b)/Integrin alpha M (ITGAM)
CD11b-DTR mice	Transgenic mice expressing diphtheria toxin receptor under the control of the Human ITGAM promoter (CD11b)
CD200	OX-2 type I membrane glycoprotein
CD200R	Cell surface transmembrane glycoprotein CD200 receptor 1
c-MYB	Protein c MYB proto-oncogene, transcription factor
CNS	Central Nervous System
CSF	Cerebrospinal fluid
CSF1R	Colony Stimulating Factor 1 Receptor
CUX-1	Homeobox protein cut-like 1
CXCL1	Keratinocytes-derived chemokine (KC)
CX3CL1	Chemokine (C-X3-C motif) ligand 1/fractalkine
CX3CR1	CX3C Chemokine receptor 1/ fractalkine receptor
C1q	Complement component 1q
C3	Complement C3
CR3	Complement receptor 3
DAM	Damage-associated microglia
DAMP	Damage-Associated Molecular Pattern
DAP12	DNAX activation protein 12
DT	Diphtheria toxin
DTR	Diphtheria toxin receptor
FDA	Food and Drug Administration
FIRE	fms-intronic regulatory element, Csf1r locus super-enhancer

dc_2027_22

dc_2027_22

G-CSF	Granulocyte colony stimulating factor
GFAP	Glial Fibrillary Acidic Protein
GFP	Green Fluorescent Protein
GWAS	Genome Wide Association Study
HMGB1	High Mobility Group Box 1
HSC	Haematopoietic Stem Cell
HSV	Herpes Simplex virus
HSVTK	Herpes Simplex viral thymidine kinase
IL-1	Interleukin 1
IL-1R1	Interleukin 1 receptor type 1
IL-1Ra	Interleukin 1 receptor 1 antagonist
IL-6	Interleukin 6
MCI	Mild Cognitive Impairment
MCP-1	Monocyte chemoattractant protein-1
MS	Multiple Sclerosis
NLR	Nod-like receptor
NLRP3	NLR family pyrin domain containing 3
NMDA	N-methyl-D-aspartate
NTPDase	Nucleoside Triphosphate Diphosphohydrolase
NVU	Neurovascular unit
LPS	Lipopolysaccharide
PAMP	Pathogen Associated Molecular Pattern
PD	Parkinson's disease
PNS	Peripheral nervous system
PRR	Pattern Recognition Receptor
PRV	Pseudorabies virus
Pu.1	Transcription factor PU.1
p-tau	phosphorylated tau
ROS	Reactive oxygen species
CCL5	Chemokine (C-C motif) ligand 5 (RANTES)
SPECT	Singlephoton emission computed tomography
TBI	Traumatic Brain Injury
TGF β	Transforming growth factor β
Tgfr2	Transforming growth factor β receptor 2
TNF α	Tumor necrosis factor α
TLR	Toll like receptor
TREM2	Triggering Receptor Expressed on Myeloid cells 2

Introduction

In the first half of the 20th century, series of groundbreaking discoveries revolutionized medicine, leading to a marked reduction in childhood mortality and deaths from infectious diseases. In line with this, advances in healthcare and socioeconomic developments among other factors have substantially contributed to increased life expectancy worldwide, particularly in developed countries¹⁻³. However, these advances have also been associated with the growing burden of age-related conditions and non-communicable diseases by the 21st century. While the battle against infections is far from over⁴⁻⁶, chronic diseases represent an unresolved and rapidly growing challenge in both developing and developed countries^{3, 7}. Of note, chronic diseases and ageing have broad associations with the development of brain disorders, which not only affect millions of people worldwide, but emerge as one of the leading causes of morbidity and mortality, not mentioning costs of treatment and their additional societal impacts⁸. Despite all medical advances to date, treatment opportunities for most brain diseases remain limited. In line with this, accumulating data indicate that targeting the mechanisms of neuronal injury alone may turn out to be ineffective. This is also indicated by the failure of numerous clinical trials in stroke, Alzheimer's disease (AD), Parkinson's disease (PD) and in other conditions. Importantly, recent research has highlighted the prominent role of brain-immune interactions and inflammatory processes in the pathophysiology of most common brain diseases, which had been largely neglected in previous studies. Neurons in the central nervous system (CNS) not only require precisely regulated blood supply and support from glial cells, but the mechanisms of neuronal injury (both acute and chronic) are also profoundly influenced by complex neuro-vascular-glial interactions, which are highly sensitive to inflammation. Of note, while systemic inflammation is known to represent a key health-damaging factor and is a primary risk factor for chronic diseases and brain disorders, the overall burden of inflammation increases by ageing alongside with the development of immune dysfunction. Moreover, inflammatory markers show strong associations with socioeconomic status and lifestyle⁹⁻¹¹. Therefore, better understanding of complex biological processes and mechanisms of disease pathophysiology are desperately needed, which is greatly supported by rapidly evolving multidisciplinary research technologies. As such, recent developments in neuroscience, imaging, molecular biology, immunology and genetics strongly support the identification of novel therapeutic targets in neurological disorders, but effective therapeutic strategies may not be developed without the extensive understanding of the interactions between the immune system and the CNS.

The emerging role of non-neuronal cells in shaping neuronal activity and fate

High energy demand and fine-tuned operation of neuronal networks rely on their interactions with non-neuronal cells that appear to be similarly complex as neuron-neuron interactions. These interactions manifest at different temporal and spatial scales, and are highly compartmentalized throughout the CNS. Of note, evolution of the CNS has not only involved increases in neuronal numbers and the complexity of their interactions, but has also been associated with marked explosion of the diversity of glial cells and the complexity of their interactions with neurons in mammals, and in particular, hominids¹²⁻¹⁵. Thus, to understand how the brain works and how given pathological processes impair the precise functioning of the brain, studies on glia-neuron interactions appear equally important to those investigating communication between neuronal cells and networks. For example, glial cells, ependymal cells, choroid plexus epithelial cells and the vasculature of the CNS not only form unique barriers, but actively control CSF production and circulation, extracellular ion gradients, changes of metabolic states and neuronal activity, and, importantly, cerebral blood flow, which fuels neuronal activity in the brain. Cerebral autoregulation (ability to maintain stable blood flow in the brain despite changes in systemic blood pressure) and functional hyperemia (increase in local blood flow in response to neuronal activity) are well-documented examples for precisely controlled blood supply to match the metabolic needs of neurons^{16, 17}. While the exact mechanisms through which complex interactions between vascular endothelial cells, smooth muscle cells, pericytes, astrocytes and other cells control blood flow in the brain remain to be defined, failure of these interactions has known pathological consequences. Importantly, reduction of cerebral blood flow, impaired neurovascular coupling and altered activity of glial cells are among the earliest changes seen in common neurological disorders such as AD, PD and other forms of neurodegeneration, even preceding the occurrence of neurological symptoms¹⁶⁻¹⁸.

It is well-established that normal functioning of neurons requires constant support from specialized glial cells, whose failure may rapidly translate into diverse forms of neuropathologies. However, while the detrimental consequences of glial dysfunction are widely recognized, the root causes remain largely unexplored. For example, while oligodendrocytes are among the most vulnerable cells of the CNS, mechanisms of oligodendrocyte loss in conditions like Multiple Sclerosis (MS) or the markedly limited efficacy of remyelination / nerve regeneration in the CNS compared to that seen in the peripheral nervous system (PNS) remains improperly defined^{19, 20}. Similar caveats exist regarding the role of different glial cells populations in shaping the ion composition of the brain parenchyma that is required for precise operation of complex neuronal networks. Maintenance of the extracellular milieu in the brain is a fine-tuned process with numerous pathological

implications, including the regulation of extracellular potassium, chloride or sodium levels, maintenance of normal pH, blood brain barrier (BBB) function and water transport, or removal of extracellular metabolites among others. Astrocytes are key contributors to all these processes, whereas their dysfunction is known to contribute to stroke, epilepsy, AD, Huntington's disease and other conditions²¹⁻²³.

In the unique microenvironment of the highly compartmentalized CNS, operation of immune processes is also challenging given the complexity of brain barriers that limit the interactions between the CNS parenchyma and humoral/cellular elements of the immune system. Low density of lymphatic vessels in the brain and limited surveillance by peripheral immune cells require fine-tuned regulation of inflammatory- and immune processes, which is further emphasized by the high sensitivity of neurons to inflammation-mediated injury²⁴⁻²⁷. To this end, specialized endothelial cells and astrocytes contribute to neuroimmune communication alongside with sustaining BBB function, while choroid plexus epithelial cells, ependymal cells, meningeal structures and lymphatic blood vessels control immune cell trafficking at the boundaries of the blood-CSF-parenchyma interface. These unique structures also contribute to the operation of the glymphatic system, which enables bulk movement of CSF from the subarachnoid space along periaxonal spaces, where it mixes with interstitial fluid within the parenchyma before ultimately exiting from the parenchyma via perivenous spaces²⁸. After all, it is not surprising that specialized myeloid cell types are also required for broad housekeeping functions, as seen in most other organs, equipped with unique phenotypes adapted to the unique microenvironment of the CNS. In particular, microglia, the most abundant immune cell population of the CNS not only play a key role to orchestrate central immune processes, but also have numerous other homeostatic roles, which have been increasingly documented in the last two decades^{25, 29-31}.

Microglia: the main immune cells of the CNS with unique origin and roles beyond immunity

Microglia are the main immune cells of the brain and the spinal cord and are key regulators of central inflammatory processes. Beyond their immune functions, recent data indicate that microglia also play instrumental roles during brain development and in the maintenance of brain homeostasis. In line with this, dysfunction or altered activity of microglia emerges as a major contributor to almost all brain diseases, including neurodevelopmental disorders, acute brain injury, neuronal hyperactivity, and age-related conditions, such as stroke, AD, PD and other forms of neurodegeneration. While similarly to microglia, other long-lived resident macrophages in peripheral tissues (e.g. in the liver or in the gut) are known to exert complex and functionally heterogeneous responses, the origin of microglial progenitors and the impact

of the CNS microenvironment on microglial function collectively grant unique roles for these cells in health and disease.

Microglia are derived from the extra-embryonic yolk sac, which is the first site for hematopoiesis during embryonic development in mammals. Recent fate-mapping studies have shown that microglia originate from primitive erythromyeloid progenitors that arise before embryonic day 8 (E8) in mice, colonize the brain from E9.5, generating the entire adult microglial population independently of any external bone-marrow-derived contribution³². Macrophages derived from erythromyeloid progenitors do not require the transcription factor c-Myb for development and maturation. As such, microglial progenitors similarly to those of Langerhans cells and Kupffer cells develop normally in c-Myb^{-/-} animals, unlike haematopoietic stem cells and macrophages that stem from them, which originate later (E10.5 in mice) in the fetal liver^{33, 34}. Proliferating microglia populate the entire CNS, reaching an „adult” phenotype by 28 days after birth in mice, following at least four stages of development³⁵. In humans, microglial progenitors colonize the developing forebrain in at least two waves: first via extravascular routes at 4.5 gestational weeks (gw) with a second wave through the vasculature at 12–13 gw^{36, 37}.

Microglia are the sole myeloid cell type in the healthy brain parenchyma, amounting to ~5–15% of total CNS cells, with large regional heterogeneities in numbers and phenotypes. Other CNS-associated macrophages include meningeal, perivascular and choroid plexus macrophages at the borders of the CNS in the respective nonparenchymal compartments^{31, 38}. Microglia comprise a self-renewing population throughout life and are long-lived. In mice, *in vivo* imaging studies have demonstrated that neocortical resident microglia died at a rate of about 26% per year, and an equal percentage of new ones formed with a median lifetime well over 15 months³⁹. Adult human microglia are also self-maintaining and long-lived: they renew slowly, at a median rate of 28% per year, which is sustained by continuous turnover throughout adult life and some microglia last for more than two decades⁴⁰. Microglial self-maintenance critically relies on Colony Stimulating Factor 1 Receptor (CSF1R)-mediated signaling. CSF1R KO mice and rats lack microglia and other tissue macrophages⁴¹, while in adults microglial CSF1R dependence appears to be stronger than in the case of most peripheral macrophage populations. Therefore, manipulation of microglia via CSF1R has become a widely used approach to investigate the role of microglia during development and in different models of brain injury, as discussed in detail below.

The role of microglia in CNS development

Evidence indicating a role for microglia in normal brain development emerged partially from gain-of-function and loss-of-function studies concerning myeloid cell development and fate.

Mice lacking Pu.1, a regulator of myeloid differentiation have no monocytes and macrophages, which is associated with decreased neuronal proliferation rate and lower macrogliogenesis. Pu.1-null mice are born with severe immune deficits and die before adulthood⁴². Another important regulator of macrophages, CSF1R has an evolutionarily conserved role in brain development. These effects are mostly attributed to impaired microglial function, although loss of the physiological functions of macrophages in the periphery is also likely to contribute to the development of different brain pathologies in CSF1R KO models⁴³. CSF1R deficiency results in an absence of microglia in zebrafish, mice, rats and humans⁴³. Mouse CSF1R mutants rarely survive into adulthood due to the lack of peripheral macrophages in addition to microglia. While in these mice embryonic development appears normal, during the postnatal period the brain architecture becomes perturbed with enlarged ventricles and regionally compressed parenchyma. This is associated with olfactory bulb deficits and increased neuronal density, elevated numbers of astrocytes and reduced numbers of oligodendrocytes in the cerebral cortex⁴¹. Loss of microglia similarly occurs in FIRE-deficient (fms-intronic regulatory element, a highly conserved super-enhancer in the *Csf1r* locus) *Csf1r*^{ΔFIRE/ΔFIRE} mice, which display apparently normal cell-type-specific transcriptomic signatures in neurons, astrocytes and oligodendrocytes⁴⁴. CSF1R KO rats also have milder neurological alterations including enlarged ventricles, reduced myelination and altered differentiation of dopaminergic neurons⁴¹. In humans, homozygous CSF1R mutations lead to the loss of microglia and different structural brain anomalies, including agenesis of the corpus callosum or absence of CUX1+ neurons, which are associated with developmental abnormalities or epilepsy in childhood⁴⁵. Neuropathological studies have also noted the accumulation of proliferating microglia at the site of white-matter injury in premature neonates and the correlation between microglial activation and developmental deficits³⁶.

The developmental roles of microglia have been attributed their effects on angiogenesis, BBB maturation, neurogenesis, axonal guidance and synaptic pruning among others. Collectively, microglia appear to contribute to a broad array of developmental processes, via vascular, neuronal and other actions with neurodevelopmental effects being best documented. These include the contribution of microglia to embryonic neurogenesis⁴⁶, neuronal differentiation⁴⁷, developmental and activity-dependent synaptic pruning^{48, 49} and formation of cortical layers⁵⁰. During embryonic development, microglia are believed to be responsible for the removal of supernumerary synapses and neurons, and contribute to neuronal network formation⁵¹. Cortical neurons are thought to require microglial support for survival during postnatal development, which was demonstrated by transient ablation of microglia in CD11b-DTR transgenic mice⁵⁰. Pharmacological depletion of microglia and

genetic models of microglial dysfunction or altered microglia-neuron interactions (e.g. in CX3CR1^{-/-}, CR3^{-/-}, and DAP12^{-/-} mutants) also result in altered axon outgrowth and cortical interneuron positioning⁵².

Phenotypes, interactions and function of microglia in the adult brain

Microglia are considered the most versatile inhabitants in the mammalian CNS with a multitude of broad functions, dynamically changing at cellular, subcellular and molecular levels to adapt to their ever-changing surroundings⁵³. Transcriptomic studies have shown that both murine and human microglia demonstrate substantial regional heterogeneity in the adult brain concerning their density, transcriptomic phenotypes and turnover rates⁵³⁻⁵⁵. This heterogeneity is believed to reflect altered functional properties of the cells, which is strongly and differentially influenced by the neurochemical milieu of their microenvironment, age, gender, composition of the gut microbiota and a number of other factors under homeostatic conditions^{53, 56}.

Another unique feature of microglia is their remarkable process motility underlying their surveillance activity. In the healthy brain, microglia constantly monitor the environment with their motile processes, which move at 1-2 μm / min speed with extensions and withdrawals exceeding the diameter of the cell body several fold. As such, individual microglial cells occupy a special territory enabling them to monitor changes that take place in the extracellular space or in different cells in their microenvironment. During their surveillance activity, microglial processes contact neurons, astrocytes, oligodendrocytes, blood vessels and other structures. Surveillance is maintained even in the injured brain, such as after cerebral ischemia or brain trauma⁵⁷⁻⁵⁹, enabling microglia to respond to diverse pathophysiological stimuli even if the brain's energetic homeostasis is compromised. This results from their remarkable metabolic flexibility, for example, the ability to consume glutamine as an alternative metabolic fuel in the absence of glucose⁶⁰.

Microglial phenotypes are plastic and are influenced by various factors inside or outside the CNS. Historically, changes in microglial shapes ranging from their „resting” state with fine, ramified branch structure around their small cell body to the „amoeboid”, phagocytic states with enlarged cell body and short, bulky processes have been widely documented in different forms of brain diseases, including viral infection, AD, PD and stroke among others⁶¹⁻⁶³. Pioneering *in vivo* two-photon imaging studies have revealed that microglia exert a rapid response to acute injury or inflammatory stimuli in the brain and the spinal cord, leading to profound changes in microglial morphology, activation states and functional responses. These include the recruitment of microglial processes to sites of injury, which can be modeled by injecting damage-associated molecules such as ATP into the brain

parenchyma^{64, 65}. In the case of small, focal injuries, these responses remain highly localized, as also shown by experimental studies using laser-induced injury^{65, 66}. More extensive tissue injury such as seen after infection, brain trauma or cerebral ischemia leads to broad alterations in the activity of microglia at the affected areas, which is characterized by withdrawal of fine processes, enlarged cell body, production of proinflammatory cytokines (e.g. IL-1 β , TNF α or IL-6), reactive oxygen species and many other substances as also shown by the markedly altered transcriptomic fingerprints of microglia after different forms of acute injury^{27, 62, 67, 68}. Marked phenotypic transformation of microglia after stroke or brain trauma may be observed for several weeks or months in both experimental models and in humans^{27, 34, 68-70}. Based on the lessons from these studies, microglial activity appears to represent a continuum, including changes in transcriptomic, proteomic, metabolic fingerprints that reflect markedly different physiological processes⁷¹. These changes are also representative of the nature and duration of insults microglia are exposed to, with strong influence by changes of the brain microenvironment – as also seen in chronic pathologies such as AD, PD or MS. The nomenclature to describe different activation states and phenotypes of microglia is far from being uniform. Nevertheless, terms like „resting” microglia have been recently updated with terms „surveilling” or „homeostatic” microglia, whereas in pathological states the old term „activated” microglia is often replaced with „primed” microglia, „microglia with altered reactivity” or „damage associated microglia (DAM)” referring to different diseases or conditions that are associated with partially distinct microglia phenotypes and responses⁷².

Accumulating data indicates that microglia are also extremely sensitive sensors to inflammatory changes that take place outside the CNS. In fact, infections, traumatic injury, metabolic disturbances, inflammatory challenges, chronic disease and systemic inflammatory conditions outside the CNS are known to be associated with altered microglial phenotypes^{27, 73, 74}, even in the absence of any obvious brain pathologies. Peripheral inflammatory challenges as often modelled by intraperitoneal or intravenous injection of bacterial cell wall components such as lipopolysaccharide (LPS) in rodents, result in major changes in microglial transcriptomic phenotypes and induce the production of various inflammatory mediators⁷³⁻⁷⁵. Importantly, inflammatory stimuli exceeding a certain threshold appear to result in epigenetic reprogramming of microglia and markedly different responses to acute challenges even months after the primary insult⁷⁶. Considering that microglia colonize the developing brain in the first trimester and microglia may live for decades in humans as discussed above, understanding microglial phenotype changes across the lifespan and their implications for the housekeeping and pathophysiological functions of microglia is of utmost importance. This is further emphasized by recent single-cell transcriptomic analyses that

identified different human microglia subsets and divergence in metabolic-, immune- and neurodegeneration-related pathways compared to non-primates¹⁴.

Housekeeping roles of microglia in the adult brain – implications for brain diseases

It has long been suggested by both experimental and clinical studies that microglia have important roles to maintain brain homeostasis. For example, loss of an important modulator of microglial activity, TGF β in the CNS disturbs microglial development after E14.5 in mice, resulting in an absence of microglia, while peripheral macrophage populations are not affected. These mice develop normally until they reach 100-120 days of age when they display motor abnormalities, progressing to paralysis and death by 23–25 weeks of age⁷⁷. Interestingly, TGF β not only suppresses activation and proliferation of microglia *in vitro*⁷⁸, but microglia are also under stringent control by TGF β 1 and other regulatory factors *in vivo*. As such, impaired TGF β signaling by deletion of the TGF β receptor, *Tgfr2*, disturbs brain homeostasis and leads to priming of microglia and altered production of inflammatory mediators in mice⁷⁹. Deficient TGF β signaling is also known to be linked with aging and facilitates the progression of neurodegenerative diseases in humans. Genetic variations of TGF β 1 increase the risk of late-onset AD⁸⁰ and cerebrovascular diseases⁸¹ among others. Similar findings exist for non-lethal CSF1R mutations, further emphasizing the importance of the CSF1-CSF1R axis in microglial biology. Patients who carry one nonfunctional copy of CSF1R develop a neurodegenerative disease known as adult-onset leukoencephalopathy with axonal spheroids and pigmented glia (ALSP), characterized by white matter degradation, dementia and motor impairment⁸². Evidence also indicates the role of deficient microglial inflammatory signaling in neurodegeneration. For example, mutations of Triggering Receptor Expressed on Myeloid cells 2 (TREM2) and DNAX activation protein 12 (DAP12), which is linked with TREM2 signaling in microglia in the CNS show strong association with a special form of frontotemporal dementia associated with cyst-like bone lesions, named Nasu-Hakola disease^{83, 84}. The available data strongly suggests that in Nasu–Hakola disease CNS damage is directly caused by microglial dysfunction⁸³⁻⁸⁶.

Despite the accumulating evidence concerning the important homeostatic roles of microglia across the lifespan, comprehensive experimental studies to modulate microglial responses in the adult brain have become available only recently. Similarly to the important developmental roles of microglia in synapse formation and elimination, neuron-to-microglia signaling appears to be also necessary for cortical synaptic remodeling postnatally in mice⁸⁷, for motor-learning-dependent synapse formation⁸⁸ or for adult neurogenesis^{89, 90} among others. Microglial transcriptomic phenotypes and states of activity also change markedly during aging in both the rodent and the human brain^{55, 91}. Therefore, it has long been assumed that

changes in the important homeostatic roles of microglia could be a major contributor to diverse age-related conditions and neurodegeneration.

Mechanisms through which inflammation, brain-immune interactions and microglial dysfunction contribute to pathology in common brain diseases

Extensive evidence exists regarding the causal and the modulatory role of immune processes in CNS injury and common brain disorders. As also seen in peripheral tissues, autoimmunity and excessive tissue inflammation can be highly damaging in the brain and the spinal cord, which is evidenced by both clinical and experimental studies on MS, Amyotrophic Lateral Sclerosis (ALS) and other conditions^{26, 92, 93}. Given the extensive available literature, autoimmune disorders are not discussed here in detail. Importantly, emerging data, with strong contribution from experimental studies demonstrate that a broad range of inflammatory mediators either produced inside or outside the CNS, as well as peripheral immune cells, CNS-resident immunocompetent myeloid cell populations and glial cells also contribute to diverse neurological conditions that have not been previously considered highly inflammatory in nature. As such, proinflammatory mediators and immune cells emerge as primary therapeutic targets in stroke, brain trauma, AD, PD and several other conditions.

Numerous studies indicate the role of IL-1, TNF and other proinflammatory mediators in neuronal hyperexcitability, seizures and epilepsy^{94, 95}. IL-1 β can also rapidly enhance focal seizure generation in brain slices⁹⁶. Reports also indicate the role of IL-1 in chronic neurodegeneration. Interestingly, misfolded proteins such as Amyloid β (A β) or phosphorylated tau (p-tau), which are considered to be major contributors to AD and other forms of neurodegeneration, act as strong inducers of IL-1 β through activating inflammasomes, complex molecular assemblies in various cell types that regulate IL-1 β release after cleavage by the enzyme, caspase-1⁹⁷. Robust data show that in experimental models of AD, neuroinflammatory processes are active contributors to disease pathophysiology, including neuronal injury, vascular inflammation and activation of glial cells, while blockade of related inflammatory pathways results in reduced neuronal loss. As such, the blockade of the NLRP3 inflammasome reduced pathology and improved cognitive outcome in APP/PS1 mice⁹⁸ and reduced tau pathology⁹⁹.

Because microglia are an important source of IL-1 β , IL-1 α , TNF α and other inflammatory mediators, whereas microglial activation parallels neuropathological changes in both experimental models of brain injury and in human post-mortem brain tissues, earlier research has implicated microglia as primary drivers of neuronal injury. However, due to the lack of appropriate tools to selectively manipulate microglia, these studies have remained largely

correlative and have yielded controversial data, showing both beneficial and detrimental roles for microglia under different conditions^{100, 101}. Microglia-mediated actions contributing to neuronal injury beyond their inflammatory mediator production have also been identified. One of the best documented examples is microglial synapse elimination that occurs under physiological conditions as part of the normal brain development program, and as a pathological process during neurodegeneration, indicated by clinical data and experimental models of AD. Because in the developing CNS microglial actions are essential to eliminate excessive synapses, disturbances in microglial function has highly detrimental consequences, as discussed above. Microglia execute these actions in a complement-mediated manner, which turned out to be also important for increased microglial synapse removal in experimental AD, contributing to neurodegeneration and impaired cognitive function. As such, blockade of the complement proteins C1q and C3, microglial C3 receptors or elimination of microglia collectively improve outcome in AD models^{102, 103}. The translational value of these observations is strengthened by the observations that complement proteins are also activated in the brains of AD patients^{104, 105}. Although the mechanisms of microglial complement-mediated removal of synapses are still not well understood, these results have indicated that fine-tuned target recognition of microglia may be impaired in different forms of brain diseases and hence, interfering with these processes may be therapeutically advantageous.

It has long been recognized that inflammatory mechanisms contribute to the formation and propagation of acute brain injury seen after brain trauma or cerebral ischemia. For example, energy failure due to the lack of oxygen and glucose supply after the cessation of blood flow is rapidly followed by a sequence of events, which is often termed as the „ischemic cascade“. The underlying pathological changes include the dysfunction of the Na⁺/K⁺-ATPase and other pumps/enzymes leading to ischaemic depolarisation and increased Ca⁺⁺ entry to the cell (excitotoxicity) via high extracellular glutamate release and stimulation of AMPA/NMDA receptors. These processes, as well as the associated production of free radicals, reactive oxygen species (ROS), activation of caspases, proapoptotic factors and lytic enzymes, mitochondrial injury, increased lactic acid production and many other pathological mechanisms are markedly influenced by glia-mediated actions (e.g. maintenance of extracellular ion balance, glutamate clearance, lactic acid metabolism, scavenging of ROS, etc.). In line with this, production of proinflammatory mediators such as IL-1 due to altered activity of astrocytes and microglia alters AMPA/NMDA receptor activation, and promotes the generation of free radicals. Inflammatory mediators may also contribute to impaired BBB function via increased production of proteases and other substances, facilitating leukocyte recruitment and entry of plasma proteins into the brain parenchyma, or platelet aggregation

in microvessels (Figure 1), which processes can act in concert to promote vascular injury, cerebral edema, and neuronal death^{27, 106, 107}.

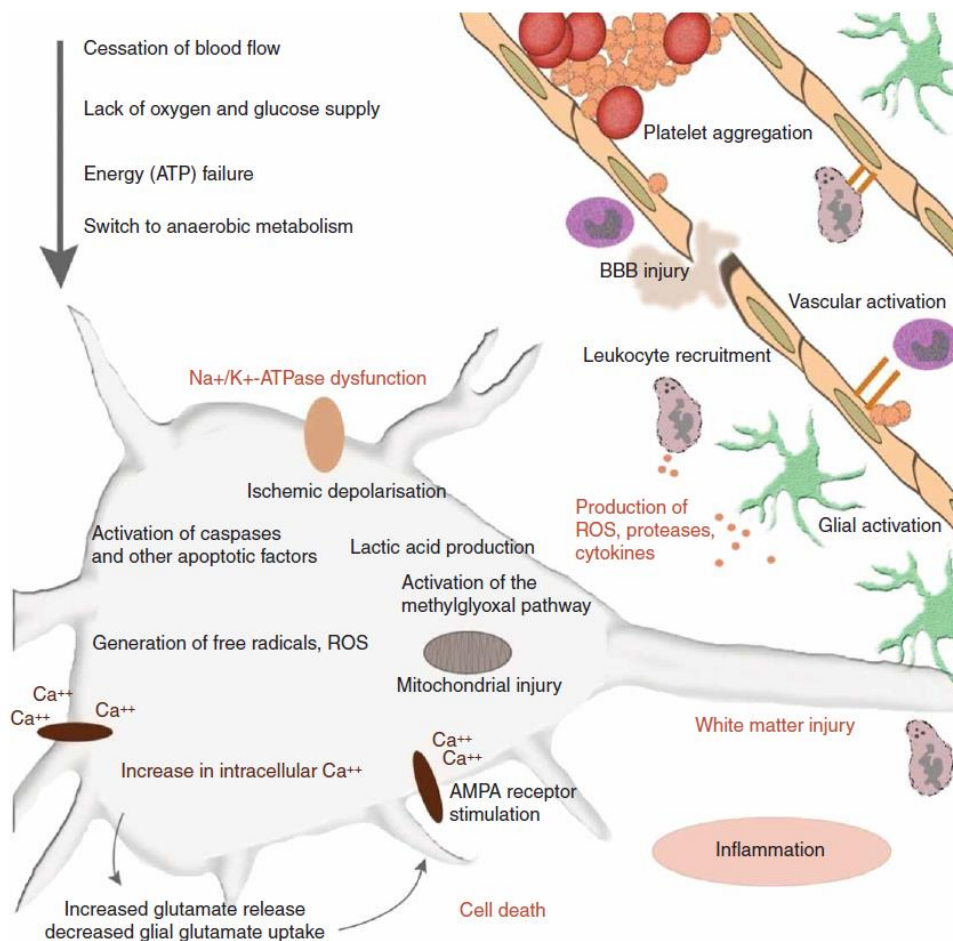


Figure 1. Schematic overview of the ischaemic cascade and related inflammatory changes. Some relevant inflammatory mechanisms with known contribution to brain injury have been depicted. See details in the text. Figure adapted from Smith et al., *Expert Opin. Investig. Drugs* (2015) 24(5)¹⁰⁶.

The contribution of inflammatory mediators to neuronal injury has been demonstrated in several experimental studies, with pioneering discoveries concerning the role of interleukin-1 (IL-1) in different forms of brain injury. IL-1, a key proinflammatory mediator produced by activated microglia and macrophages among other cells, has been shown to potentiate brain injury when injected into the brain or administered peripherally, while genetic or pharmacological blockade of IL-1 actions results in marked reduction in neuronal death following stroke, brain trauma or in different models of excitotoxicity¹⁰⁷. Among other mechanisms, IL-1 has been shown to potentiate NMDA-mediated currents, promote excitotoxic injury, augments BBB injury, results in brain endothelial activation, increases the

recruitment of leukocytes into the injured brain, promotes oxidative stress and facilitates the activation of proteases, caspases and activation of other inflammatory- and cell death-related pathways^{107, 108}. Similar data are available for TNF α , which together with IL-1 α and IL-1 β are strongly expressed in glial cells and to a lesser extent in neurons in both the rodent and the human brain after ischemic stroke¹⁰⁹.

Studies of acute brain injury have also yielded largely controversial data regarding the role of microglia to date. On the one hand, both clinical and experimental evidence indicates the important contribution of inflammatory mediators (including ROS, proteases, chemokines and cytokines) to neuronal injury, BBB breakdown, impaired recovery and poor functional outcome among others, for which microglia represent an important source in the injured brain^{27, 109, 110}. Microglia have also been suggested to promote brain injury via excessive phagocytic activity. In contrast, protective microglial actions have also been widely documented^{27, 109, 110}. As discussed in detail below, lack of appropriate tools in the past to achieve selective microglia targeting are considered to be important contributors for these controversial results. Nevertheless, it has become generally accepted that altered activity and/or dysfunction of microglia are strongly linked with diverse pathophysiological states in different neurological conditions, further emphasizing the pivotal role of these cells in health and disease.

Targeting microglia: impact on neuronal function and brain injury

Knowledge about the roles of microglia has evolved considerably alongside with the development of novel models of microglia manipulation, as supported by technological advancements in genetics, biophysical approaches and immunology. Pharmacological tools have also been developed to modulate the activity of microglia and other macrophages. For example, minocycline, a tetracycline antibiotic has been shown to dampen the production of microglial inflammatory mediators, to alter microglial activity and to improve outcome in experimental models of stroke, neonatal hypoxic-ischemia, depressive-like behavior or retinal degeneration¹¹¹⁻¹¹⁵. However, minocycline is known to act on different myeloid cell populations in addition to microglia and has broad anti-inflammatory properties¹¹⁶, therefore the exact neuroprotective role of microglia modulation by minocycline in these studies remains unclear.

Genetic models of microglia targeting have been primarily used to understand how microglial actions influence given mechanisms of neuronal activity or injury. The interactions between microglia and neurons are widely documented^{100, 117}. Along this line, it has been revealed that microglia sense various substances indicative of changes in neuronal activity, including changes in extracellular ion levels (K⁺, Cl⁻), glutamate and other neurotransmitters, purinergic

metabolites (ATP, ADP, adenosine) and others, which is also indicated by the large number of neurotransmitter receptors and ion channels expressed by microglia⁶¹. For example, studies using genetic deletion of purinergic receptors (P2X7, P2Y12, etc)¹⁰⁰ have implicated microglial mechanisms into changes in neuronal responses or disease outcome. It is important to note that only recent studies have provided conditional deletion of microglial gene products using more or less microglia-specific promoters^{118, 119} and direct versus indirect microglia-neuron interactions were not discriminated in most studies. In addition, research to date has primarily focused on microglia-neuron interactions at synapses⁴⁹. Beyond the use of genetic deletion to study the effect of impaired microglial synapse elimination during CNS development or CNS disease (e.g. C1q KO, C3 KO, CR3 KO mice), some fundamental molecular mechanisms have also been discovered through which microglia shape neuronal responses and fate. In this line of studies, one of the first important milestones concern the generation of the CX3CR1 KO mouse line by Steffen Jung and his colleagues, which has been subject to several studies of brain injury and neurodegeneration¹²⁰. CX3CR1 (fractalkine receptor) is abundantly expressed by microglia, which recognizes membrane bound fractalkine in neurons. Both the absence of CX3CR1 and fractalkine have been shown to alter microglial phenotypes and microglia-neuron interactions markedly both in developing neuronal networks and in adulthood¹²¹. Similarly complex and controversial findings are reported in mice with impaired CD200-CD200R interactions, another important signaling pathway for microglia-neuron interactions¹²².

In parallel with the increasing demand to manipulate microglial actions more selectively, some really insightful approaches have been developed. While many of these models made the disease-related roles of microglia even more enigmatic and complex, they turned out to be quite useful for the understanding of key aspects of microglial biology including the self-renewing nature of adult microglia, the impact of the brain microenvironment on microglial phenotypes or the feasibility of colonization of the disturbed microglial niche by exogenous myeloid cell populations. Bone marrow chimeric studies had suggested that microglial cells may be replaced by blood-borne myeloid cells, which is even more pronounced in case BBB injury or substantial neuronal death occurs¹²³. Later parabiosis studies (i.e. those using mice with shared circulation) have refined this view and showed that local self-renewal can sustain CNS microglia maintenance and function throughout adult life and infiltrating monocytes do not contribute to the microglia pool in large numbers^{124, 125}. In fact, brain irradiation and intravenous administration of cells for bone marrow transplantation turned out to disturb BBB integrity and cell recruitment into the CNS^{124, 125}. These observations have been refined further by studies that investigated the effects of genetic CSF1R deletion in rodents showing that disturbances in microglial niche may enable engraftment of the CNS by exogenous

myeloid cells. As $CSF1R^{-/-}$ mice lack microglia and macrophages, injected myeloid cells extensively engraft in the brain parenchyma without conditioning irradiation or chemotherapy. While haematopoietic stem cell (HSC)-derived macrophages attain a microglia-like identity in the CNS, microglia preserve their transcriptomic identity, while brain signals emerge as strong inducers of homeostatic gene expression in microglia¹²⁶. Engrafted parenchymal brain macrophages differ from microglia in transcriptome, chromatin landscape and response to inflammatory challenges¹²⁷. Microglia transplantation studies have also demonstrated that human iPSC-derived mature microglia can functionally integrate in the chimeric mouse brain and retain their identity¹²⁸.

Genetic models to deplete microglia or to reduce microglial numbers by blocking microglial proliferation have also been developed. Administration of ganciclovir to CD11b-HSVTK transgenic mice, which express herpes simplex thymidine kinase in macrophages and microglia, repressed the development of microglia activation in the facial nucleus upon axotomy and experimental autoimmune encephalomyelitis. Complete microglia depletion, however, was not possible by using this approach and haematopoietic toxicity seen in this model required the transfer of wild-type bone marrow¹²⁹. Another interesting approach to manipulate microglia or to eliminate microglia from the brain was the generation of tamoxifen-inducible $CX3CR1^{CreER}$ mice. When crossed with cre-dependent Rosa26-stop-DTR mice, microglial expression of the diphtheria toxin receptor (DTR) allows depletion of microglia after diphtheria toxin (DT) administration. This model not only achieved an over 90% depletion of microglia within 1-3 days after DT treatment, but surprisingly, spontaneous repopulation of microglia also took place 1-2 weeks thereafter, allowing the assessment of changes in microglia dynamics and its impact on outcome in different models of brain diseases⁸⁸. Some confounding effects were, however, observed in this model. Although disruption of the BBB was not observed, DT-mediated elimination of microglia paralleled astrocytosis and markedly increased in brain cytokine and chemokine levels. Not surprisingly, alongside with microglial proliferation, recruitment of $Ly6C^{hi}$ monocytes substantially contribute to repopulation of the empty microglial niche in this model¹³⁰.

Strains of $CX3CR1^{CreER}$ mice have also become essential tools for conditional deletion of different genes from microglia, leading to a better understanding of microglia-mediated actions in the brain^{88, 131, 132}. Recently, transcriptomic studies have revealed a refined group of transcripts considered to be largely microglia-specific (such as HexB), leading to the development of additional cre-driver lines allowing improved microglia-specific manipulation in future studies^{118, 119}.

Discovery of pharmacological CSF1R blockade emerged unexpectedly as a powerful tool to eliminate microglia from the brain without major inflammatory side effects and depletion of peripheral myeloid cell populations. Because expression of the CSF1 gene is elevated in most tenosynovial giant-cell tumors, Plexxikon, an American drug discovery company developed a family of CSF1R inhibitors, including PLX3397, which turned out to be effective in prolonged regression in tumor volume in most patients¹³³. Surprisingly, when administered to mice over a period of 1-3 weeks, PLX compounds were found to have no visible impact on peripheral myeloid cell populations, but were remarkably effective to eliminate microglia from the CNS, which rely on constant CSF1R signaling for their survival, without apparent major side effects. In fact, microglia depletion by PLX3397 or PLX5622 in healthy mice did not cause any obvious inflammatory changes, BBB disturbance or neuronal injury, and mice remained apparently healthy even if microglia were absent for more than two months. In addition, cessation of CSF1R inhibition was found to induce microglial repopulation within two weeks¹³⁴. Collectively, beyond the different genetic tools developed over the last two decades, pharmacological microglia manipulation have also emerged in parallel as a powerful alternative to study microglial function in health and disease.

Impact of systemic inflammation on central inflammatory actions, microglial states and brain injury

Until recently, the vast majority of experimental studies investigating microglia-neuron interactions and mechanisms of brain injury have used young rodents with no additional comorbidities. However, evidence from both clinical and experimental studies have shown that systemic inflammatory mechanisms are particularly important contributors to determine microglial states with remarkable impact on different forms of brain injury. Nevertheless, the underlying mechanisms have remained vaguely defined. Of note, even a single, acute systemic inflammatory stimulus results in marked, long-lasting changes in microglial phenotypes and inflammatory responses via epigenetic reprogramming⁷⁶. While the contribution of systemic inflammation-related alterations of microglial phenotypes to disease pathophysiology has been strongly suggested, these processes remained difficult to study in part, because systemic inflammatory changes modulate the CNS microenvironment in several different ways. These include alterations in microvessels, BBB function, CSF circulation, as well as changes in immune cells, astroglial and neuronal responses among many others. Emerging data indicates that ageing per se results in altered regulation of immune processes, an elevated systemic inflammatory burden, and markedly altered microglial responses^{9-11, 27}. Alongside with this, the rapidly growing burden of chronic disease in almost all age groups worldwide highlights the pivotal role of inflammation. It is now widely accepted that chronic conditions including atherosclerosis, hyperlipidemia, hypertension,

diabetes as well as different forms of infection are not merely key risk factors for most neurological disorders, but are collectively characterized by elevated systemic inflammatory burden. Such conditions are associated with broad changes in different vascular beds (including those in the CNS), increased expression of vascular- and cell adhesion molecules, altered leukocyte responses, altered pro- and anticoagulation balance and compromised BBB function, while changes in microglial phenotypes are also apparent^{9-11, 27}. As such, chronic inflammation emerges as an important contributor to ageing and different forms of neurodegeneration. For example, a systematic meta-analysis of 170 studies has revealed a strong association of high-sensitivity C reactive protein (CRP), interleukin-6, and other inflammatory markers with disease heterogeneity and severity in both plasma and CSF samples of patients with AD or mild cognitive impairment (MCI), indicating that these conditions are accompanied by inflammatory responses in both the periphery and CSF¹³⁵. In line with this, human PET studies also demonstrated significantly increased inflammation and altered microglial states in different forms of neuropathologies^{136, 137}, which is also reflected by the results of transcriptomic studies in both rodents and humans^{67, 75}.

The effects of systemic inflammation on brain inflammation and neuronal death have also been studied in different forms of acute brain injury, including clinical and experimental studies of ischemic stroke, brain hemorrhage or brain trauma. Results from these studies indicate that systemic inflammation may contribute to poor outcome after acute brain injury via several potential mechanisms including changes in production, mobilisation and activity of immune cells (T lymphocytes, B lymphocytes, granulocytes, monocytes, etc), altered production of acute phase proteins in the liver, altered autonomic nervous system- and neuroendocrine regulation, changes in the activity of astrocytes, microglia, increases in microvascular coagulation, BBB breakdown and other processes collectively shaping vascular and neuronal injury as well as regeneration after the acute phase of the disease^{9-11, 27}. In particular, experimental stroke models have provided remarkable insight into some of the main molecular mechanisms through which complex inflammatory actions influence brain injury and overall outcome (Figure 2).

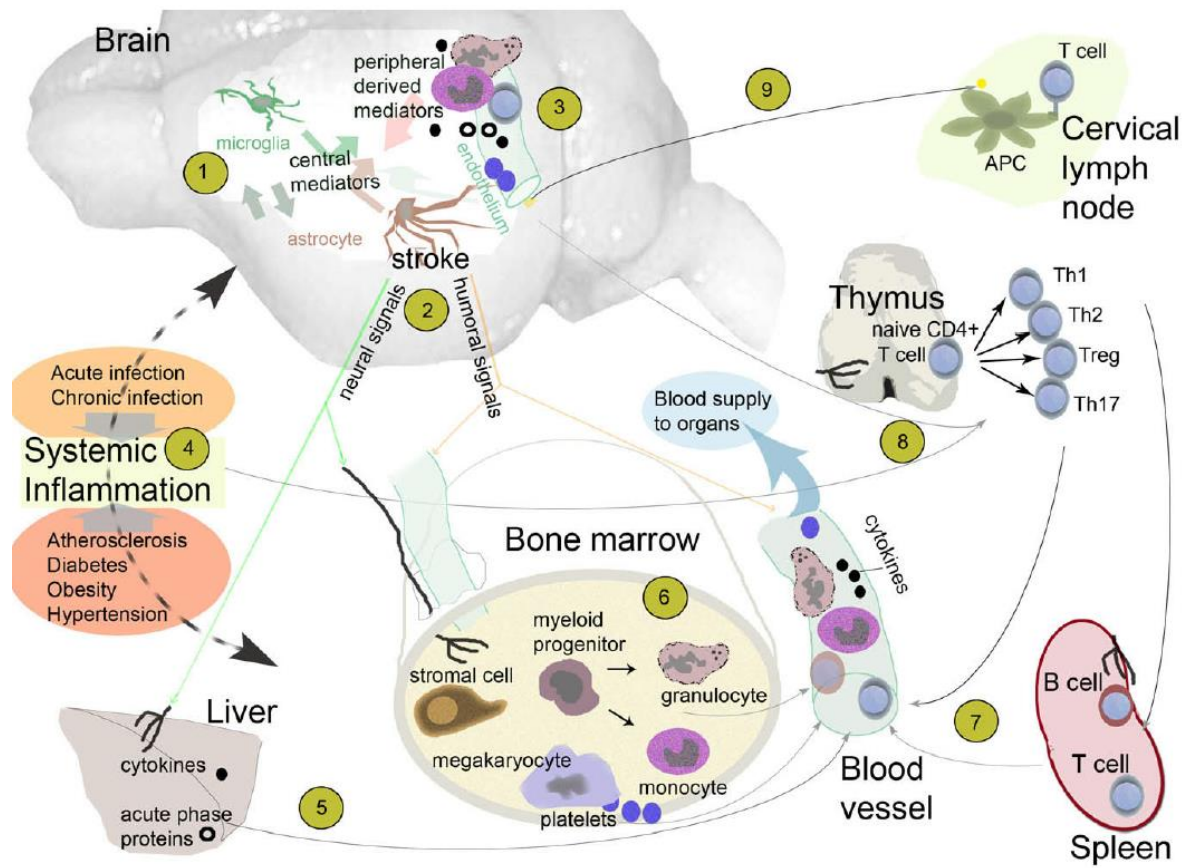


Figure 2. Brain-peripheral communication in stroke. Numbers represent different processes which may take place simultaneously after stroke but do not indicate timing. (1) Neurons, glia and cerebral endothelial cells respond to ischaemic stimuli by releasing numerous active mediators. (2) The brain signals to peripheral organs through humoral and neural routes. (3) Blood-derived mediators and infiltrating leukocytes and platelets contribute to the ischaemic processes early (breakdown of blood–brain barrier, formation of oedema, neuronal death) or late (vasculogenesis, neurogenesis) after stroke. Acute-phase proteins, chemokines and cytokines can reach the ischaemic territory directly before and after blood–brain barrier damage and modify the expression or release of centrally expressed inflammatory mediators. (4) Infectious diseases or known co-morbidities such as atherosclerosis, diabetes or obesity can lead to systemic inflammation, affecting several organs in the body. Chronic inflammation in the periphery can upregulate adhesion molecules on cerebral blood vessels and may augment vascular activation during a subsequent ischaemic event. (5) Stroke induces production and release of cytokines, chemokines and acute-phase proteins from the liver and from other organs. (6 and 7) Granulocytes, monocytes, lymphocytes and other inflammatory cells are released from immune organs such as the bone marrow or the spleen. A population of these cells migrates into the brain and contributes to the formation of ischaemic damage. (8) Acute and chronic inflammatory challenges (type of antigens and cytokine environment) in the periphery prior to stroke can determine the dominance of different T helper cell sub-types and the ratio of active leukocytes and

pro-inflammatory/anti-inflammatory cytokines. (9) Brain-derived antigens can be processed and presented in draining lymph nodes prior to (due to CNS infections, TIA, aging) and after cerebral ischaemia. This may have an effect on the acute phase of ischaemic damage or later on, in a form of neurodegenerative/autoimmune diseases of the CNS. Figure adapted from A. Denes et al. / *Brain, Behavior, and Immunity* 24 (2010) 708–723²⁷.

However, the exact mechanisms through which systemic inflammatory changes modulate or drive given pathologies following acute brain injury have remained vaguely defined. It is likely that experimental studies of brain inflammation and injury underestimate the impact of inflammatory mechanisms and in particular, the effect of microglial dysfunction on neuronal responses and fate considering the heterogeneity of the human population including genetics, the broad range of apparent comorbidities and the impact of age-related changes. It is also assumed that systemic inflammatory changes may act in part via modulating microglial actions and phenotypes. Collectively, understanding microglial actions and their role in health and disease appears to be important to identify key mechanisms of brain diseases and to find novel therapeutic targets.

Summary of research and specific aims

Since the discovery of microglia, these cells have been linked with pathophysiological changes in different disease states, which has also been supported by later observations concerning inflammation-mediated injury in the CNS. Because microglia are an important source of inflammatory mediators, earlier studies linking changes in microglial phenotypes with diverse neuropathologies have strengthened the view of their detrimental roles. However, in the absence of appropriate research tools to selectively target microglia, their contribution to CNS injury has remained highly controversial. Therefore, the key aim for my research in the last 20 years has been to understand the mechanisms through which inflammation contributes to pathological processes in the brain, by using the constantly improving methodologies in neuroscience, immunology, genetics, molecular biology, imaging and other related fields of science. Our research could benefit from some of the latest research tools to manipulate inflammatory pathways and microglial actions in different models of brain injury. For appropriate translation of research findings into possible clinical benefit, we have devoted increasing attention in recent years to also study microglia in the human brain.

First, I will discuss some of the mechanisms through which microglia may contribute to, or alter inflammation-related brain injury (**Chapter 1**). Then, I will elaborate upon the effects of systemic inflammation on microglial responses and brain injury (**Chapter 2**). Finally, I will detail our recent findings concerning the molecular mechanisms that govern fine-tuned microglia-neuron interactions, which appear to be critical contributors to neuronal health and neuronal injury (**Chapter 3**). I will intentionally devote slightly more room to discuss Chapter 3, as this part contains our latest results with some of the most advanced tools and approaches, but felt important to also include some related earlier studies to put these recent discoveries into a broader context.

- **Chapter 1: Inflammation and microglial actions modulate injury in the brain**
- **Chapter 2: Systemic inflammation promotes CNS inflammation, alters microglial function and augments brain injury**
- **Chapter 3: The role of compartment-specific microglia-neuron interactions in shaping neuronal activity and neuronal injury**

Results

Chapter 1: Inflammation and microglial actions modulate injury in the brain

This chapter is based on the following original publications:

1. Denes, A., et al., *J Cereb Blood Flow Metab*, 2007 (cited as ref. 69) ^{#,*}
2. Luheshi, N.M., et al., *J Neuroinflammation*, 2011 (cited as ref. 138) ^{#,*}
3. Savage, C.D., et al., *Front Immunol*, 2012 (cited as ref. 140) [#]
4. Denes, A., et al., *Dis Model Mech*, 2013 (cited as ref. 141) [#]
5. Denes, A., et al., *Proc Natl Acad Sci U S A*, 2015 (cited as ref. 142) ^{#,*}
6. Wong, R., et al., *Brain Behav Immun*, 2019 (cited as ref. 143) ^{#,*}
7. Allen, C., et al., *J Immunol*, 2012 (cited as ref. 144) ^{*}
8. Toth, K., et al., *PLoS Biol*, 2022 (cited as ref. 148) ^{#,*}

Author's contribution: [#]First/last or joint first/last author; ^{*}Corresponding author

While the contribution of immune cells and proinflammatory mediators to brain injury has been investigated in previous studies, the role of specific disease mechanisms including the contribution of microglia to these processes turned out to be highly controversial. In particular, whether microglial actions precede those of blood-borne macrophages after acute brain injury, had remained vaguely explored. Using *in situ* fluorescent labelling of circulating leukocytes by carboxyfluorescein succinimidyl ester (CFSE) and magnetic resonance imaging (MRI)-based tracking of peripheral macrophages labelled with iron oxide particles, we revealed that microglial response to brain injury induced by cerebral ischemia in mice precedes substantial invasion of peripheral macrophages. This was apparent both at sites of the primary injury (displaying progressive BBB breakdown) and in peri-infarct tissues (displaying increased microglial reactivity, but mostly sustained BBB function) in the striatum and the cerebral cortex. Microglial responses were characterized by rapid phenotypic transformation within a few hours upon brain injury, including altered process morphology and altered expression of activation markers (Iba1, CD34) and proliferation 24h onwards, which resulted in increased microglial cell numbers by 72h post-stroke. Importantly, we have found that microglial cell death also takes place in the acute phase of injury after stroke, while proliferating microglia phagocytosed invading neutrophil granulocytes as a possible first line of defense against harmful immune cell-mediated effects⁶⁹.

We next aimed to determine the earliest inflammatory actions, which could drive cellular responses to cerebral ischemia, and influence the evolution of brain injury. Focusing on the key proinflammatory mediator, IL-1, which is produced by microglia among other cells, we have assessed the production of the two isoforms, IL-1 α and IL-1 β at both mRNA and protein levels (with qPCR and immunofluorescence, respectively). As early as 4h after cerebral

ischemia, microglial IL-1 α production was detectable in the core of the infarct and occasionally in the peri-infarct tissue, whereas microglial IL-1 β expression was somewhat delayed, reaching its maximum levels around 24h post-injury. Microglial reactivity changes and IL-1 expression were localized to areas of primary injury¹³⁸. These results collectively suggested that the response of brain-resident microglia predominates in the injured brain tissue over blood-borne cells and highlighted injury-related production of proinflammatory mediators as a potential contributor to disease pathophysiology.

We next studied the possible triggers of injury-related stimulation of microglial reactivity and production of proinflammatory mediators. Damage associated molecular patterns (DAMPs) released from injured cells and tissues have been considered as primary candidates to trigger microglial activation. Supporting this, DAMPs such as ATP or DNA have been shown to alter microglial phenotypes and induce expression of IL-1 in both *in vivo* and *ex vivo* studies^{62, 64, 97, 106, 107}. Our results showing that between 4h and 24h after acute brain injury *in vivo*, microglia producing IL-1 are primarily localised to areas of focal neuronal loss and BBB injury in addition to penumbral tissues¹³⁸ where evolution of brain injury occurs, suggested the release of DAMPs. We also observed microglial injury and cell death at these sites, in parallel with the nuclear retention of IL-1 α in microglia, a possible mechanism to prevent release of this highly proinflammatory cytokine to the injured tissue^{69, 138}.

Production of both IL-1 isoforms can be induced by various DAMPs, and the release of IL-1 β relies on the assembly of intracellular multiprotein complexes, named inflammasomes. Release of IL-1 β typically requires two stimuli, first priming by a pathogen-associated molecular pattern (PAMP) such as LPS, followed by a DAMP such as ATP, DNA, serum proteins and other injury-related molecules to induce activation of the enzyme caspase 1 and cleavage of pro-IL-1 β into its secreted, mature form¹³⁹. In a series of *ex vivo* studies using mixed glial cultures, we found that different DAMPs (ATP, MSU or CPPD) stimulate an inflammatory response in microglia and astrocytes even in the absence of priming stimulus, as indicated by the production of cytokines and chemokines including IL-6 and CXCL1. Release of the lysosomal protease, cathepsin B, was also observed. Production of these inflammatory mediators was found to rely on IL-1 production, which was evidenced by lower levels of IL-6 and CXCL1 produced *in vivo* in mice deficient to both IL-1 isoforms (IL-1 $\alpha\beta$ KO mice)¹⁴⁰. Interestingly, we also observed that serum amyloid A (SAA), an acute phase protein, can act as a priming stimulus in glial cells, resulting in the release of IL-1 β after stimulation with ATP, comparable to that induced by the PAMP, LPS. These observations suggest that serum proteins reaching the brain parenchyma upon BBB injury together with DAMPs released from injured cells after cerebral ischemia could trigger microglial activation, production of both IL-1 isoforms and release of IL-1 β *in vivo*¹⁴⁰.

Because the pivotal role of IL-1 in different forms of brain injury has been previously established¹⁰⁷, we made efforts to understand the different cellular sources of IL-1 in the brain tissue and the mechanisms of IL-1 production in response to acute injury *in vivo*, with the aim to understand the possible contribution of microglia to these processes. To investigate the contribution of blood cell-derived vs central IL-1 sources, we performed bone marrow transplantation using WT and IL-1 $\alpha\beta$ KO mice. We found that elimination of IL-1 $\alpha\beta$ from haematopoietic cells (WT mice transplanted with IL-1 $\alpha\beta$ KO bone marrow) and the absence of IL-1 $\alpha\beta$ from the brain while present in blood-borne cells (IL-1 $\alpha\beta$ KO mice transplanted with WT bone marrow) both resulted in significantly reduced infarct size and BBB injury. Of note, mice lacking IL-1 $\alpha\beta$ from both compartments (IL-1 $\alpha\beta$ KO mice transplanted with IL-1 $\alpha\beta$ KO bone marrow) showed the highest level of protection compared to WT mice (WT mice transplanted with WT bone marrow)¹⁴¹. This study has also demonstrated the recruitment of blood-borne, donor-derived leukocytes (identified by GFP expression) to the brain 24 hours after stroke, which was most pronounced in the meninges and in large cortical blood vessels. The absence of haematopoietic IL-1 resulted in reduced circulating IL-6 levels after stroke and impaired release of granulocytes into the circulation.

To investigate how inflammasome-mediated actions contribute to the mechanisms of IL-1 production after acute brain injury, we induced experimental stroke in mice deficient for ASC, a common adaptor protein for the assembly of several inflammasomes. ASC KO mice displayed significantly reduced brain injury after stroke, alongside with dampened microglial reactivity in the affected brain areas¹⁴². The absence of ASC also resulted in reduced recruitment of CD45-positive leukocytes to the injured brain tissue, and dampened vascular inflammation as indicated by reduced binding of fluorescently labelled tomato lectin to cortical and striatal blood vessels. When further studying the mechanisms involved, we learnt that mice deficient for NLRC4 and AIM2 inflammasomes show similarly reduced brain injury and improved neurological outcome, however, this was not observed in NLRP3 KO animals. Because the AIM2 inflammasome recognizes DNA, this suggested that DNA released from injured cells in the brain could trigger inflammation and production of IL-1 β ¹⁴². Bacterial flagellin, the sole known ligand of NLRC4 may suggest the contribution of the gut microbiota to acute brain injury in these studies, but as it has turned out in the case of other inflammasomes, other endogenous ligands for NLRC4 may exist that remain to be identified⁹⁷. Nevertheless, these studies have shown that interfering with inflammasome activation could be a potentially effective therapeutic option to prevent IL-1 production and limit the evolution of brain injury after stroke.

We have also made efforts to identify specific sites of IL-1 actions that may contribute to brain injury. To this end, we have selectively eliminated the main signaling receptor, IL-1R1,

from the cerebrovascular endothelium using IL-1R1^{fl/fl} Δ Slco1c1 mice that were generated by crossing IL-1R1^{fl/fl} mice (exon 5 of the Il1r1 gene flanked with loxP sites) with tamoxifen-inducible, Slco1c1 Cre^{ERT2} mice (expressing Cre recombinase under the promoter of the thyroxine transporter). We found that vascular inflammation and recruitment of neutrophil granulocytes was reduced in these mice compared to control animals after experimental stroke, which was associated with reduced BBB injury, infarct size and improved neurological outcome¹⁴³. Neuronal IL-1R1 deletion (using IL-1R1^{fl/fl} Δ Nestin mice), and specifically, deletion from cholinergic neurons (using IL-1R1^{fl/fl} Δ ChAT mice) also turned out to result in reduced brain injury after stroke¹⁴³, without affecting vascular inflammation and granulocyte recruitment. Interestingly, microglial process coverage of neurons in the boundary zone of the infarct was increased in the absence of neuronal IL-1R1, which process may be explained by our observations presented in *Chapter 3* (Cserép et al., Science 2020). We also observed that the absence of brain endothelial IL-1R1, but not neuronal IL-1R1, resulted in the reduction of early perfusion deficits after stroke as assessed by *in vivo* laser speckle contrast imaging (LSCI). Collectively, these results suggested that IL-1 have both neuronal and vascular actions through which it can contribute to potentially harmful inflammatory responses and perfusion deficits in the brain.

What cell-specific mechanisms may link IL-1 activity and microglial responses to brain injury? In addition to its direct actions on neurons, IL-1 promotes vascular inflammation, BBB injury and also acts on leukocytes and other cell types to shape the production of a broad range of inflammatory mediators. One particular mechanism we have studied concerned the role of IL-1 to recruit potentially injury-promoting leukocyte subsets into the injured brain. The role of microglia has also turned out to be controversial in this context. While microglia are an important source of IL-1 in the injured brain (a potentially inflammation-promoting role), we have also shown that microglia act as a first line of defense to phagocytose infiltrating blood-borne cells, including neutrophil granulocytes, which are among the first cell types recruited into the brain after acute injury⁶⁹. As discussed above, mice deficient for IL-1 $\alpha\beta$ displayed reduced production of CXCL1, a potent chemokine for neutrophil recruitment¹⁴⁰ and impaired granulocyte mobilisation into the circulation was also impaired in mice lacking haematopoietic IL-1 $\alpha\beta$ ¹⁴¹, suggesting that IL-1 may facilitate neutrophil inflammatory responses in the CNS. This has been experimentally addressed in a separate study, showing that neutrophils transmigrating IL-1-stimulated endothelial cells (modelling the process that takes place during central neutrophil recruitment upon brain injury) become highly neurotoxic by producing proteases and de-condensed DNA, known as neutrophil extracellular traps (NETs)¹⁴⁴. We revealed that the neurotoxic phenotype of transmigrated neutrophils is due to the release of different proteases. A mixture of inhibitors against cathepsin-G, neutrophil

elastase, proteinase-3 and MMP-9, but not these inhibitors individually, was found to protect against neurotoxicity, while the treatment did not affect neutrophil transmigration across IL-1-activated brain endothelium. In this study, we have also demonstrated that neutrophils, which are recruited to the brain, accumulate in inflamed cerebral vessels or transmigrate the endothelial monolayer after experimental stroke *in vivo* are associated with extracellular proteases and a loss of intracellular decondensed DNA. Thus, our results suggested that microglial phagocytosis of recruited neutrophils in the brain is likely to act as an important defense mechanism, which may prevent accumulation of potentially neurotoxic immune cells that could contribute to neuronal and vascular injury. Several years after this research was published, in collaborative studies with the leadership of the laboratory of Prof. Anna Planas we confirmed that microglial cell death takes place in the acute phase of injury after stroke (showed initially in Denes et al., JCBFM 2007)⁶⁹ and that elimination of microglia indeed leads to increased neutrophil numbers in the brain¹⁴⁵. Thus, while IL-1 is produced by microglia and also by haematopoietic cells to drive the recruitment of potentially neurotoxic immune cells into the injured brain, microglia appear to be primary gatekeepers to prevent excessive neutrophil recruitment and injury to neurons.

Our recent studies also shed light on the importance of microglial functional changes in alterations of microglia-derived IL-1 production and the effects of this on inflammation and neuronal death after brain injury. To our surprise, we found that the $\text{Na}^+\text{-K}^+\text{-2Cl}^-$ cotransporter, NKCC1, which received a steeply increasing amount of attention in research on CNS diseases^{146, 147}, is highly expressed in microglia. To investigate the role of microglial NKCC1 in functional studies, we have generated a novel transgenic mouse line by crossing NKCC1^{fl/fl} (exon 8 of the Slc12a2 gene was flanked with lox P sites) and Cx3CR1-Cre^{ERT2} mice. We found that NKCC1 shapes both baseline and reactive microglia morphology, process recruitment to the site of injury, and adaptation to changes in cellular volume in a cell-autonomous manner via regulating membrane conductance¹⁴⁸. Microglial NKCC1 deficiency also resulted in NLRP3 inflammasome priming and increased production of IL-1 β , which was associated with increased brain injury and impaired functional outcome after experimental stroke. Furthermore, we found markedly different central and systemic effects of the specific NKCC1 blocker, bumetanide on the production of inflammatory mediators in the brain: systemic bumetanide reduced, while central bumetanide potentiated the production of the inflammatory mediators IL-1 β and G-CSF. These results thus suggest a key role for microglia (and microglial IL-1) in central NKCC1 actions¹⁴⁸.

Collectively, these studies highlight the importance of understanding how certain aspects of complex inflammation-related disease mechanisms may shape brain injury under different conditions and how these are influenced by the regulation of inflammation.

Chapter 2: Systemic inflammation promotes CNS inflammation, alters microglial function and augments brain injury

This chapter is based on the following original publications:

1. Denes, A., et al., *J Neurosci*, 2010 (cited as ref. 152) [#]
2. Denes, A., et al., *J Neuroinflammation* (cited as ref. 153) ^{#,*}
3. Denes, A., et al., *Ann Neurol*, 2014 (cited as ref. 154) ^{#,*}
4. Drake, C., et al., *Brain Behav Immun*, 2011 (cited as ref. 157) ⁺
5. Denes, A., et al., *J Am Heart Assoc*, 2012 (cited as ref. 158) [#]
6. Denes, A., et al., *J Cereb Blood Flow Metab*, 2011 (cited as ref. 162) ^{*}
7. Houlden, A., et al., *Brain Behav Immun*, 2016 (cited as ref. 163) ^{#,*}
8. Szigeti, K., et al., *J Cereb Blood Flow Metab*, 2015 (cited as ref. 164) ^{#,*}
9. Helyes, Z., et al., *Proc Natl Acad Sci U S A*, 2019 (cited as ref. 165) ^{#,*}

Author's contribution: [#]First/last or joint first/last author; ^{*}Corresponding author; ⁺Co-author

Chronic diseases are key risk factors for common brain disorders and are considered to be states with constantly increased systemic inflammatory burden. To this end, we aimed to understand how systemic inflammation alters central inflammatory processes and microglial actions, by developing translationally more relevant experimental models and approaches. In pioneering studies, systemic inflammation induced by administration of IL-1 or bacterial LPS was shown to result in increased brain injury after experimental stroke, partially via neutrophil-derived mechanisms¹⁴⁹.

To overcome the problems associated with inducing acute systemic inflammation with high doses of proinflammatory mediators present for short, defined periods, we performed chronic immunopolarization via inducing infection by a nematode, *Trichuris muris* (*T. muris*) prior to experimental stroke. This model allowed us to study the effect of different immune states on the evolution of acute brain injury, by using the same pathogen system: high doses of infection by this gut parasite induces a typical, T helper 2 (Th2)-polarized anti-parasitic immune response, while low doses of infection result in Th1-biased immune response and chronic inflammation due to the inability of the immune system to effectively clear the parasite on time^{150, 151}.

Using this approach, we showed that chronic Th1-biased inflammation (but not Th2-type immunopolarization) drives larger BBB injury and increased neuronal death in response to experimental stroke. To investigate the possible mechanisms involved, multiplex cytokine and chemokine measurements by cytometric bead array have been performed. We found that preceding chronic infection not only induces elevated inflammatory burden that is apparent in the mesenteric lymph nodes, the liver or the spleen, but acute brain injury-induced increases in circulating MCP-1, CXCL1 (KC) and CCL5 (RANTES) levels were

potentiated by preceding chronic infection within 2-3 hours. This was associated with delayed increases in CXCL1, IL-6, G-CSF and RANTES levels in the brain tissue as seen 48h after stroke. These inflammatory mediators are known to be markedly induced by IL-1. Selective blockade of RANTES by a specific neutralizing antibody reversed systemic inflammation-induced increases in brain injury, suggesting a functional role for this mediator¹⁵². In this study, chronic inflammation was also found to potentiate the production of leukocyte-derived proteases, namely MMP-9 in a RANTES-dependent manner, and increased platelet aggregation in brain microvessels, mechanisms, through which systemic inflammation could potentiate brain injury. Importantly, microglial phenotypes were also altered by chronic immunopolarization after stroke, and increased microglial RANTES production was observed within the territory of the infarct¹⁵².

In a subsequent study, we used two independent approaches to trigger systemic inflammation prior to experimental stroke: intraperitoneal LPS treatment or induction of anaphylaxis after sensitisation with ovalbumin. We found that microglial phenotypes are altered by systemic inflammation, which was associated with higher levels of microglial IL-1 production, increased leukocyte recruitment and more severe BBB injury¹⁵³. Both types of systemic inflammatory stimuli substantially increased brain oedema and mortality when preceding experimental stroke. Interestingly, the detrimental effects of systemic inflammation on BBB injury and brain oedema was still present when infarct size was effectively reduced by hypothermia in separate experiments, suggesting that inflammatory processes may contribute to poor outcome via mechanisms that are partially distinct from those mediating the primary cellular injury after cerebral ischemia and hence cannot be uniformly targeted¹⁵³.

The above results suggested that elevated systemic inflammatory burden may be associated with partially similar inflammatory processes in the brain during infection by different pathogens. In fact, infections (both as preceding infections and those acquired in the hospital) not only increase the risk of stroke substantially, but also contribute to poor outcome of patients¹⁰⁶. Thus, we have studied the mechanisms through which infection-induced systemic inflammation alters brain inflammation and injury after stroke. To this end, repeated intranasal inoculation of a human *Streptococcus pneumoniae* (*S. pneumoniae*) strain was performed in mice, leading to localized, subchronic, and lung-restricted infection. Infection resulted in systemic inflammation (including elevated RANTES levels in the liver) and was sufficient to drive vascular inflammation and increased microglial CD11b levels in the brain, prior to any experimentally induced injury. After the induction of experimental stroke, elevated microglial IL-1 production, increased granulocyte recruitment, platelet aggregation, as well as increased BBB injury and neuronal death were found in infected mice compared to uninfected controls. Similar infection-related effects were observed in both lean

and obese/atherosclerotic Corpulent rats. The detrimental effects of preceding *S. pneumoniae* infection were largely reversed by blockade of IL-1 actions by IL-1Ra or by blocking platelet-endothelial interactions using a selective anti-GPIIb/IIIa Fab fragment¹⁵⁴. Supporting these observations, in collaborative studies we have shown that platelet-derived IL-1 may promote cerebrovascular inflammation¹⁵⁵, in part, via interactions with the lectin complement pathway¹⁵⁶.

Proinflammatory mediators have diverse actions on the vasculature and through these actions they have also been assumed to promote atherogenesis. In fact, we found that *S. pneumoniae* infection augmented vascular pathology in different vascular beds, including the brain and the heart, resulting in increased number of plaques in the aorta of atherosclerosis-prone mice¹⁵⁴. Remarkably, we also found that systemic inflammation induced by an atherogenic diet parallels profoundly altered microglial phenotypes in the brain¹⁵⁷ similarly to that seen after different models of infection^{152, 154}. In another study, we showed that vascular inflammation and microglial alterations in atherogenic mice were largely reversed by blockade of IL-1 using IL-1R1 KO mice. However, vascular activation, but not microglial reactivity was reversed by a specific neutralizing anti-IL-1 β antibody¹⁵⁸, suggesting that blockade of circulating inflammatory mediators may not be sufficient to reverse phenotype changes of microglia in chronic disease. In line with this, we found that in patients with multiple risk factors for stroke and chronic inflammation (as shown by chronically elevated CRP levels) displayed increased microglial activity based on TSPO-PET measurements, in the absence of any obvious neurological disease (negative MR). These findings were confirmed in obese, atherosclerotic and insulin resistant Corpulent rats, which showed increased TSPO radioligand binding compared to lean rats, with increasing difference with aging¹⁵⁷. Corpulent rats also present more severe BBB injury after experimental stroke, which is partially reversed by blockade of IL-1 with IL-Ra¹⁵⁹.

In subsequent studies, we aimed to explore the early central and peripheral changes induced after brain injury and studied how these changes are influenced by systemic inflammation. We first asked, what would be the most important humoral and neural routes through which brain injury may trigger changes in peripheral immune processes. As presented in my PhD thesis (2007), I had demonstrated that immune organs such as the bone marrow and the spleen are innervated by the central autonomic nervous system^{160, 161}, suggesting that these pathways are ideally positioned to induce changes in the activity or mobilisation of immune cells upon brain injury.

We found that experimental stroke triggers rapid changes in the circulation and in the bone marrow. We have shown that brain injury leads to the release of CXCR2-positive

granulocytes from the bone marrow hours, which was associated with rapid systemic upregulation of CXCL1 (a ligand for CXCR2) and G-CSF, a key cytokine involved in the mobilisation of bone marrow leukocytes. This was associated with stroke-induced NFκB activation (phosphorylation of NFκB p65) and phosphorylation of p38 MAPK in a population of bone marrow granulocytes as assessed by western blotting and flow cytometry 10 minutes and 4 hours after reperfusion. In line with the release of granulocytes, T-cell numbers in the bone marrow increased after stroke. Stroke-induced laterality was also observed in the brain stem and in the bone marrow indicating direct involvement of the autonomic nervous system in stroke-induced cell mobilisation¹⁶². In addition, this study demonstrated that systemic inflammatory changes and leukocyte responses in the bone marrow are profoundly affected by both exposure to anaesthetic and surgical stress, suggesting that experimental studies should carefully consider the potential impact of these effects on the data obtained and the conclusions drawn.

What could be the consequences of central autonomic activation, immune cell mobilisation and other systemic inflammatory changes after brain injury? It is widely recognized that acute brain injury not only induces rapid activation of the autonomic nervous system, but this also has considerable impact on the development of clinical complications, such as infections or paralytic ileus, key contributors to prolonged hospitalization and death post-stroke. To this end, we tested in mice the hypothesis that brain damage induces changes in the gut and the intestinal microbiota. We found that both experimental stroke and traumatic brain injury markedly alter the composition of the gut microbiota according to bacterial community profiling of the caecum by Denaturing Gradient Gel Electrophoresis and 16s rRNA sequencing. In particular, relative abundance of Peptococcaceae and Prevotellaceae have been specifically influenced by brain injury and changes showed correlation with the extent of injury. Peptococcaceae in the caecum showed a significant positive correlation, whereas abundance of Prevotellaceae showed a significant negative correlation with noradrenaline levels, indicating the involvement of the autonomic nervous system in the changes observed. In line with this, we have shown that brain injury leads to increased release of noradrenaline from sympathetic nerves in the caecum as demonstrated by changes in *ex vivo* uptake and release of ³H-NE upon electric stimulation. By performing pharmacological manipulation of peripheral noradrenaline release *in vivo*, we have also demonstrated that brain injury-induced effects are mediated by noradrenaline release from the autonomic nervous system, which affects caecal mucoprotein production and goblet cell numbers¹⁶³.

We have also developed novel approaches to investigate the earliest inflammatory changes in peripheral organs after stroke. Singlephoton emission computed tomography (SPECT) imaging based on lipophilic 99mTc-hexamethylpropylene amine oxime (HMPAO) and

^{99m}Tc-DTPA (diethylene triamine pentaacetic acid) signal changes revealed that acute brain injury leads to perfusion- and barrier function changes in various peripheral organs including the lung or the gut within hours¹⁶⁴, strengthening the anatomical-functional basis for known brain injury-induced complications, such as pneumonia or paralytic ileus. Using SPECT and identical radioligands, we also found that both central and peripheral inflammatory changes were altered when experimental stroke was preceded by systemic inflammation. As such, preceding systemic inflammation induced by bacterial LPS prior to experimental stroke augmented BBB injury, and also reduced cerebral blood flow in the affected neocortex, leading to poor functional outcome¹⁶⁴. Thus, brain injury itself not only triggers rapid systemic inflammatory changes, but systemic inflammation may contribute to central inflammatory changes, brain injury and impairments in functional outcome via different routes, including elevated vascular inflammation, prothrombotic / thromboinflammatory processes, BBB injury, cerebral blood flow in addition to the direct effects of proinflammatory mediators on neurons^{154, 164}, as well as post-injury complications in the lungs or in the gut.

Among the several potentially harmful mechanisms through which peripheral inflammatory actions may impact on the CNS, the studies above highlighted that systemic inflammation is associated with marked changes in microglial phenotypes and altered neuroimmune interactions. These mechanisms are likely to contribute to CNS pathology even in the absence of direct CNS injury. For example, using a translational passive transfer trauma mouse model of complex regional pain syndrome (CRPS), we have demonstrated the key role of IL-1 and microglial IL-1 β in the maintenance of chronic pain. In this model, IgG transfer from CRPS patients into mice that have been subjected to paw incision leads to increased paw swelling, microglial IL-1 β production in the spinal cord and lasting hyperalgesia compared to mice treated with control human IgG. In turn, blockade of IL-1 actions using IL-1 $\alpha\beta$ KO mice, or perioperative IL-1R1 blockade by anakinra almost completely prevented lasting CRPS symptoms, while reduced pathology was observed in microglial IL-1 β KO mice, with no effect seen after treatment with the glucocorticoid prednisolone¹⁶⁵.

The effects of altered neuroimmune communication under inflammatory conditions and the implications of chronic and/or systemic inflammation for neurological disorders in light of the available evidence have been discussed in detail in our review articles, in collaboration with both experimental researchers and clinical experts^{27, 106, 108, 115}.

Chapter 3. The role of compartment-specific microglia-neuron interactions in shaping neuronal activity and injury

This chapter is based on the following original publications:

1. Denes, A., et al., *J Cereb Blood Flow Metab*, 2008 (cited as ref. 166) ^{#,*}
2. Szalay, G., et al., *Nat Commun*, 2016 (cited as ref. 58) ^{#,*}
3. Cserep, C., et al., *Science*, 2020 (cited as ref. 59) ^{#,*}
4. Varga, D.P., et al., *J Cereb Blood Flow Metab*, 2020 (cited as ref. 175) ^{#,*}
5. Fekete, R., et al., *Acta Neuropathol*, 2018 (cited as ref. 176) ^{#,*}
6. Csaszar, E., et al., *J Exp Med*, 2022 (cited as ref. 177) ^{#,*}

Author's contribution: [#]First/last or joint first/last author; ^{*}Corresponding author

Observations suggesting the highly complex nature of microglia-neuron interactions included early studies on mice deficient for the fractalkine receptor, CX3CR1. Because CX3CR1 is expressed only by microglia in the brain parenchyma, CX3CR1 KO mice have been identified as an informative model of microglial dysfunction due to the absence of signaling by fractalkine, which is produced by neurons and other cells in the brain¹²⁰. We found significantly reduced brain injury, neuronal death and dampened IL-1 β production in CX3CR1 KO mice after experimental stroke¹⁶⁶. This was in sharp contrast with the phenotype seen in models of chronic neurodegeneration¹⁶⁷, suggesting that the effect of altered microglia-neuron interactions on neuronal fate is likely to be highly context- and pathophysiology-dependent.

Following on from these studies, we have made several observations concerning the effects of altered microglial phenotypes on outcome after different forms of neuronal injury, but tools to selectively manipulate microglia have not been available until very recently. Synthesis of a novel family of CSF1R inhibitors such as PLX3397 and PLX5622 by Plexxikon inc. (US) represented an important milestone in microglial biology, enabling reversible depletion of microglia in mice without major detectable effects on the brain tissue¹³⁴, or peripheral monocyte/macrophage populations^{58, 134, 145}. It is important to emphasize that mice without microglia stay apparently healthy for months in the absence of pathological insults, suggesting that their actions in the otherwise normal brain may be partially compensated for by other cell types^{58, 134}. My laboratory was the first to have access to these CSF1R inhibitors to study the contribution of microglia to acute brain injury induced by experimental stroke.

In our experiments, feeding mice PLX3397 for 3 weeks resulted in close to 96% elimination of microglia from most brain regions, without toxicity to neurons, astrocytes, endothelial cells, pericytes, oligodendrocytes or smooth muscle cells. Importantly, microglia exposed to PLX3397 were found to die as a result of apoptosis, indicated by the expression of Cleaved

Caspase-3, while microglia depletion did not cause inflammation in the brain tissue⁵⁸. Thus, we considered this novel tool a promising opportunity to study the functional role of microglia in acute brain injury. To our surprise, elimination of microglia by PLX3397 resulted in significantly (by 60%) increased brain injury following experimental stroke, which was not affected by withdrawal of the drug for 24h (sufficient time to clear PLX3397 from the brain, while microglia are absent)^{58, 134}. However, withdrawal of PLX3397 for two weeks resulted in an almost complete repopulation of microglia, in which case infarct size was not different from that seen in controls (microglia competent mice fed control diet)⁵⁸.

Extent or kinetics of BBB injury in the absence of microglia was not different after stroke, therefore we concluded that effect of microglia depletion on vascular responses may not explain the marked increase in neuronal death seen in microglia-depleted animals. To study the possible mechanisms involved in microglia-mediated protection of neurons, we performed *in vivo* two-photon calcium imaging, using genetically encoded calcium indicators (GCaMP6s or RCaMP1) and monitored microglial process dynamics alongside with changes in neuronal activity. We found that microglial contacts with neurons in the boundary zone of the evolving infarct was not paralleled by changes in neuronal calcium levels, but elimination of microglia was associated with markedly dysregulated neuronal network activity patterns. Neuronal calcium load, an indicator of excitotoxicity, was also significantly increased in the absence of functional microglia⁵⁸. Thus, these experiments suggested that the formation of contacts between microglia and neurons may be an essential protective mechanism for controlling pathological neuronal activity in the injured brain, and microglia may have evolved to recognize changes in neuronal activity via specific mechanisms that remain to be explored in detail.

Our *in vivo* two-photon imaging studies have demonstrated that microglia make frequent contacts with cell bodies of affected, but viable neurons in the cerebral cortex, which displayed dysregulated calcium dynamics when microglia were absent. Moreover, these affected penumbral neurons died within a few hours in microglia depleted mice, as indicated by the absence of sustained calcium activity⁵⁸. How can microglia shape neuronal activity and protect against injury? According to the available literature, interactions between microglial processes and synapses had been considered to primarily mediate microglia-neuron communication. However, it was not explained by our observations how microglia could shape neuronal activity upon focal brain injury via interactions with often distant synapses of the given cells. Of note, while synaptic boutons and dendritic spines have high turnover, the most stable part of neurons is their cell body, where the majority of mitochondria – key determinants of energy homeostasis and cell fate decisions – are localized^{168, 169}. Therefore, we started to experimentally explore the tempting possibility that

microglia may sense and influence neuronal activity through interactions with neuronal somata, which could also suggest a role for microglia in various forms of neurodegeneration, which also involve marked changes in neuronal mitochondria^{170, 171}.

First, we performed *in vivo* two-photon imaging to study the temporal dynamics of microglia–neuron contacts. We found that microglial processes not only contacted specific somatic sites on neurons, but frequently re-contacted these „hot spots”, while the average lifetime of somatic contacts turned out to be 3-4 times longer (25 min) than those made with dendrites (7.5 min)⁵⁹. Next, we performed high resolution confocal microscopy to reconstruct neurons (somata and dendrites), contacting P2Y12-positive microglial processes and perisomatic terminals in 3D, and also studied microglial process contacts with excitatory and inhibitory synapses, in order to assess the main sites of microglia-neuron interactions in the brain. We found that both in mice and in post-mortem human brain tissues, more than 90% of pyramidal cells and interneurons receive somatic microglial contact, whereas only around 10% of GABA-ergic and glutamatergic synapses are contacted by microglia in perfusion-fixed tissues.

These observations suggested that a potentially novel form of microglia-neuron interaction may exist in the brain and somatic „hot spots” might have specific molecular composition optimized for microglia-neuron cross-talk. Interestingly, we found that contacting microglial processes preferentially touch Kv2.1 and Kv2.2 channel clusters on neuronal somata. Of note, these potassium channels do not function as ion channels in clustered form in the neuronal membrane, rather, they have long been recognized as sites for increased somatic exocytosis^{172, 173}. Thus, we speculated that Kv2.1-mediated effects may contribute to the recruitment of microglial processes to these somatic sites. In fact, transfection of HEK cells with Kv2.1 (which do not express Kv2.1 or Kv2.2. channels) turned out to be sufficient to recruit microglial processes *in vitro*, which effect was not present when HEK cells were transfected with a dominant-negative mutant Kv2.1 construct, which disables clustering of Kv2.1 in the cell membrane⁵⁹.

Using superresolution microscopy and 3D electron tomography, we revealed that enrichment of microglial P2Y12 occurs specifically at sites of somatic microglial contacts (in apposition with Kv2.1 clusters in the neuronal membrane), which were named „somatic purinergic junctions”. EM tomography also revealed a highly specialized ultrastructure in neurons at these sites characterized by closely localized mitochondria, mitochondria-derived and other vesicles, mitochondria-associated membranes and ER-like structures. Functional *in vivo* and *ex vivo* studies also revealed that microglia sense changes in neuronal mitochondrial function at these somatic sites, which was dependent on P2Y12R-mediated actions⁵⁹.

What can be the driving force for the formation or maintenance of somatic purinergic junctions? Because the main ligand for P2Y₁₂R is ADP that is generated rapidly from ATP by spontaneous hydrolysis or by Ecto ATPases, we studied the possibility of somatic ATP release from neurons. In fact, vesicular nucleotid transporter (vNUT), an enzyme responsible for packing ATP into vesicles was found to be enriched in neurons at the junctions and somatic ATP release in response to changes in neuronal activity was demonstrated⁵⁹. We have also demonstrated that the formation and lifetime of somatic junctions is promoted by neuronal activity *in vivo*, which process is P2Y₁₂R-dependent.

These studies thus collectively suggested that microglial actions may be able to interfere with neuronal function via somatic purinergic junctions by sensing changes in neuronal activity and injury via (at least in part) changes in neuronal mitochondrial function. In fact, we have shown that establishment of somatic contacts is associated with increases in neuronal NADH fluorescence, which is P2Y₁₂R-dependent. Therefore, we studied whether acute brain injury induced by experimental stroke would include microglia-mediated actions via somatic purinergic junctions. Interestingly, we found that in affected, but viable neurons at the boundary zones of the infarct, fragmentation of neuronal mitochondria and declustering of Kv2.1 was associated with P2Y₁₂R-dependent increases in microglial process coverage at somatic sites. Moreover, similarly to that seen after selective elimination of microglia by PLX3397⁵⁸, blockade of microglial P2Y₁₂ by injection of a selective inhibitor, PSB-0739 into the cisterna magna increased neuronal calcium load, dysregulated functional connectivity and led to increased brain injury and worse functional outcome in mice⁵⁹. In summary, these studies revealed a formerly unknown morpho-functional interaction site between microglial processes and neuronal cell bodies, which appears to be crucially important for microglia to monitor changes in neuronal activity and mitochondrial function, and through which, microglia can exert protective actions to limit neuronal death.

Would microglia exert general control over neuronal responses and could somatic microglia-neuron interactions be generally important to monitor changes in neuronal function, neuronal activity and fate in other forms of neuropathologies? As discussed above, microglia interact with neurons to sense alterations in their physiological activity and also contact affected neurons in the boundary zones of the infarct in an activity-dependent manner^{58, 59}. Our further findings suggest that microglia sense and influence a broad range of neuronal activity changes and modulate hyperexcitability. For example, we found that microglia respond to and influence spreading depolarization (SD) in both the injured and in the otherwise intact (uninjured) brain. SD is a form of mass neuronal depolarization that has been involved in the pathophysiology of stroke, brain trauma, migraine and other disorders¹⁷⁴. We found SD incidence and kinetics to be markedly altered in mice without functional microglia after

experimental stroke⁵⁸. Importantly, SD in the normally perfused and metabolically intact brain tissue does not lead to permanent neuronal injury, making it a useful model to study how microglia sense and influence changes in neuronal activity. Along this line, we observed that SD induced by 1mM KCl was associated with larger latency to depolarization and reduced intracellular calcium load in the otherwise intact mouse cerebral cortex⁵⁸.

Next, we studied how the absence of microglia or modulation of microglial function interferes with SD generation by inducing a series of SDs via both KCl and electrical stimulation. A series of SDs induced rapid morphological changes in microglia, facilitated microglial process recruitment to neurons, while depolarization and hyperpolarization during SD were microglia- and P2Y12R-dependent¹⁷⁵. Interestingly, microglia-mediated effects are state-dependent: DC potential signature of SD is altered by selective microglia elimination or in the absence of functional P2Y12R signaling, while the electrical threshold for SD induction differs between the first and the recurrent SDs. In line with this, the absence of microglia was associated with altered potassium uptake after SD, independently of P2Y12R¹⁷⁵.

Another likely role for fine-tuned microglia-neuron interactions at neuronal somata may concern the recognition of salvageable and terminally injured neurons, which could initiate microglial protective actions or phagocytosis in the latter case. In fact, we found that microglia and microglial P2Y12R are essential for the recognition and elimination of virally infected neurons from the brain, which process appears to be instrumental to limit the spread of neurotropic virus infection¹⁷⁶. Our *in vivo* two-photon imaging studies show that retrograde, transsynaptic infection of cortical neurons by using a recombinant pseudorabies virus strain (member of the alpha herpesvirus family) results in the recruitment of microglial processes and isolation of infected neurons by microglia within 1-3 hours. Elimination of microglia or deletion of P2Y12R resulted in markedly increased viral spread and deficient phagocytosis of infected cells due to impaired responses to ATP released from compromised neurons as a danger signal¹⁷⁶. Microglia were also found important to modulate the recruitment of peripheral monocytes into the brain in these studies, which may represent another important function to shape inflammatory changes in different brain pathologies. Moreover, we found that P2Y12R positive microglia were also recruited to and phagocytosed infected neurons in post-mortem brain tissues of patients with HSV encephalitis, suggesting that our observations regarding recognition and elimination of infected neurons by microglia may also be relevant in the human brain¹⁷⁶.

Collectively, microglia emerge as key non-neuronal cells to shape inflammatory processes, to simultaneously monitor neuronal health and pathophysiological responses, and to act as important contributors to neuronal cell fate decisions.

Our recent data further add to the complexity of microglia-mediated mechanisms that influence neuronal responses. When studying the contactomics of individual microglia, we noticed that given cells form simultaneous interactions with several neurons and blood vessels in their vicinity. Given that neuronal activity-dependent changes in cerebral blood flow (CBF) are precisely controlled via multicellular interactions in the NVU¹⁷, we argued that microglia are ideally positioned to sense and influence neurovascular responses under normal conditions or when the balance between oxygen/nutrient demand and blood supply is disturbed.

To this end, we first demonstrated by using confocal microscopy, electron microscopy and electron tomography that microglia establish direct, dynamic purinergic contacts with cells in the neurovascular unit that shape CBF, namely with endothelial cells, astrocytes, smooth muscle cells and pericytes in both mice and humans¹⁷⁷. To our surprise, electron tomography also demonstrated accumulation of microglial P2Y12R at contact sites with endothelial cells near endothelial mitochondria, suggesting that as seen in the case of somatic purinergic junctions, specific sites of ATP release may also exist in the vasculature of the cerebral cortex. Further on, we demonstrated that the absence of microglia (depletion by PLX5622) or blockade of microglial P2Y12R substantially impairs neurovascular coupling induced by whisker stimulation, as assessed by laser speckle contrast imaging (LSCI), an approach that allows detection of CBF changes through the intact skull bone in mice. These results were also confirmed by functional ultrasound imaging.

Similar observations were made by using LSCI and a novel mouse line generated in the Laboratory, namely MicroDREADD^{Dq} mice, allowing chemogenetically induced microglial dysfunction associated with impaired ATP sensitivity to be induced *in vivo* in real time¹⁷⁷. We also demonstrated that while after microglia depletion and in P2Y12R KO mice baseline cortical neuronal activity is increased, whisker stimulation-evoked neuronal calcium activity changes (assessed by *in vivo* two-photon imaging) or firing rate changes (assessed by intracortical tetrodes) do not explain altered CBF responses after microglia manipulation. Furthermore, we have shown that hypercapnia (a vascular stimulus leading to vasodilation via primarily endothelial routes) induces rapid microglial calcium changes, P2Y12R-mediated formation of perivascular filopodia, and microglial adenosine production, while depletion of microglia reduces brain pH and impairs hypercapnia-induced vasodilation.

We found that after neurovascular coupling, microglial effects were partially independent of nitric oxide, while after hypercapnia, microglial actions were found to modulate vascular cyclic GMP levels. Finally, we demonstrated that microglial dysfunction (depletion of

microglia, or both genetic and pharmacological blockade of P2Y₁₂R) markedly impairs cerebrovascular adaptation to common carotid artery occlusion resulting in hypoperfusion¹⁷⁷.

Thus, beyond compartment-specific microglia-neuron interactions, microglial mechanisms are likely to also interfere with neuronal activity indirectly by shaping activity-dependent CBF changes, or modulating vasodilation, which actions are likely to have an impact under hypoperfusion, which is a common feature of several neurological disorders. Hence, the molecular mechanisms governing complex microglia-neuron and microglia-vascular interactions require further investigations.

Conclusions

My research has been mostly focusing on neuro-immune interactions and CNS inflammatory mechanisms with the aim to understand how these processes influence the pathophysiology of common neurological disorders. Input from this research - with the contribution of many excellent colleagues - has contributed to the recognition of the pivotal modulatory role of microglia, the main immune cells of the CNS, in central inflammatory actions, neuronal activity, neuronal injury and vascular responses. Many of our studies concerned the mechanisms of acute brain injury, with strong focus on cerebral ischemia. This research avenue was intentionally chosen. First, stroke, as one of the leading causes of mortality and the primary cause of lasting disability¹⁷⁸ represents an enormous burden for patients, their families and for the healthcare systems worldwide. Inflammatory mechanisms are emerging contributors to stroke pathophysiology both concerning the formation of the primary and secondary injury in the brain. In this regard, we have made several original observations including the site-specific actions of the proinflammatory master regulator cytokine, IL-1, the role of inflammasomes, or the impact of microglial actions on neuronal activity and injury among others. Second, the remarkable disease-modifying role of chronic inflammation in different forms of neuropathologies is emerging. In fact, chronic diseases are key risk factors for not only stroke, but for virtually all neurological disorders, while the impact of age-related conditions on the dysregulation of inflammatory mechanisms is also increasingly recognized. By using experimental models of systemic inflammation and stroke, we have identified several novel, clinically relevant mechanisms of neuroimmune communication that had been previously overlooked due to the preferential use of young, apparently healthy rodents for such studies. Third, acute brain injury induced by cerebral ischemia is not only well-characterized, but using these well-established experimental stroke models in combination with recent technological developments in the field of stroke-immunology research (e.g. *in vivo* imaging, molecular anatomical, immunological, biochemical and other approaches) also enabled fundamentally new mechanisms of brain injury to be identified that could not be visualized with less advanced technologies earlier. These discoveries helped us understand how similar mechanisms may operate in other forms of CNS inflammation, injury or neurodegeneration, such as during infection, neuronal hyperexcitability or chronic pain. Fourth, knowledge originating from these studies including advances in *in vivo* microglia manipulation, imaging, or systematic comparison of inflammatory and molecular anatomical changes between the mouse and the human brain, allowed us to shed light on how microglial actions operate under physiological conditions to control neuronal activity or vascular responses. I trust that molecular imaging of vascular- and neuronal injury, purinergic actions, cellular calcium dynamics, microglia-neuron interactions, mitochondrial function and other

readouts ultimately support visualization of complex biological processes at different temporal and spatial scales, which knowledge can then be utilized to understand the mechanisms of CNS inflammation and injury in a number of additional CNS disorders better.

Lessons from neuroprotection trials and clinical studies

Why studying the role of inflammatory mechanisms in CNS disorders may be important? Interestingly, evidence that inflammatory mechanisms could be previously underestimated contributors to neurological disorders emerged in parallel with the rapidly growing burden of brain diseases worldwide. This recognition was paralleled by both medical needs and financial considerations. Beyond the high burden of brain disorders on patients, families and healthcare systems, disease costs are also extremely high and are constantly growing. In fact, the total cost of brain disorders was estimated as €798 billion in Europe in 2010⁸ and similar expenses were projected for the US. As of 2011, nearly 100 million Americans were afflicted by at least one of the over 1,000 neurological diseases¹⁷⁹. In line with this, development of effective treatment regimens proved to be particularly difficult and expensive. In the US, approximately 5 of 5,000 new drugs complete the preclinical phase and advance to clinical trials in humans. Of those five, one drug is typically approved by the Food and Drug Administration (FDA) and reaches the marketplace, a process that typically spans 12-15 years at a cost of \$2.6 billion each¹⁸⁰⁻¹⁸².

A large number of clinical trials have been designed to target mechanisms of neuronal injury to date. However, apart from the very few successful approaches used for specific neurological conditions (e.g. identification of defined targets in rare genetic disorders or endovascular thrombectomy to restore perfusion after cerebral ischemia¹⁸³), most neuroprotection trials have failed to date. These include hundreds of unsuccessful clinical trials in stroke, AD, PD and other conditions. Likely reasons for failure include uncertainties concerning disease mechanisms (e.g. the causal role of given misfolded proteins in AD pathophysiology), the low predictive value of animal studies, excessive use of young and healthy rodents in experimental research, low BBB penetration and high toxicity level of effective drug doses, lack of appropriate biomarkers and early predictors for intervention and various issues concerning study design and assessment of treatment efficacy¹⁸⁴. For example, the assumption that abnormal protein deposits are primarily responsible for neuronal loss in diverse neuropathological states has been a strong driving force behind clinical trials in AD. Even if this is the case, damage to the brain induced by abnormal deposits of amyloid β and tau tangles is believed to start decades before decline in cognitive function becomes apparent. Stroke research is another sensible example, where causes for pitfalls in clinical trials have also been extensively analyzed over the last few decades.

Despite the success of drugs improving hemodynamics (thrombolytics, antiplatelet drugs, anticoagulants, fibrinogen depleting agents) or endovascular thrombectomy to restore cerebral perfusion, neuroprotective agents have almost exclusively failed. These included drugs blocking excitotoxicity, free radical scavengers, ion channel modulators, serotonin agonists, caspase inhibitors, and also potentially anti-inflammatory agents^{106, 115, 185, 186}. These lessons strongly indicate that disease biology is complex and mechanisms of brain injury have not been appropriately understood to date. In parallel, inflammatory mechanisms emerge as pivotal contributors to CNS disorders and chronic inflammation as a multifactorial driver of CNS pathologies is also widely recognized^{3, 9, 11, 20, 21, 38, 81, 93, 94, 103, 105, 107, 171, 186-190}. Among the many possible routes through which inflammatory mechanisms may contribute to CNS pathology, which cells to target to modulate these complex processes in the CNS?

Microglia emerge as main integrators and modulators of inflammatory processes in the CNS – relevance for neurological disorders

Accumulating evidence indicates that microglia (or microglial dysfunction) are likely to be key contributors to diverse neurological conditions, even beyond their immunological or inflammatory functions. Recent genome-wide association studies (GWAS) have identified various inflammation-related genes including those highly expressed by microglia, such as CR1, SPI1, MS4As, TREM2, ABCA7, CD33, INPP5D, APOE ε4, ACADVL, TRABD, and VASP in AD, PD and other brain diseases^{54, 91, 191, 192}. Recent snRNA-seq data show that in microglia from the brains of individuals with presymptomatic sporadic AD, familial AD and sporadic AD, SNP signatures of AD-associated genes correlate with microglial activity states and changes indicative of defective meningeal lymphatics¹⁹³. Interestingly, comparison of the gene expression of neurodegenerative disease susceptibility genes from GWAS of human microglia with those of other mammalian species revealed significant over-representation of PD genes and, to a lesser extent, AD genes in the human-specific cluster and clusters shared by human and macaques as compared to rodents¹⁴. This indicates that the potential role of microglial effects in different forms of neurodegeneration may be underestimated in rodent studies. Of note, altered microglial activity is one of the earliest changes seen in neurological disorders: together with impaired cerebral blood flow and neurovascular coupling, neuroinflammation and changes in microglial function precede symptom onset in AD, Lewy body dementia, idiopathic PD, chronic hypoperfusion, or amyloid angiopathy^{16-18, 62, 190, 194-196}. This is confirmed by PET studies visualizing neuroinflammatory changes in the brain by radioligands of the translocator protein (TSPO)^{187, 191, 194, 197}. Microglial activation predicts cognitive decline in AD patients and is a better predictor of cognitive outcome in experimental AD than amyloid burden^{198, 199}, whereas microglial activation and tau propagate jointly across Braak stages²⁰⁰. There is also strong clinical evidence for the involvement of

inflammatory mechanisms and microglial actions in epilepsy^{189, 201, 202}. In ischemic or hemorrhagic stroke, TSPO studies have demonstrated markedly altered microglial reactivity 1-2 days after the acute vascular event that may last for several months and might be an indicator of secondary fiber tract degeneration from early (2 weeks) to chronic (6 months) phases after stroke²⁰³. These examples collectively implicate inflammatory and microglial actions in diverse brain disorders and suggest that a deeper understanding of the cellular-molecular mechanisms involved could have broad diagnostic and therapeutic use.

How could microglia exert protective or detrimental actions and what kind of neuroimmune interactions mediate these effects? Our research has provided evidence that microglia not only rapidly respond to injury or infection that take place in the brain parenchyma, but even in the absence of direct brain pathologies, microglial phenotypes are strongly influenced by systemic inflammatory changes. Given that microglia colonize the CNS already in the first trimester and comprise a self-renewing population thereafter, challenges that influence microglial function are expected to have life-long consequences. Our research has contributed to the understanding of microglial physiological and pathological actions at different levels, ranging from cellular-subcellular mechanisms of their interactions with neurons, soluble factors that act on, or are produced by microglia, or the effects of systemic inflammation on central inflammatory changes and microglial phenotypes. As detailed in our recent review article, long-distance or indirect interactions between microglia and neurons (and other cells) establish complex regulatory loops that include remote actions of microglia on peripheral tissues as well as effects of circulating mediators, peripheral nerves or central inflammatory processes on microglial function (Figure 3).

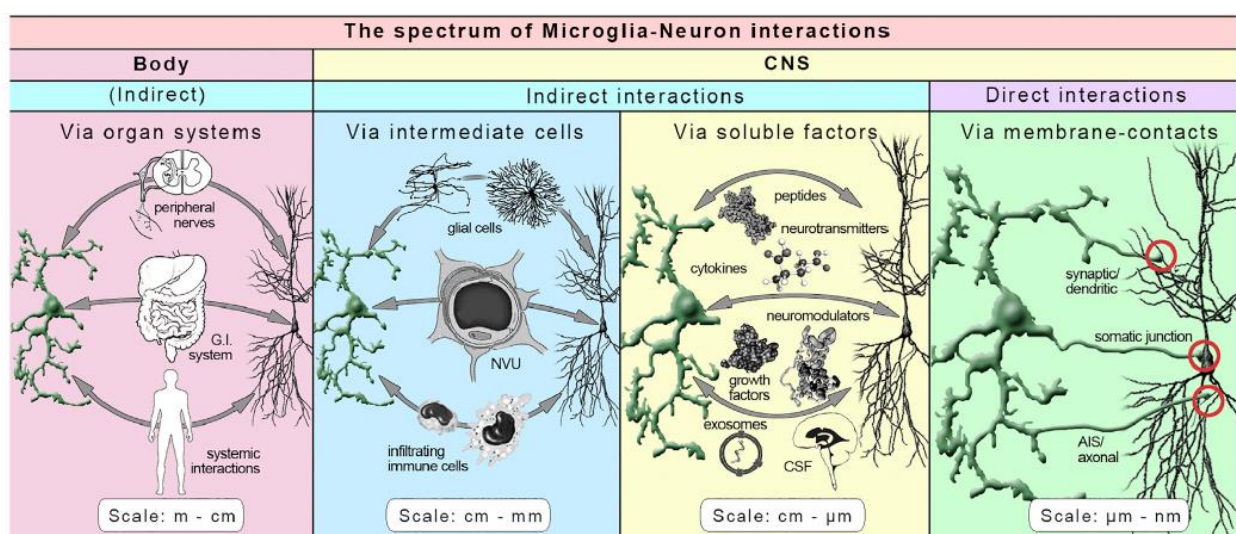


Figure 3. The spectrum of microglia-neuron interactions. Indirect, long-distance interactions between microglia and neurons establish complex regulatory loops that include remote actions of

microglial processes on neurons in peripheral tissues. In turn, circulating mediators or peripheral nerves shape microglial function. Such interactions occur during diverse forms of neuroimmune communication in health and disease. Within the CNS, indirect microglial interactions can involve communication via soluble factors and intermediate cells. These interactions may employ signaling via other glial cells (oligodendrocytes and astrocytes), cells of the neurovascular unit, or infiltrated immune cells. Indirect interactions via soluble factors (cytokines, growth factors, neuromodulators, etc.) also provide means of intercellular communication with longrange effects via the cerebrospinal fluid (CSF) or with shorter-range effects in the parenchyma limited by the diffusion and clearance of the active mediators in the extracellular space. Direct microglia-neuron interactions via tight membrane-membrane contacts permit the most effective, rapid, and dynamic communication between the two cell types. Figure adapted from Cserép et al., *Neuron* 2021²⁰⁴.

Based on the available evidence, altered production of peripheral proinflammatory cytokines, chemokines, acute phase proteins and other mediators in patients with chronic disease or infection may not only contribute to inflammation in different vascular beds (including those in the CNS), alter BBB function, the production/activity/migration of immune cells or induce changes in the autonomic nervous system or neuroendocrine regulation, but will also change microglial phenotypes via direct or indirect actions, which will eventually alter the interactions between microglia and neurons, astrocytes, microvessels or other structures. Given the instrumental role of microglia in both the maintenance of normal brain function and their emerging roles in disease, understanding of the molecular mechanisms underlying these processes, in particular, the molecular composition and functioning of compartment-specific microglial interactions is desperately needed, as discussed briefly below.

Emerging role of compartment-specific interactions between microglia, neurons and other cells in the CNS

Limited knowledge about microglial physiology, the high level of plasticity of microglial phenotypes and the lack of tools to selectively target microglia have long been suggested to underly the controversial role of these cells in brain diseases. Genetic models of altered microglial behavior and microglia-neuron interactions serve as a typical example. As discussed earlier, CX3CR1 (fractalkine receptor) is abundantly expressed by microglia, which recognize fractalkine produced by neurons and other cells in the brain. Deletion of CX3CR1 was found to result in altered microglial phenotypes and microglia-neuron interactions¹²⁰. As demonstrated in a landmark paper by the group of Richard Ransohoff using models of chronic systemic inflammation, MPTP-induced Parkinsonism and amyotrophic lateral sclerosis, dysregulated microglial responses and increased IL-1 β production in CX3CR1 KO mice were associated with increased neurotoxicity, suggesting

that augmenting CX3CR1 signaling may be neuroprotective¹⁶⁷. In our hands, CX3CR1 KO mice produced less IL-1 β in the brain tissue and had smaller infarct size after experimental stroke, which effect was also confirmed by others in different models using impaired CX3CR1 signaling^{166, 205}. Later on, we have demonstrated that elimination of microglia, or blockade of microglial P2Y12R leads to more severe brain injury after experimental stroke^{58, 59}, showing the pivotal role of sustained microglia-neuron interactions to limit neuronal loss. In contrast with these findings, excessive elimination of synapses by microglia in models of AD appear to be an important contributor to neuronal loss and cognitive decline¹⁰³. What could be the exact mechanisms regulating these complex processes under physiological or pathological conditions? What would be the exact pathological consequences of dysregulation of microglial responses in different forms of neuropathologies?

Recognition of the complexity of mechanisms through which inflammation could contribute to CNS injury, and the controversial role for microglial actions in these processes established the need to study microglia-neuron interactions with the most advanced technologies available. Recent research using genetically encoded biosensors, transgenic mice, *in vivo* imaging, transcriptomics, molecular anatomy and other approaches supported by clinical studies collectively suggest that inflammatory actions in general, and microglial actions in particular are highly compartment-dependent and also show high level of temporal dynamics. This is not only demonstrated by the stimulus-specific nature of microglial transcriptomic, proteomic and metabolic changes, but also by the high level of complexity of microglial interactions with other cells^{24, 34, 35, 42, 51, 54, 56, 57, 61}.

Among the many forms of intercellular communication ranging from remote actions of soluble messengers to direct membrane-membrane contacts, the accuracy of information transfer generally increases by the reduction of distance between the cells of interest. As such, direct membrane-membrane interactions among cells enable the most sophisticated and well-controlled forms of communication throughout the body. A good example is the highly complex dynamic cell-cell contacts that govern the activation and effector function of immune cells, such as those formed between T cells and antigen-presenting cells^{206, 207}. In the CNS, well-known forms of membrane-membrane communication include interactions between neurons via synaptic membranes or gap junctions, dynamic intercellular crosstalk within the syncytial network of astrocytes, interactions between astrocyte processes/endfeet and synapses or endothelial cells, and metabolite exchange between the myelin sheet and the axon. These interactions establish localized and functionally distinct signaling to control different biological processes. In recent years, microglia have been shown to establish complex and dynamic interactions with synapses, dendrites, axon initial segments and somata of neurons, contact Ranvier nodes, astrocytes or different cells of the neurovascular

unit. Fundamentals for these interactions include the remarkable metabolic plasticity of microglia, the high level of autonomy and constant surveillance activity of individual microglial processes and the plethora of receptors (including a broad array of neurotransmitter receptors), ion channels, transporters and soluble messengers microglia possess²⁰⁴. For example, somatic purinergic junctions, which were discovered in my laboratory, not only present a specialized ultrastructural and molecular composition optimized for dynamic intercellular communication between microglia and neurons, but similar complexity is expected for microglial interactions with synapses, axons and other cells, which is presently far from being understood (Figure 4).

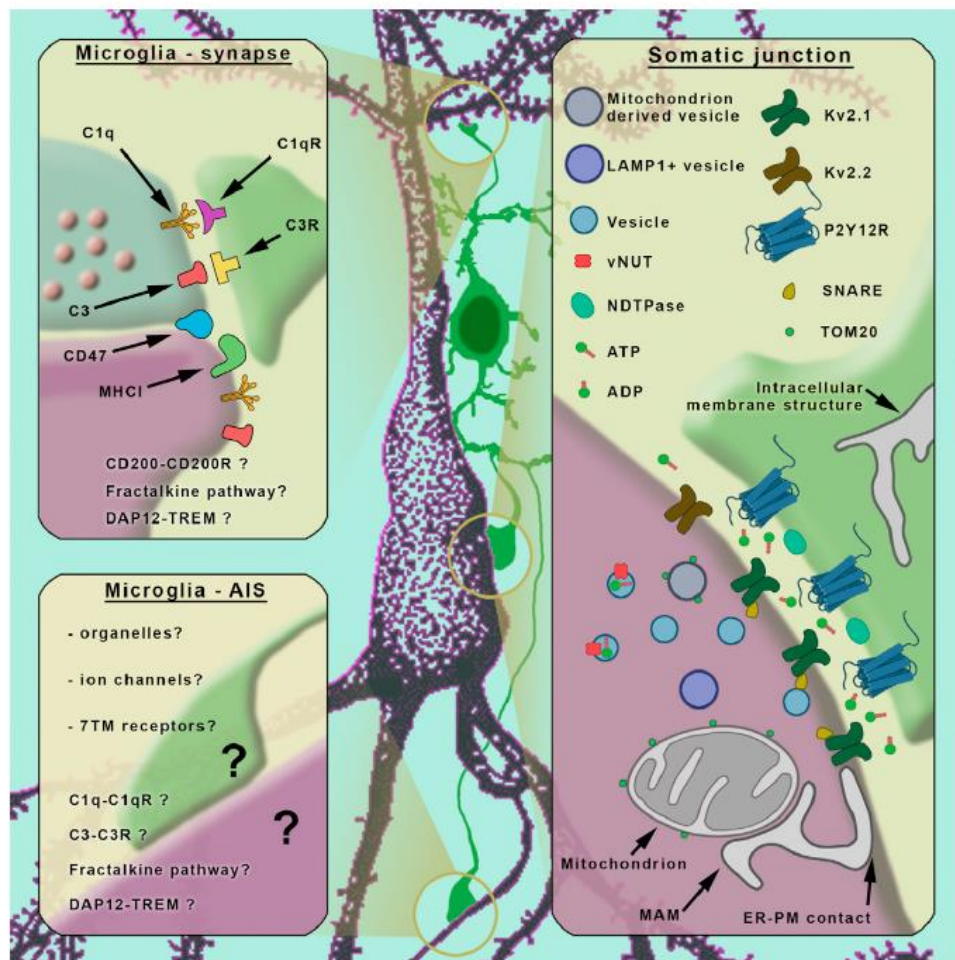


Figure 4. Compartment-dependent structural and molecular heterogeneity of microglia-neuron contacts. Microglia-synapse contacts have been shown to express elements of the complement system, namely, complement component 3 (C3) and complement component 1q (C1q). Markers of glutamatergic synapses also colocalize with CD47 and MHC class I molecules. Although the CD200-CD200R pathway, the fractalkine pathway, and DAP12-TREM signaling have also been strongly implicated as players in microglia-synapse interactions, their localization is not yet confirmed at these sites. Somatic junctions possess a specialized structure: the neuronal cytoplasm is enriched in anchored mitochondria, mitochondrion-associated membranes (MAMs), endoplasmic reticulum

plasma membrane (ER-PM) contacts, and purinergic and mitochondrion-derived vesicles (MDVs). Vesicular nucleotide transporter (vNUT) and the lysosomal marker LAMP1 are also enriched at the contact sites, whereas exocytosis-promoting Kv2.1 and Kv2.2 proteins (binding SNARE proteins) are clustered in the neuronal membrane within the contact sites. Accumulation of microglial P2Y₁₂Rs is seen in contacting microglial membranes, together with NDTase molecules that may allow ATP hydrolysis to be focally controlled by microglial processes. The expression of CD47 could also be observed at these contacts. Microglia-AIS contacts represent the lesser known area of direct microglia-neuron interactions, because no subcellular organelle or molecular element has been shown to be specifically localized at these contacts. Figure adapted from Cserép et al., *Neuron* 2021²⁰⁴.

Thus, it is likely that modulation of microglial function per se will have markedly different consequences in different cellular compartments, which should be understood in detail to aid the development of more effective therapeutic approaches. At present, the exact molecular composition and operation of these interactions is still vaguely defined, which greatly limits the efficacy of targeting pathological changes with drugs or other means. Our studies collectively suggest that purinergic and other interactions between neurons and microglia emerge as critical contributors to neuronal activity changes and cell fate decisions, in which microglia appears to play key regulatory roles. As such, microglia are likely to constantly monitor neuronal function via somatic (and other) sites, while pathophysiological activity changes, changes in mitochondrial function or somatic exocytosis, altered expression of membrane-bound molecules, as well as damage signals such as DAMPs, alarmins (e.g. ATP) and other mediators released from injured neurons drive heterogenous and context-dependent microglial actions leading to restoration of neuronal function or elimination of terminally injured cells by phagocytosis²⁰⁴. For example, our neurotropic virus research using both experimental models and post-mortem human brain tissues specifically link somatic microglia-neuron interactions with protection of the brain tissue via phagocytosis of infected cells by microglia¹⁷⁶, and suggest that the newly discovered somatic purinergic junctions could represent a key site for cell fate decisions in many other forms of neuropathologies. Dysregulation of microglial control of neuronal excitability, impaired target recognition, or off target phagocytosis, however, could lead to excessive synapse elimination or neuronal loss, with known pathophysiological consequences, as outlined above. Along this line, interactions between microglia and astrocytes may also be vital, based on recent data on task-sharing in phagocytic activity between these two cell types^{208, 209}. Furthermore, fine-tuned regulation of such processes is expected to be markedly altered in old age, under systemic inflammatory conditions, or after acute injury. Thus, alongside with the compartment-specific nature of microglial interactions with other cells, inflammatory mediators also have different, compartment-specific actions on neurons, glial cells, or the vasculature, leading to

considerable alterations of otherwise well-regulated cell-cell interactions, as also suggested by our recent studies. In fact, our recent data highlighting the pivotal role of microglia in shaping cerebral blood flow, neurovascular coupling, hypercapnia-induced vasodilation and adaptation of hypoperfusion¹⁷⁷ suggest that understanding the specific pathways regulating microglia-neuron and microglia-vascular interactions differently will be particularly important for the identification of specific drug targets for intervention in common neurological disorders, where cerebral hypoperfusion and neurodegeneration often take place simultaneously and predict poor clinical outcome^{17, 18}.

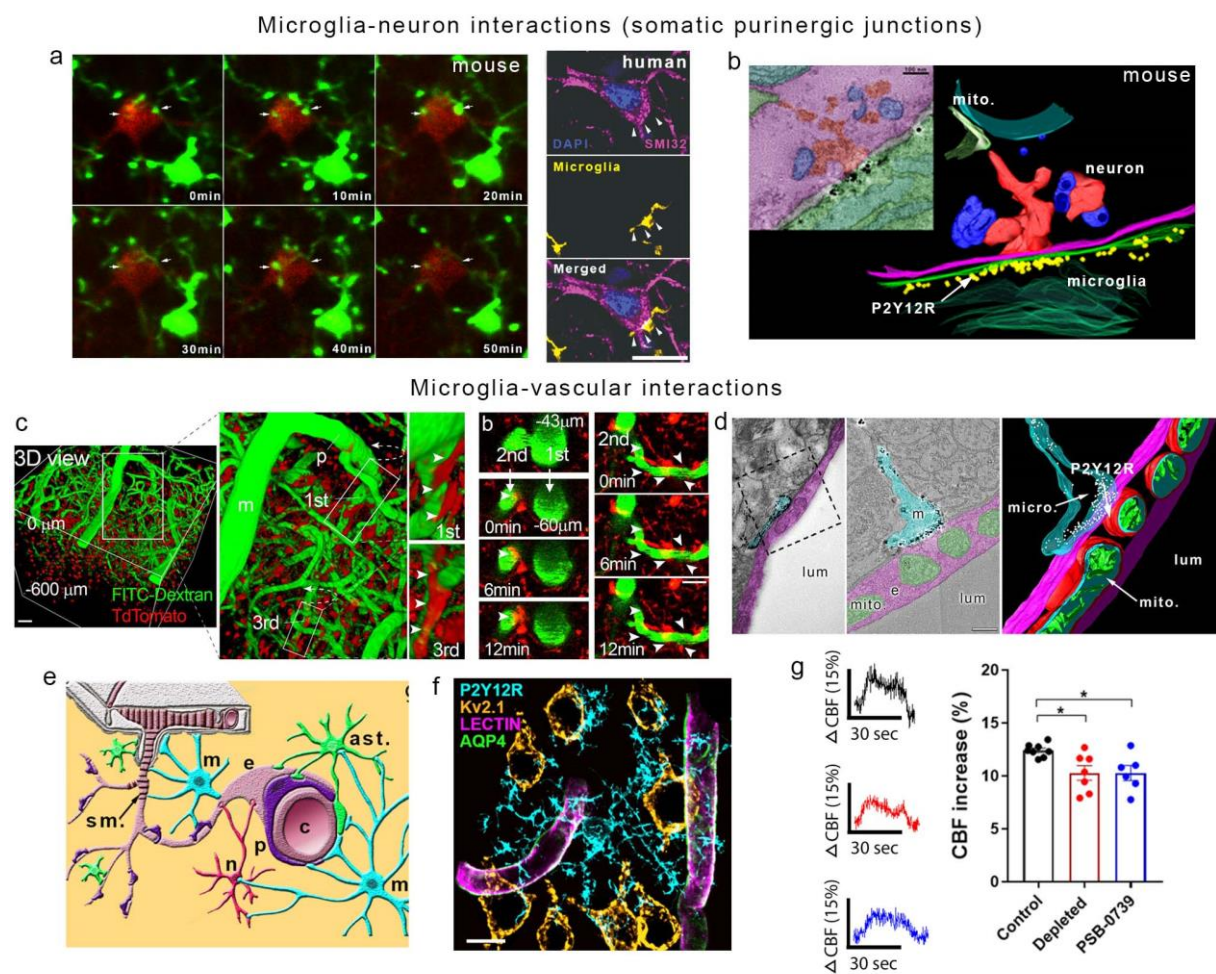


Figure 5. Microglia shape neuro-vascular responses via direct and dynamic purinergic contacts. a. In vivo two-photon imaging and confocal microscopy reveal somatic purinergic junctions in the mouse (left) and the human (right) neocortex, respectively. b. Electron tomography identifies enrichment of microglial P2Y12 receptors (yellow) at somatic neuronal contacts near mitochondria. c. 3D reconstruction of microglia-vascular interactions in the mouse neocortex. d. Electron tomography identifies enrichment of microglial P2Y12 receptors (immunogold particles are shown in white on the reconstruction) at endothelial contact sites near mitochondria. e. Schematic showing microglial contacts with cells in the NVU. f. Maximal intensity plot showing that individual microglia contact nearby neurons and microvessels simultaneously. g. Impaired neurovascular coupling in the absence

of microglia or after blockade of microglial P2Y₁₂R by PSB-0739 (Laser Speckle Contrast Imaging). a-b adapted from Cserép et al., Science 2020⁵⁹; c-g adapted from Császár et al., J Exp Med 2022¹⁷⁷.

Future prospects and challenges

Understanding the role of neuro-immune mechanisms and microglia in CNS health and disease is of pivotal importance. This is greatly supported by novel tools in neuroscience, immunology, molecular biology and imaging, with increasing demand on cross-disciplinary technologies and knowledge. Constant refinement of pharmacological and genetic microglia manipulation approaches alongside with novel experimental models and state-of-the-art imaging technologies are expected to promote better understanding of the mechanisms of CNS inflammation and injury. This should be complemented with clinical imaging studies, cross-comparison of anatomical and biochemical changes between experimental animals and humans using post-mortem tissues and *ex vivo* models of human cells/tissues (iPSCs, primary cultures, acute slices, organotypic slices, etc), to untangle complex inflammatory mechanisms for most effective translation of experimental findings into clinical benefit²¹⁰. Recent breakthroughs in omics research, including single cell transcriptomics have provided better understanding of mouse and human microglial states in diverse physiological and pathological conditions. As a challenge for the next decade, integration of information concerning defined molecular fingerprints with molecular anatomy and cellular function will be of pivotal importance. It also remains to be explored to what extent changes in microglial phenotypes and responses are responsible for certain pathological processes in given neurological conditions and how their interactions with other known pathomechanisms shape disease outcome.

Even among the well-established inflammatory targets, such as IL-1, whose pathological roles are supported by extensive experimental and clinical evidence, clinical intervention trials are expected to yield controversial results in different CNS disorders, due to the high level of genetic variability, comorbidities, age, environmental factors and many others that collectively shape disease outcome in individual patients. For example, anakinra, a recombinant form of IL-1Ra that blocks signaling via IL-1R1, is effective in a number of auto-inflammatory conditions²¹¹ and has recently been found to reduce CRP levels and mortality risk in patients admitted to hospital with moderate to severe COVID-19 pneumonia. However, no benefit was observed with dexamethasone co-administration²¹². In patients with ischemic stroke, subcutaneous IL-1Ra is not only safe and well tolerated, but was found to reduce plasma inflammatory markers associated with worse clinical outcome. However, possible interactions with thrombolysis are likely to limit its efficacy to improve long-term functional

outcome²¹³. These examples may indicate that understanding the mechanisms of production or site-specific actions of given inflammatory mediators has to be associated with understanding their complex interactome and the main confounders that limit efficacy of given treatment regimen (e.g. limited penetration of many, potentially effective drugs into the CNS).

Future clinical trials targeting neuronal injury, inflammation or microglial actions will also need to consider specific sites of actions for given pharmacological regimen, even if their main cellular targets are assumed to be already understood. As an example, our findings showing the pivotal contribution of microglial NKCC1¹⁴⁸ to central actions of bumatenide, a specific NKCC1 blocker, suggest that whether this drug indeed exerts its therapeutic effects by acting directly on NKCC1 expressed in central neurons, as widely suggested, may need to be reconsidered^{146, 147, 214}. In a similar line, immunomodulatory effects of already established drugs that had been found safe and tentatively effective in the clinic will also need to be considered, which could provide novel insights into drug repurposing research and clinical trials.

Recent challenges, such as the COVID-19 pandemic have further highlighted the importance of diverse central and systemic inflammatory mechanisms that affect given neurological states differently. In fact, beyond the observed systemic inflammatory changes including „cytokine storm”, prothrombotic states, vascular inflammation that emerge during the course of the disease, microglial phenotypes have also been found to be markedly altered^{215, 216}. The role of these changes in acute and long-term neurological alterations remain to be identified. Our unpublished data indicate marked alterations in compartment-specific microglia-neuron interactions in aging, chronic neurodegeneration or COVID-19, which suggest that understanding how neuroimmune interactions operate in different forms of CNS pathologies requires further studies enabling links between diverse and ever-changing microglial phenotypes, regulation of neuroimmune interactions and their functional consequences to be established. Such efforts will hopefully support the identification of novel diagnostic approaches and therapeutic targets in CNS disorders.

Publications

The dissertation is based on the following original publications:

Chapter 1

1. **Denes A^{*#}**, Vidyasagar R, Feng J, Narvainen J, McColl BW, Kauppinen RA, Allan SM[#] (2007) Proliferating resident microglia after focal cerebral ischaemia in mice. *Journal of cerebral blood flow and metabolism: official journal of the International Society of Cerebral Blood Flow and Metabolism* 27 (12):1941-1953. doi:10.1038/sj.jcbfm.9600495

IF: 5.147 *Independent citations: 233*

2. Luheshi NM, Kovacs KJ, Lopez-Castejon G, Brough D^{*#}, **Denes A^{*#}** (2011) Interleukin-1alpha expression precedes IL-1beta after ischemic brain injury and is localised to areas of focal neuronal loss and penumbral tissues. *Journal of neuroinflammation* 8:186. doi:10.1186/1742-2094-8-186

IF: 4.35 *Independent citations: 94*

3. Savage CD, Lopez-Castejon G, **Denes A[#]**, Brough D^{*#} (2012) NLRP3-Inflammasome Activating DAMPs Stimulate an Inflammatory Response in Glia in the Absence of Priming Which Contributes to Brain Inflammation after Injury. *Frontiers in immunology* 3:288. doi:10.3389/fimmu.2012.00288

IF: 1.552 *Independent citations: 152*

4. **Denes A[#]**, Wilkinson F, Bigger B, Chu M, Rothwell NJ, Allan SM^{*#} (2013) Central and haematopoietic interleukin-1 both contribute to ischaemic brain injury in mice. *Disease models & mechanisms* 6 (4):1043-1048. doi:10.1242/dmm.011601

IF: 5.537 *Independent citations: 20*

5. **Denes A^{*#}**, Coutts G, Lenart N, Cruickshank SM, Pelegrin P, Skinner J, Rothwell N, Allan SM, Brough D^{*#} (2015) AIM2 and NLRC4 inflammasomes contribute with ASC to acute brain injury independently of NLRP3. *Proceedings of the National Academy of Sciences of the United States of America* 112 (13):4050-4055. doi:10.1073/pnas.1419090112

IF: 9.423 *Independent citations: 138*

6. Wong R, Lenart N, Hill L, Toms L, Coutts G, Martinecz B, Csaszar E, Nyiri G, Papaemmanouil A, Waisman A, Muller W, Schwaninger M, Rothwell N, Francis S, Pinteaux E, **Denes A^{*#}**, Allan SM^{*#} (2019) Interleukin-1 mediates ischaemic brain injury via distinct actions on endothelial cells and cholinergic neurons. *Brain, behavior, and immunity* 76:126-138. doi:10.1016/j.bbi.2018.11.012

IF: 6.633 *Independent citations: 24*

7. Allen C[#], Thornton P, **Denes A^{*}**, McColl BW, Pierozynski A, Monestier M, Pinteaux E, Rothwell NJ, Allan SM[#] (2012) Neutrophil cerebrovascular transmigration triggers rapid neurotoxicity through release of proteases associated with decondensed DNA. *J Immunol* 189 (1):381-392. doi:10.4049/jimmunol.1200409

IF: 5.788 *Independent citations: 116*

8. Toth K, Lenart N, Berki P, Fekete R, Szabadits E, Posfai B, Cserep C, Alatshan A, Benko S, Kiss D, Hubner CA, Gulyas A, Kaila K, Kornyei Z, **Denes A^{*#}** (2022) The NKCC1 ion transporter modulates microglial phenotype and inflammatory response to brain injury in a cell-autonomous manner. *PLoS biology* 20 (1):e3001526. doi:10.1371/journal.pbio.3001526

IF: 8.029

Independent citations: 1

Chapter 2

1. **Denes A[#]**, Humphreys N, Lane TE, Grecis R, Rothwell N^{*#} (2010) Chronic systemic infection exacerbates ischemic brain damage via a CCL5 (regulated on activation, normal T-cell expressed and secreted)-mediated proinflammatory response in mice. *The Journal of neuroscience: the official journal of the Society for Neuroscience* 30 (30):10086-10095. doi:10.1523/JNEUROSCI.1227-10.2010

IF: 7.271

Independent citations: 73

2. **Denes A^{*#}**, Ferenczi S, Kovacs KJ (2011) Systemic inflammatory challenges compromise survival after experimental stroke via augmenting brain inflammation, blood- brain barrier damage and brain oedema independently of infarct size. *Journal of neuroinflammation* 8:164. doi:10.1186/1742-2094-8-164

IF: 4.35

Independent citations: 114

3. **Denes A^{*#}**, Pradillo JM, Drake C, Sharp A, Warn P, Murray KN, Rohit B, Dockrell DH, Chamberlain J, Casbolt H, Francis S, Martinecz B, Nieswandt B, Rothwell NJ, Allan SM[#] (2014) Streptococcus pneumoniae worsens cerebral ischemia via interleukin 1 and platelet glycoprotein Ibalpha. *Annals of neurology* 75 (5):670-683. doi:10.1002/ana.24146

IF: 11.193

Independent citations: 23

4. Drake C, Boutin H, Jones MS, **Denes A**, McColl BW, Selvarajah JR, Hulme S, Georgiou RF, Hinz R, Gerhard A, Vail A, Prenant C, Julyan P, Maroy R, Brown G, Smigova A, Herholz K, Kassiou M, Crossman D, Francis S, Proctor SD, Russell JC, Hopkins SJ, Tyrrell PJ, Rothwell NJ, Allan SM^{*#} (2011) Brain inflammation is induced by co-morbidities and risk factors for stroke. *Brain, behavior, and immunity* 25 (6):1113-1122. doi:10.1016/j.bbi.2011.02.008

IF: 4.72

Independent citations: 129

5. **Denes A[#]**, Drake C[#], Stordy J[#], Chamberlain J, McColl BW, Gram H, Crossman D, Francis S, Allan SM, Rothwell NJ^{*#} (2012) Interleukin-1 mediates neuroinflammatory changes associated with diet-induced atherosclerosis. *Journal of the American Heart Association* 1 (3):e002006. doi:10.1161/JAHA.112.002006

IF: 4.49

Independent citations: 32

6. **Denes A^{*#}**, McColl BW, Leow-Dyke SF, Chapman KZ, Humphreys NE, Grecis RK, Allan SM[#], Rothwell NJ (2011) Experimental stroke-induced changes in the bone marrow reveal complex regulation of leukocyte responses. *Journal of cerebral blood flow and metabolism: official journal of the International Society of Cerebral Blood Flow and Metabolism* 31 (4):1036-1050. doi:10.1038/jcbfm.2010.198

IF: 5.008

Independent citations: 47

7. Houlden A, Goldrick M, Brough D, Vizi ES, Lenart N, Martinecz B, Roberts IS^{*#}, **Denes A^{*#}** (2016) Brain injury induces specific changes in the caecal microbiota of mice via altered autonomic activity and mucoprotein production. *Brain, behavior, and immunity* 57:10-20. doi:10.1016/j.bbi.2016.04.003

IF: 5.964

Independent citations: 180

8. Szigeti K, Horvath I, Veres DS, Martinecz B, Lenart N, Kovacs N, Bakcsa E, Marta A, Semjeni M, Mathe D, **Denes A^{*#}** (2015) A novel SPECT-based approach reveals early mechanisms of central and peripheral inflammation after cerebral ischemia. *Journal of cerebral blood flow and metabolism: official journal of the International Society of Cerebral Blood Flow and Metabolism* 35 (12):1921-1929. doi:10.1038/jcbfm.2015.174

IF: 4.929

Independent citations: 20

9. Helyes Z^{*#}, Tekus V, Szentés N, Pohoczky K, Botz B, Kiss T, Kemeny A, Kornyei Z, Toth K, Lenart N, Abraham H, Pinteaux E, Francis S, Sensi S, **Denes A^{*#}**, Goebel A^{*#} (2019) Transfer of complex regional pain syndrome to mice via human autoantibodies is mediated by interleukin-1-induced mechanisms. *Proceedings of the National Academy of Sciences of the United States of America* 116 (26):13067-13076. doi:10.1073/pnas.1820168116

IF: 9.412

Independent citations: 25

Chapter 3

1. **Denes A^{*#}**, Ferenczi S, Halasz J, Kornyei Z, Kovacs KJ[#] (2008) Role of CX3CR1 (fractalkine receptor) in brain damage and inflammation induced by focal cerebral ischemia in mouse. *Journal of cerebral blood flow and metabolism: official journal of the International Society of Cerebral Blood Flow and Metabolism* 28 (10):1707-1721. doi:10.1038/jcbfm.2008.64

IF: 5.741

Independent citations: 202

2. Szalay G, Martinecz B, Lenart N, Kornyei Z, Orsolits B, Judak L, Csaszar E, Fekete R, West BL, Katona G, Rozsa B^{*#}, **Denes A^{*#}** (2016) Microglia protect against brain injury and their selective elimination dysregulates neuronal network activity after stroke. *Nature communications* 7:11499. doi:10.1038/ncomms11499

IF: 12.124

Independent citations: 278

3. Cserep C, Posfai B, Lenart N, Fekete R, Laszlo ZI, Lele Z, Orsolits B, Molnar G, Heindl S, Schwarcz AD, Ujvari K, Kornyei Z, Toth K, Szabadits E, Sperlagh B, Baranyi M, Csiba L, Hortobagyi T, Magloczky Z, Martinecz B, Szabo G, Erdelyi F, Szipocs R, Tamkun MM, Gesierich B, Duering M, Katona I, Liesz A, Tamas G, **Denes A^{*#}** (2020) Microglia monitor and protect neuronal function through specialized somatic purinergic junctions. *Science* 367 (6477):528-537. doi:10.1126/science.aax6752

IF: 47.728

Independent citations: 157

4. Varga DP, Menyhart A, Posfai B, Csaszar E, Lenart N, Cserep C, Orsolits B, Martinecz B, Szlepek T, Bari F, Farkas E^{*#}, **Denes A^{*#}** (2020) Microglia alter the threshold of spreading depolarization and related potassium uptake in the mouse brain. *Journal of cerebral blood flow and metabolism: official journal of the International Society of Cerebral Blood Flow and Metabolism* 40 (1_suppl):S67-S80. doi:10.1177/0271678X19900097

IF: 6.2

Independent citations: 11

5. Fekete R, Cserep C, Lenart N, Toth K, Orsolits B, Martinecz B, Mehes E, Szabo B, Nemeth V, Gonci B, Sperlagh B, Boldogkoi Z, Kittel A, Baranyi M, Ferenczi S, Kovacs K, Szalay G, Rozsa B, Webb C, Kovacs GG, Hortobagyi T, West BL, Kornyei Z, **Denes A^{*#}** (2018) Microglia control the spread of neurotropic virus infection via P2Y12 signalling and recruit monocytes through P2Y12-independent mechanisms. *Acta neuropathologica* 136 (3):461-482. doi:10.1007/s00401-018-1885-0

IF: 18.174

Independent citations: 67

6. Csaszar E, Lenart N, Cserep C, Kornyei Z, Fekete R, Posfai B, Balazsfi D, Hangya B, Schwarcz AD, Szabadits E, Szollosi D, Szigeti K, Mathe D, West BL, Sviatko K, Bras AR, Mariani JC, Kliewer A, Lenkei Z, Hricisak L, Benyo Z, Baranyi M, Sperlagh B, Menyhart A, Farkas E, **Denes A^{*#}** (2022) Microglia modulate blood flow, neurovascular coupling, and hypoperfusion via purinergic actions. *The Journal of experimental medicine* 219 (3). doi:10.1084/jem.20211071

IF: 14.307

Independent citations: 1

#First/last or joint first/last author; *Corresponding author

(Citation data: MTMT2 (<https://www.mtmt.hu/mtmt-2>) 01.06.2022)

Review articles

1. Cserep C, Posfai B, **Denes A^{*#}** (2021) Shaping Neuronal Fate: Functional Heterogeneity of Direct Microglia-Neuron Interactions. *Neuron* 109 (2):222-240. doi:10.1016/j.neuron.2020.11.007
2. Posfai, B., Cserep, C., Orsolits, B. & **Denes, A^{*#}** (2019). New Insights into Microglia-Neuron Interactions: A Neuron's Perspective. *Neuroscience* 405, 103-117.
3. Lenart, N., Brough, D. & **Denes, A^{*#}** (2016). Inflammasomes link vascular disease with neuroinflammation and brain disorders. *Journal of cerebral blood flow and metabolism : official journal of the International Society of Cerebral Blood Flow and Metabolism* 36, 1668-1685.
4. Smith CJ, **Denes A**, Tyrrell PJ, Di Napoli M (2015) Phase II anti-inflammatory and immune-modulating drugs for acute ischaemic stroke. *Expert opinion on investigational drugs* 24 (5):623-643. doi:10.1517/13543784.2015.1020110
5. Smith CJ^{*#}, Lawrence CB^{*}, Rodriguez-Grande B, Kovacs KJ, Pradillo JM, **Denes A^{*#}** (2013) The immune system in stroke: clinical challenges and their translation to experimental research. *Journal of neuroimmune pharmacology: the official journal of the Society on NeuroImmune Pharmacology* 8 (4):867-887. doi:10.1007/s11481-013-9469-1
6. **Denes A^{*#}**, Pinteaux E, Rothwell NJ, Allan SM (2011) Interleukin-1 and stroke: biomarker, harbinger of damage, and therapeutic target. *Cerebrovasc Dis* 32 (6):517-527. doi:10.1159/000332205
7. **Denes A[#]**, Thornton P, Rothwell NJ, Allan SM (2010) Inflammation and brain injury: acute cerebral ischaemia, peripheral and central inflammation. *Brain, behavior, and immunity* 24 (5):708-723. doi:10.1016/j.bbi.2009.09.010

Acknowledgements

I can't be grateful enough for all the help, support and love I have received along the way, and for which I have so many people to thank... Anna, Erika, my mother, my father, my sister, my brother, my grandparents and all of you, back to my earliest memories. You let me play all the time. I wish I could tell this to many of you, who are no longer with us...

I'm grateful to those who shaped my thinking before I had to decide what I would do for most of my life. Szabolcs Homonnay, you were not only one of the many great teachers I have had over the years, but someone to show the way when I was about to get lost.

Lucky ones get great mentors who help them to overcome obstacles, but mentors of the really lucky ones teach you that obstacles are mostly inside you...I am grateful to Krisztina Kovács, without whom I would have never grown up, to Miklós Palkovits, who opened those doors, and to Nancy Rothwell, who managed to make me believe that intellect, interest, good attitude, humanity and great science can go hand in hand and that I should never be afraid of moving out of my comfort zone. I also owe thanks to scientists, who have inspired my thinking as great minds and research leaders and supported me: Tamás Freund, Szilveszter E Vizi, László Lovász, Ferencz Hudecz, Zoltán Nusser, Gábor Tamás, István Katona, István Mody, Gyuri Buzsáki, Martin Dichgans, Uli Dirnagl and many others. Special thanks goes to all of my colleagues at KOKI and the University of Manchester.

Lucky ones have helpful colleagues for working hours and good friends to spend time with beyond that...I feel honoured that I have so many colleagues whom I can consider friends, intellectual hubs and reliable collaborators at the same time. And many of you, who have greatly influenced me, or who have managed to find solutions for problems that had appeared unmanagable before. Some of you have a very special place in my heart, and I am afraid that I cannot even list all of you: Szilvi Benkő, Andrea Fekete, Éva Mikics, Eszter Farkas, Zsuzsanna Helyes, Cath Lawrence, Arthur Liesz, István Ábrahám (†), Attila Mócsai, Zsolt Boldogkői, Tibor Hortobágyi, Beáta Sperlággh, Stuart Allan, Emmanuel Pinteaux, David Brough, Pete Thornton, Barry McColl, Ashley Houlden, Jesus Pradillo, Craig Smith, Anna Planas, Denis Vivien, Zsolt Lenkei, Andreas Meisel, and many others. Great thanks to our past and present collaborators I could not name here, from whom I have recieved a lot of help and support.

None of our discoveries would exist without my close colleagues and friends, who inspired me with their enthusiasm, untainted criticism, and the never-resting hunger for answers to those difficult questions, an attitue being strong enough to overcome all difficulties and to find the light at end of the tunnel ... *per aspera ad astra*...I would not stand here without you: Nikolett Lénárt, Eszter Császár, Zsu Környei, Rebeka Fekete, Bernadett Martinecz, Krisztina Toth, Eszter Szabadics, Csaba Cserép, Balázs Pósfai, Anett Schwarcz, Dóra Gali-Györkei, Rita Bras, Caroline Drake, Hannah Buggiey and Beatriz Rodriques-Grande.

I am also very grateful for funding agencies and research programs, who found merit in our work: Momentum Program of the Hungarian Academy of Sciences, NKFIH (OTKA), Hungarian Brain Research Program, ERC and some more. Thank you all.

References

1. Stringhini, S. *et al.* Socioeconomic status and the 25 x 25 risk factors as determinants of premature mortality: a multicohort study and meta-analysis of 1.7 million men and women. *Lancet* **389**, 1229-1237 (2017).
2. Chetty, R. *et al.* The Association Between Income and Life Expectancy in the United States, 2001-2014. *Jama* **315**, 1750-1766 (2016).
3. Mascie-Taylor, C.G. & Karim, E. The burden of chronic disease. *Science* **302**, 1921-1922 (2003).
4. Nalbandian, A. *et al.* Post-acute COVID-19 syndrome. *Nature medicine* **27**, 601-615 (2021).
5. Lopez-Leon, S. *et al.* More than 50 long-term effects of COVID-19: a systematic review and meta-analysis. *Sci Rep-Uk* **11** (2021).
6. Bedford, J. *et al.* A new twenty-first century science for effective epidemic response. *Nature* **575**, 130-136 (2019).
7. Yach, D., Hawkes, C., Gould, C.L. & Hofman, K.J. The global burden of chronic diseases: overcoming impediments to prevention and control. *Jama* **291**, 2616-2622 (2004).
8. Olesen, J., Gustavsson, A., Svensson, M., Wittchen, H.U. & Jonsson, B. The economic cost of brain disorders in Europe. *European journal of neurology* **19**, 155-162 (2012).
9. Borgoni, S., Kudryashova, K.S., Burka, K. & de Magalhaes, J.P. Targeting immune dysfunction in aging. *Ageing research reviews* **70**, 101410 (2021).
10. Fraga, S. *et al.* Association of socioeconomic status with inflammatory markers: a two cohort comparison. *Preventive medicine* **71**, 12-19 (2015).
11. Furman, D. *et al.* Chronic inflammation in the etiology of disease across the life span. *Nature medicine* **25**, 1822-1832 (2019).
12. Verkhratsky, A. & Nedergaard, M. The homeostatic astroglia emerges from evolutionary specialization of neural cells. *Philosophical transactions of the Royal Society of London. Series B, Biological sciences* **371** (2016).
13. Oberheim, N.A. *et al.* Uniquely hominid features of adult human astrocytes. *The Journal of neuroscience : the official journal of the Society for Neuroscience* **29**, 3276-3287 (2009).
14. Geirsdottir, L. *et al.* Cross-Species Single-Cell Analysis Reveals Divergence of the Primate Microglia Program. *Cell* **181**, 746 (2020).
15. Azevedo, F.A. *et al.* Equal numbers of neuronal and nonneuronal cells make the human brain an isometrically scaled-up primate brain. *The Journal of comparative neurology* **513**, 532-541 (2009).
16. Attwell, D. *et al.* Glial and neuronal control of brain blood flow. *Nature* **468**, 232-243 (2010).
17. Iadecola, C. The Neurovascular Unit Coming of Age: A Journey through Neurovascular Coupling in Health and Disease. *Neuron* **96**, 17-42 (2017).
18. Kisler, K., Nelson, A.R., Montagne, A. & Zlokovic, B.V. Cerebral blood flow regulation and neurovascular dysfunction in Alzheimer disease. *Nature reviews. Neuroscience* **18**, 419-434 (2017).
19. Bradl, M. & Lassmann, H. Oligodendrocytes: biology and pathology. *Acta neuropathologica* **119**, 37-53 (2010).
20. Franklin, R.J. & Ffrench-Constant, C. Remyelination in the CNS: from biology to therapy. *Nature reviews. Neuroscience* **9**, 839-855 (2008).
21. Siracusa, R., Fusco, R. & Cuzzocrea, S. Astrocytes: Role and Functions in Brain Pathologies. *Frontiers in pharmacology* **10**, 1114 (2019).
22. Sofroniew, M.V. & Vinters, H.V. Astrocytes: biology and pathology. *Acta neuropathologica* **119**, 7-35 (2010).

23. Escartin, C. *et al.* Reactive astrocyte nomenclature, definitions, and future directions. *Nature neuroscience* **24**, 312-325 (2021).
24. Dantzer, R. Neuroimmune Interactions: From the Brain to the Immune System and Vice Versa. *Physiological reviews* **98**, 477-504 (2018).
25. Louveau, A. *et al.* Understanding the functions and relationships of the glymphatic system and meningeal lymphatics. *The Journal of clinical investigation* **127**, 3210-3219 (2017).
26. Prinz, M. & Priller, J. The role of peripheral immune cells in the CNS in steady state and disease. *Nature neuroscience* **20**, 136-144 (2017).
27. Denes, A., Thornton, P., Rothwell, N.J. & Allan, S.M. Inflammation and brain injury: acute cerebral ischaemia, peripheral and central inflammation. *Brain, behavior, and immunity* **24**, 708-723 (2010).
28. Hablitz, L.M. & Nedergaard, M. The Glymphatic System: A Novel Component of Fundamental Neurobiology. *The Journal of neuroscience : the official journal of the Society for Neuroscience* **41**, 7698-7711 (2021).
29. Gherzi-Egea, J.F. *et al.* Molecular anatomy and functions of the choroidal blood-cerebrospinal fluid barrier in health and disease. *Acta neuropathologica* **135**, 337-361 (2018).
30. Han, R.T., Kim, R.D., Molofsky, A.V. & Liddelow, S.A. Astrocyte-immune cell interactions in physiology and pathology. *Immunity* **54**, 211-224 (2021).
31. Kierdorf, K., Masuda, T., Jordao, M.J.C. & Prinz, M. Macrophages at CNS interfaces: ontogeny and function in health and disease. *Nature reviews. Neuroscience* **20**, 547-562 (2019).
32. Ginhoux, F. *et al.* Fate mapping analysis reveals that adult microglia derive from primitive macrophages. *Science* **330**, 841-845 (2010).
33. Schulz, C. *et al.* A lineage of myeloid cells independent of Myb and hematopoietic stem cells. *Science* **336**, 86-90 (2012).
34. Marquez-Ropero, M., Benito, E., Plaza-Zabala, A. & Sierra, A. Microglial Corpse Clearance: Lessons From Macrophages. *Frontiers in immunology* **11**, 506 (2020).
35. Matcovitch-Natan, O. *et al.* Microglia development follows a stepwise program to regulate brain homeostasis. *Science* **353**, aad8670 (2016).
36. Verney, C., Monier, A., Fallet-Bianco, C. & Gressens, P. Early microglial colonization of the human forebrain and possible involvement in periventricular white-matter injury of preterm infants. *Journal of anatomy* **217**, 436-448 (2010).
37. Menassa, D.A. & Gomez-Nicola, D. Microglial Dynamics During Human Brain Development. *Frontiers in immunology* **9**, 1014 (2018).
38. Erny, D. & Prinz, M. How microbiota shape microglial phenotypes and epigenetics. *Glia* (2020).
39. Fuger, P. *et al.* Microglia turnover with aging and in an Alzheimer's model via long-term in vivo single-cell imaging. *Nature neuroscience* **20**, 1371-1376 (2017).
40. Reu, P. *et al.* The Lifespan and Turnover of Microglia in the Human Brain. *Cell reports* **20**, 779-784 (2017).
41. Erblich, B., Zhu, L., Etgen, A.M., Dobrenis, K. & Pollard, J.W. Absence of colony stimulation factor-1 receptor results in loss of microglia, disrupted brain development and olfactory deficits. *PLoS one* **6**, e26317 (2011).
42. Goldmann, T. *et al.* Origin, fate and dynamics of macrophages at central nervous system interfaces. *Nature immunology* **17**, 797-805 (2016).
43. Hume, D.A. *et al.* Phenotypic impacts of CSF1R deficiencies in humans and model organisms. *Journal of leukocyte biology* **107**, 205-219 (2020).
44. Rojo, R. *et al.* Deletion of a Csf1r enhancer selectively impacts CSF1R expression and development of tissue macrophage populations. *Nature communications* **10**, 3215 (2019).
45. Oosterhof, N. *et al.* Homozygous Mutations in CSF1R Cause a Pediatric-Onset Leukoencephalopathy and Can Result in Congenital Absence of Microglia. *American journal of human genetics* **104**, 936-947 (2019).

46. Cunningham, C.L., Martinez-Cerdeno, V. & Noctor, S.C. Microglia regulate the number of neural precursor cells in the developing cerebral cortex. *The Journal of neuroscience : the official journal of the Society for Neuroscience* **33**, 4216-4233 (2013).
47. Aarum, J., Sandberg, K., Haeberlein, S.L. & Persson, M.A. Migration and differentiation of neural precursor cells can be directed by microglia. *Proceedings of the National Academy of Sciences of the United States of America* **100**, 15983-15988 (2003).
48. Paolicelli, R.C. *et al.* Synaptic pruning by microglia is necessary for normal brain development. *Science* **333**, 1456-1458 (2011).
49. Schafer, D.P. *et al.* Microglia sculpt postnatal neural circuits in an activity and complement-dependent manner. *Neuron* **74**, 691-705 (2012).
50. Ueno, M. *et al.* Layer V cortical neurons require microglial support for survival during postnatal development. *Nature neuroscience* **16**, 543-551 (2013).
51. Eggen, B.J.L., Boddeke, E. & Kooistra, S.M. Regulation of Microglia Identity from an Epigenetic and Transcriptomic Point of View. *Neuroscience* **405**, 3-13 (2019).
52. Squarzoni, P. *et al.* Microglia modulate wiring of the embryonic forebrain. *Cell reports* **8**, 1271-1279 (2014).
53. Tan, Y.L., Yuan, Y. & Tian, L. Microglial regional heterogeneity and its role in the brain. *Molecular psychiatry* **25**, 351-367 (2020).
54. Galatro, T.F. *et al.* Transcriptomic analysis of purified human cortical microglia reveals age-associated changes. *Nature neuroscience* **20**, 1162-1171 (2017).
55. Grabert, K. *et al.* Microglial brain region-dependent diversity and selective regional sensitivities to aging. *Nature neuroscience* **19**, 504-516 (2016).
56. Hanisch, U.K. Functional diversity of microglia - how heterogeneous are they to begin with? *Frontiers in cellular neuroscience* **7**, 65 (2013).
57. Ohsawa, K. & Kohsaka, S. Dynamic motility of microglia: purinergic modulation of microglial movement in the normal and pathological brain. *Glia* **59**, 1793-1799 (2011).
58. Szalay, G. *et al.* Microglia protect against brain injury and their selective elimination dysregulates neuronal network activity after stroke. *Nat Commun* **7**, 11499 (2016).
59. Cserep, C. *et al.* Microglia monitor and protect neuronal function through specialized somatic purinergic junctions. *Science* **367**, 528-537 (2020).
60. Bernier, L.P. *et al.* Microglial metabolic flexibility supports immune surveillance of the brain parenchyma. *Nature communications* **11**, 1559 (2020).
61. Kettenmann, H., Hanisch, U.K., Noda, M. & Verkhratsky, A. Physiology of microglia. *Physiological reviews* **91**, 461-553 (2011).
62. Wolf, S.A., Boddeke, H.W. & Kettenmann, H. Microglia in Physiology and Disease. *Annual review of physiology* **79**, 619-643 (2017).
63. Tremblay, M.E., Lecours, C., Samson, L., Sanchez-Zafra, V. & Sierra, A. From the Cajal alumni Achucarro and Rio-Hortega to the rediscovery of never-resting microglia. *Frontiers in neuroanatomy* **9**, 45 (2015).
64. Davalos, D. *et al.* ATP mediates rapid microglial response to local brain injury in vivo. *Nature neuroscience* **8**, 752-758 (2005).
65. Nimmerjahn, A., Kirchhoff, F. & Helmchen, F. Resting microglial cells are highly dynamic surveillants of brain parenchyma in vivo. *Science* **308**, 1314-1318 (2005).
66. Miller, E.B., Zhang, P., Ching, K., Pugh, E.N., Jr. & Burns, M.E. In vivo imaging reveals transient microglia recruitment and functional recovery of photoreceptor signaling after injury. *Proceedings of the National Academy of Sciences of the United States of America* **116**, 16603-16612 (2019).
67. H, E.H., Noristani, H.N. & Perrin, F.E. Microglia Responses in Acute and Chronic Neurological Diseases: What Microglia-Specific Transcriptomic Studies Taught (and did Not Teach) Us. *Frontiers in aging neuroscience* **9**, 227 (2017).
68. Izzy, S. *et al.* Time-Dependent Changes in Microglia Transcriptional Networks Following Traumatic Brain Injury. *Frontiers in cellular neuroscience* **13**, 307 (2019).

69. Denes, A. *et al.* Proliferating resident microglia after focal cerebral ischaemia in mice. *Journal of cerebral blood flow and metabolism : official journal of the International Society of Cerebral Blood Flow and Metabolism* **27**, 1941-1953 (2007).
70. Donat, C.K., Scott, G., Gentleman, S.M. & Sastre, M. Microglial Activation in Traumatic Brain Injury. *Frontiers in aging neuroscience* **9**, 208 (2017).
71. Ransohoff, R.M. A polarizing question: do M1 and M2 microglia exist? *Nature neuroscience* **19**, 987-991 (2016).
72. Deczkowska, A. *et al.* Disease-Associated Microglia: A Universal Immune Sensor of Neurodegeneration. *Cell* **173**, 1073-1081 (2018).
73. Hoogland, I.C., Houbolt, C., van Westerloo, D.J., van Gool, W.A. & van de Beek, D. Systemic inflammation and microglial activation: systematic review of animal experiments. *Journal of neuroinflammation* **12**, 114 (2015).
74. Westhoff, D. *et al.* Systemic infection and microglia activation: a prospective postmortem study in sepsis patients. *Immunity & ageing : I & A* **16**, 18 (2019).
75. Sousa, C. *et al.* Single-cell transcriptomics reveals distinct inflammation-induced microglia signatures. *EMBO reports* **19** (2018).
76. Wendeln, A.C. *et al.* Innate immune memory in the brain shapes neurological disease hallmarks. *Nature* **556**, 332-338 (2018).
77. Butovsky, O. *et al.* Identification of a unique TGF-beta-dependent molecular and functional signature in microglia. *Nature neuroscience* **17**, 131-143 (2014).
78. Suzumura, A., Sawada, M., Yamamoto, H. & Marunouchi, T. Transforming growth factor-beta suppresses activation and proliferation of microglia in vitro. *J Immunol* **151**, 2150-2158 (1993).
79. Zoller, T. *et al.* Silencing of TGFbeta signalling in microglia results in impaired homeostasis. *Nature communications* **9**, 4011 (2018).
80. Bosco, P. *et al.* Role of the Transforming-Growth-Factor-beta1 Gene in Late-Onset Alzheimer's Disease: Implications for the Treatment. *Current genomics* **14**, 147-156 (2013).
81. Zhang, Y. & Yang, X. The Roles of TGF-beta Signaling in Cerebrovascular Diseases. *Frontiers in cell and developmental biology* **8**, 567682 (2020).
82. Adams, S.J., Kirk, A. & Auer, R.N. Adult-onset leukoencephalopathy with axonal spheroids and pigmented glia (ALSP): Integrating the literature on hereditary diffuse leukoencephalopathy with spheroids (HDLS) and pigmentary orthochromatic leukodystrophy (POLD). *Journal of clinical neuroscience : official journal of the Neurosurgical Society of Australasia* **48**, 42-49 (2018).
83. Paloneva, J. *et al.* Loss-of-function mutations in TYROBP (DAP12) result in a presenile dementia with bone cysts. *Nature genetics* **25**, 357-361 (2000).
84. Chouery, E. *et al.* Mutations in TREM2 lead to pure early-onset dementia without bone cysts. *Human mutation* **29**, E194-204 (2008).
85. Bianchin, M.M., Martin, K.C., de Souza, A.C., de Oliveira, M.A. & Rieder, C.R. Nasu-Hakola disease and primary microglial dysfunction. *Nature reviews. Neurology* **6**, 2 p following 523 (2010).
86. Neumann, H. & Takahashi, K. Essential role of the microglial triggering receptor expressed on myeloid cells-2 (TREM2) for central nervous tissue immune homeostasis. *Journal of neuroimmunology* **184**, 92-99 (2007).
87. Gunner, G. *et al.* Sensory lesioning induces microglial synapse elimination via ADAM10 and fractalkine signaling. *Nature neuroscience* **22**, 1075-1088 (2019).
88. Parkhurst, C.N. *et al.* Microglia promote learning-dependent synapse formation through brain-derived neurotrophic factor. *Cell* **155**, 1596-1609 (2013).
89. Diaz-Aparicio, I. *et al.* Microglia Actively Remodel Adult Hippocampal Neurogenesis through the Phagocytosis Secretome. *The Journal of neuroscience : the official journal of the Society for Neuroscience* **40**, 1453-1482 (2020).
90. De Lucia, C. *et al.* Microglia regulate hippocampal neurogenesis during chronic neurodegeneration. *Brain, behavior, and immunity* **55**, 179-190 (2016).

91. Olah, M. *et al.* A transcriptomic atlas of aged human microglia. *Nature communications* **9**, 539 (2018).
92. Pruss, H. Autoantibodies in neurological disease. *Nature reviews. Immunology* (2021).
93. Bhagavati, S. Autoimmune Disorders of the Nervous System: Pathophysiology, Clinical Features, and Therapy. *Frontiers in neurology* **12**, 664664 (2021).
94. Rijkers, K. *et al.* The role of interleukin-1 in seizures and epilepsy: a critical review. *Experimental neurology* **216**, 258-271 (2009).
95. Rana, A. & Musto, A.E. The role of inflammation in the development of epilepsy. *Journal of neuroinflammation* **15**, 144 (2018).
96. Chiavegato, A., Zurolo, E., Losi, G., Aronica, E. & Carmignoto, G. The inflammatory molecules IL-1beta and HMGB1 can rapidly enhance focal seizure generation in a brain slice model of temporal lobe epilepsy. *Frontiers in cellular neuroscience* **8**, 155 (2014).
97. Lenart, N., Brough, D. & Denes, A. Inflammasomes link vascular disease with neuroinflammation and brain disorders. *Journal of cerebral blood flow and metabolism : official journal of the International Society of Cerebral Blood Flow and Metabolism* **36**, 1668-1685 (2016).
98. Heneka, M.T. *et al.* NLRP3 is activated in Alzheimer's disease and contributes to pathology in APP/PS1 mice. *Nature* **493**, 674-678 (2013).
99. Ising, C. *et al.* NLRP3 inflammasome activation drives tau pathology. *Nature* **575**, 669-673 (2019).
100. Posfai, B., Cserep, C., Orsolits, B. & Denes, A. New Insights into Microglia-Neuron Interactions: A Neuron's Perspective. *Neuroscience* **405**, 103-117 (2019).
101. Sierra, A., Abiega, O., Shahraz, A. & Neumann, H. Janus-faced microglia: beneficial and detrimental consequences of microglial phagocytosis. *Frontiers in cellular neuroscience* **7**, 6 (2013).
102. Hong, S. *et al.* Complement and microglia mediate early synapse loss in Alzheimer mouse models. *Science* **352**, 712-716 (2016).
103. Crehan, H., Hardy, J. & Pocock, J. Microglia, Alzheimer's disease, and complement. *International journal of Alzheimer's disease* **2012**, 983640 (2012).
104. Wu, T. *et al.* Complement C3 Is Activated in Human AD Brain and Is Required for Neurodegeneration in Mouse Models of Amyloidosis and Tauopathy. *Cell reports* **28**, 2111-2123 e2116 (2019).
105. Krance, S.H. *et al.* The complement cascade in Alzheimer's disease: a systematic review and meta-analysis. *Molecular psychiatry* (2019).
106. Smith, C.J. *et al.* The immune system in stroke: clinical challenges and their translation to experimental research. *Journal of neuroimmune pharmacology : the official journal of the Society on NeuroImmune Pharmacology* **8**, 867-887 (2013).
107. Allan, S.M., Tyrrell, P.J. & Rothwell, N.J. Interleukin-1 and neuronal injury. *Nature reviews. Immunology* **5**, 629-640 (2005).
108. Denes, A., Pinteaux, E., Rothwell, N.J. & Allan, S.M. Interleukin-1 and stroke: biomarker, harbinger of damage, and therapeutic target. *Cerebrovasc Dis* **32**, 517-527 (2011).
109. Clausen, B.H. *et al.* Characterization of the TNF and IL-1 systems in human brain and blood after ischemic stroke. *Acta neuropathologica communications* **8**, 81 (2020).
110. Clausen, B.H. *et al.* Interleukin-1beta and tumor necrosis factor-alpha are expressed by different subsets of microglia and macrophages after ischemic stroke in mice. *Journal of neuroinflammation* **5**, 46 (2008).
111. Yrjanheikki, J., Keinanen, R., Pellikka, M., Hokfelt, T. & Koistinaho, J. Tetracyclines inhibit microglial activation and are neuroprotective in global brain ischemia. *Proceedings of the National Academy of Sciences of the United States of America* **95**, 15769-15774 (1998).
112. Arvin, K.L. *et al.* Minocycline markedly protects the neonatal brain against hypoxic-ischemic injury. *Annals of neurology* **52**, 54-61 (2002).

113. Han, Y. *et al.* Minocycline inhibits microglial activation and alleviates depressive-like behaviors in male adolescent mice subjected to maternal separation. *Psychoneuroendocrinology* **107**, 37-45 (2019).
114. Scholz, R. *et al.* Minocycline counter-regulates pro-inflammatory microglia responses in the retina and protects from degeneration. *Journal of neuroinflammation* **12**, 209 (2015).
115. Smith, C.J., Denes, A., Tyrrell, P.J. & Di Napoli, M. Phase II anti-inflammatory and immune-modulating drugs for acute ischaemic stroke. *Expert opinion on investigational drugs* **24**, 623-643 (2015).
116. Garrido-Mesa, N., Zarzuelo, A. & Galvez, J. Minocycline: far beyond an antibiotic. *British journal of pharmacology* **169**, 337-352 (2013).
117. Umpierre, A.D. & Wu, L.J. How microglia sense and regulate neuronal activity. *Glia* **69**, 1637-1653 (2021).
118. Kim, J.S. *et al.* A Binary Cre Transgenic Approach Dissects Microglia and CNS Border-Associated Macrophages. *Immunity* **54**, 176-190 e177 (2021).
119. Masuda, T. *et al.* Novel Hexb-based tools for studying microglia in the CNS. *Nature immunology* **21**, 802-815 (2020).
120. Jung, S. *et al.* Analysis of fractalkine receptor CX(3)CR1 function by targeted deletion and green fluorescent protein reporter gene insertion. *Molecular and cellular biology* **20**, 4106-4114 (2000).
121. Paolicelli, R.C., Bisht, K. & Tremblay, M.E. Fractalkine regulation of microglial physiology and consequences on the brain and behavior. *Frontiers in cellular neuroscience* **8**, 129 (2014).
122. Manich, G. *et al.* Role of the CD200-CD200R Axis During Homeostasis and Neuroinflammation. *Neuroscience* **405**, 118-136 (2019).
123. Larochelle, A., Bellavance, M.A., Michaud, J.P. & Rivest, S. Bone marrow-derived macrophages and the CNS: An update on the use of experimental chimeric mouse models and bone marrow transplantation in neurological disorders. *Biochimica et biophysica acta* **1862**, 310-322 (2016).
124. Ajami, B., Bennett, J.L., Krieger, C., McNagny, K.M. & Rossi, F.M. Infiltrating monocytes trigger EAE progression, but do not contribute to the resident microglia pool. *Nature neuroscience* **14**, 1142-1149 (2011).
125. Ajami, B., Bennett, J.L., Krieger, C., Tetzlaff, W. & Rossi, F.M. Local self-renewal can sustain CNS microglia maintenance and function throughout adult life. *Nature neuroscience* **10**, 1538-1543 (2007).
126. Bennett, F.C. *et al.* A Combination of Ontogeny and CNS Environment Establishes Microglial Identity. *Neuron* **98**, 1170-1183 e1178 (2018).
127. Shemer, A. *et al.* Engrafted parenchymal brain macrophages differ from microglia in transcriptome, chromatin landscape and response to challenge. *Nature communications* **9**, 5206 (2018).
128. Xu, R. *et al.* Human iPSC-derived mature microglia retain their identity and functionally integrate in the chimeric mouse brain. *Nature communications* **11**, 1577 (2020).
129. Heppner, F.L. *et al.* Experimental autoimmune encephalomyelitis repressed by microglial paralysis. *Nature medicine* **11**, 146-152 (2005).
130. Lund, H. *et al.* Competitive repopulation of an empty microglial niche yields functionally distinct subsets of microglia-like cells. *Nature communications* **9**, 4845 (2018).
131. Goldmann, T. *et al.* A new type of microglia gene targeting shows TAK1 to be pivotal in CNS autoimmune inflammation. *Nature neuroscience* **16**, 1618-1626 (2013).
132. Yona, S. *et al.* Fate mapping reveals origins and dynamics of monocytes and tissue macrophages under homeostasis. *Immunity* **38**, 79-91 (2013).
133. Tap, W.D. *et al.* Structure-Guided Blockade of CSF1R Kinase in Tenosynovial Giant-Cell Tumor. *The New England journal of medicine* **373**, 428-437 (2015).

134. Elmore, M.R. *et al.* Colony-stimulating factor 1 receptor signaling is necessary for microglia viability, unmasking a microglia progenitor cell in the adult brain. *Neuron* **82**, 380-397 (2014).
135. Shen, X.N. *et al.* Inflammatory markers in Alzheimer's disease and mild cognitive impairment: a meta-analysis and systematic review of 170 studies. *Journal of neurology, neurosurgery, and psychiatry* **90**, 590-598 (2019).
136. Nutma, E. *et al.* Cellular sources of TSPO expression in healthy and diseased brain. *European journal of nuclear medicine and molecular imaging* (2021).
137. Tournier, B.B., Tsartsalis, S., Ceyzeriat, K., Garibotto, V. & Millet, P. In Vivo TSPO Signal and Neuroinflammation in Alzheimer's Disease. *Cells* **9** (2020).
138. Luheshi, N.M., Kovacs, K.J., Lopez-Castejon, G., Brough, D. & Denes, A. Interleukin-1alpha expression precedes IL-1beta after ischemic brain injury and is localised to areas of focal neuronal loss and penumbral tissues. *Journal of neuroinflammation* **8**, 186 (2011).
139. Chan, A.H. & Schroder, K. Inflammasome signaling and regulation of interleukin-1 family cytokines. *The Journal of experimental medicine* **217** (2020).
140. Savage, C.D., Lopez-Castejon, G., Denes, A. & Brough, D. NLRP3-Inflammasome Activating DAMPs Stimulate an Inflammatory Response in Glia in the Absence of Priming Which Contributes to Brain Inflammation after Injury. *Frontiers in immunology* **3**, 288 (2012).
141. Denes, A. *et al.* Central and haematopoietic interleukin-1 both contribute to ischaemic brain injury in mice. *Disease models & mechanisms* **6**, 1043-1048 (2013).
142. Denes, A. *et al.* AIM2 and NLRC4 inflammasomes contribute with ASC to acute brain injury independently of NLRP3. *Proceedings of the National Academy of Sciences of the United States of America* **112**, 4050-4055 (2015).
143. Wong, R. *et al.* Interleukin-1 mediates ischaemic brain injury via distinct actions on endothelial cells and cholinergic neurons. *Brain, behavior, and immunity* **76**, 126-138 (2019).
144. Allen, C. *et al.* Neutrophil cerebrovascular transmigration triggers rapid neurotoxicity through release of proteases associated with decondensed DNA. *J Immunol* **189**, 381-392 (2012).
145. Otxoa-de-Amezaga, A. *et al.* Microglial cell loss after ischemic stroke favors brain neutrophil accumulation. *Acta neuropathologica* **137**, 321-341 (2019).
146. Kaila, K., Price, T.J., Payne, J.A., Puskarjov, M. & Voipio, J. Cation-chloride cotransporters in neuronal development, plasticity and disease. *Nature reviews. Neuroscience* **15**, 637-654 (2014).
147. Ben-Ari, Y. NKCC1 Chloride Importer Antagonists Attenuate Many Neurological and Psychiatric Disorders. *Trends in neurosciences* **40**, 536-554 (2017).
148. Toth, K. *et al.* The NKCC1 ion transporter modulates microglial phenotype and inflammatory response to brain injury in a cell-autonomous manner. *PLoS biology* **20**, e3001526 (2022).
149. McColl, B.W., Rothwell, N.J. & Allan, S.M. Systemic inflammatory stimulus potentiates the acute phase and CXC chemokine responses to experimental stroke and exacerbates brain damage via interleukin-1- and neutrophil-dependent mechanisms. *The Journal of neuroscience : the official journal of the Society for Neuroscience* **27**, 4403-4412 (2007).
150. Cliffe, L.J. & Grencis, R.K. The Trichuris muris system: a paradigm of resistance and susceptibility to intestinal nematode infection. *Advances in parasitology* **57**, 255-307 (2004).
151. Klementowicz, J.E., Travis, M.A. & Grencis, R.K. Trichuris muris: a model of gastrointestinal parasite infection. *Seminars in immunopathology* **34**, 815-828 (2012).
152. Denes, A., Humphreys, N., Lane, T.E., Grencis, R. & Rothwell, N. Chronic systemic infection exacerbates ischemic brain damage via a CCL5 (regulated on activation, normal T-cell expressed and secreted)-mediated proinflammatory response in mice.

- The Journal of neuroscience : the official journal of the Society for Neuroscience* **30**, 10086-10095 (2010).
153. Denes, A., Ferenczi, S. & Kovacs, K.J. Systemic inflammatory challenges compromise survival after experimental stroke via augmenting brain inflammation, blood- brain barrier damage and brain oedema independently of infarct size. *Journal of neuroinflammation* **8**, 164 (2011).
 154. Denes, A. *et al.* Streptococcus pneumoniae worsens cerebral ischemia via interleukin 1 and platelet glycoprotein Ibalpha. *Annals of neurology* **75**, 670-683 (2014).
 155. Thornton, P. *et al.* Platelet interleukin-1alpha drives cerebrovascular inflammation. *Blood* **115**, 3632-3639 (2010).
 156. Orsini, F. *et al.* Mannose-Binding Lectin Drives Platelet Inflammatory Phenotype and Vascular Damage After Cerebral Ischemia in Mice via IL (Interleukin)-1alpha. *Arteriosclerosis, thrombosis, and vascular biology* **38**, 2678-2690 (2018).
 157. Drake, C. *et al.* Brain inflammation is induced by co-morbidities and risk factors for stroke. *Brain, behavior, and immunity* **25**, 1113-1122 (2011).
 158. Denes, A. *et al.* Interleukin-1 mediates neuroinflammatory changes associated with diet-induced atherosclerosis. *Journal of the American Heart Association* **1**, e002006 (2012).
 159. Pradillo, J.M. *et al.* Delayed administration of interleukin-1 receptor antagonist reduces ischemic brain damage and inflammation in comorbid rats. *Journal of cerebral blood flow and metabolism : official journal of the International Society of Cerebral Blood Flow and Metabolism* **32**, 1810-1819 (2012).
 160. Denes, A., Boldogkoi, Z., Hornyak, A., Palkovits, M. & Kovacs, K.J. Attenuated pseudorabies virus-evoked rapid innate immune response in the rat brain. *Journal of neuroimmunology* **180**, 88-103 (2006).
 161. Denes, A. *et al.* Central autonomic control of the bone marrow: multisynaptic tract tracing by recombinant pseudorabies virus. *Neuroscience* **134**, 947-963 (2005).
 162. Denes, A. *et al.* Experimental stroke-induced changes in the bone marrow reveal complex regulation of leukocyte responses. *Journal of cerebral blood flow and metabolism : official journal of the International Society of Cerebral Blood Flow and Metabolism* **31**, 1036-1050 (2011).
 163. Houlden, A. *et al.* Brain injury induces specific changes in the caecal microbiota of mice via altered autonomic activity and mucoprotein production. *Brain, behavior, and immunity* **57**, 10-20 (2016).
 164. Szigeti, K. *et al.* A novel SPECT-based approach reveals early mechanisms of central and peripheral inflammation after cerebral ischemia. *Journal of cerebral blood flow and metabolism : official journal of the International Society of Cerebral Blood Flow and Metabolism* **35**, 1921-1929 (2015).
 165. Helyes, Z. *et al.* Transfer of complex regional pain syndrome to mice via human autoantibodies is mediated by interleukin-1-induced mechanisms. *Proceedings of the National Academy of Sciences of the United States of America* **116**, 13067-13076 (2019).
 166. Denes, A., Ferenczi, S., Halasz, J., Kornyei, Z. & Kovacs, K.J. Role of CX3CR1 (fractalkine receptor) in brain damage and inflammation induced by focal cerebral ischemia in mouse. *Journal of cerebral blood flow and metabolism : official journal of the International Society of Cerebral Blood Flow and Metabolism* **28**, 1707-1721 (2008).
 167. Cardona, A.E. *et al.* Control of microglial neurotoxicity by the fractalkine receptor. *Nature neuroscience* **9**, 917-924 (2006).
 168. Rugarli, E.I. & Langer, T. Mitochondrial quality control: a matter of life and death for neurons. *The EMBO journal* **31**, 1336-1349 (2012).
 169. Kasahara, A. & Scorrano, L. Mitochondria: from cell death executioners to regulators of cell differentiation. *Trends in cell biology* **24**, 761-770 (2014).
 170. Lin, M.T. & Beal, M.F. Mitochondrial dysfunction and oxidative stress in neurodegenerative diseases. *Nature* **443**, 787-795 (2006).

171. Burte, F., Carelli, V., Chinnery, P.F. & Yu-Wai-Man, P. Disturbed mitochondrial dynamics and neurodegenerative disorders. *Nature reviews. Neurology* **11**, 11-24 (2015).
172. Kirmiz, M., Vierra, N.C., Palacio, S. & Trimmer, J.S. Identification of VAPA and VAPB as Kv2 Channel-Interacting Proteins Defining Endoplasmic Reticulum-Plasma Membrane Junctions in Mammalian Brain Neurons. *The Journal of neuroscience : the official journal of the Society for Neuroscience* **38**, 7562-7584 (2018).
173. Johnson, B., Leek, A.N. & Tamkun, M.M. Kv2 channels create endoplasmic reticulum / plasma membrane junctions: a brief history of Kv2 channel subcellular localization. *Channels (Austin)* **13**, 88-101 (2019).
174. Dreier, J.P. The role of spreading depression, spreading depolarization and spreading ischemia in neurological disease. *Nature medicine* **17**, 439-447 (2011).
175. Varga, D.P. *et al.* Microglia alter the threshold of spreading depolarization and related potassium uptake in the mouse brain. *Journal of cerebral blood flow and metabolism : official journal of the International Society of Cerebral Blood Flow and Metabolism* **40**, S67-S80 (2020).
176. Fekete, R. *et al.* Microglia control the spread of neurotropic virus infection via P2Y12 signalling and recruit monocytes through P2Y12-independent mechanisms. *Acta neuropathologica* **136**, 461-482 (2018).
177. Csaszar, E. *et al.* Microglia modulate blood flow, neurovascular coupling, and hypoperfusion via purinergic actions. *The Journal of experimental medicine* **219** (2022).
178. Global, regional, and national burden of stroke and its risk factors, 1990-2019: a systematic analysis for the Global Burden of Disease Study 2019. *The Lancet. Neurology* **20**, 795-820 (2021).
179. Gooch, C.L., Pracht, E. & Borenstein, A.R. The burden of neurological disease in the United States: A summary report and call to action. *Annals of neurology* **81**, 479-484 (2017).
180. DiMasi, J.A., Grabowski, H.G. & Hansen, R.W. Innovation in the pharmaceutical industry: New estimates of R&D costs. *Journal of health economics* **47**, 20-33 (2016).
181. Ciociola, A.A., Cohen, L.B. & Kulkarni, P. How drugs are developed and approved by the FDA: current process and future directions. *The American journal of gastroenterology* **109**, 620-623 (2014).
182. Oxford, A.E., Stewart, E.S. & Rohn, T.T. Clinical Trials in Alzheimer's Disease: A Hurdle in the Path of Remedy. *International journal of Alzheimer's disease* **2020**, 5380346 (2020).
183. Berkhemer, O.A. *et al.* A randomized trial of intraarterial treatment for acute ischemic stroke. *The New England journal of medicine* **372**, 11-20 (2015).
184. Cummings, J. Lessons Learned from Alzheimer Disease: Clinical Trials with Negative Outcomes. *Clinical and translational science* **11**, 147-152 (2018).
185. Neuhaus, A.A., Couch, Y., Hadley, G. & Buchan, A.M. Neuroprotection in stroke: the importance of collaboration and reproducibility. *Brain : a journal of neurology* **140**, 2079-2092 (2017).
186. Cheng, Y.D., Al-Khoury, L. & Zivin, J.A. Neuroprotection for ischemic stroke: two decades of success and failure. *NeuroRx : the journal of the American Society for Experimental NeuroTherapeutics* **1**, 36-45 (2004).
187. Felsky, D. *et al.* Neuropathological correlates and genetic architecture of microglial activation in elderly human brain. *Nature communications* **10**, 409 (2019).
188. Lokman Cevik, M.J.A., José Javier Otero Neuropathologists play a key role in establishing the extent of COVID-19 in human patients. *Free Neuropathology* **1** (2020).
189. Wilcox, K.S. & Vezzani, A. Does brain inflammation mediate pathological outcomes in epilepsy? *Advances in experimental medicine and biology* **813**, 169-183 (2014).
190. Yokokura, M. *et al.* Depiction of microglial activation in aging and dementia: Positron emission tomography with [(11)C]DPA713 versus [(11)C](R)PK11195. *Journal of*

- cerebral blood flow and metabolism : official journal of the International Society of Cerebral Blood Flow and Metabolism* **37**, 877-889 (2017).
191. Efthymiou, A.G. & Goate, A.M. Late onset Alzheimer's disease genetics implicates microglial pathways in disease risk. *Molecular neurodegeneration* **12**, 43 (2017).
 192. McQuade, A. & Blurton-Jones, M. Microglia in Alzheimer's Disease: Exploring How Genetics and Phenotype Influence Risk. *Journal of molecular biology* **431**, 1805-1817 (2019).
 193. Da Mesquita, S. *et al.* Meningeal lymphatics affect microglia responses and anti-Abeta immunotherapy. *Nature* **593**, 255-260 (2021).
 194. Werry, E.L. *et al.* Recent Developments in TSPO PET Imaging as A Biomarker of Neuroinflammation in Neurodegenerative Disorders. *International journal of molecular sciences* **20** (2019).
 195. Surendranathan, A. *et al.* Early microglial activation and peripheral inflammation in dementia with Lewy bodies. *Brain : a journal of neurology* **141**, 3415-3427 (2018).
 196. Femminella, G.D. *et al.* Microglial activation in early Alzheimer trajectory is associated with higher gray matter volume. *Neurology* **92**, e1331-e1343 (2019).
 197. Patrick, E. *et al.* A cortical immune network map identifies distinct microglial transcriptional programs associated with beta-amyloid and Tau pathologies. *Translational psychiatry* **11**, 50 (2021).
 198. Malpetti, M. *et al.* Microglial activation and tau burden predict cognitive decline in Alzheimer's disease. *Brain : a journal of neurology* **143**, 1588-1602 (2020).
 199. Focke, C. *et al.* Early and Longitudinal Microglial Activation but Not Amyloid Accumulation Predicts Cognitive Outcome in PS2APP Mice. *Journal of nuclear medicine : official publication, Society of Nuclear Medicine* **60**, 548-554 (2019).
 200. Pascoal, T.A. *et al.* Microglial activation and tau propagate jointly across Braak stages. *Nature medicine* (2021).
 201. Vezzani, A. & Granata, T. Brain inflammation in epilepsy: experimental and clinical evidence. *Epilepsia* **46**, 1724-1743 (2005).
 202. Hiragi, T., Ikegaya, Y. & Koyama, R. Microglia after Seizures and in Epilepsy. *Cells* **7** (2018).
 203. Thiel, A. & Heiss, W.D. Imaging of microglia activation in stroke. *Stroke* **42**, 507-512 (2011).
 204. Cserep, C., Posfai, B. & Denes, A. Shaping Neuronal Fate: Functional Heterogeneity of Direct Microglia-Neuron Interactions. *Neuron* **109**, 222-240 (2021).
 205. Pawelec, P., Ziemka-Nalecz, M., Sypecka, J. & Zalewska, T. The Impact of the CX3CL1/CX3CR1 Axis in Neurological Disorders. *Cells* **9** (2020).
 206. Freiberg, B.A. *et al.* Staging and resetting T cell activation in SMACs. *Nature immunology* **3**, 911-917 (2002).
 207. Garcia, K.C. *et al.* An alphabeta T cell receptor structure at 2.5 Å and its orientation in the TCR-MHC complex. *Science* **274**, 209-219 (1996).
 208. Konishi, H. *et al.* Astrocytic phagocytosis is a compensatory mechanism for microglial dysfunction. *The EMBO journal* **39**, e104464 (2020).
 209. Damisah, E.C. *et al.* Astrocytes and microglia play orchestrated roles and respect phagocytic territories during neuronal corpse removal in vivo. *Science advances* **6**, eaba3239 (2020).
 210. Lee, K. *et al.* Human in vitro systems for examining synaptic function and plasticity in the brain. *Journal of neurophysiology* **123**, 945-965 (2020).
 211. Cavalli, G. & Dinarello, C.A. Anakinra Therapy for Non-cancer Inflammatory Diseases. *Frontiers in pharmacology* **9**, 1157 (2018).
 212. Kyriazopoulou, E. *et al.* Effect of anakinra on mortality in patients with COVID-19: a systematic review and patient-level meta-analysis. *The Lancet. Rheumatology* **3**, e690-e697 (2021).
 213. Smith, C.J. *et al.* SCIL-STROKE (Subcutaneous Interleukin-1 Receptor Antagonist in Ischemic Stroke): A Randomized Controlled Phase 2 Trial. *Stroke* **49**, 1210-1216 (2018).

214. Huang, H. *et al.* The WNK-SPAK/OSR1 Kinases and the Cation-Chloride Cotransporters as Therapeutic Targets for Neurological Diseases. *Aging and disease* **10**, 626-636 (2019).
215. Yang, A.C. *et al.* Dysregulation of brain and choroid plexus cell types in severe COVID-19. *Nature* **595**, 565-571 (2021).
216. Schwabenland, M. *et al.* Deep spatial profiling of human COVID-19 brains reveals neuroinflammation with distinct microanatomical microglia-T-cell interactions. *Immunity* **54**, 1594-1610 e1511 (2021).

Proliferating resident microglia after focal cerebral ischaemia in mice

Adam Denes¹, Rishma Vidyasagar², Jianghua Feng^{3,4}, Johanna Narvainen³, Barry W McColl³, Risto A Kauppinen² and Stuart M Allan³

¹Laboratory of Molecular Neuroendocrinology, Institute of Experimental Medicine, Hungarian Academy of Sciences, Budapest, Hungary; ²School of Sport and Exercise Sciences, University of Birmingham, Birmingham, UK; ³Faculty of Life Sciences, Michael Smith Building, University of Manchester, Manchester, UK; ⁴State Key Laboratory of Magnetic Resonance and Atomic and Molecular Physics, Wuhan Institute of Physics and Mathematics, The Chinese Academy of Sciences, Wuhan, China

Cerebral ischaemia usually results in the rapid death of neurons within the immediate territory of the affected artery. Neuronal loss is accompanied by a sequence of events, including brain oedema, blood–brain barrier (BBB) breakdown, and neuroinflammation, all of which contribute to further neuronal death. Although the role of macrophages and mononuclear phagocytes in the expansion of ischaemic injury has been widely studied, the relative contribution of these cells, either of exogenous or intrinsic central nervous system (CNS) origin is still not entirely clear. The purpose of this study, therefore, was to use different durations of transient middle cerebral artery occlusion (tMCAo) in the mouse to investigate fully post-occlusion BBB permeability and cellular changes in the brain during the 72 h post-MCAo period. This was achieved using *in vivo* magnetic resonance imaging (MRI) and cell labelling techniques. Our results show that BBB breakdown and formation of the primary ischaemic damage after tMCAo is not associated with significant infiltration of neutrophils, although more are observed with longer periods of MCAo. In addition, we observe very few infiltrating exogenous macrophages over a 72 h period after 30 or 60 mins of occlusion, instead a profound increase in proliferating resident microglia cells was observed. Interestingly, the more severe injury associated with 60 mins of MCAo leads to a markedly reduced proliferation of resident microglial cells, suggesting that these cells may play a protective function, possibly through phagocytosis of infiltrating neutrophils. These data further support possible beneficial actions of microglial cells in the injured brain.

Journal of Cerebral Blood Flow & Metabolism (2007) 27, 1941–1953; doi:10.1038/sj.jcbfm.9600495; published online 18 April 2007

Keywords: cell labelling; inflammation; MRI; macrophages; neurodegeneration

Introduction

Experimental paradigms of focal cerebral ischaemia show that tissue damage includes a rapidly and irreversibly damaging core and a surrounding region, known as the ‘penumbra,’ which is potentially salvageable (Ginsberg, 2003). In addition to the early events caused by compromised cerebral blood flow, there is also a delayed inflammatory response that takes place hours to days after ischaemia. Post-

ischaemic inflammatory events include activation of brain resident microglia and astrocytes (Clark *et al*, 1993; Davies *et al*, 1998; Morioka *et al*, 1993), as well as the infiltration of exogenous leukocytes such as polymorphonuclear granulocytes (Barone *et al*, 1991), macrophages (Yamagami *et al*, 1999), and lymphocytes (Schroeter *et al*, 1994) to the brain, which can increase neuronal damage (Barone *et al*, 1991; Dinkel *et al*, 2004; Jiang *et al*, 1995). The contribution of activated resident microglia versus infiltrating macrophages to ischaemic brain damage has been difficult to define because of similar immunophenotypes and other histological characteristics for these cells (Campanella *et al*, 2002; Davis *et al*, 1994; Zhang *et al*, 2005). Experiments with bone marrow chimeric mice have indicated significant differences in terms of the ratio and contribution of resident microglia versus exogenous infiltrating macrophages to early (up to 3 days) post-ischaemic inflammatory processes. After middle

Correspondence: Dr A Denes, Laboratory of Molecular Neuroendocrinology, Institute of Experimental Medicine, Szegony u. 43. Budapest H-1083, Hungary.
E-mail: denesa@koki.hu

This work was supported by EU Marie Curie Programme, The Sigrid Juselius Foundation, Medical Research Council, and the Wellcome Trust.

Received 1 December 2006; revised 31 January 2007; accepted 7 March 2007; published online 18 April 2007

cerebral artery occlusion (MCAo), massive infiltration of exogenous macrophages was reported 24 to 48 h after the insult as well as a profound dominance of resident microglia over infiltrating blood-borne macrophages during the first 4 days of reperfusion (Kokovay *et al.*, 2006; Schilling *et al.*, 2003, 2005; Tanaka *et al.*, 2003). Unfortunately, the evolution of the ischaemic damage was not correlated with the numbers of microglia/macrophage cells in these studies. It is known that microglia can enter the cell cycle and exert proliferating activity in the brain on various challenges, such as acute brain injury (Gowing *et al.*, 2006; Ladeby *et al.*, 2005) and global cerebral ischaemia (Liu *et al.*, 2001). Microglial proliferation may therefore contribute to increases in the number of mononuclear phagocytes in the brain parenchyma, although the time course and correlation with ischaemic damage of this response has not been studied in detail.

Therefore to investigate cellular changes after MCAo, we assessed the infiltration of mononuclear phagocytes into the brain *in vivo* and correlated this with intactness of the blood–brain barrier (BBB) (by contrast enhanced magnetic resonance imaging (MRI)), evolution of oedema, and tissue damage (by diffusion and T_2 MRI), as well as with histological analysis regarding the number of cells of different origin, and finally, damage formation. As it is likely that the duration of ischaemia and hence extent of neuronal injury will impact on these parameters, we studied two different MCAo periods, namely 30 and 60 mins.

We show that after tMCAo, microglial proliferation is the main factor behind the increase in the number of mononuclear phagocytes seen during the first 3 days and that the number of activated microglial cells negatively correlates with the extent of ischaemic brain damage. These findings suggest an advantageous role of newly produced brain-resident microglia in the post-ischaemic brain possibly owing to phagocytosis of neutrophils.

Materials and methods

Animals

Experiments were carried out in adult male C57Bl/6J mice (Harlan-Olac, UK) aged 12 to 14 weeks weighing 26 to 29 g ($n=62$). Animals had free access to food and water and were maintained under temperature, humidity, light-controlled conditions, under 12-h light/12-h dark cycle, with lights on at 0700 hours. All animal procedures were performed under an appropriate Home Office License and adhered to regulations as specified in the Animals (Scientific Procedures) Act (1986).

Transient Middle Cerebral Artery Occlusion

Anesthesia was induced with 1.5% isoflurane in a mixture of 30% oxygen and 70% nitrous oxide. During surgery, core temperature was monitored with a rectal

probe and maintained at $37 \pm 0.5^\circ\text{C}$, using a homeothermic blanket (Harvard Apparatus, UK). Animals were exposed to MCAo for 30 or 60 mins as described previously (Wheeler *et al.*, 2003), except that laser-Doppler was not used. Sham-operated animals had the common carotid artery clipped for 30 or 60 mins. In some control animals, the filament was advanced along the ICA until the origin of MCA and was retracted immediately, as a control for endothelial disruption by the filament.

Magnetic Resonance Imaging Scanning and Data Analysis

Mice were re-anaesthetized 4 h after tMCAo and underwent MRI scanning using a horizontal 7 T SMIS system (Guildford, Surrey, UK). A single loop surface coil (3 cm in diameter) was used for both signal reception and transmission. Ten 0.8-mm-thick coronal slices (slice gap 0.8 mm) were selected to cover the forebrain. T_1 images were acquired with $\text{TR}=700$ ms, $\text{TE}=10$ ms, $\text{FOV}=30$ mm, 256×128 (zero filled to 256×256 before FT). For T_2 images TR was 1,500 ms and TE either 30 or 60 ms. Diffusion images were obtained with $\text{TR}=1,800$ ms, $\text{TE}=60$ ms and $b=1,000$ secs/ mm^2 diffusion weighting applied along the slice selection gradient, data matrix 128×128 . AMI-227 (Ferumoxtran-10, Sinerem[®], Guerbet/France) $160 \mu\text{mol}$ of Fe/kg together with Magnevist (0.1 mmol/kg) was injected via the tail vein of conscious mice before ($n=8$) or immediately after ($n=14$) 30 mins of MCAo. Mice were re-injected with AMI-227/Magnevist 24, 48, and 72 h after MCAo occlusion (last AMI injection was injected 2 to 3 h before the last MRI scanning and 4 to 5 h before transcardial perfusion, respectively), anaesthetized with isoflurane, and scanned for MRI as described above.

The images were analysed using the software provided by SMIS. The areas with signal changes were manually delineated and percentage volumes of T_1 , T_2 , or diffusion abnormalities of total hemispheric volume determined.

In Situ Blood Cell Labelling with CFSE

Circulation-related blood cells were labelled *in situ* with carboxyfluorescein diacetate succinimidyl ester, injected via the tail vein into conscious, restrained animals. To label almost all blood cells, a slightly modified injection protocol was used (Becker *et al.*, 2004). Carboxyfluorescein diacetate succinimidyl ester (0.5 μg ; Molecular Probes, Eugene, OR, USA) was dissolved in 90 μL of high-quality dimethylsulphoxide according to the manufacturer's instructions. Stock solution (19 μL) was mixed with 80 μL of 100% ethyl alcohol, 300 μL of phosphate-buffered saline and with 0.5 μL of Pluronic F127 (Molecular Probes, Eugene, OR, USA), immediately before administration. After thorough mixing, 9 $\mu\text{L/g}$ body weight of the labelling solution was injected into the tail vein at an average rate of 50 $\mu\text{L}/\text{min}$. Carboxyfluorescein succinimidyl ester (CFSE) was administered 4 h before 30 ($n=17$) or 60 ($n=12$) mins of MCAo followed by 4, 24, 48, 72 h after MCAo, and 4, 24, 48 h after 30 ($n=14$) or 60 ($n=12$) mins of MCAo.

Blood samples were routinely collected to 3.8% sodium citrate (Sigma-Aldrich, UK) 30 mins, 4, 8, and 24 h after tracer administration. Cellular labelling with CFSE was evaluated by fluorescent microscope on native blood and bone marrow samples, as well as on leukocytes prepared from blood samples by hypoosmotic lysis with ACK solution (8.4 g/L ammonium chloride, 1 g/L potassium bicarbonate, and 1 mmol sodium ethylenediaminetetraacetic acid).

Administration of Bromodeoxyuridine

Bromodeoxyuridine (BrdU) (Sigma-Aldrich) was dissolved in 0.9% NaCl and 50 mg/kg was administered intraperitoneally twice daily after 30 or 60 mins of MCAo ($n=5$ to 7/group). Mice were killed 24, 48, and 72 h after MCAo. In a separate set of experiments, mice ($n=8$) received a single BrdU injection 22, 46, or 70 h after MCAo (2 h before transcardial perfusion). These experiments were performed to reveal the *in situ* dividing cells in the brain, testing the theoretical possibility that exogenous macrophages, which have incorporated BrdU migrate into the brain and might escape identification because of dilution of CFSE by cellular division, thereby appearing falsely as dividing microglia.

Tissue Processing

Under terminal anesthesia, mice were transcardially perfused with 10 mL saline followed by 40 mL 4% paraformaldehyde (PFA). Brain, spleen, femoral, and tibial bones (to sample bone marrow) were removed and post-fixed in 4% paraformaldehyde at 4°C for 24 h. After cryoprotection of brains and spleens in 20% sucrose/phosphate-buffered saline for 24 h, five alternate sets of 20 μ m coronal brain sections and two sets of spleen sections were cut on a sliding microtome. All sections were collected into an antifreeze solution (containing 30% ethylene glycol and 20% glycerol in phosphate-buffered saline) and stored at 20°C until processing.

Measurement of Infarct Volume using Histology

The volume of ischaemic damage was measured using a modification of the method described previously (McCull *et al*, 2004). Briefly, areas of ischaemic damage were identified on cresyl violet-stained sections at eight neuroanatomically defined coronal levels. Digitized images were created and areas of damage measured using ImageJ software. The volume of damage was calculated by integration of areas of damage with the distance between coronal levels. The end points for integration were 2.9 mm (rostral limit) and -4.9 mm (caudal limit) regarding bregma. Volumes are expressed as a percentage of total hemispheric volume.

Immunofluorescence

Double- or triple-labelling immunofluorescence was performed on free-floating sections. After blocking in 2%

normal donkey or goat sera (Vector Laboratories, Burlingame, CA, USA) sections were incubated overnight at 4°C in various mixtures of the following primary antibodies: monoclonal rat anti-mouse F4/80 1:400 (Serotec, UK), rat anti-mouse CD45 1:250 (Serotec, UK), polyclonal rabbit anti-Iba1 1:2,000 (Wako Chemicals, Germany), rat anti-mouse NIMP-R14 1:100 (Hycult Biotechnology, Uden, The Netherlands), rat anti-mouse BrdU 1:400 (Serotec, UK), goat anti-BrdU 1:1000 (Abcam, UK), rat anti-mouse CD34 1:400 (Pharmingen, San Diego, CA, USA). For detection of BrdU-labelled cells, sections were pretreated for 30 mins in 1 N HCl at 37°C.

The antigens were visualized with the adequate fluorochrome-conjugated secondary antisera (donkey anti-rat Alexa 594, goat anti-rabbit Alexa 594, donkey anti-goat Alexa 594, or donkey anti-rabbit Alexa 350, Molecular Probes) used in 1:500 dilutions for 2 h at room temperature. Sections were mounted onto gelatin-coated slides and cover-slipped with Vectashield mounting medium (Vector Laboratories) or with Vectashield mounting medium containing diamidinophenylindole.

To localize microglial cells and brain macrophages, sections were incubated with 6 μ g/mL biotinylated tomato lectin (Sigma, UK) for 2 h at room temperature according to Acarin *et al* (1994) and visualized in streptavidin-conjugated Alexa-350, 1:500 (Molecular Probes).

Mounted sections and stained cell cultures were analysed and images were viewed using an Olympus microscope. Double- or triple-fluorescent images were generated using MetaView software (Universal Imaging Corp., Downingtown, PA, USA). Quantification was performed on fluorescent images using the ImageJ (NIH, Bethesda, MD, USA) software. With the exception of phasing the brightness of the images and mild contrasting of pictures, no other modifications of presented images were done.

Histological Detection of AMI-227

Iron oxide particles were detected with Prussian Blue staining (2% HCl mixed with 2% potassium hexacyanoferrat Fe^{2+} (1:1), freshly prepared) on bone marrow and blood smears, blood leukocyte preparations, spleen, and on brain sections. On two sets of brain and spleen sections, after Prussian Blue staining diaminobenzidine enhancement was performed combined with subsequent silver/gold intensification as described recently (Schroeter *et al*, 2004). One set of sections was mounted and the histochemical iron staining was performed as originally described. The other set of free-floating sections was incubated in Prussian Blue solution and developed with diaminobenzidine, and then mounted and silver/gold intensification was performed. After the staining procedure sections were dehydrated and coverslipped with Depex mounting medium.

Statistical Analysis

Data are expressed as mean \pm s.d. One-way analysis of variance followed by *post hoc* Bonferroni's comparison was used to assess statistical differences in the cell numbers and proliferation among the different groups.

Results

Magnetic Resonance Imaging shows Blood–Brain Barrier Breakdown with no Significant Infiltration of AMI-227 Labelled Cells after Middle Cerebral Artery Occlusion

T₁-weighted MRI after Magnevist injection revealed no signs of contrast agent leakage 4 h after 30 mins of MCAo, although BBB leakage in all mice at 24 h after MCAo was evident (Figure 1A). T₂-weighted MRI showed the ischaemic lesion and oedema were complete by 24 h after MCAo, whereas diffusion MRI images revealed consistent size of abnormal brain volume with those determined by T₂-weighted MRI (Figures 1A and 1B).

AMI-227 is taken up by reticuloendothelial cells *in vivo*, including circulating macrophages. Owing to its superparamagnetic property intracellular iron oxide nanoparticles cause strong T₂^{*} (Rausch *et al*, 2001) and T₂ (Kavec *et al*, 2004) signal decrease as well as T₁-weighted signal (Rausch *et al*, 2001)

decrease. Interestingly, T₂-weighted MRI showed no signal void areas in or surrounding the ischaemic lesion in the mice injected repeatedly with AMI-227 (data not shown). This finding suggests that no leakage of this intravascular contrast agent through the BBB had occurred and/or that no significant number of AMI-227 containing cells were present in the post-ischaemic brain.

Iron-laden cells were detectable with Prussian Blue staining (with or without diaminobenzidine and silver/gold intensification) in bone marrow, blood smears, and in spleen sections up to 72 h after injection of AMI-227 (data not shown). However, although animals undergoing MCAo showed many more iron-laden cells in blood smears than sham-operated mice, in the brain parenchyma the average number of iron-laden cells was surprisingly low, with only a few single cells being seen in the ischaemic striatum (Figure 1C). Rarely, exogenous AMI-containing cells were recruited into the ischaemic striatum in small clusters, but the maximal

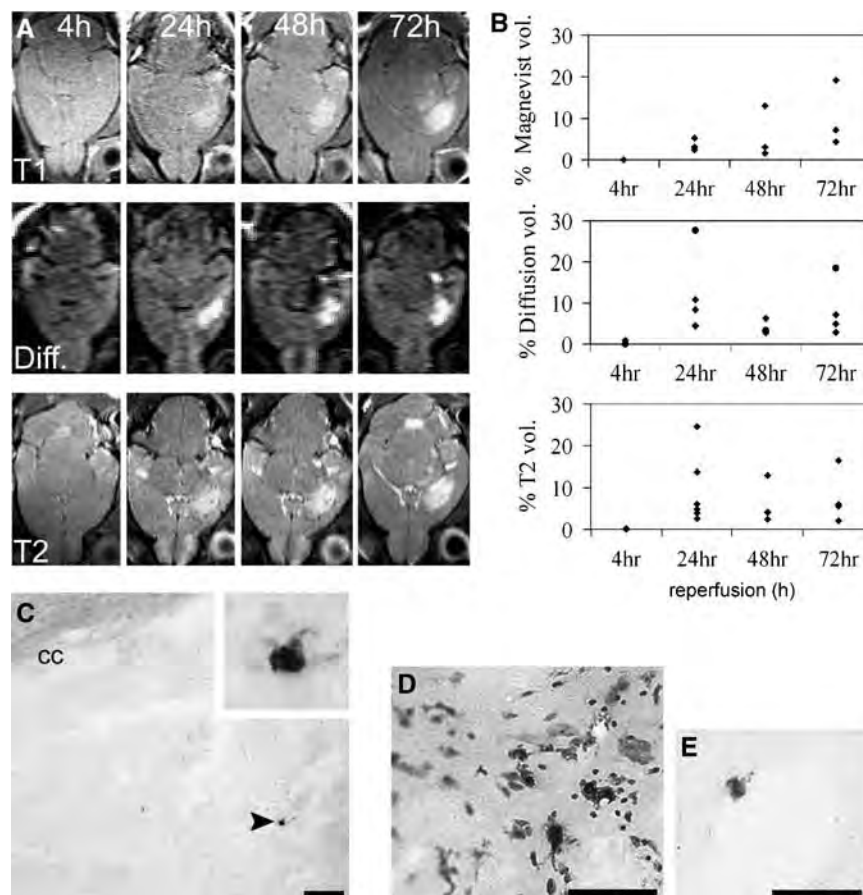


Figure 1 MR images showing damage evolution and histological verification of infiltration of iron-laden macrophages. **(A)** Axial T₁-weighted MR images through the ischaemic volume at 4, 24, 48, and 72 h after 30 mins of MCAo from a typical mouse showing responses to the Magnevist injection (labelled T₁), diffusion (diff), and T₂-weighted (T₂). MR images graphs **(B)** show the damage volume as the percentage of the ipsilateral hemisphere measured from multislice MRI data sets for individual mice. **(C)** In the ischaemic striatum, only a few exogenous, iron-labelled macrophages are found at 72 h of reperfusion time (arrowhead). **(D)** Rarely, these cells appear in small groups (brown) in the ischaemic hemisphere (cresyl violet counterstain) or located at the wall of striatal blood vessels **(E)**. Abbreviations: cc, corpus callosum. Scale bars **(C to E)**: 50 μ m.

number of these cells never exceeded 6 to 8 cells/section in any of the examined brain sections (Figure 1D). Scattered iron-laden macrophages were also sometimes found attached to the wall of blood vessels (Figure 1E). Therefore, the absence of T₂-weighted MRI or Prussian Blue staining evidence for AMI-227 labelled cells in the brain parenchyma indicates that there is virtually no exogenous macrophage infiltration into the brain after MCAo.

***In vivo* Cell Labelling Confirms the Lack of Significant Exogenous Macrophage Infiltration in the Ischaemic Brain**

To clarify further whether exogenous circulation-related cells enter the brain, CFSE leakage into the brain independent from cellular infiltration and BBB damage was determined in the brains of sham-operated animals 4 and 24 h after carboxy-fluorescein diacetate succinimidyl ester injection. Cellular CFSE labelling was never observed in the parenchyma and only occasional labelling was present in the wall of blood vessels. Strong CFSE uptake was observed in certain cells of the circumventricular organs (eminencia mediana and area postrema) and in the choroid plexus, although resident ependymal cells in these structures were not positive to the CD45 (common leukocyte) antigen (Figure 2A).

Twenty-four hours after 30 or 60 mins of MCAo, CFSE-positive macrophages appeared at the meninges, only very few being found infiltrated into the brain parenchyma (Figure 2B), which is in support of the AMI-227 findings. After MCAo (48 to 72 h), the number of CFSE-positive macrophages slightly increased in the ipsilateral hemisphere, but never exceeded 2% to 3% of the Iba1-positive cells.

Microglial Proliferation rather than Infiltration of Exogenous Macrophages Increases the Population of Mononuclear Phagocytes in the Brain Parenchyma after Middle Cerebral Artery Occlusion

Resident microglia exhibited intense proliferating activity at 48 and 72 h, as revealed by BrdU uptake (Figure 2C). CFSE-positive infiltrating macrophages were void of BrdU labelling both 48 and 72 h after 30 and 60 mins of MCAo. Processes of cellular division and BrdU uptake were observed in several diamidinophenylindole-stained microglial nuclei in the ischaemic hemisphere (Figure 2D), indicating that proliferation takes place locally in the parenchyma. Occasionally, dividing microglia contained CFSE-positive particles in their cytoplasm, as a result of phagocytosis of infiltrating neutrophils (see below), but this labelling never extended to the whole cytoplasm with either 30 or 60 mins of MCAo.

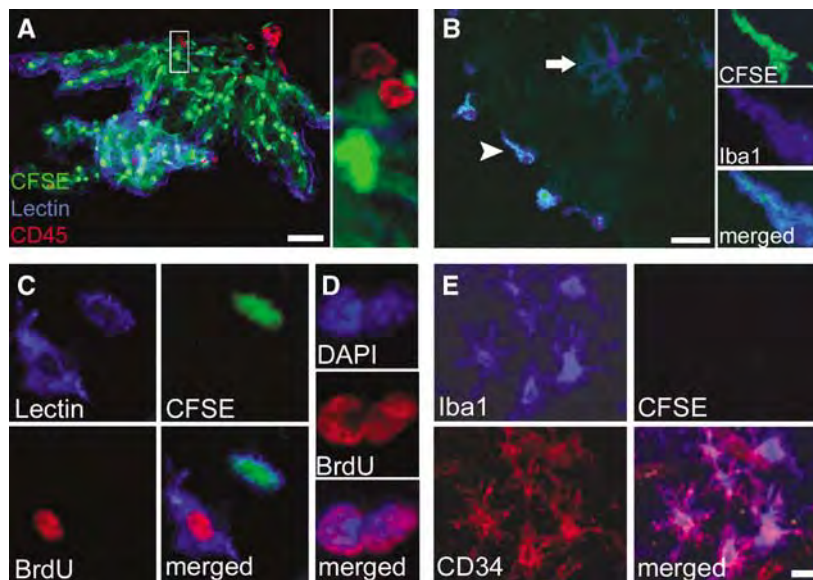


Figure 2 Proliferation, but not infiltration of exogenous macrophages, is the main mechanism underlying early increase in phagocyte numbers in the ischaemic brain. CFSE staining reveals qualitative differences between infiltrating macrophages and resident microglia in the brain parenchyma after MCAo. **(A)** Independently of BBB leakage, resident ependymal cells in CVO as well as in the choroid plexus exhibit strong CFSE labelling, but they are not positive for leukocyte antigens (CD45, red). **(B)** *In situ* stained blood-borne macrophages (arrowhead) appear at meninges in the ipsilateral hemisphere (ventral piriform area is shown), but only a small population infiltrates into the parenchyma after MCAo during 72 h of reperfusion. Resident microglial cells do not contain CFSE (arrow). **(C)** Microglia incorporate BrdU focally in the ischaemic striatum 72 h after MCAo, but show no CFSE staining. In contrast, infiltrating macrophages are CFSE-positive (green) and they do not proliferate. **(D)** Co-localization of nuclear diamidinophenylindole staining with BrdU in the ischaemic striatum reveals that cellular division takes place in the brain parenchyma. **(E)** Self-renewing resident microglia (Iba1, blue) expresses stem cell marker CD34 in the ischaemic striatum (red). Scale bars, **A**: 50 μ m; **B** and **E**: 25 μ m.

Iba1-positive microglia exhibited increased staining over time to the stem cell antigen, CD34 (Figure 2E) in the ischaemic striatum. BrdU-labelled microglia located under the corpus callosum and near the left ventricle were CD34-positive 24 h after 30 and 60 min of MCAo, the remaining dividing microglial cells in the ipsilateral hemisphere being positive by 72 h after MCAo.

Reduced Numbers of Microglia after Middle Cerebral Artery Occlusion are Associated with more Severe Injury

There was no difference in the number of Iba1-positive cells during the 72 h examination period on the contralateral hemisphere and Iba1 numbers were similar between cases of 30 and 60 mins of MCAo (207 ± 14 cells/mm² in the striatum, 223 ± 17 cells/mm² in the cortex after 30 mins of MCAo and 202 ± 12 cells/mm² in the striatum, 218 ± 12 cells/mm² in the cortex after 60 mins of MCAo at 72 h reperfusion). The number of Iba1-positive cells in the contralateral hemisphere was similar to that observed in sham animals (Figure 3D).

At 4 h after 30 mins of MCAo, no obvious cell death was apparent on cresyl violet-stained brain sections in the ipsilateral hemisphere (not shown) and there was no change in Iba1 cell numbers in the striatum or cortex compared with the contralateral hemisphere and sham animals. In contrast, 60 mins of MCAo caused significant loss of Iba1-stained microglia in the inner part of the ipsilateral striatum near the corpus callosum, and to a lesser extent in the deeper ipsilateral cortex layers (Figure 3A). Twenty-four hours after 60 mins of MCAo Iba1-positive cells were found throughout the injured striatum, but only occasionally were these cells positive to CFSE (0 to 2 cells/mm²). Microglial numbers tended to increase in the striatum over time during the 72 h after 60 mins of MCAo (Figure 3D), whereas Iba1 cell numbers remained low in the ischaemic cortex but continuously increased over time in the peri-infarct cortex (Figure 3E). The ratio of CFSE-positive Iba1 cells to total Iba1 cell population never exceeded 0.05 in the ischaemic hemisphere. The average volume of the ischaemic damage did not increase after 24 h of reperfusion (Figure 3G). After 30 mins of MCAo, the number of Iba1 cells was similar both at 4 and 24 h (Figures 3B and 3C). At 24 h, the ischaemic damage was confined to the striatum, but in two of six animals there was subsequent evolution of injury to the cortex by 48 h (Figure 3F). In these animals, the number of Iba1-positive microglia was lower both in the ipsilateral striatum (194 ± 11 cells/mm² at 48 h and 399 ± 29 cells/mm² at 72 h) and ipsilateral cortex (120 ± 21 cells/mm² at 48 h and 150 ± 2 cells/mm² at 72 h) than in the animals without visible cortical damage (282 ± 47 cells/mm² at 48 h and 475 ± 13 cells/mm² at 72 h in the striatum, 221 ± 26 cells/mm² at 48 h, $P < 0.05$ and 369 ± 28 cells/mm² at 72 h,

$P < 0.01$ in the ipsilateral cortex). Overall, the average number of Iba1-positive cells showed negative correlation with damage size both at 48 and 72 h after 30 mins of MCAo (Table 1). This correlation was not observed after 60 mins of MCAo, when neither the average size of the ischaemic damage nor the average number of microglia increased after 24 h in the ischaemic cortex.

Cortical Microglial Proliferation is Reduced by Prolonged Middle Cerebral Artery Occlusion

Only scattered BrdU-positive cells were present in the ipsilateral striatum and cortex at 24 h after 30 and 60 mins of MCAo (Figure 4A). In contrast, by 48 h reperfusion after MCAo, intensive microglial proliferation was observed in some regions of the ipsilateral hemisphere dividing cells being apparent in the inner part of the ipsilateral striatum near the subventricular zone and under the corpus callosum (Figures 4A and 4B). In animals displaying no cortical damage after 30 mins of MCAo, the ipsilateral cortex contained proliferating microglia (Figure 4B). In contrast, in the two of six animals where damage was observed in the ipsilateral cortex, only scattered dividing microglial cells, similar to the cases with 60 mins of MCAo, were seen (Figures 4B and 4C).

Seventy-two hours after 30 mins of MCAo, the entire striatum as well as the undamaged cortical MCA territory contained very high numbers of BrdU-positive microglia in four of six animals. The two animals with cortical damage after 30 mins of MCAo still only showed a few scattered dividing cells, lower in number than found in the animals exposed to 60 mins of occlusion, where numerous proliferating microglia were present in the ischaemic striatum but relatively few in the ischaemic cortex (Figures 4D and 4E).

Neutrophil Numbers are Controlled by Microglial Phagocytosis in the Ischaemic Brain

In animals undergoing 30 mins of MCAo, the number of infiltrating neutrophils were low during the first 24 h. Nevertheless, in animals with delayed cortical damage after 30 mins of MCAo, the number of neutrophils were very high in the striatum (Figure 5A) as well as the cortex compared with the ones with only striatal damage (23.4 ± 9.33 versus 2.9 ± 2.1 cells/mm² after 48 h and 11.0 ± 3.4 versus 2.5 ± 0.7 cells/mm² after 72 h of reperfusion in the left striatum; 20.2 ± 5.1 versus 1.3 ± 1 cells/mm² after 48 h and 13.6 ± 2.9 versus 2.4 ± 1.1 cells/mm² after 72 h in the left cerebral cortex, respectively; $P < 0.001$). In animals undergoing 60 mins of MCAo, the numbers of infiltrating neutrophils were low during the first 24 h, similar to those seen after 30 mins of occlusion. In contrast increasing numbers of neutrophils were seen 48 and 72 h after the insult (Figure 5B).

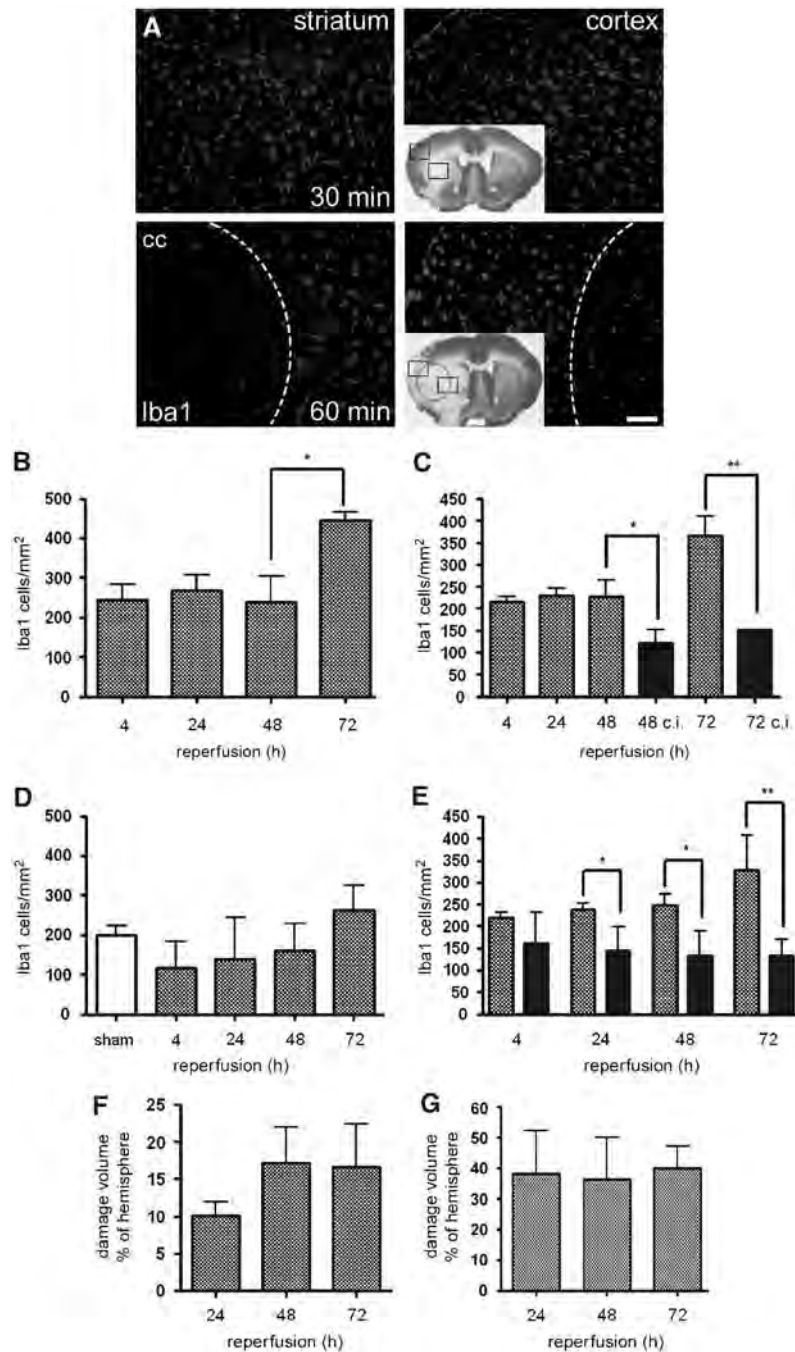


Figure 3 Effect of tMCAo of different duration on resident microglial population. (A) At 4 h after 60 mins of MCAo, significant loss of Iba1-positive microglia can be observed in the inner part of the injured striatum (near the corpus callosum, cc) and to a lesser extent in deeper ipsilateral cortex layers. In contrast, 30 mins of MCAo has no visible effect on the Iba1 cell numbers at 4 h of reperfusion. In two out of six animals, spontaneous cortical damage is evident both at 48 and 72 h after 30 mins of MCAo. Cresyl violet-stained representative brain sections (insert) showing the average size of the ischaemic damage after 60 (lower panel) and 30 (upper panel) minutes of MCAo. The site of fluorescent pictures is indicated with black frames, whereas the average place of microglial loss after 60 mins of MCAo indicated with red circle. (B and E) Graphs showing quantitative changes in Iba1 cell numbers after 30 (B and C) and 60 (D and E) mins of MCAo in specified regions of the ipsilateral hemisphere. Despite the inflammatory reaction, average striatal microglial cell numbers do not increase significantly up to 48 h of reperfusion (B) and are highly reduced in the cortex (C) if it shows signs of late ischaemic damage (black columns) by 48 (48 c.i.) and 72 h (72 c.i.) of reperfusion. (D) Continuous increase can be observed in the number of striatal Iba1 cells as referenced to the 4 h time point in the animals exposed to 60 mins of MCAo. (E) This increase is also evident in the non-ischaemic (dorsal) part of the cerebral cortex (gray columns), yet microglial numbers remain low in the ischaemic cerebral cortex (black columns). Volumes of the ischaemic damage after 30 (F) and 60 (G) mins of MCAo are expressed as the percentage of total hemispheric volume. * $P < 0.05$; ** $P < 0.01$. Scale bar = 100 μm .

Table 1 Correlation between damage size and average microglial cell numbers in the left cerebral cortex after 30 mins of MCAo

Experimental groups	N	P	r	r ²
30 mins occlusion, 48 h reperfusion	7	0.049	-0.75	0.57
30 mins occlusion, 72 h reperfusion	6	0.049	-0.81	0.66

Experimental animals exhibiting larger infarcts have significantly lower Iba1 cell numbers in the MCA area, both after 48 and 72 h of reperfusion.

NIMP staining was visualized together with CFSE to evaluate the approximate ratio of *in situ*-labelled versus all blood-derived cells infiltrated into the brain after MCAo at various time points (Figure 5C). Carboxyfluorescein succinimidyl ester-labelled cells were clearly detectable in the peripheral blood and brain neutrophils were positive to CFSE up to 72 h (Figure 6A). The ratio of labelled neutrophils (used either to evaluate the efficiency of CFSE staining or to confirm phagocytosis, see below) was dependent on the time point of *in situ* labelling and survival after MCAo (Figure 5C). The percentage of neutrophils labelled with CFSE was the highest at 4 h of reperfusion (approximately 70% of total neutrophils). Administration of the tracer 4, 24, or 48 h after the MCAo resulted in higher ratio of CFSE-labelled neutrophils in the brain compared with when given 4 h before the occlusion. This indicates that a new population of neutrophils were formed and/or released into the circulation. By 72 h of reperfusion, the percentage of labelled neutrophils was around 15% to 20% of the total infiltrated population in the animals receiving one single injection of the tracer.

Given the long half-life of CFSE in labelled leukocytes and decreasing ratio of CFSE-positive neutrophils in the brain parenchyma over time, we examined the possibility that these cells die and/or are being phagocytosed in the brain. Simultaneous visualization of Iba1, NIMP, and CFSE staining revealed phagocytosis of neutrophils by microglial cells in the ischaemic striatum and cortex (Figures 6B to E). The cytoplasm of mononuclear brain phagocytes contained NIMP-positive cells labelled with CFSE (Figure 6C) or CFSE/NIMP particles (Figure 6D). At the meninges near the ischaemic areas similar processes were seen, where infiltrating neutrophils as well as mononuclear brain phagocytes appeared in large numbers (Figure 6E). The meningeal regions likely contained both exogenous macrophages as well as resident brain phagocytes, since CFSE staining often covered the whole cytoplasm (exogenous macrophages), although sometimes staining was confined only to the phagosomes (phagocytosing microglia, data not shown). The ratio of microglia containing NIMP particles was 3% to 4% of the total microglial population at 24 h and 6% to 8% at 48 as well as 72 h of reperfusion time after both 30 and 60 mins of

MCAo (Figure 5D). Processes of cellular phagocytosis (i.e., whole NIMP-positive cells attached to microglia or being internalized in the cytoplasm of microglia) were observed mainly after 48 and 72 h of reperfusion in 0.6% to 1.8% of microglia in the ischaemic hemisphere.

Discussion

We did not observe significant invasion of blood-borne macrophages into the brain after 30 or 60 mins of MCAo, despite prolonged disruption of the BBB. This suggests that these cells are not directly involved in the infarct maturation process in the present mouse model. In contrast, we show extensive proliferation and activation of resident microglial cells in the ischaemic brain. A key function of activated microglia is, among others, to phagocytose neutrophils, and we believe that this could represent a potential protective effect, phagocytosis preventing spread, and induction of a more severe inflammatory response in the post-ischaemic brain.

Blood-brain barrier damage after MCAo was revealed with Gd-DTPA MRI both after 30 and 60 mins of occlusion, yet no evidence for leakage of AMI-227 was detected in either animal group within 3 days, suggesting that a degree of selectivity to the permeability was retained at the BBB. In the rat, 90 mins of MCAo leads to permeation of the BBB with a few AMI-227-positive macrophages (Kavec *et al*, 2004). We administered AMI-227 daily and, given the long plasma half-life (hours in rodents) of the compound (Payen *et al*, 1998), conditions were favourable for direct penetration to the brain. However, neither AMI-227 deposits nor a large number of iron-containing macrophages in the brain parenchyma were observed. Therefore, leakage of AMI-227 through the BBB was insignificant in mice and all the iron-positive cells detected histologically were likely to be blood-borne (microglia may phagocytose leaked AMI-227 as well). Overall, the number of infiltrating leukocytes was relatively low in the ischaemic striatum throughout the study and the majority of these cells were neutrophils. An explanation may be that iron-laden macrophages *in vivo* have reduced capacity to migrate into the brain on ischaemic challenge. Internalization of small superparamagnetic iron oxide/ultrasmall superparamagnetic iron oxide particles was shown to shift macrophages towards an anti-inflammatory, less responsive phenotype by enhancing interleukin (IL)-10 and inhibiting tumor necrosis factor- α production *in vitro* (Siglienti *et al*, 2006). However, we observed some CFSE-labelled exogenous macrophages in the brain, which suggests the labelling procedure did not inhibit the ability of macrophages to infiltrate into the brain.

Previous studies using AMI-227 to label peripheral macrophages in the rat *in vivo* showed that Prussian Blue-positive cells accumulate in the

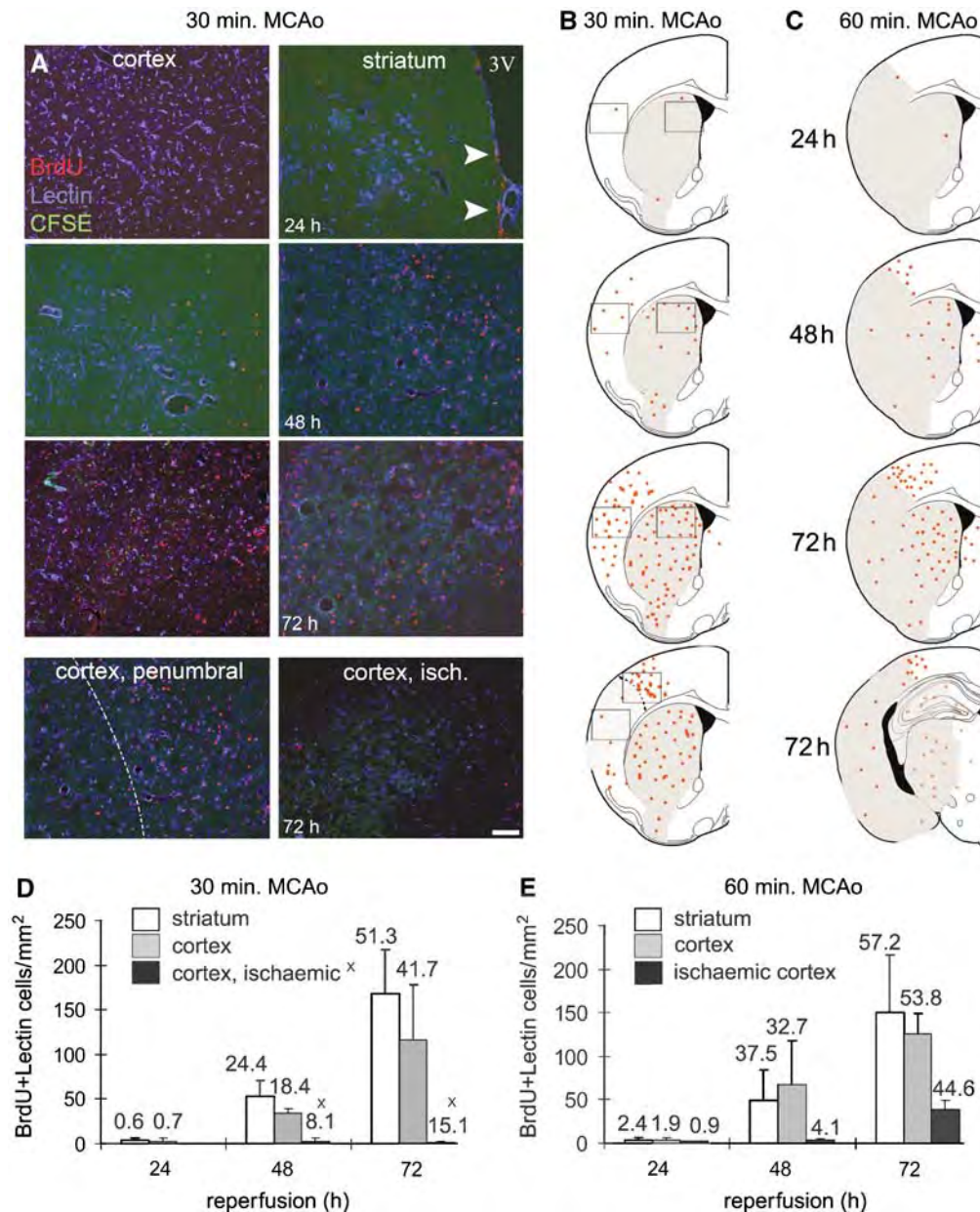


Figure 4 Cortical microglial proliferation is reduced by prolonged MCAo. **(A)** At 24 h of reperfusion, only very few BrdU-positive (red) microglial cells (blue, lectin) are found in the ipsilateral cortex and ischaemic striatum after 30 mins of MCAo. Instead, dividing cells are apparent in the subventricular zone (arrowheads). At 48 h of reperfusion time, increasing number of proliferating lectin-positive microglia is present in the non-ischaemic ipsilateral cortex as well as the ischaemic striatum, mainly immediately under the corpus callosum and in the peri-ventricular area (**A** and **B**). **(B)** Red dots represent relative distribution of BrdU-positive microglia, black squares show the site for **(A)** images in the ischaemic hemisphere. Grey shading indicate average size of the ischaemic damage after 30 and 60 mins of MCAo. By 72 h, large number of dividing cells is found throughout the ischaemic hemisphere. If the ipsilateral cerebral cortex expresses ischaemic damage as well, the number of BrdU-positive cells remain very low, but proliferating cells appear in large number in the peri-ischaemic zone, that is penumbra (**A** and **B**, lower row). **(C)** After 60 mins of MCAo, proliferating microglia appears also in the ischaemic striatum, but only few BrdU-containing cells are found in the ischaemic cortex. In addition, dividing cells are often present in the hippocampus and to a lesser extent, in the thalamus (lower row). **(D** and **E**) Graphs show average number of BrdU-positive microglia/mm² after 30 (**D**) and 60 (**E**) mins of MCAo. Numbers in the above columns represent the percentage of the BrdU/lectin-positive microglia compared with the total lectin-positive microglial population. D-cortex, ischaemic x group represent animals exhibiting delayed cortical damage after 30 mins of MCAo, $n = 2$, otherwise $n = 5$ to 6 /group. Scale bar, **A**: 100 μ m.

ischaemic core and peri-infarct zone. ED-1-positive macrophages were shown to appear in the infarct and peri-infarct areas (Rausch *et al.*, 2001; Schroeter

et al., 2004). However, direct visualization of iron-burdened macrophages by immunohistochemistry was only possible later than day 3 after transient

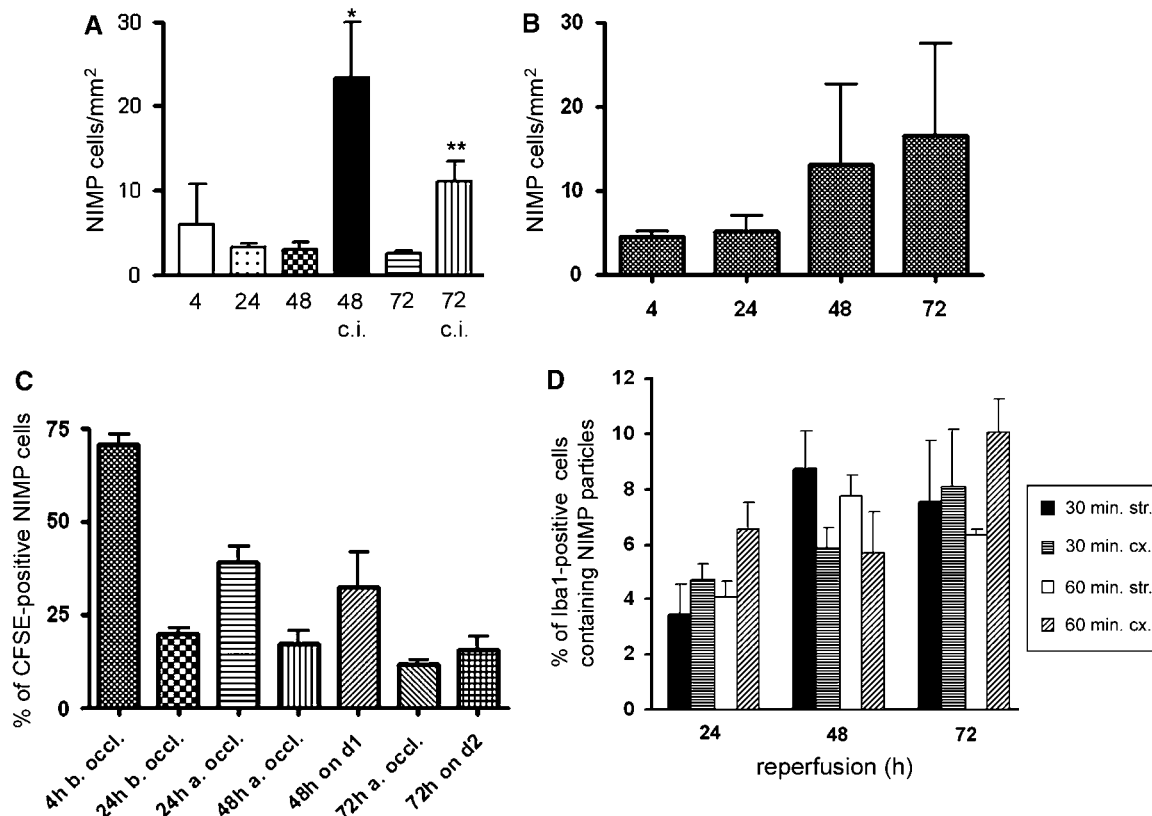


Figure 5 Microglial phagocytosis controls neutrophil granulocyte number in the ischaemic brain. **(A)** Neutrophil numbers remain low in the ischaemic striatum during the 72 h reperfusion period in the animals exposed to 30 mins of MCAo. If damage (delayed) proceeds to cortex, several infiltrating neutrophils are found in the ischaemic (c.i., $n = 2$ out of six) striatum unlike the cases where only striatal damage is present and the ipsilateral cortex shows no signs of ischaemic damage (n.i., $n = 4$ out of six). $*P < 0.001$ in animals with delayed cortical damage versus others do not exhibit cortical damage at 48 h of reperfusion and $**P < 0.05$ at 72 h of reperfusion. **(B)** Neutrophil numbers increase over time in the ischaemic striatum of animals exposed to 60 mins of MCAo. Neutrophils were counted on digital images of serial sections in the ischaemic striatum. **(C)** Percentage of neutrophils labelled with CFSE is the highest at 4 h of reperfusion and show reduction over time. Administration of the tracer 4 h (a. occl.), 24 h (on day 1), or 48 h (on day 2) after the MCA occlusion results in larger accumulation of labelled neutrophils in the brain at certain reperfusion times than in those cases when the tracer injection is performed 4 h before the occlusion (b. occl.). Quantification was performed on microphotographs captured from serial sections of the ischaemic striatum after 30 mins of MCAo at various time points. **(D)** Ratio of Iba1-positive cells containing NIMP particles in the ipsilateral striatum and cortex compared with the total Iba1-positive population.

MCAo (Rausch *et al*, 2001) or only minor iron-positive infiltrates were seen histologically, or by T_2^* -weighted MRI (Schroeter *et al*, 2006). In addition, activated phagocytic microglia express ED-1 (Rinner *et al*, 1995) and other phenotypic markers similar to macrophages (Stoll and Jander, 1999), so in these studies the possibility that phagocytosing microglia might take up iron oxide particles through the leaky BBB has not been completely excluded.

One plausible mechanism behind the beneficial action of resident microglia and perivascular macrophages might be that we observed phagocytosis of neutrophils by these cells. Polymorphonuclear granulocytes are known to accumulate in the brain after stroke and contribute to the ischaemic inflammatory damage, chiefly by producing free radicals and inflammatory molecules (Akopov *et al*, 1996; Davies *et al*, 1998; Dinkel *et al*, 2004; Matsuo *et al*,

1995). Resident microglial cells, and in lesser part, infiltrating haematogenous macrophages were shown to exert active phagocytosis of neuronal cell debris in the brain exposed to 30 mins of focal ischaemia (Schilling *et al*, 2005). In accordance with our findings, very recent studies also reported the engulfment of neutrophils and myeloperoxidase by macrophages after endothelin-1 induced MCAo. In addition, correlation of myeloperoxidase activity with temporal changes in brain injury and modulation of neutrophil infiltration as well as neutrophil phagocytosis by AM-36 (a Na^+ channel blocker antioxidant) were observed (Weston *et al*, 2006, 2007). Macrophages acquire granules by phagocytosing apoptotic neutrophils, which increases antimicrobial activity against intracellular pathogens (Tan *et al*, 2006). In the striatum after 30 mins of MCAo, the resident microglial population showed no signs of damage and these, together with

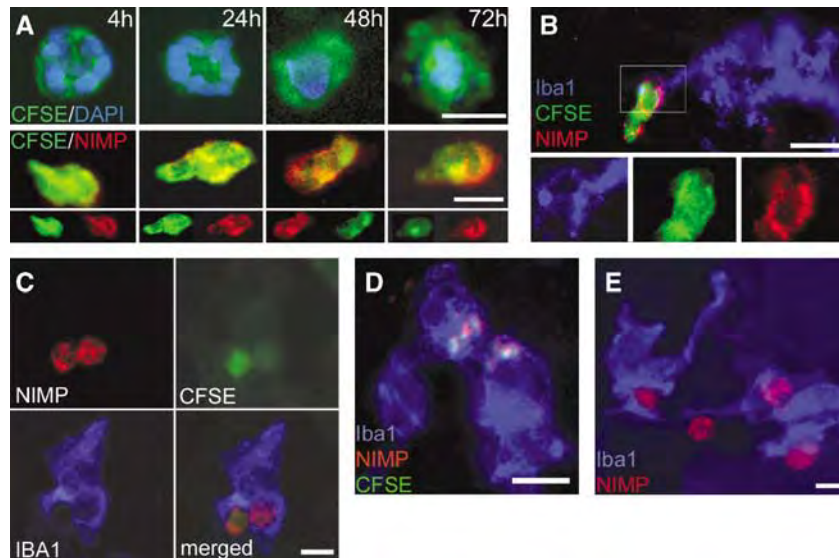


Figure 6 Cellular processes of neutrophil phagocytosis by microglia. **(A)** CFSE-positive blood leukocytes (CFSE, green; diamidinophenylindole, blue) are clearly detectable in blood smears (upper row) and CFSE is present in NIMP-positive neutrophils in the brain (lower row, ischaemic striatum is shown) up to 72 h after the labelling. **(B)** Iba1-positive microglia (blue) extend cellular processes towards neutrophils (red) in the ischaemic striatum. **(C)** In the ischaemic hemisphere (ischaemic striatum is seen, 48 h after 30 mins of MCAo), CFSE-positive neutrophils (NIMP, red) are phagocytosed by microglial cells (Iba1, blue). **(D)** The cytoplasm of Iba1-positive brain phagocytes (blue) contains CFSE/NIMP particles (ischaemic striatum is seen, 48 h after 30 mins of MCAo). **(E)** In the meninges near the ischaemic cortex, mononuclear phagocytes (Iba1, blue) engulf NIMP-positive neutrophils (48 h after 60 mins of MCAo is shown). Scale bar, **A** to **E**: 10 μ m.

meningeal and perivascular macrophages, might contribute to limiting of the effects of infiltrated neutrophils by phagocytosis. It is not clear how microglia can recognize infiltrating neutrophils in the brain parenchyma and what type of signals can trigger the phagocytotic process. It was reported that proteolytic enzymes divert the recognition and clearance of polymorphonuclear leukocytes by macrophages. Certain proteinases (of bacterial origin) can sensitize *healthy* neutrophils for uptake by macrophages due to proteolytic cleavage of an antiphagocytic signal (CD31) and the generation of a novel 'eat-me' signal on the neutrophil surface (Guzik *et al*, 2007). Similar processes might be involved after MCAo, elicited by activated brain proteases. Interestingly, our results show that a low number of microglial cells and/or a profound reduction in dividing cells strongly correlated with the number of neutrophils present in the parenchyma and, ultimately, with the extent of neuronal injury. It is possible, therefore, that increase of microglial proliferation is a direct response to the increasing neutrophil numbers in the brain parenchyma. Because degeneration of microglia was observed after prolonged MCAo it seems that proliferating microglia is protective at certain degrees of ischaemia but can be overcome by increased ischaemia, possibly as a result of increased neutrophil infiltration in these animals. These observations support the hypothesis that resident microglial activation may serve as an endogenous mechanism to limit the inflammation-mediated worsening of ischaemic brain damage.

In addition, the authors emphasize that phagocytosis of neutrophils is not the only potentially protective role of microglia after stroke.

We identified activation of microglia by means of increased expression of activation markers (Iba1, CD45, F4/80) and microglial proliferation, which profoundly increased by 72 h of reperfusion. Microglial proliferation is initially observed under the corpus callosum as well as adjacent to the lateral ventricle. Dividing microglia-expressed CD34, which is a hallmark of dividing, self-renewing microglia, as described previously after acute neuronal injury (Ladeby *et al*, 2005).

Proliferation resulted in an increase of microglial cell numbers, which was not accompanied with larger ischaemic damage. In contrast, the more extensive ischaemic injury observed after 60 mins of MCAo was associated with low microglial cell numbers and an impaired proliferative response in the cerebral cortex. Degeneration of microglia in the ischaemic core after prolonged MCAo was also reported by other studies either in a permanent model of rat (Davies *et al*, 1998) or mouse MCAo (Tanaka *et al*, 2003). Infiltrating macrophages were not positive to BrdU, which indicates that these cells may differ from resident microglia regarding their ability to divide after entering the brain. Blood-brain barrier damage and infiltrating blood-borne substances can trigger microglia to enter the cell cycle. Evidence supporting these ideas was recently provided by studies showing that pure albumin is a potent trigger of calcium signaling and

proliferation in microglial cells, but not of macrophages or astrocytes (Hooper *et al*, 2005).

The relative contribution of exogenous macrophages to post-ischaemic processes is controversial. In a permanent model of MCAo (Tanaka *et al*, 2003) as well as in a transient model (Kokovay *et al*, 2006), several Iba1-positive exogenous macrophages were found infiltrated into the brain 24 to 48 h after the insult. In contrast, others found a minor contribution of blood-borne macrophages to the inflammatory infiltrates in the 4 days after transient MCAo (Schilling *et al*, 2003, 2005). It was reported that head irradiation dose-dependently increased the number of infiltrating Iba1-positive cells in the MCA territory and the olfactory bulb in naive animals 6 weeks after bone marrow transplantation (Tanaka *et al*, 2003). Therefore, it may be difficult to compare the number and ratio of infiltrating cells between different studies using either naive or bone marrow chimeric animals.

In our experiments, the population of peripheral leukocytes labelled with CFSE or AMI-227 was in accordance with previous data (Becker *et al*, 2004; Ristevski *et al*, 2003; Weissleder *et al*, 1990), but relatively few exogenous macrophages infiltrated into brain parenchyma over the first 72 h after tMCAo, parallel to progression of the ischaemic damage. In this process, the number of microglial cells that survive the ischaemic challenge might be of importance in controlling the number of blood-borne macrophages and other proinflammatory cells. The fact that the ratio of labelled brain neutrophils in post-ischaemic brain was different depending on the time point of carboxyfluorescein diacetate succinimidyl ester administration relative to exposure to MCAo suggests that MCAo either triggers formation or release of leukocytes from the bone marrow or from peripheral pools (or both these effects), which were differently available for CFSE injected into the circulation. The gene expression profile of neutrophils are reported to undergo rapid changes and early mobilization of these cells is observed shortly after stroke in human patients, followed by a marked reduction 5 to 7 days after the insult (Emsley *et al*, 2003; Tang *et al*, 2006).

Taken together, our data show no significant exogenous macrophage infiltration early (4 to 72 h) after MCAo, but rather microglial proliferation and repopulation. The microglia can exert a phagocytic role that may be advantageous in stroke in maintaining the brain microenvironment in spite of BBB breakdown and in the prevention of ischaemic exacerbation of the damage in the penumbral region, although this remains to be demonstrated.

References

Acarin L, Vela JM, Gonzalez B, Castellano B (1994) Demonstration of poly-N-acetyl lactosamine residues in

- ameboid and ramified microglial cells in rat brain by tomato lectin binding. *J Histochem Cytochem* 42:1033–41
- Akopov SE, Simonian NA, Grigorian GS (1996) Dynamics of polymorphonuclear leukocyte accumulation in acute cerebral infarction and their correlation with brain tissue damage. *Stroke* 27:1739–43
- Barone FC, Hillegass LM, Price WJ, White RF, Lee EV, Feuerstein GZ, Sarau HM, Clark RK, Griswold DE (1991) Polymorphonuclear leukocyte infiltration into cerebral focal ischemic tissue: myeloperoxidase activity assay and histologic verification. *J Neurosci Res* 29:336–45
- Becker HM, Chen M, Hay JB, Cybulsky MI (2004) Tracking of leukocyte recruitment into tissues of mice by *in situ* labeling of blood cells with the fluorescent dye CFDA SE. *J Immunol Methods* 286:69–78
- Campanella M, Sciorati C, Tarozzo G, Beltramo M (2002) Flow cytometric analysis of inflammatory cells in ischemic rat brain. *Stroke* 33:586–92
- Clark RK, Lee EV, Fish CJ, White RF, Price WJ, Jonak ZL, Feuerstein GZ, Barone FC (1993) Development of tissue damage, inflammation and resolution following stroke: an immunohistochemical and quantitative planimetric study. *Brain Res Bull* 31:565–72
- Davies CA, Loddick SA, Stroemer RP, Hunt J, Rothwell NJ (1998) An integrated analysis of the progression of cell responses induced by permanent focal middle cerebral artery occlusion in the rat. *Exp Neurol* 154:199–212
- Davis EJ, Foster TD, Thomas WE (1994) Cellular forms and functions of brain microglia. *Brain Res Bull* 34:73–8
- Dinkel K, Dhabhar FS, Sapolsky RM (2004) Neurotoxic effects of polymorphonuclear granulocytes on hippocampal primary cultures. *Proc Natl Acad Sci USA* 101:331–6
- Emsley HC, Smith CJ, Gavin CM, Georgiou RF, Vail A, Barberan EM, Hallenbeck JM, del Zoppo GJ, Rothwell NJ, Tyrrell PJ, Hopkins SJ (2003) An early and sustained peripheral inflammatory response in acute ischaemic stroke: relationships with infection and atherosclerosis. *J Neuroimmunol* 139:93–101
- Ginsberg MD (2003) Adventures in the pathophysiology of brain ischemia: penumbra, gene expression, neuroprotection: the 2002 Thomas Willis Lecture. *Stroke* 34:214–23
- Gowing G, Vallieres L, Julien JP (2006) Mouse model for ablation of proliferating microglia in acute CNS injuries. *Glia* 53:331–7
- Guzik K, Bzowska M, Smagur J, Krupa O, Sieprawska M, Travis J, Potempa J (2007) A new insight into phagocytosis of apoptotic cells: proteolytic enzymes divert the recognition and clearance of polymorphonuclear leukocytes by macrophages. *Cell Death Differ* 14:171–82
- Hooper C, Taylor DL, Pocock JM (2005) Pure albumin is a potent trigger of calcium signalling and proliferation in microglia but not macrophages or astrocytes. *J Neurochem* 92:1363–76
- Jiang N, Moyle M, Soule HR, Rote WE, Chopp M (1995) Neutrophil inhibitory factor is neuroprotective after focal ischemia in rats. *Ann Neurol* 38:935–42
- Kavec M, Grohn O, Valonen P, Garwood M, Kauppinen RA (2004) Detection of iron oxide particle-containing inflammatory cells in developing infarction by susceptibility contrast MRI by Carr–Purcell T2. *Proc Intl Soc Magn Res Med* 12:133
- Kokovay E, Li L, Cunningham LA (2006) Angiogenic recruitment of pericytes from bone marrow after stroke. *J Cereb Blood Flow Metab* 26:545–55

- Ladeby R, Wirenfeldt M, Dalmau I, Gregersen R, Garcia-Ovejero D, Babcock A, Owens T, Finsen B (2005) Proliferating resident microglia express the stem cell antigen CD34 in response to acute neural injury. *Glia* 50:121–31
- Liu J, Bartels M, Lu A, Sharp FR (2001) Microglia/macrophages proliferate in striatum and neocortex but not in hippocampus after brief global ischemia that produces ischemic tolerance in gerbil brain. *J Cereb Blood Flow Metab* 21:361–73
- Matsuo Y, Kihara T, Ikeda M, Ninomiya M, Onodera H, Kogure K (1995) Role of neutrophils in radical production during ischemia and reperfusion of the rat brain: effect of neutrophil depletion on extracellular ascorbyl radical formation. *J Cereb Blood Flow Metab* 15:941–7
- McCull BW, Carswell HV, McCulloch J, Horsburgh K (2004) Extension of cerebral hypoperfusion and ischaemic pathology beyond MCA territory after intraluminal filament occlusion in C57Bl/6j mice. *Brain Res* 997:15–23
- Morioka T, Kolehua AN, Streit WJ (1993) Characterization of microglial reaction after middle cerebral artery occlusion in rat brain. *J Comp Neurol* 327:123–32
- Payen JF, Vath A, Koenigsberg B, Bourlier V, Decorps M (1998) Regional cerebral plasma volume response to carbon dioxide using magnetic resonance imaging. *Anesthesiology* 88:984–92
- Rausch M, Sauter A, Frohlich J, Neubacher U, Radu EW, Rudin M (2001) Dynamic patterns of USPIO enhancement can be observed in macrophages after ischemic brain damage. *Magn Reson Med* 46:1018–22
- Rinner WA, Bauer J, Schmidts M, Lassmann H, Hickey WF (1995) Resident microglia and hematogenous macrophages as phagocytes in adoptively transferred experimental autoimmune encephalomyelitis: an investigation using rat radiation bone marrow chimeras. *Glia* 14:257–66
- Ristevski B, Young AJ, Dudler L, Cahill RN, Kimpton W, Washington E, Hay JB (2003) Tracking dendritic cells: use of an in situ method to label all blood leukocytes. *Int Immunol* 15:159–65
- Schilling M, Besselmann M, Leonhard C, Mueller M, Ringelstein EB, Kiefer R (2003) Microglial activation precedes and predominates over macrophage infiltration in transient focal cerebral ischemia: a study in green fluorescent protein transgenic bone marrow chimeric mice. *Exp Neurol* 183:25–33
- Schilling M, Besselmann M, Muller M, Strecker JK, Ringelstein EB, Kiefer R (2005) Predominant phagocytic activity of resident microglia over hematogenous macrophages following transient focal cerebral ischemia: an investigation using green fluorescent protein transgenic bone marrow chimeric mice. *Exp Neurol* 196:290–7
- Schroeter M, Jander S, Witte OW, Stoll G (1994) Local immune responses in the rat cerebral cortex after middle cerebral artery occlusion. *J Neuroimmunol* 55:195–203
- Schroeter M, Oros-Peusquens AM, Irkens M, Celik A, Saleh A, Shah NJ, Jander S (2006) Spatiotemporal pattern of USPIO enhancement in experimental stroke lesions depends on the type of ischaemic injury: a 9.4 T MRI study. *Proc Int Soc Magn Reson Med* 14:1459
- Schroeter M, Saleh A, Wiedermann D, Hoehn M, Jander S (2004) Histochemical detection of ultrasmall superparamagnetic iron oxide (USPIO) contrast medium uptake in experimental brain ischemia. *Magn Reson Med* 52:403–6
- Siglienti I, Bendszus M, Kleinschnitz C, Stoll G (2006) Cytokine profile of iron-laden macrophages: implications for cellular magnetic resonance imaging. *J Neuroimmunol* 173:166–73
- Stoll G, Jander S (1999) The role of microglia and macrophages in the pathophysiology of the CNS. *Prog Neurobiol* 58:233–47
- Tan BH, Meinken C, Bastian M, Bruns H, Legaspi A, Ochoa MT, Krutzik SR, Bloom BR, Ganz T, Modlin RL, Stenger S (2006) Macrophages acquire neutrophil granules for antimicrobial activity against intracellular pathogens. *J Immunol* 177:1864–71
- Tanaka R, Komine-Kobayashi M, Mochizuki H, Yamada M, Furuya T, Migita M, Shimada T, Mizuno Y, Urabe T (2003) Migration of enhanced green fluorescent protein expressing bone marrow-derived microglia/macrophage into the mouse brain following permanent focal ischemia. *Neuroscience* 117:531–9
- Tang Y, Xu H, Du X, Lit L, Walker W, Lu A, Ran R, Gregg JP, Reilly M, Pancioli A, Khoury JC, Sauerbeck LR, Carozzella JA, Spilker J, Clark J, Wagner KR, Jauch EC, Chang DJ, Verro P, Broderick JP, Sharp FR (2006) Gene expression in blood changes rapidly in neutrophils and monocytes after ischemic stroke in humans: a microarray study. *J Cereb Blood Flow Metab* 26:1089–102
- Weissleder R, Elizondo G, Wittenberg J, Rabito CA, Bengel HH, Josephson L (1990) Ultrasmall superparamagnetic iron oxide: characterization of a new class of contrast agents for MR imaging. *Radiology* 175:489–93
- Weston RM, Jarrott B, Ishizuka Y, Callaway JK (2006) AM-36 modulates the neutrophil inflammatory response and reduces breakdown of the blood–brain barrier after endothelin-1 induced focal brain ischaemia. *Br J Pharmacol* 149:712–23
- Weston RM, Jones NM, Jarrott B, Callaway JK (2007) Inflammatory cell infiltration after endothelin-1-induced cerebral ischemia: histochemical and myeloperoxidase correlation with temporal changes in brain injury. *J Cereb Blood Flow Metab* 27:100–14
- Wheeler RD, Boutin H, Touzani O, Luheshi GN, Takeda K, Rothwell NJ (2003) No role for interleukin-18 in acute murine stroke-induced brain injury. *J Cereb Blood Flow Metab* 23:531–5
- Yamagami S, Tamura M, Hayashi M, Endo N, Tanabe H, Katsuura Y, Komoriya K (1999) Differential production of MCP-1 and cytokine-induced neutrophil chemoattractant in the ischemic brain after transient focal ischemia in rats. *J Leukoc Biol* 65:744–9
- Zhang C, Lam TT, Tso MO (2005) Heterogeneous populations of microglia/macrophages in the retina and their activation after retinal ischemia and reperfusion injury. *Exp Eye Res* 81:700–9

SHORT REPORT

Open Access

Interleukin-1 α expression precedes IL-1 β after ischemic brain injury and is localised to areas of focal neuronal loss and penumbral tissues

Nadia M Luheshi¹, Krisztina J Kovács², Gloria Lopez-Castejon¹, David Brough^{1*†} and Adam Denes^{1,2*†}

Abstract

Background: Cerebral ischemia is a devastating condition in which the outcome is heavily influenced by inflammatory processes, which can augment primary injury caused by reduced blood supply. The cytokines interleukin-1 α (IL-1 α) and IL-1 β are key contributors to ischemic brain injury. However, there is very little evidence that IL-1 expression occurs at the protein level early enough (within hours) to influence brain damage after stroke. In order to determine this we investigated the temporal and spatial profiles of IL-1 α and IL-1 β expression after cerebral ischemia.

Findings: We report here that in mice, as early as 4 h after reperfusion following ischemia induced by occlusion of the middle cerebral artery, IL-1 α , but not IL-1 β , is expressed by microglia-like cells in the ischemic hemisphere, which parallels an upregulation of IL-1 α mRNA. 24 h after ischemia IL-1 α expression is closely associated with areas of focal blood brain barrier breakdown and neuronal death, mostly near the penumbra surrounding the infarct. The sub-cellular distribution of IL-1 α in injured areas is not uniform suggesting that it is regulated.

Conclusions: The early expression of IL-1 α in areas of focal neuronal injury suggests that it is the major form of IL-1 contributing to inflammation early after cerebral ischemia. This adds to the growing body of evidence that IL-1 α is a key mediator of the sterile inflammatory response.

Findings

Inflammation is recognised as a major contributor to the worsening of acute brain injury [1]. In particular two pro-inflammatory members of the IL-1 family of cytokines, IL-1 α and IL-1 β , are considered the major effectors of injury, and inhibiting their signalling with the IL-1 receptor antagonist (IL-1Ra) is protective in experimental models of stroke [1], and has shown promise as a treatment in clinical trials [2]. Mice in which both IL-1 α and IL-1 β have been deleted (IL-1 α/β double KO) have markedly reduced damage in response to experimental stroke caused by middle cerebral artery occlusion (MCAo) [3]. However, the relative contribution of each cytokine to the evolution of the infarct is not clear since IL-1Ra inhibits both cytokines. The neuroprotective effects of IL-1Ra are

reduced when administration is delayed beyond 3 h [4], suggesting that IL-1 expressed early after the insult is important. IL-1 β mRNA is detected within 3-6 h after cerebral ischemia [5,6], although there is very little direct evidence that IL-1 β protein is produced, and almost no information is available about IL-1 α . In this study we sought to determine the spatial distribution of IL-1 α and IL-1 β in the mouse brain early (4 h) and late (24 h) after stroke induced by MCAo. Such a study was required since strategies aimed at inhibiting inflammation in the brain will be dictated by the nature of the inflammatory mediators produced.

We first investigated whether IL-1 expression could be detected early (4 h after reperfusion) after ischemic brain injury, when little neuronal death is present compared to the 24 h reperfusion time. C57BL6/H mice (male, 12-16 weeks) were subjected to 60 min MCAo and 4 h reperfusion following which they were transcardially perfused with saline followed by 4% paraformaldehyde. After cryoprotection brains were cut on a sledge microtome at a

* Correspondence: david.brough@manchester.ac.uk; Adam.denes@manchester.ac.uk

† Contributed equally

¹Faculty of Life Sciences, University of Manchester, UK

Full list of author information is available at the end of the article

thickness of 20 μm and were stored in cryoprotectant solution until use. Immunofluorescence on these sections showed IL-1 α expression (AF-400-NA, R & D Systems, 0.4 $\mu\text{g}/\text{mL}$) in microglia in the ipsilateral hemisphere as identified by co-staining for the microglial marker Iba-1 (019-19741, Wako, 1 $\mu\text{g}/\text{mL}$) (Figure 1A, B). At this time no IL-1 β expression (AF-401-NA, R & D Systems, 0.4

$\mu\text{g}/\text{mL}$) was observed in these areas, with only a few non-microglial IL-1 β -positive cells observed in the capsula interna, away from the core of the infarct, as reported previously [7]. No IL-1 expression was observed in the contralateral hemisphere, confirming that its expression was a result of the injury (Figure 1A). To further confirm early IL-1 α expression after MCAo, we performed

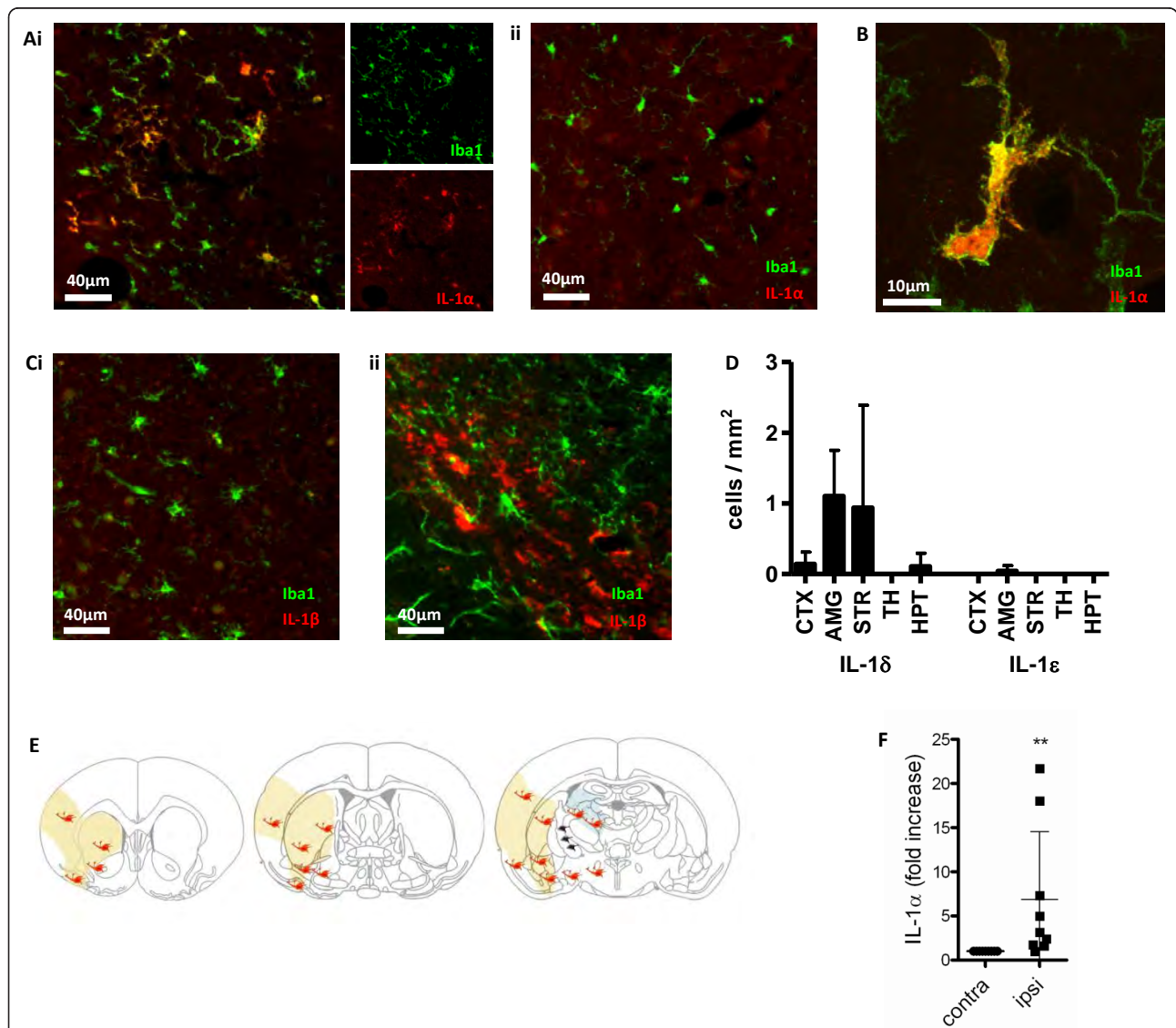


Figure 1 Early microglial IL-1 α expression after MCAo. Images are of coronal sections from the brains of C57BL6/H mice subjected to 60 min MCAo followed by 4 h reperfusion. Widefield images (A) show IL-1 α -expressing (red), Iba1 positive (green) microglia 4 h post-MCAo in the ipsilateral (Ai) but not the contralateral (ii) hemisphere. Confocal image shows the colocalization of IL-1 α and Iba-1 stains in an activated microglia in the ipsilateral hemisphere (amygdala is shown) (B). No IL-1 β -positive (red)/Iba-1 positive (green) microglia were detected in the ipsilateral amygdala at this time point (Ci, widefield). IL-1 β positive, Iba-1 negative cells were detected in the capsula interna (Cii, widefield). IL-1 α and β expressing microglia (IL-1/Iba1 positive cells) were counted (D) in the cortex (CTX), amygdala (AMG), striatum (STR), thalamus (TH) and hypothalamus (HPT). $n = 3$ C57BL6/H mice. The average distribution of IL-1 α -positive microglia (orange symbols) and a few IL-1 β expressing non-microglial cells (black symbols) are shown at 4 h reperfusion in the ipsilateral hemisphere (E), when histologically little ischemic damage is detected. Yellow shading indicates areas which typically become ischemic by 24 h reperfusion, while ischemic damage is occasionally observed in the thalamus and hippocampus (blue shading) at the same time point. Quantitative real-time PCR demonstrated a significant increase of IL-1 α mRNA in tissue homogenates of the ipsilateral hemisphere compared to the contralateral side (F). ** $P < 0.01$, unpaired t test.

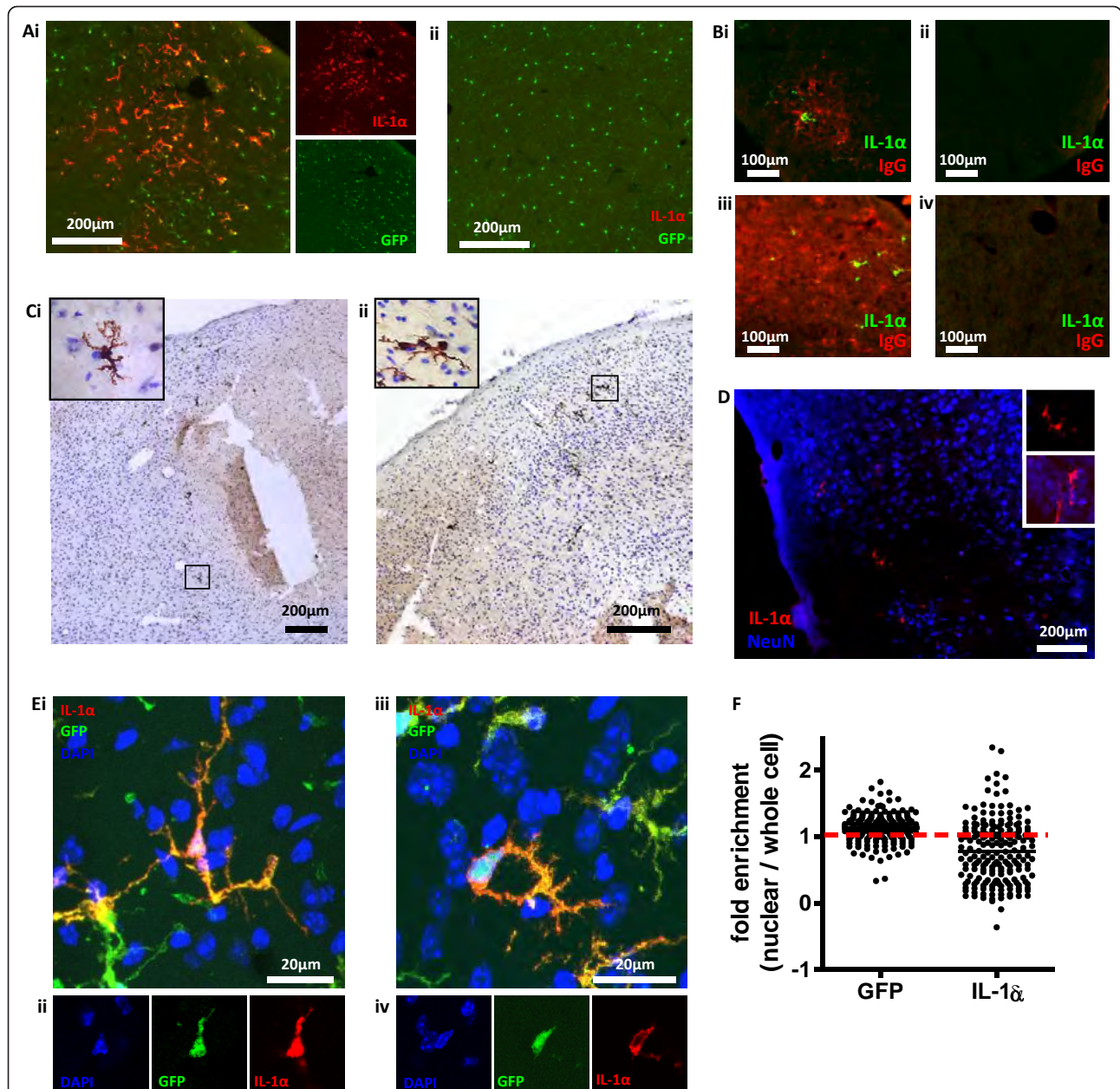


Figure 2 IL-1 α is expressed by microglia localized to focal neuronal and BBB injury 24 h after MCAO. Images are coronal sections from brains of C57BL6/H and CX3CR1-GFP +/- mice 60 min MCAO and 24 h reperfusion. Widefield images show IL-1 α -expressing (red), GFP positive (green) microglia in ipsilateral (Ai), not contralateral (ii) amygdala 24 h after MCAO in a CX3CR1-GFP +/- mouse. IL-1 α immunohistochemistry with cresyl violet co-staining localises IL-1 α expressing microglia to the peri-infarct zone in thalamus (Bi) and cortex (Bii) of a C57BL6/H mouse. Focal IgG staining (red) co-localized with IL-1 α positive microglia (green) in the ipsilateral cortex of a C57BL6/H mouse (Ci). No IgG or IL-1 α staining detected in the contralateral cortex (Cii). IL-1 α positive microglia detected in larger areas of IgG staining in the ipsilateral (Ciii), but not contralateral (Civ) hemisphere. Co-localization of IL-1 α positive microglia (red) with areas of neuronal loss (blue) in a C57BL6/H mouse (D). Occasional IL-1 α positive microglia also found in areas where neurons were morphologically intact (D, inset). Confocal images (E) are maximum Z projections (Ei, iii) and confocal slices at the level of the nucleus (Eii, iv) of IL-1 α expressing, GFP positive microglia in a CX3CR1-GFP +/- mouse. Cells with (Ei, ii), and without (Eiii, iv) nuclear IL-1 α . Nuclear fluorescence intensities for IL-1 α and GFP were quantified from confocal images, and the fold enrichment of IL-1 α and GFP in microglial nuclei was calculated in comparison to whole cell fluorescence (F). All images are representative of $n \geq 3$ mice. Quantification is of $n = 4$ CX3CR1-GFP +/- mouse brains, with each data point representing an individual cell, $n \geq 30$ cells per brain.

quantitative real-time PCR on tissue homogenates of the ipsilateral and contralateral hemispheres 4 h after reperfusion. A significant increase ($P < 0.01$) was observed in IL-1 α expression, whereas we were unable to detect IL-1 β expression at this time point (Figure 1F).

Only microglia of CX3CR1-GFP \pm mice (as used previously [7]) express GFP in the brain [8]. CX3CR1-GFP \pm mice were subjected to 60 min MCAo followed by 24 h reperfusion, when the evolution of the infarct is advanced and there is substantial neuronal death. Ramified, GFP-positive microglia-like cells in the ipsilateral hemisphere expressed IL-1 α (Figure 2A). IL-1 α -positive microglia were present in the cerebral cortex, the piriform cortex, the ventral striatum and the thalamus. Immunohistochemistry for IL-1 α , with cresyl violet co-staining, localized IL-1 α expressing microglia mainly to the penumbral tissue surrounding the infarct (Figure 2B). IgG cannot cross an intact blood brain barrier (BBB) and its presence in the brain parenchyma indicates BBB disruption and injury [9]. Staining of coronal brain sections from C57BL6/H mice (Figure 2C) and CX3CR1-GFP \pm mice (not shown) 24 h after MCAo for IL-1 α and IgG (BA-2000, Vector Labs, biotinylated horse anti-mouse IgG, 2 μ g/mL; S-32356, Invitrogen, Alexa 594 conjugated streptavidin, 5 μ g/mL) revealed that IL-1 α expressing cells co-localized to areas of focal BBB damage, mainly near the penumbral regions of the ipsilateral hemisphere (Figure 2C). The localization of IL-1 α expressing cells with injured brain tissue is also shown by the co-localization of IL-1 α positive microglia (red) with areas of focal neuronal loss within the compromised tissue (absence of NeuN (MAB377, Millipore, mouse anti-NeuN 5 μ g/mL)) (Figure 2D). IL-1 α expressing microglia increased overall after 24 h reperfusion compared to the 4 h time point (two-way ANOVA, $P < 0.05$, not shown) although the increase was not significant when comparing any particular brain regions. At 24 h IL-1 β is expressed [7]. Thus the expression of IL-1 α in microglia occurs early after an ischemic insult and is localized to areas of injury, mostly near peri-infarct regions.

IL-1 α can be actively localized to cell nuclei [10] and in microglia this may represent a mechanism of inhibiting IL-1 α release after hypoxic cellular injury [11]. 24 h after 60 min MCAo in CX3CR1-GFP \pm mice, microglia expressing GFP also expressed IL-1 α that was localized to the nucleus in some cells (Figure 2Ei, ii), but not in others (Figure 2Eiii, iv). Confocal images (Leica TCS SP5 AOBs confocal microscope) were captured from these sections and were processed and analysed with Image J <http://rsb.info.nih.gov/ij>. Regions of interest for quantification of mean fluorescence intensities (MFIs) in whole microglia and microglial nuclei were selected using the GFP and DAPI signals respectively.

MFIs were quantified for IL-1 α and GFP in whole microglia using a maximum Z projection of the confocal image stack. Nuclear IL-1 α and GFP MFIs were quantified in a confocal slice at the level of the nucleus. The fold enrichment of IL-1 α and GFP in the nucleus were calculated as follows: Fold enrichment = MFI (nucleus)/MFI (whole cell). The fold enrichment data suggest that GFP was uniformly distributed throughout the cell (Figure 2F). However the spread of IL-1 α enrichment throughout a cell was much broader suggesting that its localization between the nucleus and cytosol was regulated (Figure 2F). We have previously reported that IL-1 α is retained in the nuclei of dead and dying cells [11], and also that microglia die in the infarct following MCAo [12]. Thus it is possible that microglia in an ischemic brain undergoing cell death processes may localize IL-1 α to the nucleus to limit its release.

These data show that IL-1 α is expressed by microglia at sites of brain injury within a relevant window of time at which blocking the effects of IL-1 are known to be neuroprotective [4]. At these times, IL-1 β is not present suggesting that IL-1 α is the active IL-1 isoform in mediating the early inflammatory period following ischemic brain injury. This is consistent with recent discoveries highlighting the earlier appearance of IL-1 α in sterile inflammatory responses, with a later contribution from IL-1 β [13], although functional evidence for a role of microglia-derived IL-1 α in brain injury is not provided here. In cerebral ischemia the primary injury to brain cells is caused by the lack of blood supply and so can be considered sterile. Sterile inflammation is known as a major contributor to disease and injury [14], and IL-1 α has become recognised as a major mediator of sterile tissue injury [15,16]. Thus the data presented here extend our, and others, previous work showing that IL-1 α is a key inflammatory cytokine following tissue injury. This study also extends our previous *in vitro* studies showing that the sub-cellular distribution of IL-1 α is regulated under conditions of hypoxia, which may be relevant to the regulation of its release and sterile inflammatory responses [11].

List of abbreviations

BBB: Blood Brain Barrier; GFP: Green Fluorescent Protein; IL-1: Interleukin-1; IL-1Ra: Interleukin-1 receptor antagonist; MCAo: Middle Cerebral Artery occlusion; MFI: Mean Fluorescence Intensity.

Acknowledgements

This work was funded by the Wellcome Trust (DB, NML, GLC), and by the European Union's Seventh Framework Programme (FP7/2008-2013) under Grant Agreements 201024 and 202213 (European Stroke Network) (AD).

Author details

¹Faculty of Life Sciences, University of Manchester, UK. ²Laboratory of Molecular Neuroendocrinology, Institute of Experimental Medicine, Budapest, Hungary.

Authors' contributions

NML carried out the immune studies and analysis. KJK contributed to the design and execution of the surgical studies. GLC contributed experimentally. DB contributed to design and analysis of the study and wrote the manuscript. AD carried out the surgeries, contributed to the design and analysis of the study and wrote the manuscript. All authors read and approved the final manuscript.

Competing interests

The authors declare that they have no competing interests.

Received: 2 September 2011 Accepted: 29 December 2011

Published: 29 December 2011

References

1. Brough D, Tyrrell PJ, Allan SM: **Regulation of interleukin-1 in acute brain injury.** *Trends Pharmacol Sci* 2011, **32**:617-622.
2. Emsley HC, Smith CJ, Georgiou RF, Vail A, Hopkins SJ, Rothwell NJ, Tyrrell PJ: **A randomised phase II study of interleukin-1 receptor antagonist in acute stroke patients.** *JNeurolNeurosurgPsychiatry* 2005, **76**:1366-1372.
3. Boutin H, LeFeuvre RA, Horai R, Asano M, Iwakura Y, Rothwell NJ: **Role of IL-1alpha and IL-1beta in ischemic brain damage.** *JNeurosci* 2001, **21**:5528-5534.
4. Mulcahy NJ, Ross J, Rothwell NJ, Loddick SA: **Delayed administration of interleukin-1 receptor antagonist protects against transient cerebral ischaemia in the rat.** *BrJPharmacol* 2003, **140**:471-476.
5. Buttini M, Sauter A, Boddeke HW: **Induction of interleukin-1 beta mRNA after focal cerebral ischaemia in the rat.** *Brain Res Mol Brain Res* 1994, **23**:126-134.
6. Zhai QH, Futrell N, Chen FJ: **Gene expression of IL-10 in relationship to TNF-alpha, IL-1beta and IL-2 in the rat brain following middle cerebral artery occlusion.** *J Neurol Sci* 1997, **152**:119-124.
7. Denes A, Ferenczi S, Halasz J, Kornyei Z, Kovacs KJ: **Role of CX3CR1 (fractalkine receptor) in brain damage and inflammation induced by focal cerebral ischemia in mouse.** *J Cereb Blood Flow Metab* 2008, **28**:1707-1721.
8. Cardona AE, Piro EP, Sasse ME, Kostenko V, Cardona SM, Dijkstra IM, Huang D, Kidd G, Dombrowski S, Dutta R, et al: **Control of microglial neurotoxicity by the fractalkine receptor.** *NatNeurosci* 2006, **9**:917-924.
9. McColl BW, Rothwell NJ, Allan SM: **Systemic inflammatory stimulus potentiates the acute phase and CXC chemokine responses to experimental stroke and exacerbates brain damage via interleukin-1 and neutrophil-dependent mechanisms.** *JNeurosci* 2007, **27**:4403-4412.
10. Luheshi NM, Rothwell NJ, Brough D: **The dynamics and mechanisms of interleukin-1alpha and Beta nuclear import.** *Traffic* 2009, **10**:16-25.
11. Luheshi NM, McColl BW, Brough D: **Nuclear retention of IL-1 alpha by necrotic cells: a mechanism to dampen sterile inflammation.** *Eur J Immunol* 2009, **39**:2973-2980.
12. Denes A, Vidyasagar R, Feng J, Narvainen J, McColl BW, Kauppinen RA, Allan SM: **Proliferating resident microglia after focal cerebral ischaemia in mice.** *J Cereb Blood Flow Metab* 2007, **27**:1941-1953.
13. Rider P, Carmi Y, Guttman O, Braiman A, Cohen I, Voronov E, White MR, Dinarello CA, Apte RN: **IL-1{alpha} and IL-1{beta} Recruit Different Myeloid Cells and Promote Different Stages of Sterile Inflammation.** *J Immunol* 2011, **187**:4835-4843.
14. Rock KL, Latz E, Ontiveros F, Kono H: **The sterile inflammatory response.** *Annu Rev Immunol* 2010, **28**:321-342.
15. Kono H, Karmarkar D, Iwakura Y, Rock KL: **Identification of the cellular sensor that stimulates the inflammatory response to sterile cell death.** *J Immunol* 2010, **184**:4470-4478.
16. Chen CJ, Kono H, Golenbock D, Reed G, Akira S, Rock KL: **Identification of a key pathway required for the sterile inflammatory response triggered by dying cells.** *NatMed* 2007, **13**:851-856.

doi:10.1186/1742-2094-8-186

Cite this article as: Luheshi et al.: Interleukin-1 α expression precedes IL-1 β after ischemic brain injury and is localised to areas of focal neuronal loss and penumbral tissues. *Journal of Neuroinflammation* 2011 **8**:186.

Submit your next manuscript to BioMed Central and take full advantage of:

- Convenient online submission
- Thorough peer review
- No space constraints or color figure charges
- Immediate publication on acceptance
- Inclusion in PubMed, CAS, Scopus and Google Scholar
- Research which is freely available for redistribution

Submit your manuscript at
www.biomedcentral.com/submit





NLRP3-inflammasome activating DAMPs stimulate an inflammatory response in glia in the absence of priming which contributes to brain inflammation after injury

Catherine Diane Savage, Gloria Lopez-Castejon, Adam Denes[†] and David Brough^{*†}

Faculty of Life Sciences, University of Manchester, Manchester, UK

Edited by:

Anna Rubartelli, National Cancer Research Institute, Italy

Reviewed by:

Eicke Latz, University of Massachusetts Medical School, USA
Bruno Conti, The Scripps Research Institute, USA
Veit Hornung, University of Bonn, Germany

*Correspondence:

David Brough, Faculty of Life Sciences, University of Manchester, AV Hill Building, Oxford Road, Manchester M13 9PT, UK.
e-mail: david.brough@manchester.ac.uk

[†]Adam Denes and David Brough have contributed equally to this work.

Inflammation in the absence of infection (sterile inflammation) contributes to acute injury and chronic disease. Cerebral ischemia is a devastating condition in which the primary injury is caused by reduced blood supply and is therefore sterile. The cytokine interleukin-1 β (IL-1 β) is a key contributor to ischemic brain injury and central inflammatory responses. The release of IL-1 β is regulated by the protease caspase-1, and its activating complex, the inflammasome. Of the known inflammasomes the best characterized, and one that is perceived to sense sterile injury is formed by a pattern recognition receptor called NOD-like receptor pyrin domain containing three (NLRP3). A key feature of NLRP3-inflammasome dependent responses *in vitro* in macrophages is the requirement of an initial priming stimulus by a pathogen (PAMP), or damage associated molecular pattern (DAMP) respectively. We sought to determine the inflammatory responses of NLRP3-activating DAMPs on brain derived mixed glial cells in the absence of an initial priming stimulus *in vitro*. In cultured mouse mixed glia the DAMPs ATP, monosodium urate, and calcium pyrophosphate dehydrate crystals had no effect on the expression of IL-1 α or IL-1 β and induced release only when the cells were primed with a PAMP. In the absence of priming, these DAMPs did however induce inflammation *via* the production of IL-6 and CXCL1, and the release of the lysosomal protease cathepsin B. Furthermore, the acute phase protein serum amyloid A (SAA) acted as a priming stimulus on glial cells resulting in levels of IL-1 expression comparable to those induced by the PAMP lipopolysaccharide. *In vivo*, after cerebral ischemia, IL-1 production contributed to increased IL-6 and CXCL1 since these cytokines were profoundly reduced in the ischemic hemispheres from IL-1 α/β double KO mice, although injury-induced cytokine responses were not abolished. Thus, DAMPs augment brain inflammation by directly stimulating production of glial derived inflammatory mediators. This is markedly enhanced by DAMP-induced IL-1-release-dependent responses that require a sterile endogenous priming stimulus such as SAA.

Keywords: inflammation, caspase-1, priming, interleukin-1, NLRP3-inflammasome, cerebral ischemia

INTRODUCTION

Interleukin-1 β (IL-1 β) is a key pro-inflammatory cytokine that is central to the damaging inflammatory processes that accompany sterile disease (Dinarello, 2011). This is particularly true after an acute brain injury such as cerebral ischemia, or stroke, where IL-1 β is established as a major contributor to damage (Brough et al., 2011). It is produced during disease or after an injury as an inactive precursor (pro-IL-1 β) by cells of the innate immune system such as macrophages, or in diseases of the central nervous system (CNS), by microglia (Denes et al., 2008). In order for it to exert any biological effects it must be cleaved into an active molecule and released from the cell whereby it can act on the type I IL-1 receptor (IL-1RI) on responsive cells (Luheshi et al., 2009). A key protease required for the processing of pro-IL-1 β is caspase-1. The activity of caspase-1 is regulated by its recruitment to multi-molecular scaffolds called inflammasomes following an inflammatory stress (Schroder and Tschopp, 2010). Inflammasomes are composed of a

cytosolic pattern recognition receptor (PRR), pro-caspase-1, and, depending on the PRR, an adaptor molecule. The best characterized inflammasome forming PRR, and the one most implicated as a sensor of sterile injury, is NOD-like receptor pyrin domain containing three (NLRP3; Cassel and Sutterwala, 2010; Schroder and Tschopp, 2010). NLRP3 can be activated by a diverse array of disease associated molecules, where it oligomerizes with the adaptor ASC (apoptosis-associated speck-like protein containing a caspase recruitment domain) and caspase-1 to form the NLRP3-inflammasome, resulting in the processing of pro- to mature IL-1 β and its release.

The release of IL-1 β is considered to be a two step process (Hornung and Latz, 2010; Lopez-Castejon and Brough, 2011). IL-1 β is not normally expressed and so its expression must be induced. Stimuli that do this are pathogen associated molecular patterns (PAMPs) or damage associated molecular patterns (DAMPs; Chen and Nunez, 2010; Takeuchi and Akira, 2010). PAMPs are motifs

carried by pathogens, such as bacterial endotoxin (or lipopolysaccharide, LPS) of Gram negative bacteria, and DAMPs are endogenous molecules modified during disease or that are released by necrosis. Stimuli that prime macrophages in this way are however generally inefficient secretion stimuli for IL-1 β and the primed cells are required to encounter an additional PAMP or DAMP stimulus that triggers formation of the inflammasome, activation of caspase-1, and subsequently the processing and secretion of IL-1 β . This comes from an extensive literature on macrophages, and although there is evidence that microglia respond in a similar way to PAMP and DAMP stimulation (Brough et al., 2002; Halle et al., 2008), these responses have yet to be fully characterized. Not only are microglia a unique cell type originating from the yolk sac that are self-renewing throughout life (Ginhoux et al., 2010), but the brain is also protected by the BBB in the absence of injury, which keeps microglia isolated from potential blood-derived priming stimuli. In addition, inflammatory events triggered by DAMPs, other than IL-1 expression or release, have not been explored in glial cells previously.

The effects of NLRP3-activating DAMPs are commonly associated with IL-1 and on primed cells (Hornung and Latz, 2010). This is at least in part because NLRP3 expression is itself dependent upon priming (Bauernfeind et al., 2009). However, in many situations of acute injury, where there is rapid and localized loss of tissue (such as cerebral ischemia for example) there will be an abundance of DAMPs that may stimulate cells that have not been subject to an initial priming stimulus. LPS (often used to prime cells *in vitro*) is unlikely to be present *in vivo* during sterile injury and endogenous priming stimuli in the brain remain poorly characterized. DAMPs such as monosodium urate (MSU), and calcium pyrophosphate dehydrate (CPPD) crystals induce the production of the pro-inflammatory cytokine IL-6 in monocytes (Guerne et al., 1989) and osteoblast like cells (Bouchard et al., 2002) in the absence of a priming stimulus. MSU is also known to act as a potent adjuvant in driving adaptive immune responses independently of the NLRP3-inflammasome (Kool et al., 2011) and potentially dependent upon Syk kinase (Ng et al., 2008). Inflammatory responses in the brain (after cerebral ischemia for example) may be influenced by both local DAMPs and circulating inflammatory mediators once the breakdown of the BBB has occurred. As acute brain injury is associated with a marked central inflammatory response the aim of this research was to identify the inflammatory responses of glial cells, inflammatory cells of the CNS, to key mediators of sterile injury, NLRP3-activating DAMPs, in the absence of cell priming, and in the presence of a relevant endogenous priming stimulus.

MATERIALS AND METHODS

MATERIALS

DMEM culture media was purchased from Sigma (UK). Fetal bovine serum (FBS), glutamine, and a streptomycin/penicillin antibiotic solution were all purchased from Invitrogen (UK). Bacterial LPS (*Escherichia coli* 026:B6), Poly(IC), and ATP were purchased from Sigma (UK). MSU and CPPD crystals were from Invitrogen (UK). Serum amyloid A (SAA) was purchased from PeproTech (UK). All primers for qPCR were purchased from Qiagen (UK).

MIDDLE CEREBRAL ARTERY OCCLUSION, PERFUSION, AND TISSUE HOMOGENIZATION

We induced cerebral ischemia by middle cerebral artery occlusion (MCAo) as described previously (Denes et al., 2010a). Briefly, C57BL/6J mice (Harlan Olac) or IL-1 $\alpha\beta$ -deficient (IL-1 $\alpha\beta$ double KO) mice, weighing 26–32 g were anesthetized with isoflurane and were subjected to MCAo for 60 min using an intraluminal filament (180 μ m diameter, left side occluded) followed by 24 h reperfusion. After transcatheter perfusion with saline, brains were collected, and homogenized as described previously (Chapman et al., 2009). Protein concentrations were calculated using BCA assay (Pierce/Thermo Fisher Scientific). Some mice were perfused with 4% paraformaldehyde (PFA), and following post-fixation in PFA and cryoprotection in sucrose, brain sections were cut on a sledge microtome for immunohistochemistry and cresyl-violet staining. All animal procedures were performed under the University of Manchester project license number (40/3076) and adhered to the UK Animals (Scientific Procedures) Act (1986).

IMMUNOHISTOCHEMISTRY

Immunostaining was performed on free-floating brain sections as described (Denes et al., 2010a). After blocking with 2% normal donkey serum in PBS containing 0.3% Triton X-100, rabbit anti-Iba1 (WAKO, Germany) and rat anti-CD45 (Serotec, UK) antibodies were incubated overnight. Antigens were visualized using appropriate fluorochrome (Alexa 594, Alexa 488)-conjugated donkey secondary antibodies (Invitrogen). Mounted brain sections were coverslipped with ProLong mounting medium (Invitrogen) and analyzed on an Olympus BX51 microscope using a Coolsnap ES camera (Photometrics) through MetaVue software (Molecular Devices). CD45 and Iba 1 positive cells were quantified by counting six separate sections from the ipsilateral and contralateral hemispheres (striatum and cortex). The numbers of Iba 1 positive cells expressing CD45 were recorded for both hemispheres.

CELL CULTURE

Mixed glia were cultured from C57BL/6J at post-natal day 1–4 as described previously (Pinteaux et al., 2002). Whole brains were dissected into DMEM with 10% FBS v/v and 1% P/S. Meninges were removed and cells dissociated by trituration prior to seeding at a density equivalent to one brain/60 cm². The culture medium was changed twice a week until cultures reached confluency (14–20 days). These cultures are composed of 78% astrocytes, 12% O2A progenitor cells, and 10% microglia (Pinteaux et al., 2002). Cultures were treated with LPS (1 μ g/ml), poly(IC; 50 μ g/ml), ATP (5 mM), MSU (250 μ g/ml), CPPD (250 μ g/ml), or SAA (0.03–3 μ g/ml) for 24 h. Cultures subjected to PAMP and DAMP stimulation were treated with LPS or SAA for 24 h followed by ATP, MSU, or CPPD for 1 h.

QUANTITATIVE REAL-TIME PCR

RNA was extracted from cultured mixed glia using the TRIzol® method (Invitrogen) and reverse transcribed to cDNA using MMLV reverse transcriptase according to the manufacturer's instructions (Invitrogen). Specific primers for IL-1 β , IL-1 α , caspase-1, NLRP3, ASC, iNOS, IL-6, TNF α , CXCL1, and CXCL12 were purchased from Qiagen (QuantiTech Primer Assays) and

qPCR was performed using Power SYBR® Green PCR mastermix (Applied Biosystems) and SDS v2.3 (Applied Biosystems). For each primer set the CT threshold was set manually to achieve a slope efficiency of >99% and a single product on melt curve analysis. RNA from LPS-treated J774 macrophages was used to create a standard curve and gene expression was calculated using the relative standard curve method. Data were normalized to expression levels of the housekeeping gene SDHA (QuantiTech Primer Assays, Qiagen) across each treatment and fold change was expressed relative to basal RNA levels from untreated mixed glia.

DETECTION OF CYTOKINES BY ELISA

Measurement of key inflammatory cytokines (IL-1 β , IL-1 α , IL-6, CXCL1) released into the culture supernatant or expressed in the lysate was performed using specific ELISAs (R&D Systems, UK) according to manufacturers guidelines.

DETECTION OF CYTOKINES BY ELISA AND CYTOMETRIC BEAD ARRAY

Measurement of cytokines released into the culture supernatant or expressed in the lysate was performed using specific ELISAs (R&D Systems, UK) according to manufacturer's guidelines. Key inflammatory cytokines (IL-1 β , IL-1 α , IL-6, CXCL1) were measured in all tissues examined using appropriate cytometric bead array (CBA) Flex Sets (BD Biosciences) according to the manufacturer's protocol.

FLOW CYTOMETRIC ANALYSIS

Cultured mixed glia were resuspended using 0.5 mM EDTA in PBS. The following fluorochrome-labeled monoclonal antibodies were applied according to manufacturer's instructions: PE conjugated anti-CD11c (1:100, eBioscience), APC conjugated anti-MHCII (1:200, eBioscience), FITC conjugated anti-CD11b (1:200, eBioscience), and PerCP-Cy5.5 conjugated anti-CD45 (1:500, eBioscience). The surface expression of these markers were analyzed using CyAn advanced flow cytometer (Beckman Coulter) and Summit v4.3 software (Dako). Microglia were gated for analysis based on co-expression of CD11b and CD45.

WESTERN BLOTTING

Following the experiment supernatants were harvested and prepared in sample buffer containing 1% β -mercaptoethanol. Samples were boiled and then electrophoresed on 12% SDS-acrylamide gels. Proteins were subsequently transferred onto nitrocellulose membrane and blotted using polyclonal sheep anti-mouse IL-1 β (1:1000 in 5% milk, NIBSC, UK), or polyclonal goat anti-mouse cathepsin B (1:500, R&D Systems). The membrane was then stained with polyclonal rabbit anti-sheep IgG horse radish peroxidase (HRP) conjugate for IL-1 β (1:2000 in 5% milk, Dako, UK), or with HRP-conjugated rabbit anti-goat IgG for cathepsin B (1:1000 in 5% milk, Dako, UK), with subsequent exposure using enhanced chemi-luminescence (ECL) reagents (Amersham, UK).

GEL ZYMOGRAPHY

Released gelatinase activity was assessed by gelatin-substrate zymography as previously described (Kleiner and Stetler-Stevenson, 1994). Briefly, serum free supernatants from treated cultured mixed glia were mixed with an equal volume of loading buffer (10% SDS, 50% glycerol, 400 mM Tris-HCl pH 6.8,

250 μ g/ml bromophenol blue). All samples were loaded neat onto 8% zymography gels except for one of the ATP-treated supernatants (+*) which was diluted 1:3. Following electrophoresis, gels were washed in 2.5% Triton X-100 to remove SDS. Proteinases were renatured in activity buffer (50 mM Tris-HCl pH 7.5, 5 mM CaCl₂, 5 μ M ZnCl₂, 0.02% NaN₃) for 96 h at 37°C prior to staining in 0.5% Coomassie Brilliant Blue R-250 in 40% methanol and 10% acetic acid for 1 h at rt. Gels were destained at rt in 10% acetic acid, 10% methanol until clear bands appeared. Molecular weight of bands was estimated against molecular weight markers (BioRad).

DATA ANALYSIS

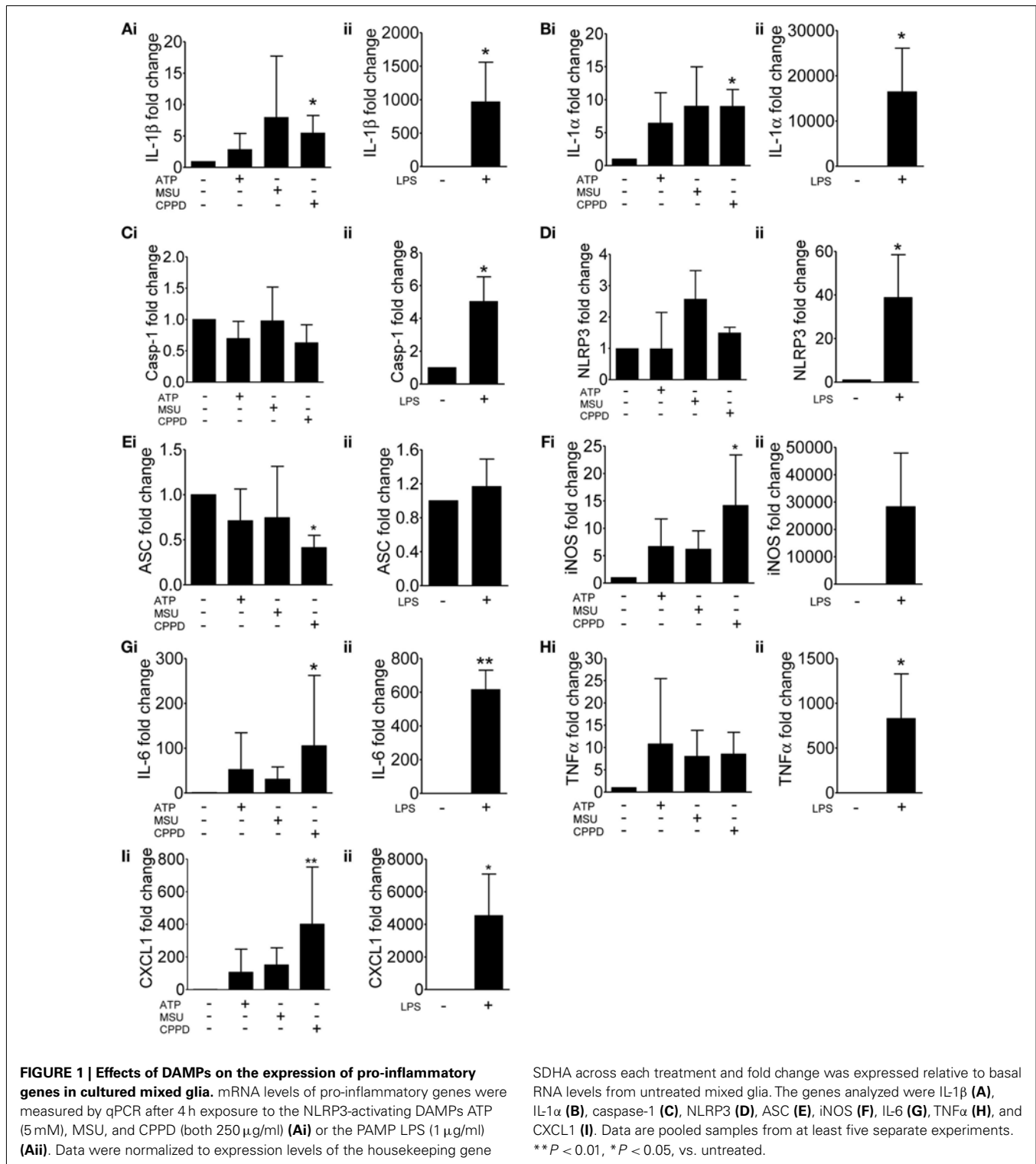
All quantitative assessments were performed in a blinded manner. Unless stated otherwise, for two groups paired *t*-test (two-tailed), for three or more groups one-way or two-way analysis of variance (ANOVA) followed by Bonferonni's *post hoc* multiple- or paired-comparison were used. All data are expressed as mean \pm SD. *** *P* < 0.001, ** *P* < 0.01, * *P* < 0.05.

RESULTS

As discussed above, NLRP3 is proposed as a sensor of sterile injury and disease and recognizes a wide range of structurally diverse DAMPs (Cassel and Sutterwala, 2010). We selected three of the best characterized NLRP3-activating DAMPs for our investigation into the effects of cell priming. ATP activates NLRP3 *via* its activation of cell surface P2X7 receptors (Mariathasan et al., 2006). MSU and CPPD crystals, inflammatory drivers of gout, and pseudogout respectively also activate the NLRP3-inflammasome (Martinon et al., 2006). Uric acid crystals are also suggested to be a general inflammatory signal released from dead and dying cells (Kono et al., 2010). We initially looked at the effects of these NLRP3-activating DAMPs on cell priming itself. Primary cultures of mouse mixed glia (composed of astrocytes and microglia; Pinteaux et al., 2002) were treated with ATP, MSU, or CPPD crystals for 4 h after which lysates were harvested and analyzed by qPCR for the expression of markers of inflammatory cell priming (Figure 1). As a positive control cultures were treated with the PAMP LPS. We initially investigated the effects of these DAMPs and LPS on the expression of genes typically associated with the inflammasome and priming e.g., IL-1 β (Figure 1Ai), IL-1 α (Figure 1Bi), caspase-1 (Figure 1Ci), NLRP3 (Figure 1Di), and ASC (Figure 1Ei). In general, DAMPs had no effect on the expression of these genes except for CPPD crystals, where a significant increase in the expression of IL-1 β and IL-1 α was observed (Figures 1Ai,Bi). LPS stimulation increased the expression of all genes, including caspase-1 (Figure 1C) and NLRP3 (Figure 1D), but did not affect ASC, whose expression did not change with any treatment except with CPPD crystals where a significant decrease was observed (Figure 1E).

In order to determine whether these NLRP3-activating DAMPs were capable of stimulating a more general inflammatory response we extended our study on gene expression to include additional inflammatory genes such as iNOS (Figure 1F), IL-6 (Figure 1G), TNF α (Figure 1H), and CXCL1 (Figure 1I). Again, DAMPs had no effect, with the exception of CPPD crystals on the expression of iNOS (Figure 1F), IL-6 (Figure 1G), and CXCL1 (Figure 1I),

dc_2027_22



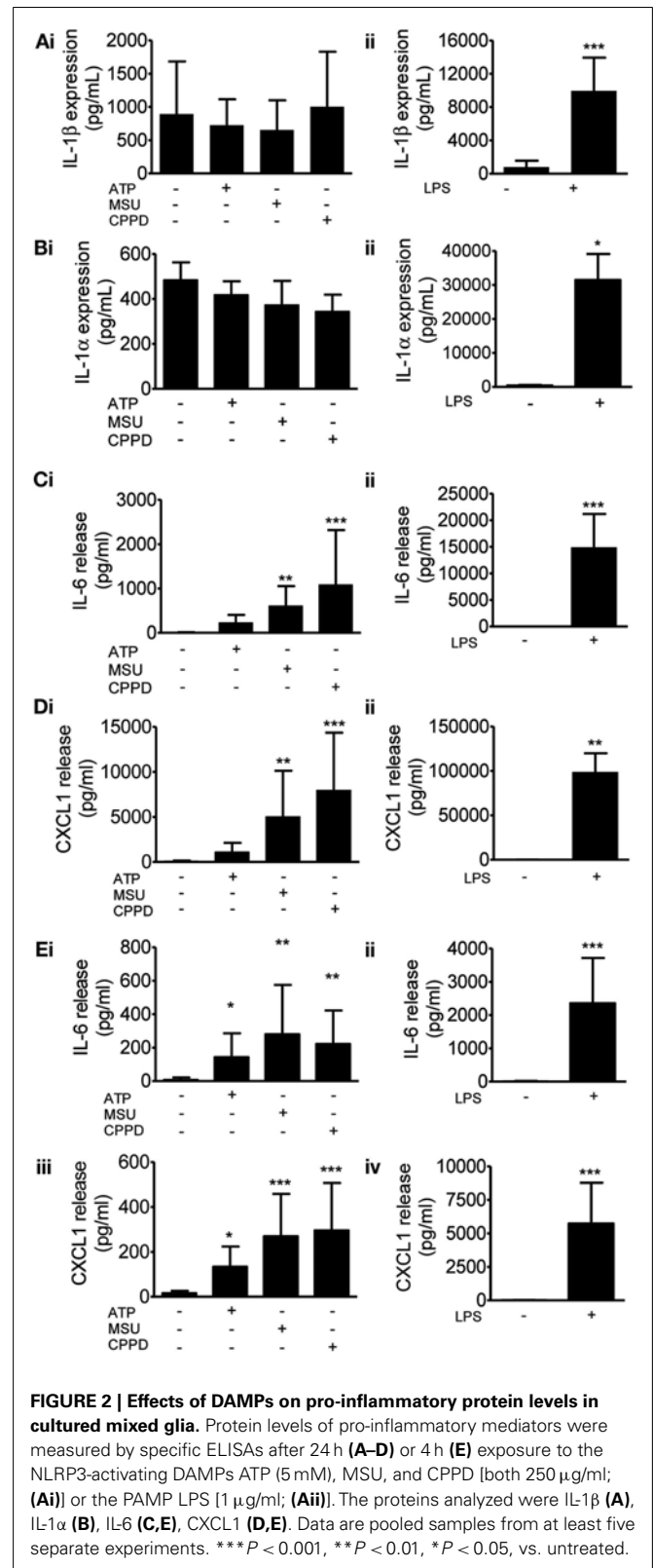
whilst LPS induced a robust response across all genes tested. These data suggest that at the level of gene expression, and within the limits of the genes investigated in this study, and with the exception of CPPD, NLRP3-activating DAMPs have a negligible effect.

We then investigated protein levels in DAMP treated mixed glial cultures for IL-1 β , IL-1 α , IL-6, and CXCL1, which we have previously reported to be upregulated in response to focal ischemic injury in both the plasma and peripheral tissues, and in the brain (Chapman et al., 2009; Denes et al., 2010a; Figure 2). After 24 h

NLRP3-activating DAMPs induced no increase in the protein levels of IL-1 β (Figure 2Ai) or IL-1 α (Figure 2Bi), whilst MSU and CPPD did induce significant increases in the production of IL-6 (Figure 2Ci) and CXCL1 (Figure 2Di). Although raised at 24 h the effects of ATP on IL-6 and CXCL1 levels were not significant, but were when we investigated the earlier time point of 4 h (Figure 2E). LPS induced a robust increase in the levels of all proteins examined (Figure 2). The production of inflammatory mediators by DAMPs alone suggest that they are capable of inducing an inflammatory response, albeit not as robust when compared to the effects of typical PAMPs such as LPS. How these DAMPs act to induce this inflammatory response is not known. None of the DAMPs tested here are reported to act as ligands for toll-like receptor (TLR). However, as mentioned in the introduction MSU can induce Syk kinase signaling (Ng et al., 2008). These DAMPs also caused some cell death within our cultures (data not shown) and so it is possible that this contributed to the effects on cytokine production observed. Microglia can upregulate CD11c and MHCII markers on the cell surface after cerebral ischemia, resulting in a phenotype resembling that of dendritic cells (Felger et al., 2010). We investigated whether PAMPs and DAMPs can directly activate an antigen-presenting phenotype in microglia. Flow cytometry showed that LPS induced an activation of cell surface CD11c and MHCII in microglia, whilst DAMPs alone had no effect (Figure 3). These data suggest that the NLRP3-inflammasome activating DAMPs investigated here, when applied alone, do not act as a priming stimulus for microglial antigen presentation.

These DAMPs are known to engage the NLRP3-inflammasome and to activate caspase-1 resulting in the processing and release of IL-1 β from primed cells. Although much of the literature on IL-1 secretion comes from work on peripheral macrophages, PAMP and DAMP-dependent IL-1 responses from microglia have been reported (e.g., Brough et al., 2002; Halle et al., 2008). The limited effects of these DAMPs observed so far was not due to their use at an insufficient concentration since priming of mixed glial cultures with LPS followed by treatment with ATP, MSU, or CPPD induced caspase-1 activation and the release of mature IL-1 β (Figure 4A), and IL-1 α (Figure 4B).

A key step during cerebral ischemia is the early breakdown of the BBB, although it is not known whether this is facilitated by the release of DAMPs from dying cells. Therefore we investigated the effects of DAMPs on the release of cathepsin B and of gelatinases which have been reported to be released following ATP-dependent activation of the P2X7 receptor in the absence of PAMP priming (Gu and Wiley, 2006; Lopez-Castejon et al., 2010), and which contribute to BBB damage after brain injury (Candelario-Jalil et al., 2009). In cultures of mixed glia ATP, MSU, CPPD, and LPS all induced the release of cathepsin B mature single chain (28–30 kDa) form (Figure 5A). Gelatin gel zymography of supernatants from cultures of mixed glia revealed that pro-MMP2 (72 kDa) was constitutively released under control conditions and that treatment of cultures with LPS, or with the DAMPs MSU or CPPD had no effect on released gelatinase activity (Figure 5B). P2X7 receptor activation in monocytes induces the release of active MMP9 (Gu and Wiley, 2006), and here in our cultures of mixed glia ATP-treatment induced a massive increase in released gelatinase activity (Figure 5B).



Although many DAMPs are reported to activate PRRs of the TLR family to prime inflammatory responses (Chen and Nunez, 2010), the priming stimulus for inflammasome function in the

dc_2027_22

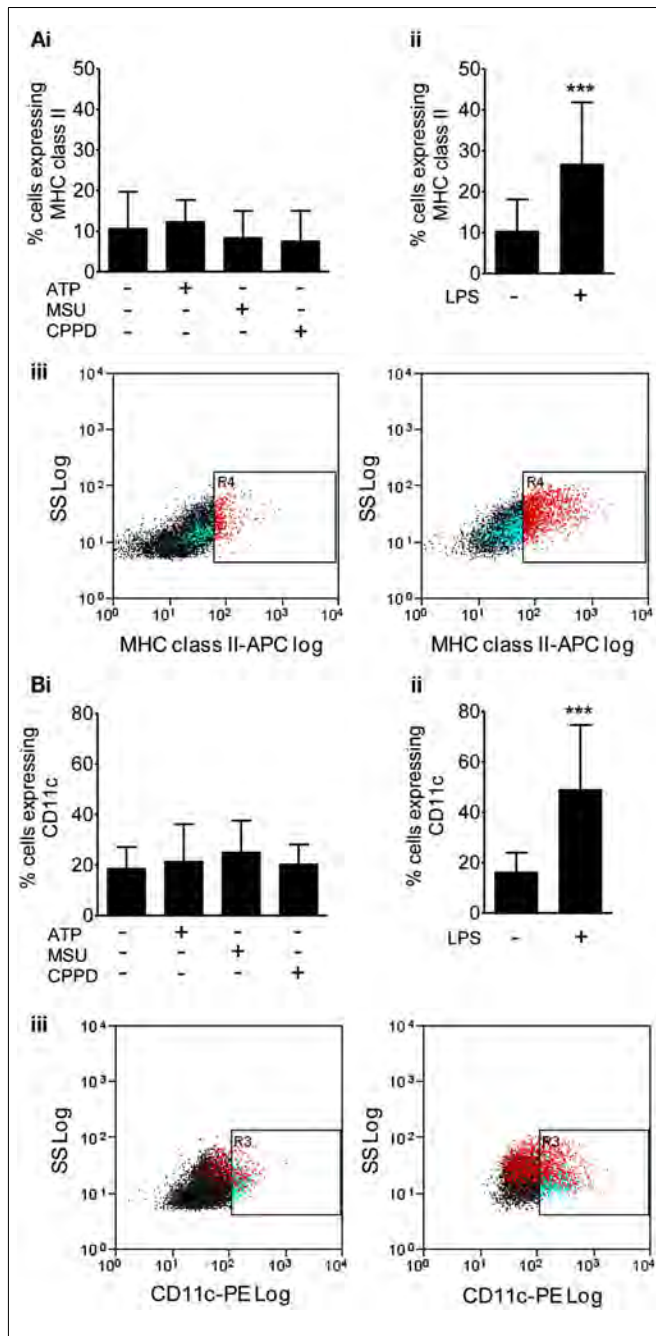


FIGURE 3 | Effects of DAMPs on surface marker expression in microglia cells. The expression of surface markers of microglia activation MHC class II (A), and CD11c (B) were measured after 24 h exposure to the NLRP3-activating DAMPs ATP (5 mM), MSU, and CPPD (both 250 μ g/ml; (Bi)) or the PAMP LPS [1 μ g/ml; (Bii)]. Flow cytometry was used to quantify surface marker expression. Data are expressed as a percentage of cells that co-express CD45 and CD11b. Representative dot plots showing the CD45 and CD11b expressing cell population plus and minus LPS treatment are also shown (Biii). Data are pooled samples from at least five separate experiments. *** $P < 0.001$ vs. untreated.

brain *in vivo* is unknown. BBB breakdown takes place early after cerebral ischemia allowing the penetration of circulating inflammatory mediators into the brain. This coincides with systemic

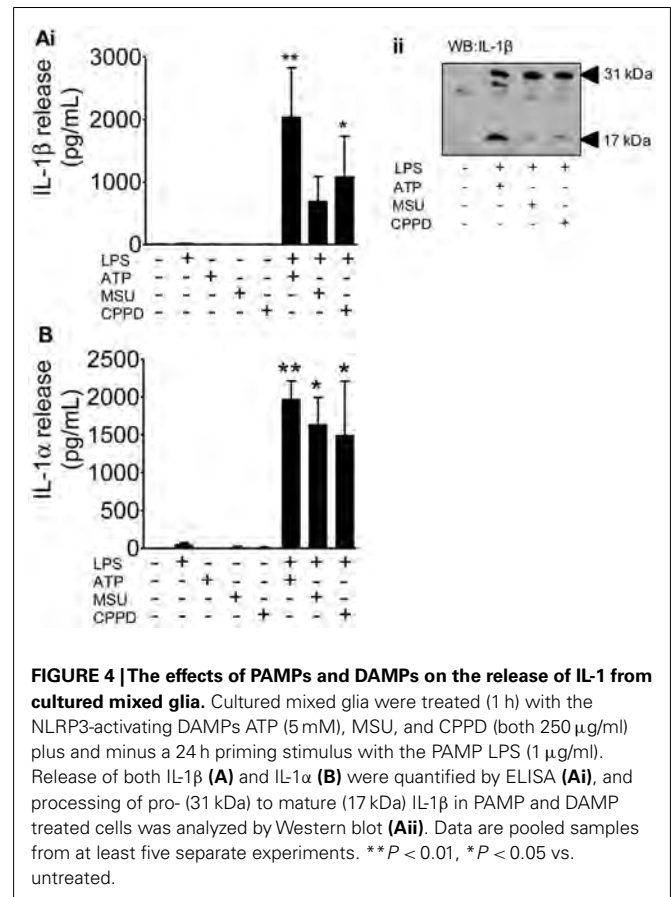
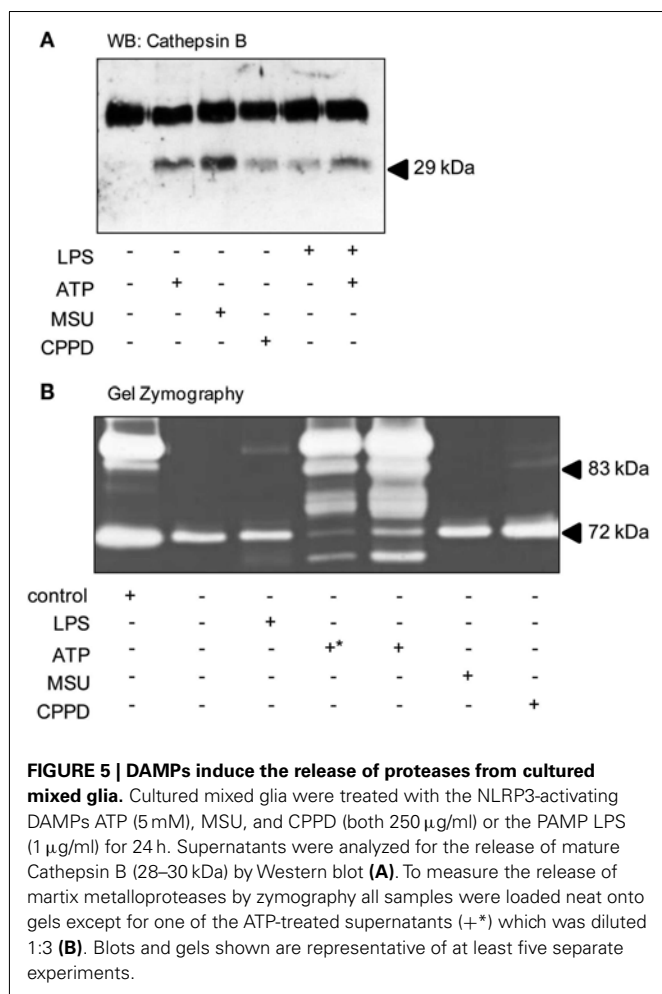


FIGURE 4 | The effects of PAMPs and DAMPs on the release of IL-1 from cultured mixed glia. Cultured mixed glia were treated (1 h) with the NLRP3-activating DAMPs ATP (5 mM), MSU, and CPPD (both 250 μ g/ml) plus and minus a 24 h priming stimulus with the PAMP LPS (1 μ g/ml). Release of both IL-1 β (A) and IL-1 α (B) were quantified by ELISA (Ai), and processing of pro- (31 kDa) to mature (17 kDa) IL-1 β in PAMP and DAMP treated cells was analyzed by Western blot (Aii). Data are pooled samples from at least five separate experiments. ** $P < 0.01$, * $P < 0.05$ vs. untreated.

upregulation of acute phase proteins such as SAA, which acts as an alternative acute phase protein to CRP in mice and is upregulated in plasma as early as 4 h after MCAo (McColl et al., 2007). Four hours after MCAo in the mouse there is disruption of the BBB and microglia localized to these areas of focal BBB disruption express IL-1 (Luheshi et al., 2011), suggesting that plasma derived factors could provide the priming stimulus. Moreover, SAA is reported to prime NLRP3-inflammasome dependent responses in macrophages (Ather et al., 2011; Niemi et al., 2011), and in synovial fibroblasts (Migita et al., 2012), although its effect on brain glia is unknown. Treatment of mixed glial cultures with SAA (0.03–3 μ g/ml, 24 h) induced the expression of IL-1 β (Figure 6A) and IL-1 α (Figure 6B). These cells were effectively primed for inflammasome dependent responses as the addition of the DAMP ATP (5 mM, 1 h) induced a significant release of IL-1 β (Figure 6C). These data suggest the possibility that DAMP-dependent inflammasome responses in the brain may be primed by endogenous plasma constituents.

Since we had found that DAMPs mediated inflammation directly and also induced IL-1 release from primed glial cells *in vitro*, we aimed to investigate the effects of DAMPs on local pro-inflammatory responses induced by brain injury *in vivo* in the absence of IL-1. NLRP3-inflammasome activating DAMPs induce the release of both IL-1 α and IL-1 β from primed macrophages (Gross et al., 2012), and so to investigate the effects of DAMPs independently of IL-1 stimulated events we subjected WT and



IL-1 α / β double KO mice to transient middle cerebral artery occlusion (tMCAo) a model of experimental stroke. Thus use of the IL-1 α / β double KO mice allowed us to dissect DAMP-dependent responses independently of any IL-1-mediated inflammation. Following tMCAo there was a large lesion in the ipsilateral hemisphere of mice, suggesting that glial cells in this hemisphere would be exposed to DAMPs (Figure 7Ai). Within this area there was significant microglial cell activation when compared to the contralateral hemisphere, observed by increased expression of Iba1 and CD45 (Figures 7Ai–iii). Twenty four hours after MCAo IL-6 and CXCL1 were increased in the ipsilateral hemisphere independently of the presence of IL-1 ($P < 0.01$ and 0.001 , respectively, two-way ANOVA) compared to the contralateral hemisphere (Figures 7B,C). WT mice demonstrated a higher level of increase (70-fold for IL-6 and 24-fold for CXCL1) than IL-1 α / β KO mice (26-fold for IL-6 and 11-fold for CXCL1), but CXCL1 was still significantly upregulated in IL-1 α / β KO mice in the ipsilateral hemisphere based on Bonferroni's *post hoc* comparison following two-way ANOVA ($P < 0.05$) and the interaction between genotype and hemispheric increase of CXCL1 was also significant (two-way ANOVA, $P < 0.01$; Figures 7B,C). IL-1 β and IL-1 α levels were undetectable in IL-1 α / β KO mice and IL-1 α displayed a significant increase after cerebral ischemia in the

ipsilateral hemisphere (two-way ANOVA followed by Bonferroni's *post hoc* test, $P < -0.05$, not shown). These data are consistent with the *in vitro* data above, suggesting that DAMPs induce a priming-independent inflammatory response, and once expression and release of IL-1 takes place, this inflammatory response is markedly augmented in the brain *in vivo*.

DISCUSSION

Here, we have analyzed the pro-inflammatory effects of NLRP3-activating DAMPs in the absence/presence of priming stimuli *in vitro* in cultures of mixed glial cells. As a result of our investigations we propose that in acute brain injury DAMPs can contribute to brain inflammation *via* at least three mechanisms: by directly stimulating the production of glial derived pro-inflammatory mediators, by contributing to BBB injury through the release of various proteases, and by inducing IL-1 release from primed cells. The presence of IL-1 in turn, markedly augments damage-induced inflammatory responses *in vivo*.

Inflammation is recognized as a major contributor to the worsening of acute brain injury and inhibiting IL-1 with the receptor antagonist (IL-1Ra) is protective in experimental models of stroke (Brough et al., 2011), and has shown promise as a treatment in clinical trials (Emsley et al., 2005). Early after cerebral ischemia (4 h) the related IL-1 family member IL-1 α is expressed by microglia in areas of brain that will become infarct (Luheshi et al., 2011), with subsequent expression of IL-1 β occurring at later time points (24 h; Denes et al., 2008). Mice in which both IL-1 α and IL-1 β have been deleted (IL-1 α / β double KO), but not single gene KOs, have markedly reduced damage in response to MCAo (Boutin et al., 2001).

Within an ischemic tissue there will be abundant levels of DAMPs that may serve to mediate local inflammatory responses. The inflammatory actions of DAMPs are most often reported as the ability to stimulate formation of the NLRP3-inflammasome, thus activating caspase-1 and inducing the release of IL-1 β (Cassel and Sutterwala, 2010). However, *in vitro* DAMPs are only reported to achieve this after the cell, typically a macrophage, has been primed with a PAMP such as LPS (Bauernfeind et al., 2009; Hornung and Latz, 2010). In monocytes and synovial cells (Guerne et al., 1989), and osteoblast like cells (Bouchard et al., 2002) release IL-6 occurs in response to the NLRP3-inflammasome activating DAMPs MSU and CPPD in the absence of priming. However, to date, an investigation of the pro-inflammatory effects of NLRP3-activating DAMPs in glial cells, in the absence of priming, has not taken place. Thus, in this study we sought to determine the pro-inflammatory effects of NLRP3-activating DAMPs in the presence and absence of PAMPs on inflammatory cells from the brain. We used cultures of mixed glia, composed mainly of astrocytes and microglia (Pinteaux et al., 2002). Both microglia and astrocytes represent a source of IL-1 in culture (Brough et al., 2002; Bianco et al., 2009) and from our experiments it was not possible to identify the relative contribution of each cell type to released cytokine levels. Given their similarity to macrophages, microglia are generally considered to be the major source of IL-1 in the brain after an injury (Denes et al., 2010b), yet astrocytes are also known to express IL-1 β following MCAo in mice (Denes et al., 2008). It is possible that a contribution from both cellular sources

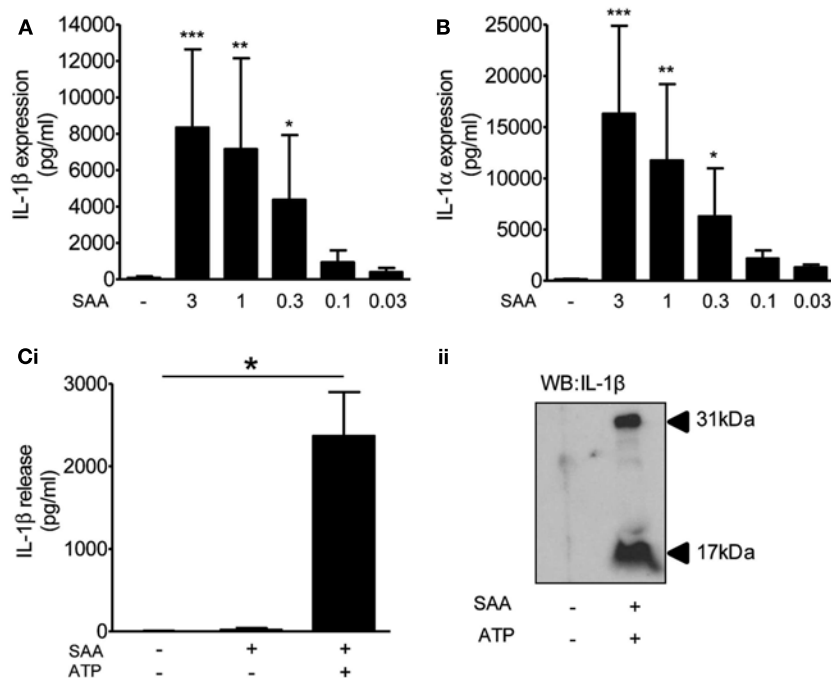


FIGURE 6 | The effects of DAMPs on the release of IL-1 from cultured mixed glia primed with serum amyloid A (SAA). Cultured mixed glia were treated with the indicated concentration of SAA for 24 h and the expression of IL-1β (A) and IL-1α (B) was measured in the cell lysate by ELISA. The NLRP3-activating DAMP ATP (5 mM) was added to the cultures

after a 24 h priming stimulus with SAA (3 μg/ml) and released IL-1β was quantified by ELISA (Ci). And processing of pro- (31 kDa) to mature (17 kDa) IL-1β was analyzed by Western blot (Cii). Data are pooled samples from at least five separate experiments. *** $P < 0.001$, ** $P < 0.01$, * $P < 0.05$ vs. untreated.

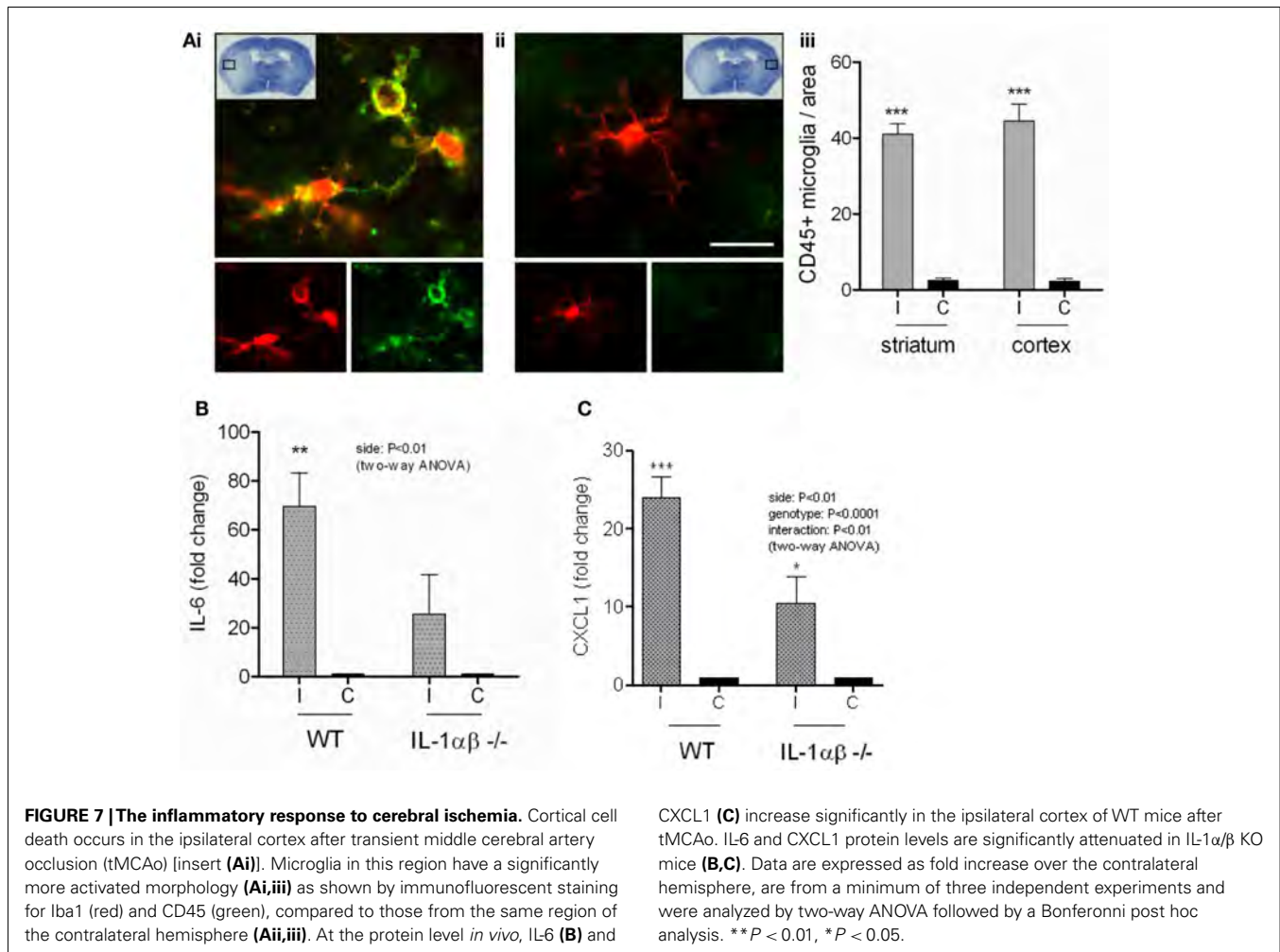
drives inflammation after brain injury, although further experiments with purified cell cultures, and animal models in which solely microglia or astrocytes can produce IL-1 are required to test this.

Entirely consistent with the literature on macrophages, we found that several well characterized DAMPs (ATP, MSU, and CPPD crystals), had no effect on IL-1β levels in the absence of prior PAMP priming (Figures 1, 2, and 4). The results for IL-1α mirrored the effects of DAMPs on IL-1β, i.e., the DAMPs had no effect except when added to a PAMP-primed cell when they induced release (Figures 1, 2, and 4). In contrast, we show that DAMPs induce IL-6 and CXCL1 release from glia *in vitro* in the absence of any priming stimulus, indicating that DAMPs have a direct pro-inflammatory effect on glial cells independently of PAMP-induced signals (Figure 2).

This priming-independent inflammatory response was also observed *in vivo* after MCAo in IL-1α/β double KO mice (Figure 7). The priming stimuli for IL-1-dependent responses in the brain after a stroke are not known. There are a number of possible candidates however. For example, after disruption of the BBB plasma derived molecules known to prime IL-1β responses such as minimally oxidized LDL, and which are associated with co-morbid diseases like type II diabetes, could prime glia at the lesion site (Masters et al., 2010). Other plasma derived molecules include acute phase reactants such as SAA which has also been reported to prime NLRP3-inflammasome dependent responses in macrophages (Ather et al., 2011; Niemi et al., 2011), and we

know that 4 h following MCAo in the mouse plasma SAA levels are elevated (McCull et al., 2007). We showed that SAA was capable of priming glial cultures to express IL-1α and IL-1β (Figure 6). Analogous to the PAMP priming observed with LPS, SAA alone did not induce the release of IL-1, but IL-1β release did occur after a SAA-primed culture was treated with ATP (Figure 6). In addition to these examples it is possible that one of a plethora of DAMPs reported to activate TLRs could provide the priming stimulus (Piccinini and Midwood, 2010). However, our study serves to highlight that brain inflammatory cells can respond to endogenous priming stimuli to promote IL-1-dependent inflammatory responses.

We also discovered that treatment of cultured mixed glia with DAMPs induced the release of cathepsin B, and that the DAMP ATP induced a massive release of gelatinase activity in the absence of priming (Figure 5). ATP induced cathepsin B release from non-primed macrophages results in the *in vitro* degradation of extracellular matrix, suggesting its pro-inflammatory action (Lopez-Castejon et al., 2010). That MSU and CPPD crystals also induce the release of active cathepsin B from non-PAMP-primed cells (Figure 5) suggest that this could be a common inflammatory mechanism of DAMPs. Furthermore, treatment with a cathepsin B inhibitor *in vivo* is neuroprotective following stroke (Benchoua et al., 2004). The effects of DAMP-induced release of gelatinases such as MMP9 could be twofold. MMP9 is known to disrupt the integrity of the BBB following MCAo (McCull et al., 2008), and is also known to be neurotoxic in neuroinflammatory



in vitro models (Thornton et al., 2008). The consequence of these IL-1-independent DAMP effects would be increased production of inflammatory mediators and acute phase reactants, leukocyte recruitment, BBB disruption, and the influx of peripheral, systemic factors.

These data reveal how DAMPs induce inflammatory responses in the absence of any bacterial infection or products, and may be relevant to a range of sterile insults in addition to the model of brain injury used here. These data support a model where DAMPs released at a site of sterile injury induce the release of cytokines and proteases that are central to the establishment of an inflammatory response. DAMPs also induce the secretion of IL-1 α and

IL-1 β from primed glia. In turn, the presence of IL-1 enhances sterile injury-induced inflammatory responses. It is not clear what primes microglia *in vivo* during ischemia but it could be one of a large number of factors, including plasma derived mediators such as SAA, and remains a subject for future investigation.

ACKNOWLEDGMENTS

The authors are grateful to the Wellcome Trust (David Brough, Gloria Lopez-Castejon), the BBSRC (Catherine Diane Savage), and the European Union's Seventh Framework Program (FP7/2008-2013) under Grant Agreements 201024 and 202213 (European Stroke Network; Adam Denes) for funding the research.

REFERENCES

- Ather, J. L., Ckless, K., Martin, R., Foley, K. L., Suratt, B. T., Boyson, J. E., Fitzgerald, K. A., Flavell, R. A., Eisenbarth, S. C., and Poynter, M. E. (2011). Serum amyloid A activates the NLRP3 inflammasome and promotes Th17 allergic asthma in mice. *J. Immunol.* 187, 64–73.
- Bauerfeind, F. G., Horvath, G., Stutz, A., Alnemri, E. S., MacDonald, K., Speert, D., Fernandes-Alnemri, T., Wu, J., Monks, B. G., Fitzgerald, K. A., Hornung, V., and Latz, E. (2009). Cutting edge: NF-kappaB activating pattern recognition and cytokine receptors license NLRP3 inflammasome activation by regulating NLRP3 expression. *J. Immunol.* 183, 787–791.
- Benchoua, A., Braudeau, J., Reis, A., Couriaud, C., and Onteniente, B. (2004). Activation of proinflammatory caspases by cathepsin B in focal cerebral ischemia. *J. Cereb. Blood Flow Metab.* 24, 1272–1279.
- Bianco, F., Perrotta, C., Novellino, L., Francolini, M., Riganti, L., Menna, E., Saglietti, L., Schuchman, E. H., Furlan, R., Clementi, E., Matteoli, M., and Verderio, C. (2009). Acid sphingomyelinase activity triggers microparticle release from glial cells. *EMBO J.* 28, 1043–1054.
- Bouchard, L., de Medicis, R., Lussier, A., Naccache, P. H., and Poubelle, P. E. (2002). Inflammatory microcrystals alter the functional phenotype of human osteoblast-like cells *in vitro*: synergism with IL-1 to overexpress cyclooxygenase-2. *J. Immunol.* 168, 5310–5317.

- Boutin, H., LeFeuvre, R. A., Horai, R., Asano, M., Iwakura, Y., and Rothwell, N. J. (2001). Role of IL-1alpha and IL-1beta in ischemic brain damage. *J. Neurosci.* 21, 5528–5534.
- Brough, D., Le Feuvre, R. A., Iwakura, Y., and Rothwell, N. J. (2002). Purinergic (P2X7) receptor activation of microglia induces cell death via an interleukin-1-independent mechanism. *Mol. Cell. Neurosci.* 19, 272–280.
- Brough, D., Tyrrell, P. J., and Allan, S. M. (2011). Regulation of interleukin-1 in acute brain injury. *Trends Pharmacol. Sci.* 32 617–622.
- Candelario-Jalil, E., Yang, Y., and Rosenberg, G. A. (2009). Diverse roles of matrix metalloproteinases and tissue inhibitors of metalloproteinases in neuroinflammation and cerebral ischemia. *Neuroscience* 158, 983–994.
- Cassel, S. L., and Sutterwala, F. S. (2010). Sterile inflammatory responses mediated by the NLRP3 inflammasome. *Eur. J. Immunol.* 40, 607–611.
- Chapman, K. Z., Dale, V. Q., Denes, A., Bennett, G., Rothwell, N. J., Allan, S. M., and McColl, B. W. (2009). A rapid and transient peripheral inflammatory response precedes brain inflammation after experimental stroke. *J. Cereb. Blood Flow Metab.* 29, 1764–1768.
- Chen, G. Y., and Nunez, G. (2010). Sterile inflammation: sensing and reacting to damage. *Nat. Rev. Immunol.* 10, 826–837.
- Denes, A., Ferenczi, S., Halasz, J., Kornyei, Z., and Kovacs, K. J. (2008). Role of CX3CR1 (fractalkine receptor) in brain damage and inflammation induced by focal cerebral ischemia in mouse. *J. Cereb. Blood Flow Metab.* 28, 1707–1721.
- Denes, A., Humphreys, N., Lane, T. E., Grecis, R., and Rothwell, N. (2010a). Chronic systemic infection exacerbates ischemic brain damage via a CCL5 (regulated on activation, normal T-cell expressed, and secreted)-mediated proinflammatory response in mice. *J. Neurosci.* 30, 10086–10095.
- Denes, A., Thornton, P., Rothwell, N. J., and Allan, S. M. (2010b). Inflammation and brain injury: acute cerebral ischaemia, peripheral, and central inflammation. *Brain Behav. Immun.* 24, 708–723.
- Dinarello, C. A. (2011). Interleukin-1 in the pathogenesis and treatment of inflammatory diseases. *Blood* 117, 3720–3732.
- Emsley, H. C., Smith, C. J., Georgiou, R. F., Vail, A., Hopkins, S. J., Rothwell, N. J., and Tyrrell, P. J. (2005). A randomised phase II study of interleukin-1 receptor antagonist in acute stroke patients. *J. Neurol. Neurosurg. Psychiatr.* 76, 1366–1372.
- Felger, J. C., Abe, T., Kaunzner, U. W., Gottfried-Blackmore, A., Gal-Too, J., McEwen, B. S., Iadecola, C., and Bulloch, K. (2010). Brain dendritic cells in ischemic stroke: time course, activation state, and origin. *Brain Behav. Immun.* 24, 724–737.
- Ginhoux, F., Greter, M., Leboeuf, M., Nandi, S., See, P., Gokhan, S., Mehler, M. F., Conway, S. J., Ng, L. G., Stanley, E. R., Samokhvalov, I. M., and Merad, M. (2010). Fate mapping analysis reveals that adult microglia derive from primitive macrophages. *Science* 330, 841–845.
- Gross, O., Yazdi, A. S., Thomas, C. J., Masin, M., Heinz, L. X., Guarda, G., Quadroni, M., Drexler, S. K., and Tschopp, J. (2012). Inflammasome activators induce interleukin-1alpha secretion via distinct pathways with differential requirement for the protease function of caspase-1. *Immunity* 36, 388–400.
- Gu, B. J., and Wiley, J. S. (2006). Rapid ATP-induced release of matrix metalloproteinase 9 is mediated by the P2X7 receptor. *Blood* 107, 4946–4953.
- Guerne, P. A., Terkeltaub, R., Zuraw, B., and Lotz, M. (1989). Inflammatory microcrystals stimulate interleukin-6 production and secretion by human monocytes and synoviocytes. *Arthritis Rheum.* 32, 1443–1452.
- Halle, A., Hornung, V., Petzold, G. C., Stewart, C. R., Monks, B. G., Reinheckel, T., Fitzgerald, K. A., Latz, E., Moore, K. J., and Golenbock, D. T. (2008). The NALP3 inflammasome is involved in the innate immune response to amyloid-beta. *Nat. Immunol.* 9, 857–865.
- Hornung, V., and Latz, E. (2010). Critical functions of priming and lysosomal damage for NLRP3 activation. *Eur. J. Immunol.* 40, 620–623.
- Kleiner, D. E., and Stetler-Stevenson, W. G. (1994). Quantitative zymography: detection of picogram quantities of gelatinases. *Anal. Biochem.* 218, 325–329.
- Kono, H., Chen, C. J., Ontiveros, F., and Rock, K. L. (2010). Uric acid promotes an acute inflammatory response to sterile cell death in mice. *J. Clin. Invest.* 120, 1939–1949.
- Kool, M., Willart, M. A., van Nimwegen, M., Bergen, I., Pouliot, P., Virchow, J. C., Rogers, N., Osorio, F., Reis e Sousa, C., Hammad, H., and Lambrecht, B. N. (2011). An unexpected role for uric acid as an inducer of T helper 2 cell immunity to inhaled antigens and inflammatory mediator of allergic asthma. *Immunity* 34, 527–540.
- Lopez-Castejon, G., and Brough, D. (2011). Understanding the mechanism of IL-1beta secretion. *Cytokine Growth Factor Rev.* 22, 189–195.
- Lopez-Castejon, G., Theaker, J., Pellegrin, P., Clifton, A. D., Braddock, M., and Surprenant, A. (2010). P2X7 receptor-mediated release of cathepsins from macrophages is a cytokine-independent mechanism potentially involved in joint diseases. *J. Immunol.* 185, 2611–2619.
- Luheshi, N. M., Kovacs, K. J., Lopez-Castejon, G., Brough, D., and Denes, A. (2011). Interleukin-1alpha expression precedes IL-1beta after ischemic brain injury and is localised to areas of focal neuronal loss and penumbra tissues. *J. Neuroinflammation* 8, 186.
- Luheshi, N. M., Rothwell, N. J., and Brough, D. (2009). Dual functionality of interleukin-1 family cytokines: implications for anti-interleukin-1 therapy. *Br. J. Pharmacol.* 157, 1318–1329.
- Mariathasan, S., Weiss, D. S., Newton, K., McBride, J., O'Rourke, K., Roose-Girma, M., Lee, W. P., Weinrauch, Y., Monack, D. M., and Dixit, V. M. (2006). Cryopyrin activates the inflammasome in response to toxins and ATP. *Nature* 440, 228–232.
- Martinon, F., Petrilli, V., Mayor, A., Tardivel, A., and Tschopp, J. (2006). Gout-associated uric acid crystals activate the NALP3 inflammasome. *Nature* 440, 237–241.
- Masters, S. L., Dunne, A., Subramanian, S. L., Hull, R. L., Tannahill, G. M., Sharp, F. A., Becker, C., Franchi, L., Yoshihara, E., Chen, Z., Mullooly, N., Mielke, L. A., Harris, J., Coll, R. C., Mills, K. H., Mok, K. H., Newsholme, P., Nuñez, G., Yodoi, J., Kahn, S. E., Lavelle, E. C., and O'Neill, L. A. (2010). Activation of the NLRP3 inflammasome by islet amyloid polypeptide provides a mechanism for enhanced IL-1beta in type 2 diabetes. *Nat. Immunol.* 11, 897–904.
- McColl, B. W., Rothwell, N. J., and Allan, S. M. (2007). Systemic inflammatory stimulus potentiates the acute phase and CXC chemokine responses to experimental stroke and exacerbates brain damage via interleukin-1- and neutrophil-dependent mechanisms. *J. Neurosci.* 27, 4403–4412.
- McColl, B. W., Rothwell, N. J., and Allan, S. M. (2008). Systemic inflammation alters the kinetics of cerebrovascular tight junction disruption after experimental stroke in mice. *J. Neurosci.* 28, 9451–9462.
- Migita, K., Koga, T., Satomura, K., Izumi, M., Torigoshi, T., Maeda, Y., Izumi, Y., Jiuchi, Y., Miyashita, T., Yamasaki, S., Aiba, Y., Komorim, A., Nakamura, M., Motokawa, S., Kawakami, A., Nakamura, T., and Ishibashi, H. (2012). Serum amyloid A triggers the monosodium urate-mediated mature interleukin-1beta production from human synovial fibroblasts. *Arthritis Res. Ther.* 14, R119.
- Ng, G., Sharma, K., Ward, S. M., Desrosiers, M. D., Stephens, L. A., Schoel, W. M., Li, T., Lowell, C. A., Ling, C. C., Amrein, M. W., and Shi, Y. (2008). Receptor-independent, direct membrane binding leads to cell-surface lipid sorting and Syk kinase activation in dendritic cells. *Immunity* 29, 807–818.
- Niemi, K., Teirila, L., Lappalainen, J., Rajamaki, K., Baumann, M. H., Oorni, K., Wolff, H., Kovanen, P. T., Matikainen, S., and Eklund, K. K. (2011). Serum amyloid A activates the NLRP3 inflammasome via P2X7 receptor and a cathepsin B-sensitive pathway. *J. Immunol.* 186, 6119–6128.
- Piccini, A. M., and Midwood, K. S. (2010). DAMPening inflammation by modulating TLR signalling. *Mediators Inflamm.* 2010, pii: 672395.
- Pinteaux, E., Parker, L. C., Rothwell, N. J., and Luheshi, G. N. (2002). Expression of interleukin-1 receptors and their role in interleukin-1 actions in murine microglial cells. *J. Neurochem.* 83, 754–763.
- Schroder, K., and Tschopp, J. (2010). The inflammasomes. *Cell* 140, 821–832.

Takeuchi, O., and Akira, S. (2010). Pattern recognition receptors and inflammation. *Cell* 140, 805–820.

Thornton, P., Pinteaux, E., Allan, S. M., and Rothwell, N. J. (2008). Matrix metalloproteinase-9 and urokinase plasminogen activator mediate interleukin-1-induced neurotoxicity. *Mol. Cell. Neurosci.* 37, 135–142.

Conflict of Interest Statement: The authors declare that the research was conducted in the absence of any commercial or financial relationships that could be construed as a potential conflict of interest.

Received: 24 May 2012; accepted: 28 August 2012; published online: 18 September 2012.

Citation: Savage CD, Lopez-Castejon G, Denes A and Brough D (2012) NLRP3-inflammasome activating DAMPs stimulate an inflammatory response in glia in the absence of priming which contributes to brain inflammation after injury. *Front. Immun.* 3:288. doi: 10.3389/fimmu.2012.00288

This article was submitted to *Frontiers in Inflammation*, a specialty of *Frontiers in Immunology*.

Copyright © 2012 Savage, Lopez-Castejon, Denes and Brough. This is an open-access article distributed under the terms of the Creative Commons Attribution License, which permits use, distribution and reproduction in other forums, provided the original authors and source are credited and subject to any copyright notices concerning any third-party graphics etc.

dc_2027_22

Central and haematopoietic interleukin-1 both contribute to ischaemic brain injury in mice

Adam Denes^{1,2}, Fiona Wilkinson³, Brian Bigger³, Michael Chu¹, Nancy J. Rothwell¹ and Stuart M. Allan^{1,*}

SUMMARY

Interleukin-1 (IL-1) is a key regulator of inflammation and ischaemic brain injury, but the contribution of central and peripheral sources of IL-1 to brain injury is not well understood. Here we show that haematopoietic-derived IL-1 is a key driver of ischaemic brain injury. Wild type (WT) mice transplanted with IL-1 α -deficient bone marrow displayed a significant (40%) reduction in brain injury induced by focal cerebral ischaemia compared with WT mice transplanted with WT bone marrow. This was paralleled by improved neurological outcome and the almost complete absence of splenic-derived, but not liver-derived, IL-1 α after stroke in WT mice lacking haematopoietic-derived IL-1. IL-1 α knockout (KO) mice transplanted with IL-1 α -deficient bone marrow showed a 60% reduction in brain injury compared with WT mice receiving WT bone marrow. Transplantation of WT bone marrow in IL-1 α KO mice resulted in a similar level of blood-brain-barrier injury to that observed in WT mice receiving IL-1 α -deficient bone marrow. Cerebral oedema after brain injury was reduced in IL-1 α KO recipients irrespective of donor-derived IL-1, but a lack of haematopoietic IL-1 has also been associated with smaller brain oedema independently of recipient status. Thus, both central and haematopoietic-derived IL-1 are important contributors to brain injury after cerebral ischaemia. Identification of the cellular sources of IL-1 in the periphery could allow targeted interventions at these sites.

INTRODUCTION

Neuroinflammatory changes in cerebral ischaemia and other central nervous system (CNS) diseases are driven by both activated glia and peripheral immune cells (Ransohoff and Brown, 2012; Denes et al., 2010a). Interleukin-1 (IL-1), a master cytokine and key inflammatory mediator, is a major contributor to ischaemic brain injury (Denes et al., 2011a; Dinarello, 2011). IL-1 also contributes to chronic diseases that are primary risk factors for cerebrovascular disease and key drivers of clinical outcome after stroke, such as diabetes, hypertension and obesity (Denes et al., 2011a; Dinarello, 2011). Hence, IL-1 of both central and peripheral origin is likely to influence CNS disease, but the cellular sources and relative contribution of endogenous peripheral versus central IL-1 to brain injury are still unclear.

In acute, experimental brain injury, microglia are considered to be the main source of central IL-1, of which IL-1 β is the best studied (Davies et al., 1999; Hanisch, 2002). However, IL-1 protein levels in microglia are very low in the first 4 hours after cerebral ischaemia in mice, and the main early isoform expressed in the brain is IL-1 α (Luheshi et al., 2011). Indeed, the time profile for the evolution of the infarct does not match the increases in cytokine mRNA and protein expression in the brain (Lambertsen et al., 2012). Thus,

peripherally-derived endogenous IL-1 might contribute to ischaemic brain injury, in both the presence and absence of comorbidities. To date, no functional studies have tested this hypothesis. To address this, we developed a chimeric mouse model in which haematopoietic-derived IL-1 is eliminated selectively, enabling us to study the role of central and blood-borne IL-1 in acute brain injury. Both brain and haematopoietic sources of IL-1 were found to contribute to ischaemic injury in mice, suggesting, at least in part, that inflammation and neuronal death after cerebral ischaemia could be limited by blocking peripheral IL-1 actions independently of drug delivery into the brain.

RESULTS

Central and haematopoietic-derived IL-1 both contribute to ischaemic brain injury

Bone marrow transplantation (Fig. 1A) was successful, as shown by the fact that blood chimerism was 88–91% in wild-type (WT) and IL-1 α knockout (KO) recipients based on flow cytometric data (Fig. 1B) and no difference in total leukocyte numbers or relative proportion of different leukocyte subsets was found among groups prior to middle cerebral artery occlusion (MCAo) (data not shown).

WT mice transplanted with IL-1 α KO bone marrow (KO to WT) displayed a 40% reduction in infarct size compared with the injury seen in WT mice receiving WT bone marrow (WT to WT), whereas IL-1 α KO mice transplanted with WT bone marrow (WT to KO) showed a 50% reduction compared with the WT to WT (Fig. 1C,D). Mice completely lacking IL-1 (KO to KO) showed a 60% reduction in infarct size compared with WT to WT mice, indicating that both central and haematopoietic-derived IL-1 are important contributors to brain injury after cerebral ischaemia. Only mice lacking both central and haematopoietic-derived IL-1 showed significantly (70%) reduced BBB injury (Fig. 1D,E) compared with fully IL-1-competent (WT to WT) mice, whereas

¹Faculty of Life Sciences, University of Manchester, Manchester, M13 9PT, UK

²Laboratory of Molecular Neuroendocrinology, Institute of Experimental Medicine, Budapest H-1450, Hungary

³Faculty of Medical and Human Sciences, University of Manchester, Manchester, M13 9PT, UK

*Author for correspondence (stuart.allan@manchester.ac.uk)

Received 21 December 2012; Accepted 12 March 2013

© 2013. Published by The Company of Biologists Ltd
This is an Open Access article distributed under the terms of the Creative Commons Attribution Non-Commercial Share Alike License (<http://creativecommons.org/licenses/by-nc-sa/3.0>), which permits unrestricted non-commercial use, distribution and reproduction in any medium provided that the original work is properly cited and all further distributions of the work or adaptation are subject to the same Creative Commons License terms.

TRANSLATIONAL IMPACT

Clinical issue

Brain diseases represent a huge burden on society, and stroke is one of the leading causes of death and morbidity worldwide. Inflammation has been identified as a key contributor to brain injury; however, the mechanisms by which inflammation mediates neuronal cell death are not fully understood. Interleukin-1 (IL-1) is an inflammatory cytokine that plays a major role in both acute and chronic diseases of the central nervous system. Although the main cellular sources of IL-1 have been extensively studied, the relative contributions of central and peripheral (blood)-derived IL-1 to brain injury have not been investigated.

Results

In this study, the authors investigated the role of central and haematopoietic-derived IL-1 in brain injury. To this end, they selectively eliminated IL-1 from blood-derived cells using bone marrow transplantation in a chimeric mouse model of focal cerebral ischaemia. The authors report that IL-1 derived from both sources contributes substantially to ischaemic brain injury. They demonstrate that deletion of blood-derived IL-1 is sufficient to improve neurological outcome of mice, and both central and peripheral IL-1 seem to contribute to the breakdown of the blood-brain barrier after cerebral ischaemia. Centrally-derived IL-1, however, seems to be the main driver of increased cerebral oedema after brain injury.

Implications and future directions

These results provide the first evidence that central and peripheral IL-1 contribute to brain injury. This finding has implications for the development of targeted interventions against detrimental inflammatory actions mediated by IL-1. Promisingly, inflammation and neuronal death after cerebral ischaemia could, at least in part, be limited by blocking peripheral IL-1 actions independently of drug delivery into the brain. Towards this goal, the identification of the exact cellular sources of peripheral IL-1 is now a key priority.

similar levels of blood-brain barrier (BBB) breakdown was observed in WT mice transplanted with IL-1 $\alpha\beta$ KO bone marrow and KO mice transplanted with WT bone marrow (45% and 48%, respectively; Fig. 1D,E). Mice lacking haematopoietic-derived IL-1 displayed improved neurological function at 24 hours reperfusion (Fig. 1F), whereas a significant reduction in brain oedema was observed in mice lacking central IL-1 irrespective of transplantation of WT or IL-1 $\alpha\beta$ KO bone marrow (Fig. 1G). Two-way ANOVA confirmed that WT recipients had reduced brain oedema independently of donor-derived IL-1 ($P=0.0065$); however, lack of haematopoietic-derived IL-1 was also associated with some reduction in brain oedema irrespective of recipient genotype ($P=0.0196$).

Haematopoietic-derived IL-1 alters systemic inflammatory responses after cerebral ischaemia

Liver homogenates showed a marked reduction in IL-1 α levels in IL-1 $\alpha\beta$ KO mice irrespective of bone marrow transplant, whereas an almost complete loss of splenic IL-1 α was seen in mice transplanted with IL-1 $\alpha\beta$ KO bone marrow (Fig. 2A). IL-1 β concentrations followed a similar trend to IL-1 α , although were frequently below the detection limit (5-10 pg/ml) of the assay, as were plasma levels 24 hours after reperfusion (not shown). In contrast, plasma IL-6 levels were significantly reduced (by 55-60%) in mice receiving IL-1 $\alpha\beta$ KO bone marrow (Fig. 2B; $P<0.05$, two-way ANOVA vs WT). No other cytokines of the 11 examined [IL-

1 α , IL-1 β , granulocyte colony-stimulating factor (G-CSF), IFN γ , IL-10, IL-17A, keratinocyte chemoattractant (KC), monocyte chemoattractant protein-1 (MCP-1), TNF α and RANTES (CCL5)] were altered (data not shown).

A rapid (within 45 minutes of onset of ischaemia) twofold rise in granulocyte numbers in response to MCAo was observed in all chimeric groups ($P<0.01$, two-way ANOVA), which was lower in WT mice receiving IL-1 $\alpha\beta$ KO bone marrow compared with WT mice transplanted with WT bone marrow (Fig. 2C; two-way ANOVA, Bonferroni's post-hoc comparison). Increases in circulating granulocytes paralleled a 10- to 20-fold rise in blood plasma KC, IL-6 and MCP-1 levels measured at reperfusion, without any changes seen among different chimeric groups (not shown). Apart from granulocytes, no changes in main leukocyte populations (T cells, B cells, monocytes) were seen in the blood, spleen or bone marrow 24 hours after MCAo in the four chimeric mouse groups.

Donor-derived (GFP+) cells were found mostly around the meninges and in association with larger cerebral blood vessels in the ipsilateral hemisphere 24 hours after MCAo (Fig. 2D). Parenchymal recruitment of GFP+ cells was observed mainly in the superficial layers of the cerebral cortex below the meninges, an area that was spared after MCAo in KO to WT mice as opposed to WT to WT animals (Fig. 2D). Only few blood-borne leukocytes were seen in the deeper cortical layers or in the striatum. Recruited donor-derived cells were mostly granulocytes and some monocyte-like cells were also observed (not shown), but microglia and macrophages (Iba1+) represented less than 4% of donor-derived cells in the brain. Very few donor-derived (GFP+/Iba-) leukocytes were found in the brain parenchyma prior to cerebral ischaemia, or in the contralateral hemisphere after MCAo, and no IgG penetration was observed in the contralateral side, arguing for minimal sustained BBB injury due to irradiation and/or bone marrow transplantation. This is in agreement with our previous data showing that microglial and macrophage repopulation after irradiation conditioning and bone marrow transplant is relatively slow, with 0.7% contribution at 2 weeks post-transplant rising to 10% by 6 months post-transplant (Wilkinson et al., 2013).

DISCUSSION

Here we demonstrate for the first time that endogenous IL-1 of both central and haematopoietic origin contributes to ischaemic brain injury, even in the absence of systemic co-morbidity. Identification of the exact cellular source(s) of IL-1 in the haematopoietic system that influence(s) brain injury needs substantially more experimental work, but our results demonstrate that blockade of peripheral IL-1 is a viable option to target brain injury without the requirement of drug delivery to the brain. Because current opportunities to block IL-1 (such as IL-1Ra) do not discriminate between the effects of IL-1 α and IL-1 β , or central and peripheral IL-1 actions, site- and isoform-specific IL-1 blockade could increase the efficacy of interventions against brain injury while maintaining essential defence mechanisms mediated by IL-1.

Microglia are radio-resistant cells in the CNS (Mildner et al., 2007). We chose an irradiation protocol for bone marrow transplantation, which resulted in minor replacement of microglia by blood-borne cells prior to cerebral ischaemia, and negligible

dc_2027_22

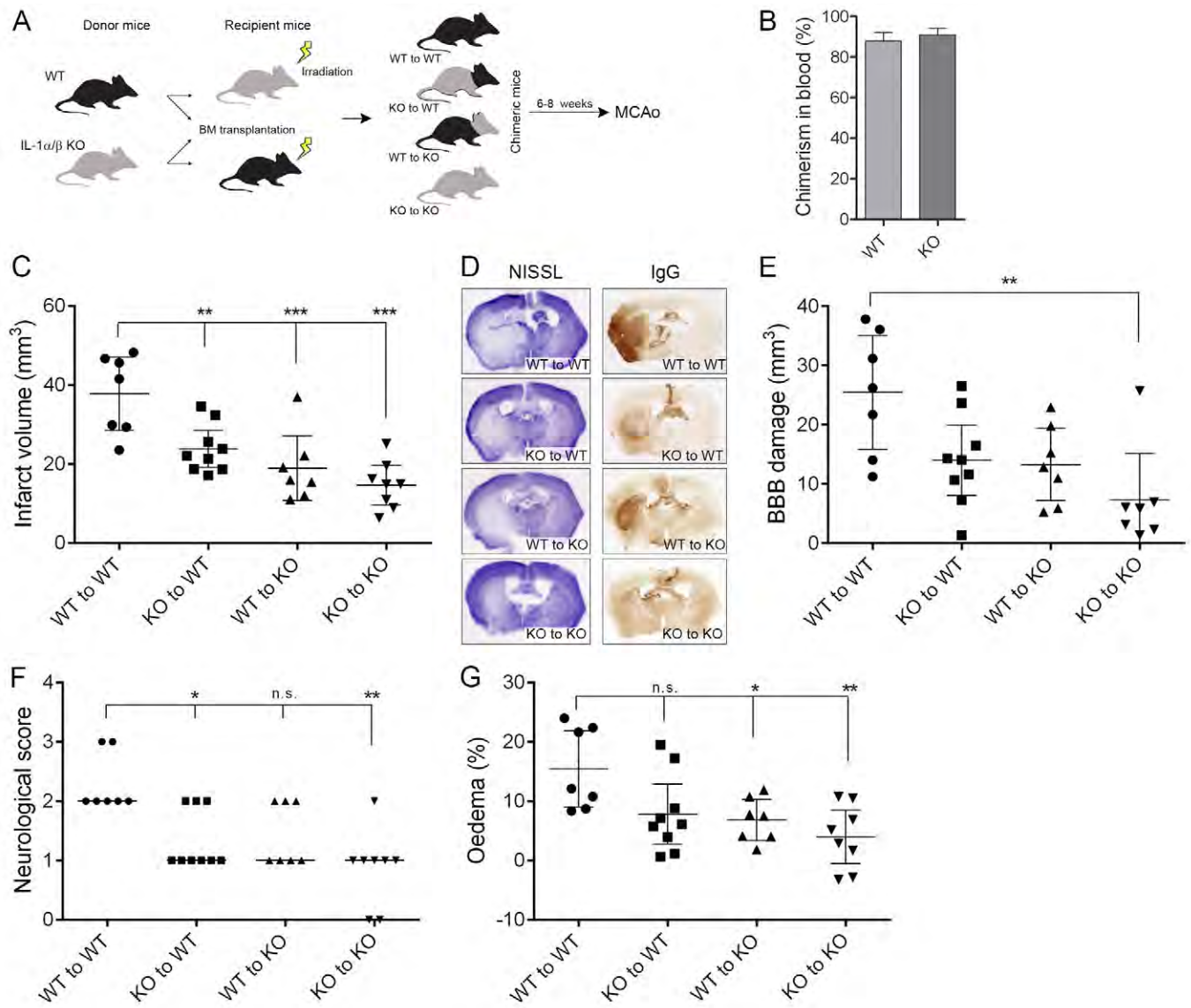


Fig. 1. Both central and haematopoietic-derived IL-1 are important contributors to brain injury after cerebral ischaemia. (A) Wild-type (WT) and IL-1 $\alpha\beta$ -deficient (KO) mice were subjected to whole body irradiation followed by transplantation of WT or IL-1 $\alpha\beta$ KO bone marrow. After 6–8 weeks of recovery, MCAo was performed. (B) Chimerism in blood as assessed by relative proportion of donor-derived (GFP+) leukocytes within the circulating CD45-positive cell population was uniform in WT and KO mice. (C) Infarct volume is significantly reduced in mice receiving KO bone marrow or in KO mice transplanted with WT bone marrow compared with WT mice reconstituted with WT bone marrow. (D) Representative images showing cresyl violet (Nissl)-stained brain sections or BBB injury (IgG infiltration). (E) Quantification of BBB injury based on IgG infiltration to the brain parenchyma. (F) Neurological deficit scores showing improved outcome in mice receiving IL-1 $\alpha\beta$ KO bone marrow. (G) Brain oedema is significantly reduced in mice lacking central IL-1. * $P < 0.05$, ** $P < 0.01$, *** $P < 0.001$, one-way ANOVA followed by Tukey's multiple post-hoc comparison (C,E,G) or Kruskal-Wallis test followed by Dunn's multiple comparison (F). Data are expressed as mean \pm s.e.m. (B; $n=9$), mean and 95% confidence interval (C–E) or median (F). n.s., non-significant.

contribution of donor-derived cells to the resident microglial pool was observed within 24 hours reperfusion after cerebral ischaemia. So, this model enabled us to study central IL-1 production separately from haematopoietic IL-1 sources. Because irradiation and bone marrow transplantation can induce changes in the recruitment of leukocytes into the brain (Ajami et al., 2007), we used WT mice transplanted with WT bone marrow for control for the effects of induction of chimerism when comparing with WT littermates receiving IL-1 $\alpha\beta$ KO bone marrow. Of note, bone

marrow transplantation did not result in the replacement of all haematopoietic-derived IL-1-producing cells in the periphery, as evidenced by maintenance of IL-1 production in the liver in WT recipients irrespective of donor-cell-derived IL-1 $\alpha\beta$ expression. Thus, it is possible that IL-1 from tissue-resident cells with slow turnover in the periphery could also contribute to brain injury. Nevertheless, previous data strongly indicate the involvement of brain-derived IL-1 to brain injury. Central (largely microglial) IL-1 levels increase in response to brain injury, IL-1Ra reaches

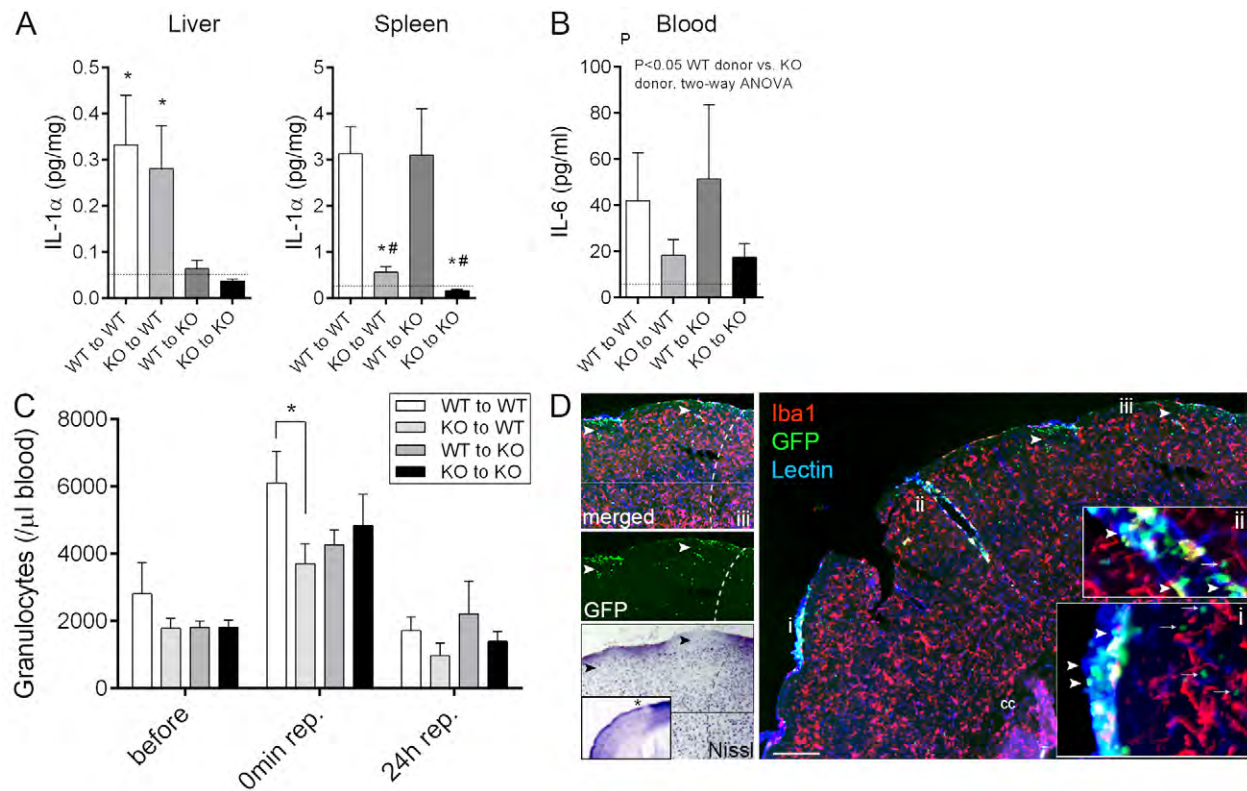


Fig. 2. Lack of haematopoietic-derived IL-1 results in altered systemic inflammatory responses after cerebral ischaemia. (A) IL-1 α production in the liver is dependent on host-derived cells with slow turnover, whereas splenic leukocytes expressing IL-1 α are readily replaced by bone-marrow-derived cells within 6–8 weeks after bone marrow transplantation. IL-1 α levels in liver and spleen homogenates at 24 hours reperfusion are shown. (B) Plasma IL-6 levels are reduced 24 hours after MCAo in mice receiving IL-1 α KO bone marrow. Dashed lines in panels A and B indicate the detection limit of the assay. (C) Stroke results in a rapid increase in circulating granulocytes ($P < 0.01$, 45 minutes after the onset of ischaemia compared with prior to occlusion), which is blunted in WT mice transplanted with IL-1 α KO bone marrow. (D) Recruitment of donor-derived (GFP+, green) leukocytes (arrowheads) to the brain 24 hours after MCAo is most pronounced in the meninges (lectin, blue) and in large cortical blood vessels (lectin, blue). Tissue infiltration of blood-borne cells is seen only in superficial cortical layers (green, arrows) and is minimal deep in the brain parenchyma, with very minor contribution of donor-derived (GFP+) macrophages (Iba1, red). Inserts show a higher magnification of the areas labelled with i and ii. (iii) Recruitment of blood-borne cells into the brain (GFP, arrowheads) is associated with neuronal loss (Nissl, asterisk in insert is showing the area of interest in the ipsilateral hemisphere). Dashed line indicates the boundary of the infarct. Cc, corpus callosum. Scale bar: 200 μ m. * $P < 0.05$ versus KO to WT, and KO to KO, respectively (A, left), * $P < 0.05$ versus WT to WT, and # $P < 0.05$ versus WT to KO (A, right), one-way ANOVA followed by Tukey's multiple post-hoc comparison (A), two-way ANOVA (B), and two-way ANOVA followed by Bonferroni's multiple comparison (C). $n = 7-9$, data are expressed as mean \pm s.e.m.

therapeutic concentrations in the brain after peripheral administration and reduces brain injury, and central administration of both IL-1Ra and IL-1 β neutralising antibodies reduces brain injury in different experimental models (Lambertsen et al., 2012; Luheshi et al., 2011; Relton and Rothwell, 1992; Yamasaki et al., 1995; Allan et al., 2005; Clausen et al., 2008; Greenhalgh et al., 2010; Clausen et al., 2011; Denes et al., 2011a; Galea et al., 2011). Therefore, we believe that, in our studies, IL-1 actions that are independent of the cells replaced by bone marrow transplantation are at least in part due to central IL-1 production, although the causal role of different central IL-1 sources in brain injury needs to be investigated further.

Our data indicate that haematopoietic-derived IL-1 might influence brain damage via different mechanisms to that of central IL-1, such as by altering leukocyte mobilisation or recruitment after injury. We found that splenic IL-1-competent cells were readily replaced by bone-marrow-derived cells within 6–8 weeks. The splenic reservoir of monocytes and CXCR2-positive granulocytes

in the bone marrow are mobilised rapidly in response to injury, infection or stroke (Shi and Pamer, 2011; Denes et al., 2011b) and are candidates for further investigation similarly to platelets that produce IL-1 α (Thornton et al., 2010). We have shown that platelet-derived IL-1 α drives cerebrovascular inflammation and facilitates the recruitment and transendothelial migration of neutrophils in an IL-1-dependent manner (Thornton et al., 2010). In addition, early recruitment of IL-1-positive, non-microglial inflammatory cells in the ischaemic brain has been reported, and some of these cells have been identified as macrophages (Lambertsen et al., 2012; Clausen et al., 2008), which in part could correspond to the cells recruited to the brain in our model. Collectively, recruitment of platelets, monocytes, macrophages or other cells into the injured brain and/or actions of inflammatory mediators released from these cells inside or outside the brain could contribute to BBB breakdown, brain oedema and neuronal injury. Cell-specific ablation of IL-1 will be essential to identify blood cell populations that contribute to brain injury. Similarly, it will be essential to investigate the

dc_2027_22

contribution of microglia and other resident brain cells to IL-1-mediated central inflammatory responses, which would allow cell-type-specific interventions. Further studies are also needed to examine the role of peripheral-IL-1-mediated actions in different models of cerebral ischaemia, such as after permanent cerebral ischaemia or when the infarct only affects cortical areas, as well as in other models of acute and chronic CNS injury.

Taken together, our results demonstrate for the first time a clear role for both central and haematopoietic-derived IL-1 in brain injury, a finding that could have an impact on the development of targeted cell therapies in CNS diseases. Importantly, by blocking peripheral IL-1 actions, drugs might not need to get through the BBB to exert beneficial effects against IL-1-mediated inflammation and injury in the brain.

MATERIALS AND METHODS

Mice

Male 7- to 9-week-old wild-type (WT) C57BL/6 and IL-1 $\alpha\beta$ -deficient (IL-1 $\alpha\beta$ KO, C57BL/6 background, bred in-house) mice were subjected to whole body irradiation (2 \times 5Gy) followed by transplantation of WT or IL-1 $\alpha\beta$ KO bone marrow (10⁷ cells/mouse) (Okabe et al., 1997). The irradiation dose was selected to enable effective repopulation of haematopoietic cells (Bigger et al., 2006), but resulted in only minor (1-4%) replacement of hemispheric microglia by donor-derived cells after 6-8 weeks. Mice recovered fully after 6 weeks, as indicated by their body weight gain, peripheral leukocyte numbers and overall fitness. Animals (3%) showing impaired recovery (decreasing body weight, prolonged piloerection, hunched posture or any other sign of illness) 4 weeks after transplantation were excluded from further experiments. All animal procedures were performed under the University of Manchester project license number (40/3076), adhered to the UK Animals (Scientific Procedures) Act (1986) and were in accordance with the ARRIVE guidelines.

Middle cerebral artery occlusion (MCAo)

Focal cerebral ischaemia was induced as described earlier (Denes et al., 2010b), 6-8 weeks after bone marrow transplantation. Mice were anaesthetised with isoflurane and were subjected to 45 minutes MCAo (left side occluded), using a silicon-coated monofilament with a tip diameter of 210 μ m (Doccol Corp., Redlands, CA) and perfused transcidentally 24 hours after reperfusion. Successful occlusion of the MCA was confirmed by laser Doppler and no difference has been found among different chimeric groups.

Transcardial perfusion and tissue processing

To isolate peripheral organs, mice were perfused transcidentally with saline under isoflurane anaesthesia. Brains were subsequently perfused with 4% paraformaldehyde, post-fixed for 24 hours, cryoprotected in 20% sucrose/PBS and sectioned (20 μ m diameter) on a sledge microtome. Organs were homogenised as described previously (Denes et al., 2010b).

Measurement of infarct volume, BBB damage and neurological deficit

The volume of ischaemic and BBB damage were measured as described previously (Denes et al., 2010b) and corrected for

oedema. IgG immunostaining was used to assess BBB permeability (Denes et al., 2010b). Neurological deficit was assessed blinded to group identity and according to a neurological grading score of increasing severity of deficit, as described previously (Denes et al., 2010b). Owing to histological problems, brain sections from a single mouse were not processed for determination of BBB injury (Fig. 1E, KO to KO group).

Measurement of inflammation

Plasma samples, and liver and spleen homogenates were processed for cytokine measurement using CBA Flex Sets (BD Biosciences, UK). Eleven key inflammatory cytokines were assessed: IL-1 α , IL-1 β , G-CSF, IFN γ , IL-6, IL-10, IL-17A, KC, MCP-1, TNF α and RANTES (CCL5). The detection limit for each cytokine was 5-10 pg/ml. Spleen, bone marrow and blood cells were isolated and stained with appropriate combinations of CD45-PerCP-Cy5.5, Ly6c-PerCP-Cy5.5, CD4-PE-Cy7, CD8-PE, CD3-APC, CD19-PE-Cy7, MHCII-APC (eBioscience, UK) and Ly6g-PE (1A8, BD Biosciences, UK) following Fc receptor blockade (eBioscience). Donor-derived WT cells were identified based on expression of green fluorescent protein (GFP) and were used to assess chimerism in WT and IL-1 $\alpha\beta$ KO recipients. Cells were acquired on an LSRII flow cytometer, using FACS Diva software (BD Biosciences, UK). Immunostaining was performed on free-floating brain sections using combinations of chicken anti-GFP (Invitrogen), rabbit anti-Iba1 (WAKO, Germany) and rabbit anti-neutrophil serum (SJC, kindly provided by Drs Daniel Anthony and Sandra Campbell, University of Oxford, Oxford, UK). Sections were incubated in primary antibody overnight followed by adequate fluorochrome (Alexa-Fluor-594, Alexa-Fluor-488)-conjugated antibodies (Invitrogen). Donor-derived microglia and macrophages were visualised using immunofluorescence against GFP and Iba1, and chimerism presented as percentage of GFP+ cells within the Iba1-positive microglial population. Biotinylated tomato lectin (Sigma-Aldrich, UK) was used to visualise blood vessels and meninges, followed by streptavidin-Alexa-Fluor-350 conjugate (Invitrogen). Images were collected on a Zeiss Axioskop or an Olympus BX51 microscope using a CoolSNAP ES camera (Photometrics, UK) through MetaVue software (Molecular Devices, UK), and processed using ImageJ and Adobe Photoshop softwares.

Randomization, quantification and statistical analysis

Group sizes were determined by power analysis based on our previous MCAo studies (Denes et al., 2010b; Denes et al., 2011b). Mice were randomly assigned to groups prior to bone marrow transplantation and were randomised in blocks for the induction of cerebral ischaemia (to ensure that all chimeric groups are represented in every day of surgery). All quantitative assessments were performed in a blinded manner. Four mice were excluded from analysis pre hoc, owing to surgical artifacts or failure to meet pre-established criteria for the MCAo model in our laboratory. Statistical analysis was performed by one-way or two-way ANOVA followed by Tukey's or Bonferroni's post-hoc multiple comparison for normally distributed data, and Kruskal-Wallis test followed by Dunn's multiple comparison for the analysis of neurological scores, using GraphPad Prism 5 software. $P < 0.05$ was considered statistically significant.

COMPETING INTERESTS

N.J.R. is the Non-Executive Director of AstraZeneca but the company has no involvement in this work.

AUTHOR CONTRIBUTIONS

A.D., S.M.A., N.J.R. and B.B. conceived and designed the experiments; A.D. and F.W. performed the experiments; A.D. and M.C. analysed the data; B.B. and F.W. contributed research tools; A.D., S.M.A. and N.J.R. wrote the paper.

FUNDING

We are grateful for funding provided by the Medical Research Council (NR MRC Research Professorship) and the European Union's Seventh Framework Programme (FP7/2008-2013) under grant agreements no. 201024 and no. 202213 (European Stroke Network; to N.J.R. and A.D.).

REFERENCES

- Ajami, B., Bennett, J. L., Krieger, C., Tetzlaff, W. and Rossi, F. M.** (2007). Local self-renewal can sustain CNS microglia maintenance and function throughout adult life. *Nat. Neurosci.* **10**, 1538-1543.
- Allan, S. M., Tyrrell, P. J. and Rothwell, N. J.** (2005). Interleukin-1 and neuronal injury. *Nat. Rev. Immunol.* **5**, 629-640.
- Bigger, B. W., Siapati, E. K., Mistry, A., Waddington, S. N., Nivsarkar, M. S., Jacobs, L., Perrett, R., Holder, M. V., Ridler, C., Kembell-Cook, G. et al.** (2006). Permanent partial phenotypic correction and tolerance in a mouse model of hemophilia B by stem cell gene delivery of human factor IX. *Gene Ther.* **13**, 117-126.
- Clausen, B. H., Lambertsen, K. L., Babcock, A. A., Holm, T. H., Dagnaes-Hansen, F. and Finsen, B.** (2008). Interleukin-1beta and tumor necrosis factor-alpha are expressed by different subsets of microglia and macrophages after ischemic stroke in mice. *J. Neuroinflammation* **5**, 46.
- Clausen, F., Hånell, A., Israelsson, C., Hedin, J., Ebendal, T., Mir, A. K., Gram, H. and Marklund, N.** (2011). Neutralization of interleukin-1 β reduces cerebral edema and tissue loss and improves late cognitive outcome following traumatic brain injury in mice. *Eur. J. Neurosci.* **34**, 110-123.
- Davies, C. A., Loddick, S. A., Toulmond, S., Stroemer, R. P., Hunt, J. and Rothwell, N. J.** (1999). The progression and topographic distribution of interleukin-1beta expression after permanent middle cerebral artery occlusion in the rat. *J. Cereb. Blood Flow Metab.* **19**, 87-98.
- Denes, A., Thornton, P., Rothwell, N. J. and Allan, S. M.** (2010a). Inflammation and brain injury: acute cerebral ischaemia, peripheral and central inflammation. *Brain Behav. Immun.* **24**, 708-723.
- Dénes, A., Humphreys, N., Lane, T. E., Grecnis, R. and Rothwell, N.** (2010b). Chronic systemic infection exacerbates ischemic brain damage via a CCL5 (regulated on activation, normal T-cell expressed and secreted)-mediated proinflammatory response in mice. *J. Neurosci.* **30**, 10086-10095.
- Denes, A., Pinteaux, E., Rothwell, N. J. and Allan, S. M.** (2011a). Interleukin-1 and stroke: biomarker, harbinger of damage, and therapeutic target. *Cerebrovasc. Dis.* **32**, 517-527.
- Denes, A., McColl, B. W., Leow-Dyke, S. F., Chapman, K. Z., Humphreys, N. E., Grecnis, R. K., Allan, S. M. and Rothwell, N. J.** (2011b). Experimental stroke-induced changes in the bone marrow reveal complex regulation of leukocyte responses. *J. Cereb. Blood Flow Metab.* **31**, 1036-1050.
- Dinarello, C. A.** (2011). Interleukin-1 in the pathogenesis and treatment of inflammatory diseases. *Blood* **117**, 3720-3732.
- Galea, J., Ogungbenro, K., Hulme, S., Greenhalgh, A., Aarons, L., Scarth, S., Hutchinson, P., Grainger, S., King, A., Hopkins, S. J. et al.** (2011). Intravenous anakinra can achieve experimentally effective concentrations in the central nervous system within a therapeutic time window: results of a dose-ranging study. *J. Cereb. Blood Flow Metab.* **31**, 439-447.
- Greenhalgh, A. D., Galea, J., Dénes, A., Tyrrell, P. J. and Rothwell, N. J.** (2010). Rapid brain penetration of interleukin-1 receptor antagonist in rat cerebral ischaemia: pharmacokinetics, distribution, protection. *Br. J. Pharmacol.* **160**, 153-159.
- Hanisch, U. K.** (2002). Microglia as a source and target of cytokines. *Glia* **40**, 140-155.
- Lambertsen, K. L., Biber, K. and Finsen, B.** (2012). Inflammatory cytokines in experimental and human stroke. *J. Cereb. Blood Flow Metab.* **32**, 1677-1698.
- Luheshi, N. M., Kovács, K. J., Lopez-Castejon, G., Brough, D. and Denes, A.** (2011). Interleukin-1 α expression precedes IL-1 β after ischemic brain injury and is localised to areas of focal neuronal loss and penumbral tissues. *J. Neuroinflammation* **8**, 186.
- Mildner, A., Schmidt, H., Nitsche, M., Merkler, D., Hanisch, U. K., Mack, M., Heikenwalder, M., Brück, W., Priller, J. and Prinz, M.** (2007). Microglia in the adult brain arise from Ly-6ChiCCR2+ monocytes only under defined host conditions. *Nat. Neurosci.* **10**, 1544-1553.
- Okabe, M., Ikawa, M., Kominami, K., Nakanishi, T. and Nishimune, Y.** (1997). 'Green mice' as a source of ubiquitous green cells. *FEBS Lett.* **407**, 313-319.
- Ransohoff, R. M. and Brown, M. A.** (2012). Innate immunity in the central nervous system. *J. Clin. Invest.* **122**, 1164-1171.
- Relton, J. K. and Rothwell, N. J.** (1992). Interleukin-1 receptor antagonist inhibits ischaemic and excitotoxic neuronal damage in the rat. *Brain Res. Bull.* **29**, 243-246.
- Shi, C. and Pamer, E. G.** (2011). Monocyte recruitment during infection and inflammation. *Nat. Rev. Immunol.* **11**, 762-774.
- Thornton, P., McColl, B. W., Greenhalgh, A., Denes, A., Allan, S. M. and Rothwell, N. J.** (2010). Platelet interleukin-1alpha drives cerebrovascular inflammation. *Blood* **115**, 3632-3639.
- Wilkinson, F. L., Sergijenko, A., Langford-Smith, K. J., Malinowska, M., Wynn, R. F. and Bigger, B. W.** (2013). Busulfan conditioning enhances engraftment of hematopoietic donor-derived cells in the brain compared with irradiation. *Mol. Ther.* **21**, 868-876.
- Yamasaki, Y., Matsuura, N., Shozuhara, H., Onodera, H., Itoyama, Y. and Kogure, K.** (1995). Interleukin-1 as a pathogenetic mediator of ischemic brain damage in rats. *Stroke* **26**, 676-680, discussion 681.

AIM2 and NLRC4 inflammasomes contribute with ASC to acute brain injury independently of NLRP3

Adam Denes^{a,b,1}, Graham Coutts^b, Nikolett Lénárt^a, Sheena M. Cruickshank^b, Pablo Pelegrin^{b,c}, Joanne Skinner^b, Nancy Rothwell^b, Stuart M. Allan^b, and David Brough^{b,1}

^aLaboratory of Molecular Neuroendocrinology, Institute of Experimental Medicine, Budapest, 1083, Hungary; ^bFaculty of Life Sciences, University of Manchester, Manchester M13 9PT, United Kingdom; and ^cInflammation and Experimental Surgery Unit, CIBERehd (Centro de Investigación Biomédica en Red en el Área temática de Enfermedades Hepáticas y Digestivas), Murcia Biohealth Research Institute–Arrixaca, University Hospital Virgen de la Arrixaca, 30120 Murcia, Spain

Edited by Vishva M. Dixit, Genentech, San Francisco, CA, and approved February 19, 2015 (received for review November 18, 2014)

Inflammation that contributes to acute cerebrovascular disease is driven by the proinflammatory cytokine interleukin-1 and is known to exacerbate resulting injury. The activity of interleukin-1 is regulated by multimolecular protein complexes called inflammasomes. There are multiple potential inflammasomes activated in diverse diseases, yet the nature of the inflammasomes involved in brain injury is currently unknown. Here, using a rodent model of stroke, we show that the NLRC4 (NLR family, CARD domain containing 4) and AIM2 (absent in melanoma 2) inflammasomes contribute to brain injury. We also show that acute ischemic brain injury is regulated by mechanisms that require ASC (apoptosis-associated speck-like protein containing a CARD), a common adaptor protein for several inflammasomes, and that the NLRP3 (NLR family, pyrin domain containing 3) inflammasome is not involved in this process. These discoveries identify the NLRC4 and AIM2 inflammasomes as potential therapeutic targets for stroke and provide new insights into how the inflammatory response is regulated after an acute injury to the brain.

inflammation | inflammasome | cerebral ischemia | brain injury | cell death

Proinflammatory cytokines of the interleukin-1 (IL-1) family are critical regulators of host responses to infection and orchestrate damaging inflammatory responses that occur during disease (1). One of the main mediators of damaging sterile inflammation is IL-1 β , which is implicated in the etiology of many major diseases, including acute cerebrovascular disease (2). Acute cerebrovascular disease presents as a range of conditions, including devastating injuries such as subarachnoid hemorrhage (SAH) and ischemic stroke, which account for up to 10% of mortality worldwide and are the leading cause of morbidity (2). Treatments for acute stroke are limited to thrombolysis for up to 10% of all strokes, antiplatelet agents, and stroke unit care. Thus, treatment of acute cerebrovascular disease remains an area of unmet clinical need. Understanding the mechanisms regulating production of IL-1 β during ischemic brain injury may lead to the identification of new therapeutic targets.

IL-1 β is produced by many cells, most commonly those of macrophage lineage, as a pro-IL-1 β precursor. Pro-IL-1 β is expressed in response to pathogen-associated molecular patterns (PAMPs) or damage-associated molecular patterns (DAMPs) that bind to pattern recognition receptors (PRRs) to up-regulate proinflammatory gene expression (3, 4). PAMPs are motifs carried by pathogens, such as bacterial endotoxin (or LPS), and DAMPs are commonly endogenous molecules released by necrosis. Pro-IL-1 β is inactive and remains intracellular until a further PAMP or DAMP stimulation activates cytosolic PRRs, often of the nucleotide-binding domain and leucine-rich repeat containing receptor (NLR) family, to form large multiprotein complexes called inflammasomes (5). These complexes consist of the PRR, procaspase-1, and, depending upon the PRR, an adaptor protein called ASC, that interact via CARD and pyrin homology-binding domains (5). When the PRR senses PAMPs

or DAMPs, it recruits ASC, which in turn recruits caspase-1, causing its activation. Caspase-1 then processes pro-IL-1 β to a mature form that is rapidly secreted from the cell (5). The activation of caspase-1 can also cause cell death (6).

A number of inflammasome-forming PRRs have been identified, including NLR family, pyrin domain containing 1 (NLRP1); NLRP3; NLRP6; NLRP7; NLRP12; NLR family, CARD domain containing 4 (NLRC4); AIM 2 (absent in melanoma 2); IFI16; and RIG-I (5). Of these inflammasomes identified to date, the best characterized, and most strongly associated with sterile inflammation, is formed by NLRP3 (7). Indeed, there are now several studies suggesting that NLRP3 inflammasomes contribute to ischemic brain injury (8, 9). However, the picture is more complicated. NLRP1 inflammasomes have been implicated in several models of brain injury (6, 10, 11), as have AIM2 inflammasomes, which are suggested to mediate pyroptotic neuronal cell death (12). There is also evidence supporting a role for caspase-1 in brain injury (13), with a selective caspase-1 inhibitor, VRT-018858, a nonpeptide, active metabolite of the prodrug pralnacasan, showing marked protection in a rat model of stroke (14). However, data for the related caspase-1 inhibitor VRT-043198 suggest that it is also an effective inhibitor of caspase-4 (15), a human ortholog of caspase-11. Caspase-11 is also implicated in ischemic brain injury (16, 17), and given that we now also know

Significance

Cerebral ischemia (CI; stroke, brain injury, vascular dementia, neonatal hypoxia, and many other conditions) affects people at all stages of life. Of the many diseases associated with CI, stroke alone causes up to 10% of deaths worldwide and is a leading cause of disability; yet treatment options are extremely limited, so this represents an area of massive unmet clinical need. Inflammation involving the cytokine interleukin-1 is a major contributor to cell death in the ischemic brain. Inflammation can be regulated by large protein complexes called inflammasomes. Here we show that the NLRC4 (NLR family, CARD domain containing 4) and AIM2 (absent in melanoma 2) inflammasomes, but not the NLRP3 (NLR family, pyrin domain containing 3) inflammasome, contribute to inflammation and injury in an ischemic brain and are thus potential therapeutic targets for these devastating diseases.

Author contributions: A.D., N.R., S.M.A., and D.B. designed research; A.D., G.C., N.L., and J.S. performed research; G.C., N.L., S.M.C., P.P., S.M.A., and D.B. contributed new reagents/analytic tools; A.D., S.M.A., and D.B. analyzed data; and A.D., N.R., S.M.A., and D.B. wrote the paper.

Conflict of interest statement: N.R. is a nonexecutive director of AstraZeneca, although the company had no involvement with this work. None of the other authors have any conflicts to declare.

This article is a PNAS Direct Submission.

¹To whom correspondence may be addressed. Email: david.brough@manchester.ac.uk or denesa@koki.hu.

This article contains supporting information online at www.pnas.org/lookup/suppl/doi:10.1073/pnas.1419090112/-DCSupplemental.

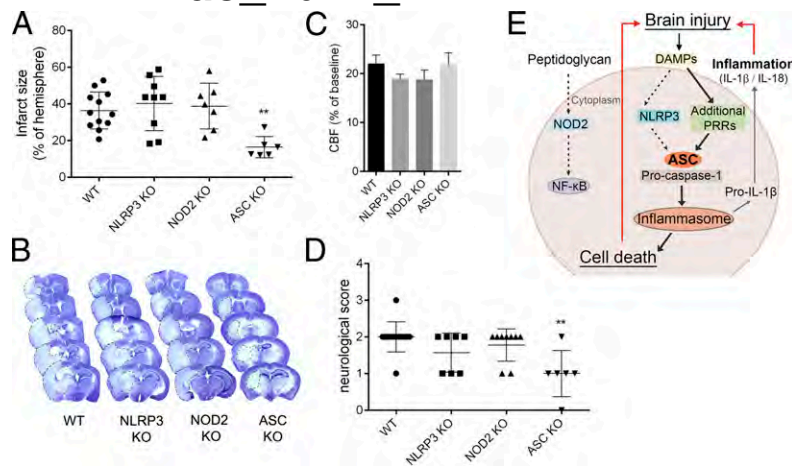


Fig. 1. ASC-dependent mechanisms contribute to brain injury induced by cerebral ischemia. Infarct volume (A) as measured on cresyl violet-stained brain sections (B) is significantly reduced in ASC^{-/-} mice (***P* < 0.01 vs. WT, NLRP3^{-/-} and NOD2^{-/-}). (C) Average cerebral blood flow (CBF) values were unaltered during occlusion of the MCA (A–C; one-way ANOVA followed by Tukey’s post hoc test). (D) Neurological outcome was improved in ASC^{-/-} mice (***P* < 0.01, Kruskal–Wallis test followed by Dunn’s multiple comparison). (E) Schematic diagram summarizing the data. The dashed lines highlight dispensable pathways.

that the original caspase-1^{-/-} mouse is also deficient in caspase-11 (18), it is clear that caspase-11 could have a role in ischemic brain injury. Our aim here was to elucidate which inflammasomes contribute to ischemic brain injury, using mice in which specific inflammasome components are deleted (^{-/-}).

Results

We initially investigated the role of NLRP3 and ASC in ischemic brain injury induced by middle cerebral artery occlusion (MCAO). We discovered that ischemic brain injury was comparable between WT and NLRP3^{-/-} mice, but ASC^{-/-} mice were significantly

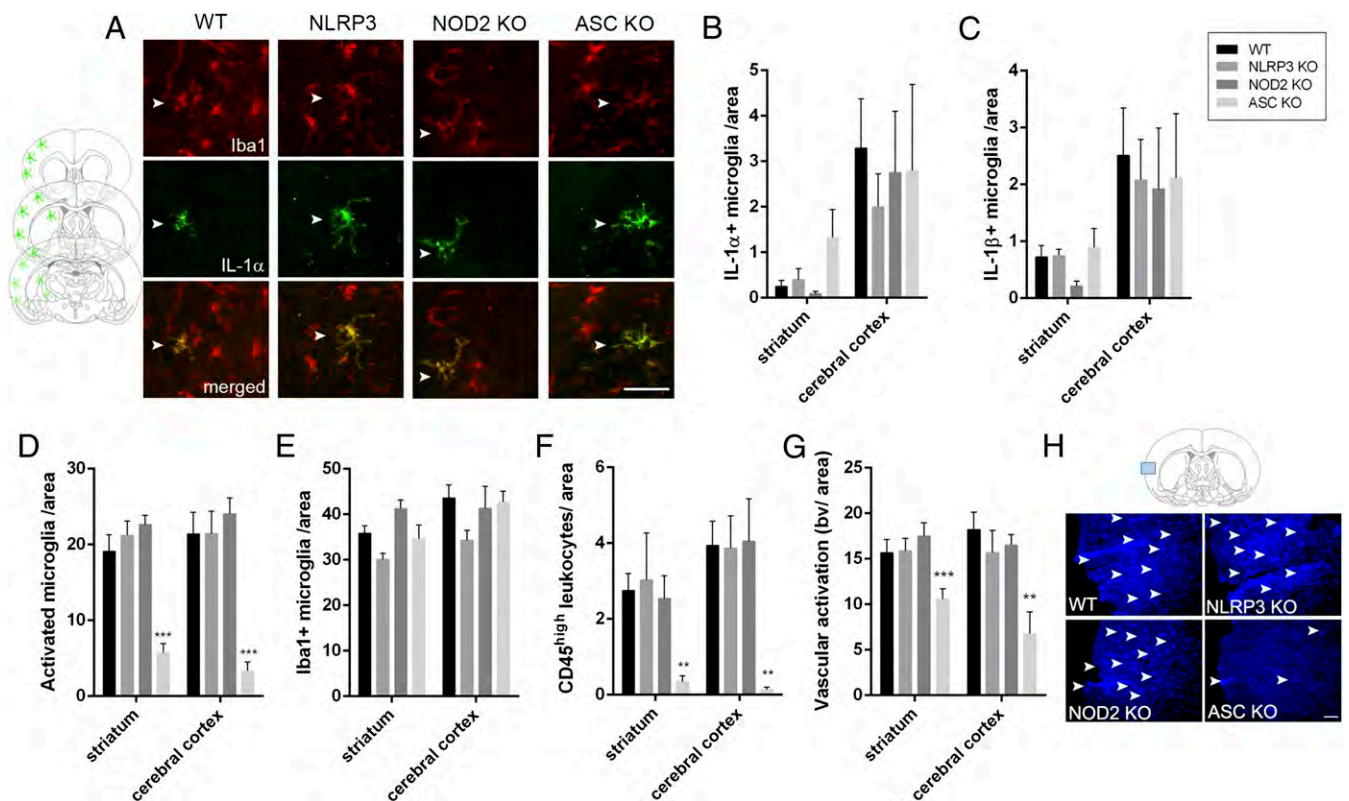


Fig. 2. ASC deficiency reduces inflammation in the brain independently of IL-1 production. Numbers of IL-1 α + (A and B) and IL-1 β + (C) positive microglia (A, Iba1+, arrowheads) are not significantly altered in the brain by NLRP3, NOD2, or ASC deficiency after cerebral ischemia. Schematic shows the location of IL-1 α -positive microglia in the ipsilateral hemisphere, which was similar in all animals. Numbers of activated microglia [D, expressing low levels of CD45 (CD45^{low}), Iba1+], total microglial numbers (E), recruitment of leukocytes expressing high levels of CD45 (CD45^{high}) (F), and vascular activation (G, blood vessels with high levels of tomato lectin staining, as shown in H in blue) have been assessed in the ipsilateral striatum and cerebral cortex. *n* = 6–9, two-way ANOVA followed by Tukey’s post hoc test. ***P* < 0.01, ****P* < 0.001. (Scale bar, A, 50 μ m; H, 100 μ m).

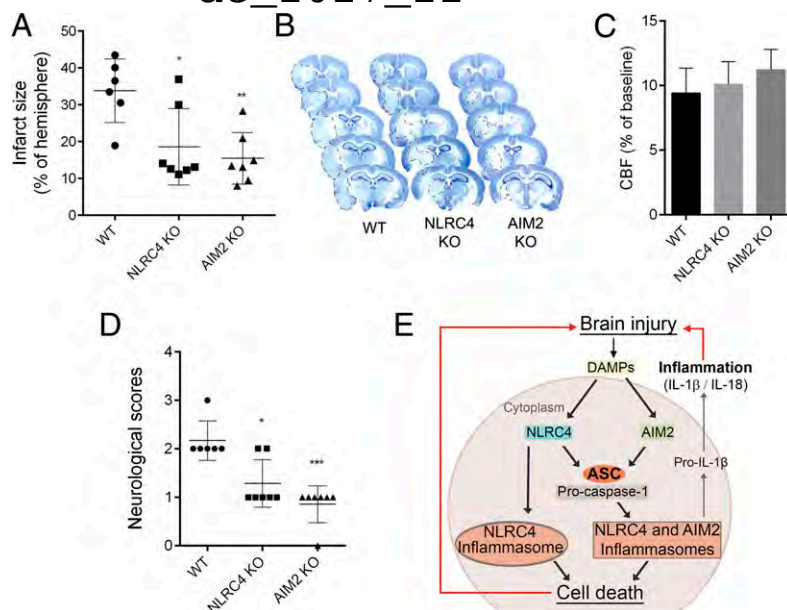


Fig. 3. AIM2- and NLR4-dependent mechanisms contribute to brain injury induced by cerebral ischemia. Infarct volume (A) as measured on cresyl violet-stained brain sections (B) was significantly reduced in AIM2^{-/-} and NLR4^{-/-} mice ($*P < 0.05$, $**P < 0.01$). (C) Average CBF values were unaltered during occlusion of the MCA (A–C, one-way ANOVA followed by Tukey's post hoc test). (D) Neurological outcome was improved in AIM2^{-/-} and NLR4^{-/-} mice ($*P < 0.05$, $***P < 0.001$), Kruskal–Wallis test followed by Dunn's multiple comparison). (E) Schematic diagram summarizing the data. $n = 6–7$.

protected (Fig. 1A and B). This was not due to altered cerebral perfusion during MCAo (Fig. 1C) or after induction of reperfusion. ASC^{-/-} mice also had improved neurological outcomes following MCAo compared with WT and NLRP3^{-/-}, which were similar (Fig. 1D). We also found that brain injury was not altered by knockout of the noninflammasome-forming PRR NOD2 (19) (Fig. 1A–D). Thus, after MCAo, ASC is likely to regulate assembly of inflammasomes via activation of PRRs other than NLRP3 (Fig. 1E).

Microglial activation (Iba1+, ramified cells, expressing low levels of CD45), leukocyte recruitment (round or elongated cells, expressing high levels of CD45; Fig. S1), and vascular activation were also reduced in the brains of ASC^{-/-} mice after MCAo (Fig. 2D–H). However, numbers of microglia expressing IL-1 α and IL-1 β after MCAo were equivalent in the brains of WT, NLRP3^{-/-}, or ASC^{-/-} mice (Fig. 2A–C and Fig. S2A). These findings suggest that following MCAo, inflammation and injury progressed independently of the canonical sensor of sterile damage, the NLRP3 inflammasome.

The lack of NLRP3 involvement after MCAo was unexpected and suggests that other inflammasomes must contribute to sterile inflammation in the brain. Available evidence suggests that AIM2 could have a role in sterile inflammatory responses (20), whereas the other inflammasome-forming receptors appear to depend upon a microbial presence. To investigate the involvement of additional PRRs, we induced MCAo in AIM2^{-/-} and NLR4^{-/-} mice. AIM2 recognizes pathogen and host double-stranded DNA and is composed of a pyrin domain and a DNA-binding HIN domain, and thus AIM2 inflammasomes have an absolute requirement for ASC to recruit and activate caspase-1 (21, 22). NLR4 has a CARD domain and can directly interact with procaspase-1, although the presence of ASC is known to enhance NLR4 inflammasome formation (5). AIM2^{-/-} and NLR4^{-/-} mice had reduced injury and improved behavioral outcomes after MCAo, compared with WT mice (Fig. 3A, B, and D). As with the ASC^{-/-} experiment above (Fig. 1), the enhanced protection in the AIM2^{-/-} and NLR4^{-/-} mice was not due to altered cerebral perfusion during MCAo occlusion (Fig. 3C).

These data suggest that NLR4 and AIM2 may interact with ASC to mediate brain injury after MCAo (Fig. 3E).

As with the ASC^{-/-} mice above, microglial activation and leukocyte recruitment were reduced in the brains of AIM2^{-/-} and NLR4^{-/-} mice after MCAo (Fig. 4D and E). Numbers of microglia expressing IL-1 β and IL-1 α after MCAo were equivalent in the brains of WT, AIM2^{-/-}, or NLR4^{-/-} mice (Fig. 4A–C and Fig. S2B). Furthermore, we did not find any significant difference in IL-1 β or IL-1 α production (Fig. 4F), as well as CXCL1, TNF α , IL-6, and IL-10 production (Fig. S3) in the liver and the spleen, two major organs that are involved in diverse inflammatory/acute phase responses that contribute to brain injury (23, 24).

Discussion

Here we have shown that ischemic brain injury was reduced in ASC^{-/-}, AIM2^{-/-}, and NLR4^{-/-} mice and not in mice deficient for the canonical sensor of sterile injury, NLRP3. These data provide the first (to our knowledge) evidence for multiple inflammasomes regulating neuronal injury, identifying AIM2 and NLR4 as key drivers of sterile inflammatory responses in the brain.

NLR4 is regarded as a sensor of pathogenic bacteria (25), and thus to see it contributing to ischemic brain injury, a model of sterile inflammation, was an unexpected result. NLR4 inflammasome activation is, however, also reported in a model of alcohol-induced liver damage (26) and also to regulate tumorigenesis in an inflammation-induced model of colorectal cancer (27). In these conditions it is possible that host microbiota contribute to the inflammatory response. However, our results may also suggest that microbiota do not contribute to brain injury via recognition of peptidoglycan-derived peptides by NOD2. We know that both systemic and central IL-1-dependent inflammation drives injury in experimental cerebral ischemia (28), and thus there is a possibility that NLR4 drives a systemic inflammatory response following the translocation of gut bacteria/products. However, although there was a characteristic systemic inflammatory response following MCAo, it was identical between the WT and inflammasome knockout strains (Fig. 4). Nevertheless, we cannot rule out the possibility that early actions

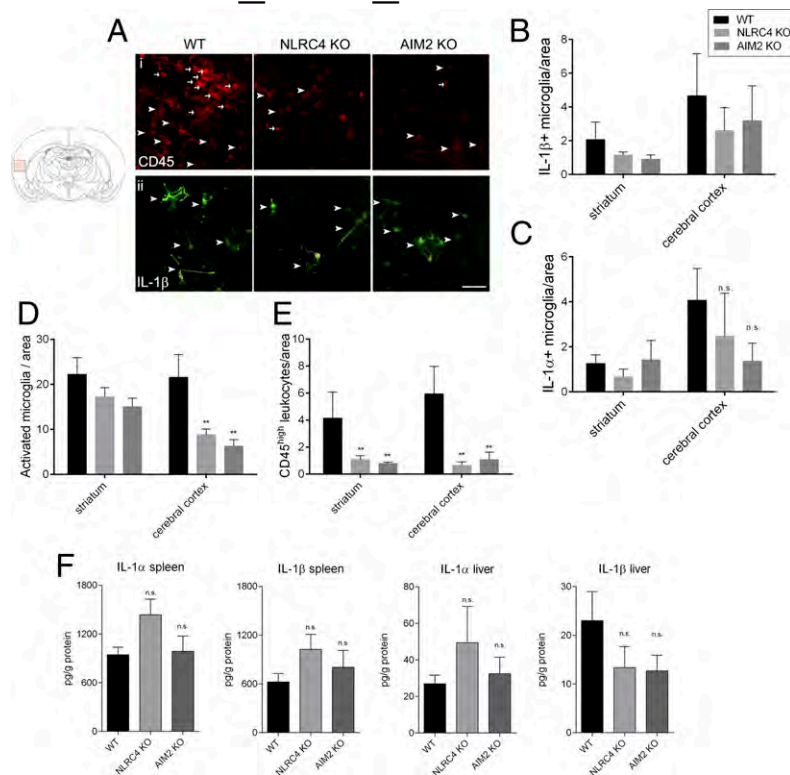


Fig. 4. AIM2 and NLRC4 deficiency reduces inflammation in the brain independently of IL-1 production. Numbers of IL-1 β - (A and B) positive microglia (arrowheads), IL-1 α -positive microglia (C), activated microglia (A and D, arrowheads), and CD45^{high} leukocytes (A and E, arrows) have been assessed in the ipsilateral hemisphere after MCAo (two-way ANOVA followed by Tukey's post hoc test). (F) Protein levels of IL-1 α and IL-1 β were measured with cytometric bead array in liver and spleen homogenates (one-way ANOVA followed by Tukey's post hoc test, ****P** < 0.01). $n = 6-7$. n.s., not significant. (Scale bar, 50 μ m.)

mediated by circulating leukocytes or inflammatory mediators could contribute to some of the differences observed in the knockout strains.

Thus, our data provide the first to our knowledge information that NLRC4 could be a DAMP sensor in brain inflammation. However, sterile inflammatory conditions involving NLRC4 in other tissues are now emerging in the literature. Autoinflammatory conditions caused by activating mutations in NLRC4 (similar to the CAPS syndromes caused by activating mutations in NLRP3) have been described recently (29–31). NLRP3 is regarded as the canonical sensor of sterile injury or stress, and so to consider how NLRC4 may sense DAMPs it is sensible to draw comparisons to NLRP3. Given the diverse structures of DAMPs that activate NLRP3 and the fact that no direct interactions have been observed, a direct interaction between a DAMP and NLRP3 is unlikely (32), and no accessory receptors have been described. Rather, the cellular stress imposed by DAMPs is suggested to give rise to a number of potential mechanisms that lead to posttranslational modification of NLRP3, leading to its activation (32). NLRC4 does not sense bacterial ligands directly but does so through coreceptors called NAIP proteins (33). Given that the NAIP proteins specifically and directly bind and sense bacterial proteins (34), it is unlikely that NAIPs also bind diverse DAMPs. This raises the possibility of specific host protein DAMPs that are homologous with bacterial NAIP ligands, or that certain DAMPs or tissue/cellular stresses activate posttranslational mechanisms, causing activation of NLRC4. Recent work from our group and others has identified ubiquitin posttranslational modification of NLRP3 inflammasome components as a key integrator of diverse DAMP signals (35–38). Interestingly, ubiquitination has also been suggested to regulate the activation of NLRC4 in a model of caspase-8-dependent cell death (39). Phosphorylation of NLRC4 is also known to be

pivotal to its activation (40). Thus, cellular/tissue stress may cause posttranslational modification of NLRC4 inflammasome components, resulting in NLRC4 inflammasome activation. A key distinction between NLRP3 and NLRC4 is that NLRP3 requires priming to induce NLRP3 expression before active NLRP3 inflammasomes can be formed (41). This priming step is not required for NLRC4 inflammasome activation (42). It is therefore possible that these pathways operate in the absence of functional NLRP3. NLRC4 has a CARD domain and can directly interact with procaspase-1, although the presence of ASC is known to enhance NLRC4-inflammasome-dependent IL-1 β processing (5). Thus, the large protective effect we also observe in the ASC^{-/-} mice could be in part due to an effect on NLRC4-inflammasome-dependent IL-1 β release. These data therefore give insights into the regulation of NLRC4 and may trigger new research into NLRC4 as a sensor of sterile injury.

AIM2 recognizes pathogen and host double-stranded DNA and is composed of a pyrin domain and a DNA-binding HIN domain, and thus to recruit caspase-1 into the inflammasome complex requires ASC as a bridging molecule (21, 22). Cultured embryonic rat cortical neurons undergo an AIM2-inflammasome-dependent cell death when challenged with the AIM2 activator poly(dA:dT) (12). AIM2 inflammasomes also drive a protective inflammatory response in the brain, and AIM2^{-/-} mice show reduced survival in response to central infection with *Staphylococcus aureus* (43). This latter study also shows a disconnect between NLRP3 and ASC because ASC^{-/-} mice are also more susceptible to central *S. aureus* infection, whereas the survival of NLRP3^{-/-} mice is comparable to WT (43). These observations, together with our data, suggest that AIM2 is an important sensor of infection and injury in the brain in vivo.

We have shown that animals deficient in both IL-1 α and IL-1 β have markedly reduced infarct size after MCAo (44), and that

Anakinra (IL-1Ra) is neuroprotective in this model (e.g., for review see ref. 45). These data, and our observations of protection in the ASC knockout mice, suggest that there is a specific regulation of IL-1 in the brain, and we also have shown previously that both central and peripheral-derived IL-1 contribute to brain injury (28). However, inflammatory caspases may also be involved in neurodegenerative disease in the absence of IL-1 (13), so NLRC4 could also regulate caspase-dependent cell death pathways. AIM2 inflammasomes may also be involved directly in neuronal cell death, and it has been reported that cultured embryonic rat cortical neurons undergo an AIM2–inflammasome-dependent cell death when challenged with the AIM2 activator poly(dA:dT) (12). Thus, inflammasomes may regulate both inflammatory and cell death pathways that modify ischemic brain injury.

We report that microglial cell activation, leukocyte recruitment, and vascular activation are reduced in the brains of ASC^{-/-}, AIM2^{-/-}, and NLRC4^{-/-} mice after MCAo (Figs. 2 and 4). It is important to note that these inflammatory changes could occur as a consequence, in addition to being a cause, of the reduced damage. Changes in inflammatory markers are likely to result from a reduction in IL-1 processing and secretion but also result from reduced injury. We have reported previously that systemic injection of IL-1 β increases leukocyte recruitment into the brain after MCAo and that induced neutropenia in this model is neuroprotective, suggesting that an IL-1 β -dependent recruitment of leukocytes exacerbates ischemic brain injury (46). We have also reported that DAMPs can induce inflammasome-independent chemokine production from cultures of mixed glia (astrocytes and microglia) in the absence of IL-1, and that in the brains of IL-1 α double-knockout mice there is chemokine production and microglial cell activation (47). Thus, the extent of microglial cell activation and leukocyte recruitment is likely to be dependent upon both IL-1–dependent inflammation and IL-1–independent cell death. In these studies we chose to study brain injury and inflammation 24 h post MCAo. In this model the extent of injury is almost completely developed at 24 h postinjury. This time point is most suitable for proof of concept studies, when both injury and neurological assessment have to be performed. Also, we have reported sustained protective effects of Anakinra up to 48 h post MCAo (48) and 7 d post MCAo, using a caspase-1 inhibitor (14). Thus, we are confident that the protective effects observed in ASC^{-/-}, AIM2^{-/-}, and NLRC4^{-/-} mice are consistent with our previous and other published work.

In the introduction we describe studies suggesting that NLRP3 inflammasomes contribute to ischemic brain injury (8, 9), but that also NLRP1 inflammasomes are implicated in several models of brain injury (6, 10, 11), as are AIM2 inflammasomes (12). Here, using mice deficient in specific inflammasome components, we have shown that ischemic brain injury is profoundly influenced by multiple inflammasomes and, importantly, here was independent of the canonical sensor of sterile inflammation, the NLRP3 inflammasome. We report here an involvement of NLRC4 and AIM2 inflammasomes, but it is possible that others known [e.g., NLRP1 (8–10)] and other yet to be fully characterized inflammasomes are also involved.

In rodent models of Alzheimer's disease the memory deficit and inflammation have been reported to depend upon the NLRP3 inflammasome (49), and aggregated A β is a DAMP known to activate NLRP3 (50). However, NLRP1 has also been implicated in a rodent model of Alzheimer's disease (51). An explanation for this difference may be the respective cellular location of the inflammasomes. NLRP3 expressed by microglia drives inflammation, and NLRP1 expressed by neurons drives pyroptotic neuronal cell death (51). Thus, activation of multiple inflammasomes in our model may reflect different cellular compartments and possibly cell death in addition to inflammatory mechanisms. The types of inflammasome activated in the brain may also depend upon the nature of the injury. For example, in

a mouse model of intracerebral hemorrhage the NLRP3 inflammasome is reported to drive brain edema and behavioral deficits (52). It was reported recently that heme, a breakdown product of blood, activates the NLRP3 inflammasome (53). Thus, in models of hemorrhagic stroke there is likely to be a significant NLRP3-driven component, which was not the case in our study on cerebral ischemia. Thus, the types of inflammasome activated reflect their cellular location, the functional output (e.g., cell death and/or inflammation), and the nature of the injury (e.g., hemorrhagic versus ischemic stroke). Following our discoveries reported here we can now investigate these mechanisms fully.

Inflammation in the brain affects the outcome of neurodegenerative disease and so is an attractive therapeutic target. However, the molecular and cellular mechanisms regulating brain inflammation remain poorly defined. We have discovered that brain inflammation after cerebral ischemia is regulated by ASC, AIM2, and NLRC4 inflammasomes. This insight now gives us the opportunity to fully elucidate inflammatory regulatory networks in the brain and to establish therapeutic targets. The complexity of inflammasome responses in the brain where multiple inflammasomes are activated in the various neurodegenerative conditions studied suggests that perhaps the most promising therapeutic antiinflammatory targets for the treatment of neurodegenerative disease will be ASC and inflammatory caspases.

Materials and Methods

Animals. Experiments were carried out in 12–16-wk-old male mice ($n = 71$), all on C57BL/6 background (WT, NLRP3^{-/-}, NOD2^{-/-}, ASC^{-/-}, NLRC4^{-/-}, and AIM2^{-/-}), breeding at the animal facility of the University of Manchester. Animals were allowed free access to food and water and maintained under temperature-, humidity-, and light-controlled conditions. All animal procedures adhered to the UK Animals (Scientific Procedures) Act (1986), and experiments were performed in accordance with STAIR and ARRIVE guidelines.

Focal Cerebral Ischemia Induced by Middle Cerebral Artery Occlusion. MCAo was performed, using the intraluminal filament technique, as described earlier (54). Animals were anesthetized with isoflurane, and a silicone-coated monofilament (210- μ m-tip diameter, Doccol) was introduced to the left external carotid artery and advanced along the internal carotid artery to occlude the MCA for 45 min, followed by 24 h reperfusion. Occlusion was confirmed by a laser Doppler (Moor Instruments) measurement of blood flow, and animals showing less than 80% signal drop compared with baseline or absence of ischemia in the striatum were excluded pre hoc. During surgery, core temperature was maintained at 37 ± 0.5 °C. Three mice were excluded pre hoc from further analysis, due to improper occlusion of the MCA ($n = 1$) or surgical artifacts ($n = 2$).

Tissue Processing. Under terminal anesthesia, animals were perfused transcardially with saline, followed by paraformaldehyde [PFA; 4% (mass/vol) in PBS, Sigma]. Brains were postfixed in 4% PFA at 4 °C for 24 h, and cryoprotected in sucrose/PBS. Twenty-micrometer-thick coronal brain sections were cut on a sledge microtome (Bright series 8000; Bright Instruments). For cytokine measurement, saline-perfused spleen and liver samples were homogenized and processed as described earlier (55).

Measurement of Infarct Size and Neurological Outcome. The size of ischemic damage was measured as described previously (54) on cresyl violet-stained brain sections, corrected for edema and expressed as the percentage of the hemisphere. There were no differences in brain size between groups. Neurological status in mice was assessed according to a neurological grading score of increasing severity of deficit (56).

Cytokine Measurement. Sample processing and protein determination were performed as described previously (55). Saline-perfused liver and spleen homogenates were measured for TNF α , CXCL1, IL-6, IL-1 β , IL-1 α , and IL-10, using CBA Flex Sets (BD Biosciences) according to the manufacturers' protocol, on a BD FACVerse flow cytometer (BD Biosciences). Values are expressed as pg/g protein, and protein concentration was determined using Pierce BCA assay kit.

Immunofluorescence. Immunostaining was performed as described earlier (10). In brief, appropriate mixtures of rat anti-mouse CD45 1:200 (Serotec), goat anti-mouse IL-1 α , goat anti-mouse IL-1 β 1:100 (R&D Systems), and rabbit anti-

Iba1 1:1,000 (Wako Chemicals) antibodies were used followed by the appropriate fluorochrome-conjugated Alexa594 or Alexa488 donkey antisera (1:500, Invitrogen). Biotinylated tomato lectin (10 μ g/mL, Sigma.) was visualized with streptavidin–Alexa 350 conjugate (Invitrogen). Activated (CD45^{low}, Iba1⁺) and total number of microglia, CD45^{high} leukocytes, activated blood vessels (based on high levels of tomato lectin staining), and IL-1 α or IL-1 β -positive microglia (Iba1⁺) were counted in the striatum and cerebral cortex on 3–3 serial sections rostrocaudally (two random 20 \times fields per section).

Quantitative Analysis and Statistics. Animals were randomized for the experiments, and surgeries were performed without the operator being aware of the genetic condition of the animals. All quantitative analysis was performed under blinded conditions. Group sizes were determined by power calculation based on results from our previous MCAo studies (5% confidence level, 80% power, and an estimated 20–40% SD). Data were analyzed with one-way or two-way

ANOVA followed by Tukey's post hoc comparison (PrismGraph 6.0). Neurological scores were analyzed with nonparametric Kruskal–Wallis test followed by Dunn's multiple comparison test. $P < 0.05$ was considered statistically significant.

ACKNOWLEDGMENTS. The authors thank Mr. László Barna, the Nikon Microscopy Center at the Institute of Experimental Medicine, Nikon Austria GmbH, and Auro-Science Consulting, Ltd., for kindly providing microscopy support and the Flow Cytometry Core Facility at the Institute of Experimental Medicine. The authors are grateful to Dr. Vishva Dixit (Genentech) for providing the NLRP3^{-/-}, NLR4^{-/-}, and AIM2^{-/-} mice. D.B. was funded by a Wellcome Trust Fellowship. We are grateful for funding provided by the Medical Research Council and the European Union's Seventh Framework Programme (FP7/2008-2013) under Grant Agreements 201024 and 202213 [European Stroke Network (to N.R. and A.D.)]. A.D. is supported by OTKA (Hungarian Scientific Research Fund) K 109743, TÁMOP-4.2.4.A/2-1/11-2012-0001, and the Hungarian Brain Research Program KTIA_13_NAP-A-1/2.

- Rock KL, Latz E, Ontiveros F, Kono H (2010) The sterile inflammatory response. *Annu Rev Immunol* 28:321–342.
- Galea J, Brough D (2013) The role of inflammation and interleukin-1 in acute cerebrovascular disease. *J Inflamm Res* 6:121–128.
- Chen GY, Nuñez G (2010) Sterile inflammation: sensing and reacting to damage. *Nat Rev Immunol* 10(12):826–837.
- Takeuchi O, Akira S (2010) Pattern recognition receptors and inflammation. *Cell* 140(6):805–820.
- Latz E, Xiao TS, Stutz A (2013) Activation and regulation of the inflammasomes. *Nat Rev Immunol* 13(6):397–411.
- de Rivero Vaccari JP, et al. (2009) Therapeutic neutralization of the NLRP1 inflammasome reduces the innate immune response and improves histopathology after traumatic brain injury. *J Cerebral Blood Flow Metabolism* 29(7):1251–1261.
- Cassel SL, Sutterwala FS (2010) Sterile inflammatory responses mediated by the NLRP3 inflammasome. *Eur J Immunol* 40(3):607–611.
- Yang F, et al. (2014) NLRP3 deficiency ameliorates neurovascular damage in experimental ischemic stroke. *J Cerebral Blood Flow Metabolism* 34(4):660–667.
- Fann DY, et al. (2013) Intravenous immunoglobulin suppresses NLRP1 and NLRP3 inflammasome-mediated neuronal death in ischemic stroke. *Cell Death Dis* 4:e790.
- Abulafia DP, et al. (2009) Inhibition of the inflammasome complex reduces the inflammatory response after thromboembolic stroke in mice. *J Cerebral Blood Flow Metabolism* 29(3):534–544.
- de Rivero Vaccari JP, Lotocki G, Marcillo AE, Dietrich WD, Keane RW (2008) A molecular platform in neurons regulates inflammation after spinal cord injury. *J Neurosci* 28(13):3404–3414.
- Adamczak SE, et al. (2014) Pyroptotic neuronal cell death mediated by the AIM2 inflammasome. *J Cerebral Blood Flow Metabolism* 34(4):621–629.
- Denes A, Lopez-Castejon G, Brough D (2012) Caspase-1: Is IL-1 just the tip of the iceberg? *Cell Death Dis* 3:e338.
- Ross J, Brough D, Gibson RM, Loddick SA, Rothwell NJ (2007) A selective, non-peptide caspase-1 inhibitor, VRT-018858, markedly reduces brain damage induced by transient ischemia in the rat. *Neuropharmacology* 53(5):638–642.
- Wannamaker W, et al. (2007) (S)-1-((S)-2-[(4-amino-3-chloro-phenyl)-methanoyl]-amino-3,3-dimethyl-butano-1-yl)-pyrrolidine-2-carboxylic acid ((2R,3S)-2-ethoxy-5-oxo-tetrahydro-furan-3-yl)-amide (VX-765), an orally available selective interleukin (IL)-converting enzyme/caspase-1 inhibitor, exhibits potent anti-inflammatory activities by inhibiting the release of IL-1 β and IL-18. *J Pharmacol Exp Ther* 321(2):509–516.
- Kang SJ, et al. (2000) Dual role of caspase-11 in mediating activation of caspase-1 and caspase-3 under pathological conditions. *J Cell Biol* 149(3):613–622.
- Shibata M, et al. (2000) Caspases determine the vulnerability of oligodendrocytes in the ischemic brain. *J Clin Invest* 106(5):643–653.
- Kayagaki N, et al. (2011) Non-canonical inflammasome activation targets caspase-11. *Nature* 479(7371):117–121.
- Pauleau AL, Murray PJ (2003) Role of nod2 in the response of macrophages to toll-like receptor agonists. *Mol Cell Biol* 23(21):7531–7539.
- Dombrowski Y, et al. (2011) Cytosolic DNA triggers inflammasome activation in keratinocytes in psoriatic lesions. *Sci Transl Med* 3(82):82ra38.
- Hornung V, et al. (2009) AIM2 recognizes cytosolic dsDNA and forms a caspase-1-activating inflammasome with ASC. *Nature* 458(7237):514–518.
- Fernandes-Alnemri T, Yu JW, Datta P, Wu J, Alnemri ES (2009) AIM2 activates the inflammasome and cell death in response to cytoplasmic DNA. *Nature* 458(7237):509–513.
- Iadecola C, Anrather J (2011) The immunology of stroke: From mechanisms to translation. *Nat Med* 17(7):796–808.
- Denes A, Thornton P, Rothwell NJ, Allan SM (2010) Inflammation and brain injury: acute cerebral ischaemia, peripheral and central inflammation. *Brain Behav Immun* 24(5):708–723.
- Franchi L, Muñoz-Planillo R, Núñez G (2012) Sensing and reacting to microbes through the inflammasomes. *Nat Immunol* 13(4):325–332.
- DeSantis DA, et al. (2013) Alcohol-induced liver injury is modulated by Nlrp3 and Nlr4 inflammasomes in mice. *Mediators Inflamm* 2013:751374.
- Hu B, et al. (2010) Inflammation-induced tumorigenesis in the colon is regulated by caspase-1 and NLR4. *Proc Natl Acad Sci USA* 107(50):21635–21640.
- Denes A, et al. (2013) Central and haematopoietic interleukin-1 both contribute to ischaemic brain injury in mice. *Dis Model Mech* 6(4):1043–1048.
- Romberg N, et al. (2014) Mutation of NLR4 causes a syndrome of enterocolitis and autoinflammation. *Nat Genet* 46(10):1135–1139.
- Canna SW, et al. (2014) An activating NLR4 inflammasome mutation causes autoinflammation with recurrent macrophage activation syndrome. *Nat Genet* 46(10):1140–1146.
- Kitamura A, Sasaki Y, Abe T, Kano H, Yasutomo K (2014) An inherited mutation in NLR4 causes autoinflammation in human and mice. *J Exp Med* 211(12):2385–2396.
- De Nardo D, De Nardo CM, Latz E (2014) New insights into mechanisms controlling the NLRP3 inflammasome and its role in lung disease. *Am J Pathol* 184(1):42–54.
- Wen H, Miao EA, Ting JP (2013) Mechanisms of NOD-like receptor-associated inflammasome activation. *Immunity* 39(3):432–441.
- Kofoed EM, Vance RE (2011) Innate immune recognition of bacterial ligands by NALPs determines inflammasome specificity. *Nature* 477(7366):592–595.
- Rodgers MA, et al. (2014) The linear ubiquitin assembly complex (LUBAC) is essential for NLRP3 inflammasome activation. *J Exp Med* 211(7):1333–1347.
- Lopez-Castejon G, et al. (2013) Deubiquitinases regulate the activity of caspase-1 and interleukin-1 β secretion via assembly of the inflammasome. *J Biol Chem* 288(4):2721–2733.
- Juliana C, et al. (2012) Non-transcriptional priming and deubiquitination regulate NLRP3 inflammasome activation. *J Biol Chem* 287(43):36617–36622.
- Py BF, Kim MS, Vakifahmetoglu-Norberg H, Yuan J (2013) Deubiquitination of NLRP3 by BRCC3 critically regulates inflammasome activity. *Mol Cell* 49(2):331–338.
- Kumar Y, Radha V, Swarup G (2010) Interaction with Sug1 enables Ipafl ubiquitination leading to caspase 8 activation and cell death. *Biochem J* 427(1):91–104.
- Qu Y, et al. (2012) Phosphorylation of NLR4 is critical for inflammasome activation. *Nature* 490(7421):539–542.
- Bauernfeind FG, et al. (2009) Cutting edge: NF- κ B activating pattern recognition and cytokine receptors license NLRP3 inflammasome activation by regulating NLRP3 expression. *J Immunol* 183(2):787–791.
- Franchi L, et al. (2006) Cytosolic flagellin requires Ipafl for activation of caspase-1 and interleukin 1 β in salmonella-infected macrophages. *Nat Immunol* 7(6):576–582.
- Hanamsagar R, Aldrich A, Kielian T (2014) Critical role for the AIM2 inflammasome during acute CNS bacterial infection. *J Neurochem* 129(4):704–711.
- Boutin H, et al. (2001) Role of IL-1 α and IL-1 β in ischemic brain damage. *J Neurosci* 21(15):5528–5534.
- Brough D, Tyrrell PJ, Allan SM (2011) Regulation of interleukin-1 in acute brain injury. *Trends Pharmacol Sci* 32(10):617–622.
- McColl BW, Rothwell NJ, Allan SM (2007) Systemic inflammatory stimulus potentiates the acute phase and CXC chemokine responses to experimental stroke and exacerbates brain damage via interleukin-1- and neutrophil-dependent mechanisms. *J Neurosci* 27(16):4403–4412.
- Savage CD, Lopez-Castejon G, Denes A, Brough D (2012) NLRP3-inflammasome activating DAMPs stimulate an inflammatory response in glia in the absence of priming which contributes to brain inflammation after injury. *Front Immunol* 3:288.
- Mulcahy NJ, Ross J, Rothwell NJ, Loddick SA (2003) Delayed administration of interleukin-1 receptor antagonist protects against transient cerebral ischaemia in the rat. *Br J Pharmacol* 140(3):471–476.
- Heneka MT, et al. (2013) NLRP3 is activated in Alzheimer's disease and contributes to pathology in APP/PS1 mice. *Nature* 493(7434):674–678.
- Halle A, et al. (2008) The NALP3 inflammasome is involved in the innate immune response to amyloid- β . *Nat Immunol* 9(8):857–865.
- Tan MS, et al. (2014) Amyloid- β induces NLRP1-dependent neuronal pyroptosis in models of Alzheimer's disease. *Cell Death Dis* 5:e1382.
- Ma Q, et al. (2014) NLRP3 inflammasome contributes to inflammation after intracerebral hemorrhage. *Ann Neurol* 75(2):209–219.
- Dutra FF, et al. (2014) Hemolysis-induced lethality involves inflammasome activation by heme. *Proc Natl Acad Sci USA* 111(39):E4110–E4118.
- Denes A, Humphreys N, Lane TE, Grecnis R, Rothwell N (2010) Chronic systemic infection exacerbates ischemic brain damage via a CCL5 (regulated on activation, normal T-cell expressed and secreted)-mediated proinflammatory response in mice. *J Neurosci* 30(30):10086–10095.
- Chapman KZ, et al. (2009) A rapid and transient peripheral inflammatory response precedes brain inflammation after experimental stroke. *J Cerebral Blood Flow Metabolism* 29(11):1764–1768.
- Bederson JB, et al. (1986) Rat middle cerebral artery occlusion: Evaluation of the model and development of a neurologic examination. *Stroke* 17(3):472–476.

Supporting Information

Denes et al. 10.1073/pnas.1419090112

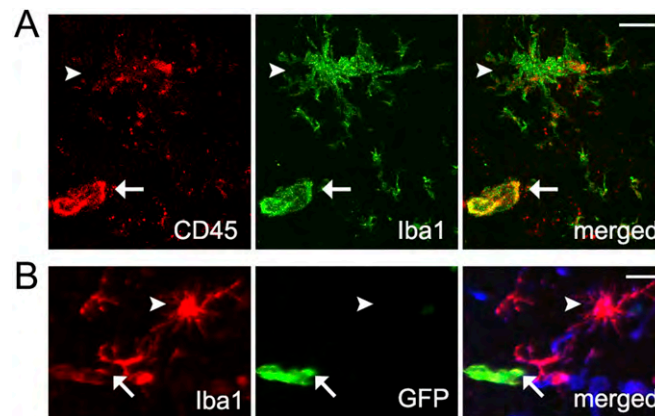


Fig. S1. (A) Iba1-positive (green) microglia showing low levels of CD45 (red) expression and ramified morphology (arrowhead) have been discriminated from elongated or amoeboid macrophages expressing high levels of CD45 (arrow) in the brain. (B) Recruited Iba1+ (red) macrophages at 24 h reperfusion are found associated to blood vessels (tomato lectin, blue) and are morphologically different from microglia as confirmed by using mice that had undergone lethal irradiation and transplantation of GFP+ bone marrow 6 wk before experimental stroke. (Scale bar, 10 μ m.)

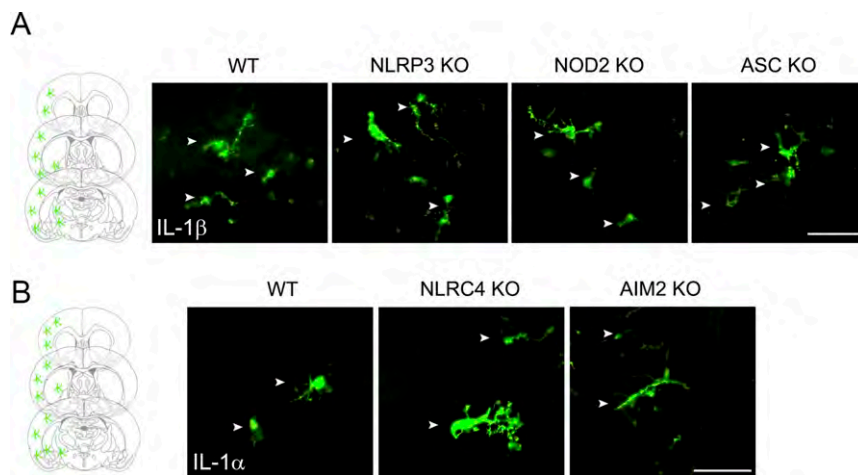


Fig. S2. (A) IL-1 β -positive microglia (green, arrowheads) in the ipsilateral cortex in WT, NLRP3 KO, NOD2 KO, and ASC KO mice. (B) IL-1 α -positive microglia (green, arrowheads) in the ipsilateral cortex in WT, NLRC4 KO, and AIM2 KO mice. Schematics show the location of IL-1 α - and IL-1 β -positive microglia in the ipsilateral hemisphere, which was similar in all animals. (Scale bars, 50 μ m.)

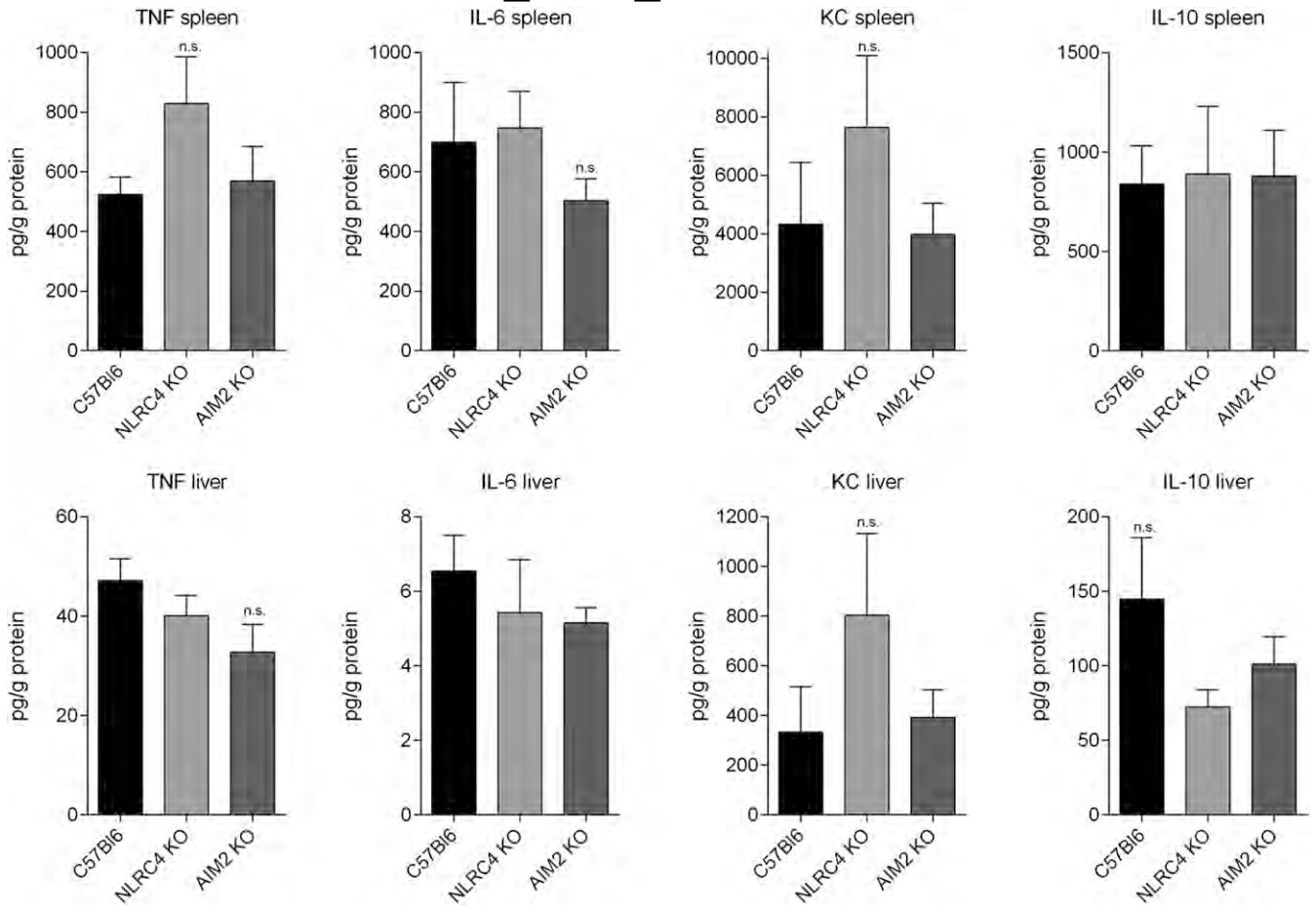
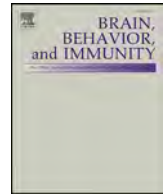


Fig. S3. KC (CXCL1), TNF α , IL-6, and IL-10 levels were measured in spleen and liver homogenates 24 h after MCAo by cytometric bead array and expressed as pg/g protein. n.s., not significant.



Contents lists available at ScienceDirect

Brain, Behavior, and Immunity

journal homepage: www.elsevier.com/locate/ybrbi

Interleukin-1 mediates ischaemic brain injury via distinct actions on endothelial cells and cholinergic neurons

Raymond Wong^{a,1}, Nikolett Lénárt^{b,1}, Laura Hill^a, Lauren Toms^a, Graham Coutts^a,
Bernadett Martinecz^b, Eszter Császár^b, Gábor Nyiri^c, Athina Papaemmanouil^a, Ari Waisman^d,
Werner Müller^a, Markus Schwaninger^e, Nancy Rothwell^a, Sheila Francis^f, Emmanuel Pinteaux^{a,2},
Adam Denés^{b,2,*}, Stuart M. Allan^{a,2,*}

^a Faculty of Biology, Medicine and Health, University of Manchester, M13 9PT Manchester, UK^b "Momentum" Laboratory of Neuroimmunology, Institute of Experimental Medicine, Szigony u. 43, 1083 Budapest, Hungary^c Laboratory of Cerebral Cortex Research, Institute of Experimental Medicine, Szigony u. 43, 1083 Budapest, Hungary^d Institute for Molecular Medicine, University Medical Center of the Johannes Gutenberg University Mainz, 55131 Mainz, Germany^e Institute of Experimental and Clinical Pharmacology and Toxicology, University of Lübeck, 23538 Lübeck, Germany^f Department of Infection, Immunity & Cardiovascular Disease, Medical School, University of Sheffield, S10 2RX Sheffield, UK

A B S T R A C T

The cytokine interleukin-1 (IL-1) is a key contributor to neuroinflammation and brain injury, yet mechanisms by which IL-1 triggers neuronal injury remain unknown. Here we induced conditional deletion of IL-1R1 in brain endothelial cells, neurons and blood cells to assess site-specific IL-1 actions in a model of cerebral ischaemia in mice. Tamoxifen treatment of IL-1R1 floxed (^{fl/fl}) mice crossed with mice expressing tamoxifen-inducible Cre-recombinase under the Slco1c1 promoter resulted in brain endothelium-specific deletion of IL-1R1 and a significant decrease in infarct size (29%), blood-brain barrier (BBB) breakdown (53%) and neurological deficit (40%) compared to vehicle-treated or control (IL-1R1^{fl/fl}) mice. Absence of brain endothelial IL-1 signalling improved cerebral blood flow, followed by reduced neutrophil infiltration and vascular activation 24 h after brain injury. Conditional IL-1R1 deletion in neurons using tamoxifen inducible nestin-Cre mice resulted in reduced neuronal injury (25%) and altered microglia-neuron interactions, without affecting cerebral perfusion or vascular activation. Deletion of IL-1R1 specifically in cholinergic neurons reduced infarct size, brain oedema and improved functional outcome. Ubiquitous deletion of IL-1R1 had no effect on brain injury, suggesting beneficial compensatory mechanisms on other cells against the detrimental effects of IL-1 on endothelial cells and neurons. We also show that IL-1R1 signalling deletion in platelets or myeloid cells does not contribute to brain injury after experimental stroke. Thus, brain endothelial and neuronal (cholinergic) IL-1R1 mediate detrimental actions of IL-1 in the brain in ischaemic stroke. Cell-specific targeting of IL-1R1 in the brain could therefore have therapeutic benefits in stroke and other cerebrovascular diseases.

1. Background

Inflammation is a major contributor to stroke pathophysiology and is therefore an attractive therapeutic target. A key mediator of inflammation is the pro-inflammatory cytokine interleukin-1 (IL-1) (Dinarelli et al., 2012). IL-1, expressed as two isoforms IL-1 α and IL-1 β , is upregulated rapidly after experimental cerebral ischaemia and very early expression is thought to occur in monocyte and macrophage lineages, whilst slightly delayed expression occurs in astrocytes, neurons, endothelial cells and invading immune cells (Ching et al., 2005; Pinteaux et al., 2009; Denes et al., 2011). Preclinical studies using experimental animal models have demonstrated the importance of IL-1 in stroke. Central or systemic administration of exogenous recombinant

IL-1 β in rodents subjected to middle cerebral artery occlusion (MCAo) exacerbates brain damage (Yamasaki et al., 1995; Stroemer and Rothwell, 1998; McColl et al., 2007), whilst disruption of both IL-1 α and IL-1 β in IL-1 α/β knockout (KO) mice results in a 70% reduction in infarct volume (Boutin et al., 2001). There is extensive experimental evidence showing that blockade of IL-1 signalling using the IL-1 receptor antagonist (IL-1Ra) is protective in stroke and other forms of brain injury, and early stage clinical trials of IL-1Ra in both ischaemic and haemorrhagic stroke have to date shown potentially promising results (Sobowale et al., 2016). However, the cellular mechanisms by which IL-1 mediates brain injury following cerebral ischaemia remain unknown.

IL-1 is known to exert its actions via binding and activation of its

* Corresponding authors.

E-mail addresses: denesa@koki.hu (A. Denés), stuart.allan@manchester.ac.uk (S.M. Allan).¹ Joint first authors.² Joint senior authors.<https://doi.org/10.1016/j.bbi.2018.11.012>

Received 31 July 2018; Received in revised form 12 November 2018; Accepted 15 November 2018

Available online 16 November 2018

0889-1591/© 2018 The Authors. Published by Elsevier Inc. This is an open access article under the CC BY license (<http://creativecommons.org/licenses/by/4.0/>).

main functional IL-1 type 1 receptor (IL-1R1) (Sims et al., 1988). IL-1R1 is expressed on the cerebrovasculature (Konsman et al., 2004) and *in vitro* studies also suggest that IL-1 acts in the brain through endothelial cells (Thornton et al., 2010; Summers et al., 2013), whilst toxic actions of IL-1 are mediated via cerebrovascular activation and transmigration of neutrophils (Allen et al., 2012) *in vitro*. The knockdown of endothelial IL-1R1 has been investigated *in vivo* (Li et al., 2011; Ching et al., 2007) but has been focussed on ubiquitous knockdown rather than inhibiting specific endothelial cell subsets, such as in the brain. IL-1 acts both peripherally and centrally (Denes et al., 2013) but precise brain specific actions have not yet been identified.

IL-1 also has diverse actions on neurons, including fast electrophysiological firing (Diem et al., 2003; Desson and Ferguson, 2003), potentiation of excitotoxicity and changes in neuronal gene expression (Denes et al., 2011; Tsakiri et al., 2008). However, functional data showing the effect of IL-1 on neurons and endothelial cells have been obtained only from *in vitro* studies (Lazovic et al., 2005; Andre et al., 2006), including our previous work showing IL-1 acts on neurons to produce inflammatory mediators (Tsakiri et al., 2008), suggesting neuronal signalling could contribute to detrimental neuroinflammatory responses, though the contribution of cell specific IL-1 actions to brain injury *in vivo* remains unknown.

The objective of this study was to determine the target cells of IL-1 action during ischaemic brain injury in mice. Tools to selectively and conditionally delete IL-1R1 in different cell types *in vivo* have become available recently (Abdulaal et al., 2016; Bruttger et al., 2015). Thus, we investigated the contribution of endothelial cells and neurons to ischaemic brain injury by deleting IL-1R1 from brain endothelial cell or neurons (including cholinergic neuronal cells). We also assessed the effects of IL-1R1 deficiency in platelets and myeloid cells, cell types that are known to contribute to diverse forms of brain injury and that are involved in systemic IL-1 actions (Thornton et al., 2010; Denes et al., 2011; Iadecola and Anrather, 2011). We show that both brain endothelial and neuronal IL-1R1 mediate the actions of IL-1 on brain injury via functionally distinct mechanisms, some of which (i.e. effects on cerebral perfusion) are apparent in the first hour after the ischaemic insult. We also reveal that IL-1R1 on cholinergic neurons themselves represent a potential therapeutic target against the detrimental effects of IL-1 after acute brain injury.

2. Materials and methods

2.1. Experimental design

Animal procedures were carried out in accordance with the Animal Scientific Procedures Act (1986) and the European Council Directive 2010/63/EU, and were approved by the Animal Welfare and Ethical Review Body, University of Manchester, UK and the Animal Care and Use Committee of the Institute of Experimental Medicine, Budapest, Hungary. Experiments followed ARRIVE (Kilkenny et al., 2010) and IMPROVE guidelines (Percie du Sert, 2017). A code was allocated to each animal by a non-experimenter and was randomly assigned to different treatment groups. During all surgical procedures and functional tests the experimenter was blinded to treatment.

2.2. Animals

All mice were on a C57BL/6J background and only males were used. Brain endothelial-specific IL-1R1 knockout (KO) mice were generated by crossing mice in which exon 5 of the *Il1r1* gene is flanked with loxP sites [IL-1R1 floxed (^{fl/fl})] (Abdulaal et al., 2016) with mice expressing Cre recombinase under the promoter of the thyroxine transporter (Slco1c1) that is specifically expressed in brain endothelial cells (Ridder et al., 2011) (thereafter named IL-1R1^{fl/fl} Δ Slco1c1) (Fig. 1A). Brain endothelial IL-1R1 deletion was achieved by injection of tamoxifen (2 mg/100 μl in corn oil, Sigma-Aldrich) for five consecutive days

in 6–9 week old male mice. Controls were IL-1R1^{fl/fl} Δ Slco1c1 male mice injected with vehicle (corn oil) as well as IL-1R1^{fl/fl} mice treated with tamoxifen. Mice allocated for the detection of IL-1R1 expression were culled 0, 7 and 14 days after tamoxifen administration, whilst mice allocated for experimental stroke underwent surgery at 21 days after the start of tamoxifen or vehicle administration. Tamoxifen inducible nestin-Cre mice were crossed with IL-1R1^{fl/fl} mice to delete IL-1R1 in neurons following two consecutive administrations of 2 mg/100 μl tamoxifen (48 h apart) in 2–4 week old male mice (thereafter named IL-1R1^{fl/fl} Δ Nestin). Ubiquitous IL-1R1 KO mice (named IL-1R1^{-/-}) were generated by crossing IL-1R1^{fl/fl} mice with K14-Cre mice, as previously reported (Couzin-Frankel, 2012). To delete IL-1R1 selectively from cholinergic neurons, IL-1R1^{fl/fl} mice were crossed with ChAT-cre mice (IL-1R1^{fl/fl} Δ ChAT). To selectively and constitutively delete IL-1R1 in myeloid cells or platelets, IL-1R1^{fl/fl} mice were crossed with LysM-Cre mice (IL-1R1^{fl/fl} Δ LysM) or PF4-Cre mice (IL-1R1^{fl/fl} Δ PF4), respectively. All animals were maintained at 21 ± 1 °C, 55 ± 10% humidity, in a 12 h light-dark cycle with free access to food and water.

In total, 10 IL-1R1^{fl/fl} Δ Slco1c1 animals injected with vehicle, 11 IL-1R1^{fl/fl} Δ Slco1c1 animals injected with tamoxifen and 11 IL-1R1^{fl/fl} animals injected with tamoxifen, were used in this study to determine the effect of brain endothelial cell IL-1R1 deletion; 10 IL-1R1^{fl/fl} and 10 tamoxifen-treated IL-1R1^{fl/fl} Δ Nestin were used to assess the effect of neuronal IL-1R1 deletion; 13 IL-1R1^{fl/fl} mice and 10 IL-1R1^{-/-} mice were used to determine the effect of ubiquitous IL-1R1 deletion; 9 IL-1R1^{fl/fl} Δ ChAT mice, 10 IL-1R1^{fl/fl} mice, 14 IL-1R1^{fl/fl} mice, 14 IL-1R1^{fl/fl} Δ PF4 and 12 IL-1R1^{fl/fl} Δ LysM mice were used to assess the effect of IL-1R1 deletion in cholinergic neurons, platelets or myeloid cells, respectively. The pre-determined inclusion criteria for analysis were as follows; decline in Doppler signal of at least 70%, no subarachnoid haemorrhages and survival to 24 h. Subarachnoid haemorrhage was identified post-mortem by the presence of excessive bleeding on the external surface of the brain, typically close to the filament location. Animals excluded from analysis due to early mortality included; two IL-1R1^{fl/fl} Δ Slco1c1 mice treated with vehicle and two with tamoxifen, four IL-1R1^{fl/fl}, one IL-1R1^{fl/fl} Δ Nestin and two IL-1R1^{fl/fl} Δ ChAT animal due to surgical artefacts, whilst a single IL-1R1^{fl/fl} Δ Slco1c1 vehicle-treated animal was culled early for welfare. Exclusions for cerebral haemorrhages included; two IL-1R1^{fl/fl} Δ Slco1c1 mice treated with vehicle, three with tamoxifen, one IL-1R1^{fl/fl} animal treated with tamoxifen and one IL-1R1^{fl/fl} Δ Nestin animal. Four additional mice were excluded from analysis pre hoc based on the criteria detailed above in that an insufficient drop (> 70%) in cerebral blood flow was observed. In total there were 23 mice excluded from the study, which is 14.6% of the total used.

2.3. Focal cerebral ischaemia

Anaesthesia was induced by inhalation of 4% isoflurane (30% oxygen and 70% nitrous oxide gas mix, AbbVie Ltd, UK or Linde Ltd, Hungary) and was maintained at 1.75%. Body temperature was monitored throughout surgery (via rectal probe) and maintained at 37 °C ± 0.5 °C using a heating blanket (Harvard Apparatus, Edenbridge, Kent, UK). A laser Doppler blood flow monitor (Oxford Optronix, Abingdon, UK) was used to monitor cerebral blood flow (CBF). Focal cerebral ischaemia was induced by MCAo based on a previously described protocol (Wong et al., 2014). Briefly, a hole was made into the temporalis muscle (6 mm lateral and 2 mm posterior from bregma) to allow a 0.5 mm diameter flexible laser-Doppler probe to be fixed onto the skull and secured in place by tissue adhesive (Vetbond, UK). A midline incision was made on the ventral surface of the neck and the right common carotid artery isolated and ligated. Topical anaesthetic (EMLA, 5% prilocaine and lidocaine, AstraZeneca, UK) was applied to skin incision sites prior to incision. The internal carotid artery and the pterygopalatine artery were temporarily ligated. A 6-0 monofilament (Doccol, Sharon, MA, USA) was introduced into the internal

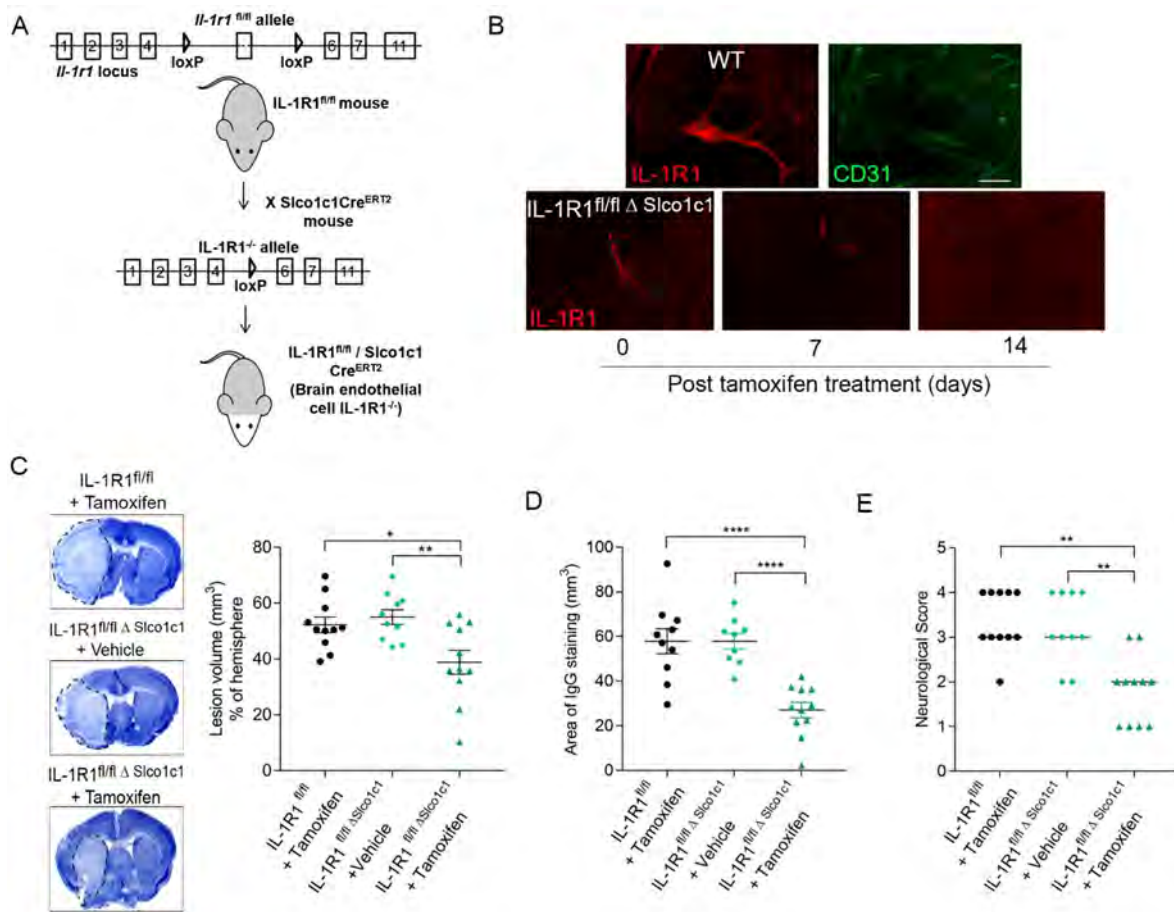


Fig. 1. Brain endothelial IL-1R1 deletion reduces infarct volume and BBB permeability and improves neurological function. IL-1R1^{fl/fl} Δ Slco1c1 (Brain endothelial-specific IL-1R1) mice were generated by crossing IL-1R1^{fl/fl} mice (exon 5 of the *Il1r1* gene flanked with loxP sites) with Slco1c1 Cre^{ERT2} mice (expressing Cre recombinase under the promoter of the thyroxine transporter) (A). IL-1R1 protein expression was reduced over time in blood vessels identified by CD31 immunostaining in IL-1R1^{fl/fl} Δ Slco1c1 animals after tamoxifen treatment to total deletion by day 14 (B). IL-1R1 deletion in brain endothelial cells (IL-1R1^{fl/fl} Δ Slco1c1 mice treated with tamoxifen) reduced infarct volume as assessed on cresyl violet stained brain sections (C), IgG leakage (D) and improved neurological function (E) compared to control group (IL-1R1^{fl/fl} Δ Slco1c1 mice treated with vehicle). IL-1R1^{fl/fl} Δ Slco1c1 mice treated with vehicle; n = 10, IL-1R1^{fl/fl} Δ Slco1c1 mice treated with tamoxifen; n = 11, IL-1R1^{fl/fl} treated with tamoxifen; n = 11. *p ≤ 0.05, **p ≤ 0.01, ***p ≤ 0.001, ****p ≤ 0.0001. All parametric data are expressed as means ± SEM, medians are shown in the case of neurological scores. (For interpretation of the references to colour in this figure legend, the reader is referred to the web version of this article.)

carotid artery via an incision in the common carotid artery (endothelial-specific IL-1R1 deletion study) or via the external carotid artery (ubiquitous, neuronal-specific-, myeloid cell-specific and platelet-specific IL-1R1 deletion studies). The filament was advanced approximately 10 mm distal to the carotid bifurcation, beyond the origin of the middle cerebral artery. Relative CBF was monitored for the first 30–45 min following MCAo, during which time relative CBF had to reduce by at least 70% of pre-ischæmic values for inclusion. After 30 min of occlusion (endothelial-specific IL-1R1 deletion study) or 45 min of occlusion (ubiquitous, neuronal-specific-, myeloid cell-specific and platelet-specific IL-1R1 deletion studies) the filament was withdrawn back into the common carotid artery to allow reperfusion to take place. The wound was sutured and mice received a subcutaneous bolus dose of saline for hydration (500 μl) and a general analgesic (Buprenorphine, 0.05 mg/kg injected subcutaneously, Vetergesic, UK). Animals were kept at 26–28 °C until they recovered from anaesthesia and surgery, before being transferred back to ventilated cages suspended over a heating pad with free access to mashed food and water in normal housing conditions.

2.4. Tissue processing

Animals were perfused transcardially with 0.9% saline followed by 4% paraformaldehyde (PFA) under either terminal 3% isoflurane (30% oxygen and 70% nitrous oxide gas mix) or ketamine-xylazine anaesthesia. Brains were then removed and left to post-fix for 24 h either in 4% PFA or in 10% sucrose 4% PFA before being transferred either to 30% sucrose or to 10% sucrose-PBS. After 24 h in 10% or 30% sucrose, brains were sectioned into 25–30 μm coronal sections using a sledge microtome (Bright, Cambridgeshire, UK or Leica, Germany) for subsequent Cresyl violet staining and immunohistochemistry.

2.5. Functional outcomes

Animals were assessed for neurological deficits 24 h after MCAo a using a 5-point scoring system (Iadecola et al., 1997). The neurological scores were as follows: 0, normal motor function; 1, flexion of torso and contralateral forelimb when mouse was lifted by the tail; 2, circling to the contralateral side when mouse is held by the tail on a flat surface, but normal posture at rest; 3, leaning to the contralateral side at rest, 4, no spontaneous motor activity. In IL-1R1^{fl/fl} Δ CHAT mice functional outcome has also been assessed by a composite neurological score

optimized for mice to obtain a more comprehensive readout (Orsini et al., 2012; Clark et al., 1997). Composite scores range from 0 (healthy mice) to 56 (worst performance) by adding up scores from 13 categories as follows: hair (0–2), ears (0–2), eyes (0–4), posture (0–4), spontaneous activity (0–4), and epileptic behavior (0–12), and focal deficits: body symmetry (0–4), gait (0–4), climbing on a surface held at 45° (0–4), circling behavior (0–4), front limb symmetry (0–4), compulsory circling (0–4), and whisker response to a light touch (0–4). Results are expressed as composite neurological score.

2.6. Laser speckle contrast imaging (LSCI)

At the end of the MCAo surgery, mice were transferred to the stereotaxic frame and LSCI measurements performed 30 min after reperfusion under isoflurane anaesthesia, using a PeriCam PSI High Resolution system (Perimed AB, Järfälla-Stockholm, Sweden). To assess CBF changes in different groups of mice in a uniform manner, tamoxifen-treated IL-1R1^{fl/fl} Δ Slco1c1 mice and IL-1R1^{fl/fl} Δ Nestin mice together with tamoxifen-treated control IL-1R1^{fl/fl} mice were subjected to MCAo for 45 min (left side occluded). LSCI measurements were performed 30 min after reperfusion. The skin on the top of the skull was opened and imaging performed through the intact skull bone to visualize cortical perfusion changes (Winship, 2014) for 10 min at 16 frames/sec in 20 μ m/pixel resolution, using a 10 \times 10 mm field of view. To evaluate recovery of blood flow in the penumbra after stroke, perfusion changes were assessed in three adjacent regions of interest (ROI) in the primary MCA area (Fig. 5A). LSCI is particularly sensitive to assess perfusion changes in the microcirculation. The area of cortical sinusoids have been excluded from ROIs and only measurements without motion artefacts have been analysed to minimize bias (Eriksson et al., 2014; Dunn, 2012). Area under the curve (AUC) values over the 10 min imaging period for each ROI were determined and data expressed as percentage values of the corresponding contralateral ROI.

2.7. Histology and immunohistochemistry

Lesion volumes were measured using Cresyl violet staining, as previously described (McCull et al., 2007). For each brain, infarcts were measured on defined coronal sections (using image J), spaced approximately 360 μ m apart. Each defined coronal section, with its brain co-ordinates and lesion was integrated to estimate total lesion volume for each brain and corrected for oedema.

Blood-brain-barrier (BBB) permeability was assessed by peroxidase-based immunohistochemistry for circulating IgG infiltration in the brain. Endogenous peroxidase activity (0.3% H₂O₂ in dH₂O for 10 min) and non-specific staining [5% normal horse serum, 0.3% triton in phosphate buffered saline (PBS) for 10 min] were blocked, and sections incubated in biotinylated anti-mouse IgG antibody (1:500, #BA-2000, Vector Laboratories, UK) for 2 h. Sections were then washed and incubated with avidin–biotin–peroxidase complex (1:500, Vectastain Elite ABC HRP Kit, #PK-6100, Vector Laboratories, UK), and detected by colorimetry using a diaminobenzidine (DAB) solution (0.05% DAB, 0.005% H₂O₂ in dH₂O). Sections were left to dry, before being mounted using DPX mounting medium (Fisher Scientific, UK), cover slipped and imaged using an Olympus BX51 upright microscope with Coolsnap ES camera (Photometrics, UK) for image capture. The total IgG volume for the brain was determined by measuring IgG on individual sections and integrating them to determine total IgG volume, as described earlier for lesion volume.

2.8. Immunofluorescence

Brain sections were incubated with blocking buffer consisting of 5% normal donkey serum (Jackson laboratories, Bar Harbor, ME, USA), 1% bovine serum albumin (BSA), 0.1% Triton X-100, 0.05% Tween 20 (Sigma-Aldrich), 0.2 M Glycine (Fisher Scientific) in PBS for 1 h.

Blocking buffer was then removed and sections were incubated with primary antibody, diluted in primary antibody buffer (1% BSA, 0.3% Triton X-100 in PBS), with Lectin (1:100, Lycopersicon esculentum, #L0651, Sigma-Aldrich) at 4 °C overnight. Primary antibodies used in this study included; goat anti-IL-1R1 (1:100, #AF771, R & D Systems, UK), sheep anti-VWF (1:100, Abcam, UK), rabbit anti-Iba1 (1:1000, #019–19741, Wako, USA), goat anti-intracellular adhesion molecule 1 (ICAM-1, 1:200, #AF796, R&D Systems, UK), goat anti-vascular cell adhesion protein 1 (VCAM-1, 1:100, R&D Systems, UK), SJC4 (1:10,000, kindly gifted by Professor Daniel Anthony, University of Oxford, UK), rat anti-CD45 (1:250, #MCA1388, AbD Serotec, UK), goat-anti MPO (1:250, #AF3667, Novus Biologicals, UK), mouse anti-neurofilament-H (1:500, #SMI-32P, Covance, USA), rabbit anti-P2RY12 (1:500, #55043AS AnaSpec, Belgium), mouse anti-Cre recombinase (1:500, #MAB3120, Millipore, Germany) and chicken-anti PGP9.5 (1:500, #ab72910, Abcam, UK), rabbit anti-Annexin V (1:250, #NB100-1930, Novus Biologicals, UK) and mouse-anti NeuN (1:500, #MAB377, Millipore, Germany). Sections were washed in 0.1% Tween in PBS, and incubated with secondary antibodies diluted in 0.05% tween in PBS. Secondary antibodies consisted of Alexa-Fluor 488 (1:500 rabbit, goat, ThermoFisher, UK), Alexa-Fluor 594 (1:500, sheep, goat, ThermoFisher, UK) and Alexa-Fluor 350 (1:100, streptavidin, ThermoFisher, UK), donkey anti-rabbit A488 (1:500, #A21206, Invitrogen, USA), streptavidin DyL405 (1:500, #016-470-084, Jackson ImmunoResearch, USA), donkey anti-goat A488 (1:500, #A11055, Invitrogen, USA), donkey anti-rat A594 (1:500, #A21209, Invitrogen, USA) and donkey anti-rabbit A647 (1:500, #711-605-152, Jackson ImmunoResearch, USA). After a 2 h incubation, secondary antibodies were removed, and sections were washed with 0.1% Tween in PBS, mounted on glass slides and left to dry in the dark, before being cover slipped with mounting medium (ProLong Gold without DAPI, ThermoFisher, UK).

2.9. Image analysis

Analyses for immunohistochemistry were conducted on coronal sections taken at the same co-ordinates (approximately +1 mm anterior to bregma), and both ipsilateral and contralateral hemispheres (to the side of the brain lesion) regions were measured in each animal. Neutrophils were counted in the middle of the striatum and in the cerebral cortex. Analysis of vascular markers (ICAM-1, VCAM-1) and Iba1 immunostaining was conducted in the penumbra region of the cortex and in the striatum. The activation states of Iba1-positive microglia were scored based on the morphology, as described previously (40), or numbers of activated microglia counted based on the levels of Iba1 and CD45 expression and morphology. Briefly, scoring was as follows: 0, Resting/Ramified; 1, De-ramifying/Re-ramifying; 2, Activated/Amoeboid; 3, Clustered & activated. Image analysis was carried out blinded to the experimental group status on three randomly selected ROI/brain region/slice on three coronal slices/animal.

2.10. Statistical analysis

Sample size for experimental stroke studies were determined by a priori power calculation using G*Power 3.1.9.2 with mean differences and standard deviations based on pilot studies and previous experiments (power 80%, α 0.05). Data were assessed for normal distribution using the Shapiro-Wilk W-test in order to determine parametric or non-parametric analysis. Lesion volume and BBB breakdown were analysed with one-way ANOVA followed by post-hoc Tukey multiple comparisons between treatments groups. Mann-Whitney test was used to analyse differences between control and IL-1R1^{fl/fl} Δ ChAT mice due to the lack of normality of data sets. Neurological scoring was analysed with non-parametric Mann-Whitney test (2 groups) or Kruskal-Wallis test combined with Dunn's multiple comparisons test. Immunofluorescence data were analysed by two-way ANOVA, and post-

hoc Tukey's multiple comparisons between matched hemisphere and treatment groups. Significant difference was considered for $p < 0.05$.

3. Results

3.1. Brain endothelial IL-1R1 deletion reduces infarct volume, BBB permeability and improves neurological function

First, we investigated brain injury after targeted deletion of IL-1R1 from the cerebrovasculature. IL-1R1^{fl/fl} Δ S1co1c1 animals (Fig. 1A) injected with tamoxifen showed reduced IL-1R1 protein expression in cerebral blood vessels at day 7 and IL-1R1 expression was completely ablated on day 14 (Fig. 1B). Experimental animals in this study were used at day 21 onwards.

Deletion of IL-1R1 in brain endothelial cells (IL-1R1^{fl/fl} Δ S1co1c1 mice) significantly reduced both ischaemic infarct (29% decrease, Fig. 1C, 95% CI: 4.33 to 27.99, $p = 0.0058$; $F(2, 29) = 6.67$) and IgG leakage (53% decrease, Fig. 1D, 95% CI: 15.27 to 46.47, $p < 0.0001$; $F(2, 27) = 17.82$) compared to vehicle-treated IL-1R1^{fl/fl} Δ S1co1c1 animals, whilst IL-1R1^{fl/fl} animals treated with tamoxifen had infarcts and BBB injury based on IgG leakage comparable to vehicle-treated IL-1R1^{fl/fl} Δ S1co1c1 mice (Fig. 1C and D). IL-1R1 deletion in brain endothelial cells resulted in reduced neurological deficits (40% decrease, Fig. 1E, $p < 0.0065$) compared to vehicle-treated IL-1R1^{fl/fl} Δ S1co1c1 mice, with experimental groups correlating similarly to infarct volume and BBB disruption.

3.2. Brain endothelial IL-1R1 deletion reduces cerebrovascular activation and neutrophil migration

As reported previously (Wang et al., 1994), MCAo increased cerebral vascular expression of ICAM-1 (Fig. 2A and B) and VCAM-1 (Fig. 2C and D) in the ipsilateral hemisphere, compared to the contralateral hemisphere [$F(1, 25) = 113.8$, $p \leq 0.001$; $F(1, 25) = 98.82$, $p \leq 0.001$, respectively]. However, brain endothelial IL-1R1 deletion reduced cerebrovascular activation in IL-1R1^{fl/fl} Δ S1co1c1 mice by 50% (95% CI: 1.86 to 12.95, $p = 0.007$) for ICAM-1 (Fig. 2B) and 55% (95% CI: 1.81–33.08, $p = 0.027$) for VCAM-1 (Fig. 2D) compared to vehicle-treated animals [$F(2, 25) = 8.919$, $p = 0.0012$; $F(2, 25) = 7.043$, $p = 0.0038$, respectively]. Cerebral activation of VWF was reduced by 56% though this was not significant (95% CI: -4.71 to 33.42, $p = 0.1668$; $F(2, 25) = 2.412$, $p = 11.02$). Tamoxifen-treated IL-1R1^{fl/fl} mice had equivalent levels of ICAM-1 (Fig. 2B) and VCAM-1 (Fig. 2D) to vehicle-treated IL-1R1^{fl/fl} Δ S1co1c1 mice.

We have demonstrated previously that IL-1 actions on brain endothelial cells *in vitro* contribute to neutrophil infiltration and subsequent neurotoxicity (Allen et al., 2012). Since our data demonstrate that brain endothelial IL-1R1 contributes to brain damage and BBB dysfunction, we next investigated the possible mechanisms underlying brain endothelial IL-1R1 deletion-induced ischaemic damage, by assessing stroke induced neutrophil infiltration after IL-1R1 deletion.

After MCAo, neutrophils migrate to the area of infarct, in significantly increased numbers compared to the undamaged contralateral side (Fig. 3A). IL-1R1^{fl/fl} Δ S1co1c1 mice treated with tamoxifen, showed almost a complete loss (94% reduction, $p = 0.0114$) of neutrophil migration compared to vehicle treatment (95% CI: 17.95 to 154.4, $p = 0.0114$; $F(2, 25) = 6.093$), whilst IL-1R1^{fl/fl} animals treated with tamoxifen had similar neutrophil numbers compared to vehicle-treated IL-1R1^{fl/fl} Δ S1co1c1 animals (Fig. 3B). Although IL-1R1 deletion on the brain endothelium dramatically reduced neutrophil migration induced by cerebral ischaemia, there was no effect on microglial activation, and the number of microglia were unchanged (data not shown) compared to vehicle-treated IL-1R1^{fl/fl} Δ S1co1c1 or IL-1R1^{fl/fl} control animals after MCAo (Fig. 3C and D).

3.3. Neuronal IL-1R1 deletion reduces infarct volume and leads to altered microglia-neuron interactions in the penumbra

To genetically delete IL-1R1 effectively from most neurons we used the nestin promoter-driven Cre recombinase expression that is expressed in neurons and a subset of glial precursors. Using our tamoxifen induction protocol we found that Cre expression was mainly confined to neurons in IL-1R1^{fl/fl} Δ Nestin mice 48 h after tamoxifen administration (Fig. 4A). Experimental stroke in IL-1R1^{fl/fl} Δ Nestin mice resulted in significantly smaller (25% reduction, $p = 0.0379$) brain injury (Fig. 4B) compared to IL-1R1^{fl/fl} mice that received identical tamoxifen treatment. In spite of this marked reduction in infarct volume, only a non-significant trend of reduced brain oedema was observed (Fig. 4C), whereas BBB breakdown was not affected in these mice (data not shown) and no difference was observed in neurological outcome (Fig. 4D). To understand these findings, we assessed changes in vascular activation and neutrophil recruitment in IL-1R1^{fl/fl} Δ Nestin and IL-1R1^{fl/fl} mice 24 h after cerebral ischaemia, as above. In contrast to the effect of brain endothelial IL-1R1 deletion, no changes in ICAM-1-positive blood vessels or the total number of CD45-positive leukocytes or neutrophils were found in the brain (Fig. 4E–G). The majority of CD45-positive leukocytes were neutrophils containing myeloperoxidase (Fig. 4E ii). The numbers of activated microglia were also not different (Fig. 4H), suggesting that an absence of IL-1R1 signalling in the brain of IL-1R1^{fl/fl} Δ Nestin mice does not influence vascular and microglial inflammatory actions in response to ischaemic injury. Since our previous research has revealed a key role for microglia in protecting injured neurons by shaping neuronal network activity and excitotoxicity, we assessed microglial process coverage of neurons as an indicator of altered neuronal activity and microglia-neuron interactions (Szalay et al., 2016). Microglial process coverage was significantly increased (by 22.29%, $p = 0.0043$) in the ischaemic penumbra of IL-1R1^{fl/fl} Δ Nestin mice (Fig. 4I), where microglia contacted both NeuN-positive neurons and Annexin V-positive cells beyond the zone of viable neurons (Fig. 4J). This suggested that neuronal IL-1R1 signalling may alter neuronal activity and/or protective microglia neuron interactions.

3.4. Brain endothelial, but not neuronal IL-1R1 deletion improves early perfusion deficits after cerebral ischaemia

To investigate whether site-specific IL-1 actions influenced brain perfusion early enough to influence the evolution of the infarct, we assessed cerebral perfusion changes 30 min after the induction of reperfusion in three adjacent regions of interest (ROI; Fig. 5A). In the absence of endothelial IL-1R1, a significantly smaller perfusion deficit was observed in the ipsilateral hemisphere at the MCA area [$p = 0.0017$, $F(1, 32) = 11.74$], which was apparent at both MCA2 and MCA3 ROIs (95% CI: 0.4004 to 49.09, $p = 0.0451$; 95% CI: 0.4911 to 49.18, $p = 0.0440$, respectively) compared to control mice (Fig. 5B and C). This phenomenon was less obvious in the lateral cortical areas (core of primary MCA territory) and was more apparent in the midline and rostral-caudal zones with more collateral supply (Fig. 5B, MCA2, MCA3 ROIs on Fig. 5C). We also assessed cerebral perfusion changes in IL-1R1^{fl/fl} Δ Nestin mice. In contrast to our findings after endothelial IL-1R1 deletion, no differences were observed between IL-1R1^{fl/fl} Δ Nestin and IL-1R1^{fl/fl} mice (Fig. 5D and E), suggesting that the absence of IL-1R1 in neurons has no major impact on cerebral perfusion.

3.5. Deletion of IL-1R1 from cholinergic neurons results in smaller infarct size, smaller brain oedema and improved functional outcome

Our findings in IL-1R1^{fl/fl} Δ Nestin mice suggest the existence of parallel, endothelium-independent neuron specific actions of IL-1R1 in ischaemic brain injury. Therefore, we investigated the effect of IL-1R1 deletion directly in choline-acetyltransferase (ChAT) positive cholinergic cells. Forebrain cholinergic neurons play a fundamental role in

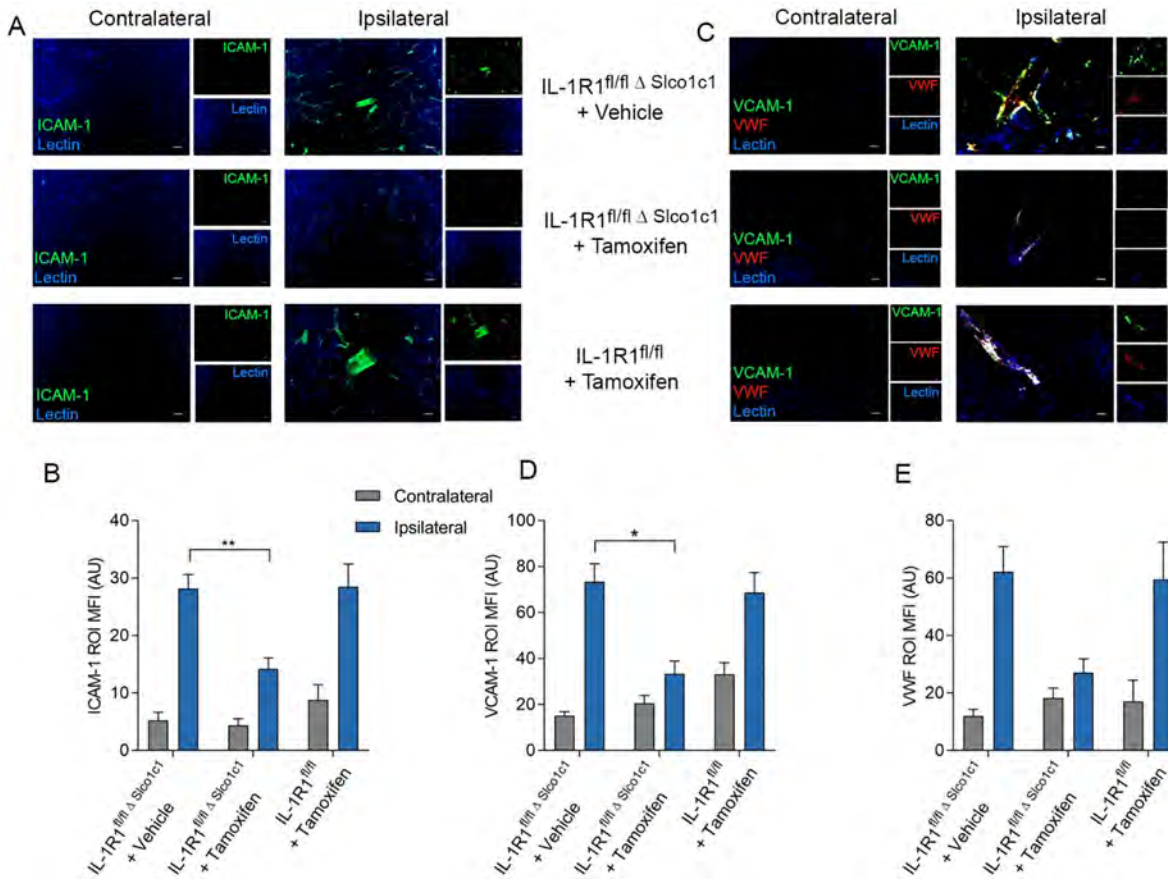


Fig. 2. Brain endothelial IL-1R1 deletion reduces vascular activation. Immunostaining with ICAM-1 (co-stained with lectin to identify cerebral blood vessels) showed increased ICAM-1 cerebrovascular staining in the ipsilateral hemisphere when compared to the contralateral side 24 h after MCAo (A), and deletion of IL-1R1 on the brain endothelium decreased ICAM-1 expression (IL-1R1^{fl/fl} Δ S1co1c1 mice treated with tamoxifen) in comparison to control (IL-1R1^{fl/fl} Δ S1co1c1 mice treated with vehicle) (B). VCAM-1 Immunostaining (co-stained with lectin to identify cerebral blood vessels and VWF for endothelial cell activation) showed increased VCAM-1 cerebrovascular staining in the ipsilateral hemisphere when compared to the contralateral side after stroke (C), and deletion of IL-1R1 on the brain endothelium decreased VCAM-1 expression (IL-1R1^{fl/fl} Δ S1co1c1 mice treated with tamoxifen) in comparison to control (IL-1R1^{fl/fl} Δ S1co1c1 mice treated with vehicle) (D). No change in the number of VWF-positive blood vessels was seen (E). IL-1R1^{fl/fl} Δ S1co1c1 mice treated with vehicle; n = 10, IL-1R1^{fl/fl} Δ S1co1c1 mice treated with tamoxifen; n = 11, IL-1R1^{fl/fl} treated with tamoxifen; n = 7. *p ≤ 0.05, **p ≤ 0.01. Region of interest MFI measured in arbitrary units (AU). Data are expressed as means ± SEM.

controlling the CNS, establish widespread innervation in the forebrain and are implicated in cognitive decline and several neurodegenerative diseases. In addition, brainstem cholinergic neurons control various physiological functions and regulate general immune response via the vagus nerve (Hoover, 2017; Mufson et al., 2008; Duris et al., 2017).

There was a significant reduction in infarct size (by 22.4%, p = 0.0279) and brain oedema (by 57.2%, p = 0.0255) in IL-1R1^{fl/fl} Δ ChAT mice when compared to IL-1R1^{fl/fl} mice (Fig. 6A and B). Deletion of IL-1R1 in cholinergic cells also improved functional outcome as assessed by Garcia’s composite neurological score (Fig. 6D, p = 0.0263), whilst a non-significant trend for improved sensory-motor function was observed by using the Bederson score (Fig. 6C).

3.6. Removal of IL-1R1 signalling ubiquitously or from platelets and myeloid cells does not influence brain injury after cerebral ischaemia

We chose to flox exon 5 in the il-1r1 locus to effectively eliminate all IL-1R1 isoforms in order to generate a new line of IL-1R1^{fl/fl} mice where the receptor is fully eliminated (Fig. 7A). Ubiquitous deletion of IL-1R1 was confirmed with PCR from tail samples and a lack of IL-1R1 immunoreactivity in the brain (Fig. 7B). In spite of the complete absence of functional IL-1R1 in these mice and the marked protective effect of endothelial and neuronal IL-1R1 deletion, ubiquitous IL-1R1 KO mice subjected to cerebral ischaemia showed no difference in infarct size

(Fig. 7C), oedema (Fig. 7D) and neurological outcome (Fig. 7E) compared to control WT (IL-1R1^{fl/fl}) mice. To investigate whether IL-1R1 signalling in blood-borne cells could explain the lack of protection in ubiquitous IL-1R1 KO mice, but significantly reduced brain injury after brain endothelial and neuronal IL-1R1 deletion, we deleted IL-1R1 from platelets and myeloid cells. Constitutive deletion of IL-1R1 in platelets or myeloid cells by crossing IL-1R1^{fl/fl} mice with PF4-Cre mice and LysM-Cre mice, respectively, had no significant impact on brain injury and other parameters measured (Fig. 7F–H). Thus, endothelial and IL-1R1 in cholinergic neurons contributes to brain injury independently of IL-1 actions on platelets and myeloid cells.

4. Discussion

In this study we have identified the cerebrovascular endothelium and cholinergic neurons as major targets for IL-1 action after ischaemic stroke. Specific deletion of the IL-1R1 in brain endothelial cells reduced infarct volume and other outcome measures (i.e. BBB disruption, neurological deficit) induced by transient MCAo to a level comparable to that seen with IL-1Ra treatment in a number of previous studies (Maysami et al., 2016; McCann et al., 2016). We show for the first time that brain endothelial IL-1 actions have a robust and very early impact on cortical perfusion after brain injury, which is associated with facilitation of vascular activation and leukocyte infiltration. In contrast,

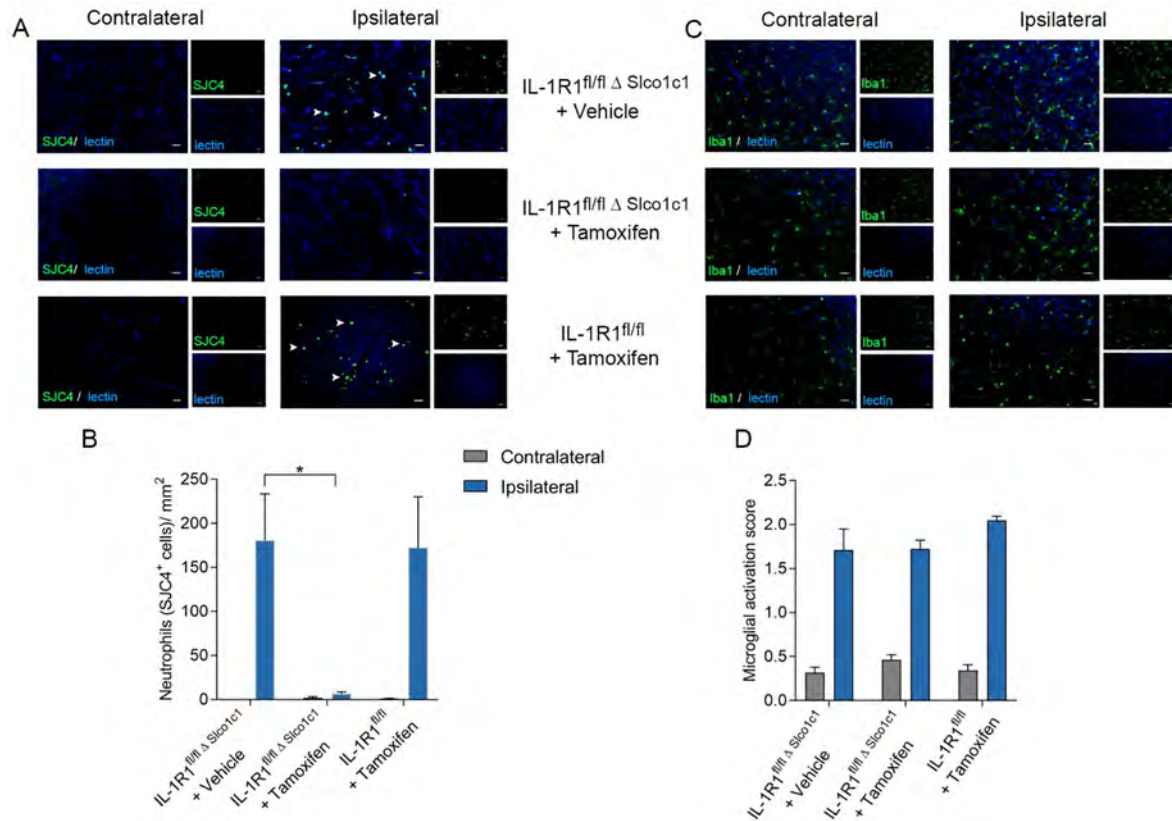


Fig. 3. Brain endothelial IL-1R1 deletion reduces neutrophil cerebrovascular migration but does not influence microglial activation. Immunostaining for neutrophils using SJC4 antibody (co-stained with lectin to identify cerebral blood vessels) reveals increased number of neutrophils in the ipsilateral hemisphere 24 h after MCAO in comparison to the contralateral side (A), and deletion of IL-1R1 on the brain endothelium reduced the number of neutrophils (IL-1R1^{fl/fl} Δ Slco1c1 mice treated with tamoxifen) in comparison to control (IL-1R1^{fl/fl} Δ Slco1c1 mice treated with vehicle) (B). Immunostaining for microglia using Iba1 (co-stained with lectin to identify cerebral blood vessels) revealed no differences in cell number (C), but did show increased cell activation in the damaged region after stroke. However, no differences in activation states were found between experimental groups (D). IL-1R1^{fl/fl} Δ Slco1c1 mice treated with vehicle; n = 10, IL-1R1^{fl/fl} Δ Slco1c1 mice treated with tamoxifen; n = 11, IL-1R1^{fl/fl} treated with tamoxifen; n = 7. * p ≤ 0.05. Data are expressed as means ± SEM.

neuronal IL-1R1 deletion reduced infarct size whilst having no influence on cerebral perfusion changes after stroke. This confirms IL-1 actions on the cerebrovascular endothelium and neurons as key events in mechanisms of IL-1-driven inflammation that depend on different mechanisms and potentially different time windows in response to stroke.

Brain endothelial cells are activated by IL-1 after stroke via binding of IL-1R1, leading to the upregulation of ICAM-1, VCAM-1 and P-Selectin expression, as well as various chemokines, resulting in neutrophil adhesion and infiltration (Thornton et al., 2010). We have demonstrated previously *in vitro* that IL-1 leads to the infiltration of neutrophils that acquire a neurotoxic phenotype (Allen et al., 2012). We now show *in vivo* that mice lacking IL-1R1 on brain endothelial cells exhibit reduced cerebrovascular expression of ICAM-1 and VCAM-1 that is accompanied by a marked reduction in the number of neutrophils infiltrating the brain in response to stroke, supporting our previous *in vitro* findings. Neutrophils are amongst the first cells to infiltrate the brain during cerebral ischaemia, amplifying cerebral inflammatory responses that exacerbate further BBB disruption, cerebral oedema and brain injury, leading to larger infarcts (Jin et al., 2010; Segel et al., 2011). Due to the key roles of neutrophils in ischaemic brain injury, it is not surprising they are of great interest as therapeutic targets (Jickling et al., 2015), and IL-1 acting on the brain endothelium to attract neutrophils and their neurotoxic intracellular content could potentially be a key mechanism. It is currently unclear whether neutrophil-dependent mechanisms contribute to changes in cerebral perfusion and/or BBB breakdown within the first hours after cerebral ischaemia. We have shown previously that IL-1-mediated systemic

inflammatory mechanisms involve neutrophils, platelets and also stimulate endothelin-1 expression (Thornton et al., 2010; Denes et al., 2007; Murray et al., 2014), which could alter cerebral perfusion. Thus, IL-1 actions on the cerebrovascular endothelium could interact with several other IL-1 dependent (and independent) inflammatory processes in the mechanisms of brain injury. The surprising finding that the absence of functional IL-1R1 signalling in brain endothelial cells profoundly determines cerebral perfusion within the first hours – a therapeutically critical time window after stroke – suggests that timely blockade of IL-1 actions could have diverse beneficial effects on blood flow recovery and the associated inflammatory response that collectively determine functional outcome. Importantly, these effects of IL-1 on brain endothelial cells are potentially modifiable without the need for direct CNS actions of a drug, opening up the possibility of targeted anti-IL-1 therapies (e.g. neutralising antibodies) that would not typically show brain penetration.

We also observed microglial cell activation in the peri-infarct area but this activation was not affected by deletion of IL-1R1 in the brain endothelial cells or in the absence of neuronal IL-1 signalling. As well as changes to activation state due to cerebral injury, microglia also proliferate when activated (Weinstein et al., 2010). We saw no difference in the numbers of microglia between any of the treatment groups in the peri-infarct zone, which could be due to the short (24 h) survival times used in this study (Denes et al., 2007).

In contrast, deletion of IL-1R1 in IL-1R1^{fl/fl} Δ Nestin mice altered microglial process coverage of neurons, which indicates changes in microglia-neuron interactions after stroke. We have demonstrated recently that microglia are key contributors to neuronal network activity

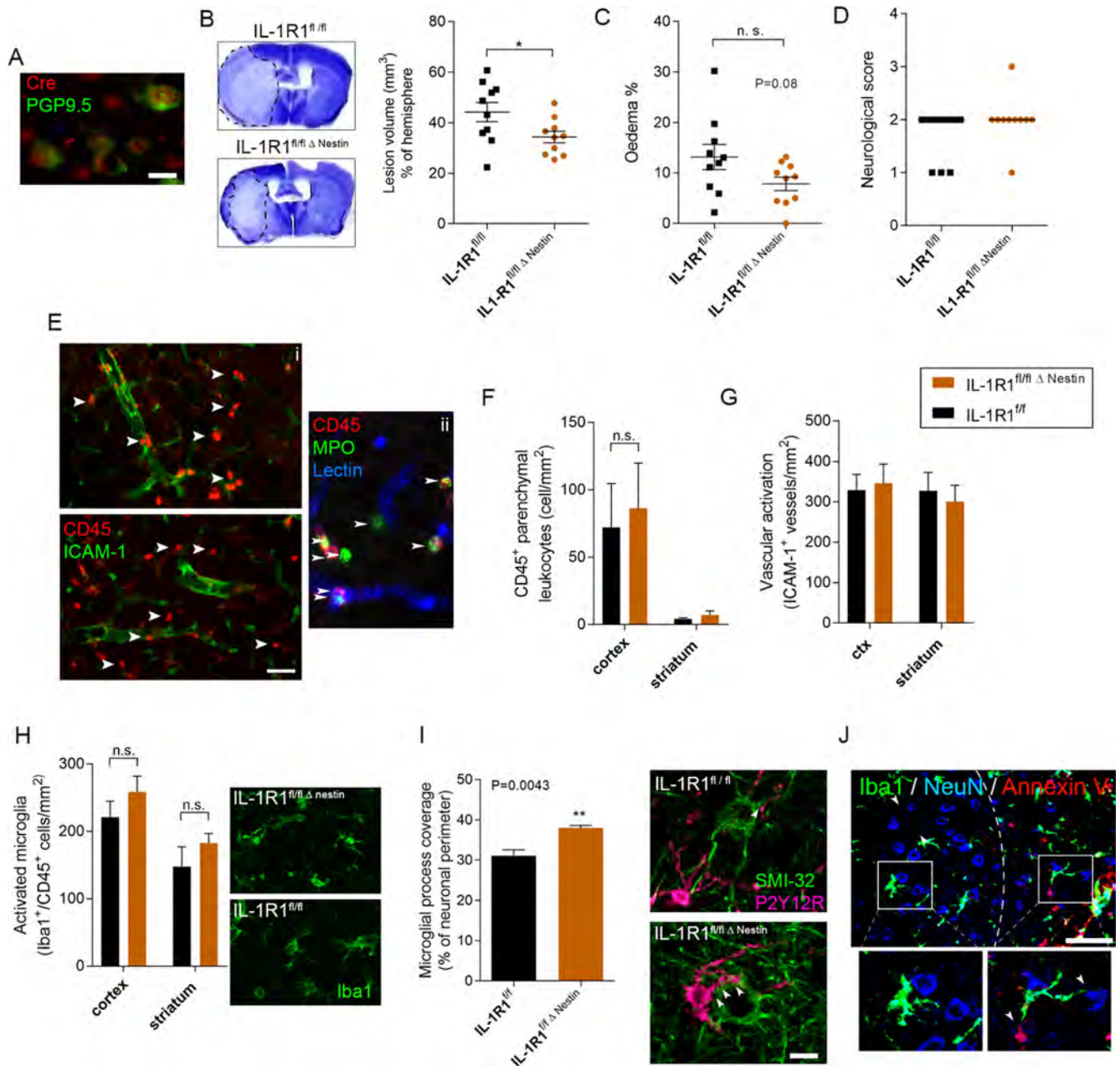


Fig. 4. IL-1R1^{fl/fl} Δ Nestin mice are protected against brain injury and alter microglia-neuron interactions. Immunostaining reveals neuronal expression of cre recombinase in IL-1R1^{fl/fl} Δ Nestin mice 48 h after tamoxifen administration (A). IL-1R1 deletion in neurons (IL-1R1^{fl/fl} Δ Nestin mice treated with tamoxifen) reduced infarct volume (B), but did not significantly alter brain oedema (C) or neurological outcome (D). Dashed line outlines the area of the infarct. Immunofluorescent assessment of ICAM-1 expression in brain microvessels and CD45-positive leukocytes (arrowheads) (E) reveals no changes in the recruitment of blood-borne cells (F) and vascular activation (G) in response to neuronal IL-1R1 deletion. The majority of CD45-positive leukocytes were neutrophils containing myeloperoxidase (MPO, arrowheads) (Eii). No differences were seen in the number of activated (Iba1 + CD45_{low}) microglia in the striatum, or in the cortex (shown in pictures) (H). In contrast, microglial process coverage of neurons (arrowheads) was increased in the absence of neuronal IL-1R1 (I). Microglia (Iba1, green) contact neurons (NeuN, blue) and Annexin V-positive cell debris (red) in the boundary zone of the infarct. Note the markedly reduced number of neurons beyond the Annexin V-positive zone (dashed line) (J). n = 10. *p \leq 0.05, **p \leq 0.01. All parametric data are expressed as means \pm SEM, medians are shown in the case of neurological scores. Scale bars: A, I, 10 μ m; E, J, 50 μ m. (For interpretation of the references to colour in this figure legend, the reader is referred to the web version of this article.)

changes in the injured brain *in vivo* and an absence of microglia leads to markedly augmented neuronal injury after stroke (Szalay et al., 2016). This is likely due in part to an early protective action of microglia against excitotoxicity in the evolving penumbra (Szalay et al., 2016), which is associated with increased microglial process coverage of neurons that increases with higher level of neuronal activity. These results are consistent with observations of microglial actions on excitotoxicity using repetitive supramaximal stimulation and the effect of IL-1 on microglial process convergence toward neuronal axons in brain

slices (Kato et al., 2016; Eyo et al., 2016). Increased microglial process coverage after neuronal, but not endothelial deletion of IL-1R1, could be linked to improved microglial control of neuronal activity, which should be investigated in detail in further studies.

To investigate the neurochemical phenotype of neurons that may mediate detrimental IL-1 effects via IL-1R1 signalling in the area of the brain supplied by the MCA, we chose to selectively eliminate IL-1R1 from cholinergic neurons. Cholinergic cells in the basal forebrain and the brainstem give rise to widespread innervation of the striatum

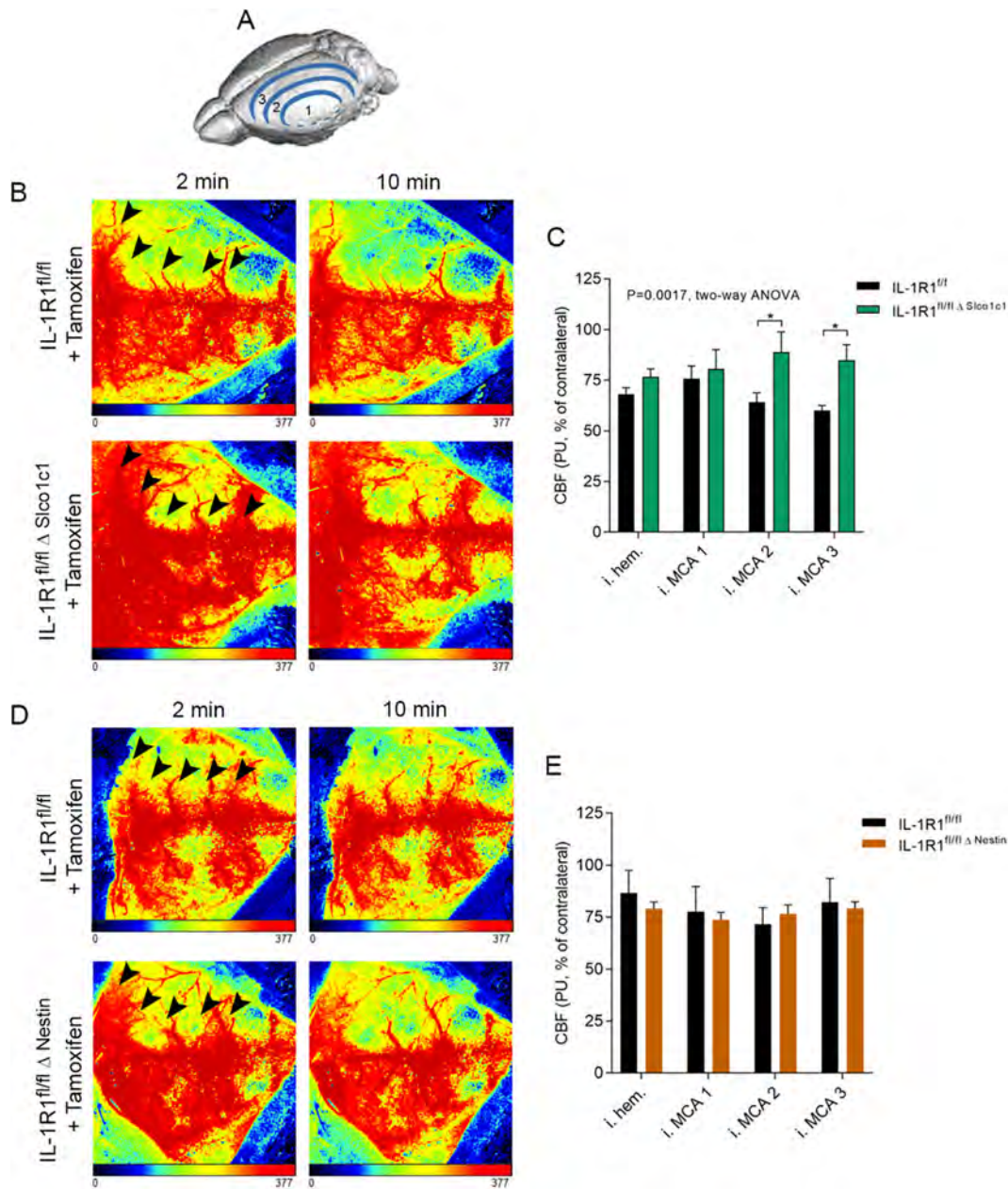


Fig. 5. Endothelial IL-1R1 deletion reduces early perfusion deficits after cerebral ischaemia and reperfusion. Cortical perfusion was assessed by laser speckle contrast imaging (LSCI) in three adjacent zones (MCA1-MCA3) centred around the primary MCA area towards the midline and rostro-caudal cortical areas (A). IL-1R1^{fl/fl} Δ Sico1c1 mice show better blood flow recovery at 30 min after the induction of reperfusion compared to IL-1R1^{fl/fl} mice, which is most apparent in zones MCA2 and 3 (arrowheads) during the 10 min measurement period. Note that cortical blood flow remains relatively uniform between the 2 min and 10 min representative time points. Quantitative analysis reveals significantly higher cerebral perfusion in the ipsilateral hemisphere ($p \leq 0.01$, two-way ANOVA, all ROIs included) with Tukey's post hoc multiple comparisons showing differences in the MCA2 and MCA3 zones ($p \leq 0.05$, $n = 5$). LSCI maps after cerebral ischaemia and reperfusion show no difference between IL and 1R1^{fl/fl} Δ Nestin mice compared to IL-1R1^{fl/fl} mice (D) and quantitative analysis shows no significant changes in cortical blood flow (E). * $p \leq 0.05$, All data are expressed as means \pm SEM.

(Dautan et al., 2014; Zaborszky et al., 2015) and the cerebral cortex. Besides the strong associations of the cholinergic system with attention, memory and cognitive function (Eckenstein et al., 1988; Rye et al., 1984; Yu and Dayan, 2005; Hasselmo and Bower, 1993; Rasmusson and Dykes, 1988; Jones, 1993), dysfunction of cholinergic neurons is linked with a wide array of neurodegenerative disorders (Tata et al., 2014). Atrophy of the basal forebrain cholinergic system is associated with cognitive impairment (Kilimann et al., 2017) and precedes Alzheimer's disease pathology (Schmitz and Nathan Spreng, 2016). The mechanisms through which IL-1R1 signalling in cholinergic cells could mediate brain injury after experimental stroke are presently unclear. However,

interactions between cholinergic pathways and the immune system are well-documented (Maurer and Williams, 2017). For example, $\alpha 7$ nicotinic acetylcholine receptors in astrocytes (Patel et al., 2017) and microglia (Suzuki et al., 2006) mediate anti-inflammatory effects including reduced release of TNF α and protect dopaminergic neurons against degeneration. In addition, systemic inflammatory responses are under the control of the cholinergic anti-inflammatory pathway (Rosas-Ballina and Tracey, 2009) supplied by connections of the vagal nerve. Activation of vagal neurons leads to smaller brain injury after experimental stroke (Jiang et al., 2014; Ay et al., 2009; Sun et al., 2012), whilst disruption to this pathway is linked with exacerbated brain

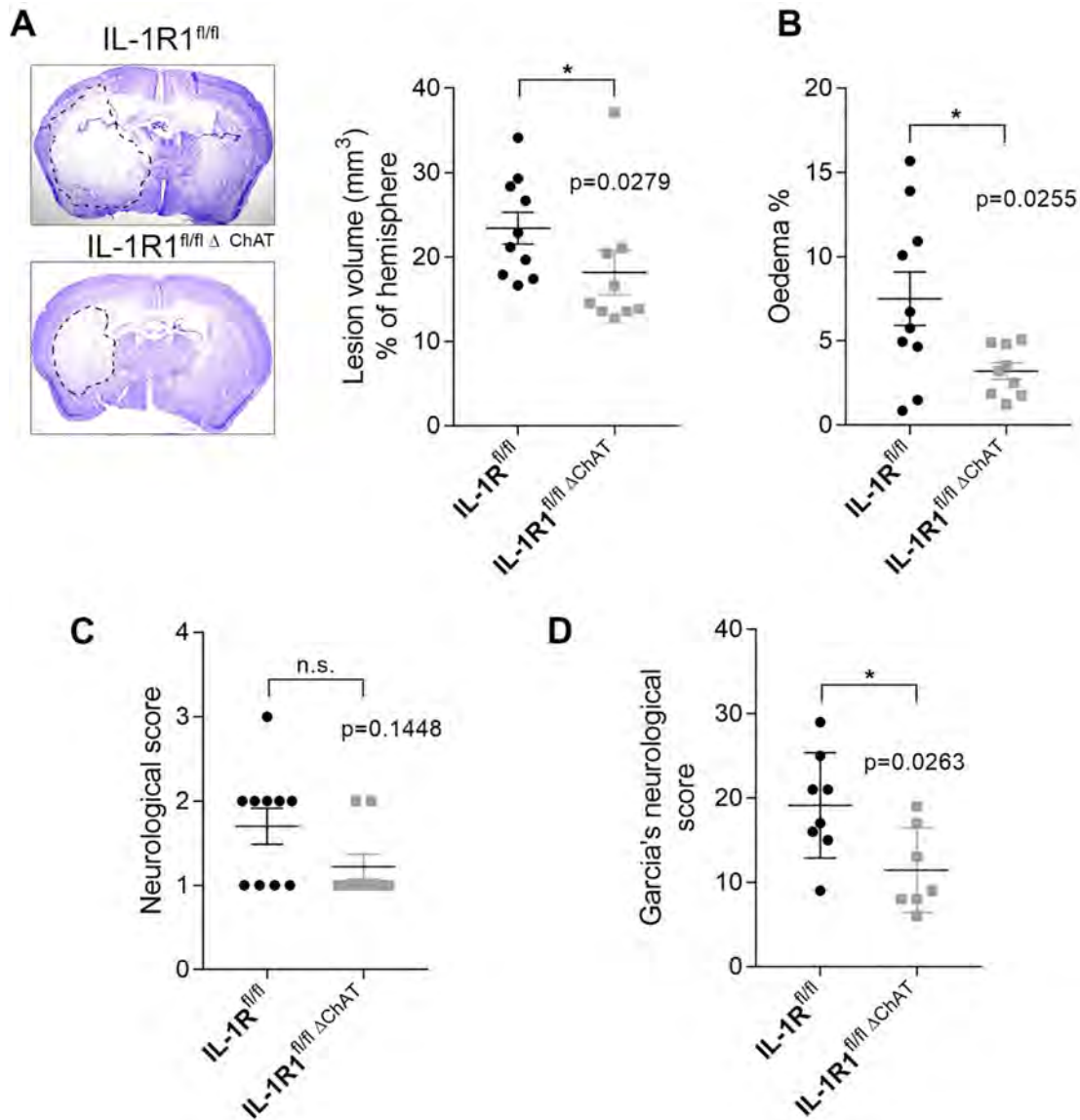


Fig. 6. Deletion of IL-1R1 in cholinergic cells reduces brain injury, brain oedema and improves functional outcome after stroke. Deletion of IL-1R1 from cholinergic neurons (IL-1R1^{fl/fl} Δ ChAT mice) results in reduced infarct size (A) and brain oedema (B). A non-significant trend for improved sensory-motor function is seen in IL-1R1^{fl/fl} Δ ChAT mice (C), whilst functional outcome is significantly improved in these animals based on Garcia's composite neurological score. n = 10 (IL-1R1^{fl/fl}) and n = 9 (IL-1R1^{fl/fl} Δ ChAT) (D). *p ≤ 0.05, All parametric data are expressed as means ± SEM, medians are shown in the case of neurological scores.

injury in both ischaemic (Han et al., 2014a,b) and haemorrhagic (Krafft et al., 2012) stroke. Although IL-1 is known to regulate acetylcholinesterase production and activity of cholinergic neurons (Li et al., 2000), our data implicate for the first time that functional IL-1R1 in cholinergic neurons directly contribute to brain injury and brain oedema in an experimental model of brain injury. The important role of cholinergic innervation in shaping neuronal network activity throughout the brain, the sensitivity of cholinergic neurons to inflammation-mediated injury, or the role of ACh as a modulator of inflammation could explain the profound effect of cholinergic IL-1R1 deletion on stroke outcome. In fact, cholinergic neurons have been shown to be vulnerable to excitotoxicity and inflammation, which may also be indicated by changes in ACh levels or cholinergic receptors described in several neurodegenerative disorders (Weiss et al., 1994; McKinney and Jacksonville, 2005). Thus, IL-1-mediated actions could promote the dysfunction of cholinergic neurons via different forms of injury including increased excitotoxicity and/or lead to impaired regulation of central and peripheral inflammatory processes by shaping the activity of the forebrain cholinergic system (Rosas-Ballina and Tracey,

2009; Allan and Rothwell, 2001), which will need to be investigated in further studies.

It is widely recognised that peripheral inflammatory disorders predispose to, or exacerbate, cardiovascular (Grundy et al., 1999) and cerebrovascular diseases (Catto and Grant, 1995). Experimental exacerbation of ischaemic brain injury by systemic infection and CNS pathology, induced by atherosclerosis, are mediated by peripheral IL-1 (Thornton et al., 2010; Denes et al., 2007, 2012). The cell targets and mechanisms of these effects are unknown, but the brain endothelium is a key candidate, since IL-1 penetrates the brain at very low levels (Banks et al., 1995). Circulating concentrations of IL-1 never reach high levels apart from in severe infection (Dinarello, 1996) but circulating immune cells may deliver IL-1 to the cerebrovasculature (Thornton et al., 2010), where IL-1R1 expression in the brain is highest (Konsman et al., 2004). We show, however, that although both platelets and myeloid cells produce IL-1 and contribute to brain injury after cerebral ischaemia (Iadecola and Anrather, 2011; Nieswandt et al., 2011), IL-1 actions via IL-1R1 in these cells are not required for these effects.

Previous research found that mice lacking IL-1R1 had comparable

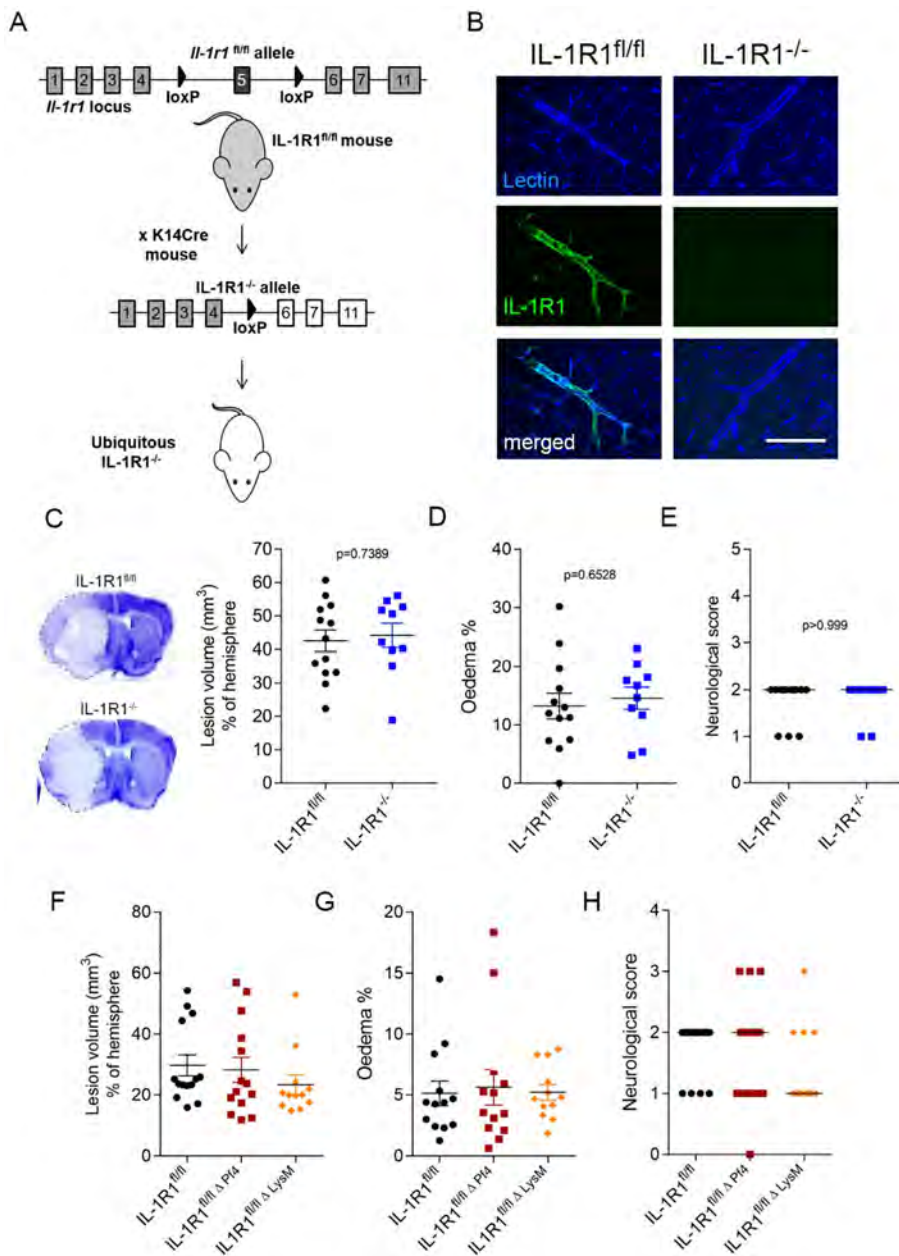


Fig. 7. Ubiquitous and haematopoietic deletion of IL-1R1 do not influence outcome after cerebral ischaemia. IL-1R1^{-/-} mice (ubiquitous IL-1R1 deletion) were generated by crossing IL-1R1^{fl/fl} mice with mice expressing K14 Cre (A). IL-1R1^{-/-} mice show deletion of IL-1R1 protein expression in blood vessels labelled with tomato lectin (B). Infarct size (C), brain oedema (D) and neurological outcome (E) are not different in IL-1R1^{-/-} mice compared to IL-1R1^{fl/fl} mice. Deletion of IL-1R1 from platelets (IL-1R1^{fl/fl} Δ^{PP4}) or from myeloid cells (IL-1R1^{fl/fl} Δ^{LysM} mice) does not influence infarct size (F), brain oedema (G), and neurological scores (H) after experimental stroke. n = 13 (IL-1R1^{fl/fl}), 10 (IL-1R1^{-/-}) in B–D; n = 14 (IL-1R1^{fl/fl}), 13 (IL-1R1^{fl/fl} Δ^{PP4}) and 12 (IL-1R1^{fl/fl} Δ^{LysM}). All parametric data are expressed as means ± SEM, medians are shown in the case of neurological scores.

infarct volumes to wild-type (WT) animals (Touzani et al., 2002). Since in these IL-1R1 KO mice the expression of a truncated form of IL-1R1 could not be excluded (Qian et al., 2012), when generating our IL-1R1^{fl/fl} mice, we chose to flox exon 5 in the *il-1r1* locus to effectively eliminate all IL-1R1 isoforms (Abdulaal et al., 2016). This new ubiquitous deletion of IL-1R1 did not significantly influence brain injury after stroke in the present experimental model, similar to what was found previously in other IL-1R1 KO mouse strains (Diem et al., 2003). It is possible therefore that a complete absence of IL-1R1 signalling could involve presently unknown compensatory effects and/or that beneficial actions via IL-1R1 might exist in the periphery or on other cells in the brain. We have not been able to explore such compensatory or potentially beneficial effects of IL-1 signalling in the present study, which we recognise as a limitation, and something that is the focus of ongoing future work. The protective effects of systemic IL-1Ra in different models of brain injury are widely recognised (Maysami et al., 2016), therefore further understanding of the cell-specific actions of IL-1 will need to be better understood to achieve a maximal potential for the therapeutic blockade of IL-1 actions in brain diseases.

In conclusion, brain endothelial and neuronal (cholinergic) IL-1R1 are key contributors to the detrimental actions of IL-1 in the brain after stroke (Fig. 8). Cell-specific targeting of IL-1R1 in the brain could have major therapeutic benefit in stroke and other cerebrovascular disease by allowing more selective targeting, improving efficacy and reducing any potential side effects.

Funding

This work was supported with funding from the British Heart Foundation (grant ref: PG/13/8/29989 to SA, EP and NJR), the Hungarian Brain Research Program [KTIA_13_NAP-A-1/2 (AD) and 2017-1.2.1-NKP-2017-00002 (GN)], National Research, Development and Innovation Office, NN 125643 (GN), the ‘Momentum’ Program of the Hungarian Academy of Sciences (AD) and ERC-CoG 724994 (AD). The generation of the IL-1R1^{fl/fl} mice was funded by FP7/EU Project MUGEN (MUGEN LSHG-CT-2005-005203) to WM and the Medical Research Council (G0801296) to SA, EP and NJR.

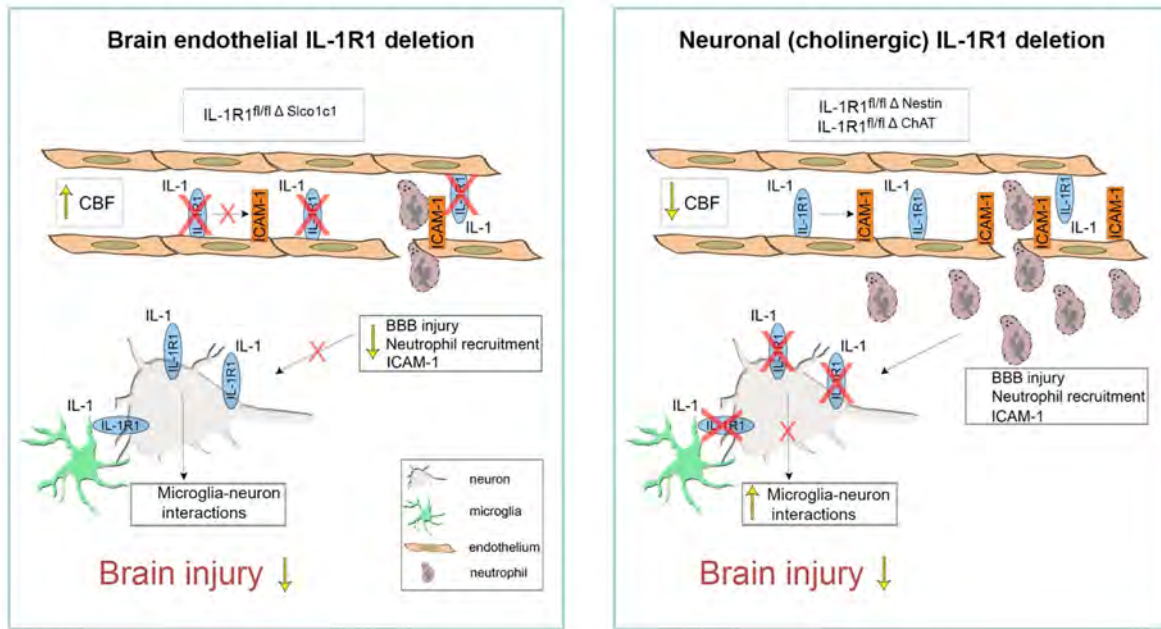


Fig. 8. Summary of the distinct mechanisms of IL-1 actions on ischaemic brain injury targeting either the cerebrovascular endothelium or neurons. Our data show that both the cerebrovascular endothelium and neurons are primary targets of detrimental IL-1 actions mediating brain injury via two distinct mechanisms. Endothelial IL-1R1 deletion results in markedly decreased infarct size, BBB injury and better neurological outcome 24 h after stroke. It is also associated with decreased vascular activation and neutrophil recruitment. Interestingly, an improved cerebral perfusion can be seen in these mice 30 min after reperfusion indicating that IL-1 has early detrimental actions on cerebral blood flow acting through the vascular endothelium. Neuronal IL-1R1 deletion is also protective regarding infarct size, however BBB injury, vascular activation, neutrophil recruitment and early cortical perfusion are unaffected by the absence of IL-1R1 in cholinergic cells or neurons. However, increased microglial process coverage can be detected around neurons in the penumbra suggesting altered microglia-neuron interactions.

Acknowledgements

The authors would like to thank the Bioimaging Facility in the Faculty of Biology, Medicine and Health at the University of Manchester for equipment and advice in imaging and the Nikon Microscopy Center at the Institute of Experimental Medicine, Nikon Austria GmbH, and Auro-Science Consulting, Ltd., for kindly providing microscopy support, and Siddharth Krishnan, Catriona Cunningham and Ivana Rajkovic for their invaluable technical expertise.

Declaration of conflicting interests

There are no relevant disclosures or conflicts of interests by authors.

Author's contributions

RW and NL conducted the experiments (RW: endothelial-specific IL-1R1 KO study; NL: neuronal-specific IL-1R1 deletion, ChAT-specific IL-1R1 deletion and ubiquitous-, myeloid cell- and platelet-specific IL-1R1 KO studies), data analysis and wrote the manuscript. AP helped design and oversaw the breeding programme, including the genotyping of animals. LH, LT, GC, BM and EC contributed to experimental design, and provided vital experimental support and data analysis. AW, WM and MS contributed to animal model development and editing of the manuscript. SF and GN contributed to experimental design and editing of the manuscript. EP, NJR, SA and AD devised the study, obtained funding and wrote the manuscript.

Appendix A. Supplementary data

Supplementary data to this article can be found online at <https://doi.org/10.1016/j.bbi.2018.11.012>.

References

- Abdulaal, W.H., et al., 2016. Characterization of a conditional interleukin-1 receptor 1 mouse mutant using the Cre/LoxP system. *Eur. J. Immunol.* 46, 912–918.
- Allan, S.M., Rothwell, N.J., 2001. Cytokines and acute neurodegeneration. *Nat. Rev. Neurosci.* 2, 734–744.
- Allen, C., et al., 2012. Neutrophil cerebrovascular transmigration triggers rapid neurotoxicity through release of proteases associated with de-condensed DNA. *J. Immunol.* 189, 381–392.
- Andre, R., Moggs, J.G., Kimber, I., Rothwell, N.J., Pinteaux, E., 2006. Gene regulation by IL-1beta independent of IL-1R1 in the mouse brain. *Glia* 53, 477–483.
- Ay, I., Lu, J., Ay, H., Gregory Sorensen, A., 2009. Vagus nerve stimulation reduces infarct size in rat focal cerebral ischemia. *Neurosci. Lett.* 459, 147–151.
- Banks, W.A., Kastin, A.J., Broadwell, R.D., 1995. Passage of cytokines across the blood-brain barrier. *Neuroimmunomodulation* 2, 241–248.
- Boutin, H., et al., 2001. Role of IL-1alpha and IL-1beta in ischemic brain damage. *J. Neurosci.* 21, 5528–5534.
- Bruttger, J., et al., 2015. Genetic cell ablation reveals clusters of local self-renewing microglia in the mammalian central nervous system. *Immunity* 43, 92–106.
- Catto, A.J., Grant, P.J., 1995. Risk factors for cerebrovascular disease and the role of coagulation and fibrinolysis. *Blood Coagul Fibrinolysis* 6, 497–510.
- Ching, S., et al., 2007. Endothelial-specific knockdown of interleukin-1 (IL-1) type 1 receptor differentially alters CNS responses to IL-1 depending on its route of administration. *J. Neurosci.* 27, 10476–10486.
- Ching, S., He, L., Lai, W., Quan, N., 2005. IL-1 type I receptor plays a key role in mediating the recruitment of leukocytes into the central nervous system. *Brain Behav. Immun.* 19, 127–137.
- Clark, W.M., Lessov, N.S., Dixon, M.P., Eckenstein, F., 1997. Monofilament intraluminal middle cerebral artery occlusion in the mouse. *Neurol. Res.* 19, 641–648.
- Couzin-Frankel, J., 2012. Cardiovascular disease. Massive trials to test inflammation hypothesis. *Science (New York, N.Y.)* 337, 1158.
- Dautan, D., et al., 2014. A major external source of cholinergic innervation of the striatum and nucleus accumbens originates in the brainstem. *J. Neurosci.* 34, 4509–4518.
- Denes, A., et al., 2007. Proliferating resident microglia after focal cerebral ischaemia in mice. *J. Cereb. Blood Flow Metab.* 27, 1941–1953.
- Denes, A., et al., 2012. Interleukin-1 mediates neuroinflammatory changes associated with diet-induced atherosclerosis. *J. Am. Heart Assoc.* 1, e002006.
- Denes, A., et al., 2013. Central and haematopoietic interleukin-1 both contribute to ischaemic brain injury in mice. *Disease Models Mech.* 6, 1043–1048.
- Denes, A., Ferenczi, S., Kovacs, K.J., 2011. Systemic inflammatory challenges compromise survival after experimental stroke via augmenting brain inflammation, blood-brain barrier damage and brain oedema independently of infarct size. *J. Neuroinflamm.* 8, 164.
- Denes, A., Pinteaux, E., Rothwell, N.J., Allan, S.M., 2011. Interleukin-1 and stroke: biomarker, harbinger of damage, and therapeutic target. *Cerebrovasc Dis.* 32, 517–527.
- Desson, S.E., Ferguson, A.V., 2003. Interleukin 1beta modulates rat subformal organ

- neurons as a result of activation of a non-selective cationic conductance. *J. Physiol.* 550, 113–122.
- Diem, R., Hobom, M., Grottsch, P., Kramer, B., Bahr, M., 2003. Interleukin-1 beta protects neurons via the interleukin-1 (IL-1) receptor-mediated Akt pathway and by IL-1 receptor-independent decrease of transmembrane currents in vivo. *Mol. Cell. Neurosci.* 22, 487–500.
- Dinareello, C.A., 1996. Biologic basis for interleukin-1 in disease. *Blood* 87, 2095–2147.
- Dinareello, C.A., Simon, A., van der Meer, J.W., 2012. Treating inflammation by blocking interleukin-1 in a broad spectrum of diseases. *Nat. Rev. Drug. Discov.* 11, 633–652.
- Dunn, A.K., 2012. Laser speckle contrast imaging of cerebral blood flow. *Ann. Biomed. Eng.* 40, 367–377.
- Duris, K., Lipkova, J., Jurajda, M., 2017. Cholinergic anti-inflammatory pathway and stroke. *Curr. Drug Deliv.* 14, 449–457.
- Eckenstein, F.P., Baughman, R.W., Quinn, J., 1988. An anatomical study of cholinergic innervation in rat cerebral cortex. *Neuroscience* 25, 457–474.
- Eriksson, S., Nilsson, J., Stureson, C., 2014. Non-invasive imaging of microcirculation: a technology review. *Med. Dev. (Auckland, N.Z.)* 7, 445–452.
- Eyo, U.B., et al., 2016. Regulation of Physical Microglia–Neuron Interactions by Fractalkine Signaling after Status Epilepticus. *eNeuro* 3 0209-0216.2016.
- Grundty, S.M., Pasternak, R., Greenland, P., Smith Jr., S., Fuster, V., 1999. Assessment of cardiovascular risk by use of multiple-risk-factor assessment equations: a statement for healthcare professionals from the American Heart Association and the American College of Cardiology. *Circulation* 100, 1481–1492.
- Han, Z., et al., 2014a. Alpha-7 nicotinic acetylcholine receptor agonist treatment reduces neuroinflammation, oxidative stress, and brain injury in mice with ischemic stroke and bone fracture. *J. Neurochem.* 131, 498–508.
- Han, Z., et al., 2014b. Activation of alpha-7 nicotinic acetylcholine receptor reduces ischemic stroke injury through reduction of pro-inflammatory macrophages and oxidative stress. *PLoS One* 9, e105711.
- Hasselmo, M.E., Bower, J.M., 1993. Acetylcholine and memory. *Trends Neurosci.* 16, 218–222.
- Hoover, D.B., 2017. Cholinergic modulation of the immune system presents new approaches for treating inflammation. *Pharmacol. Therapeutics* 179, 1–16.
- Iadecola, C., Anrather, J., 2011. The immunology of stroke: from mechanisms to translation. *Nat. Med.* 17, 796–808.
- Iadecola, C., Zhang, F.Y., Casey, R., Nagayama, M., Rose, M.E., 1997. Delayed reduction of ischemic brain injury and neurological deficits in mice lacking the inducible nitric oxide synthase gene. *J. Neurosci.* 17, 9157–9164.
- Jiang, Y., et al., 2014. Vagus nerve stimulation attenuates cerebral ischemia and reperfusion injury via endogenous cholinergic pathway in rat. *PLoS One* 9, e102342.
- Jickling, G.C., et al., 2015. Targeting neutrophils in ischemic stroke: translational insights from experimental studies. *J. Cereb. Blood Flow Metab.* 35, 888–901.
- Jin, R., Yang, G., Li, G., 2010. Inflammatory mechanisms in ischemic stroke: role of inflammatory cells. *J. Leukoc Biol.* 87, 779–789.
- Jones, B.E., 1993. The organization of central cholinergic systems and their functional importance in sleep-waking states. *Progress Brain Res.* 98, 61–71.
- Kato, G., et al., 2016. Microglial contact prevents excess depolarization and rescues neurons from excitotoxicity. *eNeuro* 3 e0004-0016.2016 0001-0009.
- Kilimann, I., et al., 2017. Parallel Atrophy of Cortex and Basal Forebrain Cholinergic System in Mild Cognitive Impairment. *Cerebral Cortex (New York, N.Y.)* 1991 27, 1841–1848.
- Kilkenny, C., Browne, W.J., Cuthill, I.C., Emerson, M., Altman, D.G., 2010. Improving bioscience research reporting: the ARRIVE guidelines for reporting animal research. *PLoS Biol.* 160, 1577–1579.
- Konsman, J.P., Vigues, S., Mackerlova, L., Bristow, A., Blomqvist, A., 2004. Rat brain vascular distribution of interleukin-1 type-1 receptor immunoreactivity: relationship to patterns of inducible cyclooxygenase expression by peripheral inflammatory stimuli. *J. Comp. Neurol.* 472, 113–129.
- Krafft, P.R., et al., 2012. alpha7 nicotinic acetylcholine receptor agonism confers neuroprotection through GSK-3beta inhibition in a mouse model of intracerebral hemorrhage. *Stroke* 43, 844–850.
- Lazovic, J., et al., 2005. Neuroinflammation and both cytotoxic and vasogenic edema are reduced in interleukin-1 type 1 receptor-deficient mice conferring neuroprotection. *Stroke* 36, 2226–2231.
- Li, Y., et al., 2000. Neuronal-glia interactions mediated by interleukin-1 enhance neuronal acetylcholinesterase activity and mRNA expression. *J. Neurosci.* 20, 149–155.
- Li, Q., et al., 2011. Endothelial IL-1R1 is a critical mediator of EAE pathogenesis. *Brain Behav. Immun.* 25, 160–167.
- Maurer, S.V., Williams, C.L., 2017. The cholinergic system modulates memory and hippocampal plasticity via its interactions with non-neuronal cells. *Front. Immunol.* 8, 1489.
- Maysami, S., et al., 2016. A cross-laboratory preclinical study on the effectiveness of interleukin-1 receptor antagonist in stroke. *J. Cereb. Blood Flow Metab.* 36, 596–605.
- McCann, S.K., Cramond, F., Macleod, M.R., Sena, E.S., 2016. Systematic review and meta-analysis of the efficacy of interleukin-1 receptor antagonist in animal models of stroke: an update. *Transl. Stroke Res.* 7, 395–406.
- McColl, B.W., Rothwell, N.J., Allan, S.M., 2007. Systemic inflammatory stimulus potentiates the acute phase and CXC chemokine responses to experimental stroke and exacerbates brain damage via interleukin-1- and neutrophil-dependent mechanisms. *J. Neurosci.* 27, 4403–4412.
- McKinney, M., Jacksonville, M.C., 2005. Brain cholinergic vulnerability: relevance to behavior and disease. *Biochem. Pharmacol.* 70, 1115–1124.
- Mufson, E.J., Counts, S.E., Perez, S.E., Ginsberg, S.D., 2008. Cholinergic system during the progression of Alzheimer's disease: therapeutic implications. *Expert Rev. Neurotherapeutics* 8, 1703–1718.
- Murray, K.N., et al., 2014. Systemic inflammation impairs tissue reperfusion through endothelin-dependent mechanisms in cerebral ischemia. *Stroke* 45, 3412–3419.
- Nieswandt, B., Kleinschnitz, C., Stoll, G., 2011. Ischaemic stroke: a thrombo-inflammatory disease? *J. Physiol.* 589, 4115–4123.
- Orsini, F., et al., 2012. Targeting mannose-binding lectin confers long-lasting protection with a surprisingly wide therapeutic window in cerebral ischemia. *Circulation* 126, 1484–1494.
- Patel, H., McIntire, J., Ryan, S., Dunah, A., Loring, R., 2017. Anti-inflammatory effects of astroglial alpha7 nicotinic acetylcholine receptors are mediated by inhibition of the NF-kappaB pathway and activation of the Nrf2 pathway. *J. Neuroinflamm.* 14, 192.
- Percie du Sert, N., et al., 2017. The IMPROVE Guidelines (Ischaemia Models: Procedural Refinements Of in Vivo Experiments). *J. Cereb. Blood Flow Metab.* 271678x17709185.
- Pinteaux, E., Trotter, P., Simi, A., 2009. Cell-specific and concentration-dependent actions of interleukin-1 in acute brain inflammation. *Cytokine* 45, 1–7.
- Qian, J., et al., 2012. Interleukin-1R3 mediates interleukin-1-induced potassium current increase through fast activation of Akt kinase. *Proc. Natl. Acad. Sci. USA* 109, 12189–12194.
- Rasmusson, D.D., Dykes, R.W., 1988. Long-term enhancement of evoked potentials in cat somatosensory cortex produced by co-activation of the basal forebrain and cutaneous receptors. *Exp. Brain Res.* 70, 276–286.
- Ridder, D.A., et al., 2011. TAK1 in brain endothelial cells mediates fever and lethargy. *J. Exp. Med.* 208, 2615–2623.
- Rosas-Ballina, M., Tracey, K.J., 2009. Cholinergic control of inflammation. *J. Int. Med.* 265, 663–679.
- Rye, D.B., Wainer, B.H., Mesulam, M.M., Mufson, E.J., Saper, C.B., 1984. Cortical projections arising from the basal forebrain: a study of cholinergic and noncholinergic components employing combined retrograde tracing and immunohistochemical localization of choline acetyltransferase. *Neuroscience* 13, 627–643.
- Schmitz, T.W., Nathan Spreng, R., 2016. Basal forebrain degeneration precedes and predicts the cortical spread of Alzheimer's pathology. *Nat. Commun.* 7, 13249.
- Segel, G.B., Halterman, M.W., Lichtman, M.A., 2011. The paradox of the neutrophil's role in tissue injury. *J. Leukoc Biol.* 89, 359–372.
- Sims, J.E., et al., 1988. cDNA expression cloning of the IL-1 receptor, a member of the immunoglobulin superfamily. *Science (New York, N.Y.)* 241, 585–589.
- Sobowale, O.A., et al., 2016. Interleukin-1 in stroke. *Stroke* 47, 2160–2167.
- Stroemer, R.P., Rothwell, N.J., 1998. Exacerbation of ischemic brain damage by localized striatal injection of interleukin-1beta in the rat. *J. Cereb. Blood Flow Metab.* 18, 833–839.
- Summers, L., et al., 2013. Activation of brain endothelial cells by interleukin-1 is regulated by the extracellular matrix after acute brain injury. *Mol. Cell. Neurosci.* 57, 93–103.
- Sun, Z., Baker, W., Hiraki, T., Greenberg, J.H., 2012. The effect of right vagus nerve stimulation on focal cerebral ischemia: an experimental study in the rat. *Brain Stimulation* 5, 1–10.
- Suzuki, T., et al., 2006. Microglial alpha7 nicotinic acetylcholine receptors drive a phospholipase C/IP3 pathway and modulate the cell activation toward a neuroprotective role. *J. Neurosci. Res.* 83, 1461–1470.
- Szalay, G., et al., 2016. Microglia protect against brain injury and their selective elimination dysregulates neuronal network activity after stroke. *Nat. Commun.* 7, 11499.
- Tata, A.M., Velluto, L., D'Angelo, C., Reale, M., 2014. Cholinergic system dysfunction and neurodegenerative diseases: cause or effect? *CNS Neurol. Disorders Drug Targets* 13, 1294–1303.
- Thornton, P., et al., 2010. Platelet interleukin-1alpha drives cerebrovascular inflammation. *Blood* 115, 3632–3639.
- Thornton, P., McColl, B.W., Cooper, L., Rothwell, N.J., Allan, S.M., 2010. Interleukin-1 drives cerebrovascular inflammation via MAP kinase-independent pathways. *Curr. Neurovascular Res.* 7, 330–340.
- Touzani, O., et al., 2002. Interleukin-1 influences ischemic brain damage in the mouse independently of the interleukin-1 type I receptor. *J. Neurosci.* 22, 38–43.
- Tsakiri, N., Kimber, I., Rothwell, N.J., Pinteaux, E., 2008. Interleukin-1-induced interleukin-6 synthesis is mediated by the neutral sphingomyelinase/Src kinase pathway in neurons. *Br J. Pharmacol.* 775–783.
- Tsakiri, N., Kimber, I., Rothwell, N.J., Pinteaux, E., 2008. Differential effects of interleukin-1 alpha and beta on interleukin-6 and chemokine synthesis in neurons. *Mol. Cell. Neurosci.* 38, 259–265.
- Wang, X., et al., 1994. Upregulation of intercellular adhesion molecule 1 (ICAM-1) on brain microvascular endothelial cells in rat ischemic cortex. *Brain Res. Mol. Brain Res.* 26, 61–68.
- Weinstein, J.R., Koerner, I.P., Möller, T., 2010. Microglia in ischemic brain injury. *Fut. Neurol* 5, 227–246.
- Weiss, J.H., Yin, H.Z., Choi, D.W., 1994. Basal forebrain cholinergic neurons are selectively vulnerable to AMPA/kainate receptor-mediated neurotoxicity. *Neuroscience* 60, 659–664.
- Winship, I.R., 2014. Laser speckle contrast imaging to measure changes in cerebral blood flow. *Methods Mol. Biol.* 1135, 223–235.
- Wong, R., Gibson, C.L., Kendall, D.A., Bath, P.M., 2014. Evaluating the translational potential of progesterone treatment following transient cerebral ischaemia in male mice. *BMC Neurosci.* 15, 131.
- Yamasaki, Y., et al., 1995. Interleukin-1 as a pathogenetic mediator of ischemic brain damage in rats. *Stroke* 26, 676–680 discussion 681.
- Yu, A.J., Dayan, P., 2005. Uncertainty, neuromodulation, and attention. *Neuron* 46, 681–692.
- Zaborszky, L., et al., 2015. Neurons in the basal forebrain project to the cortex in a complex topographic organization that reflects corticocortical connectivity patterns: an experimental study based on retrograde tracing and 3D reconstruction. *Cerebral Cortex (New York, N.Y.)* 1991 25, 118–137.



MACS® Solutions for dermatology research

Find out more about immune cells in dermatology

► miltenyibiotec.com/dermatology



Neutrophil Cerebrovascular Transmigration Triggers Rapid Neurotoxicity through Release of Proteases Associated with Decondensed DNA

This information is current as of June 25, 2012.

Charlotte Allen, Peter Thornton, Adam Denes, Barry W. McColl, Adam Pierozynski, Marc Monestier, Emmanuel Pinteaux, Nancy J. Rothwell and Stuart M. Allan

J Immunol 2012; 189:381-392; Prepublished online 1 June 2012;

doi: 10.4049/jimmunol.1200409

<http://www.jimmunol.org/content/189/1/381>

Supplementary Material <http://www.jimmunol.org/content/suppl/2012/06/01/jimmunol.1200409.DC1.html>

References This article **cites 50 articles**, 20 of which you can access for free at: <http://www.jimmunol.org/content/189/1/381.full#ref-list-1>

Subscriptions Information about subscribing to *The Journal of Immunology* is online at: <http://jimmunol.org/subscriptions>

Permissions Submit copyright permission requests at: <http://www.aai.org/ji/copyright.html>

Email Alerts Receive free email-alerts when new articles cite this article. Sign up at: <http://jimmunol.org/cgi/alerts/etoc>



Neutrophil Cerebrovascular Transmigration Triggers Rapid Neurotoxicity through Release of Proteases Associated with Decondensed DNA

Charlotte Allen,^{*,1} Peter Thornton,^{*,1,2} Adam Denes,^{*} Barry W. McColl,^{*,3} Adam Pierozynski,^{*} Marc Monestier,[†] Emmanuel Pinteaux,^{*} Nancy J. Rothwell,^{*} and Stuart M. Allan^{*}

Cerebrovascular inflammation contributes to diverse CNS disorders through mechanisms that are incompletely understood. The recruitment of neutrophils to the brain can contribute to neurotoxicity, particularly during acute brain injuries, such as cerebral ischemia, trauma, and seizures. However, the regulatory and effector mechanisms that underlie neutrophil-mediated neurotoxicity are poorly understood. In this study, we show that mouse neutrophils are not inherently toxic to neurons but that transendothelial migration across IL-1-stimulated brain endothelium triggers neutrophils to acquire a neurotoxic phenotype that causes the rapid death of cultured neurons. Neurotoxicity was induced by the addition of transmigrated neutrophils or conditioned medium, taken from transmigrated neutrophils, to neurons and was partially mediated by excitotoxic mechanisms and soluble proteins. Transmigrated neutrophils also released decondensed DNA associated with proteases, which are known as neutrophil extracellular traps. The blockade of histone–DNA complexes attenuated transmigrated neutrophil-induced neuronal death, whereas the inhibition of key neutrophil proteases in the presence of transmigrated neutrophils rescued neuronal viability. We also show that neutrophil recruitment in the brain is IL-1 dependent, and release of proteases and decondensed DNA from recruited neutrophils in the brain occurs in several *in vivo* experimental models of neuroinflammation. These data reveal new regulatory and effector mechanisms of neutrophil-mediated neurotoxicity (i.e., the release of proteases and decondensed DNA triggered by phenotypic transformation during cerebrovascular transmigration). Such mechanisms have important implications for neuroinflammatory disorders, notably in the development of antileukocyte therapies. *The Journal of Immunology*, 2012, 189: 381–392.

Cerebral ischemia and other CNS disorders induce a potent central and systemic inflammatory response. A key hallmark of CNS inflammation is the mobilization and recruitment of inflammatory cells into the brain and breakdown of the blood–brain barrier (BBB), leading to increased neuronal loss (1, 2). Neutrophils appear in the brain within hours of an ischemic event, adhering to activated blood vessels or migrating to the parenchyma, which is increased under systemic inflammatory conditions (3, 4). However, mechanisms of neutrophil activation and recruitment,

as well as their contribution to neuroinflammation and brain injury, are poorly understood.

The recruitment and migration of neutrophils during inflammation and infection are key for the subsequent activation of several inflammatory events (5). Primed neutrophils are able to activate T cells and secrete potent chemoattractants, including leukotrienes (6). Activated neutrophils also produce chemokines, cytokines, proteases, and reactive oxygen species (6), all of which could be detrimental to the surrounding healthy tissue of the host.

In peripheral tissues, migration of neutrophils to sites of inflammation reportedly changes their phenotype. Transmigration across activated endothelium *in vivo* is known to induce an increase in reactive oxygen species production and degranulation of neutrophils (7). Further work investigating *in vivo* transmigration showed the involvement of complex intravascular chemotactic gradients, which guide transmigrated neutrophils to the site of sterile injury (8).

We showed that cerebral ischemia triggers rapid neutrophil activation and release from the bone marrow (9). The infiltration of activated neutrophils to peripheral tissues is relatively well documented (10, 11), but much less is known about whether neutrophils undergo phenotypic and functional changes upon their recruitment to the brain.

We showed that the proinflammatory cytokine IL-1, a key mediator of neuroinflammation, exacerbates ischemic damage via neutrophil-dependent mechanisms, leading to increased BBB breakdown and subsequent neuronal injury (4, 12). Neutrophils exert toxicity to neuronal cell cultures within 24–72 h *in vitro* (13–15), indicating that these cells are likely to deliver neurotoxic products to the brain upon migration in response to cerebrovascular inflammatory changes *in vivo*.

^{*}Faculty of Life Sciences, University of Manchester, Manchester M13 9PT, United Kingdom; and [†]Department of Microbiology and Immunity, School of Medicine, Temple University, Philadelphia, PA 19140

¹C.A. and P.T. contributed equally to this work.

²Current address: Medimmune, Cambridge, United Kingdom.

³Current address: Neurobiology Division, The Roslin Institute, University of Edinburgh, Edinburgh, United Kingdom.

Received for publication February 6, 2012. Accepted for publication April 24, 2012.

This work was supported by the Medical Research Council, U.K.

Address correspondence and reprint requests to Dr. Adam Denes, Faculty of Life Sciences, A.V. Hill Building, University of Manchester, Oxford Road, Manchester M13 9PT, U.K. E-mail address: adam.denes@manchester.ac.uk

The online version of this article contains supplemental material.

Abbreviations used in this article: AMPA, α -amino-3-hydroxy-5-methyl-4-isoxazolepropionate; BBB, blood–brain barrier; CBA, Cytometric Bead Array; CEAM, a mixture of inhibitors against cathepsin-G, neutrophil elastase, proteinase-3 (aprotinin), and MMP-9 (SB3CT); LDH, lactate dehydrogenase; MAP2, microtubule-associated protein 2; MBEC, mouse brain endothelial cell; MCAo, middle cerebral artery occlusion; MMP-9, metalloproteinase-9; NET, neutrophil extracellular trap; NMDA, *N*-methyl-D-aspartate; PGP 9.5, protein gene product 9.5; WT, wild-type.

Copyright © 2012 by The American Association of Immunologists, Inc. 0022-1767/12/\$16.00

It is not known whether cerebrovascular extravasation causes neutrophils to acquire a neurotoxic phenotype and, if so, whether it happens rapidly enough to contribute to acute brain injury. Therefore, the aim of this study was to test the hypothesis that IL-1–induced cerebrovascular transmigration triggers neutrophils to acquire a neurotoxic phenotype. We show in this study that transendothelial migration of neutrophils across cerebral endothelium critically alters neutrophil phenotype to a neurotoxic state and that neurotoxicity of transmigrated neutrophils is mediated via rapid release of a mixture of active proteases associated with decondensed DNA, referred to as neutrophil extracellular traps (NETs). NETs contribute to the defense against extracellular bacteria (16), but actions in the brain have not been described. Collectively, our data identify novel trigger and effector mechanisms of neutrophil-mediated neurotoxicity and highlight how a key neutrophil antimicrobial strategy can also be damaging to host tissue.

Materials and Methods

Animals

Wild-type (WT) and IL-1 α / β deficient (IL-1 α / β ^{-/-}) mice, all on a C57BL/6 background, were bred in-house and maintained on a 12-h light/dark cycle. Sprague Dawley rats were purchased from Charles River (Margate, U.K.). Animal studies were performed under United Kingdom Home Office personal and project licenses, and protocols adhered to the Animals (Scientific Procedures) Act (1986).

Focal cerebral ischemia and other models of neuroinflammation

Focal cerebral ischemia was induced by transient (60 min) middle cerebral artery occlusion (MCAo), as described previously (4, 17). After MCAo, mice were subjected to 8 or 24 h of reperfusion. Some animals were injected i.p. with 00 IU vehicle or rat rIL-1 β (National Institute for Biological Standards and Controls, Potters Bar, U.K.) 30 min before undergoing MCAo, as described previously (12). LPS (4 μ g; Sigma, Gillingham, U.K.) was injected into the striatum of mice to induce parenchymal inflammation. Intrastriatal coadministration of α -amino-3-hydroxy-5-methyl-4-isoxazolepropionate (AMPA; 15 nM/ μ l; Tocris, Bristol, U.K.) and human IL-1 β (5 ng/ μ l; National Institute for Biological Standards and Controls) (2-min infusion at 0.5 μ l/min) was carried out, as described previously, to induce striatal and cortical damage in rats (18–20).

Primary mouse brain endothelial cell culture

Primary cultures of mouse brain endothelial cells (MBECs) were prepared from the brains of 8–12-wk-old C57BL/6 mice, as described previously (21), with the following modifications. Isolated brain vessels were resuspended in maintenance medium consisting of DMEM F-12 (Invitrogen, Paisley, U.K.), 10% plasma-derived serum (FirstLink, U.K.), 10% FCS, 100 μ g/ml endothelial cell growth supplement (BD Biosciences, Oxford, U.K.), 100 μ g/ml heparin, 2 mM glutamine, 1 U/ml penicillin, and 100 μ g/ml streptomycin. For neutrophil-migration assays, microvessels were plated onto murine collagen IV (50 μ g/ml; BD Biosciences)-coated 24-well cluster Transwell inserts (6.5 mm diameter, 3.0 μ m pore; Corning, Tewksbury, MA). Puromycin (3 μ g/ml) was added to the media for 3 d in vitro. Cultures were grown at 37°C in a 5% CO₂ humidified atmosphere and were used after 14 d in vitro, once cells were confluent. Cultures were 95.8 \pm 1.6% positive for PECAM-1 and expressed endothelial markers Von Willebrand factor and zona occludens-1 (data not shown).

bEnd.5 MBEC line cultures

The bEnd.5 MBEC line, which closely resembles primary brain endothelium in culture (4), was purchased from the Health Protection Agency Culture Collections (Salisbury, U.K.). Cells were grown in DMEM (high glucose, 4.5 g/l; Invitrogen), supplemented with 10% FCS, 1% nonessential amino acid, 2 mM glutamine, 1 U/ml penicillin, and 100 μ g/ml streptomycin.

Primary cortical neuronal cell cultures

Primary cortical neuronal cell cultures were prepared from embryonic (day-15) mice, as described previously (7). Cells were seeded at 180,000 cells/cm² and grown in Neurobasal Medium (Invitrogen), 2% B27 minus antioxidants (Invitrogen), 5% plasma-derived serum, 2 mM glutamine, 1 U/ml peni-

collin, and 100 μ g/ml streptomycin. Neurons were used between 10 and 13 d in vitro. Cultures were, on average, 98% pure neurons (data not shown).

Collection of naive neutrophils

Freshly isolated neutrophils (termed naive neutrophils) were collected from 8–12-wk-old mice euthanized by CO₂ inhalation. Femurs and tibias were removed, and bone marrow was flushed using a 25G needle with 1–2 ml neutrophil buffer (PBS without calcium or magnesium with 0.1% low endotoxin BSA [w/v] and 1 mM EDTA; Sigma). RBCs were lysed with 0.2% (w/v) NaCl, and osmolality was restored by the addition of 1.2% (w/v) NaCl. Ly6G⁺ neutrophils were separated immunomagnetically by passing the previously labeled cell suspension through an LS column and magnet (Miltenyi Biotec, Bisley, U.K.). The column was removed from the magnet, and the eluted cells were washed and resuspended in serum-free neurobasal medium at 4 \times 10⁶ cells/ml. The average purity of neutrophil preparations was 96%, as identified by flow cytometry (see below).

Neutrophil transendothelial migration assay

MBECs or bEnd.5 cells grown to confluence on Transwell inserts were pretreated for 4 h with rat IL-1 β (100 ng/ml; R&D Systems, Abingdon, U.K.) in the absence or presence of human IL-1 receptor antagonist (100 μ g/ml; R&D Systems). Following treatment, cells were washed twice with fresh medium and transferred to fresh tissue culture plates. Purified neutrophil suspensions of 2 \times 10⁵ were added to the luminal (top) compartment of each 24-well Transwell. After an incubation period of 24 h, the abluminal-transmigrated fraction of neutrophils (termed transmigrated neutrophils) was collected and centrifuged at 400 \times g for 10 min, and cells were counted using a hemocytometer. Neutrophil transmigration was expressed as the fold increase compared with vehicle-treated (control) cultures.

Collection of transmigrated neutrophils

To obtain transmigrated neutrophils in sufficient quantities to analyze their phenotypes, we collected neutrophils that had migrated across IL-1 β –stimulated brain endothelium grown on larger six-well–format Transwell inserts (4.7 cm² area/Transwell). For this purpose, and because of low yields of MBEC primary cultures, we used the bEnd.5 cell line to support neutrophil transmigration. For this transendothelial migration using larger Transwell inserts, a concentration of 10 ng/ml IL-1 β for 4 h was used. This concentration induced a similar increase in neutrophil transmigration across bEnd.5 cells as observed with 100 ng/ml (Supplemental Fig. 1a), and it reduced the possibility of IL-1 carried over after activation. This allowed us to determine the effects of activated versus nonactivated endothelial-derived factors on nonmigrated neutrophil phenotypes. A purified neutrophil suspension containing 3.5 \times 10⁶ cells was added to the luminal (top) compartment of each six-well Transwell. After the specified incubation period, the abluminal-transmigrated fraction of neutrophils (termed transmigrated neutrophils) was collected and centrifuged at 400 \times g for 10 min. For the direct addition of neutrophils to neuronal cultures, transmigrated neutrophils were collected from the abluminal compartments 4 h after application of naive neutrophils to the luminal compartment. All nonmigrated neutrophil controls were exposed to bEnd.5 cells, which had also been treated previously with vehicle or IL-1 β (10 ng/ml) for 4 h, in the abluminal compartment of the Transwell insert. Previous studies showed that >1 h is sufficient to allow neutrophils to respond to endothelial-derived factors (13). In addition, naive neutrophils were incubated for 4 h in the presence of conditioned medium obtained from activated endothelium, washed, and incubated for 4 h. For the addition of neutrophil-conditioned medium to neuronal cultures, transmigrated neutrophils were collected 20 h after the addition of naive neutrophils to the luminal compartment. This time point allowed collection of sufficient neutrophils for subsequent analysis.

To induce neutrophil transendothelial migration outside the brain in vivo, a model of thioglycollate-induced peritonitis was used. Thioglycollate medium (3%), aged for 1 mo, was injected into the peritoneal cavity, and neutrophils were recovered by peritoneal lavage 4 h after injection. Contaminating RBCs were lysed, and neutrophils were washed and resuspended in neurobasal medium for addition to neurons.

Collection of neutrophil lysates and neutrophil-conditioned medium

To determine the effects of neutrophil-secreted factor(s) on neurons, neutrophil-conditioned medium was collected by resuspending neutrophils in serum-free neurobasal medium, at 1.2 \times 10⁶ cells/ml, and seeding into tissue culture plates for 3 h. Cells were collected and centrifuged at 400 \times g for 10 min, and pellets were lysed in lysis buffer containing protease

inhibitors. Supernatants were further centrifuged at $10,000 \times g$ for 10 min. Lysates and cleared supernatants were aliquoted and stored at -80°C .

Treatment of neurons with neutrophils or neutrophil-conditioned medium

Direct application of neutrophils onto primary neuronal cultures was performed by adding $10 \mu\text{l}$ age-matched naive neutrophils, nonmigrated neutrophils (using nonactivated endothelium, activated endothelium, or neutrophils that were also incubated for 4 h in the presence of conditioned medium obtained from activated endothelium, washed, and incubated for 4 h), or transmigrated neutrophils (suspended at 4×10^6 cells/ml) to neurons grown in 96-well plates, corresponding to $120,000$ neutrophils/ cm^2 of neurons. Neutrophil-conditioned medium was added to neuronal cultures at a 1:4 dilution (one quarter of neuronal media was removed and replaced with neutrophil-conditioned medium). Neurons were treated with $10 \mu\text{M}$ MK-801 (Tocris), $10 \mu\text{M}$ cathepsin-G inhibitor (Calbiochem, Watford, U.K.), $10 \mu\text{M}$ elastase IV inhibitor (Calbiochem), $20 \mu\text{M}$ aprotinin (Sigma), or $12.5 \mu\text{M}$ metalloproteinase-9 (MMP-9) inhibitor (SB3CT; Enzo, Exeter, U.K.) added 20 min prior to treatment with neutrophil-conditioned medium. Neutrophil-conditioned medium was also pretreated with washed trypsin-agarose beads (1 U, 30 min at 37°C ; Sigma) or was heat inactivated for 30 min at 95°C , prior to application to neurons. PL2-3 monoclonal anti-mouse Ab (anti-H2A-H2B-DNA) or an IgG2a isotype control (22, 23) was incubated ($15 \mu\text{g}/\text{ml}$) with prechilled neutrophil-conditioned medium for 10 min before addition to neurons. Neutrophil-conditioned medium was also pretreated or not with DNase I (Invitrogen), at a concentration of $30 \text{ U}/\text{ml}$ for 30 min at 37°C , before being added to neuronal cultures (as described above) for additional incubation lasting 24 h.

Live cell imaging

Neurons were loaded with $1 \mu\text{M}$ CellTracker Red (Invitrogen) for 30 min and washed into imaging buffer: 121 mM NaCl, 5.4 mM KCl, 0.8 mM MgCl_2 , 1.8 mM CaCl_2 , 6 mM NaHCO_3 , 5.5 mM glucose, 25 mM HEPES (pH 7.3). Neurons were imaged every 30 s in the absence or presence of transmigrated neutrophils (neutrophils added to neuronal cultures at $120,000$ cells/ cm^2) on a transmitted light channel and on an Alexa Fluor 594 red fluorescent channel using a BD Pathway Bioimager (BD Biosciences). Live cell microscopy was performed locally (<http://www.lsm.manchester.ac.uk/research/facilities/bioimaging/>). All offline analysis of images and movies was processed using ImageJ software (<http://rsb.info.nih.gov/ij/>). Movies (6 h of footage) are shown at 15 frames/s.

Immunohistochemistry

Tissue processing for immunohistochemistry was performed, as described previously (4, 17). Abs used were goat anti-ICAM-1 (1:500; R&D Systems), goat anti-VCAM-1 (1:500; R&D Systems), mouse anti-fibronectin (1:100; Sigma), rabbit anti-glial fibrillary acidic protein (1:500; Abcam, Cambridge, U.K.), rabbit anti-neutrophil elastase (1:500; Abcam), chicken anti-protein gene product 9.5 (PGP 9.5; 1:500; Abcam), mouse anti-microtubule-associated protein 2 (MAP2; 1:500; Sigma), mouse anti-H2A-H2B-DNA complex (PL2-3; 1:1000; Temple University), rat anti-CD45 (1:500; Serotec), and rabbit anti-granulocyte serum, SJC (1:5000; kindly provided by Drs. Daniel Anthony and Sandra Campbell, University of Oxford, Oxford, U.K.). Biotinylated tomato lectin was purchased from Sigma. Endogenous peroxidase activity was blocked with 0.3% H_2O_2 in methanol, and nonspecific binding sites were blocked with 10% normal serum (Vector Laboratories, Peterborough, U.K.). Sections were incubated in primary Ab (diluted in 5% normal serum in PBS) overnight at 4°C . For peroxidase-based staining, sections were incubated with anti-rabbit biotinylated secondary IgG (1:200 in PBS) before incubation in VECTAS-TAIN ABC solution and development of staining by diaminobenzidine reaction (all from Vector Laboratories). Sections were lightly counterstained with cresyl violet. The number of SJC⁺ cortical neutrophils was determined in the hemisphere ipsilateral to MCAo at four coronal levels (1.1 , 0.2 , -0.5 , -1.1 mm relative to bregma), and the mean was calculated. For double-labeling immunofluorescence, following primary Ab incubation, sections were incubated with Alexa Fluor-conjugated secondary Abs (1:1000 in PBS; Invitrogen) and mounted with ProLong Gold, with or without DAPI counterstain (Invitrogen). Bright-field images were collected on a Zeiss Axioskop upright microscope and captured using Zeiss AxioVision software. Wide-field fluorescence images were collected on an Olympus BX51 upright microscope and captured using MetaVue software (Molecular Devices, CA). The images were collected using a CoolSNAP HQ camera (Photometrics, AZ), and the raw images were deconvolved using softWoRx software.

Immunocytochemistry

Neurons cultured on poly-D-lysine-coated 12-mm glass coverslips were fixed in 4% paraformaldehyde/ 4% sucrose (w/v), permeabilized with 0.1% (v/v) Triton X-100 in PBS, quenched with 0.25% (w/v) NH_4Cl_2 , and blocked with 5% (w/v) BSA in PBS. Cultures were immunostained with a combination of the following Abs: neurofilament (1:500; Millipore, Watford, U.K.), neuronal nucleus (1:200; Chemicon, Watford, U.K.), neutrophil elastase (1:500; Abcam), PL2-3 (1:500; anti-H2A-H2B-DNA complex), and SJC (1:5000). Immunodetection was performed with Alexa Fluor-conjugated secondary Abs (1:1000; Invitrogen), and cells were mounted with ProLong Gold, with or without DAPI counterstain. Wide-field fluorescence images were collected on an Olympus BX51 upright microscope and captured using MetaVue software (Molecular Devices, Uckfield, U.K.). Z-stacked images were acquired on a Delta Vision (Applied Precision, WA) restoration microscope objective.

Scanning electron microscopy

Transmigrated neutrophils were added to neuronal cultures, as described above, and fixed with 2.5% (w/v) glutaraldehyde (Sigma). The fixed cells then underwent three 5-min washes with 0.1 M PBS (Sigma). After the final wash, 1% (v/v) osmium tetra-oxide (Sigma) in 0.1 M PBS was added to the cells for a minimum of 1 h at 4°C . The cells were rinsed with 0.1 M PBS and dehydrated with a 15-min incubation in increasing alcohol solutions (70 and 95%) and then three additional incubations in 100% alcohol for 10 min. The tissue was dried to the critical drying point and then mounted for 3 min of sputter coating. The samples were viewed using the Gatan 3View System (Gatan, Abingdon, U.K.).

Flow cytometry

Cells were fixed in FACS/FIX buffer (1% [w/v] PFA and 0.1% [w/v] low-endotoxin BSA [Sigma]) for 15 min at room temperature. Cells were washed with FACS buffer (0.1% BSA [w/v] PBS) and pelleted at $400 \times g$ for 5 min. Neutrophils were incubated with anti-CD16/CD32 for 30 min at 4°C (1:200 in FACS buffer; BD Biosciences) and then washed and pelleted, as described before. Staining was carried out with anti-Ly6G-allophycocyanin (1:200; eBiosciences, Hatfield, U.K.), anti-CD11b-Alexa Fluor 488-conjugated Ab (1:100; Serotec, Oxford, U.K.), or isotype control for 30 min at 4°C before final wash and centrifugation. Neutrophils were identified by flow cytometry. Ninety-six percent of the purified, naive neutrophil population was CD11b/Ly6G⁺.

For the staining of intracellular phosphorylated proteins, neutrophils were labeled with Ly6G, as before, but then permeabilized with PerIII (BD Biosciences) for 30 min. Cells were washed and collected by centrifugation at $400 \times g$ for 5 min and incubated with anti-p-NF- κB -PE, anti-p-p38-PE, or anti-p-Akt-PE (1:25 in FACS buffer; eBiosciences) for 30 min at 4°C in the dark. After a final wash and centrifugation, the cells were resuspended in FACS/FIX buffer and analyzed by a Cyan ADP (Beckman Coulter, High Wycombe, U.K.) flow cytometer.

Tissue homogenization

WT or IL-1 α / $\beta^{-/-}$ mice were anesthetized 8 h after MCAo and perfused with 0.9% saline, and brain samples were rapidly removed and frozen on dry ice. Frozen cortical samples were homogenized on ice in buffer (50 mM Tris-HCl [pH 7.6], 150 mM NaCl, 5 mM CaCl_2 , 0.02% NaN_3 , 1% Triton X-100) and centrifuged ($15,000 \times g$; Hettich Mikro 200R; Hettich, Salford, U.K.); protein concentration was determined in supernatants by bicinchoninic acid protein assay (detection range: 800 – $1.55 \mu\text{g}/\text{ml}$; Pierce, Cramlington, U.K.).

ELISA

ICAM-1 and VCAM-1 concentrations in cortical homogenates were quantified by ELISA, according to the manufacturer's instructions (R&D Systems). Samples were read at $450/570 \text{ nm}$ on a plate reader (Biotek, Bedford, U.K.), with a detection range of $8 \text{ ng}/\text{ml}$ – $13.25 \text{ pg}/\text{ml}$ and intra-assay variation $< 3\%$. Data obtained were analyzed using GraphPad Prism 5.0 software (GraphPad, CA).

Because of the high sensitivity and specificity of PL2-3 Ab (22), a specific histone-DNA complexes ELISA was developed in-house. PL2-3 Ab was used to detect the H2A-H2B-DNA complex immobilized from neutrophil-conditioned medium samples on Nunc (Sigma) microplates. Following incubation with biotinylated horse anti-mouse Ab (Vector Laboratories) and streptavidin-HRP (R&D Systems), the reaction was developed with tetramethylbenzidine substrate solution (BD Biosciences). Samples were read at $450/570 \text{ nm}$ on a Biotek plate reader (Biotek, Potton, U.K.).

Cytometric bead array

Lysates of naive neutrophils, nonmigrated neutrophils, and transmigrated neutrophils were assayed by Cytometric Bead Array (CBA) analysis (BD Biosciences) for the following 14 inflammatory mediators: MIP-1, TNF- α , RANTES (CCL5), MCP, CXCL1, IL-6, IL-1 α , IL-1 β , IL-17, IL-10, IFN- γ , G-CSF, L-selectin, and E-selectin.

Identification of nuclear and mitochondrial DNA by PCR

Neutrophil-conditioned medium prepared from naive or transmigrated neutrophils was assayed for the presence of mitochondrial or nuclear DNA as follows: DNA was precipitated from a fixed volume of conditioned medium using sodium acetate/ethanol protocol before resuspension in 10 μ l RNase-free distilled water. To confirm the presence of mitochondrial or nuclear DNA, sections of DNA within unique mitochondrial or nuclear genes were targeted by PCR using specific primers (sequence available on request) as follows. Because a fixed volume of neutrophil-conditioned medium was used for precipitation, a fixed volume of 1 μ l was used for each PCR reaction. Each PCR reaction contained 1 mM MgCl₂, 1 \times reaction buffer, 1.2 mM 2'-deoxynucleoside 5'-triphosphate, 1 pmol forward and reverse primer, and 2.5 U Taq polymerase (all reagents were from Biotool, London, U.K.) for 5 min at 94°C; 30 cycles of 30 s at 94°C, 30 s at 56°C, and 30 s at 72°C; 5 min at 72°C and then a final step of 4°C for 15 min. Products were detected on a 1.5% (w/v) agarose gel containing 5 μ g/ml ethidium bromide (Sigma) at 100 V for 45 min and visualized using ImageQuant LAS 400 (GE Healthcare, Chalfont St. Giles, U.K.).

Gel zymography

To determine the presence of active mature MMP-9, neutrophil-conditioned medium was collected from naive or transmigrated neutrophils and subjected to gelatin zymography, as described previously (21).

Western blot analysis

Total protein content of bEnd.5 lysates was determined using bicinchoninic acid assay. A fixed protein concentration of each sample was diluted in 5 \times dissociation buffer (200 mM Tris/HCl [pH 6.8], 10% SDS, 20% [v/v] glycerol, 10 mM DTT, 0.05% bromophenol blue). Samples were heated at 95°C for 5 min prior to being resolved by 12% SDS-PAGE. Proteins were then transferred onto a Hybond (polyvinylidene difluoride; GE Healthcare) membrane. ICAM-1 and VCAM-1 were then detected using specific Abs (as mentioned above) diluted in PBS 0.1% Tween (v/v) and 2% BSA. All bound Abs were detected using specific HRP-conjugated secondary Abs, which were detected using the ECL system (GE Healthcare). Actin was detected using an HRP-conjugated primary Ab to determine protein loading (Sigma). Images were captured using ImageQuant LAS 400 (GE Healthcare) and saved as 8-bit TIFF files for densitometric analysis using Northern Eclipse Software 6.0 (Empix Imaging, ON, Canada).

Cell death assays

Lactate dehydrogenase assay. Cell death was assayed by measuring the release of lactate dehydrogenase (LDH) into cell culture supernatants using a CytoTox96 assay (Promega, Southampton, U.K.).

MTT assay. Viability of neuronal cultures was measured through the addition of MTT (5 μ g/ml; Sigma), directly to neuronal cultures in the absence or presence of neutrophils. The production of formazan was observed after 2 h of incubation. Bright-field micrographs of neurons (pre- and postaddition of MTT) were collected on an Olympus CKX31 cell culture microscope using Motic imaging software.

Trypan blue assay. Nonmigrated or transmigrated neutrophils were collected 20 h after isolation or application to bEnd.5 cells and were incubated with a 1:2 dilution of the vital dye trypan blue (Sigma); the percentage of trypan blue⁺ cells was determined.

Statistical analysis

Data are expressed as mean (\pm SEM) from a minimum of three independent experiments carried out on separate cultures. Depending on the number of groups within the data set, data were analyzed using either the Student *t* test (two groups) or one-way ANOVA with the Bonferroni post hoc test (three or more groups) using GraphPad Prism 5.0 (GraphPad). The *p* values < 0.05 were considered statistically significant.

Results

IL-1 mediates cerebrovascular activation and recruitment of neutrophils in vivo and induces cerebrovascular transmigration of neutrophils in vitro

We first used MCAo as a model to induce neuroinflammation and found that neutrophil migration in the brain was significantly reduced in IL-1 α / β ^{-/-} mice compared with WT mice (Supplemental Fig. 1a–c). These observations were supported by the altered IL-1–dependent ICAM-1 and VCAM-1 levels in vivo (Supplemental Fig. 1e–g) and IL-1–treated bEnd.5 cells in vitro (Supplemental Fig. 1h). IL-1 β induced the migration of neutrophils (CD11b/Ly6G⁺; Supplemental Fig. 2a) across primary cultures of MBECs and bEnd.5 cells (Fig. 1a) into the abluminal compartments of Transwell inserts. Treatment with vehicle had little effect on migration (<3%) across MBECs or bEnd.5 cells. Activation of MBECs by IL-1 β caused a 4.5-fold increase in neutrophil migration compared with the vehicle-treated control (Fig. 1a), which was blocked by IL-1 receptor antagonist (Supplemental Fig. 2b). A comparable increase was seen in bEnd.5 cultures treated with the same concentration of IL-1 β (Fig. 1a).

Cerebrovascular transmigration induces a neurotoxic phenotype in neutrophils, leading to rapid neuronal death

Transmigrated neutrophils applied to neurons for 3 h induced significant loss of neuronal viability (Fig. 1b), which was comparable to the neurotoxicity induced by treatment with *N*-methyl-D-aspartate (NMDA; 600 μ M) for 24 h (Fig. 1b). Real-time CellTracker monitoring of healthy neurons showed that transmigrated neutrophils induced rapid neuronal death (Fig. 1ci, 1cii). Neuronal cell bodies loaded with CellTracker Red and their processes were visualized every 30 s for 6 h, in the absence or the presence of transmigrated neutrophils (Supplemental Videos 2 and 1, respectively). Neurons exposed to transmigrated neutrophils swelled rapidly (within 180 min), rounded up, and lost CellTracker Red staining intensity (Fig. 1cii, Supplemental Video 1). Loss of CellTracker Red labeling was not apparent over a similar time period in untreated neurons (Fig. 1ci, Supplemental Video 2). Neuronal processes became bead-like and fragmented within 30 min of application of transmigrated neutrophils (Fig. 1cii, Supplemental Video 1). Addition of transmigrated neutrophils to neuronal cultures for 24 h induced a marked loss of neuronal cell bodies and processes, as identified by PGP 9.5 staining (Fig. 1dii).

Neurotoxicity induced by the application of transmigrated neutrophils was confirmed by LDH release: a 3-fold increase in neuronal death was observed after 24 h (Fig. 1e). Application of naive neutrophils or nonmigrated neutrophils, which had been incubated with nonactivated or IL-1 β –activated brain endothelial cells or incubated with conditioned medium from activated endothelium after washing, did not significantly affect neuronal viability after 24 h of incubation (Fig. 1e). Cell death was not due to IL-1 β being carried over, because naive neutrophils incubated with neurons in the presence of IL-1 β did not induce a significant increase in cell death within the same time frame (Supplemental Fig. 2d). This increase in LDH release observed within neurons after exposure to transmigrated neutrophils was not due to compromised neutrophil viability, which was determined through trypan blue staining: the viability of transmigrated neutrophils 20 h after isolation was 40% less than that observed for the naive neutrophils (Supplemental Fig. 2e).

The neurotoxicity of transmigrated neutrophils was also conveyed through the release of soluble factors from the neutrophils, because conditioned medium from transmigrated neutrophils (applied at 1:4 dilution to the primary neuronal cultures) induced

dc_2027_22

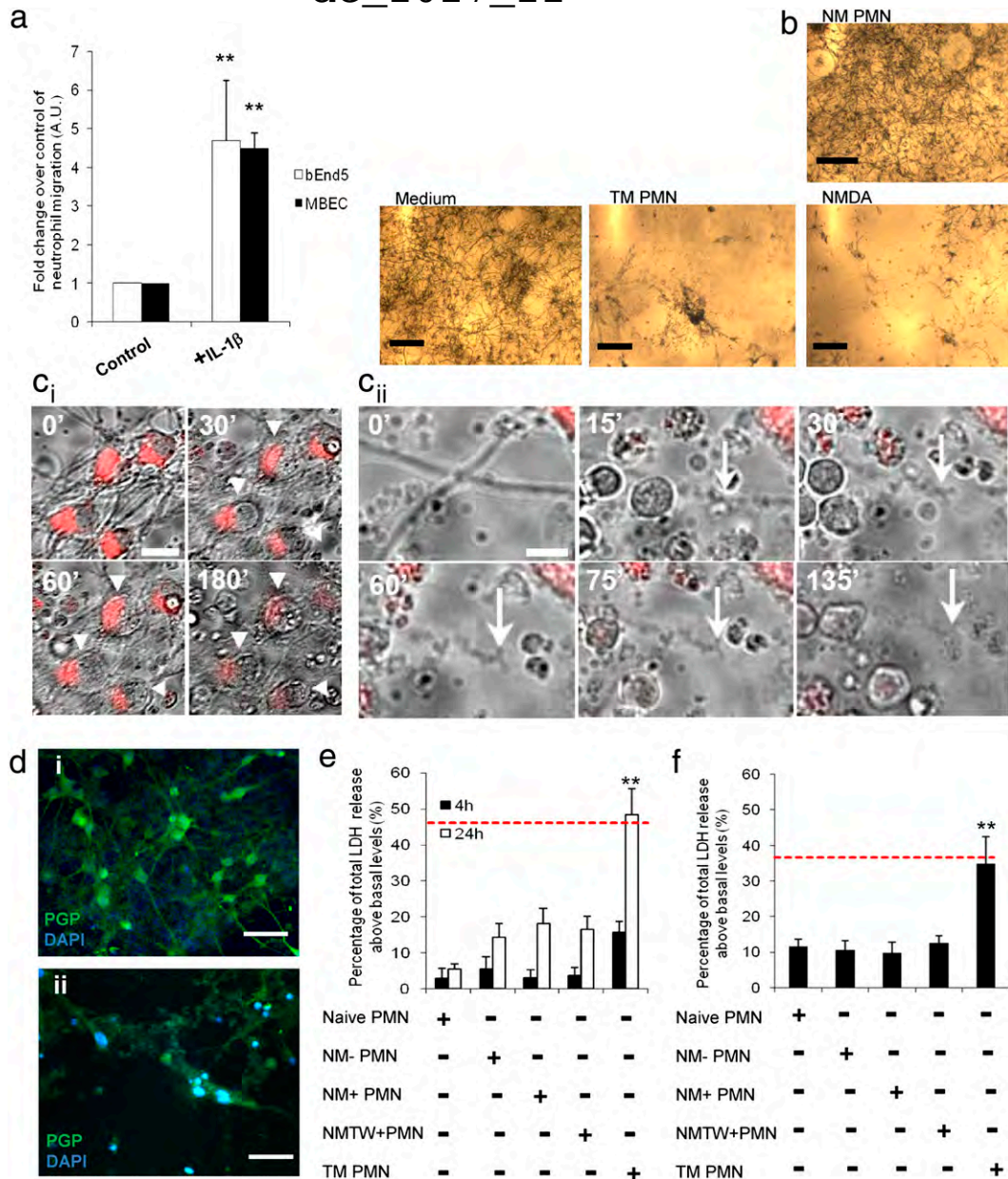


FIGURE 1. Neutrophils acquire a neurotoxic phenotype after transmigration across activated brain endothelium. **(a)** Transmigration of neutrophils across brain endothelioma cells (bEnd.5) and primary MBECs treated with IL-1 β (4 h) after 24 h. **(b)** Bright-field images of neurons exposed to Neurobasal Medium, nonmigrated neutrophils (NM PMN), transmigrated neutrophils (TM PMN) (120,000 cells/cm²), or 600 μ M NMDA in the presence of MTT (5 μ g/ml) for 24 h. Neuronal viability under these conditions is indicated by the presence or absence of MTT crystals. Scale bar, 300 μ m. **(c)** Bright-field and CellTracker Red images of stained neurons (arrowheads) exposed to TM PMN for 0–180 min (Supplemental Video 1). Scale bar, 15 μ m. **(c)** Bright-field and CellTracker Red images of a neuronal process (arrows) exposed to TM PMN for 0–135 min. Scale bar, 5 μ m. **(d)** Immunofluorescent images of neurons (PGP 9.5, green) exposed to naive PMN **(i)** or TM PMN **(ii)** (120,000 PMN/cm²) for 24 h. Scale bars, 30 μ m. **(e)** Quantification of total LDH release from neurons 4 or 24 h after application of naive neutrophils (PMN), nonmigrated neutrophils that were incubated with nonactivated endothelial cells (NM-PMN), nonmigrated neutrophils that had been incubated with IL-1 β -activated brain endothelial cells (NM+ PMN) or incubated with conditioned medium from activated endothelium after washing (NMTW+PMN), or transmigrated neutrophils (TM PMN) (120,000 cells/cm²). Red dashed line indicates neuronal death induced by 600 μ M NMDA. **(f)** Effect of conditioned medium (applied at 1:4 dilution) from naive PMN, NM- PMN, NM+ PMN, NMTW+ PMN, or TM PMN on neuronal viability, as assessed by LDH release after 24 h. Bars represent mean \pm SEM for a minimum of three independent experiments carried out on separate cultures. Red dashed line indicates neuronal death induced by 600 μ M NMDA. ** p < 0.01, one-way ANOVA, with a Bonferroni post hoc test.

a >4-fold increase in neuronal death (overall 30–40% increase in neuronal LDH release) after 24 h of incubation (Fig. 1f). Conditioned medium from naive neutrophils or nonmigrated neutrophils induced a reduction in neuronal viability to a much smaller extent compared with that induced by the conditioned medium from transmigrated neutrophils (Fig. 1f), which was comparable to the neurotoxicity induced by NMDA (600 μ M) after 24 h of incu-

bation (red dashed line). An increase in neurotoxicity was also observed in and the presence of transmigrated neutrophils after migration across IL-1 α -stimulated bEnd.5 (Supplemental Fig. 2f). Therefore, this rapid induction in neuronal death could be solely attributed to the transmigration of neutrophils across activated brain endothelium, because no increase was observed in any of the four nonmigrated control groups.

dc_2027_22

We also investigated whether transendothelial migration-induced neutrophil neurotoxicity is unique to activated brain endothelium. To this end, we used a thioglycollate-induced peritonitis model, which also allowed us to assess the role of *in vivo* neutrophil transmigration on neurotoxicity *in vitro*. Conditioned medium from neutrophils collected from the peritoneal cavity after thioglycollate injection was neurotoxic and led to increased LDH release and reduced MTT metabolism in neuronal cultures (Supplemental Fig. 2g, 2h).

Cerebrovascular transmigration profoundly alters neutrophil phenotype

The morphology of naive neutrophils and transmigrated neutrophils was determined by immunofluorescence. Compared with naive neutrophils, transmigrated neutrophils were devoid of lobed nuclei (Fig. 2bA, arrow) and displayed extracellular decondensed DNA (Fig. 2bB, arrow), which was associated with an increase in the abundance of elastase staining (Fig. 2bB, 2bC). Using immunofluorescence, the loss of neuronal MAP2 staining observed after 4 h of incubation with transmigrated neutrophils was extensive in comparison with the neurons incubated with the naive controls (Fig. 2c, 2d). In this instance, the neutrophils were also stained with CD45, as well as MMP-9, indicating the presence of the secondary and tertiary granules. A three-dimensional z-stack was produced from the wide-field fluorescent images, allowing visualization of the morphology of naive and transmigrated neutrophils in the presence of the neuronal cultures in a transverse cross section (Fig. 2cii, 2dii). The presence of the punctuate MMP-9 staining within the spherical naive neutrophils can be clearly seen, resting above the neuronal cultures (Fig. 2cii). This MMP-9 staining was lost in the transmigrated neutrophils, which, together with the altered shape and appearance, suggests their degranulation (Fig. 2dii).

We then determined the inflammatory phenotype of the transmigrated neutrophils in comparison with naive neutrophils by CBA analysis (Table I). Transmigrated neutrophils had increased inflammatory profiles, with reduced cell-associated CD62L (L-selectin) indicative of activation-induced CD62L shedding, as well as significantly increased neutrophil CXCL1 and IL-6 expression. We also detected a significant increase (six-fold) in neutrophil cell-associated (but not secreted) inflammatory factors RANTES and MCP-1 (Table I). These results show that cerebrovascular transmigration profoundly alters neutrophil viability, activation, and inflammatory phenotype.

Flow cytometric analysis demonstrated a rapid activation of transmigrated neutrophils after transmigration (Supplemental Fig. 3ai–iii). The percentage of transmigrated neutrophils staining positive for both p-p38 and p-Akt was significantly increased in comparison with the naive neutrophils, and a trend toward increased p-NF- κ B was observed (Supplemental Fig. 3ai, 3aiii). Activation of the p-NF- κ B, p38, and Akt pathways was shown to promote survival of activated neutrophils (24–26). These data are consistent with previous studies on noncerebral endothelium, demonstrating that neutrophil transmigration across endothelium prolongs neutrophil viability (27, 28).

Release of neutrophil proteases associated with decondensed DNA is linked with neuronal death *in vitro*

Following our previous observation of decondensed DNA within transmigrated neutrophils (Fig. 2bB), we hypothesized that the neurotoxicity of transmigrated neutrophils was mediated by histone–DNA complexes or neutrophil-derived proteases, which are released upon degranulation and are associated with NETs (29). Through the use of a mAb to histone–DNA complexes (PL2-3, H2A–H2B–DNA) (22), a significant reduction in intracellular H2A–H2B–DNA staining *in vitro* in transmigrated neutrophils was

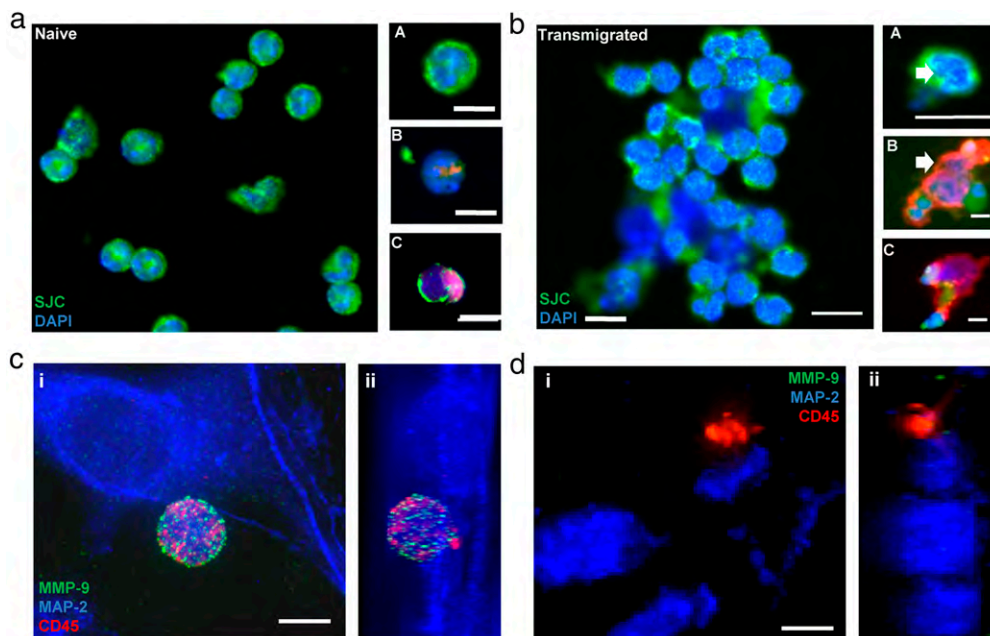


FIGURE 2. Neutrophils migrated across IL-1 β -activated cerebrovascular endothelium show altered phenotype in comparison with naive controls. (a) Naive neutrophils stained with anti-neutrophil serum (SJC, green) and DAPI (blue) (aA), SJC (red), DAPI (blue), and PL2-3 (green) (aB), or elastase (red), DAPI (blue), and PL2-3 (green) (aC). Scale bars, 10 μ m. (b) Transmigrated neutrophils stained with SJC (green) and DAPI (blue) (bA), SJC (red), DAPI (blue), and PL2-3 (green) (bB), or elastase (red), DAPI (blue), and PL2-3 (green) (bC). White arrows indicate delobulated nuclei and the presence and protrusion of elastase. Scale bars, 10 μ m. Immunofluorescent images of neurons (MAP2, blue) exposed to naive (ci) or z-stack (cii) or transmigrated neutrophils (di) or z-stack (dii) (120,000 neutrophils/cm²) for 4 h. Neutrophils (CD45, red) contain high levels of MMP-9 (green) (ci), which is lost from transmigrated neutrophils added to neurons (di). Scale bars, 5 μ m.

Table I. Cytokine profile of naive neutrophil and transmigrated neutrophil lysates determined using CBA analysis

Cytokine	Naive (pg/ml)	Transmigrated (pg/ml)
CD62E	34 ± 12	116 ± 34
CD62L	569 ± 73	177 ± 63*
IL-1 α	13 ± 3	12 ± 4
TNF- α	24 ± 7	19 ± 8
MIP-1	36 ± 5	17 ± 6
G-CSF	22 ± 4	23 ± 41
MCP-1	85 ± 12	579 ± 110*
RANTES	55 ± 11	507 ± 80**
IL-6	7 ± 2	46 ± 14*
IL-1 β	30 ± 6	16 ± 5
KC	21 ± 3	1159 ± 290*
IL-10	37 ± 27	46 ± 10
IL-17	4 ± 1	4 ± 12

Data (corrected) are mean \pm SEM from a minimum of three independent experiments carried out on separate cultures.

* $p < 0.05$, ** $p < 0.01$, Student unpaired t test.

observed compared with in naive controls (Fig. 3ai–iii), implying that the decondensed DNA was released upon or after transmigration. Using PCR and specific mitochondrial or nuclear gene primers, we found that extracellular DNA was present in the conditioned medium of transmigrated neutrophils and the conditioned medium of naive neutrophils (Fig. 3bi, 3bii). The presence of extracellular decondensed DNA was confirmed by ELISA using the PL2-3 Ab: a significant increase in the abundance of decondensed DNA was detected in the conditioned medium of transmigrated neutrophils in comparison with the naive neutrophil-conditioned medium (Fig. 3c).

Neutrophil proteases contribute to tissue injury during inflammation (30–32) and brain injury after MCAo (21, 33, 34). Extensive work also showed that neutrophil elastase is associated with NETs (16, 35, 36). The mAb PL2-3 was also effective in identifying NETosis and associated inflammation in the periphery (16). After the direct transmigration of neutrophils onto neuronal cultures in the presence of PL2-3, an improvement in neuronal viability was observed using immunofluorescence: MAP2 staining was retained in comparison with vehicle-treated controls (Fig. 3diii, 3div). The maintained integrity of neuronal cell bodies was also quantified in both the PL2-3-treated and vehicle-treated control after neutrophil transmigration: a significant increase in cell body integrity was observed in the presence of PL2-3 (Fig. 3e). This could not be attributed to compromised neutrophil migration due to the PL2-3 Ab, because the transmigration of neutrophils across IL-1-activated brain endothelium was not affected when the Ab was present (Fig. 3f). We also determined whether the presence of the PL2-3 Ab altered the neurotoxicity induced by the application of conditioned medium from transmigrated neutrophils. LDH assay detected a small and nonsignificant, but consistent, reduction (mean, 16%) in neuronal death after PL2-3 Ab treatment in the presence of conditioned medium of transmigrated neutrophils (Supplemental Fig. 3b). This difference suggests the impedance of NETosis in the presence of PL2-3 during migration, rather than the inhibition of NET release. These results suggest that the release of decondensed DNA–protease complexes is likely to be involved in the process of neutrophil activation and protease release, but transmigrated neutrophil-mediated neurotoxicity was not directly induced by histone–DNA complexes. Together with NET production, degranulation of the transmigrated neutrophils could also contribute to the acquired neurotoxicity. As shown previously, the loss of MMP-9 staining was observed in transmigrated neutrophils, suggesting degranulation (Fig. 2d). A significant increase in the

presence of active MMP-9 was detected in conditioned medium of transmigrated neutrophils in comparison with the naive control (Supplemental Fig. 3c). Because neutrophil proteases are known to be associated with decondensed DNA, their potential involvement in the acquired neurotoxic phenotype of transmigrated neutrophils was investigated further.

Neutrophil proteases mediate rapid neurotoxicity of transmigrated neutrophils

To evaluate the potential role of the released proteases and other substances in the neurotoxic mechanisms induced by transmigrated neutrophils, we first performed interventions using conditioned medium from transmigrated neutrophils. Pretreatment of neurons with MK-801 (NMDA receptor antagonist) partially, but significantly, reduced the neurotoxicity induced by conditioned medium from transmigrated neutrophils (Fig. 4a). Heat inactivation or trypsin treatment of conditioned medium from transmigrated neutrophils also inhibited its neurotoxic effect (Fig. 4a), suggesting a proteinaceous neurotoxin.

Neutrophil-derived proteases are associated with NETs (36); therefore, we tested whether MMP-9, cathepsin-G, proteinase-3, or elastase, released from transmigrated neutrophils, may be responsible for the observed neurotoxicity. No effect was seen when specific inhibitors against certain proteases were used alone (data not shown). Because these proteases exhibit their actions in concert (37), a mixture of inhibitors against cathepsin-G (C), neutrophil elastase (E), proteinase-3 (aprotinin; A) and MMP-9 (SB3CT; M) was also tested (defined as CEAM, a mixture of inhibitors against cathepsin-G, neutrophil elastase, proteinase-3 [aprotinin], and MMP-9 [SB3CT]). CEAM did not affect neutrophil transmigration across IL-1-activated brain endothelium (Fig. 4b). Immunofluorescence showed maintained integrity, reduced degranulation, and less elastase/MMP-9 staining in transmigrated neutrophils in the presence of CEAM compared with vehicle-treated transmigrated neutrophils (Fig. 4cii, 4ciii). Neutrophils were directly migrated onto neuronal cultures across activated bEnd.5 cells in the presence of vehicle or CEAM for 2 h (Fig. 4diii, 4div). Importantly, neuronal structural integrity appeared to be maintained after the migration of transmigrated neutrophils in the presence of CEAM (Fig. 4div) in comparison with the vehicle-treated–transmigrated neutrophils (Fig. 4diii), thus supporting the link between neuronal toxicity and the proteases released from transmigrated neutrophils.

When transmigrated neutrophils were added directly to neurons, the presence of CEAM significantly rescued neuronal viability compared with the vehicle-treated–transmigrated neutrophil control (Fig. 4e). The presence of CEAM was ineffective when using conditioned medium from transmigrated neutrophils, suggesting that the cascade of events subsequent to full degranulation involving these neutrophil-derived proteases might result in neurotoxicity. This is supported by the observation that neurotoxicity could be successfully inhibited on site in neuronal cultures while maintaining transmigrated neutrophil integrity, but it could not be inhibited in conditioned medium from transmigrated neutrophils, in which it is possible that proteolytic events had already occurred, and full degranulation had taken place.

DNase treatment of conditioned medium from transmigrated neutrophils failed to restore neuronal viability, indicating that DNA released from transmigrated neutrophils was not directly responsible for the observed neurotoxicity (Supplemental Fig. 2i). Several other inhibitors (calcium channel blocker nifedipine, broad-spectrum caspase inhibitor BOC-Asp(OMe)-FMK, cysteine protease inhibitor E64, protease-activated receptor inhibitor-1, L- α -aminoadipate, EDTA, EGTA, BAPTA to chelate-free calcium, apocynin to inhibit NAPDH oxidase, MEK1 inhibitor, the MAC-1 inhibitor clusterin, and the four individual CEAM components) all failed to rescue the

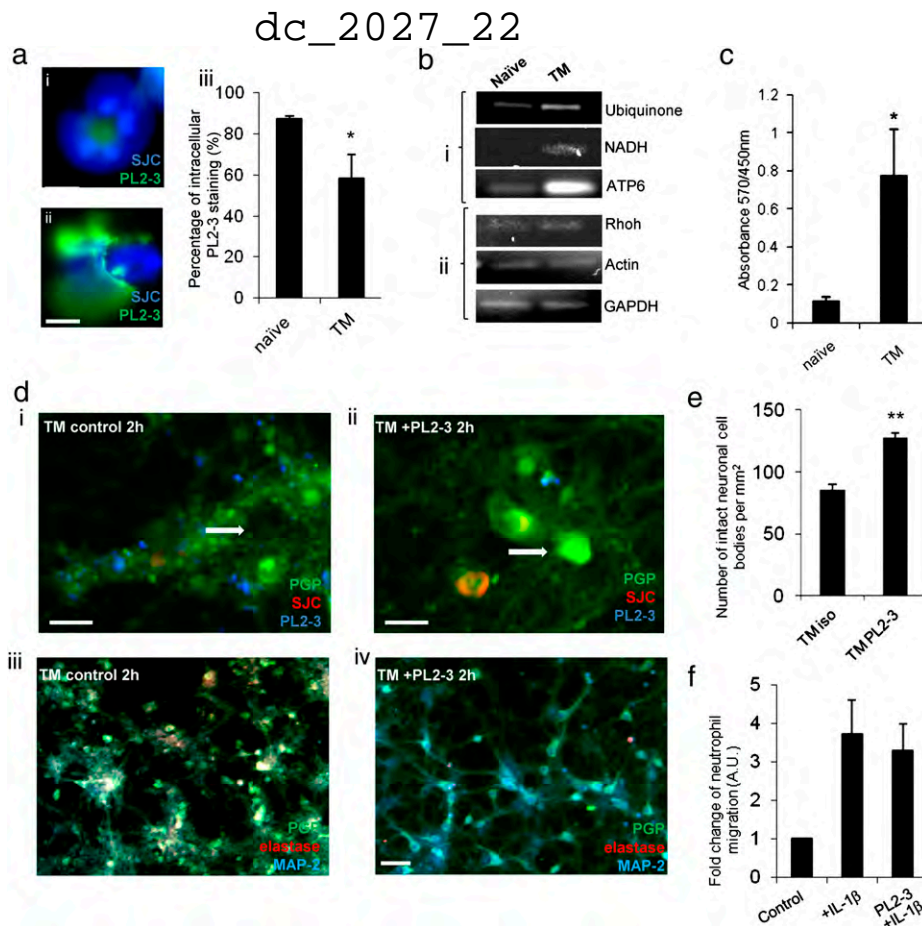


FIGURE 3. Neutrophil proteases are associated with NETs and neuronal death in vitro. Intracellular PL2-3 staining is significantly reduced in transmigrated (TM) neutrophils (**aii**) compared with naive neutrophils (**ai**) (DAPI and PL2-3). Scale bar, 5 μ m. (**aiii**) Bar graph shows the percentage of neutrophils present with intracellular PL2-3 staining. (**b**) Neutrophil-derived mitochondrial DNA is increased in conditioned medium from transmigrated neutrophils (TM) but not in that from naive neutrophils, as determined by PCR. Mitochondrial (**bi**) and nuclear (**bii**) DNA were observed in the conditioned medium of transmigrated neutrophils compared with naive controls. (**c**) Elevated levels of extracellular histone–DNA were detected in conditioned medium of naive neutrophils and transmigrated neutrophils (TM). (**d**) Neurons were incubated for 2 h and stained with PGP 9.5 (green), neutrophils were stained with SJC (red), and NETs were stained with PL2-3 (blue). Reduction in neurotoxicity of transmigrated neutrophils in the presence of PL2-3 (15 μ g/ml) is seen in neuronal cultures stained with PGP 9.5 (green) and MAP2 (blue) (**diii**) compared with isotype-treated control (**dii**). Scale bar, 30 μ m. Maintained structural integrity is shown in cultured neurons (arrows) after exposure to transmigrated neutrophils treated with PL2-3 (15 μ g/ml) (**dii**) in comparison with neutrophils transmigrated across activated endothelium in the presence of an isotype control (**di**). Scale bar, 10 μ m. (**e**) Percentage of maintained integrity of neuronal cell bodies after exposure to transmigrated neutrophils treated with PL2-3 (15 μ g/ml) in comparison with isotype-treated control. (**f**) Presence of PL2-3 Ab (15 μ g/ml) does not affect neutrophil migration across IL-1 β -activated brain endothelium after 24 h of migration. Bars represent the mean \pm SEM from a minimum of three independent experiments carried out on separate cultures. * $p < 0.05$, ** $p < 0.01$, Student t test or one-way ANOVA, with a Bonferroni post hoc test or Student t test, where appropriate.

neuronal viability in the presence of conditioned medium from transmigrated neutrophils (data not shown).

These data indicate that neuronal viability can be maintained if neutrophil degranulation and release of multiple proteases are prevented in the presence of neurons. Time-lapse imaging indicated the presence of transmigrated neutrophils that were moving continually, as well as degranulated neutrophils that were in close association with neurons (Supplemental Video 2). Scanning electron microscopy was used to visualize the transmigrated neutrophils and neurons in greater detail (Fig. 4f–h, 4j). Transmigrated neutrophils were associated with the neurons (Fig. 4f) and were attached to intact neuronal cell bodies (Fig. 4gi, 4gii). In contrast, neuronal death, as evidenced by the presence of disintegrated neuronal cell bodies, was seen in the vicinity of collapsed neutrophils (Fig. 4gi, 4giii). Degranulation and NET release from transmigrated neutrophils were observed: the strand-like globular structures of the decondensed DNA were found protruding from the disintegrating neutrophil cell membrane (Fig. 4h, 4j).

Neutrophils recruited to the brain in vivo are associated with extracellular proteases and a loss of intracellular decondensed DNA

Decondensed DNA associated with neutrophils and loss of intracellular histone–DNA complexes were observed in animal models of neuroinflammation tested in vivo (Fig. 5a), such as after intracerebral LPS administration or MCAo (Fig. 5ai), MCAo in the presence of peripherally administered IL-1 β (Fig. 5aii), MCAo preceded by systemic infection (Fig. 5aiii), and AMPA/IL-1–induced neurotoxicity (Fig. 5aiv). Within these models of neuroinflammation, intracellular PL2-3 staining was reduced or uneven in close proximity to the nuclear DNA staining, as indicated by DAPI (Fig. 5b). In general, the presence of neutrophil-associated decondensed DNA was reduced in the brain (80% of intracerebral neutrophils were PL2-3⁻) (Fig. 5ci, 5cii) in comparison with meningeal neutrophils (20% were PL2-3⁻). This provides further evidence for an altered state of recruited neutrophils in vivo. There was no significant difference in neutrophilic intracellular PL2-3 staining between different neuro-

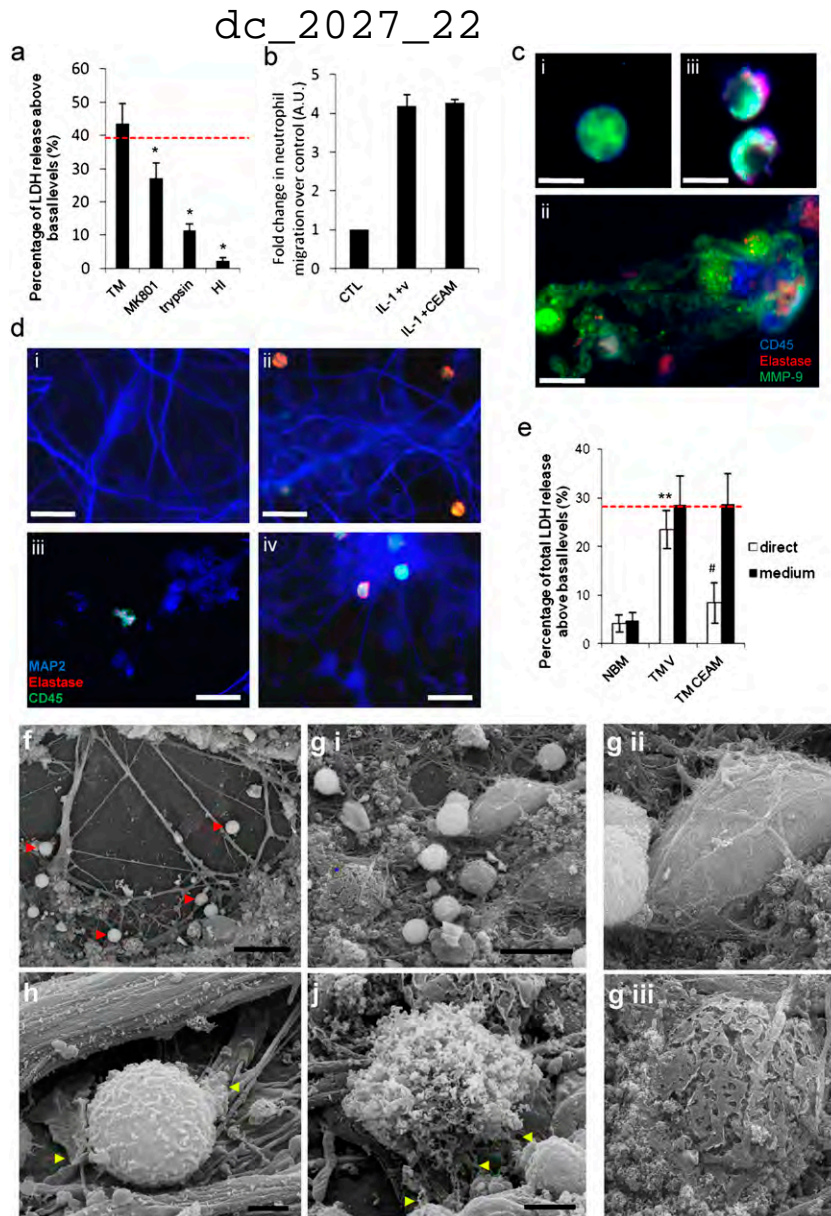


FIGURE 4. Degranulation and NET release are associated with neurotoxicity in transmigrated neutrophils through neutrophil proteases. **(a)** Neuronal LDH release is shown 24 h after treatment with conditioned medium (CM) from transmigrated neutrophils (TM), with or without pretreatment of neurons with MK801 (10 μ M), trypsin, or heat-inactivated CM (HI). Red dashed line indicates neuronal death induced by 600 μ M NMDA. **(b)** The transmigration of neutrophils across IL-1 β -activated brain endothelium (bEnd.5) is not significantly altered by the presence of CEAM after 24 h. **(c)** Neutrophil morphology indicated by the presence of elastase (red), CD45 (blue), and MMP-9 (green) using immunofluorescence in naive neutrophils. Attenuation of degranulation in the presence of CEAM (**ciii**) compared with the vehicle-treated transmigrated neutrophils (**cii**). Scale bars, 5 μ m. Maintained neuronal structural integrity shown in neuronal cultures after exposure to transmigrated neutrophils in the presence of CEAM (**dii**) compared with neutrophils transmigrated across activated endothelium (**diii**). Vehicle-treated transmigrated neutrophils induced extensive neuronal damage compared with naive neutrophils. Neurons were incubated for 4 h and stained with MAP2 indicating neuronal viability (blue); neutrophils were stained with CD45 (green) and elastase (red). Scale bars, 30 μ m. **(d)** Neuronal cultures in the presence of vehicle, **(dii)** neuronal cultures in the presence of naive neutrophils. **(e)** Neuronal viability was established using LDH assay after the direct application of naive and transmigrated neutrophils (white bars) or naive and transmigrated neutrophil-conditioned medium (black bars) in the presence of CEAM or a vehicle control. Red dashed line indicates neuronal death induced by 600 μ M NMDA. **(f)** Scanning electron micrograph images of transmigrated neutrophils in primary murine neuronal cultures after 1 h of incubation. The presence of neutrophils is indicated by arrowheads. Scale bar, 30 μ m. **(g)** Identification and comparison of a healthy neuronal body (white asterisk) with a dying neuronal body (blue asterisk). Scale bar, 20 μ m. **(gii** and **giii**) Neuronal bodies are shown at higher magnification. Scale bar, as shown in (g). **(h)** Transmigrated neutrophil in initial phases of degranulation (yellow arrowheads) surrounding neuronal processes. Yellow arrowheads indicate the presence of strands of DNA. Scale bar, 2 μ m. **(j)** Full degranulation of the transmigrated neutrophils; the granules and globular structures of NETs are clearly visualized (yellow arrowheads). Scale bar, 2 μ m. Bar graphs show mean \pm SEM for a minimum of three independent experiments carried out on separate cultures. * p < 0.05, versus TM, ** p < 0.01, TM versus naive (NBM), # p < 0.05, TM versus TM CEAM, one-way ANOVA, with Bonferroni post hoc test.

inflammatory conditions. Quantification revealed extracellular neutrophil-associated DNA (PL2-3) in $4 \pm 1\%$ of recruited neutrophils after intracerebral LPS administration, whereas a trend toward more neutrophils with extracellular PL2-3 was observed

after AMPA/IL-1-induced neurotoxicity, MCAo in the presence of peripherally administered IL-1 β , or after MCAo preceded by systemic infection ($9 \pm 5\%$, $11 \pm 5\%$, and $15 \pm 5\%$, respectively). Extracellular neutrophil-associated PL2-3 staining was mostly

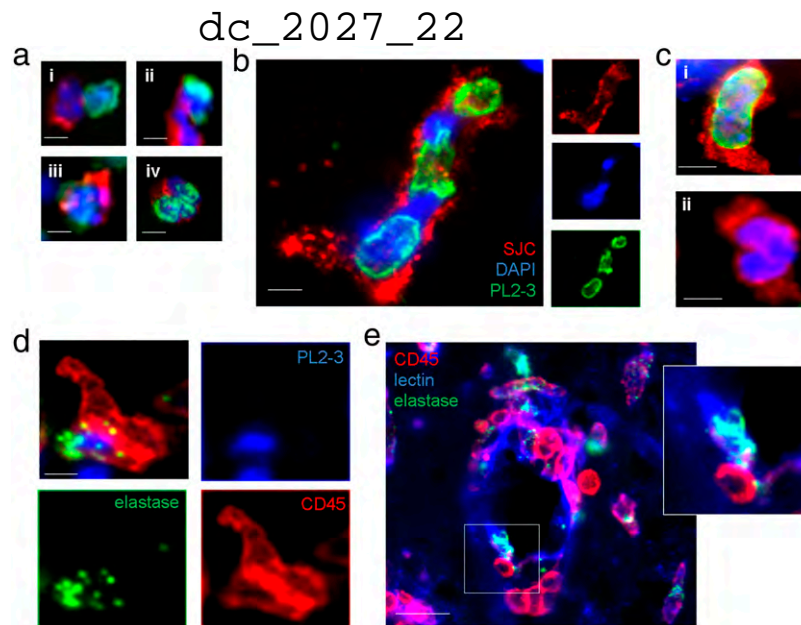


FIGURE 5. Neutrophil recruitment in acute brain injury is associated with extracellular proteases and loss of intracellular decondensed DNA in vivo. **(a)** Loss of intracellular histone–DNA complexes (PL2-3 staining) in neutrophils identified in the cerebral cortex in vivo in different established models of neuroinflammation after induction of cerebral ischemia **(i)**, after induction of cerebral ischemia in the presence of peripherally injected IL-1 β **(ii)**, after induction of cerebral ischemia following systemic infection with *Trichuris muris* (3) **(iii)**, and after stereotactic intrastriatal administration of IL-1 and AMPA **(iv)** in rat. Scale bars, 5 μm . **(b)** In a population of recruited neutrophils in the inflamed brain, PL2-3 staining is uneven, and decondensed DNA is observed in close proximity to nuclear DNA (DAPI, blue). Scale bar, 10 μm . **(c)** Meningeal neutrophils contain high amounts of intracellular histone–DNA complexes (PL2-3) after stereotactic injection of LPS. Scale bar, 10 μm . **(cii)** Neutrophils recruited to the inflamed cerebral cortex contain less decondensed DNA (PL2-3) after stereotactic injection of LPS. Scale bar, 10 μm . **(d)** Extracellular PL2-3 and elastase are found in the cerebral cortex in vivo after stereotactic injection of LPS. Scale bar, 5 μm . **(e)** Immunofluorescence showing perivascular inflammatory cells (CD45, red) containing neutrophil elastase (green) adhering to the endothelial monolayer (lectin, blue) in the brain. *Inset* shows enlargement of area in box. Scale bar, 20 μm .

punctuate and appeared in close proximity to neutrophils (Supplemental Fig. 4a). Long NET-like structures containing both nuclear DNA and PL2-3 were not observed in the brain. Neutrophil elastase was also determined through immunofluorescence in vivo and was associated with decondensed DNA (Fig. 5d). The presence of extracellular elastase associated with recruited neutrophils was observed in vivo, along the blood vessel wall and occasionally in the parenchyma after MCAo (Supplemental Fig. 4b). Disintegration of the perivascular basement membrane from the endothelial monolayer after MCAo was also observed in vivo (Supplemental Fig. 4c), indicating that products derived from recruited neutrophils could reach nearby neurons via the compromised BBB. In addition to this, populations of elastase⁺ neutrophils were observed perivascularly inside and outside the endothelial monolayer (Fig. 5e, Supplemental Fig. 4d).

Discussion

We show in this study that transmigration through activated cerebrovascular endothelium critically alters neutrophils, leading to a proinflammatory, neurotoxic phenotype. Using established in vitro and in vivo models of neuroinflammation, we show the presence of released decondensed DNA (NETs) associated with key proteases after neutrophil transendothelial migration. Neurotoxicity of neutrophils was demonstrated previously, but over a 1–3-d period (13, 15), whereas, in this study, the transmigration-induced neurotoxicity developed very rapidly (within 30 min). Therefore, these data identify a novel neuroinflammatory mechanism: the development of rapid neurotoxicity of neutrophils by IL-1–induced cerebrovascular transmigration.

Neutrophil recruitment through endothelial activation is a common observation in inflammatory disease: the two-stage process of neutrophil activation of priming and mobilization leads to their adherence, rolling, and transmigration (6). The stimulation of this priming and recruitment can occur via the presence of pathogen

associated molecular patterns or, in the case of sterile injury, damage associated molecular patterns produced by necrotic and apoptotic cells (5). Previous studies highlighting the importance of neutrophil recruitment in peripheral inflammation demonstrated a clear role for NETs through pathogen associated molecular patterns and damage associated molecular pattern stimulation linking both in vitro and in vivo observations (30–32).

Systemic inflammatory changes in response to cerebral ischemia also lead to the mobilization of peripheral inflammatory cells, which takes place in parallel to activation of the cerebrovascular endothelium (1, 17, 21). The release of neutrophils from the bone marrow in response to MCAo is associated with an increase in pro-MMP9 in circulating blood cells within hours (9). Activated neutrophils are recruited and adhere to inflamed blood vessels in the brain in response to neuroinflammation (38, 39). Their extravasation, which is associated with vascular leakage in the brain, was demonstrated with in vivo two-photon imaging (40). Intrastriatal injection of LPS or coinjection of AMPA and IL-1 into the striatum provided us additional in vivo paradigms of neuroinflammation that induce neutrophil recruitment and that are relevant to pathogen- and sterile-induced brain inflammatory conditions. Our in vivo data showed that most recruited neutrophils were associated with blood vessels in the ipsilateral hemisphere after MCAo and in excitotoxic- or endotoxin-induced neuroinflammation. Transmigrated neutrophils contained high levels of proinflammatory cytokines (e.g., KC and RANTES), indicating that such cells may contribute further to cerebrovascular activation and leukocyte recruitment to the brain.

The degranulation of neutrophils and the release of NETs containing decondensed DNA and proteases takes place normally as part of an antibacterial defense (16, 36, 41, 42). This might be initiated in vivo to prevent the bacterial invasion of seriously injured tissues. These properties could contribute to the poor out-

come observed in stroke patients with systemic inflammation (43, 44). Murine *in vivo* models also reflect this, because the upregulation observed in neutrophil recruitment and neutrophil-derived proteases might account for BBB damage and increased neuronal death (4, 21). Through the release of decondensed DNA and proteases during extravasation, these neurotoxic products could reach neurons through the disrupted basement membrane of the glia limitans and lead to their demise. Additional stimuli received from parenchymal cells or extracellular matrix may also exacerbate the effects of the transmigrated neutrophils. Although neutrophils are not recruited to the brain until several hours after acute brain injury, once transendothelial migration takes place, neutrophils can exert rapid toxicity (within 30 min, based on our *in vitro* data) to neurons. Therefore, it is not surprising that powerful mechanisms have evolved to prevent parenchymal infiltration of neutrophils, such as the complex barrier structures of the neurovascular unit or phagocytosis of invading neutrophils by microglia (45, 46).

Although our data suggest that the process of transmigration itself is a sufficient stimulus to endow neutrophils with neurotoxic properties and, thus, the ability to kill neurons immediately, it does not imply that diapedesis of neutrophils is the sole factor that contributes to their neurotoxicity. Adherence to activated brain endothelium, partial diapedesis, or the initiation of transmigration could also contribute to the development of a neurotoxic phenotype *in vivo*; these mechanisms warrant further investigation. Proinflammatory alterations in neutrophils induced by their transmigration may reflect a heightened state of activation, such that they are primed to respond to additional stimuli, which may indirectly contribute to further neurotoxicity *in vivo*. Similarly, the pro-survival effect of transmigration on neutrophils is likely to further exacerbate the neurotoxic potential of neutrophils in the injured brain. Although the release of NETs often occurs in association with neutrophil death, recent data indicate that viable neutrophils can form NETs, which parallels the release of mitochondrial, but not nuclear, DNA (35). This is strikingly similar to our findings: release of proteases and mitochondrial DNA in neutrophil-conditioned medium and *in vivo* and the restricted release of nuclear DNA released in the brain. This might indicate that the release of proteases and decondensed DNA from neutrophils in the brain is an active process and not simply a consequence of neutrophil death. It is not known when the release of proteases and DNA takes place *in vivo*, but most recruited neutrophils lacked intracellular PL2-3 immunopositivity in the brain. It is also possible that classical NETosis involving the release of nuclear DNA, as observed *in vitro* or in peripheral tissues, is restricted in the brain or such cells are rapidly phagocytosed by resident microglia.

Our data also show that the neurotoxic phenotype of neutrophils after transendothelial migration is not unique to activated brain endothelium, because conditioned medium of neutrophils collected *in vivo* after thioglycollate-induced peritonitis also exerts toxicity in neuronal cultures. Irrespective of whether neurotoxicity is triggered by peripheral or central transendothelial migration, neutrophils recruited to the brain parenchyma can exert neurotoxicity, which is likely to be further increased by the fact that toxic products could reach nearby neurons from transmigrating neutrophils if the BBB is compromised. Our *in vitro* data show that neuron–neutrophil contact is not required for neutrophil neurotoxicity. Furthermore, peripherally located transmigrating neutrophils could exert toxicity to neurons outside the brain as well, which has to be further investigated in the context of peripheral neuropathies.

Elastase, cathepsin-G, and proteinase-3 are known to be present in neutrophil primary granules, whereas tertiary granules contain, among other components, MMP-9 (47). Other studies showed the localization of NETs with elastase, cathepsin-G, and proteinase-3

(16, 42, 48), which suggests that the release of primary granules and NETs is the last line of defense for a neutrophil before apoptosis (29). The formation of NETs provides a link between the released proteases and decondensed DNA: the presence of elastase was identified attached to the NET itself (16, 49). Elastase is involved in the very first stages of nuclear DNA decondensation through its exit from the primary granules directly to the nucleus (48). The fact that CEAM was not protective when added to conditioned medium of transmigrated neutrophils indicates that a cascade of events, subsequent to protease and decondensed DNA release, is responsible for neurotoxicity; this needs to be investigated in further studies. Similarly, considerable further work is required to establish the functional link between mitochondrial DNA and protease activation in neutrophils during NETosis, although it is relevant that mitochondrial DNA can activate human neutrophils, resulting in the release of proteases, such as MMP-9 (50).

Our *in vitro* imaging data and scanning electron microscopic observations indicated that transmigrated neutrophils are closely associated with neurons. This accords with the fact that inhibition of the proteases present after degranulation is successful only if transmigrated neutrophils are applied directly to neuronal cultures and not when in the presence of just the conditioned medium of transmigrated neutrophils. This implies that proteolytically cleaved products of these proteases are neurotoxic. CEAM provided almost full protection against neurotoxicity when applied in the presence of transmigrated neutrophils, indicating that proteases are the main mediators of toxicity in this model. The possibility that the actual presence of neurons triggers the degranulation of neutrophils is not known and remains to be determined in future studies.

In conclusion, we show that neutrophils that have migrated across an activated cerebrovascular endothelium profoundly change their phenotype and secrete decondensed DNA and proteases that contribute to neuronal death. IL-1 has a key role in cerebrovascular activation, neutrophil recruitment, and transendothelial migration, which contribute to brain inflammation and neuronal death. Therefore, inhibition of neutrophil recruitment and extravasation from cerebral vessels by blocking IL-1 actions might be a preferable strategy to inhibiting the various factors released by neutrophils once they have migrated, because it is likely to offer more effective protection against neutrophil-mediated neuronal death, a significant component in ischemic and other inflammatory brain injuries. Therefore, these findings further support the development of inhibitors of IL-1 as neuroprotective agents.

Acknowledgments

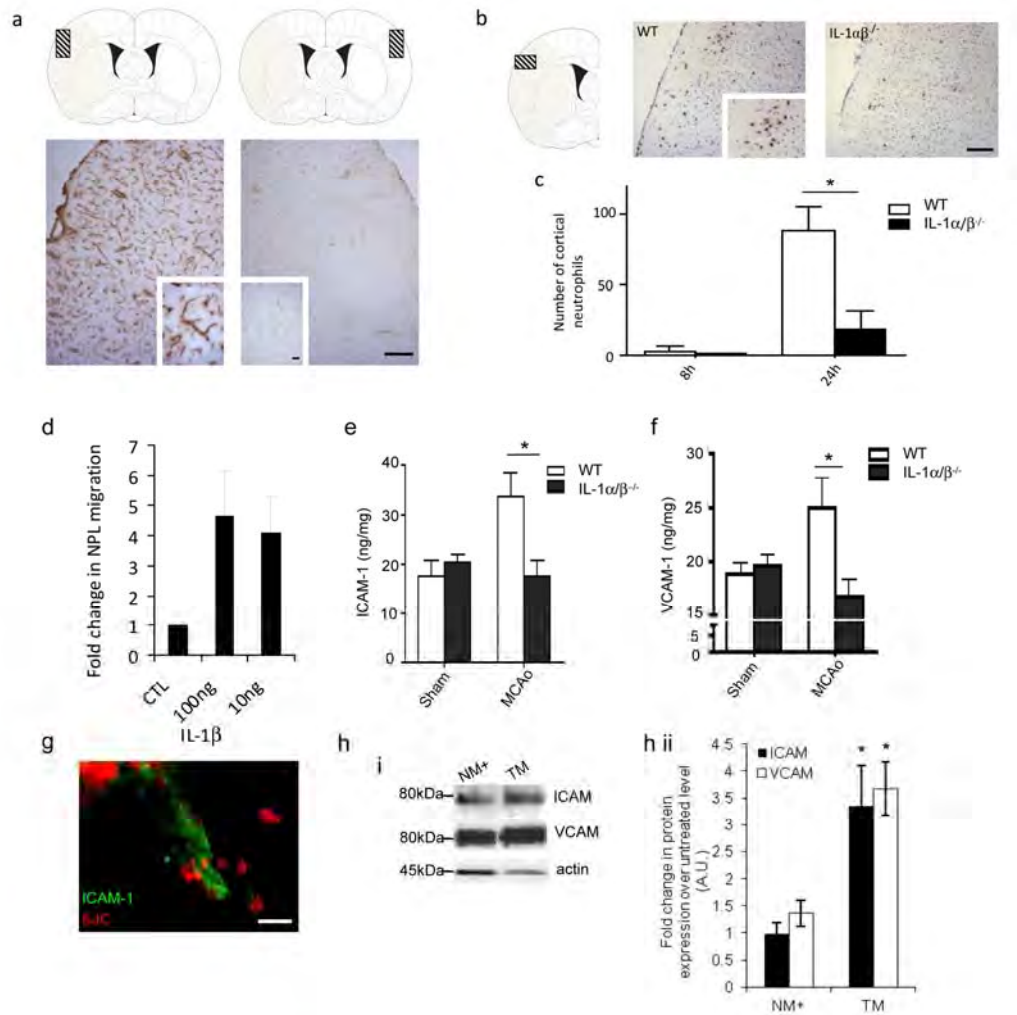
We thank Hannah Buggey, James Giles, and Emily Robinson for *in vivo* tissue samples, Laura Cooper for immunohistochemistry, and Catherine Smedley for technical assistance. We also thank Joel Pachter (University of Connecticut Health Center, Farmington, CT) for advice with the preparation of MBEC culture and Drs. Sandra Campbell and Daniel Anthony (University of Oxford) for the SJC Ab. IL-1 α / β ^{-/-} mice were kindly provided by Prof. Yoichiro Iwakura (Institute of Medical Science, University of Tokyo, Tokyo, Japan). The Bioimaging Facility microscopes in the Faculty of Life Sciences, University of Manchester used in this study were purchased with grants from the Biotechnology and Biological Sciences Research Council, the Wellcome Trust, and the University of Manchester Strategic Fund, and we acknowledge the support of Peter March and Steve Marsden within this core facility for help with microscopy. We also express our gratitude for the assistance of Tobias Starbourg in the Faculty of Life Sciences electron microscopy facility, supported by a Wellcome Trust equipment grant.

Disclosures

N.J.R. is a nonexecutive director of AstraZenca, but this has no relation to the current research. The other authors have no financial conflicts of interest.

References

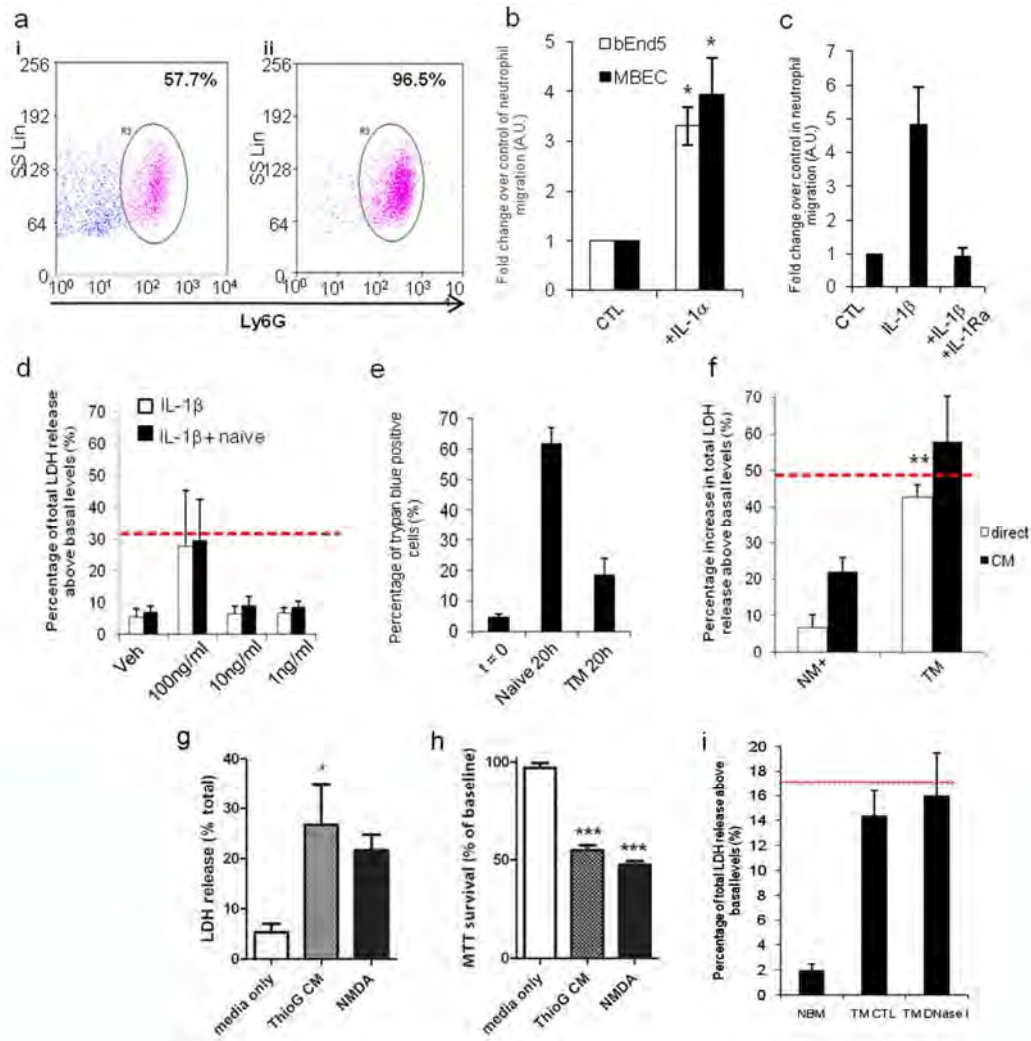
- Allan, S. M., P. J. Tyrrell, and N. J. Rothwell. 2005. Interleukin-1 and neuronal injury. *Nat. Rev. Immunol.* 5: 629–640.
- Neumann, J., S. Sauerzweig, R. Rönicke, F. Gunzer, K. Dinkel, O. Ullrich, M. Gunzer, and K. G. Reymann. 2008. Microglia cells protect neurons by direct engulfment of invading neutrophil granulocytes: a new mechanism of CNS immune privilege. *J. Neurosci.* 28: 5965–5975.
- Dénes, A., N. Humphreys, T. E. Lane, R. Grecnis, and N. Rothwell. 2010. Chronic systemic infection exacerbates ischemic brain damage via a CCL5 (regulated on activation, normal T-cell expressed and secreted)-mediated proinflammatory response in mice. *J. Neurosci.* 30: 10086–10095.
- McColl, B. W., N. J. Rothwell, and S. M. Allan. 2008. Systemic inflammation alters the kinetics of cerebrovascular tight junction disruption after experimental stroke in mice. *J. Neurosci.* 28: 9451–9462.
- Soehnlein, O., and L. Lindbom. 2010. Phagocyte partnership during the onset and resolution of inflammation. *Nat. Rev. Immunol.* 10: 427–439.
- Wright, H. L., R. J. Moots, R. C. Bucknall, and S. W. Edwards. 2010. Neutrophil function in inflammation and inflammatory diseases. *Rheumatology (Oxford)* 49: 1618–1631.
- Nourshargh, S., and F. M. Marelli-Berg. 2005. Transmigration through venular walls: a key regulator of leukocyte phenotype and function. *Trends Immunol.* 26: 157–165.
- McDonald, B., K. Pittman, G. B. Menezes, S. A. Hirota, I. Slaba, C. C. Waterhouse, P. L. Beck, D. A. Muruve, and P. Kubers. 2010. Intravascular danger signals guide neutrophils to sites of sterile inflammation. *Science* 330: 362–366.
- Denes, A., B. W. McColl, S. F. Leow-Dyke, K. Z. Chapman, N. E. Humphreys, R. K. Grecnis, S. M. Allan, and N. J. Rothwell. 2011. Experimental stroke-induced changes in the bone marrow reveal complex regulation of leukocyte responses. *J. Cereb. Blood Flow Metab.* 31: 1036–1050.
- Nathan, C. 2006. Neutrophils and immunity: challenges and opportunities. *Nat. Rev. Immunol.* 6: 173–182.
- Phillipson, M., and P. Kubers. 2011. The neutrophil in vascular inflammation. *Nat. Med.* 17: 1381–1390.
- McColl, B. W., N. J. Rothwell, and S. M. Allan. 2007. Systemic inflammatory stimulus potentiates the acute phase and CXC chemokine responses to experimental stroke and exacerbates brain damage via interleukin-1- and neutrophil-dependent mechanisms. *J. Neurosci.* 27: 4403–4412.
- Dinkel, K., F. S. Dhabhar, and R. M. Sapolsky. 2004. Neurotoxic effects of polymorphonuclear granulocytes on hippocampal primary cultures. *Proc. Natl. Acad. Sci. USA* 101: 331–336.
- Nguyen, H. X., T. J. O'Barr, and A. J. Anderson. 2007. Polymorphonuclear leukocytes promote neurotoxicity through release of matrix metalloproteinases, reactive oxygen species, and TNF- α . *J. Neurochem.* 102: 900–912.
- Shaw, S. K., S. A. Owolabi, J. Bagley, N. Morin, E. Cheng, B. W. LeBlanc, M. Kim, P. Harty, S. G. Waxman, and C. Y. Saab. 2008. Activated polymorphonuclear cells promote injury and excitability of dorsal root ganglia neurons. *Exp. Neurol.* 210: 286–294.
- Brinkmann, V., U. Reichard, C. Goosmann, B. Fauler, Y. Uhlemann, D. S. Weiss, Y. Weinrauch, and A. Zychlinsky. 2004. Neutrophil extracellular traps kill bacteria. *Science* 303: 1532–1535.
- Boutin, H., R. A. LeFeuvre, R. Horai, M. Asano, Y. Iwakura, and N. J. Rothwell. 2001. Role of IL-1 α and IL-1 β in ischemic brain damage. *J. Neurosci.* 21: 5528–5534.
- Allan, S. M., L. C. Parker, B. Collins, R. Davies, G. N. Luheshi, and N. J. Rothwell. 2000. Cortical cell death induced by IL-1 is mediated via actions in the hypothalamus of the rat. *Proc. Natl. Acad. Sci. USA* 97: 5580–5585.
- Lawrence, C. B., S. M. Allan, and N. J. Rothwell. 1998. Interleukin-1 β and the interleukin-1 receptor antagonist act in the striatum to modify excitotoxic brain damage in the rat. *Eur. J. Neurosci.* 10: 1188–1195.
- McCluskey, L., S. Campbell, D. Anthony, and S. M. Allan. 2008. Inflammatory responses in the rat brain in response to different methods of intra-cerebral administration. *J. Neuroimmunol.* 194: 27–33.
- Thornton, P., B. W. McColl, A. Greenhalgh, A. Denes, S. M. Allan, and N. J. Rothwell. 2010. Platelet interleukin-1 α drives cerebrovascular inflammation. *Blood* 115: 3632–3639.
- Losman, M. J., T. M. Fasy, K. E. Novick, and M. Monestier. 1992. Monoclonal autoantibodies to subnucleosomes from a MRL/Mp(-)/+ mouse. Oligoclonality of the antibody response and recognition of a determinant composed of histones H2A, H2B, and DNA. *J. Immunol.* 148: 1561–1569.
- Losman, M. J., T. M. Fasy, K. E. Novick, and M. Monestier. 1993. Relationships among antinuclear antibodies from autoimmune MRL mice reacting with histone H2A-H2B dimers and DNA. *Int. Immunol.* 5: 513–523.
- Arruda, M. A., A. G. Rossi, M. S. de Freitas, C. Barja-Fidalgo, and A. V. Graça-Souza. 2004. Heme inhibits human neutrophil apoptosis: involvement of phosphoinositide 3-kinase, MAPK, and NF- κ B. *J. Immunol.* 173: 2023–2030.
- Rane, M. J., Y. Pan, S. Singh, D. W. Powell, R. Wu, T. Cummins, Q. Chen, K. R. McLeish, and J. B. Klein. 2003. Heat shock protein 27 controls apoptosis by regulating Akt activation. *J. Biol. Chem.* 278: 27828–27835.
- Sunil, V. R., A. J. Connor, N. Lavnikova, C. R. Gardner, J. D. Laskin, and D. L. Laskin. 2002. Acute endotoxemia prolongs the survival of rat lung neutrophils in response to 12-O-tetradecanoyl-phorbol 13-acetate. *J. Cell. Physiol.* 190: 382–389.
- McGettrick, H. M., J. M. Lord, K. Q. Wang, G. E. Rainger, C. D. Buckley, and G. B. Nash. 2006. Chemokine- and adhesion-dependent survival of neutrophils after transmigration through cytokine-stimulated endothelium. *J. Leukoc. Biol.* 79: 779–788.
- Watson, R. W., O. D. Rotstein, A. B. Nathens, J. Parodo, and J. C. Marshall. 1997. Neutrophil apoptosis is modulated by endothelial transmigration and adhesion molecule engagement. *J. Immunol.* 158: 945–953.
- Remijsen, Q., T. W. Kuijpers, E. Wirawan, S. Lippens, P. Vandenabeele, and T. Vanden Berghe. 2011. Dying for a cause: NETosis, mechanisms behind an antimicrobial cell death modality. *Cell Death Differ.* 18: 581–588.
- Mitroulis, I., K. Kambas, A. Chrysanthopoulou, P. Skendros, E. Apostolidou, I. Kourtzelis, G. I. Drosos, D. T. Boumpas, and K. Ritis. 2011. Neutrophil extracellular trap formation is associated with IL-1 β and autophagy-related signaling in gout. *PLoS ONE* 6: e29318.
- Narasaraju, T., E. Yang, R. P. Samy, H. H. Ng, W. P. Poh, A. A. Liew, M. C. Phoon, N. van Rooijen, and V. T. Chow. 2011. Excessive neutrophils and neutrophil extracellular traps contribute to acute lung injury of influenza pneumonia. *Am. J. Pathol.* 179: 199–210.
- Villanueva, E., S. Yalavarthi, C. C. Berthier, J. B. Hodgson, R. Khandpur, A. M. Lin, C. J. Rubin, W. Zhao, S. H. Olsen, M. Klinker, et al. 2011. Netting neutrophils induce endothelial damage, infiltrate tissues, and expose immunostimulatory molecules in systemic lupus erythematosus. *J. Immunol.* 187: 538–552.
- Kumari, R., L. B. Willing, S. D. Patel, K. A. Baskerville, and I. A. Simpson. 2011. Increased cerebral matrix metalloproteinase-9 activity is associated with compromised recovery in the diabetic db/db mouse following a stroke. *J. Neurochem.* 119: 1029–1040.
- Stowe, A. M., T. L. Adair-Kirk, E. R. Gonzales, R. S. Perez, A. R. Shah, T. S. Park, and J. M. Gidday. 2009. Neutrophil elastase and neurovascular injury following focal stroke and reperfusion. *Neurobiol. Dis.* 35: 82–90.
- Yousefi, S., C. Mihalache, E. Kozlowski, I. Schmid, and H. U. Simon. 2009. Viable neutrophils release mitochondrial DNA to form neutrophil extracellular traps. *Cell Death Differ.* 16: 1438–1444.
- Urban, C. F., D. Ermert, M. Schmid, U. Abu-Abed, C. Goosmann, W. Nacken, V. Brinkmann, P. R. Jungblut, and A. Zychlinsky. 2009. Neutrophil extracellular traps contain calprotectin, a cytosolic protein complex involved in host defense against *Candida albicans*. *PLoS Pathog.* 5: e1000639.
- Heinz, A., M. C. Jung, G. Jahreis, A. Rusciani, L. Duca, L. Debelle, A. S. Weiss, R. H. Neubert, and C. E. Schmelzer. 2012. The action of neutrophil serine proteases on elastin and its precursor. *Biochimie* 94: 192–202.
- Wewer, C., A. Seibt, H. Wollburg, L. Greune, M. A. Schmidt, J. Berger, H. J. Galla, U. Quitsch, C. Schwerk, H. Schroten, and T. Tenenbaum. 2011. Transcellular migration of neutrophil granulocytes through the blood-cerebrospinal fluid barrier after infection with *Streptococcus suis*. *J. Neuroinflammation* 8: 51.
- Gurney, K. J., E. Y. Estrada, and G. A. Rosenberg. 2006. Blood-brain barrier disruption by stromelysin-1 facilitates neutrophil infiltration in neuroinflammation. *Neurobiol. Dis.* 23: 87–96.
- Kim, S., P. Ubel, and R. De Vries. 2009. Pruning the regulatory tree. *Nature* 457: 534–535.
- Pham, C. T. 2006. Neutrophil serine proteases: specific regulators of inflammation. *Nat. Rev. Immunol.* 6: 541–550.
- Urban, C. F., U. Reichard, V. Brinkmann, and A. Zychlinsky. 2006. Neutrophil extracellular traps capture and kill *Candida albicans* yeast and hyphal forms. *Cell. Microbiol.* 8: 668–676.
- Worthmann, H., A. B. Tryc, M. Deb, A. Goldbecker, Y. T. Ma, A. Tountopoulou, R. Lichtinghagen, and K. Weissenborn. 2010. Linking infection and inflammation in acute ischemic stroke. *Ann. N. Y. Acad. Sci.* 1207: 116–122.
- McColl, B. W., S. M. Allan, and N. J. Rothwell. 2009. Systemic inflammation, inflammation and acute ischemic stroke. *Neuroscience* 158: 1049–1061.
- Cardoso, F. L., D. Brites, and M. A. Brito. 2010. Looking at the blood-brain barrier: molecular anatomy and possible investigation approaches. *Brain Res. Brain Res. Rev.* 64: 328–363.
- Denes, A., R. Vidyasagar, J. Feng, J. Narvainen, B. W. McColl, R. A. Kauppinen, and S. M. Allan. 2007. Proliferating resident microglia after focal cerebral ischemia in mice. *J. Cereb. Blood Flow Metab.* 27: 1941–1953.
- Borregaard, N., K. Lollike, L. Kjeldsen, H. Sengeløv, L. Bastholm, M. H. Nielsen, and D. F. Bainton. 1993. Human neutrophil granules and secretory vesicles. *Eur. J. Haematol.* 51: 187–198.
- Papayannopoulos, V., K. D. Metzler, A. Hakkim, and A. Zychlinsky. 2010. Neutrophil elastase and myeloperoxidase regulate the formation of neutrophil extracellular traps. *J. Cell Biol.* 191: 677–691.
- Fuchs, T. A., U. Abed, C. Goosmann, R. Hurwitz, I. Schulze, V. Wahn, Y. Weinrauch, V. Brinkmann, and A. Zychlinsky. 2007. Novel cell death program leads to neutrophil extracellular traps. *J. Cell Biol.* 176: 231–241.
- Zhang, Q., K. Itagaki, and C. J. Hauser. 2010. Mitochondrial DNA is released by shock and activates neutrophils via p38 map kinase. *Shock* 34: 55–59.



Supplementary Figure 1. Recruitment of neutrophils and vascular activation are IL-1 dependent. (a) Schematic showing cortical regions from hemispheres ipsilateral (grey left region) or contralateral (white right region) to brain infarct used for ICAM-1 immunocytochemistry (lower panels, scale bar 100 μ m, inner panel, scale bar 20 μ m). (b) Numbers of neutrophils (SJC-positive cells) in WT and IL-1 $\alpha/\beta^{-/-}$ mice were immunolocalised and (c) quantified in cortical regions 24 h after MCAo (scale bar 100 μ m). (d) Transmigration of neutrophils across bEnd5 cells activated with 10ng/ml

dc_2027_22

IL-1 β (4 h) is not altered in comparison to bEnd.5 activated with 100ng/ml of IL-1 β (4 h) after 24 h of transmigration. (e) Brain homogenates of WT and IL-1 $\alpha/\beta^{-/-}$ mice harvested 24 h after exposure to MCAo were assayed for levels of ICAM-1, or (f) VCAM-1 by ELISA. (g) In WT mice, neutrophils localised to regions surrounding activated cerebral endothelium (ICAM-1-positive vessels, scale bar 25 μ m) (h) Cellular ICAM-1 and VCAM-1 levels detected by (i) Semi-quantitative Western blot analysis on lysates of untreated or IL-1 β -treated bEnd.5, (ii) a significant fold increase in both ICAM-1 and VCAM-1 after neutrophil transmigration was observed. Bars represent the mean data \pm SEM for a minimum of 3 independent experiments carried out on separate cultures. *P<0.05 (one-way ANOVA, with a Bonferroni *post hoc* test).

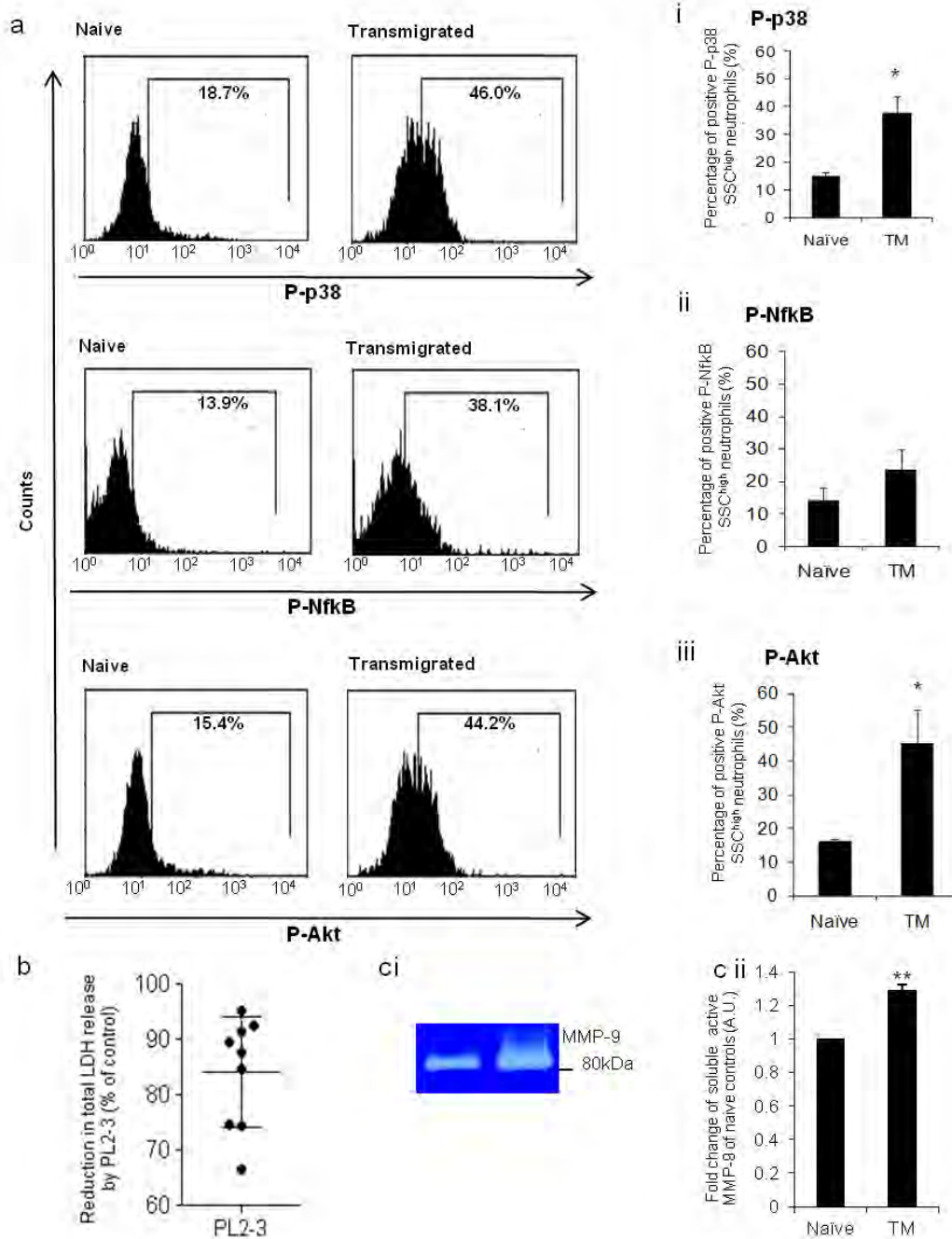


Supplementary Figure 2. Altered phenotype of transmigrated neutrophils cannot be attributed to cell death or IL-1 carry-over (a) Isolation of Ly6G-positive neutrophils from the bone marrow (i) original suspension before purification resulted in a cell suspension shown in (ii) containing 96 % CD11b/SSC^{high} cells as demonstrated by flow cytometry. (b) Transmigration of neutrophils across MBECs and brain endothelioma cells (bEnd5) activated with IL-1 α (100ng/ml, 4 h). (c) Transmigration of neutrophils across MBECs treated with IL-1 β (100 ng/ml) in the absence or presence of IL-1Ra (100 ng/ml) after 24 h. (d) Quantification of total LDH release from neurons 24 h after application of 120,000 naive neutrophils/cm² in the absence or presence of increasing concentrations of IL-1 β . (e) Level of cell death of

naive neutrophils and transmigrated (TM) neutrophils was determined using trypan blue and expressed a percentage of positive cells within the total population observed.

(f) Quantification of total LDH release from neurons 24 h after application of 120,000 cells/cm² non-migrated neutrophils, which had been incubated with IL-1 α -activated brain endothelial cells (NM+) or transmigrated neutrophils (TM) that had migrated across IL-1 α -stimulated endothelial cells (bEnd.5). Red dotted line indicates neuronal death induced by 600 μ M NMDA. (g) Quantification of total LDH release and (h) MTT metabolism in neuronal cultures after addition of neutrophils collected after *in vivo* transendothelial migration in thioglycollate induced peritonitis. (i) Neurotoxicity of conditioned medium from transmigrated neutrophils in presence of 30U/ml DNase I. Red dotted line indicates neuronal death induced by 600 μ M NMDA.

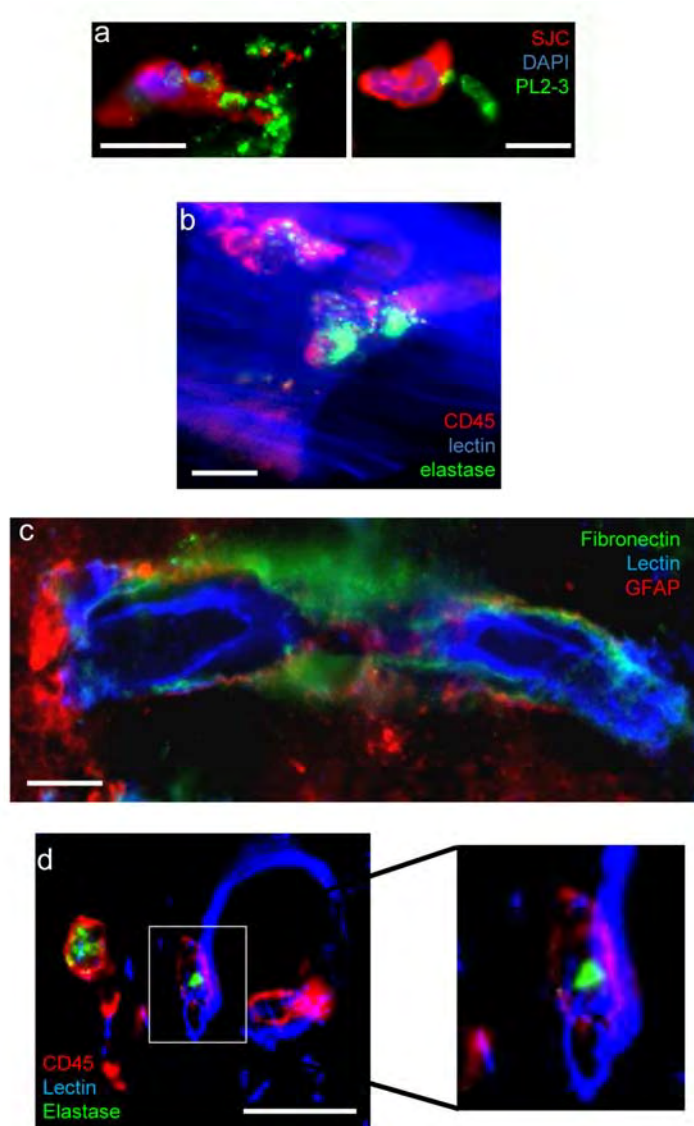
Bars represent the mean data \pm SEM for a minimum of 3 independent experiments carried out on separate cultures, *P<0.05, **P<0.01 (one-way ANOVA, with a Bonferroni *post hoc* test).



Supplementary Figure 3. Neutrophils migrated across IL-1 β -activated cerebrovascular endothelium show altered viability and phenotype in comparison to naïve controls (a) Flow cytometry demonstrated a significant increase in the key cell signaling proteins (i) P-p38 and (iii) P-Akt and a trend towards

dc_2027_22

increased (ii) P-NF κ B, present in CD11b/SSC^{high} transmigrated (TM) neutrophils vs naïve neutrophils. Representative histograms (left) are shown from three independent experiments (graphs, right). Mean values represent a minimum of three independent experiments. Error bars: SEM, *P < 0.05 (). (b) Presence of PL2-3 (15 μ g/ml) in the conditioned medium of transmigrated neutrophils results in a trend to reduced neurotoxicity in neuronal cultures after 24 h as determined using an LDH assay. (c) Conditioned medium from transmigrated neutrophils contains greater levels of active MMP-9 than naïve neutrophil conditioned medium, as determined through gelatine gel zymography. Bars represent the mean data +/- SEM for a minimum of 3 independent experiments carried out on separate cultures *P<0.05, **P<0.01 (Student's t-test or one-way ANOVA, with a Bonferroni *post hoc* test).



Supplementary Figure 4. Neutrophil recruitment in acute brain injury *in vivo*.

(a) Neutrophils (SJC) showing extracellular PL2-3 immunostaining after intra-striatal LPS (left) or AMPA+IL-1 injection (right). Scale bars, 10 μ m. (b) Recruited inflammatory cells (CD45) containing neutrophil elastase are associated with blood vessels (lectin) in the brain *in vivo* after stereotaxic injection of LPS (scale bar, 10 μ m). (c) Immunofluorescence showing disintegration of the perivascular basement membrane (fibronectin, green) and detachment of astrocyte endfeet (GFAP, red) from the endothelial monolayer (lectin, blue) after MCAo (scale bar, 20 μ m). (d)

dc_2027_22

Immunofluorescence showing perivascular neutrophil elastase containing (green) inflammatory cells (CD45, red) around the endothelial monolayer (lectin, blue) in the inflamed cerebral cortex (scale bar, 20 μ m).

Movies 1-2.

Real-time imaging of neuronal loss induced by the application of transmigrated neutrophils. Cortical neurons were labelled with CellTracker Red and visualised every 30 sec with (movie 1) or without (movie 2) application of transmigrated neutrophils (added $t = 4$ min, movie 1). Arrowheads (movie 1) indicate the position of neuronal cell bodies (highlighted in Fig. 2c), which become rounded, swollen and necrotic, losing CellTracker Red dye within 6 h of applying transmigrated neutrophils. Arrow (movie 1) indicates the position of a neuronal process (highlighted in Fig. 2c) which becomes fragmented and degraded by closely-opposed transmigrated neutrophils. After application of transmigrated neutrophils, several neutrophils become labelled with the CellTracker Red dye, which may have leaked from necrotic neurons.

RESEARCH ARTICLE

The NKCC1 ion transporter modulates microglial phenotype and inflammatory response to brain injury in a cell-autonomous manner

Krisztina Tóth^{1,2}, Nikolett Lénárt¹, Péter Berki^{1,2,3}, Rebeka Fekete¹, Eszter Szabadits¹, Balázs Pósfai^{1,2}, Csaba Cserép¹, Ahmad Alatshan^{4,5}, Szilvia Benkó^{4,5}, Dániel Kiss⁶, Christian A. Hübner⁷, Attila Gulyás³, Kai Kaila⁸, Zsuzsanna Környei¹, Ádám Dénes^{1*}

1 Momentum Laboratory of Neuroimmunology, Institute of Experimental Medicine, Budapest, Hungary, **2** János Szentágotthai Doctoral School of Neurosciences, Semmelweis University, Budapest, Hungary, **3** Laboratory of Cerebral Cortex Research, Institute of Experimental Medicine, Budapest, Hungary, **4** Department of Physiology, Faculty of Medicine, University of Debrecen, Debrecen, Hungary, **5** Doctoral School of Molecular Cellular and Immune Biology, Faculty of Medicine, University of Debrecen, Debrecen, Hungary, **6** Software Engineering Institute, John von Neumann Faculty of Informatics, Óbuda University, Budapest, Hungary, **7** University Hospital Jena, Friedrich Schiller University, Jena, Germany, **8** Molecular and Integrative Biosciences and Neuroscience Center (HiLIFE), University of Helsinki, Helsinki, Finland

* denes.adam@koki.hu



OPEN ACCESS

Citation: Tóth K, Lénárt N, Berki P, Fekete R, Szabadits E, Pósfai B, et al. (2022) The NKCC1 ion transporter modulates microglial phenotype and inflammatory response to brain injury in a cell-autonomous manner. *PLoS Biol* 20(1): e3001526. <https://doi.org/10.1371/journal.pbio.3001526>

Academic Editor: Ulrich Dirnagl, Charité Universitätsmedizin Berlin, GERMANY

Received: January 22, 2021

Accepted: January 4, 2022

Published: January 27, 2022

Copyright: © 2022 Tóth et al. This is an open access article distributed under the terms of the [Creative Commons Attribution License](https://creativecommons.org/licenses/by/4.0/), which permits unrestricted use, distribution, and reproduction in any medium, provided the original author and source are credited.

Data Availability Statement: All relevant data are within the paper and its [Supporting Information](#) files.

Funding: This work was supported by "Momentum" research grant from the Hungarian Academy of Sciences (LP2016-4/2016 to A.D.; <https://mta.hu/lendulet>) and ERC-CoG 724994 (to A.D.; <https://erc.europa.eu/>), with contribution from 2019-2.1.7-ERA-NET-2020-00004 (<https://nkfi.gov.hu>). Additionally, this work was funded by Hungarian National Scientific Research Fund

Abstract

The NKCC1 ion transporter contributes to the pathophysiology of common neurological disorders, but its function in microglia, the main inflammatory cells of the brain, has remained unclear to date. Therefore, we generated a novel transgenic mouse line in which microglial NKCC1 was deleted. We show that microglial NKCC1 shapes both baseline and reactive microglia morphology, process recruitment to the site of injury, and adaptation to changes in cellular volume in a cell-autonomous manner via regulating membrane conductance. In addition, microglial NKCC1 deficiency results in NLRP3 inflammasome priming and increased production of interleukin-1 β (IL-1 β), rendering microglia prone to exaggerated inflammatory responses. In line with this, central (intracortical) administration of the NKCC1 blocker, bumetanide, potentiated intracortical lipopolysaccharide (LPS)-induced cytokine levels. In contrast, systemic bumetanide application decreased inflammation in the brain. Microglial NKCC1 KO animals exposed to experimental stroke showed significantly increased brain injury, inflammation, cerebral edema and worse neurological outcome. Thus, NKCC1 emerges as an important player in controlling microglial ion homeostasis and inflammatory responses through which microglia modulate brain injury. The contribution of microglia to central NKCC1 actions is likely to be relevant for common neurological disorders.

(NKFIH-OTKA Grant No. K131844 to S.B.), the János Bolyai Research Scholarship of the Hungarian Academy of Sciences (to C.C. and N.L., BO/00558/19/5; <https://mta.hu/bolyai-osztondij/bolyai-janos-kutatasi-osztondij-105319>), ÚNKP-20-3-II (to B.P.) and ÚNKP-21-5 (to C.C. and N.L.; <http://www.unkp.gov.hu/unkp-rol>) of the New National Excellence Program of the Ministry for Innovation and Technology, Hungary; German Research Foundation (SPP 1665; <https://www.dfg.de/en/>) and the Federal Ministry of Education and Research (NEURON ACRoBAT 01EW1706) to C.A.H.; and the Academy of Finland and Sigrid Jusélius Foundation (<https://www.sigridjuselius.fi/en/>) to K.K.. Prepared with the professional support of the Doctoral Scholarship Program of the Cooperative Doctoral Program of the Ministry of Innovation and Technology Financed from The National Research, Development and Innovation Fund (to B.P.). A.A. holds a Stipendium Hungaricum Scholarship from the Government of Hungary (<https://stipendiumhungaricum.hu/>). The funders had no role in study design, data collection and analysis, decision to publish, or preparation of the manuscript.

Competing interests: The authors have declared that no competing interests exist.

Abbreviations: BBB, blood–brain barrier; CCA, common carotid artery; CCC, cation-chloride cotransporter; ECA, external carotid artery; FBS, fetal bovine serum; G-CSF, granulocyte colony stimulating factor; ICA, internal carotid artery; IL-1 α , interleukin-1 α ; IL-1 β , interleukin-1 β ; IL-6, interleukin-6; ip., intraperitoneal; KC, keratinocyte chemoattractant; KCC, K⁺-Cl⁻ cotransporter; LPS, lipopolysaccharide; MCAo, middle cerebral artery occlusion; M-CSF, macrophage colony-stimulating factor; NKCC1, Na⁺-K⁺-2Cl⁻ cotransporter; NLRP3, NLR family pyrin domain containing 3; PB, phosphate buffer; PBS, phosphate-buffered saline; qRT-PCR, real-time quantitative PCR; TNF- α , tumor necrosis factor α ; VRAC, volume-regulated anion channel.

Introduction

Members of the plasmalemmal cation-chloride cotransporter (CCC) family, such as the neuron-specific K⁺/Cl⁻ extruder, KCC2, and the ubiquitously expressed Na⁺-K⁺-2Cl⁻ cotransporter, NKCC1 (coded by the *Slc12a2* gene), have received a steeply increasing amount of attention in research on central nervous system (CNS) diseases, ranging from neuropsychiatric diseases to epilepsy, stroke, and dementia [1–6]. Notably, there is an abundance of studies, which have shown that the mRNA and protein expression levels as well as the functionality of NKCC1 are enhanced in injured and posttraumatic neurons [7,8]. This, in turn, has raised the obvious possibility that assuming a pathophysiological role for NKCC1, therapeutic actions might be achieved by pharmacological inhibition of this transporter. Indeed, data in a number of experimental studies based on systemic application of the selective NKCC1 blocker, the loop diuretic bumetanide, have suggested that this drug has therapeutic actions in diverse neuropathological conditions. These include neonatal seizures, temporal lobe epilepsy, autism spectrum disorders, schizophrenia, and brain edema after traumatic or hypoxic/ischemic injury [1–4,7–12]. In most of these studies, bumetanide has been suggested to exert its therapeutic effects by acting directly on NKCC1 expressed in central neurons.

While bumetanide is routinely used to block neuronal NKCC1 in experiments performed *in vitro* [3,8,12], the view that the drug might have direct effects on central neurons *in vivo* has raised numerous questions. First, the poor pharmacokinetic properties of bumetanide, including a low penetration across the blood–brain barrier (BBB) implies that when applied systemically at clinically relevant doses, the drug may not reach pharmacologically relevant concentrations in the brain parenchyma, a prediction that has been experimentally verified [10,13,14]. Another important point in the present context is that NKCC1 is expressed within the immature and mature CNS mainly in nonneuronal cell types [15], such as oligodendrocytes and their precursors [16,17], ependymal cells, and astrocytes [18–21]. Thus, even if applied directly into brain tissue, bumetanide or any other NKCC1 blockers would be expected to inhibit this ion transporter in a wide variety of cell types.

Interestingly, common neurological disorders including those with altered NKCC1 activity [6,7,22] display broad neuroinflammatory changes. While the impact of NKCC1 function on inflammatory cytokine production has not been widely studied, emerging evidence indicates up-regulated NKCC1 expression in response to inflammatory stimuli (LPS, IL-1 β , TNF- α) [23–26]. Notably, while microglia are the main inflammatory cell type in the CNS, there is no information about the functional role of NKCC1 in microglia and whether microglial NKCC1 could provide a significant contribution to central NKCC1 actions under inflammatory conditions or after brain injury.

In the healthy brain, microglia regulate a wide variety of neuronal functions, whereas altered microglial activity is linked with the pathophysiology of most common brain disorders, such as neurodegenerative and psychiatric diseases, stroke, and epilepsy [27–33]. Extracellular accumulation of potassium is related to diverse neuropathological alterations [32,34], and the contribution of microglial potassium channels and transporters to microglial activity is widely recognized. These include membrane-expressed potassium channels (Kv1.3, THIK-1, Kir2.1) that regulate microglial motility, immune surveillance, and cytokine release, among others [35,36]. Moreover, changes in intracellular potassium and chloride levels are associated with inflammasome activation contributing to the regulation of interleukin-1 β (IL-1 β) release [37–39]. Interestingly, recent transcriptomic data verified high-level NKCC1 expression in microglia [21,40]. However, currently no experimental data are available on the function of microglial NKCC1 under physiological and pathological conditions. To this end, we studied whether central and systemic NKCC1 blockade impact on central inflammatory changes differently

and tested the hypothesis that NKCC1 is involved in the regulation of microglial inflammatory mediator production, neuroinflammation, and brain injury.

Results

Systemic and central blockade of NKCC1 regulate LPS-induced inflammatory cytokine production in the brain in an opposite manner

To investigate whether systemic blockade of NKCC1 actions by bumetanide could alter inflammatory responses in the CNS, we injected mice either intraperitoneally or intracortically with bacterial lipopolysaccharide (LPS), while NKCC1 actions were blocked by systemic (intraperitoneal (ip.), 2 mg/kg) bumetanide administration (Fig 1A). As expected, LPS administration by ip. injection triggered marked inflammation in the spleen and the liver (S1A Fig), but caused low cytokine production in cortical brain tissues, which was not influenced by ip. bumetanide treatment (Fig 1A). However, bumetanide resulted in a small but significant increase in LPS-induced IL-1 β production in the spleen (S1A Fig). In contrast, intracortical LPS administration triggered a robust inflammatory response in the brain as seen earlier [41], which was reduced by ip. bumetanide treatment. This was demonstrated by lower G-CSF, KC, IL-1 β , and IL-1 α levels in the brain (by 39.8%, 43%, 54.6%, and 41%, respectively), while systemic cytokine levels were not altered (S1A Fig).

To compare the effects of systemic versus central NKCC1 blockade by bumetanide, we next investigated the impact of central (intracortical) bumetanide administration on LPS-induced cytokine responses, by coinjecting bumetanide with LPS (50 μ M bumetanide in 200 nl final volume, rate: 200 nl/10 minutes; Fig 1B) into the cerebral cortex. As expected, intracortical LPS without bumetanide resulted in a 20- to 50-fold increase in inflammatory cytokines/chemokines in the cerebral cortex compared to vehicle. Surprisingly, on top of this, bumetanide markedly potentiated LPS-induced G-CSF, KC, IL-1 β , and IL-1 α levels in the brain (by 86.1%, 31.2%, 82.5%, and 72.4%, respectively), in sharp contrast with the effects of ip. bumetanide treatment (Fig 1A). Intracortical bumetanide had no effect on systemic cytokine levels (S1B Fig).

We next tested whether the effects of central bumetanide administration on increasing cytokine production might be explained by altered LPS-induced recruitment of leukocytes. However, while flow cytometry revealed increased number of infiltrating CD45^{high} leukocytes, in particular CD11b⁺ Ly6G^{high} granulocytes, and CD11b⁺ Ly6G⁻ Ly6C^{high} monocytes in response to central LPS injection compared to vehicle administration (Fig 1C), this was not altered by central bumetanide. The number of CD45^{int} CD11b⁺ microglia was not affected either (Fig 1C), indicating that the increased LPS-induced cytokine production observed upon central bumetanide treatment is not due to altered inflammatory cell numbers in the cerebral cortex. Unbiased densitometric analysis revealed that GFAP and AQP4 immunopositivity 24 hours after intracortical LPS injection were not altered by central bumetanide treatment (S2 Fig), suggesting that while bumetanide may also act on astroglial NKCC1 [18–20], marked changes in astrocyte phenotypes or perivascular astrocyte endfeet are unlikely to explain the effect of bumetanide on central inflammatory responses in the present study.

Microglia are the primary source of inflammatory cytokines in a number of neuropathologies, and IL-1 β , also produced by microglia, is a key proinflammatory cytokine regulating the brain's cytokine network [42,43]. To investigate the cellular source of IL-1 β in this experimental model, we injected LPS intracortically into Cx3CR1^{+/GFP} (microglia reporter) mice. Multi-label immunostainings confirmed that Cx3CR1-GFP microglia coexpressing P2Y12R and CD45 displayed cytoplasmic IL-1 α and IL-1 β production (Fig 1D). These findings collectively suggested that microglia are likely to be major mediators of central bumetanide actions under inflammatory conditions. Supporting this, central LPS administration resulted in a significant

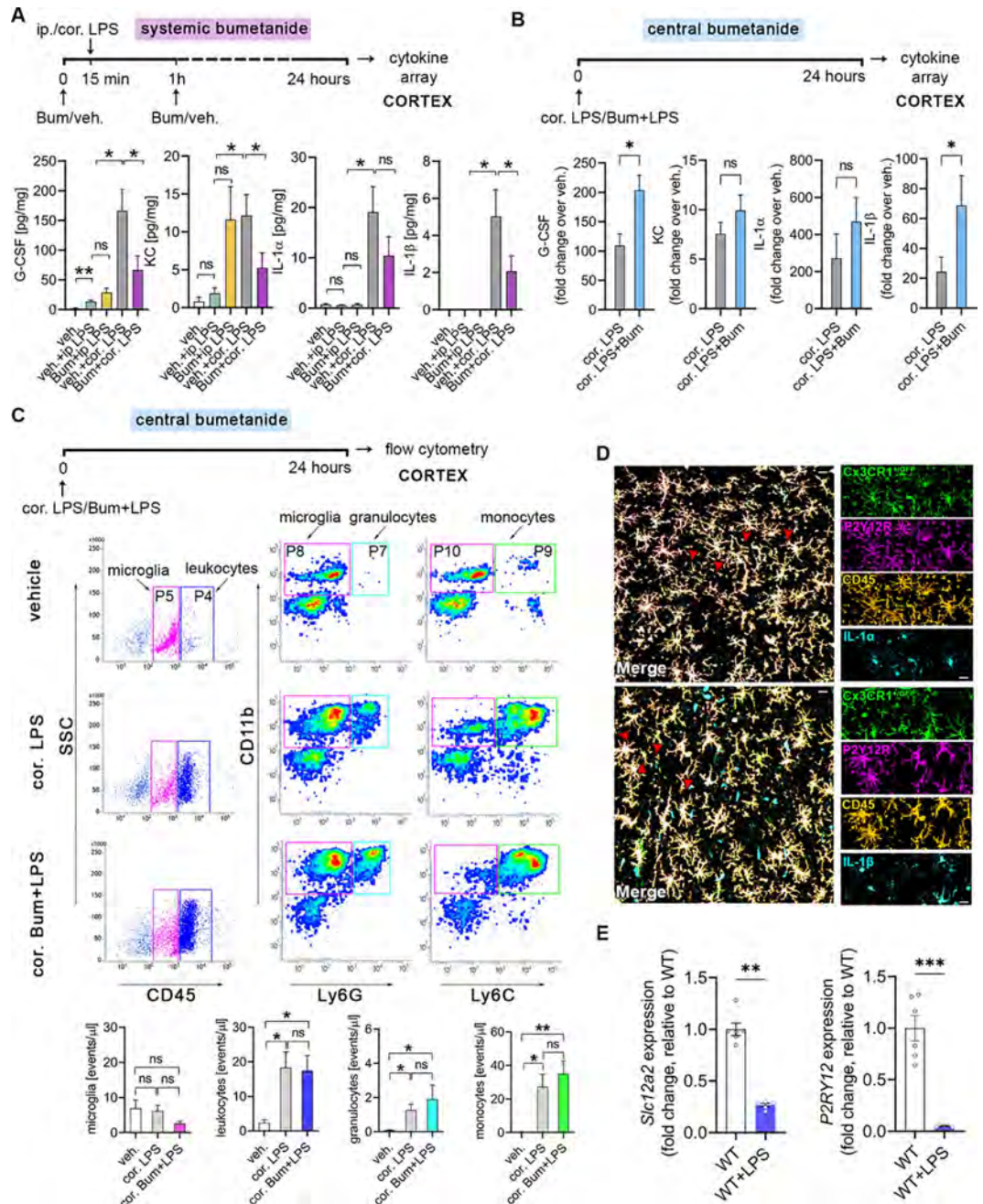


Fig 1. Systemic and central (intracortical) blockade of NKCC1 regulate LPS-induced inflammatory cytokine production in the brain in an opposite manner. (A) Mice were subjected to either ip. or cor. LPS injections, while NKCC1 was blocked by ip. Bum administration. Central LPS injection triggers high cytokine (G-CSF, IL-1 α , IL-1 β) and KC responses in the brain compared to ip. LPS injection, which is blocked by ip. Bum administration. (B) Central NKCC1 inhibition by cor. Bum administration significantly increases G-CSF and IL-1 β levels. See also S1 Fig for effects of systemic vs. central blockade of NKCC1 on LPS-induced cytokine responses in the periphery. (C) Flow cytometric dot plots show that cortical administration of Bum does not affect the number of microglia (CD45^{int}/P5 gate), and recruitment of leukocytes (CD45^{high}/P4 gate), including monocytes (CD11b⁺, Ly6C^{high}/P9 gate), and granulocytes (CD11b⁺, Ly6G^{high}/P7 gate) upon central LPS injection. (D) The main source of IL-1 α and IL-1 β in the brain are microglia cells. Confocal images of Cx3CR1^{+/GFP} brain slices show IL-1 α -CD45-P2Y12R (above, red arrowheads) and IL-1 β -CD45-P2Y12R (below, red arrowheads) labeled cells after cortical LPS injection-induced inflammation. (E) NKCC1 (encoded by *Slc12a2*) and P2Y12R gene expression is down-regulated in microglia isolated from adult mice 24 hours after cisterna magna LPS application. (A) Kruskal–Wallis followed by Dunn’s multiple comparison test; **p* < 0.05; *N* (veh.) = 5, *N* (veh. + ip. LPS) = 5, *N* (Bum + ip. LPS) = 5, *N* (veh. + cor. LPS) = 5, *N* (Bum + cor. LPS) = 9. (B) Unpaired *t* test; **p* < 0.05; *N* = 9/group; data were pooled from two independent

studies. (C) One-way ANOVA followed by Tukey's multiple comparison test; * $p < 0.05$; N (veh.) = 5, N (cor. LPS) = 6, N (cor. Bum + LPS) = 6. (D) Scale: 25 μm . (E) Unpaired t test; ** $p < 0.01$, *** $p < 0.001$; N (WT) = 6, N (WT + LPS) = 5. Data underlying this figure can be found in [S1 Data](#). Bum, bumetanide; cor., cortical; ip., intraperitoneal; ns, not significant; veh., vehicle; WT, wild type.

<https://doi.org/10.1371/journal.pbio.3001526.g001>

decrease of NKCC1 (encoded by *Slc12a2*) mRNA levels, along with a decline of P2Y₁₂R mRNA, a key purinergic receptor reportedly associated with homeostatic microglial actions, microglial activation, and response to injury ([Fig 1E](#)) [[31,44–46](#)].

Deletion of microglial NKCC1 markedly impacts on baseline cell morphology and alters transformation to reactive microglia

Available RNA-seq data as well as our results ([Fig 1E](#)) demonstrate that the *Slc12a2* gene is expressed by microglia [[21,40](#)]. In line with this, our further qPCR data revealed that mRNA levels of NKCC1 in microglial cells isolated from newborn (1.052 ± 0.054) or adult (0.89 ± 0.098) C57BL/6J mice are comparable to those in neural progenitors derived from embryonic brains (1.30 ± 0.05 ; [Fig 2A](#)). However, NKCC1 mRNA expression markedly decreased when cells were grown in culture for 10 days ([Fig 2A](#)), making it difficult to study NKCC1 function in microglia using in vitro techniques (see also [[58](#)]).

To study the functional role of NKCC1 in microglia in vivo, we generated a novel transgenic mouse line in which microglial NKCC1 was deleted ([Fig 2B](#)). *Slc12a2* expression in isolated microglia derived from tamoxifen-inducible microglial NKCC1 knockout (KO) mice was markedly reduced in comparison with wild-type (WT) littermates (WT: 1.46 ± 0.11 , KO: 0.50 ± 0.016 ; [Fig 2C](#)) as assessed by qPCR. Reduced NKCC1 protein expression was also confirmed by unbiased fluorescent density measurements after systematic random sampling of a great number of individual microglial cells from Iba1/NKCC1 stained slices. In fact, a discrete NKCC1 labeling was seen in the plasma membrane of microglial cells in WT mice, which was absent in microglial NKCC1 KO mice ([Fig 2D and 2E](#)).

Microglia are known to respond to physiological and pathological challenges with fast morphological transformation [[47](#)], while the role of NKCC1 in cell volume regulation has been highlighted in previous studies concerning other cell types [[48,49](#)]. To study the role of NKCC1 in microglial cell shape, we performed automated morphological analysis using perfusion-fixed brain sections obtained from WT and microglial NKCC1 KO mice ([Fig 2F and 2G](#)). First, we aimed to test whether microglial NKCC1 deficiency has any impact on baseline cell morphology. Our data revealed that NKCC1-deficient microglia displayed a 23.8% higher cell surface, 19% higher branch volume, and 33.5% more branches compared to WT cells ([Fig 2F and 2G](#)), while we observed no changes in the cell body volume of KO versus WT microglia ([Fig 2G](#)). According to these data, microglial NKCC1 is likely to be involved in shaping baseline cell morphology.

Microglial process motility is altered by central NKCC1 inhibition

To assess whether NKCC1 is involved in the regulation of dynamic microglial process surveillance and injury-induced microglial responses, we performed in vivo 2-photon imaging in microglia reporter Cx3CR1^{+/GFP} mice in combination with bumetanide treatment ([Fig 3](#)). We tracked pre-lesion (baseline) process motility followed by focal laser-induced lesioning, which was repeated after bumetanide administration into the cisterna magna in a different (undisturbed) part of the cerebral cortex in the same animals ([Fig 3A and 3B](#)). The cisterna magna application protocol had been extensively tested in previous studies for effective drug penetration into the brain parenchyma and direct actions on microglia by using PSB0739, a selective P2Y₁₂R antagonist [[31](#)].

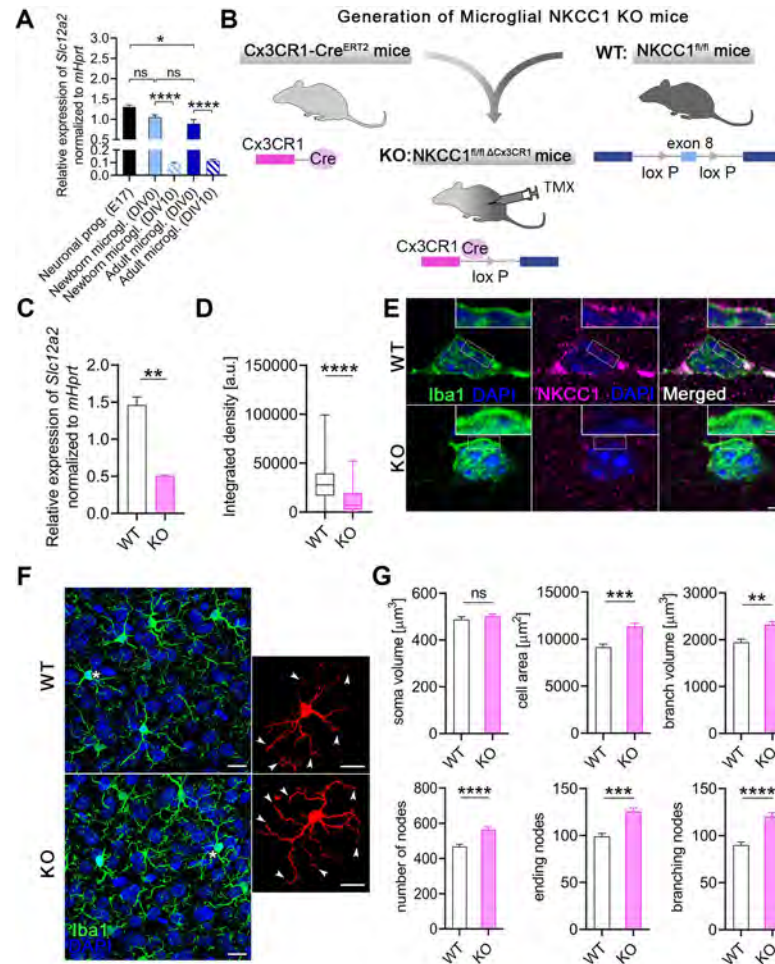


Fig 2. Deletion of microglial NKCC1 markedly impacts on baseline cell morphology and alters transformation to reactive microglia. (A) NKCC1 mRNA expression levels in newborn and adult microglia isolated from C57BL/6j mice compared to neural progenitors derived from E17 embryonic hippocampi. Note that NKCC1 mRNA levels decrease dramatically during in vitro maintenance (DIV10). (B) We generated a novel microglia-specific conditional NKCC1 KO transgenic mouse line by crossing NKCC1^{fl/fl} (exon 8 of the *Sclt2a2* gene was flanked by lox P sites) and Cx3CR1-Cre^{ERT2} mice. (C) NKCC1 mRNA levels in isolated NKCC1 KO microglia was markedly reduced in comparison to WT cells. (D, E) NKCC1 protein expression in a large number of randomly sampled NKCC1 KO microglia cells is markedly reduced compared to WT cells. Inserts show plasma membrane localization of NKCC1. (F, G) Automated morphological analysis and maximum intensity projections of confocal images. Inserts show cells marked with white asterisks in 3D. Arrowheads indicate altered branch structure of NKCC1 KO microglia. Automated morphological analysis shows that features of NKCC1-deficient microglia significantly differ from WT microglia. (A) One-way ANOVA, followed by Holm-Sidak's post hoc test. *N* (Neuronal progenitor) = 3, *N* (Newborn microglia DIV0) = 6, *N* (Newborn microglia DIV10) = 5, *N* (Adult microglia DIV0) = 7, *N* (Adult microglia DIV10) = 6. **: $p < 0.01$. (C) Unpaired *t* test, $N = 3/\text{group}$. **: $p < 0.01$. (D) Mann-Whitney test, N (WT) = 142 cells from 2 mice, N (KO) = 83 cells from 1 mouse. ****: $p < 0.0001$. (E) Scale: 2 μm , in inserts: 1 μm . (F, G) Scale: 25 μm ; Mann-Whitney test, N (WT) = 162 cells from 3 mice, N (KO) = 281 cells from 5 mice. **: $p < 0.01$, ***: $p < 0.001$, ****: $p < 0.0001$. Data underlying this figure can be found in [S1 Data](#). DIV, days in vitro; E17, embryonic day 17; KO, knockout; ns, not significant; TMX, tamoxifen; WT, wild type.

<https://doi.org/10.1371/journal.pbio.3001526.g002>

Bumetanide caused a small but observable (7%) increase in the mean velocity of microglial processes (Fig 3C). In contrast, lesion-induced recruitment of microglial processes showed a marked, 31.7% reduction after bumetanide treatment ($N = 7$) (Fig 3D and 3E and see [S1 Video](#)). These experiments indicate that beyond shaping cell morphology, microglial NKCC1 also regulates dynamic microglial actions both under physiological and pathological conditions.

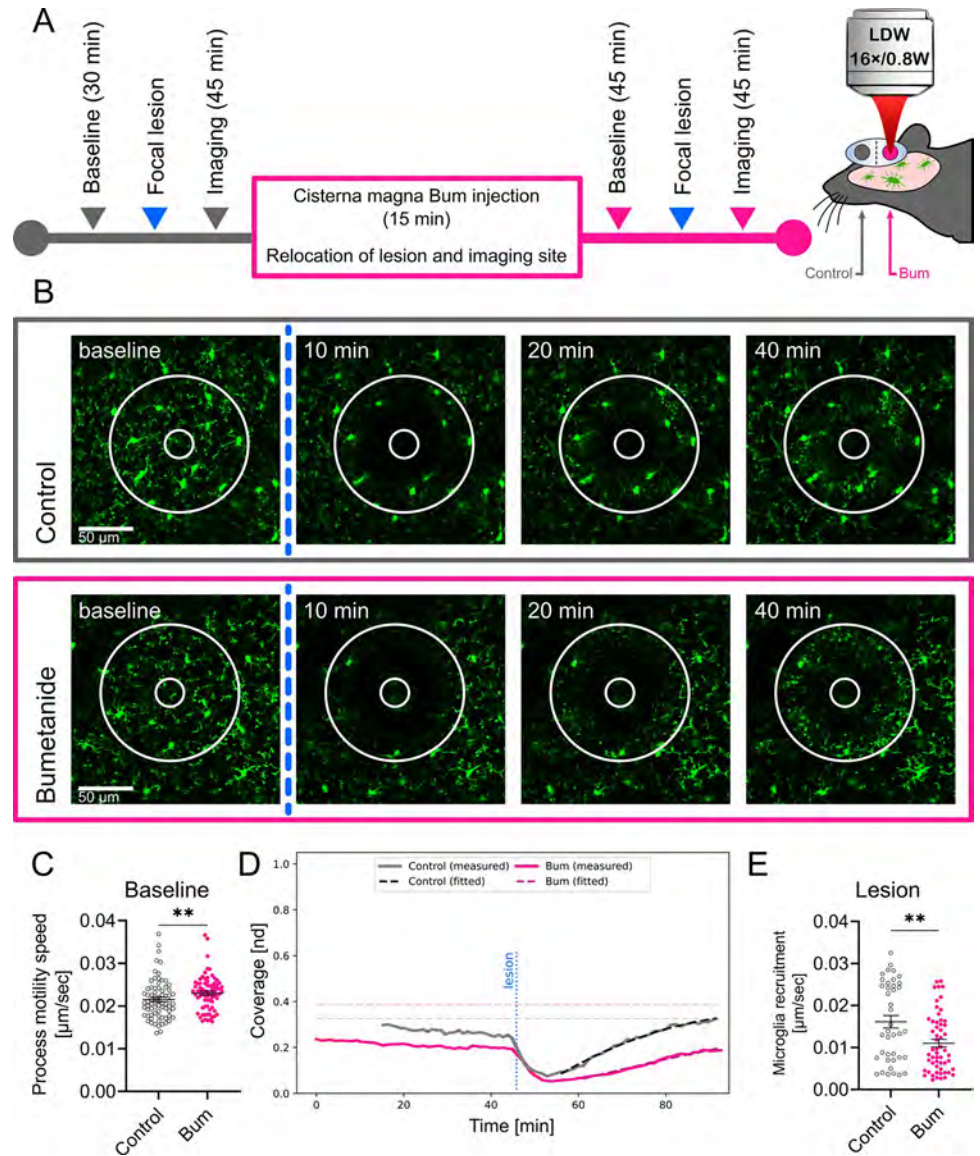


Fig 3. Microglial process dynamics and injury-induced process recruitment are altered by bumetanide. (A) Outline of the 2-photon imaging experiment performed in *Cx3CR1^{+/GFP}* (microglia reporter) mice. Imaging was performed to assess baseline microglial process motility and response to laser-induced injury followed by Bum administration into the cisterna magna and identical measurements at a different, undisturbed cortical region. (B) Representative images of microglial responses at selected time points, taken from *S1 Video*. The lesion site is marked with a circle that completely covers the area of the lesion. The ablation zone (i.e., the inner circle) was excluded from the analysis (see *Materials and methods*). (C) Mean base-state velocity distribution of processes from manual image tracking. Data show a 7% higher mean velocity of cell processes after Bum administration. (D) Evaluation of microglial process coverage over time in the lesion-centered circular area generated by a custom image analysis pipeline. Solid lines show the proportion of the area covered by microglial GFP signal. Dashed curves show the calculated values of coverage from the best-fitting curves. Horizontal lines are the predicted maximal coverage values for the lesion site; vertical line is the time point of the lesioning. (E) Calculated postlesion velocities of microglial process recruitment using automated image analysis followed by model fitting. Data show a significant decrease (31.7%) in mean frontline velocity of cells with Bum administration. (B) Scale: 50 µm. (C) Mann–Whitney test, $N_{\text{Control}} = 73$, $N_{\text{Bum}} = 76$ processes from 5 mice, **: $p < 0.01$. (E) Mann–Whitney test, $N_{\text{Control}} = 40$, $N_{\text{Bum}} = 56$ fitted values from 5 and 7 mice, respectively, **: $p < 0.01$. Data underlying this figure can be found in *S1 Data*. Bum, bumetanide.

<https://doi.org/10.1371/journal.pbio.3001526.g003>

The absence of microglial NKCC1 induces NLRP3 and potentiates inflammatory cytokine production in the cerebral cortex

To assess the effect of NKCC1 deletion on microglial inflammatory states and responses, we first examined the expression of IL-1 β and NLRP3. Assembly of the NLRP3 inflammasome is known to be a key step for processing of pro-IL-1 β by caspase-1, and the release of mature IL-1 β from microglia or macrophages [50,51]. qPCR data revealed elevated expression of both IL-1 β and NLRP3 in NKCC1 KO microglia even in the absence of inflammatory stimulus (Fig 4A). Next, we examined the impact of NKCC1 deficiency on morphological characteristics of microglia after activation by endotoxin that primes microglial inflammatory responses and leads to morphological transformation [52]. Unbiased, automated morphological analysis showed that both WT and NKCC1 KO microglia respond to intracortical LPS administration with dramatic morphological conversion (Fig 4B and 4C). However, NKCC1-deficient microglia were significantly smaller than their WT counterparts, displaying a 10% smaller cell surface, 12.5% smaller cell volume, and 13.7% smaller branch volume (Fig 4D). According to these data, microglial NKCC1 is likely to be involved in shaping cell morphology and regulation of cell volume after inflammatory challenges.

To test the impact of microglial NKCC1 deletion on the production of central inflammatory mediators, we examined LPS-induced cytokines and chemokines in microglial NKCC1 KO and WT mice 24 hours after intracortical LPS injections in brain homogenates (Fig 4E). Importantly, deletion of microglial NKCC1 markedly potentiated LPS-induced levels of G-CSF (3.53-fold), KC (2.12-fold), IL-1 α (3.98-fold), IL-1 β (3.96-fold), IL-6 (4.35-fold), and TNF- α (3-fold) in the cerebral cortex compared to controls (Fig 4E). In contrast, intracortical LPS treatment did not alter cytokine levels or T cell, B cell, monocyte, or granulocyte numbers in the spleen or liver (S3A–S3C Fig). Similarly to that seen after intracortical pharmacological inhibition of NKCC1 by bumetanide, neither the number of CD11b⁺ CD45^{int} microglial cells nor blood-borne CD11b⁺ CD45^{high} leukocytes, CD11b⁺ Ly6C^{high} monocytes, or CD11b⁺ Ly6G^{high} granulocytes were altered as a result of microglial NKCC1 deficiency (Fig 4F). We also tested whether increased baseline IL-1 β and NLRP3 mRNA levels seen in NKCC1 KO microglia (Fig 4A) were maintained in these cells 24 hours after intracisternal LPS administration. We found that significantly increased NLRP3 mRNA levels (by 100%) were still present in NKCC1 KO microglia isolated from the brain by using magnetic separation, while a strong trend ($p = 0.057$) to increased IL-1 β mRNA by 50% was also observed (Fig 4G). These findings corroborated our previous results on cortical NKCC1 blockade by bumetanide, confirming that the inhibition of microglial NKCC1 markedly potentiates central cytokine production upon inflammatory challenges, with a likely role for the NLRP3 inflammasome in the excessive production of IL-1 β .

Deletion of NKCC1 from microglia results in altered membrane currents and a hyperpolarizing shift in the reversal of swelling-induced current

To study the consequences of NKCC1 deletion on microglial ion regulation and membrane currents, we made perforated patch-clamp recordings on native microglia in acute hippocampal slice preparations from WT and microglial NKCC1 KO mice. With this method, the intracellular Cl⁻ concentration remains unaffected by the pipette solution. Recordings were done in voltage-clamp mode at a holding potential of -40 mV, while voltage steps (-140 mV to +60 mV with 20 mV increments and 100 ms duration) were delivered to construct I-V plots for individual cells (Fig 5A). An exposure to hypotonic ACSF solution (50% dilution, 5 minutes) was used to identify the outwardly rectifying current in response to cellular swelling, which is considered to be mainly mediated by the largely Cl⁻ permeable volume-regulated anion

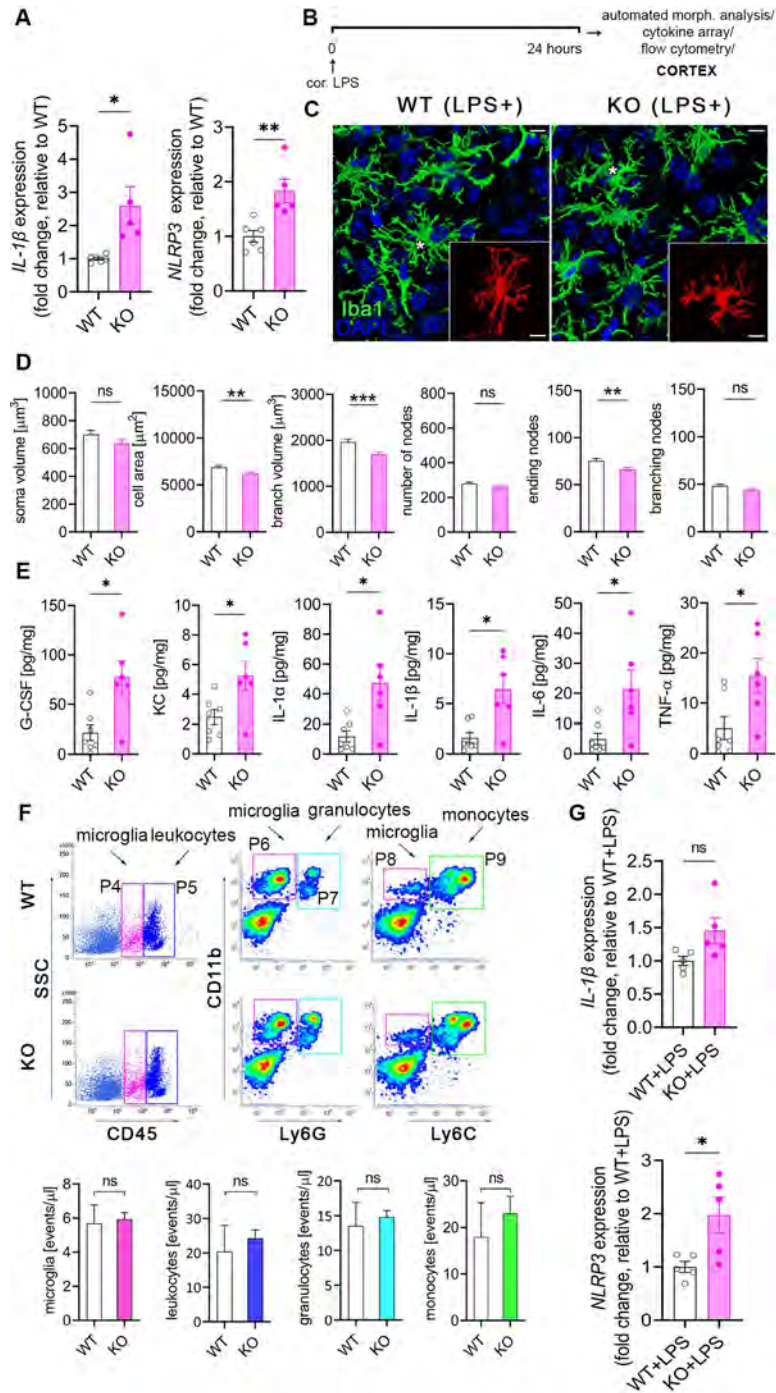


Fig 4. The absence of microglial NKCC1 boosts inflammatory cytokine production in the cerebral cortex in response to an inflammatory stimulus. (A) Baseline NLRP3 and IL-1β mRNA expression is increased in isolated NKCC1 KO microglia compared to WT cells. (B) Experimental outline of automated morphological analysis, cytokine array, and flow cytometry. (C, D) Automated morphological analysis shows that activated NKCC1-deficient microglia are slightly smaller than their WT counterparts. (E) LPS-induced cytokine levels are significantly higher in the cortices of microglial NKCC1 KO mice than in WT. (F) Flow cytometric dot plots show that microglial NKCC1 deficiency does not alter the number of CD11b⁺, CD45^{int} microglia (P4 gate) or numbers of infiltrating CD11b⁺, CD45^{high} leukocytes (P5 gate), CD11b⁺, Ly6G^{high} monocytes (P9 gate) and CD11b⁺, Ly6G^{high} granulocytes (P7 gate) in response to intracortical LPS administration. See corresponding data on peripheral cytokine levels and immune cell populations in S3 Fig. (G) Increased NLRP3 and IL-1β mRNA levels are sustained in NKCC1 KO and WT microglia 24 hours after intracisternal LPS administration. (A) Unpaired *t* test; **p* < 0.05, ***p* < 0.01; *N* (WT) = 6, *N* (KO) = 5. (C) Scale:

25 μm . (D) Mann–Whitney test, N (WT) = 108 cells from 6 mice, N (KO) = 92 cells from 4 mice, $**p < 0.01$, $***p < 0.001$. (E) Unpaired t test, $*$: $p < 0.05$; N (WT) = 7, N (KO) = 6. (F) Unpaired t test, N (WT) = 4, N (KO) = 4. (G) Unpaired t test; $*$: $p < 0.05$; N (WT + LPS) = 5, N (KO + LPS) = 5. Data underlying this figure can be found in [S1 Data](#). KO, knockout; ns, not significant; WT, wild type.

<https://doi.org/10.1371/journal.pbio.3001526.g004>

channels (VRACs) [53–55]. Our results showed that current responses under normotonic and hypotonic conditions (Fig 5B) were qualitatively similar to those published previously regarding WT microglia in acute slice preparations [56]. I–V curves (Fig 5C and 5D) indicated a much higher resistance of the KO versus WT cells, especially at more positive voltage levels under both normotonia and hypotonia. The slope of I–V curves between the -40 mV and 0 mV voltage steps (Fig 5E and 5F) showed significantly higher input resistance of KO microglia both in normotonia (WT: 1.91 G Ω , q1: 1.71 , q3: 2.38 versus KO: 3.00 G Ω , q1: 2.20 , q3: 4.50 ; Mann–Whitney, $p < 0.05$) and hypotonia (WT: 0.78 G Ω , q1: 0.66 , q3: 1.11 versus KO: 2.47 G Ω , q1: 0.94 , q3: 4.25 ; Mann–Whitney, $p < 0.05$). We also measured resting membrane potential of microglia (Fig 5G) where no statistically significant difference was observed between WT and KO (WT: -20 mV, q1: -21 , q3: -18 versus KO: -19 mV, q1: -26 , q3: -17 ; Mann–Whitney, not significant). In order to compare the responses of WT and KO microglial cells to cell swelling, we isolated the swelling-induced current component by subtracting the currents obtained at each point of voltage in normotonic conditions from those recorded during the hypotonic response (S4A Fig). The resulting I–V plot of the swelling-induced currents showed a reversal potential (E_{swell} —a rough estimate of the Cl^- equilibrium potential, E_{Cl^-}), which was more negative in the KO cells (WT: -47 mV, q1: -53 , q3: -38 versus KO: -68 mV, q1: -91 , q3: -46 ; Mann–Whitney, $p < 0.05$; S4B Fig). Because of the variation of the individual data points related to reversal and resting potentials, we calculated the driving force ($\text{DF} = V_{\text{rest}} - E_{\text{swell}}$) for each WT and KO cell (S4B Fig), which provides a more direct parameter of the efficacy of ion regulation than ionic reversal potentials [1]. We found significantly higher DF values in the case of NKCC1 KO versus WT microglia (WT: 28 mV, q1: 21 , q3: 33 versus KO: 50 mV, q1: 30 , q3: 65 ; Mann–Whitney, $p < 0.05$), supporting the view that the lack of microglial NKCC1 results in a lower intracellular Cl^- concentration.

To investigate the potential compensatory mechanisms that may arise in response to NKCC1 deletion in microglial cells, we evaluated the expression of some relevant genes that are reportedly expressed by microglia and are known to regulate ion concentrations, membrane potential or response to osmotic stress (S5 Fig; [57,58]). *Slc9a1*, *Slc8a1*, *Slc12a6*, *Clic1*, *Cln3*, *Kcnk13*, *Kcnk6*, *Kcnj2*, *Kcna3*, and *Sgk1* mRNAs did not show altered expression between WT and NKCC1 KO microglia (S5A and S5C Fig), but we found a more than 2-fold increase in *Lrrc8d*, the D subunit of VRAC in response to NKCC1 deletion (S5A Fig). Importantly, *Lrrc8d* (VRAC) is involved in increasing the permeability for a broad range of uncharged organic osmolytes [59]. Interestingly, intracisternal LPS treatment resulted in a marked reduction of NKCC1 and P2Y12R mRNA levels (Fig 1E), in line with the down-regulation of *Slc9a1*, *Slc8a1*, *Lrrc8d*, *Clic1*, *Cln3*, *Kcnk13*, *Kcnk6*, *Kcnj2*, *Sgk1* genes (S5B Fig) of which *Slc9a1*, *Clic1*, *Kcna3*, *Kcnj2*, *Kcnk13* genes are known to play a role in maintaining ramified morphology and resting state under physiological conditions [35,39,58,60].

Deletion of microglial NKCC1 increases infarct volume, brain edema and worsens neurological outcome after MCAo

Because Na^+ -coupled Cl^- importers and their upstream regulatory serine–threonine kinases (WNK–SPAK–OSR1) are involved in maintaining intracellular ionic homeostasis as well as regulation of cell volume [2,49], inhibiting these cotransporters is a subject of interest in

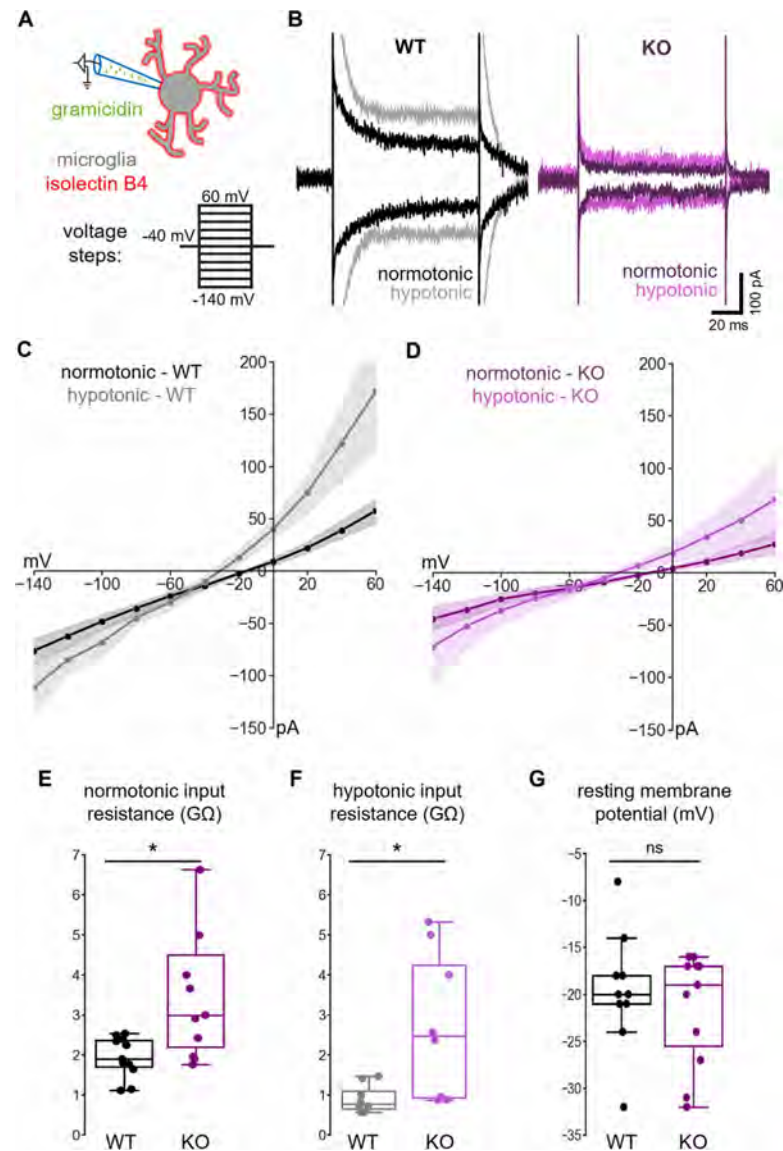


Fig 5. Deletion of NKCC1 from microglia results in altered membrane currents. (A) Schematic representation of the experiment. Perforated patch-clamp recordings were performed on isolectin B4-labeled microglial cells in acute hippocampal slice preparations. Current responses to a train of voltage steps from -140 to 60 mV with 20 mV increments and a duration of 100 ms were measured in voltage-clamp mode (holding potential: -40 mV) both in normotonic, and after 5 -minute perfusion with hypotonic ACSF (50% dilution). (B) Example traces of recordings from WT (black: normotonic, gray: hypotonic ACSF) and NKCC1 KO (purple: normotonic, violet: hypotonic ACSF) animal. Traces show responses at -140 and $+60$ mV voltage steps in both conditions. (C) Average I-V curve responses from WT in normotonic ($N = 11$ cells, black with SEM) and in hypotonic ($N = 8$ cells, gray with SEM) condition. (D) Average I-V curves from NKCC1 KO in normotonic ($N = 11$ cells, purple with SEM) and in hypotonic ($N = 8$ cells, violet with SEM) condition. (E) Input resistance of WT versus KO cells in normotonic condition. (F) Input resistance of WT versus KO cells in hypotonic condition. (G) Resting membrane potential in normotonic condition of WT versus NKCC1 KO microglial cells measured in current-clamp mode (0 pA injected current). (E) Mann-Whitney; N (WT) = 11 cells from 8 animals, N (KO) = 11 cells from 7 animals; $*$; $p < 0.05$. (F) Mann-Whitney; N (WT) = 8 cells from 6 animals, N (KO) = 8 cells from 5 animals; $*$; $p < 0.05$. (G) Mann-Whitney; N (WT) = 10 cells from 8 animals, N (KO) = 11 cells from 7 animals. Data underlying this figure can be found in [S1 Data](#). KO, knockout; ns, not significant; WT, wild type.

<https://doi.org/10.1371/journal.pbio.3001526.g005>

ischemic stroke therapy and in other forms of acute brain injury (brain trauma, SAH) where cerebral edema is a major contributor to poor clinical outcome [2,49]. Thus, we investigated whether microglial NKCC1 deficiency influences the severity of brain injury after experimental stroke in microglial NKCC1 KO mice subjected to transient, 45-minute long middle cerebral artery occlusion (MCAo). Twenty-four hours after reperfusion, elimination of microglial NKCC1 was not associated with obvious alterations in astroglial GFAP levels or AQP4 levels in perivascular astrocyte endfeet (S6 Fig). However, we observed a significant increase in brain edema, which was accompanied by a 47% increase in lesion volume (Fig 6A and 6B; $p = 0.0262$) and poor neurological outcome in NKCC1 KO mice (Fig 6B; Bederson's score: WT: 1.2 ± 0.2 , KO: 2.1 ± 0.2 ; composite neurological score: WT: 14.4 ± 1.5 , KO: 20.5 ± 1.5). Furthermore, experimental stroke induced a 4-fold up-regulation of IL-1 α and 4.8-fold increase in IL-1 β expressing NKCC1 KO microglia cells compared to WT animals, while the

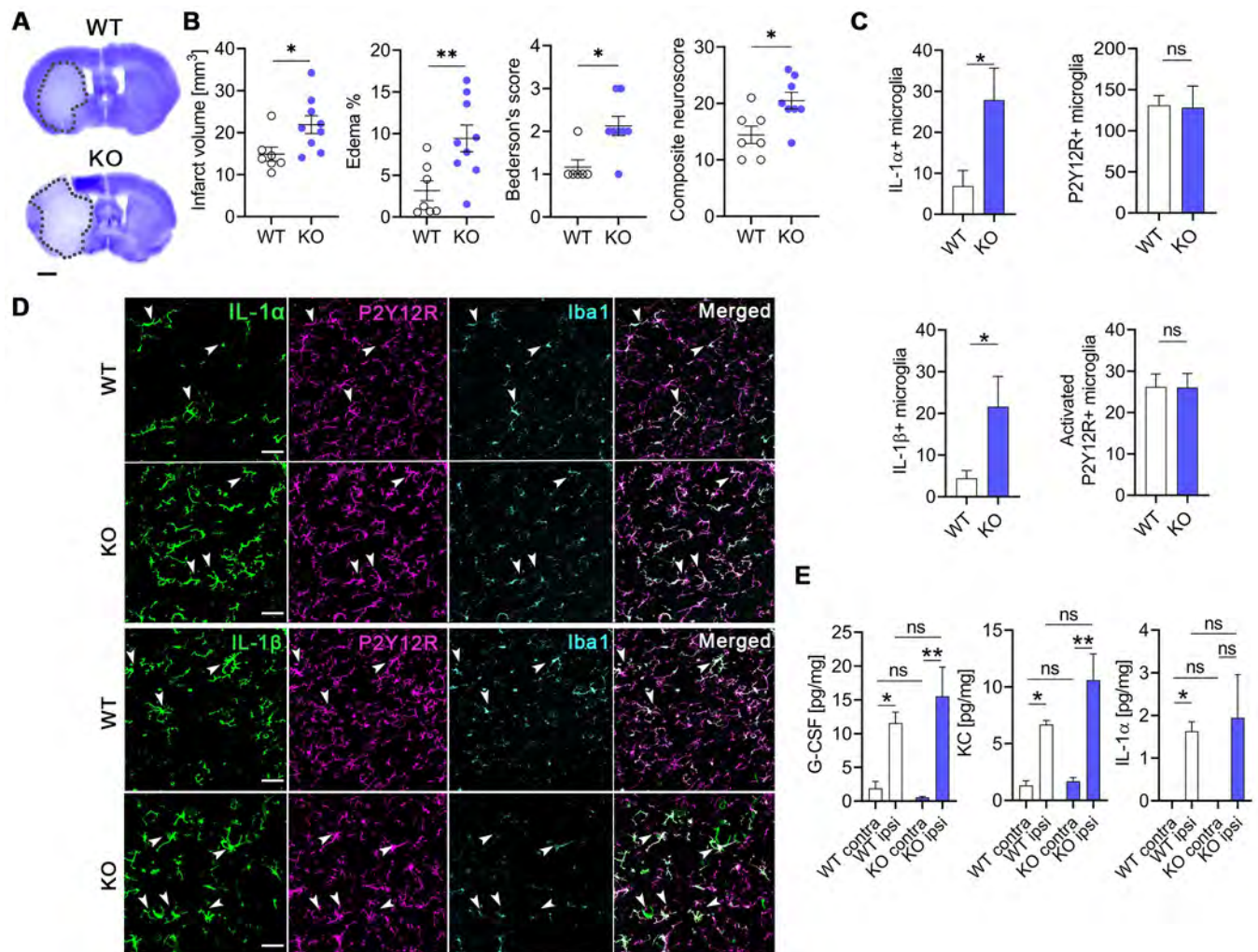


Fig 6. Deletion of microglial NKCC1 increases infarct volume, brain edema, and worsens neurological outcome after MCAo. (A, B) Microglial NKCC1-deficient mice (KO) show larger infarct volume as assessed on cresyl violet-stained brain sections and more severe neurological outcome compared to WT mice. (C, D) Microglial NKCC1 deletion results in higher levels of IL-1 α and IL-1 β 24 hours after MCAo. (E) Cytokine levels in the cortex do not differ 8 hours after MCAo in KO mice compared to WT. (A) Scale: 1 mm. (B) Unpaired *t* test, N (WT) = 7, N (KO) = 9; *: $p < 0.05$, **: $p < 0.01$. (C) Mann-Whitney test, *: $p < 0.05$; N (WT) = 7, N (KO) = 8. (D) Scale: 50 μ m. (E) Kruskal-Wallis test followed by Dunn's multiple comparison test; $N = 6$ /group. *: $p < 0.05$, **: $p < 0.01$. Data underlying this figure can be found in S1 Data. KO, knockout; MCAo, middle cerebral artery occlusion; ns, not significant; WT, wild type.

<https://doi.org/10.1371/journal.pbio.3001526.g006>

overall microglia density and the number of activated microglia were not different at 24-hour reperfusion (Fig 6C and 6D). We also assessed whether increases in IL-1 production take place early after brain injury before the majority of the infarct is formed. Cytometric bead array did not reveal altered cytokine production in cortical homogenates shortly (8 hours) after MCAo (Fig 6E). Taken together, these results indicate that microglial NKCC1 deficiency results in augmented brain inflammation, brain edema, and increased brain injury after experimental stroke.

Discussion

To our knowledge, we show for the first time that NKCC1 is functionally active in microglia in the adult mouse brain and that microglial NKCC1 is involved in shaping both baseline and reactive microglia morphology and responses. We present evidence that NKCC1 regulates microglial membrane conductance and adaptation to swelling-induced volume changes in a cell-autonomous manner, while the lack of NKCC1 results in primed microglial inflammatory states as evidenced by elevated NLRP3 and IL-1 β levels. In line with this, while systemic NKCC1 blockade attenuates LPS-induced inflammation in the brain, central pharmacological inhibition or genetic deletion of microglial NKCC1 potentiates inflammatory cytokine production. Microglial NKCC1 deletion also increases brain injury, inflammation, and cerebral edema and leads to worse neurological outcome after acute brain injury induced by experimental stroke. Thus, microglial NKCC1 emerges as an important regulator of central inflammatory responses.

As pointed out in the Introduction, there is little direct information on whether systemically applied bumetanide might exert therapeutic effects by directly blocking NKCC1 in the brain and, particularly, in central neurons. To unravel the effects of pharmacological inhibition of NKCC1 in the periphery and the brain, we investigated the systemic versus central effects of bumetanide in response to bacterial endotoxin (LPS) administration, which is widely used to trigger inflammatory cytokine responses [41,52]. Intraperitoneally injected bumetanide reduced intracortical LPS-induced proinflammatory cytokine/chemokine responses in the brain, similarly to that found in the case of LPS-induced lung injury attributed to NKCC1-mediated macrophage activation [61]. These findings are also consistent with the suggested beneficial therapeutic effects of systemic NKCC1 blockade in CNS pathologies, which are associated with inflammation [1,7,8,10–12,62].

Importantly, intracortical administration of bumetanide had exactly the opposite effect on intracortical LPS-induced cytokine production to that seen after systemic bumetanide treatment, resulting in elevated cytokine levels in the cortex. These markedly different outcomes clearly demonstrate the difficulty to interpret pharmacological interventions in the absence of data on the precise cellular targets of NKCC1 actions in the brain and highlight the need for cell-specific NKCC1 targeting studies.

Because microglia are the key source of inflammatory cytokines in the brain, we tested whether microglial activity could be directly related to NKCC1 function. Indeed, we observed comparable *Slc12a2* expression in microglia, isolated from either newborn or adult mouse brains, to that seen in neural progenitors. We also revealed NKCC1 protein in cortical microglial cells, which is in line with recent observations showing microglial NKCC1 expression in the superficial spinal dorsal horn in rats [63], and also supported by single-cell transcriptomic studies [21,40]. Further on, we demonstrated that NKCC1 levels are markedly down-regulated in microglia in response to LPS, alongside with decreased P2Y₁₂R levels (a purinergic receptor regulating microglial cell–cell interactions under both physiological conditions and in response to injury [21,44,64–66]), suggesting that impaired microglial NKCC1 function alters microglial responses to injury or inflammatory stimuli.

To investigate the cell-autonomous effects of NKCC1 in microglia, we generated a new, microglial NKCC1 KO transgenic mouse line. We found that the absence of NKCC1 resulted in a more branching microglial morphology in resting state and a more amoeboid shape under inflammatory conditions. These results paralleled enhanced baseline process motility in the intact brain, *in vivo*, and significantly reduced process recruitment to the site of the acute lesion, when microglial NKCC1 was blocked by intracisternal bumetanide during 2-photon imaging. While the use of bumetanide was required for *in vivo* imaging of microglia due to the absence of microglial reporter protein expression in microglial NKCC1 KO mice, the cisterna magna application protocol had been previously shown to effectively target parenchymal microglia by using PSB0739, a selective P2Y₁₂R antagonist [31]. As centrally administered bumetanide may also reach other NKCC1-expressing cells (e.g., neurons and astrocytes), we cannot exclude the possibility that microglial responses might have been influenced indirectly by other cell types in this experiment. Nevertheless, the net effect of central NKCC1 blockade by bumetanide leads to markedly impaired microglial process response to acute injury. Associations of NKCC1 with actin cytoskeleton dynamics [67,68] are well documented, which take place via controlling F-actin organization through Cofilin-1 and RhoGTPase activity [67]. Collectively, our results suggest that regulation of targeted process outgrowth in microglia is NKCC1 dependent, in addition to its known dependency on microglial P2Y₁₂R, while THIK-1, a potassium channel that regulates baseline microglial surveillance and process dynamics, is not required for this process [35].

Importantly, we also found that the absence of microglial NKCC1 renders microglia to express higher levels of NLRP3 and IL-1 β mRNA even without any exposure to inflammatory stimuli. It is well established that changes in microglial membrane potential and ion currents markedly determine cell volume regulation, process dynamics, and inflammatory responses of microglia. For example, depolarization is associated with reduced branching in microglia [35,69], while potassium or chloride efflux are essential for NEK7-NLRP3 interaction during the assembly of the NLRP3 inflammasome [38,50], which is required for the production of mature IL-1 β [37,38,50]. The regulation of these processes appears to be highly complex. The TWIK2 two-pore domain K⁺ channel (K_{2p}) mediates K⁺ efflux triggering NLRP3 activation in lung macrophages [37], while THIK-1 has been identified as the main K⁺ channel in microglia [35], although RNA profiling [21,40] also revealed high expression of TWIK2 in this cell type. In line with this, blocking THIK-1 function inhibits the release of IL-1 β from activated microglia, consistent with potassium efflux being necessary for inflammasome activation [35].

To reveal how microglial NKCC1 may contribute to these processes, we investigated whether deletion of NKCC1 leads to altered expression of ion channels or transporters that have been linked with microglial ion- and volume regulation and with inflammatory cytokine production (see references in S4D Fig). We could not observe changes in THIK-1 or TWIK2 mRNA levels by qPCR, but the subunit D of VRAC was up-regulated in KO animals. Subunit D is involved in the transport of uncharged organic osmolytes by VRAC, and it may be important for volume reduction without a major release of inorganic ions [59] for a cell coping with potentially lowered inorganic ion levels due to NKCC1 loss. Changes in the expression of other VRAC subunits may also be important for microglial inflammatory processes. For example, LRRC8A-containing anion channels are known associate with NADPH oxidase 1 (Nox1) and regulate superoxide production and TNF- α signaling in vascular smooth muscle cells [59,70]. Thus, changes in microglial ROS production in the absence of NKCC1 will need to be investigated in future studies.

To examine the effects of NKCC1 deletion on microglial membrane properties, we conducted perforated patch recordings in hippocampal slices from WT and KO animals. Importantly, we found that NKCC1 KO cells had an input resistance almost twice as high as that

measured in WT under both normotonia and hypotonia. We also characterized the swelling-induced current for WT and KO microglia, which is considered to be mainly mediated by the largely Cl^- permeable VRACs [53–55]. In agreement with an expected decrease in cellular Cl^- uptake upon NKCC1 deletion [1], E_{swell} was significantly more negative in the KO versus WT microglia, which was further supported by comparing the driving forces of swelling-induced currents in individual cells, yielding higher values in KO cells. However, the driving force at V_{rest} had a positive polarity (outward current) in all cells of both genotypes, which indicates that in addition to NKCC1 and VRAC, an active Cl^- extruder is likely to be present in microglia. While the identity of the latter cannot be deduced from the present data, there is evidence that K^+ - Cl^- cotransporter (KCC) isoforms, such as the volume-sensitive KCC1, are expressed in microglia [71]. It is worth noting here that in numerous cell types, NKCC1 and KCCs are simultaneously involved in chloride regulation [72]. Our data indicate that the increased input resistance in KO was also paralleled with a decrease in the swelling-induced current. We have no mechanistic explanation for these two effects, but they are likely to reflect adaptations of microglia to genetic NKCC1 deletion with compensatory changes not revealed by our qPCR studies. Such a coordinated adaptive response could involve down-regulation of VRACs and/or K^+ channels among others. Upregulation of VRAC subunit D in NKCC1 KO microglia could represent a compensatory response to impaired VRAC function, as suggested by the reduced swelling-related conductance in these cells.

We also found that in line with increased NLRP3 and IL-1 β mRNA levels in NKCC1 KO microglia, LPS stimulation resulted in elevated NLRP3 mRNA levels even after 24 hours upon LPS treatment and potentiated the production of IL-1 β and other cytokines in the cortex of microglial NKCC1 KO mice compared to control mice. Importantly, deletion of microglial NKCC1 had an identical effect on inflammatory cytokine levels to that seen after NKCC1 inhibition by bumetanide, suggesting that central bumetanide actions involve blockade of microglial NKCC1. In line with this, we could not find significant changes in two key astroglial markers, GFAP and AQP4, after central bumetanide application in response to LPS treatment, arguing against a major role of astroglial NKCC1 in the observed differences on the timescale of the present study. While a role for astroglial NKCC1 in mediating central bumetanide actions has been previously reported [18,19], our present work shows that central bumetanide effects involve a substantial microglial component via NKCC1.

Proinflammatory cytokine production, particularly the effects mediated by IL-1, are known to influence acute brain injury induced by brain trauma or stroke [73–75]. We found significantly increased infarct volume (by 47%) in microglial NKCC1 KO mice after experimental stroke comparable to a striking, 60% increase in infarct size caused by highly efficient, selective microglia elimination [32]. Microglia depletion resulted in dysregulated neuronal network activity, an effect that is likely to be mediated via elimination of protective microglia–neuron interactions at somatic purinergic junctions [31]. It remains to be investigated in future studies, whether microglia–neuron interactions are altered in microglial NKCC1 KO mice, which could shape neuronal injury via diverse mechanisms related to changes in neuronal excitability [29,30,32,33]. In line with this, the absence of microglial NKCC1 may have contributed to increased neuronal injury via increased IL-1 production, as suggested by the established pathophysiological role of IL-1-mediated actions in different forms of brain injury [73,76].

In our experimental stroke studies, we could not detect increased cytokine production in the absence of microglial NKCC1 early (8 hours) after MCAo, while both IL-1 α and IL-1 β expression were markedly up-regulated in NKCC1 KO microglia 24 hours after reperfusion. Following stroke, impaired cell volume regulation results in cytotoxic cell swelling and edema formation, which peaks beyond the first 24 hours in both patients and experimental animals [77,78]. Cerebral edema was shown to be associated with increased phosphorylation of the

SPAK/OSR1 kinases playing a key role in NKCC1 activation in various neural cell types [2,48,49] and a SPAK kinase inhibitor, ZT-1a, attenuated cerebral edema after stroke [79]. In line with this, NKCC1 is involved in homeostatic cell volume regulation [48,49], and bumetanide attenuates edema formation in response to ischemic or traumatic brain injury [2]. In light of these findings, our data showing impaired volume regulation and exaggerated cytokine production in NKCC1 KO microglia have a potentially high pathophysiological and clinical relevance.

In conclusion, we show that microglial NKCC1 plays a previously unrecognized role in shaping microglial phenotype and inflammatory responses. Strikingly, bumetanide-induced enhancement of neuroinflammation was mimicked by conditional deletion of microglial NKCC1, suggesting that microglial NKCC1 is a significant target of NKCC1 blockers, given that brain tissue levels of such drugs are sufficiently high [10,13,14]. Our results implicating microglial NKCC1 in inflammation, brain edema formation, and responses to injury suggest that microglial NKCC1 actions should be considered when studying the effects of NKCC1 inhibitors in different CNS functions and pathologies. This is further emphasized by the broad clinical interest in pharmacological NKCC1 blockade. The present results also call for a reevaluation of the pharmacological effects of bumetanide in brain diseases with a significant inflammatory component.

Materials and methods

Experimental animals

Experiments were performed on adult male C57BL/6J (RRID: IMSR JAX:000664), NKCC1^{fl/fl}, and NKCC1^{fl/fl} ΔCx3CR1 (microglial NKCC1 KO) mice (all on C57BL/6J background). For experiments using LPS treatment P90-110 (postnatal day 90-110), and for MCAo experiments, P70-90 day-old mice were used. NKCC1^{fl/fl} mice were provided by Dr. Christian A. Hübner of University Hospital Jena of Friedrich Schiller University, Jena, Germany. Ubiquitous NKCC1 KO mice (P15-20, NKCC1 full KO, NKCC1^{-/-}), generated by crossing C57BL/6NTac-Gt (ROSA)26Sor^{tm16(cre)Arte} and NKCC1^{fl/fl} mice, were used as immunostaining controls and were not subjected to other experimental procedures. Mice were housed in a 12-hour dark/light cycle environment, under controlled temperature and humidity and ad libitum access to food and water. All experimental procedures were in accordance with the guidelines set by the European Communities Council Directive (86/609 EEC) and the Hungarian Act of Animal Care and Experimentation (1998; XXVIII, Sect. 243/1998) and approved by the Animal Care and Experimentation Committee of the Institute of Experimental Medicine and the Government Office of Pest Country Department of Food Chain Safety, Veterinary Office, Plant Protection and Soil Conservation Budapest, Hungary under the number PE/EA/1021-7/2019 and Department of Food Chain Safety and Animal Health Directorate of Csongrád County Hungary. All experiments followed ARRIVE and IMPROVE guidelines [80,81]. A code was allocated to each animal using GraphPad's random number generator and was randomly assigned to different treatment groups. During all surgical procedures and functional tests, the experimenter was blinded to the treatment.

Generation and genotyping of the microglial NKCC1 knockout mouse line

Microglial NKCC1 deletion (NKCC1^{fl/fl} ΔCx3CR1) was achieved by crossing tamoxifen-inducible B6.129P2(C)-CX3CR1tm2.1 (cre/ERT2)Jung/J mice (RRID:IMSR_JAX:020940JAX) [82] with the NKCC1^{fl/fl} mouse line [83], in which a region between exon 7 and exon 10 of *Slc12a2* gene was flanked with lox P sites. Microglial NKCC1 deletion was achieved by 2 intraperitoneally administered tamoxifen injections (100 μl of 20 mg/ml in corn oil, #T5648, Sigma-

Aldrich) 48 hours apart in 3- to 4-week-old male mice, shortly after weaning. In all functional experiments, mice were studied more than 3 weeks after the last tamoxifen injection to avoid interference with Cre-dependent recombination in peripheral myeloid cells [82]. In the case of selective microglia isolation by magnetic cell sorting, we used animals exposed to tamoxifen for at least 2 weeks as Cre activity was shown to increase most dramatically within the first week after initiating treatment [84].

In all experiments, conditional mutant mice heterozygous for cre and homozygous for NKCC1 flox ($^{cre/+} fl/fl$), referred to as NKCC1 KO throughout the manuscript, were used. In all cases, littermate controls—referred to as WT—were used, which were negative for cre and homozygous for NKCC1 flox ($^{+/+} fl/fl$). Heterozygous, conditional mutant mice were viable, fertile, average in size, and did not display any gross physical or marked behavioral abnormalities. Genotypes for *Slc12a2* encoding NKCC1 were determined from tail biopsy samples by conventional PCR using the following primers: 5'-GCAATTAAGTTTGGAGGTTCCCTT, 5'-CCAACAGTATGCAGACTCTC and 5'-CCAACAGTATGCAGACTCTC; product sizes: 200 bps for WT, 260 bps for floxed, and 460 bps for KO.

Microglia cell preparations and cultures

Microglia cells from either newborn (P0-1, male or female) or adult (P40-55, male) C57BL/6J, NKCC1 $^{fl/fl}$ (WT), or NKCC1 $^{fl/fl} \Delta Cx3CR1$ (KO) mice were isolated by magnetic separation using anti-CD11b microbeads (Miltenyi Biotec, Germany), with slight modification of the protocol described by Otxoa-de-Amezaga [85]. After transcardial perfusion with ice-cold phosphate-buffered saline (PBS), the brain tissues (cortices and hippocampi) were enzymatically dissociated with Neural Tissue Dissociation Kit-P (#130-092-628; Miltenyi Biotec). Myelin was removed by MACS Myelin Removal Beads II (#130-096-733, Miltenyi Biotec), then cells in a single-cell suspension were magnetically labeled with MACS CD11b microbeads (#130-093-634, Miltenyi Biotec) and were separated using MS columns (#130-042-201, Miltenyi Biotec, Germany). Cells selected with CD11b microbeads were plated onto poly-L-lysine precoated 96-well or 386-well plates at 3×10^4 cell/cm² density and were cultured at 37°C in a 95% air/5% CO₂ incubator in DMEM/Glutamax medium (#31966-021, Gibco) supplemented with 10% fetal bovine serum (FBS, #FB-1090, Biosera), 1% Pen/Strep (10,000 U/ml; #15140-122, ThermoFisher Scientific), and 10 nM macrophage colony-stimulating factor (M-CSF; #PMC2044, ThermoFisher Scientific) for 10 days.

Embryonic neural progenitor cell preparations

Embryonic hippocampal cells were prepared from C57BL/6J mice on embryonic day 17. After aseptically removing the hippocampi from the skull, tissue was freed from meninges and incubated in 0.05% trypsin-EDTA (#T4549, Sigma-Aldrich) solution with 0.05% Dnase I (#DN25, Sigma-Aldrich) in PBS for 15 minutes at 37°C.

Intracortical and intracisternal injections

P90-110 mice were deeply anesthetized with fentanyl (0.05 mg/kg) and mounted into a stereotaxic frame, then were subjected to either single saline or LPS (lipopolysaccharide from *Escherichia coli* O26:B6; 200 nl of 5 mg/ml, rate = 200 nl/10 minutes; #L8274, Sigma-Aldrich) injections using a glass micropipette [86]. The coordinates for the injection were anterior-posterior -2.5 mm, lateral +1.5 mm, and ventral -0.25 mm from the bregma. Bumetanide, a specific inhibitor of NKCC1 in the brain, was coinjected with LPS (50 μM; #3108, Tocris). At 24 hours, mice were transcardially perfused with saline, and approximately 0.5 × 0.5 × 0.5 cm sized tissue pieces from the center of each injected cortical region were cut off and collected

for cytokine array and flow cytometric analysis. For tissue sectioning, mice were perfused with saline followed by 4% paraformaldehyde in PBS. For real-time quantitative PCR (qRT-PCR) experiments to assess the effect of NKCC1 deficiency on microglial expression of genes, which contribute to ion homeostasis, membrane potential, cell volume regulation, or inflammation, LPS (5 μ g dissolved in ACSF) was administered into the cisterna magna in 5 μ l final volume, using a glass capillary. At 24 hours, mice were transcardially perfused with saline followed by CD11b+ magnetic cell sorting.

Systemic administration of LPS and bumetanide

Male adult NKCC1^{fl/fl} mice were injected intraperitoneally with saline, LPS (2 mg/kg; O26:B6, #L8274, Sigma-Aldrich) or LPS (2 mg/kg) and bumetanide (25 mg/kg; #3108, Tocris). Intraperitoneal bumetanide injections were repeated twice, the first one 15 minutes prior to LPS injection, the second one 1 hour after LPS administration. The double injection aimed to ensure that in the critical time window, we have effective concentrations of bumetanide in the circulation. At 24 hours, saline-perfused spleen and brain samples were collected for cytokine measurements or flow cytometric analysis.

Cytokine measurement

The levels of inflammatory cytokines and chemokines were measured in spleen and brain samples. Sample processing and protein determination were performed as described previously [87]. Mice were transcardially perfused with saline prior to the collection of spleen and brain samples (ipsilateral to injections). Tissue samples were homogenized in TritonX-100 and protease inhibitor-containing (1:100, #539131, Calbiochem) Tris-HCl buffer (TBS (pH 7.4)) and centrifuged at 17,000 g, for 20 minutes at 4°C. Protein level was quantified for every sample using BCA Protein Assay Kit (#23225, ThermoFisher Scientific). Then, measured cytokine levels were normalized for total protein concentrations. The concentrations of cytokines and chemokines were determined by BD Cytometric Bead Array (CBA) using BD CBA Flex Sets (G-CSF: #560152, KC: #558340, IL-1 α : #560157, IL-1 β : #560232, IL-6: #558301, TNF- α : #558299, BD, Becton, Dickinson and Company) according to the manufacturer's instructions. Samples were acquired using a BD FACSVerser flow cytometer (BD, Becton, Dickinson and Company), and the results were analyzed by FCAP Array software (BD, Becton, Dickinson and Company).

Flow cytometric analysis of brain and spleen and liver samples

For flow cytometric analysis, cells were isolated from mouse brains with Collagenase D (0.5 mg/ml, #11088866001, Roche), DNase I (10 μ g/ml, #DN25, Sigma-Aldrich) dissolved in 10% FBS containing DMEM (#6546, Sigma-Aldrich), then the cell suspension was passed through a 40- μ m cell strainer (Corning). After enzymatic dissociation, the cells were resuspended in 40% Percoll solution and overlaid on 70% Percoll (#17-0891-01, GE Healthcare). After a density centrifugation step (at 2,100 rpm, 30 minutes), mononuclear cells were collected from the interphase of 40%/70% Percoll. Spleen and liver were mechanically homogenized, and red blood cells were removed by centrifugation. Before acquisition, brain, spleen, and liver cells were diluted with FACS buffer and were incubated with anti-mouse CD16/32 to block Fc receptor. Brain cells or spleen and liver leukocytes were incubated with cocktails of selected antibodies: T cells—anti-mouse CD8a-PE (1:200, #12-0081-82, eBioscience), anti-mouse CD3-APC clone 17A2 (1:200, #17-0032-80, eBioScience), anti-mouse CD4-FITC (1:200, #11-0043-82, eBioscience), anti-mouse CD45-PerCP/Cy5.5 (1:200, #103131, BioLegend); B cells/granulocytes—anti-mouse CD19-FITC (1:200, #11-0193-81, eBioScience), anti-mouse Ly-

6C-PE-Cy7 (1:500, #25-5932-80, eBioscience), anti-mouse Ly-6G-APC (1:500, #127613, BioLegend); monocytes/granulocytes—anti-mouse CD11b-FITC (1:200, #11-0112-81, eBioscience); anti-mouse Ly-6C-PE-Cy7; anti-mouse Ly-6G-APC, CD45-PerCP/Cy5.5. To exclude dead cells, some cocktails contained propidium iodide (3 μ M; #P1304MP, ThermoFisher). Cells were acquired on a BD FACSVerser flow cytometer, and data were analyzed using FACSsuite software (BD, Becton, Dickinson and Company). Cell counts were calculated by using 15 μ m polystyrene microbeads (#18328–5, Polysciences).

RNA isolation and cDNA reverse transcription

For qRT-PCR measurements, CD11b+ magnetic sorted microglia cells or embryonic neural progenitor cells were homogenized in QIAzol Lysis Reagent (#79306, QIAGEN) either immediately after isolation or after 10 days of in vitro culturing. Total RNA was isolated using Direct-zol RNA Miniprep Kits (#R2052, Zymo Research) following the manufacturer's protocol. The RNA purity and concentration were assessed by NanoDrop ND-1000 spectrophotometer (Nanodrop Technologies). The isolated RNA was then stored at -80°C . RNA was subjected to DNase I (#AM2224, Ambion) treatment in the presence of RNase H inhibitor (#AM2682, Ambion). Standardized quantities of RNA were reverse transcribed to cDNA using the SuperScript II First-strand Reverse Transcriptase system (#18064014, ThermoFisher Scientific) and random hexamers (#48190011, Invitrogen) supplemented with RNase H inhibitor (#AM2682, Ambion).

Real-time quantitative PCR (qRT-PCR)

qRT-PCR was performed with QuantStudio12K Flex qPCR instrument (Applied Biosystems), using TaqMan Gene Expression Assays and the TaqMan Gene Expression Master Mix (#4369016, ThermoFisher Scientific). All mouse TaqMan Gene Expression Assays used for amplification reactions were obtained from ThermoFisher Scientific: *Slc12a2* (Mm01265951_m1, targeting exon 1 to 10); (Mm00436546_m1, targeting exon 8 to 10, used for the validation of microglia-specific NKCC1 deletion; see Fig 2C), *Hprt* (Mm03024075_m1), *Slc12a6* (Mm01334052_m1), *Slc8a1* (Mm01232254_m1), *Slc9a1* (Mm00444270_m1), *Clcn3* (Mm01348786_m1), *Clic1* (Mm00446336_m1), *Kcnk6* (Mm01176312_g1), *Kcnj2* (Mm00434616_m1), *Kcna3* (Mm00434599_s1), *Lrrc8d* (Mm01207167_m1), *Sgk1* (Mm00441380_m1), *NLRP3* (Mm00840904_m1), *pro-IL-1 β* (Mm00434228_m1). The amplification was performed under the following cycling conditions: 95°C for 10 minutes, followed by 40 cycles of 95°C for 10 seconds, and 60°C for 1 minutes. The comparative Ct method ($\Delta\Delta\text{Ct}$ method) was used to analyze the relative expression values for each transcript using *Hprt* as a reference gene.

In vivo 2-photon imaging and assessment of microglial process dynamics

Cx3CR1^{+/GFP} microglia reporter mice were anesthetized using fentanyl. As previously has reported [31], fentanyl did not influence microglial process motility compared to the effects of different anesthetics. Cranial window with 3 mm diameter was opened on the left hemisphere centered 1.5 mm lateral and 1 mm posterior to bregma without hurting the dura mater. After removal of the skull bone, a 3-mm and 5-mm double glass coverslip construct was fixed with 3M Vetbond tissue glue on top of the dura mater. Then, a custom-made metal headpiece (Femtonics, Budapest, Hungary) was fixed with dental cement on the surface of the skull. All experiments were performed on a Femto2D-DualScanhead microscope (Femtonics, Budapest, Hungary) coupled with a Chameleon Discovery laser (Coherent, Santa Clara, USA). Following excitation, the fluorescent signal was collected using a Nikon 18X water immersion objective.

Data acquisition was performed by MES software (Femtonics). Galvano Z-stacks of 8 images (500 × 500 pixels, 3 μm step size, range = 100 to 125 μm from pial surface) were made at every minute. Two-photon image sequences were exported from MES and analyzed using FIJI. Microglial baseline process velocity was measured on time-series images acquired with 2P microscopy. Following motion correction, images from the same region of Cx3CR1^{+/GFP} mice were analyzed with the Manual Tracking plugin of FIJI. We applied a local maximum centring correction method with a search square of 5 pixels. Pixel size was 0.65 μm/px. Processes were included in the measurement when they were clearly traceable for at least 10 minutes. To compare how fast microglia cells are responding to injuries, cortical lesion was formed using laser beam. Focal lesion was induced with a 1,040-nm fix laser, and the laser power was 300 mW for 1,000 ms. The area of focal lesion was defined by a circle with 7.5 to 12.5 μm radius originating from the focal point of the laser beam. Baseline process motility was recorded before focal lesion, followed by a cell recruitment phase, and it was all repeated 15 minutes later after bumetanide administration (0.3 mg/kg body weight, in 5 μl final volume) into the cisterna magna in a different (undisturbed) part of the cerebral cortex in each animal.

Then, based on the idea of the procedure proposed by Davalos and colleagues [45], we created an automated image processing pipeline using CellProfiler [88] to determine the proportion of area over time covered by microglia cells on each image. We defined 2 concentric circles so that the whole area of the lesion is surrounded by the outer one, and the focal point of the ablation is covered by the inner one. The same dimensions were used among all images in the data set. We chose 25 μm for the inner diameter and 130 μm for the outer diameter on experimental basis. Only cells inside this region were taken into account, excluding the inner site as there were autofluorescent artifacts detected there. To differentiate between cells (high-intensity areas) and background (low-intensity areas), an adaptive threshold value was calculated from the per-image median intensities. The coverage was then measured as the proportion of pixels classified as cell and the total number of pixels in the area. Coverage values in the initial (baseline) phase of the experiment kept stable, no remarkable oscillation was recorded in any cases. Based on the observed data, we assumed that coverage reaches a minimum value Q_{min} as a result of the injury, then at time t_s , microglia cells start to extend their processes into the lesion area uniformly from its perimeter with velocity v , and saturate at a final coverage Q_{max} from this assumption, we created a simple mathematical model that predicts the coverage values over time inside the investigated area.

$$C(t) = (Q_{max} - Q_{min}) \frac{r_o^2 - (r_o - v(t - t_s))^2}{r_o^2 - r_i^2} + Q_{min}$$

In this equation, r_i and r_o denote the inner and outer radii of the ring-shaped region, respectively. See S7 Fig for a visual explanation of the model. For each measured coverage data set, we fitted this model by choosing values for v , Q_{max} and t_s that minimize the mean squared difference between the observed and predicted values. To find the best fitting values, a grid search-based optimizer algorithm was used. We found that the model is able to describe the observed behavior of cell flow from the external areas inside the lesion, and it also gives an estimate for the cell's mean velocity, which is in good agreement with those from the manual tracking of cell processes.

Middle cerebral artery occlusion (MCAo)

To assess the functional contribution of microglial NKCC1 to ischemic brain injury, mice were subjected to a 45-minute long MCAo using a silicone-coated filament, as described earlier by Dénes and colleagues [89]. Surgery was performed under isoflurane (1.5% in a 30% O₂

and 70% N₂O gas mixture) anesthesia and core body temperature was tightly controlled (37°C ± 0.5°C) during the whole procedure using a homeothermic heating blanket. Laser Doppler flowmetry was used to validate the occlusion of the MCA. In brief, after a midline incision made on the ventral surface of the neck, the right common carotid artery (CCA) was isolated, and a silicone-coated monofilament (210 to 230 μm tip diameter, Doccol, Sharon, USA) was introduced to the left external carotid artery (ECA) and advanced along the internal carotid artery (ICA) to occlude the MCA. Animals were kept in a postoperative chamber at 26 to 28°C until the functional assessment having free access to mashed food and water. Neurological outcome was assessed at 24-hour reperfusion using corner test and the 5-point Bederson's sensory motor deficit scoring system [90–92]. Briefly, the following scores were given: a 0, no motor deficit; 1, flexion of torso and contralateral forelimb when mouse was lifted by the tail; 2, circling to the contralateral side when mouse is held by the tail on a flat surface, but normal posture at rest; 3, leaning to the contralateral side at rest; 4, no spontaneous motor activity; 5, early death due to stroke. Functional outcome has also been assessed by a complex neurological scoring system to obtain a more comprehensive readout [93]. Results are expressed as composite neurological score. Composite scores range from 0 (healthy mice) to 56 (worst performance) by adding up scores from 13 categories as follows: hair (0 to 2), ears (0 to 2), eyes (0 to 4), posture (0 to 4), spontaneous activity (0 to 4), and epileptic behavior (0 to 12); and focal deficits: body symmetry (0 to 4), gait (0 to 4), climbing on a surface held at 45° (0 to 4), circling behavior (0 to 4), front limb symmetry (0 to 4), compulsory circling (0 to 4), and whisker response to a light touch (0 to 4).

Infarct volume and brain edema were calculated after 24-hour survival on cresyl violet stained coronal brain sections using ImageJ as described previously [94]. In brief, lesion volume was determined at 8 neuroanatomically defined coronal levels (between +2 mm rostral and –4 mm caudal to bregma) by integrating measured areas of damage and correcting for edema size. The predetermined inclusion criteria for analysis were as follows: decline in Doppler signal of at least 70%, no cerebral hemorrhages, and survival to 24 hours. Cerebral hemorrhage was identified postmortem by the presence of excessive bleeding on the external surface of the brain, typically close to the filament location.

Immunohistochemistry

Perfusion, tissue processing, and immunostaining for histology. Mice were anesthetized and transcardially perfused with 0.9% NaCl solution for 1 minute, followed by 4% PFA in 0.1 M phosphate buffer (PB) for 40 minutes, followed by 0.1 M PB for 10 minutes to wash the fixative out. Blocks containing the primary somatosensory cortex and dorsal hippocampi were dissected, and coronal sections were prepared on a vibratome (VT1200S, Leica, Germany) at 50 μm thickness for immunofluorescent histological and 100 μm thickness for the automated morphological analysis. Sections were washed in 0.1 M PB, incubated in 10% and 30% sucrose containing 0.1 M PB for 3 and 12 hours, respectively. Then the samples were placed into cryovials, snap frozen in liquid nitrogen, and stored at –80°C for further use. For the free-floating immunohistochemical detection of NKCC1, each vial contained sections from NKCC1^{fl/fl} (WT), NKCC1^{fl/fl} ΔC_{x3}CR1 (KO), and NKCC1^{-/-} mice, which sections were marked by different cuts, enabling that all experimental parameters were completely identical for all samples. The sections were washed in TBS, blocked with a Mouse-on-Mouse blocker solution (MOM blocker, #BMK-2202, Vectorlabs) for 1 hour, washed in TBS 2 × 5 minutes, and washed with MOM diluent 2 × 5 minutes. The diluted anti-NKCC1 primary antibodies (NKCC1 Rb: 1:4,000, #13884-1-AP, Proteintech, NKCC1 M: 1:2,000, diluted in MOM diluent; DSHB) were preincubated for 48 hours with brain slices from NKCC1^{-/-} mice in order to

remove the fraction of immunoglobulins that could potentially cause non-specific binding. After discarding these slices, the guinea pig anti-Iba1 antibody (#234004, Synaptic Systems) was added to reach a 1:1,000 final dilution. This antibody mixture was applied on the samples for 48 hours at 4°C during gentle shaking. After intensive washes in TBS, sections were incubated with a mixture of secondary antibodies (donkey anti-mouse Alexa 647, 1:1,000, #715-605-150; donkey anti-rabbit Alexa 488, 1:1,000, #711-546-152; donkey anti-guinea pig Alexa 594, 1:1,000, #706-586-148; Jackson ImmunoResearch, diluted in TBS) for 24 hours. After subsequent washes in TBS and 0.1 M PB, DAPI staining was performed and the sections were mounted on glass slides and covered with Diamond Antifade (#P36961, ThermoFisher) or Aquamount (#18606-5, Polysciences). Immunofluorescence was analyzed using a Nikon Eclipse Ti-E inverted microscope (Nikon Instruments Europe B.V., Amsterdam, the Netherlands), with a CFI Plan Apochromat VC 60X oil immersion objective (numerical aperture: 1.4) and an A1R laser confocal system. We used 405, 488, 561, and 647 nm lasers (CVI Melles Griot), and scanning was done in line serial mode. Single-image planes were exported from the ND2 files, the outline of microglial cells was drawn using the Iba1-labeling, and the integrated density of the NKCC1 fluorescence signal was measured within these respective ROIs. This section is related to [Fig 2](#).

Perfusion, processing, and immunostaining of ischemic and LPS-injected tissues. In terminal ketamine-xylazine anesthesia (100 mg/kg-10 mg/kg), mice were transcardially perfused with 0.9% NaCl solution, followed by 4% phosphate-buffered PFA. Brains of microglial NKCC1 KO mice subjected to 45-minute MCAo were postfixed and cryoprotected overnight (in 4% phosphate-buffered PFA-10% sucrose solution), then immersed into a cryoprotective solution (10% sucrose in PBS) at least 2 hours before 25 µm coronal sections were cut using a sledge microtome. Immunofluorescent staining was performed on free-floating coronal brain sections. Brain sections were blocked with 5% normal donkey serum followed by overnight incubation at 4°C using the following mixture of primary antibodies: goat anti-IL-1β/ILF2 (1:250; #AF-401-NA, R&D Systems), rat anti-CD45 (1:250; #MCA1388, AbD Serotec), rabbit anti-P2Y12R (1:500; #55043AS, AnaSpec). After the incubation with the primaries, sections were washed several times in TBS and were incubated with mixture of corresponding secondary antibodies at room temperature for 2 hours. The following secondaries were used: donkey anti-goat CF568 (1:1,000; #20106, Biotium), donkey anti-rabbit Alexa 647 (1:1,000; #711-605-152, Jackson ImmunoResearch), donkey anti-rat Alexa 488 (1:1,000; #712-546-153, Jackson ImmunoResearch). Slices were washed in TBS and were mounted to microscope slides using Fluoromount-G (#0100-01, SouthernBiotech). Representative images were captured with a 20X objective (Plan Apo VC, numerical aperture: 0.75, FOV = 645.12 µm) on a Nikon A1R confocal system. Quantitative analysis was performed on widefield images, captured with a 20X objective (Plan, numerical aperture: 0.4) on a Nikon Eclipse Ti-E inverted microscope (Nikon Instruments Europe B.V., Amsterdam, the Netherlands). IL-1α and IL-1β positive cells in the penumbral region, P2Y12R positive and CD45 positive cells in the whole cortex were counted on 3–3 serial coronal sections for a given brain area. This methodical description is related to [Fig 6](#).

The following primaries and secondaries were used for GFAP and AQP4 immunolabeling: chicken anti-GFAP (1:1,000, #173006, Synaptic Systems) and guinea pig anti-AQP4 (1:500, #429004, Synaptic Systems), donkey anti-chicken A594 (1:500, #703-586-155, Jackson ImmunoResearch) and donkey anti-guinea pig A647 (1:500, #706-606-148, Jackson ImmunoResearch). For imaging, fluorescent slide scanner (Panoramic MIDI 3D HISTECH) with 20X Plan-Apochromat objective was used. Raw integrated densities were automatically measured on all images in selected ROIs from the striatum, and then their per-animal average was calculated and used for statistical analysis. This methodical description is related to [S2](#) and [S6](#) Figs.

Electrophysiology

Hippocampal slices. Mice (56 to 65 days) were decapitated under deep isoflurane anesthesia. The brain was removed and placed into an ice-cold cutting solution. The cutting solution contained (in mM): 205 sucrose, 2.5 KCl, 26 NaHCO₃, 0.5 CaCl₂, 5 MgCl₂, 1.25 NaH₂PO₄, 10 glucose, saturated with 95% O₂–5% CO₂. Horizontal hippocampal slices of 250 μm thickness were cut using a Vibratome (Leica VT1000S). Slices were placed into an interface-type incubation chamber, which contained standard ACSF at 35 °C that gradually cooled down to room temperature. At the beginning of the incubation period, a solution of 25 μM/ml Alexa 594 conjugated isolectin B4 (I21413, ThermoFisher) dissolved in ACSF was pipetted on top of each slice (15 ml/slice). After this, slice preparations were incubated in darkness for 1 hour before measurement. All measurements took place within 4 hours after slicing. The ACSF contained (in mM): 126 NaCl, 2.5 KCl, 26 NaHCO₃, 2 CaCl₂, 2 MgCl₂, 1.25 NaH₂PO₄, 10 glucose, saturated with 95% O₂–5% CO₂.

Perforated patch recordings. After incubation for at least 1 hour, slices were transferred individually into a submerged-type recording chamber with a superfusion system allowing constantly bubbled (95% O₂–5% CO₂) ACSF to flow at a rate of 3 to 3.5 ml/min. The ACSF was adjusted to 300 to 305 mOsm (normotonic control solution), and the hypotonic solution was made by 50% dilution of control ACSF. Both normotonic and hypotonic solutions were constantly saturated with 95% O₂–5% CO₂ during measurements. All measurements were carried out at room temperature. A stock solution of 100 mg/ml gramicidin B (G5002, Sigma-Aldrich) diluted in DMSO was prepared daily and further diluted to 100 μg/ml concentration in the filtered pipette solution. We also added 100 μM Alexa Fluor 488 (A10436, ThermoFisher) to monitor membrane integrity during measurements. Before each recording, patch pipettes were fabricated from borosilicate glass and prefilled with gramicidin-free intracellular solution, and then backfilled with the intracellular solution containing gramicidin and Alexa 488. The pipette solution contained (in mM) the following: 120 KCl, 1 CaCl₂, 2 MgCl₂, 10 HEPES, and 11 EGTA (pH 7.3), 280 to 300 mOsm. Pipette resistances were 3 to 6 MΩ when filled with pipette solution. Visualization of slices and selection of cells (guided by isolectin B signal) was done under an upright microscope (BX61WI; Olympus, Tokyo, Japan, equipped with infrared-differential interference contrast optics and a UV lamp). Only cells located deeper than 15 to 20 μm measured from the slice surface were targeted. During recordings, Alexa 488 signal was constantly monitored to make sure that the membrane of cells did not suffer a rupture. Cells with an intracellular Alexa 488 signal were discarded. All cells were initially recorded in voltage-clamp mode at –40 mV holding potential. Series resistance was constantly monitored, and perforation was considered to be formed when the resistance fell to 35 to 50 MΩ (this regularly happened after 25 to 30 minutes after gigaseal formation). Individual recordings taken for analysis showed stability in series resistance and current response values between a 15% margin during the whole recording. After the perforated-patch configuration formed, resting membrane potential values were measured by changing the recording configuration to current-clamp mode at 0 pA for a short period of time (2 to 5 seconds). Thereafter, current responses to a pulse train of voltage steps from –140 mV to 60 mV with 20 mV increments were recorded in voltage-clamp mode with –40 mV holding potential. Each voltage step was 100 ms in duration and repeated 3 times. The interpulse interval was 2,000 ms. Pulse trains were recorded in the normotonic ACSF and after 5 minutes of perfusion with the hypotonic solution. Recordings were performed with a Multiclamp 700B amplifier (Molecular Devices). Data were digitized at 10 kHz with a DAQ board (National Instruments, USB-6353) and recorded with a custom software developed in C#.NET and VB.NET in the laboratory. For the extraction of current values, the last 40 ms of each voltage-step was used, during which the

current responses were in a steady-state. Analysis was done using custom software developed in Delphi and Python environments. Input resistance of cells were determined by calculating the slope of I-V curves between the -40 mV and 0 mV voltage steps both in WT and KO.

Automated morphological analysis of microglial cells

Mouse brains were cut into $100\mu\text{m}$ thick coronal slices and were immunostained with guinea pig anti-Iba1 (1:500; #234004, Synaptic Systems), Alexa 647 donkey anti-guinea pig (1:500; #706-606-148, Jackson ImmunoResearch) antibodies, and DAPI. Imaging was carried out in 0.1 M PB, using a Nikon Eclipse Ti-E inverted microscope (Nikon Instruments Europe B.V., Amsterdam, the Netherlands), with a CFI Plan Apochromat VC 60X water immersion objective (numerical aperture: 1.2) and an A1R laser confocal system. For 3D morphological analysis of microglial cells, the open-source MATLAB-based Microglia Morphology Quantification Tool was used (available at <https://github.com/isdneuroimaging/mmqt>). This method uses microglia and cell nuclei labeling to identify microglial cells. Briefly, 59 possible parameters describing microglial morphology are determined through the following automated steps: identification of microglia (nucleus, soma, branches) and background, creation of 3D skeletons, watershed segmentation, and segregation of individual cells [47].

Quantification and statistical analysis

All quantitative assessment was performed in a blinded manner. Based on the type and distribution of data populations (examined with Shapiro–Wilk normality tests), we applied appropriate statistical tests: In the case of 2 independent groups, Student *t* test or Mann–Whitney *U*-test was applied; for 3 or more independent groups, one-way ANOVA followed by Tukey’s post hoc comparison or Kruskal–Wallis test with Dunn’s multiple comparison test was applied. Data were analyzed using the GraphPad Prism version 8.2 for Windows software (GraphPad Software, San Diego, California, USA). In this study, data are expressed as mean \pm SEM, $p < 0.05$ was considered statistically significant.

Supporting information

S1 Fig. Effects of systemic vs. central blockade of NKCC1 on LPS-induced cytokine responses in the periphery. (A) ip. Bum injections further enhance the ip. LPS-induced G-CSF, IL- 1α , and IL- 1β production, while cor. LPS alone or with Bum has no significant effect on cytokine levels in the spleen and liver. (B) cor. LPS injection does not induce cytokine production, and Bum has no effect on baseline cytokine levels in the spleen and liver. (C, D) Flow cytometric dot plots show that cortical administration of Bum does not alter the numbers of CD4⁺ (P3 gate) and CD8⁺ (P4 gate) T cells and CD19⁺ MHCII⁺ (P6 gate) B cells in the spleen. All data are expressed as mean \pm SEM. (A) One-way ANOVA followed by Sidak’s multiple comparison test (spleen) and Kruskal–Wallis test followed by Dunn’s multiple comparison test (liver); * $p < 0.05$; ** $p < 0.01$; *** $p < 0.001$; N (veh.) = 5, N (veh. + ip. LPS) = 5, N (Bum + ip. LPS) = 5, N (veh. + cor. LPS) = 6, N (Bum + cor. LPS) = 9. (B) One-way ANOVA followed by Holm–Sidak’s multiple comparison test $N = 6$ /group. (D) Kruskal–Wallis test followed by Dunn’s multiple comparison test; N (veh.) = 4, N (cor. LPS) = 4, N (cor. Bum + LPS) = 5. Data underlying this figure can be found in [S1 Data](#). Bum, bumetanide; cor., cortical; ip., intraperitoneal; ns, not significant; veh., vehicle. (TIF)

S2 Fig. Intracortical blockade of NKCC1 does not alter astroglial GFAP or AQP4 levels. (A, B) CLSM images show immunolabeling for GFAP (yellow) and AQP4 (cyan) in NKCC1^{fl/}

ⁿ¹ animals 24 hours after cortical injection of LPS or LPS + Bum and in the corresponding contralateral areas. (C) Raw integrated densities were automatically measured on all images in randomly selected ROIs from the injected ipsilateral cortical and contralateral regions prior to statistical analysis. No statistically significant difference in GFAP and AQP4 expression levels is seen in parenchymal astrocytes or perivascular astrocyte endfeet. (B) Scale: 25 μ m. (C) One-way ANOVA followed by Holm–Sidak’s multiple comparisons test; $N = 4$ mice/group and 3–3 ROIs/animal. Data underlying this figure can be found in [S1 Data](#). Bum, bumetanide; LPS, lipopolysaccharide; ns, not significant; ROI, region of interest. (TIF)

S3 Fig. Microglial NKCC1 deficiency does not alter cytokine levels and main leukocyte populations in the spleen after intracortical LPS injection. (A, B) Cytokine levels in the spleen and liver do not differ between WT and NKCC1 KO mice after intracortical LPS administration. (C) Numbers of CD4⁺ (P4 gate), CD8⁺ (P5 gate) T cells, and CD19⁺ MHCII⁺ B cells (P6 gate) are not altered in the spleen of NKCC1 KO mice compared to WT. Microglial NKCC1 deficiency does not affect the proportion of monocytes (P8 gate) or granulocytes (P7 gate) compared to WT. (A, B) Mann–Whitney test, N (WT) = 8, N (KO) = 6. (C) Unpaired t test; N (WT) = 4, N (KO) = 4. Data underlying this figure can be found in [S1 Data](#). KO, knockout; ns: not significant; WT, wild type. (TIF)

S4 Fig. Deletion of NKCC1 from microglia results in a hyperpolarizing shift in the reversal of swelling-induced current. (A) I–V curves calculated by the subtraction of measured values in normotonic conditions from ones in hypotonic medium (WT: $N = 8$ cells, green with SEM; KO: $N = 8$ cells, blue with SEM), resulting in I–V curves representing the currents evoked by cell swelling due to osmotic change. (B) Reversal potentials of the swelling-induced currents measured from WT (green) or NKCC1 KO (blue) animals (left). Driving force was calculated for individual cells in WT (green) or KO (blue) by the subtraction of swelling-induced current reversal potentials from measured resting membrane potential (right). (B) Mann–Whitney; N (WT) = 8 cells, N (KO) = 8 cells; *: $p < 0.05$. Data underlying this figure can be found in [S1 Data](#). KO, knockout; WT, wild type. (TIF)

S5 Fig. Changes in mRNA levels of microglial ion channels, transporters, and exchangers in the absence of microglial NKCC1 and after LPS treatment. (A) The expression of most genes that contribute to ion regulation, membrane potential, and cell volume regulation (anion channels (CLIC1); K⁺ channels (Kv1.3; Kir2.1; THIK-1; TWIK-2); ion exchangers (NH1E Na⁺/H⁺ exchanger; NCX1 Na⁺/Ca²⁺ exchanger; CLCN3 H⁺/Cl⁻ exchanger); and transporters (KCC3 K⁺/Cl⁻ transporter)) are not altered in NKCC1 KO microglia. However, *Lrrc8d* mRNA levels show a 2-fold increase in NKCC1 KO microglia cells. (B) *Slc9a1*, *Slc8a1*, *Lrrc8d*, *Clic1*, *Cln3*, *Kcnk13*, *Kcnk6*, *Kcnj2*, *Sgk1* gene show decreased expression level in microglial cells 24 hours after intracisternal LPS injection. (C) *Slc9a1*, *Slc8a1*, *Slc12a6*, *Clic1*, *Cln3*, *Kcnk13*, *Kcnk6*, *Kcnj2*, *Sgk1*, *P2RY12* gene did not show altered expression between WT and NKCC1 KO microglia after intracisternal LPS treatment. (D) Summary table of investigated genes. (A–C) Unpaired t test. (A) N (WT) = 6, N (KO) = 5; **: $p < 0.01$. (B) N (WT) = 6, N (WT + LPS) = 5, *: $p < 0.05$, **: $p < 0.01$, *** $p < 0.001$. (C) N (WT + LPS) = 5, N (KO + LPS) = 6, *: $p < 0.05$. Data underlying this figure can be found in [S1 Data](#). KO, knockout; LPS, lipopolysaccharide; ns, not significant; WT, wild type. (TIF)

S6 Fig. Deletion of microglial NKCC1 does not alter astroglial GFAP and AQP4 levels. (A, B) CLSM images show immunolabeling for GFAP (yellow) and AQP4 (cyan) in microglial NKCC1 KO animals 24 hours after MCAo. (C) Raw integrated densities were automatically measured on all images in selected ROIs from the striatum, then, their per-animal average was calculated and used for statistical analysis. Data show no statistically significant differences in GFAP and AQP4 expression levels. (B) Scale: 25 μ m. (C) One-way ANOVA followed by Holm–Sidak’s multiple comparisons tests; N (WT) = 7, N (KO) = 8 mice and 3–3 ROIs/animal. Data underlying this figure can be found in [S1 Data](#). KO, knockout; MCAo, middle cerebral artery occlusion; ns, not significant; ROI, region of interest; WT, wild type. (TIF)

S7 Fig. Visual representation of the mathematical model of microglial process recruitment. (TIF)

S1 Video. In vivo 2P time-lapse imaging of Cx3CR1^{+/GFP} mice shows microglial responses to focal lesion-induced injury under control conditions (left) and after cisterna magna bumetanide injection (right). Lesion-induced microglial process recruitment was determined by model fitting using image data from the circular region marked on the video. The outer perimeter of this region corresponds to the lesion site. Scale: 50 μ m. (AVI)

S1 Data. Underlying numerical data for Figs 1A–1C, 1E, 2A, 2C, 2D, 2G, 3C–3E, 4A, 4D–4G, 5C–5G, 6B, 6C, and 6E and S1A, S1B, S1D, S2C, S3A–S3C, S4A, S4B, S5A–S5C, and S6C. (XLSX)

Acknowledgments

We thank János Szabadics for his valuable remarks on the electrophysiology part of the manuscript; László Barna and the Nikon Imaging Center at the Institute of Experimental Medicine for kindly providing microscopy support; Dóra Gali-Györkei for her excellent technical assistance; and the Cell Biology Center at the Institute of Experimental Medicine.

Author Contributions

Conceptualization: Christian A. Hübner, Kai Kaila, Zsuzsanna Környei, Ádám Dénes.

Data curation: Krisztina Tóth, Ádám Dénes.

Formal analysis: Krisztina Tóth, Nikolett Lénárt, Péter Berki, Balázs Pósfai, Szilvia Benkő, Dániel Kiss.

Funding acquisition: Ádám Dénes.

Investigation: Krisztina Tóth, Nikolett Lénárt, Péter Berki, Rebeka Fekete, Eszter Szabadits, Balázs Pósfai, Csaba Cserép, Ahmad Alatshan, Zsuzsanna Környei.

Methodology: Krisztina Tóth, Nikolett Lénárt, Péter Berki, Eszter Szabadits, Christian A. Hübner, Attila Gulyás, Ádám Dénes.

Project administration: Ádám Dénes.

Resources: Szilvia Benkő, Christian A. Hübner, Ádám Dénes.

Software: Dániel Kiss.

Supervision: Zsuzsanna Környei, Ádám Dénes.

Validation: Krisztina Tóth, Nikolett Lénárt, Péter Berki, Eszter Szabadits, Balázs Pósfai.

Visualization: Krisztina Tóth, Eszter Szabadits, Balázs Pósfai, Csaba Cserép, Dániel Kiss.

Writing – original draft: Krisztina Tóth, Zsuzsanna Környei, Ádám Dénes.

Writing – review & editing: Krisztina Tóth, Zsuzsanna Környei, Ádám Dénes.

References

1. Kaila K, Price TJ, Payne JA, Puskarjov M, Voipio J. Cation-chloride cotransporters in neuronal development, plasticity and disease. *Nat Rev Neurosci*. 2014; 15:637–54. <https://doi.org/10.1038/nrn3819> PMID: 25234263
2. Huang H, Song S, Banerjee S, Jiang T, Zhang J, Kahle KT, et al. The WNK-SPAK/OSR1 Kinases and the Cation-Chloride Cotransporters as Therapeutic Targets for Neurological Diseases. *Aging Dis*. 2019; 10:626. <https://doi.org/10.14336/AD.2018.0928> PMID: 31165006
3. Huberfeld G, Wittner L, Clemenceau S, Baulac M, Kaila K, Miles R, et al. Perturbed chloride homeostasis and GABAergic signaling in human temporal lobe epilepsy. *J Neurosci*. 2007; 27:9866–73. <https://doi.org/10.1523/JNEUROSCI.2761-07.2007> PMID: 17855601
4. Kaila K, Ruusuvuori E, Seja P, Voipio J, Puskarjov M. GABA actions and ionic plasticity in epilepsy. *Curr Opin Neurobiol*. 2014;34–41. <https://doi.org/10.1016/j.conb.2013.11.004> PMID: 24650502
5. Shekarabi M, Zhang J, Khanna AR, Ellison DH, Delpire E, Kahle KT. WNK Kinase Signaling in Ion Homeostasis and Human Disease. *Cell Metab*. 2017;285–99. <https://doi.org/10.1016/j.cmet.2017.01.007> PMID: 28178566
6. Schulte JT, Wierenga CJ, Bruining H. Chloride transporters and GABA polarity in developmental, neurological and psychiatric conditions. *Neurosci Biobehav Rev*. 2018;260–71. <https://doi.org/10.1016/j.neubiorev.2018.05.001> PMID: 29729285
7. Ben-Ari Y. NKCC1 Chloride Importer Antagonists Attenuate Many Neurological and Psychiatric Disorders. *Trends Neurosci*. 2017;536–54. <https://doi.org/10.1016/j.tins.2017.07.001> PMID: 28818303
8. Kharod SC, Kang SK, Kadam SD. Off-label use of bumetanide for brain disorders: An overview. *Front Neurosci*. 2019. <https://doi.org/10.3389/fnins.2019.00310> PMID: 31068771
9. Lemonnier E, Degrez C, Phelep M, Tyzio R, Josse F, Grandgeorge M, et al. A randomised controlled trial of bumetanide in the treatment of autism in children. *Transl Psychiatry*. 2012; 2:202. <https://doi.org/10.1038/tp.2012.124> PMID: 23233021
10. Puskarjov M, Kahle KT, Ruusuvuori E, Kaila K. Pharmacotherapeutic targeting of cation-chloride cotransporters in neonatal seizures. *Epilepsia*. 2014;806–18. <https://doi.org/10.1111/epi.12620> PMID: 24802699
11. Löscher W, Puskarjov M, Kaila K. Cation-chloride cotransporters NKCC1 and KCC2 as potential targets for novel antiepileptic and antiepileptogenic treatments. *Neuropharmacology*. 2013;62–74. <https://doi.org/10.1016/j.neuropharm.2012.05.045> PMID: 22705273
12. Töllner K, Brandt C, Töpfer M, Brunhofer G, Erker T, Gabriel M, et al. A novel prodrug-based strategy to increase effects of bumetanide in epilepsy. *Ann Neurol*. 2014; 75:550–62. <https://doi.org/10.1002/ana.24124> PMID: 24615913
13. Töllner K, Brandt C, Römermann K, Löscher W. The organic anion transport inhibitor probenecid increases brain concentrations of the NKCC1 inhibitor bumetanide. *Eur J Pharmacol*. 2015; 746:167–73. <https://doi.org/10.1016/j.ejphar.2014.11.019> PMID: 25449033
14. Römermann K, Fedrowitz M, Hampel P, Kaczmarek E, Töllner K, Erker T, et al. Multiple blood-brain barrier transport mechanisms limit bumetanide accumulation, and therapeutic potential, in the mammalian brain. *Neuropharmacology*. 2017; 117:182–94. <https://doi.org/10.1016/j.neuropharm.2017.02.006> PMID: 28192112
15. Virtanen MA, Uvarov P, Hübner CA, Kaila K. NKCC1, an Elusive Molecular Target in Brain Development: Making Sense of the Existing Data. *Cell*. 2020; 9:2607. <https://doi.org/10.3390/cells9122607> PMID: 33291778
16. Wang H, Yan Y, Kintner DB, Lytle C, Sun D. GABA-mediated trophic effect on oligodendrocytes requires Na-K-2Cl cotransport activity. *J Neurophysiol*. 2003; 90:1257–65. <https://doi.org/10.1152/jn.01174.2002> PMID: 12904508

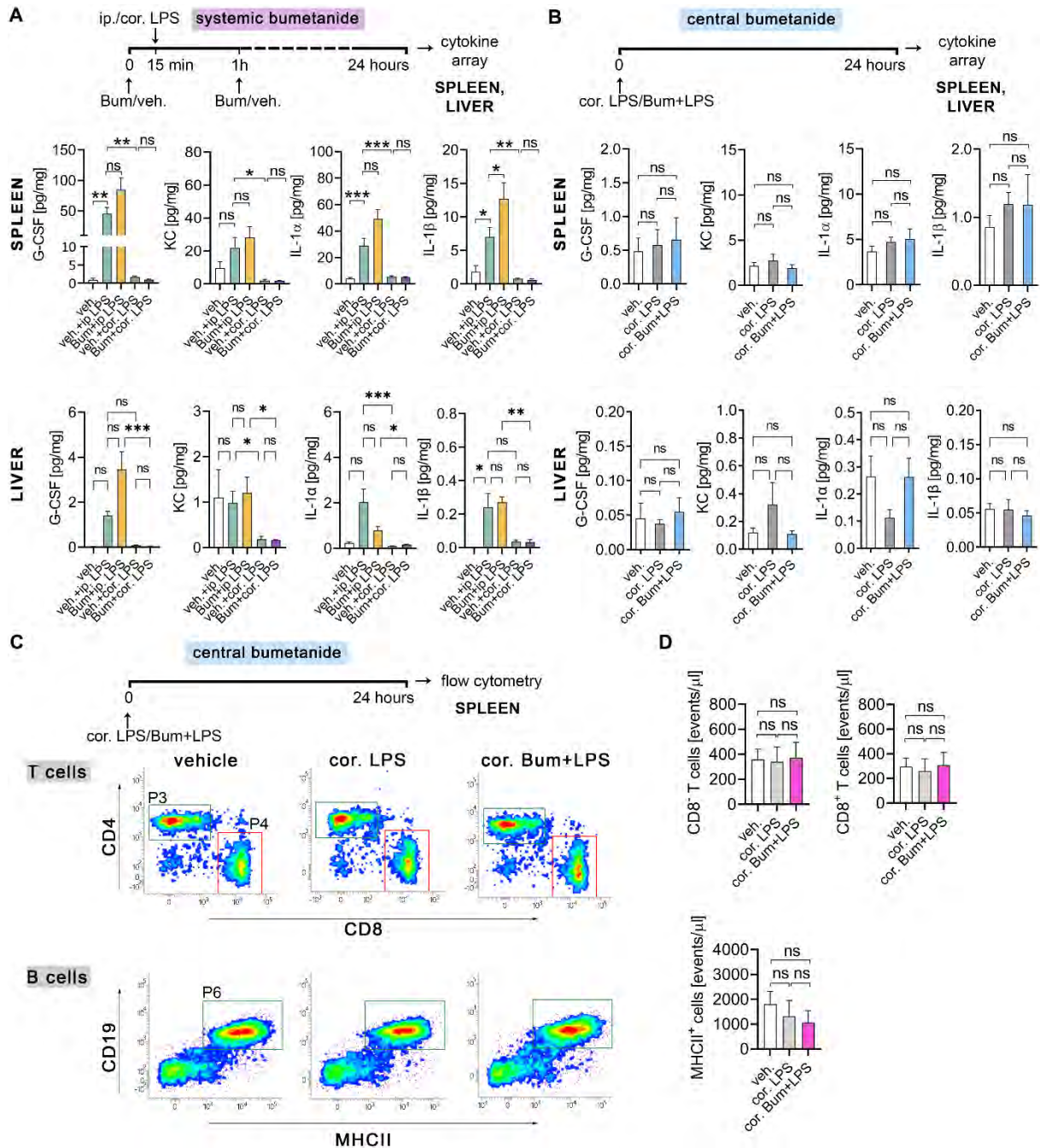
17. Yu Y, Fu P, Yu Z, Xie M, Wang W, Luo X. NKCC1 Inhibition Attenuates Chronic Cerebral Hypoperfusion-Induced White Matter Lesions by Enhancing Progenitor Cells of Oligodendrocyte Proliferation. *J Mol Neurosci*. 2018; 64:449–58. <https://doi.org/10.1007/s12031-018-1043-0> PMID: 29502291
18. Henneberger C, Bard L, Panatier A, Reynolds JP, Kopach O, Medvedev NI, et al. LTP Induction Boosts Glutamate Spillover by Driving Withdrawal of Perisynaptic Astroglia. *Neuron*. 2020 [cited 2020 Nov 15]. <https://doi.org/10.1016/j.neuron.2020.08.030> PMID: 32976770
19. Noor ZN, Deitmer JW, Theparambil SM. Cytosolic sodium regulation in mouse cortical astrocytes and its dependence on potassium and bicarbonate. *J Cell Physiol*. 2019; 234:89–99. <https://doi.org/10.1002/jcp.26824> PMID: 30132845
20. Su G, Kintner DB, Flagella M, Shull GE, Sun D. Astrocytes from Na⁺-K⁺-Cl⁻ cotransporter-null mice exhibit absence of swelling and decrease in EAA release. *Am J Physiol Cell Physiol*. 2002;282. <https://doi.org/10.1152/ajpcell.00538.2001> PMID: 11940530
21. Zhang Y, Chen K, Sloan SA, Bennett ML, Scholze AR, O’Keefe S, et al. An RNA-sequencing transcriptome and splicing database of glia, neurons, and vascular cells of the cerebral cortex. *J Neurosci*. 2014; 34:11929–47. <https://doi.org/10.1523/JNEUROSCI.1860-14.2014> PMID: 25186741
22. Kaila K, Price TJ, Payne JA, Puskarjov M, Voipio J. Cation-chloride cotransporters in neuronal development, plasticity and disease. *Nat Rev Neurosci*. 2014;637–654. <https://doi.org/10.1038/nrn3819> PMID: 25234263
23. Huang LQ, Zhu GF, Deng YY, Jiang WQ, Fang M, Chen CB, et al. Hypertonic saline alleviates cerebral edema by inhibiting microglia-derived TNF- α and IL-1 β -induced Na-K-Cl Cotransporter up-regulation. *J Neuroinflammation*. 2014;11. <https://doi.org/10.1186/1742-2094-11-11> PMID: 24447830
24. Pozdeev VI, Lang E, Görg B, Bidmon HJ, Shinde P V., Kircheis G, et al. TNF α induced up-regulation of Na⁺,K⁺,2Cl⁻ cotransporter NKCC1 in hepatic ammonia clearance and cerebral ammonia toxicity. *Sci Rep*. 2017;7. <https://doi.org/10.1038/s41598-017-00035-9> PMID: 28127057
25. Reid AY, Riazi K, Campbell Teskey G, Pittman QJ. Increased excitability and molecular changes in adult rats after a febrile seizure. *Epilepsia*. 2013;54. <https://doi.org/10.1111/epi.12278> PMID: 24001074
26. Weidenfeld S, Kuebler WM. Cytokine-regulation of Na⁺-K⁺-Cl⁻ cotransporter 1 and cystic fibrosis transmembrane conductance regulator-potential role in pulmonary inflammation and edema formation. *Front Immunol*. 2017:393. <https://doi.org/10.3389/fimmu.2017.00393> PMID: 28439270
27. Salter MW, Stevens B. Microglia emerge as central players in brain disease. *Nat Med*. 2017; 23:1018–1027. <https://doi.org/10.1038/nm.4397> PMID: 28886007
28. Song WM, Colonna M. The identity and function of microglia in neurodegeneration. *Nat Immunol*. 2018:1048–1058. <https://doi.org/10.1038/s41590-018-0212-1> PMID: 30250185
29. Wu W, Li Y, Wei Y, Bosco DB, Xie M, Zhao MG, et al. Microglial depletion aggravates the severity of acute and chronic seizures in mice. *Brain Behav Immun*. 2020; 89:245–55. <https://doi.org/10.1016/j.bbi.2020.06.028> PMID: 32621847
30. Badimon A, Strasburger HJ, Ayata P, Chen X, Nair A, Ikegami A, et al. Negative feedback control of neuronal activity by microglia. *Nature*. 2020; 586:417–23. <https://doi.org/10.1038/s41586-020-2777-8> PMID: 32999463
31. Cserép C, Pósfai B, Lénárt N, Fekete R, László ZI, Lele Z, et al. Microglia monitor and protect neuronal function through specialized somatic purinergic junctions. *Science*. 2020; 367:528–37. <https://doi.org/10.1126/science.aax6752> PMID: 31831638
32. Szalay G, Martinecz B, Lénárt N, Környei Z, Orsolits B, Judák L, et al. Microglia protect against brain injury and their selective elimination dysregulates neuronal network activity after stroke. *Nat Commun*. 2016; 7:11499. <https://doi.org/10.1038/ncomms11499> PMID: 27139776
33. Eyo UB, Peng J, Swiatkowski P, Mukherjee A, Bispo A, Wu L-J. Neuronal hyperactivity recruits microglial processes via neuronal NMDA receptors and microglial P2Y₁₂ receptors after status epilepticus. *J Neurosci*. 2014; 34:10528–40. <https://doi.org/10.1523/JNEUROSCI.0416-14.2014> PMID: 25100587
34. Ayata C, Lauritzen M. Spreading depression, spreading depolarizations, and the cerebral vasculature. *Physiol Rev*. 2015; 95:953–93. <https://doi.org/10.1152/physrev.00027.2014> PMID: 26133935
35. Madry C, Kyrargyri V, Arancibia-Cárcamo IL, Jolivet R, Kohsaka S, Bryan RM, et al. Microglial Ramification, Surveillance, and Interleukin-1 β Release Are Regulated by the Two-Pore Domain K⁺ Channel THIK-1. *Neuron*. 2018; 97:299–312.e6. <https://doi.org/10.1016/j.neuron.2017.12.002> PMID: 29290552
36. Nguyen HM, Grössinger EM, Horiuchi M, Davis KW, Jin L-W, Maezawa I, et al. Differential Kv1.3, KCa3.1, and Kir2.1 expression in “classically” and “alternatively” activated microglia. *Glia*. 2017; 65:106–21. <https://doi.org/10.1002/glia.23078> PMID: 27696527
37. Di A, Xiong S, Ye Z, Malireddi RKS, Kometani S, Zhong M, et al. The TWIK2 Potassium Efflux Channel in Macrophages Mediates NLRP3 Inflammasome-Induced Inflammation. *Immunity*. 2018; 49:56–65.e4. <https://doi.org/10.1016/j.immuni.2018.04.032> PMID: 29958799

38. He Y, Zeng MY, Yang D, Motro B, Núñez G. NEK7 is an essential mediator of NLRP3 activation downstream of potassium efflux. *Nature*. 2016; 530:354–7. <https://doi.org/10.1038/nature16959> PMID: [26814970](https://pubmed.ncbi.nlm.nih.gov/26814970/)
39. Tang T, Lang X, Xu C, Wang X, Gong T, Yang Y, et al. CLICs-dependent chloride efflux is an essential and proximal upstream event for NLRP3 inflammasome activation. *Nat Commun*. 2017;8. <https://doi.org/10.1038/s41467-017-00021-9> PMID: [28364116](https://pubmed.ncbi.nlm.nih.gov/28364116/)
40. Bennett ML, Bennett FC, Liddelov SA, Ajami B, Zamanian JL, Fernhoff NB, et al. New tools for studying microglia in the mouse and human CNS. *Proc Natl Acad Sci U S A*. 2016; 113:E1738–46. <https://doi.org/10.1073/pnas.1525528113> PMID: [26884166](https://pubmed.ncbi.nlm.nih.gov/26884166/)
41. Giles JA, Greenhalgh AD, Davies CL, Denes A, Shaw T, Coutts G, et al. Requirement for interleukin-1 to drive brain inflammation reveals tissue-specific mechanisms of innate immunity. *Eur J Immunol*. 2015; 45:525–30. <https://doi.org/10.1002/eji.201444748> PMID: [25367678](https://pubmed.ncbi.nlm.nih.gov/25367678/)
42. Heneka MT, Kummer MP, Latz E. Innate immune activation in neurodegenerative disease. *Nat Rev Immunol*. 2014:463–477. <https://doi.org/10.1038/nri3705> PMID: [24962261](https://pubmed.ncbi.nlm.nih.gov/24962261/)
43. Allan SM, Tyrrell PJ, Rothwell NJ. Interleukin-1 and neuronal injury. *Nature Reviews Immunology*. *Nat Rev Immunol*. 2005:629–40. <https://doi.org/10.1038/nri1664> PMID: [16034365](https://pubmed.ncbi.nlm.nih.gov/16034365/)
44. Nimmerjahn A, Kirchhoff F, Helmchen F. Neuroscience: Resting microglial cells are highly dynamic surveillants of brain parenchyma in vivo. *Science*. 2005; 308:1314–8. <https://doi.org/10.1126/science.1110647> PMID: [15831717](https://pubmed.ncbi.nlm.nih.gov/15831717/)
45. Davalos D, Grutzendler J, Yang G, Kim JV, Zuo Y, Jung S, et al. ATP mediates rapid microglial response to local brain injury in vivo. *Nat Neurosci*. 2005; 8:752–8. <https://doi.org/10.1038/nn1472> PMID: [15895084](https://pubmed.ncbi.nlm.nih.gov/15895084/)
46. Fekete R, Cserép C, Lénárt N, Tóth K, Orsolits B, Martinecz B, et al. Microglia control the spread of neurotropic virus infection via P2Y12 signalling and recruit monocytes through P2Y12-independent mechanisms. *Acta Neuropathol*. 2018; 136:461–82. <https://doi.org/10.1007/s00401-018-1885-0> PMID: [30027450](https://pubmed.ncbi.nlm.nih.gov/30027450/)
47. Heindl S, Gesierich B, Benakis C, Llovera G, Duering M, Liesz A. Automated morphological analysis of microglia after stroke. *Front Cell Neurosci*. 2018;12. <https://doi.org/10.3389/fncel.2018.00012> PMID: [29440991](https://pubmed.ncbi.nlm.nih.gov/29440991/)
48. Kahle KT, Khanna AR, Alper SL, Adragna NC, Lauf PK, Sun D, et al. K-Cl cotransporters, cell volume homeostasis, and neurological disease. *Trends Mol Med*. 2015:513–23. <https://doi.org/10.1016/j.molmed.2015.05.008> PMID: [26142773](https://pubmed.ncbi.nlm.nih.gov/26142773/)
49. Russell JM. Sodium-potassium-chloride cotransport. *Physiol Rev*. 2000:211–76. <https://doi.org/10.1152/physrev.2000.80.1.211> PMID: [10617769](https://pubmed.ncbi.nlm.nih.gov/10617769/)
50. Swanson K V., Deng M, Ting JPY. The NLRP3 inflammasome: molecular activation and regulation to therapeutics. *Nature Reviews Immunology*. Nature Publishing Group; 2019. pp. 477–489. <https://doi.org/10.1038/s41577-019-0165-0> PMID: [31036962](https://pubmed.ncbi.nlm.nih.gov/31036962/)
51. Heneka MT, McManus RM, Latz E. Inflammasome signalling in brain function and neurodegenerative disease. *Nat Rev Neurosci*. 2018:610–621. <https://doi.org/10.1038/s41583-018-0055-7> PMID: [30206330](https://pubmed.ncbi.nlm.nih.gov/30206330/)
52. Wendeln AC, Degenhardt K, Kaurani L, Gertig M, Ulas T, Jain G, et al. Innate immune memory in the brain shapes neurological disease hallmarks. *Nature*. 2018; 556:332–8. <https://doi.org/10.1038/s41586-018-0023-4> PMID: [29643512](https://pubmed.ncbi.nlm.nih.gov/29643512/)
53. Eder C, Klee R, Heinemann U. Involvement of stretch-activated Cl⁻ channels in ramification of murine microglia. *J Neurosci*. 1998; 18:7127–37. <https://doi.org/10.1523/JNEUROSCI.18-18-07127.1998> PMID: [9736636](https://pubmed.ncbi.nlm.nih.gov/9736636/)
54. Ducharme G, Newell EW, Pinto C, Schlichter LC. Small-conductance Cl⁻ channels contribute to volume regulation and phagocytosis in microglia. *Eur J Neurosci*. 2007; 26:2119–30. <https://doi.org/10.1111/j.1460-9568.2007.05802.x> PMID: [17927776](https://pubmed.ncbi.nlm.nih.gov/17927776/)
55. Schlichter LC, Mertens T, Liu B. Swelling activated Cl⁻ channels in microglia: Biophysics, pharmacology and role in glutamate release. *Channels*. 2011; 5:128–37. <https://doi.org/10.4161/chan.5.2.14310> PMID: [21150294](https://pubmed.ncbi.nlm.nih.gov/21150294/)
56. Murana E, Pagani F, Basilico B, Sundukova M, Batti L, Di Angelantonio S, et al. ATP release during cell swelling activates a Ca²⁺-dependent Cl⁻—Current by autocrine mechanism in mouse hippocampal microglia. *Sci Rep*. 2017;7. <https://doi.org/10.1038/s41598-017-00035-9> PMID: [28127057](https://pubmed.ncbi.nlm.nih.gov/28127057/)
57. Luo L, Song S, Ezenwukwa CC, Jalali S, Sun B, Sun D. Ion channels and transporters in microglial function in physiology and brain diseases. *Neurochem Int*. 2021;142. <https://doi.org/10.1016/j.neuint.2020.104925> PMID: [33248207](https://pubmed.ncbi.nlm.nih.gov/33248207/)

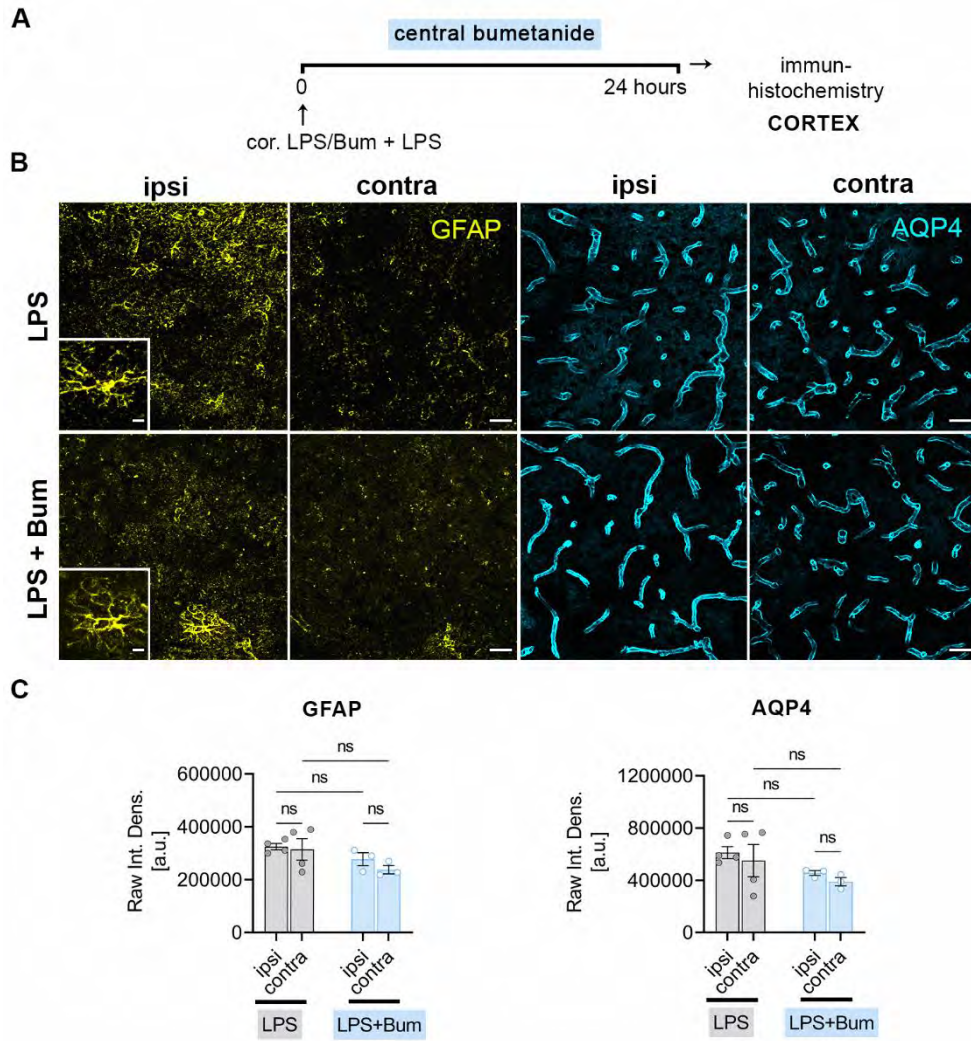
58. Izquierdo P, Attwell D, Madry C. Ion Channels and Receptors as Determinants of Microglial Function. *Trends Neurosci.* 2019;278–92. <https://doi.org/10.1016/j.tins.2018.12.007> PMID: 30678990
59. Chen L, König B, Liu T, Pervaiz S, Razzaque YS, Stauber T. More than just a pressure relief valve: Physiological roles of volume-regulated LRRC8 anion channels. *Biol Chem.* 2020;1481–96. <https://doi.org/10.1515/hsz-2019-0189> PMID: 31091194
60. Luo L, Song S, Ezenwukwa CC, Jalali S, Sun B, Sun D. Ion Channels and Transporters in Microglial Function in Physiology and Brain Diseases. *Neurochem Int.* 2020;104925. <https://doi.org/10.1016/j.neuint.2020.104925> PMID: 33248207
61. Hung CM, Peng CK, Sen YS, Shui HA, Huang KL. WNK4–SPAK modulates lipopolysaccharide-induced macrophage activation. *Biochem Pharmacol.* 2020;171. <https://doi.org/10.1016/j.bcp.2019.113738> PMID: 31786261
62. Lemonnier E, Degrez C, Phelep M, Tyzio R, Josse F, Grandgeorge M, et al. A randomised controlled trial of bumetanide in the treatment of autism in children. *Transl Psychiatry.* 2012; 2:202. <https://doi.org/10.1038/tp.2012.124> PMID: 23233021
63. Javdani F, Hegedűs K, Miranda CO, Hegyi Z, Holló K, Antal M. Differential expression of Na⁺/K⁺/Cl⁻ cotransporter 1 in neurons and glial cells within the superficial spinal dorsal horn of rodents. *Sci Rep.* 2020;10. <https://doi.org/10.1038/s41598-019-56089-4> PMID: 32001736
64. Davalos D, Grutzendler J, Yang G, Kim JV, Zuo Y, Jung S, et al. ATP mediates rapid microglial response to local brain injury in vivo. *Nat Neurosci.* 2005; 8:752–8. <https://doi.org/10.1038/nn1472> PMID: 15895084
65. Haynes SE, Hollopeter G, Yang G, Kurpius D, Dailey ME, Gan WB, et al. The P2Y₁₂ receptor regulates microglial activation by extracellular nucleotides. *Nat Neurosci.* 2006; 9:1512–9. <https://doi.org/10.1038/nn1805> PMID: 17115040
66. Butovsky O, Jedrychowski MP, Moore CS, Cialic R, Lanser AJ, Gabriely G, et al. Identification of a unique TGF- β -dependent molecular and functional signature in microglia. *Nat Neurosci.* 2014; 17:131–43. <https://doi.org/10.1038/nn.3599> PMID: 24316888
67. Schiapparelli P, Guerrero-Cazares H, Magaña-Maldonado R, Hamilla SM, Ganaha S, Goulin Lippi Fernandes E, et al. NKCC1 Regulates Migration Ability of Glioblastoma Cells by Modulation of Actin Dynamics and Interacting with Cofilin. *EBioMedicine.* 2017; 21:94–103. <https://doi.org/10.1016/j.ebiom.2017.06.020> PMID: 28679472
68. Ma H, Li T, Tao Z, Hai L, Tong L, Yi L, et al. NKCC1 promotes EMT-like process in GBM via RhoA and Rac1 signaling pathways. *J Cell Physiol.* 2019; 234:1630–42. <https://doi.org/10.1002/jcp.27033> PMID: 30159893
69. Madry C, Arancibia-Cárcamo IL, Kyrargyri V, Chan VTT, Hamilton NB, Attwell D. Effects of the ecto-ATPase apyrase on microglial ramification and surveillance reflect cell depolarization, not ATP depletion. *Proc Natl Acad Sci U S A.* 2018; 115:E1608–17. <https://doi.org/10.1073/pnas.1715354115> PMID: 29382767
70. Choi H, Rohrbough JC, Nguyen HN, Dikalova A, Lamb FS. Oxidant-resistant LRRC8A/C anion channels support superoxide production by NADPH oxidase 1. *J Physiol.* 2021; 599:3013–36. <https://doi.org/10.1113/JP281577> PMID: 33932953
71. Bhandage AK, Kanatani S, Barragan A. Toxoplasma-Induced Hypermigration of Primary Cortical Microglia Implicates GABAergic Signaling. *Front Cell Infect Microbiol.* 2019; 0:73. <https://doi.org/10.3389/fcimb.2019.00073> PMID: 30949457
72. Gillen CM, Forbush B. Functional interaction of the K-Cl cotransporter (KCC1) with the Na-K-Cl cotransporter in HEK-293 cells. *Am J Physiol Cell Physiol.* 1999;276. <https://doi.org/10.1152/ajpcell.1999.276.2.C328> PMID: 9950760
73. Brough D, Rothwell NJ, Allan SM. Interleukin-1 as a pharmacological target in acute brain injury. *Exp Physiol.* 2015;1488–94. <https://doi.org/10.1113/EP085135> PMID: 26096539
74. Lambertsen KL, Biber K, Finsen B. Inflammatory cytokines in experimental and human stroke. *Journal of Cerebral Blood Flow and Metabolism. J Cereb Blood Flow Metab.* 2012;1677–98. <https://doi.org/10.1038/jcbfm.2012.88> PMID: 22739623
75. Wofford KL, Loane DJ, Cullen DK. Acute drivers of neuroinflammation in traumatic brain injury. *Neural Regen Res.* 2019;1481–9. <https://doi.org/10.4103/1673-5374.255958> PMID: 31089036
76. Denes A, Thornton P, Rothwell NJ, Allan SM. Inflammation and brain injury: Acute cerebral ischaemia, peripheral and central inflammation. *Brain, Behavior, and Immunity.* 2010;708–23. <https://doi.org/10.1016/j.bbi.2009.09.010> PMID: 19770034
77. Battey TWK, Karki M, Singhal AB, Wu O, Sadaghiani S, Campbell BCV, et al. Brain edema predicts outcome after nonlacunar ischemic stroke. *Stroke.* 2014; 45:3643–8. <https://doi.org/10.1161/STROKEAHA.114.006884> PMID: 25336512

78. Yao Y, Zhang Y, Liao X, Yang R, Lei Y, Luo J. Potential Therapies for Cerebral Edema After Ischemic Stroke: A Mini Review. *Front Aging Neurosci*. 2021. <https://doi.org/10.3389/fnagi.2020.618819> PMID: 33613264
79. Zhang J, Bhuiyan MIH, Zhang T, Karimy JK, Wu Z, Fiesler VM, et al. Modulation of brain cation-Cl⁻ cotransport via the SPAK kinase inhibitor ZT-1a. *Nat Commun*. <https://doi.org/10.1038/s41467-019-13851-6> PMID: 31911626
80. Kilkenny C, Browne WJ, Cuthill IC, Emerson M, Altman DG. Improving Bioscience Research Reporting: The ARRIVE Guidelines for Reporting Animal Research. *PLoS Biol*. 2010; 8:e1000412. <https://doi.org/10.1371/journal.pbio.1000412> PMID: 20613859
81. Percie du Sert N, Alfieri A, Allan SM, Carswell HVO, Deuchar GA, Farr TD, et al. The IMPROVE Guidelines (Ischaemia Models: Procedural Refinements Of in Vivo Experiments). *J Cereb Blood Flow Metab*. 2017:3488–517. <https://doi.org/10.1177/0271678X17709185> PMID: 28797196
82. Yona S, Kim K-W, Wolf Y, Mildner A, Varol D, Breker M, et al. Fate Mapping Reveals Origins and Dynamics of Monocytes and Tissue Macrophages under Homeostasis. *Immunity*. 2013; 38:79–91. <https://doi.org/10.1016/j.immuni.2012.12.001> PMID: 23273845
83. Antoine MW, Hübner CA, Arezzo JC, Hébert JM. A causative link between inner ear defects and long-term striatal dysfunction. *Science*. 2013; 341:1120–3. <https://doi.org/10.1126/science.1240405> PMID: 24009395
84. Donocoff RS, Teteloshvili N, Chung H, Shoulson R, Creusot RJ. Optimization of tamoxifen-induced Cre activity and its effect on immune cell populations. *Sci Rep*. 2020;10. <https://doi.org/10.1038/s41598-019-56089-4> PMID: 32001736
85. Otxoa-de-Amezaga A, Miró-Mur F, Pedragosa J, Gallizioli M, Justicia C, Gaja-Capdevila N, et al. Microglial cell loss after ischemic stroke favors brain neutrophil accumulation. *Acta Neuropathol*. 2019; 137:321–41. <https://doi.org/10.1007/s00401-018-1954-4> PMID: 30580383
86. Giles JA, Greenhalgh AD, Denes A, Nieswandt B, Coutts G, McColl BW, et al. Neutrophil infiltration to the brain is platelet-dependent, and is reversed by blockade of platelet GPIIb₃. *Immunology*. 2018; 154:322–8. <https://doi.org/10.1111/imm.12892> PMID: 29325217
87. Denes A, Coutts G, Lénárt N, Cruickshank SM, Pelegrin P, Skinner J, et al. AIM2 and NLRP4 inflammasomes contribute with ASC to acute brain injury independently of NLRP3. *Proc Natl Acad Sci U S A*. 2015; 112:4050–5. <https://doi.org/10.1073/pnas.1419090112> PMID: 25775556
88. McQuin C, Goodman A, Chernyshev V, Kamensky L, Cimini BA, Karhohs KW, et al. CellProfiler 3.0: Next-generation image processing for biology. *PLoS Biol* 2018;16. <https://doi.org/10.1371/journal.pbio.2005970> PMID: 29969450
89. Dénes Á, Humphreys N, Lane TE, Grecis R, Rothwell N. Chronic systemic infection exacerbates ischemic brain damage via a CCL5 (regulated on activation, normal T-cell expressed and secreted)-mediated proinflammatory response in mice. *J Neurosci*. 2010; 30:10086–95. <https://doi.org/10.1523/JNEUROSCI.1227-10.2010> PMID: 20668193
90. Bederson JB, Pitts LH, Tsuji M, Nishimura MC, Davis RL, Bartkowski H. Rat middle cerebral artery occlusion: Evaluation of the model and development of a neurologic examination. *Stroke*. 1986; 17:472–6. <https://doi.org/10.1161/01.str.17.3.472> PMID: 3715945
91. Iadecola C, Zhang F, Casey R, Nagayama M, Elizabeth RM. Delayed reduction of ischemic brain injury and neurological deficits in mice lacking the inducible nitric oxide synthase gene. *J Neurosci*. 1997; 17:9157–64. <https://doi.org/10.1523/JNEUROSCI.17-23-09157.1997> PMID: 9364062
92. Schaar KL, Brenneman MM, Savitz SI. Functional assessments in the rodent stroke model. *Exp Transl Stroke Med*. 2010. <https://doi.org/10.1186/2040-7378-2-13> PMID: 20642841
93. Orsini F, Villa P, Parrella S, Zangari R, Zanier ER, Gesuete R, et al. Targeting mannose-binding lectin confers long-lasting protection with a surprisingly wide therapeutic window in cerebral ischemia. *Circulation*. 2012; 126:1484–94. <https://doi.org/10.1161/CIRCULATIONAHA.112.103051> PMID: 22879370
94. McColl BW, Rothwell NJ, Allan SM. Systemic inflammatory stimulus potentiates the acute phase and CXC chemokine responses to experimental stroke and exacerbates brain damage via interleukin-1- and neutrophil-dependent mechanisms. *J Neurosci*. 2007; 27:4403–12. <https://doi.org/10.1523/JNEUROSCI.5376-06.2007> PMID: 17442825

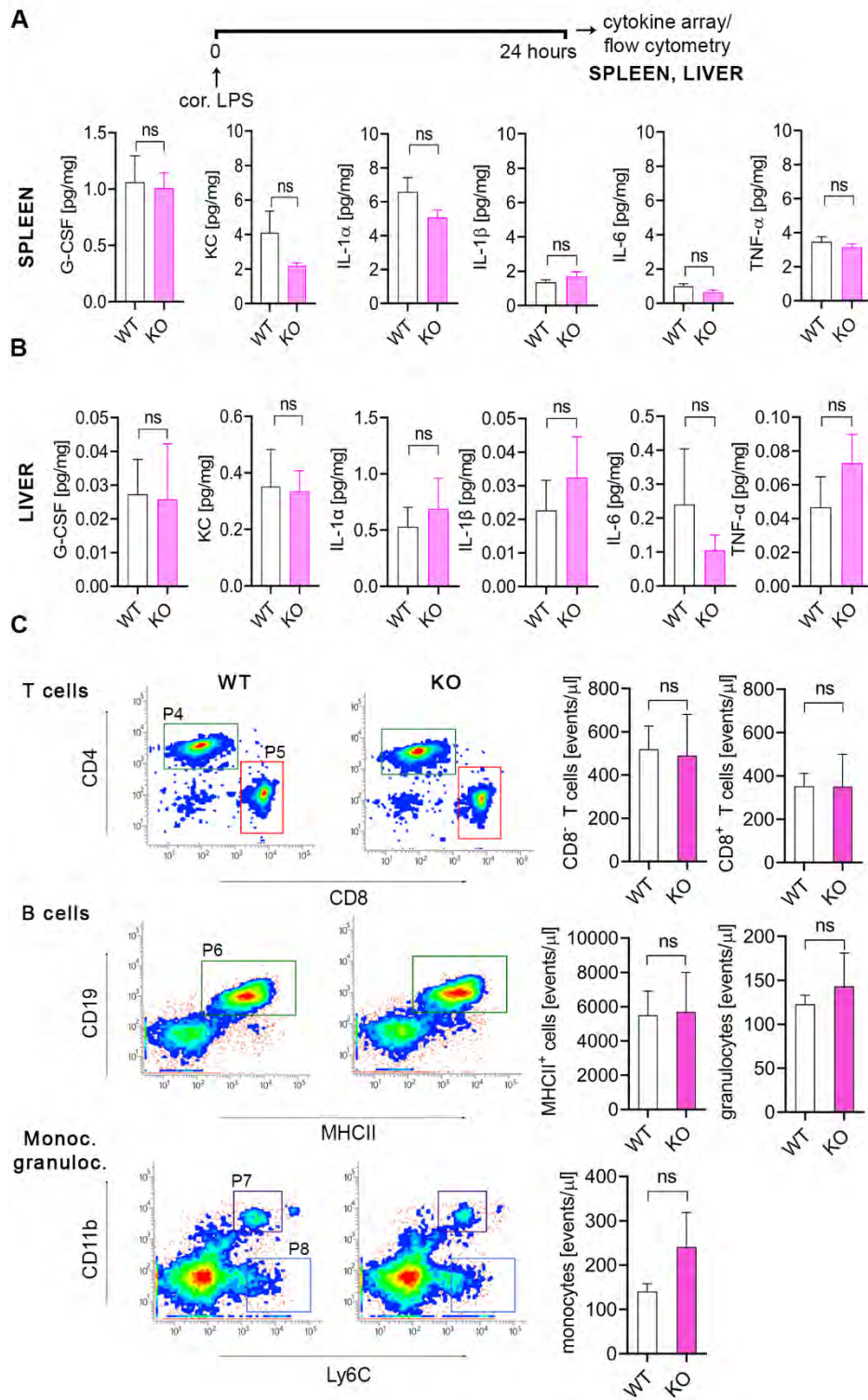
S1 Fig.



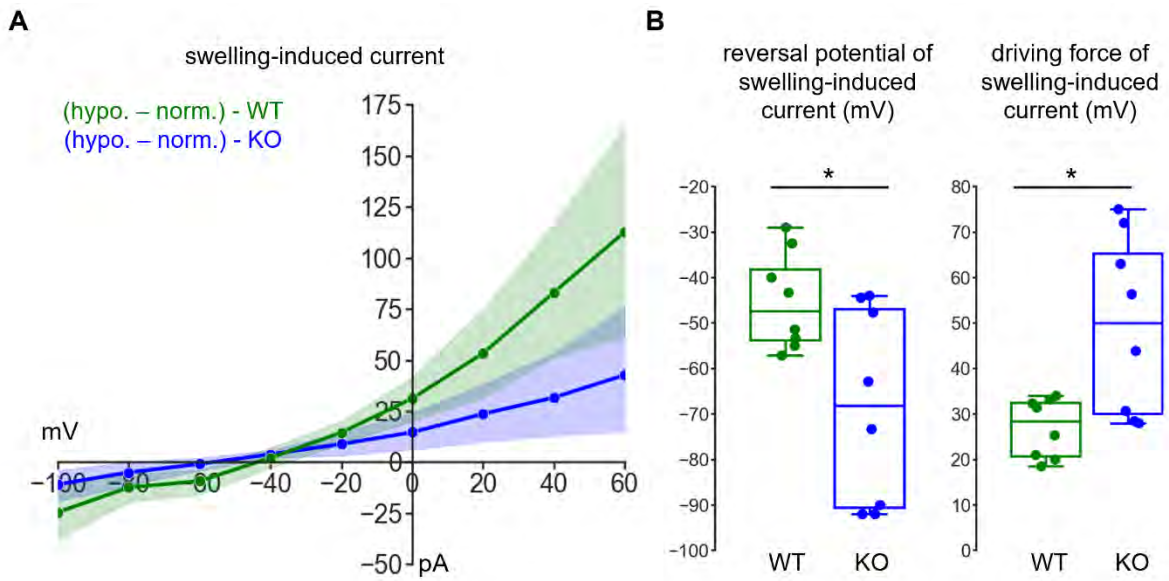
S2 Fig.



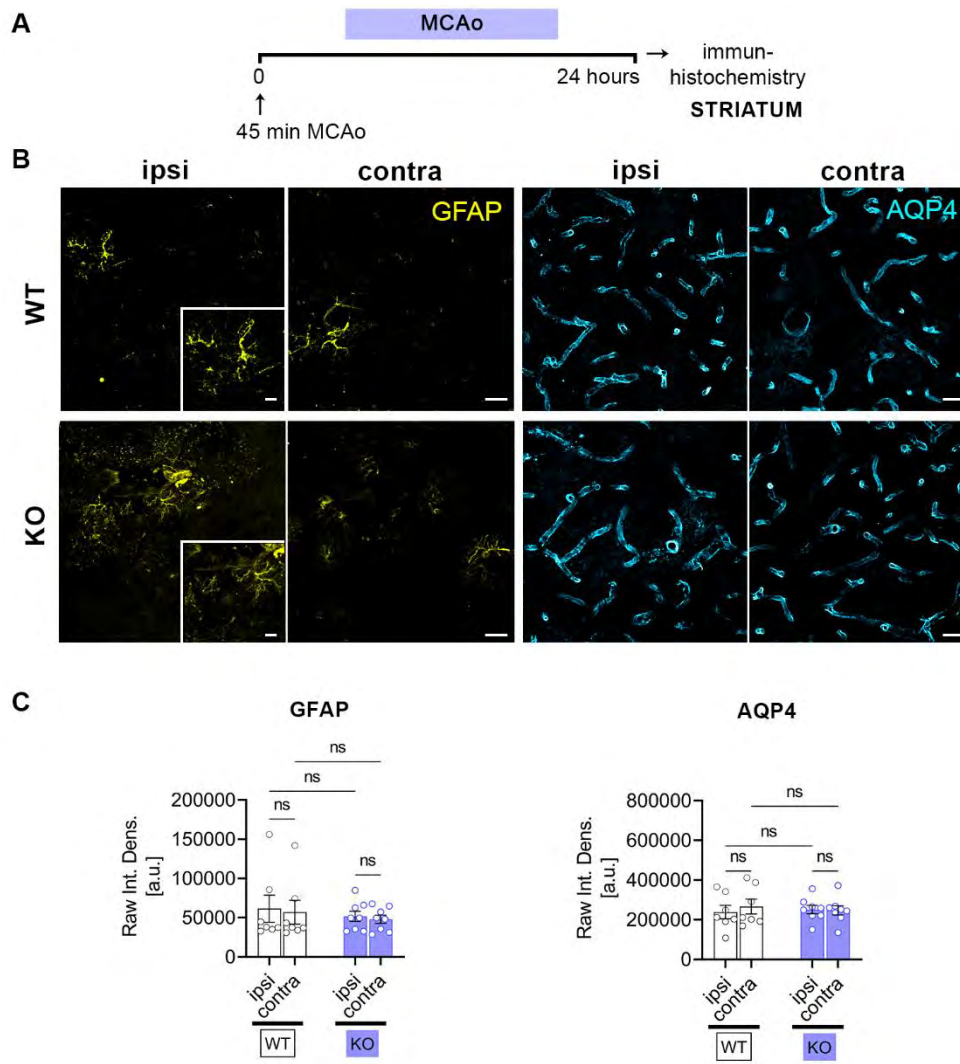
S3 Fig.



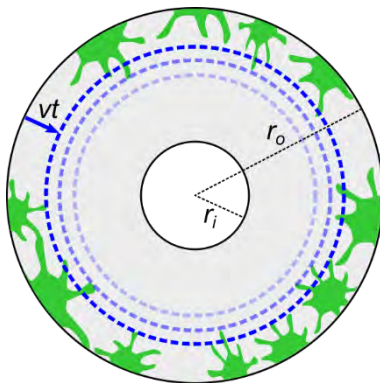
S4 Fig.



S5 Fig.



S6 Fig.



Chronic Systemic Infection Exacerbates Ischemic Brain Damage via a CCL5 (Regulated on Activation, Normal T-Cell Expressed and Secreted)-Mediated Proinflammatory Response in Mice

Ádám Dénes,¹ Neil Humphreys,¹ Thomas E. Lane,² Richard Grecis,¹ and Nancy Rothwell¹

¹Faculty of Life Sciences, University of Manchester, Manchester M13 9PT, United Kingdom, and ²Department of Molecular Biology and Biochemistry, University of California, Irvine, Irvine, California 92697

Infection and systemic inflammation are risk factors for cerebrovascular diseases and poststroke infections impair outcome in stroke patients, although the mechanisms of their contribution are mostly unknown. No preclinical studies have identified how chronic infection affects ischemic brain damage and which key inflammatory mediators are involved. We used a well established model of gut infection (*Trichuris muris*) to study how chronic infection contributes to brain injury. We show that, in mice, infection that leads to a chronic Th1-polarized immune response dramatically (60%) exacerbates brain damage caused by experimental stroke. Chronic Th1-type infection resulted in systemic upregulation of proinflammatory mediators and profoundly altered stroke-induced early (40 min to 4 h) and late (48 h) inflammation in the brain and peripheral tissues. Using the same infection, we show that a Th1-, but not Th2-polarized response augments brain injury by increasing the Th1 chemokine CCL5 [regulated on activation, normal T-cell expressed and secreted (RANTES)] systemically. This infection-associated response paralleled altered regulatory T-cell response, accelerated platelet aggregation in brain capillaries, and increased microvascular injury and matrix metalloproteinase activation after stroke. Antibody neutralization of RANTES reversed the effect of chronic infection on brain damage, microvascular MMP-9 activation, and cellular inflammatory response. Our results suggest that chronic infection exacerbates ischemic brain damage via a RANTES-mediated systemic inflammatory response, which leads to delayed resolution of inflammation and augmented microvascular injury in the brain.

Introduction

Cerebrovascular disease is profoundly influenced by peripheral immune and inflammatory processes. Comorbidities and known causes of stroke such as atherosclerosis, diabetes, obesity, or systemic infection all involve chronic inflammation, which can directly contribute to ischemic damage and adversely impact on recovery (Emsley and Hopkins, 2008; McColl et al., 2009; Dénes et al., 2010). Infections may trigger up to one-third of ischemic strokes and worsen outcome (Emsley and Hopkins, 2008). In addition to the potentially harmful effects of pathogen-derived factors, the host immune response itself appears to be a major contributor to ischemic brain damage. Recent experimental data highlight the importance of interleukin-1 β (IL-1 β) or endotoxin-induced systemic inflammation (McColl et al., 2008), T-cell-associated interferon- γ (IFN- γ) (Yilmaz et al., 2006), regulatory T-cells (Liesz et al., 2009), and IL-17-producing $\gamma\delta$ T-cells (Shichita et al., 2009), which all influence the development of ischemic brain injury.

Peripheral inflammatory processes can induce changes in the kinetics of blood–brain barrier (BBB) disruption, increase in neurovascular gelatinolytic activity, and altered activation of inflammatory cells and cytokines in the brain after stroke (McColl et al., 2007, 2008; Liesz et al., 2009; Shichita et al., 2009). However, we do not know which inflammatory substances mediate the effect of chronic peripheral inflammation on brain damage and how. Furthermore, it is not known how peripheral immune processes relate to changes in neurovascular milieu, such as capillary coagulation, microvascular injury, and impaired blood flow recovery after stroke. Relevant experimental models of comorbidities in stroke provide valuable tools to study some of these mechanisms, but most models are highly complex. Moreover, no study has investigated the effect of infection-induced chronic peripheral inflammation on experimental stroke.

Thus, we used the murine intestinal parasitic whipworm *Trichuris muris* to induce a chronic, systemic inflammatory response dominated by CD4⁺ T helper-1 (Th1)/Th17 cells (Cliffe and Grecis, 2004; Hayes et al., 2004; Owyang et al., 2006) to investigate brain and peripheral inflammatory responses after transient middle cerebral artery occlusion (MCAo). In this well established model, low-dose parasite infection results in an IFN- γ -induced class switch to parasite-specific IgG2a, and this response persists to chronicity (Bancroft et al., 2001; Cliffe and Grecis, 2004). This has been confirmed by depletion of IFN- γ , which results in expulsion of the parasite via the development of a protective Th2-type response (Else et al., 1994; Helmby et al., 2001).

Received March 9, 2010; revised May 13, 2010; accepted June 8, 2010.

This work was supported by the Medical Research Council (MRC) (N.R.) (MRC Research Professorship), European Union's Seventh Framework Programme (FP7/2008–2013) under Grant Agreements 201024 and 202213 (European Stroke Network) (N.R., A.D.), and the Wellcome Trust (N.H., R.G.). We thank Dr. Allison Bancroft and Dr. Kelly Millar for help with the *T. muris* model and cytometric bead array.

Correspondence should be addressed to Nancy Rothwell, Faculty of Life Sciences, University of Manchester, AV Hill Building, Oxford Road, Manchester M13 9PT, UK. E-mail: nancy.rothwell@manchester.ac.uk.

DOI:10.1523/JNEUROSCI.1227-10.2010

Copyright © 2010 the authors 0270-6474/10/3010086-10\$15.00/0

Using *T. muris*, we identify mechanisms whereby chronic, systemic inflammation markedly exacerbates experimental stroke and show that this is mediated by the chemokine CCL5 [regulated on activation, normal T-cell expressed and secreted (RANTES)].

Materials and Methods

Mice and *T. muris* infection. Experiments were performed in adult male C57BL/6J mice (Harlan Olac), maintained in individually ventilated cages, under temperature-, humidity-, and light-controlled conditions. Mice were orally infected with ~20 infective eggs (low dose) when 12–16 weeks of age and incubated for 35 d when chronic Th1-polarized response is well established (Bancroft et al., 1994, 2001; Else et al., 1994) before surgery. Th1-polarized response is dominated by proinflammatory cytokines such as IFN- γ or tumor necrosis factor- α (TNF α), whereas during a Th2-polarized response cytokines such as IL-4, IL-9, IL-10, and IL-13 are expressed. To induce Th2-polarized response, mice were given ~100 eggs (high dose) followed by 21 d incubation (peak of Th2-polarized infection). No mortality or behavioral changes were observed in infected mice. All animal procedures were performed under an appropriate Home Office license and adhered to regulations as specified in the Animals (Scientific Procedures) Act (1986).

Filament MCAo and perfusion. Focal cerebral ischemia or sham surgery were performed on infected mice and age/weight-matched controls weighing 26–32 g. Anesthesia was induced with isoflurane. During surgery, core temperature was maintained at $37 \pm 0.5^\circ\text{C}$. We investigated whether body temperature was altered in infected mice before surgery or after experimental stroke. No significant difference in rectal temperature was observed between infected and uninfected mice before surgery (36.9 ± 0.2 vs $36.8 \pm 0.3^\circ\text{C}$). Animals were exposed to sham surgery or MCAo for 45 min using an intraluminal filament (180 μm diameter, left side occluded) followed by 4, 24, or 48 h reperfusion. After MCAo, mice developed mild hypothermia, which was normalized by 24 h. No significant difference in body temperature was observed after MCAo between infected and uninfected animals (35.1 ± 0.8 vs $35.1 \pm 1.1^\circ\text{C}$ at 3 h reperfusion). Serial blood samples (typically seven times 20 μl /mouse) were obtained from the tail vein before surgery and after MCAo. Before whole-body transcardial perfusion with saline, blood was taken from the heart using 3.8% sodium citrate as an anticoagulant (1:10). The upper body (above the diaphragm) was perfused with 4% paraformaldehyde, whereas unfixed (saline-perfused) liver, spleen, femoral-tibial bone marrow, mesenteric lymph nodes, and cecum were frozen. In separate experiments, saline-perfused brains were collected at various time points after MCAo. Paraformaldehyde-fixed brains were sectioned on a freezing microtome and kept at -20°C in cryoprotectant solution.

Measurement of infarct volume and BBB damage. The volume of ischemic and BBB damage was measured as described previously (Dénes et al., 2007). Briefly, areas of ischemic damage were identified on cresyl violet-stained sections at eight neuroanatomically defined coronal levels (between 2.9 mm rostral and -4.9 mm caudal to bregma). Digitized images were created, and areas of damage were measured using ImageJ software. The volume of damage was calculated by integration of areas of damage with the distance between coronal levels. Leakage of plasma-derived IgG (BBB damage) was detected with biotinylated horse anti-mouse IgG (1:500) followed by incubation with ABC solution (Vector; 1:500), and the color was developed by diaminobenzidine tetrahydrochloride. Calculation of BBB damage was performed as described above.

Assessment of neurological deficit. Neurological status was assessed blinded to drug treatment and according to a neurological grading score of increasing severity of deficit (Bederson et al., 1986): 0, no observable deficit; 1, torso flexion to right; 2, spontaneous circling to right; 3, leaning/falling to right; 4, no spontaneous movement.

Systemic neutralization of RANTES. Monoclonal antibody recognizing RANTES [clone R6G9 (Glass et al., 2004)] or control IgG were administered intraperitoneally, 24 h before and immediately before MCAo (two times 0.25 mg/mouse in 200 μl of sterile PBS).

Cytokine measurements with cytometric bead array and ELISA. Liver, spleen, and ipsilateral brain hemisphere samples were homogenized as described previously (Chapman et al., 2009). Protein concentrations

were calculated using BCA assay (Pierce/Thermo Fisher Scientific). Lymph node cells were isolated and restimulated *in vitro* with *T. muris* excretory/secretory (ES) antigen. Sixteen key inflammatory cytokines [granulocyte-macrophage colony-stimulating factor (GM-CSF), granulocyte colony-stimulating factor (G-CSF), IFN- γ , IL-1 β , IL-10, IL-13, IL-17A, IL-2, IL-4, IL-5, IL-6, IL-9, KC, MCP-1, TNF α , RANTES] were measured in all tissues examined using appropriate cytometric bead array (CBA) Flex Sets (BD Biosciences) according to the manufacturer's protocol. GM-CSF, IL-2, IL-4, IL-5, and IL-17A were not routinely measured all the time because of their low or tissue-specific expression found in pilot experiments. Parasite-specific IgGs were measured by ELISA as described previously (Else et al., 1993).

Flow cytometry. Spleen and bone marrow cells were isolated and stained with Gr1-APC, CD4-FITC, CD3-PerCP, CD11b-PE, Foxp3-APC (BD Biosciences) alone or in combination. Cells were acquired on a FACSCalibur (BD Biosciences). Acquisition and analysis of data were performed using CellQuest Pro software (BD Biosciences).

Immunohistochemistry and immunofluorescence. Immunostaining was performed on free-floating brain sections using various combinations of primary antibodies: rat anti-mouse CD45 (Serotec), goat anti-Iba1 (Abcam), rabbit anti-SJC (kindly provided by Drs. Daniel Anthony and Sandra Campbell, University of Oxford, Oxford, UK) (Anthony et al., 1998), goat anti-RANTES (R&D Systems), goat anti-MMP-9 (R&D Systems), rat anti-mouse CD41 (BD Biosciences), mouse anti-NeuN (Millipore), and rabbit anti-cleaved caspase-3 (Cell Signaling). Sections were incubated in primary antibody (diluted in PBS and 0.3% Triton X-100) for 12–48 h at 4°C . For fluorescent detection, adequate fluorochrome (Alexa 594, Alexa 488)-conjugated antibodies (Invitrogen) were used. Cell nuclei were stained with DAPI (4',6'-diamidino-2-phenylindole). Biotinylated tomato lectin (Sigma-Aldrich) was visualized with streptavidin-Alexa 350 conjugate (Invitrogen). Peroxidase staining was developed with diaminobenzidine tetrahydrochloride alone or in the presence of nickel ammonium sulfate.

Microscopy. Images were collected on a Zeiss Axioskop or an Olympus BX51 microscope using a Coolsnap ES camera (Photometrics) through MetaVue software (Molecular Devices). Fluorescent images were processed using ImageJ and Adobe Photoshop softwares.

Quantitative analysis of neuronal death and immunostaining for inflammatory markers. Quantification was performed on parallel series of coronal brain sections using a stereological approach (typically 8–12 sections per hemisphere were counted rostrocaudally, 400 μm apart). In each brain ($n = 8$ –10), two to three randomly selected fields of the ischemic striatum or cerebral cortex were viewed on each section in a live CCD camera window and cells positive to NeuN and/or cleaved caspase-3 were counted. SJC-, RANTES-, CD41 ($n = 6$ –10)-, and MMP-9 ($n = 5$ –7)-positive profiles were quantified as above. Data were expressed as the average number of objects per square millimeter or area in the given brain region.

Randomization, quantification, and statistical analysis. Animals were randomized for experiments where it was possible (e.g., anti-RANTES treatment). All quantitative assessments were performed in a blinded manner. For two groups, Student's *t* test (two-tailed), and for three or more groups, one-way or two-way ANOVA followed by Bonferroni's *post hoc* multiple-comparison or paired comparison were used. For correlation analysis, *p* value (two-tailed) and R^2 were determined.

Results

Chronic infection exacerbates ischemic brain damage

First, we examined the effect of chronic peripheral infection on ischemic brain damage, by using low-dose parasite infection to induce a chronic, Th1-polarized immune response. The chronic Th1-polarized response resulted in a 60% increase in brain ischemic damage ($p < 0.01$), which paralleled augmented BBB damage ($p < 0.001$) compared with uninfected mice, 48 h after MCAo (Fig. 1A–C). Neuronal loss was significantly increased ($p < 0.01$) in the ipsilateral hemisphere in infected mice (Fig. 1D,E). This was attributable mainly to necrotic cell death, as cleaved caspase-3-positive apoptotic neurons in the core of the infarct were also significantly reduced ($p < 0.01$) in mice with chronic Th1-type

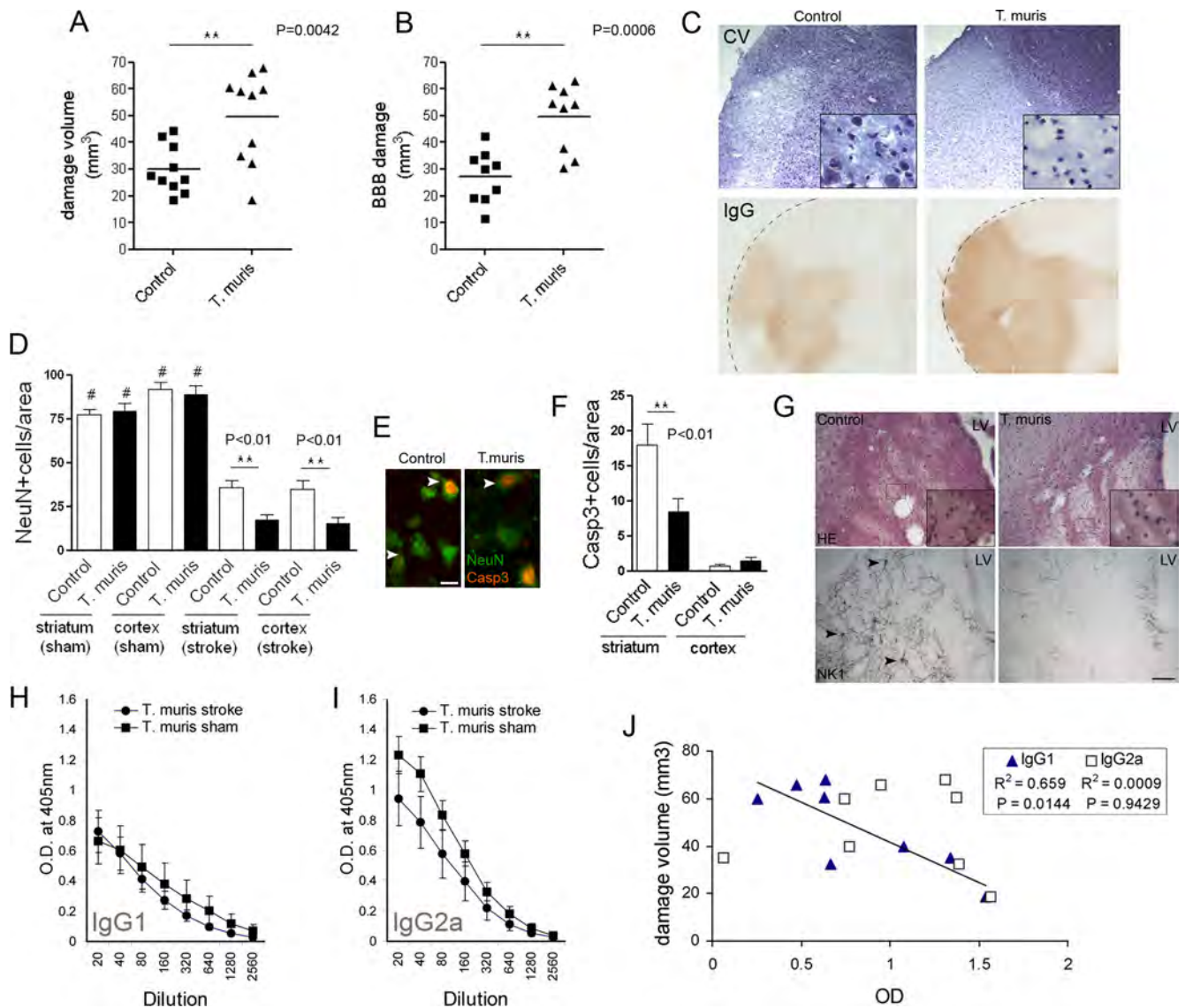


Figure 1. Chronic Th1-type peripheral immune response augments ischemic brain damage. Ischemic (**A**) and BBB (**B**) damage are significantly larger in infected mice compared with uninfected mice at 48 h reperfusion after 45 min MCAo, as identified by cresyl violet staining (**C**) and leakage of plasma-derived IgG (*t* test, two-tailed). Quantitative analysis of NeuN (**D**) and cleaved caspase-3 (**F**) immunofluorescence (**E**) shows augmented neuronal loss after chronic infection (ANOVA, followed by Bonferroni's multiple-comparison test; #*p* < 0.001 sham vs stroke; ***p* < 0.01). **G**, Hematoxylin and eosin staining shows significant loss of neurons in the ipsilateral striatum at 48 h reperfusion after 45 min MCAo, which is more pronounced in infected mice. Chronic peripheral infection causes marked degeneration and loss of NK1-positive cell bodies (arrowheads) and neuronal processes after MCAo. Measurement of parasite-specific IgG1 (**H**) and IgG2a (**I**) indicates the development of a Th1-polarized response. **J**, Correlation analysis indicates significant negative correlation between anti-parasitic IgG1 (dominant in Th2-type response) levels in the plasma and the volume of ischemic damage. Data are expressed as means ± SEM. LV, Lateral ventricle. Scale bars: **E**, 10 μm; **G**, 100 μm. Data shown are representative of 10 mice in each group corresponding to two independent experiments.

response, corresponding to low numbers of surviving cells (Fig. 1*E,F*). To investigate the loss of neuronal processes after MCAo, expression of NK1 [Substance P receptor, which is distributed widely on striatal GABAergic interneurons and cholinergic projection neurons (Gerfen, 1991; Stumm et al., 2001; Blomeley et al., 2009)] was assessed by immunohistochemistry. MCAo upregulated neuronal NK1, whereas marked degeneration of NK1-positive processes and boutons was observed in the core of the infarct in infected mice compared with uninfected animals (Fig. 1*G*; supplemental Fig. 1, available at www.jneurosci.org as supplemental material).

Next, we investigated whether parasite-specific IgG levels in the plasma, which reflect infection status and polarization of the immune response, show correlation with the size of infarct after MCAo. Elevated parasite-specific IgG2a levels in the plasma after both MCAo and sham surgery (Fig. 1*I*) and parasite-specific IgG1 (Fig. 1*H*) demonstrated the predicted development of a

chronic Th1-type response in this model (Else et al., 1993, 1994; Bancroft et al., 2001; Cliffe and Grecis, 2004). Th1 cytokines, such as IFN-γ, can promote class switching to IgG2a antibody production in B-cells (Snapper et al., 1997), which leads to elevated serum IgG2a levels. Antiparasitic IgG1, which is dominant in the Th2-type response, during which IgG2a is not elevated (Bancroft et al., 1994; Cliffe and Grecis, 2004), showed a negative correlation (*p* < 0.05; *R*² = 0.66) with the volume of ischemic brain damage in infected mice (Fig. 1*J*). This indicated that the exacerbation of the ischemic brain damage is caused by the Th1-polarized response induced by chronic infection.

Chronic type 1 cytokine-dominated infection results in systemic inflammation

We looked at different organs known to be involved in the generation of the systemic inflammatory response to reveal whether

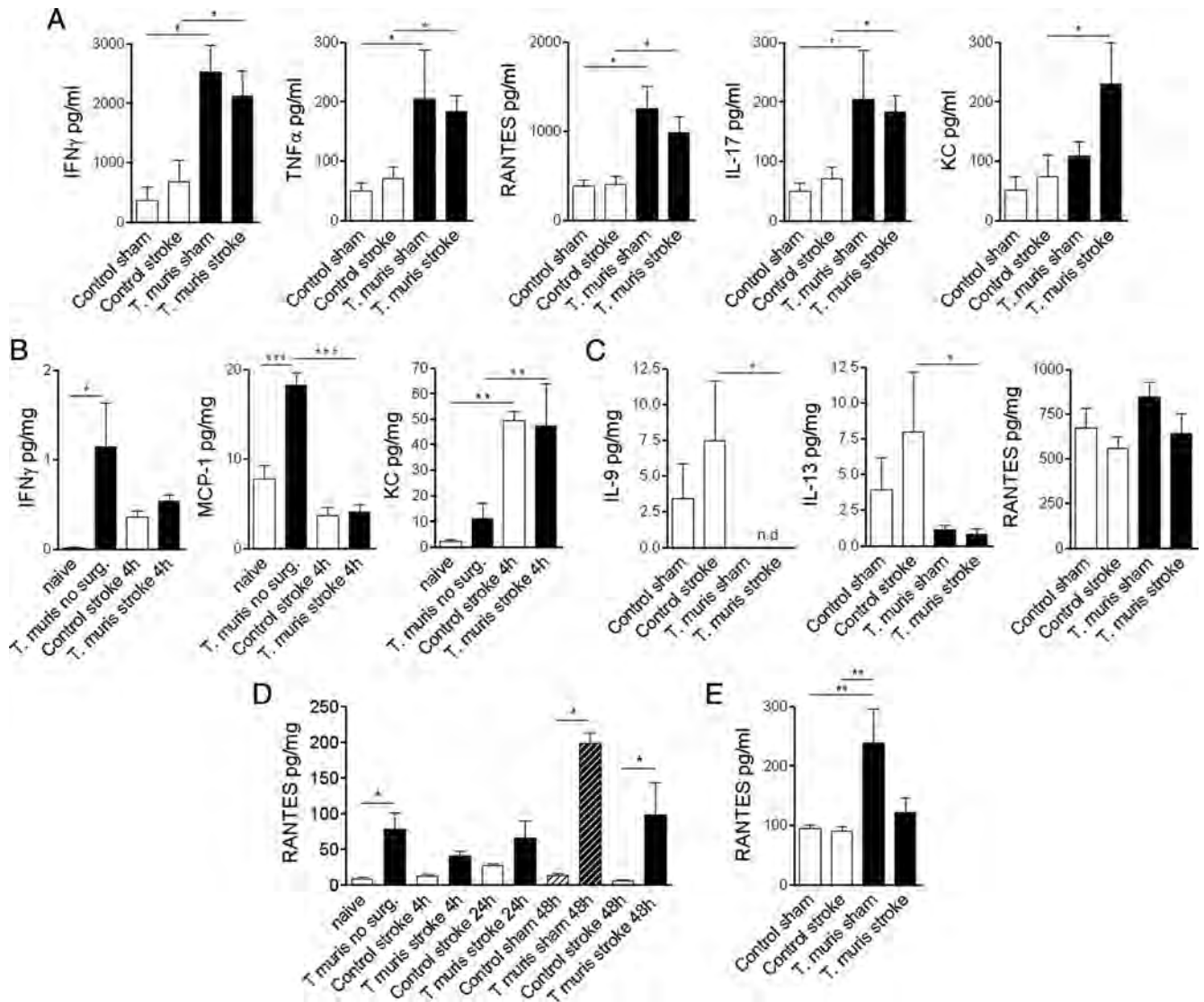


Figure 2. Chronic Th1-type infection results in organ-specific proinflammatory activation and systemic upregulation of RANTES. **A**, Mesenteric lymph node cells isolated 48 h after sham surgery or MCAo were restimulated with parasite ES antigens *in vitro*. CBA analysis was performed on spleen homogenates of mice without surgery (0 h), at 4 h reperfusion (**B**), and after 48 h reperfusion (**C**). **D**, Liver homogenates harvested at various time points show chronically elevated RANTES in infected mice. **E**, Plasma samples show elevated RANTES in sham mice at 48 h reperfusion. * $p < 0.05$, ** $p < 0.01$, *** $p < 0.001$, one-way ANOVA followed by Bonferroni's multiple-comparison test. Data are expressed as means \pm SEM. Data shown are representative of 6–10 mice in each group from two independent experiments.

chronic infection had systemic effects and to see how stroke-induced inflammatory changes were altered by chronic infection. In the mesenteric lymph node (the major draining lymph node of the gut), infected animals expressed elevated IFN- γ , TNF α , RANTES, and IL-17 (proinflammatory cytokines) compared with uninfected controls after both sham and MCAo surgery (Fig. 2A), indicating a well established chronic Th1-polarized response. In infected mice, induction of KC (CXCL1) was observed in the mesenteric lymph node in response to MCAo, which was not seen in uninfected animals (Fig. 2A). In spleen homogenates, IFN- γ and MCP-1 were increased in infected mice before surgery (Fig. 2B). MCAo caused induction of splenic KC and G-CSF within 4 h (Fig. 2B; supplemental Fig. 2, available at www.jneurosci.org as supplemental material) in both infected and uninfected mice. In contrast, splenic IL-9 and IL-13 (type 2 cytokines) expression was blunted in infected animals at 48 h reperfusion after MCAo, but proinflammatory cytokines were not different (Fig. 2C; supplemental Fig. 2, available at www.jneurosci.org as supplemental material).

In the liver of infected mice, RANTES was elevated at most time points examined, compared with uninfected mice (Fig. 2D). Other liver cytokines were not significantly different at 4 h (supplemental Fig. 3, available at www.jneurosci.org as supplemental material) or 48 h after stroke (data not shown). Importantly, only RANTES was significantly increased in the plasma of infected mice up to 48 h after sham surgery (Fig. 2E) compared with uninfected animals of the 16 key inflammatory cytokines examined.

Chronic infection alters the acute phase response to stroke and leads to sustained inflammation in the brain

Plasma IFN- γ and TNF α were moderately elevated (2 ± 2 vs 12 ± 4 and 6 ± 1 vs 24 ± 6 pg/ml, respectively; $p < 0.05$) in infected mice compared with uninfected animals before surgery (data not shown). After the induction of ischemia, circulating cytokines MCP-1, KC, IL-6, and G-CSF increased significantly (20- to 200-fold) within 40–120 min and returned to baseline

24–48 h after reperfusion (Fig. 3A). In infected mice, the increases in MCP-1, KC, and G-CSF in response to ischemia were attenuated, whereas RANTES was elevated.

In the brain, induction of inflammatory cytokines in uninfected mice peaked 24 h after MCAo (Fig. 3B), and MCP-1, KC, IL-6, and RANTES levels had declined by 48 h. In uninfected mice, brain IL-6 levels were significantly higher 24 h after stroke compared with infected animals. In contrast, MCP-1, KC, and IL-6 showed sustained upregulation, whereas G-CSF and RANTES exhibited additional increases by 48 h in infected mice (Fig. 3B), indicating slower resolution of inflammation in the brain after stroke.

Infection-induced systemic RANTES is associated with microvascular dysfunction and increased platelet aggregation in the brain after stroke

Immunohistochemistry revealed strong vascular RANTES labeling after MCAo (in both small-medium size blood vessels and in microvessels) in the ischemic hemisphere of infected mice (Fig. 4A,B), but not in uninfected controls. RANTES immunostaining was most marked in the ipsilateral thalamus and hippocampus, which were ischemic in 90% of *T. muris*-infected mice, but showed only marginal damage (in 40–50% of mice) or were not affected in uninfected mice. These areas are especially sensitive to remote damage after stroke in rodents and primates (Dihné et al., 2002; Ling et al., 2009; Bihel et al., 2010). In infected mice, an increased number of RANTES-positive platelets (average diameter, 2.4 μm) was found in capillaries (Fig. 4A, I, inset). Glial RANTES expression was also markedly enhanced in these mice 48 h after stroke (Fig. 4A, III–IV; C). A population of these cells was CD45-positive microglia/macrophages that coexpressed Iba1 (supplemental Fig. 4A, available at www.jneurosci.org as supplemental material). Immunofluorescence revealed CD41-positive platelets in the areas of vascular RANTES deposition, mostly in microvessels. Platelet aggregates occluding capillaries were numerous in the ischemic hemisphere of infected mice after stroke (Fig. 4D; supplemental Fig. 4B, available at www.jneurosci.org as supplemental material) compared with uninfected mice. We found no significant differences in cerebral blood flow recovery after MCAo between infected and uninfected mice as measured by laser Doppler flowmetry.

RANTES was also upregulated in pelleted blood cell and platelet lysates in infected mice before surgery and up to 48 h after sham surgery compared with uninfected mice ($p < 0.01$). Blood cells contained elevated RANTES in infected mice 4 h after

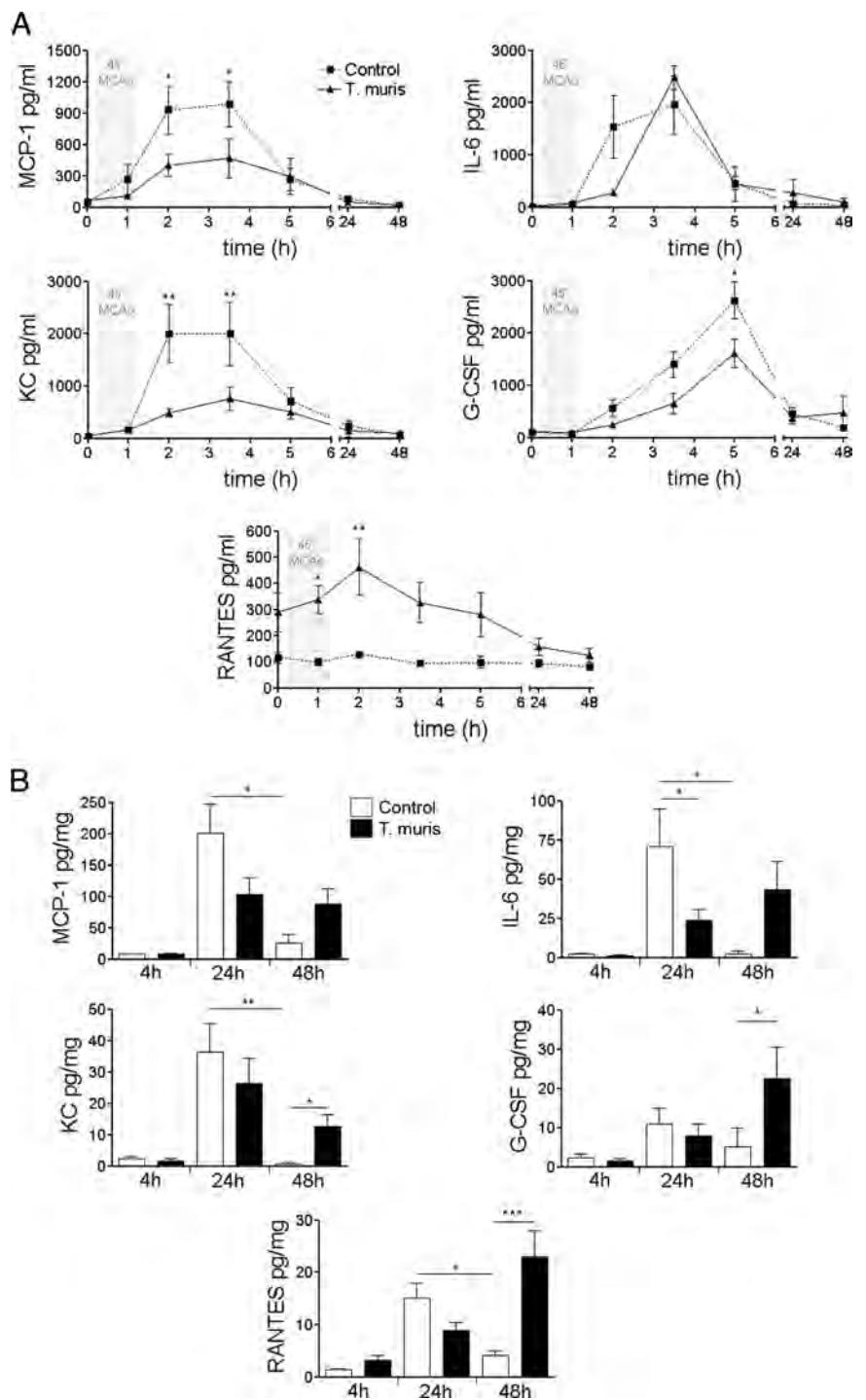


Figure 3. Chronic infection alters MCAo-induced acute phase response in the plasma and the brain. **A**, Serial plasma samples. **B**, Ipsilateral brain hemisphere homogenates. * $p < 0.05$, ** $p < 0.01$, two-way ANOVA followed by Bonferroni's posttest. Data are expressed as means \pm SEM. Data shown are representative of two independent experiments.

MCAo, which reduced by 48 h, indicating altered production or enhanced release during the formation of ischemic damage (Fig. 4E). Compared with uninfected mice, infected mice displayed elevated RANTES in the brain after sham surgery (0.7 ± 0.2 vs 3.6 ± 1.5 pg/mg, respectively; $p < 0.05$) or without surgery (data not shown), indicating cerebrovascular inflammation before the induction of experimental stroke. RANTES deposition on cerebral blood vessels in the ipsilateral hemisphere was also associated with increased vascular adhesion of CD45-positive leukocytes in

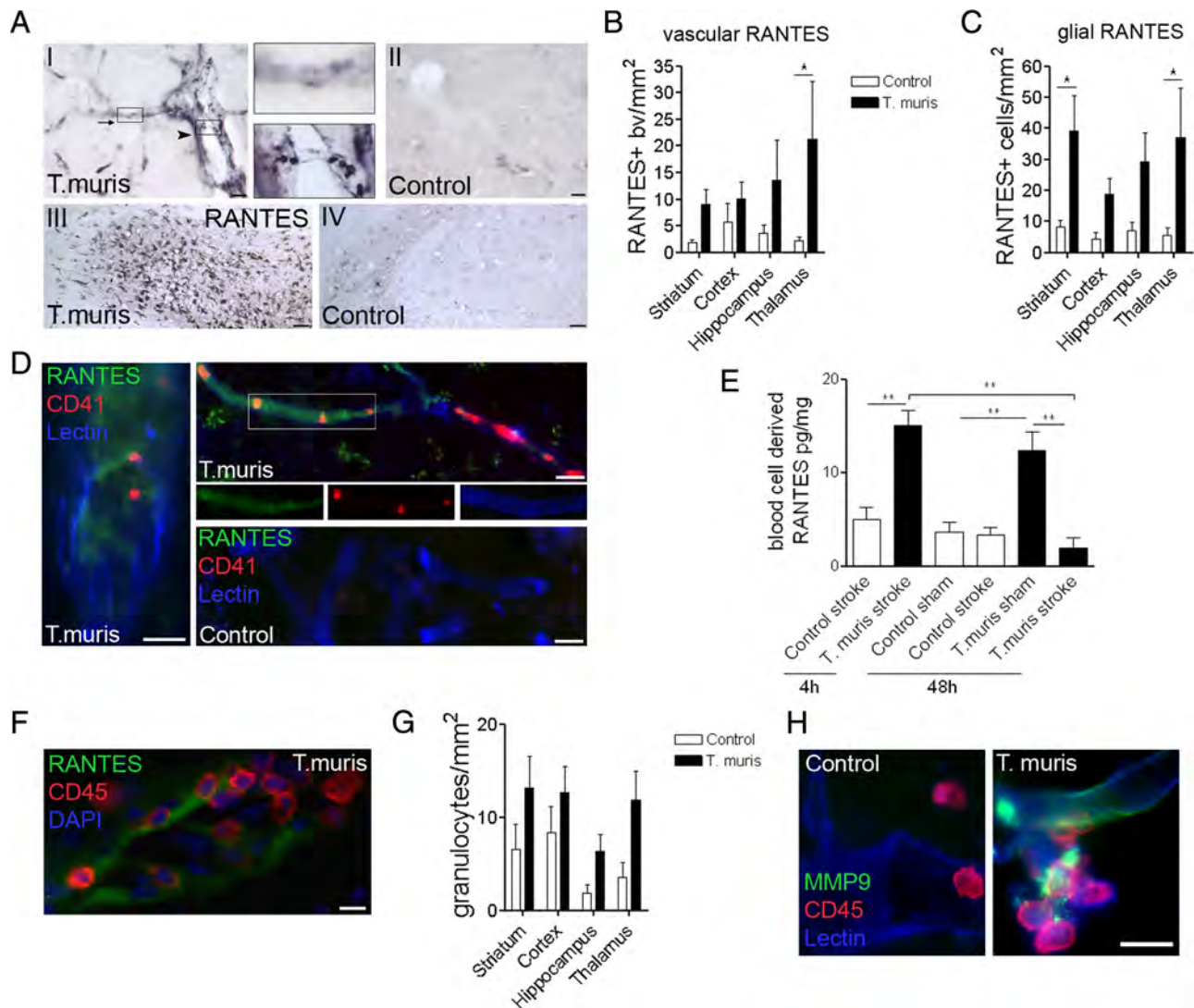


Figure 4. Chronic Th1-polarized response increases RANTES, platelet aggregation, leukocyte recruitment, and matrix metalloproteinase activity in the ischemic hemisphere. **A**, Immunohistochemistry reveals increased RANTES in microvessels (top inset, arrow) and platelets (bottom inset, arrowhead) in Th1-polarized mice (**I**), but not in uninfected animals (**II**) after MCAo. Glial RANTES expression was augmented in the affected hippocampus (**III**) of infected but not in uninfected mice (**IV**). Quantification of vascular (**B**) and glial (**C**) RANTES staining 48 h after MCAo (infected vs uninfected; $p < 0.001$, two-way ANOVA; Bonferroni's posttest, $*p < 0.05$). **D**, Vascular deposition of RANTES (green) and platelet aggregates (CD41, red) are increased in infected mice. **E**, Blood cell lysates contain elevated RANTES at 4 h reperfusion in infected mice compared with uninfected animals, which is reduced by 48 h reperfusion ($**p < 0.01$, one-way ANOVA followed by Bonferroni's multiple-comparison test). **F**, Vascular RANTES deposition was associated with leukocyte recruitment (CD45; red). **G**, Granulocyte numbers (SJC) were increased in the ipsilateral hemisphere in infected mice (infected vs control; $p < 0.01$, two-way ANOVA). **H**, Vascular MMP-9 (green) expression was enhanced after MCAo in the ischemic striatum of Th1-polarized mice. Scale bars: **D**, **F**, **H**, 10 μm ; **A**, **I**, **II**, 20 μm ; **A**, **III**, **IV**, 100 μm . Data are expressed as means \pm SEM. Data shown are representative of 6–10 mice in each group from two independent experiments.

Th1-polarized mice (Fig. 4*F*) after MCAo. Granulocytes as identified by SJC immunostaining were more numerous in the ischemic brains of infected mice after MCAo compared with uninfected mice ($p < 0.01$) (Fig. 4*G*). This was accompanied by increased number and proportion of Gr1-positive (a marker of neutrophils and monocytes) leukocytes in the spleen ($4.4 \pm 0.3\%$ in uninfected vs $9.1 \pm 2\%$ in infected mice; $p < 0.05$).

To investigate whether chronic infection modified neurovascular gelatinase expression in the brain after MCAo, we used immunostaining to MMP-9. MMP-9 is augmented in the brain by acute systemic inflammatory challenge after experimental stroke, which is associated with increased BBB permeability (McCull et al., 2008). Microvessels showed markedly increased MMP-9 immunostaining within the ischemic hemisphere in infected mice compared with uninfected animals (Fig. 4*H*), after MCAo. It indicated that chronic Th1-polarized response to in-

fection was associated with augmented vascular injury in the brain after experimental stroke, corresponding to increased ischemic and BBB damage observed in infected mice (Fig. 1*B*).

Systemic neutralization of RANTES reverses the effect of chronic infection on brain injury

We investigated whether systemic blockade of RANTES has an effect on ischemic brain damage and inflammation after MCAo in uninfected and infected mice, using a specific neutralizing antibody (Glass et al., 2004). Anti-RANTES treatment prevented the infection-driven exacerbation of ischemic damage ($p < 0.01$) (Fig. 5*A*) but had no significant effect in uninfected mice. After systemic RANTES neutralization, analysis of mesenteric lymph nodes showed successful inhibition of RANTES (1005 ± 63 pg/ml after control IgG vs 630 ± 57 pg/ml after anti-RANTES; $p < 0.01$) and KC (718 ± 110 pg/ml after control IgG vs $383 \pm$

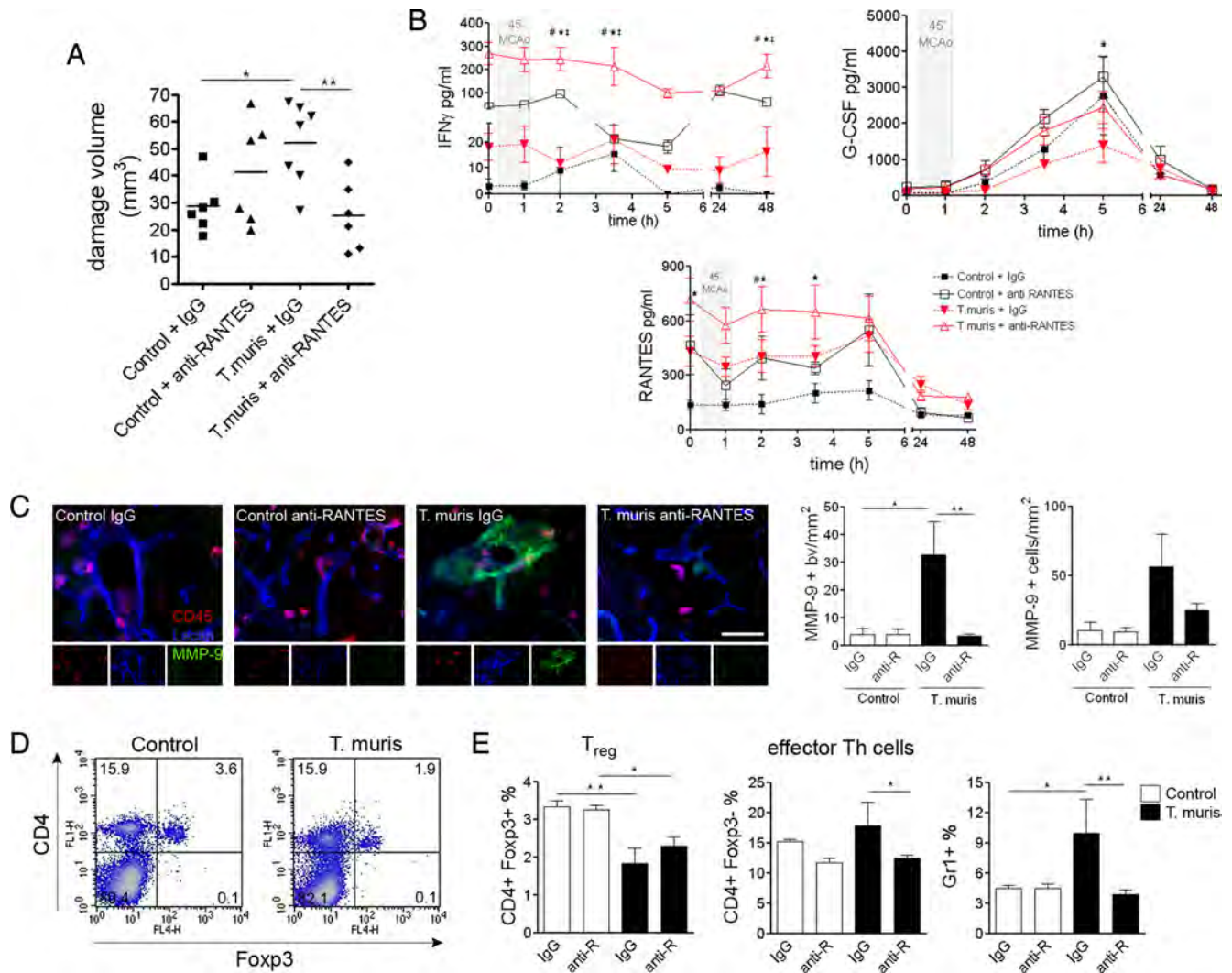


Figure 5. Systemic neutralization of RANTES reverses the effects of Th1-type infection on brain damage. **A**, The exacerbation of the ischemic brain damage is prevented by RANTES inhibition. $*p < 0.05$, $**p < 0.01$, one-way ANOVA followed by Bonferroni's multiple-comparison test. **B**, Effect of RANTES neutralization on plasma cytokine levels. Two-way ANOVA followed by Bonferroni's posttest. Infection versus control: $p < 0.01$ for IFN- γ , G-CSF, RANTES, two-way ANOVA (*T. muris* anti-RANTES vs *control anti-RANTES, #control IgG, †*T. muris* IgG). **C**, Vascular MMP-9 immunostaining, expressed as the number of MMP-9-positive blood vessels (bv) per square millimeter, was significantly increased in infected, control IgG-treated mice in the ipsilateral hemisphere after MCAo, compared with uninfected animals. This was reversed in response to anti-RANTES treatment. The number of CD45/MMP-9-positive cells was not significantly different (right). Fluorescent micrographs showing MMP-9, CD45, and lectin triple-immunofluorescent staining in the ipsilateral striatum (left). **D**, Flow cytometric analysis shows that Th1-polarized mice have reduced CD4⁺/Foxp3⁺ (T_{reg}) cells in the spleen 48 h after MCAo. **E**, The effect of systemic neutralization of RANTES on effector Th cells, T_{reg} , and Gr1-positive leukocytes in the spleen. Scale bar, 50 μ m. Data are expressed as means \pm SEM. Data shown are representative of two independent experiments.

121 pg/ml after anti-RANTES; $p = 0.02$), whereas a trend was observed for reduced TNF α (630 ± 202 pg/ml after control IgG vs 404 ± 42 pg/ml after anti-RANTES). IFN- γ markedly increased in the plasma after anti-RANTES treatment compared with infected, control IgG-treated mice. Inhibition of stroke-induced G-CSF by chronic Th1-type infection was reversed (Fig. 5B), whereas levels of neutralized RANTES increased. Infected, control IgG-treated mice displayed increased vascular MMP-9 immunostaining in the ischemic hemisphere ($p < 0.05$), whereas the number of MMP-9/CD45-positive cells was not significantly different. Anti-RANTES treatment inhibited vascular MMP-9 expression ($p < 0.01$) in infected mice (Fig. 5C).

We investigated whether infection and systemic neutralization of RANTES influenced regulatory T-cells (T_{reg}), which play a key protective role in cerebral ischemia (Liesz et al., 2009) and increase in number after stroke in the spleen (Offner et al., 2006). Infected mice exhibited reduced numbers of T_{reg} in the spleen

(Fig. 5D) after MCAo compared with uninfected mice, whereas a similar ratio of effector CD4-positive T-cells was found. Anti-RANTES treatment reduced splenic effector Th cells but had no effect on T_{reg} . Anti-RANTES also reversed increased Gr1-positive leukocyte numbers in infected mice (Fig. 5E).

Th2-polarized peripheral immune response after *T. muris* infection does not modify ischemic brain damage

We also investigated whether the *T. muris* effect was specific to the parasite infection or dependent on the induced Th1 response. We infected mice with a high dose of *T. muris* before MCAo. This regimen activates a Th2-polarized immune response against the intestinal parasite and results in expulsion of worms from the host (Bancroft et al., 2001; Cliffe and Grencis, 2004). Low levels of parasite-specific IgG2a levels confirmed the development of a Th2-polarized response (Fig. 6A,B). Eosinophil granulocyte numbers increased significantly in the bone marrow in Th2-

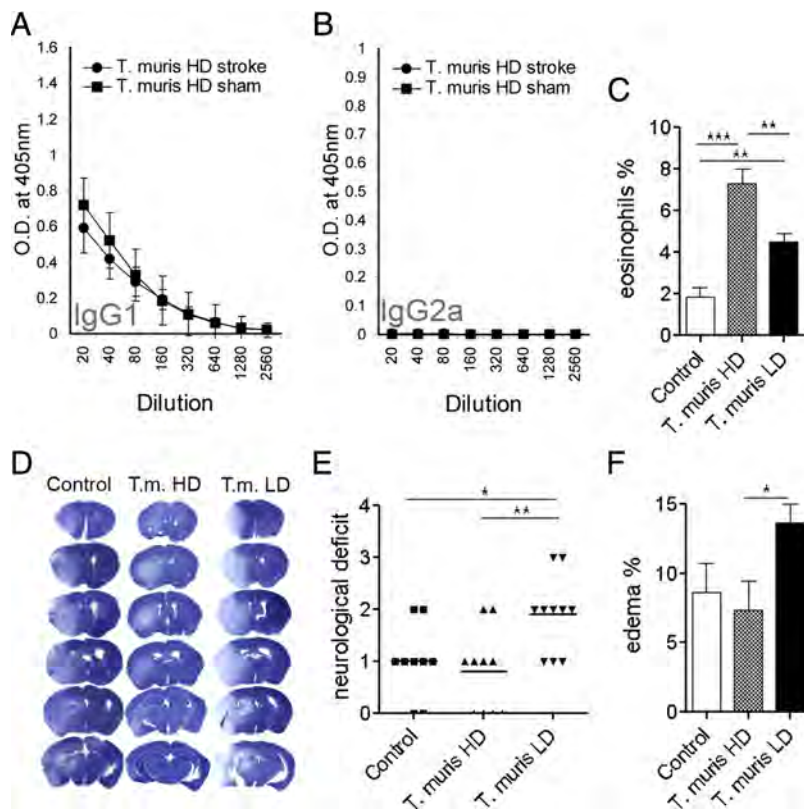


Figure 6. *T. muris* high-dose infection results in Th2-polarized immune response, which does not exacerbate brain damage. **A**, **B**, Antiparasitic IgG levels in the plasma of *T. muris* high-dose (HD)-infected (Th2-polarized) mice. **C**, Eosinophil granulocytes are elevated in the bone marrow in *T. muris* HD mice compared with uninfected (control) and *T. muris* low-dose (LD)-infected (Th1-polarized) mice. **D**, Representative cresyl violet-stained brain sections from uninfected, *T. muris* HD, and *T. muris* LD mice after 45 min MCAo and 48 h reperfusion. **E**, Neurological deficit is significantly exacerbated in *T. muris* LD mice compared with uninfected and *T. muris* HD mice. **F**, Brain edema is larger in *T. muris* LD mice compared with *T. muris* HD animals. * $p < 0.05$, ** $p < 0.01$, *** $p < 0.001$, one-way ANOVA followed by Bonferroni's posttest. Data are expressed as means \pm SEM. Data shown are representative of two independent experiments ($n = 10$).

polarized mice compared with uninfected and Th1-polarized mice (Fig. 6C). The ischemic brain damage was not exacerbated in Th2-polarized mice (Fig. 6D) compared with uninfected animals but was significantly smaller ($p < 0.05$) than that of Th1-polarized mice (29.8 ± 2.8 , 28.9 ± 6.0 , and 49.6 ± 5.3 mm³ in uninfected, *T. muris* high-dose-, and *T. muris* low-dose-infected animals, respectively). Neurological deficit was significantly augmented in Th1-polarized mice compared with Th2-polarized and uninfected mice (Fig. 6E), after MCAo. The extent of brain edema was also significantly smaller in Th2-polarized mice compared with Th1-polarized animals (Fig. 6F). Proinflammatory cytokines were not increased in mesenteric lymph nodes (supplemental Fig. 5A, available at www.jneurosci.org as supplemental material) after high-dose infection. Stroke-induced changes in G-CSF and KC levels in the plasma were not different from low-dose infection. Importantly, plasma RANTES was not elevated at any time point before or after MCAo after high-dose (Th2-type) infection compared with uninfected mice (supplemental Fig. 5B, available at www.jneurosci.org as supplemental material).

Discussion

We show for the first time that chronic peripheral infection in mice, dominated by type 1 cytokines, exacerbates ischemic brain damage, which is associated with delayed resolution of brain inflammation and augmented microvascular dysfunction after stroke. We identify RANTES as a key mediator of these events,

whereby chronic peripheral inflammation affects brain injury. In light of clinical studies, which usually fail to distinguish between infections that trigger stroke and an aggravation of stroke pathophysiology, our data confirm that preexisting infections can exacerbate infarct evolution if the ischemic event occurs.

No experimental studies have implicated RANTES as a mediator of chronic inflammation, which impacts on remote injury or specifically exacerbates ischemic brain damage. Recent preclinical data indicate reduced ischemic brain damage in RANTES-deficient mice (Terao et al., 2008). In contrast, the present study shows that RANTES neutralization did not modify brain damage in uninfected mice. However, we show for the first time that the exacerbation of ischemic damage caused by chronic infection is prevented by RANTES inhibition. The clinical relevance of our findings is supported by several reports, which implicate RANTES as an atherogenic chemokine in vascular disease and in comorbidities associated with stroke. Inhibition of RANTES-dependent pathways is protective in experimental models of atherosclerosis (Zernecke et al., 2006; Koenen et al., 2009). In peripheral tissues, platelet-derived RANTES is deposited on the inflamed endothelium where it triggers monocyte arrest (von Hundelshausen et al., 2001; Schober et al., 2002). Our results show for the first time that vascular RANTES is increased in the brain in response to chronic infection after stroke. Human aortic aneurysms release high levels of RANTES, which recruits neutrophils to the intraluminal thrombi (Houard et al., 2009). In patients, RANTES plasma levels correlate with acute-phase proteins C-reactive protein (CRP) and fibrinogen in coronary artery diseases (Koh et al., 2009). RANTES gene polymorphism is associated with relative risk of coronary arteriosclerosis (Simeoni et al., 2004) and cerebral ischemia (Um and Kim, 2009). Therefore, blood RANTES may be a potential biomarker to identify patients at risk of stroke by indicating the presence of high level of chronic inflammation.

T. muris is a model for a human pathogen, *Trichuris trichiura*. To our knowledge, gastrointestinal helminth infections are not associated with negative outcome after stroke in clinical practice, although these types of infection are relatively rare in well developed countries where the incidence of stroke is high. In addition, although nematodes favor to polarize the immune response away from Th2 dominance, protection against nematodes mostly leads to a Th2-type response, and a well established infection model (using appropriate strain, dose, and timing) is needed to establish a chronic Th1-polarized infection in this case. Interestingly, a comprehensive set of data link Chagas' disease, caused by a parasite, *Trypanosoma cruzi*, to increased stroke prevalence, which is an emerging health problem in Europe and the United States after Latin America (Carod-Artal and Gascon, 2010). Therefore, other parasitic diseases may have previously unrecognized role in stroke. Our aim here was to use *T. muris* infection as a well char-

acterized model in mice to induce a chronic peripheral inflammation (which is an important contributor to poor outcome in patients) by modulating the immune response rather than modeling certain known comorbidities in stroke, which are highly complex. We used well established markers to characterize the immune state of the animal such as antigen-specific IgG subclasses or key inflammatory cytokines, which also correlate with outcome in stroke patients. For example, elevated serum *Chlamydia pneumoniae*- or *Helicobacter pylori*-specific IgGs in patients are predictive of cerebrovascular and cardiovascular events and extent of brain injury, similarly to infection burden and elevated serum CRP (Corrado et al., 2006; Smith et al., 2006). Our results indicate that the chronic Th1-polarized immune response, but not *T. muris* infection itself or the protective Th2-type response is detrimental. Although high-dose-infected (Th2-polarized) mice mostly expelled their parasites by 21 d after infection, low-dose-infected (Th1-polarized) mice had adult worms in the cecum after anti-RANTES treatment, whereas their ischemic brain damage was not different from uninfected mice. Our data also show that excess plasma IgG1 levels, which indicate more pronounced resistance to infection and Th2-type regulation (Bellaby et al., 1996; Perrigou et al., 2009), correlate negatively with infarct size, whereas the Th2-polarized response to *T. muris* did not worsen brain damage.

Chronic Th1-polarized response was also associated with increased platelet aggregation in the brain after stroke. Some observations link chronic inflammation to a procoagulant state, including the effect of proinflammatory mediators on platelet activation, aggregation, or reduction of anticoagulant factors (Levi et al., 2004). These mechanisms are involved in diabetes (Stegenga et al., 2008), obesity, and hypertension (Alessi and Juhan-Vague, 2008), which are individual risk factors in stroke. RANTES may not mediate platelet aggregation or adhesion alone (Shenkman et al., 2004), but interaction among multiple cytokines and pathways is likely to occur in inflammation and stroke. For example, IL-6, which was reduced in the first 24 h after MCAo in the brain of type 1-polarized mice, is protective against coagulatory and hemostatic disturbance (Inoue et al., 2004). G-CSF, which showed blunted early (4 h) production, but delayed (48 h) upregulation after MCAo in type 1-polarized mice, is a wide-action neuroprotectant in transient experimental stroke models if administered within 4 h (England et al., 2009). One other example of the complex interactions between systemic infection and stroke in our model is the downregulation of infection-induced proinflammatory cytokines such as MCP-1 and IFN- γ in the spleen within 4 h or RANTES in the plasma and blood cells between 4 and 48 h, in response to MCAo. We think that either enhanced release, deposition and proteolytic cleavage, or reduced production because of stroke-induced immunosuppression (Prass et al., 2003) are possible mechanisms. Nevertheless, these data argue for the need of precise understanding of these interactions to deliver appropriate medicines for patients with different comorbidities.

RANTES contributes to the proinflammatory response to IFN- γ (Ma et al., 2005), which is controlled by T_{reg}. These cells protect against focal cerebral ischemia (Liesz et al., 2009). Interestingly, obesity, a major risk factor for stroke, leads to profound and site-specific loss of T_{reg} cells in the adipose tissue and highly upregulated RANTES expression (Feuerer et al., 2009). Low-dose-infected mice had low worm burden in the cecum, which may account for less pronounced regulation of the ongoing chronic inflammatory response. This is clearly indicated by reduced T_{reg} (but not effector Th cells) in the spleen of infected compared with uninfected mice. The present study did not inves-

tigate whether a causal role exists for T_{reg} in inflammation-induced brain damage after stroke or not. It is also unclear whether increased leukocyte recruitment, microvascular injury, and BBB disruption contribute to brain damage in infected, Th1-polarized mice or simply reflect larger infarcts in these animals. In addition to reducing brain injury, the effect of anti-RANTES treatment on splenic inflammatory cells indicates an important role for this chemokine in the modulation of infection-induced leukocyte responses after stroke.

Additional investigation is required to understand how systemic inflammation and Th1 prepolarization of the immune system interact with stroke-induced immune changes in the late phases of infarct evolution and affect recovery. As the ischemic brain injury itself can polarize the immune system toward a Th2 state, induce immunosuppression, and lead to poststroke infections (Prass et al., 2003), it is possible that this response is altered by preexisting infection or chronic inflammation. Recent data indicate that IL-17-producing $\gamma\delta$ T-cells (Shichita et al., 2009) or T_{reg} (Liesz et al., 2009), which play an important role in multiple infectious diseases, can also influence delayed brain injury after experimental stroke. Therefore, it is important for future studies to establish how these inflammatory pathways interact and affect damage formation or recovery in stroke patients with comorbidities such as infection or chronic inflammatory disease.

Together, our results demonstrate for the first time that chronic peripheral infection exacerbates ischemic brain damage by systemic upregulation of RANTES. Targeted modulation of RANTES-dependent pathways may be therapeutically useful in several known comorbidities that augment the effects of stroke and impair outcome. Moreover, given ~1 billion people infected with similar intestinal nematodes worldwide, these data extend our understanding of the immunomodulatory capacity of such pathogens and their potential effects in vascular diseases.

References

- Alessi MC, Juhan-Vague I (2008) Metabolic syndrome, haemostasis and thrombosis. *Thromb Haemost* 99:995–1000.
- Anthony D, Dempster R, Fearn S, Clements J, Wells G, Perry VH, Walker K (1998) CXC chemokines generate age-related increases in neutrophil-mediated brain inflammation and blood-brain barrier breakdown. *Curr Biol* 8:923–926.
- Bancroft AJ, Else KJ, Grecis RK (1994) Low-level infection with *Trichuris muris* significantly affects the polarization of the CD4 response. *Eur J Immunol* 24:3113–3118.
- Bancroft AJ, Else KJ, Humphreys NE, Grecis RK (2001) The effect of challenge and trickle *Trichuris muris* infections on the polarisation of the immune response. *Int J Parasitol* 31:1627–1637.
- Bederson JB, Pitts LH, Tsuji M, Nishimura MC, Davis RL, Bartkowski H (1986) Rat middle cerebral artery occlusion: evaluation of the model and development of a neurologic examination. *Stroke* 17:472–476.
- Bellaby T, Robinson K, Wakelin D (1996) Induction of differential T-helper-cell responses in mice infected with variants of the parasitic nematode *Trichuris muris*. *Infect Immun* 64:791–795.
- Bihel E, Pro-Sistiaga P, Letourneur A, Toutain J, Saulnier R, Insausti R, Bernaudin M, Roussel S, Touzani O (2010) Permanent or transient chronic ischemic stroke in the non-human primate: behavioral, neuroimaging, histological, and immunohistochemical investigations. *J Cereb Blood Flow Metab* 30:273–285.
- Blomeley CP, Kehoe LA, Bracci E (2009) Substance P mediates excitatory interactions between striatal projection neurons. *J Neurosci* 29:4953–4963.
- Carod-Artal FJ, Gascon J (2010) Chagas disease and stroke. *Lancet Neurol* 9:533–542.
- Chapman KZ, Dale VQ, Denes A, Bennett G, Rothwell NJ, Allan SM, McColl BW (2009) A rapid and transient peripheral inflammatory response precedes brain inflammation after experimental stroke. *J Cereb Blood Flow Metab* 29:1764–1768.

- Cliffe LJ, Grecnis RK (2004) The *Trichuris muris* system: a paradigm of resistance and susceptibility to intestinal nematode infection. *Adv Parasitol* 57:255–307.
- Corrado E, Rizzo M, Tantillo R, Muratori I, Bonura F, Vitale G, Novo S (2006) Markers of inflammation and infection influence the outcome of patients with baseline asymptomatic carotid lesions: a 5-year follow-up study. *Stroke* 37:482–486.
- Dénes A, Vidyasagar R, Feng J, Narvainen J, McColl BW, Kauppinen RA, Allan SM (2007) Proliferating resident microglia after focal cerebral ischaemia in mice. *J Cereb Blood Flow Metab* 27:1941–1953.
- Dénes A, Thornton P, Rothwell NJ, Allan SM (2010) Inflammation and brain injury: acute cerebral ischaemia, peripheral and central inflammation. *Brain Behav Immun* 24:708–723.
- Dihné M, Grommes C, Lutzenburg M, Witte OW, Block F (2002) Different mechanisms of secondary neuronal damage in thalamic nuclei after focal cerebral ischemia in rats. *Stroke* 33:3006–3011.
- Else KJ, Entwistle GM, Grecnis RK (1993) Correlations between worm burden and markers of Th1 and Th2 cell subset induction in an inbred strain of mouse infected with *Trichuris muris*. *Parasite Immunol* 15:595–600.
- Else KJ, Finkelman FD, Maliszewski CR, Grecnis RK (1994) Cytokine-mediated regulation of chronic intestinal helminth infection. *J Exp Med* 179:347–351.
- Emsley HC, Hopkins SJ (2008) Acute ischaemic stroke and infection: recent and emerging concepts. *Lancet Neurol* 7:341–353.
- England TJ, Gibson CL, Bath PM (2009) Granulocyte-colony stimulating factor in experimental stroke and its effects on infarct size and functional outcome: a systematic review. *Brain Res Rev* 62:71–82.
- Feuerer M, Herrero L, Cipolletta D, Naaz A, Wong J, Nayer A, Lee J, Goldfine AB, Benoist C, Shoelson S, Mathis D (2009) Lean, but not obese, fat is enriched for a unique population of regulatory T cells that affect metabolic parameters. *Nat Med* 15:930–939.
- Gerfen CR (1991) Substance P (neurokinin-1) receptor mRNA is selectively expressed in cholinergic neurons in the striatum and basal forebrain. *Brain Res* 556:165–170.
- Glass WG, Hickey MJ, Hardison JL, Liu MT, Manning JE, Lane TE (2004) Antibody targeting of the CC chemokine ligand 5 results in diminished leukocyte infiltration into the central nervous system and reduced neurologic disease in a viral model of multiple sclerosis. *J Immunol* 172:4018–4025.
- Hayes KS, Bancroft AJ, Grecnis RK (2004) Immune-mediated regulation of chronic intestinal nematode infection. *Immunol Rev* 201:75–88.
- Helmby H, Takeda K, Akira S, Grecnis RK (2001) Interleukin (IL)-18 promotes the development of chronic gastrointestinal helminth infection by downregulating IL-13. *J Exp Med* 194:355–364.
- Houard X, Touat Z, Ollivier V, Louedec L, Philippe M, Sebbag U, Meilhac O, Rossignol P, Michel JB (2009) Mediators of neutrophil recruitment in human abdominal aortic aneurysms. *Cardiovasc Res* 82:532–541.
- Inoue K, Takano H, Yanagisawa R, Sakurai M, Shimada A, Morita T, Sato M, Yoshino S, Yoshikawa T, Tohyama C (2004) Protective role of interleukin-6 in coagulatory and hemostatic disturbance induced by lipopolysaccharide in mice. *Thromb Haemost* 91:1194–1201.
- Koenen RR, von Hundelshausen P, Nesselmeier IV, Zerneck A, Liehn EA, Sarabi A, Kramp BK, Piccinini AM, Paludan SR, Kowalska MA, Kungl AJ, Hackeng TM, Mayo KH, Weber C (2009) Disrupting functional interactions between platelet chemokines inhibits atherosclerosis in hyperlipidemic mice. *Nat Med* 15:97–103.
- Koh SJ, Kim JY, Hyun YJ, Park SH, Chae JS, Park S, Kim JS, Youn JC, Jang Y, Lee JH (2009) Association of serum RANTES concentrations with established cardiovascular risk markers in middle-aged subjects. *Int J Cardiol* 132:102–108.
- Levi M, van der Poll T, Büller HR (2004) Bidirectional relation between inflammation and coagulation. *Circulation* 109:2698–2704.
- Liesz A, Suri-Payer E, Veltkamp C, Doerr H, Sommer C, Rivest S, Giese T, Veltkamp R (2009) Regulatory T cells are key cerebroprotective immunomodulators in acute experimental stroke. *Nat Med* 15:192–199.
- Ling L, Zeng J, Pei Z, Cheung RT, Hou Q, Xing S, Zhang S (2009) Neurogenesis and angiogenesis within the ipsilateral thalamus with secondary damage after focal cortical infarction in hypertensive rats. *J Cereb Blood Flow Metab* 29:1538–1546.
- Ma B, Kang MJ, Lee CG, Chapoval S, Liu W, Chen Q, Coyle AJ, Lora JM, Picarella D, Homer RJ, Elias JA (2005) Role of CCR5 in IFN- γ -induced and cigarette smoke-induced emphysema. *J Clin Invest* 115:3460–3472.
- McColl BW, Rothwell NJ, Allan SM (2007) Systemic inflammatory stimulus potentiates the acute phase and CXC chemokine responses to experimental stroke and exacerbates brain damage via interleukin-1- and neutrophil-dependent mechanisms. *J Neurosci* 27:4403–4412.
- McColl BW, Rothwell NJ, Allan SM (2008) Systemic inflammation alters the kinetics of cerebrovascular tight junction disruption after experimental stroke in mice. *J Neurosci* 28:9451–9462.
- McColl BW, Allan SM, Rothwell NJ (2009) Systemic infection, inflammation and acute ischemic stroke. *Neuroscience* 158:1049–1061.
- Offner H, Subramanian S, Parker SM, Wang C, Afentoulis ME, Lewis A, Vandenbark AA, Hurn PD (2006) Splenic atrophy in experimental stroke is accompanied by increased regulatory T cells and circulating macrophages. *J Immunol* 176:6523–6531.
- Owyang AM, Zaph C, Wilson EH, Guild KJ, McClanahan T, Miller HR, Cua DJ, Goldschmidt M, Hunter CA, Kastelein RA, Artis D (2006) Interleukin 25 regulates type 2 cytokine-dependent immunity and limits chronic inflammation in the gastrointestinal tract. *J Exp Med* 203:843–849.
- Perrigoue JG, Zaph C, Guild K, Du Y, Artis D (2009) IL-31-IL-31R interactions limit the magnitude of Th2 cytokine-dependent immunity and inflammation following intestinal helminth infection. *J Immunol* 182:6088–6094.
- Prass K, Meisel C, Höflich C, Braun J, Halle E, Wolf T, Ruscher K, Victorov IV, Priller J, Dirnagl U, Volk HD, Meisel A (2003) Stroke-induced immunodeficiency promotes spontaneous bacterial infections and is mediated by sympathetic activation reversal by poststroke T helper cell type 1-like immunostimulation. *J Exp Med* 198:725–736.
- Schober A, Manka D, von Hundelshausen P, Huo Y, Hanrath P, Sarembock IJ, Ley K, Weber C (2002) Deposition of platelet RANTES triggering monocyte recruitment requires P-selectin and is involved in neointima formation after arterial injury. *Circulation* 106:1523–1529.
- Shenkman B, Brill A, Brill G, Lider O, Savion N, Varon D (2004) Differential response of platelets to chemokines: RANTES non-competitively inhibits stimulatory effect of SDF-1 α . *J Thromb Haemost* 2:154–160.
- Shichita T, Sugiyama Y, Ooboshi H, Sugimori H, Nakagawa R, Takada I, Iwaki T, Okada Y, Iida M, Cua DJ, Iwakura Y, Yoshimura A (2009) Pivotal role of cerebral interleukin-17-producing γ delta T cells in the delayed phase of ischemic brain injury. *Nat Med* 15:946–950.
- Simeoni E, Winkelmann BR, Hoffmann MM, Fleury S, Ruiz J, Kappenberger L, März W, Vassalli G (2004) Association of RANTES G-403A gene polymorphism with increased risk of coronary arteriosclerosis. *Eur Heart J* 25:1438–1446.
- Smith CJ, Emsley HC, Vail A, Georgiou RF, Rothwell NJ, Tyrrell PJ, Hopkins SJ (2006) Variability of the systemic acute phase response after ischemic stroke. *J Neurosci* 26:77–81.
- Snapper CM, Marcu KB, Zelazowski P (1997) The immunoglobulin class switch: beyond “accessibility.” *Immunity* 6:217–223.
- Stegenga ME, van der Crabben SN, Blümer RM, Levi M, Meijers JC, Serlie MJ, Tanck MW, Sauerwein HP, van der Poll T (2008) Hyperglycemia enhances coagulation and reduces neutrophil degranulation, whereas hyperinsulinemia inhibits fibrinolysis during human endotoxemia. *Blood* 112:82–89.
- Stumm R, Culmsee C, Schafer MK, Krieglstein J, Weihe E (2001) Adaptive plasticity in tachykinin and tachykinin receptor expression after focal cerebral ischemia is differentially linked to GABAergic and glutamatergic cerebrocortical circuits and cerebrovascular endothelium. *J Neurosci* 21:798–811.
- Terao S, Yilmaz G, Stokes KY, Russell J, Ishikawa M, Kawase T, Granger DN (2008) Blood cell-derived RANTES mediates cerebral microvascular dysfunction, inflammation, and tissue injury after focal ischemia-reperfusion. *Stroke* 39:2560–2570.
- Um JY, Kim HM (2009) Polymorphisms of RANTES and IL-4 genes in cerebral infarction. *J Mol Neurosci* 37:1–5.
- von Hundelshausen P, Weber KS, Huo Y, Proudfoot AE, Nelson PJ, Ley K, Weber C (2001) RANTES deposition by platelets triggers monocyte arrest on inflamed and atherosclerotic endothelium. *Circulation* 103:1772–1777.
- Yilmaz G, Arumugam TV, Stokes KY, Granger DN (2006) Role of T lymphocytes and interferon- γ in ischemic stroke. *Circulation* 113:2105–2112.
- Zerneck A, Liehn EA, Gao JL, Kuziel WA, Murphy PM, Weber C (2006) Deficiency in CCR5 but not CCR1 protects against neointima formation in atherosclerosis-prone mice: involvement of IL-10. *Blood* 107:4240–4243.

RESEARCH

Open Access

Systemic inflammatory challenges compromise survival after experimental stroke via augmenting brain inflammation, blood- brain barrier damage and brain oedema independently of infarct size

Ádám Dénes^{1,2*}, Szilámér Ferenczi¹ and Krisztina J Kovács¹

Abstract

Background: Systemic inflammation impairs outcome in stroke patients and experimental animals via mechanisms which are poorly understood. Circulating inflammatory mediators can activate cerebrovascular endothelium or glial cells in the brain and impact on ischaemic brain injury. One of the most serious early clinical complications of cerebral ischaemia is brain oedema, which compromises survival in the first 24-48 h. It is not understood whether systemic inflammatory challenges impair outcome after stroke by increasing brain injury only or whether they have direct effects on brain oedema, cerebrovascular inflammation and blood-brain barrier damage.

Methods: We used two different systemic inflammatory stimuli, acute endotoxin treatment and anaphylaxis to study mechanisms of brain injury after middle cerebral artery occlusion (MCAo). Ischaemic brain injury, blood-brain barrier damage and oedema were analysed by histological techniques. Systemic cytokine responses and inflammatory changes in the brain were analysed by cytometric bead array, immunofluorescence, *in situ* hybridization and quantitative real-time PCR.

Results: Systemic inflammatory challenges profoundly impaired survival in the first 24 h after experimental stroke in mice, independently of an increase in infarct size. Systemic lipopolysaccharide (LPS) dose-dependently increased mortality (50-100%) minutes to hours after cerebral ischaemia. Acute anaphylactic challenge in ovalbumin-sensitised mice affected stroke more seriously when induced via intraperitoneal administration compared to intravenous. Both LPS and anaphylaxis induced inflammatory changes in the blood and in the brain prior to experimental stroke. Plasma cytokine levels were significantly higher after LPS, while increased IL-10 levels were seen after anaphylaxis. After MCAo, both LPS and anaphylaxis increased microglial interleukin-1 α (IL-1 α) expression and blood-brain barrier breakdown. LPS caused marked granulocyte recruitment throughout the ipsilateral hemisphere. To investigate whether reduction of ischaemic damage can improve outcome in systemic inflammation, controlled hypothermia was performed. Hypothermia reduced infarct size in all treatment groups and moderately improved survival, but failed to reduce excess oedema formation after anaphylaxis and LPS-induced neuroinflammation.

Conclusions: Our results suggest that systemic inflammatory conditions induce cerebrovascular inflammation via diverse mechanisms. Increased brain inflammation, blood-brain barrier injury and brain oedema formation can be major contributors to impaired outcome in mice after experimental stroke with systemic inflammatory stimuli, independently of infarct size.

Keywords: cerebral ischaemia, blood-brain barrier, oedema, IL-1 α , inflammation, systemic, LPS, anaphylaxis

* Correspondence: adam.denes@manchester.ac.uk

¹Laboratory of Molecular Neuroendocrinology, Institute of Experimental Medicine, Budapest, Hungary

Full list of author information is available at the end of the article

Background

Considerable research supports a relationship between systemic inflammation and poor outcome in stroke patients and in models of experimental stroke [1,2]. Animal models of co-morbidities in stroke have revealed various systemic inflammatory mechanisms which contribute to brain damage. These include peripheral immune cells, proteases, cytokines and chemokines, which can increase ischaemia-induced vascular permeability, excitotoxicity and brain oedema resulting in impaired blood flow recovery, leading to augmented neuronal loss [3,4]. There is a correlation between the size of ischaemic brain injury and the level of central and peripheral inflammatory changes in experimental animals, but this may not be translated easily to stroke patients. It is partially due to the large variability of co-morbidities, age, gender, time of admission after the event and exposure to a wide array of different medicines, which make the influence of systemic inflammation on outcome difficult to assess. In patients acute infection, usually respiratory and of bacterial origin and particularly in the week preceding stroke, is a significant risk factor for cerebral infarction [1]. Inflammatory processes other than infection are also associated with worse outcome after stroke. For example, activation of mast cells, a key cell type in allergy and anaphylaxis is also linked to increased mortality and brain oedema in stroke [5,6].

The treatment of patients with large hemispheric ischaemic stroke accompanied by massive space-occupying oedema represents one of the major unsolved problems in neurocritical care medicine [7]. Some clinical data indicate that neuroprotective approaches may not be sufficient to prevent brain oedema in cerebral ischaemia. For example, hypothermia, a promising treatment for ischaemic stroke due to its neuroprotective effect, was associated with an increase in intracranial pressure and early mortality in a high percentage of patients [7]. In experimental animals, increase in infarct size mostly parallels increased brain oedema and blood-brain barrier (BBB) breakdown, which correlates with worse outcome. However, stroke patients display large variability in recovery depending on location of the infarct and differences in apparent comorbidities [8,9]. This indicates that there is a need to understand the mechanisms how clinically relevant inflammatory events influence outcome after stroke. Therefore we asked whether brain oedema, BBB injury and inflammation are affected similarly by different systemic inflammatory challenges and whether reducing the size of the ischaemic brain damage by hypothermia can lead to proportional reduction of oedema and BBB damage during acute systemic inflammatory conditions. Using two independent peripheral inflammatory stimuli, endotoxin (LPS) and

anaphylaxis, in acute cerebral ischaemia in mice we noticed that these conditions can be associated with increased BBB breakdown, inflammation and brain oedema, without significantly affecting infarct size. Moreover, infarct, but not brain oedema was significantly reduced by hypothermia after anaphylactic challenge. Our data indicate that circulating inflammatory markers in different acute systemic inflammatory conditions may worsen outcome after focal cerebral ischaemia by directly increasing BBB damage and brain oedema formation, with a possible involvement of mediators other than most commonly measured cytokines.

Methods

Animals

Male, 8-14 weeks old C57BL/6 mice, weighing 25-30 g were used for the study ($n = 109$). Mice were bred in house, had free access to water and food and were maintained under temperature ($21^{\circ}\text{C} \pm 1^{\circ}\text{C}$), humidity (65%) and light-controlled conditions (12-h light/12-h dark cycle, with lights on at 0700 hours). All animal procedures were carried out in accordance with the European Communities Council Directive (86/609 EEC) and Hungarian Government directive 243/98. Experiments were approved by the Institutional Animal Care and Use Committee at the Institute of Experimental Medicine.

Systemic inflammatory challenge with Lipopolysaccharide (LPS), ovalbumin sensitisation (OVA) and anaphylaxis (OVA+A) prior to MCAo

Lipopolysaccharide (LPS, serotype: 0111:B4, Sigma L4391) was administered intraperitoneally at doses of 100 $\mu\text{g}/\text{mouse}$ (4 mg/kg) 25 $\mu\text{g}/\text{mouse}$ (1 mg/kg), 10 $\mu\text{g}/\text{mouse}$ (400 $\mu\text{g}/\text{kg}$) and 5 $\mu\text{g}/\text{mouse}$ (200 $\mu\text{g}/\text{kg}$). The highest doses (25-100 $\mu\text{g}/\text{mouse}$) were selected to induce substantial systemic inflammation, without compromising survival (LD_{50} value for LPS in mice after intraperitoneal administration is 10-20 mg/kg [10,11]). No animals died or needed to be terminated as a result of LPS injection alone in our experiments. A separate group of mice were sensitised intraperitoneally with 100 μg ovalbumin (Sigma A5378, dissolved in 200 μl saline containing 1 mg $\text{Al}(\text{OH})_3$). Anaphylaxis was induced 14 days later via injection of 1 mg ovalbumin intraperitoneally (ip.) or intravenously (iv.). Mice were subjected to MCAo 3 h after LPS or anaphylactic challenge.

Transient focal cerebral ischaemia

Middle cerebral artery occlusion (MCAo) was performed using the intraluminal filament technique as described previously [12]. Anaesthesia was induced with 2% halothane and maintained in 1% halothane-air mixture. For normothermic experiments, core temperature was

monitored with a rectal probe and maintained at $37 \pm 0.5^\circ\text{C}$, using a homeothermic blanket during the surgery. For controlled hypothermia, unheated, anaesthetised mice were allowed to spontaneously lose temperature during the surgery until reaching $33 \pm 0.5^\circ\text{C}$ and then body temperature was maintained between $33\text{--}34^\circ\text{C}$ during occlusion. MCAo was performed with a nylon filament (tip diameter $180\ \mu\text{m}$, silicone coated), which was introduced into the origin of the external carotid artery and advanced through the internal carotid artery to occlude the MCA. After 60 minutes of occlusion, reperfusion was induced and both normothermic and hypothermic mice were kept at 27°C for 4 h before returning to normal housing. Sham surgery was performed exactly the same as MCAo, but the filament was immediately withdrawn after reaching the origin of the MCA. Mice were subcutaneously injected with 1 mL of sterile saline after the surgery and continuously monitored for neurologic symptoms. Animals were euthanised if they were unable to move spontaneously after 3 h recovery period, or if breathing was seriously compromised. Otherwise, mice were terminated after 24 h reperfusion. Due to the mild to moderate sickness behaviour seen after systemic LPS and anaphylaxis, induction of ischaemia blinded to treatment groups was not fully possible.

Histology

Mice were anaesthetised and perfused transcardially with 10 mL saline followed by 40 mL 4% paraformaldehyde in 0.1 M Phosphate buffer (pH = 7.4). After cryoprotection of brains in 20% sucrose-KPBS for 24 h, five alternate sets of $20\ \mu\text{m}$ coronal brain sections were cut on a sledge microtome. All sections were collected in an anti-freeze solution (30% ethylene glycol and 20% glycerol in phosphate-buffered saline) and stored at -20°C until processing.

Measurement of infarct volume and BBB damage

The volume of ischaemic damage was measured using a modification of a method described previously [12]. Briefly, areas of ischaemic damage were identified on cresyl-violet-stained sections at eight neuroanatomically defined coronal levels. Digitized images were created and the areas of damage measured using ImageJ software (NIH, Bethesda, MD, USA). The volume of damage was calculated by integration of areas of damage with the distance between coronal levels. The end points for integration were 2.9 mm (rostral limit) and -4.9 mm (caudal limit) relative to bregma. Volumes are expressed as a percentage of the total hemispheric volume. Leakage of plasma derived IgG into the brain parenchyma was detected by biotinylated horse anti-mouse IgG (Vector Laboratories, BA-2000, 1:500) following blocking nonspecific binding in 5% normal horse serum and 1% BSA. After 30 min incubation with ABC solution (1:500, Vector Laboratories) the reaction was

developed with 3,3'-diaminobenzidine (DAB). The volume of BBB damage was calculated as described above. Brain oedema was measured on cresyl violet-stained brain sections and was expressed as a percentage increase of the volume of the ipsilateral hemisphere compared to the contralateral side.

Immunofluorescence

Free-floating brain sections were blocked with 2% normal donkey serum and incubated overnight with primary antibodies: goat anti-IL-1 α (R&D Systems, AF-400-NA) and rabbit anti-granulocyte serum (SJC, kindly provided by Drs. Daniel Anthony and Sandra Campbell, University of Oxford). Then, donkey anti-goat Alexa 488 and donkey anti-rabbit Alexa 594 fluorescent secondary antibodies were used. Sections were stained with biotinylated tomato lectin, which was visualised with streptavidin Alexa 350 conjugate.

In Situ Hybridization Histochemistry

To monitor IL-1 β mRNA, a riboprobe complementary to 373 to 940 nucleotides of the mouse IL-1 β gene was transcribed from plasmid (S. Ferenczi) in the presence of ^{35}S -UTP. Tissue sections were mounted onto SuperFrost Ultra Plus (Menzer-Glazer) slides post-fixed with 4% paraformaldehyde, digested with Proteinase K (10 in 50 mmol/L Tris, pH = 8 and 5 mmol/L EDTA at 37°C , 5 mins), acetylated (0.25% acetic anhydride in 0.1 mol/L triethanolamine, pH = 8), and dehydrated. Hybridization mixture (50% formamide, 0.3 mol/L NaCl, 10 mmol/L Tris (pH = 8), 2 mmol/L EDTA, 1X Denhardt's, 10% dextran sulfate, 0.5 mg/mL yeast tRNA) was pipetted onto the slides (100 mL, containing probe at 10^7 d.p.m./mL) and hybridized overnight at 56°C . Sections were then rinsed in 4X SSC (1X SSC: 0.15 mol/L NaCl and 15 mmol/L trisodiumcitrate buffer, pH = 7), digested with ribonuclease A (20 mg/mL in Tris-EDTA buffer with 0.5 mol/L NaCl at 37°C for 30 min), gradually desalted, and washed in 0.1X SSC at 65 to 75°C for 30 min. Slides were dipped in NTB nuclear emulsion (Kodak) and exposed for 2 weeks, developed in D-19 developer, and lightly counterstained with cresyl violet.

Quantitative Real-Time PCR

Total RNA was isolated from brain samples with QIAGEN RNeasy Mini Kit (Qiagen, Valencia, CA, USA) according the manufacturer's instruction. To eliminate genomic DNA contamination DNase I treatment was used (100 μl Rnase-free DNase I (1u DNase) solution (Fermentas) was added. Sample quality control and the quantitative analysis were carried out by NanoDrop (Thermo Scientific). Amplification was not detected in the RT-minus controls. cDNA synthesis was performed with the High Capacity cDNA Reverse Transcription Kit

(Applied Biosystems, Foster City, CA, USA). The designed primers (Invitrogen, Table 1) were used in the Real-Time PCR reaction with Fast EvaGreen qPCR Master Mix (Biotium, CA, USA) on ABI StepOnePlus instrument. Gene expression was analyzed by ABI StepOne 2.1 program. The amplicon was tested by Melt Curve Analysis on ABI StepOnePlus instrument. GAPDH and β -actin were used as endogenous control reference genes. Experiments were normalized to GAPDH expression.

Measurement of plasma IL-1 β and OVA-specific IgE by ELISA

Blood was taken from the right heart ventricle immediately before transcatheter perfusion. 3.8% sodium citrate (1:10) was used as an anticoagulant. IL-1 β was measured by using mouse IL-1 beta/IL-1F2 DuoSet ELISA kit (DY401, R&D Systems) according to the manufacturers protocol. For the measurement of OVA-specific IgE, Nunc-Immuno™ plates (Sigma) were coated with plasma samples in bicarbonate coating buffer (0.1 M NaHCO₃, 0.1 M NaCl, pH 8.2) and then blocked with 1% BSA in PBS. Biotinylated anti-mouse IgE antibody was used to detect plasma OVA-specific IgE and mouse anti-ovalbumin IgE (Serotec, MCA2259) antibody was used as standard. The reaction was developed with SAV-HRP (R&D Systems) followed by OptEIA™ TMB Substrate Reagent Set (BD Biosciences).

Cytokine measurements with cytometric bead array (CBA)

Plasma samples were analysed for 11 key inflammatory cytokines (G-CSF, IFN γ , IL-1 β , IL-1 α , IL-10, IL-17, IL-6, KC, MCP-1, TNF α , RANTES) by using appropriate CBA Flex Sets (BD Biosciences) according to the manufacturer's protocol. To measure the same cytokines in brain homogenates, animals were transcatheterially perfused with saline 3 hours after systemic inflammatory challenges. Brain

hemispheres were homogenised as described elsewhere [13].

Data analysis

Quantitative analysis was done in a blinded manner whenever it was possible. Data were analysed by using One-way or Two-way analysis of variance (ANOVA) followed by Bonferroni's post hoc multiple- or paired comparison. Data are expressed as mean \pm SEM.

Results

Systemic inflammation impairs survival after experimental stroke

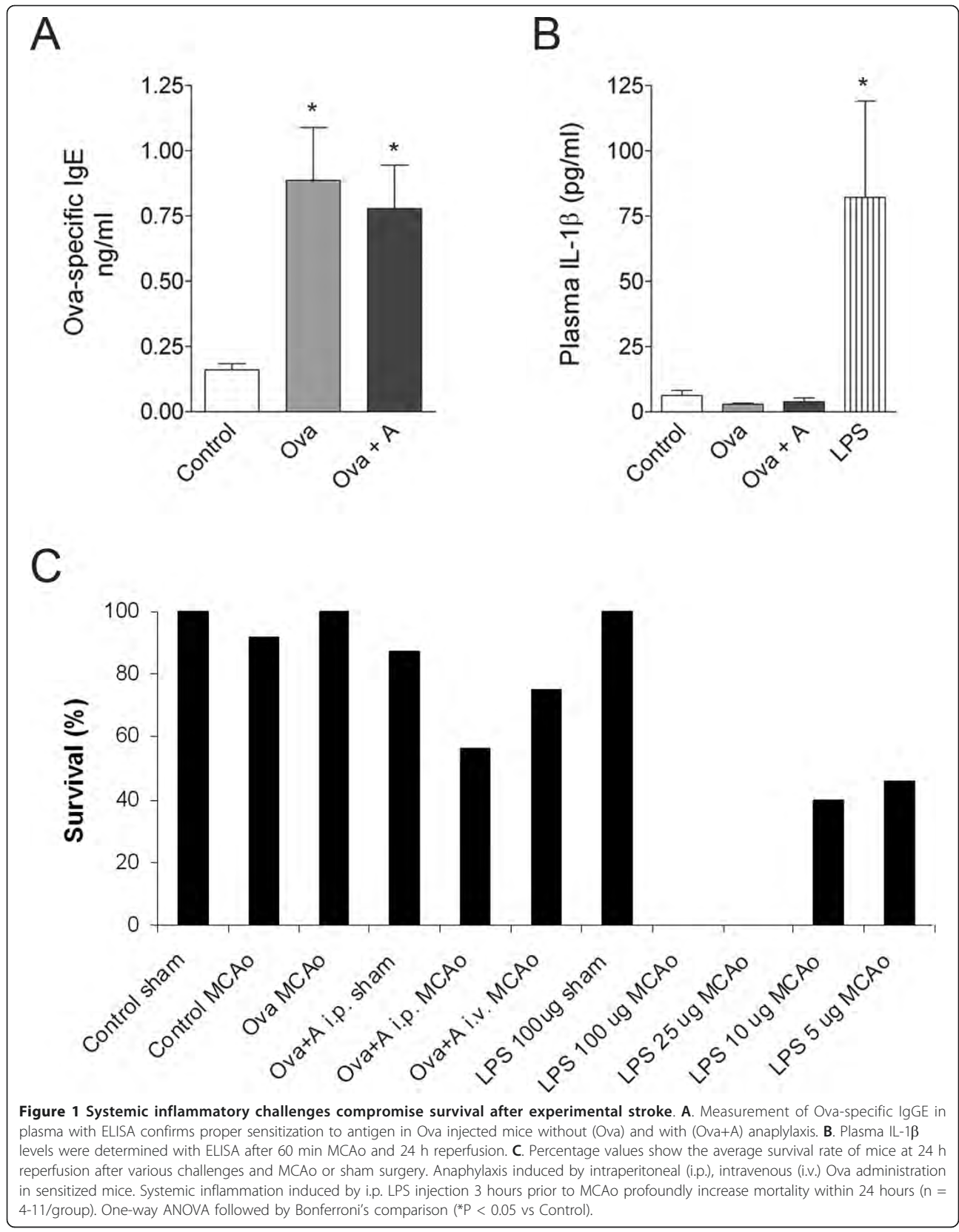
Mice were challenged with LPS or Ova+A 3 h before MCAo to develop a systemic inflammatory response [14-17] by the time experimental stroke was induced. Mice injected with LPS (25-100 μ g/mouse) displayed mild to moderate sickness behaviour, respectively, which was less pronounced at doses of 5-10 μ g. Ova sensitised mice showed signs of ear swelling and itching after anaphylactic challenge, which largely resolved after 1-2 h. Successful sensitisation against Ova was confirmed by elevated circulating Ova-specific IgE levels (Figure 1A). Plasma IL-1 β was upregulated in LPS-treated animals (Figure 1B), indicating the development of a systemic inflammatory response. Only actively moving animals which showed no signs of serious illness 3 h after LPS or Ova+A challenge were subjected to 60 min MCAo.

Mice challenged intraperitoneally with Ova+A showed impaired recovery after MCAo and only 56% of mice survived for 24 h (Figure 1C). However, 75% of the animals survived if mice were challenged with intravenous Ova indicating that Ova is likely to be acting locally on sensitised peritoneal cells to initiate a systemic inflammatory response, compromising survival after experimental

Table 1 Primers used for real-time PCR

	FORWARD	REVERSE	R ²	EFF (%)
GAPDH	TGACGTGCCGCTGGAGAAA	AGTGTAGCCCAAGATGCCCTTCAG	0,996	91,7
ACTIN- β	CGTAAAGACCTCTATGCCAA	GCGCAAGTTAGGTTTTGTC	0,988	92,5
IL-1 β	GCCTCGTGCTGTCGGACCCA	TGAGGCCCAAGGCCACAGGT	0,953	98,1
IL-1 α	CCATAACCCATGATCTGGAAGAG	GCTTCATCAGTTTGTATCTCAAATCAC	0,998	104,0
IL-17 α	CCTGGCGGTACAGTGAAG	GGAAGTCCTTGGCCTCAGTGT	0,959	95,8
IL-6	CAGTTGCCTTCTGGGACTGA	GGGAGTGGTATCCTCTGTGAAGTCT	0,959	108,0
IL-10	AGTGAGAAGCTGAAGACCCTCAGG	TTCATGGCCTTGTAGACACCTTGGT	0,970	107,2
G-CSF	TGCCCAGAGGCGCATGAAGC	GGGGAACGGCCTCTCGTCCT	0,997	102,5
MCP-1	CCAGCACCAGCACCAGCCAA	TGGATGCTCCAGCCGGCAAC	0,967	94,8
TNF α	CAGCCGATGGGTTGTACCTT	GGCAGCCTTGTCCCTTGA	0,985	102,4
KC	GAGTGCGCTGTCACTGCCT	CAAGGCAAGCCTCGCGACCA	0,997	105,2

Primers used for real-time PCR (comparative CT experiments) were designed by the Primer Express 3.0 program. Oligonucleotide primer sequences, R² (regression coefficient) and efficiency (eff %) of the PCR reactions are listed for all primer pairs.



stroke. Mice sensitised with Ova without anaphylaxis expressed no mortality during these studies after MCAo.

No mice survived after MCAo if they received 25-100 µg LPS. Very poor recovery and high mortality (50-60%) was observed with 5-10 µg LPS after MCAo, whereas even high doses of LPS did not compromise survival after sham surgery (Figure 1C). These data showed that circulating inflammatory mediators induced by two completely different stimuli can profoundly impair survival after experimental stroke.

Systemic inflammatory challenges augment cerebrovascular inflammation, BBB damage and brain oedema after experimental stroke, independently of infarct size

Mice that survived for 24 h were investigated to reveal how different systemic stimuli affected brain damage caused by focal cerebral ischaemia. No significant increase of ischaemic brain damage was observed after LPS or Ova+A challenges (Figure 2A). However, both

conditions increased BBB damage (Figure 2B). Systemic inflammation resulted in increased brain oedema (systemic inflammatory challenges versus control conditions, $P < 0.05$, Two-way ANOVA). Sensitisation with Ova without anaphylaxis did not have any detrimental effect on oedema or BBB damage (Figure 2B-D). Next, we examined whether different systemic inflammatory conditions had an effect on brain inflammation after MCAo. Anaphylaxis significantly increased the expression of IL-1 α in the ipsilateral cerebral cortex (Figure 3A, C), while endotoxin-induced systemic response was associated with profound increases of IL-1 α in remote areas, such as the thalamus and the hypothalamus ($P < 0.05$). In addition to parenchymal cells, several IL-1 α -positive cells were observed perivascularly around dilated blood vessels after anaphylaxis, indicating that IL-1 α expression may be associated with the development of vasogenic oedema (Figure 3C, i). In contrast, LPS-treated mice displayed mostly parenchymal, elongated, IL-1 α -positive cells with microglial morphology

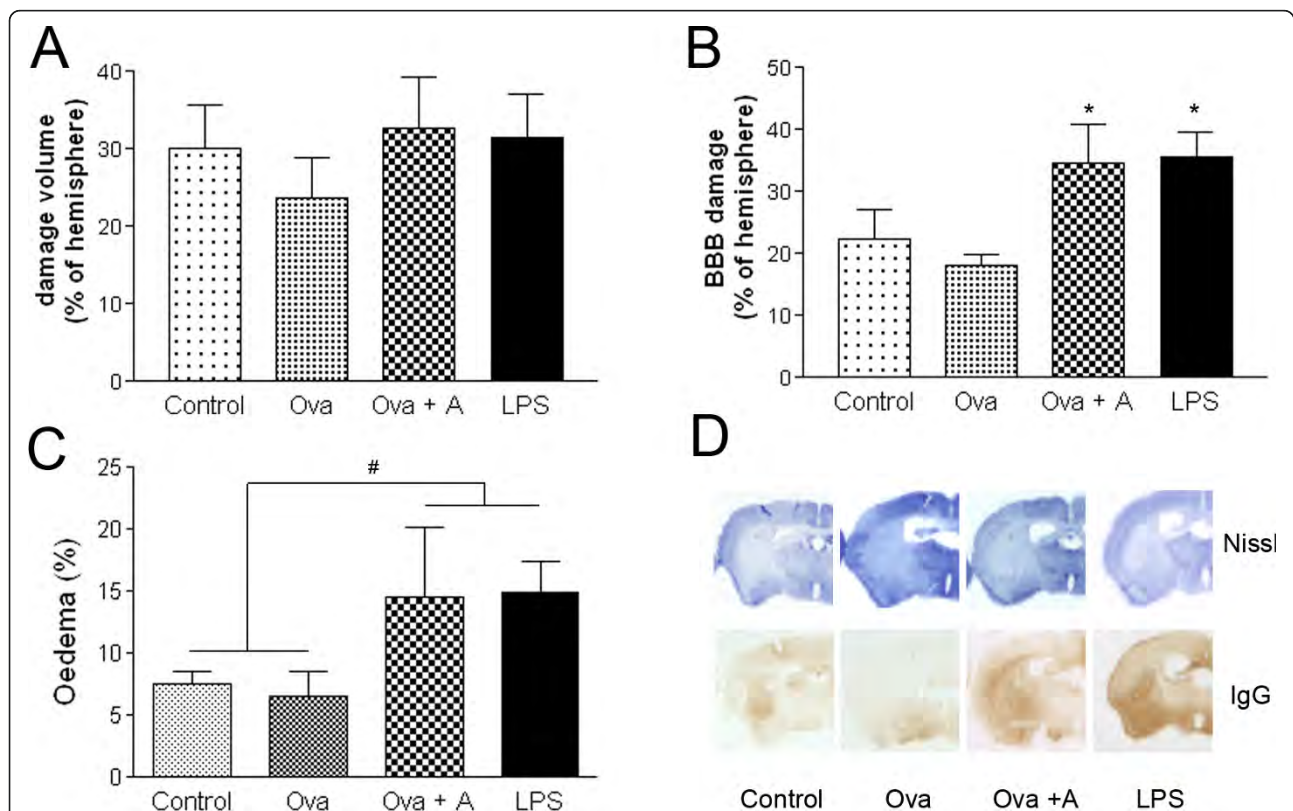


Figure 2 Systemic inflammation increases BBB damage and brain oedema independently of infarct size. **A.** The volume of the ischaemic damage was measured on cresyl violet (Nissl) stained serial brain sections. **B.** BBB damage was assessed by immunostaining for mouse IgG on free floating brain sections. Intraperitoneal LPS injection and anaphylaxis 3 hours prior to MCAo significantly augment BBB disruption at 24 hours of reperfusion ($P < 0.05$, One-way ANOVA, Bonferroni's post-hoc comparison). **C.** Oedema is expressed as percentage increase of the ipsilateral hemispheric volume compared to the contralateral hemisphere (# $P < 0.05$, systemic inflammatory challenges versus control conditions, Two-way ANOVA). **D.** Representative images show the ischaemic brain- (Nissl) or BBB (IgG) damage in different treatment groups. Data are representative of 4-5 mice/group.

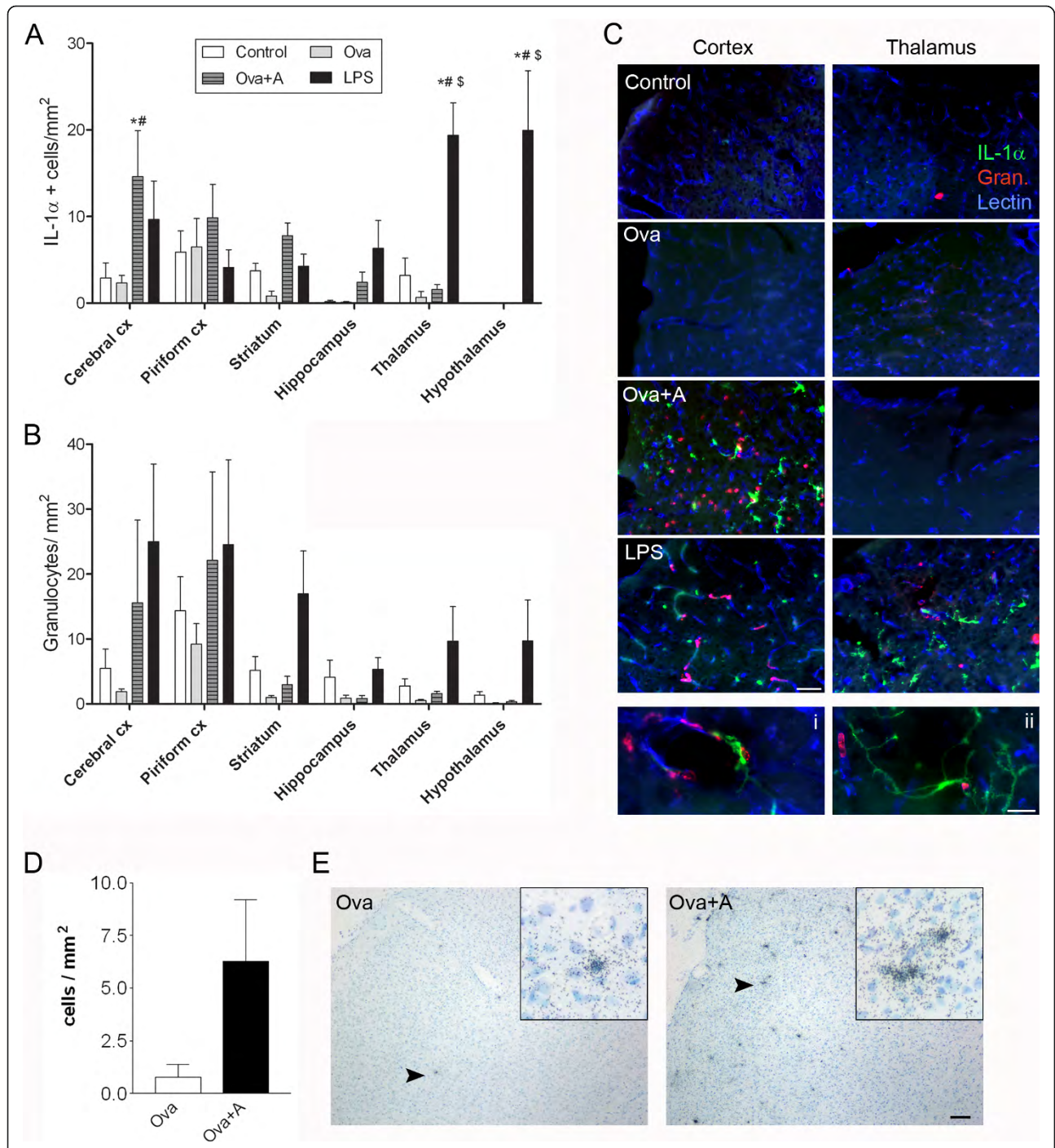


Figure 3 Experimental stroke-induced IL-1 expression is increased in the brain after LPS administration and anaphylaxis. Quantification of IL-1 α -positive cells (**A**) and granulocytes (**B**) in the ipsilateral hemisphere. **C**. Immunofluorescence shows IL-1 α -positive cells (green), granulocytes (red) and tomato lectin-positive blood vessels (blue) and microglia/macrophage cells in the ipsilateral cerebral cortex and thalamus after 24 h reperfusion. Perivascular cells in the cerebral cortex (i) and parenchymal cells in the thalamus (ii) expressing IL-1 α after MCAo are abundant in mice with anaphylaxis and LPS treatment, respectively. **D**. *In situ* hybridization reveals increased number of cells expressing IL-1 β mRNA in the ischaemic cerebral cortex of mice 24 h after MCAo with anaphylaxis (Ova+A) compared to MCAo and Ova sensitization (Ova). **E**. Silver grains indicate the presence of IL-1 β mRNA in Ova and Ova+A mice after MCAo (counterstained with cresyl violet). Inserts show higher magnification of IL-1 β mRNA containing cells indicated by arrowheads. Data are representative of 4-5 mice in each group. One-way ANOVA followed by Bonferroni's comparison ($P < 0.05$ vs * Control, # Ova, \$ Ova+A). Scale bars: Cii - 20 μ m, C - 50 μ m, E - 100 μ m.

(Figure 3C, ii). IL-1 α expression was detected mostly in tomato lectin-positive ramified microglia/macrophage cells (not shown). LPS treatment resulted in an overall increase of granulocytes in the ipsilateral hemisphere ($P < 0.05$), whereas this was only observed in the cerebral cortex after anaphylaxis (Figure 3B, C).

We also measured IL-1 β expression in the brain after MCAo, using *in situ* hybridization. IL-1 β has been associated with brain oedema formation after stroke [4,18-20]. We did not find significant changes in IL-1 β mRNA expression after MCAo in LPS-treated mice (data not shown) compared to controls, but observed markedly increased numbers of IL-1 β mRNA expressing cells after anaphylaxis (Figure 3D, E). In line with the IL-1 α data, IL-1 β mRNA expression was augmented mostly in the ischaemic cerebral cortex (Figure 3B, C) at 24 h reperfusion, whereas we only occasionally observed IL-1 β -positive cells in the ipsilateral striatum (data not shown).

LPS and anaphylaxis-induced systemic inflammatory responses are dominated by different circulating cytokines

To investigate whether these fundamentally different systemic inflammatory stimuli drive different systemic inflammatory responses, we investigated the plasma levels of 11 key cytokines 3 h after LPS or anaphylaxis (at the time MCAo is performed). LPS induced profound (10-1000 fold) increases in G-CSF, IL-6, KC, MCP-1, TNF α , and RANTES and a 4-fold, but significant increase in IL-1 β , without significantly affecting IFN γ , IL-17A, IL-1 α and IL-10 levels (Figure 4). Anaphylaxis increased G-CSF, IL-6, KC, MCP-1, TNF α , and RANTES levels 4-30 fold (not significant), and significantly elevated IL-10 levels (80 fold) while no IL-1 β or IL-1 α was detected (Figure 4).

Systemic inflammatory challenges induce neuroinflammatory changes in the brain

In order to examine inflammatory changes in the brain in response to systemic inflammatory challenges, we measured central IL-1 α , IL-1 β and IL-10 expression with real-time PCR, 3 h after LPS treatment or anaphylaxis. In the absence of any direct brain injury, intraperitoneal LPS caused a 2-3 fold increase in central IL-1 α and IL-1 β mRNA levels in brain hemispheres compared to control mice (Figure 5A). In contrast, IL-10 mRNA levels were decreased in LPS and Ova treated mice and after anaphylaxis compared to controls (Figure 5A).

Cytometric bead array did not show significant elevation in IL-1 α , IL-1 β or IL-10 protein concentration in the brain after LPS administration or anaphylaxis (data not shown), but revealed a significant increase in MCP-1 (6 fold), RANTES (3-4 fold), G-CSF (17 fold) and IL-6

(9 fold) levels in response to LPS (Figure 5B). KC (CXCL-1) was elevated in the brain 2-40 fold after LPS treatment, which was not significant due to large variations among individual animals (data not shown).

Real-time PCR confirmed the induction of MCP-1, G-CSF, and KC in the brain after intraperitoneal LPS treatment and also revealed higher levels of TNF α mRNA compared to control mice (Figure 5C). Interestingly, IL-6 mRNA levels were significantly reduced after LPS administration (Figure 5C).

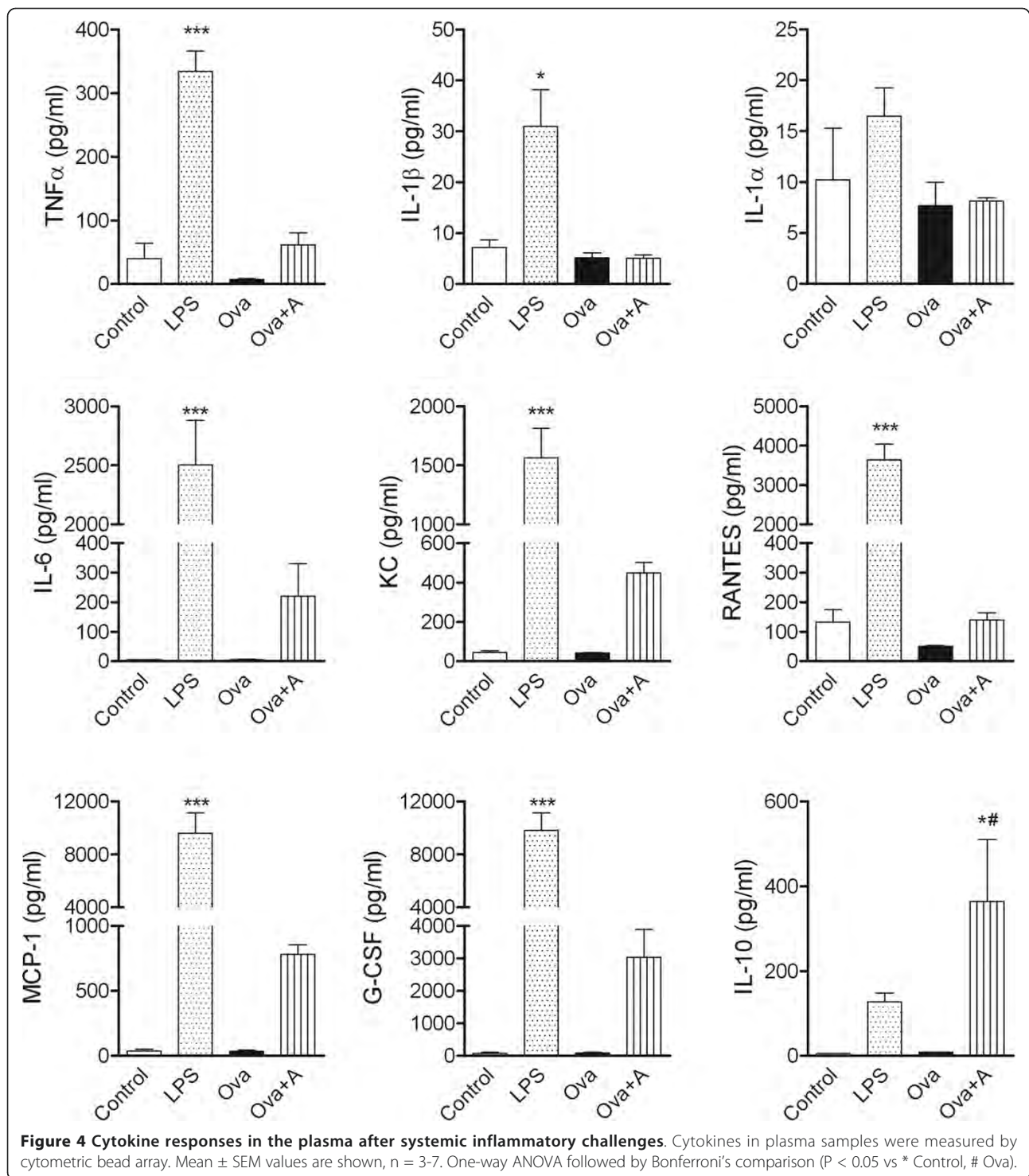
Hypothermia profoundly reduces ischaemic brain injury, but does not prevent the effect of systemic inflammation on brain oedema and survival

To further investigate the mechanisms of how peripheral inflammatory challenges affect ischaemic brain damage and inflammation, we subjected mice to hypothermia during occlusion, using the same experimental groups as above. Overall, hypothermia profoundly reduced ischaemic brain damage ($P < 0.001$) and brain oedema ($P < 0.01$) compared to normothermia (Figure 6A, B). Only LPS-treated mice showed elevated granulocyte levels and IL-1 α expressing cells in the ipsilateral hemisphere after hypothermia and MCAo (not shown), indicating that peripheral LPS initiates brain inflammation even if the ischaemic brain damage is reduced. Hypothermia was not sufficient to protect against increased brain oedema caused by anaphylaxis compared to control mice (Figure 6C). Moreover, hypothermia only moderately reduced mortality in mice exposed to LPS or anaphylaxis (72% survival after LPS and 67% survival after anaphylaxis).

Discussion

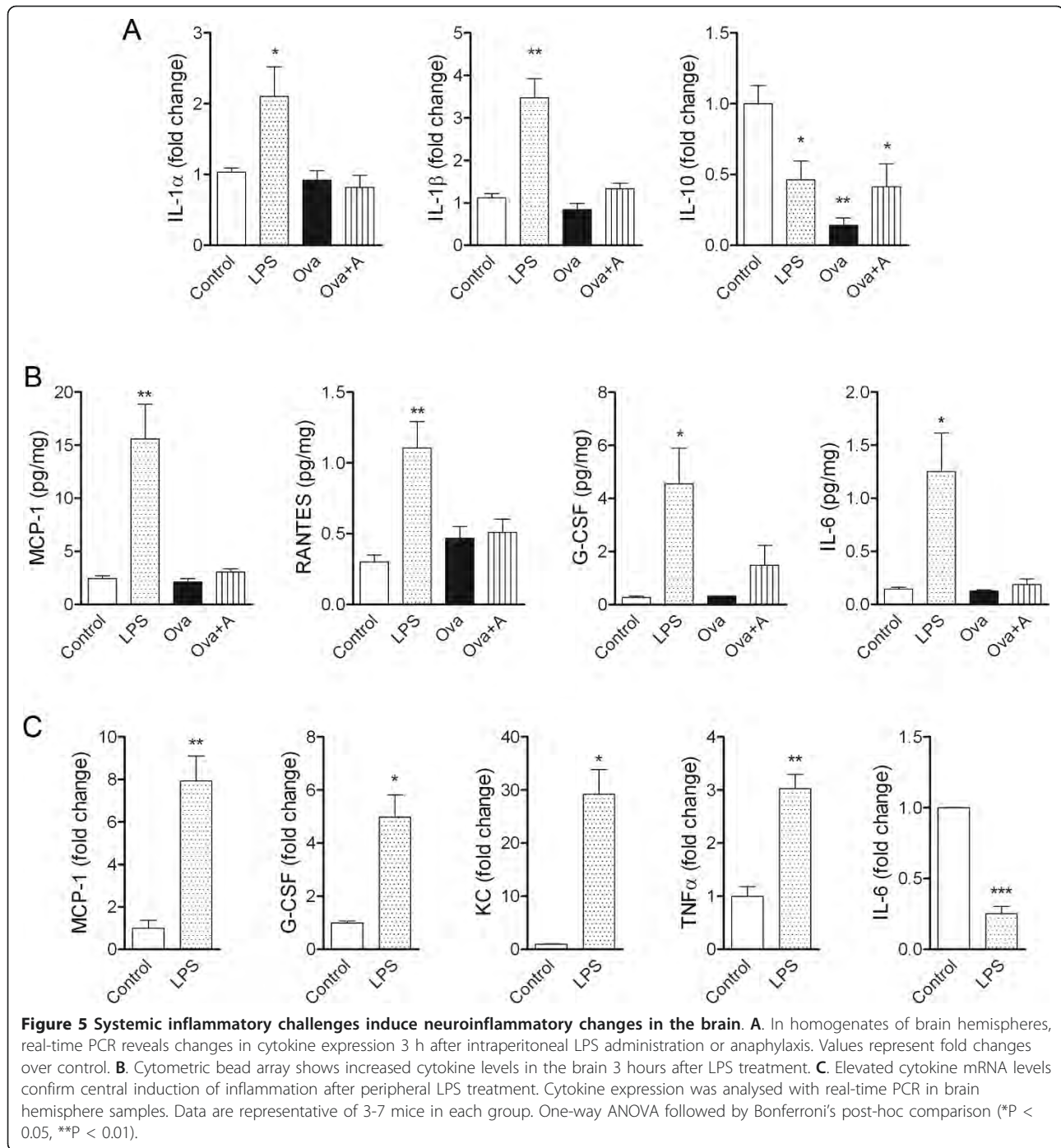
Here we present experimental evidence that two different systemic inflammatory conditions, endotoxin treatment and anaphylaxis markedly compromise survival, augment brain oedema, BBB damage and cerebrovascular inflammation after experimental cerebral ischaemia. We also show that this effect is not a direct consequence of increased ischaemic brain damage in the current model, and reduction of the infarct by hypothermia cannot fully prevent increased mortality (after both LPS and anaphylaxis) and oedema (after anaphylaxis). The key message of our study is that a number of complications associated with systemic inflammation in stroke patients may be in part caused by an elevated inflammatory burden and not only consequences of a large infarct in response to pre-existing inflammation or infection.

Our aim was to investigate the effect of two acute systemic inflammatory conditions, which involve fundamentally different mechanisms of induction, on brain injury and survival. LPS stimulates toll-like receptor 4 (TLR4), which results in the release of key proinflammatory cytokines from various cell types [21]. Elevated levels of IL-1 β ,



TNF α and IL-6 have been reported in the circulation, while IL-6 can also be detected in the cerebrospinal fluid (CSF) within 2-5 h after intraperitoneal LPS administration [15,22]. We found high levels of circulating inflammatory cytokines and elevated IL-1 β levels 3 h after LPS challenge, the time when MCAo was induced. It is likely that

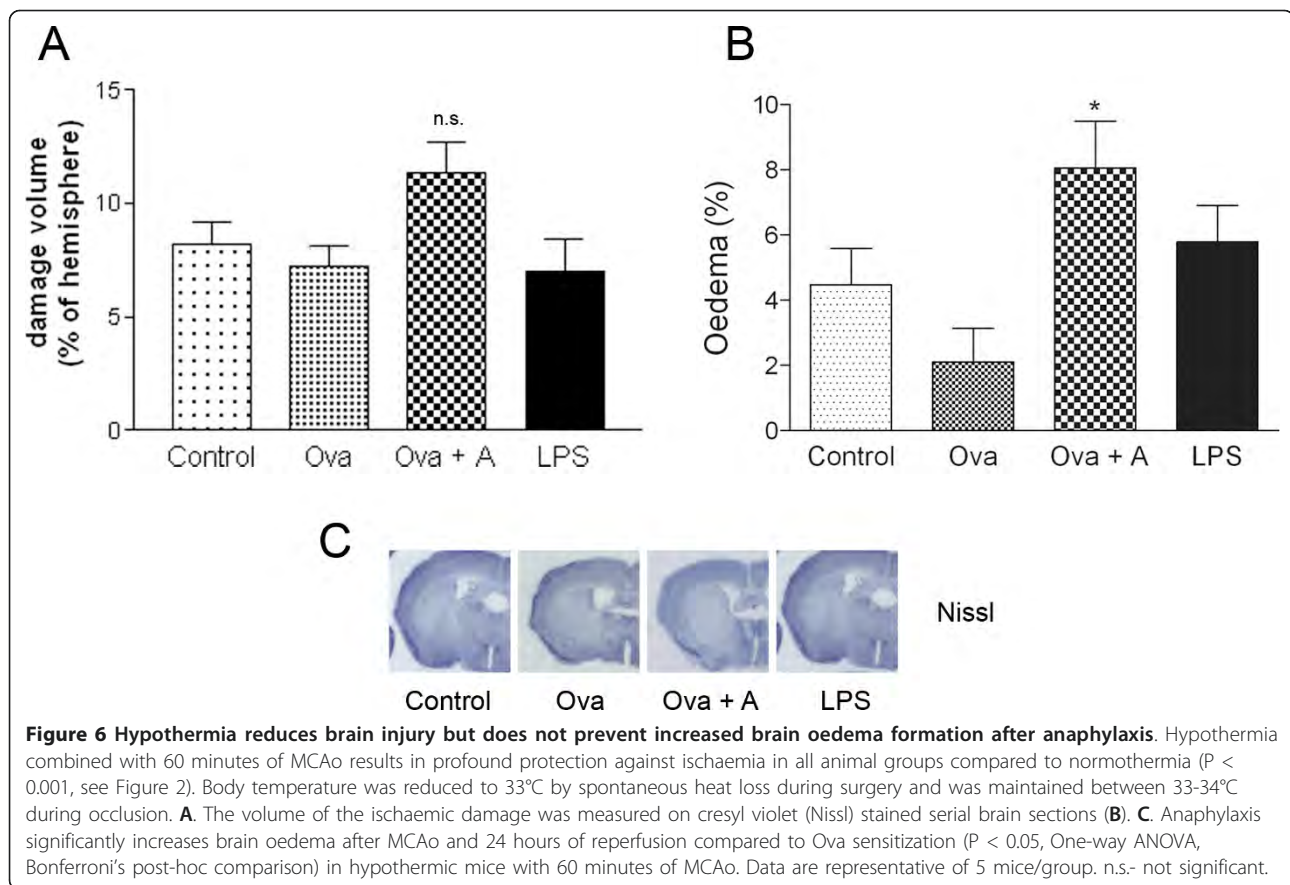
activation of TLR4 by host-derived ligands can also impact on stroke outcome as TLR4-deficient mice are protected against the ischaemic injury [23]. The classic pathway of systemic anaphylaxis is induced largely by activation of mast cells and results in the release of various vasoactive and inflammatory mediators, such as histamine and



platelet-activating factor [24]. In our study, successful activation of Ova-sensitized mast cells was also indicated by elevated levels of IL-10 [25]. Mast cells are early responders to stroke and are involved in the regulation of acute BBB changes after cerebral ischaemia [6]. Inhibition of mast cell function reduces brain oedema formation after intracerebral haemorrhage [26]. Therefore, our data show that the induction of systemic inflammation was successful

with two independent models, which are both relevant to ischaemic stroke.

It is generally difficult to evaluate the exact mechanisms whereby systemic inflammation affects ischaemic brain injury in experimental studies, because larger strokes are mostly associated with elevated levels of inflammation in the brain. The key finding of our study was the profound effect of systemic inflammatory challenges on survival and



brain inflammation after stroke, which took place independently of the increase in infarct size. Moreover, both conditions (LPS and anaphylaxis) increased BBB damage compared to control animals, which is likely to contribute to the formation of brain oedema. Peripherally administered LPS has minimal penetration across the murine blood-brain barrier [27] but LPS and circulating inflammatory mediators can induce central inflammatory actions through receptors expressed in the circumventricular organs [28,29]. Our data show that central inflammatory responses have been altered due to systemic LPS challenge and anaphylaxis prior to the induction of experimental stroke. Increased BBB damage, brain oedema and the induction of IL-1 α in the hypothalamus, thalamus and in perivascular macrophages/microglia after MCAo in response to LPS might be associated with direct effects of LPS on circumventricular organs or signals mediated by perivascular receptors of LPS and/or other inflammatory mediators. A previous study showed low mortality, but increased ischaemic- and BBB damage after MCAo and intraperitoneal LPS administration compared to MCAo alone [18]. However, in that study the time of LPS administration was 30 min, and not 3 h prior to MCAo as in our model, which may result in different systemic levels of

proinflammatory mediators by the time MCAo is performed. In contrast, intraperitoneal IL-1 β administration was found to increase mortality by 60% [18], which is strikingly similar to what we observed after LPS challenge.

Analysis of central cytokine changes indicated an altered inflammatory status in the brain after systemic inflammatory challenges. The induction of IL-1 α , IL-1 β , TNF α , MCP-1, RANTES, G-CSF, KC mRNA and increased MCP-1, RANTES, G-CSF protein levels in the brain after systemic LPS challenge are likely to result in a primed proinflammatory response by the time experimental stroke is induced. This, together with altered IL-10 mRNA levels after both anaphylaxis and LPS may partially explain elevated microglia-derived IL-1, increased brain oedema and BBB damage seen after MCAo. The downregulation of IL-6 mRNA and the increase in IL-6 protein levels 3 h after LPS administration are controversial and may indicate a complex and time-dependent regulation of central inflammatory responses at mRNA and peptide levels by systemic challenges.

To our knowledge, no studies have investigated the effect of anaphylaxis on experimental stroke so far. We show that anaphylaxis profoundly impaired survival in

the same time frame as LPS treatment did, in spite of the fundamentally different mechanisms of induction as outlined above. After anaphylaxis, we found upregulation of several proinflammatory cytokines, although high levels of circulating IL-10 were measured. IL-10 protects against brain injury [30,31], which may explain why we did not observe an increase in infarct volume after MCAo in these mice. In contrast, high numbers of IL-1 α -immunopositive and IL-1 β mRNA expressing cells and dilated blood vessels were seen in the brain after anaphylaxis and MCAo, which indicates that these changes were initiated in response to systemic inflammatory challenge. Anaphylaxis may exert its effects on brain inflammation through other inflammatory mediators than the cytokines examined. Although LPS increased proinflammatory cytokines several fold compared to anaphylactic challenge and initiated a more pronounced granulocyte response, IL-1 α -positive cells after endotoxin treatment were dominantly expressed in remote areas. However, our data show that both LPS and anaphylaxis result in the release of various vasoactive substances into the circulation, which can alter vascular permeability and therefore lead to oedema in central and peripheral tissues [32-35].

One possible explanation for not observing increased infarct volume in these studies may be the loss of the most serious cases prior to 24 h reperfusion, which could result in increased numbers of mice with smaller infarct after systemic inflammatory challenge. However, in our hands the current MCAo model did not result in maximal cortical damage in any of the treatment groups (Figure 2), which argues against this explanation. To further examine mechanisms whereby systemic inflammatory challenges affect brain injury, we also repeated MCAo and all treatments under hypothermic conditions. Although we found significant protection with respect to ischaemic brain damage by hypothermia in all groups, mice that underwent anaphylaxis and MCAo displayed increased brain oedema compared to controls. Hypothermia has been shown to exert neuroprotection and can markedly reduce infarct size in experimental rodent models [36,37]. However, our data indicate that at least in part, brain oedema may be directly affected by circulating inflammatory mediators and is not only a consequence of increased brain damage after stroke with systemic anaphylaxis. These results indicate the need for precise understanding of the effect of systemic inflammatory changes on oedema formation after stroke. Systemic inflammation is not only a predictor to worse outcome in stroke patients [2,3] but anaphylactoid reactions may occur in response to thrombolytic treatment in stroke patients taking an angiotensin-converting-enzyme inhibitor [38,39]. Cerebral ischaemia can also occur in patients after wasp sting anaphylaxis

[40,41] indicating that changes in blood coagulation may be involved in this process.

Taken together, these data demonstrate the involvement of acute systemic inflammation in increased mortality, BBB damage and brain oedema formation after experimental stroke. The fact that these changes are not necessarily linked to increased ischaemic brain damage indicate that appropriate management of stroke patient with various comorbidities in the future may require precise understanding of the interaction between peripheral inflammatory processes and cerebral ischaemia.

Acknowledgements

This work was supported by grants from the Hungarian Science Research Foundation (OTKA-NKTH K68574 to KJK), grant from Hungarian Ministry of Health and Welfare (ETT 300/2006 to KJK), and the Wellcome International Collaboration Award.

Author details

¹Laboratory of Molecular Neuroendocrinology, Institute of Experimental Medicine, Budapest, Hungary. ²Faculty of Life Sciences, University of Manchester, Manchester, M13 9PT, UK.

Authors' contributions

AD and KJK designed the studies. AD performed experiments, AD and SF performed measurements and analysed the data. AD and KJK wrote the paper. All authors read and approved the final manuscript.

Competing interests

The authors declare that they have no competing interests.

Received: 23 July 2011 Accepted: 24 November 2011

Published: 24 November 2011

References

1. Emsley HC, Hopkins SJ: **Acute ischaemic stroke and infection: recent and emerging concepts.** *Lancet Neurol* 2008, **7**:341-353.
2. McColl BW, Allan SM, Rothwell NJ: **Systemic infection, inflammation and acute ischemic stroke.** *Neuroscience* 2009, **158**:1049-1061.
3. Denes A, Thornton P, Rothwell NJ, Allan SM: **Inflammation and brain injury: Acute cerebral ischaemia, peripheral and central inflammation.** *Brain Behav Immun* 2009.
4. McColl BW, Rothwell NJ, Allan SM: **Systemic inflammation alters the kinetics of cerebrovascular tight junction disruption after experimental stroke in mice.** *J Neurosci* 2008, **28**:9451-9462.
5. Strbian D, Karjalainen-Lindsberg ML, Kovanen PT, Tatlisumak T, Lindsberg PJ: **Mast cell stabilization reduces hemorrhage formation and mortality after administration of thrombolytics in experimental ischemic stroke.** *Circulation* 2007, **116**:411-418.
6. Lindsberg PJ, Strbian D, Karjalainen-Lindsberg ML: **Mast cells as early responders in the regulation of acute blood-brain barrier changes after cerebral ischemia and hemorrhage.** *J Cereb Blood Flow Metab* 2007, **27**:689-702.
7. Juttler E, Schellinger PD, Aschoff A, Zweckberger K, Unterberg A, Hacke W: **Clinical review: Therapy for refractory intracranial hypertension in ischaemic stroke.** *Crit Care* 2007, **11**:231.
8. Wardlaw JM: **Neuroimaging in acute ischaemic stroke: insights into unanswered questions of pathophysiology.** *J Intern Med* 2007, **267**:172-190.
9. Teeling JL, Perry VH: **Systemic infection and inflammation in acute CNS injury and chronic neurodegeneration: underlying mechanisms.** *Neuroscience* 2009, **158**:1062-1073.
10. Agelaki S, Tsatsanis C, Gravanis A, Margioris AN: **Corticotropin-releasing hormone augments proinflammatory cytokine production from macrophages in vitro and in lipopolysaccharide-induced endotoxin shock in mice.** *Infect Immun* 2002, **70**:6068-6074.

11. Reynolds K, Novosad B, Hoffhines A, Gipson J, Johnson J, Peters J, Gonzalez F, Gimble J, Hill M: **Pretreatment with troglitazone decreases lethality during endotoxemia in mice.** *J Endotoxin Res* 2002, **8**:307-314.
12. Denes A, Ferenczi S, Halasz J, Kornyei Z, Kovacs KJ: **Role of CX3CR1 (fractalkine receptor) in brain damage and inflammation induced by focal cerebral ischemia in mouse.** *J Cereb Blood Flow Metab* 2008, **28**:1707-1721.
13. Denes A, Humphreys N, Lane TE, Grecnis R, Rothwell N: **Chronic systemic infection exacerbates ischemic brain damage via a CCL5 (regulated on activation, normal T-cell expressed and secreted)-mediated proinflammatory response in mice.** *J Neurosci* 2010, **30**:10086-10095.
14. Wieczorek M, Swiergiel AH, Pournajafi-Nazarloo H, Dunn AJ: **Physiological and behavioral responses to interleukin-1beta and LPS in vagotomized mice.** *Physiol Behav* 2005, **85**:500-511.
15. Kim YW, Kim KH, Ahn DK, Kim HS, Kim JY, Lee DC, Park SY: **Time-course changes of hormones and cytokines by lipopolysaccharide and its relation with anorexia.** *J Physiol Sci* 2007, **57**:159-165.
16. Peavy RD, Metcalfe DD: **Understanding the mechanisms of anaphylaxis.** *Curr Opin Allergy Clin Immunol* 2008, **8**:310-315.
17. Wierberton AD, Wright SH, Knight PA, Miller HR: **Anaphylactic release of mucosal mast cell granule proteases: role of serpins in the differential clearance of mouse mast cell proteases-1 and -2.** *J Immunol* 2006, **176**:899-904.
18. McColl BW, Rothwell NJ, Allan SM: **Systemic inflammatory stimulus potentiates the acute phase and CXC chemokine responses to experimental stroke and exacerbates brain damage via interleukin-1 and neutrophil-dependent mechanisms.** *J Neurosci* 2007, **27**:4403-4412.
19. Lazovic J, Basu A, Lin HW, Rothstein RP, Krady JK, Smith MB, Levison SW: **Neuroinflammation and both cytotoxic and vasogenic edema are reduced in interleukin-1 type 1 receptor-deficient mice conferring neuroprotection.** *Stroke* 2005, **36**:2226-2231.
20. Schielke GP, Yang GY, Shivers BD, Betz AL: **Reduced ischemic brain injury in interleukin-1 beta converting enzyme-deficient mice.** *J Cereb Blood Flow Metab* 1998, **18**:180-185.
21. Lu YC, Yeh WC, Ohashi PS: **LPS/TLR4 signal transduction pathway.** *Cytokine* 2008, **42**:145-151.
22. Wakahara K, Kobayashi H, Yagyu T, Matsuzaki H, Kondo T, Kurita N, Sekino H, Inagaki K, Suzuki M, Kanayama N, Terao T: **Bikunin suppresses lipopolysaccharide-induced lethality through down-regulation of tumor necrosis factor- alpha and interleukin-1 beta in macrophages.** *J Infect Dis* 2005, **191**:930-938.
23. Caso JR, Pradillo JM, Hurtado O, Lorenzo P, Moro MA, Lizasoain I: **Toll-like receptor 4 is involved in brain damage and inflammation after experimental stroke.** *Circulation* 2007, **115**:1599-1608.
24. Finkelman FD: **Anaphylaxis: lessons from mouse models.** *J Allergy Clin Immunol* 2007, **120**:506-515, quiz 516-507.
25. Hakim-Rad K, Metz M, Maurer M: **Mast cells: makers and breakers of allergic inflammation.** *Curr Opin Allergy Clin Immunol* 2009, **9**:427-430.
26. Strbian D, Tatlisumak T, Ramadan UA, Lindsberg PJ: **Mast cell blocking reduces brain edema and hematoma volume and improves outcome after experimental intracerebral hemorrhage.** *J Cereb Blood Flow Metab* 2007, **27**:795-802.
27. Banks WA, Robinson SM: **Minimal penetration of lipopolysaccharide across the murine blood-brain barrier.** *Brain Behav Immun* 2010, **24**:102-109.
28. Rivest S: **Molecular insights on the cerebral innate immune system.** *Brain Behav Immun* 2003, **17**:13-19.
29. Roth J, Harre EM, Rummel C, Gerstberger R, Hubschle T: **Signaling the brain in systemic inflammation: role of sensory circumventricular organs.** *Front Biosci* 2004, **9**:290-300.
30. Spera PA, Ellison JA, Feuerstein GZ, Barone FC: **IL-10 reduces rat brain injury following focal stroke.** *Neurosci Lett* 1998, **251**:189-192.
31. Liesz A, Suri-Payer E, Veltkamp C, Doerr H, Sommer C, Rivest S, Giese T, Veltkamp R: **Regulatory T cells are key cerebroprotective immunomodulators in acute experimental stroke.** *Nat Med* 2009, **15**:192-199.
32. Yamashita T, Kawashima S, Ohashi Y, Ozaki M, Ueyama T, Ishida T, Inoue N, Hirata K, Akita H, Yokoyama M: **Resistance to endotoxin shock in transgenic mice overexpressing endothelial nitric oxide synthase.** *Circulation* 2000, **101**:931-937.
33. Lee KS, Kim SR, Park SJ, Min KH, Lee KY, Choe YH, Park SY, Chai OH, Zhang X, Song CH, Lee YC: **Mast cells can mediate vascular permeability through regulation of the PI3K-HIF-1alpha-VEGF axis.** *Am J Respir Crit Care Med* 2008, **178**:787-797.
34. Czabanka M, Peter C, Martin E, Walther A: **Microcirculatory endothelial dysfunction during endotoxemia—insights into pathophysiology, pathologic mechanisms and clinical relevance.** *Curr Vasc Pharmacol* 2007, **5**:266-275.
35. Abbott NJ: **Inflammatory mediators and modulation of blood-brain barrier permeability.** *Cell Mol Neurobiol* 2000, **20**:131-147.
36. Burk J, Burggraf D, Vosko M, Dichgans M, Hamann GF: **Protection of cerebral microvasculature after moderate hyperthermia following experimental focal cerebral ischemia in mice.** *Brain Res* 2008, **1226**:248-255.
37. Ren Y, Hashimoto M, Pulsinelli WA, Nowak TS Jr: **Hypothermic protection in rat focal ischemia models: strain differences and relevance to "reperfusion injury".** *J Cereb Blood Flow Metab* 2004, **24**:42-53.
38. Hill MD, Barber PA, Takahashi J, Demchuk AM, Feasby TE, Buchan AM: **Anaphylactoid reactions and angioedema during alteplase treatment of acute ischemic stroke.** *Cmaj* 2000, **162**:1281-1284.
39. Rudolf J, Grond M, Prince WS, Schmulling S, Heiss WD: **Evidence of anaphylaxis after alteplase infusion.** *Stroke* 1999, **30**:1142-1143.
40. Riggs JE, Ketonen LM, Bodensteiner JB, Benesch CG: **Wasp sting-associated cerebral infarction: a role for cerebrovascular sympathetic innervation.** *Clin Neuropharmacol* 1993, **16**:362-365.
41. Riggs JE, Ketonen LM, Wymer JP, Barbano RL, Valanne LK, Bodensteiner JB: **Acute and delayed cerebral infarction after wasp sting anaphylaxis.** *Clin Neuropharmacol* 1994, **17**:384-388.

doi:10.1186/1742-2094-8-164

Cite this article as: Denes et al.: Systemic inflammatory challenges compromise survival after experimental stroke via augmenting brain inflammation, blood- brain barrier damage and brain oedema independently of infarct size. *Journal of Neuroinflammation* 2011 **8**:164.

Submit your next manuscript to BioMed Central and take full advantage of:

- Convenient online submission
- Thorough peer review
- No space constraints or color figure charges
- Immediate publication on acceptance
- Inclusion in PubMed, CAS, Scopus and Google Scholar
- Research which is freely available for redistribution

Submit your manuscript at
www.biomedcentral.com/submit



Streptococcus pneumoniae Worsens Cerebral Ischemia via Interleukin 1 and Platelet Glycoprotein Iba

Ádám Dénes, PhD,^{1,2} Jesus M. Pradillo, PhD,¹ Caroline Drake, PhD,¹
Andrew Sharp, PhD,³ Peter Warn, PhD,³ Katie N. Murray, MSc,¹
Bazaz Rohit, PhD,⁴ David H. Dockrell, PhD,⁴ Janet Chamberlain, PhD,⁴
Helen Casbolt, PhD,⁴ Sheila Francis, PhD,⁴ Bernadett Martinecz, MSc,²
Bernhard Nieswandt, PhD,⁵ Nancy J. Rothwell, PhD,¹ and Stuart M. Allan, PhD¹

Objective: Bacterial infection contributes to diverse noninfectious diseases and worsens outcome after stroke. *Streptococcus pneumoniae*, the most common infection in patients at risk of stroke, is a major cause of prolonged hospitalization and death of stroke patients, but how infection impacts clinical outcome is not known.

Methods: We induced sustained pulmonary infection by a human *S. pneumoniae* isolate in naive and comorbid rodents to investigate the effect of infection on vascular and inflammatory responses prior to and after cerebral ischemia.

Results: *S. pneumoniae* infection triggered atherogenesis, led to systemic induction of interleukin (IL) 1, and profoundly exacerbated (50–90%) ischemic brain injury in rats and mice, a response that was more severe in combination with old age and atherosclerosis. Systemic blockade of IL-1 with IL-1 receptor antagonist (IL-1Ra) fully reversed infection-induced exacerbation of brain injury and functional impairment caused by cerebral ischemia. We show that infection-induced systemic inflammation mediates its effects via increasing platelet activation and microvascular coagulation in the brain after cerebral ischemia, as confirmed by reduced brain injury in response to blockade of platelet glycoprotein (GP) Iba. IL-1 and platelet-mediated signals converge on microglia, as both IL-1Ra and GPIba blockade reversed the production of IL-1a by microglia in response to cerebral ischemia in infected animals.

Interpretation: *S. pneumoniae* infection augments atherosclerosis and exacerbates ischemic brain injury via IL-1 and platelet-mediated systemic inflammation. These mechanisms may contribute to diverse cardio- and cerebrovascular pathologies in humans.

ANN NEUROL 2014;75:670–683

Community-acquired pneumonia is a common condition that leads to prolonged hospitalization, impaired clinical outcome, and increased mortality of patients, especially those with compromised immunity, such as children, the elderly, and those with immune suppression as a result of disease or injury.^{1,2} The gram-positive bacterium *Streptococcus pneumoniae* is a major human pathogen, and the most common cause of bacterial community-acquired pneumonia.³

Infection also contributes to the development of cardio- and cerebrovascular diseases and is associated with poor outcomes after heart disease and stroke.^{4–8} *S. pneumoniae* infection could contribute to stroke or cardioembolism by triggering the rupture of an atherosclerotic plaque in humans,^{7–10} and molecular signatures of common bacteria, including *Streptococcus* species, have been identified in atherosclerotic lesions.^{11,12} Vaccination

View this article online at wileyonlinelibrary.com. DOI: 10.1002/ana.24146

Received Oct 7, 2013, and in revised form Mar 17, 2014. Accepted for publication Mar 17, 2014.

Address correspondence to Dr Dénes, Faculty of Life Sciences, University of Manchester, AV Hill Building, Oxford Road, Manchester, M13 9PT, United Kingdom. E-mail: denesa@koki.hu

From the ¹Faculty of Life Sciences, University of Manchester, Manchester, United Kingdom; ²Laboratory of Molecular Neuroendocrinology, Institute of Experimental Medicine, Budapest, Hungary; ³Manchester Academic Health Science Centre, National Institute for Health Research Translational Research Facility in Respiratory Medicine, University of Manchester, University Hospital of South Manchester National Health Service Foundation Trust, Manchester, United Kingdom; ⁴Department of Cardiovascular Science, Medical School, University of Sheffield, Sheffield, United Kingdom; ⁵Department of Vascular Medicine, University Hospital and Rudolf Virchow Center for Experimental Biomedicine, University of Würzburg, Würzburg, Germany.

against *S. pneumoniae* reduces atherosclerosis; however, the effect of *S. pneumoniae* infection on atherogenesis has not been demonstrated experimentally.

Infection is a key risk factor for stroke in young patients,⁵ a cohort without any atherosclerotic burden, suggesting that infection could contribute to an ischemic event independently of inducing plaque rupture. Clinical data indicate that *S. pneumoniae*, together with other common infections such as *Chlamydia pneumoniae* and *Haemophilus influenzae*, also contributes to impaired outcome, prolonged hospitalization, and death after stroke.⁵ Experimental stroke in mice propagates pneumonia.^{13,14} However, it is not known if sustained bacterial infections preceding an acute cerebrovascular event could trigger stroke or contribute to increased stroke pathophysiology. Therefore, the main hypothesis tested in the study was whether preceding infection by a clinically highly relevant bacterial strain, *S. pneumoniae*, induces systemic vascular inflammation and worsens stroke outcome and whether this occurs via inflammatory mechanisms that could be blocked therapeutically.

Here we demonstrate that *S. pneumoniae* infection promotes atherogenesis, and exacerbates inflammatory responses to cerebral ischemia, leading to increased brain injury via platelets and interleukin (IL) 1. Thus, we suggest that complications after acute vascular events is preceded by a rapid systemic inflammatory response and excessive coagulation induced by pre-existing infection that profoundly impairs outcome. This could be prevented by treatment with IL-1 receptor antagonist (IL-1Ra).

Materials and Methods

Animals

Experiments were carried out in adult male wild-type (WT; C57BL/6J; Harlan-Olac, Blackthorn, UK) and ApoE^{-/-} (JAX 2052; Jackson Laboratory, Bar Harbor, ME) mice, aged 12 to 20 weeks. Male Wistar rats were 8 weeks old (250–300g). Aged (15 months) lean and (JCR:LA-cp; *cp/cp*) corpulent rats, which are obese, atherosclerotic, and insulin resistant,¹⁵ were also used. Animals were allowed free access to food and water and maintained under temperature-, humidity-, and light-controlled conditions. All animal procedures adhered to the UK Animals (Scientific Procedures) Act (1986), and experiments were performed in accordance with STAIR and ARRIVE guidelines.

Infection with *S. pneumoniae*

A protocol for doses and timing of *S. pneumoniae* (American Type Culture Collection [ATCC] 49619, capsular serotype 19F [Danish]) challenge was established to allow low-grade, indolent pulmonary exposure to *S. pneumoniae* infection that is sustained in animals for a period of 6 to 7 days. Animals were lightly anesthetized with 2.5% isoflurane, and *S. pneumoniae* or phosphate-buffered saline (PBS; mock infection, 50 μ l, pH 7.4)

was slowly pipetted onto the nostrils to allow subsequent dissemination throughout the lungs. An ascending infectious challenge was used on day 0 (2×10^8 cfu/ml), day 2 (4×10^8 cfu/ml), and day 5 (8×10^8 cfu/ml). Mild piloerection and slightly increased respiration rate were observed after infection in 30% of the animals, but none of the infected mice showed any neurological symptoms, including signs of meningitis, intracranial hemorrhage, or visible neuronal injury in the absence of experimental stroke. Animals showing signs of more severe infection, such as markedly reduced activity, weight loss, or a hunched appearance were excluded from further experiments (3 mice, 0 rats). Blood pH, pCO₂, pO₂, and O₂ saturation were analyzed with a 248 Blood Gas Analyser (Siemens Healthcare Diagnostics, Surrey, UK).

Middle Cerebral Artery Occlusion

Middle cerebral artery occlusion (MCAo) was performed using the intraluminal filament technique as described earlier¹⁶ on mice infected with *S. pneumoniae* and age/weight-matched controls weighing 25 to 30g. In brief, animals were anesthetized with isoflurane and a silicone-coated monofilament (210 μ m tip diameter; Docol, Redlands, CA) was introduced into the left external carotid artery and advanced along the internal carotid artery to occlude the MCA for 30 minutes. Occlusion was confirmed by a laser Doppler (Moor Instruments, Axminster, UK). During surgery, core temperature was maintained at $37 \pm 0.5^\circ\text{C}$. Due to the large size and multiple comorbidities of corpulent rats, a distal MCAo model was used in all rat experiments to avoid extensive tissue dissection and mortality. Rats were anesthetized with isoflurane and subjected to cerebral ischemia by transient occlusion of the distal MCA for 60 minutes using a 10-0 suture as described earlier.¹⁷ After experimental stroke, 3 mice and 2 rats were excluded pre hoc due to improper occlusion of the MCA (n = 2) and surgical artifacts (n = 3).

Experimental Design

To investigate whether *S. pneumoniae* infection contributes to atherogenesis or vascular inflammation in different vascular beds, ApoE^{-/-} and C57BL/6J mice aged 12 weeks were fed either an atherogenic Paigen diet (18.5% fat, 0.9% cholesterol, 0.5% cholate, 0.26% sodium; Special Diet Services, Witham, UK) or a normal chow diet (4.3% fat, 0.02% cholesterol; Special Diet Services) for 8 weeks prior to mock infection or infection with *S. pneumoniae* (8 experimental groups). Corpulent rats that spontaneously develop atherosclerosis as they age¹⁵ were fed a chow diet throughout. Mice and rats were sacrificed 6 or 7 days after the first infection, respectively.

For the experiments investigating how *S. pneumoniae* infection preceding experimental stroke influences outcome, all animals were fed a chow diet. Naive male C57BL/6J mice aged 14 to 16 weeks were infected with *S. pneumoniae* on day 0, day 2, and day 5 followed by 30 minutes of MCAo¹⁶ on day 6 and 4 hours or 24 hours of reperfusion. In separate experiments, mice were treated intraperitoneally with a single bolus of recombinant IL-1Ra (100mg/kg; Biovitrium, Stockholm, Sweden) or placebo

(0.5% bovine serum albumin in PBS, pH 7.4). To block platelet adhesion through glycoprotein (GP) Ib α , mice received 100 μ g anti-GPIb α Fab (p0p/B),¹⁸ or control immunoglobulin (Ig) G intravenously. IL-1Ra or anti-GPIb α was administered 1 hour after 30-minute MCAo, and mice were euthanized at 24-hour reperfusion.

Aged lean and (JCR:LA-cp; cp/cp) corpulent rats or young Wistar rats were mock infected/infected with *S. pneumoniae* on day 0, day 2, and day 5 followed by 60 minutes of transient distal MCAo¹⁷ on day 7 and 24 hours of reperfusion. A group of Wistar rats received a single dose of IL-1Ra (100mg/kg) or placebo subcutaneously at 1 hour of reperfusion.

Tissue Processing

Under terminal anesthesia, blood was taken from the heart using 3.8% sodium citrate (1:10) as an anticoagulant. Animals were then perfused transcardially with saline followed by paraformaldehyde (PFA; 4% in PBS; Sigma-Aldrich, Dorset, UK). Brains were postfixed in 4% PFA at 4°C for 24 hours, and cryoprotected in sucrose/PBS. Coronal brain sections (20 μ m thick for mice and 30 μ m thick for rats) were cut on a sledge microtome (Bright series 8000; Bright Instruments, Huntingdon, UK). For cytokine measurement, saline-perfused brain, lung, spleen, and liver samples were homogenized, and processed as described earlier.¹⁹ Except for the lungs, *S. Pneumoniae* was not recovered from any other tissues examined, as expected in the case of the ATCC 49619 strain.

Measurement of Infarct Volume and Blood-Brain Barrier Damage

The volume of ischemic and blood-brain barrier (BBB) damage was measured as described previously and corrected for edema.¹⁶ Leakage of plasma-derived IgG (BBB damage) was detected with biotinylated horse antimouse IgG (1:500; Vector Laboratories, Burlingame, CA) followed by incubation with ABC solution (1:500; Vector), and the color was developed by diaminobenzidine tetrahydrochloride (DAB).

Analysis of Functional and Behavioral Outcome

Neurological status in mice was assessed according to a neurological grading score of increasing severity of deficit²⁰: 0, no observable deficit; 1, torso flexion to right; 2, spontaneous circling to right; 3, leaning/falling to right; 4, no spontaneous movement. In rats an additive neurobehavioral scoring system was used as described earlier²¹: body position (completely flat, 0 to upright position, 4); spontaneous activity (none, 0 to repeated vigorous movement, 3); transfer arousal (coma, 0 to extremely excited, 5); gait (absolute incapacity, 0 to normal, 3); touch escape (none, 0 to extremely vigorous, 3), and positional passivity (no struggle when held, 0 to maximal struggle, 4).

Cytokine Measurement

Sample processing and protein determination were performed as described previously.¹⁹ In mice, plasma samples and saline-perfused brain, liver, spleen, and lung homogenates were measured for tumor necrosis factor (TNF) α , RANTES, chemokine

(C-C motif) ligand 2, chemokine (C-X-C motif) ligand 1 (CXCL1), IL-6, IL-1 β , IL-1 α , IL-17 α , interferon γ , granulocyte colony-stimulating factor (G-CSF), and IL-10 using CBA Flex Sets (BD Biosciences, Oxford, UK) according to the manufacturers protocol, with FACSArray and LRSII flow cytometers (BD Biosciences). Rat cytokines IL-1 β , IL-6, CXCL1, and TNF α in plasma, liver, spleen, and lung were measured with DuoSet ELISA kits (R&D Systems, Abingdon, UK).

Flow Cytometry

Following Fc receptor blockade (antimouse CD16/CD32, clone 93; eBioscience, Hatfield, UK), cells were stained with cocktails of selected antibodies: T cells (CD4-FITC, CD8-PE, CD3-APC, CD45-PerCP-Cy5.5), B cells/dendritic cells (CD19-FITC, CD11c-PE, MHCII-APC \pm CD45-PerCP-Cy5.5), B cells/granulocytes (CD19-FITC, Ly6G-PE, MHCII-APC, Ly6c-PerCP-Cy5.5), granulocytes/monocytes (CD11b-FITC, Ly6G-PE, Ly6c-PerCP-Cy5.5, CD115-APC), and platelets (CD61-FITC, CD42d-PE, CD62P-APC). Antibodies were purchased from eBioscience except for Ly6g-PE (1A8; BD Biosciences, Oxford, UK). Cells were acquired on an LSRII flow cytometer (BD Biosciences, Franklin Lake, NJ), and data were analyzed using FACS Diva software (BD Biosciences, Franklin Lake, NJ).

Immunohistochemistry and Immunofluorescence

Immunostaining was performed as described earlier.¹⁶ For immunohistochemistry, goat antimouse vascular cell adhesion molecule (VCAM) 1 (1:250; R&D Systems) and rabbit anti-Iba1 (1:1,000; Wako Chemicals, Neuss, Germany) primary antibodies were used, and the staining was developed with nickel DAB. For immunofluorescence, appropriate mixtures of rat antimouse CD45 (1:200; AbD Serotec, Oxford, UK), goat antimouse VCAM-1 (1:250; R&D Systems), rabbit anti-Iba1 (1:1,000; Wako Chemicals), goat anti-IL-1 α (1:100; R&D Systems), or rat anti-CD41 (1:100; BD Biosciences, Oxford, UK) antibodies were used followed by the adequate fluorochrome-conjugated Alexa 594 or Alexa 488 donkey antisera (1:500; Invitrogen, Paisley, UK). Biotinylated tomato lectin (10 μ g/ml, Sigma-Aldrich) was visualized with streptavidin-Alexa 350 conjugate (Invitrogen). VCAM-positive blood vessels were counted in 3 random fields of view for each serial section (typically 8–10) in the cerebral cortex. Activated microglia were counted in the striatum, cerebral cortex, and hippocampus on 10 serial sections rostrocaudally (3–4 fields per section). CD45-positive cells were counted in the caudal lateral ventricle on 5 serial sections (starting at -1.58 mm from Bregma). The ventricular ependyma was visualized by using VCAM immunofluorescence. Images were viewed on an Olympus (Tokyo, Japan) BX51 upright microscope using $\times 4$, $\times 10$, $\times 40$, and $\times 60$ objectives and captured using a Cool-snap ES camera (Photometrics, Tucson, AZ, USA) with Meta-Vue Software (Molecular Devices, Warriner, UK). Images were processed and figures assembled in Adobe (San Jose, CA) Photoshop CS6. Except for mild changes to brightness and contrast applied uniformly across experimental groups, no other modifications to digital images has been made.

Staining of Aortae

Oil Red O staining was performed as described earlier.²² Plaque density was calculated on Oil Red O–stained en face preparations of the aorta by light microscopy/image capture analysis to determine the percentage lesion of the total area of the aorta. For E-selectin staining, antigen retrieval was performed followed by incubation with E-selectin antibody (1:25; Abcam, Cambridge, UK), secondary biotinylated antibody (1:200), and ABC / DAB for detection.

Quantitative Analysis and Statistics

Animals were randomized for the experiments by GraphPad Random Number Generator (<http://graphpad.com/quickcalcs/randomN1.cfm>). All quantitative analysis was performed under blinded conditions. Group sizes were determined by power calculation using DSS Research (<https://www.dssresearch.com/>) and Stattol.net (http://www.stattol.net/SSizAOV_Pgm.php) online resources, and based on results from previous studies using the MCAo model in mice or rats with identical age, gender, and genetic background (5% confidence level, 80% power, and an estimated 20–40% standard deviation, resulting in $n = 5–8$ for most experiments). Statistical power was also assessed in individual experiments with *S. pneumoniae*. Data were analyzed with Student *t* test (comparing 2 experimental groups, Prism 6.0; GraphPad, La Jolla, CA), and 1-way or 2-way analysis of variance (ANOVA), followed by Tukey and Bonferroni post hoc comparison, respectively (comparing ≥ 3 groups, Prism 6.0), or 3-way ANOVA followed by Scheffe post hoc test (comparing 8 groups, 3 variables; Fig 1D, F; analyzed with StatView; SAS Institute, Cary, NC). Neurological scores were analyzed with nonparametric *t* test (Mann–Whitney test, 2 groups), or Kruskal–Wallis test followed by Dunn multiple comparison (4 experimental groups). $p < 0.05$ was considered statistically significant.

Results

S. Pneumoniae Infection Induces Systemic Inflammation, Accelerates Atherosclerosis, and Results in Cerebrovascular Inflammation

As atherosclerosis is the main risk factor for thromboembolism, and clinical data indicate an increased risk of thrombotic events in patients with pneumonia,^{7–10} we infected C57BL/6J and ApoE^{−/−} mice fed a chow or a high-fat (Paigen) diet with increasing doses of a human isolate, *S. pneumoniae* ATCC 49619, to mimic sustained bacterial infection, and investigated cardio- and cerebrovascular responses. Infection caused a >2-fold increase in the number of aortic plaques within 6 days in high fat-fed WT mice, but had no additional effect on aortic plaque formation in ApoE^{−/−} mice, which already showed advanced aortic plaques after 8 weeks of Paigen diet, as also observed in our earlier studies (see Fig 1).^{22,23} The atherogenic effect of infection was also confirmed in aged, obese, and atherosclerotic corpulent rats based on increased E-selectin expression by the aortic endothelium.

Analysis of peripheral cytokines showed elevated circulating IL-1 α and IL-17 levels and increased IL-6 production in the spleen in response to infection in mice. Atherogenic diet also increased plasma IL-1 α , but no additive effect of infection was observed.

Next, we investigated whether infection caused cerebrovascular inflammation. VCAM levels on the cerebrovascular endothelium increased significantly in response to infection, whereas atherogenic diet caused vascular activation only in ApoE^{−/−} mice, as we reported earlier (see Fig 1).^{22,23} There was no synergistic effect between diet and infection. Microglial CD11b levels were elevated in WT mice in response to infection, but the number of Iba1⁺ microglia was not altered. We reported earlier that atherogenic diet induces leukocyte accumulation in the choroid plexus that is most apparent in atherosclerosis-prone ApoE^{−/−} mice.²² *S. pneumoniae* infection significantly reduced (by 40%) diet-induced accumulation of CD45⁺ cells in the lateral ventricle, indicating that infection-induced systemic responses modify inflammatory changes in the brain. No acute cardio- or cerebrovascular events were observed in mice or rats during the course of infection.

Preceding *S. Pneumoniae* Infection Exacerbates Brain Injury and Potentiates BBB Breakdown in Association with Age and Comorbidities

Sustained *S. pneumoniae* infection in young, healthy C57BL/6J mice prior to experimental stroke resulted in a significant (60%) exacerbation of brain injury induced by cerebral ischemia and markedly impaired neurological outcome 24 hours after reperfusion (Fig 2). Infected mice showed a trend for reduced O₂ saturation and had significantly reduced pO₂ levels in the blood before experimental stroke compared to uninfected mice, as expected in animals with pneumonia, similarly to patients with community- or hospital-acquired pneumonia.²⁴

To investigate the effect of *S. pneumoniae* infection on stroke outcome in a comorbid rodent model, we infected aged lean and corpulent (obese and atherosclerotic) rats prior to MCAo. Infection significantly exacerbated brain injury in both lean (by 55%) and corpulent (by 90%) rats (see Fig 2). Aged, infected rats had markedly increased BBB injury as identified by parenchymal infiltration of plasma-derived IgG. Corpulent rats displayed significantly higher (by 40%) BBB breakdown in response to infection compared to lean rats. Infection worsened both behavioral outcome and sensory–motor functions after experimental stroke, which paralleled increased granulocyte recruitment in the ischemic hemisphere (Fig 3). Splenic IL-1 α and IL-6 levels were increased after infection in corpulent, but not lean rats,

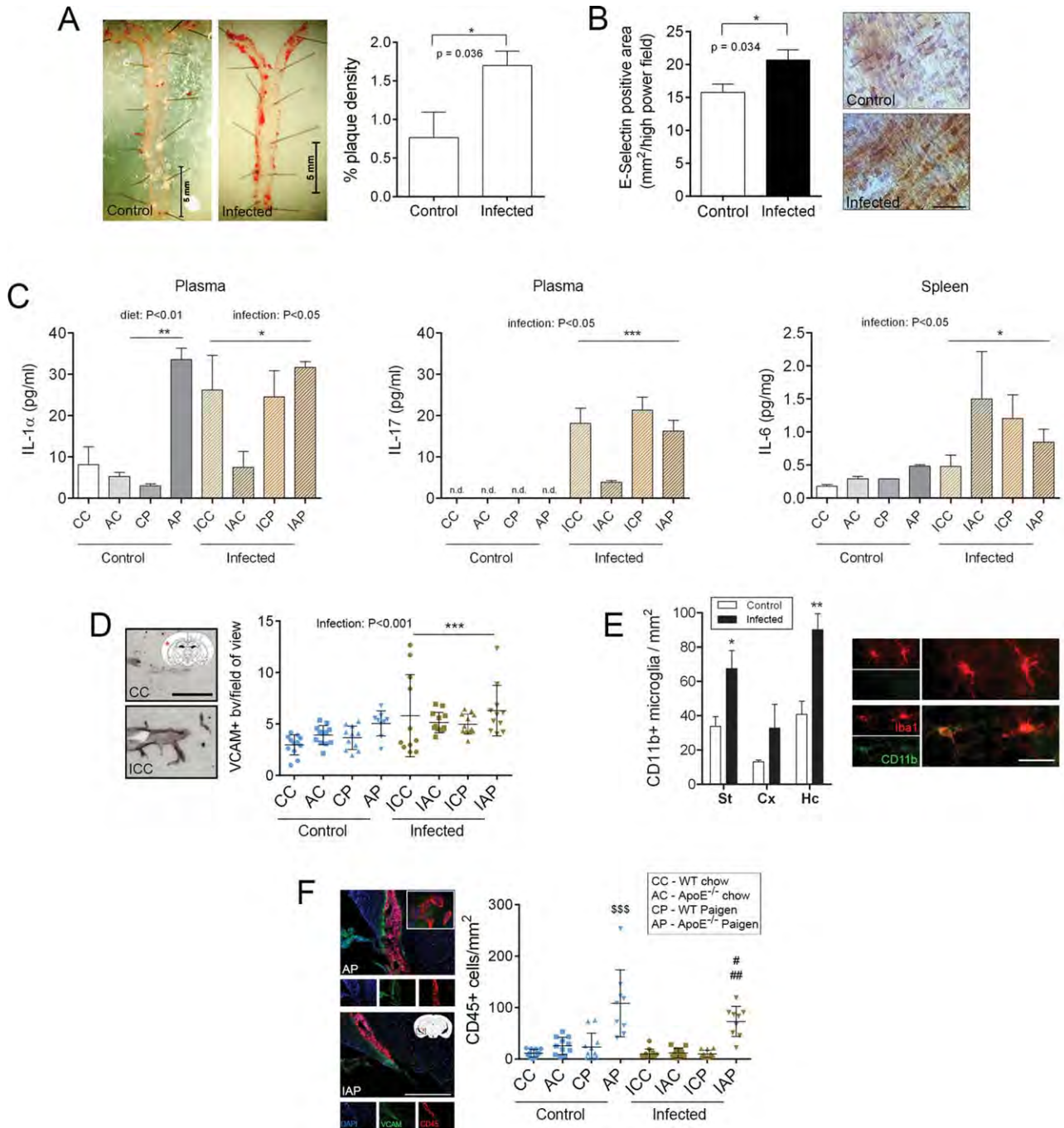


FIGURE 1: *Streptococcus pneumoniae* infection facilitates aortic plaque formation and results in cerebrovascular inflammation. (A) Aortic plaque number was assessed by en face Oil Red O staining of whole aortae in wild-type (WT) mice after 6 days of infection with *S. pneumoniae* (n = 4–5). (B) Pulmonary *S. pneumoniae* infection increases aortic E-selectin expression in obese and atherosclerotic corpulent rats. (C) Cytokine levels shown in the blood and the spleen after infection (n = 6–12). (D) Vascular cell adhesion molecule (VCAM) immunohistochemistry reveals increased cerebrovascular activation in response to pulmonary *S. pneumoniae* infection (n = 9–12). (E) Microglia display higher CD11b levels in the brain after infection as assessed in the striatum (St), cerebral cortex (Cx), and hippocampus (Hc; n = 5). (F) Diet-induced accumulation of CD45-positive leukocytes in the caudal lateral ventricle is reduced in ApoE^{-/-} mice in response to infection. \$\$\$p < 0.001 vs CC, AC, CP, ICC, IAC, and ICP; #p < 0.05 vs CC, AC, and CP; ##p < 0.01 vs ICC, IAC, and ICP; *p < 0.05, **p < 0.01, ***p < 0.001. Location of pictures in D and F is shown on the schematic with red asterisks. AC = uninfected ApoE^{-/-} mice on chow diet; AP = uninfected ApoE^{-/-} mice on Paigen diet; bv = blood vessels; CC = uninfected WT mice on chow diet; CP = uninfected WT mice on Paigen diet; DAPI = 4',6-diamidino-2-phenylindole; IAC = infected ApoE^{-/-} mice on chow diet; IAP = infected ApoE^{-/-} mice on Paigen diet; ICC = infected WT mice on chow diet; ICP = infected WT mice on Paigen diet; IL = interleukin; n.d. = not detectable. Scale bars: A, 5mm; B, 25 μ m; D, E, 50 μ m; F, 200 μ m.

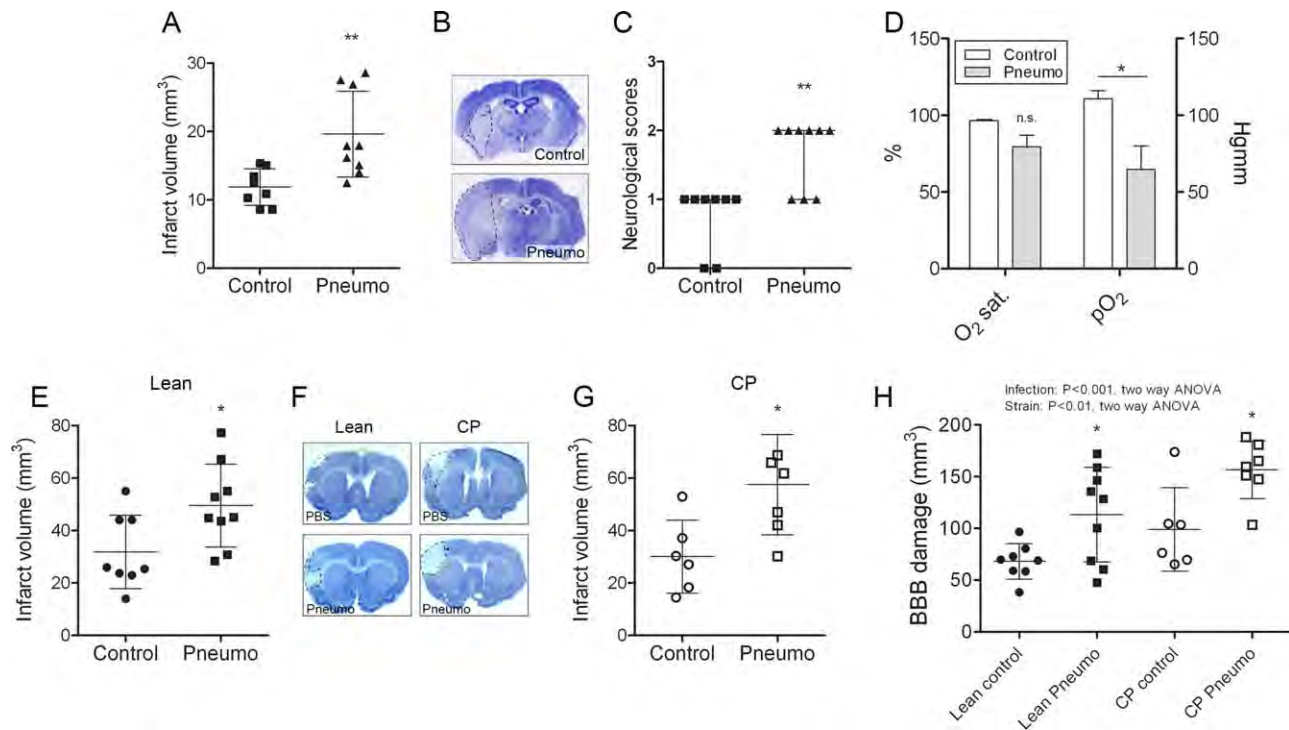


FIGURE 2: *Streptococcus pneumoniae* infection worsens brain injury after experimental stroke and induces granulocytosis. (A) Mice were infected with increasing challenges of *S. pneumoniae* over 6 days prior to middle cerebral artery occlusion (MCAo) that leads to an exacerbation of brain injury 24 hours after cerebral ischemia. (B) Cresyl violet (Nissl) staining shows the infarct (dashed lines) in representative animals 24 hours after MCAo. (C) Neurological deficit is significantly impaired 24 hours after cerebral ischemia in infected mice. (D) pO_2 levels are lower in infected mice prior to MCAo. (E–G) Ischemic brain injury is exacerbated in response to infection in aged lean (E) and corpulent (CP) rats (G). Brain injury is shown 24 hours after MCAo as identified on cresyl violet–stained (Nissl; F) brain sections. (H) Infection prior to stroke augments blood–brain barrier (BBB) injury that is more serious in corpulent rats. A–G, unpaired *t* test; H, two-way analysis of variance (ANOVA); * $p < 0.05$, ** $p < 0.01$; $n = 8–9$ mice, $n = 7–9$ rats. n.s. = not significant; PBS = phosphate-buffered saline. [Color figure can be viewed in the online issue, which is available at www.annalsofneurology.org.]

indicating that animals with chronic vascular disease develop an exaggerated systemic inflammatory response to *S. pneumoniae* after cerebral ischemia.

***S. Pneumoniae* Infection Causes Granulocytosis and IL-1–Mediated Systemic Inflammatory Response**

Infected mice had elevated circulating granulocytes prior to experimental stroke, which was associated with reduced B-cell numbers in the blood (Fig 4). Bone marrow granulocyte levels were also elevated, indicating that although the infection is localized to the lung, infection-induced systemic inflammatory responses involve increased granulopoiesis in the bone marrow and release of granulocytes into the circulation. In addition to innate immune mechanisms, T cells play a role in defense against *S. pneumoniae* infection.^{25–27} However, we found that infected mice had reduced CD8⁺ T cells in the blood prior to cerebral ischemia.

Next, we investigated cytokine changes in the blood and in peripheral organs after infection and cerebral ischemia. *S. pneumoniae* infection led to a 30- to 80-fold elevation in IL-1 α and IL-1 β levels in the lung, where the

infection was localized, 4 hours after MCAo, paralleled by an increase in G-CSF, IL-6, and TNF α levels (20–30-fold, Fig 5A). RANTES and TNF α levels were increased in the liver in response to infection; IL-1 α , IL-1 β , G-CSF, peaked 4 hours after cerebral ischemia (see Fig 5B) in infected animals. No cytokine changes were detected in the spleen between control and infected mice (not shown).

In infected mice, experimental stroke led to 2.5-fold higher levels of MCP-1 and 5-fold higher levels of KC in the brain compared to controls (see Fig 5C), two key chemokines responsible for the recruitment of monocytes and granulocytes to the brain.^{28,29}

***S. Pneumoniae* Infection-Induced Brain Injury is IL-1 Dependent**

In mice, blocking IL-1 actions by IL-1Ra fully reversed the increase in ischemic brain injury induced by infection and restored impairment in sensory–motor performance (Fig 6). Infection induced a 3-fold increase in BBB injury, which was reduced by 40% after IL-1Ra treatment. We have reported previously that chronic infection preceding stroke increases granulocyte numbers in the spleen, and

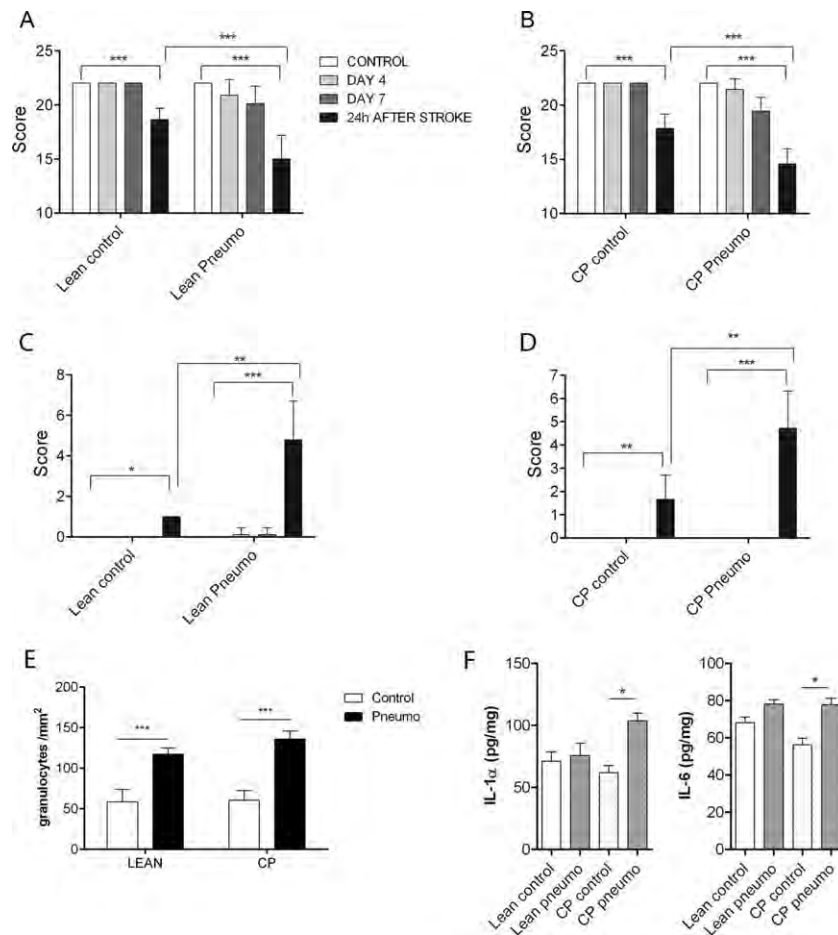


FIGURE 3: *Streptococcus pneumoniae* infection impairs functional outcome in aged rats in synergy with comorbidities following cerebral ischemia. (A–D) Behavioral (A, B) and sensory–motor (C, D) outcome was assessed in infected (Pneumo) and uninfected (control), 16-month-old lean rats (A, C) and obese, atherosclerotic corpulent (CP) rats (B, D) 24 hours after cerebral ischemia. (E) Increased numbers of granulocytes were found in the ipsilateral hemisphere in infected rats 24 hours after middle cerebral artery occlusion (as assessed by immunostaining with an antigranulocyte serum, SJC4). (F) Interleukin (IL) 1 α and IL-6 levels were measured by enzyme-linked immunosorbent assay in spleen homogenates. Two-way analysis of variance followed by Bonferroni post hoc comparison, * $p < 0.05$, ** $p < 0.01$, *** $p < 0.001$; $n = 7–9$.

that granulocytes contribute to ischemic injury and BBB breakdown mediated by systemic inflammation.^{16,30} IL-1Ra significantly reduced granulocyte numbers in the spleen (by >50%) and had similar effects on CD4⁺ T cells in the bone marrow, irrespective of infection status.

Similarly to mice, Wistar rats displayed significantly elevated IL-1 β levels (2-fold) in the liver in response to infection, confirming the development of a systemic inflammatory response (see Fig 6). Infection significantly (by 40%) increased brain injury induced by cerebral ischemia. IL-1Ra administration fully reversed the infection-induced increase in brain injury and BBB breakdown after cerebral ischemia, suggesting that impaired outcome after stroke in response to *S. pneumoniae* is IL-1 dependent in both rodent models. IL-1Ra treatment after cerebral ischemia also reversed brain edema in infected rats, improved behavioral outcome, and rescued motor performance.

***S. Pneumoniae* Infection Drives Brain Injury Via Platelet-Dependent Inflammatory Responses**

As infection could facilitate coagulatory processes,⁵ we examined platelet aggregation in the brain. We found an increased number of platelet aggregates in the area of the infarct in infected mice after experimental stroke, and this was also confirmed in the ipsilateral hemisphere of both aged lean and corpulent rats in response to infection (Fig 7). Platelet accumulation was observed mostly in small cerebral arteries, resulting in partial or complete coverage of the vascular lumen, and was not affected by IL-1Ra. Flow cytometric analysis confirmed increased platelet activation in infected mice prior to MCAo as identified by higher levels of P-selectin (CD62P) on CD42d/CD61-positive circulating platelets. Blockade of platelet GPIIb/IIIa (using a specific Fab fragment, which does not induce depletion of platelets¹⁸) significantly reduced infarct size and BBB injury, and improved

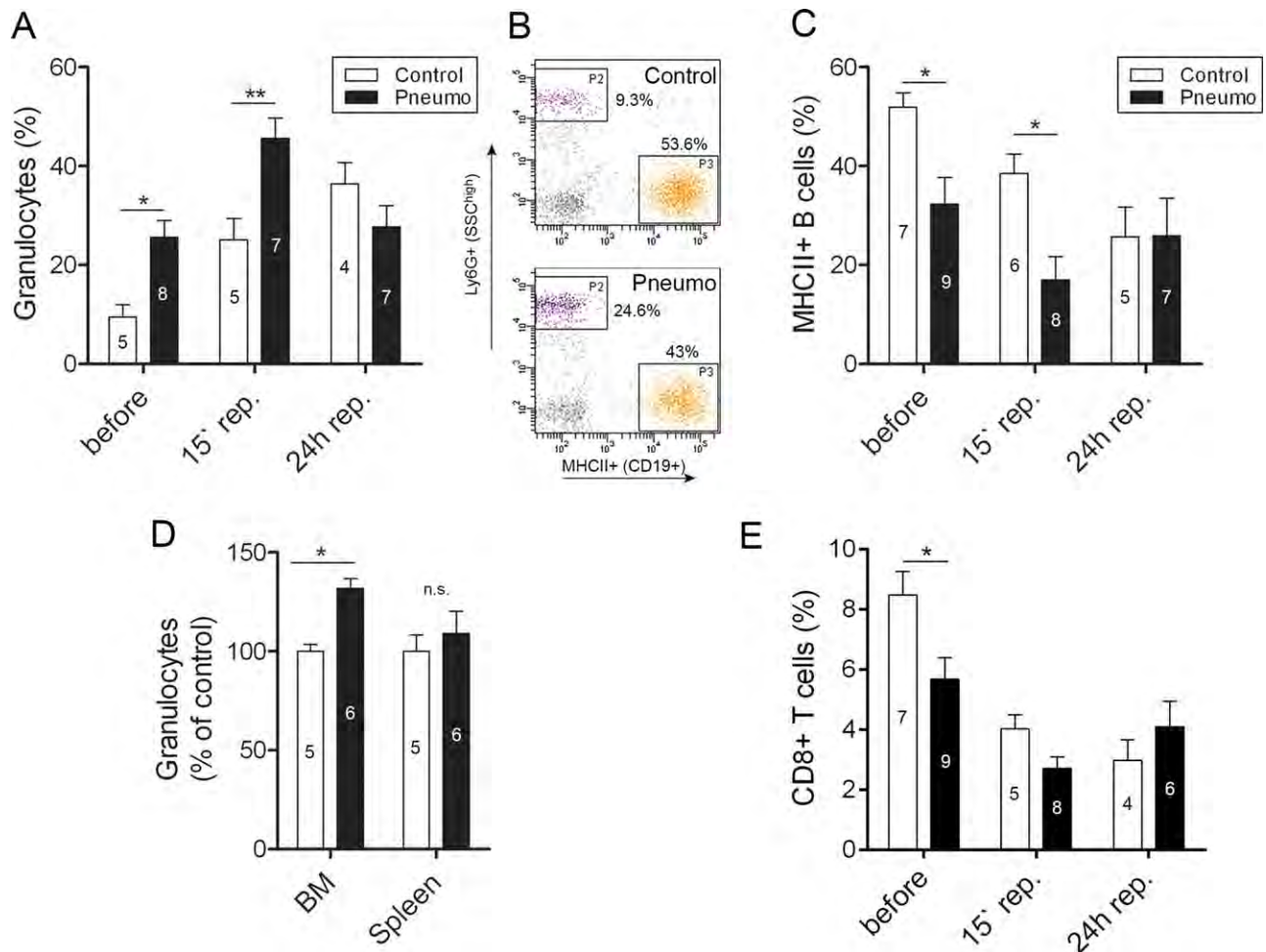


FIGURE 4: *Streptococcus pneumoniae* infection induces granulocytosis and a reduction in circulating B cells and CD8⁺ T cells. (A–C) Flow cytometric analysis indicates higher granulocyte (A) and lower MHCII⁺ B cell (C) numbers before middle cerebral artery occlusion and 15 minutes after reperfusion in mice infected with *S. pneumoniae* (two-way analysis of variance [ANOVA] followed by Bonferroni multiple comparison). (B) Representative dot blots showing granulocytes (P2 gate, Ly6G⁺, SSC^{high}) and MHCII⁺ B cells (P3 gate, MHCII⁺ CD19⁺). (D) Granulocytes are increased in the bone marrow after infection. (E) CD8⁺ T cells (CD3⁺) are reduced in the circulation in infected mice. * $p < 0.05$, ** $p < 0.01$, two-way ANOVA, followed by Bonferroni post hoc comparison; $n = 4–9$ (number of individual cohorts has been displayed on the graphs). n.s. = not significant. [Color figure can be viewed in the online issue, which is available at www.annalofneurology.org.]

neurological outcome in infected mice, but did not alter platelet accumulation in the brain, suggesting an inflammatory role for platelets. GPIIb α blockade did not facilitate intracranial bleedings in infected mice. Only 2 mice receiving control IgG and 1 mouse receiving anti-GPIIb α Fab showed minor hemorrhagic transformation (<0.1% of the volume of the infarct). GPIIb α blockade did not mediate protection against the small, primarily striatal injury in uninfected mice.

Blockade of platelet GPIIb α reduced infection-induced granulocyte recruitment in the brain by 50% (see Fig 7). As both IL-1Ra and blockade of GPIIb α reversed brain injury in infected mice, we further investigated whether systemic inflammatory changes alter microglial activation, which are the primary inflammatory cells in the brain. Microglial (lectin⁺/Iba1⁺) IL-1 α was highly expressed in the ipsilateral hemisphere in infected mice

after cerebral ischemia, which was significantly reduced after platelet GPIIb α blockade. This reduction was most apparent in the ipsilateral cerebral cortex (see Fig 6H). Analysis of brain sections in infected mice also showed a comparable reduction in cortical IL-1 α -positive microglia in response to IL-1Ra administration (see Fig 7J), indicating that IL-1- and platelet-dependent mechanisms contribute to microglial inflammatory changes and brain injury in response to infection after cerebral ischemia. We have also assessed whether infection could contribute to increased BBB injury, microglial IL-1 α expression, or granulocyte recruitment independently of increased infarct size. Mice displaying the smallest infarcts from the infection group across different studies had comparable infarct size to those showing the largest infarct volumes in the control group ($21.2 \pm 6\text{mm}^2$ vs $22.8 \pm 6.8\text{mm}^2$, respectively, $n = 5$). Granulocyte numbers were not (5 ± 1 cells/ mm^2

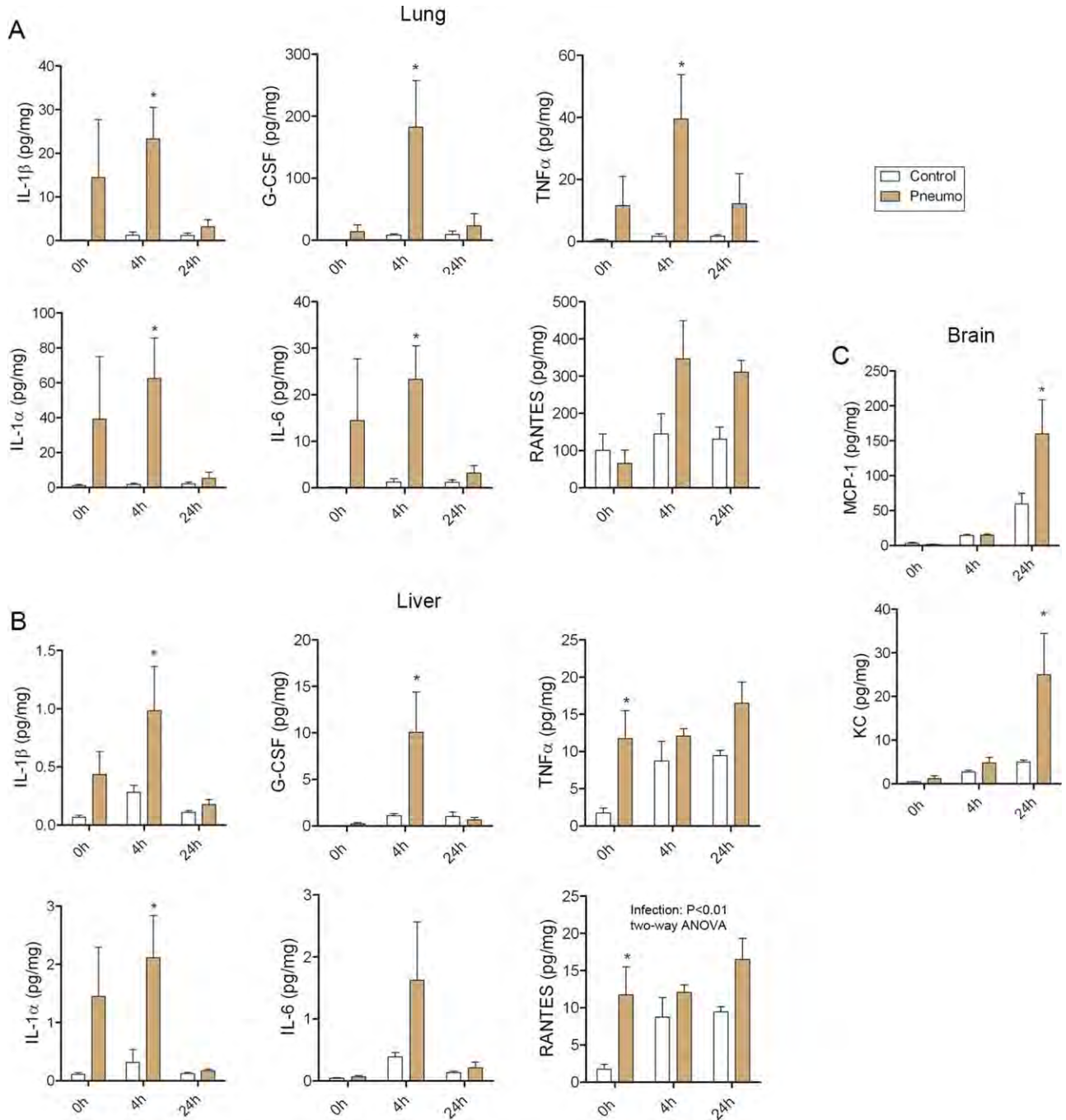


FIGURE 5: *Streptococcus pneumoniae* infection induces systemic interleukin (IL) 1 and exacerbates brain inflammation after cerebral ischemia. (A) Infection (Pneumo) leads to elevated IL-1β and IL-1α levels after cerebral ischemia in the lung compared to uninfected (Control) mice as well as increases in granulocyte colony-stimulating factor (G-CSF) and tumor necrosis factor (TNF) α. (B) IL-1α and IL-1β levels in the liver before and after cerebral ischemia, accompanied by elevated G-CSF, TNFα, and RANTES levels. (C) Twenty-four hours after middle cerebral artery occlusion, brain homogenates contain increased levels of proinflammatory chemokines KC and MCP-1. *p<0.05 two-way analysis of variance followed by Bonferroni multiple comparison; n = 3 (0 hours) and n = 5 (4 hours and 24 hours). [Color figure can be viewed in the online issue, which is available at www.annalsofneurology.org.]

vs 5 ± 2 cells/mm²), but BBB injury volume ($22.9 \pm 3.8\text{mm}^2$ vs $13.8 \pm 4.8\text{mm}^2$, $p < 0.01$) and number of IL-1α-positive microglia (18 ± 7 cells/mm² vs 5 ± 4 cells/mm², $p < 0.01$) were significantly higher in infected animals with even small infarcts compared to control mice after cerebral ischemia.

Discussion

We present evidence that sustained pulmonary *S. pneumoniae* infection, the most common cause of bacterial community-acquired pneumonia, generates an IL-1-mediated systemic inflammatory response involving granulocytosis and platelet activation that accelerates

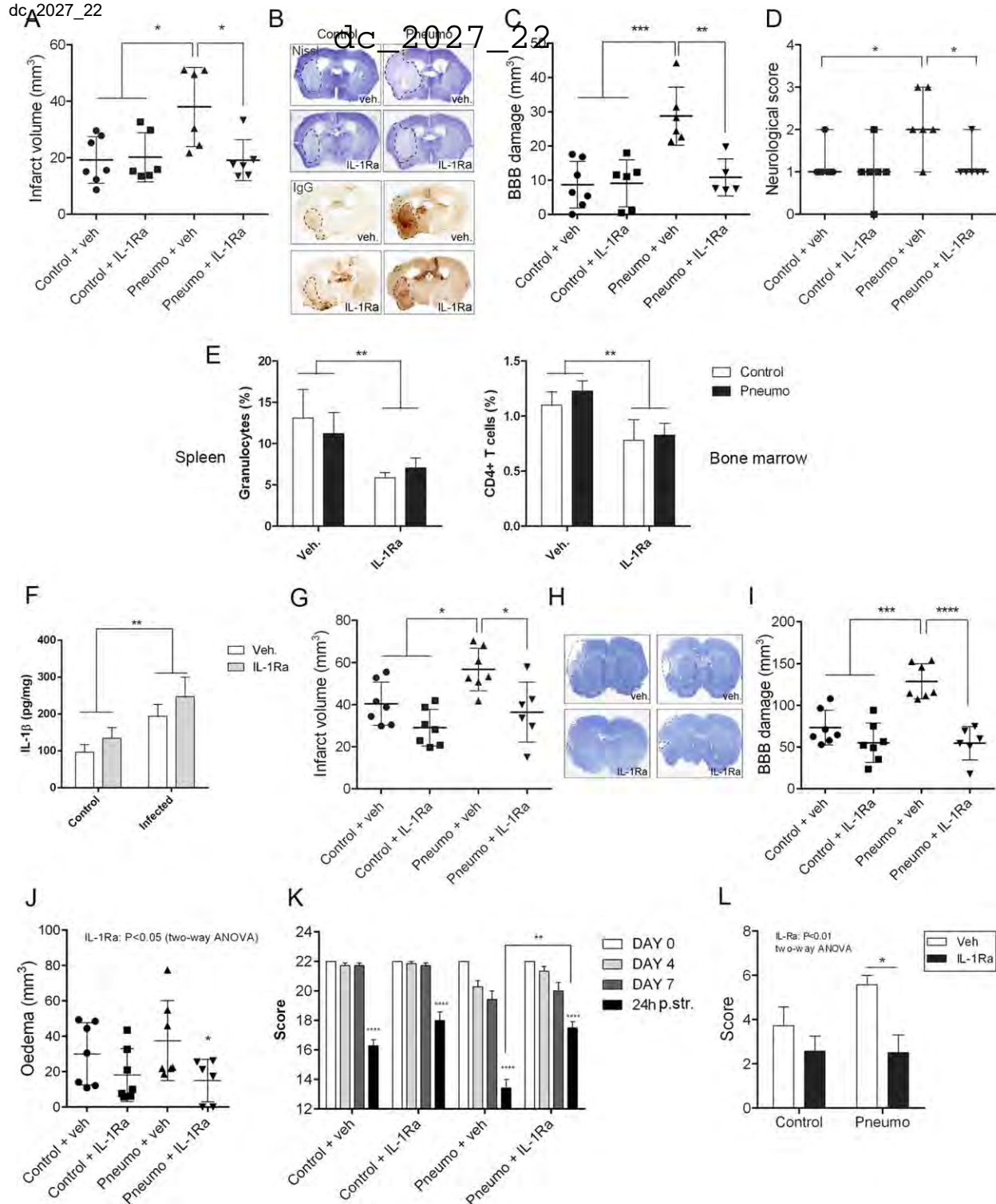


FIGURE 6: Blockade of interleukin (IL) 1 actions by IL-1 receptor antagonist (IL-1Ra) reverses the effects of *Streptococcus pneumoniae* infection on outcome after cerebral ischemia in rodents. (A) The increase in infarct volume caused by infection is reversed after IL-1Ra administration 1 hour after reperfusion, as measured on cresyl violet (Nissl)-stained brain sections. (B) Cresyl violet (Nissl) staining and immunohistochemical detection of plasma-derived immunoglobulin (Ig) G in the brain in uninfected (Control) and *S. pneumoniae*-infected (Pneumo) mice. (C) Blood-brain barrier (BBB) damage was measured by IgG staining. (D) Neurological outcome is impaired after infection, which is fully reversed by IL-1Ra administration. (E) IL-1Ra administered to infected and uninfected mice 1 hour after reperfusion results in reduced splenic granulocyte and bone marrow T-cell numbers 24 hours after cerebral ischemia (two-way analysis of variance [ANOVA] followed by Bonferroni post hoc comparison, $n = 5-6$). (F) IL-1 β levels in the liver were measured by enzyme-linked immunosorbent assay in control and infected Wistar rats after middle cerebral artery occlusion (MCAo). (G) IL-1Ra administration 1 hour after reperfusion reverses infection-induced exacerbation of the ischemic brain injury in Wistar rats. (H) Cresyl violet-stained, representative brain sections are shown in uninfected and infected mice with or without IL-1Ra. (I) BBB injury is increased in response to infection, and this is reversed by IL-1Ra. (J) IL-1Ra reduced brain edema in infected rats after cerebral ischemia. (K) Behavioral outcome was assessed at various time points in control and infected rats before stroke (days 0, 4, and 7 postinfection) and 24 hours after MCAo (24 hours p.str., $n = 6-7$). (L) Neurological outcome is significantly improved in infected mice after IL-1Ra treatment ($n = 6-7$; two-way ANOVA followed by Bonferroni post hoc comparison). * $p < 0.05$, ** $p < 0.01$, *** $p < 0.001$, **** $p < 0.0001$. veh. = vehicle. [Color figure can be viewed in the online issue, which is available at www.annalsofneurology.org.]

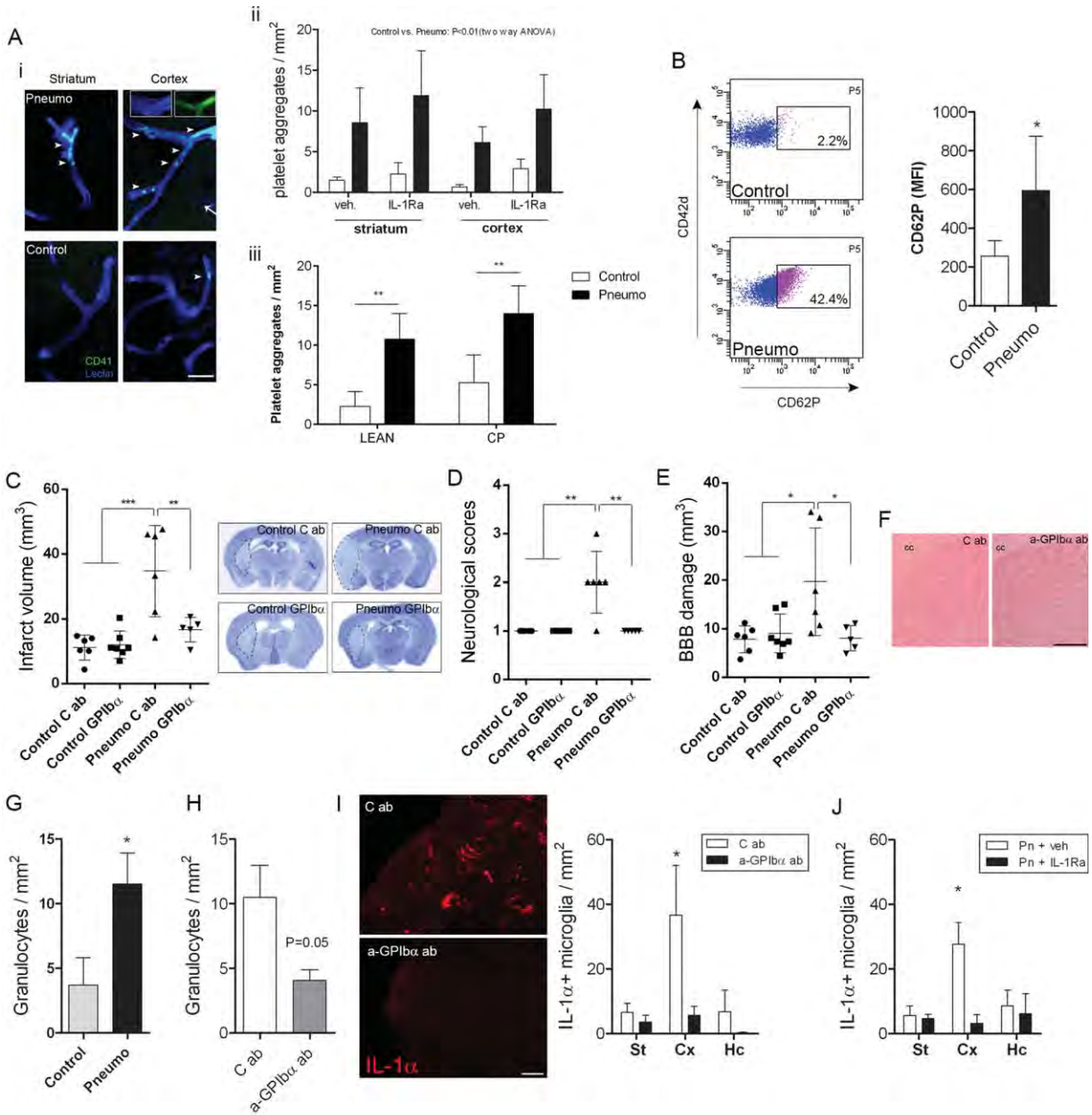


FIGURE 7: *Streptococcus pneumoniae* infection exacerbates brain injury in mice after cerebral ischemia via platelet-dependent responses. (A, i) Platelets in microvessels (lectin, blue) of the ipsilateral striatum and cortex have been identified by anti-CD41 (green) staining 24 hours after middle cerebral artery occlusion (MCAo) in mice. Arrowheads show intravascular platelet aggregates; arrow shows the location of the inserts (upper right panel). Quantification shows the number of intravascular platelet aggregates in the brain in mice (ii, control vs infected $p < 0.01$, two-way analysis of variance [ANOVA]) and in lean and corpulent (CP) rats (iii, $p < 0.01$, two-way ANOVA followed by Bonferroni post hoc test). (B) Flow cytometric analysis of circulating platelets identified by CD42d-PE indicates increased surface levels of CD62P (gate P5). (C) Increased infarct size in *S. pneumoniae*-infected mice (Pneumo) compared to uninfected mice (Control) is significantly reduced after blockade of glycoprotein (GP) I β x with pOp/B Fab fragment, administered 1 hour after MCAo, compared to control immunoglobulin (Ig) G (C ab). (D) Neurological scores indicate better functional recovery after GPIIb/3 blockade in infected mice. (E) Blood–brain barrier (BBB) injury is reduced in infected mice after GPIIb/3 blockade. (F) Blockade of platelet GPIIb/3 does not increase the risk of intracranial hemorrhage in infected mice as assessed on hematoxylin and eosin–stained brain sections (ipsilateral striatum is shown; cc = corpus callosum). (G) Granulocyte numbers (identified by an antigranulocyte serum, SJC4) were increased in the ipsilateral striatum in infected mice 24 hours after MCAo. (H) Striatal granulocytes are reduced by >50% (not significant, $p = 0.05$) after platelet GPIIb/3 blockade compared to control IgG (C ab). (I) Treatment with anti-GPIIb/3 antibody reduces microglial interleukin (IL) 1 α expression in the ipsilateral cerebral cortex ($p < 0.05$, two-way ANOVA followed by Bonferroni post hoc comparison). (J) IL-1 receptor antagonist (IL-1Ra) reduces microglial IL-1 α expression in the ipsilateral cerebral cortex. Scale bars: A, 10 μm ; F, 500 μm ; I, 50 μm ; $n = 6-7$ (A, G, J), $n = 5-8$ (B), $n = 5-7$ (C, D, E, F, H, I). * $p < 0.05$, ** $p < 0.01$, *** $p < 0.001$. Cx = cerebral cortex; Hc = hippocampus; MFI = mean fluorescence intensity; St = striatum; veh. = vehicle.

atherogenesis and leads to cerebrovascular inflammation. *S. pneumoniae*-induced systemic inflammation preceding an acute cerebrovascular event profoundly exacerbates inflammation in the brain via IL-1- and platelet-dependent mechanisms that augment microglial IL-1 α production and lead to increased neuronal injury.

Clinical data indicate that infection contributes to the development of vascular disease, is a trigger for an acute vascular event, and/or contributes to outcome once an acute vascular event has occurred. In patients, infection could mediate all of these effects in both heart disease and stroke,^{5,8,10} although the mechanisms are not known, and current experimental evidence is insufficient. Chlamydia pneumoniae infection has been shown to induce an unstable atherosclerotic plaque phenotype in low-density lipoprotein receptor, ApoE double-knockout mice.³¹ There is clinical evidence to show that *S. pneumoniae* contributes to atherogenesis,^{11,12} although the efficacy of antibiotic treatment on heart disease is controversial.³² However, no experimental studies have addressed the role of sustained *S. pneumoniae* infection in plaque growth or plaque rupture to date. We show that systemic effects of infection induce inflammation in distant vascular beds, and lead to vascular pathologies in both the aorta and the brain, although the extent of the response in individual mice was different. Our study was not designed to specifically investigate plaque rupture, hence it is not surprising that no acute cardio- or cerebrovascular events were observed in infected, atherosclerotic rodents. In contrast, our data clearly indicate the acceleration of atherogenesis by *S. pneumoniae* infection in atherosclerosis-prone rodent models, arguing for a contribution of *S. pneumoniae* to vascular disease.

To examine the effects of sustained and localized pulmonary *S. pneumoniae* infection on systemic inflammatory changes and stroke outcome, we infected mice intranasally with *S. pneumoniae* ATCC 49619 serotype 19F (Danish), a clinically relevant, human isolate. Because major virulence factors such as pneumolysin are conserved across all *S. pneumoniae* strains, we used mock infection in control mice to account for any unexpected effects caused by the inoculum in the lungs. In general, serotype 19F isolates are associated with colonization of mucosa,³³ and are less commonly associated with invasive disease (serotype 19F is included in the 7-valent conjugated pneumococcal polysaccharide vaccine PCV-7). Lack of invasiveness of ATCC 49619 was also confirmed in our experimental model. The infectious challenge was titrated over 5 days to maximize the stimulation of the immune system while minimizing the incidence of invasive disease in the acute phase. Although in this model the infection is localized to the lung, we found marked

systemic inflammatory changes in several organs, dominated by the key proinflammatory cytokine, IL-1. It has been shown that serious pulmonary infection can cause multiorgan dysfunction and a high level of mortality.³⁴ We developed our inoculation protocol to result in sustained infection over a course of several days using intermittent sublethal challenges, without causing major weight loss, fever, behavioral alterations, or death.

In patients, infections preceding a stroke are associated with increased stroke risk and result in impaired outcome, similarly to infections that develop post-stroke.^{5,8,35,36} Our data clearly show that although pneumonia was associated with reduced pO₂ levels (with O₂ saturation unchanged) prior to stroke that could contribute to poor outcome, intervention against both IL-1 and platelet GPIb α reversed infection-induced cerebrovascular inflammation, neuronal injury, and impaired functional outcome, arguing for a major role of inflammation in brain pathologies caused by systemic effects of pulmonary *S. pneumoniae* infection. It is also possible that local and/or systemic inflammation could compromise perfusion and oxygen uptake/release in various organs including the lung or the brain. However, mild hypoxia due to lung inflammation was found to have no direct effect on infarct size.³⁷ Nevertheless, our results strongly suggest that patients with stroke and pneumonia could benefit substantially from anti-inflammatory therapies, such as IL-1Ra. We investigated central and systemic inflammatory mechanisms in detail to explain how IL-1 can mediate injury after infection. As in our rodent model, infection-induced neutrophil and platelet activation has been documented in patients with pneumococcus-induced lung infection.^{26,38} Granulocyte levels were increased after infection and cerebral ischemia in the brain, and were marginally reduced by GPIb α blockade, but not IL-1Ra, indicating that granulocyte responses might not fully explain the effect of infection on brain injury. Granulocyte numbers were not increased in infected mice independently of infarct size either. Although after IL-1-mediated cerebrovascular transmigration granulocytes acquire a neurotoxic phenotype, and IL-1 actions can worsen injury in the brain via granulocytes in vivo,^{30,39} increased numbers of parenchymal granulocytes in the current experimental model might be indirectly associated with infection status and thus bigger infarcts. Nevertheless, systemic or perivascular granulocyte responses might mediate brain injury independently of the cells in the brain parenchyma, although this was not tested experimentally in the present study. In contrast, both platelet intervention and IL-1Ra uniformly reversed microglial IL-1 α after cerebral ischemia in infected mice, suggesting that altered microglial

activation (which was evident even prior to infection) could contribute to infection-induced inflammatory responses. Similarly, increased BBB injury was evident in infected mice with even smaller infarcts, supporting our earlier observations that systemic inflammatory mechanisms could mediate inflammation and injury in the brain independently of changes in infarct size.⁴⁰

Vascular activation after infection, and increased platelet aggregation in infected mice after cerebral ischemia, suggested that inflammatory signals in the brain might be mediated by activated platelets. According to a recent study, *S. pneumoniae* can induce platelet aggregation in a strain-specific manner via toll-like receptor 2, which is dependent on GPIIb/IIIa, but is not affected by aspirin.⁴¹ In addition, our previous data indicated that a chronic infection resulting in a systemic, Th1-polarized immune response leads to the accumulation of platelets in brain microvessels after cerebral ischemia,¹⁶ although the functional role of platelets in the brain has not been investigated earlier after infection. GPIIb/IIIa blockade did not reduce microvascular platelet aggregates in the ischemic brain after *S. pneumoniae* infection, arguing for an inflammatory role for platelet GPIIb/IIIa-mediated interactions in augmenting cerebrovascular pathologies. We reported recently that platelet-derived IL-1 α can induce cerebrovascular inflammation.⁴² Activated platelets release IL-1 and/or IL-1-containing microparticles upon interacting with the endothelium.^{42,43}

We have demonstrated previously that peripheral IL-1 administration exacerbates brain injury,³⁰ and inflammatory mechanisms reportedly contribute to cerebral ischemia even in the absence of systemic inflammation.^{28,29} Both GPIIb/IIIa blockade and IL-1Ra have been shown to be protective in uninfected animals.^{17,18} However, due to the small cerebral injury (that mostly corresponded to the core of the infarct) seen in uninfected animals, we did not expect these interventions to significantly reduce brain injury in control animals in the current experimental model. Importantly, our present results indicate that IL-1-dependent systemic inflammation and pathologies in the central nervous system can develop in response to sustained bacterial infection in vivo, and this disease mechanism is central to the pathologies caused by a clinically important gram-positive bacterium, *S. pneumoniae*. It is likely that such mechanisms could be important in other vascular, noncommunicable diseases as well, such as myocardial infarction, and liver or kidney ischemia.

In conclusion, our data identify IL-1 as a key mediator of infection-induced brain injury and indicate that selective targeting of IL-1- and platelet-mediated mechanisms could be therapeutically useful to prevent

infection-induced thromboinflammatory mechanisms, which predispose to acute vascular events and lead to profound impairment in outcome after stroke.

Acknowledgment

Funding was provided by the Medical Research Council (NJR MRC Research Professorship; S.M.A.) and the European Union's Seventh Framework Programme (FP7/2008-2013) under grant agreements 201024 and 202213 (European Stroke Network; N.J.R., A.D.).

We thank OTKA K 109743 (A.D., B.M.), TÁMOP-4.2.4.A/2-11/1-2012-0001 (A.D.), and the Hungarian Brain Research Program KTIA 13 NAP-A-I/3 (A.D.) for their support; the Bioimaging facility of the University of Manchester; and J. Russell and S. Proctor for the corpulent rats.

Authorship

A.D., N.J.R., and S.M.A. designed research. A.D., J.M.P., C.D., A.S., P.W., K.N.M., B.R., J.C., H.C., and B.M. performed research. P.W., D.H.D., S.F., and B.N. contributed new reagents/analytic tools. A.D., J.M.P., C.D., A.S., P.W., K.N.M., B.R., J.C., H.C., and B.M. analyzed data. A.D., N.J.R., and S.M.A. wrote the article. A.D. and J.M.P. contributed equally.

Potential Conflicts of Interest

D.H.D.: funding, Wellcome Trust, MRC, GSK (no direct conflict of interest in the results of this research). N.J.R.: nonexecutive director of AstraZeneca (no involvement in this work).

References

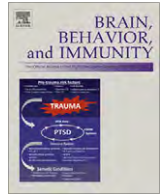
1. Marrie TJ. Community-acquired pneumonia in the elderly. *Clin Infect Dis* 2000;31:1066-1078.
2. O'Brien KL, Wolfson LJ, Watt JP, et al. Burden of disease caused by *Streptococcus pneumoniae* in children younger than 5 years: global estimates. *Lancet* 2009;374:893-902.
3. Marrie TJ. Community-acquired pneumonia. *Clin Infect Dis* 1994; 18:501-513; quiz 514-515.
4. Denes A, Pinteaux E, Rothwell NJ, Allan SM. Interleukin-1 and stroke: biomarker, harbinger of damage, and therapeutic target. *Cerebrovasc Dis* 2012;32:517-527.
5. Emsley HC, Hopkins SJ. Acute ischaemic stroke and infection: recent and emerging concepts. *Lancet Neurol* 2008;7:341-353.
6. Marijon E, Mirabel M, Celermajer DS, Jouven X. Rheumatic heart disease. *Lancet* 2012;379:953-964.
7. Musher DM, Rueda AM, Kaka AS, Mapara SM. The association between pneumococcal pneumonia and acute cardiac events. *Clin Infect Dis* 2007;45:158-165.
8. Smeeth L, Thomas SL, Hall AJ, et al. Risk of myocardial infarction and stroke after acute infection or vaccination. *N Engl J Med* 2004;351:2611-2618.

9. Vila-Corcoles A, Ochoa-Gondar O, Rodriguez-Blanco T, et al. Clinical effectiveness of pneumococcal vaccination against acute myocardial infarction and stroke in people over 60 years: the CAPAMIS study, one-year follow-up. *BMC Public Health* 2012;12:222.
10. Tseng HF, Slezak JM, Quinn VP, et al. Pneumococcal vaccination and risk of acute myocardial infarction and stroke in men. *JAMA* 2010;303:1699–1706.
11. Binder CJ, Horkko S, Dewan A, et al. Pneumococcal vaccination decreases atherosclerotic lesion formation: molecular mimicry between *Streptococcus pneumoniae* and oxidized LDL. *Nat Med* 2003;9:736–743.
12. Ott SJ, El Mokhtari NE, Musfeldt M, et al. Detection of diverse bacterial signatures in atherosclerotic lesions of patients with coronary heart disease. *Circulation* 2006;113:929–937.
13. Prass K, Meisel C, Hoflich C, et al. Stroke-induced immunodeficiency promotes spontaneous bacterial infections and is mediated by sympathetic activation reversal by poststroke T helper cell type 1-like immunostimulation. *J Exp Med* 2003;198:725–736.
14. Prass K, Braun JS, Dirnagl U, et al. Stroke propagates bacterial aspiration to pneumonia in a model of cerebral ischemia. *Stroke* 2006;37:2607–2612.
15. Mangat R, Su J, Scott PG, et al. Chylomicron and apoB48 metabolism in the JCR:LA corpulent rat, a model for the metabolic syndrome. *Biochem Soc Trans* 2007;35:477–481.
16. Denes A, Humphreys N, Lane TE, et al. Chronic systemic infection exacerbates ischemic brain damage via a CCL5 (regulated on activation, normal T-cell expressed and secreted)-mediated proinflammatory response in mice. *J Neurosci* 2010;30:10086–10095.
17. Pradillo JM, Denes A, Greenhalgh AD, et al. Delayed administration of interleukin-1 receptor antagonist reduces ischemic brain damage and inflammation in comorbid rats. *J Cereb Blood Flow Metab* 2012;32:1810–1819.
18. Kleinschnitz C, Pozgajova M, Pham M, et al. Targeting platelets in acute experimental stroke: impact of glycoprotein Ib, VI, and IIb/IIIa blockade on infarct size, functional outcome, and intracranial bleeding. *Circulation* 2007;115:2323–2330.
19. Chapman KZ, Dale VQ, Denes A, et al. A rapid and transient peripheral inflammatory response precedes brain inflammation after experimental stroke. *J Cereb Blood Flow Metab* 2009;29:1764–1768.
20. Bederson JB, Pitts LH, Tsuji M, et al. Rat middle cerebral artery occlusion: evaluation of the model and development of a neurologic examination. *Stroke* 1986;17:472–476.
21. Madrigal JL, Caso JR, de Cristobal J, et al. Effect of subacute and chronic immobilisation stress on the outcome of permanent focal cerebral ischaemia in rats. *Brain Res* 2003;979:137–145.
22. Drake C, Boutin H, Jones MS, et al. Brain inflammation is induced by co-morbidities and risk factors for stroke. *Brain Behav Immun* 2011;25:1113–1122.
23. Denes A, Drake C, Stordy J, et al. Interleukin-1 mediates neuroinflammatory changes associated with diet-induced atherosclerosis. *J Am Heart Assoc* 2012;1:e002006.
24. Lim WS, Boudouin SV, George RC, et al. BTS guidelines for the management of community acquired pneumonia in adults: update 2009. *Thorax* 2009;64(suppl 3):iii1–iii55.
25. Henriques-Normark B, Normark S. Commensal pathogens, with a focus on *Streptococcus pneumoniae*, and interactions with the human host. *Exp Cell Res* 2010;316:1408–1414.
26. Kadioglu A, Andrew PW. The innate immune response to pneumococcal lung infection: the untold story. *Trends Immunol* 2004;25:143–149.
27. Koppe U, Suttorp N, Opitz B. Recognition of *Streptococcus pneumoniae* by the innate immune system. *Cell Microbiol* 2012;14:460–466.
28. Iadecola C, Anrather J. The immunology of stroke: from mechanisms to translation. *Nat Med* 2012;17:796–808.
29. Denes A, Thornton P, Rothwell NJ, Allan SM. Inflammation and brain injury: acute cerebral ischaemia, peripheral and central inflammation. *Brain Behav Immun* 2011;24:708–723.
30. McColl BW, Rothwell NJ, Allan SM. Systemic inflammatory stimulus potentiates the acute phase and CXC chemokine responses to experimental stroke and exacerbates brain damage via interleukin-1- and neutrophil-dependent mechanisms. *J Neurosci* 2007;27:4403–4412.
31. Ezzahiri R, Stassen FR, Kurvers HA, et al. Chlamydia pneumoniae infection induces an unstable atherosclerotic plaque phenotype in LDL-receptor, ApoE double knockout mice. *Eur J Vasc Endovasc Surg* 2003;26:88–95.
32. Stassen FR, Vainas T, Bruggeman CA. Infection and atherosclerosis. An alternative view on an outdated hypothesis. *Pharmacol Rep* 2008;60:85–92.
33. Kronenberg A, Zucs P, Droz S, Muhlemann K. Distribution and invasiveness of *Streptococcus pneumoniae* serotypes in Switzerland, a country with low antibiotic selection pressure, from 2001 to 2004. *J Clin Microbiol* 2006;44:2032–2038.
34. Andonegui G, Goring K, Liu D, et al. Characterization of *S. pneumoniae* pneumonia-induced multiple organ dysfunction syndrome: an experimental mouse model of gram-positive sepsis. *Shock* 2009;31:423–428.
35. Grau AJ, Bugge F, Becher H, et al. Recent bacterial and viral infection is a risk factor for cerebrovascular ischemia: clinical and biochemical studies. *Neurology* 1998;50:196–203.
36. Grau AJ, Bugge F, Heindl S, et al. Recent infection as a risk factor for cerebrovascular ischemia. *Stroke* 1995;26:373–379.
37. Muhammad S, Haasbach E, Kotchourko M, et al. Influenza virus infection aggravates stroke outcome. *Stroke* 2011;42:783–791.
38. McNicol A, Israels SJ. Mechanisms of oral bacteria-induced platelet activation. *Can J Physiol Pharmacol* 2010;88:510–524.
39. Allen C, Thornton P, Denes A, et al. Neutrophil cerebrovascular transmigration triggers rapid neurotoxicity through release of proteases associated with decondensed DNA. *J Immunol* 2012;189:381–392.
40. Denes A, Ferenczi S, Kovacs KJ. Systemic inflammatory challenges compromise survival after experimental stroke via augmenting brain inflammation, blood-brain barrier damage and brain oedema independently of infarct size. *J Neuroinflammation* 2011;8:164.
41. Keane C, Tilley D, Cunningham A, et al. Invasive *Streptococcus pneumoniae* trigger platelet activation via Toll-like receptor 2. *J Thromb Haemost* 2012;8:2757–2765.
42. Thornton P, McColl BW, Greenhalgh A, et al. Platelet interleukin-1 α drives cerebrovascular inflammation. *Blood* 2010;115:3632–3639.
43. Boilard E, Nigrovic PA, Larabee K, et al. Platelets amplify inflammation in arthritis via collagen-dependent microparticle production. *Science* 2010;327:580–583.



Contents lists available at ScienceDirect

Brain, Behavior, and Immunity

journal homepage: www.elsevier.com/locate/ybrbi

Brain inflammation is induced by co-morbidities and risk factors for stroke

Caroline Drake^a, Hervé Boutin^a, Matthew S. Jones^b, Adam Denes^a, Barry W. McColl^{a,1}, Johann R. Selvarajah^c, Sharon Hulme^c, Rachel F. Georgiou^c, Rainer Hinz^b, Alexander Gerhard^b, Andy Vail^d, Christian Prenant^b, Peter Julyan^e, Renaud Maroy^f, Gavin Brown^b, Alison Smigova^b, Karl Herholz^b, Michael Kassiou^{g,h,i}, David Crossman^j, Sheila Francis^k, Spencer D. Proctor^l, James C. Russell^l, Stephen J. Hopkins^c, Pippa J. Tyrrell^c, Nancy J. Rothwell^a, Stuart M. Allan^{a,*}

^a Faculty of Life Sciences, University of Manchester, Manchester, UK^b Wolfson Molecular Imaging Centre, University of Manchester, Manchester, UK^c Clinical Neurosciences Group and Stroke Medicine, Salford Royal Foundation Trust, UK^d Health Methodology Research Group, University of Manchester, UK^e North Western Medical Physics, Christie Hospital, Manchester, UK^f SHFJ – CEA Orsay, France^g Brain and Mind Research Institute, University of Sydney, NSW 2050, Australia^h Discipline of Medical Radiation Sciences, University of Sydney, NSW 1825, Australiaⁱ School of Chemistry, University of Sydney, NSW 2006, Australia^j NIHR Biomedical Research Unit, University of Sheffield, Sheffield, UK^k Department of Cardiovascular Science, University of Sheffield, UK^l Metabolic and Cardiovascular Diseases Laboratory, Alberta Institute for Human Nutrition, University of Alberta, Edmonton, Alberta, Canada

ARTICLE INFO

Article history:

Received 16 December 2010

Received in revised form 11 February 2011

Accepted 12 February 2011

Available online 26 February 2011

Keywords:

Brain
Co-morbidity
Inflammation
Risk factors
Stroke
Systemic

ABSTRACT

Chronic systemic inflammatory conditions, such as atherosclerosis, diabetes and obesity are associated with increased risk of stroke, which suggests that systemic inflammation may contribute to the development of stroke in humans. The hypothesis that systemic inflammation may induce brain pathology can be tested in animals, and this was the key objective of the present study. First, we assessed inflammatory changes in the brain in rodent models of chronic, systemic inflammation. PET imaging revealed increased microglia activation in the brain of JCR-LA (corpulent) rats, which develop atherosclerosis and obesity, compared to the control lean strain. Immunostaining against Iba1 confirmed reactive microgliosis in these animals. An atherogenic diet in apolipoprotein E knock-out (ApoE^{-/-}) mice induced microglial activation in the brain parenchyma within 8 weeks and increased expression of vascular adhesion molecules. Focal lipid deposition and neuroinflammation in periventricular and cortical areas and profound recruitment of activated myeloid phagocytes, T cells and granulocytes into the choroid plexus were also observed. In a small, preliminary study, patients at risk of stroke (multiple risk factors for stroke, with chronically elevated C-reactive protein, but negative MRI for brain pathology) exhibited increased inflammation in the brain, as indicated by PET imaging. These findings show that brain inflammation occurs in animals, and tentatively in humans, harbouring risk factors for stroke associated with elevated systemic inflammation. Thus a “primed” inflammatory environment in the brain may exist in individuals at risk of stroke and this can be adequately recapitulated in appropriate co-morbid animal models.

© 2011 Elsevier Inc. Open access under [CC BY license](http://creativecommons.org/licenses/by/3.0/).

1. Introduction

Clinical and experimental evidence implicates inflammation in multiple phases of stroke aetiology and pathology (Allan et al.,

2005; Amor et al., 2010; Denes et al., 2010a,b; McColl et al., 2009; Muir et al., 2007). Several of the risk factors for stroke, such as atherosclerosis, hypertension and diabetes/obesity are triggered and/or propagated by dysregulated systemic inflammatory processes (Dandona et al., 2004; Ross, 1999; Savoia and Schiffrin, 2006). Markers of elevated systemic inflammation are associated with increased stroke risk and brain lesions detected by magnetic resonance imaging (MRI) (Fornage et al., 2008; van Dijk et al., 2005). Like other statins, rosuvastatin, has multiple anti-inflammatory properties. It reduces cerebrovascular events in patients without hyperlipidemia but with raised C-reactive protein (CRP) levels

* Corresponding author. Address: Faculty of Life Sciences, University of Manchester, AV Hill Building, Oxford Road, Manchester M13 9PT, UK. Fax: +44 (0) 161 275 3938.

E-mail address: stuart.allan@manchester.ac.uk (S.M. Allan).

¹ Present address: The Roslin Institute and R(D)SVS, University of Edinburgh, Edinburgh, UK.

(Ridker et al., 2008). Angiotensin-converting enzyme (ACE) inhibitors can lower median CRP levels and result in better long-term outcome in stroke patients, after controlling for confounding variables and concomitant treatments (Di Napoli and Papa, 2003). Similarly, aspirin or other anti-platelet treatments are used prophylactically in patients at risk, but it is still unclear whether their beneficial properties are due to anti-aggregation effects or to a combination of anti-platelet and anti-inflammatory effects (Franks et al., 2010). Therefore, although inflammation-driven co-morbidities are common and aetiologically important in stroke patients, exactly how systemic inflammation contributes to risk of stroke and to other neurological conditions remains to be determined.

Despite the almost ubiquitous nature of co-morbidities preceding stroke, there has been a relative paucity of studies incorporating these in experimental stroke research. This may have contributed to the lack of successful translation for a number of potential stroke treatments identified in pre-clinical studies (Endres et al., 2008; Fisher et al., 2009). One reason for the failure of translation may be that underlying inflammation associated with atherosclerotic risk factors modifies the mechanisms of post-ischaemic brain damage, including the type, magnitude and kinetics of the damaging processes. In support of this, we and others have shown that the extent of brain injury is exacerbated, and mechanisms of damage altered and/or aggravated, when experimental stroke is induced in animals with hypertension, diabetes, obesity or acute/chronic infection/inflammation (Coyle, 1984; Denes et al., 2010a,b; McColl et al., 2007; Terao et al., 2008; Vannucci et al., 2001). However, it is unclear whether co-morbid stroke risk factors can drive brain inflammation and induce a “primed” inflammatory state in the brain prior to a cerebrovascular event.

Here we undertook a translational study to determine if risk factors for stroke, which involve chronic systemic inflammation, also induce brain inflammation in rodents and humans. We show that brain inflammation is present in rats and mice harbouring systemic vascular and/or metabolic disease and that analogous changes may be present in patients with clinical risk factors and evidence of systemic inflammation, as indicated by a raised concentration of circulating CRP.

2. Materials and methods

2.1. Pre-clinical studies

These studies were performed on (JCR:LA-cp) (*cp/cp*) corpulent rats, which are obese, atherosclerotic and insulin resistant and ApoE-deficient (ApoE^{-/-}) mice fed an atherogenic diet, which exhibit severe atherosclerosis.

Animals were allowed free access to food and water and were maintained under temperature, humidity and light-controlled conditions. All animal procedures adhered to the UK Animals (Scientific Procedures) Act (1986).

Corpulent and lean heterozygous control rats (+/?), obtained from an established breeding colony at The University of Alberta, Edmonton, Canada (Mangat et al., 2007); were subject to PET scanning using specific translocator protein (TSPO; formerly known as peripheral benzodiazepine receptor) radiotracers [¹⁸F]DPA-714, at 9 (average body weight; +/? : 411 ± 14 g; *cp/cp*: 720 ± 22 g), 12 (+/? : 438 ± 18 g; *cp/cp*: 918 ± 33 g) (*n* = 4 per group) and 15 months of age (+/? : 452 ± 15 g, *n* = 4; *cp/cp*: 0.979 ± 0.054 kg, *n* = 3).

Experiments were carried out in male ApoE^{-/-} (JAX 2052, Jackson Laboratories, USA) and C57BL/6 control mice (Jackson Laboratories, USA) bred in-house at the University of Sheffield. Mice aged 8 weeks were fed normal chow (4.3% fat, 0.02% cholesterol) or a high fat/high cholate (Paigen; 18.5% fat, 0.9% cholesterol, 0.5% cholate, 0.26% sodium) diet (Special Diet Services, UK) for 8 weeks.

2.1.1. Positron emission tomography

Rats were anaesthetised by isoflurane inhalation (induction, 5%; maintenance, 2–2.5%) in oxygen. [¹⁸F]DPA-714, a specific tracer for the TSPO (Boutin et al., 2008; Chauveau et al., 2009) was synthesised (James et al., 2008), and injected intravenously in the tail vein as a bolus (10.8–19.8 MBq, 0.03–2.79 nmol). Respiration and temperature was monitored throughout using a pressure sensitive pad and rectal probe, Model 1025L interface and PC-SAM software (SA Instruments, NJ, USA). Body temperature was maintained at 37 ± 0.5 °C by use of a heating pad and the heating and fan module connected to the rectal probe via the interface and controlled by the PC-SAM software. Whole-body images were acquired in list-mode with a non-rotating 16-module quad-HIDAC PET camera (Oxford Positron Systems, UK) for 1 h (Hastings et al., 2007). The list-mode data were reconstructed directly into 5 min time-frame images (without resorting to histogramming) via the one-pass-list-mode-expectation maximisation (OPL-EM) algorithm (Reader et al., 2002) with one iteration of 16 sub-sets into images of dimensions 120² (transaxially) × 240 (axially) with isotropic 1 mm³ voxels. Absolute calibration of the images was achieved by reference to a [²²Na] source imaged in the field of view in each scan. This had been validated with a uniformly filled mouse-sized [¹⁸F] phantom imaged over 2 h. Dynamic images were calibrated in kBq/cm⁻³.

Images were segmented using the Local Means Analysis method and the organ mean Time Activity Curves were corrected for Partial Volume Effect using the Geometric Transfer Matrix (GTM) method with a selection of 20% of the organ voxels (GTM20) (Maroy et al., 2008a,b). The segmentation method extracts regions with homogeneous TACs, as required by the GTM20 method. The latter was designed to be more robust than the original GTM method to segmentation errors through the automated selection of adequate voxels in the segmented organs. Both methods were applied using the BrainVisa and Anatomist framework. For more accurate quantification and illustration purposes, PET images were co-registered with the rat MRI template (Schwarz et al., 2006), generously provided by GlaxoSmithKline (Verona, Italy). Automatic segmentation of PET images revealed 1–2 regions of interest (ROI) with different [¹⁸F]DPA-714 (low and high) uptake in the brain of both the lean and corpulent rats. These ROIs were used to compare the genotypes and the different ages.

To account for the differences (~2-fold) in body-weight between lean and corpulent rats, we expressed all uptake values as standardised uptake value (SUV) (i.e. percentage of injected dose per cubic centimetre corrected for body weight: %ID · kg/cm³). Until now the problem of comparing obese and lean animals or patients, and using SUV, has been mainly applied to [¹⁸F]fluoro-deoxy-glucose PET imaging. However, considering the controversial literature on SUV, and the fact it has been reported that correcting for the absolute body-weight was likely to over-compensate for the difference (Boellaard, 2009; Keyes, 1995; Sugawara et al., 1999) we have used a slightly different approach. Indeed, the over-compensation of SUV is due to the fact that it assumes that the excess of weight mainly due to adipose tissue has the same metabolic activity than the rest of the body (Keyes, 1995; Sugawara et al., 1999), and therefore that corpulent rats have a metabolic activity twice that observed in lean controls. To the contrary, we considered that correcting for the lean body-weight was likely to under-compensate since it assumes that the excess of adipose tissue is completely inert (Keyes, 1995). Both assumptions being wrong, we decided to adjust the body-weight to calculate the SUV according to Kleiber laws (Kleiber, 1947), in which the metabolic activity is proportional to a factor equal to $m^{0.74}$ (*m* being the body-weight in g of the animal).

2.1.2. Tissue processing

Under terminal anaesthesia, mice and rats were perfused transcardially with saline followed by 4% paraformaldehyde

(PFA; Sigma, UK). Brains were removed and postfixed in 4% PFA at 4 °C for 24 h. Brains were subjected to cryoprotection in phosphate-buffered saline containing 20% sucrose for 24 h. Five alternate sets of 20 µm (mice) or 30 µm (rats) thick coronal brain sections were cut on a sledge microtome (Bright series 8000; Bright Instruments, Huntingdon, UK). All sections were collected into an antifreeze solution (containing 30% ethylene glycol (Sigma, UK) and 20% glycerol (Fisher, UK) in phosphate-buffered saline) and stored at –20 °C until processing.

2.1.3. Immunohistochemistry

Immunohistochemistry was performed on free-floating brain sections. Endogenous peroxidase activity was blocked with 0.3% hydrogen peroxide (Sigma) in dH₂O and sections were treated with 2% normal serum (Vector Laboratories, Burlingame, CA) for 1 h at room temperature. Sections were incubated overnight in antibody diluent (0.1 M PBS + 0.3 % Triton X-100, Sigma) using the following primary antibodies: goat anti-mouse VCAM-1 1:250 (R&D Systems, UK), goat anti-mouse ICAM-1 1:250 (R&D Systems, UK), goat anti-mouse Iba1 1:500 (Abcam, UK), rabbit anti-Iba1 (Wako Chemicals, Germany) and rat anti-mouse CD45 1:250 (Serotec, UK). Sections were then incubated in appropriate biotinylated secondary antibody for 1 h (rabbit anti-goat 1:1000 and rabbit anti-rat 1:750, Vector Laboratories, UK). Sections were then incubated in Vectastain ABC solution (Vector laboratories, UK) and colour was developed by nickel enhanced diaminobenzidine (50 mg/ml) incubation (Vector Laboratories, UK). Sections were mounted onto gelatine coated slides, dehydrated and coverslipped using Depex (Fisher, UK). Images were collected on an Axiocam colour CCD camera (Zeiss, Germany) upright microscope using 20× and 60× objectives and captured using a Coolsnap ES camera (Photometrics) through Axiovision software (Zeiss, Germany).

2.1.4. Immunofluorescence

Double or triple immunofluorescence was performed on free-floating brain sections. After blocking in 2% normal donkey serum (Vector Laboratories) sections were incubated overnight at 4 °C in primary antibodies: rat anti-mouse CD45 1:200 (Serotec, UK), goat anti-mouse VCAM-1 1:250 (R&D Systems), goat anti-mouse ICAM-1 1:250 (R&D Systems), rat anti-CD3 (Serotec), goat anti-Iba1 (Abcam, UK), rabbit anti-Iba1 (Wako Chemicals, Germany) and rabbit anti-neutrophil serum (SJC), kindly provided by Drs. Daniel Anthony and Sandra Campbell, University of Oxford (Anthony et al., 1998). The antigens were visualised with the adequate fluorochrome-conjugated (Alexa 594 1:750 or Alexa 488 1:500, Molecular Probes) secondary donkey antisera or with biotinylated secondary antibodies followed by streptavidin Alexa 350 conjugate, for 2 h at room temperature. Sections were mounted onto gelatin-coated slides and cover-slipped Vectashield mounting medium containing diamidinophenylindole (Vector Laboratories, Burlingame, CA).

Images were collected on an Olympus BX51 upright microscope using 40× and 60× objectives and captured using a Coolsnap ES camera (Photometrics, UK) through MetaVue Software (Molecular Devices, UK). Specific band pass filter sets for DAPI, FITC and Texas red were used to prevent bleed through from one channel to the next.

2.1.5. Quantitative analysis

All quantitative analysis was performed under blinded conditions and confirmed by at least two independent researchers. VCAM-positive blood vessels were counted in three random fields of view for each section (typically 8–10) containing rostro-caudal cerebral cortex. A score for the whole brain was obtained by averaging individual counts and this was expressed as positive blood vessels per mm².

Activated microglia were identified as showing: (1) increased Iba1 immunopositivity, (2) enlarged and/or amoeboid cell body, (3) complete or partial loss of thin, elongated processes. Round shaped, small Iba1-positive cells with leucocyte morphology were not counted. Regions analysed for microglial activation were also stained with mouse anti-rat CD68 (corpulent rats) and rat anti-mouse CD45 (mice) to assess the number of parenchymal macrophages and other leucocytes. Activated microglia were counted throughout the striatum and expressed as activated microglia per mm².

Fluorescently labelled CD45 positive cells were counted in two randomly selected fields of view of the caudal choroid plexus (–1.82 mm from Bregma) and the lateral ventricle (–1.58 mm from Bregma). The choroid plexus and ventricular ependyma were visualised by using VCAM immunofluorescence.

2.1.6. Histology

After CD45 immunohistochemistry (see above) sections were rinsed in dH₂O and incubated in 60% v/v isopropanol/dH₂O (Fischer, UK) for 2 min. Sections were transferred to Oil red O (ORO; Sigma, UK) (0.05% w/v ORO/99% isopropanol) for 15 min, rinsed in 60% v/v isopropanol, rinsed in dH₂O and coverslipped with an aqueous glycerol jelly mount (7.7% w/v Gelatine (BDH, UK) and 54% glycerol in water). Haematoxylin & Eosin (H&E) staining was performed on mounted brain sections. Following staining sections were dehydrated and cover-slipped with Depex mounting medium.

2.1.7. Statistical analysis

Quantitative analysis of data was performed in a blinded manner. PET image quantifications were analysed using Mann–Whitney for comparison between lean and corpulent animals and for comparing 9 vs 15 and 9 vs 12 month age groups. Because the same group of animals was scanned at 12 and 15 months of age, a non-parametric paired Wilcoxon test was used to compare these two groups.

Quantitative data from immunohistochemical and immunofluorescence studies were analysed by one- or two-way analysis of variance (ANOVA) followed by *post-hoc* Bonferroni's correction. All data are expressed as mean ± SD. Statistical significance is reported at the 0.05 level.

2.2. Clinical study

2.2.1. Patients

This small, preliminary study was undertaken to assess cerebral inflammation in humans with multiple risk factors for stroke, but no evidence of cerebral damage, in order to investigate the relevance of our experimental findings in a translational context. One hundred and twenty-one subjects were screened, and rigorous criteria were applied to identify patients at risk of stroke, while excluding patients with existing brain pathology. Subjects were deemed eligible if having multiple (three or more) risk factors for stroke, and/or established arterial disease (hypertension, dyslipidemia, atrial fibrillation, left ventricular hypertrophy, ischaemic heart disease, diabetes mellitus, peripheral vascular disease, carotid disease and smoking), and CRP >3 mg/L on two separate occasions. All subjects underwent MRI scans to exclude any intracranial pathology, and subjects with a history of a previous cerebrovascular event were not involved in the study. MR scans were reviewed by neuroradiologists. Only four patients fulfilled all inclusion criteria and were subjected to PET imaging to assess microglial activation in the brain (see below). Age matched control participants were chosen on the basis of having two or fewer major vascular risk factors and plasma CRP ≤1 mg/L (see Table 1). All participants were also screened to exclude cognitive impairment and a

Table 1
Clinical study group characteristics.

	At risk subjects (n = 4)	Control participants (n = 4)
Mean age in years [range]	63 [58–72]	64 [58–68]
Sex M:F	3:1	1:3
Number of risk factors [range]	3–4	1–2
Mean CRP at screening [range]	9.15 [2.99–13.26]	0.76 [0.55–1.00]
Mean interleukin-6 at screening [range]	12.00 [1.98–33.40]	2.46 [1.10–3.61]
Mean CRP at PET [range]	11.93 [8.98–15.73]	1.56 [1.18–2.05]
Mean interleukin-6 at PET [range]	10.55 [3.70–25.00]	4.79 [1.00–8.08]

telephone consultation was used to exclude symptoms of acute infection prior to PET scanning. All participants gave written informed consent.

2.2.2. Positron emission tomography

Participants underwent MRI scans on a 3 T Philips Achieva system using a T1 weighted inversion recovery SENSE sequence for co-registration of PET images and to exclude visible evidence of stroke. PET studies were performed on a high resolution research tomograph (CTI/Siemens). [¹¹C](R)-PK11195 (TSPO ligand) was used to assess microglial activation in the brain. Following a 6 min transmission scan, [¹¹C](R)-PK11195 was injected as a slow bolus over 20 s and data were acquired during a 60 min emission scan. The injected radioactivity dose was 465 ± 121 MBq and radiochemical purity was always greater than 98.9%. The injected mass of cold (R)-PK11195 was 2.4 ± 1.0 µg. Binding potential (BP_{ND}) images were generated using the simplified reference tissue model and a supervised clustering algorithm was used to extract a reference tissue input function (Turkheimer et al., 2007). The study was approved by the local research and ethics committee.

3. Results

3.1. PET imaging reveals neuroinflammation in cp/cp JCR-LA cp rats

There was no significant difference in microglial activation as determined by PET imaging between lean and corpulent rats at 9 months of age (Fig. 1A). By 12 months of age, microglial activation was increased significantly in the brains of the corpulent rats in the ROI with the lowest tracer uptake (+35%, Fig. 1B). [¹⁸F]DPA-714 uptake increased further in 15 month old animals (+32% and +53% in low and high uptake ROI respectively; Fig. 1C). We also observed a trend for an increase in neuroinflammation with age in both lean and corpulent animals, although this was significant only in the corpulent in the low uptake ROI when comparing 15 with 9 month old animals (+28%, $P < 0.05$, Fig. 1C). Although the [¹⁸F]DPA-714 uptake was increased by a similar magnitude (+29 to 33%, Fig. 1B and C) between 12 and 15 months in the corpulent rats, the differences were not significant. In reference organs, known to express high level of TSPO (heart, lungs and kidneys), there were no significant differences between lean and corpulent rats (Supplementary Fig. 1).

3.2. Immunohistochemical evidence of microglial activation in rodents with peripheral disease

Immunohistochemistry revealed activated microglial cells in the brains of 15 month old corpulent rats (Fig. 2A). We found no activated microglial cells in the brains of corpulent rats aged 9 months or in heterozygous (lean) rats at any age (9–15 months) examined.

In ApoE^{-/-} mice fed Paigen diet Iba1 immunohistochemistry revealed activated microglial cells (Fig. 2B). Microglia displaying thickened processes and increased levels of Iba1 were observed in multiple brain regions such as the cerebral cortex, striatum, hypothalamus, periventricular areas and meninges. Chow or Paigen-diet fed C57BL/6 control mice and chow-fed ApoE^{-/-} mice lacked activated brain microglia.

3.3. Atherogenic mice develop vascular inflammation and leucocyte infiltration in the brain

C57BL/6 or ApoE^{-/-} mice fed a chow diet did not show elevated vascular ICAM or VCAM expression in the brain. A trend for increased vascular ICAM and VCAM expression was observed in C57BL/6 mice fed the Paigen diet (not significant). In contrast, ICAM and VCAM expression was significantly augmented in ApoE^{-/-} mice on the Paigen diet (Fig. 3A and B). Increased VCAM staining was present mainly on medium sized or large blood vessels in the cerebral cortex, striatum, thalamus and hippocampus. Quantitative analysis of VCAM immunohistochemistry revealed significantly stronger staining in Paigen fed groups compared to chow diet ($P < 0.01$, data not shown). Post-hoc comparison revealed significant differences between ApoE^{-/-} chow and Paigen fed animals (Fig. 3C), but not in C57BL/6 mice, indicating that diet-induced pro-inflammatory changes are augmented in ApoE^{-/-} mice.

We also investigated the possibility that diet-induced atherosclerosis was associated with leucocyte infiltration into the brain parenchyma and ventricles, using immunofluorescent staining of the common leucocyte antigen CD45. Microglial CD45 expression was relatively dim throughout the brain and was well discriminated from that of bright and round shaped or elongated leucocytes. Profound enrichment of ventricular leucocytes was found in ApoE^{-/-} mice fed with Paigen diet, and this was associated with increased VCAM expression in the choroid plexus (Fig. 4A). Invasion of the choroid plexus by CD45-positive cells was significantly elevated in ApoE^{-/-} animals on the Paigen diet compared to ApoE^{-/-} animals on normal diet, but this was not observed in C57BL/6 mice fed with Paigen diet (Fig. 4B). In Paigen-fed ApoE^{-/-} mice, CD45-positive cells were numerous in the choroid plexus of the lateral ventricles from the *fimbria hippocampi* to the caudal areas of the ventricle. Caudally, infiltration of ventricular-associated cells into the surrounding parenchyma was also observed in ApoE^{-/-} mice (Fig. 4C). The size of the lateral ventricle was not significantly different among experimental groups and no correlation between CD45-positive cells and ventricle size was found in individual mice. The choroid plexus was found to contain a number of different cell types including granulocytes (identified by an anti-neutrophil serum, SJC) and CD3-positive T cells (Fig. 4D). Granulocytes represented a large proportion of the cells and were uniformly distributed along the VCAM-positive areas of the choroid plexus, in partial overlap with T cells. Activated microglia/macrophages lined the walls of the caudal lateral ventricle, showed increased CD45 expression (Fig. 4E).

3.4. Atherogenic diet results in focal lipid deposition and inflammation in ApoE^{-/-} mice

In peripheral tissues, particularly in large blood vessels, ApoE^{-/-} mice develop atherosclerotic plaques, as identified by lipid deposition, leucocyte infiltration and vascular stenosis (Stoll and Bendzus, 2006; Zadelaar et al., 2007). However, it is not known whether such focal vascular pathologies appear in the brain in these animals or not. In 40% of the Paigen fed ApoE^{-/-} mice, focal pathologies were observed in the brain parenchyma (typically in the hypothalamus, near the third ventricle). Oil red staining identified blood vessel-associated lipid deposition (Fig. 5A and B),

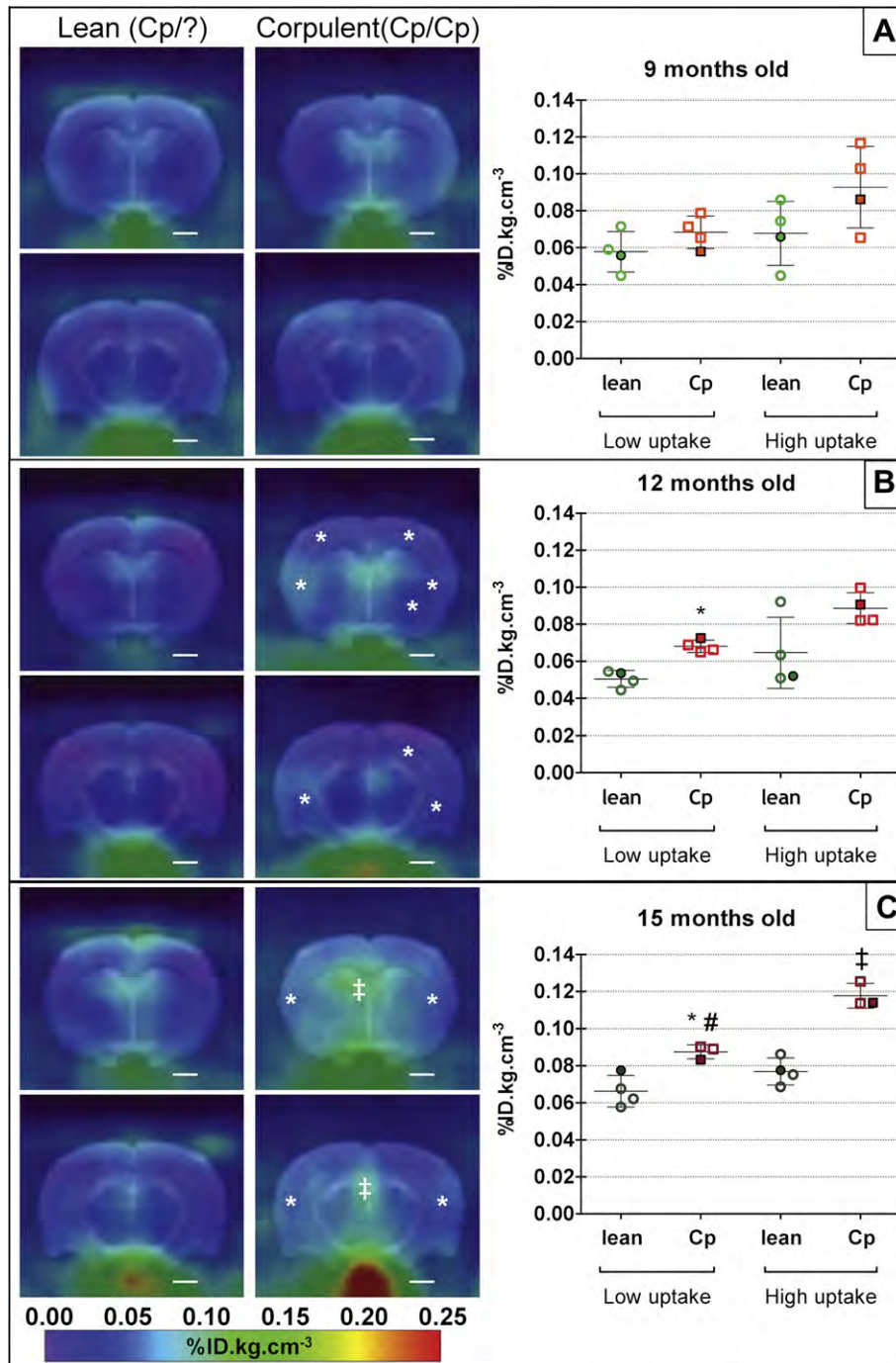


Fig. 1. Sum images (20–60 min post-injection; left panel) and respective quantification (graphs on the right panel) of $[^{18}\text{F}]\text{DPA-714}$ uptake in the brain of lean (+/?) and corpulent (*cp/cp*) rats at 9 (A), 12 (B) and 15 months (C) of age. * and ‡ indicate a significant difference between lean and corpulent animals of the same age in respectively low and high uptake regions of interest ($P < 0.05$, Mann–Whitney test). # indicates a significant difference between 9 (A) and 15 (B) months old animals ($P < 0.05$, Mann–Whitney test). Data are expressed as mean \pm SD (filled symbols correspond to the respective image on the left panel).

accompanied by microglial activation and leucocyte recruitment (identified by H&E), as well as CD45 and Iba1 staining (Fig. 5C). VCAM expression was increased focally around lipid rich areas and also in the ipsilateral wall of the third ventricle, indicating ongoing inflammatory responses in the brain (Fig. 5D).

3.5. PET imaging: pilot study reveals neuroinflammation in human subjects with risk factors for stroke

Peripheral inflammatory markers increased in both groups of subjects between screening and time of PET but remained higher

in the at risk group (Table 1). Visual inspection of the participants' BP_{ND} maps revealed increased $[^{11}\text{C}](\text{R})\text{-PK11195}$ binding in three of the subjects with increased risk factors (Fig. 6). The distribution of the $[^{11}\text{C}](\text{R})\text{-PK11195}$ signal showed individual differences and was seen across neocortical areas and other brain regions, including the thalamus and brain stem. There was no evidence of raised $[^{11}\text{C}](\text{R})\text{-PK11195}$ binding in periventricular or deep white matter regions. There was no pattern of activity in a particular vascular territory, as one might see with established stroke. These preliminary results indicate that neocortical inflammation is present in the brain of subjects with chronic

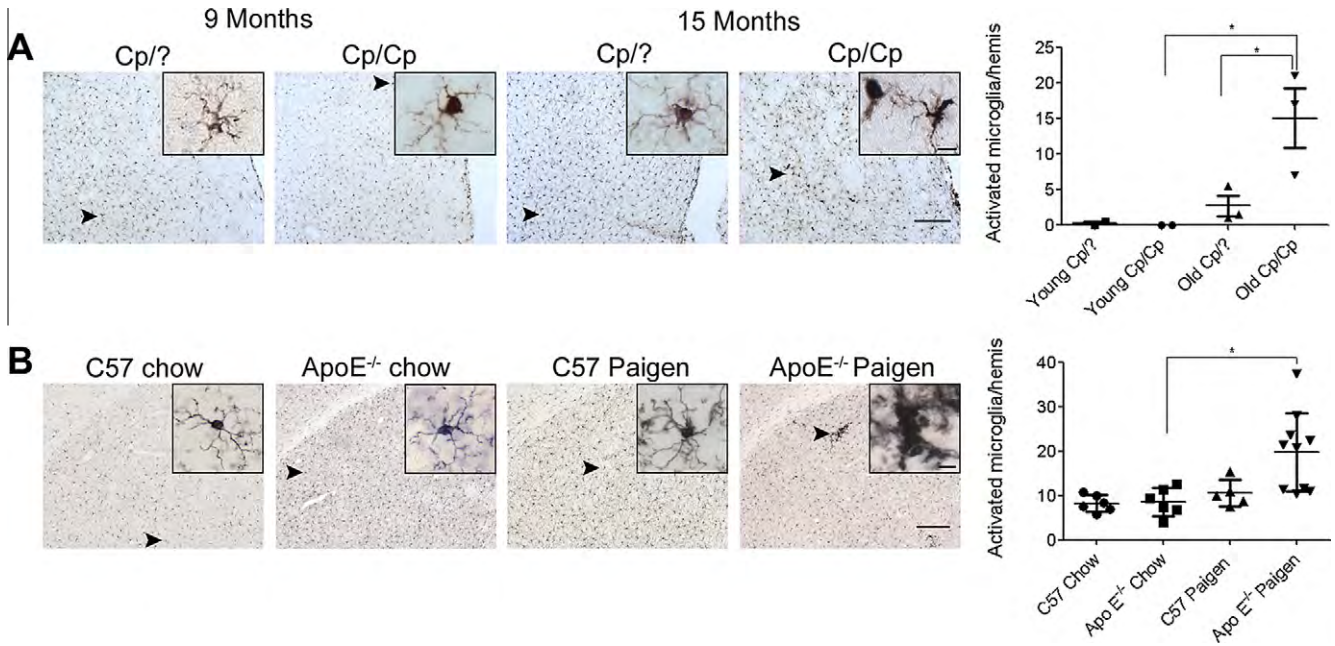


Fig. 2. Rodent models of atherosclerosis involve microglial activation in the brain. (A) Activated microglia as identified by increased Iba1 immunopositivity, thickened processes and irregular cell bodies were seen in the striatum of 15 month old corpulent rats, but not in 9 month old animals. Aged corpulent rats had a significantly increased number of activated microglia compared to young corpulent, or 15 month old heterozygous rats. (B) Activated, Iba1-positive microglia was numerous in ApoE^{-/-} mice fed a Paigen diet. Insets show representative images of microglial cells from the different groups of mice. Quantitative analysis revealed significantly more activated microglial cells in the striatum of ApoE^{-/-} mice fed a Paigen diet compared with ApoE^{-/-} mice fed chow diet. *P < 0.05. Scale bars: 200 and 10 μm (insets).

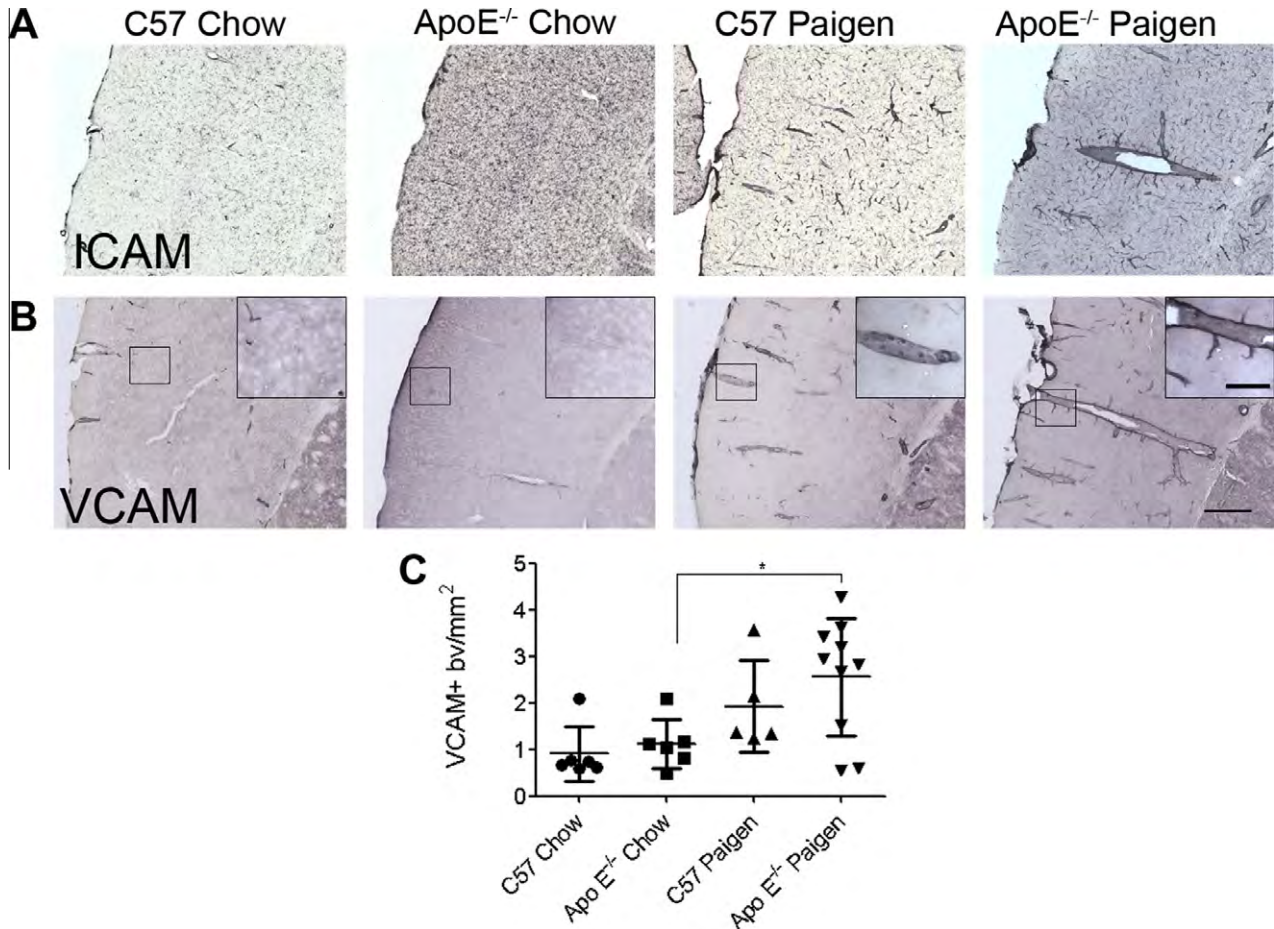


Fig. 3. Cerebrovascular activation occurs in the brain in association with peripheral atherosclerosis. Vascular activation was assessed in the cerebral cortex using immunostaining to the adhesion molecules (A) ICAM and (B) VCAM. Unlike mice fed a chow diet, mice fed a Paigen diet showed an increased number of ICAM and VCAM-positive blood vessels in the brain. (C) Quantitative analysis of VCAM-positive blood vessels in the cerebral cortex. Scale bars: 200 and 50 μm (inset).

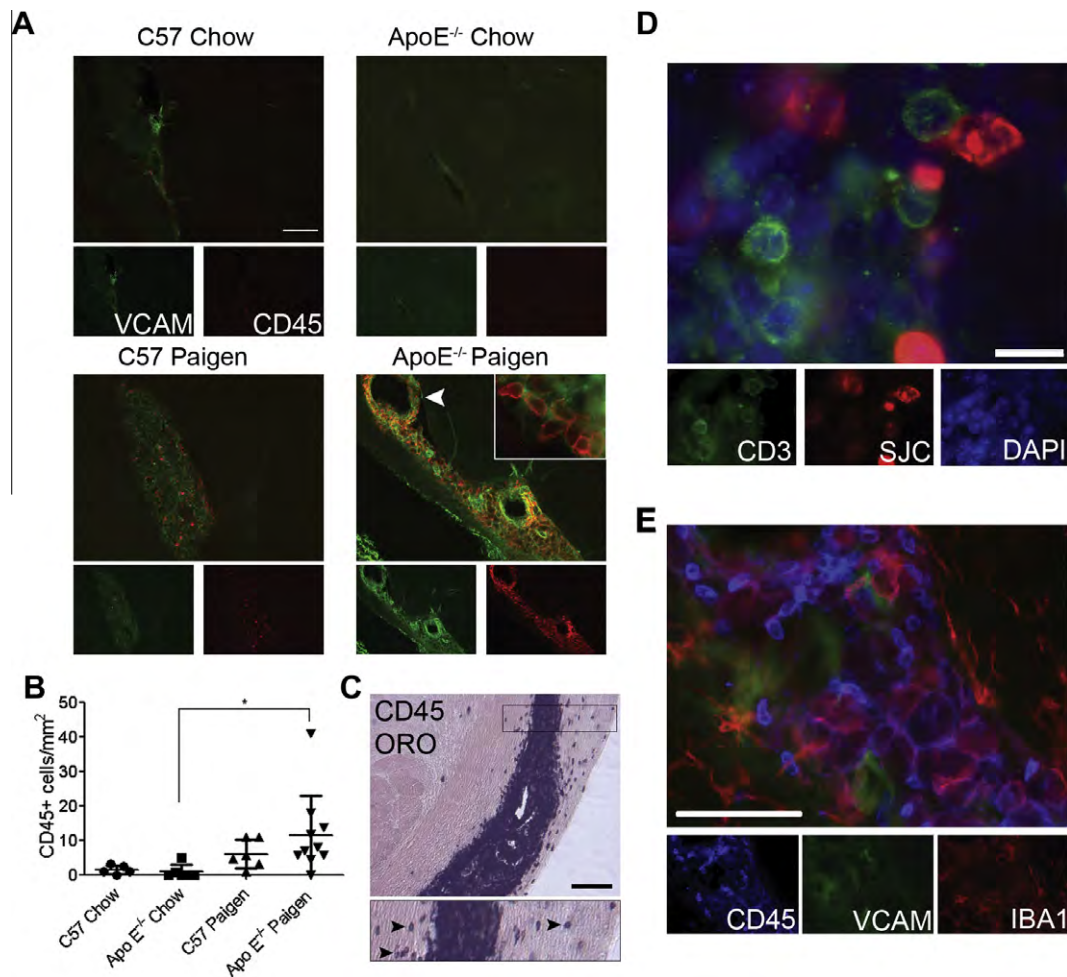


Fig. 4. Microglia/macrophages, granulocytes and T cells accumulate in the choroid plexus of the caudal lateral ventricle in response to peripheral atherosclerosis. (A) ApoE^{-/-} mice fed a Paigen diet show accumulation of CD45⁺ leucocytes (red) in the choroid plexus of the caudal lateral ventricle, which display increased VCAM (green) immunopositivity. (B) Quantification of CD45⁺ leucocytes in the choroid plexus of the lateral ventricles. (C) CD45-positive cells, which are numerous in the choroid plexus, also appear in the parenchyma (Oil red O counterstain) on both sides of the lateral ventricle (inset, arrowheads). (D) CD3 positive T cells (green) were found to accumulate in a partially overlapping area with granulocytes, identified with an anti-neutrophil serum (SJC, red). (E) A population of microglia/macrophages (Iba1, red) shows increased CD45 immunopositivity (blue) in the caudal choroid plexus among other CD45-positive leucocytes (possibly granulocytes). **P* < 0.05. Scale bars: A; 200 μ m; C; 100 μ m; D; 10 μ m and E; 50 μ m.

systemic inflammation, which is consistent with our findings in rodents with risk factors for stroke.

4. Discussion

Here we show that major risk factors for stroke such as atherosclerosis, hyperlipidemia and obesity, which involve chronic systemic inflammation, are associated with brain inflammation in relevant animal models and in a small cohort of humans, in the absence of any cerebrovascular events. These data suggest that systemic inflammation can drive brain inflammation prior to stroke presentation, leading to a “primed” inflammatory environment in the brain.

We used PET imaging to identify microglial activation, because these cells are early responders to pathological changes in the CNS and microglial activation is a hallmark of multiple brain diseases in patients and rodent models (Hanisch and Kettenmann, 2007; Teeling and Perry, 2009). The advantage of assessing neuroinflammation by *in vivo* PET imaging in rodents is that these measurements are comparable with clinical imaging data, and is therefore highly translatable to clinical settings. Both [¹¹C]PK11195 and [¹⁸F]DPA-714 bind to TSPO, but despite that [¹⁸F]DPA-714 has the

advantages of better signal to noise ratio (Chauveau et al., 2009) and the longer half-life of [¹⁸F], which allow PET imaging of 2–3 animal per batch of tracer, [¹⁸F]DPA-714 is not yet available for clinical use in our facilities. Corpulent rats exhibited focal areas of microglial activation, as assessed by increased [¹⁸F]DPA-714 binding *in vivo*. Increased TSPO-ligand binding was observed in various brain areas, including periventricular regions and some subcortical and cortical regions in the corpulent rats (Fig. 1B and C). Imaging data correlated well with the immunohistochemistry findings, which revealed an increase in the number of activated microglial cells. In line with the experimental data, the presence of [¹¹C](R)-PK11195 binding indicated neuroinflammation in subjects with multiple risk factors.

Microglial activation was also detected in several brain regions in atherosclerotic ApoE^{-/-} mice, indicating that neuroinflammation is likely to be a common link among animal models of chronic systemic inflammatory diseases. Although the exact mechanism of microglial activation needs to be further investigated, such “priming” of microglia in response to peripheral inflammatory changes has important implications to multiple cerebrovascular diseases. It is now established that microglia primed by central neurodegeneration or amyloidosis respond more vigorously to subsequent systemic or central inflammatory insults. For example, in a murine

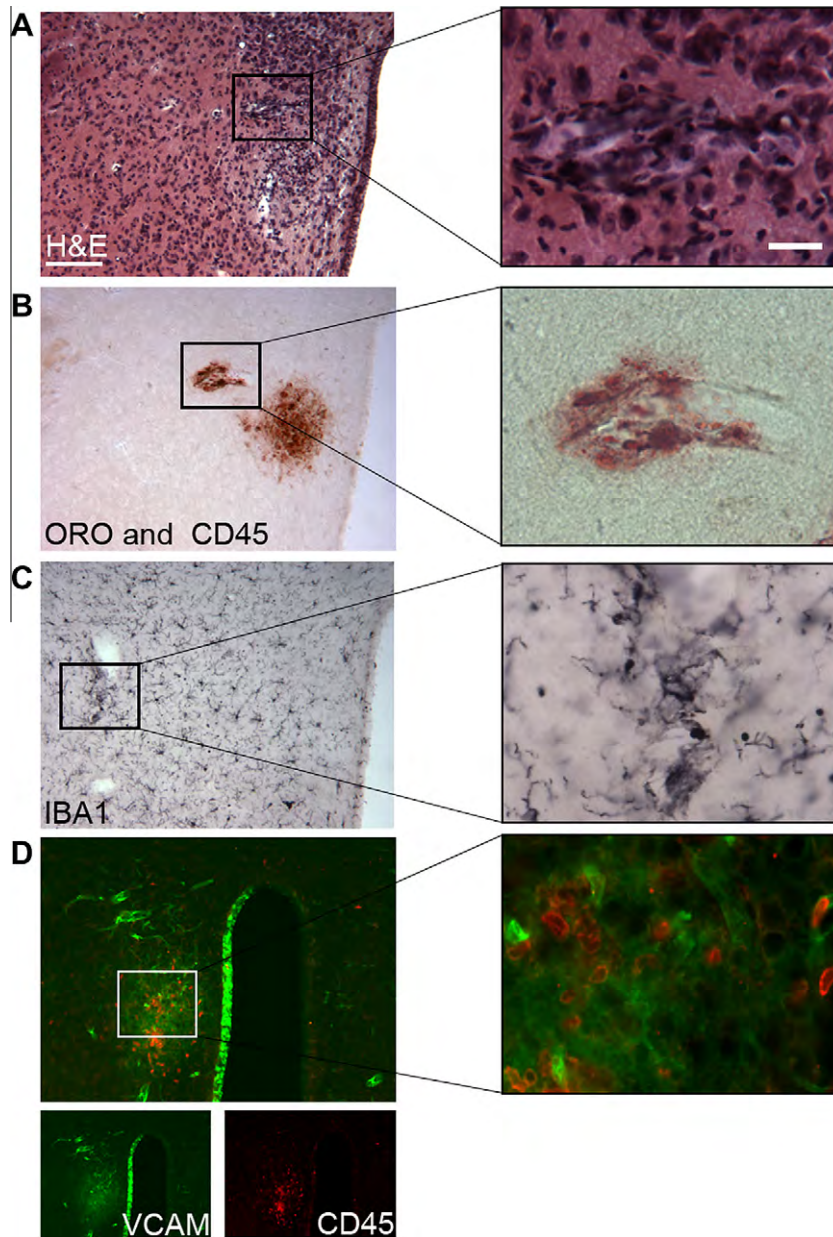


Fig. 5. Focal pathological changes are present in the brain in response to peripheral atherosclerosis. Haematoxylin & Eosin (H&E) staining (A) reveals vascular inflammation as indicated by dilated blood vessels and inflammatory infiltrates in the hypothalamus adjacent to the third ventricle in Paigen fed ApoE^{-/-} mice. Focal lipid deposition as identified by Oil red O staining is observed in the vicinity of perivascular CD45-positive leucocytes (B). This is associated with an increase in the number of activated, Iba1-positive microglia (C) recruitment of CD45⁺ cells (D, red) and focally upregulated VCAM immunostaining (D, green). VCAM expression is also seen in the ipsilateral wall of the third ventricle but not in the contralateral part. Parallel brain sections from a representative brain are shown. **P* < 0.05. Scale bars: 100 and 12.5 μm. (For interpretation of the references to colour in this figure legend, the reader is referred to the web version of this paper.)

model of prion disease, intracerebral or systemic LPS challenge induced augmented microglial activation and cytokine expression compared to control mice (Cunningham et al., 2005). Our data indicate that systemic influences are also capable of priming the inflammatory response of the brain. The presence of activated microglia and cerebrovascular inflammation may not only lead to irreversible neuroinflammatory alterations in the brain, but probably contribute to outcome if an ischaemic event occurs. Given that the vast majority of experimental stroke studies are undertaken in 'normal' animals with no underlying inflammation this might explain the lack of translation of potential treatments to the clinic.

We performed further characterisation of the vascular and cellular response in the brain of C57BL/6 and ApoE^{-/-} mice, to explore the possible effects of atherogenic diet on neuroinflammation.

Although the atherogenic "Paigen" diet alone reportedly induces inflammation in peripheral organs (Desai et al., 2008), we found significant vascular activation or enrichment of CD45-positive cells in the choroid plexus only in ApoE^{-/-} mice fed the Paigen diet, not in C57BL/6 mice. No sign of intraluminal plaques was observed in cerebral blood vessels in our study, which is in line with a report showing increased oxidative stress and endothelial dysfunction in cerebral arterioles in high-fat fed ApoE^{-/-} mice, but in the absence of atherosclerotic lesions (Kitayama et al., 2007).

Our results indicate that brain inflammation is associated with chronic systemic inflammation, and an atherogenic diet further augments this process. In Paigen-fed ApoE^{-/-} mice an increase in T lymphocytes in the choroid plexus at the areas of granulocyte recruitment was seen. A recent report in experimental autoimmune

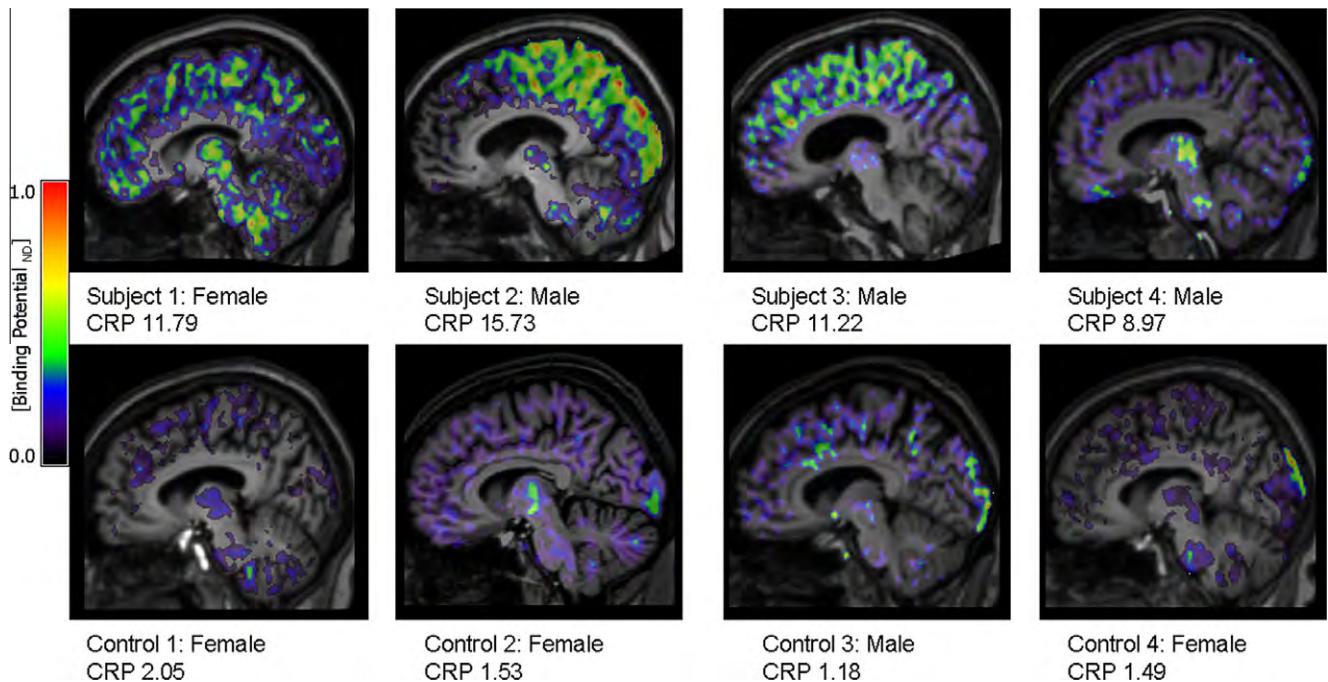


Fig. 6. [^{11}C](R)-PK11195 binding potential (BP_{ND}) images are shown for all subjects and control participants. Images are displayed on each subject's respective T1 MRI scan normalised to the SPM5 T1 brain template. The value for each individual's CRP at the time of PET scanning is also shown.

encephalomyelitis highlights a key role of interleukin-17-producing T helper cells in recruiting immune cells into the choroid plexus (Reboldi et al., 2009). It is intriguing to speculate, therefore, that our data also highlight the possibility that such a process may occur as a result of chronic systemic inflammation alone. Alternatively, the brain inflammation may be driven by metabolic disturbances alone without the need for systemic inflammation.

Some ApoE $^{-/-}$ mice fed a Paigen diet also displayed brain perivascular areas with focal lipid deposition and with microglial and vascular inflammation, similar to that seen in large peripheral blood vessels in these mice (Stoll and Bendszus, 2006; Zedelaa et al., 2007). Our data cannot confirm whether lipid deposition in the brain is a trigger of focal inflammatory changes or only a consequence of an ongoing inflammatory response. Nevertheless, we show that atherogenic diet is associated with focal inflammatory changes in the brain of animals that develop systemic vascular disease.

In summary, we demonstrate that chronic systemic inflammatory diseases, which are primary risk factors for stroke, are associated with inflammatory changes in the brain of rodents and humans. Our data support the existence of a causal relationship between systemic inflammation and brain inflammation that may contribute to stroke and other neurological disorders. An augmented inflammatory environment in the brain of stroke-prone individuals could aggravate post-ischaemic damage if stroke occurs and further studies will address this issue. Our translational approach has shown that appropriate co-morbid animal models exist that replicate important aspects of the stroke-prone state in humans, and that these co-morbid models could help facilitate translation from experimental studies to the clinic by providing a more realistic pre-clinical setting for testing novel therapies.

Conflict of interest

Prof. N. Rothwell is a non-executive director of AstraZeneca, but there was no involvement of the company in any of these studies.

Acknowledgments

The authors wish to thank Prof. Alan Jackson for support in MRI scanning and reporting the participants of our clinical study, Glaxo-SmithKline and more particularly Dr. A. Bifone for providing the rat brain MRI template used for co-registration with the PET images and the personnel of the Wolfson Molecular Imaging Centre for facilitating the PET scanning procedures, especially Messrs Mike Fairclough, Michael Green for their support of the preclinical study. Thanks to Dr. Federico Turkheimer (Imperial College London) for provision of the cluster analysis software used in the clinical study. Grateful thanks also to Drs. Daniel Anthony and Sandra Campbell, University of Oxford who kindly provided the anti-neutrophil serum (S.J.C.).

The clinical study was funded by the Sir Jules Thorn Charitable Trust.

Prof. N. Rothwell, Dr. H. Boutin and C. Drake are funded by MRC, UK. We are grateful for funding provided by the European Union's Seventh Framework Programme (FP7/2008–2013) under grant agreements Nos. 201024 and 202213 (European Stroke Network, NR, AD). This study was carried out within the EC-FP6 project DiMI (LSHB-CT-2005-512146) framework.

Investigators Francis and Crossman are funded by the BHF and the National Institute for Health Research (NIHR), UK. The Bioimaging Facility microscopes used in this study were purchased with grants from BBSRC, Wellcome and the University of Manchester Strategic Fund. Special thanks goes to Peter March, Jane Kott and Robert Fernandez for their help with the microscopy.

Appendix A. Supplementary data

Supplementary data associated with this article can be found, in the online version, at [doi:10.1016/j.bbi.2011.02.008](https://doi.org/10.1016/j.bbi.2011.02.008).

References

- Allan, S.M., Tyrrell, P.J., Rothwell, N.J., 2005. Interleukin-1 and neuronal injury. *Nat. Rev.* 5, 629–640.

- Amor, S., Puentes, F., Baker, D., van der Valk, P., 2010. Inflammation in neurodegenerative diseases. *Immunology* 129, 154–169.
- Anthony, D., Dempster, R., Fearn, S., Clements, J., Wells, G., Perry, V.H., Walker, K., 1998. CXC chemokines generate age-related increases in neutrophil-mediated brain inflammation and blood–brain barrier breakdown. *Curr. Biol.* 8, 923–926.
- Boellaard, R., 2009. Standards for PET image acquisition and quantitative data analysis. *J. Nucl. Med.* 50 (Suppl. 1), 11S–20S (Epub 2009 April 20).
- Boutin, H., Prenant, C., Galea, J., Greenhalgh, A., Julyan, P., Brown, G., Herholz, K., Rothwell, N., Kassiou, M., 2008. [18F]DPA-714: a new ligand for neuroinflammation, evaluation in a model of cerebral ischemia in rats. First World Molecular Imaging Congress, Program No. 0629.
- Chauveau, F., Van Camp, N., Dolle, F., Kuhnast, B., Hinnen, F., Damont, A., Boutin, H., James, M., Kassiou, M., Tavitian, B., 2009. Comparative evaluation of the translocator protein radioligands 11C-DPA-713, 18F-DPA-714, and 11C-PK11195 in a rat model of acute neuroinflammation. *J. Nucl. Med.* 50, 468–476.
- Coyle, P., 1984. Outcomes to middle cerebral artery occlusion in hypertensive and normotensive rats. *Hypertension* 6, 169–174.
- Cunningham, C., Wilcockson, D.C., Campion, S., Lunnion, K., Perry, V.H., 2005. Central and systemic endotoxin exacerbates ischemic brain damage via a CCL5 (regulated on activation, normal T-cell expressed and secreted)-mediated proinflammatory response in mice. *J. Neurosci.* 25, 9275–9284.
- Dandona, P., Aljada, A., Bandyopadhyay, A., 2004. Inflammation: the link between insulin resistance, obesity and diabetes. *Trends Immunol.* 25, 4–7.
- Denes, A., Humphreys, N., Lane, T.E., Grecnis, R., Rothwell, N., 2010a. Chronic systemic infection exacerbates ischemic brain damage via a CCL5 (regulated on activation, normal T-cell expressed and secreted)-mediated proinflammatory response in mice. *J. Neurosci.* 30, 10086–10095.
- Denes, A., Thornton, P., Rothwell, N.J., Allan, S.M., 2010b. Inflammation and brain injury: acute cerebral ischaemia, peripheral and central inflammation. *Brain Behav. Immun.* 24, 708–723.
- Desai, M.S., Mariscalco, M.M., Tawil, A., Vallejo, J.G., Smith, C.W., 2008. Atherogenic diet-induced hepatitis is partially dependent on murine TLR4. *J. Leukoc. Biol.* 83, 1336–1344.
- Di Napoli, M., Papa, F., 2003. Angiotensin-converting enzyme inhibitor use is associated with reduced plasma concentration of C-reactive protein in patients with first-ever ischemic stroke. *Stroke* 34, 2922–2929.
- Endres, M., Engelhardt, B., Koistinaho, J., Lindvall, O., Meairs, S., Mohr, J.P., Planas, A., Rothwell, N., Schwabinger, M., Schwab, M.E., Vivien, D., Wieloch, T., Dirnagl, U., 2008. Improving outcome after stroke: overcoming the translational roadblock. *Cerebrovasc. Dis.* 25, 268–278.
- Fisher, M., Feuerstein, G., Howells, D.W., Hurn, P.D., Kent, T.A., Savitz, S.I., Lo, E.H., 2009. Update of the stroke therapy academic industry roundtable preclinical recommendations. *Stroke* 40, 2244–2250.
- Fornage, M., Chiang, Y.A., O'Meara, E.S., Psaty, B.M., Reiner, A.P., Siscovick, D.S., Tracy, R.P., Longstreth Jr., W.T., 2008. Biomarkers of inflammation and MRI-defined small vessel disease of the brain: the cardiovascular health study. *Stroke* 39, 1952–1959.
- Franks, Z.G., Campbell, R.A., Weyrich, A.S., Rondina, M.T., 2010. Platelet–leukocyte interactions link inflammatory and thromboembolic events in ischemic stroke. *Ann. NY Acad. Sci.* 1207, 11–17.
- Hanisch, U.K., Kettenmann, H., 2007. Microglia: active sensor and versatile effector cells in the normal and pathologic brain. *Nat. Neurosci.* 10, 1387–1394.
- Hastings, D.L., Reader, A.J., Julyan, P.J., Zweit, J., Jeavons, A.P., Jones, T., 2007. Performance characteristics of a small animal PET camera for molecular imaging. *Nucl. Instrum. Methods Phys. Res. A* 573, 80–83.
- James, M.L., Fulton, R.R., Vercoullie, J., Henderson, D.J., Garreau, L., Chalou, S., Dolle, F., Costa, B., Guilloteau, D., Kassiou, M., 2008. DPA-714, a new translocator protein-specific ligand: synthesis, radiofluorination, and pharmacologic characterization. *J. Nucl. Med.* 49, 814–822.
- Keyes Jr., J.W., 1995. SUV: standard uptake or silly useless value? *J. Nucl. Med.* 36, 1836–1839.
- Kitayama, J., Faraci, F.M., Lentz, S.R., Heistad, D.D., 2007. Cerebral vascular dysfunction during hypercholesterolemia. *Stroke* 38, 2136–2141.
- Kleiber, M., 1947. Body size and metabolic rate. *Physiol. Rev.* 27, 511–541.
- Mangat, R., Su, J., Scott, P.G., Russell, J.C., Vine, D.F., Proctor, S.D., 2007. Chylomicron and apoB48 metabolism in the JCR:LA corpulent rat, a model for the metabolic syndrome. *Biochem. Soc. Trans.* 35, 477–481.
- Maroy, R., Boisgard, R., Comtat, C., Frouin, V., Cathier, P., Duchesnay, E., Dolle, F., Nielsen, P.E., Trebossen, R., Tavitian, B., 2008a. Segmentation of rodent whole-body dynamic PET images: an unsupervised method based on voxel dynamics. *IEEE Trans. Med. Imaging* 27, 342–354.
- Maroy, R., Boisgard, R., Comtat, C., Trebossen, R., Tavitian, B., 2008b. Fast and accurate PET preclinical data analysis: Segmentation and Partial Volume Effect correction with no anatomical priors. In: Nuclear Science Symposium Conference Record 2008, pp. 5498–5501.
- McColl, B.W., Allan, S.M., Rothwell, N.J., 2009. Systemic infection, inflammation and acute ischemic stroke. *Neuroscience* 158, 1049–1061.
- McColl, B.W., Rothwell, N.J., Allan, S.M., 2007. Systemic inflammatory stimulus potentiates the acute phase and CXC chemokine responses to experimental stroke and exacerbates brain damage via interleukin-1- and neutrophil-dependent mechanisms. *J. Neurosci.* 27, 4403–4412.
- Muir, K.W., Tyrrell, P., Sattar, N., Warburton, E., 2007. Inflammation and ischaemic stroke. *Curr. Opin. Neurol.* 20, 334–342.
- Reader, A.J., Ally, S., Bakatselos, F., Manavaki, R., Walledge, R.J., Jeavons, A.P., Julyan, P.J., Sha, Z., Hastings, D.L., Zweit, J., 2002. One-pass list-mode EM algorithm for high-resolution 3-D PET image reconstruction into large arrays. *IEEE Trans. Nucl. Sci.* 49, 693–699.
- Reboldi, A., Coisne, C., Baumjohann, D., Benvenuto, F., Bottinelli, D., Lira, S., Uccelli, A., Lanzavecchia, A., Engelhardt, B., Sallusto, F., 2009. C–C chemokine receptor 6-regulated entry of TH-17 cells into the CNS through the choroid plexus is required for the initiation of EAE. *Nat. Immunol.* 10, 514–523.
- Ridker, P.M., Danielson, E., Fonseca, F.A., Genest, J., Gotto Jr., A.M., Kastelein, J.J., Koenig, W., Libby, P., Lorenzatti, A.J., MacFadyen, J.G., Nordestgaard, B.G., Shepherd, J., Willerson, J.T., Glynn, R.J., 2008. Rosuvastatin to prevent vascular events in men and women with elevated C-reactive protein. *N. Engl. J. Med.* 359, 2195–2207.
- Ross, R., 1999. Atherosclerosis is an inflammatory disease. *Am. Heart J.* 138, S419–S420.
- Savoia, C., Schiffrin, E.L., 2006. Inflammation in hypertension. *Curr. Opin. Nephrol. Hypertens.* 15, 152–158.
- Schwarz, A.J., Danckaert, A., Reese, T., Gozzi, A., Paxinos, G., Watson, C., Merlo-Pich, E.V., Bifone, A., 2006. A stereotaxic MRI template set for the rat brain with tissue class distribution maps and co-registered anatomical atlas: application to pharmacological MRI. *Neuroimage* 32, 538–550.
- Stoll, G., Bendszus, M., 2006. Inflammation and atherosclerosis: novel insights into plaque formation and destabilization. *Stroke* 37, 1923–1932.
- Sugawara, Y., Zasadny, K.R., Neuhoff, A.W., Wahl, R.L., 1999. Reevaluation of the standardized uptake value for FDG: variations with body weight and methods for correction. *Radiology* 213, 521–525.
- Teeling, J.L., Perry, V.H., 2009. Systemic infection and inflammation in acute CNS injury and chronic neurodegeneration: underlying mechanisms. *Neuroscience* 158, 1062–1073.
- Terao, S., Yilmaz, G., Stokes, K.Y., Ishikawa, M., Kawase, T., Granger, D.N., 2008. Inflammatory and injury responses to ischemic stroke in obese mice. *Stroke* 39, 943–950.
- Turkheimer, F.E., Edison, P., Pavese, N., Roncaroli, F., Anderson, A.N., Hammers, A., Gerhard, A., Hinz, R., Tai, Y.F., Brooks, D.J., 2007. Reference and target region modeling of [11C]-(R)-PK11195 brain studies. *J. Nucl. Med.* 48, 158–167.
- van Dijk, E.J., Prins, N.D., Vermeer, S.E., Vrooman, H.A., Hofman, A., Koudstaal, P.J., Breteler, M.M., 2005. C-reactive protein and cerebral small-vessel disease: the Rotterdam Scan Study. *Circulation* 112, 900–905.
- Vannucci, S.J., Willing, L.B., Goto, S., Alkayed, N.J., Brucklacher, R.M., Wood, T.L., Towfighi, J., Hurn, P.D., Simpson, I.A., 2001. Experimental stroke in the female diabetic, db/db, mouse. *J. Cereb. Blood Flow. Metab.* 21, 52–60.
- Zadelaar, S., Kleemann, R., Verschuren, L., de Vries-Van der Weij, J., van der Hoorn, J., Princen, H.M., Kooistra, T., 2007. Mouse models for atherosclerosis and pharmaceutical modifiers. *Arterioscler. Thromb. Vasc. Biol.* 27, 1706–1721.

Interleukin-1 Mediates Neuroinflammatory Changes Associated With Diet-Induced Atherosclerosis

Adam Denes, PhD*; Caroline Drake, PhD*; Jing Stordy, PhD*; Janet Chamberlain, PhD; Barry W. McColl, PhD; Hermann Gram, PhD; David Crossman, MD; Sheila Francis, PhD; Stuart M. Allan, PhD; Nancy J. Rothwell, PhD

Background—Systemic inflammation contributes to brain pathology in cerebrovascular disease through mechanisms that are poorly understood.

Methods and Results—Here we show that atherosclerosis, a major systemic inflammatory disease, is associated with severe cerebrovascular inflammation in mice and that this effect is mediated by the proinflammatory cytokine interleukin-1 (IL-1). Apolipoprotein E-deficient mice fed Paigen or Western diets develop vascular inflammation, microglial activation, and leukocyte recruitment in the brain, which are absent in apolipoprotein E-deficient mice crossed with IL-1 type 1 receptor-deficient mice. Systemic neutralization of IL-1 β with an anti-IL-1 β antibody reversed aortic plaque formation (by 34% after a Paigen and 45% after a Western diet) and reduced inflammatory cytokine expression in peripheral organs. Central, lipid accumulation-associated leukocyte infiltration into the choroid plexus was reversed by IL-1 β antibody administration. Animals fed a Western diet showed 57% lower vascular inflammation in the brain than that of mice fed a Paigen diet, and this was reduced further by 24% after IL-1 β antibody administration.

Conclusions—These results indicate that IL-1 is a key driver of systemically mediated cerebrovascular inflammation and that interventions against IL-1 β could be therapeutically useful in atherosclerosis, dementia, or stroke. (*J Am Heart Assoc.* 2012;1:e002006 doi: 10.1161/JAHA.112.002006.)

Key Words: interleukin-1 • atherosclerosis • cerebrovascular inflammation • leukocyte • microglia

Inflammation is a key driver of cardiovascular and cerebrovascular disease, including atherosclerosis, and contributes to diseases such as myocardial infarction, stroke, and dementia. These diseases share common risk factors, such as obesity, hypertension, and diabetes,^{1,2} that are associated with inflammation. In patients, a clear association exists between cardiovascular risk factors or carotid atherosclerosis and dementia, progression of Alzheimer's disease, or depression.³⁻⁵ Animal studies demonstrate that peripheral inflammatory conditions are associated with increased neuroinflammatory responses in the brain and enhanced damage in response to experimentally induced stroke.⁶⁻⁹

From the Faculty of Life Sciences, University of Manchester, Manchester, UK (A.D., C.D., S.M.A., N.J.R.); the Department of Cardiovascular Science, Medical School, University of Sheffield, Sheffield, UK (J.S., J.C., D.C., S.F.); The Roslin Institute and R(D)SVS, University of Edinburgh, UK (B.W.M.); Norwich Medical School, University of East Anglia, Norwich, UK (D.C.); and Novartis Institutes of BioMedical Research, Basel, Switzerland (H.G.)

*Authors A. Denes, C. Drake and J. Stordy contributed equally to this article.

Correspondence to: Dr. Stuart M. Allan, AV Hill Building, Oxford Rd, Manchester, M13 9PT. E-mail: stuart.allan@manchester.ac.uk

Received April 3, 2012; accepted May 3, 2012.

© 2012. The Authors. Published on behalf of the American Heart Association, Inc., by Wiley-Blackwell. This is an Open Access article under the terms of the Creative Commons Attribution Noncommercial License, which permits use, distribution, and reproduction in any medium, provided the original work is properly cited and is not used for commercial purposes.

Interleukin (IL)-1 is a key contributor to a diverse range of diseases, demonstrated by the beneficial effects of blocking endogenous IL-1 in experimental models, most commonly with the IL-1 receptor antagonist (IL-1Ra).¹⁰ Evidence indicates that IL-1 contributes to peripherally induced neuroinflammatory diseases. Mice that lack IL-1 type 1 receptor (IL-1R1), when subjected to experimental autoimmune encephalomyelitis, show significantly reduced neuroinflammation, as indicated by a reduction in vascular adhesion molecule (VCAM)-1 and infiltrating immune cells.¹¹ IL-1 expression is increased in human coronary arteries affected by atherosclerosis^{12,13} and is also associated with arterial inflammation, oxidative stress, and increased blood pressure.¹⁴

In apolipoprotein E-knockout (ApoE^{-/-}) mice fed high-fat diets, atheroma development is related to the composition of the diet; a high-fat, high-cholesterol (Paigen) diet produces the largest effect.¹⁴ Genetic deletion of IL-1R1 in ApoE^{-/-}, Paigen diet-fed mice (ApoE^{-/-}/IL-1R1^{-/-}) markedly reduces inflammatory responses in the periphery.¹⁴ Similar results were seen in Paigen diet-fed ApoE^{-/-} mice treated with a neutralizing antibody to IL-1 β .¹⁵ These findings suggest that IL-1 mediates the effects of high-fat diets on peripheral vascular atherosclerotic pathology.

Our recent studies show increased cerebrovascular and brain inflammation in ApoE^{-/-} mice fed an atherogenic

high-fat diet, though the mechanisms of this response are not known.⁶ The primary objective of the present study was to test the hypothesis that the neuroinflammatory responses associated with atherosclerosis induced by high-fat feeding in susceptible (ApoE^{-/-}) mice is mediated by IL-1. To address this, we determined the neuroinflammatory response to fat feeding in ApoE^{-/-}/IL-1R1^{-/-} mice and the effect of immunoneutralization of IL-1 β on peripheral and central pathology in atherogenic mice.

Methods

Animals

Experiments were carried out in male ApoE^{-/-} (JAX 2052, Jackson Laboratories, Bar Harbor, Maine, USA) and ApoE^{-/-}/IL-1R1^{-/-} mice, the latter generated as described previously.¹⁴ Both strains were bred in house at the University of Sheffield, UK, were allowed free access to food and water, and were maintained under temperature-, humidity-, and light-controlled conditions. All animal procedures adhered to the UK Animals (Scientific Procedures) Act (1986).

Ten-week-old mice were fed a control (4.3% fat, 0.02% cholesterol), Paigen (18.5% fat, 0.9% cholesterol, 0.5% cholate, 0.26% sodium), or Western (21% fat, 0.15% cholesterol, 0.03% cholate, 0.296% sodium) diet for a period of 8 weeks, as described previously.¹⁴ Body weight was recorded weekly, and, as a measure of well-being and overall fitness, voluntary wheel running activity was assessed. Blood pressures were recorded weekly by using a Visitech tail cuff system, as previously described.¹⁴ At the end of the experimental period, blood was taken from the heart, before transcardial perfusion. Brain, liver, and spleen samples were taken and prepared as described previously,^{6,16} and the aortae were fixed and harvested for en face Oil Red O staining and aortic root analysis.¹⁴

Treatment

Mice were dosed with an anti-mouse anti-IL-1 β or anti-cyclosporin A isotype control antibody^{17,18} according to weight (10 mg/kg IP).

Cytokine Measurements

Eleven cytokines were measured in plasma (at weeks 0, 4, and 8), liver homogenates, and spleen homogenates: tumor necrosis factor- α , RANTES (CCL5), monocyte chemoattractant protein-1 (CCL2), KC (CXCL1), IL-6, IL-1 β , IL-1 α , IL-17 α , interferon- γ , granulocyte-colony stimulating factor, and IL-10. These were measured with appropriate Cytometric Bead Array Flex Sets (BD Biosciences, UK) according to the manufacturer's protocol. Protein concentrations were calculated by bicinchoninic acid assay (Pierce/Thermo Fisher Scientific, UK).

Assessment of Vascular and Microglial Activation by Immunohistochemistry

Immunohistochemistry for vascular (VCAM) and microglial ionized calcium binding adaptor molecule 1 (Iba1) activation was performed on free-floating brain sections. Endogenous peroxidase activity and blocking treatment were performed as stated previously. Primary antibody incubation was performed overnight with goat anti-mouse VCAM-1 1:250 (R&D Systems, Abingdon, UK) or rabbit anti-Iba1 1:1000 (Wako Chemicals, Nuss, Germany). Sections were then incubated in appropriate biotinylated secondary antibody for 1 hour (rabbit anti-goat 1:1000 and goat anti-rabbit 1:750, Vector Laboratories, UK), followed by Vectastain ABC solution (Vector Laboratories, UK), before visualization with nickel-enhanced diaminobenzidine (50 mg/mL) (Vector Laboratories, UK). Sections were mounted onto gelatin-coated slides and dehydrated, and coverslips were applied with Depex (Fisher, UK). Images were collected on an Axiocam color charge-coupled device camera (Zeiss, Germany) upright microscope with 10 \times and 20 \times objectives and were captured by a Coolsnap ES camera (Photometrics, Tucson, Arizona, USA) through Axiovision software (Zeiss, Germany).

Assessment of Leukocyte Recruitment in the Brain

Double immunofluorescence was performed to detect leukocytes (CD45) and vascular activation (VCAM) on free-floating brain sections. After blocking in 2% normal donkey serum (Vector Laboratories, Burlingame, CA), sections were incubated overnight at 4 $^{\circ}$ C with primary antibodies: rat anti-mouse CD45 1:200 (Serotec, UK) and goat anti-mouse VCAM-1 1:250 (R&D Systems). The antigens were visualized with the adequate fluorochrome-conjugated (Alexa 594 1:750 or Alexa 488 1:500, Molecular Probes, Eugene, OR) secondary donkey anti-sera for 2 hours at room temperature. Sections were mounted onto gelatin-coated slides and coverslipped with Vectashield mounting medium containing diamidinophenylindole (DAPI, Vector Laboratories, Burlingame, CA).

Images were collected on an Olympus BX51 upright and captured by a Coolsnap ES camera (Photometrics, UK) through MetaVue Software (Molecular Devices, UK).

Histology

Oil Red O staining combined with CD45 immunohistochemistry was performed as described earlier.⁶

Quantitative Analysis

All analyses were performed blinded. VCAM-positive blood vessels were counted in 3 random fields of view for each

section (typically 8 to 10) containing rostral-caudal cerebral cortex. A score for the whole brain was obtained by averaging individual counts and was expressed as positive blood vessels per square millimeter. Activated microglia were identified as showing: (1) increased Iba1 immunopositivity, (2) enlarged or amoeboid cell body, and (3) complete or partial loss of thin, elongated processes. Round, small Iba1-positive cells with leukocyte morphology were not counted. Activated microglia were counted throughout the striatum and expressed as activated microglia per square millimeter. Fluorescently labeled CD45-positive cells were counted in the caudal choroid plexus (−1.82 mm from bregma) and the lateral ventricle (−1.58 mm from bregma). The choroid plexus and ventricular ependyma were visualized by VCAM immunofluorescence. Data on the control mice used to evaluate CD45, VCAM, and Iba1 staining in ApoE^{−/−}/IL-R1^{−/−} have been published previously.⁶

Statistical Analysis

Normal distribution of experimental data was examined by Shapiro-Wilk normality test. Only a minority of data sets did not pass the normality test (see Results), in which cases appropriate nonparametric tests (Mann-Whitney test for 2 groups and Kruskal-Wallis test followed by Dunn multiple-comparison test for ≥3 groups) also were performed. When normality of the data had been confirmed, comparisons between 2 experimental groups were made with unpaired *t* tests. Data from 4 groups (ApoE^{−/−}/IL-R1^{−/−} experiment) were analyzed by one-way analysis of variance (ANOVA), followed by Bonferroni multiple-comparison post-test with GraphPad Prism 5 software. Two-way ANOVA was used to determine the overall effect of diet and IL-1β on the levels of vascular and microglial activation and recruitment of CD45-positive cells. Body weight changes were analyzed by repeated-measures ANOVA. Blood pressure measurements were analyzed by global nonlinear regression (to fit blood pressure data over a defined period of time for a group of animals), followed by an F test (GraphPad Prism 5). Data are presented as mean±SEM. A probability of <5% was regarded as statistically significant.

Results

Neuroinflammation in Atherosclerotic ApoE^{−/−} Mice Is Abolished in ApoE^{−/−}/IL-R1^{−/−} Mice

Diet-induced atherosclerosis in ApoE^{−/−} mice was associated with marked neuroinflammatory responses in the brain, which were abolished in animals in which the IL-1 receptor was deleted. Specifically, in ApoE^{−/−}/IL-R1^{−/−} mice fed a Paigen diet, microglial activation was significantly reduced compared to ApoE^{−/−} mice fed a Paigen diet and was similar to that of mice fed a control diet (Figure 1A and 1D). VCAM-1 was upregulated throughout the brain in ApoE^{−/−} mice fed a Paigen diet,

whereas there was little or no evidence of vascular activation in ApoE^{−/−}/IL-R1^{−/−} mice fed a Paigen diet, and in these animals vascular activation was comparable to that of mice fed a control diet and was significantly lower than in ApoE^{−/−} mice fed a Paigen diet (Figure 1B and 1E). The enhanced leukocyte accumulation in ApoE^{−/−} mice fed a Paigen diet was reversed in ApoE^{−/−}/IL-R1^{−/−} mice to levels comparable to the mice fed a control diet (Figure 1C and 1F). The marked decline in voluntary physical activity in ApoE^{−/−} mice was also reversed by genetic deletion of the IL-1 receptor in the ApoE^{−/−}/IL-R1^{−/−} mice (Figure 1G).

Neutralization of IL-1β Reduces Atherosclerotic Lesion Size in ApoE^{−/−} Mice Fed a High-Fat Diet

Peripheral administration of an anti-IL-1β antibody successfully neutralized IL-1β (an average 89% reduction in IL-1 concentrations) in all organs where IL-1β expression was detectable, regardless of diet (Figure 2).

Lesion coverage in the descending aorta was reduced significantly in IL-1β antibody-treated mice fed either a Paigen or a Western diet, as compared to control mice (by 34% and 45% respectively; Figure 3A and 3B). Mice treated with IL-1β antibody had significantly smaller lesion areas after having been fed the Paigen diet, as compared to control antibody-treated mice (Figure 3D). There was no diet-dependent difference in lesion size or percentage coverage in either the IL-1β or control antibody treatment groups. Treatment with IL-1β antibody had no statistically significant effect on systemic blood pressure in mice fed either diet (data and statistical analysis are not shown).

IL-1 neutralization reversed the weight loss in mice fed a Paigen diet over the course of the study period (*P*<0.001), whereas there was no difference in the body weight of mice fed a Western diet, with or without intervention (Figure 1).

IL-1β Neutralization Reduces Peripheral Inflammation

Consistent with the markedly reduced IL-1β levels described above, IL-1α was also reduced significantly (37%) in the livers of mice fed the Paigen diet and in the spleens of mice fed the Western diet (42%; Figure 4), but no significant reduction was seen in the spleens of mice fed a Paigen diet and in the livers of mice fed a Western diet. IL-1β neutralization also reduced hepatic concentrations of CCL2 (33%) in mice fed a Paigen diet and interleukin-6 (80%) and CXCL1 (79%) levels in spleens from mice fed a Western diet (Figure 4). No significant differences were observed in CCL2, interleukin-6, or CXCL1 levels in other organs in mice fed a Paigen or Western diet. Levels of IL-17, interferon-γ, IL-10, or tumor necrosis factor-α were mostly below the detection limit of the assay or the results were inconsistent; therefore, no significant effect of IL-1β neutralization

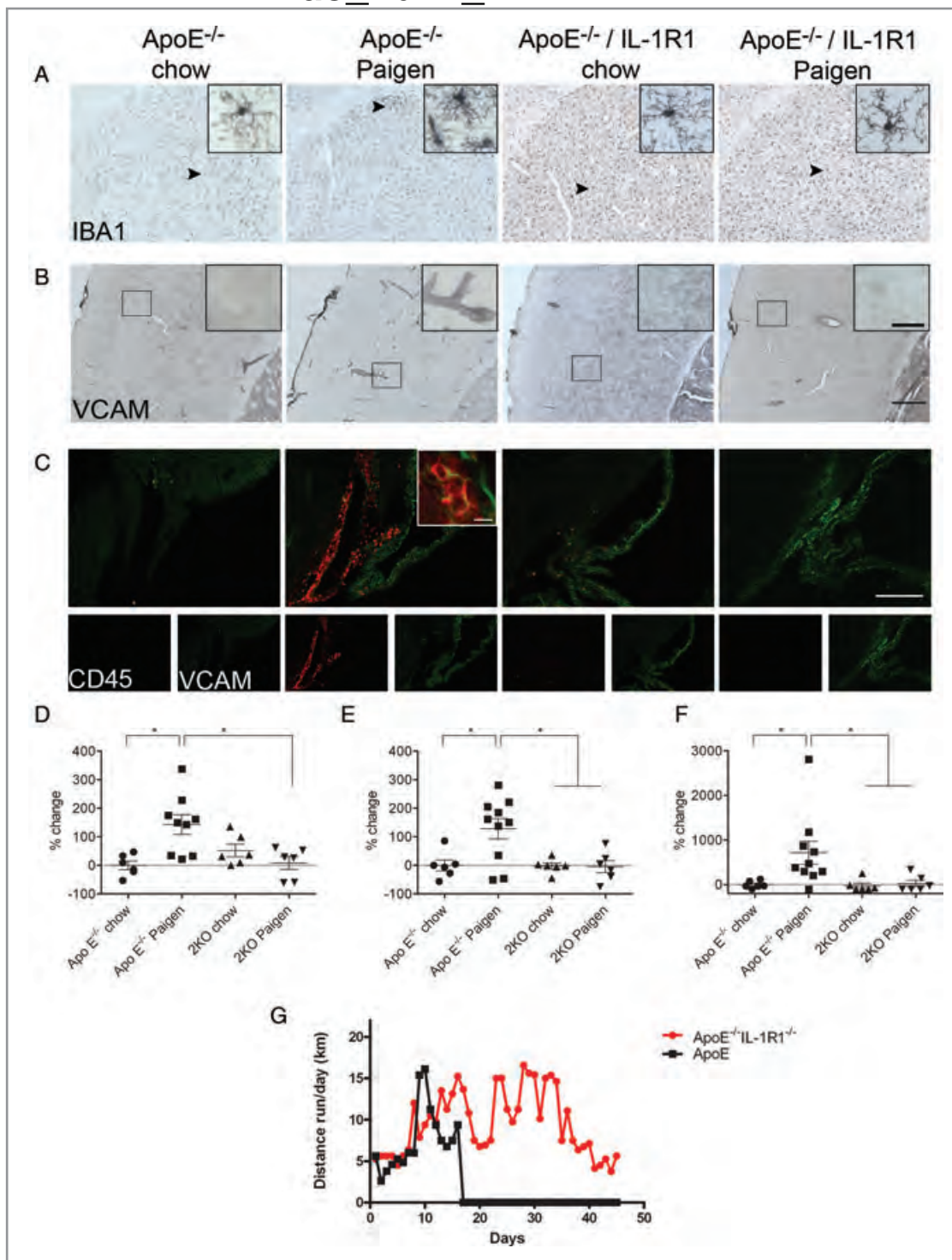


Figure 1. Vascular activation, microglial activation, and leukocyte accumulation are reduced in ApoE^{-/-}/IL-1R1^{-/-} mice fed a Paigen diet. Activated microglia as identified by increased Iba1 immunopositivity, thickened processes, and irregular cell bodies were seen in ApoE^{-/-} mice fed a Paigen diet. Microglial activation was significantly reduced, to control levels, in ApoE^{-/-}/IL-1R1^{-/-} mice fed a Paigen diet (A). Vascular activation was assessed through the immunostaining of the adhesion molecule VCAM. Atherosclerotic ApoE^{-/-} mice show increased vascular activation, which is significantly reduced in ApoE^{-/-}/IL-1R1^{-/-} mice fed a Paigen diet (B). Leukocyte accumulation as shown by CD45 immunostaining was increased in ApoE^{-/-} mice fed a Paigen diet. Leukocyte accumulation was significantly reduced, to control levels, in ApoE^{-/-}/IL-1R1^{-/-} mice fed a Paigen diet (C). D, Quantification of Iba1-positive microglia. E, Quantification of VCAM-positive blood vessels. F, Quantification of CD45-positive leukocytes. The “vehicle” data in F were not normally distributed; therefore, in addition to one-way ANOVA ($P=0.017$) followed by Bonferroni multiple-comparison post-test, nonparametric Kruskal-Wallis test ($P=0.0065$) followed by Dunn multiple-comparison test also were performed. Post-hoc comparisons gave identical results. A through F: $n=6-10$. G, Voluntary wheel running actogram for ApoE^{-/-} and ApoE^{-/-}/IL-1R1^{-/-} mice ($n=2-3$). Error bars represent standard error, $*P<0.05$. Scale bars: 200 μm (A through C) and 10 μm (inset in C).

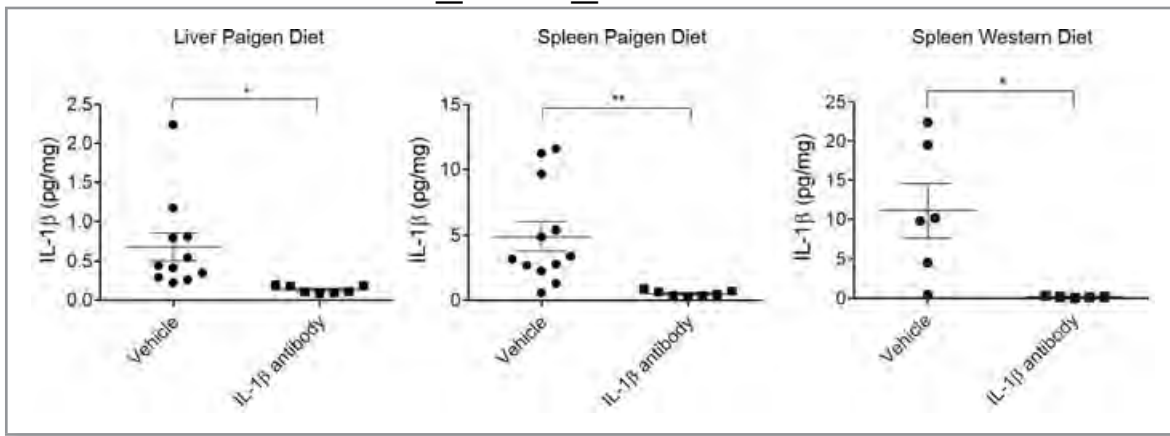


Figure 2. Neutralization of IL-1 β in anti-IL-1 β antibody-treated mice. Cytokines were measured by Cytometric Bead Array. IL-1 β was neutralized in the livers and spleens of ApoE $^{-/-}$ mice fed a Paigen diet and in the spleens of mice fed a Western diet, as compared with mice treated with control antibody. Error bars represent standard error, * $P < 0.05$ and ** $P < 0.01$ vs ApoE $^{-/-}$ mice treated with a control antibody ($n = 7-11$).

was observed. The lack of statistical significance might be a result of underpowered analysis in some cases.

IL-1 β Neutralization Attenuates Vascular Activation in ApoE $^{-/-}$ Mice Fed a Western Diet

Microglial and vascular activation have been reported previously in the brains of atherosclerotic ApoE $^{-/-}$ mice fed a Paigen diet, but no information is available on mice fed a Western diet. Mice fed a Paigen diet showed microglial activation that was 41% higher than in mice fed a Western diet (Figure 5). Microglial activation was observed in the cerebral cortex, striatum, periventricular areas, and meninges, as reported previously.⁶ The number of activated microglial cells in mice fed a Paigen or Western diet was not different after IL-1 β neutralization (Figure 5). Mice fed the cholate-free, high-fat, Western diet showed a 57% reduction in vascular activation when compared to mice fed a Paigen diet, as indicated by a lower number of VCAM-positive blood vessels (Figure 6B and 6C). IL-1 β neutralization had no significant effect on vascular activation in ApoE $^{-/-}$ mice fed a Paigen diet, although a trend toward reduced activation was observed (the lack of statistical significance might be a result of underpowered analysis). In contrast, the neutralization of IL-1 β significantly reduced (24%) vascular activation in mice fed a Western diet (Figure 6B and 6C).

IL-1 β Neutralization Attenuates the Accumulation of CD45+ Leukocytes in ApoE $^{-/-}$ Mice in the Lateral Ventricle

Diet-dependent leukocyte accumulation was assessed in coronal brain sections and was found to occur in 2 different regions of the lateral ventricle (Figure 7A and 7D). Mice fed a Paigen diet showed increased leukocyte accumulation, principally in

an area of the dorsal lateral ventricle between the hippocampus and the thalamus, as previously shown.⁶ Treatment with the anti-IL-1 β antibody significantly ($P < 0.05$) attenuated the number of leukocytes accumulating in the dorsal lateral ventricle in response to the Paigen diet (Figure 7A). In contrast, mice fed a Western diet showed little accumulation of leukocytes in this region of the lateral ventricle as compared to mice fed the Paigen diet (Figure 7B). The accumulation of leukocytes was found to extend ventrally to the choroid plexus of the ventricular space in mice fed a Paigen diet (Figure 7C), and mice fed a Western diet also show increased leukocyte infiltration in this ventral region, though numbers are reduced compared to the Paigen diet-fed mice (Figure 7D). Overall, the anti-IL-1 β antibody reduced leukocyte accumulation in the ventral ventricle independently of diet, as compared to control antibody ($P < 0.05$, two-way ANOVA).

Atherogenic Diet Results in Lipid Accumulation in the Brain, and IL-1 β Neutralization Reduces Lipid-Associated Inflammation in the Lateral Ventricle

We have previously reported that mice fed a Paigen diet display focal lipid deposition and inflammation in the brain parenchyma.⁶ In the present study, the number of focal pathologies was relatively low in the parenchyma and was not affected by IL-1 β neutralization. However, Oil Red O staining revealed lipid accumulation in the lateral ventricle in mice fed a Paigen diet, which was associated with recruitment of CD45-positive cells and microglial activation (Figure 8A Through 8F). Lipid accumulation and inflammation were observed in the choroid plexus, the lumen of the dorsal (rostral) and ventral (caudal) parts of the lateral ventricle, and both the thalamic and hippocampal ventricular walls near the ependyma (Figure 8A Through 8C). Lipid

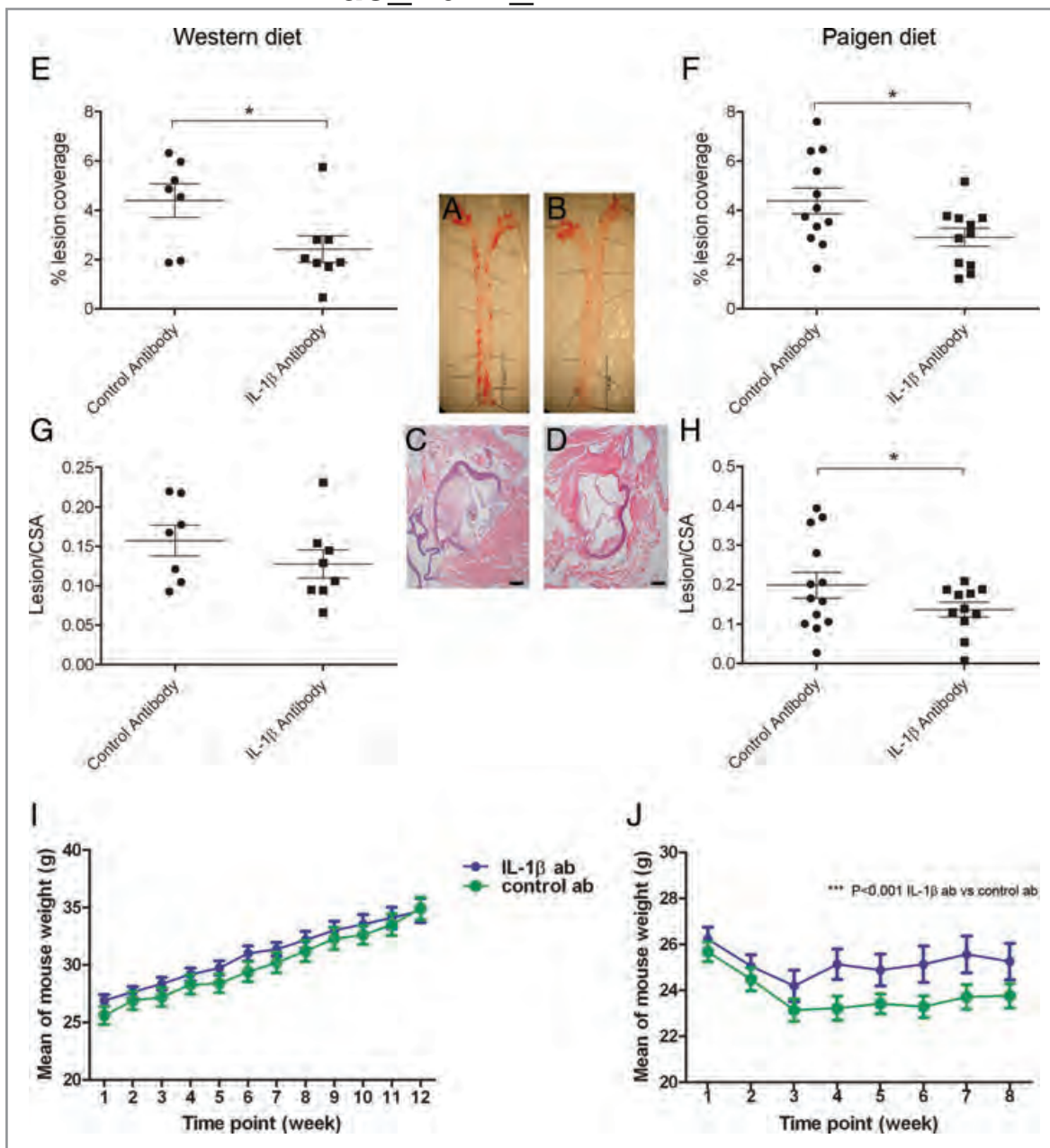


Figure 3. Atherosclerotic burden is reduced after treatment with an IL-1 β antibody. Atherosclerosis was assessed by Oil Red O staining of whole aortae and histology of lesions at aortic roots. Inset (A through D), Representative histology from Paigen diet-fed mice. Whole aortae in A (control antibody) and B (IL-1 β antibody), with en face Oil Red O staining; aortic root in C (control antibody) and D (IL-1 β antibody), with Miller's elastic van Gieson staining. Reduction in percent coverage of lesions in aortae from ApoE^{-/-} mice fed a Western (E) and Paigen diet (F) with and without antibody treatment (both * $P < 0.05$). Aortic root lesion size in mice fed a Western (G) and Paigen (H) diet (* $P < 0.05$) when treated with an IL-1 β antibody. Body weight changes in mice fed a Western (I) or Paigen (J) diet over the course of the study. Scale bars: 0.5 mm (A and B) and 50 μ m (C and D). $n = 7-8$ for E and G; $n = 11-13$ for F and H.

deposition was frequently seen on the wall of larger ventricle-associated blood vessels (Figure 8D) and occasionally in small parenchymal arteries. Lipid droplets were found inside choroid plexus cells (Figure 8F) and in the subfornical organ, associated with the accumulation of CD45-positive cells. Anti-IL-1 β antibody greatly reduced CD45-positive cells with leukocyte

and microglial morphology in the caudal lateral ventricle (Figure 8A) but had no effect on lipid accumulation. Lipid deposition and inflammation were far less pronounced in the brains of mice fed a Western diet. Lipid droplets in the ependymal wall of the third ventricle were seen in mice fed both Paigen and Western diets (Figure 8F).

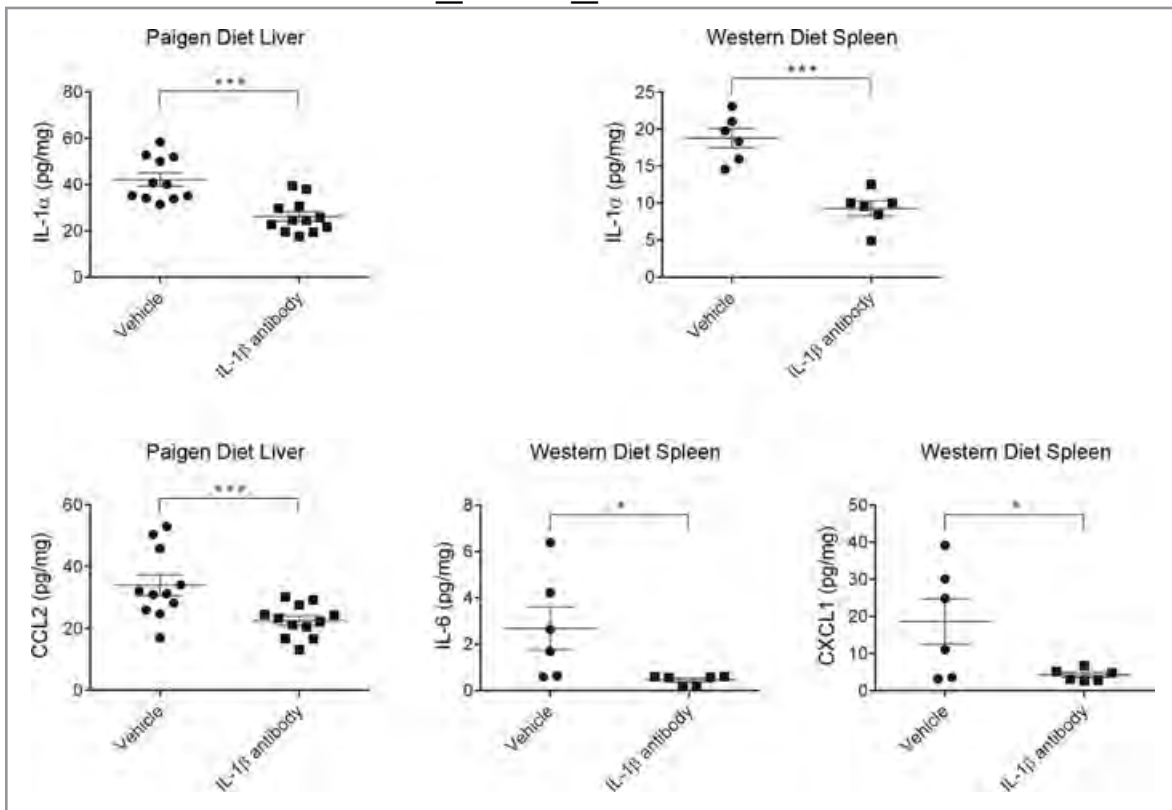


Figure 4. IL-1 β neutralization has secondary antiinflammatory effects in peripheral organs. Cytometric Bead Array was used to measure the cytokine and chemokine levels in homogenized livers and spleen samples. IL-1 α was significantly reduced in livers of ApoE $^{-/-}$ mice fed a Paigen diet and the spleens of mice fed a Western diet. The chemokine CCL2 was reduced in the livers of ApoE $^{-/-}$ mice fed a Paigen diet. The concentrations of interleukin-6 and CXCL1 were significantly reduced in response to IL-1 β neutralization in mice fed a Western diet. Error bars represent standard error, * P <0.05, ** P <0.01 and *** P <0.001 vs ApoE $^{-/-}$ mice treated with a control antibody (n=6–12).

Discussion

We show that central nervous system inflammatory pathology is associated with the development of atherosclerosis in high-fat diet-fed ApoE $^{-/-}$ mice and, through genetic deletion of IL-1R1 or neutralization of IL-1 β , provide evidence that this is mediated by IL-1. These findings identify IL-1 as a key driver in the development of cerebrovascular inflammation in response to atherogenic diet and systemic vascular disease.

Neutralization of IL-1 β had antiinflammatory effects in peripheral organs. High-fat feeding increases hepatic inflammation, presumably because of an increased accumulation of cholesterol.¹⁹ Treatment of hepatic cells with IL-1 β also raises the level of cholesterol uptake and accumulation.²⁰ Therefore, the reduced hepatic inflammation seen in the present study could be due to the decreased availability of IL-1 β to the hepatic cells and thus a decreased uptake of cholesterol.

Treatment with an anti-IL-1 β antibody attenuated brain leukocyte accumulation in ApoE $^{-/-}$ mice in the lateral ventricle, but this effect was confined to the ventral ventricular region in mice fed the less aggressive Western diet,²¹ with the latter showing a much lower brain leukocyte invasion than Paigen diet-fed animals. Vascular activation was reduced by

neutralization of IL-1 β in mice fed a Western diet, but only a trend toward reduction was seen in Paigen diet-fed animals (which had much higher number of VCAM-positive blood vessels), and no effect was seen on microglial activation in mice fed either diet. These observations are not fully consistent with the findings in ApoE $^{-/-}$ /IL-1R1 $^{-/-}$ mice fed a Paigen diet and may be because of limited brain penetration of the anti-IL-1 β antibody, or because IL-1 α , which can also mediate activation of IL-1R1, contributes to changes in the brain and cerebrovasculature.

ApoE $^{-/-}$ mice fed either a Western or Paigen diet are known to develop atheroma throughout the aorta.²² Treatment with an anti-IL-1 β antibody caused a significant reduction in the atherosclerotic lesion area in the descending aorta in mice fed both a Paigen and Western diet and in the aortic root in mice fed a Paigen diet. These data are consistent with a recent study that reported similar effectiveness of another anti-IL-1 β antibody treatment for atherosclerosis.¹⁵ Because ApoE $^{-/-}$ /IL-1R1 $^{-/-}$ mice fed an atherosclerotic diet also develop reduced peripheral pathology,¹⁴ it is not possible from the findings of this study to determine the specific site of IL-1 action in driving central nervous system pathology. Reversal

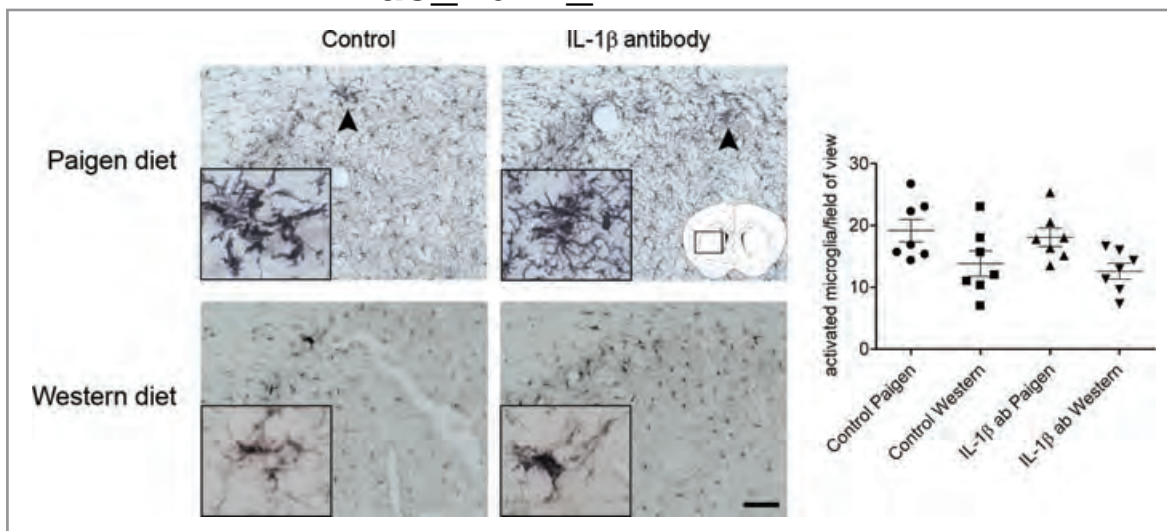


Figure 5. Levels of microglial activation differed between ApoE^{-/-} mice fed a Paigen or Western diet. Levels of microglial activation were assessed through the immunostaining of Iba1. Microglial activation was assessed throughout the striatum, and the location of images shown is indicated in the schematic diagram. Levels of microglial activation differed for each diet, but IL-1 β neutralization had no effect. Error bars indicate standard error (n=7), scale bars 200 μ m and 10 μ m.

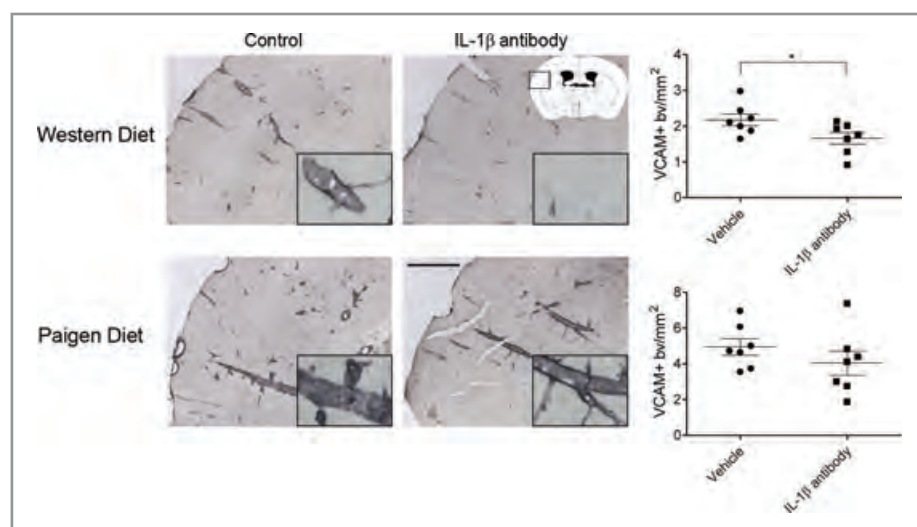


Figure 6. IL-1 β neutralization reduces vascular activation in ApoE^{-/-} mice fed a Western diet. Levels of vascular activation were assessed with immunostaining for the adhesion molecule VCAM. Vascular activation was assessed throughout the cerebral cortex; locations of images shown are indicated in the schematic diagram. Vascular activation was significantly reduced in ApoE^{-/-} mice fed a Western diet compared to those fed a Paigen diet. IL-1 β neutralization caused a significant reduction in vascular activation in ApoE^{-/-} mice fed a Western diet. Error bars indicate standard error, * P <0.05 vs ApoE^{-/-} fed a Western diet (n=7). Scale bars 200 μ m and 50 μ m.

specific effects of IL-1 in response to atherogenic diet and systemic vascular inflammation. Regardless of the site of IL-1 action, these data show benefits of IL-1 blockade on multiple tissues, notably the brain.

Central nervous system inflammation is observed in response to peripheral disease and may itself contribute to the development of vascular diseases. Recent experimental data indicate a role for centrally mediated signaling by inflammatory cytokines such as IL-1 β and tumor necrosis factor- α in neurogenic hypertension or metabolic disease.^{23–25} Neutralization of IL-1 β reversed weight loss in mice fed a Paigen diet, and the decline in voluntary physical activity in ApoE^{-/-} mice was also reversed by genetic deletion of the IL-1 receptor. Central IL-1-mediated effects on weight loss might be important in light of recent data that implicated inflammation-

of the effects of high-fat diet in mice lacking the IL-1 receptor may be due to the absence of IL-1 signaling within the cerebral vasculature or in the brain or may be secondary to the amelioration of peripheral pathology. The fact that there was no diet-dependent difference in atherosclerotic lesion size but Paigen diet induced more substantial cerebrovascular inflammation than did Western diet argues for some brain-

induced central IL-1 signaling in muscle atrophy, which was found to be dependent on the hypothalamic-pituitary-adrenal axis.²⁶ Paigen diet induces more substantial proinflammatory changes than does the Western diet, which was also indicated by the higher levels of CD45-positive cells in the lateral ventricle and the reduction of body weight, as opposed to the body weight increase seen in Western diet-fed mice. The

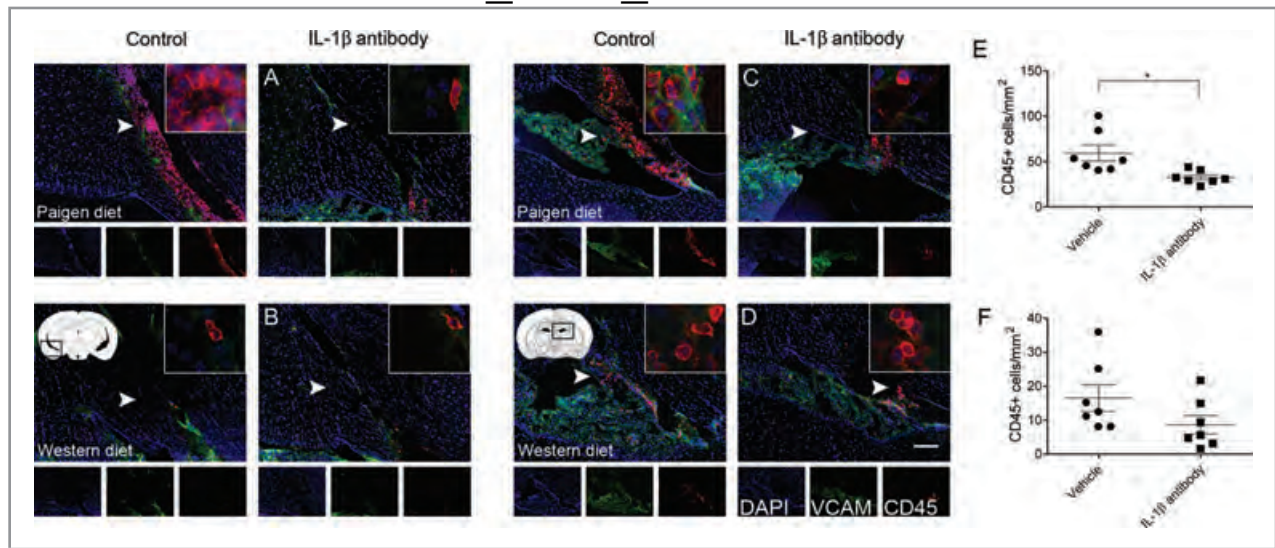


Figure 7. Leukocytes accumulate in the choroid plexus of the lateral ventricle in ApoE^{-/-} mice fed a Paigen diet and, to a lesser extent, a Western diet, which is attenuated in the Paigen diet-fed mice by an anti-IL-1β antibody. A, CD45-positive leukocytes accumulate in the ventral, caudal part of the lateral ventricle in ApoE^{-/-} mice fed a Paigen diet, which is attenuated by IL-1β antibody treatment. B, Accumulation of leukocytes in this region is not seen in mice fed a Western diet. C, CD45-positive leukocytes accumulate in the choroid plexus of the lateral ventricle in ApoE^{-/-} mice fed a Paigen diet, which is attenuated by IL-1β antibody treatment. Data in C were not normally distributed; therefore in addition to unpaired *t* test ($P=0.013$), nonparametric Mann-Whitney test ($P=0.0041$) was also performed. D, Fewer CD45-positive cells accumulated in this region in mice fed a Western diet, but IL-1β antibody treatment had no significant effect. Schematic diagram indicates the location of images. E and F, Quantification of the total number of CD45-positive leukocytes in mice fed a Paigen (E) or Western (F) diet. Error bars represent standard error, * $P<0.05$ vs ApoE^{-/-} mice treated with a control antibody ($n=7$).

different mechanisms of action of Paigen and Western diets^{21,22} and, therefore, the different levels of systemic and central inflammation induced might also explain differences seen in the effect of IL-1β neutralization on the various inflammatory parameters we studied in the brain.

Lipid deposition in ventricle-associated blood vessels, choroid plexus, circumventricular organs, and ventricles indicates pronounced vascular effects elicited by an atherogenic diet in the brains of mice fed a Paigen diet. Lipid accumulation appeared to take place independently from IL-1β. However, recruitment of inflammatory cells was localized to lipid accumulation in the brain and was markedly reduced in response to IL-1β neutralization, which suggests that local lipid deposition-induced stimuli might be directly involved in inflammatory cellular responses in the brain. Collectively, our data suggest that interventions against central and systemic effects of vascular diseases could have therapeutic potential. Elevated systemic inflammatory burden is considered a high risk for cardiovascular and cerebrovascular diseases.²⁷⁻²⁹ Clear association exists between depression and cardiovascular/metabolic disease,³⁰⁻³² and IL-1 signaling has been linked closely with the development of decreased motivational disorders such as depression.³³⁻³⁵

Therefore, patients with multiple risk factors for heart disease or stroke might benefit from neutralization of systemic IL-1β activity. Similarly, the potential effects of high-fat diet

and atherosclerosis on cognitive decline and depression might be reduced by interventions against IL-1 signaling.

Conclusions

We present evidence that the cytokine IL-1 contributes to neuroinflammatory changes in mice developing diet-induced atherosclerosis. IL-1β blockade provides a potential therapeutic opportunity to limit atherosclerosis, associated neuroinflammation, and hence cerebrovascular disease such as stroke and vascular dementia.

Acknowledgments

We give special thanks to the Bioimaging Facility staff (University of Manchester, Manchester, UK) for their help with the microscopy.

Sources of Funding

We thank the Medical Research Council, Centre for Integrative Mammalian Biology, Biotechnology and Biological Sciences Research Council, and the European Union's Seventh Framework Programme for funding (under Grant Agreements 201024 and 202213). Anti-IL-1β and control antibodies were supplied by Novartis. The Bioimaging Facility microscopes used in this study were purchased with grants from Biotechnology and

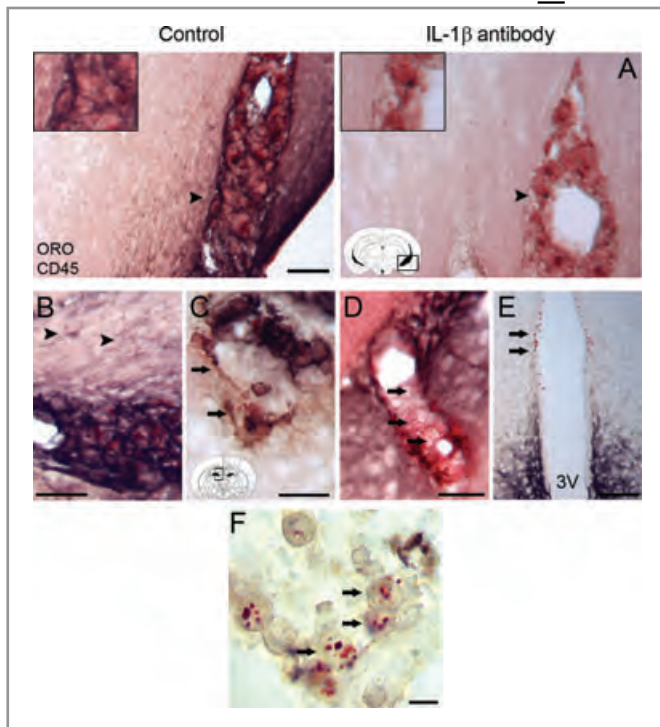


Figure 8. Atherogenic diet results in lipid accumulation in the brain, and IL-1 β neutralization reduces lipid-associated inflammation in the lateral ventricle. Immunostaining for CD45 (dark brown/purple) followed by Oil Red O staining (lipids; red) was performed on brain sections from mice fed Paigen or Western diet. A, IL-1 β antibody treatment reduces the recruitment of CD45-positive cells in the ventral (caudal) lateral ventricle and periventricular microglial activation but has no effect on lipid accumulation (insets show higher magnification of the areas marked by arrowheads). B, Lipid accumulation is observed in the rostral ventricle below the hippocampus, associated with hippocampal microglial activation (arrowheads). C, Inflammatory cells are found recruited to lipid droplets (arrows) around the ventricular ependyma in the dorsal thalamus in mice fed Paigen diet. Lipid deposition (arrows) is seen in the wall of ventricle-associated blood vessels (D) in animals fed a Paigen diet. E, Mice fed Western diet display lipid droplets (arrows) in the wall of the third (3V) ventricle and microglial activation in the arcuate nucleus. F, Lipid droplets are observed in choroid plexus cells (arrows) in mice fed a Paigen diet. Location of panels B through D and F in the brain is shown on schematic on panel C. n=7. Scale bars: 50 μ m (A through D), 100 μ m (E), and 10 μ m (F).

Biological Sciences Research Council, Wellcome, and the University of Manchester Strategic Fund.

Disclosures

Dr Rothwell is a nonexecutive director of AstraZenca, but this has no relation to the current research. Dr Gram is an employee of Novartis Pharma AG.

References

1. Savoia C, Schiffrin EL. Inflammation in hypertension. *Curr Opin Nephrol Hypertens.* 2006;15:152–158.

2. Dandona P, Aljada A, Bandyopadhyay A. Inflammation: the link between insulin resistance, obesity and diabetes. *Trends Immunol.* 2004; 25:4–7.

3. Silvestrini M, Viticchi G, Falsetti L, Balucani C, Vernieri F, Cerqua R, Luzzi S, Bartolini M, Provinciali L. The role of carotid atherosclerosis in Alzheimer's disease progression. *J Alzheimers Dis.* 2011; 25:719–726.

4. Dolan H, Crain B, Troncoso J, Resnick SM, Zonderman AB, Obrien RJ. Atherosclerosis, dementia, and Alzheimer disease in the Baltimore Longitudinal Study of Aging cohort. *Ann Neurol.* 2010; 68:231–240.

5. Altman R, Rutledge JC. The vascular contribution to Alzheimer's disease. *Clin Sci (Lond).* 2010;119:407–421.

6. Drake C, Boutin H, Jones MS, Denes A, McColl BW, Selvarajah JR, Hulme S, Georgiou RF, Hinz R, Gerhard A, Vail A, Prenant C, Julian P, Maroy R, Brown G, Smigova A, Herholz K, Kassio M, Crossman D, Francis S, Proctor SD, Russell JC, Hopkins SJ, Tyrrell PJ, Rothwell NJ, Allan SM. Brain inflammation is induced by co-morbidities and risk factors for stroke. *Brain Behav Immun.* 2011; 25:1113–1122.

7. Terao S, Yilmaz G, Stokes KY, Ishikawa M, Kawase T, Granger DN. Inflammatory and injury responses to ischemic stroke in obese mice. *Stroke.* 2008; 39:943–950.

8. McColl BW, Rose N, Robson FH, Rothwell NJ, Lawrence CB. Increased brain microvascular MMP-9 and incidence of haemorrhagic transformation in obese mice after experimental stroke. *J Cereb Blood Flow Metab.* 2010; 30:267–272.

9. Laskowitz DT, Sheng HX, Bart RD, Joyner KA, Roses AD, Warner DS. Apolipoprotein E-deficient mice have increased susceptibility to focal cerebral ischemia. *J Cereb Blood Flow Metab.* 1997;17:753–758.

10. Dinarello CA. Interleukin-1 in the pathogenesis and treatment of inflammatory diseases. *Blood.* 2011;117:3720–3732.

11. Li Q, Powell N, Zhang H, Belevych N, Ching S, Chen O, Sheridan J, Whitacre C, Qian N. Endothelial IL-1R1 is a critical mediator of EAE pathogenesis. *Brain Behav Immun.* 2011; 25:160–167.

12. Galea J, Armstrong J, Gadsdon P, Holden H, Francis SE, Holt CM. Interleukin-1 beta in coronary arteries of patients with ischemic heart disease. *Arterioscler Thromb Vasc Biol.* 1996;16:1000–1006.

13. Dewberry R, Holden H, Crossman D, Francis S. Interleukin-1 receptor antagonist expression in human endothelial cells and atherosclerosis. *Arterioscler Thromb Vasc Biol.* 2000; 20:2394–2400.

14. Chamberlain J, Francis S, Brookes Z, Shaw G, Graham D, Alp NJ, Dower S, Crossman DC. Interleukin-1 regulates multiple atherogenic mechanisms in response to fat feeding. *PLoS One.* 2009;4.

15. Bhaskar V, Yin J, Mirza AM, Phan D, Vanegas S, Issafras H, Michelson K, Hunter JJ, Kantak SS. Monoclonal antibodies targeting IL-1 beta reduce biomarkers of atherosclerosis in vitro and inhibit atherosclerotic plaque formation in apolipoprotein E-deficient mice. *Atherosclerosis.* 2011; 216:313–320.

16. Chapman KZ, Dale VQ, Denes A, Bennett G, Rothwell NJ, Allan SM, McColl BW. A rapid and transient peripheral inflammatory response precedes brain inflammation after experimental stroke. *J Cereb Blood Flow Metab.* 2009;29:1764–1768.

17. Osborn O, Brownell SE, Sanchez-Alavez M, Salomon D, Gram H, Bartfai T. Treatment with an interleukin 1 beta antibody improves glycemic control in diet-induced obesity. *Cytokine.* 2008; 44:141–148.

18. Geiger T, Towbin H, Cosenti-Vargas A, Zingel O, Arnold J, Rordorf C, Glatt M, Vosbeck K. Neutralization of interleukin-1 beta activity in vivo with a monoclonal antibody alleviates collagen-induced arthritis in DBA/1 mice and prevents the associated acute-phase response. *Clin Exp Rheumatol.* 1993; 11:515–522.

19. Tous M, Ferre N, Camps J, Riu F, Joven J. Feeding apolipoprotein E-knockout mice with cholesterol and fat enriched diets may be a model of non-alcoholic steatohepatitis. *Mol Cell Biochem.* 2005; 268:53–58.

20. Ma KL, Ruan XZ, Powis SH, Chen Y, Moorhead JF, Varghese Z. Inflammatory stress exacerbates lipid accumulation in hepatic cells and fatty livers of apolipoprotein E-knockout mice. *Hepatology.* 2008; 48:770–781.

21. Vergnes L, Phan J, Strauss M, Tafuri S, Reue K. Cholesterol and cholate components of an atherogenic diet induce distinct stages of hepatic inflammatory gene expression. *J Biol Chem.* 2003; 278:42774–42784.

22. Getz GS, Reardon CA. Diet and murine atherosclerosis. *Arterioscler Thromb Vasc Biol.* 2006; 26:242–249.

23. Shi P, Diez-Freire C, Jun JY, Qi Y, Katovich MJ, Li Q, Sriramula S, Francis J, Summers C, Raizada MK. Brain microglial cytokines in neurogenic hypertension. *Hypertension.* 2010; 56:297–303.

24. Ye SH, Mozayani P, Gamburd M, Zhong HQ, Campese VM. Interleukin-1 beta and neurogenic control of blood pressure in normal rats and rats with chronic renal failure. *Am J Physiol Heart Circ Physiol.* 2000; 279:H2786–H2796.

25. Purkayastha S, Zhang G, Cai D. Uncoupling the mechanisms of obesity and hypertension by targeting hypothalamic IKK-beta and NF-kappa B. *Nat Med*. 2011;17:883-U255.
26. Braun TP, Zhu X, Szumowski M, Scott GD, Grossberg AJ, Levasseur PR, Graham K, Khan S, Damaraju S, Colmers WF, Baracos VE, Marks DL. Central nervous system inflammation induces muscle atrophy via activation of the hypothalamic-pituitary-adrenal axis. *J Exp Med*. 2011; 208:2449-2463.
27. Denes A, Thornton P, Rothwell NJ, Allan SM. Inflammation and brain injury: acute cerebral ischaemia, peripheral and central inflammation. *Brain Behav Immun*. 2010; 24:708-723.
28. Spagnoli LG, Bonanno E, Sangiorgi G, Mauriello A. Role of inflammation in atherosclerosis. *J Nucl Med*. 2007; 48:1800-1815.
29. McColl BW, Allan SM, Rothwell NJ. Systemic infection, inflammation and acute ischemic stroke. *Neuroscience*. 2009;158:1049-1061.
30. Somberg TC, Arora RR. Depression and heart disease: therapeutic implications. *Cardiology*. 2008;111:75-81.
31. Williams ED, Steptoe A. The role of depression in the etiology of acute coronary syndrome. *Curr Psychiatry Rep*. 2007;9:486-492.
32. Plante GE. Depression and cardiovascular disease: a reciprocal relationship. *Metabolism*. 2005;54:45-48.
33. Koo JW, Duman RS. Evidence for IL-1 receptor blockade as a therapeutic strategy for the treatment of depression. *Curr Opin Investig Drugs*. 2009;10:664-671.
34. Diniz BS, Teixeira AL, Talib L, Gattaz WF, Forlenza OV. Interleukin-1 beta serum levels is increased in antidepressant-free elderly depressed patients. *Am J Geriatr Psychiatry*. 2010;18:172-176.
35. Lehto SM, Niskanen L, Miettola J, Tolmunen T, Viinamaki H, Mantyselka P. Serum anti-inflammatory markers in general population subjects with elevated depressive symptoms. *Neurosci Lett*. 2010;484:201-205.

Experimental stroke-induced changes in the bone marrow reveal complex regulation of leukocyte responses

Adam Denes¹, Barry W McColl², Sophie F Leow-Dyke¹, Katie Z Chapman^{1,3}, Neil E Humphreys¹, Richard K Grecnis¹, Stuart M Allan¹ and Nancy J Rothwell¹

¹Faculty of Life Sciences, University of Manchester, Manchester, UK; ²Neuropathogenesis Division, The Roslin Institute and R(D)SVS, University of Edinburgh, Roslin, UK

Stroke induces a systemic response that involves rapid activation of inflammatory cascades, followed later by immunodepression. Experimental stroke-induced responses in the bone marrow, which is the primary source of circulating monocytes and granulocytes, have not been investigated previously. We show that cerebral ischaemia induced early (4 hours) release of CXCR2-positive granulocytes from the bone marrow, which was associated with rapid systemic upregulation of CXCL1 (a ligand for CXCR2) and granulocyte-colony-stimulating factor, a key cytokine involved in the mobilisation of bone marrow leukocytes. This process involves rapid activation of nuclear factor- κ B and p38 mitogen-activated protein kinase in bone marrow myeloid cells. T-cell numbers in the bone marrow increased after stroke, and bone marrow cells did not show suppressed cytokine response to bacterial endotoxin stimulation *in vitro*. Stroke-induced laterality observed in the brain stem and in the bone marrow indicates direct involvement of the autonomic nervous system in stroke-induced cell mobilisation. We also show that systemic inflammatory changes and leukocyte responses in the bone marrow are profoundly affected by both anaesthetic and surgical stress. We conclude that stroke influences leukocyte responses in the bone marrow through multiple mechanisms and suggest that preclinical studies should take into consideration the effect of surgical manipulation in experimental models of stroke.

Journal of Cerebral Blood Flow & Metabolism advance online publication, 3 November 2010; doi:10.1038/jcbfm.2010.198

Keywords: acute-phase response; autonomic; bone marrow; cytokine; granulocyte; stroke

Introduction

It is now accepted that inflammatory processes originating both inside and outside the brain are important aetiological and pathologic factors in stroke. Acute or chronic inflammatory diseases often precede and contribute to the onset and outcome of stroke in humans and experimental animals, in part through immune cells such as neutrophils or monocytes and various soluble inflammatory mediators

(Denes *et al*, 2010; Emsley and Hopkins, 2008; McColl *et al*, 2009). Both clinical and experimental cerebral ischaemia induces activation of the sympathetic nervous system and lymphoid organs such as the spleen, followed by later immunosuppression and splenic atrophy (Dirnagl *et al*, 2007; Offner *et al*, 2006b, 2009; Prass *et al*, 2003). These data indicate that the generation of the stroke-induced acute-phase response involves both humoral and neural signals to various peripheral organs.

We are aware of no previous studies that have examined the consequences of cerebral ischaemia on bone marrow cell composition, activation, and mobilisation. The bone marrow is the primary source of granulocytes and monocytes, which are recruited to the inflamed brain and reportedly contribute to many brain diseases, including stroke (D'Mello *et al*, 2009; Kim *et al*, 2009; McColl *et al*, 2008). Notably, the signals that trigger leukocyte mobilisation from the bone marrow in acute brain diseases are unknown and may represent potential targets for therapy. We showed previously that the bone marrow receives central autonomic innervation, which involves forebrain areas such as the insular and

Correspondence: Dr A Denes, Faculty of Life Sciences, University of Manchester, AV Hill Building, Oxford Road, Manchester M13 9PT, UK.

E-mail: adam.denes@manchester.ac.uk

³Current address: Laboratory of Neurogenesis and Cell Therapy, Section of Restorative Neurology, Wallenberg Neuroscience Center, University Hospital, Lund, Sweden.

The authors are grateful for funding provided by the Medical Research Council (NJR MRC Research Professorship), the European Union's Seventh Framework Programme (FP7/2008-2013) under grant agreements no. 201024 and no. 202213 (European Stroke Network, NJR, AD), and the Wellcome Trust (NH, RG).

Received 26 July 2010; revised 22 September 2010; accepted 11 October 2010

piriform cortex (Denes *et al.*, 2005), which often become ischaemic after experimental stroke. It is also known that humoral factors, including cytokines and chemokines are rapidly elevated in both the brain and the periphery after stroke (Offner *et al.*, 2006a). In addition, we recently showed that cerebral ischaemia induces systemic upregulation of CXCL1 (KC), a chemokine that acts in concert with granulocyte-colony-stimulating factor (G-CSF) to mobilise neutrophils from the bone marrow in response to inflammatory challenges (Chapman *et al.*, 2009; Wengner *et al.*, 2008). The release of neutrophil granulocytes from the bone marrow is a complex process, which involves an antagonistic interaction between the neutrophil chemokine receptors CXCR2 and CXCR4 (Eash *et al.*, 2010). Activation of CXCR2 by its ligands, CXCL1 and/or CXCL2, is a key step in neutrophil mobilisation and recruitment to inflamed tissues in various diseases, including arthritis, ischaemia-reperfusion injury, or inflammatory demyelination in the central nervous system (Jacobs *et al.*, 2010; Li *et al.*, 2010; Liu *et al.*, 2010; Martin *et al.*, 2003; von Vietinghoff *et al.*, 2010; Wengner *et al.*, 2008). Other chemokine receptors such as CCR5 can also interact with key leukocyte mobilisation responses and can promote the recruitment of monocytes, granulocytes, and T cells to the sites of inflammation (Balistreri *et al.*, 2007; Honczarenko *et al.*, 2002; Kohlmeier *et al.*, 2008). Leukocyte mobilisation responses also involve several acutely synthesised inflammatory mediators, such as matrix metalloproteinase protein-9 (MMP-9), which besides its proposed role in the release of leukocytes from the bone marrow, makes a profound contribution to brain damage after stroke (McColl *et al.*, 2008; Pelus *et al.*, 2004).

These findings implicate the bone marrow in inflammatory responses to brain injury; hence, we tested the hypothesis that experimental stroke leads to the activation and mobilisation of bone marrow leukocytes. We show that middle cerebral artery occlusion (MCAo) in mice induced rapid activation of myeloid cells and mobilisation of CXCR2-positive granulocytes, which was followed by changes in bone marrow lymphocytes. Our results also show effects of anaesthesia and surgical stress, which not only altered leukocyte responses but also had a considerable impact on the systemic levels of inflammatory mediators. These findings reveal a previously unrecognised effect of stroke on bone marrow leukocyte responses and have important implications for both therapeutic and modelling aspects of experimental stroke research.

Materials and methods

Animals

Male C57BL6/J mice (Harlan-Olac, Bicester, UK) aged 12 to 14 weeks (weighing 24 to 30 g) were used for the study. Animals had free access to food and water and were

maintained under temperature-, humidity-, and light-controlled conditions. All animal procedures were performed under an appropriate Home Office License and adhered to regulations as specified in the Animals (Scientific Procedures) Act (1986).

Surgical Procedures

Transient MCAo was performed using the intraluminal filament method as described previously (Denes *et al.*, 2007). Anaesthesia was induced with 4%, and maintained with 1.5%, isoflurane (Baxter Healthcare Corporation, Thetford, UK) in a mixture of 30% oxygen and 70% nitrous oxide. During surgery, core body temperature was monitored using a rectal probe and maintained at $37^{\circ}\text{C} \pm 0.5^{\circ}\text{C}$, using a homeothermic blanket (Harvard Apparatus, Kent, UK). After surgical exposure of the bifurcation of the external carotid artery and the internal carotid artery on the left side, a silicone-coated nylon monofilament (tip diameter $180\ \mu\text{m}$) was introduced into the origin of the external carotid artery and advanced through the internal carotid artery to occlude the MCA. Reperfusion was induced 60 minutes later, and animals were allowed to recover. In sham-operated animals, the filament was advanced along the internal carotid artery until the origin of the MCA and was retracted immediately. In the case of both MCAo and sham surgery, mice were kept anaesthetised throughout the whole surgical procedure. To control for the effect of isoflurane on bone marrow cells, a group of mice were anaesthetised for 90 minutes (average duration of the complete surgery), without any surgical intervention.

In a separate set of experiments, mice were allowed to recover during occlusion and reanaesthetised at the end of the occlusion to remove the filament, which reduced anaesthesia duration from ~ 90 minutes to 20 to 30 minutes (the time spent during surgery to insert the filament and to suture the surgical territory after the occlusion). Control (sham, isoflurane) groups were adjusted accordingly.

After surgery, mice were subjected to 10 minutes to 72 hours reperfusion. Neurologic status was assessed immediately after recovery to confirm successful occlusion, according to a neurologic grading score of increasing severity of deficit (Bederson *et al.*, 1986): (0) no observable deficit; (1) torso flexion to right; (2) spontaneous circling; (3) leaning/falling to right; and (4) no spontaneous movement. Mice showing no functional deficit (i.e., without clear torso flexion and/or circling) after MCAo were excluded from the study. Mice were subcutaneously injected with 0.5 mL of sterile saline daily and continuously monitored for neurologic symptoms.

Tissue Processing

Serial blood samples were obtained from the tail vein and cardiac blood was collected from the right ventricle before perfusion. The plasma was separated with centrifugation at $1,700 \times g$, 4°C , and blood cells were lysed in ice-cold lysis buffer (50 mmol/L Tris-HCl, pH 7.4, 150 mmol/L NaCl, 5 mmol/L CaCl_2 , 0.02% NaN_3 , 1% Triton X). Mice were transcardially perfused with 0.9% saline, and then the

brains were removed and snap frozen on dry ice. For cytokine measurement, the bone marrow from femurs and tibia was flushed with lysis buffer. For flow cytometric cell surface labelling and for *in vitro* stimulation assays, bone marrow cells were isolated in medium (RPMI, supplemented with 10% fetal calf serum and penicillin/streptomycin). Bone marrow cells were flushed with 1% paraformaldehyde in phosphate-buffered saline (PBS) for phospho-flow cytometric labelling. In some experiments, the left and right tibial and femoral bone marrow was isolated separately to assess laterality after MCAo. Some animals were perfused with 4% paraformaldehyde for immunohistochemistry and the brains were sectioned on a sledge microtome (Bright, Huntingdon, UK).

Flow Cytometry

Bone marrow cells were isolated as described above. For cell surface labelling, after Fc receptor blocking, cells were incubated with fluorescently conjugated antibodies against CD4 (GK1.5), CD8 (53-6.7), CD3 (17A2), CD19 (MB19-1), MHCII (M5/114.15.2), Gr-1 (RB6-8C5), CD11b (M1/70), c-kit (2B8), CD49b (DX5) (eBioscience, Hatfield, UK), CXCR2 (242216, R&D Systems, Abingdon, UK), and CCR5 (C34-3448, BD Biosciences, Oxford, UK).

For single-cell phosphorylation-state analysis, fixed cells were first incubated with anti-Gr-1 (eBioscience), then permeabilised with BD Phosflow Perm III buffer (BD Biosciences), and then stained with either phospho-nuclear factor (NF) κ B p65 (Ser536, Cell Signaling Technology, Danvers, MA, USA, 1:25) or phospho-p38 mitogen-activated protein kinase (MAPK) (pT180/pY182, BD Biosciences, 1:25). Before intracellular cytokine staining, bone marrow cells isolated from naive animals or from mice exposed to anaesthesia, stroke, or sham surgery were incubated with 3 μ mol/L monensin (Golgi Stop; BD Biosciences) for 2 hours. Subsequently, cell surface labelling was performed as described above, before permeabilisation and incubation with goat anti-mouse CXCL1 (R&D Systems) overnight and then with donkey anti-goat Alexa 488 (Invitrogen, Paisley, UK) for 1 hour.

Labelled cells were acquired on FACS Calibur (BD Biosciences) and Cyan ADP (Beckman Coulter, High Wycombe, UK) flow cytometers. Data were analysed using CellQuest pro (BD Biosciences), FACSDiva (BD Biosciences), and Summit 4.3 (Dako Ltd, Glostrup, Denmark) software.

Lateralisation of the bone marrow was evaluated by determining the ratio of Gr-1^{high} granulocytes or CD19-positive B cells in the left and right femur/tibia by flow cytometry, and was then laterality expressed as the % difference between them.

Western Blotting

For NF κ B western blots, cell lysates were separated on 4% to 12% SDS-polyacrylamide gels under reducing conditions. Proteins were transferred to polyvinylidene difluoride membrane (Scientific Laboratory Supplies Ltd, Wilford, UK). Membranes were blocked with 10% nonfat milk in PBS-0.1% Tween 20 for 1 hour at room temperature.

Membranes were incubated with the primary antibody (rabbit anti-NF κ B p65, Santa Cruz Biotechnology, Wembley, UK) diluted 1:200 in 1% bovine serum albumin/PBS-0.1% Tween 20 at 4°C. Loading volumes were normalised against anti- β -actin peroxidase (1:1,500 dilution, Sigma-Aldrich, St Louis, MO, USA). Membranes were washed with PBS-0.1% Tween 20 and incubated with horseradish peroxidase-conjugated secondary antibody (goat anti-rabbit-horseradish peroxidase, Dako Ltd) diluted 1:1,000 in 5% nonfat milk/PBS-0.1% Tween 20 for 1 to 3 hours at room temperature. Membranes were developed by reaction with ECL chemiluminescent substrate (GE Healthcare, Pittsburgh, PA, USA), onto photographic film (Fischer Scientific, Pittsburgh, PA, USA).

Gel Zymography

Bone marrow lysates equilibrated for total protein concentration (2 mg/mL) (25 μ L) were separated on SDS-polyacrylamide gels impregnated with 1.5 mg/mL gelatin under nonreducing, nondenaturing conditions. The SDS was removed to renature enzymes by incubating gels in the wash buffer (50 mmol/L Tris-HCl, pH 7.6, 5 mmol/L CaCl₂, 1 μ mol/L ZnCl₂, 2.5% Triton X-100). Gels were then incubated in the reaction buffer (wash buffer without detergent) for 72 hours at 37°C to stimulate gelatinolysis. Gels were stained with Coomassie Brilliant Blue R-250 (0.1%) diluted in 40% methanol and 10% acetic acid for 1 hour, and destained in a solution containing 10% methanol and 1% acetic acid until clear gelatinolytic bands appeared.

In Vitro Stimulation of Bone Marrow Cells

Total bone marrow cells collected 72 hours after sham or stroke surgery were stimulated with 1 μ g/mL lipopolysaccharide (*E. coli* O26:B6), at a density of 7.5×10^6 cells/mL in RPMI medium, supplemented with 10% fetal calf serum and penicillin/streptomycin. After 3 hours incubation at 37°C, cells were pelleted with centrifugation at $400 \times g$, the supernatant was collected, and cells were lysed in lysis buffer.

Cytokine Measurement

For the measurement of CXCL1 (KC), proMMP-9, and interleukin-6, DuoSet ELISA (enzyme-linked immunosorbent assay) kits were purchased from R&D Systems and used according to the manufacturer's protocol. Granulocyte-colony-stimulating factor was measured using the cytometric bead array (BD Biosciences).

Immunohistochemistry

Free-floating, 20- μ m-thick brain sections were blocked in 2% normal goat serum and then incubated with rabbit anti-STAT3 (signal transducer and activator of transcription 3) phosphorylation (Cell Signaling Technology) or rabbit anti-neurokinin receptor-1 (NK1) (Millipore,

Watford, UK) antibodies. After incubation with biotinylated goat anti-rabbit secondary antibody (Vector Laboratories, Peterborough, UK) and ABC solution (Vector Laboratories) for 1 hour, colour was developed with diaminobenzidine-tetrahydrochloride (Sigma-Aldrich) in the presence of nickel-ammonium sulphate.

Statistical Analysis

For comparing two groups, Student's *t*-test (two tailed) was used. Comparison of three or more groups was carried out by one-way or two-way ANOVA (analysis of variance), followed by Bonferroni's correction. Data are expressed as mean \pm s.e.m. $P < 0.05$ was considered statistically significant.

Results

CXCR2-Positive Granulocytes are Released from the Bone Marrow in Response to Experimental Stroke

Sixty-minute MCAo resulted in ischaemic brain damage in the left hemisphere affecting 35% to 65% of the hemisphere (lesion volume, 40 to 70 mm³), in the MCA territory, including the striatum, the insular, the somatosensory and the somatomotor cortex. Neurologic scores were two or three in average (data not shown). Activation of myeloid cells was associated with mobilisation of Gr-1-positive cells from the bone marrow within 4 hours after MCAo (Figures 1A and 1B) as identified by flow cytometry. Identical results were obtained using CD11b, another marker of granulocytes–monocytes (Figures 1C and 1D). To investigate which population of myeloid cells responds specifically to stroke, we looked at CXCR2-positive granulocytes, because our recent findings indicated a key role for CXCL1 (a CXCR2 ligand) in the stroke-induced early systemic response (Chapman *et al*, 2009). We observed a marked reduction in CXCR2-positive cells at 4 hours reperfusion (60%, compared with naive mice) in the granulocyte pool of the bone marrow in response to stroke (Figures 1F and 1G). Sham surgery seemed to cause a slight reduction in this population (not significant at 4 hours reperfusion), whereas stroke resulted in a significant (47%) reduction in CXCR2-positive granulocytes (CD11b+ SSC^{high} cells) in the bone marrow compared with sham surgery (Figure 1H). CCR5-positive cells increased in the bone marrow, indicating that stroke is likely to have a differential effect on different populations of leukocytes (Figure 1I).

Both isoflurane and sham surgery seemed to disturb leukocyte responses. A marked increase in bone marrow cell numbers was observed as a result of surgical stress 72 hours after sham or stroke surgery (Figure 1E), which was caused by an increase in the myeloid cell lineage. Total and myeloid cell numbers were significantly lower (20% to 25%) after stroke compared with sham surgery (Figures 1A to 1E). CXCR2-positive granulocytes were less abundant in the bone marrow at 72 hours reperfusion after

stroke compared with sham surgery (Supplementary Figure A).

Experimental Stroke Induces Rapid Activation of Myeloid Cells in the Bone Marrow

We evaluated whether experimental stroke led to the activation of leukocytes in the bone marrow, by assessing NF κ B and p38 MAPK, two common signalling pathways in various haematopoietic cells (Bottero *et al*, 2006; Geest and Coffey, 2009). Western blotting identified rapid induction of NF κ B p65 in the bone marrow after stroke at 10 minutes reperfusion (70 minutes onset of ischaemia), which was further augmented by 4 hours (Figure 2A). Single-cell analysis with flow cytometry revealed that phosphorylation of NF κ B p65 occurs in myeloid cells after stroke, predominantly in Gr-1-positive SSC^{high} granulocytes (Figure 2B). Phosphorylation of NF κ B p65 was significantly increased in granulocytes at 4 hours reperfusion after stroke compared with sham surgery (Figure 2C). Flow cytometry showed a significant increase in phosphorylated p38 MAPK in Gr-1^{int} SSC^{int} cells (a population corresponding to various mature and immature myeloid populations including monocytes) at 4 hours reperfusion after stroke (Figures 2D and 2E). These data indicate that experimental stroke induces rapid activation of bone marrow myeloid cells.

Early Inflammatory Changes in the Bone Marrow Parallel the Systemic Response to Experimental Stroke

Stroke induced a transient (50-fold) elevation of CXCL1 (KC) in the circulation 4 hours after reperfusion, which was significantly higher than the effect (25-fold) of surgical stress alone (Figure 3A). At the same time point, CXCL1 was also induced in the bone marrow, but levels were significantly (50%) lower in stroke animals (Figure 3B), which may indicate the increased release of bone marrow-derived CXCL1 (or CXCL1-containing cells) into the blood.

Bone marrow proMMP-9 levels reduced markedly (by 70%) at 4 hours reperfusion after MCAo (Figure 3C) compared with naive animals. Gelatinase activity in the bone marrow decreased equally after stroke and surgical stress caused by sham surgery (Figure 3D). These results indicated that surgical stress is sufficient to induce inflammatory changes in the bone marrow. Intracellular staining and flow cytometric analysis confirmed upregulation of CXCL1 in granulocytes (CD11b⁺ Gr-1⁺ SSC^{high} cells) in the bone marrow after both sham and stroke surgery (Figure 3E and Supplementary Figure B). Correspondingly, at 4 hours reperfusion, CXCL1 levels in circulating blood cells increased in response to surgery and MCAo (25- to 30-fold; Figure 3F). Moreover, surgical stress alone increased proMMP-9 in circulating blood cells by 10 minutes after reperfusion

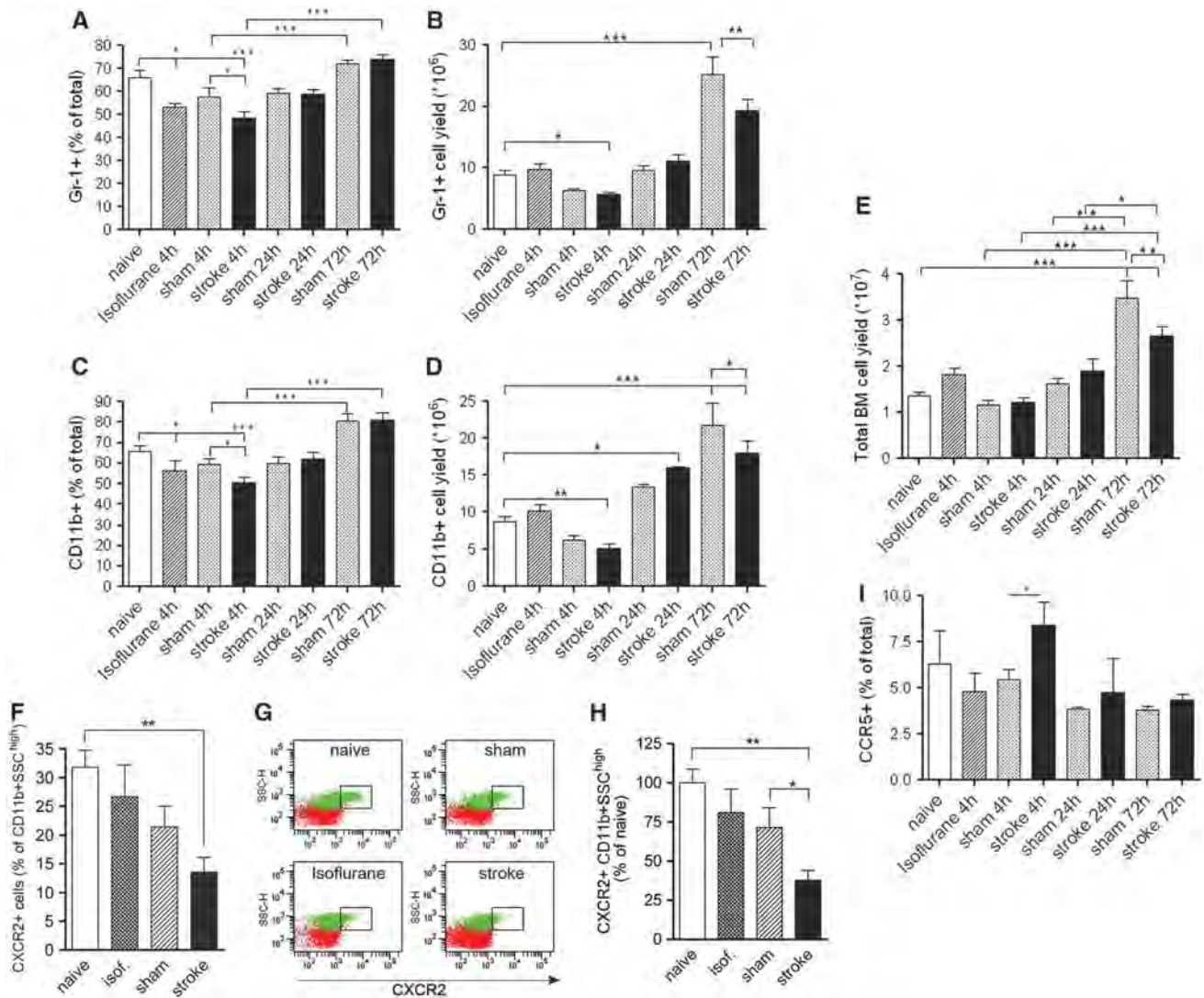


Figure 1 Experimental stroke induces a rapid release of CXCR2-positive granulocytes from the bone marrow. Flow cytometric analysis was used to assess changes in myeloid cell populations in the bone marrow after isoflurane anaesthesia, sham, or stroke surgery at various reperfusion times. Release of Gr-1- and CD11b-positive cells was induced predominantly by stroke at 4 hours reperfusion, which was followed by a reduction in surgery-induced increase in cell numbers after stroke at 72 hours reperfusion. Both (A) proportion and (B) total number of Gr-1-positive cells in the bone marrow indicate comparable changes to the (C) proportion or (D) total number of CD11b-positive cells over time. (E) Total cell yield in the bone marrow after various reperfusion times. (F) Stroke-induced granulocyte release from the bone marrow was predominantly caused by a marked reduction in CXCR2-positive (CD11b + SSC^{high}) cells at 4 hours reperfusion. (G) Representative dot blots showing reduction of CXCR2-expressing CD11b + SSC^{high} cells in the bone marrow at 4 hours reperfusion. Green: gated on CD11b-positive cells. (H) Reduction of CXCR2 + granulocytes in the bone marrow 4 hours after stroke is significantly augmented compared with both naive and sham mice. (I) The proportion of CCR5-positive cells increased in the bone marrow at 4 hours reperfusion. * $P < 0.05$; ** $P < 0.01$; *** $P < 0.001$. Data shown are representative of five to nine mice in each group corresponding to at least two independent experiments. isof., isoflurane.

(Figure 3G). Blood cell-derived CXCL1 and proMMP-9 were reduced after stroke compared with sham surgery at 10 minutes and 4 hours, respectively, which indicate that stroke alters the production and/or release of inflammatory mediators compared with surgical stress alone (Figures 3F and 3G).

We also investigated whether circulating levels of key neutrophil-mobilising cytokines are upregulated early enough to drive the release of CXCR2-positive granulocytes from the bone marrow after stroke. Ten minutes after reperfusion, CXCL1 levels were not

different after sham and stroke surgery (Figure 3H); in contrast, G-CSF exhibited a rapid increase after stroke, but not sham surgery (Figure 3I).

Experimental Stroke Causes Increased Bone Marrow T Cells and Natural Killer Cells

Isoflurane alone induced an increase in T and B cells in the bone marrow 4 hours after induction, which correlated with lymphocyte responses in

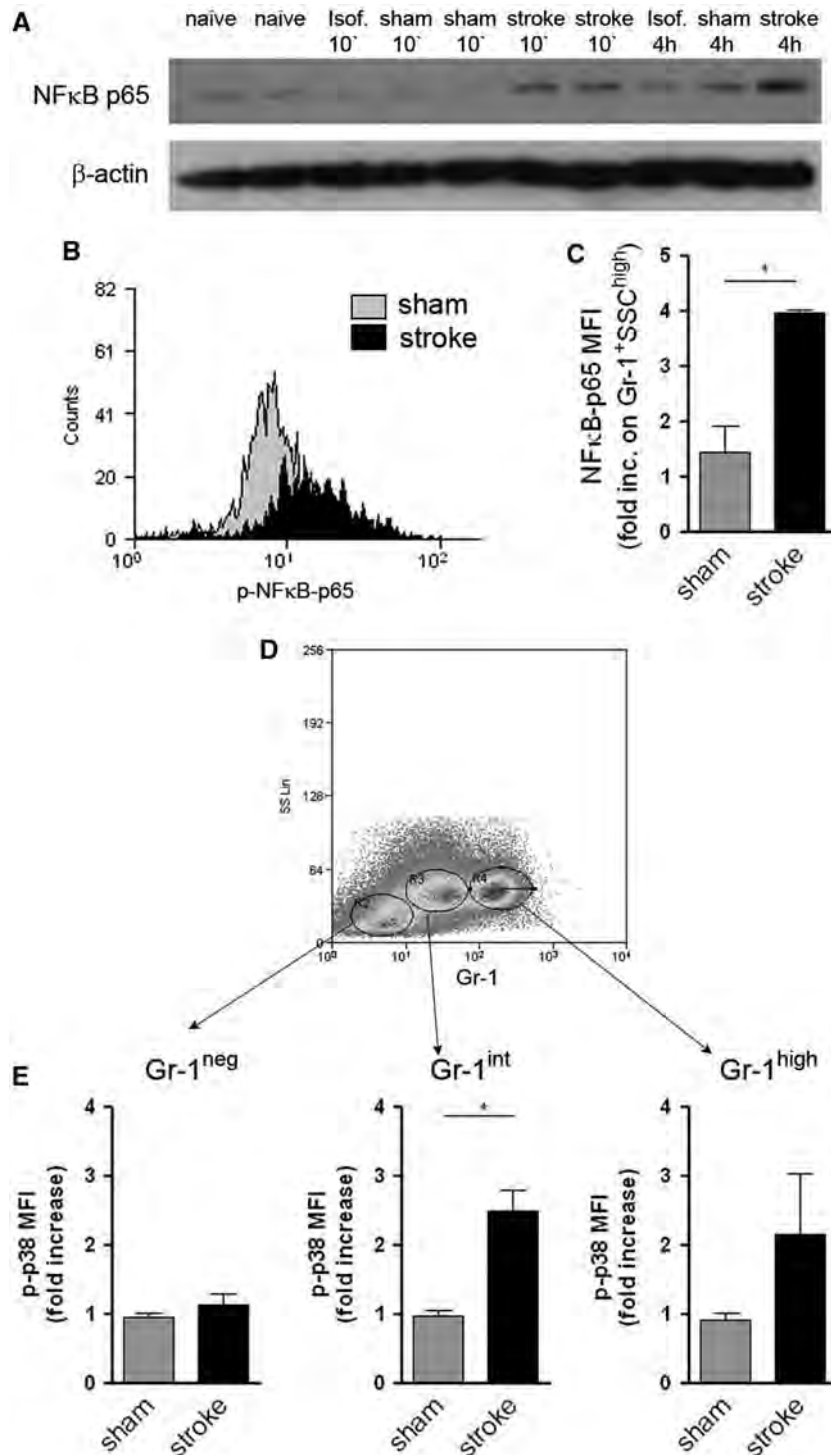


Figure 2 Experimental stroke results in rapid activation of myeloid cell populations in the bone marrow. **(A)** Stroke-induced NFκB activation between 10 minutes and 4 hours reperfusion as assessed by western blotting, using a specific antibody recognising the NFκB p65 subunit. Isoflurane anaesthesia alone (Isof.) or sham surgery also led to mild p65 activation at 4 hours reperfusion. **(B)** Phosphorylation of NFκB p65 at residues surrounding Ser536 was detected with flow cytometry in Gr-1-positive SSC^{high} granulocytes in the bone marrow. Histogram shows stroke-induced NFκB p65 phosphorylation, which led to increased intracellular mean fluorescent intensity (MFI) after permeabilisation and immunostaining. **(C)** NFκB p65 phosphorylation was significantly increased after stroke in bone marrow granulocytes at 4 hours reperfusion compared with sham surgery. **(D)** Dot plot showing the gates used to assess the phosphorylation of p38 MAPK in different Gr-1-positive cell populations in the bone marrow by flow cytometry. **(E)** Stroke resulted in a significant increase in phosphorylated p38 MAPK (p-p38) in Gr-1^{int} cells after 4 hours reperfusion. **P* < 0.05. One representative experiment (*n* = 3) out of two independent experiments is shown. MAPK, mitogen-activated protein kinase; NFκB, nuclear factor-κB.

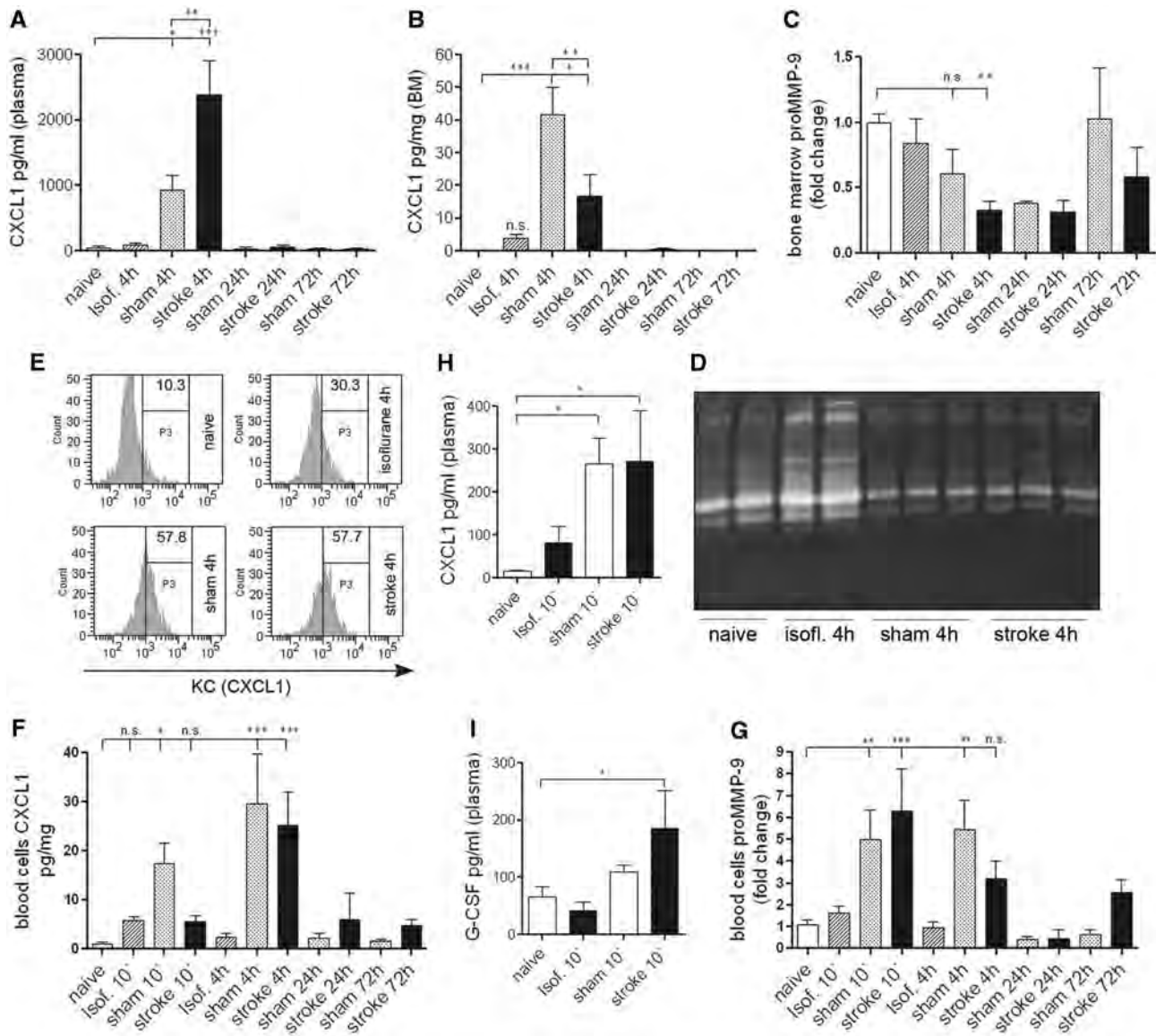


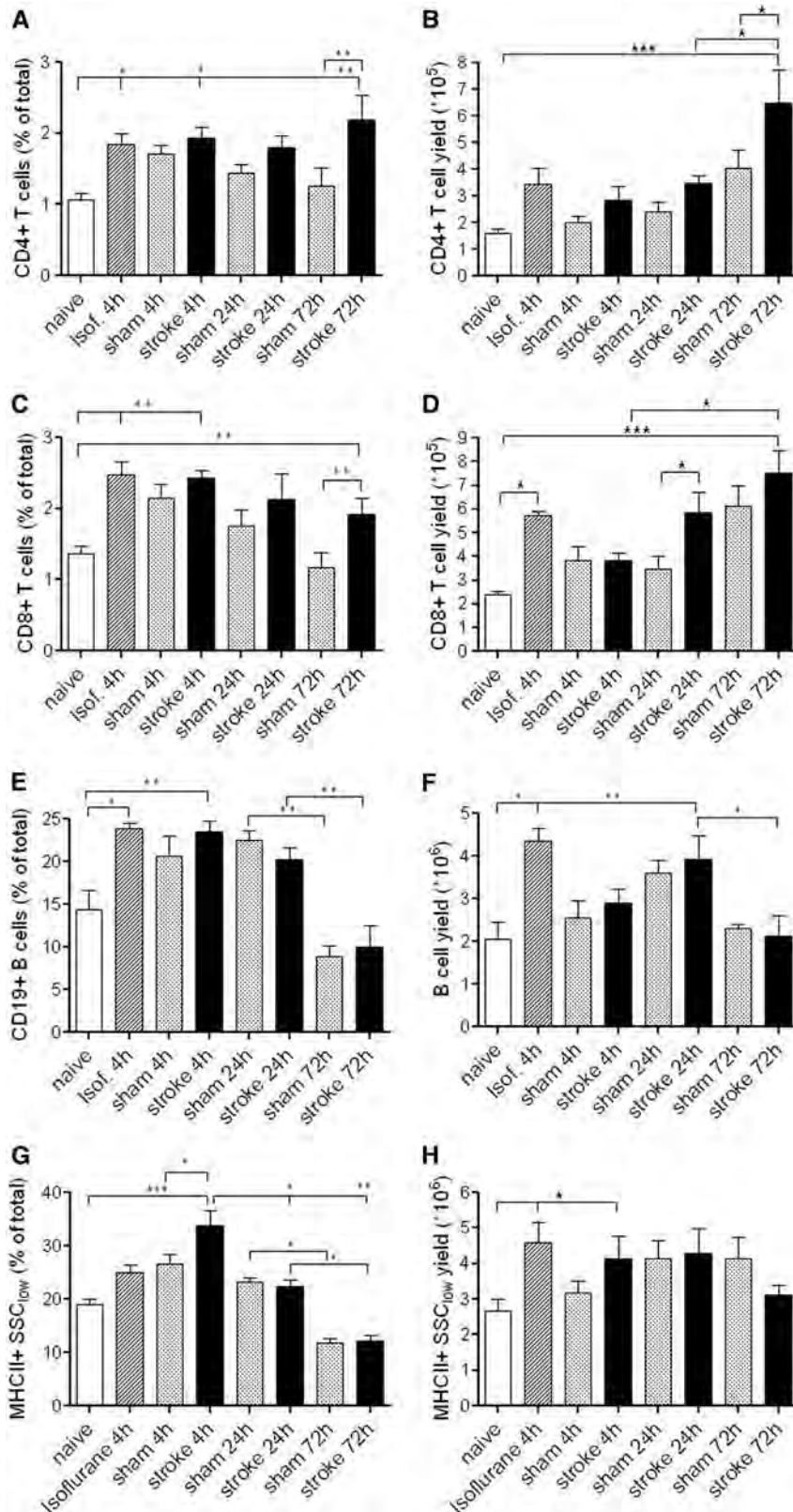
Figure 3 Rapid systemic induction of CXCL1 and proMMP-9 parallel cellular changes in response to experimental stroke and surgical stress. **(A)** Plasma CXCL1 was induced 4 hours after MCAo at a significantly higher level than sham surgery alone. **(B)** CXCL1 was upregulated in the bone marrow at 4 hours reperfusion, which was less pronounced after MCAo than after sham surgery. **(C)** Changes in proMMP-9 levels were measured by ELISA in the bone marrow (fold increase over naive is shown). **(D)** Gelatinase activity, measured by gel zymography decreases markedly in the bone marrow by 4 hours reperfusion after both sham and MCAo surgery. **(E)** Intracellular cytokine staining revealed upregulated CXCL1 in CD11b/Gr-1 double-positive, SSC^{high} bone marrow cells after sham and stroke surgery after 4 hours reperfusion. Circulating blood cells were lysed and **(F)** CXCL1 or **(G)** proMMP-9 were detected with ELISA at various reperfusion times. By 10 minutes reperfusion, plasma **(H)** CXCL1 was elevated after both sham and MCAo surgeries, whereas **(I)** plasma G-CSF showed a significant increase only after stroke. * $P < 0.05$; ** $P < 0.01$; *** $P < 0.001$. Data from two to three independent experiments are shown. ELISA, enzyme-linked immunosorbent assay; G-CSF, granulocyte-colony-stimulating factor; MCAo, middle cerebral artery occlusion; MMP-9, matrix metalloproteinase protein-9; NS, not significant.

animals that had undergone sham or stroke surgery (Figures 4A to 4F). This was largely normalised by 24 to 72 hours reperfusion in sham animals. In contrast, MCAo increased CD4- and CD8-positive T cells in the bone marrow between 24 and 72 hours reperfusion, compared with sham surgery. Total bone marrow T-cell numbers markedly increased at 72 hours after stroke compared with naive mice (Figures 4A to 4D). B cells were significantly reduced in the bone

marrow by 72 hours in response to surgical stress, which corresponded to the increase in proportion and number of granulocytes/monocytes (Figures 1A to 1E). In contrast, the ratio of major histocompatibility complex II (MHCII)-positive B cells showed a transient (4 hours) elevation after stroke (Figure 4G). Natural killer cells (Figures 5A and 5B) showed an increase after stroke compared with sham surgery between 24 and 72 hours reperfusion, whereas mast

cells increased by 72 hours reperfusion in response to surgical stress (Figures 5C and 5D). The main leukocyte population changes in the bone marrow are summarised in Table 1.

In a separate set of experiments, we investigated whether shortening the duration of anaesthesia would prevent the confounding effects seen on various leukocyte populations (see the 'Materials



and methods' section). The effect of an average of 20- to 30-minute anaesthesia on leukocyte responses in the bone marrow was largely indistinguishable from what we observed earlier with a longer period of anaesthesia, indicating that isoflurane effects occur relatively early after induction (data not shown).

Bone Marrow Cells do not Exhibit a Suppressed Response to Endotoxin after Experimental Stroke

As stroke-induced immunodeficiency is a known cause of serious bacterial infections in stroke patients and impairs outcome (Dirnagl *et al.*, 2007; Prass *et al.*, 2003), we investigated whether this response can manifest in the bone marrow. Total

bone marrow cells isolated at 72 hours reperfusion expressed and released high levels of interleukin-6 after stimulation with lipopolysaccharide *in vitro* (Figures 6A and 6B). CXCL1 was also induced, but was not released from the cells during the 3-hour incubation period (Figures 6C and 6D). However, no difference between stroke and sham surgery was observed (Figures 6A to 6D), indicating that bone marrow cells after stroke retain their ability to respond to stimulation by bacterial cell-wall compounds. The chronic effect of stroke on lymphopaenia in the blood, thymus, and spleen, and impaired cytokine expression by blood cells in response to lipopolysaccharide or mitogens, are apparent 12 to 48 hours after stroke in mice (Prass *et al.*, 2003).

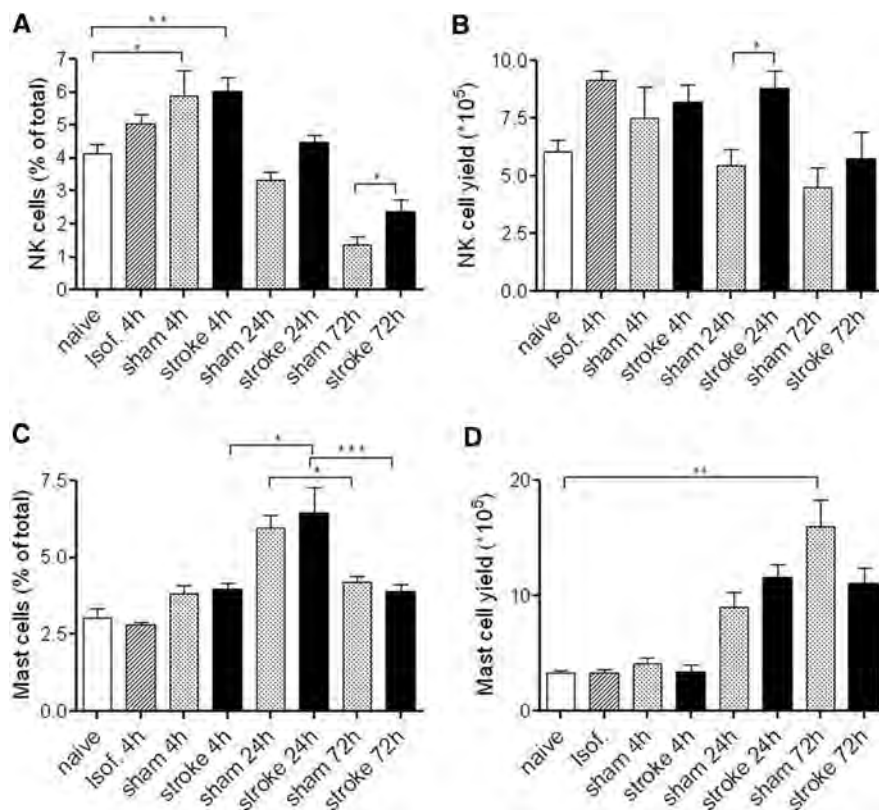


Figure 5 Flow cytometric analysis of natural killer (NK) cells and mast cells in the bone marrow after experimental stroke. (**A**, **B**) Stroke resulted in an increase in NK cells in the bone marrow between 24 and 72 hours reperfusion compared with sham surgery. (**C**) C-kit + Gr-1^{int} mast cell proportions and (**D**) yield at various reperfusion times. * $P < 0.05$; ** $P < 0.01$; *** $P < 0.001$. Data shown are representative of three to eight mice in each group, corresponding to at least two independent experiments.

Figure 4 Differential effects of anaesthetic, surgery, and experimental stroke on lymphocyte populations in the bone marrow. Isoflurane increased T and B cells in the bone marrow at 4 hours reperfusion (**A–E**) as revealed by flow cytometric analysis. (Panels **A** and **B**) CD4-positive and (panels **C** and **D**) CD8-positive T cells were more abundant at 72 hours reperfusion after stroke surgery compared with sham animals, which is indicated by (panels **A** and **C**) increased percentage and by (panels **B** and **D**) cell yield. Surgical stress resulted in reduced B cell ratio (**E**) and numbers (**F**) after 72 hours reperfusion, which was associated with an increased proportion of myeloid cells (see Figure 1) and no significant effect of stroke surgery versus sham was seen. (**G**, **H**) In contrast, MCAO resulted in upregulated MHCII on B cells at 4 hours reperfusion compared with sham surgery. * $P < 0.05$; ** $P < 0.01$; *** $P < 0.001$. Data shown are representative of five to nine mice in each group, corresponding to at least two independent experiments. MCAO, middle cerebral artery occlusion.

Table 1 Changes in cells populations in the bone marrow over time after experimental stroke

	Early (4 hours)			Late (24–72 hours)		
	Anaesthetic	Surgery	Stroke	Anaesthetic	Surgery	Stroke
Total BM cells						
Granulocytes (CXCR2+)			↓↓		↑↑	↓
Myeloid cells (total)			↓		↑↑	↑
CCR5+			↑			
Mast cells					↑	
CD4+ T cells	↑					↑
CD8+ T cells	↑↑					↑
B cells	↑				↓	
MHCII+			↑			
NK cells						↑

The main effects of isoflurane anaesthesia, surgical stress, and stroke were summarized at the time points examined. Arrows indicate cell population changes: ↑, increase; ↓, decrease. It must be noted that trends, or transient changes in cell population ratio without real effect in total cell numbers were not included.

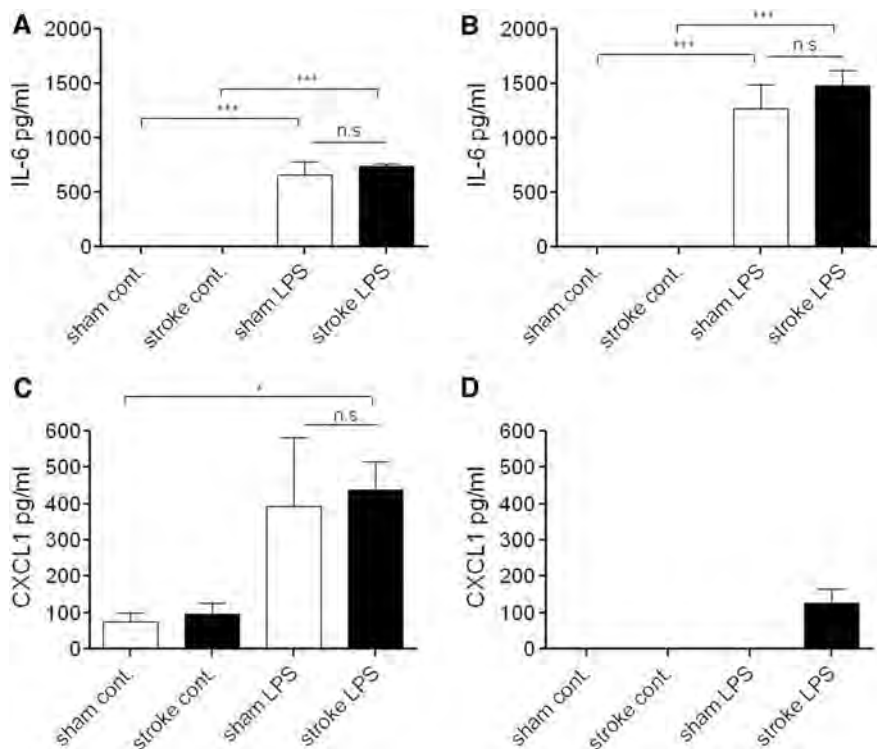


Figure 6 Bone marrow cell response to endotoxin stimulation after experimental stroke. Seventy-two hours after stroke or sham surgery, total bone marrow cells were isolated and stimulated with LPS *in vitro*. **(A)** IL-6 and **(C)** CXCL1 became upregulated in cell lysates after 3 hours stimulation, but no difference was observed between cells isolated from sham or stroke animals. **(B)** High levels of IL-6 and **(D)** low levels of CXCL1 were released into the medium in response to LPS, but no difference in cytokine levels was observed between sham and stroke surgery. * $P < 0.05$; *** $P < 0.001$. Data are representative of two independent experiments. IL-6, interleukin-6; LPS, lipopolysaccharide; NS, not significant.

Lateralisation of the Bone Marrow in Response to Experimental Stroke

Preautonomic neural efferents in the brain stem control the bone marrow (Denes *et al.*, 2005), and two-thirds of the projections originating from the ventrolateral medulla are considered ipsilateral (Moon *et al.*, 2002). Hence, we investigated whether stroke could induce laterality in the brain or in the

bone marrow. In the nucleus ambiguus and pre-Bötzing complex, the adrenal medulla and in the dorsal vagal nucleus (Figures 7A and 7B), obvious ipsilateral–contralateral differences were observed in STAT3 phosphorylation, which was present in most animals up to 48 to 72 hours reperfusion. These medullary neurones are involved in the autonomic regulation of various organs, including respiratory and cardiovascular processes (Doi and Ramirez,

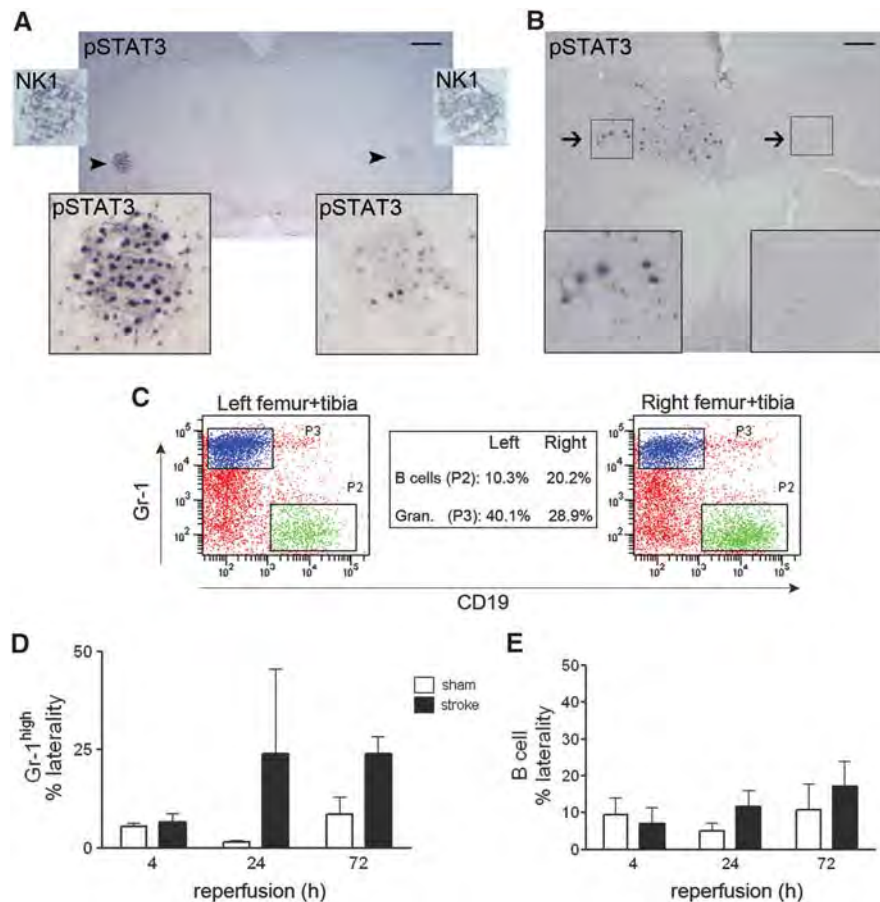


Figure 7 Experimental stroke resulted in lateralisation in the autonomic brainstem nuclei and in the bone marrow. (A) Marked differences were observed in STAT3 phosphorylation (pSTAT3) in the adrenal medulla, the nucleus ambiguus, and pre-Bötzing complex between the ipsilateral and contralateral medulla (bottom inserts, arrowhead) at 48 hours reperfusion. Neurokinin receptor-1 (NK1) expression is shown on the corresponding area of parallel sections (top inserts). (B) Laterality was seen in the nucleus tractus solitarius/dorsal motor nucleus of the vagus (inserts, arrows). (C) Overall, 30% of animals after MCAo exhibited marked lateralisation in the bone marrow when comparing left and right femurs/tibia. Gr-1^{high} granulocytes and CD19-positive B cells are shown. (D) The average difference in Gr-1^{high} granulocyte proportions between the left and right bones was significantly greater after stroke than sham surgery ($P < 0.05$, two-way ANOVA), (E) whereas laterality was not different for B cells. Scale bars: panel A, 250 μm ; panel B, 100 μm . ANOVA, analysis of variance; MCAo, middle cerebral artery occlusion; STAT3, signal transducer and activator of transcription 3.

2010; Elenkov *et al*, 2000). Consequently, 30% to 40% of mice after stroke, but not sham surgery, exhibited marked laterality when comparing the left and right femoral/tibial bone marrow (Figure 7C). The average difference in the ratio of Gr-1^{high} granulocytes between the left and right bones after stroke was significantly greater than that of sham animals (18% versus 5%, respectively, $P < 0.05$, Figure 7D), whereas B-cell proportions were not different (Figure 7E). Laterality in naive animals did not exceed 2% on average for all cell populations examined (data not shown). No obvious ipsilateral or contralateral dominance was observed in any leukocyte populations in the bone marrow after stroke, indicating that although autonomic projections are likely involved in the regulation of the bone marrow, their lateralisation may be more variable at the individual level than in the case of somatomotor projections.

Discussion

We show in this study that the bone marrow responds rapidly to experimental stroke, which involves changes in various leukocyte populations and inflammatory mediators in concert with the development of the stroke-induced systemic response. These findings have implications for at least three different, but largely overlapping research areas. First, the role of systemic inflammatory changes in stroke is increasingly recognised; our data identify key targets for intervention and show that inflammatory leukocyte responses after stroke are likely to be affected directly by changes in the bone marrow microenvironment. Second, our results may serve as important indications for clinical and experimental stem-cell therapy approaches, which largely rely on the transplantation of bone

marrow-derived cells after ischaemia, without fully understanding how the bone marrow itself is affected by the ischaemic challenge. Third, the influence of anaesthetic and surgical stress on the bone marrow indicates that experimental stroke studies need to consider these effects in a translational context.

Myeloid cells in the bone marrow responded rapidly (10 minutes to 4 hours after reperfusion) to experimental stroke. We observed p38 MAPK phosphorylation in Gr-1^{int} SSC^{int} cells, which represent a diverse population of immature and mature myeloid cells, including a subset of monocytes. p38 MAPKs are involved in the regulation of various haematopoietic processes, including granulocyte differentiation and respond to a wide range extracellular cues particularly cellular stressors such as ultraviolet radiation, osmotic shock, hypoxia, proinflammatory cytokines, and less often growth factors (Geest and Coffey, 2009; Raman *et al*, 2007). Activation of the NF κ B pathway in neutrophils occurs in response to various stimuli and is involved in the production of inflammatory cytokines (McDonald *et al*, 1997; McDonald and Cassatella, 1997; Vancurova *et al*, 2001). Nuclear factor- κ B signalling has a key role in granulopoiesis and granulocyte release; mice with I-kappa-B (I κ B) deficiency (which leads to constitutive NF κ B activation) exhibit granulocytosis and blood neutrophilia (Beg *et al*, 1995). CXCL1 (KC) production and NF κ B activation are involved in neutrophil recruitment to the ischaemic tissue in various organs (Chandrasekar *et al*, 2001; Ishibashi *et al*, 1999; Souza *et al*, 2005). CXCR2 is not only a receptor for CXCL1 but also has a crucial role in neutrophil release from the bone marrow. Defective regulation of CXCR2 facilitates neutrophil release from the bone marrow, whereas CXCR2^{-/-} neutrophils are retained in the bone marrow (Eash *et al*, 2010; von Vietinghoff *et al*, 2010). Our data indicate that Gr-1-positive cells become rapidly activated in response to stroke in the bone marrow, which causes the release of the CXCR2-positive myeloid population within 4 hours reperfusion. It has been shown that CXCL1 and G-CSF exert coordinated actions on neutrophil mobilisation from the bone marrow (Wengner *et al*, 2008). Although in our study CXCL1 was upregulated in bone marrow-derived neutrophils/monocytes after both sham and stroke surgery, our results indicate a more pronounced release of CXCL1 (at 4 hours reperfusion) and G-CSF (at 10 minutes reperfusion) into the circulation in response to stroke, which correlates with increased stroke-induced cell mobilisation from the bone marrow. Granulocyte-colony-stimulating factor can induce the expression of CXCL2 (another CXCR2 agonist) in bone marrow endothelial cells; therefore, CXCR2-positive cells may be activated synergistically by CXCL1 and CXCL2 (Eash *et al*, 2010). In contrast to the reduction of CXCR2-positive cells in the bone marrow, we found a transient increase in CCR5 after 4 hours reperfusion. Among several cell types, CCR5 is expressed on murine neutrophils and

monocytes, and the absence of CCR5 results in deficient neutrophil migration responses after ischaemia (Reichel *et al*, 2006). Therefore, our data indicate that experimental stroke may not only exert differential effects on bone marrow myeloid/lymphoid cell populations but is also likely to have differential effects on specific chemokine receptors, which determine leukocyte mobilisation and recruitment.

Neutrophil-derived MMP-9 is involved in the mobilisation of bone marrow cells by G-CSF and CXCR2 ligands in mice (Pelus *et al*, 2004). Production of MMP-9 by activated human monocytes also involves NF κ B activation (Lu and Wahl, 2005). We did not investigate whether proMMP-9 is directly involved in stroke-induced cell mobilisation, but our results indicate that changes in proMMP-9 after MCAo in the bone marrow largely correspond to the release of source cells into the circulation. It is noteworthy that sham surgery alone induced CXCL1 and proMMP-9 in neutrophils between 10 minutes and 4 hours reperfusion. Furthermore, surgical stress and anaesthesia exerted profound effects on both early (4 hours) and late (24 to 72 hours) cellular responses in the bone marrow. Lymphocytes seemed to respond to isoflurane with early (within 4 hours) recruitment into the bone marrow, whereas surgical stress caused a marked increase in bone marrow myeloid cells 72 hours after surgery. Volatile anaesthetics reportedly affect leukocyte responses; e.g., they alter neutrophil adherence to blood vessels (Heindl *et al*, 1999), induce apoptosis of lymphocytes (Matsuoka *et al*, 2001), or affect the resolution of inflammation (Chiang *et al*, 2008). They also contribute to ischaemic brain injury (Lee *et al*, 2007; Li and Zuo, 2009), but our results are the first to show that both surgery and anaesthesia interact with experimental stroke to cause cellular and cytokine changes directly in the bone marrow. Therefore, these data may have important implications for experimental stroke modelling.

The importance of stroke-induced increases in T cells and natural killer cells in the bone marrow between 24 to 72 hours reperfusion is unclear. Bone marrow T cells have been recently shown to maintain and modulate haematopoiesis. T cell-deficient mice have impaired haematopoietic activity and reduced granulocyte numbers, which can be reversed by intravenous injection of T cells (Monteiro *et al*, 2005). Further studies are required to determine whether T cells influence granulocyte responses in the bone marrow after stroke.

Brain damage leads to suppression of host immune responses in experimental animals and humans, which then enables opportunistic pathogens to develop serious posttraumatic infections (Dirnagl *et al*, 2007; Meisel *et al*, 2004; Prass *et al*, 2003). We found no evidence of suppressed bone marrow cell responses to bacterial endotoxin, which indicates that myeloid cells in the bone marrow likely

retain their ability to respond to infectious stimuli. This is also supported by the fact that although bone marrow cells were less abundant in animals that had undergone stroke surgery compared with sham surgery alone, cellular responses in the bone marrow were largely determined by surgical stress at 72 hours reperfusion as compared with naive animals. Furthermore, T-cell numbers were found to increase in the bone marrow after stroke, and not decrease, as occurs in the case of the spleen after cerebral ischaemia (Offner *et al*, 2006b).

Lateralisation of the autonomic nervous system in the brain is one of the proposed causes of stroke-induced immunodepression (Dirnagl *et al*, 2007). Laterality, seen after MCAo in our experiments, indicates that direct neuronal mechanisms are likely to be involved in the activation and/or mobilisation of leukocytes from the bone marrow. This is supported by published findings. Substance P, a neuropeptide released from sensory nerves in the bone marrow controlling haematopoietic cell maturation and release (Broome and Miyan, 2000; Rameshwar *et al*, 1993) induces NF κ B-dependent chemotaxis of neutrophils by upregulation of CXCR2 (Sun *et al*, 2007). The key role of the autonomic nervous system and bone marrow nerves in haematopoiesis and cell mobilisation has also been confirmed in elegant studies (Busik *et al*, 2009; Mendez-Ferrer *et al*, 2008). Further studies are required to assess the role of the autonomic nervous system in bone marrow cell mobilisation after stroke. However, these studies need to consider the difficulty in undertaking specific interventions targeting the bone marrow without affecting the ischaemic brain injury. Our data indicate that neuronal processes are likely to be involved in bone marrow cell mobilisation after experimental stroke, but their impact on immunosuppression may be less than that in other lymphoid organs, such as the spleen.

In conclusion, our results reveal previously unrecognised responses of the bone marrow to experimental stroke, which are likely to affect outcome. Our data also indicate the need to reconsider the relevance of experimental studies on stroke, given the major impacts of anaesthesia and sham surgery.

Disclosure/conflict of interest

NJR is a nonexecutive director of AstraZenca, but this has no relation to the current research.

References

Balistreri CR, Caruso C, Grimaldi MP, Listi F, Vasto S, Orlando V, Campagna AM, Lio D, Candore G (2007) CCR5 receptor: biologic and genetic implications in age-related diseases. *Ann NY Acad Sci* 1100:162–72

- Bederson JB, Pitts LH, Tsuji M, Nishimura MC, Davis RL, Bartkowski H (1986) Rat middle cerebral artery occlusion: evaluation of the model and development of a neurologic examination. *Stroke* 17:472–6
- Beg AA, Sha WC, Bronson RT, Baltimore D (1995) Constitutive NF-kappa B activation, enhanced granulopoiesis, and neonatal lethality in I kappa B alpha-deficient mice. *Genes Dev* 9:2736–46
- Bottero V, Withoff S, Verma IM (2006) NF-kappaB and the regulation of hematopoiesis. *Cell Death Differ* 13:785–97
- Broome CS, Miyan JA (2000) Neuropeptide control of bone marrow neutrophil production. A key axis for neuroimmunomodulation. *Ann NY Acad Sci* 917:424–34
- Busik JV, Tikhonenko M, Bhatwadekar A, Opreanu M, Yakubova N, Caballero S, Player D, Nakagawa T, Afzal A, Kielczewski J, Sochacki A, Hasty S, Li Calzi S, Kim S, Duclas SK, Segal MS, Guberski DL, Esselman WJ, Boulton ME, Grant MB (2009) Diabetic retinopathy is associated with bone marrow neuropathy and a depressed peripheral clock. *J Exp Med* 206:2897–906
- Chandrasekar B, Smith JB, Freeman GL (2001) Ischemia-reperfusion of rat myocardium activates nuclear factor-kappaB and induces neutrophil infiltration via lipopolysaccharide-induced CXC chemokine. *Circulation* 103:2296–302
- Chapman KZ, Dale VQ, Denes A, Bennett G, Rothwell NJ, Allan SM, McColl BW (2009) A rapid and transient peripheral inflammatory response precedes brain inflammation after experimental stroke. *J Cereb Blood Flow Metab* 29:1764–8
- Chiang N, Schwab JM, Fredman G, Kasuga K, Gelman S, Serhan CN (2008) Anesthetics impact the resolution of inflammation. *PLoS One* 3:e1879
- Denes A, Boldogkoi Z, Uherezky G, Hornyak A, Rusvai M, Palkovits M, Kovacs KJ (2005) Central autonomic control of the bone marrow: multisynaptic tract tracing by recombinant pseudorabies virus. *Neuroscience* 134:947–63
- Denes A, Thornton P, Rothwell NJ, Allan SM (2010) Inflammation and brain injury: acute cerebral ischaemia, peripheral and central inflammation. *Brain Behav Immun* 24:708–23
- Denes A, Vidyasagar R, Feng J, Narvainen J, McColl BW, Kauppinen RA, Allan SM (2007) Proliferating resident microglia after focal cerebral ischaemia in mice. *J Cereb Blood Flow Metab* 27:1941–53
- Dirnagl U, Klehmet J, Braun JS, Harms H, Meisel C, Ziemssen T, Prass K, Meisel A (2007) Stroke-induced immunodepression: experimental evidence and clinical relevance. *Stroke* 38:770–3
- D'Mello C, Le T, Swain MG (2009) Cerebral microglia recruit monocytes into the brain in response to tumor necrosis factor alpha signaling during peripheral organ inflammation. *J Neurosci* 29:2089–102
- Doi A, Ramirez JM (2010) State-dependent interactions between excitatory neuromodulators in the neuronal control of breathing. *J Neurosci* 30:8251–62
- Eash KJ, Greenbaum AM, Gopalan PK, Link DC (2010) CXCR2 and CXCR4 antagonistically regulate neutrophil trafficking from murine bone marrow. *J Clin Invest* 120:2423–31
- Elenkov IJ, Wilder RL, Chrousos GP, Vizi ES (2000) The sympathetic nerve—an integrative interface between two supersystems: the brain and the immune system. *Pharmacol Rev* 52:595–638
- Emsley HC, Hopkins SJ (2008) Acute ischaemic stroke and infection: recent and emerging concepts. *Lancet Neurol* 7:341–53

- Geest CR, Coffey PJ (2009) MAPK signaling pathways in the regulation of hematopoiesis. *J Leukoc Biol* 86:237–50
- Heindl B, Reichle FM, Zahler S, Conzen PF, Becker BF (1999) Sevoflurane and isoflurane protect the reperfused guinea pig heart by reducing postischemic adhesion of polymorphonuclear neutrophils. *Anesthesiology* 91:521–30
- Honczarenko M, Le Y, Glodek AM, Majka M, Campbell JJ, Ratajczak MZ, Silberstein LE (2002) CCR5-binding chemokines modulate CXCL12 (SDF-1)-induced responses of progenitor B cells in human bone marrow through heterologous desensitization of the CXCR4 chemokine receptor. *Blood* 100:2321–9
- Ishibashi N, Weisbrot-Lefkowitz M, Reuhl K, Inouye M, Mirochnitchenko O (1999) Modulation of chemokine expression during ischemia/reperfusion in transgenic mice overproducing human glutathione peroxidases. *J Immunol* 163:5666–77
- Jacobs JP, Ortiz-Lopez A, Campbell JJ, Gerard CJ, Mathis D, Benoist C (2010) Deficiency of CXCR2, but not other chemokine receptors, attenuates autoantibody-mediated arthritis in a murine model. *Arthritis Rheum* 62:1921–32
- Kim JV, Kang SS, Dustin ML, McGavern DB (2009) Myelomonocytic cell recruitment causes fatal CNS vascular injury during acute viral meningitis. *Nature* 457:191–5
- Kohlmeier JE, Miller SC, Smith J, Lu B, Gerard C, Cookenham T, Roberts AD, Woodland DL (2008) The chemokine receptor CCR5 plays a key role in the early memory CD8+ T cell response to respiratory virus infections. *Immunity* 29:101–13
- Lee HT, Kim M, Kim M, Kim N, Billings FTt, D'Agati VD, Emala CW, Sr (2007) Isoflurane protects against renal ischemia and reperfusion injury and modulates leukocyte infiltration in mice. *Am J Physiol Renal Physiol* 293:F713–22
- Li L, Huang L, Vergis AL, Ye H, Bajwa A, Narayan V, Strieter RM, Rosin DL, Okusa MD (2010) IL-17 produced by neutrophils regulates IFN-gamma-mediated neutrophil migration in mouse kidney ischemia-reperfusion injury. *J Clin Invest* 120:331–42
- Li L, Zuo Z (2009) Isoflurane preconditioning improves short-term and long-term neurological outcome after focal brain ischemia in adult rats. *Neuroscience* 164:497–506
- Liu L, Belkadi A, Darnall L, Hu T, Drescher C, Cotleur AC, Padovani-Claudio D, He T, Choi K, Lane TE, Miller RH, Ransohoff RM (2010) CXCR2-positive neutrophils are essential for cuprizone-induced demyelination: relevance to multiple sclerosis. *Nat Neurosci* 13:319–26
- Lu Y, Wahl LM (2005) Production of matrix metalloproteinase-9 by activated human monocytes involves a phosphatidylinositol-3 kinase/Akt/IKKalpha/NF-kappaB pathway. *J Leukoc Biol* 78:259–65
- Martin C, Burdon PC, Bridger G, Gutierrez-Ramos JC, Williams TJ, Rankin SM (2003) Chemokines acting via CXCR2 and CXCR4 control the release of neutrophils from the bone marrow and their return following senescence. *Immunity* 19:583–93
- Matsuoka H, Kurosawa S, Horinouchi T, Kato M, Hashimoto Y (2001) Inhalation anesthetics induce apoptosis in normal peripheral lymphocytes *in vitro*. *Anesthesiology* 95:1467–72
- McColl BW, Allan SM, Rothwell NJ (2009) Systemic infection, inflammation and acute ischemic stroke. *Neuroscience* 158:1049–61
- McColl BW, Rothwell NJ, Allan SM (2008) Systemic inflammation alters the kinetics of cerebrovascular tight junction disruption after experimental stroke in mice. *J Neurosci* 28:9451–62
- McDonald PP, Bald A, Cassatella MA (1997) Activation of the NF-kappaB pathway by inflammatory stimuli in human neutrophils. *Blood* 89:3421–33
- McDonald PP, Cassatella MA (1997) Activation of transcription factor NF-kappa B by phagocytic stimuli in human neutrophils. *FEBS Lett* 412:583–6
- Meisel C, Prass K, Braun J, Victorov I, Wolf T, Megow D, Halle E, Volk HD, Dirnagl U, Meisel A (2004) Preventive antibacterial treatment improves the general medical and neurological outcome in a mouse model of stroke. *Stroke* 35:2–6
- Mendez-Ferrer S, Lucas D, Battista M, Frenette PS (2008) Haematopoietic stem cell release is regulated by circadian oscillations. *Nature* 452:442–7
- Monteiro JP, Benjamin A, Costa ES, Barcinski MA, Bonomo A (2005) Normal hematopoiesis is maintained by activated bone marrow CD4+ T cells. *Blood* 105:1484–91
- Moon EA, Goodchild AK, Pilowsky PM (2002) Lateralisation of projections from the rostral ventrolateral medulla to sympathetic preganglionic neurons in the rat. *Brain Res* 929:181–90
- Offner H, Subramanian S, Parker SM, Afentoulis ME, Vandenbark AA, Hurn PD (2006a) Experimental stroke induces massive, rapid activation of the peripheral immune system. *J Cereb Blood Flow Metab* 26:654–65
- Offner H, Subramanian S, Parker SM, Wang C, Afentoulis ME, Lewis A, Vandenbark AA, Hurn PD (2006b) Splenic atrophy in experimental stroke is accompanied by increased regulatory T cells and circulating macrophages. *J Immunol* 176:6523–31
- Offner H, Vandenbark AA, Hurn PD (2009) Effect of experimental stroke on peripheral immunity: CNS ischemia induces profound immunosuppression. *Neuroscience* 158:1098–111
- Pelus LM, Bian H, King AG, Fukuda S (2004) Neutrophil-derived MMP-9 mediates synergistic mobilization of hematopoietic stem and progenitor cells by the combination of G-CSF and the chemokines GRObeta/CXCL2 and GRObetaT/CXCL2delta4. *Blood* 103:110–9
- Prass K, Meisel C, Hoflich C, Braun J, Halle E, Wolf T, Ruscher K, Victorov IV, Priller J, Dirnagl U, Volk HD, Meisel A (2003) Stroke-induced immunodeficiency promotes spontaneous bacterial infections and is mediated by sympathetic activation reversal by post-stroke T helper cell type 1-like immunostimulation. *J Exp Med* 198:725–36
- Raman M, Chen W, Cobb MH (2007) Differential regulation and properties of MAPKs. *Oncogene* 26:3100–12
- Rameshwar P, Ganea D, Gascon P (1993) *In vitro* stimulatory effect of substance P on hematopoiesis. *Blood* 81:391–8
- Reichel CA, Khandoga A, Anders HJ, Schlondorff D, Luckow B, Krombach F (2006) Chemokine receptors Ccr1, Ccr2, and Ccr5 mediate neutrophil migration to postischemic tissue. *J Leukoc Biol* 79:114–22
- Souza DG, Vieira AT, Pinho V, Sousa LP, Andrade AA, Bonjardim CA, McMillan M, Kahn M, Teixeira MM (2005) NF-kappaB plays a major role during the systemic and local acute inflammatory response following intestinal reperfusion injury. *Br J Pharmacol* 145:246–54
- Sun J, Ramnath RD, Bhatia M (2007) Neuropeptide substance P upregulates chemokine and chemokine receptor expression in primary mouse neutrophils. *Am J Physiol* 293:C696–704

- Vancurova I, Miskolci V, Davidson D (2001) NF-kappa B activation in tumor necrosis factor alpha-stimulated neutrophils is mediated by protein kinase Cdelta. Correlation to nuclear Ikappa Balpha. *J Biol Chem* 276:19746–52
- von Vietinghoff S, Asagiri M, Azar D, Hoffmann A, Ley K (2010) Defective regulation of CXCR2 facilitates neutrophil release from bone marrow causing spontaneous inflammation in severely NF-kappaB-deficient mice. *J Immunol* 185:670–8
- Wengner AM, Pitchford SC, Furze RC, Rankin SM (2008) The coordinated action of G-CSF and ELR + CXC chemokines in neutrophil mobilization during acute inflammation. *Blood* 111:42–9

Supplementary Information accompanies the paper on the Journal of Cerebral Blood Flow & Metabolism website (<http://www.nature.com/jcbfm>)



Contents lists available at ScienceDirect

Brain, Behavior, and Immunity

journal homepage: www.elsevier.com/locate/ybrbi

Full-length Article

Brain injury induces specific changes in the caecal microbiota of mice via altered autonomic activity and mucoprotein production

A. Houlden^a, M. Goldrick^a, D. Brough^a, E.S. Vizi^{c,d}, N. Lénárt^b, B. Martinecz^b, I.S. Roberts^{a,*}, A. Denes^{a,b,*}^a Faculty of Life Sciences, University of Manchester, Manchester, UK^b Laboratory of Neuroimmunology, Institute of Experimental Medicine, Budapest, Hungary^c Laboratory of Drug Research, Institute of Experimental Medicine, Hungarian Academy of Sciences, P.O.B. 67, H-1450 Budapest, Hungary^d Department of Pharmacology and Pharmacotherapy, Semmelweis University, Budapest, Hungary

ARTICLE INFO

Article history:

Received 13 January 2016

Received in revised form 9 March 2016

Accepted 5 April 2016

Available online 6 April 2016

Keywords:

Stroke
Microbiota
Cerebral ischemia
Inflammation
Noradrenaline
Gut
Mucoprotein

ABSTRACT

Intestinal microbiota are critical for health with changes associated with diverse human diseases. Research suggests that altered intestinal microbiota can profoundly affect brain function. However, whether altering brain function directly affects the microbiota is unknown. Since it is currently unclear how brain injury induces clinical complications such as infections or paralytic ileus, key contributors to prolonged hospitalization and death post-stroke, we tested in mice the hypothesis that brain damage induced changes in the intestinal microbiota. Experimental stroke altered the composition of caecal microbiota, with specific changes in Peptococcaceae and Prevotellaceae correlating with the extent of injury. These effects are mediated by noradrenaline release from the autonomic nervous system with altered caecal mucoprotein production and goblet cell numbers. Traumatic brain injury also caused changes in the gut microbiota, confirming brain injury effects gut microbiota. Changes in intestinal microbiota after brain injury may affect recovery and treatment of patients should appreciate such changes.

© 2016 The Authors. Published by Elsevier Inc. This is an open access article under the CC BY license (<http://creativecommons.org/licenses/by/4.0/>).

1. Introduction

It is becoming clear that intestinal microbiota play key roles in both host development and in maintaining homeostasis. Intestinal microbiota change with age and are also influenced by environmental factors such as diet, and disease (Flint et al., 2012; Wu, 2011; Spor et al., 2011). Recent research highlights the key role of microbial communities in the large intestine in essential immune defence mechanisms and control of inflammatory responses (Abt et al., 2012; Ganal et al., 2012). Impaired regulation of the intestinal microbiota is also known to contribute to diseases of the intestinal tract, and is linked with the development of diverse inflammatory conditions such as sepsis, metabolic disease or cancer (Ayres et al., 2012; Dupont and Dupont, 2011; Le Chatelier et al., 2013; Yoshimoto et al., 2013). Altered intestinal microbiota have also recently been linked to neuro-behavioural problems such as autism (Hsiao et al., 2013; Kang et al., 2013). In

fact the effect of microbiota on brain function is profound with microbiota known to influence brain specific activity such as anxiety like behaviour, learning and memory, microglial activity and blood brain barrier integrity (Luczynski, 2016). However, much less is known about whether changes in the intestinal microbiota are themselves influenced by central nervous system function. Brain injury caused by stroke is the most common cause of lasting disability worldwide and has a huge socio-economic impact. Beyond the detrimental effects of the initial injury on outcome after acute cerebrovascular events, one of the key causes for death or prolonged hospitalization and impaired recovery of patients is the development of post-stroke infections (Dirnagl et al., 2007). In some clinical studies, preventive antibiotic therapy was found beneficial (Hetze et al., 2013), and recent data indicate that pattern recognition receptors that can recognise microbiota-derived products could contribute to stroke outcome (Denes et al., 2015; Caso et al., 2008). The enteric nervous system is under central autonomic control and it is believed that the autonomic nervous system contributes to regulation of intestinal immunity and microbiota (de Jonge, 2013). We and others have shown that acute brain injury induces diverse autonomic, neuroendocrine and inflammatory changes, which manifest in several organs in the body, leading to immunosuppression and the development of

* Corresponding authors at: Faculty of Life Sciences, University of Manchester, Manchester, UK (I.S. Roberts); Laboratory of Neuroimmunology, Institute of Experimental Medicine, Budapest, Hungary (A. Denes).

E-mail addresses: i.s.roberts@manchester.ac.uk (I.S. Roberts), denesa@koki.hu (A. Denes).

infectious complications (Dirnagl et al., 2007; Denes et al., 2010). The impact of an acute brain injury on the intestinal microbiota, and whether this is also influenced by neuroendocrine and inflammatory changes as a result of injury, is not known, but could be of importance to the outcome and recovery of the patient.

Here we tested the hypothesis that an acute brain injury induced by experimental stroke or traumatic brain injury would induce specific changes in the gut microbiota. We demonstrate that brain injury profoundly impacts on microbial communities in the caecum and that brain injury is associated with specific changes in microbiota. We propose that these changes are due to increased noradrenaline (NE) release from the autonomic nervous system into the gut. These changes may influence recovery after an acute brain injury.

2. Methods

2.1. Mice

Male 10–14 week-old C57BL/6 mice were kept at 22 °C ± 1 °C and 65% humidity with a 12 h light-dark cycle and had free access to food and water. All animal procedures were performed under appropriate project licence authority and adhered to the UK Animals (Scientific Procedures) Act (1986) and the Hungarian Act of Animal Care and Experimentation (1998; XXVIII, Section 243/1998), approved by the Animal Care and Use Committee of the IEM.

2.2. Middle cerebral artery occlusion (MCAo)

Transient focal cerebral ischemia was induced as described previously (Denes et al., 2010). Briefly, mice were anaesthetised with isoflurane, the common carotid artery was exposed and cerebral ischemia was induced by an intraluminal filament that was advanced along the internal carotid artery, to occlude middle cerebral artery. After 60 min of MCAo, reperfusion was induced for 4 h or 72 h prior to sacrifice. Core body temperature was maintained at 37.0 °C ± 0.5 °C throughout the surgery by a heating blanket (Homeothermic Blanket Control Unit; Harvard Apparatus, Kent, UK) and monitored after recovery. After surgery, animals were returned to their cages and allowed free access to water and food. Neurological deficit in mice was assessed by using Bederson scores (4 point scale of increasing neurological deficit) as described previously (Denes et al., 2010). Animals that showed no obvious neurological deficit at 4 h reperfusion after MCAo (score 1 at minimum) have been excluded from the studies pre hoc (n = 1).

2.3. Surgical controls

We investigated the effect of surgical manipulation and anaesthesia in the absence of experimental stroke on changes in the intestinal microbiota. To achieve this, two separate experimental conditions were used; the first involved only anaesthesia with no surgical manipulation, the second sham surgery, during which mice underwent all procedures as in the MCAo group, except for occlusion of the MCA with an intraluminal filament.

2.4. Traumatic brain injury (TBI)

A closed head model of TBI was performed in mice under isoflurane anaesthesia similarly to what has been described earlier, with slight modifications (Umschweif et al., 2014). After induction of anaesthesia, the skull was exposed by a small, midline longitudinal incision. The head was held in place and a plastic cone was placed on the skull 2 mm lateral of the midline after which a 100 g weight was allowed to fall on the top of the cone from a preestablished

height resulting in injury to the left hemisphere, which localised around the affected cerebral cortex (Fig. 7). Mice were allowed to recover and 1 ml of saline was injected subcutaneously for rehydration. We used a relative mild form of TBI resulting in 2 out of 7 mice with substantial neurological deficit as assessed 72 h later. Sham animals were subjected to the same procedure except for head injury.

2.5. Pharmacological manipulation of the sympathetic nervous system

A group of mice was injected with the NE reuptake inhibitor atomoxetine (Sigma, 0.1 mg kg⁻¹) and the α2-adrenergic receptor antagonist yohimbine (Sigma, 1 mg kg⁻¹) administered intraperitoneally (0.2 ml/mouse in total), once daily for three subsequent days. Another group of mice received a single intraperitoneal injection of 6-hydroxydopamine (6-OHDA) (0.2 ml, Sigma, 100 mg kg⁻¹) followed by 0.2 ml sterile saline for two subsequent days. Control mice were administered 0.2 ml saline daily for three days. Mice were sacrificed 72 h after the first injection; the caecum was quickly removed and was kept at –80 °C until use.

2.6. ELISA

To measure inflammatory changes and neurotransmitter levels in the gut, caecum tissues were washed in sterile saline and homogenised as described previously (Denes et al., 2010). Samples were kept at –20 °C until processing. Protein concentrations calculated using a BCA assay (Pierce/Thermo Fisher Scientific). Caecum homogenates were measured for granulocyte-colony stimulating factor (G-CSF), RANTES (CCL5), KC (CXCL1), MMP-9, interleukin 6 (IL-6), ICAM-1, VCAM-1 (R & D Systems, UK), adrenaline and noradrenaline (Eagle Biosciences, NH, USA), substance P (R & D Systems, UK), and serotonin (Enzo, UK) according to the manufacturers protocol.

2.7. DNA extraction

Genomic DNA was extracted directly from total caecal content (~250 mg) using the QIAamp DNA Stool Mini Kit (Qiagen) with pathogen protocol.

2.8. Community profiling

Bacterial communities were profiled in the mouse caecum using Denaturing Gradient Gel Electrophoresis (DGGE), 454 sequencing (Roche, USA), and Illumina MiSeq (USA). DGGE assessment of the bacterial communities was as follows: PCR amplification of the 16S rRNA gene used universal primers 341F-GC and 518R (Muyzer et al., 1993), and reaction conditions: 5U BioTaq polymerase in 1X buffer (Bioline, UK), 1.5 mM MgCl₂, 20 pmol primers, 0.2 mM dNTPs, 5 µg BSA, and 10–50 ng of template DNA in a final volume of 50 µL. The cycle sequence consisted of initial denaturation step of 95 °C 5 min, then 30 cycles of 95 °C 1 min; 55 °C 1 min; 72 °C 1 min, and final extension of 72 °C 10 min. PCR products were purified (QiaGEN Minelute kit) before loading onto a DGGE gel (150 ng/lane). Samples were separated using the D-code system (Bio-Rad, USA) on 10% w/v acrylamide gel with a gradient of 30–70% denaturant at 60 °C for 16 h at 63 V. Gels were stained for 30 min using SYBR Gold (Invitrogen, USA). DGGE Gels were analysed with Phoretix 1D Advanced gel analysis software (Ver. 5.0, Nonlinear Dynamics Ltd.), with binary matrix of band presence/absence of individual bands used for sample comparison.

2.8.1. Pyrosequencing

454 sequencing of the bacterial communities were as follows: The 16S rRNA gene was amplified using the modified 16S primers 66f and 518R (italicised) to include Lib-A (underlined) linker

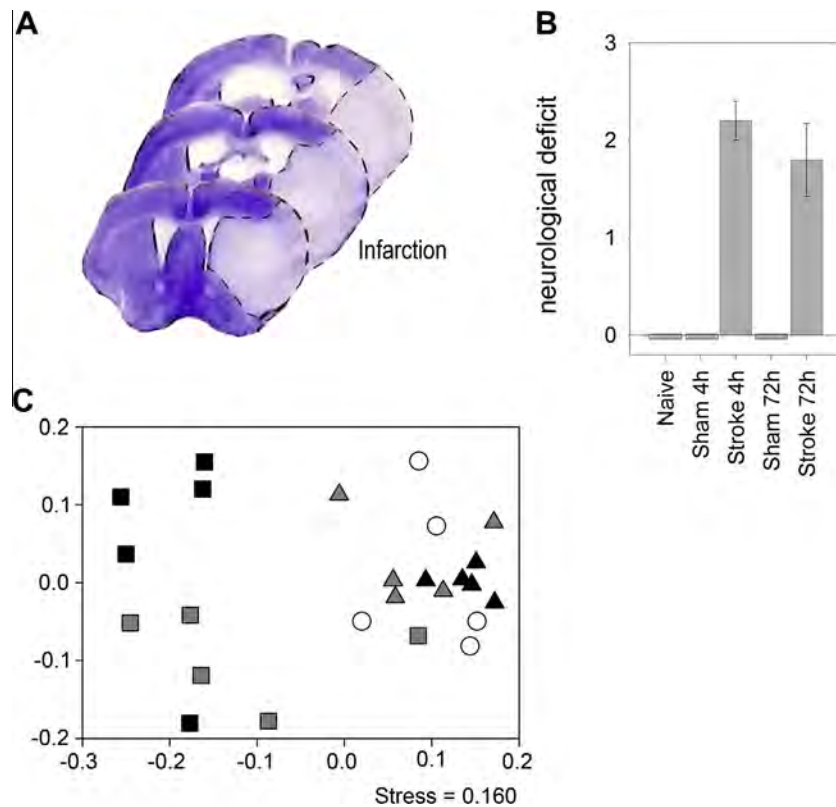


Fig. 1. Neurological deficit and bacterial community profiling of brain injury mice and controls by DGGE: (A) Brain injury is shown after 60 min MCAo and 72 h reperfusion as identified by cresyl violet staining, dotted line indicates infarct boarder. (B) Neurological deficit score for mice post surgery significant effect of treatment (ANOVA: $F_{4,20} = 33.88$, $p < 0.01$) post hoc TukeyHSD confirmed stroke increase neurological deficit ($p < 0.001$), with no difference between 4 h or 72 h post brain injury ($p = 0.58$). Error bars are standard error of the mean, $n = 5$. (C) NMDS analysis of caecal bacterial communities assessed by DGGE of the 16S rRNA gene, profile of Naïve, Sham and Brain injury mice caecal bacterial communities at $t = 4$ h and 72 h post operation. Samples are as follows: $\circ = t 0$; $\triangle = t 4$ h; $\square = t 72$ h post treatment; white = naïve; grey = sham; black = brain injury. Axis represent scale for similarity distance scores between sample centered to (0,0). PERMANOVA: Naïve vs. Sham and Brain injury at 4 h post operation (adonis: $F.Model_{2,12} = 1.34$, $p = 0.159$), Naïve vs. Sham 72 h (adonis: $F.Model_{1,8} = 3.59$, $p = 0.016$); Naïve vs. Brain Injury 72 h, (adonis: $F.Model_{1,8} = 5.90$, $p = 0.008$); Sham 72 h vs. Brain Injury 72 h, (adonis: $F.Model_{1,8} = 1.51$, $pr = 0.17$). (For interpretation of the references to colour in this figure legend, the reader is referred to the web version of this article.)

primer sequences required to 454 sequencing and a MID tag to allow sample pooling (Forward primer (Primer A-Key): 5'-CGTATCGCCTCCCTCGCGCCATCAG(MID)CAGGCTAACACATGCAAGTC-3'.

Reverse primer (Primer B-Key): 5'-CTATGCGCCTTGCAGCCCGCTCAGATTACCGCGGCTGCTGG-3'.

Roche multiplex identifiers (MID tags), which are unique “barcode” sequences for each amplified sample were used to allow the pooling of different samples into the same sequencing run. Post sequencing these samples could then be separated on their MIDs back into the individual sample amplified for analysis. MIDs used are detailed in Table S1. All samples were amplified by PCR using the same batch of reagents/buffers to eliminate reagent difference effects, they were also amplified in triplicate to reduce variation in PCR amplicon products (Polz and Cavanaugh, 1998). Samples were amplified using the following reaction conditions: 3U Velocity polymerase in 1X buffer (Bioline, UK), 20 pmol primers, 0.2 mM dNTPs, and 10–50 ng of template DNA in a final volume of 50 μ L. The cycle parameters used a low cycle number to reduce chimera production (Thompson et al., 2002), and were as follows: Initial denaturation 95 $^{\circ}$ C 2 min 30 s, then 18 cycles of 95 $^{\circ}$ C 10 s; 55 $^{\circ}$ C 10 s; 72 $^{\circ}$ C 30 s; with final extension of 72 $^{\circ}$ C 2 min. Triplicate PCR reactions were pooled, before size selection by gel extraction with the QIAquick gel extraction kit, concentrated by using MinElute PCR Purification Kit (Qiagen), quantified using Qubit dsDNA HS Assay (Life technologies) before pooling of MID tagged products in equimolar amounts in preparation for multiplex barcode pyrosequencing. Roche 454 GS-FLX sequencing was undertaken

at the Centre for Genome Research, University of Liverpool, yielding a total of 305,216 reads Sequences were processed with flows trimmed to 400 and processed/cleaned using PyroDist for distance

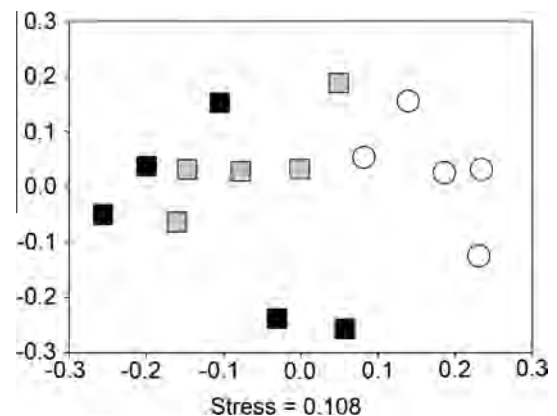


Fig. 2. 16S amplicon pyrosequencing analysis of mouse caecum from naive, sham and brain injury mice. Bacterial species relative abundances from rarefied OTU data (1866 sequences) were used for NMDS analysis. Samples are as follows: $\circ = t 0$; $\square = t 72$ h post treatment; white = naïve; grey = sham; black = brain injury. Axis represent scale for similarity distance scores between sample centered to (0,0). Pair-wise comparisons were undertaken to identify significant differences using PERMANOVA. Naïve vs. Sham (adonis: $F.Model_{1,8} = 2.12$, $p = 0.008$); Naïve vs. Brain Injury (adonis: $F.Model_{1,8} = 2.24$, $p = 0.008$); Sham vs. Brain injury, (adonis: $F.Model_{1,8} = 1.02$, $p = 0.484$).

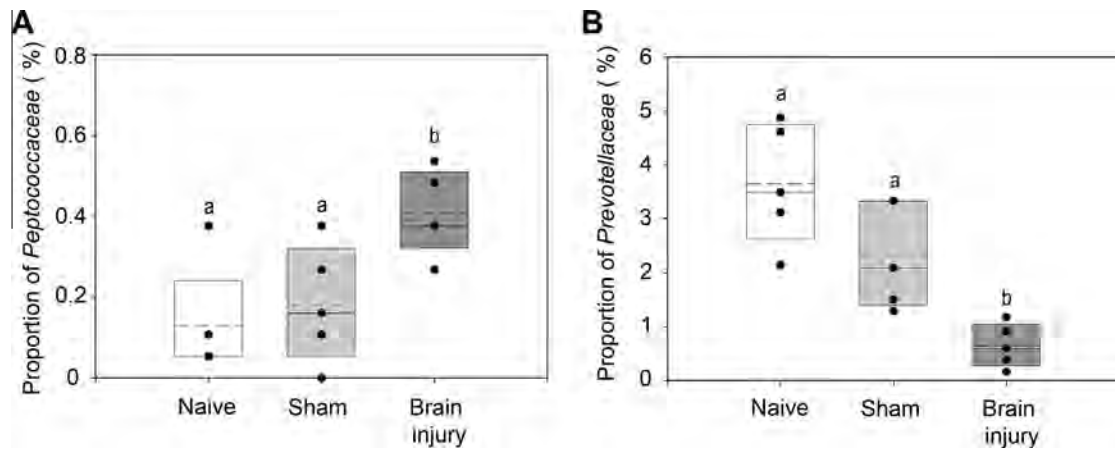


Fig. 3. Proportions of bacterial taxa that were identified to change significantly as a result of experimental stroke or sham surgery. ANOVA was undertaken on all taxa identified with FDR correction of P-values. (A) *Peptococcaceae* proportions of community between naïve, sham, and brain injury mice were significantly different (p -adjust = 0.026), with labels a and b denoting treatments significantly different ($p < 0.05$) identified using TukeyHSD posthoc test, (B) *Prevotellaceae* proportions of community between naïve, sham, and brain injury mice were significantly different (p -adjust = 0.019) with labels a and b denoting treatments significantly different ($p \leq 0.05$) identified using TukeyHSD posthoc test. Upper and lower limits of box represent 75th and 25th percentile, solid line in median, dotted line mean. Dots represent actual values for each mouse.

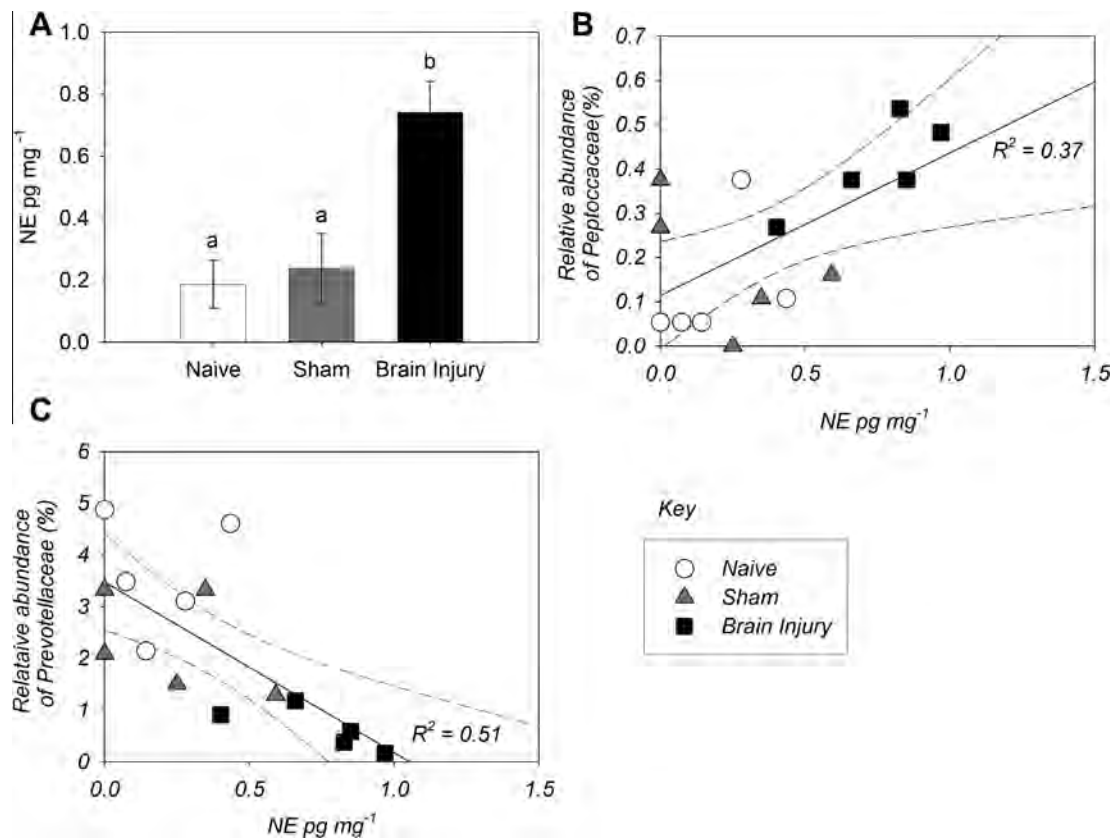


Fig. 4. Intestinal microbiota changes correlate with gut noradrenaline (NE) levels (A) Mice that had undergone 60 min MCAo and 72 h reperfusion show significantly increased NE levels in gut tissue homogenates (ANOVA: $F_{2,12} = 10.02$, $p = 0.003$; Posthoc TukeyHSD significance < 0.001 , with the labels a and b denoting samples significantly different, error bars are standard error of the mean, $n = 5$). (B) *Peptococcaceae* relative abundance correlate with intestinal NE levels (Regression: $R^2 = 0.370$, $F_{1,13} = 7.56$, $p = 0.02$), Equation of line $y = 0.322x + 0.114$. (C) *Prevotellaceae* decrease in the intestinal proportionally to increasing NE levels after injury (Regression: $R^2 = 0.512$, $F_{1,13} = 13.58$, $p = 0.003$), Equation of line $y = -3.299x + 3.480$. Samples are as follows: \circ = Naive; \triangle = Sham 72 h post treatment; \square = Brain injury 72 h post treatment.

calculation, FCluster for clustering analysis, PyroNoise in mothur based on AmpliconNoiseV1.25 (Quince et al., 2011).

2.8.2. Illumina MiSeq

Sequencing of the bacterial communities were undertaken by Centre for Genome Research, University of Liverpool using paired end Illumina MiSeq, and library prep was as follows: The 16S rRNA

gene was amplified using the primers described by Caporaso et al. (2011) producing 254 bp insert, and then nested PCR to add MID tags and including Illumina adaptor sequences as in the Illumina Nextera protocol. Samples were amplified using the following reaction conditions: 1X Kapa Mastermix (KapaBiosystems, UK) 10 μ M primers, and 5–10 ng of template DNA in 20 μ l final volume. Samples were then purified using Ampure beads and resuspend

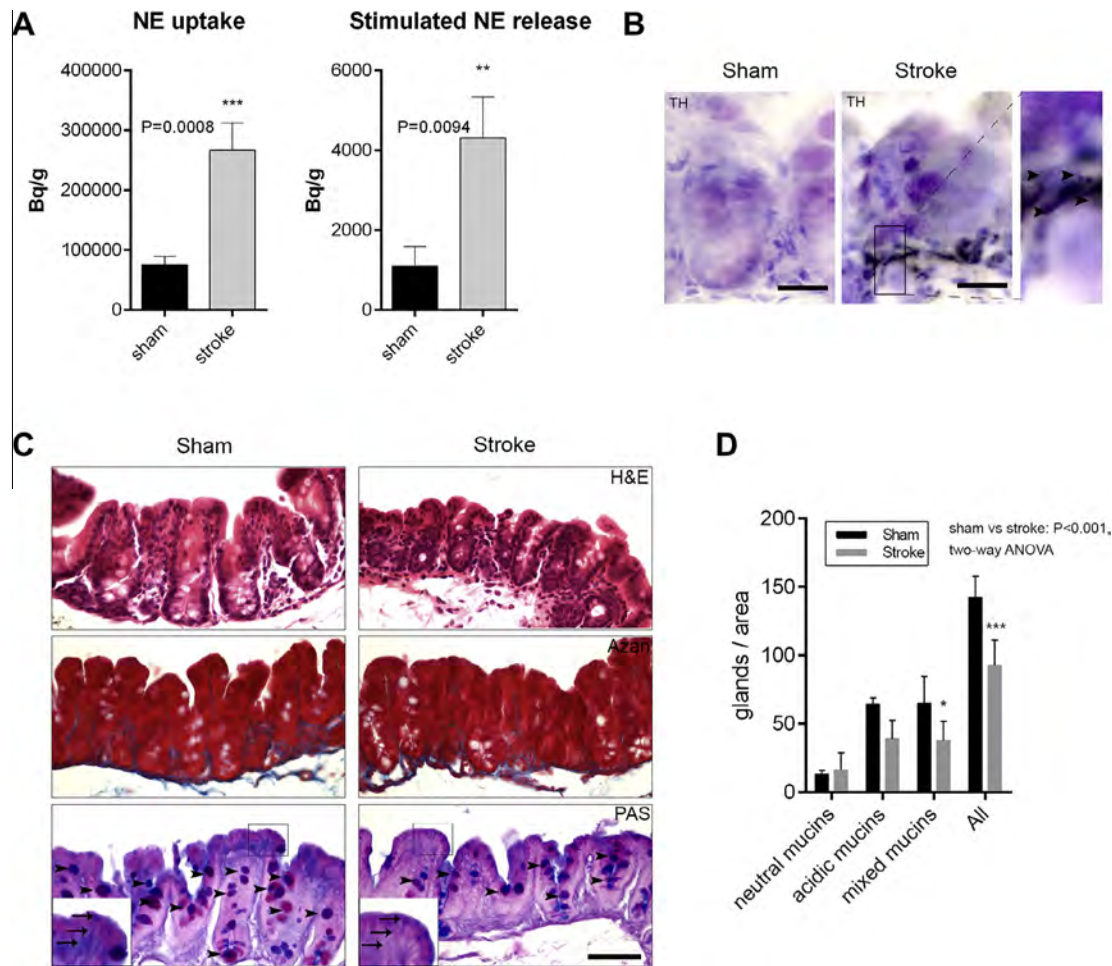


Fig. 5. Brain injury results in altered noradrenaline (NE) release and mucoprotein production in the caecum. (A) Tissue uptake and stimulated release of ^3H -NE was significantly increased in the caecum 72 h after experimental stroke ($^{**}P < 0.01$, $^{***}P < 0.0001$, unpaired t test), error bars are standard error of the mean, $n = 6-8$). (B) Tyrosine hydroxylase immunopositive nerve fibers (arrowheads) are most abundant at the basis of the intestinal epithelium found often in the proximity of goblet cells in mice 72 h after brain injury (cresyl violet counterstain). (C) Haematoxylin and eosin (H&E), Azan and periodic acid-Schiff-alcian blue (PAS) staining of paraffin-embedded caecum sections is shown, 72 h after sham surgery or experimental stroke. PAS staining identifies mucoprotein-containing cells (magenta – neutral mucins, blue – acidic mucins, magenta/blue – mixed mucins) and indicates less mucoproteins associated with the apical part of intestinal epithelial cells (shown by arrowheads on insert). (D) Quantification of PAS staining (C). Brain injury is associated with less mucin-containing cells in the caecum compared to sham animals ($^{*}P < 0.05$, $^{***}P < 0.0001$, one-way ANOVA followed by TukeyHSD posthoc test), error bars are standard error of the mean, $n = 4$. Scale bars: B – 50 μm; C – 100 μm. (For interpretation of the references to colour in this figure legend, the reader is referred to the web version of this article.)

in 10 μl. In the second round PCR 5 ng of template DNA is replaced with 9 μl of purified PCR product. The cycle parameters used a low cycle number to reduce chimera production (Thompson et al., 2002), and were as follows for both rounds of PCR: Initial denaturation 98 °C 2 min, then 10 cycles of 95 °C 20 s; 65 °C 15 s; 70 °C 30 s; with final extension of 72 °C 5 min. Samples were quantified using Qubit dsDNA HS Assay (Life technologies) before pooling. The sequencing run had on average of 111,536 sequences per sample. Samples were paired and quality trimmed to q20. OTUs were picked at 97% using Open-reference OTU picking strategy (utilizing Greengenes database release Feb-2011; <http://greengenes.lbl.gov>), and chimera checked with cluster less than 4 sequences removed using scripts in QIIME.

NMDS statistical analysis of all sequencing and the community compositional analysis were undertaken in R statistical package.

All sequencing data has been deposited in the European nucleotide archive and available under accession number PRJEB12833.

2.9. [^3H]NE uptake and release from the caecum

Mice 72 h after sham surgery or experimental stroke were killed by decapitation and the caecum was rapidly removed. Caecum

tissues without caecal content were dissected into 2–3 mm pieces, immediately placed into ice-cold Krebs' solution (113 mM NaCl, 4.7 mM KCl, 1.2 mM MgSO_4 , 2.5 mM CaCl_2 , 25 mM NaHCO_3 , 1.2 mM KH_2PO_4 , 115 mM glucose, 0.3 mM Na_2EDTA , and 0.03 mM ascorbic acid), and continuously gassed with a mixture of 95% O_2 and 5% CO_2 . Caecum slices were washed with 5 ml of Krebs' solution, and loaded for 45 min with [^3H]NE at a concentration of 10 μCi in 1 ml of Krebs' solution. Slices then were washed three times with 10 ml of ice-cold oxygenated Krebs' solution and transferred into a four-channel microvolume (100 μl) super-perfusion system kept at 37 °C (Vizi et al., 1985) superfused with Krebs' solution at a rate of 0.5 ml min^{-1} for 60 min (preperfusion period), and the effluent was discarded. After preperfusion, 19 × 3 min fractions were collected. Electrical stimulation (20 V; 10 Hz; 2 ms; 1200 impulses) was applied during the third (S_1) and the thirteenth sample (S_2). In some experiments tetrodotoxin (3 μM) was added during the ninth sample (after S_1) which was present thereafter in the perfusion fluid to investigate its effect on S_2 -induced NE release. Then, the caecum slices were removed from the chamber and homogenised in 5 ml of 10% trichloroacetic acid. A 0.5 ml aliquot of the supernatant was added to 2 ml of scintillation mixture (Ultima Gold; Packard, Meridian, CT), and the

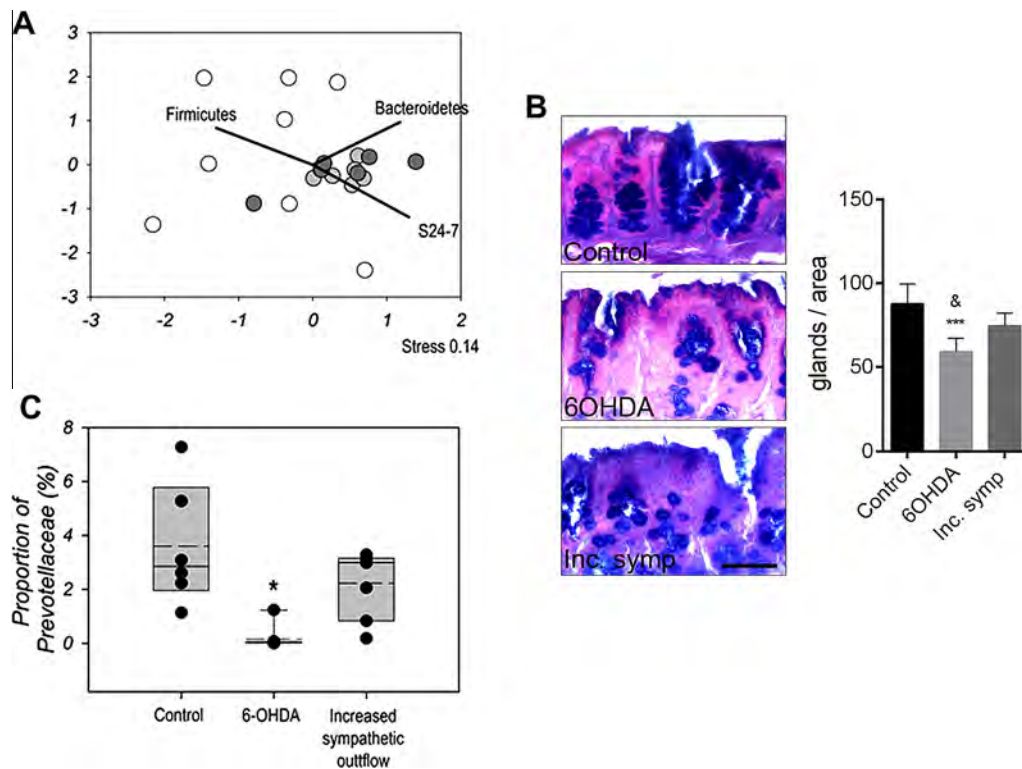


Fig. 6. Impact of manipulations of the sympathetic nervous system. (A) Impact on community microbiota assessed by NMSD analysis of 16S amplicon illumina sequencing relative abundances from rarefied OTU data (36,904 sequences). Controls = white, 6-OHDA treated = Light grey, Increased systemic sympathetic autonomic tone = dark grey. 6-OHDA samples were significantly different to controls (adonis F.model_{1,12} = 2.90, $p = 0.0012$), whereas Increased systemic sympathetic autonomic tone had no impact. Significant correlations were identified with the Phyla of Firmicutes ($R^2 = 0.60, p = 0.008$), Bacteroidetes ($R^2 = 0.58, p = 0.01$) and the Bacteroidetes family S24-7 ($R^2 = 0.78, p = 0.017$). (B) *Periodic acid-Schiff-alcian blue* (PAS) staining of paraffin-embedded caecum sections is shown in control mice and after 6-OHDA administration or atomoxetine/yohimbine treatment that leads to mild increase in sympathetic tone (Inc. symp). Number of PAS-positive goblet cells is significantly reduced 72 h after 6-OHDA compared to Control ($p < 0.001$) and Inc. symp. ($^*p < 0.05$) mice. Scale bar: 100 μ m. Error bars are standard error of the mean, $n = 5-6$. (C) Significant shifts (*) in the proportions of Prevotellaceae as a result of 6-OHDA treatment $p < 0.05$. Upper and lower limits of box represent 75th and 25th percentile, solid line in median, dotted line mean. Dots represent actual values for each mouse.

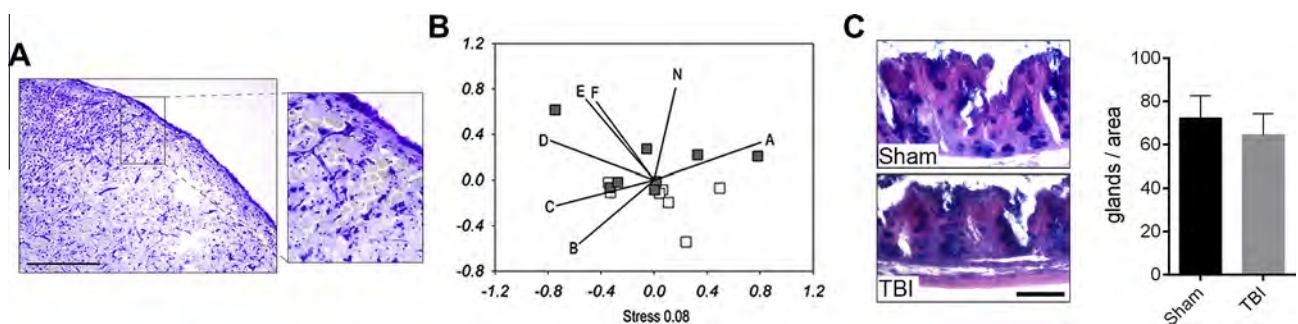


Fig. 7. Impact of traumatic brain injury (TBI) on microbiota. (A) Cresyl violet staining indicates brain injury induced by TBI in the cerebral cortex. Scale bar: 500 μ m. (B) Impact on community microbiota as a result of TBI assessed by NMSD analysis of 16S amplicon illumina sequencing. Rarefied OTU data (36,904 sequences) was used with samples as follows: Controls = white, TBI = dark grey. A strong correlation between neurological deficit and community compositions was seen label N ($R^2 = 0.6797, p = 0.0013$). Other significant correlations explaining the shifts in NMSD were identified and marked with the letters as follows (A) Clostridiales ($R^2 = 0.76, p = 0.015$), (B) Bacteroidetes ($R^2 = 0.63, p = 0.02$), (C) α -proteobacteria ($R^2 = 0.59, p = 0.039$), (D) Proteobacteria ($R^2 = 0.73, p = 0.008$), (E) Cyanobacteria ($R^2 = 0.76, p = 0.002$), (F) Porphyromonadaceae ($R^2 = 0.66, p = 0.027$). (C) *Periodic acid-Schiff-alcian blue* (PAS) staining of paraffin-embedded caecum sections is shown 72 h after sham surgery or traumatic brain injury (TBI). Scale bar: 100 μ m. Error bars are standard error of the mean, $n = 7-8$. (For interpretation of the references to colour in this figure legend, the reader is referred to the web version of this article.)

radioactivity was measured with a Packard 1900 TR liquid scintillation counter. Radioactivity was expressed in terms of disintegration per minute per gram of wet tissue (becquerels per gram). The [3 H]NE uptake of slices was defined as the tissue content of radioactivity at the beginning (C_B) of the perfusion period. This value was calculated according to the following equation: $\sum_{i=1-19} FR_i + C_E = C_B$, where FR_i is the released radioactivity in the fraction number i , and C_E is the tissue content measured at the end of the experiment. The neuronal release of [3 H]NE was measured by the

integration of the surplus release over baseline in response to electrical stimulation.

2.10. Histology

72 h after sham surgery or experimental stroke the caecum was removed and placed immediately into 4% paraformaldehyde (PFA, pH = 7.4) for 24 h prior to paraffin embedding. 5 μ m thick sections were mounted onto gelatin-coated slides, deparaffinized and

stained with haematoxylin and eosin (H&E), Azan or *periodic acid Schiff–alcian blue* (PAS), then dehydrated and coverslipped with Depex mounting medium. Mucin-containing cells visualized by PAS staining have been quantified in a blinded manner on 3–3 randomly selected caecum sections in each mouse ($n = 4$). Catecholaminergic nerve fibers in the caecum were visualized with immunohistochemistry using mouse-anti TH monoclonal antibody (1:100, DiaSorin). The staining was developed with anti-mouse ImmPRESS reagent followed by DAB-Ni peroxidase kit (Vector Laboratories, Burlingame, CA, US), and sections counterstained with cresyl violet.

2.11. Statistical analysis

Statistics were undertaken using the R-package, with multivariate analysis was undertaken on these data using the Vegan (Oksanen et al., 2012) and Ecodist (Goslee and Urban, 2007) packages in R. A Non parametric version of multidimensional scaling (NMDS) was used to assess communities using bray-curtis dissimilarities to characterise the difference between communities. The calculated dissimilarity matrix is compressed and modelled in 2 dimensions for NMDS figures in which the physical distances represent the level of similarity between samples, and permutational multivariate analysis of variance using distance matrices (Adonis in Vegan) for comparisons between groups on the distance matrix to give significance values.

3. Results

3.1. Experimental cerebral ischemia

Experimental stroke induced in mice by occlusion of the middle cerebral artery (MCAo) resulted in cerebral ischemia affecting the ipsilateral striatum and the cerebral cortex consistent with our earlier studies (Dénes et al., 2010, 2011) (Fig. 1A). Sensory-motor functional assessment indicated severe neurological deficit in mice that had undergone 60 min MCAo and 4 or 72 h reperfusion, but no deficit was observed in naïve or sham mice (Fig. 1B). We then sought to determine the effects of this injury on the intestinal microbiota. Since experimental stroke induced by MCAo requires acute surgical intervention that includes anaesthesia, we set up additional experimental groups to control for the potential effects of surgical stress and the anaesthetic isoflurane.

3.2. Characterisation of microbial communities

To determine the effects of experimental stroke on intestinal microbiota we initially used bacterial community profiling of the caecum by DGGE. Caeca were removed and total genomic DNA was extracted for bacterial community profiling by DGGE. Data were analysed using non-metric multidimensional scaling (NMDS). Fig. 1C reveals specific changes in the bacterial communities. No significant change was observed between naïve mice, sham mice, or mice that had undergone MCAo at 4 h post operation using PERMANOVA on the distance matrix created. However, at 72 h post operation there was a shift in microbial populations as result of surgery with an indication of the separation of sham and brain injury animals on their community profile (Fig. 1C). The caecal microbial community composition in mice that had experimental stroke and 72 h reperfusion had significantly different communities to naïve mice. Sham operated individuals also had a significantly different microbial community to the naïve population (Fig. 1C), indicating that sham surgery alone causes a profound change in caecal microbial community structure. To determine whether differences in caecal microbiota between naïve and

operated mice were a result of anaesthesia rather than surgery, we analysed the caecal microbiota in animals that had received anaesthetic alone. Caeca were sampled 72 h post anaesthesia, and from control mice, and community profiled as described above by DGGE (data not shown). NMDS analysis demonstrated that there was no significant difference between mice as a result of the anaesthetic (S1 Figure, adonis: F.Model_{1,9} = 1.83, $pr = 0.081$). Therefore the changes identified in the sham mice were mostly a result of the surgery, not the anaesthetic with the small sample ($n = 5–6$) tested.

To characterise the specific changes occurring as a result of brain injury the composition of the caecal microbiota were determined by 16S rRNA gene amplification followed by pyrosequencing generating an average of 12,335 sequences per sample. Samples demonstrated deep coverage by the levelling of rarefaction curves (S2 Figure) and using goods coverage estimate (Good, 1953) we found on average 98.99% coverage of operational taxonomic units in samples (OTUs: bacterial species defined at the level of >97% similarity on sequence level of the 16S rRNA gene).

Assessment of the Shannon diversity index (Shannon, 1948) of the sequence data showed that there were no significant differences between samples (ANOVA: $F_{2,12} = 0.50$, $p = 0.62$). However, NMDS analysis identified that there was a significant shift in communities as result of stroke or surgery (Fig. 2). To identify any specific bacterial taxa that change as a result of brain injury alone the rarefied sequence data was analysed using proportional data for each taxa calculated using QIIME. ANOVA tests were undertaken for each taxa to identify if treatment had a significant effect on their proportion. To account for any increases in type I errors, the resulting p values table was corrected using the commonly used FDR correction which is commonly used for this type of analysis (Benjamini and Hochberg, 1995). We identified that brain injury had a significant effect on the proportion of Peptococcaceae (Fig. 3A). TukeyHSD posthoc tests confirmed that as a result of brain injury there was a significant increase in the proportion of Peptococcaceae in comparison to Naïve and Sham mice ($p < 0.05$). The proportions of Prevotellaceae decreased as a result of either treatment (Fig. 3B). TukeyHSD posthoc tests identified that there was a decrease in the proportions of Prevotellaceae as a result of sham in comparison to naïve although not significant ($p = 0.08$), which declined further as a result of stroke ($p \leq 0.05$). Therefore these data establish that there are specific significant changes to the caecal microbiota as a consequence of experimental stroke that cannot be attributed to the effects of surgery alone.

To assess whether changes as a result of brain injury could occur by chance variation in microbial communities, another experiment was undertaken where 10 naïve mice ($n = 5$ per cage) were monitored by stool sampling at 0, 28, and 41 days, with the samples subjected to 454 pyrosequencing as detailed above. No significant effect of time or cage housed was found in Shannon bacterial diversity (ANOVA: $F_{2,16} = 0.40$, $p = 0.676$) and (ANOVA: $F_{1,8} = 1.46$, $p = 0.261$) respectively (S3 Figure). NMDS analysis of bacterial composition (S4 Figure), identified a small time dependent change on the bacterial community composition (adonis: F.Model_{1,28} = 1.71, $p = 0.022$), which would not be unexpected over 41 days. ANOVA with FDR correction did not identify any taxa that changed with time between samples. This would indicate that microbial communities are very stable in C57BL/6 mice caged in our animal facility, giving us confidence in the brain injury effects identified.

3.3. Linking bacterial changes to functional outcome after stroke

To investigate whether brain injury drives autonomic changes in the gut, we assessed levels of key neurotransmitters in the tissue of the caecum. Levels of adrenaline, serotonin, and substance P in the caecum did not change (S4 Figure), but noradrenaline (NE) was sig-

nificantly increased 72 h after experimental stroke (Fig. 4A). Increased NE levels positively correlated with neurological deficit scores (S5 Figure). Relative abundance of Peptococcaceae in the caecum showed a significant positive correlation, whereas abundance of Prevotellaceae showed a significant negative correlation with NE levels (Fig. 4B & C) and neurological deficit demonstrated the same correlations (S5 Figure). We have also tested changes in several inflammatory markers in the intestinal tissue, which are known to be associated with alterations in the microbiota. Of these markers RANTES (CCL5) levels showed a positive correlation with the relative abundance of Peptococcaceae in the caecum (S6 Figure).

3.4. Brain injury leads to increased release of NE from sympathetic nerves in the caecum and altered mucoprotein production

To investigate how brain injury leads to increased NE production in the caecum, we used a well-established *ex vivo* approach allowing selective assessment of noradrenergic autonomic regulation in the tissue. Caecum tissue blocks isolated 72 h after sham surgery or experimental stroke were rinsed carefully to eliminate caecal content and were incubated with ^3H -NE, allowing uptake and release of ^3H -NE upon electric stimulation. Brain injury resulted in a profound increase in autonomic outflow in the caecum indicated by an over threefold increase in ^3H -NE tissue uptake and release induced by a 10 Hz stimulation (Fig. 5A). To further confirm that brain injury altered autonomic nerve function in the gut and increased NE production/release (Fig. 5A) is not due to other cells, such as macrophages that can produce catecholamines (Nguyen et al., 2011), tetrodotoxin was used that selectively blocks the firing of action potentials in nerves by inhibiting voltage-gated sodium channels (Vizi et al., 1995). Tetrodotoxin completely prevented stimulation-evoked ^3H -NE release in the caecum (S7 Figure), indicating that brain injury increases noradrenergic autonomic outflow in the caecum. Histology also confirmed that nerves containing tyrosine hydroxylase (TH, a rate-limiting enzyme of catecholamine biosynthesis) were more abundant in the caecum of mice 72 h after brain injury compared to sham animals (Fig. 5B). TH-positive nerve fibers and nerve endings were mostly found in close proximity to mucoprotein-containing cells at the basis of the intestinal epithelium (Fig. 5B). To test whether the increased levels of NE were directly affecting the growth of Peptococcaceae and Prevotellaceae in the caecum, caecal contents were obtained from naive mice and cultured anaerobically for 24 h with increased levels of NE. Analysis by Q-PCR showed no correlation between the level of NE and the growth of both bacterial genera (S8 Figure). As such it is our hypothesis that the effects of increased levels of NE on the Peptococcaceae and Prevotellaceae are indirect. It is known that autonomic regulation could indirectly influence the gut microbiota via altered goblet cell function (Kim and Ho, 2010). To test whether brain injury had any effect on mucoprotein production in the caecum the number of cells in the intestinal mucosa containing mixed (both acidic and neutral) mucoproteins and the total number of goblet cells was counted. Both the number of cells containing mixed mucoproteins and the total number of goblet cells were significantly reduced 72 h after brain injury compared to sham mice (Fig. 5C and D). However, no sign of local tissue inflammation, leukocyte infiltration, fibrosis or tissue lesions were seen in the caecum after brain injury as assessed on haematoxylin and eosin (H&E)- and Azan-stained caecum sections (Fig. 5C).

3.5. Manipulation of the sympathetic nervous system leads to altered mucoprotein production, bacterial community changes, and reduced Prevotellaceae levels in the caecum

To investigate whether changes in sympathetic activity lead to similar alterations in the caecal microbiota *in vivo* to those seen

after ischemic brain injury, two different pharmacological approaches were used 1) A mild increase in systemic sympathetic autonomic tone induced by daily administration of atomoxetine (a NE reuptake inhibitor) and yohimbine (an α_2 -adrenergic receptor antagonist) or 2) intraperitoneal administration of 6-hydroxydopamine (6-OHDA), which leads to robust NE release followed by depletion of noradrenergic nerve terminals in peripheral tissues. Impact on microbial communities was assessed by sequencing of 16 rRNA gene amplicons using illumina Mi-seq platform resulting in an average of 111,536 sequences per sample with greater than 99.8% coverage of OTUs estimated by good coverage estimates (Good, 1953). A rarefied subset of 36,904 sequences was used for all subsequent analysis. The mild increase in systemic sympathetic autonomic tone had no effect on microbial communities in the caecum 72 h later, as identified by 16S rRNA sequencing (Fig. 6A). In contrast, the administration of 6-OHDA resulted in profound changes in the gut microbiota (Fig. 6A). The 6-OHDA treatment resulted in differential perturbations of the microbial community causing a significant spread and separation from the control mice when assessed by NMDS (adonis F.model_{1,12} = 2.90, $p = 0.0012$). Correlation of bacterial abundances in relation to the NMDS plot identified significant correlations with the Phyla of Firmicutes ($R^2 = 0.60$, $p = 0.008$) and Bacteroidetes ($R^2 = 0.58$, $p = 0.01$) and the Bacteroidetes family S24-7 ($R^2 = 0.78$, $p = 0.017$) (Fig. 6A) populations indicating dramatic and differential shifts in the populations. 6-OHDA treatment significantly decreased goblet cell numbers in the caecum, whilst atomoxetine/yohimbine treatment had no effect (Fig. 6B). Moreover, 6-OHDA treatment specifically resulted in a 20-fold reduction in Prevotellaceae levels in the caecum, a reduction also observed after experimental stroke (Fig. 6C).

3.6. Severity of traumatic brain injury correlates with changes in the gut microbiota

We next investigated the impact of alternative models of brain injury on the gut microbiota, and thus subjected mice to mild traumatic brain injury (TBI) using a closed-head injury model (Fig. 7A). As with the manipulation of the sympathetic nervous system, communities were assessed using illumina Mi-Seq multiplexed with the run described above. The severity of injury from TBI, as with ischemic brain injury described above, correlated with changes in caecal microbiota (Fig. 7B). Bacterial population shifts on NMDS that indicate correlations with neurological deficit as a result of TBI, were identified in Bacteroidetes, the Bacteroidetes family Porphyromonadaceae, Firmicutes and α -Proteobacteria. However in contrast to ischemic brain injury, TBI did not result in changes in Peptococcaceae and Prevotellaceae. Correspondingly, goblet cell numbers after TBI were identical to that seen in control mice (Fig. 7C), suggesting that different forms of brain injury shape changes in the gut microbiota through multiple mechanisms.

4. Discussion

There is an increasing appreciation of the importance of the intestinal microbiota and its contribution to the development and maintenance of physiological systems and homeostasis. Altered intestinal microbiota are linked to neuro-developmental disorders (Kang et al., 2013), in addition to a number of immune and inflammatory disease states (Flint et al., 2012; Wu, 2011; Spor et al., 2011; Abt et al., 2012; Ganai et al., 2012; Ayres et al., 2012; Dupont and Dupont, 2011; Le Chatelier et al., 2013; Yoshimoto et al., 2013). While a number of factors are known to influence the intestinal microbiota, such as diet, age, and disease, the effects of brain function per se have not been studied. We show that impair-

ment in brain function, induced by experimental stroke, caused specific and significant changes in the caecal microbiota. These stroke-specific changes occur relatively rapidly, within 72 h, and involve a significant decrease in the levels of Prevotellaceae and an increase in the levels of Peptococcaceae. Prevotellaceae have been shown to be part of the core microbiota of C57Bl/6 mice (Gu et al., 2013), as such the consequences of reducing the prevalence of Prevotellaceae is likely to be significant. In humans Prevotellaceae are associated with agrarian diets rich in plant derived material and reductions in the abundance of Prevotellaceae have been detected in the microbiota of autistic children (Luczynski, 2016), Crohn's disease (Prindiville et al., 2004) and in children suffering from type 1 diabetes (Mejía-León et al., 2014). In contrast, abnormal increases in Prevotellaceae has been found to exacerbate DSS-induced colitis in mice (Elinav et al., 2011). The significance of the increase in the abundance of Peptococcaceae is less clear since little is known about their role in the intestinal microbiota. Peptococcaceae are relatively minor components of the intestinal microbiota of both mice and humans, and the changes we detect here may be a consequence of the decrease in the levels of Prevotellaceae. Nevertheless, since only brain injury, but not surgical stress resulted in changes (over 3-fold) in Peptococcaceae, these changes could be specific indicators of brain injury and their predictive value for functional outcome should be tested in patients with various forms of brain injury. Interestingly, the proinflammatory cytokine, CCL5 (RANTES), which we found to positively correlate with Peptococcaceae levels, has been linked with the development of colitis (Elinav et al., 2011), therefore the functional role of RANTES in stroke-induced gut microbiota changes will need to be investigated in future studies.

These changes in the caecal microbiota were correlated both with increased levels of NE and noradrenergic innervation as well as the severity of injury. It is well known that NE levels increase following trauma or injury (Millen et al., 1985; Woolf et al., 1992; Lyte and Bailey, 1997) and stroke is known to induce NE in the circulation in line with increased sympathetic activity in both humans and experimental animals (Myers et al., 1981; Cechetto et al., 1989). However this is the first evidence for increased NE release and noradrenergic innervation in the caecum following stroke. It is known that NE can be sensed and utilised by bacteria in caecal microbiota and that NE-like molecules can be synthesised by bacteria (Karavolos et al., 2013; Asano et al., 2012; Lyte, 2004). However the anatomical and neurochemical evidence data presented here demonstrate the source of the NE in the caecum following stroke would appear to be host derived from sympathetic innervation. It is currently unclear whether brain injury-induced increases in sympathetic outflow in the caecum are due to direct actions of altered central sympatho-motor responses or could also be influenced by changes in parasympathetic activity mediated by the vagus nerve. However these data suggest that specific brain-induced changes in gut NE will influence the microbiome-gut-brain axis and thus affect outcome and behaviour. The effect of early life stress on microbiota has been demonstrated previously, suggesting that stress-induced central or peripheral events could alter the intestinal microbiota (O'Mahony et al., 2009).

Gastrointestinal dysfunction occurs frequently in stroke patients in the form of altered intestinal motility, abdominal pain, gastric distension, constipation or ulcers that are linked to altered autonomic activity (Korpelainen et al., 1999; Su et al., 2009; Bracci et al., 2007; Hilz et al., 2011). Increasing stroke severity is associated with progressive loss of overall autonomic modulation and a progressive shift toward sympathetic dominance in stroke patients (Hilz et al., 2011). These data therefore suggest that a specific neuronal input or an imbalance in neuro and inflammatory mediators (such as NE reported here for example) in the interstitial intestinal

tissue contribute to the signals that regulate the structure of the intestinal microbiota. Although it is known that the growth in pure culture of *Prevotella intermedia* is inhibited by the presence of stress hormones such as NE (Jentsch et al., 2013), when the mouse microbiota was cultured *in vitro* in increasing concentrations of NE we did not detect any difference on the levels of Prevotellaceae or Peptococcaceae (S8 Figure). This difference may well reflect that in our experiments we were studying the growth of caecal microbiota consisting of many interacting bacterial species, an approach more likely to reproduce effects inside the caecum rather than pure culture. As such the increase in host-derived NE seen in the experimental stroke may be indirectly affecting the relative growth of Prevotellaceae and Peptococcaceae within the caecal microbiota resulting their changes in abundance. Pharmacological manipulation of the peripheral autonomic nervous system by 6-OHDA strengthened our conclusions that a decrease in Prevotellaceae in the caecum seen after experimental stroke could be due to altered autonomic activity. Intraperitoneally administered 6-OHDA does not cross the BBB (Williams et al., 1981) and leads to rapid release of NE in the periphery, which has been shown to lead to immediate changes in diverse bacterial species (Lyte, 2014; Pullinger et al., 2010). This is followed by depletion of noradrenergic terminals. We found decreased Prevotellaceae levels 72 h after 6-OHDA administration, which was similar to what seen after experimental stroke. It is currently unclear whether ischemic brain injury leads to increased sympathetic outflow in the caecum via increasing central autonomic tone, or whether cessation of central autonomic control after brain injury is compensated by local increases in NE in the gut. Nevertheless, increased NE release or the dysregulation of autonomic control of the gut after both ischemic brain injury and 6-OHDA would explain similar changes seen in Prevotellaceae.

It is known that autonomic regulation can effect goblet cell function (Kim and Ho, 2010). As such NE could indirectly influence the gut microbiota via altered goblet cell function (Kim and Ho, 2010). Analysis of caecal tissue from stroke animals demonstrated that the number of cells containing mixed mucoproteins and the total number of goblet cells were significantly reduced 72 h after brain injury compared to sham mice (Fig. 5C and D). As such changes to the mucosal surface are likely to be generated as a consequence of brain injury. Changes in mucin levels have been linked to gut health and susceptibility to infection (Kim and Ho, 2010), of which bacteria from the family Prevotellaceae have been demonstrated to colonise and utilise mucin (Wright et al., 2000). The autonomic nervous system is also known to dampen immune responses (Reyes-García and García-Tamayo, 2009) although here no sign of local tissue inflammation, leukocyte infiltration, fibrosis or tissue lesions were seen in the caecum after brain injury as assessed on haematoxylin and eosin (H&E)- and Azan-stained caecum sections (Fig. 5C). Importantly, 6-OHDA treatment resulted in reduced number of goblet cells in the caecum similarly to what was found after experimental stroke and a decrease in Prevotellaceae was observed in both cases. In contrast, traumatic brain injury did not alter goblet cell numbers or Prevotellaceae levels in the caecum, and caused different community changes.

It should be noted that an important observation of our studies was the effect of sham surgery on the caecal microbiota. We have previously reported the surprisingly significant effects of sham surgery on levels of inflammatory mediators in peripheral tissues and the circulation (Denes et al., 2011). In the closed head model of mild traumatic brain injury used here, sham mice only experienced a relatively small manipulation (a small cut on the skin covering the skull) compared to the sham surgery required for the MCAo model of experimental stroke, whilst brain injury and functional deficit were much smaller in the TBI model. This could explain why TBI did not lead to profound changes in goblet cell function and a decrease in Prevotellaceae in the gut, whilst a

correlation between increasing neurological deficit and specific changes in microbiota were found. Thus, microbiota changes after TBI could be in part due to a generic stress response that follows tissue injury and also to a different form of brain injury compared to that seen after experimental stroke. Whether the changes we observe on the intestinal microbiota in response to sham surgery and levels of systemic inflammation reported are functionally linked is unknown. However the implications of these observations are far reaching. Firstly, these data indicate that any surgical intervention may profoundly and rapidly influence the caecal microbiota. Such changes could have effects on post-surgical outcome, particularly if the dysbiosis (microbial imbalance on or inside the body) results in changes that favour the growth of potential opportunistic pathogens within the host microbiota. Secondly, the interpretations of experimental observations made from models that utilise surgical intervention may be confounded by surgery-induced changes in the caecal microbiota and inflammatory status. Thus surgical intervention essentially changes the organisms' baseline and could in effect create a comorbid state.

In conclusion, our results are the first to show specific changes in the microbiota due to a change in brain function, and also to surgical stress following tissue injury, with the likely involvement of the autonomic nervous system and goblet cells under certain conditions. Identification of the mechanisms involved in this dysbiosis could help us understand how the connectivity between brain function and the intestinal microbiota contributes to health and disease and have important implications in the treatment of patients following traumatic brain injury.

Acknowledgments

We are grateful to Thomas Curl-Roper and Erica Roche who performed experiments on this project as part of their degree programmes at the University of Manchester. We thank Mária Bakó for her help and advice in histology. We thank Ping Wang for assistance in denoising sequencing data. We thank Prof. Ulrich Dirnagl and Prof. Andreas Meisel for the critical discussions of the work. We are also grateful to Prof. Mark Lyte (Texas Tech University Health Sciences Center) for useful discussions. This work was in part funded through Medical Research Council grant G1100076 to ISR. Funding for AD was provided by OTKA K109743 and the Hungarian Brain Research Program KTIA_13_NAP-A-1/2. AD is supported by the Bolyai Janos Research Scholarship from the Hungarian Academy of Sciences.

Appendix A. Supplementary data

Supplementary data associated with this article can be found, in the online version, at <http://dx.doi.org/10.1016/j.bbi.2016.04.003>.

References

- Abt, M.C. et al., 2012. Commensal bacteria calibrate the activation threshold of innate antiviral immunity. *Immunity* 37, 158–170.
- Asano, Y. et al., 2012. Critical role of gut microbiota in the production of biologically active, free catecholamines in the gut lumen of mice. *Am. J. Physiol. Gastrointest. Liver Physiol.* 303, G1288–95.
- Ayres, J.S., Trinidad, N.J., Vance, R.E., 2012. Lethal inflammasome activation by a multidrug-resistant pathobiont upon antibiotic disruption of the microbiota. *Nat. Med.* 18, 799–806.
- Benjamini, Y., Hochberg, Y., 1995. Controlling the false discovery rate: a practical and powerful approach to multiple testing. *J. R. Stat. Soc. Ser. B* 57, 289–300.
- Bracci, F. et al., 2007. Chronic constipation in hemiplegic patients. *World J. Gastroenterol.* 13, 3967–3972.
- Caporaso, J.G. et al., 2011. Global patterns of 16S rRNA diversity at a depth of millions of sequences per sample. *Proc. Natl. Acad. Sci. U.S.A.* 108 (Suppl.), 4516–4522.
- Caso, J.R. et al., 2008. Toll-like receptor 4 is involved in subacute stress-induced neuroinflammation and in the worsening of experimental stroke. *Stroke* 39, 1314–1320.
- Cechetto, D.F. et al., 1989. Autonomic and myocardial changes in middle cerebral artery occlusion: stroke models in the rat. *Brain Res.* 502, 296–305.
- de Jonge, W.J., 2013. The gut's little brain in control of intestinal immunity. *ISRN Gastroenterol.* 2013 630159.
- Denes, A., Thornton, P., Rothwell, N.J., Allan, S.M., 2010. Inflammation and brain injury: acute cerebral ischaemia, peripheral and central inflammation. *Brain Behav. Immun.* 24, 708–723.
- Dénes, A., Humphreys, N., Lane, T.E., Grecis, R., Rothwell, N., 2010. Chronic systemic infection exacerbates ischemic brain damage via a CCL5 (regulated on activation, normal T-cell expressed and secreted)-mediated proinflammatory response in mice. *J. Neurosci.* 30, 10086–10095.
- Dénes, Á., Ferenczi, S., Kovács, K.J., 2011. Systemic inflammatory challenges compromise survival after experimental stroke via augmenting brain inflammation, blood-brain barrier damage and brain oedema independently of infarct size. *J. Neuroinflammation* 8, 164.
- Denes, A. et al., 2011. Experimental stroke-induced changes in the bone marrow reveal complex regulation of leukocyte responses. *J. Cereb. Blood Flow Metab.* 31, 1036–1050.
- Denes, A. et al., 2015. AIM2 and NLR4 inflammasomes contribute with ASC to acute brain injury independently of NLRP3. *Proc. Natl. Acad. Sci. U.S.A.* 112, 4050–4055.
- Dirnagl, U. et al., 2007. Stroke-induced immunodepression: experimental evidence and clinical relevance. *Stroke* 38, 770–773.
- Dupont, A.W., Dupont, H.L., 2011. The intestinal microbiota and chronic disorders of the gut. *Nat. Rev. Gastroenterol. Hepatol.* 8, 523–531.
- Elinav, E. et al., 2011. NLRP6 inflammasome regulates colonic microbial ecology and risk for colitis. *Cell* 145, 745–757.
- Flint, H.J., Scott, K.P., Louis, P., Duncan, S.H., 2012. The role of the gut microbiota in nutrition and health. *Nat. Rev. Gastroenterol. Hepatol.* 9, 577–589.
- Ganal, S.C. et al., 2012. Priming of natural killer cells by nonmucosal mononuclear phagocytes requires instructive signals from commensal microbiota. *Immunity* 37, 171–186.
- Good, I.J., 1953. The population frequencies of species and the estimation of population parameters. *Biometrika* 40, 237–264.
- Goslee, S., Urban, D., 2007. The ecodist package: dissimilarity-based functions for ecological analysis. *J. Stat. Softw.* 22, 1–19.
- Gu, S. et al., 2013. Bacterial community mapping of the mouse gastrointestinal tract. *PLoS One* 8, e74957.
- Hetze, S. et al., 2013. Superiority of preventive antibiotic treatment compared with standard treatment of poststroke pneumonia in experimental stroke: a bed to bench approach. *J. Cereb. Blood Flow Metab.* 33, 846–854.
- Hilz, M.J. et al., 2011. High NIHSS values predict impairment of cardiovascular autonomic control. *Stroke* 42, 1528–1533.
- Hsiao, E.Y. et al., 2013. Microbiota modulate behavioral and physiological abnormalities associated with neurodevelopmental disorders. *Cell* 155, 1451–1463.
- Jentsch, H.F.R., März, D., Krüger, M., 2013. The effects of stress hormones on growth of selected periodontitis related bacteria. *Anaerobe* 24, 49–54.
- Kang, D.-W. et al., 2013. Reduced incidence of *Prevotella* and other fermenters in intestinal microflora of autistic children. *PLoS One* 8, e68322.
- Karavolos, M.H., Winzer, K., Williams, P., Khan, C.M.A., 2013. Pathogen espionage: multiple bacterial adrenergic sensors eavesdrop on host communication systems. *Mol. Microbiol.* 87, 455–465.
- Kim, Y.S., Ho, S.B., 2010. Intestinal goblet cells and mucins in health and disease: recent insights and progress. *Curr. Gastroenterol. Rep.* 12, 319–330.
- Korpelainen, J.T., Sotaniemi, K.A., Myllylä, V.V., 1999. Autonomic nervous system disorders in stroke. *Clin. Auton. Res.* 9, 325–333.
- Le Chatelier, E. et al., 2013. Richness of human gut microbiome correlates with metabolic markers. *Nature* 500, 541–546.
- Luczynski, P. et al., 2016. Growing up in a bubble: using germ-free animals to assess the influence of the gut microbiota on brain and behaviour. *Int. J. Neuropsychopharmacol.*, pii=020 101093/ijnp/pyw020.
- Lyte, M., 2004. Microbial endocrinology and infectious disease in the 21st century. *Trends Microbiol.* 12, 14–20.
- Lyte, M., 2014. Host-microbiota neuroendocrine interactions influencing brain and behavior. *Gut Microbes* 5, 381–389.
- Lyte, M., Bailey, M.T., 1997. Neuroendocrine-bacterial interactions in a neurotoxin-induced model of trauma. *J. Surg. Res.* 70, 195–201.
- Mejía-León, M.E., Petrosino, J.F., Ajami, N.J., Domínguez-Bello, M.G., de la Barca, A.M.C., 2014. Fecal microbiota imbalance in Mexican children with type 1 diabetes. *Sci. Rep.* 4, 3814.
- Millen, J.E., Glauser, F.L., Fairman, R.P., 1985. A comparison of physiological responses to percussive brain trauma in dogs and sheep. *J. Neurosurg.* 62, 587–591.
- Muyzer, G., de Waal, E.C., Uitterlinden, A.G., 1993. Profiling of complex microbial populations by denaturing gradient gel electrophoresis analysis of polymerase chain reaction-amplified genes coding for 16S rRNA. *Appl. Environ. Microbiol.* 59, 695–700.
- Myers, M.G., Norris, J.W., Hachniski, V.C., Sole, M.J., 1981. Plasma norepinephrine in stroke. *Stroke* 12, 200–204.
- Nguyen, K.D. et al., 2011. Alternatively activated macrophages produce catecholamines to sustain adaptive thermogenesis. *Nature* 480, 104–108.

- O'Mahony, S.M. et al., 2009. Early life stress alters behavior, immunity, and microbiota in rats: implications for irritable bowel syndrome and psychiatric illnesses. *Biol. Psychiatry* 65, 263–267.
- Oksanen, J. et al., 2012. Vegan: Community Ecology Package, R Package Version 2.0-4.
- Polz, M.F., Cavanaugh, C.M., 1998. Bias in template-to-product ratios in multitemplate PCR. *Appl. Environ. Microbiol.* 64, 3724–3730.
- Prindiville, T., Cantrell, M., Wilson, K.H., 2004. Ribosomal DNA sequence analysis of mucosa-associated bacteria in Crohn's disease. *Inflamm. Bowel Dis.* 10, 824–833.
- Pullinger, G.D. et al., 2010. 6-Hydroxydopamine-mediated release of norepinephrine increases faecal excretion of *Salmonella enterica* serovar Typhimurium in pigs. *Vet. Res.* 41.
- Quince, C., Lanzen, A., Davenport, R.J., Turnbaugh, P.J., 2011. Removing noise from pyrosequenced amplicons. *BMC Bioinformatics* 12, 38.
- Reyes-García, M.G., García-Tamayo, F., 2009. A neurotransmitter system that regulates macrophage pro-inflammatory functions. *J. Neuroimmunol.* 216, 20–31.
- Shannon, C.E., 1948. The mathematical theory of communication. *Bell Syst. Tech. J.* 27, 379–423.
- Spor, A., Koren, O., Ley, R., 2011. Unravelling the effects of the environment and host genotype on the gut microbiome. *Nat. Rev. Microbiol.* 9, 279–290.
- Su, Y. et al., 2009. New-onset constipation at acute stage after first stroke: incidence, risk factors, and impact on the stroke outcome. *Stroke* 40, 1304–1309.
- Thompson, J.R., Marcelino, L.A., Polz, M.F., 2002. Heteroduplexes in mixed-template amplifications: formation, consequence and elimination by 'reconditioning PCR'. *Nucleic Acids Res.* 30, 2083–2088.
- Umschweif, G. et al., 2014. Neuroprotection after traumatic brain injury in heat-acclimated mice involves induced neurogenesis and activation of angiotensin receptor type 2 signaling. *J. Cereb. Blood Flow Metab.* 34, 1–10.
- Vizi, S. et al., 1985. Release and turnover of noradrenaline in isolated median eminence: lack of negative feedback modulation. *Neuroscience* 16, 907–916.
- Vizi, E.S., Orsó, E., Osipenko, O.N., Haskó, G., Elenkov, I.J., 1995. Neurochemical, electrophysiological and immunocytochemical evidence for a noradrenergic link between the sympathetic nervous system and thymocytes. *Neuroscience* 68, 1263–1276.
- Williams, J.M. et al., 1981. Sympathetic innervation of murine thymus and spleen: evidence for a functional link between the nervous and immune systems. *Brain Res. Bull.* 6, 83–94.
- Woolf, P.D. et al., 1992. The catecholamine response to multisystem trauma. *Arch. Surg.* 127, 899–903.
- Wright, D.P., Rosendale, D.J., Robertson, A.M., 2000. Prevothella enzymes involved in mucin oligosaccharide degradation and evidence for a small operon of genes expressed during growth on mucin. *FEMS Microbiol. Lett.* 190, 73–79.
- Wu, G.D. et al., 2011. Linking long-term dietary patterns with gut microbial enterotypes. *Science* (80-) 334, 105–108.
- Yoshimoto, S. et al., 2013. Obesity-induced gut microbial metabolite promotes liver cancer through senescence secretome. *Nature* 499, 97–101.

ORIGINAL ARTICLE

A novel SPECT-based approach reveals early mechanisms of central and peripheral inflammation after cerebral ischemia

Krisztián Szigeti¹, Ildikó Horváth¹, Dániel S Veres¹, Bernadett Martinecz², Nikolett Lénárt², Noémi Kovács³, Erika Bakcsa¹, Alexa Márta¹, Mariann Semjéni³, Domokos Máthé³ and Ádám Dénes²

Inflammation that develops in the brain and peripheral organs after stroke contributes profoundly to poor outcome of patients. However, mechanisms through which inflammation impacts on brain injury and overall outcome are improperly understood, in part because the earliest inflammatory events after brain injury are not revealed by current imaging tools. Here, we show that single-photon emission computed tomography (NanoSPECT/CT Plus) allows visualization of blood brain barrier (BBB) injury after experimental stroke well before changes can be detected with magnetic resonance imaging (MRI). Early ^{99m}Tc-DTPA (diethylene triamine pentaacetic acid) signal changes predict infarct development and systemic inflammation preceding experimental stroke leads to very early perfusion deficits and increased BBB injury within 2 hours after the onset of ischemia. Acute brain injury also leads to peripheral inflammation and immunosuppression, which contribute to poor outcome of stroke patients. The SPECT imaging revealed early (within 2 hours) changes in perfusion, barrier function and inflammation in the lungs and the gut after experimental stroke, with good predictive value for the development of histopathologic changes at later time points. Collectively, visualization of early inflammatory changes after stroke could open new translational research avenues to elucidate the interactions between central and peripheral inflammation and to evaluate *in vivo* 'multi-system' effects of putative anti-inflammatory treatments.

Journal of Cerebral Blood Flow & Metabolism (2015) **35**, 1921–1929; doi:10.1038/jcbfm.2015.174; published online 29 July 2015

Keywords: BBB; brain injury; cerebral ischemia; SPECT imaging; systemic inflammation

INTRODUCTION

Stroke is the leading cause of permanent disability worldwide and represents a huge socio-economic burden.¹ Treatment opportunities are currently limited to tissue plasminogen activator (tPA), which is available for the minority of stroke patients.² Recent data indicate that common comorbidities for stroke (atherosclerosis, diabetes, obesity or infection) are associated with an elevated systemic inflammatory burden and, since inflammation both in the brain and in the periphery contributes to poor clinical outcome,^{3,4} interest has focused on anti-inflammatory therapies.⁵ Since neurons die rapidly during ischemia,⁶ decision making in the clinic largely relies on early imaging data from CT or magnetic resonance imaging (MRI). However, these essential imaging tools give little information about inflammatory changes in the brain and do not reveal earliest signs of blood brain barrier (BBB) injury after stroke that could be negatively influenced by systemic inflammation.^{3,7} Therefore, development of novel imaging approaches could largely support translational research and development of personalized therapies. Stroke and other forms of acute brain injury also result in systemic immunosuppression, which often leads to poststroke infections. Infectious complications that affect the lungs or the urinary tract contribute profoundly to mortality and poor recovery of stroke patients.⁸ In addition, stroke patients often present with diverse gut-associated symptoms such as paralytic ileus. Translocation of gut bacteria after stroke has also been documented.^{9–11} However, it is currently

unclear whether brain injury has organ-specific effects, which could be revealed with imaging techniques *in vivo*.

Single-photon emission tomography (SPECT) has been used previously to visualize cerebral blood flow and BBB injury in patients 24 to 72 hours after stroke.^{12,13} The clinical application of SPECT largely relies on BBB injury imaging using water-soluble small molecular radiopharmaceuticals such as diethylene triamine pentaacetic acid (DTPA), which stably chelates ^{99m}Tc isotope atoms. Imaging of the penetration of hydrophilic ^{99m}Tc-DTPA into the brain parenchyma after injury allows the assessment of BBB breakdown. However, a lipophilic molecule, hexamethylpropylene amine oxime (HMPAO) when radiolabeled with ^{99m}Tc ions can be applied to image cerebral blood flow. It is postulated that lipophilic ^{99m}Tc-HMPAO complex *D,L* isoform is predominantly taken up by brain gray-matter tissue proportionally to cerebral blood flow. Upon entering the BBB and the cell membranes, ^{99m}Tc-HMPAO *D,L*-isoform molecules are thought to be transformed to a hydrophilic complex by interaction with intracellular glutathione and they are thus entrapped within the cells, which allows for monitoring of brain perfusion and its changes.^{14,15} In addition, radiolabeled human serum albumin (HSA) has been used previously to visualize plasma extravasation and inflammation in the brain.¹⁶

However, early events of BBB injury and perfusion changes have not been investigated by SPECT in clinical or experimental stroke studies and the predictive value of SPECT imaging for infarct evolution and the developments of central or peripheral

¹Department of Biophysics and Radiation Biology, Semmelweis University, Budapest, Hungary; ²Laboratory of Neuroimmunology, Institute of Experimental Medicine, Budapest, Hungary and ³CROmed Translational Research Centers, Budapest, Hungary. Correspondence: Dr A Dénes, Laboratory of Neuroimmunology, Institute of Experimental Medicine, Szigony u. 43, IX. Tuzoltó u. 37-47, Budapest 1083, Hungary.

E-mail: denesa@koki.hu

Received 23 April 2015; revised 8 June 2015; accepted 17 June 2015; published online 29 July 2015

inflammation after brain injury are not known. Here, we reveal a previously unrecognized potential for SPECT imaging in translational stroke research. First, we developed novel SPECT-based imaging approaches in a mouse model of experimental stroke that show remarkable sensitivity and allow early visualization of BBB injury with strong predictive value for infarct evolution. Second, we show that SPECT imaging reveals mechanisms through which preceding systemic inflammation has very early and detrimental effects on acute brain injury. Third, this is the first *in vivo* imaging study to identify brain injury-induced changes in peripheral organs that are most commonly affected in stroke patients, within 2 hours after experimental stroke. These novel imaging protocols make use of clinically approved radioligands, and give sufficient resolution in the small mouse brain, thus could facilitate the understanding of inflammatory events after stroke and translation of experimental data to clinical benefit.

MATERIALS AND METHODS

Animals

Experiments were performed in adult male C57BL/6J mice ($n=46$) aged 12 to 16 weeks, breeding in the Specific Pathogen Free unit of the IEM (Institute of Experimental Medicine). Animals were allowed free access to food and water and maintained under temperature, humidity, and light-controlled conditions. All procedures were conducted in accordance with the ARRIVE guidelines and the guidelines set by the European Communities Council Directive (86/609 EEC) and approved by the Animal Care and Use Committee of the IEM and the Semmelweis University (XIV-I-001/29-7/2012).

Middle Cerebral Artery Occlusion

Middle cerebral artery occlusion (MCAo) was performed using the intraluminal filament technique as described earlier.^{17,18} In brief, animals were anesthetized with isoflurane and a silicone-coated monofilament (210 μm tip diameter, Doccol Corporation, Sharon, MA, USA) was introduced to the left external carotid artery and advanced along the internal carotid artery to occlude the MCA for 30 minutes or 45 minutes. Different occlusion times were used to produce both small striatal infarcts (30 minutes MCAo) and striatal and cortical injury (45 minutes MCAo) to assess the sensitivity of SPECT imaging to perfusion deficits and BBB injury changes after experimental stroke. During surgery, core temperature was maintained at $37 \pm 0.5^\circ\text{C}$. Sham animals were anesthetized for the same period of time and all surgical procedures were identical to the stroke group except that the filament was not advanced to the MCA. In a group of animals, cerebral blood flow was assessed by a laser Doppler (Moor Instruments, Axminster, UK). After experimental stroke, four mice were excluded pre hoc due to incomplete occlusion of the MCA (lack of striatal infarction, $n=2$) and surgical artifacts (subarachnoid hemorrhage, $n=1$; vagus injury $n=1$). Two further mice died (24 hours and 48 hours after lipopolysaccharide (LPS) and MCAo, respectively).

Systemic Inflammation

Systemic inflammation was induced by intraperitoneal injection of LPS (serotype: 0111:B4, Sigma-Aldrich, St. Louis, MO, USA, L4391, 40 $\mu\text{g}/\text{kg}$) 3 hours before experimental stroke as described earlier.¹⁹

Single-Photon Emission Computed Tomography and Magnetic Resonance Imaging

Multimodal imaging studies were conducted with multiple radiotracers in different time points after MCAo. During the acquisitions, mice were placed in prone position in a dedicated mouse bed, and were anesthetized with 2% isoflurane in oxygen. In all, 63 ± 4 MBq $^{99\text{m}}\text{Tc}$ -DTPA or $^{99\text{m}}\text{Tc}$ -HMPAO was administered intravenously via tail vein injection followed by an anatomic T2-weighted MRI scan. An hour after the isotope administration—mice remaining in the same bed and position—a whole body CT and afterwards a whole body SPECT scan was started. A group of mice were prescanned 7 days before MCAo to assess baseline DTPA binding. Mice were scanned 2 hours after MCAo for $^{99\text{m}}\text{Tc}$ -DTPA or $^{99\text{m}}\text{Tc}$ -HMPAO uptake. One day after MCAo, 22 ± 3 MBq ^{125}I -HSA administration was embedded in the above protocol right before the SPECT-CT imaging. Duration of anesthesia and all treatment protocols were identical in the

sham and the stroke group during and after imaging. Temperature of the animals was kept at $37.2 \pm 3^\circ\text{C}$ during imaging.

Magnetic resonance imaging measurements were performed on a nanoScan 1T MRI system (Mediso Ltd., Budapest, Hungary) equipped with an actively shielded 450 mT/m gradient system and volume coils for both receiving and transmitting. As anatomic imaging, a T2-weighted fast spin echo sequence was acquired with three-dimensional acquisition scheme having the squared axial field of view 42 mm and the in-plane resolution of 0.3 mm, the same as the slice thickness. Imaging parameters were repetition time/echo time 2,200/92.8 ms, 25 μs dwell time and two excitations resulting in a 35-minute scan. A diffusion-weighted spin echo scan followed the anatomic scan. Ten axial slices were acquired with 1 mm slice thickness (0.2 mm gap between the slices) and in-plane resolution of 0.4 mm. To calculate mean apparent diffusion coefficient map diffusion weighting was created in three orthogonal directions with the parameters repetition time/echo time 600/18 ms, Δ/δ 2.4/10 ms and two b values of (1; 600) s/mm^2 .

The SPECT-CT measurements were performed on NanoSPECT/CT PLUS (Mediso Ltd.) equipped with multi-pinhole mouse collimators with a system SPECT resolution of 0.8 mm and the detection limit of a focal signal of 0.064 mm^3 . The semicircular CT scanning was acquired with 45 kV tube voltage, 500 ms of exposure time, 1:4 binning and 360 projections in 9 minutes. In the reconstruction 0.16 mm in-plane resolution and slice thickness were set and Butterworth filter was applied. Whole-body SPECT scanning was performed with 45 frames per cycle and termination condition of 135 seconds per frame in a scan range of 96.6 mm resulting in a 100-minute scan. The detection peak energies were set to 24 keV in case of ^{125}I and 140.51 keV in case of $^{99\text{m}}\text{Tc}$ with a 20% energy window. Two different SPECT reconstruction was performed concerning the resolution: 0.45 mm isovoxel in case of the whole body and 0.3 mm isovoxel in a reduced field of view centered to the head only. Data from SPECT measurements in the brain were presented as a ratio to cerebellum, which brain region was not affected by cerebral ischemia and levels of $^{99\text{m}}\text{Tc}$ -HMPAO, $^{99\text{m}}\text{Tc}$ -DTPA, and ^{125}I -HSA remained unaltered throughout the study. Peripheral SPECT imaging data are presented as a percentage of whole body radioactivity. In preliminary experiments we have assessed in three control mice and in four mice after MCAo whether any remaining $^{99\text{m}}\text{Tc}$ radioactivity after $^{99\text{m}}\text{Tc}$ -DTPA injection could interfere with subsequent measurements performed 24 hours later. Except for a low level of background remaining in the urinary bladder, no detectable signal was present in the brain parenchyma or in peripheral organs.

Tissue Processing

Under terminal anesthesia, animals were perfused transcardially with saline followed by paraformaldehyde (4% in phosphate-buffered saline). Brains were postfixed in 4% paraformaldehyde at 4°C for 24 hours, and cryoprotected in sucrose/phosphate-buffered saline. In all, 25 μm thick coronal brain sections were cut on a sledge microtome (Leica SM2010R, Leica Biosystems Nussloch GmbH, Nussloch, Germany). Gut and lung tissues were embedded into paraffin and 5 μm thick sections were cut (Leica SM2010R) before Hematoxylin and Eosin and periodic acid-Schiff alcian blue staining.

Measurement of Infarct Volume and Neurologic Outcome

The volume of ischemic brain damage was measured on cresyl violet-stained brain sections and corrected for edema as described previously.¹⁷ Neurologic status in mice was assessed according to a neurologic grading score of increasing severity of deficit:²⁰ 0, no observable deficit; 1, torso flexion to right; 2, spontaneous circling to right; 3, leaning/falling to right; 4, no spontaneous movement.

Immunohistochemistry and Immunofluorescence

Leakage of plasma-derived IgG (BBB damage) was detected with biotinylated horse anti-mouse IgG (Vector Laboratories, Burlingame, CA, USA, 1:500) followed by incubation with ABC solution (Vector, 1:500). The color was developed by diaminobenzidine tetrahydrochloride. Immunofluorescence was performed as described earlier,¹⁷ using rat anti-mouse CD45 1:200 (Bio-Rad AbD Serotec, Kidlington, UK) and rabbit anti-Iba1 1:1,000 (Wako Chemicals GmbH, Neuss, Germany) primary antibodies followed by fluorochrome-conjugated donkey anti-rat Alexa594 and donkey anti-rabbit Alexa488 antisera (1:500, Thermo Fisher Scientific, Waltham, MA, USA). Activated microglia (Iba1+, CD45low ramified cells with thickened processes and enlarged cell body) and recruited leukocytes (CD45 highly expressing round or elongated cells) were counted in the

striatum, cerebral cortex, hippocampus, and thalamus on four serial sections rostro-caudally (2-2 fields per section).

Quantitative Analysis and Statistics

Mice were randomly assigned to experimental groups. All quantitative analysis was performed under blinded conditions. CD45-positive cells were quantified in two randomly selected fields on 3-3 coronal brain sections each according to appropriate bregma levels to cover the striatum, the cerebral cortex, the hippocampus, and the thalamus. Normality of data sets was assessed with Kolmogorov-Smirnov test. Parametric data were analyzed with Student's *t*-test or two-way ANOVA followed by Sidak's *post hoc* comparison (GraphPadPrism6.0, GraphPad Software Inc., La Jolla, CA, USA). Neurologic scores were analyzed with Mann-Whitney test. Linear regression was performed with GraphPadPrism6.0. $P < 0.05$ was considered as statistically significant.

RESULTS

Single-Photon Emission Computed Tomography Imaging Reveals Early Events of Blood Brain Barrier Injury in the Brain After Experimental Stroke with Predictive Value for Infarct Development

To visualize early changes in perfusion, BBB injury and inflammation after experimental stroke, we used SPECT/CT imaging with combination of radioligands ^{99m}Tc -HMPAO or ^{99m}Tc -DTPA with I125-HSA. HMPAO signal was significantly decreased in the ipsilateral striatum and cerebral cortex 2 hours after MCAo whereas no changes were seen in mice subjected to sham surgery (Figures 1A and 1D). Laser Doppler confirmed that this effect was not due to incomplete reperfusion after MCAo, since cerebral blood flow in the MCA area returned to baseline levels within 5 minutes after the withdrawal of the filament (Figure 1C). The HMPAO signal did not show significant difference 24 hours after MCAo compared with that of sham animals, but was significantly lower after 72 hours reperfusion (Figure 1E). Using SPECT imaging, we found increased DTPA signal in the ipsilateral striatum as early as 2 hours after 30 minutes MCAo, in overlapping areas with leakage of plasma-derived IgG (indicative of BBB breakdown) as detected on coronal brain sections (Figures 1F and 1G). No changes in the ipsilateral hemisphere were detectable with MRI using T2 (Supplementary Figure 1) or diffusion-weighted imaging (not shown) 2 hours after MCAo. Twenty-four hours after 30 minutes MCAo, a regimen that leads to mostly striatal infarcts, DTPA signal was increased in the ipsilateral striatum, whereas DTPA uptake was extended to the cerebral cortex after 45 minutes MCAo, a regimen that leads to both striatal and cortical infarction, as confirmed by MRI and SPECT coregistration (Figure 1H). DTPA uptake in the striatum at 2 hours reperfusion showed good correlation ($R^2 = 0.57$, $P = 0.031$) with infarct size measured on cresyl violet-stained brain sections 24 hours after MCAo (Figure 1I). Two hours after MCAo, DTPA uptake was significantly increased in the ipsilateral striatum in mice with an infarction larger than 20 mm^3 twenty-four hours after stroke compared with sham animals (Figure 1J), and DTPA uptake at 24h showed a significant correlation ($R^2 = 0.55$, $P = 0.022$) with BBB injury as measured by leakage of plasma-derived IgG into the brain on coronal brain sections (Figure 1K), irrespective of infarct size. Histologic analysis revealed that small infarcts (below 20 mm^3) in this study showed an average BBB injury of $4.7 \pm 3.5\text{ mm}^3$ based on IgG penetration whereas infarcts above 20 mm^3 were associated with $21.9 \pm 12\text{ mm}^3$ BBB injury twenty-four hours after MCAo. The system resolution of our imaging device allows the accurate quantification of 4.1 mm^3 volumes with over 96% recovery factor. No changes in I125-HSA uptake were seen in the brain after experimental stroke up to 24 hours reperfusion (not shown).

Single-Photon Emission Computed Tomography Imaging Reveals Early Detrimental Effects of Systemic Inflammation on Cerebral Perfusion and Blood Brain Barrier Injury After Experimental Stroke Since we found that central HMPAO and DTPA signal changes revealed early events of cerebral perfusion and BBB injury, we

used these novel imaging protocols to investigate the impact of systemic inflammation on brain injury after stroke. Systemic inflammation induced by intraperitoneal administration of LPS 2 hours before 30 minutes MCAo reduced cerebral perfusion in the ipsilateral cortex (by 17% in the cerebral cortex, $P = 0.048$ and by 25% in the MCA area, $P = 0.0067$, as measured by ^{99m}Tc -HMPAO uptake), compared with stroke alone. No changes were seen in the striatum or the thalamus (Figures 1A and 1C). Systemic inflammation resulted in increased DTPA uptake in the ipsilateral hemisphere as early as 2 hours after reperfusion ($P < 0.001$), which was most apparent in the cortical MCA area (36% higher compared with stroke alone, Figures 2D and 2E). The effect of systemic inflammation on increased DTPA uptake in the brain was also seen 24 hours after reperfusion ($P < 0.01$, Figure 2F). Systemic inflammation did not increase DTPA uptake after stroke in the core of the infarct (striatum), but a significantly higher DTPA uptake was found at 24 hours reperfusion compared with the 2-hour time point ($P < 0.05$), indicating the development of larger BBB injury over time (Figure 2G). No changes in the ipsilateral hemisphere were detectable with MRI 2 hours after MCAo and preceding systemic inflammation (Supplementary Figure 1).

Systemic Inflammation Increases Brain Inflammation After Stroke and Leads to Markedly Impaired Neurologic Outcome

We found that increased DTPA uptake in the ipsilateral hemisphere was associated with increased microglial activation (Figures 3A and 3B) after experimental stroke in mice with preceding systemic inflammation. There was a marked increase in leukocyte recruitment within the MCA area of the ipsilateral cerebral cortex in response to systemic inflammation after stroke (Figures 3B and 3C; 0.1 ± 0.1 cells after stroke and 3.4 ± 1.5 cells after systemic inflammation and stroke). There was a trend toward increased infarct size (Figure 3D, not significant), whereas profoundly impaired neurologic outcome was observed in mice with preceding systemic inflammation (Figure 3E), in accordance with our previous findings.¹⁹

Single-Photon Emission Computed Tomography Imaging Reveals Early Events of Inflammation and Perfusion Changes in the Lung After Experimental Stroke

Since infectious complications that manifest in the lung, the gut, or the urinary tract are critical contributors to poor outcome and survival of stroke patients,⁸ we assessed whether our novel SPECT imaging protocols reveal early changes in these organs after experimental stroke. ^{99m}Tc -HMPAO signal showed a marked increase in the lung as early as 2 hours after experimental stroke, which was most apparent in the upper lobes of the lung (Figures 4A and 4B), to different extent in individual mice. Lung inflammation was also evident in mice showing the highest HMPAO uptake in MRI (Figure 4B). The HMPAO signal showed a significant increase 24 hours after MCAo in the upper lobes of the lung (Figure 4C) compared with sham mice (by 50%, $P = 0.027$, Figure 4D). Similarly to HMPAO, 24 hours after experimental stroke I125-HSA signal increased significantly in the lung compared with sham mice (by 27%, $P = 0.011$), which was most apparent in the upper lobes of the lung (71% increase over sham mice, $P = 0.003$). There was a good correlation between HSA and HMPAO signal increases in individual mice 24 hours after stroke ($R^2 = 0.64$), whereas only 20% of the mice showed any changes in the lung based on CT or MR images of those having increased HSA or HMPAO uptake in the upper lobes of the lung (not shown). No significant difference in lung DTPA signal was found between sham and stroke mice. Histologic analysis identified inflammatory changes (alveolar space collapse, edema) in the lungs after stroke at 24 hours reperfusion (Figure 4H). This was not seen in sham animals. Seventy-two hours after MCAo 30% of the animals developed pneumonia based on microhemorrhages and increased mucus production in the lungs as assessed on

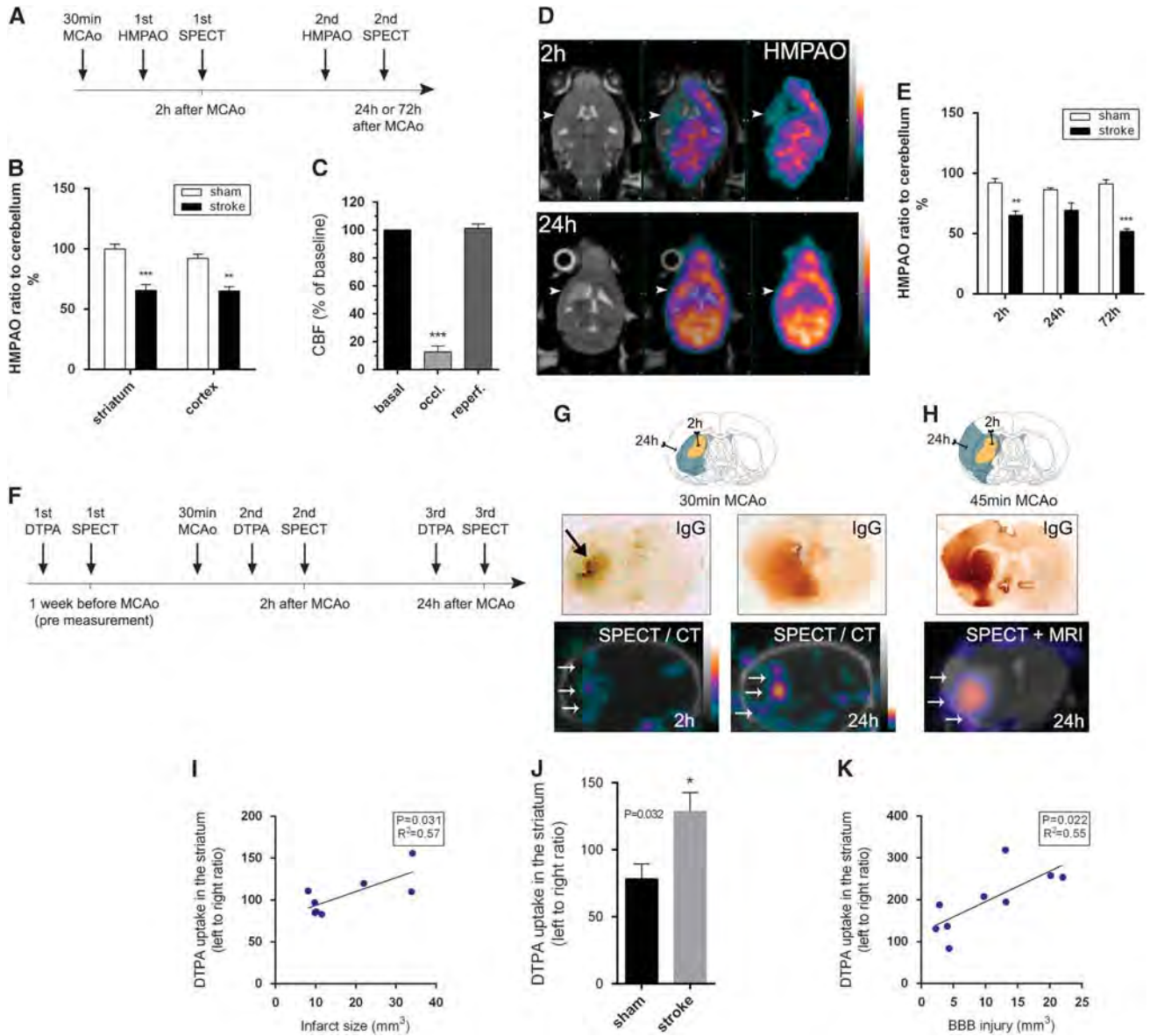


Figure 1. Single-photon emission computed tomography (SPECT) imaging reveals early events of blood brain barrier (BBB) injury after experimental stroke. **(A)** Experimental protocol for SPECT imaging with ^{99m}Tc-HMPAO. **(B)** HMPAO signal is reduced 2 hours after occlusion in the ipsilateral striatum and cerebral cortex. **(C)** Cerebral blood flow was measured by a laser Doppler using an optical probe placed above the ipsilateral middle cerebral artery (MCA). **(D)** SPECT coregistration with magnetic resonance imaging (MRI) showing HMPAO signal changes after MCA occlusion (MCAo). Arrowheads indicate the ipsilateral striatum where infarction is formed by 24 hours reperfusion. **(E)** Time scale of HMPAO signal changes in sham animals and after MCAo. **(F)** Experimental protocol for SPECT imaging with ^{99m}Tc-DTPA. **(G)** Areas of BBB breakdown as revealed by detection of plasma-derived IgG leakage into the brain parenchyma on coronal brain sections overlap with increases of DTPA signal 2 hours and 24 hours after 30 minutes MCAo (arrows). **(H)** SPECT imaging with MRI coregistration showing the location of BBB injury (DTPA) within the infarct after 45 minutes MCAo, which corresponds to leakage of plasma-derived IgG into the brain. **(I)** DTPA signal 2 hours after experimental stroke is predictive of infarct size as measured 24 hours after MCAo on cresyl violet-stained brain sections. **(J)** DTPA signal is significantly increased in the ipsilateral striatum 2 hours after MCAo compared with sham animals in mice showing infarct size larger than 20 mm² 24 hours after stroke. **(K)** Twenty-four hours after MCAo, DTPA signal intensity in the striatum correlates significantly with BBB injury as measured by IgG staining on brain sections. $n = 4$ to 7, * $P < 0.05$, ** $P < 0.01$, *** $P < 0.001$, two-way ANOVA followed by Sidak's multiple comparison (**B** and **E**); one-way ANOVA followed by Tukey's multiple comparison (**C**); unpaired t test (**J**); linear regression (**I** and **K**). DTPA, diethylene triamine pentaacetic acid; HMPAO, hexamethylpropylene amine oxime.

Hematoxylin and Eosin- and periodic acid-Schiff alcian blue-stained lung sections (Figure 4H).

Experimental Stroke Leads to Rapid Gut Barrier Function Changes that can be Detected *In Vivo* by Single-Photon Emission Computed Tomography

Stroke patients have diverse gut associated symptoms, including constipation, reduced bowel motility, paralytic ileus, and dysphagia,

whereas bacterial translocation from the gut to the circulation has also been documented after stroke.^{9-11,21} However, no *in vivo* imaging studies showed previously that acute brain injury results in robust and rapid changes in the gut and gave insight into the mechanisms. The SPECT imaging with ^{99m}Tc-DTPA revealed early and transient changes in the gut after experimental stroke as identified by increases in DTPA signal 2 hours after reperfusion (by 64%, $P = 0.025$, Figures 5A and 5C), which recovered fully by

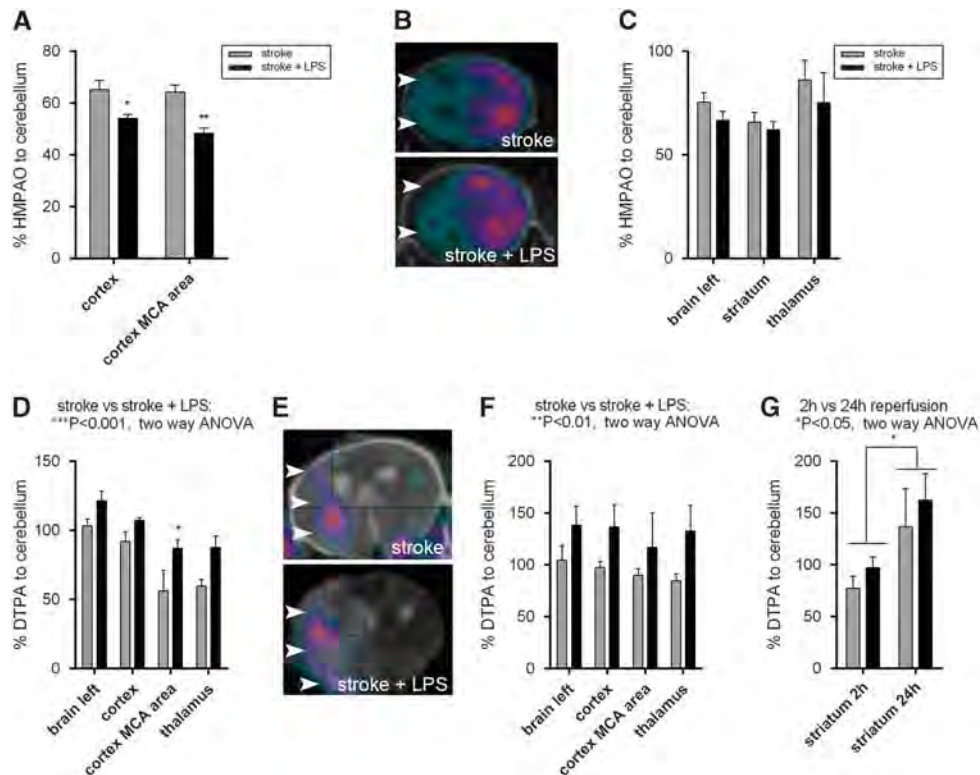


Figure 2. Systemic inflammation reduces cerebral perfusion and rapidly augments blood brain barrier (BBB) injury after experimental stroke. (A and B) ^{99m}Tc -HMPAO signal is reduced significantly in the ipsilateral cerebral cortex in mice with preceding systemic inflammation (lipopolysaccharide (LPS)+stroke) 2 hours after middle cerebral artery occlusion (MCAo), compared with animals without systemic inflammation (stroke). Arrowheads on single-photon emission computed tomography (SPECT)/computed tomography (CT) images showing the superficial zones of the cerebral cortex when HMPAO signal reduction is most apparent (B and C). No changes in HMPAO signal are seen in other brain areas. (D and E) ^{99m}Tc -DTPA uptake is significantly increased in the ipsilateral hemisphere 2 hours after MCAo (arrowheads on E) in mice with preceding systemic inflammation. (F) DTPA uptake is increased in the ipsilateral hemisphere after stroke and systemic inflammation compared with stroke mice, 24 hours after MCAo. (G) DTPA in the ipsilateral striatum 2 and 24 hours after MCAo. $n=4$ to 5, $*P < 0.05$, $**P < 0.01$, $***P < 0.001$, two-way ANOVA followed by Sidak's multiple comparison. DTPA, diethylene triamine pentaacetic acid; HMPAO, hexamethylpropylene amine oxime.

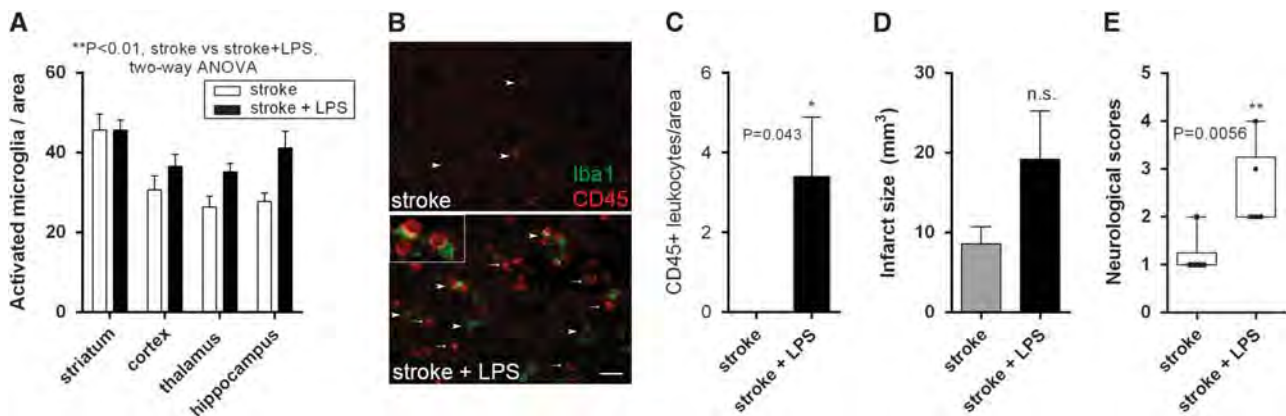


Figure 3. Systemic inflammation increases brain inflammation after stroke and leads to markedly impaired neurologic outcome. (A and B) Microglial activation (ramified, Iba1/CD45_{low} cells with enlarged cell body and thickened processes, arrowheads on B) was assessed 24 hours after experimental stroke in the ipsilateral hemisphere. (C) Recruitment of CD45+ leukocytes to middle cerebral artery (MCA) area of the ipsilateral cerebral cortex 24 hours after MCAo was markedly increased in mice with preceding systemic inflammation (arrows on B). (D) Infarct size was measured on cresyl violet-stained brain sections 24 hours after MCAo. (E) Mice with preceding systemic inflammation show markedly impaired neurologic outcome 24 hours after experimental stroke. $n=5$ to 6, $*P < 0.05$, $**P < 0.01$, $P < 0.001$, two-way ANOVA (A), unpaired t test (C and D) and Mann-Whitney test (E). Scale bar, 50 μm .

24 hours reperfusion (Figure 5C). No perfusion changes were detected in the gut after MCAo as identified by ^{99m}Tc -HMPAO. Histologic analysis on hematoxylin and eosin-stained gut tissues has not revealed any obvious sign of tissue injury or inflammation

infiltrates after experimental stroke (Figure 5D), suggesting that brain injury-induced effects alone could be insufficient to cause lasting gut inflammation. Since bacterial cell wall products released to the circulation after stroke could facilitate gut inflammation and

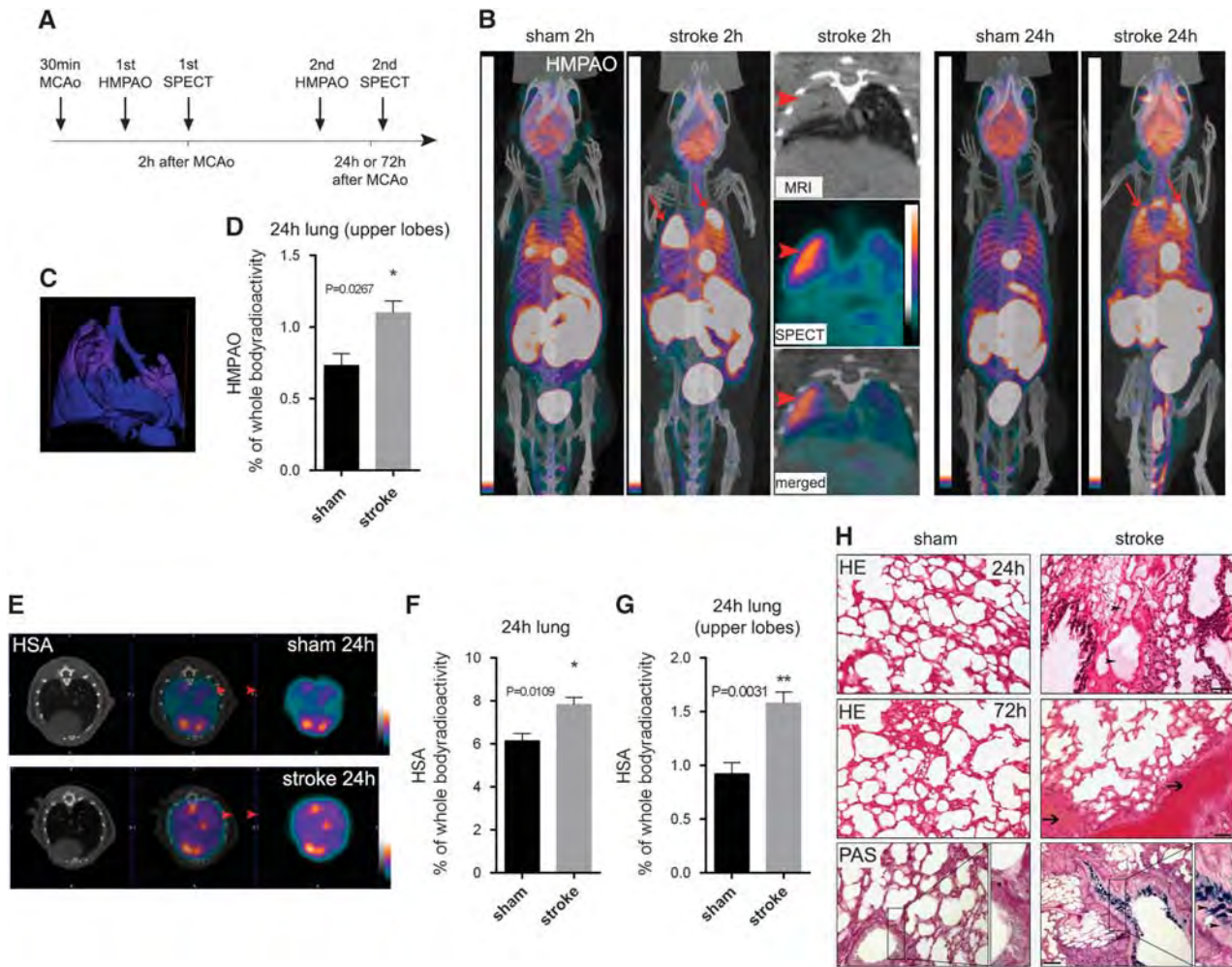


Figure 4. Single-photon emission computed tomography (SPECT) imaging reveals early inflammatory changes in the lung after experimental stroke. **(A)** Experimental protocol for SPECT imaging with ^{99m}Tc -HMPAO. **(B)** HMPAO signal changes in the lung are evident in mice as early as 2 hours after experimental stroke (arrows) and mostly confined to the upper lobes of the lung was also confirmed by magnetic resonance imaging (MRI) coregistration (arrowheads). Increased lung HMPAO signal in the upper lobes of the lung is also seen 24 hours after middle cerebral artery occlusion (MCAo) (arrows). **(C)** 3D reconstruction outlines affected areas in the lung 24 hours after MCAo. **(D)** HMPAO signal in the lung is significantly different in mice after experimental stroke compared with sham animals at 24 hours after surgery. **(E)** I125-HSA signal is increased after experimental stroke in the lung at 24 hours reperfusion. Quantitative analysis showing that HSA signal is significantly increased in the lung **(F)**, which is most apparent in the upper lobes **(G)**. **(H)** Histologic analysis showing inflammatory changes (alveolar space collapse, edema, arrowheads) in the upper lobes of the lung after stroke at 24 hours reperfusion. Seventy-two hours after stroke microhemorrhages (arrows) and increased mucus production (arrowheads) are seen in the lungs as assessed on Hematoxylin and Eosin- and periodic acid-Schiff (PAS) alcian blue-stained lung sections. $n=4$ to 5, $*P < 0.05$, $**P < 0.01$, unpaired t test. Scale bar, $100\ \mu\text{m}$. HMPAO, hexamethylpropylene amine oxime; HSA, human serum albumin.

also contribute to systemic inflammatory changes, we have investigated gut DTPA signal changes in mice with preceding systemic inflammation. Systemic inflammation preceding stroke prolonged DTPA signal increases in the gut as suggested by increased DTPA uptake compared with mice that had undergone experimental stroke only (Figure 5E), indicating that increased systemic inflammatory burden could facilitate brain injury-induced changes in the gut.

DISCUSSION

In this research paper, we reveal very early events of inflammation and injury in both the brain and peripheral organs after experimental stroke, using novel SPECT imaging approaches combined with CT and MRI. These new imaging protocols highlight a previously unrecognized potential for SPECT imaging

to detect BBB injury within a clinically relevant time window, 2 hours after stroke with predictive value for infarct development. SPECT imaging revealed that systemic inflammation preceding experimental stroke leads rapidly to reduced cortical perfusion and increased BBB injury, primarily in penumbral tissues after induction of cerebral ischemia that is associated with markedly augmented brain inflammation and impaired neurologic outcome. In addition, we show that SPECT-based imaging protocols can detect inflammatory changes in peripheral organs (the lungs and the gut) as early as 2 hours after stroke, which are frequently affected in stroke patients and this contributes profoundly to poor clinical outcome and worse recovery. Early inflammatory changes in the lungs as revealed by SPECT were followed by the development of pulmonary inflammation 24 to 72 hours later in experimental animals.

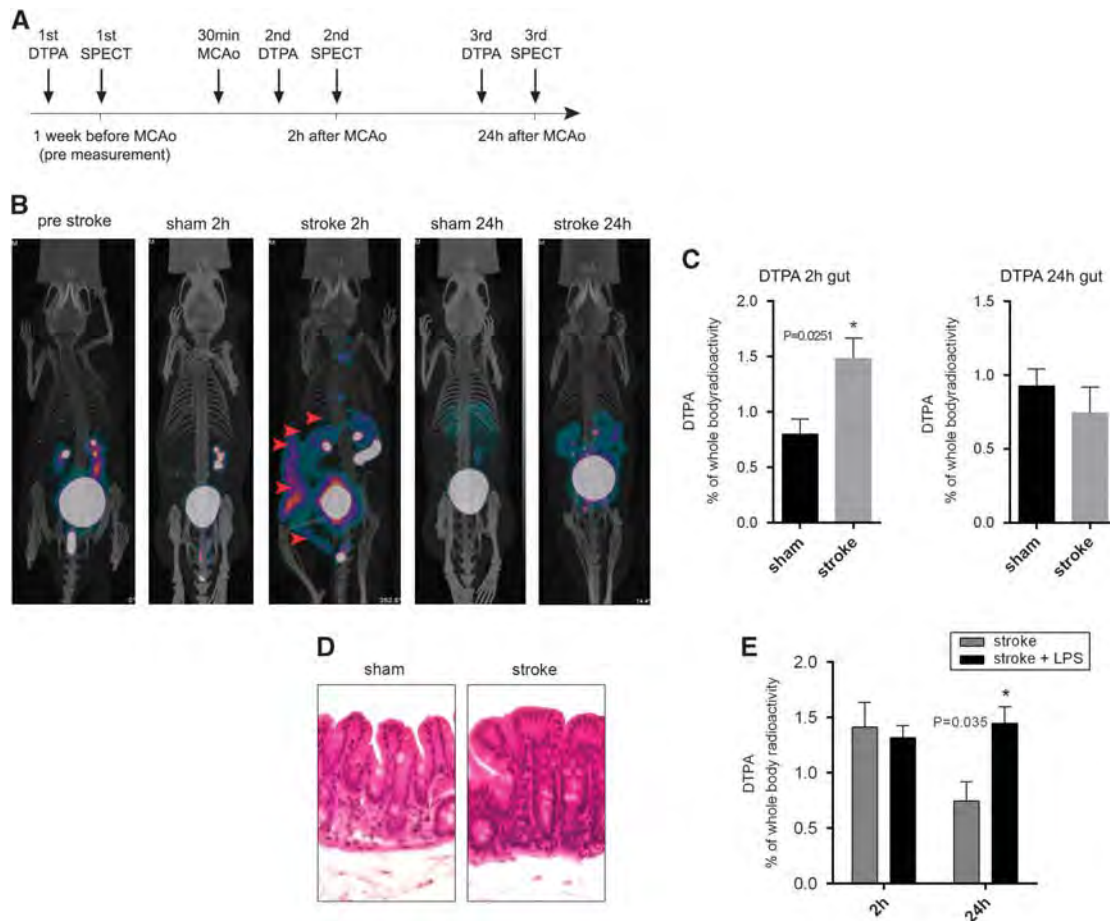


Figure 5. Single-photon emission computed tomography (SPECT) imaging reveals early and transient barrier function changes in the gut after experimental stroke. **(A)** Experimental protocol for SPECT imaging with ^{99m}Tc -DTPA. **(B and C)** DTPA signal intensity markedly increases in the gut 2 hours after experimental stroke (arrowheads), which effect is abolished by 24 hours reperfusion. **(D)** Hematoxylin and eosin staining does not show changes in the gut after experimental stroke compared with sham mice. **(E)** Systemic inflammatory stimulus preceding experimental stroke results in prolonged DTPA signal increases in the gut, which are maintained up to 24 hours reperfusion. $n=4$ to 5 , $*P < 0.05$, unpaired t test **(C)** and two-way ANOVA followed by Sidak's multiple comparison **(E)**. DTPA, diethylene triamine pentaacetic acid.

At present, the clinically accepted method in early diagnostic imaging of acute ischemic stroke is the determination of perfusion-weighted imaging/diffusion-weighted imaging mismatch to identify the core and the penumbra. However, limitations of mismatch detection in both preclinical and clinical research have been recognized, especially in the context of comorbidities,^{22,23} while early events of BBB injury are not assessed routinely in patients.

To our knowledge, this is the first study that used SPECT imaging to visualize early disruption of the BBB after experimental stroke. Our SPECT image acquisition system and reconstruction algorithm were suited to detection of small focal brain lesions in mice and the ^{99m}Tc -DTPA SPECT results correlated well with histologic data. The limitation of SPECT imaging in detection of very small injury in the brain was due to the fact that small, striatal infarcts after MCAo are associated with very low level of BBB breakdown in most of the experimental animals. Earlier studies could detect BBB breakdown with MRI using Gadolinium-DTPA (Gd-DTPA) as contrast agent and with near-infrared fluorescence imaging, using near-infrared fluorescence imaging-BSA, 4 to 24 hours after focal cerebral ischemia in the rodent brain.^{24–27} So far, clinical imaging studies have assessed only delayed phases of BBB injury with SPECT, using ^{99m}Tc -DTPA 48 to 72 hours after stroke,^{12,28,29} in which correlation between BBB injury and neurologic outcome has been reported.¹² In our experimental model, DTPA uptake in the ipsilateral hemisphere 2 hours after

stroke was predictive of infarct size measured at 24 hours reperfusion, particularly in the case of large infarcts. Importantly, early DTPA uptake was significantly augmented by preceding systemic inflammation, which was most apparent in the penumbra, affecting the MCA area of the ipsilateral cerebral cortex. This suggests that evolution of BBB breakdown was facilitated by preceding systemic inflammation, which was represented by ^{99m}Tc -DTPA SPECT signals. Similarly to our observations, previous studies confirmed that changes in BBB breakdown after brain injury show linear correlation with ^{99m}Tc -DTPA SPECT signals.³⁰ At present, assessment of detrimental systemic inflammatory processes in stroke patients largely relies on blood markers (increased white blood cell count, erythrocyte sedimentation rate or plasma C-reactive protein), while there are no imaging tools that could visualize systemic inflammation or its early effect on brain injury. Whole-body SPECT imaging could be used in experimental and clinical studies to determine *in vivo* regional differences in inflammatory activation in the brain and peripheral tissues, to address key research questions and improve the predictive value of blood biomarkers. We have shown earlier that in patients with multiple risk factors for stroke and chronically elevated C-reactive protein, brain inflammation (microglial activation as assessed by positron emission tomography) is apparent even before the occurrence of any acute cerebrovascular events, independently of any obvious neurologic disease. Similar changes

have been found in the brain in relevant co-morbid animal models.³¹ Underlying systemic inflammation due to old age, chronic diseases or infection results in markedly impaired outcome after stroke in patients and in experimental animals.^{7,17–19,32} However, mechanisms by which systemic inflammation impacts on brain injury are improperly understood. Recent data suggest that peripheral inflammatory stimuli (induced by LPS or the proinflammatory cytokine interleukin-1) could alter cerebral perfusion, lead to larger BBB injury or cerebral edema after stroke that might happen independently of increases in infarct size.^{19,33,34} In fact, we have found reduced 99mTc-HMPAO uptake in the cerebral cortex early (2 hours) after experimental stroke that was further reduced by preceding systemic inflammation. In contrast, systemic inflammation did not significantly reduce cerebral perfusion and did not augment BBB injury in the striatum (infarct core), where cerebral blood flow was maximally reduced during MCAo. The HMPAO signal showed an increase in subnormal values after 24 hours reperfusion and decreased again by 72 hours after stroke. The sole study that used 99mTc-HMPAO and SPECT in an MCAo model found similar reduction in HMPAO signal upon occlusion followed by a gradual increase between 2 days and 7 days after reperfusion.³⁵ It is believed that the SPECT signal is derived from the accumulation of a hydrophilic metabolite of 99mTc-HMPAO in the brain parenchyma,¹³ but HMPAO signal changes could also be due to elevated glutathione levels.³⁶ Inflammation could contribute to both reduced cerebral perfusion several hours after the induction of reperfusion after stroke (often termed as the 'no-reflow phenomenon') and increased levels of oxidative stress,^{37,38} therefore mechanisms of HMPAO signal changes after stroke need to be investigated in detail in future studies. Measurements by laser Doppler have shown that blood flow in the MCA was fully restored upon the induction of reperfusion. Nevertheless, this technique does not give information about whether reflow takes place at the level of capillaries in deeper brain tissues. Thus, HMPAO appears to be a sensitive marker of compromised blood flow after cerebral ischemia in the brain parenchyma and correlations between HMPAO signal changes and tissue oxygenation will need to be investigated further. Importantly, our SPECT imaging studies using 99mTc-HMPAO and histologic data suggest that systemic inflammation has very early and negative impact on cerebral perfusion, inflammation and BBB injury, well within the relevant therapeutic time window after stroke, which indicates a good potential for anti-inflammatory therapies in patients with high systemic inflammatory burden. For example, therapeutic blockade of actions of IL-1, a key proinflammatory cytokine, was effective to prevent increased BBB injury, infarct size and worse neurologic outcome induced by a human *Streptococcus pneumoniae* isolate in mice and rats after experimental stroke.¹⁸

Brain injury induces profound inflammatory changes in the periphery in both patients and experimental animals that turn into immunosuppression. One of the most detrimental clinical consequences of poststroke immunosuppression is the development of infectious complications that lead to long hospitalization, impaired recovery or death in patients.⁸ Our SPECT imaging results identify for the first time obvious changes in some of the most affected peripheral organs after stroke, namely in the lungs and the gut, as early as from 2 hours to 24 hours after acute experimental brain injury. At present, the precise cellular-molecular mechanisms underlying early 99mTc-HMPAO, 99mTc-DTPA, and I125-HSA signal are currently unclear, but are likely to reflect alterations in inflammatory processes, perfusion, and barrier function. Uptake of 99mTc-HMPAO by bronchoalveolar cells in the inflamed lung of smokers or after lung toxicity is supposedly reflective of altered glutathione concentrations.³⁹ Our histologic data confirmed the development of inflammation in the lung starting from 24 hours after experimental stroke. This is also supported by increased pulmonary uptake of I125-HSA after

stroke. Constipation, dysphagia, paralytic ileus, digestion problems, and other gut symptoms are often seen in stroke patients and bacterial translocation across the gut epithelium has also been reported.^{9–11,21,40} Since the gut barrier structures resemble those of the central nervous system⁴¹ and 99mTc-DTPA identified early, but transient changes in the gut after stroke, whereas no changes in I125-HSA or 99mTc-HMPAO signal were observed, it is possible that 99mTc-DTPA signal increases are reflective of changes in the gut barrier structures in response to brain injury. The autonomic nervous system has been implicated in the development of poststroke immunosuppression.^{8,42} Both the gut and the lungs receive rich autonomic innervation that could directly dampen immune responses,⁴³ thus it is possible that brain injury-induced changes in these organs are due to autonomic activation or lack of central autonomic control; however, this must be functionally investigated in further studies. Nevertheless, currently no imaging tools can visualize early events of peripheral inflammation or infection after brain injury in patients or experimental animals, while early diagnosis of infection would have profound clinical benefits. Poststroke infections are not only associated with a lower survival rate, but preventive antibacterial therapy is very effective to reduce infections after severe nonlacunar ischemic stroke.⁴⁴

Translation of experimental findings to clinical benefit is one of the biggest challenges of current research in the field of brain diseases. We have developed a set of new imaging applications using SPECT to investigate mechanisms of stroke-induced pathologies in mice. While our imaging tools could be effectively used to understand mechanisms of brain diseases in experimental models, there is a good potential to translate these findings into clinical application. The image resolution used was sufficient to identify detailed functional and anatomic changes in different areas of the small mouse brain, which could be markedly improved in the human brain. In addition, we used radioligands that are already approved for clinical use, which may largely support clinical studies with the overall aim to develop protocols for improved diagnosis of disease.

In conclusion, we developed novel, SPECT-based imaging applications for complex assessment of inflammatory, perfusion and barrier function changes in experimental stroke that could support understanding of mechanisms of stroke and other brain diseases with good potential for clinical translation.

AUTHOR CONTRIBUTIONS

KSz, DM, and AD designed research; KSz, IH, DSV, BM, NL, NK, EB, AM, MS, and AD performed research; DM contributed new reagents/analytic tools; KSz, IH, DSV, BM, NL, NK, EB, AM, MS, DM, and AD analyzed the data; and KSz, DM, and AD wrote the paper.

DISCLOSURE/CONFLICT OF INTEREST

The authors declare no conflict of interest.

ACKNOWLEDGMENTS

Funding was provided by OTKA K109743 (AD), TÁMOP-4.2.4.A/2-11/1-2012-000 (AD), the Hungarian Brain Research Program KTIA_13_NAP-A-1/2 (AD), and the European Union's Seventh Framework Program (FP7/2007-2013) under grant agreements n° HEALTH-F2-2011-278850 (INMiND, KSZ) and n° 305311 (INSERT). AD is supported by the Bolyai Janos Research Scholarship of the Hungarian Academy of Sciences.

REFERENCES

- 1 Feigin VL, Forouzanfar MH, Krishnamurthi R, Mensah GA, Connor M, Bennett DA et al. Global and regional burden of stroke during 1990–2010: findings from the Global Burden of Disease Study 2010. *Lancet* 2014; **383**: 245–254.
- 2 Emberson J, Lees KR, Lyden P, Blackwell L, Albers G, Bluhmki E et al. Effect of treatment delay, age, and stroke severity on the effects of intravenous

- thrombolysis with alteplase for acute ischaemic stroke: a meta-analysis of individual patient data from randomised trials. *Lancet* 2014; **384**: 1929–1935.
- 3 Emsley HC, Smith CJ, Tyrrell PJ, Hopkins SJ. Inflammation in acute ischemic stroke and its relevance to stroke critical care. *Neurocrit Care* 2008; **9**: 125–138.
 - 4 Macrez R, Ali C, Toutirais O, Le Mauff B, Defer G, Dirnagl U et al. Stroke and the immune system: from pathophysiology to new therapeutic strategies. *Lancet Neurol* 2011; **10**: 471–480.
 - 5 Smith CJ, Denes A, Tyrrell PJ, Di Napoli M. Phase II anti-inflammatory and immunomodulating drugs for acute ischaemic stroke. *Expert Opin Investig Drugs* 2015; **24**: 623–643.
 - 6 Saver JL. Time is brain—quantified. *Stroke* 2006; **37**: 263–266.
 - 7 McColl BW, Allan SM, Rothwell NJ. Systemic infection, inflammation and acute ischemic stroke. *Neuroscience* 2009; **158**: 1049–1061.
 - 8 Dirnagl U, Klehmet J, Braun JS, Harms H, Meisel C, Ziemssen T et al. Stroke-induced immunodepression: experimental evidence and clinical relevance. *Stroke* 2007; **38**: 770–773.
 - 9 Su Y, Zhang X, Zeng J, Pei Z, Cheung RT, Zhou QP et al. New-onset constipation at acute stage after first stroke: incidence, risk factors, and impact on the stroke outcome. *Stroke* 2009; **40**: 1304–1309.
 - 10 Tang WH, Wang Z, Levison BS, Koeth RA, Britt EB, Fu X et al. Intestinal microbial metabolism of phosphatidylcholine and cardiovascular risk. *N Engl J Med* 2013; **368**: 1575–1584.
 - 11 Korpelainen JT, Sotaniemi KA, Myllyla VV. Autonomic nervous system disorders in stroke. *Clin Auton Res* 1999; **9**: 325–333.
 - 12 Lorberboym M, Lampl Y, Sadeh M. Correlation of 99mTc-DTPA SPECT of the blood-brain barrier with neurologic outcome after acute stroke. *J Nucl Med* 2003; **44**: 1898–1904.
 - 13 Sperling B, Lassen NA. Hyperfixation of HMPAO in subacute ischemic stroke leading to spuriously high estimates of cerebral blood flow by SPECT. *Stroke* 1993; **24**: 193–194.
 - 14 Sasaki T, Senda M. Technetium-99m-meso-HMPAO as a potential agent to image cerebral glutathione content. *J Nucl Med* 1997; **38**: 1125–1129.
 - 15 Khalil MM, Tremoleda JL, Bayomy TB, Gsell W. Molecular SPECT imaging: an overview. *Int J Mol Imaging* 2011; **2011**: 796025.
 - 16 Knotkova H, Pappagallo M. Imaging intracranial plasma extravasation in a migraine patient: a case report. *Pain Med* 2007; **8**: 383–387.
 - 17 Denes A, Humphreys N, Lane TE, Grecnis R, Rothwell N. Chronic systemic infection exacerbates ischemic brain damage via a CCL5 (regulated on activation, normal T-cell expressed and secreted)-mediated proinflammatory response in mice. *J Neurosci* 2010; **30**: 10086–10095.
 - 18 Denes A, Pradillo JM, Drake C, Sharp A, Warn P, Murray KN et al. Streptococcus pneumoniae worsens cerebral ischemia via interleukin 1 and platelet glycoprotein Ibalph. *Ann Neurol* 2014; **75**: 670–683.
 - 19 Denes A, Ferenczi S, Kovacs KJ. Systemic inflammatory challenges compromise survival after experimental stroke via augmenting brain inflammation, blood-brain barrier damage and brain oedema independently of infarct size. *J Neuroinflammation* 2011; **8**: 164.
 - 20 Bederson JB, Pitts LH, Tsuji M, Nishimura MC, Davis RL, Bartkowski H. Rat middle cerebral artery occlusion: evaluation of the model and development of a neurologic examination. *Stroke* 1986; **17**: 472–476.
 - 21 Caso JR, Hurtado O, Pereira MP, Garcia-Bueno B, Menchen L, Alou L et al. Colonic bacterial translocation as a possible factor in stress-worsening experimental stroke outcome. *Am J Physiol Regul Integr Comp Physiol* 2009; **296**: R979–R985.
 - 22 Reid E, Graham D, Lopez-Gonzalez MR, Holmes WM, Macrae IM, McCabe C. Penumbra detection using PWI/DWI mismatch MRI in a rat stroke model with and without comorbidity: comparison of methods. *J Cereb Blood Flow Metab* 2012; **32**: 1765–1777.
 - 23 Sobesky J, Zaro Weber O, Lehnhardt FG, Hesselmann V, Neveling M, Jacobs A et al. Does the mismatch match the penumbra? Magnetic resonance imaging and positron emission tomography in early ischemic stroke. *Stroke* 2005; **36**: 980–985.
 - 24 Kastrup A, Engelhorn T, Beaulieu C, de Crespigny A, Moseley ME. Dynamics of cerebral injury, perfusion, and blood-brain barrier changes after temporary and permanent middle cerebral artery occlusion in the rat. *J Neurol Sci* 1999; **166**: 91–99.
 - 25 Klohs J, Steinbrink J, Bourayou R, Mueller S, Cordell R, Licha K et al. Near-infrared fluorescence imaging with fluorescently labeled albumin: a novel method for non-invasive optical imaging of blood-brain barrier impairment after focal cerebral ischemia in mice. *J Neurosci Methods* 2009; **180**: 126–132.
 - 26 Nagel S, Wagner S, Koziol J, Kluge B, Heiland S. Volumetric evaluation of the ischemic lesion size with serial MRI in a transient MCAO model of the rat: comparison of DWI and T1WI. *Brain Res Brain Res Protoc* 2004; **12**: 172–179.
 - 27 Zhang Z, Zhang L, Yepes M, Jiang Q, Li Q, Arniago P et al. Adjuvant treatment with neuroserpin increases the therapeutic window for tissue-type plasminogen activator administration in a rat model of embolic stroke. *Circulation* 2002; **106**: 740–745.
 - 28 Inoue Y, Momose T, Machida K, Honda N, Mamiya T, Takahashi T et al. Delayed imaging of Tc-99m-DTPA-HSA SPECT in subacute cerebral infarction. *Radiat Med* 1993; **11**: 214–216.
 - 29 Lampl Y, Sadeh M, Lorberboym M. Prospective evaluation of malignant middle cerebral artery infarction with blood-brain barrier imaging using Tc-99m DTPA SPECT. *Brain Res* 2006; **1113**: 194–199.
 - 30 Lin KJ, Liu HL, Hsu PH, Chung YH, Huang WC, Chen JC et al. Quantitative micro-SPECT/CT for detecting focused ultrasound-induced blood-brain barrier opening in the rat. *Nucl Med Biol* 2009; **36**: 853–861.
 - 31 Drake C, Boutin H, Jones MS, Denes A, McColl BW, Selvarajah JR et al. Brain inflammation is induced by co-morbidities and risk factors for stroke. *Brain Behav Immun* 2011; **25**: 1113–1122.
 - 32 Iadecola C, Anrather J. The immunology of stroke: from mechanisms to translation. *Nat Med* 2011; **17**: 796–808.
 - 33 Murray KN, Girard S, Holmes WM, Parkes LM, Williams SR, Parry-Jones AR et al. Systemic inflammation impairs tissue reperfusion through endothelin-dependent mechanisms in cerebral ischemia. *Stroke* 2014; **45**: 3412–3419.
 - 34 McColl BW, Rothwell NJ, Allan SM. Systemic inflammation alters the kinetics of cerebrovascular tight junction disruption after experimental stroke in mice. *J Neurosci* 2008; **28**: 9451–9462.
 - 35 Martin A, Mace E, Boisgard R, Montaldo G, Theze B, Tanter M et al. Imaging of perfusion, angiogenesis, and tissue elasticity after stroke. *J Cereb Blood Flow Metab* 2012; **32**: 1496–1507.
 - 36 Sasaki T, Senda M. Evaluation of glutathione localization in brain using 99mTc meso-HMPAO. *J Nucl Med* 1999; **40**: 1056–1060.
 - 37 Rezkalla SH, Kloner RA. No-reflow phenomenon. *Circulation* 2002; **105**: 656–662.
 - 38 Lakhani SE, Kirchgessner A, Hofer M. Inflammatory mechanisms in ischemic stroke: therapeutic approaches. *J Transl Med* 2009; **7**: 97.
 - 39 Durak H, Kilinc O, Ertay T, Ucan ES, Kargi A, Kaya GC et al. Tc-99m-HMPAO uptake by bronchoalveolar cells. *Ann Nucl Med* 2003; **17**: 107–113.
 - 40 Bracci F, Badiali D, Pezzotti P, Scivoletto G, Fuoco U, Di Lucente L et al. Chronic constipation in hemiplegic patients. *World J Gastroenterol* 2007; **13**: 3967–3972.
 - 41 Daneman R, Rescigno M. The gut immune barrier and the blood-brain barrier: are they so different? *Immunity* 2009; **31**: 722–735.
 - 42 Prass K, Meisel C, Hoflich C, Braun J, Halle E, Wolf T et al. Stroke-induced immunodeficiency promotes spontaneous bacterial infections and is mediated by sympathetic activation reversal by poststroke T helper cell type 1-like immunostimulation. *J Exp Med* 2003; **198**: 725–736.
 - 43 Elenkov IJ, Wilder RL, Chrousos GP, Vizi ES. The sympathetic nerve—an integrative interface between two supersystems: the brain and the immune system. *Pharmacol Rev* 2000; **52**: 595–638.
 - 44 Harms H, Prass K, Meisel C, Klehmet J, Rogge W, Drenckhahn C et al. Preventive antibacterial therapy in acute ischemic stroke: a randomized controlled trial. *PLoS One* 2008; **3**: e2158.

Supplementary Information accompanies the paper on the Journal of Cerebral Blood Flow & Metabolism website (<http://www.nature.com/jcbbfm>)

Correction

NEUROSCIENCE

Correction for “Transfer of complex regional pain syndrome to mice via human autoantibodies is mediated by interleukin-1–induced mechanisms,” by Zsuzsanna Helyes, Valéria Tékus, Nikolett Szentes, Krisztina Pohóczky, Bálint Botz, Tamás Kiss, Ágnes Kemény, Zsuzsanna Környei, Krisztina Tóth, Nikolett Lénárt, Hajnalka Ábrahám, Emmanuel Pinteaux, Sheila Francis, Serena Sensi, Ádám Dénes, and Andreas Goebel, which was first published June 10, 2019; 10.1073/pnas.1820168116 (*Proc. Natl. Acad. Sci. U.S.A.* **116**, 13067–13076).

The authors note that, due to a printer’s error, the affiliations for Ádám Dénes appeared incorrectly. They should instead appear as Momentum Laboratory of Neuroimmunology, Institute of Experimental Medicine, H-1083, Budapest, Hungary; and Division of Neuroscience and Experimental Psychology, University of Manchester, Manchester M13 9PT, United Kingdom. The corrected author and affiliation lines appear below. The online version has been corrected.

Zsuzsanna Helyes^{a,b,c}, Valéria Tékus^{a,b}, Nikolett Szentes^{a,b}, Krisztina Pohóczky^{a,b,d}, Bálint Botz^{a,b}, Tamás Kiss^{a,b}, Ágnes Kemény^{a,b,e}, Zsuzsanna Környei^f, Krisztina Tóth^f, Nikolett Lénárt^f, Hajnalka Ábrahám^e, Emmanuel Pinteaux^g, Sheila Francis^h, Serena Sensiⁱ, Ádám Dénes^{f,g}, and Andreas Goebel^{i,j}

^aDepartment of Pharmacology and Pharmacotherapy, Medical School, University of Pécs, H-7624, Pécs, Hungary; ^bJános Szentágothai Research Centre & Centre for Neuroscience, University of Pécs, H-7624, Pécs, Hungary; ^cPharmlnVivo Ltd., H-7629, Pécs, Hungary; ^dFaculty of Pharmacy, Department of Pharmacology, University of Pécs, H-7624, Pécs, Hungary; ^eDepartment of Biology and Electron Microscopy, Medical School, University of Pécs, H-7624, Pécs, Hungary; ^fMomentum Laboratory of Neuroimmunology, Institute of Experimental Medicine, H-1083, Budapest, Hungary; ^gDivision of Neuroscience and Experimental Psychology, University of Manchester, Manchester M13 9PT, United Kingdom; ^hDepartment of Infection, Immunity and Cardiovascular Disease, University of Sheffield, Sheffield S10 2RX, United Kingdom; ⁱDepartment of Translational Medicine, University of Liverpool, Liverpool L9 7AL, United Kingdom; and ^jDepartment of Pain Medicine, The Walton Centre National Health Service Foundation Trust, Liverpool L9 7LJ, United Kingdom

Published under the [PNAS license](#).

www.pnas.org/cgi/doi/10.1073/pnas.1910290116

Transfer of complex regional pain syndrome to mice via human autoantibodies is mediated by interleukin-1-induced mechanisms

Zsuzsanna Helyes^{a,b,c,1,2}, Valéria Tékus^{a,b,1}, Nikolett Szentes^{a,b,1}, Krisztina Pohóczky^{a,b,d}, Bálint Botz^{a,b}, Tamás Kiss^{a,b}, Ágnes Kemény^{a,b,e}, Zsuzsanna Környei^f, Krisztina Tóth^f, Nikolett Lénárt^f, Hajnalka Ábrahám^e, Emmanuel Pinteaux^g, Sheila Francis^h, Serena Sensiⁱ, Ádám Dénes^{e,g,2,3}, and Andreas Goebel^{i,j,2,3}

^aDepartment of Pharmacology and Pharmacotherapy, Medical School, University of Pécs, H-7624, Pécs, Hungary; ^bJános Szentágotthai Research Centre & Centre for Neuroscience, University of Pécs, H-7624, Pécs, Hungary; ^cPharmInVivo Ltd., H-7629, Pécs, Hungary; ^dFaculty of Pharmacy, Department of Pharmacology, University of Pécs, H-7624, Pécs, Hungary; ^eDepartment of Biology and Electron Microscopy, Medical School, University of Pécs, H-7624, Pécs, Hungary; ^fMomentum Laboratory of Neuroimmunology, Institute of Experimental Medicine, H-1083, Budapest, Hungary; ^gDivision of Neuroscience and Experimental Psychology, University of Manchester, Manchester M13 9PT, United Kingdom; ^hDepartment of Infection, Immunity and Cardiovascular Disease, University of Sheffield, Sheffield S10 2RX, United Kingdom; ⁱDepartment of Translational Medicine, University of Liverpool, Liverpool L9 7AL, United Kingdom; and ^jDepartment of Pain Medicine, The Walton Centre National Health Service Foundation Trust, Liverpool L9 7LJ, United Kingdom

Edited by David Julius, University of California, San Francisco, CA, and approved May 13, 2019 (received for review December 1, 2018)

Neuroimmune interactions may contribute to severe pain and regional inflammatory and autonomic signs in complex regional pain syndrome (CRPS), a posttraumatic pain disorder. Here, we investigated peripheral and central immune mechanisms in a translational passive transfer trauma mouse model of CRPS. Small plantar skin-muscle incision was performed in female C57BL/6 mice treated daily with purified serum immunoglobulin G (IgG) from patients with longstanding CRPS or healthy volunteers followed by assessment of paw edema, hyperalgesia, inflammation, and central glial activation. CRPS IgG significantly increased and prolonged swelling and induced stable hyperalgesia of the incised paw compared with IgG from healthy controls. After a short-lasting paw inflammatory response in all groups, CRPS IgG-injected mice displayed sustained, profound microglia and astrocyte activation in the dorsal horn of the spinal cord and pain-related brain regions, indicating central sensitization. Genetic deletion of interleukin-1 (IL-1) using IL-1 α knockout (KO) mice and perioperative IL-1 receptor type 1 (IL-1R1) blockade with the drug anakinra, but not treatment with the glucocorticoid prednisolone, prevented these changes. Anakinra treatment also reversed the established sensitization phenotype when initiated 8 days after incision. Furthermore, with the generation of an IL-1 β floxed^(fl/fl) mouse line, we demonstrated that CRPS IgG-induced changes are in part mediated by microglia-derived IL-1 β , suggesting that both peripheral and central inflammatory mechanisms contribute to the transferred disease phenotype. These results indicate that persistent CRPS is often contributed to by autoantibodies and highlight a potential therapeutic use for clinically licensed antagonists, such as anakinra, to prevent or treat CRPS via blocking IL-1 actions.

CRPS | autoantibody | complex regional pain syndrome | interleukin-1 | anakinra

Complex regional pain syndrome (CRPS), with a prevalence of about 1:2,000, is a chronic pain condition experienced by humans. CRPS is usually triggered by trauma to the distal regions of a limb and is further associated with limb-restricted edema; sensory, vasomotor, sudomotor, motor, and trophic abnormalities; and profound sensory central nervous system (CNS) reorganization (1). In CRPS, typically no or only minimal tissue destruction occurs (2), and although morphological change, such as disuse atrophy, can sometimes be observed, this is not thought to explain the experienced intense pain (3). The underlying pathophysiological mechanisms are poorly understood. Systemic inflammatory markers remain normal in CRPS patients, but regional inflammatory mediators and autoimmunity are suggested to contribute to the manifestation of the symptoms (4). Furthermore, neuroplasticity mechanisms within the spinal cord and the brain are believed to sustain persistent pain (5).

While most patients with CRPS show an improvement within months, either with or without treatment (6), 20% of patients develop persistent pain, often lasting for years or even through their lifetime (7). This type of persistent pain is intrusive and results in among the lowest quality of life scores in medical conditions (8). Among the few drug trials performed to date (9), neither conventional drugs used to relieve pain, (i.e., nonsteroidal antiinflammatory drugs, opioids, antidepressants, or anticonvulsants) nor steroids have shown significant efficacy in persistent CRPS. Implantation of a spinal cord stimulator, which delivers electrical impulses to the dorsal column, can override CRPS pain in about 50% of patients, but the duration of the optimum effect is limited (9). Since many patients cannot be successfully treated, the treatment of CRPS remains an important unresolved problem and is still an unmet medical need (10). Thus, to better understand the peripheral and

Significance

Complex regional pain syndrome (CRPS) is a poorly understood painful condition, which typically arises after distal limb trauma; 20% of patients may develop lifelong severe incessant pain with few therapeutic options. In this study, we show that immunoglobulin G autoantibodies from patients with severe, persistent CRPS, on transfer to hind paw-injured mice, elicit important features of the clinical condition and profound glial activation in pain-related brain regions. Blockade of the proinflammatory cytokine interleukin-1 (IL-1) both prevents and reverses these changes. Our findings suggest that antibody-mediated autoimmunity contributes to the development of severe CRPS after injury and that blockade of IL-1 actions may be an attractive therapeutic prospect. Investigation of autoantibody contribution to other unexplained chronic pain syndromes seems warranted.

Author contributions: Z.H., V.T., E.P., Á.D., and A.G. designed research; Z.H., V.T., N.S., K.P., B.B., T.K., Á.K., Z.K., K.T., N.L., H.Á., S.F., S.S., Á.D., and A.G. performed research; Z.K., K.T., N.L., E.P., S.F., and Á.D. contributed new reagents/analytic tools; Z.H., V.T., N.S., K.P., B.B., H.Á., E.P., Á.D., and A.G. analyzed data; and Z.H., N.S., K.P., E.P., S.F., Á.D., and A.G. wrote the paper.

The authors declare no conflict of interest.

This article is a PNAS Direct Submission.

Published under the PNAS license.

¹Z.H., V.T., and N.S. contributed equally to this work.

²To whom correspondence may be addressed. Email: zsuzsanna.helyes@aok.pte.hu, denes.adam@koki.mta.hu, or andreasgoebel@rocketmail.com.

³Á.D. and A.G. contributed equally to this work.

This article contains supporting information online at www.pnas.org/lookup/suppl/doi:10.1073/pnas.1820168116/-DCSupplemental.

Published online June 10, 2019.

central pathophysiological mechanisms underlying CRPS, reliable and validated animal models are desperately needed (2).

We have recently shown that passive transfer of serum immunoglobulin G (IgG) from CRPS patients to hind paw-injured rodents elicits key features (unilateral hyperalgesia and edema) of the clinical condition (11). This suggests a “two-hit” process, where circulating IgG autoantibodies (i.e., the first hit) are rendered pathogenic in the context of paw injury (the second hit)-related regional or central modifications (2). Although these behavioral results indicated that serum IgG autoantibodies contribute to the disease pathophysiology and thus, provided first evidence for the construct validity of the transfer model, the observed abnormalities were modest and short-lasting, and the mechanisms mediating them have remained unknown.

Using samples available from patients who consented to repeat donation of larger blood volumes or who had received plasma exchange treatment (12), we have now developed an enhanced passive IgG transfer trauma model and have examined its translational validity. We investigated (i) whether and how the transferred behavioral signs in rodents are augmented and sustained with daily human IgG injections and whether there are differences between preparations from different patients; (ii) the degree of regional posttraumatic immune activation in the paw given that mild, transient immune activation in the affected skin is sometimes detected in patients (13) and its correlation to behavioral parameters; (iii) the degree and mechanisms of posttraumatic glial activation in the spinal dorsal horn, since strong CNS reorganization is recognized in the clinical cases (5); and finally, (iv) whether targeting specific inflammatory pathways at the time of or after trauma can prevent or reverse transferred complex regional pain syndrome (tCRPS) to provide a translatable therapeutic approach.

Results

Daily Administration of Serum IgG from CRPS Patients Induces Profound and Persistent Postincisional Mechanical Hyperalgesia.

The preoperation mechanonociceptive threshold values of the affected limbs were 8.65 ± 0.08 , 8.69 ± 0.09 , and 8.60 ± 0.07 in the saline, healthy IgG-, and CRPS IgG-treated mice, respectively (not significantly different) (Fig. 1A). Plantar skin and muscle incision induced a 45–50% relative decrease of the mechanonociceptive threshold in all groups 1 d after the surgery. On daily injections, paw sensitivity quickly recovered to mild hyperalgesia in both saline and healthy IgG-injected animals, with mild, nonsignificantly enhanced values remaining in the healthy IgG group vs. the saline group throughout the experimental period. Injection of IgG from CRPS patients caused significantly augmented hyperalgesia compared with IgG from healthy volunteers, which seemed to be further enhanced toward the end of the experimental period. This effect was evident in the IgG preparations from each individually tested patient ($n = 7$) as well as a preparation pooled from seven separate patients (SI

Appendix, Fig. S1). The observed 15–32% absolute threshold reduction was twofold compared with that seen in our previously published experimental model (injections on days –1, 0, 5, and 6) (11). Contralateral paws retained normal sensitivity in all groups (SI Appendix, Fig. S2).

In all groups, injured paws developed about 30% relative paw swelling (defined as edema) on day 1, but there were no changes in contralateral paws (SI Appendix, Fig. S3). Edema resolved in healthy IgG and saline groups, but CRPS IgG injection significantly slowed edema resolution (Fig. 1B). While the pattern of transferred hyperalgesia was uniform, there was important variability in the degree and pattern of transferred swelling between different patient preparations, with no correlation between these two parameters (SI Appendix, Figs. S2 and S3). Postsurgery minimal weight loss was observed compared with baseline for a few days, and the weights of the animal then fully recovered without significant differences between groups (SI Appendix, Fig. S4). We observed no spontaneous nocifensive behaviors, such as paw biting, lifting, or licking.

CRPS IgG Does Not Alter Vascular Plasma Leakage but Increases Neutrophil Myeloperoxidase Activity Early After Paw Incision.

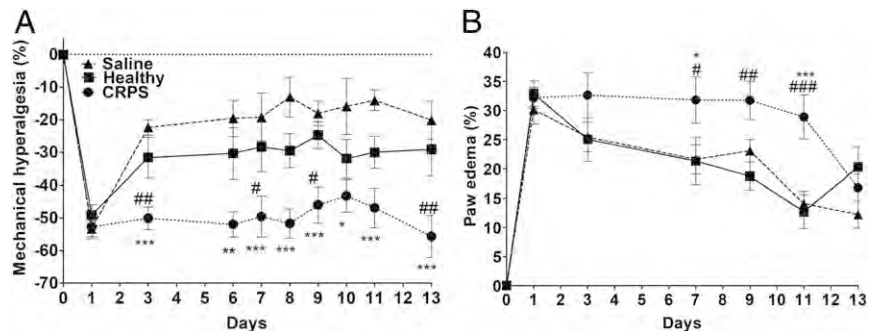
Indocyanin green (ICG)-derived fluorescence detecting vascular leakage showed a nonsignificant trend to increase in the injured paws in all groups 2 d after paw incision; CRPS IgG did not specifically affect plasma extravasation [saline injured: $1.52 \times 10^9 \pm 1.11 \times 10^8$; healthy IgG injured: $1.42 \times 10^9 \pm 1.54 \times 10^8$; CRPS IgG injured: $1.70 \times 10^9 \pm 2.2 \times 10^8$; fluorescence intensity: (photons per second per 1 cm^2 per steradian) per microwatt per 1 cm^2].

As expected, in vivo imaging of 8-amino-5-chloro-7-phenylpyrido[3,4-d]pyridazine-1,4(2H,3H) dione (L-012)-derived bioluminescence, used as a sensitive marker of inflammatory cell activity [most prominently neutrophil-derived myeloperoxidase (MPO)], showed increased signal in response to limb trauma alone (Fig. 2). We found a significant increase in neutrophil MPO activity in the CRPS IgG-treated animals on the affected side 2 d after the incision compared with in the control groups. Differences in MPO activity in CRPS IgG vs. healthy IgG groups had disappeared by day 6, although significant increases in the injured paw were still present compared with the intact side on day 13. Importantly, while strong variability was observed between different IgG preparations in influencing MPO activity (SI Appendix, Fig. S5 and Table S2), bioluminescence measured on day 2 or 6 did not correlate with either maximal paw swelling or hyperalgesia on day 6. This suggests that altered MPO activity in the injured paw of tCRPS mice is an unrelated IgG effect that is unlikely to explain the marked impact of CRPS IgG on paw hypersensitivity.

CRPS IgG Does Not Promote Inflammation or Neuropathy in the Paw.

We further examined whether the tCRPS behavioral signs were related to locally augmented inflammatory responses or to neuropathic changes. In successive experiments, animals were

Fig. 1. Effect of intraperitoneal injection of serum IgG derived from CRPS patients or healthy controls on plantar incision-induced mechanical hyperalgesia (A) and swelling (B) of the injured mouse hind paw. IgG was administered daily starting on day 0. The right hind paws were incised on day 0 about 6 h after Ig injection. Shown are pooled results from all three long-term experiments to either day 10 or 13 with three different IgG preparations (2–4) (individual results are in Fig. 2, and patients details are in SI Appendix, Table S1). Data are means \pm SEM. Two-way ANOVA was followed by Bonferroni's multiple comparison test. Healthy indicates the healthy control IgG-injected group, and CRPS indicates the CRPS IgG-injected group. * $P < 0.05$ (vs. saline-treated control mice); ** $P < 0.01$ (vs. saline-treated control mice); *** $P < 0.001$ (vs. saline-treated control mice); # $P < 0.05$ (vs. healthy IgG-treated mice); ## $P < 0.01$ (vs. healthy IgG-treated mice); ### $P < 0.001$ (vs. healthy IgG-treated mice).



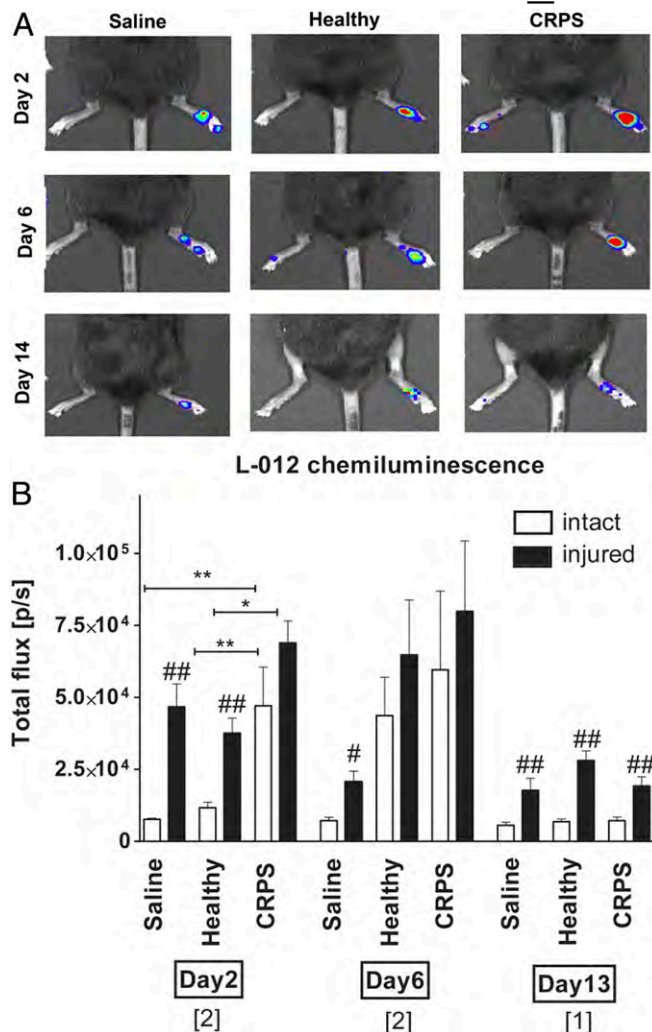


Fig. 2. Imaging ROS demonstrates the development of inflammation in the injured hind paws of mice. In vivo images of L-012-derived bioluminescence were obtained during general anesthesia on days 2, 6, and 13 after paw incision. Typical images, with red color indicating strong bioluminescence, are shown in *A*, and quantification of the bioluminescence intensity is in *B*. Data at each time point represent the pooled results from experiments conducted with separate CRPS/healthy control IgG preparations (numbers of preparations per time point are in brackets) (details are in *SI Appendix, Fig. S4 and Table S2*) and are shown as means \pm SEM of $n = 6-18$ mice per group. One-way ANOVA was followed by Bonferroni's multiple comparison test. Healthy indicates the healthy control IgG-injected group, and CRPS indicates the CRPS IgG-injected group. * $P < 0.05$ vs. respective control groups; ** $P < 0.01$ vs. respective control groups; # $P < 0.05$ vs. respective intact side; ## $P < 0.01$ vs. respective intact side.

killed between experimental days 1 and 13, and paw tissues were harvested to assess various inflammatory changes (animal numbers and preparations are in *SI Appendix, Table S3*).

Substance P (SP) levels increased in the injured paw, with higher levels in the CRPS IgG group on day 6 (Fig. 3*A*), whereas calcitonin gene-related peptide (CGRP) levels were not significantly altered (Fig. 3*B*), consistent with earlier findings (11). Increased levels of inflammatory mediators were seen in the injured paws, with gradual decrease over time [shown in Fig. 3 *C-F* for interleukin-6 (IL-6), tumor necrosis factor- α (TNF- α), monocyte chemoattractant protein-1 (MCP-1), and IL-1 β and in *SI Appendix, Fig. S6* for additional mediators]. We detected no differences in the levels of inflammatory mediators between the CRPS and healthy IgG groups (Fig. 3 *C-F* and *SI Appendix, Fig. S6*) at any

time point, except for a mild CRPS IgG-induced MCP-1 increase at day 13 (Fig. 3*E*). Notably, at the time of maximum hyperalgesia (13 d postinjury), most mediators were undetectable. There were no significant changes in plasma concentrations of any cytokines after correction for multiple testing (*SI Appendix, Fig. S7*).

Histological examination revealed moderate infiltration of inflammatory cells into areas immediately adjacent to the incision early after surgery, with no obvious difference between groups; there was no evidence of infiltration by inflammatory cells on day 13 in any experimental group. Since some patients with persistent CRPS exhibit mild small fiber neuropathy (14), we also examined mouse paw biopsies from CRPS IgG-injected animals for any evidence of structural changes to small skin nerves with both light and electron microscopy. The morphology of the axons in the right (injured) and left (intact) paws as well as the ultrastructure of nonmyelinated and thin-myelinated axons in the dermis appeared very similar on aspect, and there were no significant differences between sides on quantification of axon numbers and diameters (*SI Appendix, Table S4*).

CRPS IgG Facilitates Sustained Microglia Activation in the CNS. We next investigated whether altered activity of microglia or astrocytes in pain-related circuits (15) would reflect the marked effects of CRPS IgG on pain sensitivity responses. In CNS areas receiving input from the injured paw, CRPS IgG induced remarkable increases in both astrocyte and microglia cell activities compared with both saline and healthy IgG groups. In the dorsal horn, this response was sometimes much stronger than the increases representing the incision trauma (Fig. 4). Astrocyte reactivity in the CRPS IgG animals was augmented in all CNS areas at early time points (days 3 and 6), whereas microglia staining was enhanced throughout the experimental period (including day 13) (Fig. 4 and *SI Appendix, Fig. S9*), indicating that increased mechanical hypersensitivity in this model is associated with transient astrocyte and persistent microglial activation in the CNS.

Early IL-1 Receptor Blockade with Anakinra Prevents the Development of tCRPS, While Delayed Anakinra Treatment Reverses Established tCRPS and Reduces Glial Activation.

Since both microglia and astrocytes are important sources of proinflammatory cytokines that are known to contribute to pain hypersensitivity responses (16, 17) and IL-1 is a key mediator that influences neuronal activity (18, 19), we investigated the effects of glucocorticoid (prednisolone) treatment or interleukin-1 receptor (IL-1R) antagonist (anakinra) treatment on CRPS IgG-induced behavioral signs and inflammatory changes. Prednisolone (4 mg/kg) or anakinra (10 mg/kg) was daily administered intraperitoneally, starting 5 h before surgery (day 0) and extending throughout the experimental period. One day after surgery, mechanical hyperalgesia developed equally in all groups (Fig. 5*A* and *B*). Glucocorticoid treatment transiently reduced CRPS IgG-induced mechanical hyperalgesia (between days 2 and 3), but this effect was lost by day 7. In contrast, anakinra prevented all CRPS IgG-induced effects throughout the experimental period (Fig. 5*B*). Anakinra, but not prednisolone treatment, almost completely reversed glia cell activation in the ipsilateral dorsal horn on day 6 (Fig. 5*D* and *E*). Notably, anakinra treatment also significantly reduced paw MCP-1 levels on day 3; however, there were no other differential effects on levels of peripheral mediators between these two treatments (*SI Appendix, Fig. S10*). Furthermore, delayed administration of anakinra starting from day 8 onward reversed the established tCRPS phenotype (Fig. 5*C*) and completely reversed the associated increased dorsal horn microglia activation on day 13 (Fig. 5*F*).

Selective Deletion of Microglial IL-1 β Ameliorates While Ubiquitous Deletion of IL-1 α Completely Prevents tCRPS. Given that CRPS IgG caused significant dorsal horn glia cell activation without influencing paw IL-1 levels and that blockade of IL-1 prevented

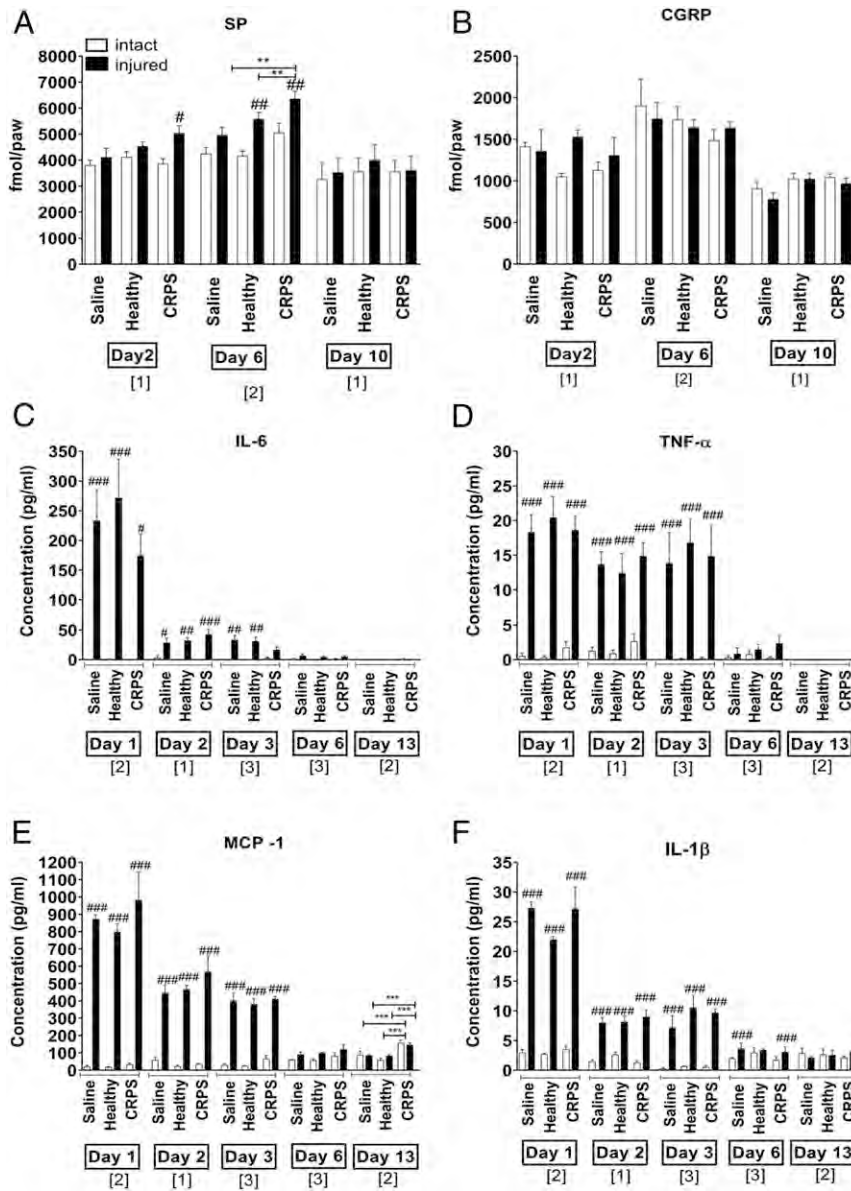


Fig. 3. Effects of human IgG transfer on sensory neuropeptide and inflammatory cytokine concentrations in the hind paws. Concentrations of (A) SP and (B) CGRP were measured by RIA in hind paw homogenates excised after they were killed. Concentrations of (C) IL-6, (D) TNF- α , (E) MCP-1, and (F) IL-1 β were measured by cytometric bead array from the same samples. Data are from one to three experiments per time point (brackets below x axes) each with different patient preparations. Shown are means \pm SEM. One-way ANOVA was followed by Bonferroni's multiple comparison test. Healthy indicates the healthy control IgG-injected group, and CRPS indicates the CRPS IgG-injected group. ** $P < 0.01$ vs. respective control groups; # $P < 0.05$ vs. respective intact side; ## $P < 0.01$ vs. respective intact side; ### $P < 0.001$ vs. respective intact side;

the tCRPS phenotype, we then investigated whether tCRPS was associated with enhanced glial IL-1 production in the dorsal horn. Immunofluorescence revealed increased microglial IL-1 β production in lumbar (L)4/L5 dorsal horn microglia cells only in the tCRPS group (Fig. 6A), while IL-1 α was not detected. We then examined whether the tCRPS phenotype would be altered by genetic knockout (KO) of IL-1. We found that CRPS IgG-injected IL-1 $\alpha\beta$ KO mice failed to develop enhanced hyperalgesia and showed even less posttraumatic paw swelling (Fig. 6B and C) than mice treated with healthy IgG. To investigate whether increased microglial IL-1 β production is sufficient to mediate the effects of CRPS IgG on increased mechanical hyperalgesia, we generated an IL-1 β floxed ($^{fl/fl}$) mouse line. Exons 4 and 5 of the *IL-1B* gene were flanked with loxP sites, resulting in the generation of IL-1 $\beta^{fl/fl}$ allele (SI Appendix, Fig. S11). IL-1 $\beta^{fl/fl}$ mice were crossed with Cx3cr1^{CreER} mice (20), resulting in microglial deletion of IL-1 β on tamoxifen administration (M-IL-1 β KO), while most peripheral Cx3cr1-positive cells recovered IL-1 β production due to their higher turnover as shown by using other cre-dependent reporter lines previously (20). In fact, IL-1 β protein levels were markedly reduced in IL-1 β

KO microglia after repeated intraperitoneal injections of bacterial lipopolysaccharide compared with wild-type (WT) microglia, but no changes were seen in splenic macrophages derived from tamoxifen-treated Cx3cr1^{CreER} \times IL-1 $\beta^{fl/fl}$ mice compared with controls (SI Appendix, Fig. S12). Elimination of microglial IL-1 β significantly reduced mechanical hyperalgesia and paw edema in mice treated with CRPS IgG, although this effect was smaller than in the case of IL-1 $\alpha\beta$ KO mice (Fig. 6B and C). Total numbers of microglia were reduced in IL-1 $\alpha\beta$ KO mice but were not altered in response to microglial IL-1 β deletion in the CRPS group (Fig. 6D), suggesting that, while microglial IL-1 β is an important driver of chronic neuroinflammation contributing to persistent pain, other IL-1 β -producing cells or actions mediated by IL-1 α could also contribute to CRPS symptoms in mice.

Discussion

Here, we show in an enhanced passive transfer trauma model that daily administration of IgG from patients with persistent CRPS to mice elicits intense, unilateral static mechanical hyperalgesia after hind paw injury, which remains stable through the experimental period. This is associated with increased paw edema

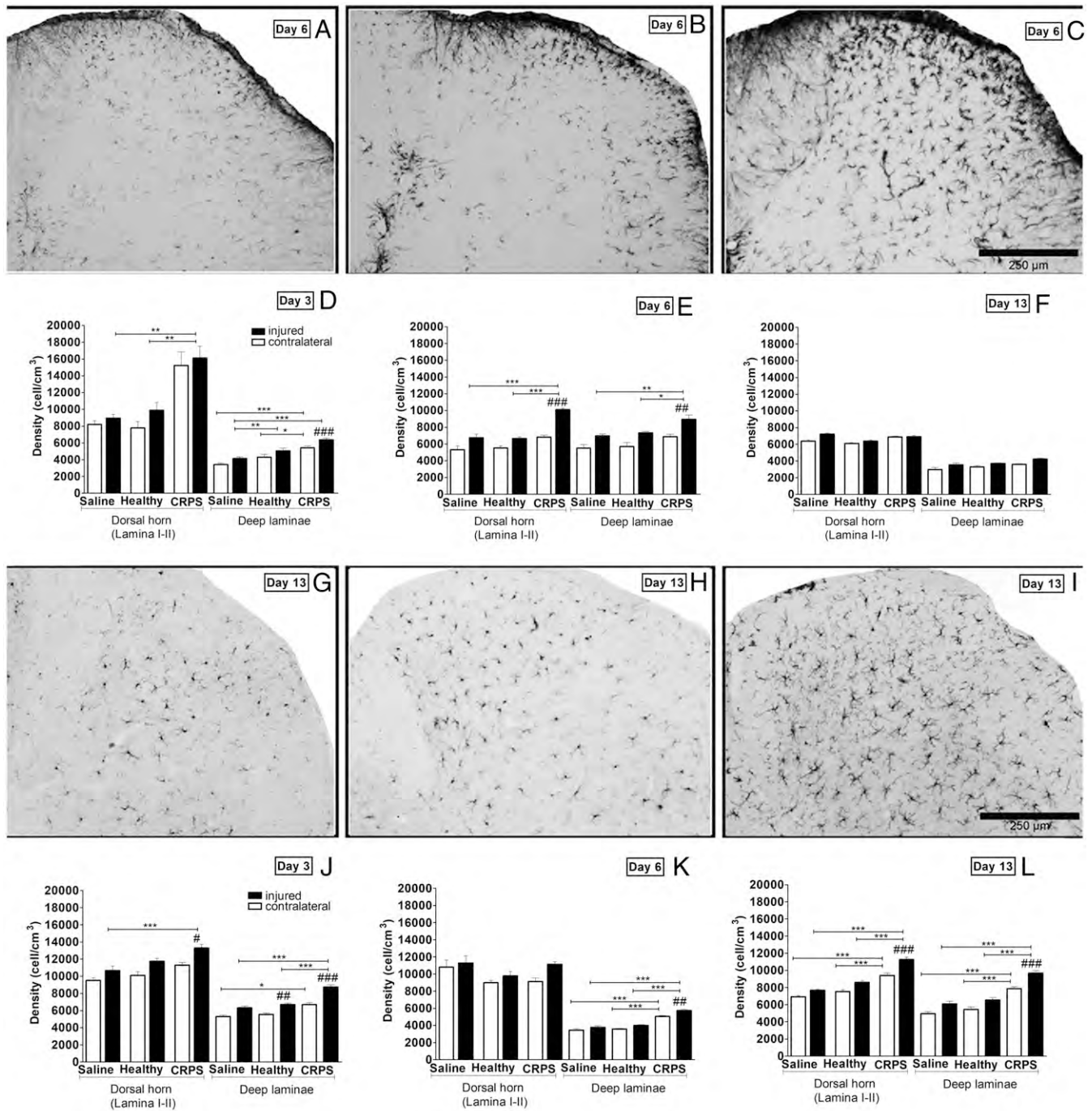


Fig. 4. Glial activation in the L5 spinal cord dorsal horn ipsilateral to the paw injury. A–C show GFAP immunopositivity marking astrocytes, and G–I show Iba1 immunopositivity marking microglia cells, with (A and G) saline, (B and H) healthy control IgG, and (C and I) CRPS IgG injections. The GFAP-immunopositive sections shown are from day 6, and Iba1 sections are from day 13 after paw incision. Quantification of astrocyte reactivity (D–F) and microglia staining (J–L) in lamina I–II dorsal horn of the L4–L6 spinal cord and deeper laminae at 3, 6, and 13 d after hind paw incision. Each panel represents the pooled results from two experiments with two different samples (3 and 4). Shown are means \pm SEM of six to seven mice per group. One-way ANOVA was followed by Bonferroni's modified post hoc test. Healthy indicates the healthy control IgG-injected group, and CRPS indicates the CRPS IgG-injected group. * $P < 0.05$ vs. respective control groups; ** $P < 0.01$ vs. respective control groups; *** $P < 0.001$ vs. respective control groups; # $P < 0.05$ vs. respective contralateral side; ## $P < 0.01$ vs. respective contralateral side; ### $P < 0.001$ vs. respective contralateral side.

that resolves over time. Collectively, these features resemble the course and pathophysiology of the clinical disease (1). In these extensive integrative studies, a uniform pattern of transferred static mechanical hyperalgesia was seen with all patient preparations, highlighting that seronegativity is unlikely to be common in patients with severe, persistent CRPS. The results emphasize

the translational validity of the model and the importance of autoimmune mechanisms underpinning the pathophysiology of both clinical CRPS and experimental transferred tCRPS.

We found that the normal posttraumatic inflammatory response in the incised paws rapidly declined and fully settled by days 6–13 postincision; the paw inflammation did not correlate

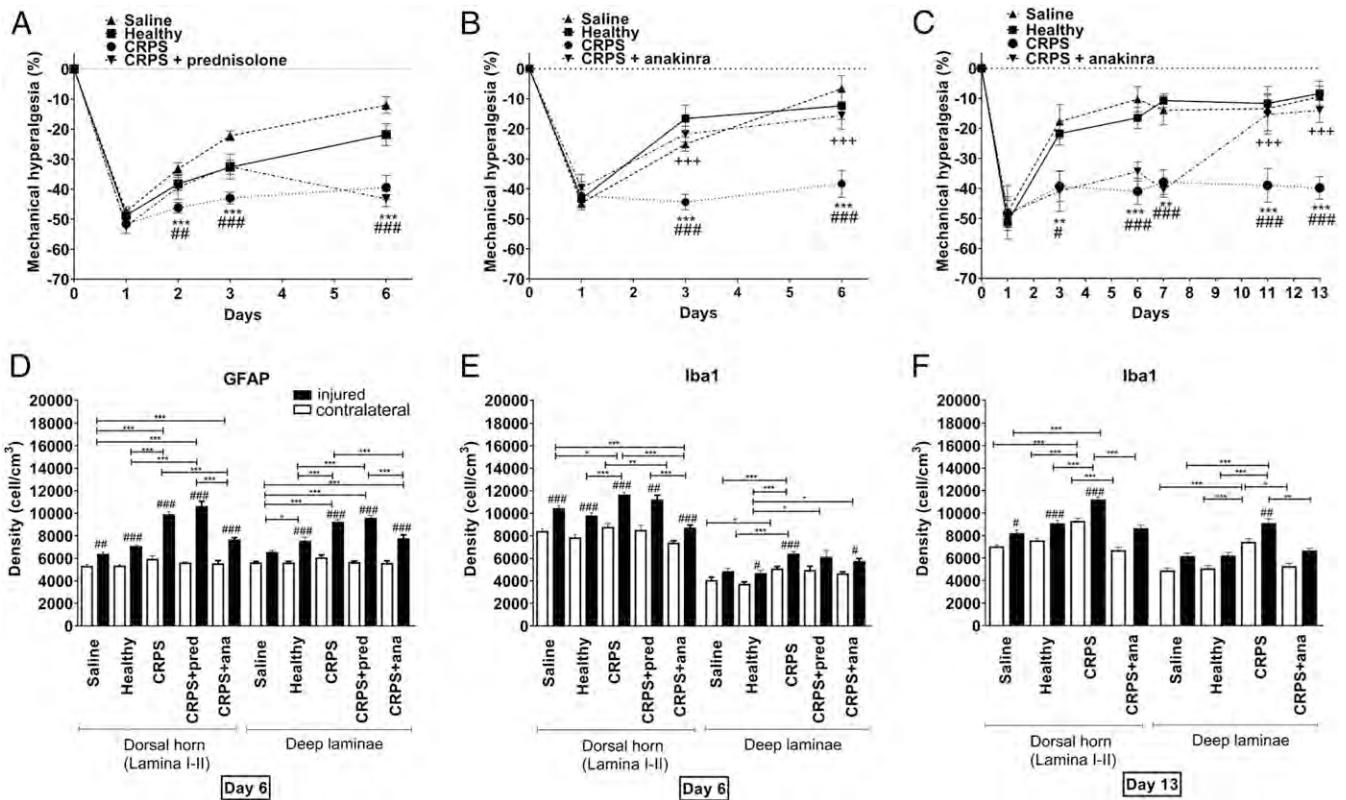


Fig. 5. Effects of prophylactic steroid or anakinra treatment (days 0–6) and delayed (therapeutic) anakinra treatment on CRPS IgG-induced mechanical hyperalgesia and glial activation in the spinal cord. *A* and *B* show mechanical hyperalgesia in groups of animals injected intraperitoneally first with human IgG or saline and 3 h later with 4 mg/kg prednisolone, 10 mg/kg anakinra, or saline vehicle on each day between days 0 and 6. *D* and *E* show dorsal horn glia cell activation in these mice on day 6: (*D*) GFAP (astrocyte) and (*E*) Iba-1 (microglia). Results represent the average values derived from two independent experiments with different preparations for each treatment, with four experiments in total; saline, healthy control IgG, and CRPS IgG outcomes are pooled from these experiments. (*C* and *F*) Late anakinra treatment starting on day 8: (*C*) behavioral outcome and (*F*) dorsal horn microglia cell count on day 13. Data are shown as means \pm SEM. Two-way ANOVA was followed by Bonferroni's multiple comparison test. One-way ANOVA was followed by Bonferroni's modified post hoc test. Healthy indicates the healthy control IgG-injected group, and CRPS indicates the CRPS IgG-injected group. Significance symbols for the behavioral data as follows: * $P < 0.05$ (CRPS IgG vs. saline-treated control mice); ** $P < 0.01$ (CRPS IgG vs. saline-treated control mice); *** $P < 0.001$ (CRPS IgG vs. saline-treated control mice); # $P < 0.05$ (CRPS IgG vs. healthy control IgG-treated mice); ### $P < 0.001$ (CRPS IgG vs. healthy control IgG-treated mice); +++ $P < 0.001$ (anakinra plus CRPS IgG vs. CRPS IgG-injected mice). Significance immunohistochemistry data: * $P < 0.05$ vs. respective control groups; ** $P < 0.01$ vs. respective control groups; *** $P < 0.001$ vs. respective control groups; # $P < 0.05$ vs. respective contralateral side; ## $P < 0.01$ vs. respective contralateral side; ### $P < 0.001$ vs. respective contralateral side.

with the degree of CRPS IgG-induced paw hyperalgesia. We found little evidence for any CRPS IgG-related enhanced paw inflammation. Our results thus demonstrate that static mechanical hyperalgesia may not depend on persistent inflammatory mediator release, highlighting that tCRPS is not a model of enhanced posttraumatic inflammatory pain. There was, however, some evidence for abnormal production of two specific mediators in the CRPS group: SP production was increased at early time points, in line with some clinical observations (21) and our earlier results (11), and there was also a mild but significant bilateral increase in MCP-1 on day 13, the role of which will require additional investigations. Although we measured common mediators of inflammation in the injured paws and these were normal, the involvement of additional mediators cannot be excluded.

In mice, the development of tCRPS remained restricted to the injured paw, consistent with the clinical situation, where about 90% of the cases show symptoms in only one traumatized limb (22). The precise mechanisms through which circulating pathogenic IgG antibodies mediate both the regionally restricted posttraumatic clinical CRPS and tCRPS are presently unclear. Early transient trauma-induced inflammatory changes or regional opening of blood–nerve and blood–brain barriers may play a role by promoting the expression of neoantigens or by

providing IgG access to privileged sites (23). The presence of such facilitating mechanisms is supported by our *in vivo* imaging results, which showed plasma leakage and increased MPO activity in the injured paw.

Interestingly, MPO activity was variably enhanced in the animal groups injected with different CRPS IgG preparations, and there was no correlation with mechanical hyperalgesia or swelling in these same animals. These findings may resemble the strong heterogeneity seen between patients in the extent of their limb swellings, color changes, or temperature changes and may also reflect the observation that these clinical parameters do not necessarily correlate with the patients' perceived pain intensities or recorded skin sensitivities (2).

Since inflammatory changes in the paw did not seem to explain the increased mechanical hyperalgesia in the tCRPS mice, we investigated the potential role of glial responses in pain-related neuronal circuits, which have been suggested to contribute to chronification processes in posttraumatic pain models (15, 24, 25). We found that tCRPS was associated with strong microglia and astrocyte activation at all three tested levels of the nociceptive pathway, the ipsilateral spinal cord dorsal horn, the periaqueductal gray, and the contralateral somatosensory cortex. In the dorsal horn, the increases in glial responses in the tCRPS

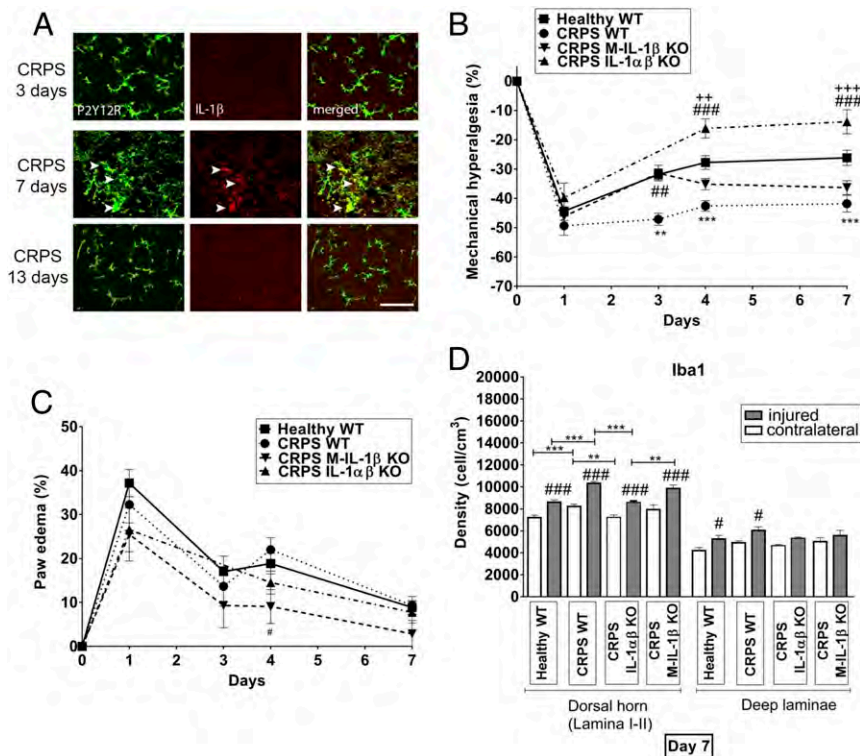


Fig. 6. Deletion of IL-1 α or microglia-derived IL-1 β fully or partially prevents development of the CRPS IgG-induced phenotype in mice. (A) A population of microglia identified by immunostaining against P2Y12, a specific microglial marker in the brain (59), displays a morphologically activated phenotype and shows immunopositivity for IL-1 β at day 7 in the deep laminae of the L4–L5 spinal cord near the central canal. (Scale bar: 50 μ m.) (B and C) IL-1 α KO mice are fully protected and M-IL-1 β KO mice are partially protected from the development of the CRPS IgG-induced phenotype: (B) paw hyperalgesia and (C) paw edema. Two-way ANOVA was followed by Bonferroni's multiple comparison test. Significance in B and C: ** P < 0.01 (CRPS IgG WT vs. healthy IgG WT); *** P < 0.001 (CRPS IgG WT vs. healthy IgG WT); * P < 0.05 (CRPS IgG M-IL-1 β KO vs. CRPS IgG WT); *** P < 0.001 (CRPS IgG M-IL-1 β KO vs. CRPS IgG WT); *** P < 0.001 (CRPS IgG IL-1 α KO vs. CRPS IgG WT); ** P < 0.01 (CRPS IgG IL-1 α KO vs. CRPS IgG M-IL-1 β KO); *** P < 0.001 (CRPS IgG IL-1 α KO vs. CRPS IgG M-IL-1 β KO). (D) CRPS IgG-induced microglia activation is abrogated in IL-1 α KO but not in M-IL-1 β KO mice. Data are pooled from two experiments with different CRPS IgG preparations for each mouse type and are shown as means \pm SEM. Healthy indicates the healthy control IgG-injected group, and CRPS indicates the CRPS IgG-injected group. One-way ANOVA was followed by Bonferroni's modified post hoc test. Significance values in D: ** P < 0.01 vs. respective control groups; *** P < 0.001 vs. respective control groups; * P < 0.05 vs. respective contralateral side; *** P < 0.001 vs. respective contralateral side.

vs. control groups were sometimes severalfold larger than the extent of glia activation caused by the paw incision (Fig. 4), suggesting a powerful central effect of the transferred IgG.

These results raise the question of how the observed profound central glial cell activation is mediated. Possible mechanisms may include (i) modification of nociceptor function after direct antibody binding in the periphery as an "autoimmune channelopathy" (26), (ii) release of yet undetermined peripheral mediators (27), (iii) direct binding in the dorsal horn after temporary post-traumatic opening of the blood spinal cord barrier (28), or (iv) a missing link. Independent of the nature of these upstream mechanisms, glial activation is likely to result in the release of mediators, such as IL-1 β , TNF- α , or brain-derived neurotrophic factor, with consequent modification of central pain processing (15, 29).

We hypothesized that perioperative antiinflammatory interventions might be effective, and we initially thought that such interventions might act through the blockade of perioperative regional facilitatory factors required to render circulating CRPS autoantibodies pathogenic (4). To investigate whether such interventions could prevent the disease phenotype, we treated mice peritraumatically with high-dose prednisolone. Prednisolone treatment temporarily interrupted the process of antibody-dependent sensitization, but it did not stop it. Systemic glucocorticoids are considered potentially effective in very early CRPS based on the results of one preliminary trial (9). These data suggest that, where patients produce harmful autoantibodies, the peritraumatic application of glucocorticoids is unlikely to stop disease progression. In contrast, perioperative treatment with the IL-1R antagonist anakinra in this CRPS model consistently prevented the tCRPS phenotype. Notably, we found that there were only minor differences in the regional paw inflammatory environment based on the production of cytokines and chemokines after treatment with (ineffective) prednisolone and (effective) anakinra (SI Appendix, Fig. S10); furthermore, even delayed blockade of IL-1 actions with anakinra starting on day 8 after the incision trauma, when trauma-induced peripheral inflammatory responses had largely resolved, was highly effective,

suggesting that the pertinent biological effect of anakinra treatment was not restricted to the injured paw.

IL-1 is a potent activator of astrocytes through actions via IL-1R1, whereas both activated microglia and astrocytes can contribute to painful central sensitization through secreting IL-1 (29, 30). These actions can be effectively blocked by anakinra (31–34). In our model, augmented dorsal horn glia cell activation in the tCRPS group was fully reversed by anakinra. Since IL-1-mediated actions are involved in the cross-talk between neurons, microglia, and astrocytes in promoting neuroinflammation (35, 36), we assessed glial IL-1 β and IL-1 α production in the spinal cord and found that microglial IL-1 β production was increased on day 7 in the CRPS IgG-treated group. In agreement with these data, we found that IL-1 α KO mice were fully protected from developing the tCRPS phenotype and associated glial activation. To specifically assess the functional role of microglial IL-1 β in tCRPS-associated hyperalgesia and swelling, we generated a mouse strain (IL-1 β ^{fl/fl} mice), enabling the deletion of IL-1 β from microglia. Consistent with earlier data showing prolonged cre-dependent transgene expression in long-lived microglia but not in peripheral macrophage populations with short turnover (20), tamoxifen treatment of Cx3cr1^{CreER} \times IL-1 β ^{fl/fl} mice resulted in a marked reduction of microglial, but not splenic, IL-1 β production (SI Appendix, Fig. S12). As seen in IL-1 α KO mice, the absence of microglial IL-1 β production fully protected from tCRPS-associated mechanical hyperalgesia up to day 3, whereas it had a weaker effect thereafter. This highlights the importance of microglial IL-1 β in the tCRPS disease process but also, the likely involvement of other cells and/or IL-1 α (35).

Strengths of our study include the robust, multidimensional evaluation of an enhanced CRPS disease transfer model with preparations from patients whose clinical presentations differed using outcomes designed to provide translational validity. Additional strengths are the comprehensive assessment of both peripheral and central markers of immune activation and of several antiinflammatory treatments as well as gene KO strategies, which

have allowed an informed suggestion for clinical studies with a licensed drug not previously reported in this patient group.

Limitations include the upper transfer limit cutoff at 13 d, which was necessary to avoid the adverse effects of serum sickness (37). However, it may be argued that the “chronic phase” in this disease model starts from the second week after incision, when peripheral inflammation and symptoms in the control group resolve. As is often observed with IgG disease transfer in other disease models, tCRPS does not fully match the symptoms of clinical CRPS (38). For example, overt motor dysfunction was not detected, and commonly encountered central features, such as body perception abnormalities, were not revealed. In line with most behavioral studies in animal models of chronic pain (39), we did not demonstrate the presence of spontaneous pain but ascertained nociceptor hypersensitivity by assessing stimulus-evoked pain (mechanical hypersensitivity). Independently, we only transferred serum IgG that was derived from patients suffering from persistent (7) Budapest CRPS with high pain intensities (numeric rating scale > 7); however, these are also the patients who present the most difficult situation in the clinical practice. We cannot rule out the possibility that some patients in this group do not have these antibodies. Since each of the seven individually tested serum IgG preparations induced the abnormal phenotype (*SI Appendix, Fig. S1*), the likelihood that we have missed the absence of such antibodies in more than one-half of patients of a similar population seems very low (<1%) (*Patients, Healthy Controls, and Serum Preparation*); the development of serum diagnostic tests will be required to further detail the proportion of seronegative patients. We did not measure epidermal nerve fiber density or length in the mouse paw skin; therefore, our studies may not fully rule out mild small fiber neuropathy.

In summary, we have devised a robust translational model reproducing pertinent aspects of an “idiopathic,” posttraumatic chronic pain condition. The consistent pathogenicity of various serum IgG preparations indicates that, among patients who have severe forms of this condition, autoantibody contribution is ubiquitous. Since abnormal signs were entirely confined to the injured side, we also established a general principle suggesting that pathogenic circulating autoantibodies can cause regionally restricted disease when triggered by local trauma.

Our results support previous clinical observations that patients with persistent CRPS should respond to immune treatments with a reduction of at least some of their disease features (12). The clinical use of IL-1R antagonists in CRPS has a broad therapeutic potential. Anakinra is clinically licensed both in the United States and in Europe, and short-term use has an acceptable side effect profile (40, 41). Since CRPS regularly develops in the context of elective operations, such as arthroscopy or bunion surgery, prevention of such cases would have very important implications for both patients and procedure-related health care as well as societal costs (42). As our results also suggest that treatment initiated after injury resolution reverts the established transferred phenotype, clinical treatment of patients with persistent CRPS could now be tested in a trial setting.

The cellular and molecular targets of the patient autoantibodies need to be clarified; recent results in other conditions that are not associated with trauma (26, 27) have indicated that pain-sensitizing autoantibodies may directly bind to sensory neurons or indirectly bind to juxtapositioned cells, which then release nerve-sensitizing mediators. The duration of beneficial effects after the drug is withdrawn should be investigated in this experimental model. In addition, identifying the exact cellular targets for IL-1 actions in the pathophysiology of tCRPS could facilitate the development of alternative IL-1 targeting approaches in the prevention or treatment of the clinical disease. The results of this study highlight the important role that auto-

antibodies can play in causing detrimental symptoms, absent tissue destruction and systemic inflammation.

Materials and Methods

Patients, Healthy Controls, and Serum Preparation. NorthWest Ethics Haydock UK approved serum donations. Written informed consent was obtained from all patients. Serum or plasma samples were obtained (*i*) via a dedicated study designed to repeatedly acquire large volumes, (*ii*) from waste plasma after patients’ plasma exchange treatment, and (*iii*) from patients participating in a clinical trial who never had plasma exchange (43)—the latter samples were pooled to minimize animal use. Details are provided in *SI Appendix*. The patients’ baseline characteristics are provided in Table 1. We calculated the probability that we missed an event rate of >50% of patients having no pain-sensitizing autoantibodies by $[0.5^{(\text{number of experiments} \times \text{fraction of positive experiments})}]$: $0.5^7 = 0.008125$ (i.e., <1%). IgG was prepared from plasma or serum of patients as previously described using Protein G columns for affinity purification followed by elution, buffering, dialysis in normal saline, and concentration to about 8 mg/mL IgG for injection (pooled preparations 12 mg/mL) (11).

Animals. The Ethics Committee on Animal Research of the University of Pecs approved experiments involving rodents. Since CRPS affects women two to three times more frequently than men, experiments were carried out on female mice on C57BL/6 background (10–12 wk old, 18–22 g). Breeding, maintenance, and ethical procedures were as previously described (11) (details are in *SI Appendix*).

Experimental Design. After acclimatization and conditioning, three control measurements of nociception and paw volume were performed on days –4, –3, and –2. Day 0 was the starting day of intraperitoneal injections (*SI Appendix, Fig. S13*). Mice (five to seven per group) were treated daily to compensate for rapid metabolism of human IgG in the mouse (*SI Appendix, Methods*) with 1 mL of IgG fractions (8 mg/mL) obtained from CRPS patients or healthy volunteers or saline.

Six hours after the injection on day 0, a standardized incision trauma was applied to the right hind paw as described below. All mice removed their stitches within 16 h postsurgery. Measurements (see below) were performed repeatedly starting on day 1 until the respective termination day.

Animals were killed at various time points, and tissues were harvested as previously described (11). In some experiments, animals were perfused transcardially with phosphate buffered saline (PBS) followed by 4% paraformaldehyde as previously described, and the whole brains and spinal cords were excised and prepared for additional immunohistochemistry analyses.

Plantar Skin and Muscle Incision. To model a CRPS-triggering injury, we used the hind paw plantar skin muscle incision method under general anesthesia as described earlier (11, 44) and detailed in *SI Appendix*. This model evokes a significant decline of the mechanonociceptive threshold, with a maximum 1 d after surgery, which persists for 7–8 d; the model’s early threshold normalization was considered advantageous, minimizing any animal suffering and allowing for early assessment of IgG-induced changes. All measurements were carried out by two investigators (V.T. and N.S.) who were blinded to treatment assignment. Blinding was performed by the technicians who performed all injections but were otherwise not involved in the study; they differentially coded the animal cages and provided the decoding key after completion of the last measurements.

Determination of the Mechanosensitivity of the Paw. Most patients with CRPS have, in addition to their spontaneous pain, pain with the application of pressure to the CRPS-affected limb (“mechanical hyperalgesia”) (45, 46), and all patients included in this study experienced this feature. The corresponding mechanonociceptive threshold of the plantar surface of the mouse hind paw was determined with a dynamic plantar aesthesiometer (Ugo Basile 37400)—a modified electronic von Frey technique—as previously described (11). The blunt-end needle exerting an increasing force to the mouse paw provides a mild but basically painful stimulus activating A δ and C fibers (47). Threshold decreases are considered as mechanical hyperalgesia and are expressed as percentage decrease of the mechanonociceptive thresholds compared with the baseline values (48, 49).

Paw Volume Measurement. Limb swelling is a common feature of CRPS-affected limbs, and all included patients reported intermittent limb swelling. Mouse paw volume was measured using plethysmometry (Ugile Basile

Table 1. Baseline characteristics of the patient serum donors

No.	Sex/age	Limb/DD	Pain	Dx	Plex
1	M/62	U/9	10	+II	Y
2	F/37	L/15	7.5	+I	N
3	F/38	L/10	9.5	+I	Y
4	F/36	L/10	7	+I	Y
5	F/40	L/5	7.5	+I	Y
6	F/51	L/8	8	+I	N
7	F/49	L/7	8	+I	Y

Age indicates age in years at the time of plasma/serum acquisition. Limb indicates the affected limb. DD is the disease duration in years. Pain indicates 24-h average pain intensity on a 11-point numeric rating scale (0–10, with 10 = pain as bad as you can imagine). Dx indicates diagnosis, with + indicating that the patient fulfills Budapest research diagnostic criteria (new International Association for the Study of Pain criteria); II denotes trigger injury to a major nerve, and I denotes no trigger injury to a major nerve. Plex indicates plasma derived from plasma exchange. N, no; Y, yes; U, upper limb; L, lower limb.

Plethysmometer 7140). Edema was expressed as a percentage increase compared with the baseline paw volume (48).

In Vivo Optical Imaging of Plasma Leakage and Neutrophil MPO Activity. The mechanisms underpinning CRPS IgG-enhanced paw swelling are unknown, but one possibility is augmented plasma extravasation. Intravenous injected ICG, a fluorescent cyanine dye, binds to plasma proteins and remains in the healthy vasculature. Under inflammatory conditions, it can be used to evaluate capillary leakage. ICG (0.5 mg/kg) was dissolved freshly in 5% (wt/vol) aqueous solution of Kolliphor HS 15 and a macrogol-based surfactant and injected intravenously (retrobulbar sinus) under ketamine (100 mg/kg; Calypsol; Gedeon Richter Plc.) and xylazine (10 mg/kg; Sedaxylan; Eurovet Animal Health B.V.) anesthesia 2 d after the paw incision. Fluorescence imaging was performed 20 min postinjection using an IVIS Lumina II in vivo optical imaging system (PerkinElmer; autoacquisition time, f/stop = 1, binning = 2, excitation: 745 nm, emission filter: >800 nm) (50).

A luminol analog chemiluminescent probe, L-012 (Wako Pure Chemical Industries Ltd.) was used for in vivo visualization of reactive oxygen species (ROS)/reactive nitrogen species (RNS) produced by MPO in neutrophils and macrophages; L-012 has a high sensitivity toward ROS/RNS (51). Mouse preparation, injection, imaging, and analysis procedures were conducted as previously described and highlighted in *SI Appendix* (52).

Measurement of Inflammatory Mediators. Proinflammatory neuropeptides peripherally released from sensory nerves and inflammatory cytokines released by perineuronal cells are abnormal in some patients with CRPS, and we measured their concentrations in the model.

The preserved frozen paws (see above) were thawed, chopped, and then homogenized in Triton X-100 and Calbiochem Protease Inhibitor Cocktail containing Tris-HCl homogenization buffer at 0 °C. Additional processing details are provided in *SI Appendix*. We measured CGRP- and SP-like immunoreactivities in the paws by a sensitive radioimmunoassay (RIA) technique developed in our laboratory as previously described (11, 53, 54).

Concentrations of IL-1 α , IL-1 β , IL-6, TNF- α , KC (CXCL1), MCP-1, G-CSF, RANTES (CCL5), interferon- γ , IL-4, and IL-10 in mouse plasma and the paw homogenates were measured by cytometric bead array (BD Biosciences) as previously described (34, 55), and transforming growth factor- β and NGF were measured by sandwich enzyme-linked immunosorbent assay according to the manufacturers' instructions (56).

Paw Skin Light and Electron Microscopy. After biopsy, samples were immersed into a fixative containing 2.5% glutaraldehyde buffered with phosphate buffer (0.1 M, pH 7.4) overnight at 4 °C, fixed in 1% osmium tetroxide for 35 min, and dehydrated with increasing concentration of ethanol. After complete dehydration, they were transferred to propylene oxide before being placed into aluminum foil boats and then embedded into gelatin capsule containing Durcupan resin (Sigma).

Semithin and ultrathin sections were cut with Leica ultramicrotome. Semithin sections were mounted on glass slides, stained with toluidine blue, and examined under a light microscope. Ultrathin sections were mounted on collodion-coated (Parlodion; Electron Microscopy Sciences) single-slot copper grids contrasted with uranyl acetate and lead citrate, and were examined in a

JEOL 1200EX-II electron microscope. Small nerve fiber quantification methods are detailed in *SI Appendix, Methods*.

Immunohistochemistry. Brains and L4–L6 segments of the spinal cord were removed and postfixed for 4 h in 4% paraformaldehyde before being placed into 30% sucrose (Duchefa Biochemie) in 0.1 M PBS overnight at 4 °C. Sections (30 μ m) were prepared using a freezing microtome (Leica Biosystems Nussloch GmbH) as free-floating sections (57, 58), and they were stained and mounted as described in *SI Appendix*. The sections ($n = 3$ –4 animal per group) were examined by NeuroLucida software (v07; MBF Bioscience) using a Nikon Eclipse Ni-E bright-field microscope with a computer-controlled stage. A modified unbiased stereology protocol was used for quantification of glial fibrillary acidic protein (GFAP) or Iba1 immunoreactive cells along the nociceptive pathway as previously described (50).

Immunofluorescence. Immunofluorescence to detect microglial P2Y₁₂ (59) and the production of IL-1 α and IL-1 β was performed on free-floating brain sections. Images were captured with a Nikon Ni-E C2+ confocal microscope.

Antiinflammatory Interventions. We investigated whether early immune suppression would alter the disease course in the model. We administered the synthetic glucocorticoid prednisolone (4 mg/kg intraperitoneally) (60, 61) or the IL-1R antagonist anakinra [10 mg/kg intraperitoneally; Swedish Orphan Biovitrum AB (publ), SE-112 76]. This prednisolone dose corresponds to the highest dose range used in humans [pulse therapy (62)], and the anakinra dose is known to be pharmacologically active in mice and und is comparable with human therapeutic dosages (63–65). Control animals received respective vehicles. The first drug injection was 3 h before the plantar skin and muscle incision and at least 4 h after IgG or control treatment. Drug treatment was then repeated daily through the experimental period. Delayed anakinra treatment was administered daily between days 8 and 13.

Generation of IL-1 β Floxed Mice and Microglial IL-1 β KO Mice. Il1b^{tm1a(EUCOMM)Hmgu} embryonic stem cells (66) were purchased from the European Mouse Mutant Cell Repository. Cells from clone HEPD0840-8-E03 were prepared for microinjection according to previously published protocols (67) with minor modifications (*SI Appendix, Methods*) and then microinjected into four- to eight-cell B6N-Tyr^{c-Brd}/BrdCrCl embryos. Surviving embryos were surgically implanted into the oviduct of day 0.5 postcoitum pseudopregnant mice. Resulting black/white C57BL/6N chimeras were backcrossed onto C57BL/6N WT mice to assess germline penetrance. Potential founder mice were screened by PCR for LacZ, Neo, and LoxP sites. This line was further crossed with C57BL/6N-Tg(CAG-Flp)1Afst/Mmud mice. The flip recombinase expression by this line resulted in a "conditional ready" (floxed) Il1b^{tm1c(EUCOMM)Hmgu} allele where exons 4 and 5 are flanked by loxP sites. To generate microglial IL-1 β KO mice, IL-1 β floxed mice were crossed with tamoxifen-inducible B6.129P2(C)-CX3CR1^{tm2.1(cre/ERT2)Jung/J} mice (JAX stock 020940) (20).

Statistical Analysis. Data shown are means \pm SEM, and two-way repeated measures ANOVA followed by Bonferroni's post hoc test was used for comparison of threshold values between groups at respective timepoints. One-way ANOVA followed by Bonferroni's post hoc test was used for analysis of the immunohistochemistry and cytokine results. A value of $P < 0.05$ was considered statistically significant.

ACKNOWLEDGMENTS. This research was supported by National Brain Research Program 2017-1.2.1-NKP-2017-00002 (NAP-2; Chronic Pain Research Group), the Pain Relief Foundation Liverpool, Gazdaságfejlesztési és Innovációs Operatív Program (Economy Development and Innovation Operative Programme) (GINOP)-2.3.2-15-2016-00050 (Peptidergic Signaling in Health and Disease; PEPSYS), Emberi Erőforrás Operatív Program (Human Resource Operative Programme) (EFOP) 3.6.2-17-2017-00008 N (2017-2019), and Társadalmi Megújulás Operatív Program (Social Renewal Operative Programme) (TAMOP) 4.2.4. A/2-11-1-2012-0001 "National Excellence Program—Elaborating and operating an inland student and researcher personal support system convergence program." A.D. is supported by Hungarian Brain Research Program KTIA_13_NAP-A-1/2, the "Momentum" Program of the Hungarian Academy of Sciences, European Research Council (ERC)-CoG 724994, and TÉT_16-1-2016-0104. The generation of IL-1 β /fl mouse line was funded by British Heart Foundation Grant PG/13/55/30365 (to E.P. and S.F.). We thank Dóra Önböli and Lilla Draskóczy for their expert technical assistance in the animal experiments and tissue preparation; Jenny Hawkes for her expert technical assistance in the IgG preparation; and Deborah Bently for proofreading the manuscript.

1. R. N. Harden *et al.*, Validation of proposed diagnostic criteria (the "Budapest criteria") for complex regional pain syndrome. *Pain* **150**, 268–274 (2010).
2. F. Birklein, S. K. Ajit, A. Goebel, R. S. G. M. Perez, C. Sommer, Complex regional pain syndrome—Phenotypic characteristics and potential biomarkers. *Nat. Rev. Neurol.* **14**, 272–284 (2018).
3. M. Nicholas *et al.*; IASP Taskforce for the Classification of Chronic Pain, The IASP classification of chronic pain for ICD-11: Chronic primary pain. *Pain* **160**, 28–37 (2019).
4. A. Goebel, F. Blaes, Complex regional pain syndrome, prototype of a novel kind of autoimmune disease. *Autoimmun. Rev.* **12**, 682–686 (2013).
5. C. Maihöfner, H. O. Handwerker, B. Neundörfer, F. Birklein, Patterns of cortical reorganization in complex regional pain syndrome. *Neurology* **61**, 1707–1715 (2003).
6. A. Zyluk, The natural history of post-traumatic reflex sympathetic dystrophy. *J. Hand Surg. [Br.]* **23**, 20–23 (1998).
7. M. de Mos *et al.*, Outcome of the complex regional pain syndrome. *Clin. J. Pain* **25**, 590–597 (2009).
8. M. A. Kemler, C. A. Furnée, Economic evaluation of spinal cord stimulation for chronic reflex sympathetic dystrophy. *Neurology* **59**, 1203–1209 (2002).
9. N. E. O'Connell, B. M. Wand, J. McAuley, L. Marston, G. L. Moseley, Interventions for treating pain and disability in adults with complex regional pain syndrome. *Cochrane Database Syst. Rev.* **4**, CD009416 (2013).
10. A. B. Ch. Goebel *et al.*, *Complex Regional Pain Syndrome in Adults* (Royal College of Physicians, London, ed. 2, 2018).
11. V. Tékus *et al.*, A CRPS-IgG-transfer-trauma model reproducing inflammatory and positive sensory signs associated with complex regional pain syndrome. *Pain* **155**, 299–308 (2014).
12. J. Schwartz *et al.*, Guidelines on the use of therapeutic apheresis in clinical practice—evidence-based approach from the writing committee of the American Society for apheresis: The seventh special issue. *J. Clin. Apher.* **31**, 149–162 (2016).
13. F. J. Huygen *et al.*, Evidence for local inflammation in complex regional pain syndrome type 1. *Mediators Inflamm.* **11**, 47–51 (2002).
14. A. L. Oaklander *et al.*, Evidence of focal small-fiber axonal degeneration in complex regional pain syndrome-I (reflex sympathetic dystrophy). *Pain* **120**, 235–243 (2006).
15. K. Inoue, M. Tsuda, Microglia in neuropathic pain: Cellular and molecular mechanisms and therapeutic potential. *Nat. Rev. Neurosci.* **19**, 138–152 (2018).
16. Z. J. Zhang, B. C. Jiang, Y. J. Gao, Chemokines in neuron-glia cell interaction and pathogenesis of neuropathic pain. *Cell. Mol. Life Sci.* **74**, 3275–3291 (2017).
17. K. Popiolek-Barczyk, J. Mika, Targeting the microglial signaling pathways: New insights in the modulation of neuropathic pain. *Curr. Med. Chem.* **23**, 2908–2928 (2016).
18. S. M. Allan, P. J. Tyrrell, N. J. Rothwell, Interleukin-1 and neuronal injury. *Nat. Rev. Immunol.* **5**, 629–640 (2005).
19. A. Denes, E. Pinteaux, N. J. Rothwell, S. M. Allan, Interleukin-1 and stroke: Biomarker, harbinger of damage, and therapeutic target. *Cerebrovasc. Dis.* **32**, 517–527 (2011).
20. S. Yona *et al.*, Fate mapping reveals origins and dynamics of monocytes and tissue macrophages under homeostasis. *Immunity* **38**, 79–91 (2013).
21. M. Weber, F. Birklein, B. Neundörfer, M. Schmelz, Facilitated neurogenic inflammation in complex regional pain syndrome. *Pain* **91**, 251–257 (2001).
22. P. H. Veldman, H. M. Reynen, I. E. Arntz, R. J. Goris, Signs and symptoms of reflex sympathetic dystrophy: Prospective study of 829 patients. *Lancet* **342**, 1012–1016 (1993).
23. N. P. Staff *et al.*, Post-surgical inflammatory neuropathy. *Brain* **133**, 2866–2880 (2010).
24. M. R. Suter, Microglial role in the development of chronic pain. *Curr. Opin. Anaesthesiol.* **29**, 584–589 (2016).
25. E. D. Milligan, L. R. Watkins, Pathological and protective roles of glia in chronic pain. *Nat. Rev. Neurosci.* **10**, 23–36 (2009).
26. J. M. Dawes *et al.*, Immune or genetic-mediated disruption of CASPR2 causes pain hypersensitivity due to enhanced primary afferent excitability. *Neuron* **97**, 806–822.e10 (2018).
27. G. Wigerblad *et al.*, Autoantibodies to citrullinated proteins induce joint pain independent of inflammation via a chemokine-dependent mechanism. *Ann. Rheum. Dis.* **75**, 730–738 (2016).
28. L. S. Cahill *et al.*, Quantifying blood-spinal cord barrier permeability after peripheral nerve injury in the living mouse. *Mol. Pain* **10**, 60 (2014).
29. W. Guo *et al.*, Glial-cytokine-neuronal interactions underlying the mechanisms of persistent pain. *J. Neurosci.* **27**, 6006–6018 (2007).
30. C. Y. Chiang, B. J. Sessle, J. O. Dostrovsky, Role of astrocytes in pain. *Neurochem. Res.* **37**, 2419–2431 (2012).
31. J. M. Pradillo *et al.*, Delayed administration of interleukin-1 receptor antagonist reduces ischemic brain damage and inflammation in comorbid rats. *J. Cereb. Blood Flow Metab.* **32**, 1810–1819 (2012).
32. A. Denes, P. Thornton, N. J. Rothwell, S. M. Allan, Inflammation and brain injury: Acute cerebral ischaemia, peripheral and central inflammation. *Brain Behav. Immun.* **24**, 708–723 (2010).
33. A. Denes *et al.*, Interleukin-1 mediates neuroinflammatory changes associated with diet-induced atherosclerosis. *J. Am. Heart Assoc.* **1**, e002006 (2012).
34. Á. Dénes *et al.*, Streptococcus pneumoniae worsens cerebral ischemia via interleukin 1 and platelet glycoprotein Iba. *Ann. Neurol.* **75**, 670–683 (2014).
35. S. A. Liddel *et al.*, Neurotoxic reactive astrocytes are induced by activated microglia. *Nature* **541**, 481–487 (2017).
36. W. Liu, Y. Tang, J. Feng, Cross talk between activation of microglia and astrocytes in pathological conditions in the central nervous system. *Life Sci.* **89**, 141–146 (2011).
37. K. V. Toyka, D. B. Brachman, A. Pestronk, I. Kao, Myasthenia gravis: Passive transfer from man to mouse. *Science* **190**, 397–399 (1975).
38. P. Silveius Smitt *et al.*, Paraneoplastic cerebellar ataxia due to autoantibodies against a glutamate receptor. *N. Engl. J. Med.* **342**, 21–27 (2000).
39. J. S. Mogil *et al.*, Hypolocomotion, asymmetrically directed behaviors (licking, lifting, flinching, and shaking) and dynamic weight bearing (gait) changes are not measures of neuropathic pain in mice. *Mol. Pain* **6**, 34 (2010).
40. G. Lopalco *et al.*, Safety profile of anakinra in the management of rheumatologic, metabolic and autoinflammatory disorders. *Clin. Exp. Rheumatol.* **34**, 531–538 (2016).
41. M. T. Nurmohamed, B. A. Dijkman, Efficacy, tolerability and cost effectiveness of disease-modifying antirheumatic drugs and biologic agents in rheumatoid arthritis. *Drugs* **65**, 661–694 (2005).
42. SUVA, *CRPS (Complex Regional Pain Syndrome)*, W. Jänig, R. Schaumann, W. Vogt, Eds. (SUVA, 2013).
43. A. Goebel *et al.*, Mycophenolate for persistent complex regional pain syndrome, a parallel, open, randomised, proof of concept trial. *Scand. J. Pain* **18**, 29–37 (2018).
44. E. M. Pogatzki, S. N. Raja, A mouse model of incisional pain. *Anesthesiology* **99**, 1023–1027 (2003).
45. J. Gierthmühlen *et al.*; German Research Network on Neuropathic Pain (DFNS) Study Group Sensory signs in complex regional pain syndrome and peripheral nerve injury. *Pain* **153**, 765–774 (2012).
46. V. Hugel *et al.*, Complex interaction of sensory and motor signs and symptoms in chronic CRPS. *PLoS One* **6**, e18775 (2011).
47. S. Ventéo *et al.*, Fxyd2 regulates Aδ- and C-fiber mechanosensitivity and is required for the maintenance of neuropathic pain. *Sci. Rep.* **6**, 36407 (2016).
48. A. Szabó *et al.*, Role of transient receptor potential vanilloid 1 receptors in adjuvant-induced chronic arthritis: In vivo study using gene-deficient mice. *J. Pharmacol. Exp. Ther.* **314**, 111–119 (2005).
49. K. Bölskei *et al.*, Investigation of the role of TRPV1 receptors in acute and chronic nociceptive processes using gene-deficient mice. *Pain* **117**, 368–376 (2005).
50. Á. Horváth *et al.*, Transient receptor potential ankyrin 1 (TRPA1) receptor is involved in chronic arthritis: In vivo study using TRPA1-deficient mice. *Arthritis Res. Ther.* **18**, 6 (2016).
51. I. Imada *et al.*, Analysis of reactive oxygen species generated by neutrophils using a chemiluminescence probe L-012. *Anal. Biochem.* **271**, 53–58 (1999).
52. B. Botz *et al.*, Differential regulatory role of pituitary adenylate cyclase-activating polypeptide in the serum-transfer arthritis model. *Arthritis Rheumatol.* **66**, 2739–2750 (2014).
53. J. Németh *et al.*, Substance P radioimmunoassay for quantitative characterization of sensory neurotransmitter release. *Neurobiology (Bp.)* **7**, 437–444 (1999).
54. J. Németh *et al.*, Development of a new sensitive CGRP radioimmunoassay for neuropharmacological research. *Neurobiology (Bp.)* **6**, 473–475 (1998).
55. A. Denes *et al.*, AIM2 and NLR4 inflammasomes contribute with ASC to acute brain injury independently of NLRP3. *Proc. Natl. Acad. Sci. U.S.A.* **112**, 4050–4055 (2015).
56. J. B. Davis, ELISA for monitoring nerve growth factor. *Methods Mol. Biol.* **1606**, 141–147 (2017).
57. M. G. Giovannini *et al.*, Mitogen-activated protein kinase regulates early phosphorylation and delayed expression of Ca²⁺/calmodulin-dependent protein kinase II in long-term potentiation. *J. Neurosci.* **21**, 7053–7062 (2001).
58. F. Cerbai *et al.*, The neuron-astrocyte-microglia triad in normal brain ageing and in a model of neuroinflammation in the rat hippocampus. *PLoS One* **7**, e45250 (2012).
59. R. Fekete *et al.*, Microglia control the spread of neurotropic virus infection via P2Y₁₂ signalling and recruit monocytes through P2Y₁₂-independent mechanisms. *Acta Neuropathol.* **136**, 461–482 (2018).
60. L. He *et al.*, Methylprednisolone prevents nerve injury-induced hyperalgesia in neprilysin knockout mice. *Pain* **155**, 574–580 (2014).
61. M. Suzuki, H. Yoshida, M. Hashizume, K. Tanaka, Y. Matsumoto, Blockade of interleukin-6 receptor enhances the anti-arthritis effect of glucocorticoids without decreasing bone mineral density in mice with collagen-induced arthritis. *Clin. Exp. Immunol.* **182**, 154–161 (2015).
62. F. Buttgerit *et al.*, Standardised nomenclature for glucocorticoid dosages and glucocorticoid treatment regimens: Current questions and tentative answers in rheumatology. *Ann. Rheum. Dis.* **61**, 718–722 (2002).
63. R. G. Iannitti *et al.*, IL-1 receptor antagonist ameliorates inflammasome-dependent inflammation in murine and human cystic fibrosis. *Nat. Commun.* **7**, 10791 (2016).
64. A. de Luca *et al.*, IL-1 receptor blockade restores autophagy and reduces inflammation in chronic granulomatous disease in mice and in humans. *Proc. Natl. Acad. Sci. U.S.A.* **111**, 3526–3531 (2014).
65. J. Petrasek *et al.*, IL-1 receptor antagonist ameliorates inflammasome-dependent alcoholic steatohepatitis in mice. *J. Clin. Invest.* **122**, 3476–3489 (2012).
66. M. Gertsenstein *et al.*, Efficient generation of germ line transmitting chimeras from C57BL/6N ES cells by aggregation with outbred host embryos. *PLoS One* **5**, e11260 (2010).
67. W. C. Skarnes *et al.*, A conditional knockout resource for the genome-wide study of mouse gene function. *Nature* **474**, 337–342 (2011).

SI APPENDIX:**Methods****Patients, healthy controls, and serum preparation**

Ethics permission was obtained to repeatedly sample larger volumes of CRPS patient sera as well as age (± 10 years) and sex matched healthy control sera (15/NW/0467, NorthWest Ethics Haydock, UK). Waste plasma samples were obtained between 2014-2017 from patients ($n=5$) newly undergoing plasma exchange treatment for persistent CRPS at the Walton Centre NHS Foundation Trust, a tertiary care hospital in Northern England (UK). Use of waste-plasma does not require ethics committee approval; all patients provided individual written informed consent. Small volumes of serum were pooled from samples taken at screening from all participants in a recent clinical trial ($n=7$, 15/NW/0135, NorthWest Ethics Haydock, UK) who had baseline pain intensities of $\geq 7/10$ on a 11-point numeric rating scale (NRS, 0='no pain', 10='pain as bad as you can imagine'). Their baseline pain intensity scores are provided in Table S1. The patients had provided written informed consent for the use of their serum samples for research purposes, as part of their overall consent for this study (1).

Human IgG injection protocol

In all studies mice were injected with 8mg human IgG daily, following the classical immunoglobulin disease transfer protocol established for neurological conditions (2). This daily injection regimen compensates for losses of transferred human immunoglobulin G induced by rapid metabolism in the rodent. To clarify the rate of decline of human IgG levels in our mouse model, we injected groups of hind paw injured animals on days 0 and 1 with 12mg and 8mg human IgG respectively. We then measured human IgG concentrations in mouse plasma, after humane sacrifice ($n=4$ per time point) 5h after the second IgG injection and then on days 3, 6, and 13 by using Human total IgG Platinum ELISA kit (BMS2091, ThermoFisher Scientific, US) according to the manufacturer's protocol. The initial half-life of human IgG in mice was less than 3 days, with a slowing decline after day 7 (1.77 ± 0.4 (SEM) mg/ml 5h after the second injection (day 1), 0.93 ± 0.3 mg/ml at day 3, 0.32 ± 0.1 mg/ml at day 7, and 0.18 ± 0.06 mg/ml at day 13, respectively), confirming the expected rapid metabolism.

Animals

The original breeding pairs were purchased from Jackson Laboratories (USA) through Charles River Hungary or obtained from breeding pairs at the Institute of Experimental Medicine,

Budapest, Hungary. Animals were bred and kept in the conventional animal house of the Department of Pharmacology and Pharmacotherapy of the Medical School, University of Pécs at 24 °C, in a 12 h light–dark cycle and had access to standard rodent chow and water ad libitum. Mice were housed in groups of 5–10 in polycarbonate cages (330 cm² floor space, 12 cm height) upon a bedding consisting of wood shavings. All procedures were performed according to the 1998/XXVIII Act of the Hungarian Parliament on Animal Protection and Consideration Decree of Scientific Procedures of Animal Experiments (243/1988), complied with the recommendations of the International Association for the Study of Pain. Ethical approval was given by the Ethics Committee on Animal Research of University of Pécs according to the Ethical Codex of Animal Experiments (licence No.: BA02/2000-31/2016).

Plantar skin-muscle incision

Mice were anesthetized with ketamine (100 mg/kg; Calypsol, Gedeon Richter Plc., Budapest, Hungary) and xylazine (10 mg/kg; Sedaxylan, Eurovet Animal Health B.V., Bladel, Netherlands) on day 0. The operation site was prepared in a sterile manner, and the plantar surface of one right hindpaw was incised longitudinally, starting 0.2 cm from the heel, over a distance of 0.5 cm, intersecting the skin, fascia and plantar muscle. The skin was then opposed with interrupted stitches, using 5-0 nylon. The wound site was treated with povidone iodine solution.

***In vivo* optical imaging of neutrophil myeloperoxidase (MPO) activity as a marker of cellular inflammation**

On days 2, 6 or 13 following incision, mice were anaesthetised, hair was removed from both hindlegs to prevent scattering/absorbing of the light signal. L-012 (25 mg/kg) in sterile phosphate-buffered saline (PBS, 20 mg/ml) was injected i.p.. Bioluminescence was measured 10 min post-injection using the IVIS Lumina II *in vivo* optical imaging system (180 s acquisition, F/stop = 1, Binning = 8). Data were analysed using Living Image® software (Perkin-Elmer, Waltham, USA).

In both cases identical Region of Interests (ROIs) were applied around both hind paws up to the ankles. Fluorescence was expressed as total radiant efficiency ($[\text{photons/s/cm}^2/\text{sr}]/[\mu\text{W/cm}^2]$), whilst luminescence was expressed as total radiance (total photon flux/s) originating from the analysed ROIs.

Measurement of sensory neuropeptides, inflammatory cytokines and nerve growth factor in the paw and cytokines in the plasma

dc_2027_22

In every case, 400 µl homogenisation buffer was used for 50 mg tissue sample weight to normalise the difference of the sample size. The homogenate was centrifuged at 15,000-20000 g for 20 min at 4 °C and the supernatant was immediately collected and stored frozen for later measurement of inflammatory sensory neuropeptides and cytokines.

Quantification of small nerve fibre axons in paw skin biopsies

Numbers and diameters of thin unmyelinated axons in the dermis were quantitatively assessed on EM photomicrographs of ultrathin sections from the left and right paws using iTEM software (Olympus Corp., Japan). When axons appeared to be cut oblique or longitudinally, the smaller diameter was taken. Numbers and diameters of axons were averaged and the standard deviation (SD) was determined. The differences between the two sides were evaluated with Student's t-test, and the levels of significance was set at $p \leq 0.05$.

Immunohistochemistry

Sections were washed in 0.05M Tris buffered saline (TBS, pH 7.6), incubated in 0.3% H₂O₂/methanol (Szkarabeusz Ltd, Hungary) for 30 min to inhibit endogenous peroxidase activity, then incubated in primary antibodies for 48 h at 4°C (GFAP dilution: 1:1000, Novocastra™ Leica Biosystems, or Iba1 dilution: 1:500, Wako Chemicals GmbH, Germany). After washing steps, sections were incubated with Vectastain Elite ABC HRP Kit (Vector Labs, USA). Antibodies were visualized using Nickel (II) sulphate hexahydrate/3,3'-diaminobenzidine tetrahydrochloride (DAB, Sigma-Aldrich, USA) as chromogen, and glucose oxidase (Sigma-Aldrich, USA), which resulted in a black precipitate within the labelled cells. The sections were mounted onto gelatinized slides, allowed to dry overnight, dehydrated through increasing concentrations of ethanol; they were then coverslipped with DPX (Sigma-Aldrich, USA), and allowed to dry again.

Immunofluorescence

25 µm thick free-floating brain sections were incubated with 5% normal donkey serum and then incubated overnight at 4°C with the appropriate combination of primary antibodies: rabbit anti-P2Y₁₂ (dilution 1:500, #55043A, AnaSpec), goat anti-IL-1α (dilution 1:500, #AF-400-NA R&D Systems), and goat anti-IL-1β (dilution 1:500, #AF-401-NA R&D Systems). For visualization donkey anti-rabbit Alexa 488 and donkey anti-goat Alexa 647 secondary antibodies (1:500) were used. Images were captured with a Nikon Ni-E C2+ (Nikon, Tokyo, Japan) confocal microscope, and image processing was performed using the NIKON NIS Elements Viewer 4.20 software (Auroscience Ltd., Budapest, Hungary).

Cytometric bead array

Cytometric bead Array (CBA) was performed by using BD™ CBA Flex Sets (BD Biosciences, Franklin Lakes, New Jersey USA) according to the manufacturers' protocol. Samples were acquired using a BD FACSVerser flow cytometer and data analysed by FCAP Array v3 software (BD Biosciences). Concentrations of nerve growth factor (NGF) and transforming growth factor beta (TGF-β) in the paw homogenates were measured by Sandwich ELISA kit (ChemiKine™, Merck, Germany) according to the manufacturers' instructions. The concentrations of all cytokines and chemokines were expressed as pg mediator per ml wet tissue homogenate.

Generation of IL-1β floxed mice and microglial IL-1β KO mice

I11b^{tm1a(EUCOMM)Hmgu} embryonic stem cells were purchased from the European Mouse Mutant Cell Repository (EuMMCR). Cells from clone HEPD0840-8-E03 were prepared for microinjection according to previously published protocol(92) with minor modifications. Briefly, ES cells were cultured in KO-DMEM + KOSR + 2i (MEK inhibitor and GSK3 inhibitor) on a gelatinized (0.1% gelatin in PBS) cell culture dish maintained in standard culture conditions (37°C, 5% CO₂, humidified). The culture medium was changed daily, and the cells were passaged when 75-80% confluent using accutase to dissociate the cells. Cells were passaged no more than 3 times and were transferred to media without 2i reagents for 24 h prior to microinjection. Cells were then microinjected into 4 to 8 cell B6N-Tyr^{c-Brd}/BrdCrCl embryos. Surviving embryos were surgically implanted into the oviduct of day 0.5 post-coitum pseudopregnant mice. Resulting black/white C57BL/6N chimeras were back-crossed onto C57BL/6N wild-type mice to assess germline penetrance. Potential founder mice were screened by PCR for LacZ, Neo and LoxP sites. This line was further crossed with C57BL/6N-Tg(CAG-Flp)1Afst/Mmucd mice. The flp recombinase expression provided by this line resulted in a "conditional ready" (floxed) I11b^{tm1c(EUCOMM)Hmgu} allele where exons 4 and 5 are flanked by loxP sites. To generate microglial IL-1β KO mice, IL-1β floxed mice were crossed with tamoxifen-inducible B6.129P2(C)-CX3CR1^{tm2.1(cre/ERT2)Jung/J} mice (JAX stock #020940 (3)). Cre recombinase activity was induced by two intraperitoneal injections of tamoxifen (2mg/100μl, Sigma-Aldrich, dissolved in corn oil), 48h apart in 3-4 weeks old male mice, shortly after weaning.

Quantification of immunohistochemistry to assess glial activation

Cell counting was conducted as follows: we traced the contours of the specific areas under low magnification (4x) with the help of Paxinos and Franklin mouse brain atlas, then we counted

labelled astrocytes and microglia cells using higher magnification (10x). Since the thickness of the section was 30 μ m, cells were counted in a 3-dimensional tissue and we calculated the 3D cellular volume using Neurolucida software. The density of GFAP and Iba1 immunopositive cells was determined as the number of counted cells divided by the volume of the measured area, expressed as cell number/ cm³.

Results

Table S1

R-no	Baseline
P01002	6.8
P01004	*9.3
P01005	*8.2
P01006	*8.4
P01009	*7.2
P01012	5.9
P01001	*7.6
P01003	6.8
P01007	6.6
P01008	6.2
P01010	*8.5
P01011	*9.1

Table S1. Pain intensities at baseline of all randomized patients in the MYPS trial, including seven patients selected for pooled testing in the passive-transfer-trauma model. R-no= randomization number; baseline= pain intensity at baseline (average of daily average pain intensity ratings on a 0-10 numeric rating scale, during the screening period, maximally 14 entries); data from (1); *denotes patients whose serum was used for a pooled experiment, see methods section ('patients, healthy controls and serum preparation'), results are shown in Figure S1 (L, P).

Figure S1

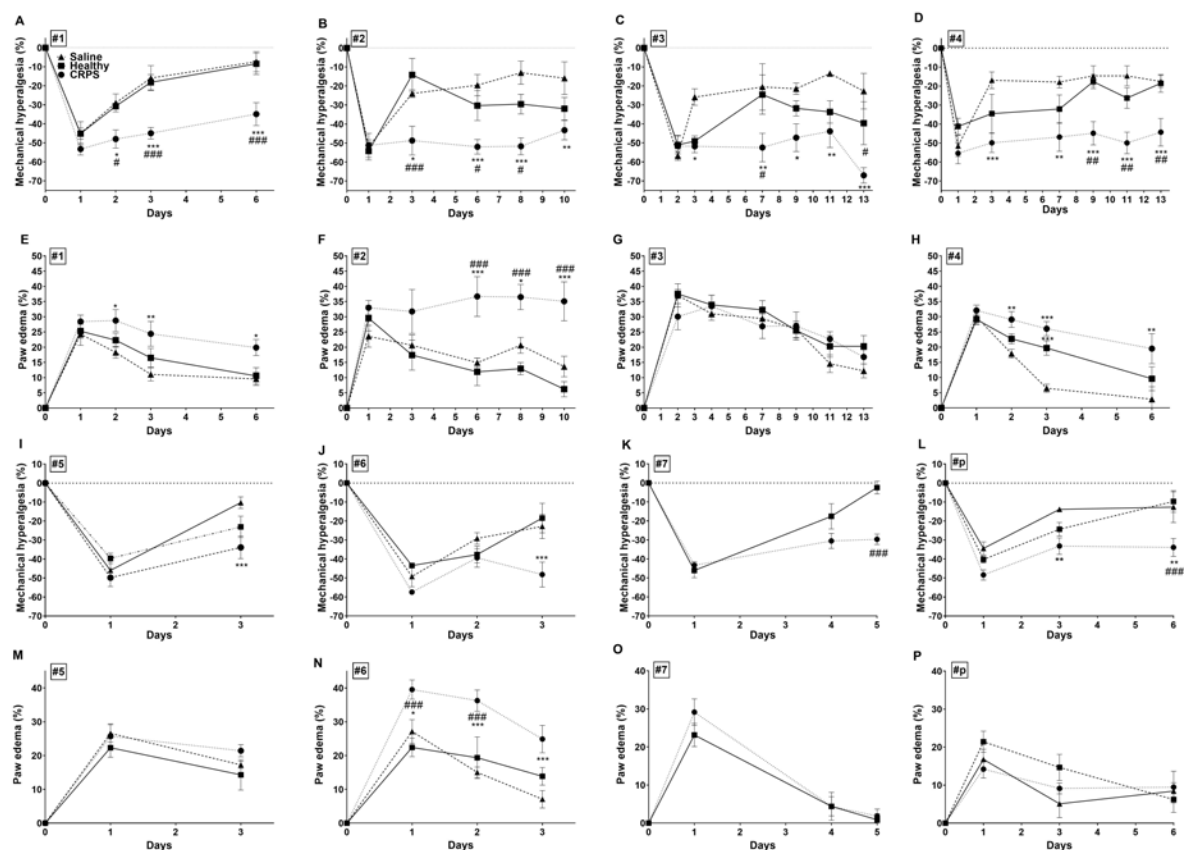


Fig. S1. Behavioural effects of injection with individual CRPS/healthy serum IgG samples, and pooled samples from the MYPS trial. Effects of serum IgG from individual CRPS patients #1-#7 (manuscript Table 1), and of one serum IgG preparation pooled from seven additional CRPS patients (#p, Table S1), or healthy controls, or saline on plantar incision-induced mechanical hyperalgesia and swelling, with data shown as means \pm SEM, * $p < 0.05$, ** $p < 0.01$, *** $p < 0.001$ (vs. saline-treated control mice), # $p < 0.05$, ## $p < 0.01$, ### $p < 0.001$ (vs. healthy IgG-treated mice); two-way ANOVA followed by Bonferroni's multiple comparison test. 'Healthy'=healthy control IgG injected group; 'CRPS'=CRPS IgG injected group.

Figure S2

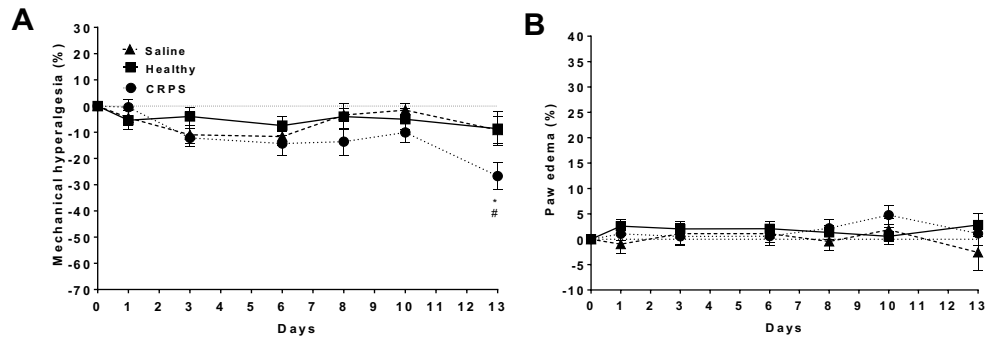


Fig. S2. Effect of serum IgG derived from CRPS patients or healthy controls, or saline on mechanical hyperalgesia (A) and swelling (B) of the *intact* hind paw. Pooled results from the long-term experiments (preparations #2, #3, #4, injured paw results: Figure 1). Data are means \pm SEM, * $p < 0.05$ (vs. saline-treated control mice), # $p < 0.05$ (vs. healthy IgG-treated mice); two-way ANOVA followed by Bonferroni's multiple comparison test. 'Healthy'=healthy control IgG injected group; 'CRPS'=CRPS IgG injected group.

Figure S3

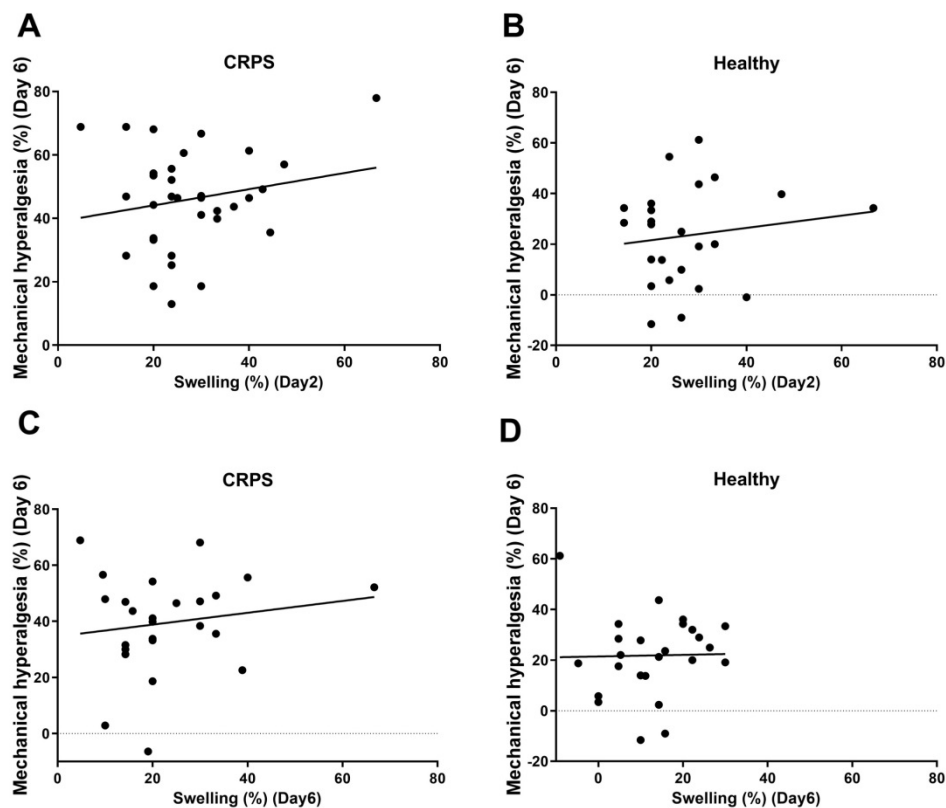


Fig. S3. Correlation between mechanical hyperalgesia and paw swelling. Panels (A, B) show correlation between the mechanical hyperalgesia on day 6 and paw edema on day 2 (when this was usually maximal), while (C, D) show correlations between both parameters on day 6 respectively. Dot plot data represent individual animal data, as obtained from 4-5 experiments using different patient preparations per time point, 6 mice/ experiment. There is no correlation at any measured time point. (A, B) n=30-32 animals; Spearman $r=0.056$; $p=0.741$ in the CRPS IgG group and $r=0.103$; $p=0.632$ in the healthy control group. (C, D) n=24-26 animals; Spearman $r=0.116$; $p=0.577$ in the CRPS IgG group and $r=0.202$, $p=0.331$ in the healthy control group. ‘Healthy’=healthy control IgG injected group; ‘CRPS’=CRPS IgG injected group.

Figure S4

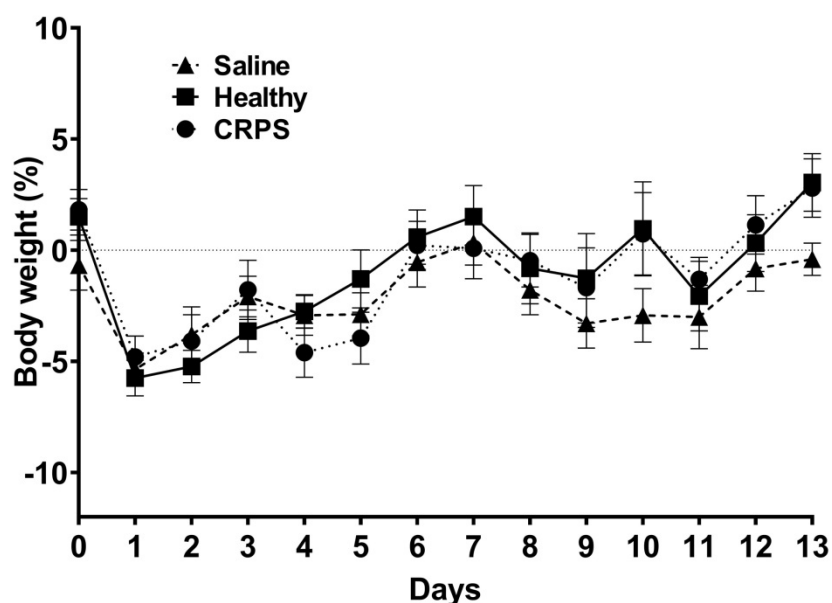


Fig. S4. Typical weight change over time. Minimal weight loss was observed in all groups in the first few days after surgery, followed by recovery. Weights were measured in the mornings, before injection treatment and/or surgery. Values are in percent of baseline (the average of 3 measurements in the preceding week). Numbers represent the average of two experiments conducted with two different CRPS IgG (#3, #4), or healthy control IgG preparations. Error bars denote SEM. ‘Healthy’=healthy control IgG injected group; ‘CRPS’=CRPS IgG injected group.

Figure S5

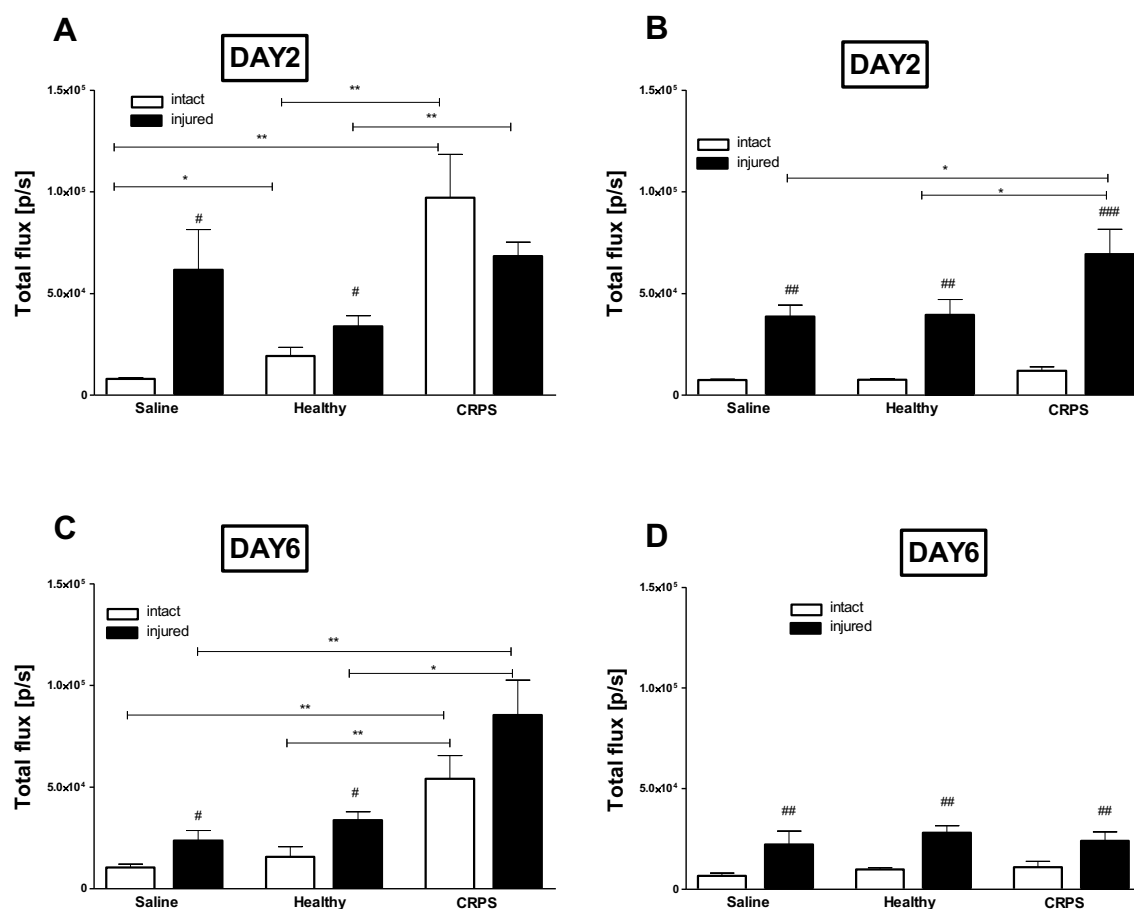


Fig. S5: *L-012* - derived bioluminescence for individual CRPS patient/healthy control preparations on days 2 and 6. Data were obtained from animals treated with various serum IgG preparations or saline under general anaesthesia on days 2 and 6 after paw incision. Panel (A) shows results from patient #1 IgG on day 2, (B) shows pooled results of 2 repeated experiments of patient #3 IgG on day 2. Panels (C, D) represent the bioluminescence results of patient #1 IgG and patient #4 IgG on day 6, respectively. Data are means \pm SEM of $n=6-12$ mice/group, * $p < 0.05$, ** $p < 0.01$, *** $p < 0.001$ vs. respective control groups, # $p < 0.05$, ## $p < 0.01$, ### $p < 0.001$ vs. respective intact hind paw, one-way ANOVA followed by Bonferroni's multiple comparison test. 'Healthy'=healthy control IgG injected group; 'CRPS'=CRPS IgG injected group.

Table S2

Day 2	animal number	Day 6	animal number	Day 13	animal number
#1	7	#1	6	#4	6
#3	6	#4	6		
#3	6				
total animal number	19		12		6

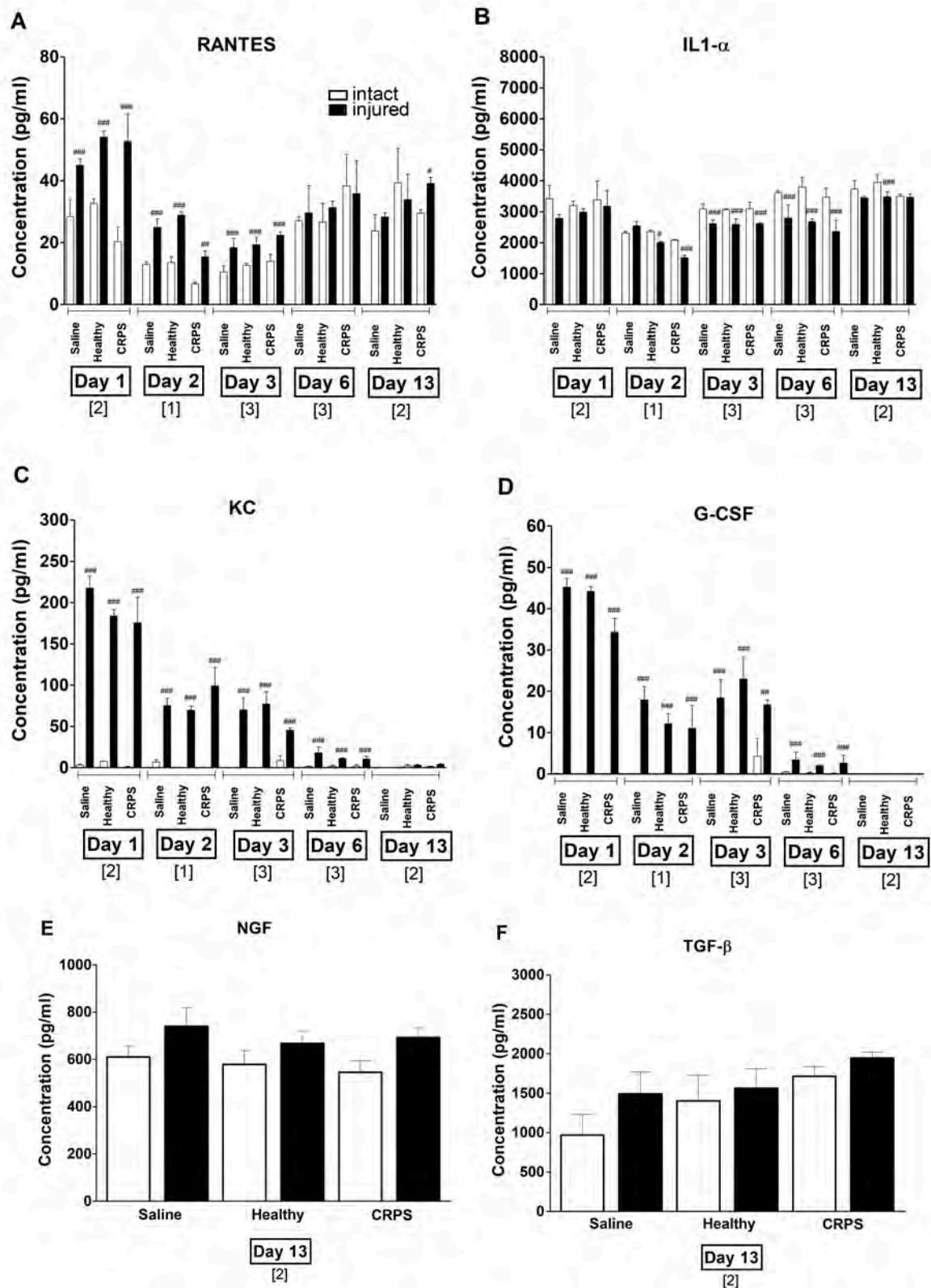
Table S2. Preparations and animal numbers for *in vivo* testing (corresponding Figures 3 and S5). #1-#4 = individual patient IgG preparations used (patient details in Table 1)

Table S3

Days	1	2	3	5	6	10	13
#2						7 ^c	
#1					7 ^c		
#5			6 ^c				
#3			6 ^{b,c}				
#3	6 ^c						
#3		6 ^c					
#3					6 ^c		
#3		6 ^c					
#3					6 ^{b,c}		
#3			6 ⁺				
#3			6 ^{b,c}				
#3							6 ^{b,c}
#4			6 ^c				
#4		6 ^c					
#4					6 ^{b,c}		
#3			7 ⁺				
#4							6 ^{b,c}
#4	6 ^c						
#4					5 ⁺		
#4					6 [*]		
#3					6 [*]		
#3							6 ^{*b}
#3							6 ^{*b}
#4					6-6 ^{b,c}		
#7				6 ^c			
#6					6 ^{b,c}		
Pooled serum					6 ^c		
#4 IL-1 α β KO					6 ^{b,c}		
#3 IL-1 α β KO					6 ^{b,c}		
#8 M-IL-1 β KO					4 ^{b,c}		
#3 M-IL-1 β KO					4 ^{b,c}		

Table S3. List of experiments in the order in which they were done, with animal numbers per group. #1-#7=individual patient IgG preparations used (patient details in Table 1); +/* steroid/anakinra experiment; ^b sera were applied for central nervous system (CNS) immunochemistry, ^c sera were used for behavioural assessment, and evaluation of the mediator levels only (no therapy).

Figure S6



dc_2027_22

Fig. S6. *Effects of human IgG treatments and trauma on inflammatory mediator concentrations in the hind paws.* Concentrations of **(A)** regulated on activation, normal T cell expressed and secreted (Rantes), **(B)** keratinocyte chemoattractant (KC), **(C)** granulocyte-colony stimulating factor (G-CSF), and **(D)** interleukin-1-alpha (IL-1 α) were measured by cytometric bead array from the same samples (CBA). Concentrations of **(E)** nerve growth factor (NGF) and **(F)** transforming growth factor beta (TGF- β) were measured by Sandwich ELISA kit. Levels of interferon-gamma (IFN- γ), interleukin-4 (IL-4) and interleukin-10 (IL-10) were below the detection limit (not shown). Data are from 1-3 experiments with different patient IgG preparations (brackets under the x-axis) per time point, 6 mice/ experiment. The preparations are specified in Table S3. Shown are means \pm SEM; #p < 0.05, ##p < 0.01, ###p < 0.001 vs. respective intact side, one-way ANOVA followed by Bonferroni's multiple comparison test. 'Healthy'=healthy control IgG injected group; 'CRPS'=CRPS IgG injected group.

Figure S7

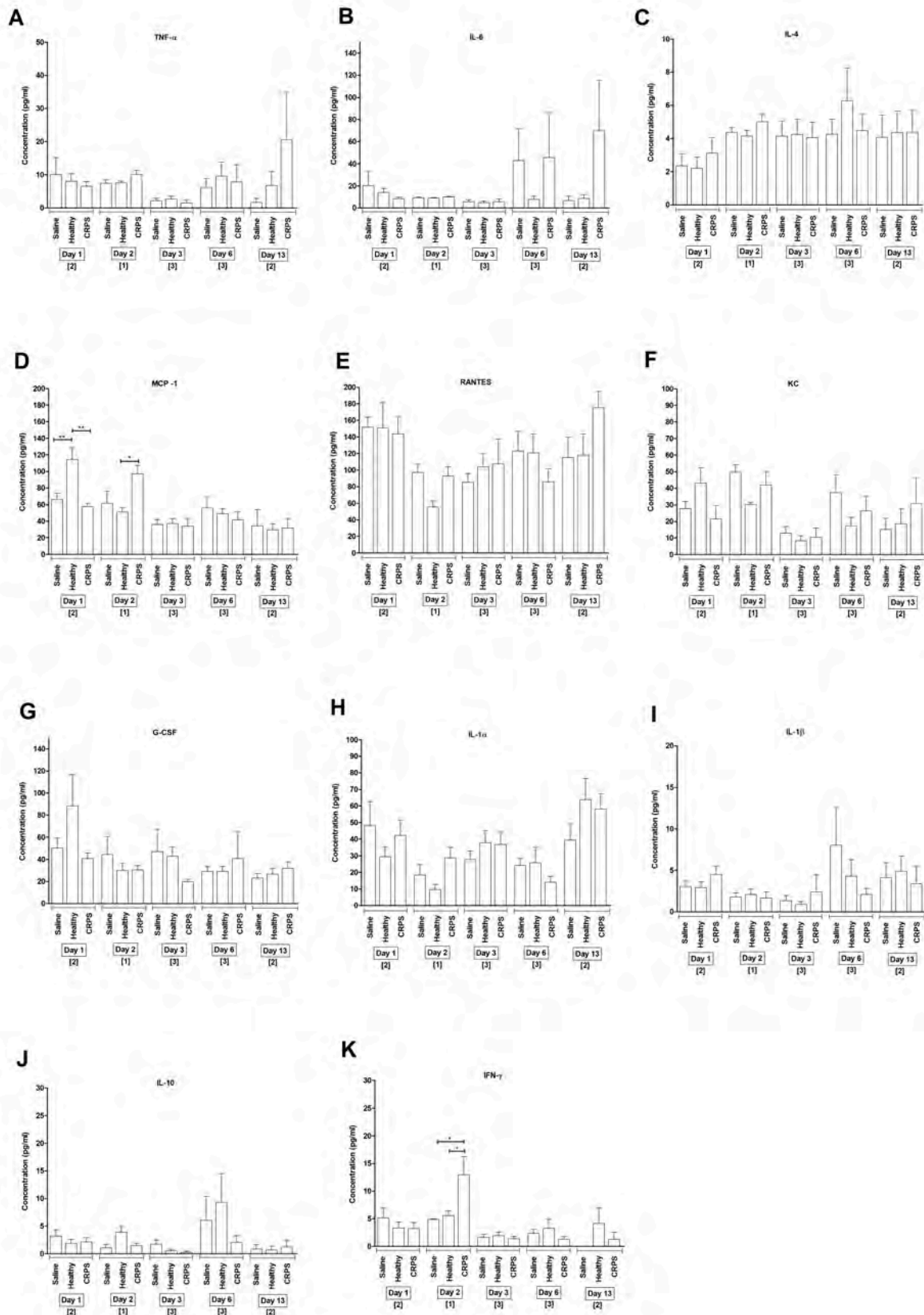


Figure S7. *Effects of human IgG treatments on inflammatory mediator concentrations in the mouse plasma.* Concentrations of (A) TNF- α , (B) IL-6, (C) IL-4, (D) MCP-1, (E) RANTES, (F) KC, (G) G-CSF, (H) IL- α , (I) IL-1 β , (J) IL-10 and (K) IFN- γ were measured by CBA from the same plasma samples. Data are from 1-3 experiments (brackets under x-axis) with different patient preparations per time point, 6 mice/ experiment. Preparations used are specified in Table S3. Shown are means \pm SEM; *p < 0.05, **p < 0.01, ***p < 0.001 respective control groups, one-way ANOVA followed by Bonferroni's multiple comparison test. After correction for 10 tests, no significant result remained. 'Healthy'='healthy control IgG injected group; 'CRPS'=CRPS IgG injected group.

Figure S8

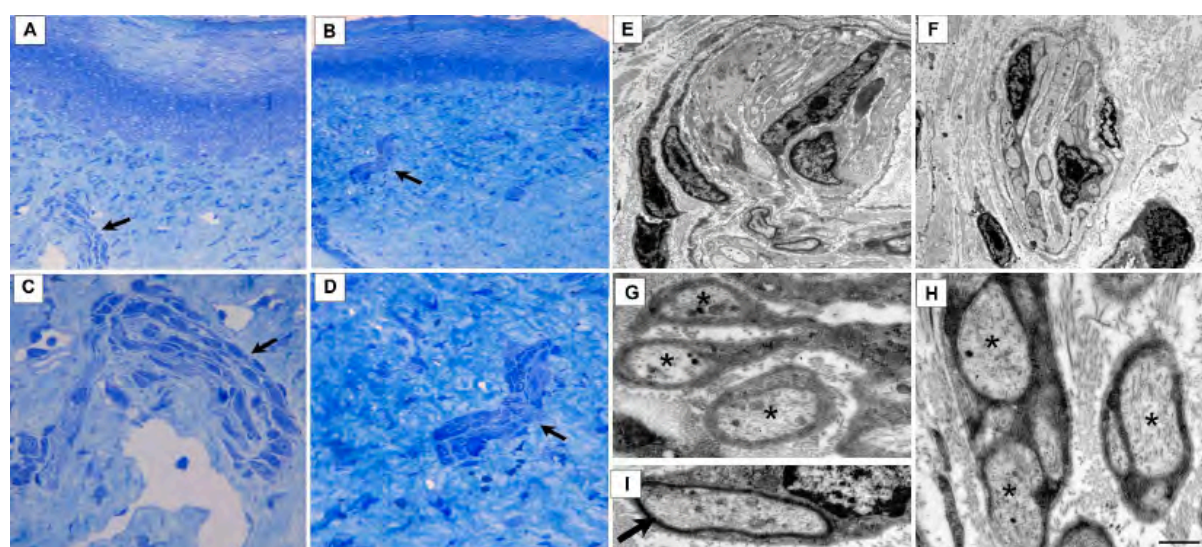


Fig. S8. *Small nerve fibres in the paw skin of CRPS Ig- injected mice on day 13.* (A-D) Semithin sections of the right (A, C) and left (B, D) paws of the CRPS IgG injected group. Arrows point to bundles containing non-myelinated, thinly-myelinated and myelinated axons. Structures shown in (A, B) are visible in (C, D) with higher magnification. Scale bar is 50 μ m in (A, B), 20 μ m in (C, D). (E-I) Photomicrographs of ultrathin transmission EM sections of the right (E, G, I) and the left (F, H) paws of the CRPS IgG injected group. (E, F) show small magnification images of thin nerves containing non-myelinated, thinly-myelinated and myelinated axons. (G) Ultrastructure of non-myelinated axons (asterisks), and (I) of a thinly-myelinated axon in an oblique section (arrow). (H) Ultrastructure of non-myelinated axons (asterisks) from the left paw. Scale bar is 3 μ m in (E, F), 500 nm in (G, H) and 750 nm in (I).

Table S4

	Right paw (injured)	Left paw (intact)
Number of axons per nerve \pm SD (number of nerves)	29.67 \pm 12.74 (3)	25.67 \pm 12.09 (3)
Axonal diameter \pm SD (number of axons measured)	339.08nm \pm 159.80 (221)	356.38nm \pm 145.73 (192)

Table S4. *Axon number/nerve, and diameter of unmyelinated axons in the right and left paws of CRPS IgG injected animals.* EM photomicrographs of three nerves were used to determine the axon number per nerve; to calculate the average axonal diameter, the diameters of all axons visible on all available EM sections were counted; all right-left differences were non-significant with $p > 0.2$ (Student's t-test). SD=standard deviation.

Figure S9

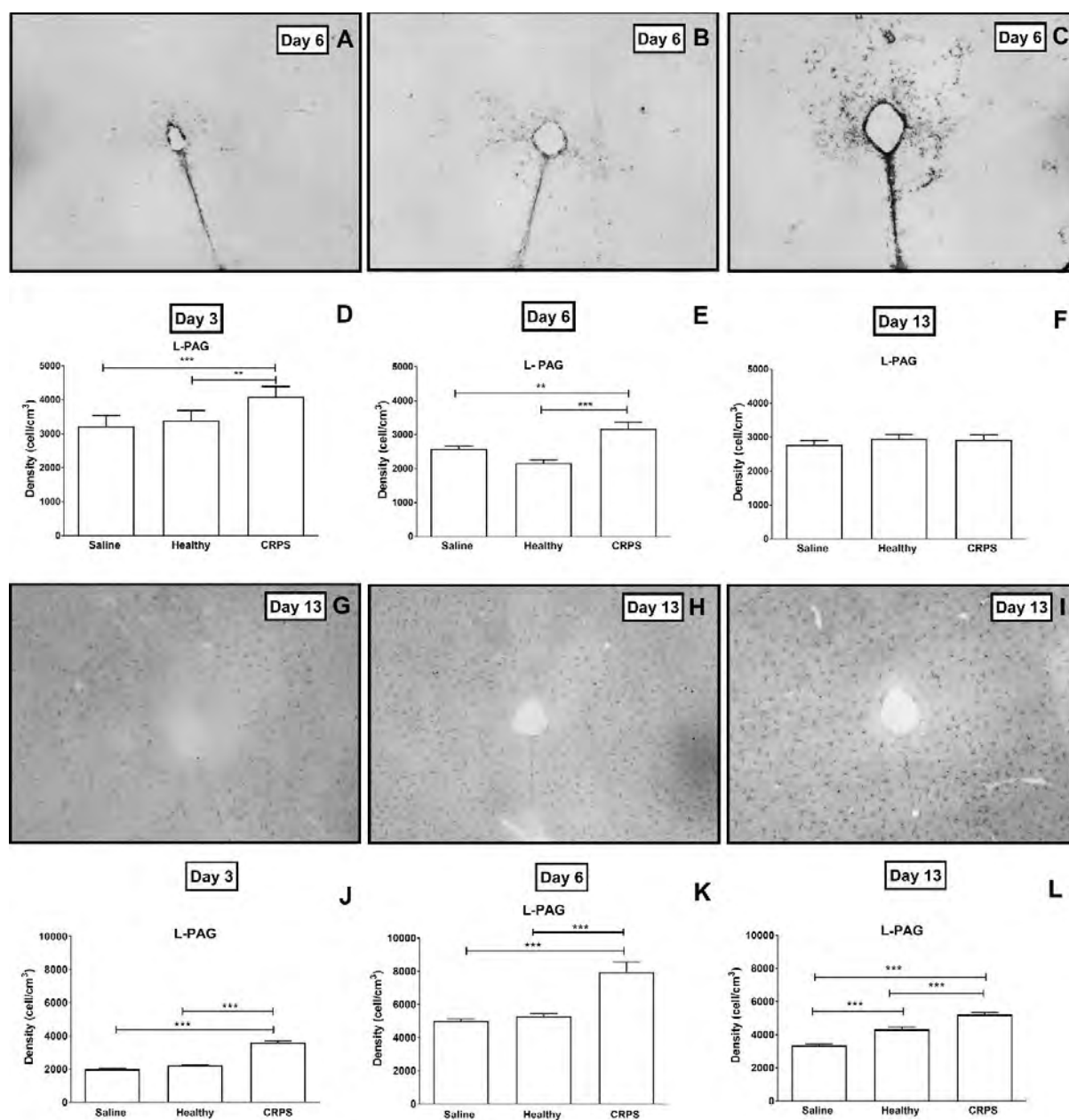


Figure S9A. Representative photomicrographs and quantification of glia cells within the lateral periaqueductal grey matter. Panels (A-C) show GFAP immunopositivity indicating astrocytes, and panels (G-I) show Iba1 immunopositivity indicating microglia cells ((A, G) saline, (B, H) healthy, (C, I) CRPS groups). The GFAP immunopositive sections shown are from day 6-, and Iba1 sections from day 13 after paw incision. Magnifications are 4x. Panels (D-F): quantification of astrocyte reactivity, and panels (J-L) microglia staining at 3, 6, and 13 days post hindpaw incision. Each panel represents the pooled results from 2 experiments with 2 different patient IgG samples (#3, #4) or control IgG. Shown are means \pm SEM of 6-7 mice per group, * $p < 0.05$, ** $p < 0.01$, *** $p < 0.001$ vs. respective control groups; one-way ANOVA followed by Bonferroni's modified post hoc test. 'Healthy'=healthy control IgG injected group; 'CRPS'=CRPS IgG injected group.

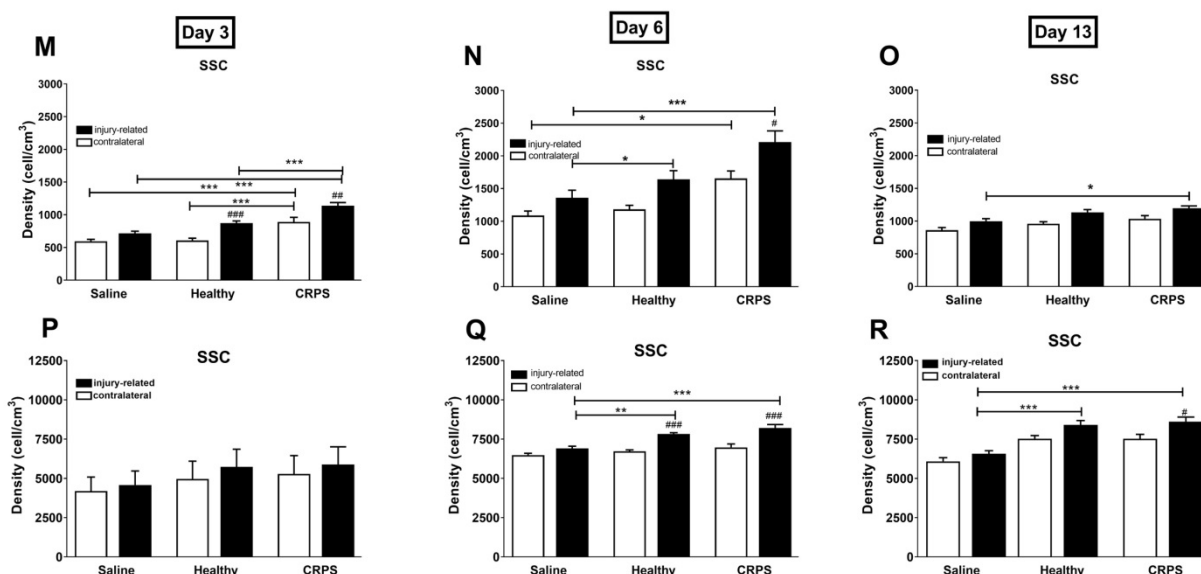


Figure S9B Somatosensory cortex glia cell staining. Quantification of astrocyte (M-O) and microglia staining (P-R) in the somatosensory cortex ('SSC') at 3, 6, and 13 days post hindpaw incision. Each panel represents the pooled results from 2 experiments with 2 different CRPS IgG samples (#3, #4). Shown are means \pm SEM of 6-7 mice per group * $p < 0.05$, ** $p < 0.01$, *** $p < 0.001$ vs. respective control groups; # $p < 0.05$, ## $p < 0.01$, ### $p < 0.001$ vs. respective contralateral side; one-way ANOVA followed by Bonferroni's modified post hoc test. 'Healthy'=healthy control IgG injected group; 'CRPS'=CRPS IgG injected group; 'injury-related' refers to the left brain in all cases, i.e. the side that is contralateral to the (right) paw injury side.

Figure S10

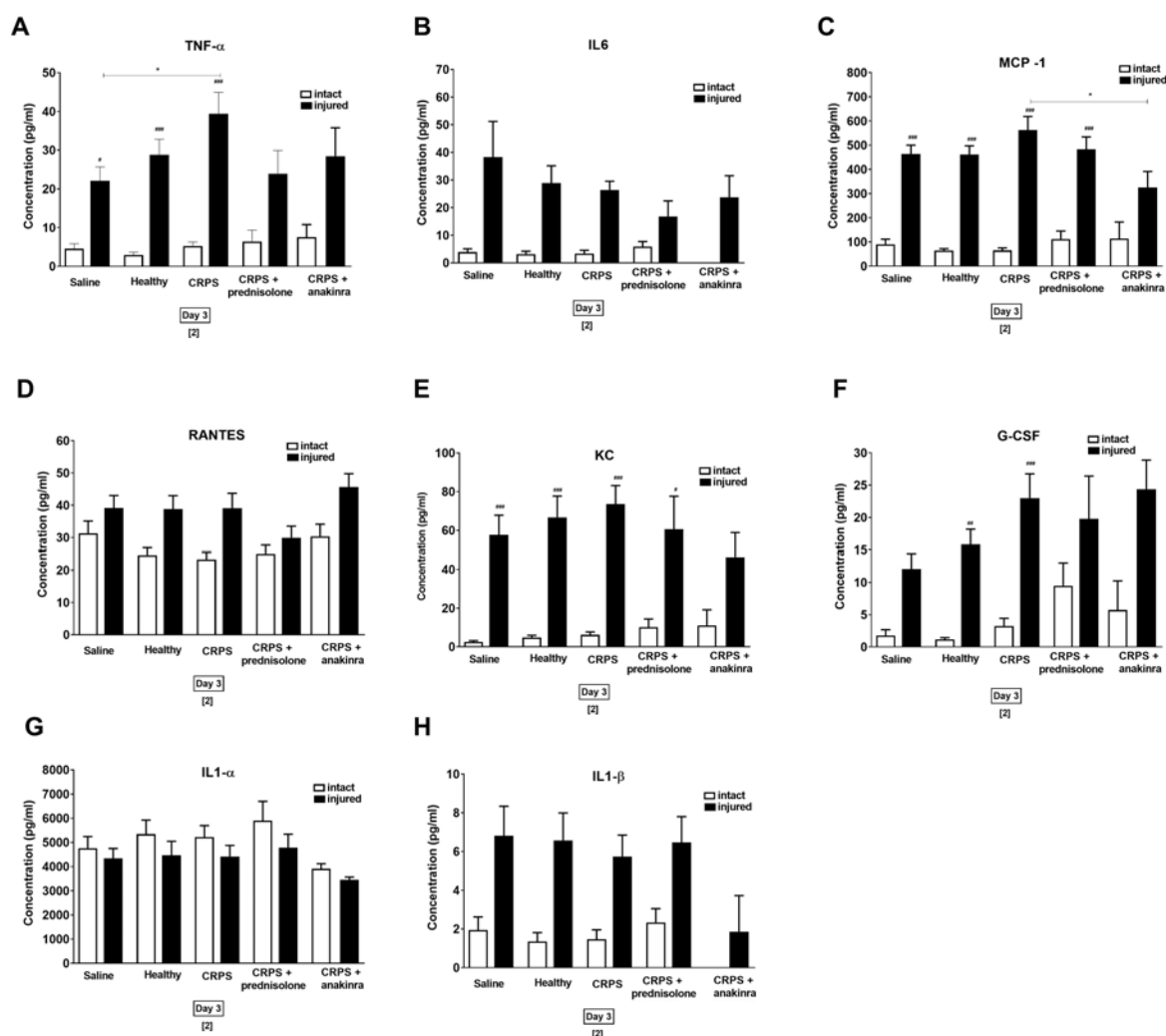


Figure S10. Effects of prednisolone and anakinra treatment on inflammatory cytokine concentrations in the hindpaws on day 3. (A) TNF- α , (B) IL-6, (C) MCP-1, (D) RANTES, (E) KC, (F) G-CSF, (G) IL-1 α , (H) IL-1 β were measured by cytometric bead array (CBA) from the same paw samples. Other cytokines (IL-4, IL-10 and IFN- γ) were under detection limit. Data are from 2 experiments (brackets under x-axis) with different patient IgG and control IgG preparations per time point, 6 mice/experiment (Table S3). Results shown are means \pm SEM, # p < 0.05, ## p < 0.01, ### p < 0.001 vs. respective intact side, one-way ANOVA followed by Bonferroni's multiple comparison test. 'Healthy'=healthy control IgG injected group; 'CRPS'=CRPS IgG injected group.

Figure S11

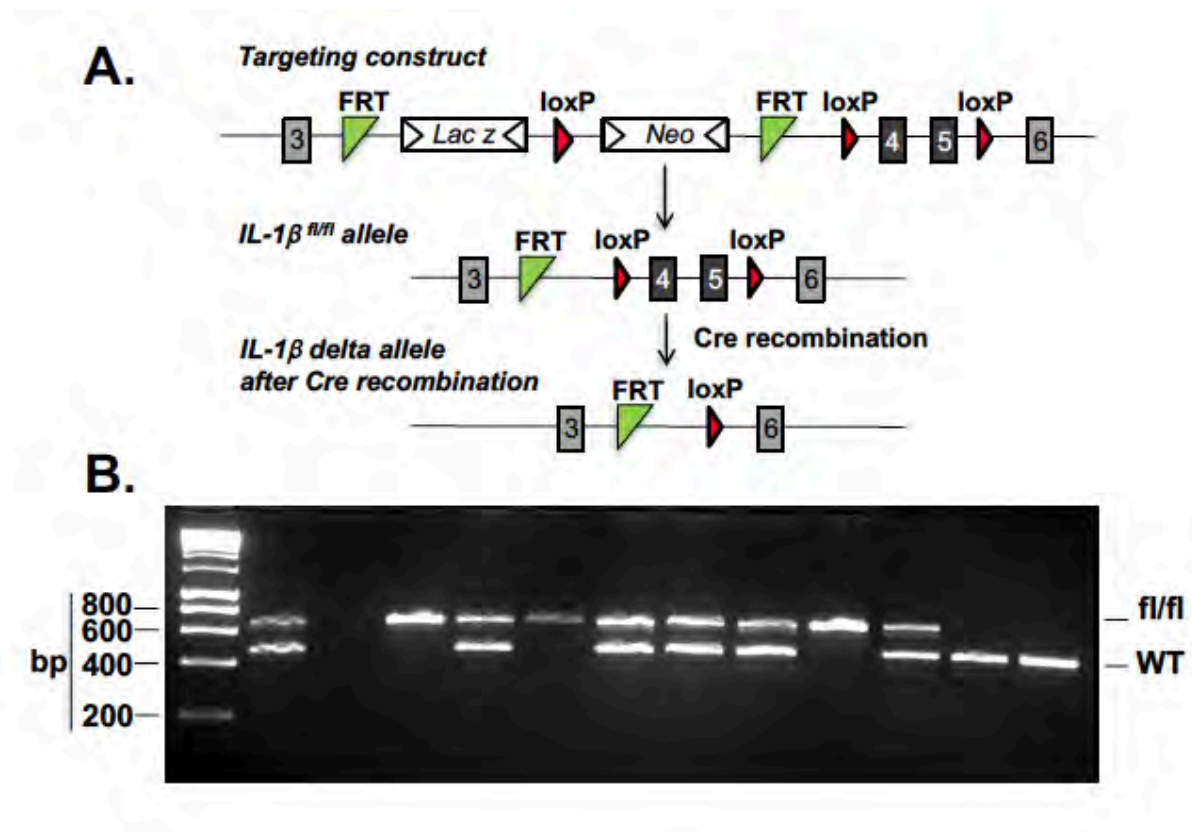


Figure S11. Generation of $IL-1\beta^{fl/fl}$ mice. A) Genetic targeting shows exon 4-5 flanked with loxP sites, positioned upstream of a lacZ/Neo resistance cassette, which is excised upon FLP recombination, resulting in the generation of $IL-1\beta^{fl/fl}$ allele. Cre recombinase leads to exon 4-5 deletion, generating cell-specific $IL-1\beta$ KO mice. B) Genotyping PCR showing amplification of the WT (480bp) and $IL-1\beta$ floxed allele (673bp).

Figure S12

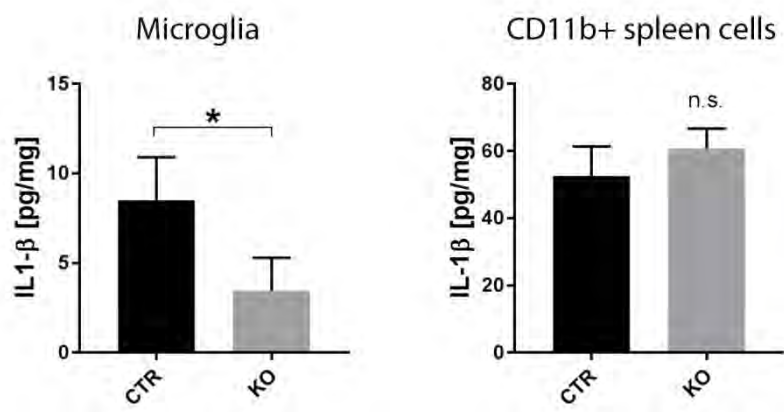


Figure S10. Microglia, but not splenic macrophages derived from tamoxifen-treated *Cx3cr1^{CreER} x IL-1 β ^{fl/fl}* mice show elimination of IL-1 β . Microglia and splenic monocytes/macrophages were isolated by magnetic separation using anti-CD11b microbeads after 12h after priming with intraperitoneal LPS administration, *in vivo*. IL-1 β levels were measured by cytometric bead array and values expressed as pg/mg following correction for protein content. Note that only microglia but not spleen cells show a reduction in IL-1 β levels confirming the specific elimination of IL-1 β from microglia.

Figure S13

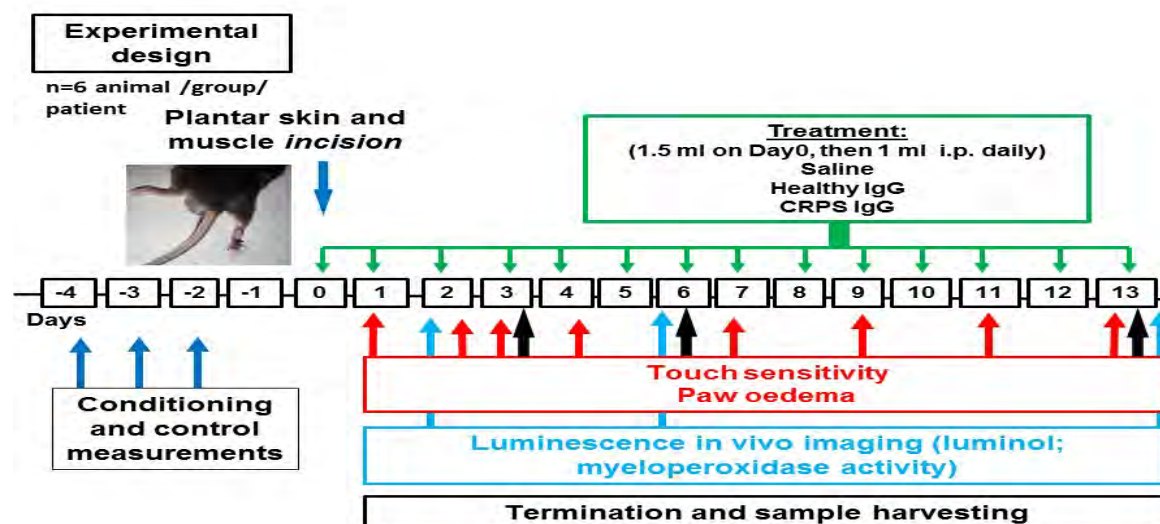


Figure S13. Scheme of the experimental paradigms and investigational techniques. i.p. intraperitoneally; IgG immunoglobulin G, black arrows indicate the time of sample harvesting for central nervous system (CNS) immunochemistry, paws were also harvested on days 1,2, and 10.

dc_2027_22

Bibliography

1. Goebel A, *et al.* (2018) Mycophenolate for persistent complex regional pain syndrome, a parallel, open, randomised, proof of concept trial. *Scandinavian Journal of Pain* 18(1):29-37.
2. Toyka KV, Brachman DB, Pestronk A, & Kao I (1975/10/24) Myasthenia gravis: passive transfer from man to mouse. *Science* 190(4212):397-399.
3. Yona S, *et al.* (2013) Fate mapping reveals origins and dynamics of monocytes and tissue macrophages under homeostasis. *Immunity* 38(1):79-91.

Role of CX3CR1 (fractalkine receptor) in brain damage and inflammation induced by focal cerebral ischemia in mouse

Ádám Dénes¹, Szilamér Ferenczi¹, József Halász², Zsuzsanna Környei³
and Krisztina J Kovács¹

¹Laboratory of Molecular Neuroendocrinology, Institute of Experimental Medicine, Budapest, Hungary;

²Department of Psychiatry, St George University Teaching Hospital, Szekesfehervar, Hungary; ³Laboratory of Cellular and Developmental Neurobiology, Institute of Experimental Medicine, Budapest, Hungary

CX3CR1 (fractalkine receptor) is important for sustaining normal microglial activity in the brain. Lack of CX3CR1 reportedly results in neurotoxic microglial phenotype in disease models. The objective of this study was to test the hypothesis that the absence of CX3CR1 worsens the outcome in cerebral ischemia. We observed significantly smaller (56%) infarcts and blood–brain barrier damage in CX3CR1-deficient (CX3CR1^{-/-}) animals compared with CX3CR1^{+/-} and wild-type mice after transient occlusion of the middle cerebral artery (MCAo). Functional recovery of CX3CR1^{-/-} animals was enhanced, while less number of apoptotic cells and infiltrating leukocytes were found in the ipsilateral hemisphere. Expression of IL-1 β mRNA, protein, and interleukin (IL)-1Ra and tumor necrosis factor (TNF)- α mRNAs was lower in CX3CR1^{-/-} mice, whereas no difference was observed in the number of IL-1 β -expressing microglia or plasma IL-1 β concentration. We observed early IL-1 β expression in astrocytes *in vivo* after MCAo and after oxygen–glucose deprivation *in vitro*, which might contribute to the ischemic damage. Our findings indicate that lack of CX3CR1 does not result in microglial neurotoxicity after MCAo, but rather significantly reduces ischemic damage and inflammation. Reduced IL-1 β and TNF α expression as well as decreased leukocyte infiltration might be involved in the development of smaller infarcts in CX3CR1^{-/-} animals.

Journal of Cerebral Blood Flow & Metabolism (2008) **28**, 1707–1721; doi:10.1038/jcbfm.2008.64; published online 25 June 2008

Keywords: CX3CR1; IL-1 β ; inflammation; microglia; mouse; transient MCAo

Introduction

The pathophysiology of ischemic stroke includes a sequence of inflammatory events that involves several central and peripheral cell types as well as large number of inflammatory molecules (McColl *et al*, 2007; Muir *et al*, 2007). Microglia are among the first candidates to contribute to ischemic damage, as these cells display very early activation in stroke and are capable of expressing potentially harmful molecules, such as interleukin (IL)-1 β ,

tumor necrosis factor (TNF)- α , and reactive oxygen species (Chong *et al*, 2005; Zheng and Yenari, 2004). Although the processes of microglial activation, proliferation, cytokine production, and phagocytosis have been studied extensively in animal models of cerebral ischemia, the exact function of these cells is not fully understood and several controversial findings have been reported. For example, inhibition of microglial activation by minocycline was shown to result in better outcome (Yenari *et al*, 2006; Yrjanheikki *et al*, 1998), whereas selective ablation of proliferating microglia worsened the outcome (Lalancette-Hebert *et al*, 2007) after experimental stroke. This might indicate that the large complexity of central ischemic processes as well as involvement of peripheral inflammatory events in stroke makes it difficult to study the exact microglial function *in vivo*.

CX3CR1 is the only known receptor of fractalkine (CX3CL1), and has been implicated in several inflammatory processes in the periphery, such as recruitment, adhesion, and vascular transmigration

Correspondence: Dr Á Dénes, Laboratory of Molecular Neuroendocrinology, Institute of Experimental Medicine, Hungarian Academy of Sciences, Szigony u. 43, Budapest H-1083, Hungary. E-mail: denesa@koki.hu

This work was supported by grants from the Hungarian Science Research Foundation (OTKA-NKTH K68574 to KJK), grant from Hungarian Ministry of Health and Welfare (ETT 300/2006 to KJK), and the Wellcome International Collaboration Award.

Received 18 February 2008; revised 20 May 2008; accepted 22 May 2008; published online 25 June 2008

of leukocytes (Imai *et al*, 1997). In the brain, neurons constitutively express high levels of the chemokine CX3CL1, which has been suggested to be responsible for sustaining normal microglial activity through interaction with microglial CX3CR1 (Biber *et al*, 2007; Hanisch and Kettenmann, 2007). It was recently shown that CX3CR1 deficiency dysregulates microglial responses, resulting in microglial neurotoxicity *in vivo* in three different disease models using transgenic mice (Cardona *et al*, 2006), in which the *cx3cr1* gene was replaced by a green fluorescent protein (GFP) reporter gene (Jung *et al*, 2000). Unlike peritoneal macrophages, microglia isolated from homozygote (CX3CR1^{-/-}) mice expressed significantly more IL-1 β in response to activation by lipopolysaccharides (LPS) than microglia derived from heterozygote (CX3CR1^{+/-}) mice (Cardona *et al*, 2006). Interleukin-1 β was shown to contribute to the formation of ischemic damage through various mechanisms (Touzani *et al*, 1999, 2002) and microglia are considered to be its primary source in the brain (Gosselin and Rivest, 2007). Therefore, we hypothesized that lack of CX3CR1 might result in increased brain damage and cell death in cerebral ischemia. To this end, we subjected CX3CR1^{-/-}, CX3CR1^{+/-} mice and their wild-type (WT) C57Bl6 littermates to transient middle cerebral artery occlusion (MCAo), to reveal the role of CX3CR1 deficiency in ischemic damage, neuronal apoptosis, and inflammation.

Materials and methods

Animals

Experiments were performed in adult male CX3CR1^{+GFP}, CX3CR1^{GFP/GFP}, and C57Bl/6H mice aged 12 to 16 weeks, weighing 26 to 28 g ($n=58$). CX3CR1/GFP mice were obtained from the European Mouse Mutant Archive (EMMA), backcrossed for more than 10 generations to C57Bl/6 (Jung *et al*, 2000). In these mice, the *cx3cr1* gene was replaced by a GFP reporter gene such that heterozygote CX3CR1^{+GFP} (CX3CR1^{+/-}) mice express GFP in cells that retain receptor function, whereas cells in homozygote CX3CR1^{GFP/GFP} (CX3CR1^{-/-}, knockout (KO)) mice are labeled with GFP and also lack CX3CR1. Animals had free access to food and water and were maintained under temperature, humidity, and light-controlled conditions (21°C \pm 1°C, 65% humidity, 12-h light/12-h dark cycle, with lights on at 0700 hours). All procedures were conducted in accordance with the guidelines set by the European Communities Council Directive (86/609 EEC) and approved by the Institutional Animal Care and Use Committee of the Institute of Experimental Medicine.

Transient Middle Cerebral Artery Occlusion

Anesthesia was induced with 2% halothane and maintained in 1% halothane-air mixture. During surgery, the

core temperature was monitored with a rectal probe and maintained at 37 \pm 0.5°C, using a homeothermic blanket. Animals were exposed to transient MCAo for 60 mins, as described previously (Wheeler *et al*, 2003). Briefly, a nylon filament (tip diameter 180 μ m) was introduced into the origin of the external carotid artery and advanced through the internal carotid artery to occlude the MCA. A total of 60 mins later, reperfusion was induced and animals were allowed to recover. Mice were subcutaneously injected with 1 mL of sterile saline daily and continuously monitored for neurologic symptoms. To investigate that heterozygote mice maintain CX3CR1 receptor function completely, they were compared with C57Bl/6 mice (having two copies of the CX3CR1 gene) after MCAo. The volume of ischemic damage and blood-brain barrier (BBB) breakdown was not different at any reperfusion intervals.

After 4, 24, or 72 h of reperfusion, mice were anaesthetized and perfused transcardially with 10 mL saline followed by 40 mL 4% paraformaldehyde (pH = 7.4). After cryoprotection of brains in 20% sucrose-KPBS for 24 h, five alternate sets of 20 μ m coronal brain sections were cut on a sliding microtome. All sections were collected in an antifreeze solution (30% ethylene glycol and 20% glycerol in phosphate-buffered saline) and stored at -20°C until processing.

Measurement of Infarct Volume

The volume of ischemic damage was measured using a modification of a method described previously (McColl *et al*, 2004). Briefly, areas of ischemic damage were identified on cresyl-violet-stained sections at eight neuro-anatomically defined coronal levels. Digitized images were created and the areas of damage measured using ImageJ software (NIH, Bethesda, MD, USA). The volume of damage was calculated by integration of areas of damage with the distance between coronal levels. The end points for integration were 2.9 mm (rostral limit) and -4.9 mm (caudal limit) regarding bregma. Volumes are expressed as a percentage of the total hemispheric volume.

Evaluation of Blood-Brain Barrier Permeability

The BBB damage was determined using a modified protocol of immunostaining for IgG (Richmon *et al*, 1998). Free floating sections were rinsed in 1% H₂O₂ for 10 mins to quench endogenous peroxidase activity, washed 3 \times in KPBS, and blocked for 1 h in KPBS containing 0.3% Triton-X-100, 2% bovine serum albumin, and 5% normal horse serum (Vector Laboratories, Burlingame, CA, USA). After overnight incubation in biotinylated horse anti-mouse IgG (1:500; Vector Laboratories) at 4°C, the sections were rinsed in KPBS and incubated in avidin-biotin horseradish peroxidase complex (ABC; Vector Laboratories) for 1 h. Staining was visualized with 3,3-diaminobenzidine tetrachloride. The volume of BBB damage was calculated as described above.

Immunofluorescence and Immunoperoxidase Labeling

Double- or triple-labeling immunofluorescence was performed on free-floating brain sections or on astroglial cell cultures. After blocking in 2% normal donkey or goat sera (Vector Laboratories), the sections were incubated overnight at 4°C in various mixtures of the following primary antibodies: monoclonal mouse anti-GFP (1:1,000; Molecular Probes, Eugene, OR, USA); polyclonal rabbit anti-Iba1 (1:1,000; Wako Chemicals, Neuss, Germany); monoclonal rat anti-mouse CD45 (1:250; Serotec, Oxford, UK); monoclonal rat anti-mouse NIMP-R14 (1:100; Hycult Biotechnology, Uden, The Netherlands); monoclonal mouse anti-GFAP (1:1,000; Sigma, Oxford, UK); polyclonal rabbit anti-glutamine synthetase (1:1,000; Sigma); polyclonal sheep anti-IL-1 β (1:500; affinity purified; NIBSC); polyclonal goat anti-IL-1 β (1:500; R&D Systems, Minneapolis, MN, USA); and polyclonal rabbit-anti Annexin V (1:500; Novus Biologicals, Littleton, CO, USA). The antigens were visualized with appropriate fluorochrome-conjugated secondary antisera (donkey anti-mouse Alexa 488, donkey anti-rabbit Alexa 488, donkey anti-mouse Alexa 594, donkey anti-rabbit Alexa 594, donkey anti-sheep Alexa 594, or donkey anti-goat Alexa 594; Molecular Probes) used in 1:500 dilutions for 2 h at room temperature. In some cases, immunostaining was visualized with an adequate biotinylated secondary antibody, followed by streptavidine-Alexa 350 or 594 conjugates. Microglial cells were also labeled with biotinylated tomato lectin (10 μ g/mL) and streptavidine-Alexa 594. Some sections were counterstained with 2 μ g/mL of diamidinophenylindole (Molecular Probes) for 1 min. Apoptotic cells were identified by using an affinity-purified antibody to detect endogenous Annexin V, which binds to phosphatidyl serine residues on the cell surface. The ratio of apoptotic neurons was evaluated by NeuN/Annexin V immunofluorescence as described by Cardona *et al* (2006). Sections were mounted onto gelatin-coated slides and coverslipped with Vectashield mounting medium (Vector Laboratories). Goat anti-IL-1 β (gIL-1 β) staining was also visualized by biotinylated rabbit anti-goat antisera and developed with 3,3-diaminobenzidine tetrachloride-nickel, with or without preincubation of gIL-1 β with 180 ng/mL recombinant mouse IL-1 β (R&D Systems).

Images were viewed using a Nikon Eclipse 6000 microscope equipped with Spot RTcolor digital camera (Diagnostic Instruments Inc., IL, USA). Confocal images were captured using Olympus BX-61 microscope. Double or triple-fluorescent images were generated using SPOT Advanced software and Adobe Photoshop. Quantification of fluorescent images and 3D reconstruction of confocal images were performed using the ImageJ software (NIH).

In Situ Hybridization Histochemistry

To monitor IL-1 β mRNA, a riboprobe complementary to 373 to 940 nucleotides of the mouse IL-1 β gene was transcribed from plasmid in the presence of ³⁵S-UTP. Hybridization and autoradiographic techniques were

modified following the method described by Simmons *et al* (1989). Tissue sections were mounted onto SuperFrost Ultra Plus (Menzer-Glazer) slides post-fixed with 4% paraformaldehyde, digested with Proteinase K (10 in 50 mmol/L Tris, pH = 8 and 5 mmol/L EDTA at 37°C, 5 mins), acetylated (0.25% acetic anhydride in 0.1 mol/L triethanolamine, pH = 8), and dehydrated. Hybridization mixture (50% formamide, 0.3 mol/L NaCl, 10 mmol/L Tris (pH = 8), 2 mmol/L EDTA, 1 \times Denhardt's, 10% dextran sulfate, 0.5 mg/mL yeast tRNA) was pipetted onto the slides (100 μ L, containing probe at 10⁷ d.p.m./mL) and hybridized overnight at 56°C. Sections were then rinsed in 4 \times SSC (1 \times SSC: 0.15 mol/L NaCl and 15 mmol/L trisodiumcitrate buffer, pH = 7), digested with ribonuclease A (20 mg/mL in Tris-EDTA buffer with 0.5 mol/L NaCl at 37°C for 30 mins), gradually desalted, and washed in 0.1 \times SSC at 65 to 75°C for 30 mins. Slides were dipped in NTB nuclear emulsion (Kodak) and exposed for 2 weeks, developed in D-19 developer, and lightly counterstained with cresyl violet.

Adhesive Removal Test

The motor response to sensory stimuli was measured with a stimulation test developed for rats (Marshall and Gotthelf, 1979; Schallert *et al*, 1983) and adopted for mice (Fleming *et al*, 2004). Small adhesive stimuli (50 mm²) were placed on the snout of the mouse in their home cages. The behavior was video-recorded and later analyzed by an observer blind to the treatment schedules. The following behavioral variables were assessed: the time to remove the stimulus and the number of attempts for tape removal. To remove the stimulus, animals would raise both forelimbs toward their face and swipe off the stimulus with both forepaws. Typically, both intact WT, CX3CR1 +/–, and CX3CR1 –/– mice make contact and remove the stimulus within 15 secs, without differences according to genotype. Each animal ($n = 4$ /group) was tested 24, 48, and 72 h after MCAo. If the animal did not remove the stimulus within 60 secs, the experimenter removed it and the trial for the next mouse was initiated. On each experimental day, the average performance of three trials was calculated and used for later statistical analysis. The intertrial interval differed between 12 and 15 mins for the experimental subjects.

Sample Preparation and IL-1 β ELISA

Blood samples were routinely collected from the right heart ventricle before transcatheter perfusion (4, 24, and 72 h after MCAo) in the presence of K-EDTA (10 μ L of 20% K-EDTA/1 mL blood). Samples were centrifuged at 8,000 r.p.m., aliquoted, and stored at –20°C.

Brain homogenates were prepared from CX3CR1 –/– and +/– mice ($n = 5$ /group) 24 h after 60 mins MCAo. One mouse among the CX3CR1 +/– mice was excluded from further analysis because of surgical artifact. Animals were anaesthetized and the chest was opened. After blood sampling from the right ventricle, the brain was removed and immediately frozen in dry ice. The brainstem and

cerebellum were removed, and the forebrain was dissected into hemispheres. The cortex was separated around the corpus callosum. To preserve the whole striatum, majority of the hypothalamus and thalamus was removed from the rest of the hemisphere. Brain samples of 50 mg were homogenized in 300 μ L of sterile phosphate-buffered saline (pH=7.4) containing protease inhibitors (Complete Mini; Roche, Mannheim, Germany), sonicated for 30 secs on ice, and centrifuged at 13,000 r.p.m. Supernatants were stored at -70°C until ELISA or quantitative real-time PCR measurement.

The concentration of IL-1 β peptide in plasma samples and brain homogenates was measured using mouse IL-1 β /IL-1F2 DuoSet kit (DY401; R&D Systems) according to the manufacturer's recommendations. Samples were diluted 1:1 in Tris-buffered saline (20 mmol/L Trizma base, 150 mmol/L NaCl, pH=7.4) containing 0.1% bovine serum albumin and 0.05% Tween 20.

Quantitative Real-Time PCR

Total RNA was isolated from homogenates (same samples as used for IL-1 β ELISA) of the ipsilateral-contralateral striatum and cortex, using RNeasy Mini Kit (Qiagen, Valencia, CA, USA) and then converted to cDNA by high-capacity cDNA reverse transcription kit (Applied Biosystems, Foster City, CA, USA). Real-time PCR was performed using Power SYBR Green PCR Master Mix (Applied Biosystems) on ABI StepOne instrument according to the manufacturer's instructions. Primers used for the comparative C_T experiments were designed by the Primer Express 3.0 program. Gene expression was analyzed by ABI StepOne program. Primer sequences for the following genes are

GAPDH:

(f) TGACGTGCCGCCTGGAGAAA

(r) AGTGTAGCCCAAGATGCCCTTCAG

IL-1 β :

(f) TTGACGGACCCCAAAGATG

(r) TGGACAGCCCAGGTCAAAG

IL-1Ra:

(f) CTTTACCTTCATCCGCTCTGAGA

(r) TCTAGTGTGTGCAGAGGAACCA

TNF α :

(f) CAGCCGATGGGTTGTACCTT

(r) GGCAGCCTTGTCCTTGA

GAPDH message was used as internal control. Relative quantity of mRNAs was referred to corresponding brain sites of an intact CX3CR1 $-/-$ mouse. Melting curve analysis to confirm the identity of PCR products had been performed by using StepOne instrument's Software v.2.0 according to the instructions of the manufacturer.

Astroglial and Microglia-Enriched Cultures

Astrocytes were isolated from the forebrains of neonatal (P2) CD1 mice and transgenic mice expressing eGFP under the control of human GFAP promoter (Nolte *et al.*, 2001) or

in knockin constructs within the CX3CR1 gene (Jung *et al.*, 2000). Meninges were removed and the tissue was minced with razor blades. The tissue pieces were subjected to enzymatic dissociation, using 0.05% w/v trypsin and 0.05% w/v DNase I (Sigma) for 10 mins at room temperature. The cells were plated onto poly-L-lysine-coated plastic surfaces and grown in MEM supplemented with 10% fetal calf serum, 4 mmol/L glutamine, and 40 μ g/mL gentamycin (Sigma) in humidified air atmosphere containing 5% CO $_2$ at 37 $^{\circ}\text{C}$. The culture medium was changed on the first 2 days and thereafter every second to third day. Confluent primary cultures were harvested by trypsinization and subjected to fluorescence-activated cell sorting (FACS) to eliminate microglial contamination. Microglia-enriched cultures from CX3CR1 $-/-$ and $+/-$ mice were obtained by sorting microglial cells (see below) from glial cultures prepared in the same way as described above. Cells were grown in the same media as used for astrocyte cultures.

Fluorescence-Activated Cell Sorting

Flow cytometry was undertaken using FACS Vantage flow cytometry analysis system (BD Biosciences). Single-cell suspensions were first gated on forward scatter, and, subsequently, within this population based on GFP expression. Non-GFP-expressing cells were used as negative control for background fluorescence. To obtain microglia-enriched cultures, GFP-positive microglia from CX3CR1 $-/-$ and $+/-$ glial cultures were sorted by FACS 3 days before oxygen-glucose deprivation (OGD). To optimize survival of microglial cells after separation by FACS, cultures contained 7% to 10% of astrocytes.

To obtain pure astroglial cultures, we used two different approaches. In the first series of experiments, we used astrocytic cultures prepared from CX3CR1 $+/-$ mice (Jung *et al.*, 2000). The contaminating microglial (GFP-positive) cells were removed from the cultures by fluorescent cell sorting. In the second set of experiments, cultures were prepared from the forebrains of hGFAP-GFP mice (Nolte *et al.*, 2001). Astrocytes expressing GFP were subjected to FACS before the experiments. In this way, we eliminated microglial cells in two different ways from the astrocytic cultures. The sorted hGFAP-GFP-positive or CX3CR1-negative cells were replated onto poly-L-lysine-coated dishes. The purified cultures reached confluency within 3 days when they were used for determination of IL-1 β production in response to OGD.

Oxygen-Glucose Deprivation on Microglia-Enriched Cultures and on Cultured Astrocytes

Culture medium was replaced with sterile, deoxygenated HEPES (145 mmol/L NaCl, 3 mmol/L KCl, 1 mmol/L MgCl $_2$, 2 mmol/L CaCl $_2$, 10 mmol/L HEPES; 288 to 300 mOsm, pH=7.2) without glucose, or with HEPES supplemented with 10 mmol/L glucose (control cultures). Astrocyte cultures were then placed into an airtight incubating chamber, flushed with a gas mixture of 94% N $_2$, 5% CO $_2$, and 1% O $_2$ for 15 mins, and the chamber was

closed and the cultures incubated for 3 h at 37°C. At the end of OGD, incubation medium (HEPES) was collected and the cultures were incubated in MEM. Supernatants from astrocyte cultures were collected 4 and 24 h after OGD and stored at -70°C. Astrocytes were harvested 4 and 24 h after hypoxia, centrifuged at 2,000 rpm, and placed in sterile phosphate-buffered saline (pH=7.4) containing protease inhibitors (Complete Mini; Roche). Samples were then sonicated for 30 secs and stored at -70°C before IL-1 β ELISA. Microglia-enriched cultures were harvested 4 h after 3 h of OGD and samples were treated as described above.

Statistical Analysis

Statistical analysis was performed using Student's *t*-test or one-way ANOVA (analysis of variance) followed by Bonferroni's *post hoc* test. Behavioral data were analyzed by repeated-measure ANOVA (the two factors were genotype and time). Where interaction between the two factors was observed, Fischer LSD *post hoc* comparisons were also run.

Results

Absence of CX3CR1 Results in Significantly Smaller Infarct Size, which is Associated with Smaller BBB Damage

Four hours after MCAo, mild pathologic changes were observed in the ipsilateral striatum of cresyl-violet-stained brain sections. Loss of staining intensity was obvious in the lateral globus pallidus in CX3CR1 $-/-$, CX3CR1 $+/-$, and C57Bl6 (WT) animals. Blood-brain barrier damage identified by using immunostaining to mouse IgG was seen in the striatum as early as 4 h after MCAo, whereas one-third of CX3CR1 $+/-$ and C57Bl6 mice displayed IgG labeling in some part of the ipsilateral cerebral cortex.

After 24 h of reperfusion, 23.1% \pm 3.3% of the ipsilateral hemisphere displayed ischemic damage in CX3CR1 $-/-$ mice, compared with 36.0% \pm 4.7% and 33.8% \pm 5.9% in CX3CR1 $+/-$ and WT animals, respectively (Figure 1A). The BBB breakdown at 24 h of reperfusion was smaller in CX3CR1 $-/-$ mice than that seen in CX3CR1 $+/-$ mice (Figure 1B). Data were not significantly different at the 24-h time point using one-way ANOVA followed by Bonferroni's *post hoc* test.

A total of 72 h after MCAo, the volume of ischemic damage assessed by cresyl violet staining was significantly smaller in CX3CR1 $-/-$ mice than in mice expressing the fractalkine receptor ($P < 0.05$; 25.8% \pm 4.0% in CX3CR1 $-/-$ mice versus 45.6% \pm 2.2% in CX3CR1 $+/-$ and 47.4% \pm 2.9% in WT mice). In heterozygous and WT mice, 60% to 90% of the ipsilateral cerebral cortex in the territory of the MCA, as well as 50% to 70% of the ipsilateral hippocampus and thalamus, became ischemic by

72 h after MCAo, and sometimes the damage was also extended to the lateral hypothalamus (Figure 1C). In contrast, only two out of six CX3CR1 $-/-$ animals displayed ischemic damage in the hippocampus and thalamus, and the extent of cortical infarct was also significantly smaller. Corresponding to the ischemic damage, integrity of BBB was seriously affected in 50% to 90% of the ipsilateral cortex, thalamus, and hippocampus in all mice having functional CX3CR1, whereas in three out of six CX3CR1 $-/-$ animals, BBB damage was confined to the striatum and the hippocampus, the thalamus being only partially affected in the rest of the CX3CR1 $-/-$ animals (Figure 1D). A total of 72 h after MCAo, the volume of BBB damage in CX3CR1 $-/-$ mice was significantly smaller (28.0% \pm 6.61%) compared with CX3CR1 $+/-$ (54.5% \pm 4.1%) and WT (45.7 \pm 1.8) animals. To investigate if CX3CR1 deficiency had any direct effect on BBB disruption after MCAo, values of BBB damage were normalized to the infarct size. Values of BBB damage/ischemic damage ratio were between 0.88 and 1.19 in all groups, and no significant differences were observed among CX3CR1 $-/-$, CX3CR1 $+/-$, and WT animals (1.00 \pm 0.12, 1.07 \pm 0.11, and 0.88 \pm 0.06 after 24 h and 1.09 \pm 0.1, 1.19 \pm 0.21, and 0.96 \pm 0.19 after 72 h of MCAo). These results indicate that fractalkine receptor deficiency had no direct effect on BBB disruption after MCAo.

CX3CR1 $-/-$ Mice Exhibit Lower Number of Apoptotic Cells in the Brain After MCAo, Compared with Animals Expressing CX3CR1

Annexin V immunohistochemistry was used to investigate whether marked CX3CR1-dependent differences seen in the size of ischemic damage and BBB breakdown are associated with different numbers of apoptotic cells in the brains of CX3CR1 $-/-$ and CX3CR1 $+/-$ animals.

A total of 4 h after MCAo, only occasional Annexin V labeling was observed in the ipsilateral cerebral cortex in both genotypes and rarely in the striatum. Ependymal cells displayed Annexin V staining in the lateral and sometimes in the third ventricle.

A total of 24 h after MCAo, more Annexin V-positive cells were found in heterozygote mice than in CX3CR1 $-/-$ mice, except for the ischemic striatum, where the number of apoptotic cells was relatively low. Annexin V-positive cells appeared in the ischemic cortex (207 \pm 134 cells/mm² in CX3CR1 $-/-$; 624 \pm 443 cells/mm² in CX3CR1 $+/-$ mice) and several cells were observed in the nonischemic penumbral cortex as well as in the piriform area (Figures 2A and 2B). Marked differences were observed in the left hippocampus and the thalamus between the two genotypes (20 \pm 33 versus 199 \pm 127 cells/mm² in the hippocampus;

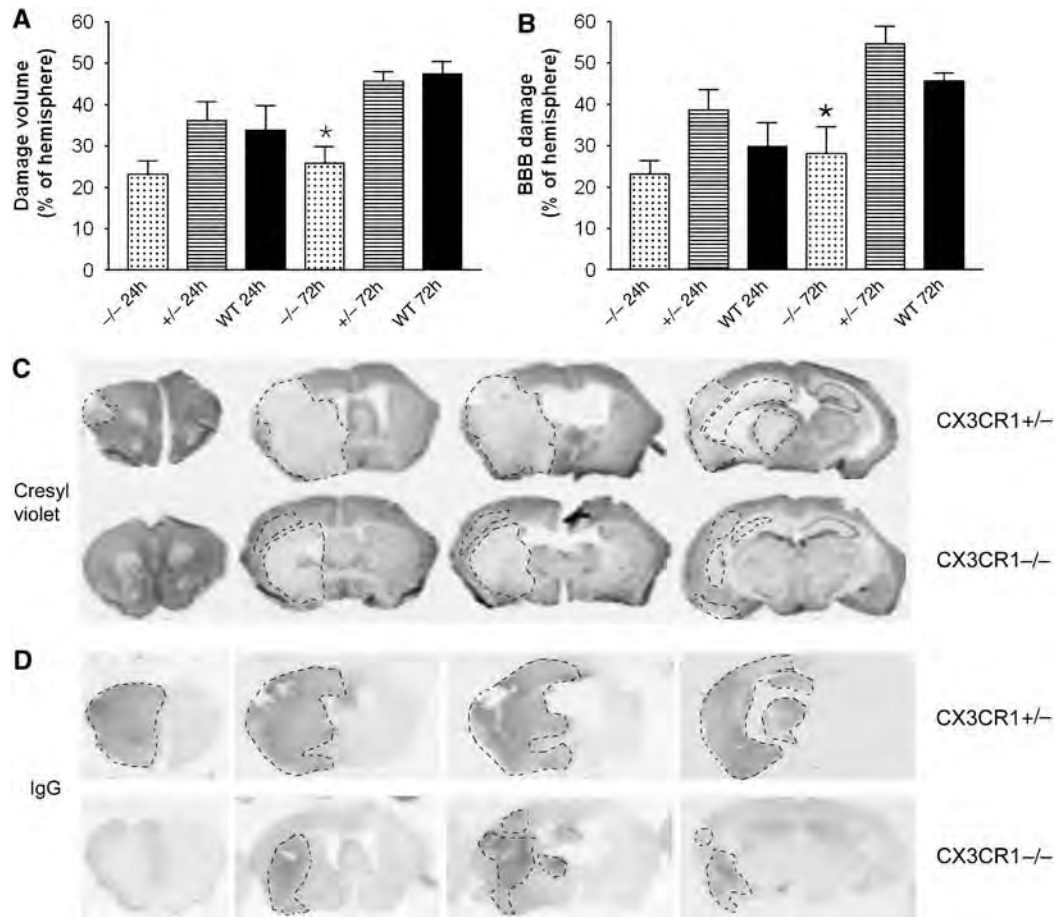


Figure 1 CX3CR1^{-/-} mice have smaller infarct size compared with mice expressing CX3CR1, which is associated with reduced BBB damage. **(A)** The mean \pm s.e.m. values of ischemic damage are shown according to the loss of cresyl violet staining 24 and 72 h after MCAo. The volume of ischemic damage is expressed as the percent of total hemispheric volume. CX3CR1^{-/-} mice (-/-) have significantly smaller infarcts at 72 h of reperfusion than do CX3CR1^{+/-} (+/-) and WT animals (* $P < 0.05$; -/- versus +/- and WT). **(B)** Corresponding to smaller infarcts, the mean volume of BBB breakdown, identified by IgG leakage to the brain parenchyma, is similarly smaller in CX3CR1^{-/-} animals compared with mice expressing CX3CR1. **(C)** Bright field photographs showing damaged areas 72 h after MCAo in cresyl violet-stained brain sections. Although +/- and WT mice exhibit large infarct in the majority of the ipsilateral cerebral cortex, hippocampus, and thalamus, only a part of the cortex becomes ischemic in CX3CR1^{-/-} animals and only occasional damage is seen in the hippocampus or thalamus. The rostro-caudal extent of the damage is also smaller in the case of -/- mice compared with mice expressing CX3CR1. **(D)** At 72 h, in heterozygote and WT mice, BBB damage (as revealed by IgG immunostaining) is seen in the majority of the ipsilateral hemisphere, whereas in CX3CR1^{-/-} animals, it is confined to the striatum.

57 \pm 66 versus 564 \pm 168 cells/mm² in the thalamus of CX3CR1^{-/-} and CX3CR1^{+/-} mice, respectively ($P < 0.05$)).

At 72 h of reperfusion, the number of Annexin V-positive cells was much lower than that seen at 24 h (not shown). Late cellular death was observed mainly in the ipsilateral cerebral cortex and thalamus in heterozygote mice, whereas only two out of six CX3CR1^{-/-} mice displayed Annexin V labeling in these areas.

To reveal the phenotype of apoptotic cells, Annexin V immunostaining was colocalized with tomato lectin, CD45, GFAP, GFP, and NeuN markers. Annexin V labeling was colocalized with NeuN in 40% to 70% of apoptotic cells. (Figure 2C). However, more intensive Annexin V-immunostaining was often accompanied with the reduction or complete loss of NeuN immunopositivity. Annexin V

labeling was also seen in some microglial cells, astrocytes, and CD45-positive leukocytes and was often associated with tomato lectin-positive vascular elements (not shown).

In both CX3CR1^{-/-} and heterozygote mice, microglia were consequently found attached to Annexin V-positive cells. High-resolution confocal microscopy revealed that microglia extended its processes toward apoptotic cells sometimes from a relatively large distance (Figure 2D; see Supplementary Video).

Adhesive Removal Test Indicates Better Recovery in KO Mice After MCAo

The number of attempts to remove the stimulus showed genotype-specific differences (Figure 3).

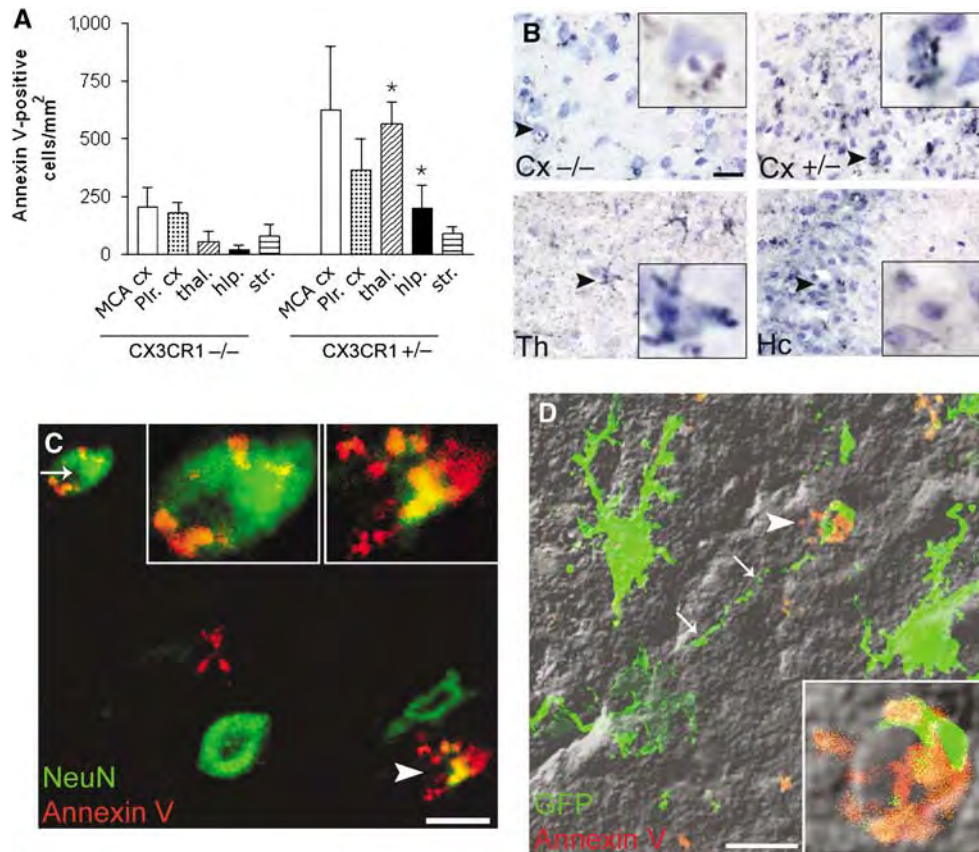


Figure 2 CX3CR1 +/– mice have more Annexin V-positive cells in the ipsilateral hemisphere after MCAo. **(A)** A total of 24 h after MCAo, more Annexin V cells are present in the left cerebral cortex, thalamus, and hippocampus of heterozygote mice than in that of CX3CR1 –/– animals, whereas no difference can be observed in the striatum. * $P < 0.05$; Bonferroni's *post hoc* comparison after one-way ANOVA. **(B)** Annexin V immunohistochemistry with cresyl violet counter-staining reveals apoptotic cells in the ipsilateral cerebral cortex of CX3CR1 –/– (Cx –/–) and CX3CR1 +/– (Cx +/–) mice (top photographs). In the thalamus (Th, lower left picture) and hippocampus (Hc, lower right picture) of CX3CR1 +/– animals, several Annexin V-positive cells are found at 24 h of reperfusion. Arrowheads point toward cells appearing in the insets at higher magnification. **(C)** Apoptotic neurons (NeuN, green) in the ipsilateral cerebral cortex display Annexin V labeling (red, arrow). More intensive Annexin V-staining is often associated with the loss or reduction of NeuN immunopositivity (arrowhead). **(D)** Three dimensional reconstruction of stacks of confocal images using the volume-rendering method, Volume J (Image J), with DIC. The GFP-positive CX3CR1 +/– microglia extending processes (arrows) toward an apoptotic cell (arrowhead). Inset showing the Annexin V-positive cell indicated with the arrowhead at a different Z position. Scale bars: 10 μm (C, D), 20 μm (B).

CX3CR1 –/– animals made a faster and more pronounced recovery after MCAo compared with heterozygote control ones. The overall difference between mice with different genetic background reached significance ($F_{\text{genotype}(1,6)} = 4.326$, $P < 0.083$), the repeated-measure factor ($F_{\text{time}(2,12)} = 5.148$, $P < 0.03$), and the interaction between the factors were significant ($F_{\text{interaction}(2,12)} = 4.469$, $P < 0.04$). With *post hoc* test, compared with the first post-operative day, when the number of attempts for tape removal was very low, CX3CR1 –/– but not heterozygote animals showed a pronounced increase in the number of attempts, indicating a less-severe impairment and faster recovery after MCA manipulation in CX3CR1 –/– animals.

The adhesive removal latencies tended to be lower in the CX3CR1 –/– group compared with the heterozygote animals, but were not significant

($F_{\text{genotype}(1,6)} = 2.271$, $P < 0.18$; $F_{\text{time}(2,12)} = 1.337$, $P < 0.30$; $F_{\text{interaction}(2,12)} = 1.522$, $P < 0.26$). By the third postoperative day, half of the CX3CR1 –/– animals were able to remove the adhesive tape compared with none in the heterozygote group.

GFP/CD45-Staining Reveals Less-Infiltrating Leukocytes in the Ipsilateral Hemisphere after MCAo in CX3CR1 –/– Mice

The GFP-positive microglia in CX3CR1 –/– and +/– mice were colocalized with Iba1 and tomato lectin in all animals examined, and the microglial expression of CD45 and CD34 markers increased in the ipsilateral hemisphere after MCAo. Astrocytes expressing GFAP or glutamine synthetase as well as neurons identified by NeuN expression were not positive to GFP in intact mice and in mice subjected

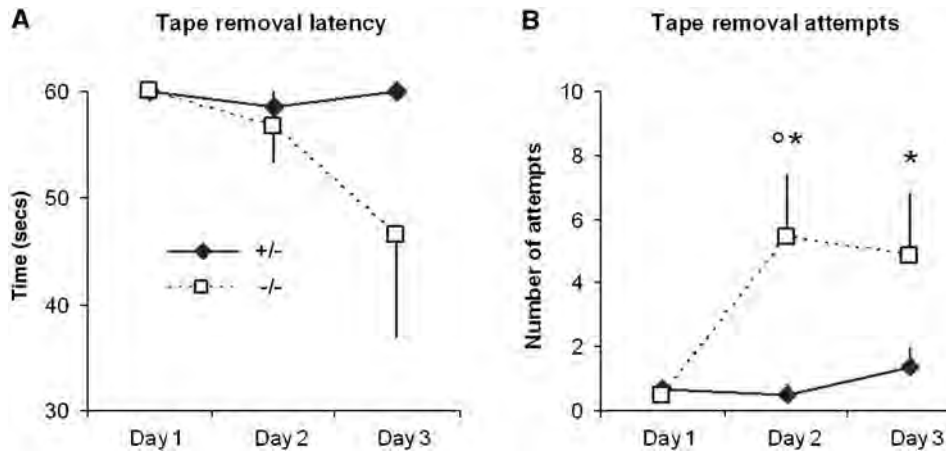


Figure 3 The sensorimotor performance of mice with different CX3CR1 background after MCAo. The adhesive removal test was performed on postoperative days 1, 2, and 3. Both the adhesive removal latency (**A**) and the number of attempts for tape removal (**B**) indicate a more pronounced recovery of CX3CR1^{-/-} animals compared with heterozygotes. *Significantly different from Day 1 ($P < 0.05$). °Different from heterozygote control ($P < 0.08$).

to MCAo (not shown), confirming previous observations by others (Cardona *et al*, 2006).

To reveal infiltrating leukocytes in the brains of CX3CR1^{-/-} and CX3CR1^{+/-} mice, CD45 immunostaining was used, which labels all leukocyte populations, including resident microglia of hematopoietic origin. CD45/GFP-positive microglia and macrophages are thereby discriminated from potentially infiltrating other leukocytes negative to CX3CR1 (GFP), which include mature neutrophils, eosinophils, T and B lymphocytes as well as most of the natural killer cells (Jung *et al*, 2000).

Microglia become widely activated in both genotypes after MCAo in the ipsilateral hemisphere. There was no significant difference in the phenotype and the number of GFP⁺/CD45⁺ microglia and macrophage cells between CX3CR1^{-/-} and ^{+/-} animals in the ipsilateral hemisphere 24 h after MCAo. In contrast, the microglial cell number was significantly higher in the ipsilateral cerebral cortex of CX3CR1^{-/-} animals (Figure 4A) than in that of heterozygote mice 72 h after MCAo (346 ± 58 versus 221 ± 57 cells/mm², respectively; $P < 0.05$).

A total of 72 h after MCAo, both in ipsilateral cerebral cortex and striatum, CX3CR1^{-/-} mice had significantly less GFP⁻/CD45⁺ leukocytes (Figures 4B–4E) than CX3CR1^{+/-} animals (11.6 ± 7.7 versus 38.6 ± 9.2 cells/mm² in the cortex and 14.8 ± 12.3 versus 54.5 ± 25.6 cells/mm² in the striatum, respectively; $P < 0.05$). About 50% to 70% of CD45⁺/GFP⁻ leukocytes were neutrophils, expressing the NIMP marker (not shown).

IL-1 β Production is Blunted in the Brain of CX3CR1^{-/-} Mice after MCAo: a Possible Role for Astrocytes

IL-1 β in plasma samples: Plasma IL-1 β levels did not show any difference among CX3CR1^{-/-}, CX3CR1^{+/-}, and C57Bl6 mice in either the 4, 24, or 72 h

reperfusion intervals after MCAo. Only half of the animals (irrespective of genotype) had a detectable amount of IL-1 β in the plasma samples after 4 and 24 h of reperfusion between 11.4 and 18.5 pg/mL and between 9.8 and 29.5 pg/mL, respectively. After 72 h of reperfusion, IL-1 β was detectable only in 20% to 40% of the animals.

Microglial IL-1 β production after MCAo: Using two different affinity-purified antibodies against IL-1 β , we could not detect microglial cells expressing IL-1 β in the brain 4 h after MCAo. A total of 24 h after ischemia, a relatively low number of IL-1 β -positive microglia (not exceeding 15% of the total in either brain section) was detected in the ipsilateral cerebral cortex in both genotypes (Figures 5A, 5B, and 6A), and some of these cells were also seen in the ipsilateral thalamus and hippocampus in both genotypes. The average cell number was not significantly different between CX3CR1^{-/-} and ^{+/-} mice (14.4 ± 14.2 versus 7.7 ± 10.1 cells/mm² with sheep anti-IL-1 β ; 10.8 ± 8.1 versus 5 ± 7.3 cells/mm² with goat anti-IL-1 β antibody, respectively) in the cortex, and IL-1 β -positive microglia were just occasionally observed in the ischemic striatum. *In situ* hybridization revealed IL-1 β -expressing cells in the ipsilateral hemisphere at 24 h of reperfusion. In the ipsilateral cerebral cortex, the location and average number of cells containing elevated IL-1 β mRNA (Figure 6B) corresponded to microglia showing IL-1 β immunofluorescence (Figure 6A).

By 72 h after MCAo, the number of IL-1 β -positive microglia did not exceed 2 to 5 cells/mm². No IL-1 β -positive microglia were observed in the contralateral hemisphere.

IL-1 β expression in brain homogenates: ELISA measurement revealed high IL-1 β peptide levels 24 h after MCAo in the ipsilateral (left) hemisphere (Figure 5C). CX3CR1^{-/-} mice exhibited signifi-

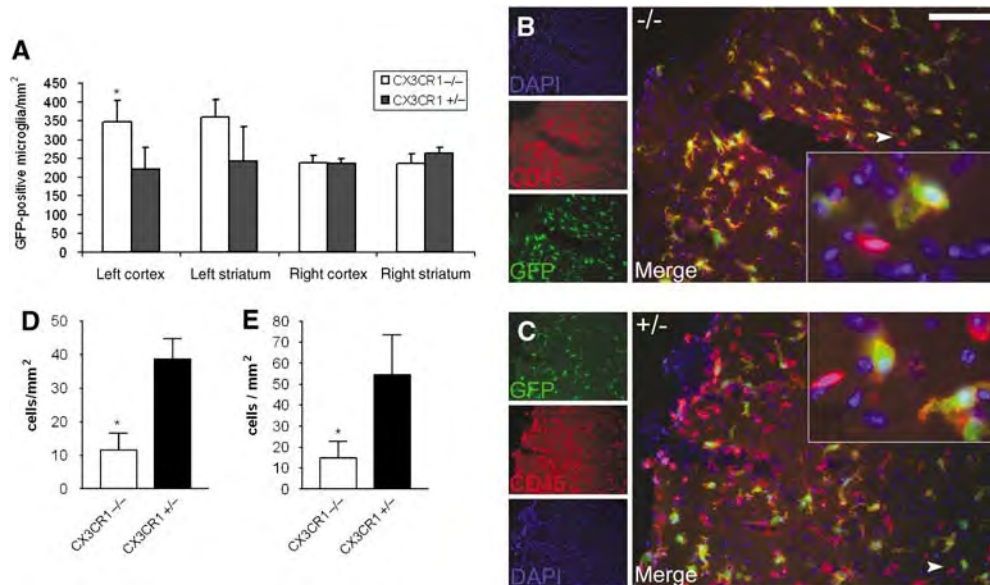


Figure 4 CX3CR1^{-/-} mice have more microglia and less infiltrating CD45-positive leukocytes in the brain after MCAo. The figure shows the amount of GFP-positive microglia and CD45-positive/GFP-negative (possibly infiltrating) leukocytes in the ischemic hemisphere 72 h after MCAo. **(A)** CX3CR1 knockout mice display more GFP-positive microglia in the ipsilateral cerebral cortex and striatum than do CX3CR1^{+/-} mice, whereas no difference is observed in the contralateral hemisphere. **(B)** In CX3CR1^{-/-} mice, only some GFP⁻/CD45⁺ (red) leukocytes are found in the ipsilateral cerebral cortex, and several GFP/CD45 double-positive microglial (macrophage) cells are seen at 72 h of reperfusion. **(C)** In CX3CR1^{+/-} animals, less microglia and more GFP⁻/CD45⁺ leukocytes are observed in the ipsilateral cerebral cortex at 72 h of reperfusion. **(D, E)** Graphs showing the average number (mean \pm s.e.m.) of GFP⁻/CD45⁺ leukocytes in the brain of CX3CR1^{-/-} and CX3CR1^{+/-} mice 72 h after MCAo. GFP⁻/CD45⁺ leukocyte numbers are significantly lower in CX3CR1^{-/-} mice in the ipsilateral cerebral cortex **(D)** and in the ischemic striatum **(E)** compared with CX3CR1^{+/-} mice. * $P < 0.05$. Scale bar: 100 μ m.

cantly lower amount of IL-1 β compared with CX3CR1^{+/-} animals in the left striatum (245 ± 125 versus 1025 ± 289 pg/mL, respectively; $P < 0.05$). This difference was also seen in the left cortex (330 ± 192 versus 1526 ± 1048 pg/mL, respectively). Elevated IL-1 β peptide levels were also observed in the contralateral hemisphere in both genotypes after MCAo. Real-time PCR measurement revealed increased IL-1 β mRNA levels in the ipsilateral hemisphere 24 h after MCAo. CX3CR1^{-/-} mice showed a blunted elevation of IL-1 β mRNA after MCAo, compared with CX3CR1^{+/-} mice (Figure 5D). The difference was significant in the left striatum (7.6 ± 2 -fold increase in CX3CR1^{-/-} versus 83.1 ± 23 -fold increase in heterozygote mice; $P < 0.05$). Elevation of IL-1 β mRNA after MCAo was also observed in the contralateral striatum and cortex in both genotypes compared with control (2.7 ± 0.7 in CX3CR1^{-/-} versus 9.6 ± 10.4 -fold increase in heterozygote in the right striatum, and 1.3 ± 0.3 in CX3CR1^{-/-} versus 2.7 ± 0.6 -fold increase in heterozygote in the right cortex).

Because the very low number of IL-1 β -positive microglia found in the ipsilateral striatum, as well as the complete absence of these cells in the contralateral hemisphere, did not explain the results of IL-1 β ELISA and real-time PCR measurements of brain homogenates, we investigated the possibility of IL-1 β production by astrocytes.

IL-1 β expression in astrocytes: As early as 4 h after MCAo, IL-1 β -expressing GFP-negative cells were observed in the ipsilateral hemisphere in both CX3CR1 genotypes as well as in WT mice. A population of these cells located in the caudal striatum (sometimes near the ependyma of the lateral ventricle; Figure 6C) and the corpus callosum appeared to be GFAP- or glutamine synthetase-positive. Elongated IL-1 β -positive cells were seen in the capsula interna, thalamus, and in the ventricular part of the dorsal ipsilateral thalamus and hippocampus expressing GFAP or glutamine synthetase (not shown). Some cells expressing IL-1 β mRNA were also observed in these brain sites (Figure 6D).

A total of 24 h after MCAo, gIL-1 β -positive astrocytes were seen in the ipsilateral hippocampus (Figure 6E) and thalamus in three out of five CX3CR1^{+/-} mice, which were only seen in one CX3CR1^{-/-} animal. To confirm the specificity of labeling, gIL-1 β antibody was preabsorbed with 180 ng/mL recombinant mouse IL-1 β peptide before overnight incubation. Preabsorption prevented both astrocyte- and microglia-like IL-1 β immunostaining in the brain parenchyma (Figure 6F) at 24 h, but was able to prevent cellular staining in 50% astrocyte-like cells at 4 h. Neuronal-like gIL-1 β staining was also observed 24 h after MCAo, even on the contralateral hemisphere, which was absent if

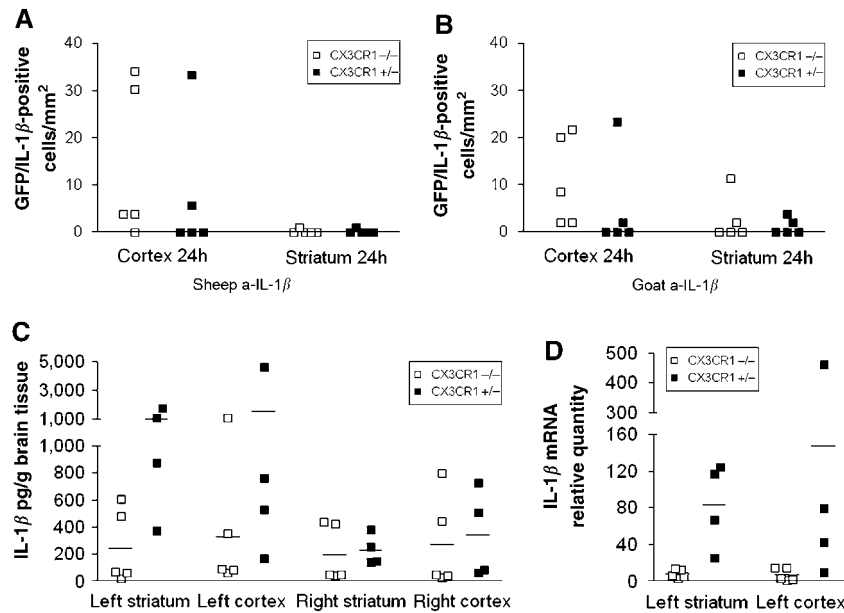


Figure 5 Interleukin-1 β in microglia and in brain homogenates after MCAo. The figure shows the expression of IL-1 β in microglia and the amount of IL-1 β peptide and mRNA in brain homogenates of CX3CR1 $^{-/-}$ and CX3CR1 $^{+/-}$ mice after MCAo. (A, B) Quantification of IL-1 β -positive microglia on brain sections of CX3CR1 $^{-/-}$ and $^{+/-}$ mice 24 h after MCAo, using sheep anti-IL-1 β antibody (A, sIL-1 β) or goat anti-IL-1 β antibody (B, gIL-1 β). Squares represent the average number of microglia in individual animals. (C) The amount of IL-1 β peptide was measured with ELISA from homogenates of the ipsilateral (left) and contralateral (right) striatum and cortex 24 h after MCAo. Squares represent the amount of IL-1 β in individual animals. (D) Graph showing the relative quantity of IL-1 β mRNA determined by real-time PCR in the same brain homogenates of the ipsilateral striatum and cortex as used for IL-1 β peptide measurement. (C) Squares represent the fold increase of IL-1 β mRNA in individual mice after MCAo compared with corresponding brain sites of an intact CX3CR1 $^{-/-}$ mouse.

preabsorption with recombinant mouse IL-1 β was performed.

IL-1 β expression *in vitro* after OGD in microglia-enriched cultures and in astrocytes: To investigate microglial IL-1 β expression *in vitro*, microglia-enriched cultures were prepared (Figure 7A). A total of 4 h after OGD, elevated IL-1 β expression was observed in cell lysates of microglia-enriched cultures derived from CX3CR1 $^{-/-}$ and CX3CR1 $^{+/-}$ mice compared with control cultures. Culture supernatants (MEM) were devoid of IL-1 β peptide 4 h after OGD, and only slight increase was observed in the incubation media (HEPES) compared with control cultures. No significant difference in IL-1 β production was observed in cell lysates between CX3CR1 $^{-/-}$ and CX3CR1 $^{+/-}$ microglia-enriched cultures (Figure 7B). To confirm early astrocytic IL-1 β expression after OGD, astrocyte cultures were prepared from GFP/GFAP, CX3CR1 $^{+/-}$, and CD1 mice. The IL-1 β peptide was not detected in culture supernatants (MEM) 4 h after OGD, but incubation media (HEPES) taken minutes after the end of 3 h of hypoxia contained 15 to 30 pg/mL IL-1 β in different cultures. Cell lysates of astrocytes contained elevated IL-1 β levels compared with controls (Figure 7C) 4 h after OGD. Sorting GFP-positive astrocytes (from cultures derived from GFP/GFAP mice) or removing GFP-positive microglia (from cultures

derived from CX3CR1 $^{+/-}$ mice) by FACS to get very pure astrocyte cultures did not have any effect on IL-1 β production at 4 h, indicating that IL-1 β production was not because of microglial contamination. Immunofluorescence revealed a few IL-1 β /GFAP-positive astrocytes in GFP/GFAP and CX3CR1 $^{+/-}$ cultures, but more IL-1 β /GFAP-positive cells were detected in CD1 astrocyte cultures 4 h after OGD (Figures 7D and 7E). A population of IL-1 β -expressing cells was not positive to GFAP but was labeled with glutamine synthetase, an alternative marker for astrocytic cells. 24 h after OGD, cell lysates contained more IL-1 β compared with 4 h in both GFP/GFAP and CX3CR1 $^{+/-}$ astroglial cultures (75 and 103 pg/mL, respectively).

Quantitative Real-Time PCR Measurement Reveals Elevated Levels of IL-1Ra and TNF α mRNA after MCAo in CX3CR1 $^{+/-}$ Mice

A total of 24 h after MCAo, IL-1Ra and TNF α mRNA expression was increased in brain homogenates of CX3CR1 $^{+/-}$ mice compared with CX3CR1 $^{-/-}$ animals both in the ipsilateral striatum and cortex (Figures 8A–8D). Irrespective of the CX3CR1 genotype, significant correlation was observed between IL-1 β and IL-1Ra and TNF α mRNA levels ($P < 0.001$). The level of TNF α mRNA was also elevated in mice expressing higher amount of IL-1 β .

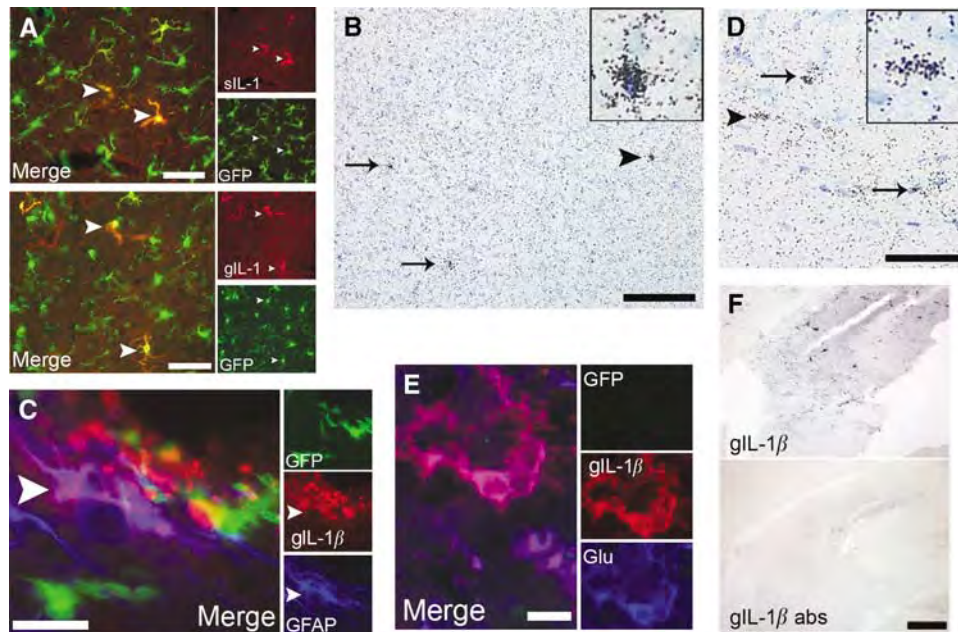


Figure 6 Distribution of IL-1 β -positive microglia and astrocytes in the brain after MCAo. The IL-1 β -positive cells in the brain after MCAo were revealed by immunofluorescence and *in situ* hybridization. **(A)** Representative fluorescent images showing the insular part of the ipsilateral cerebral cortex in a CX3CR1 $^{-/-}$ animal 24 h after MCAo. Immunostaining to IL-1 β (red) and GFP (green) using sheep (upper panel) or goat (lower panel) IL-1 β antibodies. **(B)** *In situ* hybridization reveals IL-1 β -expressing cells in the ipsilateral cerebral cortex (arrows, inset showing higher magnification of the cell indicated by arrowhead). **(C)** A total of 4 h after MCAo, some astrocytes (GFAP, blue) are positive to gIL-1 β (red) in the caudal, ipsilateral striatum near the ependyma of the lateral ventricle. **(D)** *In situ* hybridization reveals IL-1 β -expressing cells in the white matter in the ipsilateral thalamus (arrows, inset showing higher magnification of the cell indicated by arrowhead). **(E)** Glutamine synthetase-positive (Glu, blue), GFP-negative cell expressing gIL-1 β in the ipsilateral hippocampus 24 h after MCAo. **(F)** In a CX3CR1 $+/+$ mouse 24 h after MCAo, IL-1 β immunostaining (upper picture, gIL-1 β) is absent in the left hippocampus if goat anti-IL-1 β is preabsorbed with recombinant mouse IL-1 β peptide (gIL-1 β antibodies, lower picture). Scale bars: **(B, F)** 100 μ m; **(A, D)** 50 μ m; **(C)** 25 μ m, and **(E)** 10 μ m.

Elevation of IL-1Ra and TNF α mRNAs was observed on the contralateral hemisphere after MCAo, but it was only 2% to 10% of that seen in homogenates of the ipsilateral hemisphere. The levels of IL-1Ra and TNF α mRNAs were higher in CX3CR1 $+/+$ mice on the contralateral hemisphere, compared with CX3CR1 $^{-/-}$ animals 24 h after MCAo (Figures 8E–8H).

Discussion

We observed reduced brain damage, a lower number of apoptotic cells, CD45-positive infiltrating leukocytes, and highly blunted IL-1 β expression after MCAo in mice lacking the CX3CR1 (fractalkine) receptor. These results indicate that CX3CR1 is involved in the pathophysiology of cerebral ischemia in the current mouse model and the absence of this receptor results in better general recovery and reduced inflammation in the brain.

One possible explanation for our findings is that fractalkine–CX3CR1 signaling modulates microglial acute and/or late response to ischemic challenge. Microglial activation after MCAo and phagocytosis of Annexin V-positive cells were observed in both genotypes, indicating that CX3CR1 deficiency does

not profoundly affect microglial movement and detection of apoptotic signals.

Absence of fractalkine receptor in CX3CR1 $^{-/-}$ mice was reported to cause cell-autonomous microglial neurotoxicity after systemic LPS treatment in a toxic model of Parkinson's disease and a transgenic model of amyotrophic lateral sclerosis (Cardona *et al*, 2006). Furthermore, CX3CR1 $^{-/-}$ microglia were shown to accumulate and promote retinal degeneration (Combadiere *et al*, 2007). In contrast, we observed significantly smaller ischemic damage/neuronal apoptosis after MCAo in CX3CR1 $^{-/-}$ mice than in mice having CX3CR1, suggesting that loss of CX3CR1 confers neuroprotection in ischemia. Supporting this finding, fractalkine knockout mice were similarly shown to be less susceptible to cerebral ischemia–reperfusion injury (Soriano *et al*, 2002), which indicates that loss of CX3CR1–fractalkine signaling mediates these changes. In addition, CX3CR1 inhibition is protective against ischemic acute renal failure in mice (Oh *et al*, 2008). Therefore, it seems that lack of CX3CR1 has different consequences under different pathologic conditions. One plausible mechanism could be the altered IL-1 β secretion by microglia/macrophages in the absence of CX3CR1. After activation by LPS, microglia derived from CX3CR1 $^{-/-}$ mice expressed more

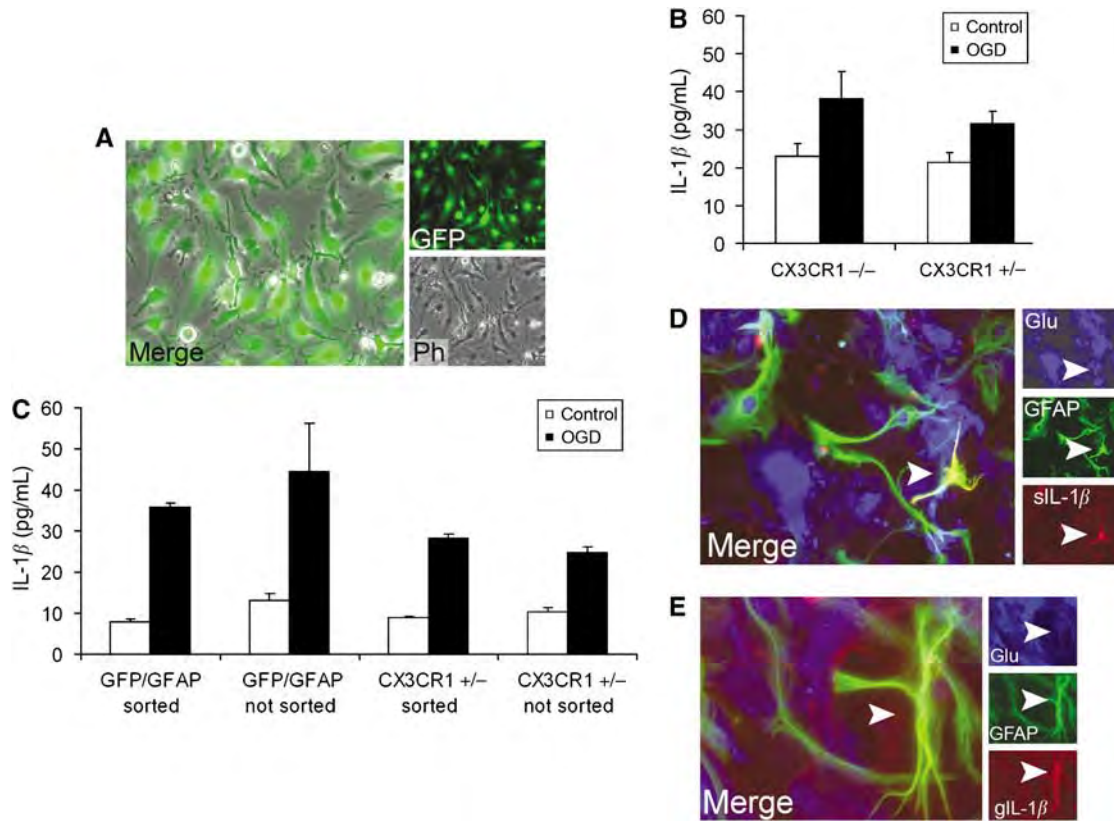


Figure 7 Interleukin-1 β expression *in vitro* after OGD in microglia-enriched cultures and astrocytes. **(A)** Representative fluorescent images showing a 95% purity microglia-enriched culture prepared from CX3CR1 +/– mice. Most cells (Ph, phase contrast image) in the culture express GFP (green). **(B)** Graph showing the amount of IL-1 β peptide in cell lysates of CX3CR1^{–/–} and CX3CR1 +/– microglia-enriched cultures 4 h after OGD compared with control. **(C)** A total 4 h after 3 h of OGD in glucose-free HEPES, astrocyte cell lysates were shown to contain elevated amount of IL-1 β peptide compared with control cells in both GFP/GFAP and CX3CR1 +/– cultures. Sorting merely GFP-positive astrocytes (GFP/GFAP sorted) or removing GFP-positive microglia (CX3CR1 +/– sorted) by FACS does not have any effect on IL-1 β production. After 4 h of OGD, a population of cultured CD1 astrocytes shows positive staining to IL-1 β , using sheep **(D)** or goat **(E)** anti-IL-1 β .

IL-1 β , and adoptive transfer of these cells resulted in increased neuronal death, which was blocked by IL-1Ra (Cardona *et al*, 2006). In contrast, we observed blunted IL-1 β mRNA and protein expression in CX3CR1^{–/–} mice 24 h after MCAO, which correlated with smaller infarcts, whereas no difference was seen in the number of IL-1 β -positive microglia and in *in vitro* IL-1 β production by microglia-enriched cultures after OGD. It is likely, therefore, that CX3CR1^{–/–} microglia are not neurotoxic in stroke and/or microglia are not directly involved in worsening the outcome after MCAO. Experiments that usually show the toxic potential of microglia *in vitro* often use stimuli eliciting defense-oriented reactions, such as LPS (Hanisch and Kettenmann, 2007), which results in production of a high amount of proinflammatory cytokines. This situation is not identical to other challenges, such as hypoxia and ischemia. It has previously been reported in several studies that microglia have beneficial as well as detrimental effects in cerebral ischemia, which indicate a highly complex microglial acute/late function in damage formation, inflammation, and repair. It is not clear whether loss of CX3CR1 might

have led to reduced microglial inflammatory function after MCAO or decrease in microglial-derived inflammatory molecules directly contributed to the formation of smaller ischemic damage. Therefore, it cannot be completely excluded that the reduced level of inflammatory cytokines and lower number of infiltrating leukocytes in KO mice after MCAO were (at least in part) because of the smaller ischemic damage itself. Inflammation is observed in the brain after several types of pathologic insults. However, it has also been reported that inflammatory mediators can profoundly exacerbate ischemic damage in the MCAO model (McColl *et al*, 2007).

It is possible that lack of CX3CR1 modifies microglial response in response to MCAO, which, in turn, could blunt the release of inflammatory molecules from other cells too, resulting in a better outcome in CX3CR1^{–/–} mice. It was reported recently that IL-1 β induces neuronal death through an astrocyte-dependent mechanism (Thornton *et al*, 2006). In a prion model of chronic neurodegeneration and inflammation, CX3CL1 immunoreactivity is upregulated in astrocytes and CX3CR1 expression is elevated on microglia (Hughes *et al*, 2002). Our

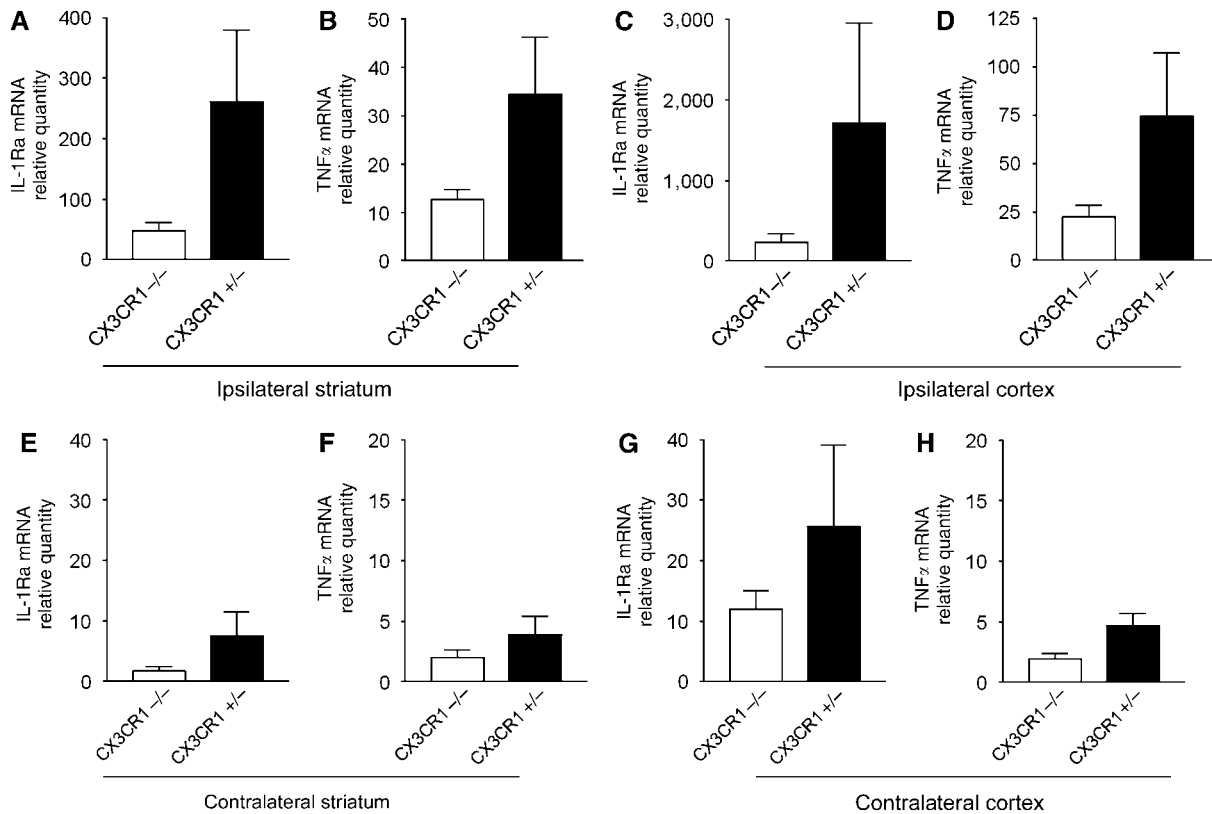


Figure 8 CX3CR1 +/– mice express higher amount of IL-1Ra and TNF α mRNA after MCAo than CX3CR1 –/– animals. Quantitative real-time PCR measurement reveals elevated amount of IL-1Ra and TNF α mRNA after MCAo. Graphs showing the relative quantity of mRNAs in the same brain homogenates of the ipsilateral (left) striatum (A, B) and cerebral cortex (C, D) as used for IL-1 β mRNA and peptide measurement. CX3CR1 +/– mice express more IL-1Ra mRNA (A, C) and TNF α mRNA (B, D) after MCAo than do KO mice. The IL-1Ra (E, G) and TNF α (F, H) mRNAs are also higher in the contralateral (right) striatum (E, F) and cerebral cortex (G, H) in CX3CR1 +/– mice than in CX3CR1 –/– animals, but the elevation of mRNAs after MCAo is much lower than that seen in the ipsilateral hemisphere.

results might also indicate that fractalkine–CX3CR1 signaling could modulate synthesis, cleavage, and/or release of IL-1 β directly. It has recently been shown that fractalkine exerts a dose-dependent differential regulation of cytokine secretion from macrophages. Relatively low concentrations of fractalkine suppressed LPS-induced TNF α secretion, but higher concentrations of fractalkine, which may represent a local inflammatory condition, was not immunosuppressive; instead, upregulation of IL-23 was seen (Mizutani *et al*, 2007). Our data indicate that fractalkine receptor deficiency may not increase microglial neurotoxicity or IL-1 β release from microglia after transient MCAo in the current model.

We found that astrocytes (and in less part neurons) can represent a significant source of IL-1 β *in vivo*, after MCAo, and *in vitro* after OGD at 4 to 24 h in both models. Furthermore, the appearance of these cells near the ependyma and meninges (and possibly neuronal IL-1 β -expression) would, in part, explain elevated IL-1 β peptide levels measured in the contralateral hemisphere after MCAo. It has been previously reported that astrocytes express IL-1 β 2 to 7 days after MCAo in the rat (Pearson *et al*, 1999), and that hypoxia-inducible factor-1 mediates trans-

criptional activation of IL-1 β in astrocyte cultures (Zhang *et al*, 2006). Interestingly, endogenous caspase-1 activation and bioactive IL-1 β production are prerequisites for iNOS induction and excessive NO formation in brain-derived endothelia and astrocytes after challenge with proinflammatory cytokines (Juttler *et al*, 2007). Recent data indicate the potential cytotoxicity of astrocytes *in vitro* and *in vivo* in neurodegenerative diseases (Hashioka *et al*, 2008; Thornton *et al*, 2006). However, it requires further investigation whether IL-1 β is released early from astrocytes in response to hypoxia or needs contribution of other cells/stimuli *in vivo*. Because cytokines, including IL-1 β , can be released into the extracellular space and into the cerebrospinal fluid from the cells of origin, brain homogenates might have contained more IL-1 β peptide than the amount indicated by IL-1 β -immunopositive cells. In addition, the detection of elevated amount of IL-1 β and TNF mRNAs in heterozygote mice with real-time PCR, even on the contralateral side, indicates local expression of these cytokines. Moreover, IL-1 β *in situ* hybridization data were compatible with results of IL-1 β immunohistochemistry regarding the number and

location of IL-1 β -expressing microglia and astrocytes.

It is not clear how fractalkine–CX3CR1 signaling could affect late central inflammatory events and how peripheral components contribute to the formation of ischemic damage. A total of 12 h after transient MCAo in rat, fractalkine expression was lost from the ischemic striatum, but fractalkine immunoreactivity was strongly increased in morphologically intact cortical neurons of the ischemic penumbra 24 and 48 h after ischemia as well as in endothelial cells 48 h and 7 days after ischemia (Tarozzo *et al*, 2002). We observed significantly less CD45+/GFP– leukocytes in the ipsilateral hemisphere in CX3CR1–/– mice 72 h after MCAo. CX3CR1–/– mice were reported to have a significant reduction in macrophage recruitment to the vessel wall and decreased atherosclerotic lesion formation (Lesnik *et al*, 2003). Others found that the CX3CR1^{high}CCR2–Gr1– subset of murine blood monocytes is characterized by CX3CR1-dependent recruitment to noninflamed tissues and that a short-lived CX3CR1^{low}CCR2–Gr1– cell population is actively recruited to inflamed tissue (Geissmann *et al*, 2003). We observed a lower number of GFP+/CD45+ microglia/macrophages in the ipsilateral cerebral cortex of CX3CR1+/- mice at 72 h, possibly as a result of more serious ischemia and decreased microglial proliferation (Denes *et al*, 2007) and/or recruitment. Our results indicate that a reduction in damage formation observed relatively early in CX3CR1–/– mice, and large differences seen in IL-1 β expression in the brain at 24 h, may be explained by central effects rather than by the result of reduced macrophage infiltration and/or peripheral monocytic IL-1 β secretion in the current model.

Fractalkine has been shown to serve as a potent chemoattractant for natural killer cells, CD8⁺ T cells (Imai *et al*, 1997), and mast cells (Papadopoulos *et al*, 2000). Neutrophils can be recruited to the brain independently of fractalkine by various substances released under pathologic conditions. For example, cytokine-induced neutrophil chemoattractant-1 is expressed by astrocytes under inflammatory conditions (Koyama *et al*, 2007). In addition, hypoxic challenge increases the expression of fractalkine and intercellular adhesion molecule-1 on human endothelial cells and promotes neutrophil adhesion through activation of the Jak-Stat5 pathway (Yang *et al*, 2007). The fact that significantly more CD45+/GFP– (i.e., CX3CR1-negative) leukocytes were recruited to the brain in heterozygote mice than in CX3CR1–/– mice indicates that the fractalkine receptor may not be directly involved in recruitment and adhesion of these cells after MCAo. In addition, loss of central CX3CR1–fractalkine signaling in CX3CR1–/– mice could result in reduced amount of other brain-derived chemokines and adhesion molecules too. The lower number of leukocytes in the brain and reduced IL-1 β , TNF α ,

and IL-1Ra expression in CX3CR1–/– mice together indicate a lower level of central inflammation after MCAo.

Taken together, we identify CX3CR1 as an important contributor to cerebral ischemia and postischemic inflammation. Through modulation of microglial and/or astrocytic function and IL-1 β expression, CX3CR1 might be an important target in clinical approaches of treatment of ischemic stroke.

Disclosure/conflict of interest

The authors state no conflict of interest or personal financial holdings that would affect the content of the article.

References

- Biber K, Neumann H, Inoue K, Boddeke HW (2007) Neuronal 'On' and 'Off' signals control microglia. *Trends Neurosci* 30:596–602
- Cardona AE, Piro EP, Sasse ME, Kostenko V, Cardona SM, Dijkstra IM, Huang D, Kidd G, Dombrowski S, Dutta R, Lee JC, Cook DN, Jung S, Lira SA, Littman DR, Ransohoff RM (2006) Control of microglial neurotoxicity by the fractalkine receptor. *Nat Neurosci* 9:917–24
- Chong ZZ, Li F, Maiese K (2005) Oxidative stress in the brain: novel cellular targets that govern survival during neurodegenerative disease. *Prog Neurobiol* 75:207–46
- Combadiere C, Feumi C, Raoul W, Keller N, Rodero M, Pezard A, Lavalette S, Houssier M, Jonet L, Picard E, Debre P, Sirinyan M, Deterre P, Ferroukhi T, Cohen SY, Chauvaud D, Jeanny JC, Chemtob S, Behar-Cohen F, Sennlaub F (2007) CX3CR1-dependent subretinal microglia cell accumulation is associated with cardinal features of age-related macular degeneration. *J Clin Invest* 117:2920–8
- Denes A, Vidyasagar R, Feng J, Narvainen J, McColl BW, Kauppinen RA, Allan SM (2007) Proliferating resident microglia after focal cerebral ischaemia in mice. *J Cereb Blood Flow Metab* 27:1941–53
- Fleming SM, Salcedo J, Fernagut PO, Rockenstein E, Masliah E, Levine MS, Chesselet MF (2004) Early and progressive sensorimotor anomalies in mice overexpressing wild-type human alpha-synuclein. *J Neurosci* 24:9434–40
- Geissmann F, Jung S, Littman DR (2003) Blood monocytes consist of two principal subsets with distinct migratory properties. *Immunity* 19:71–82
- Gosselin D, Rivest S (2007) Role of IL-1 and TNF in the brain: twenty years of progress on a Dr. Jekyll/Mr. Hyde duality of the innate immune system. *Brain Behav Immun* 21:281–9
- Hanisch UK, Kettenmann H (2007) Microglia: active sensor and versatile effector cells in the normal and pathologic brain. *Nat Neurosci* 10:1387–94
- Hashioka S, Klegeris A, Schwab C, McGeer PL (2008) Interferon-gamma-dependent cytotoxic activation of human astrocytes and astrocytoma cells. *Neurobiol Aging*; doi: 10.1016/j.neurobiolaging.2008.02.019 (in press)
- Hughes PM, Botham MS, Frentzel S, Mir A, Perry VH (2002) Expression of fractalkine (CX3CL1) and its receptor, CX3CR1, during acute and chronic inflammation in the rodent CNS. *Glia* 37:314–27

- Imai T, Hieshima K, Haskell C, Baba M, Nagira M, Nishimura M, Kakizaki M, Takagi S, Nomiya H, Schall TJ, Yoshie O (1997) Identification and molecular characterization of fractalkine receptor CX3CR1, which mediates both leukocyte migration and adhesion. *Cell* 91:521–30
- Jung S, Aliberti J, Graemmel P, Sunshine MJ, Kreutzberg GW, Sher A, Littman DR (2000) Analysis of fractalkine receptor CX(3)CR1 function by targeted deletion and green fluorescent protein reporter gene insertion. *Mol Cell Biol* 20:4106–14
- Juttler E, Bonmann E, Spranger M, Kolb-Bachofen V, Suschek CV (2007) A novel role of interleukin-1-converting enzyme in cytokine-mediated inducible nitric oxide synthase gene expression: implications for neuroinflammatory diseases. *Mol Cell Neurosci* 34:612–20
- Koyama Y, Baba A, Matsuda T (2007) Production of monocyte chemoattractant protein-1 and cytokine-induced neutrophil chemoattractant-1 in rat brain is stimulated by intracerebroventricular administration of an endothelin ETB receptor agonist. *Neuroreport* 18:1275–9
- Lalancette-Hebert M, Gowing G, Simard A, Weng YC, Kriz J (2007) Selective ablation of proliferating microglial cells exacerbates ischemic injury in the brain. *J Neurosci* 27:2596–605
- Lesnik P, Haskell CA, Charo IF (2003) Decreased atherosclerosis in CX3CR1^{-/-} mice reveals a role for fractalkine in atherogenesis. *J Clin Invest* 111:333–40
- Marshall JF, Gotthelf T (1979) Sensory inattention in rats with 6-hydroxydopamine-induced degeneration of ascending dopaminergic neurons: apomorphine-induced reversal of deficits. *Exp Neurol* 65:398–411
- McCull BW, Allan SM, Rothwell NJ (2007) Systemic inflammation and stroke: aetiology, pathology and targets for therapy. *Biochem Soc Trans* 35:1163–5
- McCull BW, Carswell HV, McCulloch J, Horsburgh K (2004) Extension of cerebral hypoperfusion and ischaemic pathology beyond MCA territory after intraluminal filament occlusion in C57Bl/6J mice. *Brain Res* 997:15–23
- Mizutani N, Sakurai T, Shibata T, Uchida K, Fujita J, Kawashima R, Kawamura YI, Toyama-Sorimachi N, Imai T, Dohi T (2007) Dose-dependent differential regulation of cytokine secretion from macrophages by fractalkine. *J Immunol* 179:7478–87
- Muir KW, Tyrrell P, Sattar N, Warburton E (2007) Inflammation and ischaemic stroke. *Curr Opin Neurol* 20:334–42
- Nolte C, Matyash M, Pivneva T, Schipke CG, Ohlemeyer C, Hanisch UK, Kirchhoff F, Kettenmann H (2001) GFAP promoter-controlled EGFP-expressing transgenic mice: a tool to visualize astrocytes and astrogliosis in living brain tissue. *Glia* 33:72–86
- Oh DJ, Dursun B, He Z, Lu L, Hoke TS, Ljubanovic D, Faubel S, Edelstein CL (2008) Fractalkine receptor (CX3CR1) inhibition is protective against ischemic acute renal failure in mice. *Am J Physiol Renal Physiol* 294:F264–71
- Papadopoulos EJ, Fitzhugh DJ, Tkaczyk C, Gilfillan AM, Sasseti C, Metcalfe DD, Hwang ST (2000) Mast cells migrate, but do not degranulate, in response to fractalkine, a membrane-bound chemokine expressed constitutively in diverse cells of the skin. *Eur J Immunol* 30:2355–61
- Pearson VL, Rothwell NJ, Toulmond S (1999) Excitotoxic brain damage in the rat induces interleukin-1beta protein in microglia and astrocytes: correlation with the progression of cell death. *Glia* 25:311–23
- Richmon JD, Fukuda K, Maida N, Sato M, Bergeron M, Sharp FR, Panter SS, Noble LJ (1998) Induction of heme oxygenase-1 after hyperosmotic opening of the blood-brain barrier. *Brain Res* 780:108–18
- Schallert T, Upchurch M, Wilcox RE, Vaughn DM (1983) Posture-independent sensorimotor analysis of inter-hemispheric receptor asymmetries in neostriatum. *Pharmacol Biochem Behav* 18:753–9
- Simmons DM, Arriza JL, Swanson LW (1989) A complete protocol for *in situ* hybridization of messenger RNAs in brain and other tissues with radiolabeled single-stranded RNA probes. *J Histochemol* 12:169–181
- Soriano SG, Amaravadi LS, Wang YF, Zhou H, Yu GX, Tonra JR, Fairchild-Huntress V, Fang Q, Dunmore JH, Huszar D, Pan Y (2002) Mice deficient in fractalkine are less susceptible to cerebral ischemia-reperfusion injury. *J Neuroimmunol* 125:59–65
- Tarozzo G, Campanella M, Ghiani M, Bulfone A, Beltramo M (2002) Expression of fractalkine and its receptor, CX3CR1, in response to ischaemia-reperfusion brain injury in the rat. *Eur J Neurosci* 15:1663–8
- Thornton P, Pinteaux E, Gibson RM, Allan SM, Rothwell NJ (2006) Interleukin-1-induced neurotoxicity is mediated by glia and requires caspase activation and free radical release. *J Neurochem* 98:258–66
- Touzani O, Boutin H, Chuquet J, Rothwell N (1999) Potential mechanisms of interleukin-1 involvement in cerebral ischaemia. *J Neuroimmunol* 100:203–15
- Touzani O, Boutin H, LeFeuvre R, Parker L, Miller A, Luheshi G, Rothwell N (2002) Interleukin-1 influences ischemic brain damage in the mouse independently of the interleukin-1 type I receptor. *J Neurosci* 22:38–43
- Wheeler RD, Boutin H, Touzani O, Luheshi GN, Takeda K, Rothwell NJ (2003) No role for interleukin-18 in acute murine stroke-induced brain injury. *J Cereb Blood Flow Metab* 23:531–5
- Yang XP, Mattagajasingh S, Su S, Chen G, Cai Z, Fox-Talbot K, Irani K, Becker LC (2007) Fractalkine upregulates intercellular adhesion molecule-1 in endothelial cells through CX3CR1 and the Jak Stat5 pathway. *Circ Res* 101:1001–8
- Yenari MA, Xu L, Tang XN, Qiao Y, Giffard RG (2006) Microglia potentiate damage to blood-brain barrier constituents: improvement by minocycline *in vivo* and *in vitro*. *Stroke* 37:1087–93
- Yrjanheikki J, Keinanen R, Pellikka M, Hokfelt T, Koistinaho J (1998) Tetracyclines inhibit microglial activation and are neuroprotective in global brain ischemia. *Proc Natl Acad Sci USA* 95:15769–74
- Zhang W, Petrovic JM, Callaghan D, Jones A, Cui H, Howlett C, Stanimirovic D (2006) Evidence that hypoxia-inducible factor-1 (HIF-1) mediates transcriptional activation of interleukin-1beta (IL-1beta) in astrocyte cultures. *J Neuroimmunol* 174:63–73
- Zheng Z, Yenari MA (2004) Post-ischemic inflammation: molecular mechanisms and therapeutic implications. *Neurol Res* 26:884–92

Supplementary Information accompanies the paper on the Journal of Cerebral Blood Flow & Metabolism website (<http://www.nature.com/jcbfm>)

ARTICLE

Received 26 Nov 2015 | Accepted 4 Apr 2016 | Published 3 May 2016

DOI: 10.1038/ncomms11499

OPEN

Microglia protect against brain injury and their selective elimination dysregulates neuronal network activity after stroke

Gergely Szalay^{1,*}, Bernadett Martinecz^{2,*}, Nikolett Lénárt^{2,*}, Zsuzsanna Környei², Barbara Orsolits², Linda Judák^{1,3}, Eszter Császár², Rebeka Fekete², Brian L. West⁴, Gergely Katona³, Balázs Rózsa^{1,3,**} & Ádám Dénes^{2,**}

Microglia are the main immune cells of the brain and contribute to common brain diseases. However, it is unclear how microglia influence neuronal activity and survival in the injured brain *in vivo*. Here we develop a precisely controlled model of brain injury induced by cerebral ischaemia combined with fast *in vivo* two-photon calcium imaging and selective microglial manipulation. We show that selective elimination of microglia leads to a striking, 60% increase in infarct size, which is reversed by microglial repopulation. Microglia-mediated protection includes reduction of excitotoxic injury, since an absence of microglia leads to dysregulated neuronal calcium responses, calcium overload and increased neuronal death. Furthermore, the incidence of spreading depolarization (SD) is markedly reduced in the absence of microglia. Thus, microglia are involved in changes in neuronal network activity and SD after brain injury *in vivo* that could have important implications for common brain diseases.

¹Two-Photon Imaging Center, Institute of Experimental Medicine, Hungarian Academy of Sciences, Szigyony U. 43, Budapest 1083, Hungary. ²Laboratory of Neuroimmunology, Institute of Experimental Medicine, Hungarian Academy of Sciences, Szigyony U. 43, Budapest 1083, Hungary. ³MTA-PPKE ITK-NAP B - Two-photon measurement Technology Research Group, Pázmány Péter University, Budapest 1083, Hungary. ⁴Plexxikon, Inc., Berkeley, California 94710, USA. * These authors contributed equally to this work. ** These authors jointly supervised this work. Correspondence and requests for materials should be addressed to Á.D. (email: denes.adam@koki.mta.hu) or to B.R. (email: rozsa.balazs@koki.mta.hu).

dc_2027_22

Microglia are the main resident immune-competent cell population of the central nervous system (CNS), and play an essential role in CNS development, maintenance and repair¹. However, altered microglial activity is associated with common human diseases, such as migraine, stroke, dementia, traumatic injury, epilepsy and Parkinson's disease: these affect millions of people worldwide, representing a high socioeconomic burden^{2–4}. In fact, microglia are capable of producing a diverse array of inflammatory mediators in response to injury or infection, and inflammation is linked with poor clinical outcome in CNS diseases^{3–5}. At the same time, data also indicate that specific microglial actions can be neuroprotective⁶. Thus, the role of microglia in brain injury is controversial and disease dependent, whereas the mechanisms through which microglia contribute to brain injury or repair are unclear.

Microglia are highly dynamic, and constantly survey the brain parenchyma, showing rapid activation in response to harmful stimuli⁷. *In vivo* two-photon imaging studies have revealed that microglial processes interact with capillaries, react to vascular or parenchymal injury in the brain, monitor the state of synapses and remove injured neurons, their processes or synaptic structures in different models of brain injury^{7–11}. Recently, microglia have also been shown to react to changes in extracellular calcium levels¹². It is currently debated whether microglia could promote excitotoxicity (a major cause of neuronal death induced by calcium overload) via production of proinflammatory mediators^{13,14}, or whether specific microglial actions could reduce excitotoxic neuronal death^{15,16}. It is also unclear whether microglia could play a role in spreading depolarization (SD), one of the most fundamental processes of brain pathology¹⁷ that involves swelling of neurons, injury to dendritic spines and subsequent silencing of brain electrical activity, which is linked with excitotoxicity and general outcome in common brain diseases such as stroke, brain haemorrhage, epilepsy and migraine^{18–20}. However, the functional role of microglia in shaping the activity of complex neuronal networks is difficult to study *in vivo*, since the large similarity between microglia and other tissue macrophages has not allowed selective *in vivo* manipulation of microglia until very recently^{6,21}. Also, it has proved to be difficult to perform long-term monitoring of fast neuronal responses in the context of microglial activity in real time.

Microglia arise from yolk sac-derived precursors that populate the brain during early development²¹. Microglia genesis is dependent on the transcription factors IRF8 and PU.1 (ref. 22), but, once migrated to the neuroectoderm, microglia become self-renewing, which requires colony-stimulating factor 1 receptor (CSF1R)-dependent signalling²³. High-dose treatment with a brain-penetrant CSF1R kinase inhibitor reversibly depletes microglia, an effect that has no apparent gross deleterious results in healthy mice, but that provides a powerful tool for inferring the various roles of microglia in more detail²⁴.

Strikingly, we found that selective elimination of microglia from the brain leads to markedly augmented neuronal death after acute brain injury. To study the mechanisms involved, we combined fast multicolour two-photon imaging of genetically encoded calcium indicators (GECI) with a recently developed remote filament model of middle cerebral artery occlusion (MCAo) allowing us to monitor microglial responses and fast neuronal activity changes simultaneously, in real time. We show that an absence of microglia results in dysregulated neuronal responses, lack of SD and increased excitotoxic injury. Thus, supporting beneficial microglial–neuronal interactions could have profound therapeutic implications.

Results

CSF1R blockade leads to selective microglia depletion. Microglia have been implicated in both vascular^{9,25} and neuronal injury^{26,27}, and neuroprotection^{28,29}, but tools to selectively manipulate microglia have become available only very recently^{24,30,31}. To reduce the potential side effects of microglia manipulation to the minimum, we made use of the discovery that microglial survival is critically dependent on CSF1R signalling, in contrast to other tissue macrophages^{23,24,31}. Feeding a chow diet containing the CSF1R antagonist PLX3397 (290 p.p.m.) for 3 weeks resulted in an almost complete elimination of microglia from the brain in *Cx3Cr1^{GFP/+}* mice, as confirmed by the absence of green fluorescent protein (GFP)-positive cells that co-expressed the microglia/macrophage marker Iba1 (Fig. 1a). Quantitative analysis showed that after 3 weeks, 97% of microglia were eliminated from the cerebral cortex and 93% from the striatum, compared with control mice (Fig. 1b). Microglia were eliminated as a result of apoptosis, as indicated by the expression of the apoptotic marker Cleaved Caspase-3 in microglia, but not in neurons (Fig. 1c) or other cells (not shown). Correspondingly, no sign of brain inflammation, leukocyte recruitment, weight loss or increases in circulating inflammatory cytokines were observed over 3 weeks of PLX3397 treatment (Supplementary Fig. 1), confirming previous results^{24,32}. No sign of blood brain barrier (BBB) injury, as assessed by IgG penetration into the brain parenchyma was found similarly to earlier observations²⁴. The number of neurons, pericytes, astrocytes and levels of the tight junction protein claudin 5 were not altered in the brain (Supplementary Fig. 2a, b) and no changes were seen in spleen macrophages and splenic or blood leukocyte populations (Supplementary Figs 3 and 4). Thus, we argued that this model of selective microglial ablation introduces minimal disturbance to the brain and does not alter peripheral leukocytes, enabling us to study the role of microglia in brain injury.

Absence of microglia results in increased brain injury. Next, we designed a series of experiments to assess the role of microglia in brain injury and to control for the potential confounding effects PLX3397 might exert on neuronal injury. As earlier, an almost complete elimination of microglia (Iba1+ cells) from the brain was observed after feeding mice a chow diet containing PLX3397 for 21 days (Fig. 1d). Since PLX3397 is quickly cleared from central and peripheral tissues²⁴, the PLX3397 diet was withdrawn for 24 h after 21 days of microglia depletion in a separate group of animals, after which microglia remained fully depleted, but only trace amounts of the drug were detected in the brain²⁴. Indeed, we found that 98% of microglia were absent from the cerebral cortex 24 h after drug withdrawal (Fig. 1d). In a further group of animals, the drug was withdrawn for 2 weeks after 21 days of treatment, which led to full repopulation of microglia (Fig. 1d). No changes in splenic Iba1+ macrophages were seen in any of the experimental groups (Fig. 1e). The absence of microglia resulted in a striking, 60% increase in infarct size 24 h after MCAo (26.8 mm³ in control versus 42.8 mm³ in microglia-depleted animals), which was not affected by the presence of PLX3397, as increased infarct size (41.2 mm³) was also seen if PLX3397 was withdrawn 24 h before cerebral ischaemia (Fig. 1f). In contrast, repopulation of microglia completely reversed the effect of microglia depletion on increased infarct size (22.5 mm³), implying that the presence of microglia influences the severity of brain injury after cerebral ischaemia. We also investigated whether any of the treatment protocols affected cerebral blood flow (CBF), but no differences in CBF values were found after occlusion of the MCA (Fig. 1g) or at reperfusion (not shown) compared with baseline. Levels of interleukin 6 (IL-6)—a

dc_2027_22

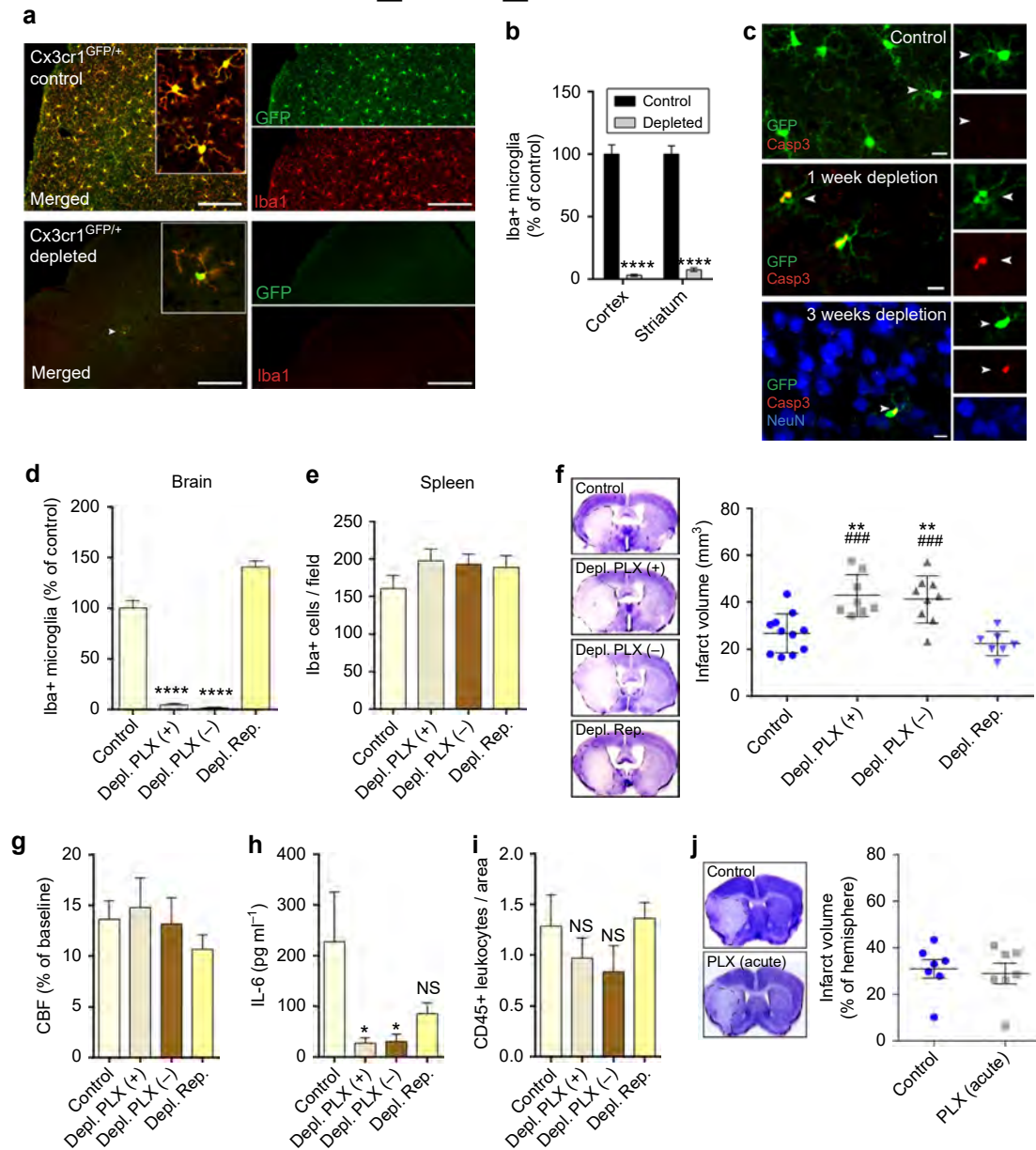


Figure 1 | Absence of microglia results in markedly increased brain injury after cerebral ischaemia. (a) *Cx3Cr1^{GFP/+}* mice were fed a chow diet containing the CSF1R antagonist PLX3397 (290 p.p.m.) for 21 days, which resulted in an almost complete elimination of resident brain microglia. Absence of microglia was confirmed by the lack of both GFP (green) and Iba1 (red) signal. Arrowhead indicates microglia (bottom panel). (b) Quantification of microglia in C57BL6/J mice after control or PLX3397 diet. (c) PLX3397 results in microglial apoptosis as indicated by the activation of Cleaved Caspase-3 (Casp3, red) in microglia (GFP, green) in *Cx3Cr1^{GFP/+}* mice (arrowheads). No Caspase-3 expression is seen in neurons (NeuN, blue). (d) Elimination of microglia (Iba1-positive cells) from the brain is seen after feeding mice a chow diet containing PLX3397 for 21 days (Depl. PLX +). Microglia remain depleted when the diet is withdrawn for 24 h after 21 days of treatment (Depl. PLX -). Microglial repopulation occurs 2 weeks after diet withdrawal (Depl. Rep.). (e) No changes are seen in Iba1-positive spleen macrophages in response PLX3397 or after microglial repopulation. (f) An absence of microglia leads to markedly increased infarct size 24 h after cerebral ischaemia, which is reversed by microglial repopulation. (g) Cerebral blood flow (CBF) was measured by a laser Doppler during MCA occlusion (expressed as % of baseline). (h) IL-6 levels in the CSF 24 h after cerebral ischaemia. (i) Elimination of microglia did not increase the recruitment of CD45-positive leukocytes into the brain 24 h after cerebral ischaemia. (j) Intraperitoneal administration of PLX3397 1 h after the onset of ischaemia did not alter brain injury as assessed 24 h after MCAo. Data are expressed as mean ± s.e.m. **b**: two-way analysis of variance (ANOVA) followed by Sidak's multiple comparison, *N* = 8-10; **d-i**: one-way ANOVA followed by Tukey's multiple comparison, *N* = 7-11; **j**: unpaired *t* test, *N* = 7, **P* < 0.05, ***P* < 0.01, *****P* < 0.0001 versus the control group; ####*P* < 0.001 versus Depl. Rep.; NS, not significant. Scale bars, **a**, 100 μm; **c**, 10 μm.

cytokine produced by microglia¹—in the cerebrospinal fluid mirrored the differences seen in microglial numbers across the different experimental groups 24 h after cerebral ischaemia (Fig. 1h). Absence of microglia did not lead to increased leukocyte recruitment to the brain 24 h (Fig. 1i) and 72 h

(Supplementary Fig. 5) after cerebral ischaemia or inflammation as observed previously by others after hippocampal injury²⁴. In addition, Iba1-positive microglia/macrophages were still profoundly reduced in the brain 72 h after MCAo, suggesting that an absence of microglia (and larger brain injury) does

dc_2027_22

not lead to significantly increased monocyte influx compared with control mice. We also investigated whether a single, intraperitoneal injection of 20 mg kg^{-1} PLX3397, which resulted in $25,930 \pm 3,600 \text{ ng ml}^{-1}$ PLX3397 concentrations in the plasma and $1,160 \pm 290 \text{ ng g}^{-1}$ ($2.8 \pm 0.7 \mu\text{M}$) concentrations in the intact (non-ischaemic) brain tissue (Supplementary Fig. 6) could exert any effect on neuronal injury. This regimen yields higher PLX3397 levels than that needed to maintain depletion of microglia²⁴, but does not lead to microglia depletion. Mice that received a single, acute dose of 20 mg kg^{-1} PLX3397 60 min after MCAo, when BBB injury takes place based on our two-photon imaging data (see below), showed no changes in infarct size 24 h after reperfusion compared with controls (Fig. 1j), while microglial numbers were not reduced (Supplementary Fig. 6). Thus, these data suggest that an absence of microglia leads to increased brain injury independently of PLX3397 and that PLX3397 itself has no detrimental effect on neuronal injury in this model.

Absence of microglia facilitates excitotoxicity. Next, we used *in vivo* two-photon calcium imaging combined with a recently developed remote filament model of MCAo to investigate the mechanisms through which microglia contribute to brain protection after acute injury. To this end, adeno-associated virus (AAV)-mediated delivery of the GECIs, GCaMP6s or RCaMP1 was performed using a micropipette distant from the imaging site. This minimized disturbance to the brain tissue, as evidenced by the absence of microglial activation in the imaging area where the dura mater was not injured (see Methods section and Supplementary Fig. 7a). This system enabled precise and continuous monitoring of neuronal calcium changes and network activity in the cerebral cortex in real time, up to several hours post reperfusion (Fig. 2a). In a separate set of experiments, series of CBF measurements were performed by laser Doppler flowmetry to establish the site of our imaging window (30 measurements performed in $n = 5$ mice). To capture neuronal GCaMP6s signal changes in the evolving infarct, the imaging site was positioned between an area with close to maximal CBF reduction (80% reduction to baseline) and an area with sub-ischaemic levels of blood flow (30% reduction to baseline, Fig. 2b). In response to induction of cerebral ischaemia for 60 min, we noticed minor increases of the GCaMP6s signal in cortical neurons and the neuropil followed by low levels of GCaMP6s signal up to 1–1.5 h after the induction of reperfusion (Fig. 2c,d). In contrast, a marked increase in intracellular calcium was observed 1.5–3 h after reperfusion in the same neurons and the neuropil caused by the initiation of SD, a basic phenomenon of brain pathology thought to contribute to excitotoxicity and linked with neuronal injury in diverse neurological diseases^{18,20} (Fig. 2d,e and Supplementary Video 1). Series of two to four SDs in individual mice were followed by a reduction in neuronal calcium signals by 4 h of reperfusion (Fig. 2d–f), which remained similar 24 h after cerebral ischaemia (Supplementary Fig. 7B). Quantitative analysis of GCaMP6s signal changes over time showed that significant increases in neuronal calcium levels develop only 1.5–3 h after the induction of reperfusion due to repeated SDs (Fig. 2f). The GCaMP6s signal remained unaltered in sham animals over the whole imaging period.

Microglia contact neurons in an activity-dependent manner. Several excellent previous studies have investigated microglial responses after brain injury using two-photon microscopy^{1,7,8,10}, but *in vivo* two-photon imaging to evaluate the relationship between microglial actions and neuronal network activity has not been performed in real time. Our histological data suggested that

after cerebral ischaemia, microglia and their processes surround neurons showing high GCaMP6s signal in the boundary zones of the infarct (Fig. 3a). To investigate this in real time, neuronal calcium responses were monitored with two-photon microscopy using the GECI RCaMP1, in *Cx3Cr1^{GFP/+}* (microglia reporter) mice (Fig. 3b). Cerebral ischaemia resulted in similar RCaMP1 changes as seen earlier with GCaMP6s. Morphological signs of microglial activation (reduced ramification and thickened processes) were seen between 1 and 4 h after the onset of ischaemia in the evolving infarct as also confirmed by Sholl analysis³³. Microglial activation was associated with enlargement of the cell body and increased Iba1 expression from 6 h after cerebral ischaemia (Supplementary Fig. 8). Importantly, microglial processes, which were frequently found to touch neuronal cell bodies and dendrites already before MCAo, were extended to neurons showing increasing RCaMP1 signal over time, surrounding the cell body and the main dendrites, whereas microglial processes were withdrawn after prolonged reduction in neuronal intracellular calcium levels (Fig. 3b–d and Supplementary Video 2). We also assessed changes in the density of microglial processes in concentric circles around individual neurons (a modification of Sholl analysis³³, see Methods section), which showed increasing microglial process coverage ($R^2 = 0.9$, $P = 0.0038$) of neurons showing a sustained rise in intracellular calcium after cerebral ischaemia (Fig. 3e). Surprisingly, we also found that SDs that typically occurred 1.5–3 h after the onset of cerebral ischaemia increased microglial process coverage of neuronal cell bodies within 30 min in both neurons showing increasing RCaMP1 signal before and after an SD (termed as Group 1 cells) and in those cells where intracellular calcium returned to near-baseline levels after SD (termed as Group 2 cells; Fig. 3f–h, Supplementary Fig. 9 and Supplementary Video 3). Super-resolution microscopy revealed that fine microglial processes form tight contacts with the neuronal cell body in the evolving infarct, whereas fewer microglia–neuron contacts were seen around the neuronal cell body in sham animals. Microglial P2Y₁₂ receptors were found clustering at the microglia–neuron interface independently of location of astrocyte endfeet (Fig. 3i–j and Supplementary Fig. 10). Thus, microglia react rapidly to changes in intracellular calcium in neurons and SD is associated with microglial process recruitment to neurons independently of sustained calcium changes in the injured brain.

Lack of microglia alters neuronal activity and SD after injury.

Our imaging data indicated that microglia contact neurons in an activity-dependent manner after brain injury, which led us to investigate neuronal calcium responses in the absence of microglia. To this end, two weeks after GCaMP6s delivery, repeated 2-min-long, fast two-photon imaging recordings were performed by resonant scanning, separated by 5 min breaks over a 5.5–6 h period before and after the induction of 60 min MCAo followed by reperfusion. Selective microglia depletion did not influence GCaMP6s delivery to cortical neurons (456 ± 78 neurons per mm^2 in control and 504 ± 35 neurons per mm^2 in microglia-depleted mice were GCaMP6s-positive in the imaging area before MCAo being induced). As earlier, we found that cerebral ischaemia resulted in negligible GCaMP6s signal changes in control mice during occlusion and early reperfusion, followed by the occurrence of repeated SDs 1.5–3 h after reperfusion in the evolving infarct. Calcium imaging revealed few changes in individual neurons or in the neuropil before SD (Fig. 4a, left). In contrast, in the absence of microglia striking increases in slow neuronal oscillations were observed 15–25 min after the onset of ischaemia, which continued after the induction of reperfusion up to 3–5 h post MCAo (Fig. 4a right, and Supplementary Video 4).

dc_2027_22

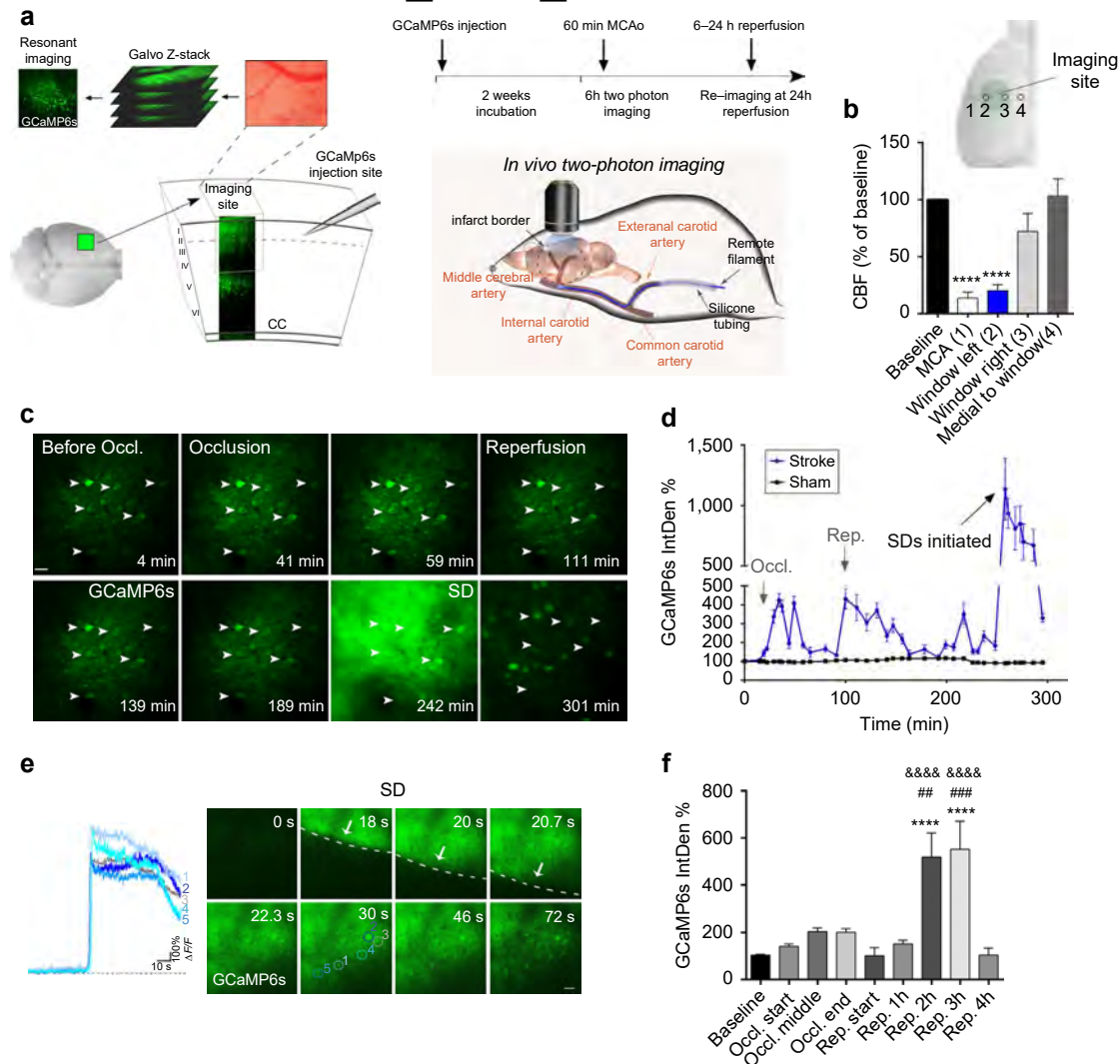


Figure 2 | Fast *in vivo* two-photon calcium imaging reveals delayed development of excitotoxicity in the cerebral cortex after cerebral ischaemia.

(a) AAV-mediated delivery of the genetically encoded calcium indicator GCaMP6s was performed two weeks before *in vivo* two-photon imaging with an injection site distant from the imaging area to minimize disturbance to the brain tissue. Cerebral ischaemia was induced by a remote filament approach of MCAo allowing precise control of occlusion and reperfusion during *in vivo* two-photon imaging. To monitor neuronal calcium responses in all stages of cerebral ischaemia, fast resonant scanning was performed at repeated 2 min recordings at 31.25 frames second followed by a 5-min break, continuously for up to 6 h including the assessment of baseline neuronal activity, 60 min occlusion of the MCA and 4-5 h reperfusion. (b) Cerebral blood flow (CBF) was measured by a laser Doppler over the MCA (1) and at different sites within (2-3) and outside (4) the area of the cranial window (N = 5 mice). (c) Representative images showing GCaMP6s signal changes in a group of neurons (arrows) imaged *in vivo* before and during MCA occlusion followed by reperfusion in the cerebral cortex over a 310 min period. Images represent average intensity projections of a 2 min resonant scanning session for each data point. (d) Representative graph showing GCaMP6s signal changes over time in mice (N = 4) that had been subjected to 60 min MCAo followed by 4 h reperfusion (blue line) and in sham animals (black line). Integrated density values were expressed as a percentage of baseline (IntDen%). (e) Spreading depolarizations (SD) are initiated 2.5-4 h after the onset of ischemia. Images show neuronal calcium changes during a single 2 min resonant scanning session, arrows indicate the wavefront of depolarization. Calcium curves from five representative neurons are shown in different colours. (f) Quantification of average GCaMP6s signal changes reveals delayed development of excitotoxic responses after stroke (N = 38 neurons from 4 mice). Data are expressed as mean ± s.e.m. **b,f**: one-way analysis of variance followed by Tukey's multiple comparison. Scale bars, **c,e**: 50 μm.

Surprisingly, an absence of microglia was associated with the complete lack of SD in microglia-depleted animals after brain injury (Fig. 4a,b). Hence, average GCaMP6s signal levels did not increase 1.5-3 h after reperfusion as seen in control mice (Fig. 4c). However, cumulative calcium load as calculated by summing up calcium curve integrals from the 2-min resonant scanning sessions of individual neurons over an 5.5 h imaging period, was significantly (over fourfold) higher in microglia-depleted mice compared with controls (Fig. 4d). This difference was striking considering that SDs contributed substantially to cumulative

calcium load in control mice, whereas no SDs were seen in the absence of microglia. Moreover, we calculated the time spent before increases in intracellular calcium load become evident in individual neurons, which was markedly shorter in the absence of microglia (Fig. 4e). To investigate whether the increased cumulative calcium load seen in the first hours after ischaemia/reperfusion is associated with subsequent neuronal injury, we investigated the fate of affected neurons at the imaging site 24 h after cerebral ischaemia. We found a significant (20%) reduction in the number of cresyl violet-stained neurons 24 h after cerebral

dc_2027_22

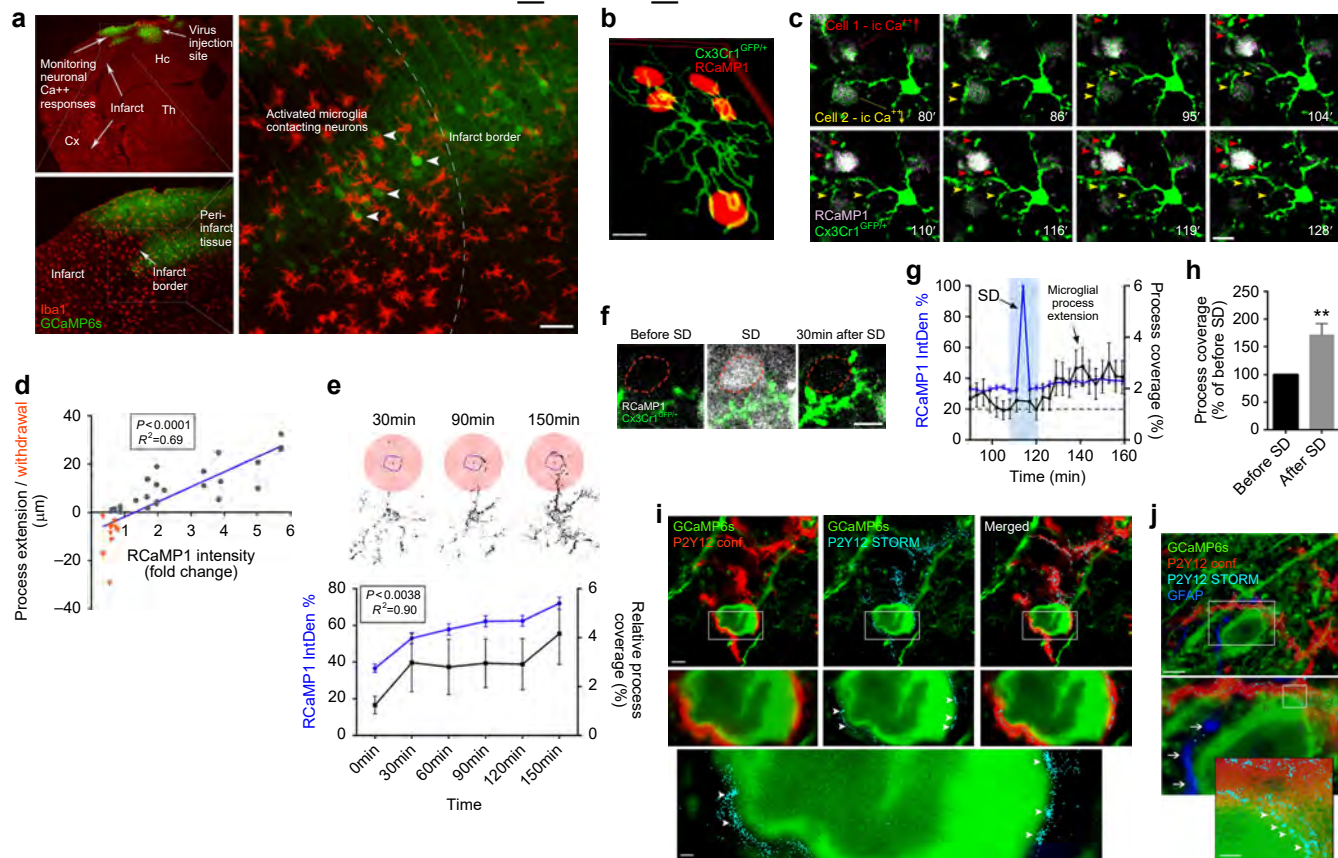


Figure 3 | Microglia interact with neurons in an activity-dependent manner and respond to SD after cerebral ischaemia. (a) Activated microglial cells (Iba1, red) surround neurons showing high GCaMP6s signal (green, arrowheads), in the boundary zone of the infarct after cerebral ischaemia. (b) Reconstruction of *in vivo* two-photon images at different Z-planes show microglial process coverage of neurons (RCaMP1, red) in the cerebral cortex in *Cx3Cr1^{GFP/+}* microglia reporter mice (arrowheads) 2 h after the onset of ischaemia (c) *In vivo* two-photon imaging reveals microglial process extension (red arrowheads) to neurons with increasing intracellular calcium levels (RCaMP1, pseudocolored) after cerebral ischaemia, whereas decreasing neuronal RCaMP1 signal is associated with microglial process withdrawal (yellow arrowheads). (d) Microglial process recruitment correlates significantly with changes in neuronal calcium levels after cerebral ischaemia (linear regression, $N = 35$ microglial processes). (e) Measurement of microglial process density in concentric circles around individual neurons (modified Sholl analysis, $N = 35$) showing microglial process recruitment to the neuronal cell body (circled in blue) over time after MCAo. Graph showing significant correlation between intracellular calcium levels in neurons ($N = 45$) based on RCaMP1 signal changes (blue line) and microglial process coverage (black line) over time. (f) Spreading depolarization (SD) initiated after cerebral ischaemia rapidly increase microglial process coverage of neurons in the cerebral cortex. (g) Graph showing the kinetics of microglial process recruitment after SD. After SD, microglial process coverage of neurons ($N = 41$) increases, even if intracellular calcium returns to near-baseline levels ((h), $N = 17$ neurons, unpaired *t* test). Integrated density values on e.g were expressed as a percentage of baseline (IntDen%). (i) STORM super-resolution microscopy reveals a close contact between P2Y12-positive microglial processes (cyan) and GCaMP6s-positive neurons (green). P2Y12 receptors form clusters at sites of microglia-neuron interaction (arrowheads). (j) Microglial processes and P2Y12 clusters (arrowheads) are found in close proximity to the neuronal cell membrane distant from GFAP-positive (dark blue) astrocyte processes (arrows). (i,j) Representative images from the cerebral cortex of mice subjected to MCAo. Data are expressed as mean \pm s.e.m. Scale bars, a: 50 μ m; b,c,f: 10 μ m; i,j: 5 μ m (inserts 500 nm).

ischaemia in control mice, which was markedly augmented (by over twofold) in microglia-depleted animals (Fig. 4f,g).

Lack of microglia alters neuronal responses to KCl. To test whether an absence of microglia leads to altered neuronal calcium dynamics in the non-ischaemic brain, we applied potassium chloride (KCl) topically to the surface of the cerebral cortex, which is widely used to induce neuronal depolarization and SD^{19,34}. Spontaneous calcium responses before KCl application and calcium responses during SD showed a good correlation with changes in local field potential (Supplementary Fig. 11). In control mice, SD was readily induced within 0.5–3 min after administration of 100 mM KCl with an obvious propagating wavefront as evidenced by GCaMP6s signal changes during fast *in vivo* two-photon imaging (Fig. 5a,b and Supplementary

Video 5). In contrast, similar SD to that seen in control mice was rarely observed in the absence of microglia. In some cases a pale wavefront was seen, resulting from increases of GCaMP6s signal (considered as an SD for quantification) in neuronal cell bodies and the neuropil (Fig. 5b and Supplementary Video 6). Repeated KCl application (three times, over the course of 2 h) resulted in only 20% probability of SD in the absence of microglia as opposed to 80% in animals with functional microglia in the brain (Fig. 5c). Quantitative analysis showed that GCaMP6s signal increases in individual neurons over baseline values after KCl administration took place with significant latency (mean 17 min) in the absence of microglia, compared to control mice (2.5 min, Fig. 5d). In addition, integration of calcium curves of individual neurons revealed a marked reduction in KCl-induced depolarization in microglia-depleted mice (Fig. 5e). Thus, modulation of neuronal activity by microglia-mediated actions appears to be a basic

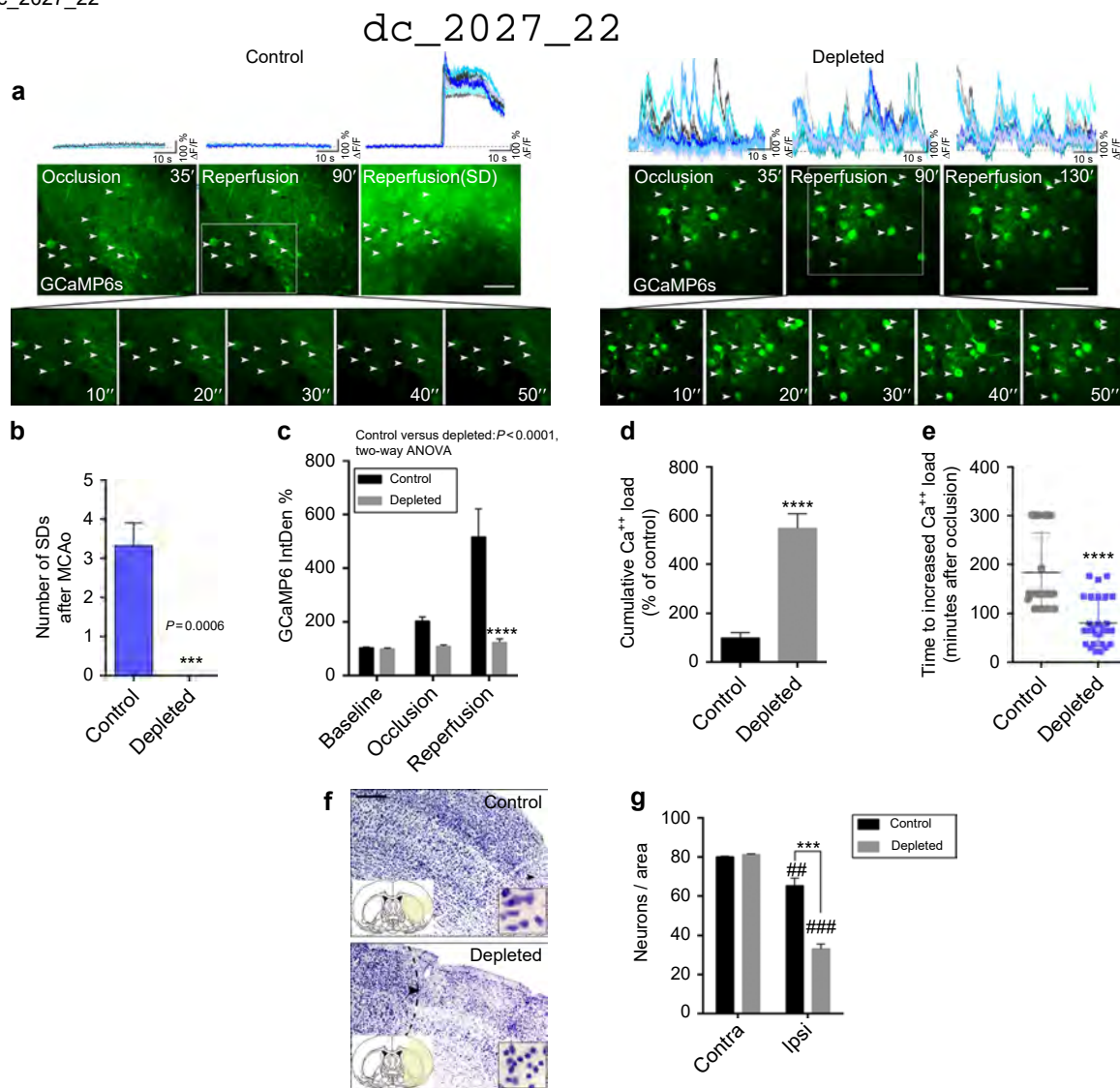


Figure 4 | Microglia shape neuronal activity after cerebral ischaemia. (a) Neuronal GCaMP6s signal changes were assessed by *in vivo* two-photon imaging in the cerebral cortex using 2 min long recordings with fast resonant scanning (31.25 frames per second), separated by 5 min breaks. In control mice no significant GCaMP6s signal intensity changes were seen before the occurrence of spreading depolarizations (SD) starting typically 1.5–3 h post-reperfusion (left panel, inserts shown at Reperfusion 90'). In contrast, an absence of microglia resulted in slow neuronal oscillations (at ≈ 0.1 Hz frequency) already during occlusion, with similar changes seen after reperfusion (right panel). Representative calcium transients from 10–10 individual neurons (white arrows, calcium responses are indicated by different colours) are shown on the top panels from control and microglia-depleted mice. (b) Lack of microglia resulted in the absence of SD. (c) Average GCaMP6s intensity of 2 min recordings was increased at late reperfusion in control mice due to initiation of SDs, compared to microglia-depleted animals. Integrated density values were expressed as a percentage of baseline (IntDen%). (d) In contrast, cumulative calcium load (expressed in % of control) as calculated by summing up calcium curve integrals of individual neurons during the 2 min long two-photon recordings over a course of 5.5 h (baseline, 60 min occlusion and 4 h reperfusion) was significantly increased in microglia-depleted animals. (e) Microglia-depleted animals reach increased calcium load over baseline significantly earlier (due to continuous neuronal depolarizations) than control mice (due to delayed initiation of SD). (f) Cresyl violet staining reveals marked neuronal death in the imaging site in microglia-depleted mice compared to controls. (g) Quantification of cresyl violet-stained neurons ($N = 8$ mice, two-way analysis of variance (ANOVA), followed by Sidak's multiple comparison) at the imaging site in the cerebral cortex and the corresponding contralateral hemisphere. Data are expressed as mean \pm s.e.m. **b:** $N = 4$ mice per group, unpaired *t*-test; **c:** two-way ANOVA followed by Dunn's multiple comparison; **d, e:** unpaired *t*-test, **c–e:** $N = 52$ neurons from 4 individual mice. $\#\#P < 0.01$, $\#\#\#P < 0.001$ versus contralateral, $***P < 0.001$ control versus depleted. Scale bars, **a**, 50 μ m; **f**, 200 μ m.

physiological phenomenon that is evident in both the intact and the injured brain.

Lack of microglia does not augment BBB injury after stroke.

Since previous studies implicated microglia in vascular injury after cerebral ischaemia⁹, we tested whether altered BBB injury could be responsible for some of the changes we observed in microglia-depleted animals. *In vivo* two-photon recordings of

Z-stacks in *Cx3Cr1^{GFP/+}* mice with RCaMP1 (Fig. 3b) and histological analysis (Supplementary Fig. 12A) revealed that individual microglial cells extended processes to 6–12 nearby neurons on average, located 15–80 μ m away from the microglial cell body. In addition, microglia contacting neurons were often found in the vicinity of capillaries, or extended their processes to distant microvessels. Using *Cx3Cr1^{GFP/+}* mice injected intravenously with a red fluorescent tracer, Dextran rhodamine (70,000 molecular weight), we set out to visualize sites

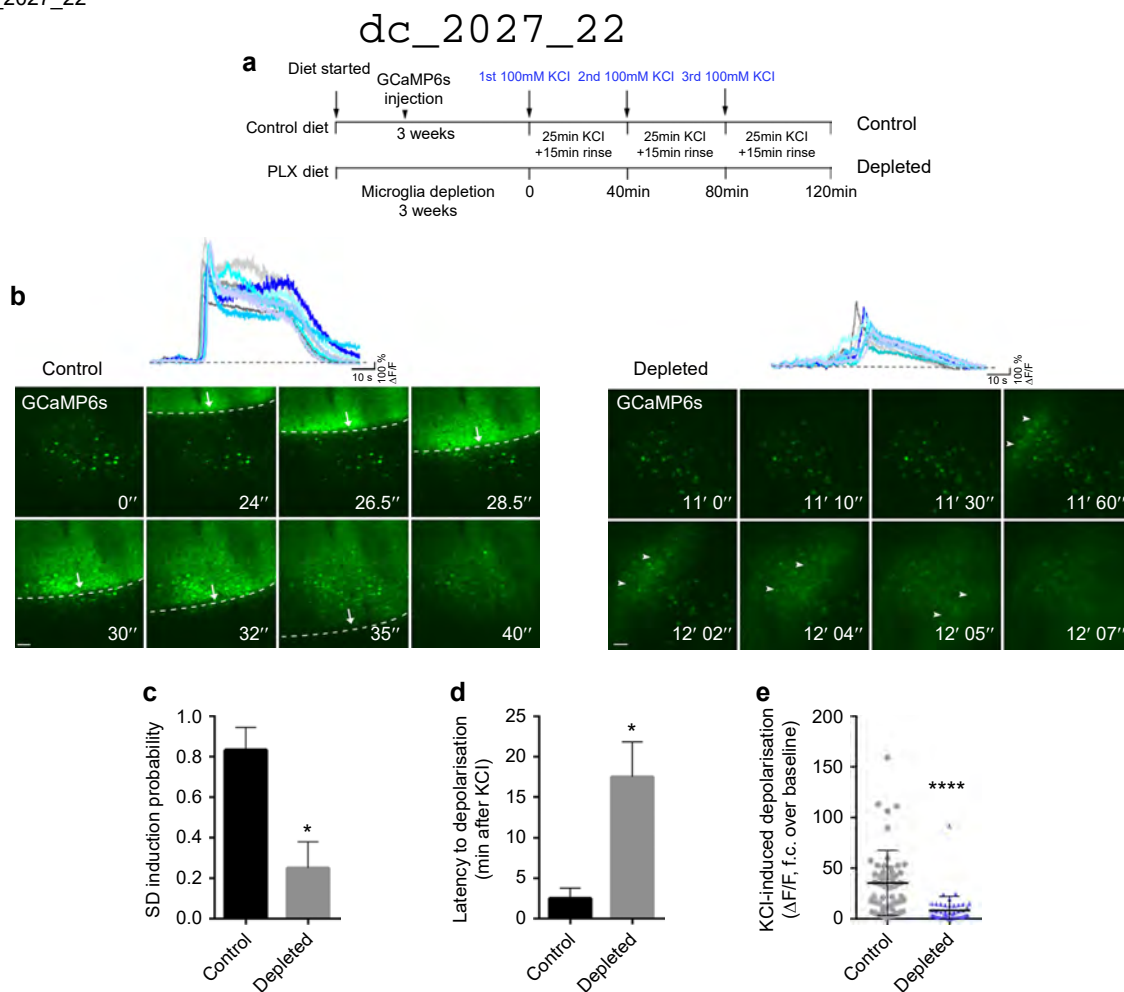


Figure 5 | Microglia shape neuronal activity in the non-ischaemic brain (a) Outline of experimental procedures to investigate KCl-induced neuronal depolarization in the absence of microglia. Three weeks after feeding mice a control or a PLX3397 diet (290 p.p.m.), and two weeks following GCaMP6s delivery, spreading depolarizations (SDs) were induced by 100 mM KCl for 25 min followed by a 15 min rinse: the protocol was repeated three times. (b) Neurons in the cerebral cortex of control mice displayed rapid SD generation after induction by KCl (left panel, arrows indicate the evolving SD wavefront). An absence of microglia resulted in a very low incidence of SD and a low level of depolarizations compared to that seen in control animals (arrowheads indicate a pale depolarization wave seen in the absence of microglia). Representative calcium curves of 10 individual neurons are shown on the top of the panel. (c) SD induction probability (number of successful SD inductions/number of KCl applications) was markedly reduced in the absence of microglia. (d) Latency to depolarisation after KCl administration was significantly increased in microglia-depleted animals. (e) KCl-induced depolarization resulted in significantly lower levels of GCaMP6s signal in the absence of microglia compared to control mice. **c, d** and **e** graphs show mean \pm s.e.m. $N = 102$ neurons from 4 individual mice. **c**, Mann-Whitney test; **d, e**, unpaired *t*-test. * $P < 0.05$, **** $P < 0.0001$. Scale bar, **b**, 50 μ m.

of BBB injury that have been associated with altered microglial activity in previous studies^{25,35}. BBB injury at the level of microvessels and arterioles occurred typically 50–90 min after the onset of ischaemia. Microglia located in the vicinity of blood vessels were recruited to the injured sites and displayed an activated phenotype within 15–40 min followed by partial withdrawal of their processes (Supplementary Fig. 12b). However, we found that elimination of microglia did not result in any significant alterations in the kinetics of BBB injury as assessed by *in vivo* two-photon imaging (Fig. 6) based on the extravasation of intravenously injected Dextran rhodamine in *Cx3Cr1^{GFP/+}* mice. Quantitative analysis showed that significant BBB injury in the brain parenchyma takes place 60 min after the onset of ischaemia (analysis of variance, $P < 0.05$) in both control and microglia-depleted animals, but control and microglia-depleted animals did not significantly differ (Fig. 6b). Similarly, no differences were seen in the glia limitans in control versus microglia-depleted mice (Fig. 6c). In addition, an absence of microglia did not alter BBB injury 24 h after MCAo as assessed on coronal brain sections based on leakage of circulating IgG into the brain parenchyma

(Fig. 6d). Thus, these data strongly suggest that microglia-mediated protective effects after brain injury are due to the regulation of neuronal activity by microglia and not to effects on the extent or kinetics of vascular injury. We also found blunted upregulation of IL-1 α , tumour necrosis factor- α (TNF α), IL-6, monocyte chemoattractant protein-1 (MCP-1), KC (CXCL1) and IL-4 in the ipsilateral hemisphere 8 h after cerebral ischaemia in the absence of microglia (Supplementary Fig. 13), indicating that increased brain injury and changes in neuronal responses are not explained by exaggerated inflammatory responses in this model of microglia depletion.

Discussion

Here we identify microglia as important components of the neuronal response to brain injury and show that microglia protect against neuronal injury. Selective removal of microglia from the brain leads to the dysregulation of neuronal calcium responses and network activity, increased calcium accumulation and markedly reduced SD incidence after brain injury, which is

dc_2027_22

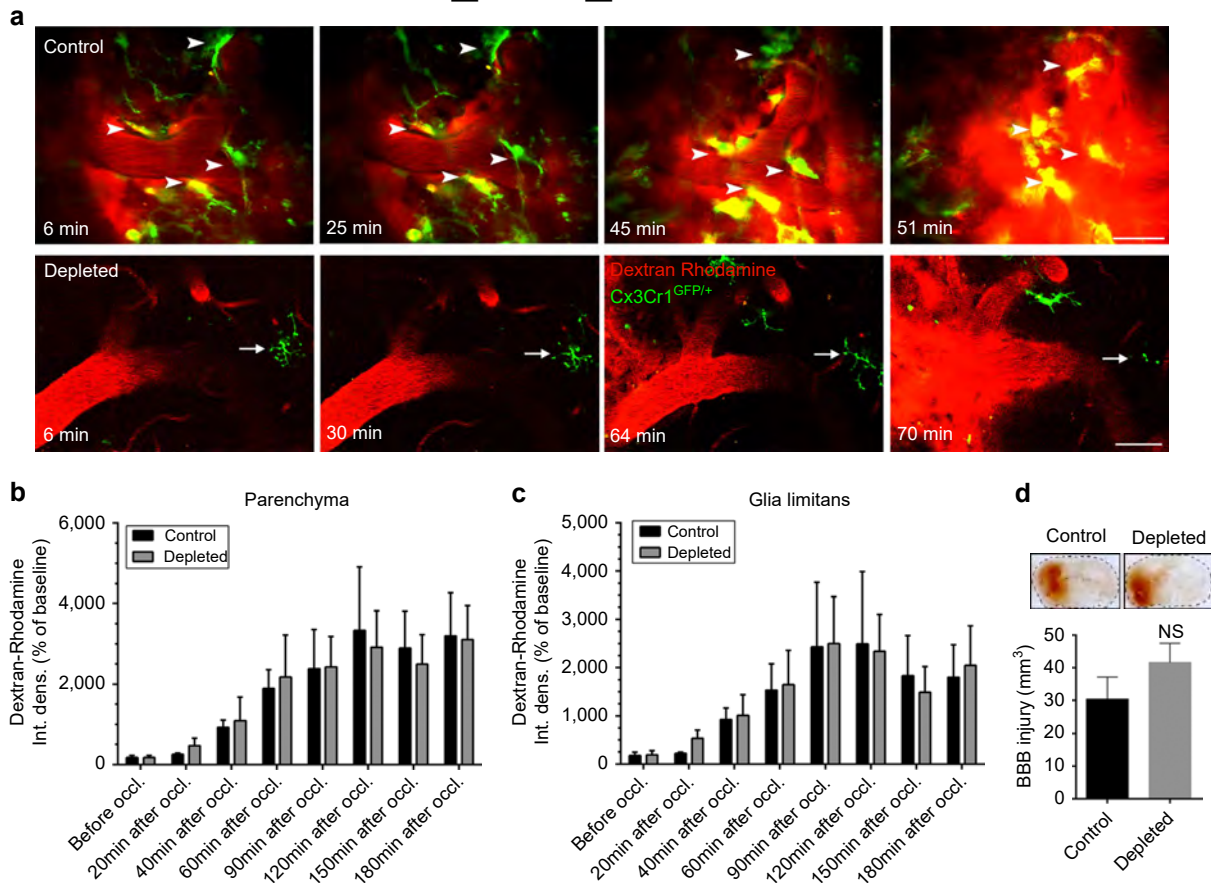


Figure 6 | Selective depletion of microglia does not alter blood brain barrier injury after cerebral ischaemia *In vivo* two-photon imaging was performed in control mice and in mice that were fed a chow diet containing PLX3397 (290 p.p.m.) for three weeks to selectively eliminate microglia from the brain. In *Cx3Cr1^{GFP/+}* mice, Dextran rhodamine (1 mg per mouse in 150 μ l volume) was administered via the jugular vein 15 min before MCAo. Z-stacks between 100 and 300 μ m below the dura mater were recorded every 3 min over a 4–5 h period before, and after the onset of ischaemia. **(a)** *In vivo* two-photon microscopy revealed increasing Dextran Rhodamine fluorescence signal in the extravascular space indicating blood brain barrier damage following cerebral ischaemia. Areas of blood brain barrier breakdown in control mice were monitored by microglia (arrowheads), which acquire an activated phenotype over time. Remaining microglia in a microglia-depleted mouse is indicated by an arrow. **(b)** Quantification of Dextran rhodamine intensity changes in the brain parenchyma over time, before and after cerebral ischaemia in control and microglia-depleted animals. Integrated density values were expressed as a percentage of baseline. **(c)** Quantification of Dextran Rhodamine intensity changes in the glia limitans. Quantitative data (mean \pm s.e.m.) from $N = 12$ blood vessels in control and $N = 8$ blood vessels in microglia-depleted animals, from 3 mice per group, analysed with two-way analysis of variance followed by Dunn's multiple comparison. **(d)** BBB injury (mm^3) in control and microglia-depleted mice (mean \pm s.e.m., $N = 8$ –10 mice, unpaired *t*-test) as measured by leakage of plasma-derived IgG into the brain parenchyma 24 h after MCAo. NS, not significant. Scale bar, **a**, 50 μ m.

associated with profoundly increased neuronal loss. Therefore, selective targeting of the pathways involved could have a critical impact on understanding the pathophysiology of common human diseases and the development of novel therapeutic approaches.

The role of microglia in the healthy brain and in neurological diseases remains highly controversial, in spite of the substantial research effort and recent breakthroughs in this field^{1,2,21}. Microglia, the resident immune cells of the brain, appear to be essential for normal brain function, whereas altered microglial function has been linked with diverse brain pathologies in both humans and experimental animals. These include diseases with a high socioeconomic burden such as depression, psychiatric diseases, epilepsy, stroke, migraine, Parkinson's disease and various forms of dementia such as Alzheimer's disease^{2,3,5,6,26,28,36}. The controversies regarding the possible detrimental or protective role for microglia in different models of neurological diseases are likely due to multiple factors. Of these, the immunological and functional similarities between microglia and peripheral macrophages have made it difficult, until very

recently, to selectively manipulate microglia^{6,24}. Most microglia in the brain are protected by the BBB (except for the cells that reside in the circumventricular organs), and are hence difficult to target, while microglia become rapidly activated in response to any disturbance to the brain or after peripheral inflammatory challenges, which can shape microglial responses and outcome after different forms of brain injury^{1,5,7}. It is important to note that none of the previous studies combined selective microglial depletion with high-resolution two-photon calcium imaging *in vivo*, to link microglial function with neuronal activity and injury in real time.

We, therefore, established a model of brain injury that allowed us to monitor both microglia–neuron interactions in real time and the effects of microglial depletion on neuronal activity and injury. During preliminary experiments, a model for GCaMP6s delivery was developed to minimize the disturbance of neurons or microglia at the imaging site, while the remote filament model of cerebral ischaemia allowed us to induce targeted injury in the brain without focal surgical intervention in the cerebral cortex. Elimination of microglia using CSF1R blockade was selective, as it

dc_2027_22

did not deplete peripheral myeloid cells, although a small, non-significant reduction in CD11b_{low} Ly6c^{high} monocytes that correspond to ~2% of total blood leukocytes was noticed. This is unlikely to have a major impact on neuronal activity and injury in this model, especially considering the limited recruitment of monocytes/macrophages compared to microglia in the brain at 24 h reperfusion after transient focal cerebral ischaemia^{37,38}. Depletion of microglia also had minimal impact on other cell types in the brain. This is in line with previous observations using the same approach²⁴, which also demonstrated a lack of illness and behavioural alterations in microglia-depleted animals^{24,32}. This might be due to the cessation of an essential survival signal mediated by CSF1R, leading to the apoptotic death of microglia, without the induction of inflammation. This regimen is expected to cause fewer disturbances to the brain than applying toxic substances that could lead to microglial activation or inflammation. Depletion of microglia by genetic expression of diphtheria toxin could lead to deficits in learning and contextual fear conditioning³⁹, or cause cytokine expression in the brain³¹, whereas toxicity to hematopoietic cells was observed in *CD11b-HSVTK* mice in response to ganciclovir⁴⁰. In addition, microglia ablation by CSF1R blockade did not affect astrocytes, in contrast to observations in microglia-depleted animals using the *Cx3Cr1^{CreER};iDTR* model³¹.

Excitotoxicity is considered to be a major mechanism of neuronal death that occurs due to intracellular calcium overload followed by the activation of various cell death pathways⁴¹. After global cerebral ischaemia, rapid, but reversible damage to dendrites and spines was found to be caused by ischaemic depolarizations immediately after cessation of blood flow⁴². SD was also observed with *in vivo* calcium imaging propagating from the core of cortical microinfarcts⁴³. We observed delayed occurrence of SD in control mice after focal cerebral ischaemia with small increases in intracellular calcium during MCA occlusion. To our surprise, an absence of microglia completely prevented SD after ischaemia, and markedly reduced the incidence of SD following KCl administration in the non-ischaemic brain. SD has been associated with neuronal injury in stroke, epilepsy, migraine and other forms of brain injury^{18–20,34}. *In vitro* studies on rat hippocampal brain slices have suggested that microglial polarization states could affect the SD threshold⁴⁴. However, the lack of SD in the ischaemic brain in the absence of microglia *in vivo* was unexpected. Instead, the development of slow neuronal oscillations as early as 15–25 min after the onset of ischaemia was seen, which was not due to immediate injury to neurons, since slow oscillations were observed even 2–3 h after reperfusion in the same cells. The majority of the affected neurons died within 24 h in the absence of microglia at the imaging site unlike in control mice, indicating that altered calcium responses could be involved in more pronounced neuronal injury as widely supported by literature data^{45,46}. Due to the lack of research tools to influence SD independently of changing neuronal activity, no mechanistic experiments could be performed in this study to functionally link SD with neuronal injury. However, our data suggest that at least after ischaemia, neuronal death in complex neuronal networks following a series of SDs could be lower than in response to dysregulated neuronal network activity and long-lasting oscillations as seen in the absence of microglia. Altered neuronal responses were observed already 30–45 min before BBB injury in microglia-depleted animals after stroke and were also seen after KCl administration, which does not lead to the disruption of the BBB. Therefore, these data suggest that microglia could impact on neuronal calcium responses and protect against neuronal injury independently of vascular injury. Mice were anaesthetized during imaging, which could alter neuronal responses⁴⁷. However,

control and microglia-depleted mice were exposed to uniformly low isoflurane levels (between 0.8 and 1.1%), hence the anaesthetic is unlikely to contribute to the profoundly altered neuronal responses seen in the absence of microglia. We have not found differences in CBF after MCA occlusion and reperfusion between control and microglia-depleted mice either, although we are aware that laser Doppler measurements only reveal changes in blood flow relative to baseline values in the superficial areas of the cerebral cortex.

We have also investigated whether PLX3397 has any effect on neuronal injury independently of microglia depletion. It has been postulated that CSF1R signalling could contribute to neuronal survival independently of microglia⁴⁸. However, in our experiments withdrawal of PLX3397 for 24 h, which reduces drug concentrations to below detection level²⁴, while microglia remained depleted, resulted in increased brain injury, similar to that seen in mice fed a PLX3397 diet at the time of MCAo. Increases in brain injury were completely reversed after repopulation of microglia. In addition, acute treatment with a PLX3397 dose higher than that needed to block microglial repopulation²⁴ did not result in depletion of microglia and did not alter brain injury. It is expected that BBB injury after cerebral ischaemia would further increase PLX3397 levels in the brain. These experiments suggest that larger brain injury in this model is due to the absence of functional microglia. Data from previous studies also support our conclusions. Elimination of microglia from rat organotypic slice cultures in a CSF1R-independent manner reduced the incidence of SD, whereas dampening of microglial M1 signalling by minocycline or conditioned medium from M2a-polarized primary microglia led to higher SD threshold⁴⁴. In addition, inhibition of proliferating microglial cells in *CD11b-TK^{mt-30}* transgenic mice resulted in larger ischaemic injury⁴⁹. The effects of microglia depletion on cerebral perfusion, somatosensory and motor responses, delayed phases of neuronal injury and functional recovery, will need to be investigated in future studies using models of brain injury and neurodegeneration.

The exact molecular mechanisms through which microglia sense and regulate neuronal activity are presently unclear but investigation of the molecular pathways involved extends beyond the scope of this already complex study. It is likely that microglia–neuron signalling involves highly complex interactions between metabolic pathways, neurotransmitters and their receptors, ion channels and inflammatory mediators. Microglia–neuron interactions in the optic tectum of the larval zebrafish were found to be dependent on neuronal pannexin-1 hemichannels and the small Rho GTPase, Rac in microglia⁵⁰. ATP triggers microglial migration and process extension in both zebrafish larvae and the mammalian brain *in vivo*^{8,50}. In fact, super-resolution microscopy revealed increased microglial process coverage of neuronal cell bodies after ischaemia and clustering of P2Y12 receptors on fine microglial processes at sites of microglia–neuron contacts, although the functional role of purinergic signalling was not investigated in this study. Glial fibrillary acidic protein (GFAP)-positive astrocyte processes have not been observed at the microglia–neuron interface, but it is possible that some microglial actions on neurons could be mediated via astrocytes. Microglia are known to produce a diverse array of inflammatory mediators that act directly on neurons and impact on neuronal activity and injury. Some of these, such as IL-1 potentiate excitotoxicity and neuronal injury⁵, while TNF α is known to alter the balance between neuronal excitation and inhibition via different, complementary mechanisms that involve neuronal AMPA, NMDA and GABA_A receptors⁵¹. Despite larger brain injury, an absence of microglia was associated with blunted ischaemia-induced production of both proinflammatory cytokines

dc_2027_22

(IL-1 α , TNF α) and cytokines that are considered to be neuroprotective in the brain (IL-6, IL-4)^{52,53}. Thus, the possible contribution of these cytokines to brain injury remains to be investigated further. The net effect of different microglial actions on neuronal activity and injury could be highly dependent on the dominance of certain pathophysiological mechanisms in different CNS diseases. However, our data are the first to demonstrate that microglia markedly protect neurons against excitotoxicity and injury after cerebral ischaemia *in vivo*, in spite of the plethora of inflammatory mediators they produce.

Taken together, our results obtained by the combination of high speed *in vivo* two-photon imaging with selective microglia manipulation revealed a previously unrecognized link between protective microglial actions and neuronal activity and injury. These results could have profound implications on the pathophysiology and potential treatment of major human diseases.

Methods

Mice. Experiments were carried out in 12–16 weeks old male C57BL/6J and *Cx3Cr1^{GFP/+}* mice, breeding in the specific-pathogen-free (SPF) unit of the Institute of Experimental Medicine. Animals were allowed free access to food and water and were maintained under controlled temperature, humidity and light conditions. All procedures were in accordance with STAIR and ARRIVE guidelines, and the guidelines set by the European Communities Council Directive (86/609 EEC) and the Hungarian Act of Animal Care and Experimentation (1998; XXVIII, section 243/1998), approved by the Animal Care and Use Committee of the Institute of Experimental Medicine.

Selective elimination and repopulation of microglia. PLX3397 was provided by Plexxikon and formulated in AIN-76A standard chow by Research Diets (290 p.p.m.; 290 mg PLX3397 in 1 kg chow). Mice were fed a PLX3397 diet for 3 weeks to eliminate microglia²⁴. One group of mice was given PLX3397 for 3 weeks, followed by withdrawal of the drug by replacing the PLX3397 diet with control chow diet for 24 h before experiments. Another group of mice was fed PLX3397 for 3 weeks followed by 2 weeks on control diet to allow for the repopulation of microglia in the brain. In agreement with earlier results²⁴, we have not found any obvious behavioural alterations, weight loss or sign of illness in mice fed a PLX3397 diet for 3 weeks or longer. Individual mice were observed for a 5-min period once daily for any changes in activity, exploratory behaviour and social interaction. Baseline temperature was recorded for every mouse before surgery or imaging. No mice were excluded from these studies due to fever, weight loss, infection or behavioural alterations as a result of PLX3397 diet.

AAV vector injection. The injection procedure was performed as described previously⁵⁴, with some modifications. A 0.5-mm hole was opened in the skull with the tip of a dental drill over the S1 cortical region (centred 1.5 mm lateral and 1.5 mm posterior to the bregma). A glass micropipette was lowered 300 μ m under the pia, at a 60° angle towards the imaging area to minimize tissue disturbance at the imaging site, followed by slow injection (300 nl over 5 min) of either AAV1.Syn.GCaMP6s.WPRE.SV40 or AAV1.Syn.RCaMP1h.WPRE.SV40 viral vectors (Penn Vector Core, Philadelphia, PA; titre 6.32×10^{11} IU ml⁻¹).

Cranial window surgery. Two weeks after injection mice were anaesthetized using isoflurane (3% for induction, 1.5–2% during surgery). First, a custom-made aluminium head plate was fixed to the skull using cyanoacrylate glue and dental cement. Then, the skull was either thinned to 20 μ m over the imaging site or a circular craniotomy (3 mm diameter) was made above the S1 cortex (centred 2.7 mm lateral and 1 mm posterior to the bregma) without touching the dura mater. During drilling, the place of craniotomy was rinsed continuously with cold Ringer solution. The location of the imaging window was defined in a separate set of experiments by series of CBF measurements using laser Doppler flowmetry (30 measurements performed at 6 different sites, in $n = 5$ mice). This was done by recording baseline blood flow followed by the occlusion of the MCA with an intraluminal filament for ~15 s after which reperfusion was induced and the Doppler probe repositioned repeating this procedure several times between the MCA and the midline in the same mouse. The area of the craniotomy was covered with a 3-mm cover glass and fixed with dental cement. In preliminary experiments, microglial activation and neuronal calcium responses were assessed in the case of thinned skull preparations and after craniotomy without dura mater injury. No changes in neuronal calcium signals, microglial CD45, Iba1 or *Cx3Cr1* expression were found in either case as opposed to craniotomy with durectomy (Supplementary Fig. 1, and not shown).

Imaging fast calcium responses and BBB injury. All experiments were performed on a Femto2D-DualScanhead microscope (Femtonics Ltd., Budapest, Hungary). Laser pulses were generated by a Mai Tai HP laser (SpectraPhysics, Santa Clara, CA) or by a Chameleon Ultra II laser (Coherent, Inc., Santa Clara, CA). The wavelength was set to 910 nm for GCaMP6s and to 980 nm when RCaMP1 and microglia in *Cx3Cr1^{GFP/+}* mice were measured simultaneously. For excitation and signal collection, a CF175 LWD 16XW/0.8 lens (Nikon, 16 \times , NA 0.8) was used, separated using a dichroic mirror (700dxcru, Chroma Technology) before the two channel detector unit, which was sitting on the objective arm (travelling detector system) as described in detail elsewhere^{55,56}. The DualScanhead microscope (Femtonics Ltd., Budapest, Hungary) is coupled with two parallel light paths, which allows imaging at the same imaging site either with a galvanic mirror or with resonant scanner without moving or changing the sample. First, the galvo-scanning light path was used to acquire Z-stacks from 200 to 80 μ m under the dura mater, with 12 images per stack at 800 \times 800 pixel resolution (0.75 μ m per pixel). Then, the light path was changed to the resonant scanning mode and two-photon imaging at video rate (31.25 frames per second) was performed at 512 \times 512 pixel resolution (1 μ m per pixel) for 60–120 s. This protocol was repeated every 5 min over the whole (5.5–6 h) imaging period for cerebral ischaemia studies. Data acquisition was performed by MesC software (Femtonics Ltd.). To image microglia in *Cx3Cr1^{GFP/+}* mice simultaneously with the assessment of BBB injury the galvo-scanning light path was used. Z-stacks were recorded in the cerebral cortex (same area as used for neuronal calcium measurements) continuously from 200 μ m to 110 μ m under the dura mater every 3 min for a 5–6 h period before, and after the onset of ischaemia. Integrated density (area of the ROI \times the mean of the ROI) was assessed at 6–6 randomly selected areas over the brain parenchyma and the glia limitans in every stack, using ImageJ. Integrated density values were expressed as a percentage of baseline (IntDen%). The occlusion of the MCA during *in vivo* two-photon imaging was verified by blood flow velocity changes measured using the line-scan mode of the galvo-scanning light path. Dextran rhodamine signal was recorded along a linear scanning trajectory perpendicular to the blood vessels' wall (measuring a single, 1.5 μ m linear line with 3–5 kHz temporal resolution) on the red channel. Blood flow velocity was calculated as earlier³⁷. Three mice in total were excluded from the imaging studies *pre hoc*, one control mouse after cerebral ischaemia due to improper laser intensity during imaging and two (one control and one microglia depleted) mice from KCl studies due to inappropriate anaesthesia.

SD induction with KCl solution. In one group of mice, a small area of the cranial window was left uncovered laterally to the cover glass (where the dura mater was not injured). The dura mater was focally opened using a syringe needle and SD was induced by applying 100 mM KCl solution to the surface of the brain for 25 min. Three repeated SD induction periods were recorded. During SD induction, animals were continuously imaged with resonant scanning for repeated 2 min periods. Then, a 15-min resting period was put in the protocol when the KCl solution was replaced with Ringer solution until the beginning of the next SD induction. In a set of studies, local field potential was measured simultaneously with GCaMP6s signal changes before and after KCl application, using a borosilicate glass electrode (~0.1 M Ω) filled with ACSF. Recordings were made in IC mode at 0 mV holding potential.

Remote filament model of MCAo. Cranial window preparation was followed by remote filament implantation under isoflurane anaesthesia. The common carotid, the external carotid and the internal carotid arteries were exposed and the common carotid artery temporarily clipped. A 5 cm long, 5.0 monofilament with silicon rubber coating (210 μ m tip diameter), residing in a silicone guiding tube was introduced into the left external carotid artery and advanced along the internal carotid artery up to 8 mm, without occluding the MCA. Blood flow was restored in the common carotid artery and the silicone guiding tube was secured, followed by closure of the wound at the site of surgery, to allow free manipulation of the monofilament during *in vivo* two-photon imaging. Mice were positioned into the two-photon microscope, after which 15–30 min baseline imaging was performed followed by the induction of 60 min of MCA occlusion and 4–5 h reperfusion.

Middle cerebral artery occlusion. MCAo was performed using the intraluminal filament technique as described earlier⁵⁸. In brief, animals were anaesthetized with isoflurane and a silicone-coated monofilament (210 μ m tip diameter, Doccol, US) was introduced into the left external carotid artery and advanced along the internal carotid artery to occlude the MCA for 45 min. Occlusion was confirmed by a laser Doppler (Moor Instruments, UK). During surgery, core temperature was maintained at 37 \pm 0.5 °C. After experimental stroke, four mice were excluded *pre hoc* due to incomplete occlusion of the MCA or surgical artifacts.

Tissue processing and immunostaining. After terminal anaesthesia, mice were perfused transcardially with saline followed by ice-cold 4% paraformaldehyde. Brains and spleens were post-fixed for 24 h, cryoprotected in 10% sucrose/PBS and sectioned (25 μ m diameter) on a sledge microtome. Detection of IgG leakage to the brain parenchyma by immunostaining (Vector, NBA-2000, horse anti-mouse biotinylated IgG 1:500) was used to assess BBB permeability on brain sections

as described earlier⁵⁸. Immunofluorescence was performed on free-floating brain sections using combinations of rabbit anti-Iba1 (WAKO, 019-19741, 1:500), rat anti-CD45 (AbD Serotec, MCA1388, 1:250), mouse anti-GFAP (Sigma, G3893, 1:500), rabbit anti-Claudin-5 (Invitrogen, 34-1600, 1:500) and goat anti-PDGFR β (R&D Systems, AF1042, 1:500) antibodies. Sections were incubated in a primary antibody cocktail overnight followed by adequate fluorochrome (Invitrogen, A21206, donkey anti-rabbit Alexa 488 1:500; Invitrogen, A21203, donkey anti-mouse Alexa 594 1:500)-conjugated antibodies. Biotinylated tomato lectin (Sigma-Aldrich, L0651-1 mg, 1:100) was used to visualize blood vessels, followed by streptavidin Alexa 350 conjugate (Invitrogen, S11249, 1:200). Images were captured using a Zeiss Axiovert 200M microscope with Axiovision 4.8 software.

Super-resolution microscopy. Free-floating brain sections were blocked with 2% normal donkey serum followed by immunostaining with rabbit anti-P2Y12 (Anaspec, AS-55043A, 1:500) antibody and anti-rabbit Alexa 647 secondary antibody (Jackson ImmunoResearch, 711-605-152, 1:400). Neurons were visualized by GCaMP6s signal and astrocytes detected using a mouse anti-GFAP antibody (Sigma, G3893, 1:500) developed by anti-mouse DyLight 405-Streptavidin secondary antibody (Jackson ImmunoResearch, 016-470-084, 1:400). Sections were mounted onto #1.5 borosilicate coverslips and covered with imaging medium containing 5% glucose, 0.1 M mercaptoethylamine, 1 mg ml⁻¹ glucose oxidase, and catalase (Sigma, 1500 U ml⁻¹) in Dulbecco's PBS (Sigma), immediately before imaging⁵⁹. STORM imaging was performed for P2Y12 (stimulated by a 647 nm laser) by using a Nikon N-STORM C2+ super-resolution system that combines 'Stochastic Optical Reconstruction Microscopy' technology and Nikon's Eclipse Ti research inverted microscope to reach a lateral resolution of 20 nm and axial resolution of 50 nm (refs 60,61).

Cytokine measurement. IL-6 was measured in cerebrospinal fluid samples and IL-1 α , IL-1 β , TNF α , IFN γ , IL-6, MCP-1, RANTES (CCL5), G-CSF, KC (CXCL1), IL-10 and IL-4 were measured in homogenates of saline perfused ipsilateral and contralateral brain hemispheres⁶² by cytometric bead array using CBA Flex Sets (all from BD Biosciences, 560157, 560232, 558299, 558296, 558301, 558342, 558345, 560152, 558340, 558300, 558294, respectively). Measurements were performed on a BD FACSVerser machine and data analysed using FACSArray software (BD Biosciences). Brain tissue cytokine levels were corrected for the total protein content of the samples as measured by BCA assay (Pierce).

Flow cytometry. Following Fc receptor blockade (eBioscience, 16-0161-85 anti-mouse CD16/CD32, 1:100), blood cells and splenic leukocytes cells were stained with cocktails of selected antibodies: T cells (all from eBioscience, 11-0043-82 anti-mouse CD4-FITC, 1:100; 12-0081-82 anti-mouse CD8 α -PE, 1:400; 17-0031-80 anti-mouse CD3e-APC, 1:200), B cells (all from eBioscience, 11-0193-81 anti-mouse CD19-FITC, 1:100; 17-5321-81 anti-mouse MHCII (I-A/I-E)-APC, 1:400); granulocytes/monocytes (all from eBioscience, 11-0112-81 anti-mouse CD11b-FITC, 1:100; 25-5932-80 anti-mouse Ly-6C-PE-Cy7, 1:400) and macrophages (BD Biosciences, 563900 rat anti-mouse F4/80-like receptor-Violet, 1:200). Antibodies were purchased from eBioscience. Cells were acquired on a BD FACSVerser flow cytometer (BD Biosciences, US) and data were analysed using FACSsuite software (BD Biosciences). Total blood cell counts were calculated by using 15 μ m polystyrene microbeads (Polysciences, 18328-5).

Quantitative analysis. Animals were randomized for MCAo experiments using GraphPad Random Number Generator. All quantitative analysis was performed under blinded conditions. The volume of ischaemic brain damage was measured on cresyl violet-stained brain sections. Infarct size and BBB injury at 24 h reperfusion were calculated by integration of areas of damage measured at eight neuroanatomically defined coronal levels (between 2.9 mm rostral and -4.9 mm caudal to bregma) with the distance between coronal levels followed by correction for oedema, as described previously⁵⁸. Quantitative analysis of immunostaining was performed on at least three, randomly selected fields within the region of interest for each brain section, on 4-4 serial coronal sections separated by 400 μ m for the striatum and 800 μ m for the cerebral cortex (between 0.8 posterior and 0.8 anterior and between 2.4 posterior and 0.8 anterior to the bregma, respectively). The border of infarct was defined on cresyl violet-stained brain sections and microglial activation was also visualized on adjacent sections based on Iba1 immunofluorescence. Two-photon image sequences were analysed using ImageJ. Measurement units were collected from MesC files with HDF5 importer plugin. Background intensity was measured in a dark region of the field of view and was subtracted from each image sequence. The GCaMP6s signal of individual neurons was collected with ImageJ Plot-axis Z profile into the MES (Femtonics Ltd.) curve analysis modul. The trace of the individual cells was normalized to the baseline level of signal (a time interval without calcium activity, typically the beginning of the image sequence). Then, the area under the curve was calculated for calcium curves after cerebral ischaemia or SD induction with KCl. Microglia-neuron interactions were assessed on Z-stacks recorded every 3 min between 200 and 11 μ m under the dura mater. Microglia contacting neurons were randomly selected and neurons showing at least 1.5-foldchange in RCaMP1 signal were used to study microglial process recruitment over a 150 min period after the onset of ischaemia. The net

extension/withdrawal of microglial processes to individual neurons was plotted against relative RCaMP1 signal intensity changes measured during the same period. Changes in microglial ramification were investigated with Sholl analysis as described earlier³⁵. Two-photon images of individual microglial cells were converted into a minimum intensity projection image using the concentric circles plugin of the ImageJ with a 2 μ m step size. The intersections between the circles and the cell processes were calculated manually for each cell. To evaluate microglia process recruitment to neuronal soma, a concentric circle macro (modification of a Sholl analysis) was written for Fiji. Microglia process coverage around neurons was assessed in 30 circles (0.5 μ m step size) with an r step of 4. For three-dimensional reconstruction of *in vivo* two-photon images at different Z-planes to visualize the relationship between neuronal RCaMP1 and microglial processes in Cx3Cr1^{GFP/+} mice, the Simple Neurite Tracer plugin (Fiji) was used.

Statistics. Group sizes for MCAo studies with infarct size assessment were determined by power calculation (GPower 3.1) based on results from our representative previous studies (α error probability: 0.05, power: 0.8 and an estimated 20% s.d.). This resulted in $n=7$ for two experimental groups (Cohen's d effect size: 1.66) and $n=9$ for four experimental groups (effect size f : 0.6). No formal power calculation was performed for imaging studies. Data were analysed using Student's t -test or Mann-Whitney test (comparing two experimental groups), one-way or two-way analysis of variance followed by Tukey's and Sidak's *post hoc* comparison, respectively (comparing three or more groups) and linear regression was used for correlation analysis (GraphPad Prism 6.0). $P < 0.05$ was considered statistically significant.

References

1. Kettenmann, H., Hanisch, U. K., Noda, M. & Verkhratsky, A. Physiology of microglia. *Physiol. Rev.* **91**, 461–553 (2011).
2. Block, M. L., Zecca, L. & Hong, J. S. Microglia-mediated neurotoxicity: uncovering the molecular mechanisms. *Nat. Rev. Neurosci.* **8**, 57–69 (2007).
3. Dheen, S. T., Kaur, C. & Ling, E. A. Microglial activation and its implications in the brain diseases. *Curr. Med. Chem.* **14**, 1189–1197 (2007).
4. Iadecola, C. & Anrather, J. The immunology of stroke: from mechanisms to translation. *Nat. Med.* **17**, 796–808 (2011).
5. Denes, A., Thornton, P., Rothwell, N. J. & Allan, S. M. Inflammation and brain injury: acute cerebral ischaemia, peripheral and central inflammation. *Brain Behav. Immun.* **24**, 708–723 (2010).
6. Prinz, M. & Priller, J. Microglia and brain macrophages in the molecular age: from origin to neuropsychiatric disease. *Nat. Rev. Neurosci.* **15**, 300–312 (2014).
7. Nimmerjahn, A., Kirchhoff, F. & Helmchen, F. Resting microglial cells are highly dynamic surveillants of brain parenchyma *in vivo*. *Science* **308**, 1314–1318 (2005).
8. Davalos, D. *et al.* ATP mediates rapid microglial response to local brain injury *in vivo*. *Nat. Neurosci.* **8**, 752–758 (2005).
9. Jolivel, V. *et al.* Perivascular microglia promote blood vessel disintegration in the ischaemic penumbra. *Acta Neuropathol.* **129**, 279–295 (2015).
10. Winship, I. R. & Murphy, T. H. *In vivo* calcium imaging reveals functional rewiring of single somatosensory neurons after stroke. *J. Neurosci.* **28**, 6592–6606 (2008).
11. Wake, H., Moorhouse, A. J., Jinno, S., Kohsaka, S. & Nabekura, J. Resting microglia directly monitor the functional state of synapses *in vivo* and determine the fate of ischaemic terminals. *J. Neurosci.* **29**, 3974–3980 (2009).
12. Eyo, U. B. *et al.* Modulation of microglial process convergence toward neuronal dendrites by extracellular calcium. *J. Neurosci.* **35**, 2417–2422 (2015).
13. Kaindl, A. M. *et al.* Activation of microglial N-methyl-D-aspartate receptors triggers inflammation and neuronal cell death in the developing and mature brain. *Ann. Neurol.* **72**, 536–549 (2012).
14. Mohebiany, A. N. & Schneider, R. Glutamate excitotoxicity in the cerebellum mediated by IL-1beta. *J. Neurosci.* **33**, 18353–18355 (2013).
15. Turrin, N. P. & Rivest, S. Tumor necrosis factor alpha but not interleukin 1 beta mediates neuroprotection in response to acute nitric oxide excitotoxicity. *J. Neurosci.* **26**, 143–151 (2006).
16. Vinet, J. *et al.* Neuroprotective function for ramified microglia in hippocampal excitotoxicity. *J. Neuroinflammation* **9**, 27 (2012).
17. Dreier, J. P. & Reiffurth, C. The stroke-migraine depolarization continuum. *Neuron* **86**, 902–922 (2015).
18. Dreier, J. P. The role of spreading depression, spreading depolarization and spreading ischaemia in neurological disease. *Nat. Med.* **17**, 439–447 (2011).
19. Dreier, J. P. *et al.* Spreading convulsions, spreading depolarization and epileptogenesis in human cerebral cortex. *Brain* **135**, 259–275 (2012).
20. Hinzman, J. M., DiNapoli, V. A., Mahoney, E. J., Gerhardt, G. A. & Hartings, J. A. Spreading depolarizations mediate excitotoxicity in the development of acute cortical lesions. *Exp. Neurol.* **267**, 243–253 (2015).
21. Ginhoux, F. *et al.* Fate mapping analysis reveals that adult microglia derive from primitive macrophages. *Science* **330**, 841–845 (2010).
22. Kierdorf, K. *et al.* Microglia emerge from erythromyeloid precursors via Pu.1- and Irf8-dependent pathways. *Nat. Neurosci.* **16**, 273–280 (2013).

23. Erbllich, B., Zhu, L., Etgen, A. M., Dobrenis, K. & Pollard, J. W. Absence of colony stimulation factor-1 receptor results in loss of microglia, disrupted brain development and olfactory deficits. *PLoS ONE* **6**, e26317 (2011).
24. Elmore, M. R. *et al.* Colony-stimulating factor 1 receptor signalling is necessary for microglia viability, unmasking a microglia progenitor cell in the adult brain. *Neuron* **82**, 380–397 (2014).
25. Fumagalli, S., Perego, C., Ortolano, F. & De Simoni, M. G. CX3CR1 deficiency induces an early protective inflammatory environment in ischemic mice. *Glia* **61**, 827–842 (2013).
26. Frakes, A. E. *et al.* Microglia induce motor neuron death via the classical NF-kappaB pathway in amyotrophic lateral sclerosis. *Neuron* **81**, 1009–1023 (2014).
27. Neher, J. J. *et al.* Phagocytosis executes delayed neuronal death after focal brain ischemia. *Proc. Natl Acad. Sci. USA* **110**, E4098–E4107 (2013).
28. Faustino, J. V. *et al.* Microglial cells contribute to endogenous brain defenses after acute neonatal focal stroke. *J. Neurosci.* **31**, 12992–13001 (2011).
29. Neumann, J. *et al.* Microglia cells protect neurons by direct engulfment of invading neutrophil granulocytes: a new mechanism of CNS immune privilege. *J. Neurosci.* **28**, 5965–5975 (2008).
30. Goldmann, T. *et al.* A new type of microglia gene targeting shows TAK1 to be pivotal in CNS autoimmune inflammation. *Nat. Neurosci.* **16**, 1618–1626 (2013).
31. Bruttger, J. *et al.* Genetic cell ablation reveals clusters of local self-renewing microglia in the mammalian central nervous system. *Immunity* **43**, 92–106 (2015).
32. Rice, R. A. *et al.* Elimination of microglia improves functional outcomes following extensive neuronal loss in the hippocampus. *J. Neurosci.* **35**, 9977–9989 (2015).
33. Morrison, H. W. & Filosa, J. A. A quantitative spatiotemporal analysis of microglia morphology during ischemic stroke and reperfusion. *J. Neuroinflammation* **10**, 4 (2013).
34. Farkas, E., Pratt, R., Sengpiel, F. & Obrenovitch, T. P. Direct, live imaging of cortical spreading depression and anoxic depolarisation using a fluorescent, voltage-sensitive dye. *J. Cereb. Blood Flow Metab.* **28**, 251–262 (2008).
35. Yang, Y. & Rosenberg, G. A. Blood-brain barrier breakdown in acute and chronic cerebrovascular disease. *Stroke* **42**, 3323–3328 (2011).
36. Brown, G. C. & Neher, J. J. Microglial phagocytosis of live neurons. *Nat. Rev. Neurosci.* **15**, 209–216 (2014).
37. Schilling, M. *et al.* Microglial activation precedes and predominates over macrophage infiltration in transient focal cerebral ischemia: a study in green fluorescent protein transgenic bone marrow chimeric mice. *Exp. Neurol.* **183**, 25–33 (2003).
38. Denes, A. *et al.* Central and haematopoietic interleukin-1 both contribute to ischaemic brain injury in mice. *Dis. Model. Mech.* **6**, 1043–1048 (2013).
39. Parkhurst, C. N. *et al.* Microglia promote learning-dependent synapse formation through brain-derived neurotrophic factor. *Cell* **155**, 1596–1609 (2013).
40. Heppner, F. L. *et al.* Experimental autoimmune encephalomyelitis repressed by microglial paralysis. *Nat. Med.* **11**, 146–152 (2005).
41. Sattler, R. & Tymianski, M. Molecular mechanisms of glutamate receptor-mediated excitotoxic neuronal cell death. *Mol. Neurobiol.* **24**, 107–129 (2001).
42. Murphy, T. H., Li, P., Betts, K. & Liu, R. Two-photon imaging of stroke onset in vivo reveals that NMDA-receptor independent ischemic depolarization is the major cause of rapid reversible damage to dendrites and spines. *J. Neurosci.* **28**, 1756–1772 (2008).
43. Shih, A. Y. *et al.* The smallest stroke: occlusion of one penetrating vessel leads to infarction and a cognitive deficit. *Nat. Neurosci.* **16**, 55–63 (2013).
44. Pusic, K. M., Pusic, A. D., Kemme, J. & Kraig, R. P. Spreading depression requires microglia and is decreased by their M2a polarization from environmental enrichment. *Glia* **62**, 1176–1194 (2014).
45. Bano, D. & Nicotera, P. Ca²⁺ signals and neuronal death in brain ischemia. *Stroke* **38**, 674–676 (2007).
46. Lai, T. W., Zhang, S. & Wang, Y. T. Excitotoxicity and stroke: identifying novel targets for neuroprotection. *Prog. Neurobiol.* **115**, 157–188 (2014).
47. Heinke, W. & Koelsch, S. The effects of anesthetics on brain activity and cognitive function. *Curr. Opin. Anaesthesiol.* **18**, 625–631 (2005).
48. Luo, J. *et al.* Colony-stimulating factor 1 receptor (CSF1R) signaling in injured neurons facilitates protection and survival. *J. Exp. Med.* **210**, 157–172 (2013).
49. Lalancette-Hebert, M., Gowing, G., Simard, A., Weng, Y. C. & Kriz, J. Selective ablation of proliferating microglial cells exacerbates ischaemic injury in the brain. *J. Neurosci.* **27**, 2596–2605 (2007).
50. Li, Y., Du, X. F., Liu, C. S., Wen, Z. L. & Du, J. L. Reciprocal regulation between resting microglial dynamics and neuronal activity *in vivo*. *Dev. Cell* **23**, 1189–1202 (2012).
51. Olmos, G. & Llado, J. Tumor necrosis factor alpha: a link between neuroinflammation and excitotoxicity. *Mediators Inflamm.* **2014**, 861231 (2014).
52. Jung, J. E., Kim, G. S. & Chan, P. H. Neuroprotection by interleukin-6 is mediated by signal transducer and activator of transcription 3 and antioxidative signaling in ischemic stroke. *Stroke* **42**, 3574–3579 (2011).
53. Gadani, S. P., Cronk, J. C., Norris, G. T. & Kipnis, J. IL-4 in the brain: a cytokine to remember. *J. Immunol.* **189**, 4213–4219 (2012).
54. Chen, T. W. *et al.* Ultrasensitive fluorescent proteins for imaging neuronal activity. *Nature* **499**, 295–300 (2013).
55. Katona, G. *et al.* Fast two-photon in vivo imaging with three-dimensional random-access scanning in large tissue volumes. *Nat. Methods* **9**, 201–208 (2012).
56. Chiovini, B. *et al.* Dendritic spikes induce ripples in parvalbumin interneurons during hippocampal sharp waves. *Neuron* **82**, 908–924 (2014).
57. Drew, P. J., Blinder, P., Cauwenberghs, G., Shih, A. Y. & Kleinfeld, D. Rapid determination of particle velocity from space-time images using the Radon transform. *J. Comput. Neurosci.* **29**, 5–11 (2010).
58. Denes, A., Humphreys, N., Lane, T. E., Grecnis, R. & Rothwell, N. Chronic systemic infection exacerbates ischemic brain damage via a CCL5 (regulated on activation, normal T-cell expressed and secreted)-mediated proinflammatory response in mice. *J. Neurosci.* **30**, 10086–10095 (2010).
59. Dani, A., Huang, B., Bergan, J., Dulac, C. & Zhuang, X. Superresolution imaging of chemical synapses in the brain. *Neuron* **68**, 843–856 (2010).
60. Dudok, B. *et al.* Cell-specific STORM super-resolution imaging reveals nanoscale organization of cannabinoid signaling. *Nat. Neurosci.* **18**, 75–86 (2015).
61. Barna, L. *et al.* Correlated confocal and super-resolution imaging by VividSTORM. *Nat. Protoc.* **11**, 163–183 (2016).
62. Denes, A. *et al.* Streptococcus pneumoniae worsens cerebral ischemia via interleukin 1 and platelet glycoprotein Ibalpha. *Ann. Neurol.* **75**, 670–683 (2014).

Acknowledgements

Funding was provided by OTKA K109743 (A.D.) and the Hungarian Brain Research Program KTIA_13_NAP-A-I/2 (A.D.). A.D. is supported by the Bolyai Janos Research Scholarship from the Hungarian Academy of Sciences. The authors thank the Hungarian-French grant (TÉT_10-1-2011-0389), OTKA (K105997), FP7-ICT-2011-C-323945 (3 × 3DImaging), VKSZ_14-1-2015-0155, ERC 682426, KTIA_NAP_13-2-2015-0006 and Swiss-Hungarian grant (SH/7/2/8) for additional support. We thank the Cell Biology Center (Flow Cytometry Core Facility) at the Institute of Experimental Medicine of the Hungarian Academy of Sciences, Budapest, Hungary for their assistance and Csaba Dávid for his help in the development of macros used for analysis of microglia process coverage. We thank László Barna, Vivien Miczán and the NMC Imaging Center at the Institute of Experimental Medicine for kindly providing microscopy support.

Author contributions

A.D. and B.R. designed research; G.S., B.M., N.L., Z.K., L.J., E.C., B.O., R.F. and A.D. performed research; B.R. and G.K. designed the two-photon imaging and electrophysiological recording setup and wrote the analysis software package and the new Ca⁺⁺ image acquisition software; B.R. and G.S. designed the new imaging methods; B.L.W. and G.K. contributed new reagents/analytic tools; G.S., B.M., N.L., Z.K., L.J., E.C.S., G.K., B.R. and A.D. analysed data; A.D. prepared the first draft of the manuscript with input from B.R., G.S., B.M., N.L. and Z.K.; A.D., B.R., G.S., B.M., N.L., Z.S.K. and B.O. contributed to the revised version of the paper. A.D. and B.R. supervised the study.

Additional information

Supplementary Information accompanies this paper at <http://www.nature.com/naturecommunications>

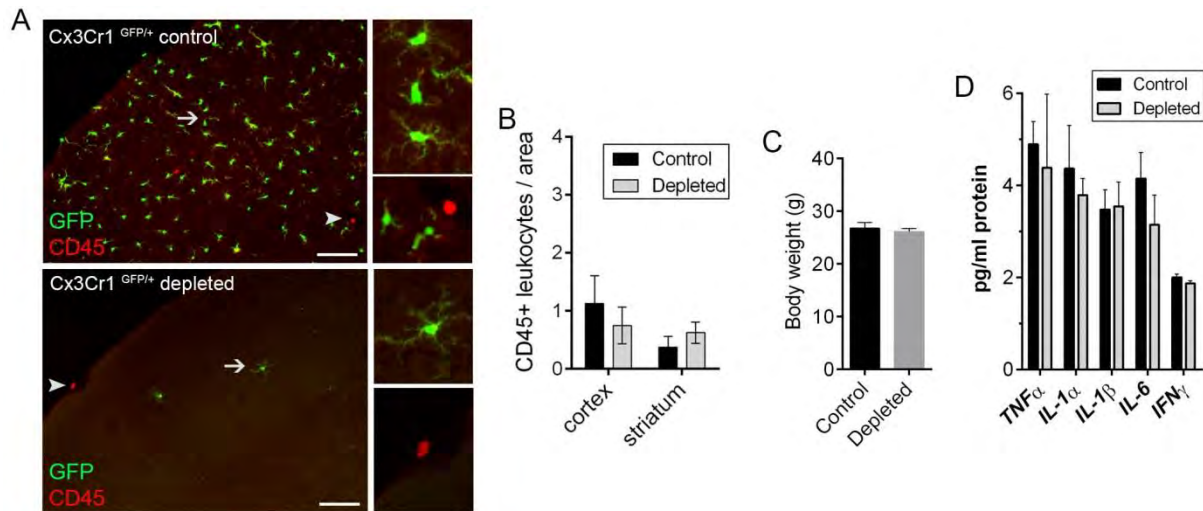
Competing financial interests: B.L.W. is an employee of Plexxikon. G.K. and B.R. are founders of Femtonics Kft. B.R. is a member of its scientific advisory board.

Reprints and permission information is available online at <http://npg.nature.com/reprintsandpermissions/>

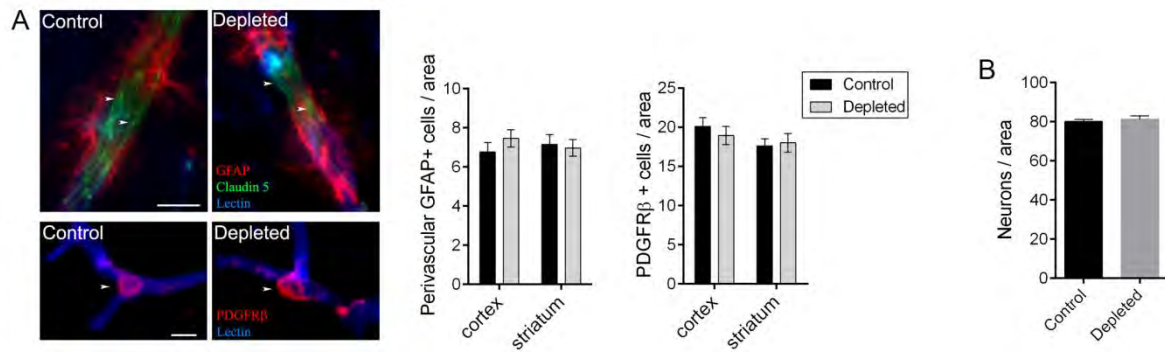
How to cite this article: Szalay, G. *et al.* Microglia protect against brain injury and their selective elimination dysregulates neuronal network activity after stroke. *Nat. Commun.* **7**:11499 doi: 10.1038/ncomms11499 (2016).



This work is licensed under a Creative Commons Attribution 4.0 International License. The images or other third party material in this article are included in the article's Creative Commons license, unless indicated otherwise in the credit line; if the material is not included under the Creative Commons license, users will need to obtain permission from the license holder to reproduce the material. To view a copy of this license, visit <http://creativecommons.org/licenses/by/4.0/>

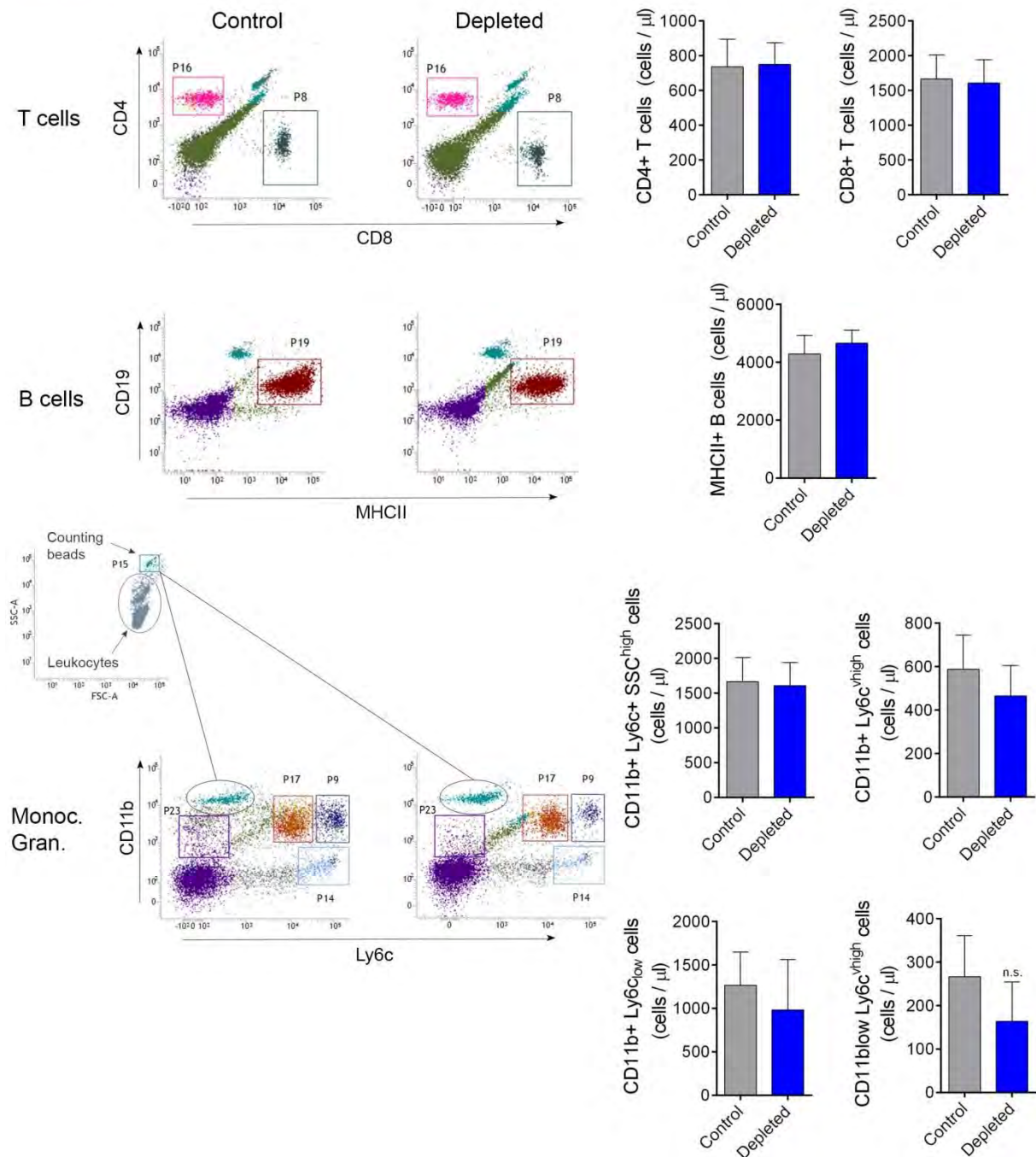


Supplementary Figure 1. Selective depletion of microglia does not result in leukocyte infiltration into the brain and does not cause illness or weight loss. A. In $Cx3Cr1^{GFP/+}$ (microglia reporter) mice an almost complete elimination of microglia (arrows, green) is seen after feeding mice a chow diet containing PLX3397 (290 ppm) for 21 days. Depletion of microglia does not result in recruitment of CD45+ leukocytes (arrowhead, red) into the brain. **B.** No infiltration of CD45+ leukocytes is seen in the brain parenchyma in C57BL6/J mice as quantified in the striatum and the cerebral cortex. **C.** Microglia depletion does not result in weight loss in mice fed a chow diet containing PLX3397 (290 ppm) for 21 days. **D.** Plasma cytokines were measured by cytometric bead array after feeding mice a control or a PLX3397 diet for 21 days. Data are expressed as mean \pm s.e.m., $n=8-10$. B, D: two-way ANOVA followed by Dunn's multiple comparison; C: unpaired t test. Scale bar: A, 50 μ m.



Supplementary Figure 2. Selective elimination of microglia does not affect other cell types in the brain. A. Depletion of microglia does not result in any changes in the morphology or the number of perivascular astrocytes (GFAP, red, top panel), or endothelial cells (lectin, blue) expressing the tight junction protein claudin-5 (green, arrowheads). Depletion of microglia does not result in any changes in the morphology or the number of pericytes (PDGFR β + cells, red, bottom panel). **B.** Depletion of microglia does not result in any changes in the number of cresyl violet–stained neurons in the cerebral cortex. Data are expressed as mean \pm s.e.m., $n=8$. A: two-way ANOVA followed by Dunn’s multiple comparison; B: unpaired t test. Scale bars: A, top panel 20 μ m, bottom panel 10 μ m.

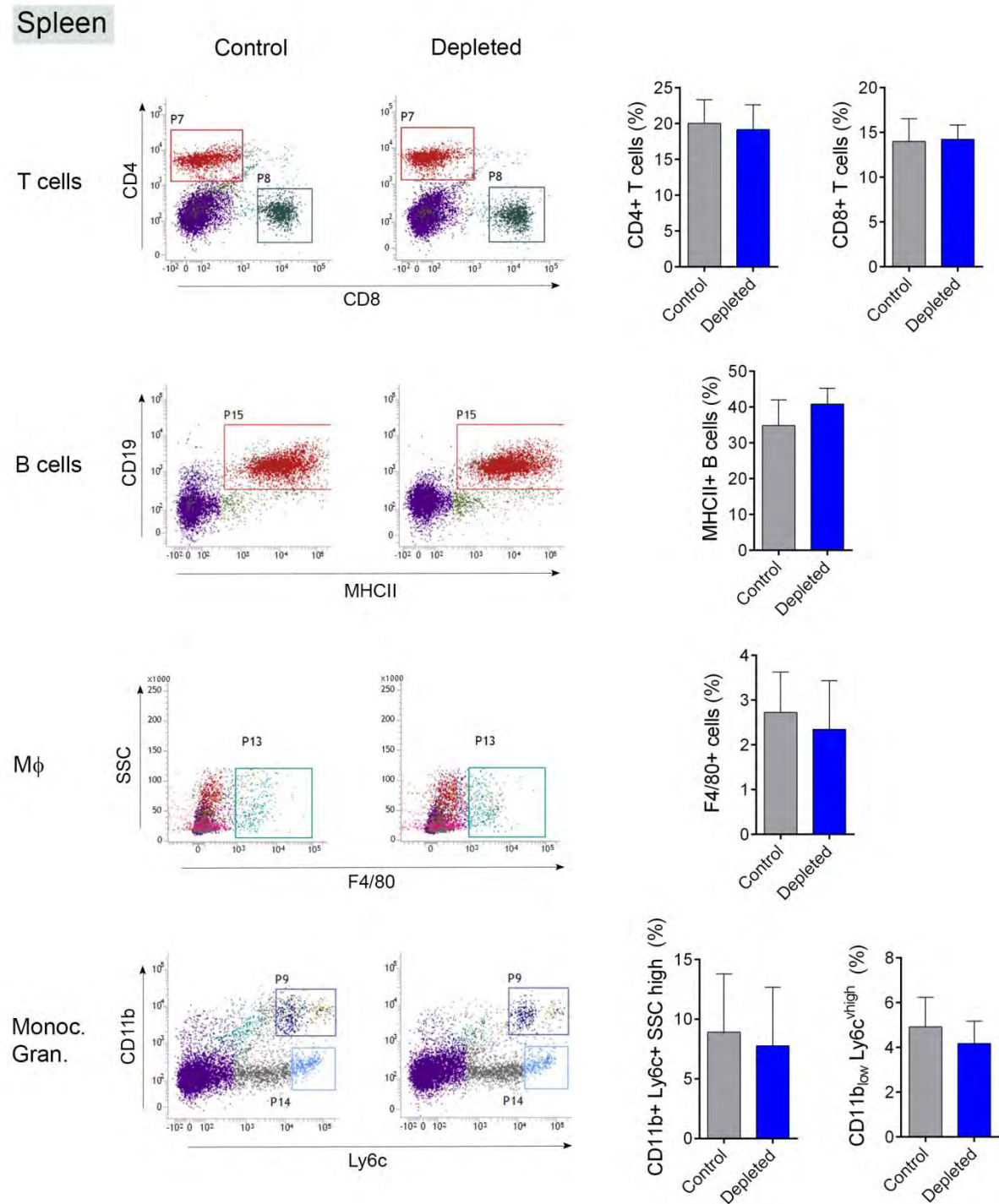
Blood



Supplementary Figure 3. Selective depletion of microglia does not alter main blood cell populations. C57BL6/J mice were fed a chow diet for 21 days containing the CSF1R antagonist PLX3397 (290 ppm). Blood samples were labelled with mixtures of specific antibodies against leukocyte populations and subjected to flow cytometric analysis. Total blood cell counts were calculated by using 15 μ m polystyrene microbeads (Polysciences,

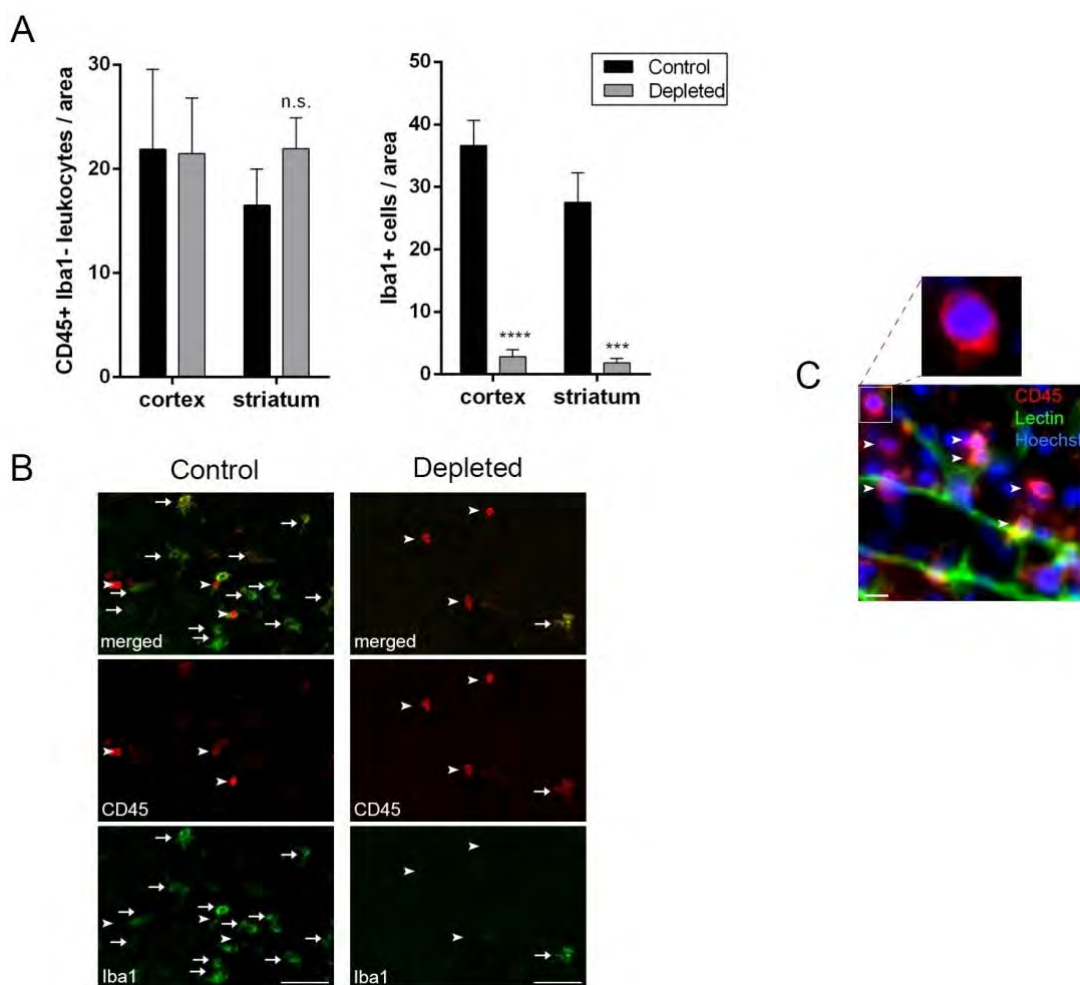
dc_2027_22

18328-5). The number of CD4⁺ T lymphocytes (P16 gate, also gated on CD3), CD8⁺ T lymphocytes (P8 gate, also gated on CD3) and CD19⁺ MHCII⁺ B cells (P19 gate) were no different between control and microglia-depleted animals. Similarly, the number of granulocytes (P17 gate, CD11b⁺, Ly6c⁺, SSC^{high} cells), CD11b⁺ Ly6c^{high} monocytes (P9 gate), CD11b_{low} Ly6c^{high} cells (P14 gate) and CD11b⁺ Ly6c_{low} cells (P23 gate) were no different between control and microglia depleted mice. Data are expressed as mean \pm s.e.m. Unpaired t-test, n=4-5. n.s. – not significant.



Supplementary Figure 4. Selective depletion of microglia does not alter main leukocyte populations in the spleen. C57BL6/J mice were fed a chow diet for 21 days containing the CSF1R antagonist PLX3397 (290 ppm). Spleen cells were isolated and labelled with mixtures of specific antibodies against leukocyte populations followed by flow cytometric analysis. The proportion of CD4+ T lymphocytes (P7 gate, also gated on CD3),

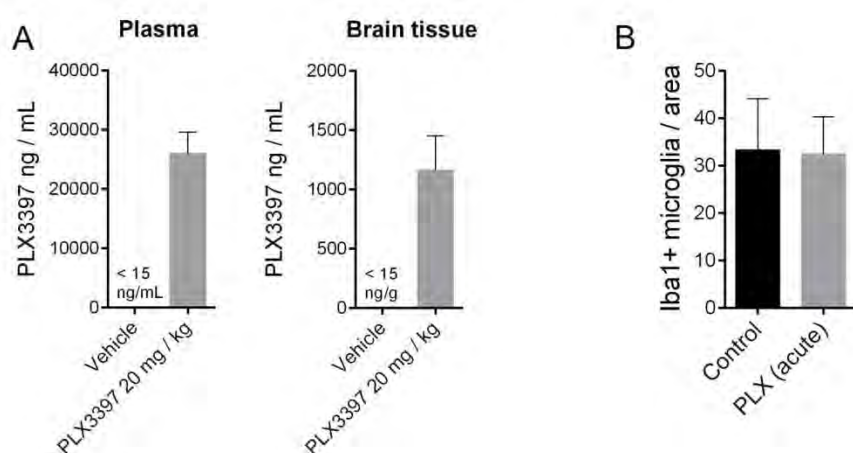
CD8+ T lymphocytes (P8 gate, also gated on CD3) and CD19+ MHCII+ B cells (P15 gate) in the spleen were not different between control and microglia depleted animals. Spleen macrophages (F4/80+ cells), granulocytes (P9 gate, CD11b+, Ly6c+, SSC^{high} cells) and CD11b_{low} Ly6c^{high} monocytes (P9 gate) were not different between control and microglia depleted animals. Data are expressed as mean \pm s.e.m., Unpaired t-test, n=4-5.



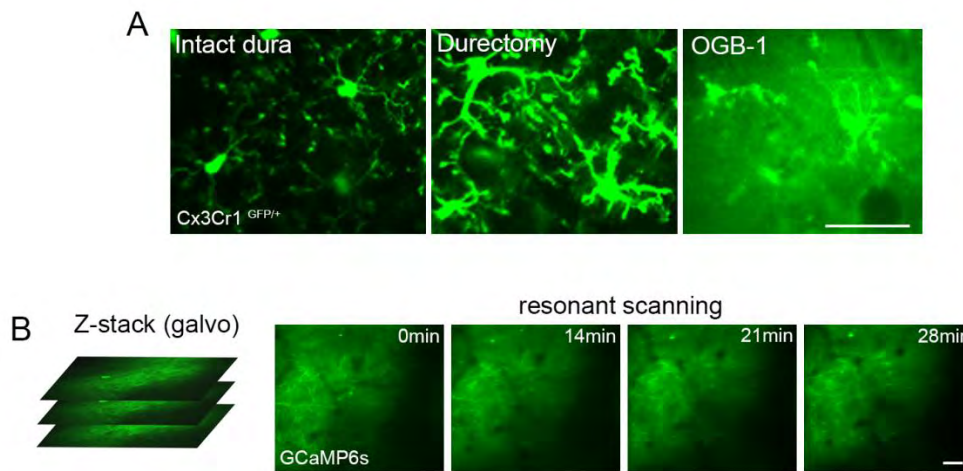
Supplementary Figure 5. Depletion of microglia does not alter leukocyte recruitment into the brain 72h after cerebral ischemia. C57BL6/J mice were fed a chow diet containing the CSF1R antagonist PLX3397 (290 ppm) or control diet for 21 days and were subjected to cerebral ischemia and 72 h reperfusion. **A.** CD45-positive, Iba1-negative leukocytes and Iba1-positive microglia/macrophages were counted in the ipsilateral striatum and the cerebral cortex. **B.** Fluorescent images showing CD45-positive Iba1-negative leukocytes

dc_2027_22

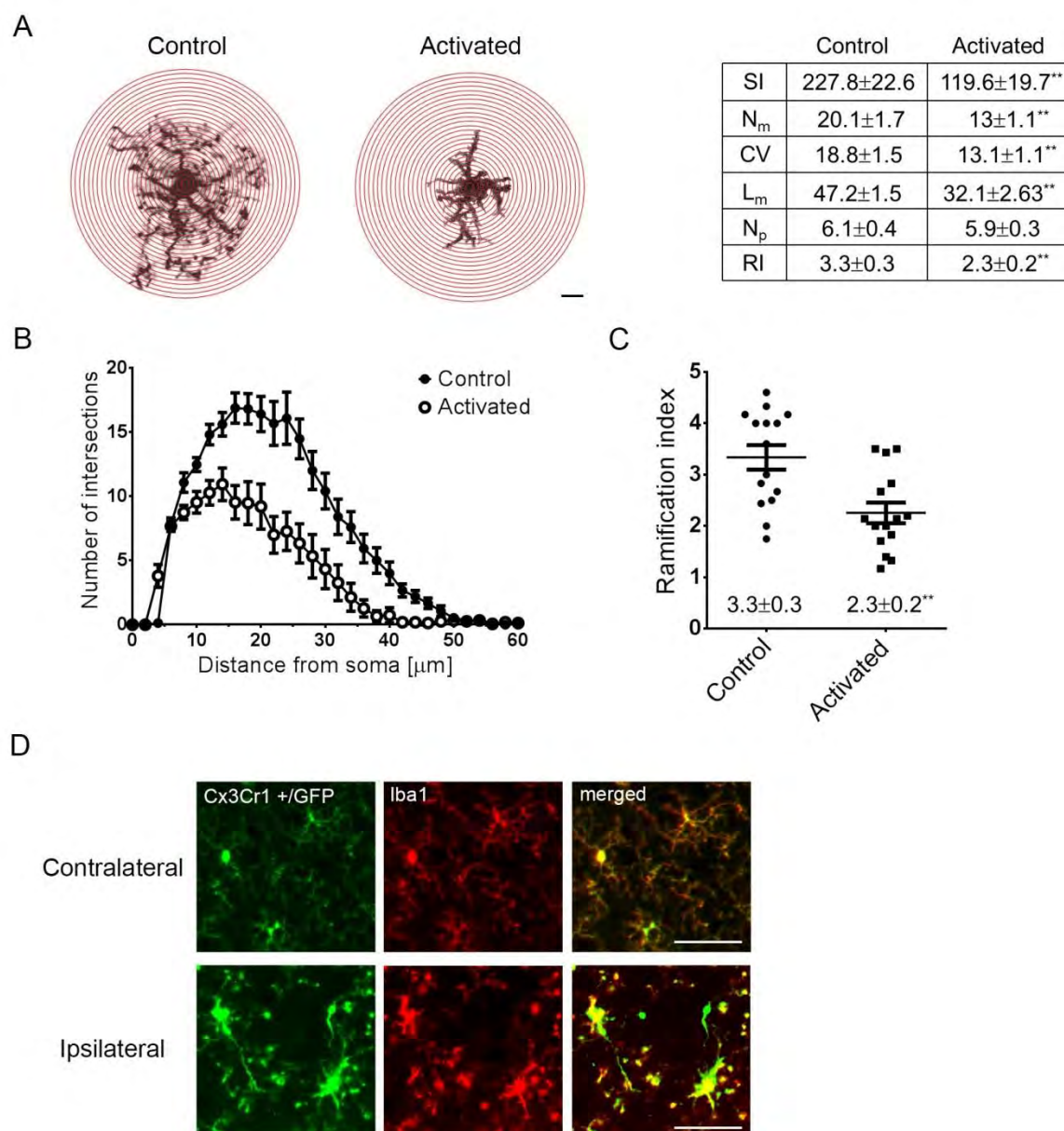
(arrowheads) and Iba1-positive microglia/macrophages (arrows) in the ipsilateral cerebral cortex. **C.** Image showing CD45-positive leukocytes (arrowheads, red) associated with a blood vessel (tomato lectin, green), cell nuclei were labelled with Hoechst (blue). *** $P < 0.001$, **** $P < 0.0001$, two-way ANOVA followed by Sidak's multiple comparisons test. Scale bars: B, 50 μm ; C, 10 μm . Data are expressed as mean \pm s.e.m., $n=8$. A: two-way ANOVA followed by Dunn's multiple comparison. n.s. – not significant.



Supplementary Figure 6. Acute treatment with PLX3397 does not reduce microglial numbers within 24 h. **A.** For pharmacokinetic studies, PLX3397 (20 mg/kg) or vehicle (PBS) was administered intraperitoneally to control C57BL6/J mice 2h before sample collection ($n=3$). PLX3397 levels were measured by extraction into acetonitrile (containing an internal standard) and quantification by liquid chromatography-tandem mass spectrometry (LC/MS/MS). **B.** C57BL6/J mice were subjected to 45 min MCAo and received an intraperitoneal injection of either vehicle or PLX3397 (20 mg/kg) 60 min after occlusion. 24 h after reperfusion mice were sacrificed and Iba1-positive cell numbers determined in the cerebral cortex. Data are expressed as mean \pm s.e.m., A: $n=3$; B: unpaired t test, $n=7$.



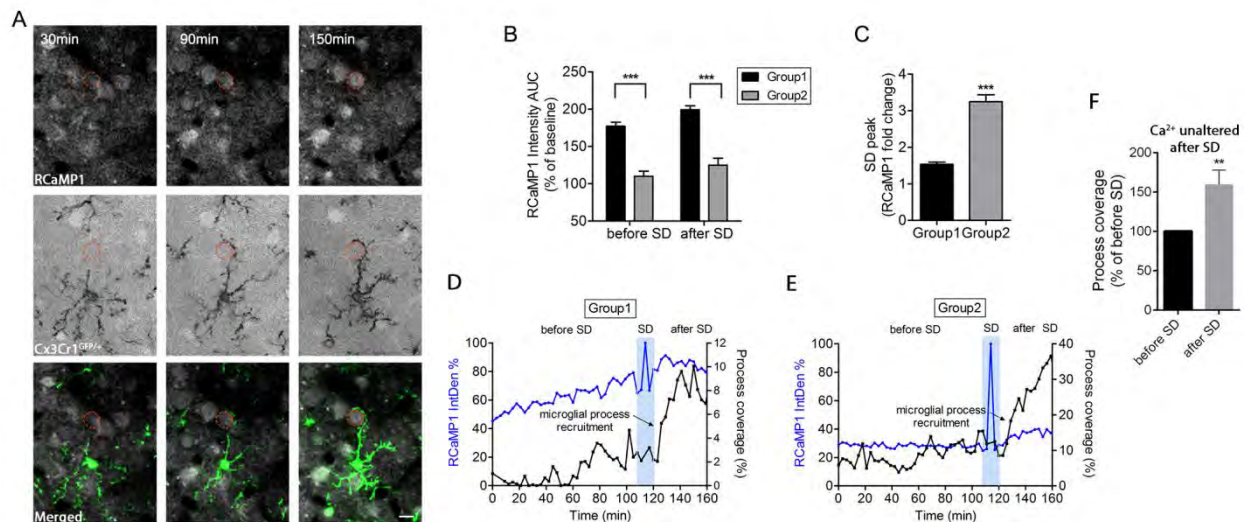
Supplementary Figure 7. Effect of genetically encoded calcium indicator delivery on microglial activation and two-photon imaging in the cerebral cortex 24h after cerebral ischemia. **A.** Injection of genetically encoded calcium indicators into the brain parenchyma was performed distant from the imaging area at a 60° angle, to minimize disturbance to the brain tissue. This protocol does not induce microglial activation at the imaging site, unless durectomy is performed, as assessed in Cx3Cr1^{GFP/+} microglia reporter mice. Injection of the calcium indicator Oregon Green 488 BAPTA-1 (OGB-1) prior to *in vivo* two-photon imaging leads to microglial activation based on withdrawal of cellular processes and enlargement of the cell body. **B.** *In vivo* neuronal calcium imaging 24 h after MCAo in the cerebral cortex reveals very few changes in GCaMP6s signal over time. Scale bars: 50µm.



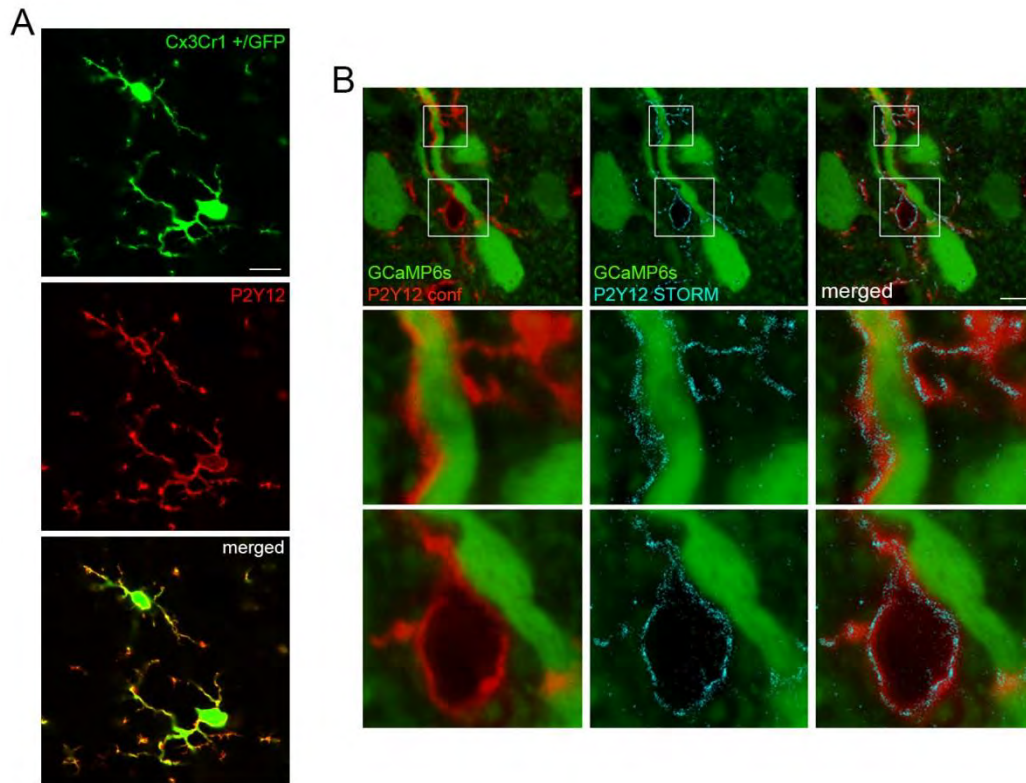
Supplementary Figure 8. Microglial morphology is altered rapidly in response to cerebral ischemia. **A.** Representative diagrams used for classical Sholl analysis showing microglial cells from a control mouse and 1h after cerebral ischemia (activated) in the cerebral cortex. Microglia in Cx3Cr1^{+/GFP} reporter mice were visualized by *in vivo* two-photon imaging. Series of concentric circles were spaced at 2 μ m intervals from the center of the soma. The number of process intersections with each circle was counted. SI = Sum of Intersections, the total number of intersections per cell; N_m = process maximum, the maximum number of intersections at radius r; CV = critical value, the radius r [μ m] with the maximum number of intersections; N_p = the number of primary branches originating at the cell's soma;

dc_2027_22

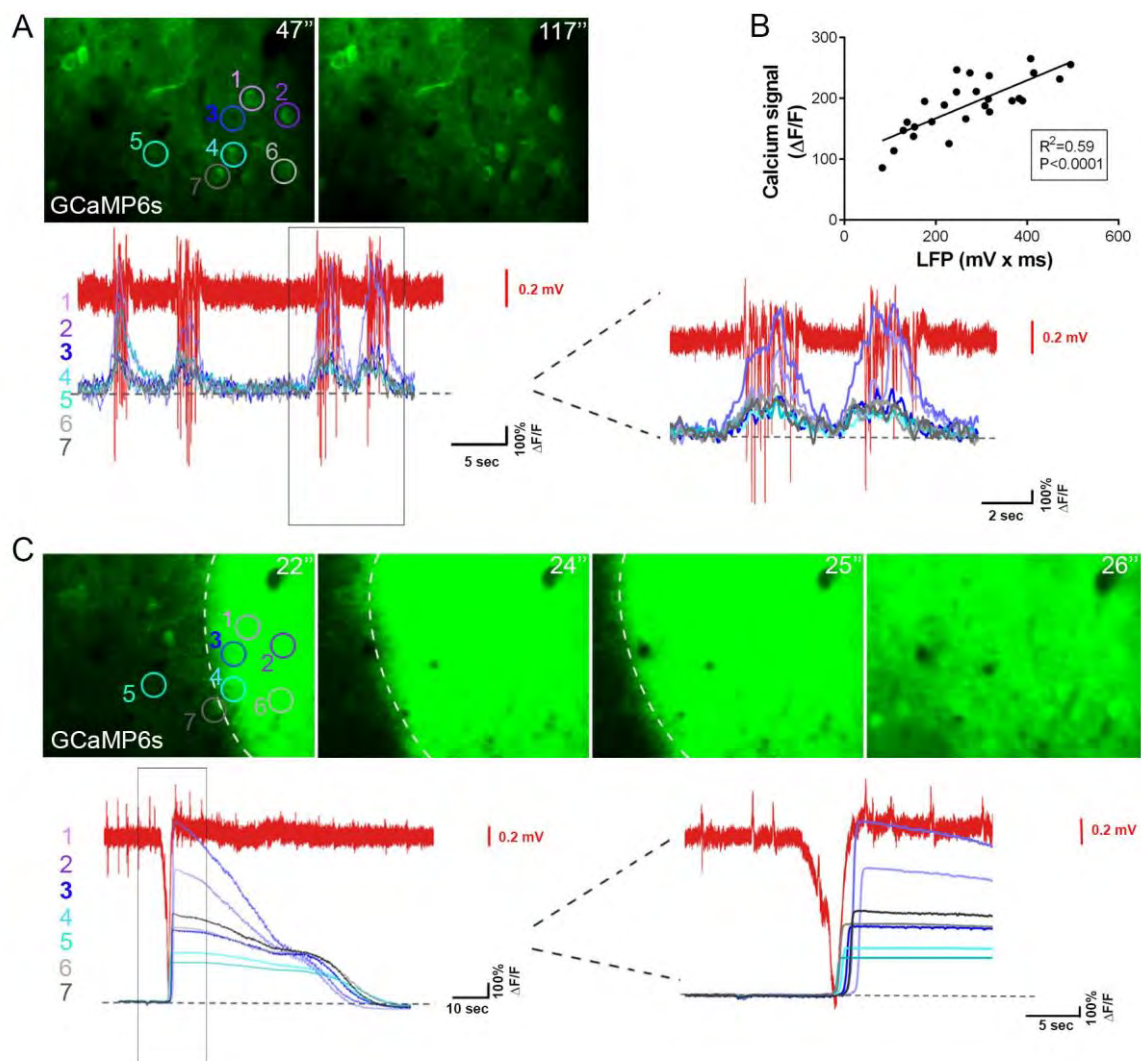
RI = Schoenen Ramification Index, a measure of the branching of the cell calculated by dividing the process maximum by the number of primary branches; L_m = maximum branch length, the maximum radius where an intersection with a process occurs (μm). **B.** Number (mean \pm s.e.m.) of intersections in control (n=15) and activated (n=15) microglial cells as a function of distance from the soma. **C.** Schoenen Ramification Index, a measure of the branching of the cells was calculated by dividing the maximum process number by the number of primary branches. The data indicate significantly reduced branching in response to cerebral ischemia. (**p=0.0017, unpaired t-test). **D.** Histological analysis in Cx3Cr1^{+GFP} mice indicates higher Iba1 (red) expression in activated microglial cells 6 h after cerebral ischemia. Scale bars: A, 10 μm ; D, 50 μm .



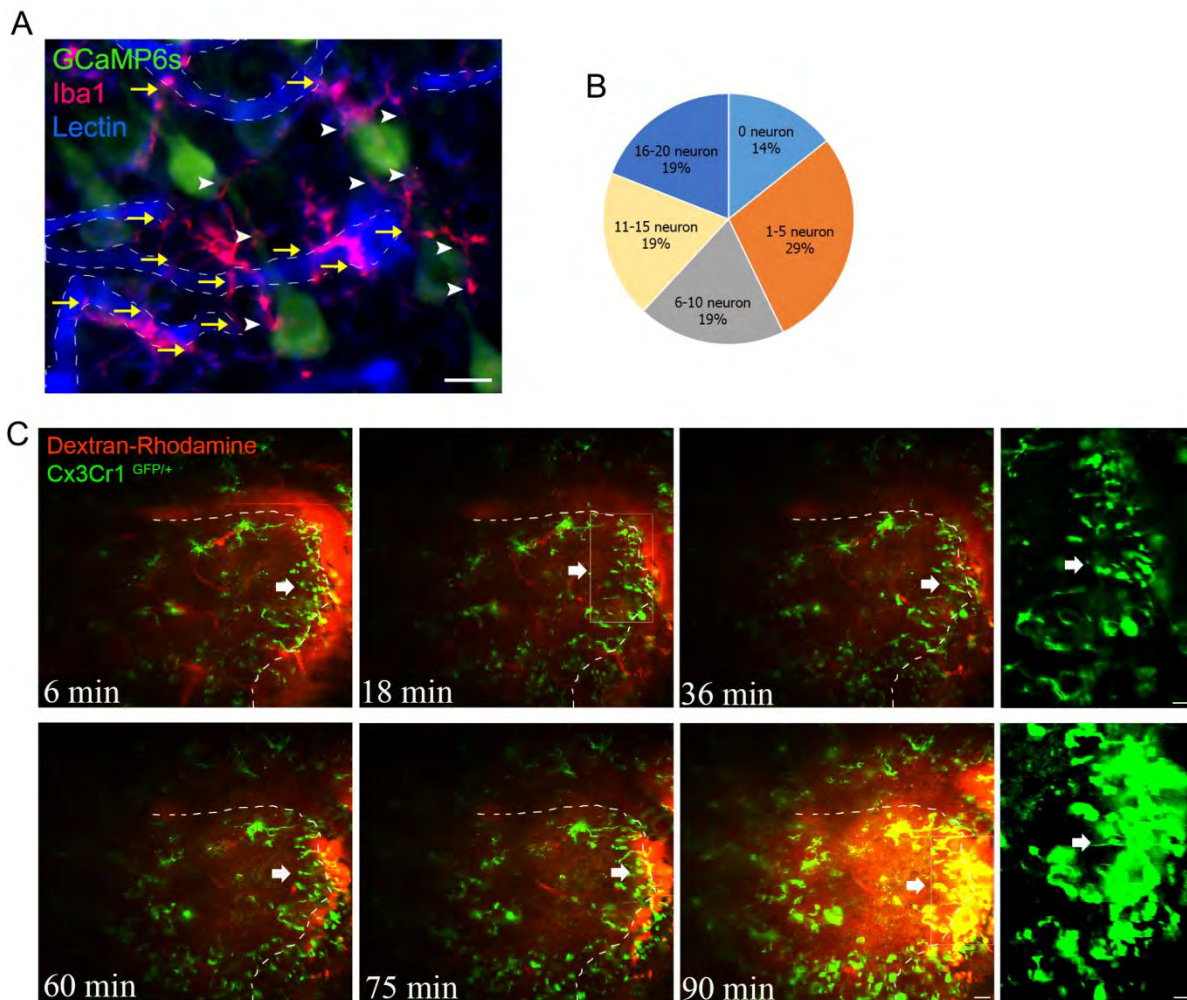
Supplementary Figure 9. Microglial process coverage of neuronal cell bodies follows neuronal calcium changes and SD after cerebral ischemia. **A.** *In vivo* two-photon imaging was performed every 3 min (Z-stacks recorded with galvo scanning) starting 15 min prior to the onset of cerebral ischemia. Monochromatic images have been thresholded and used for analysis of microglia process coverage (area) of neuronal cell bodies by a custom made concentric circle macro (modified Sholl analysis) that was run using Image J. **B.** After the induction of cerebral ischemia, one population of neurons showed increasing RCaMP1 signal ($P < 0,0001$, two-way ANOVA) over time (termed as "Group 1" cells, $P_{\text{baseline vs before SD}} < 0,0001$; $P_{\text{before vs after SD}} < 0,05$; $P_{\text{baseline vs after SD}} < 0,0001$ one-way ANOVA) whereas another population displayed minimal RCaMP1 signal increases over baseline (termed as "Group 2" cells) before and after SD. **C.** Group 2 cells, however, showed a larger RCaMP1 signal increase during SD (unpaired t test, $P < 0.0001$). **D.** Representative graph showing Group 1 cell with increasing RCaMP1 signal and increasing microglial process coverage after SD. **E.** Representative graph showing Group 2 cell with negligible RCaMP1 signal changes and increasing microglial process coverage after SD. **F.** Neurons with no significant RCaMP1 signal change after SD (Group 2 cells) show significantly increased microglial process recruitment in response to SD (unpaired t test, $P < 0.01$). Data are expressed as percentage of baseline ($n = 33$ Group 1 and $n = 17$ Group 2 neurons).



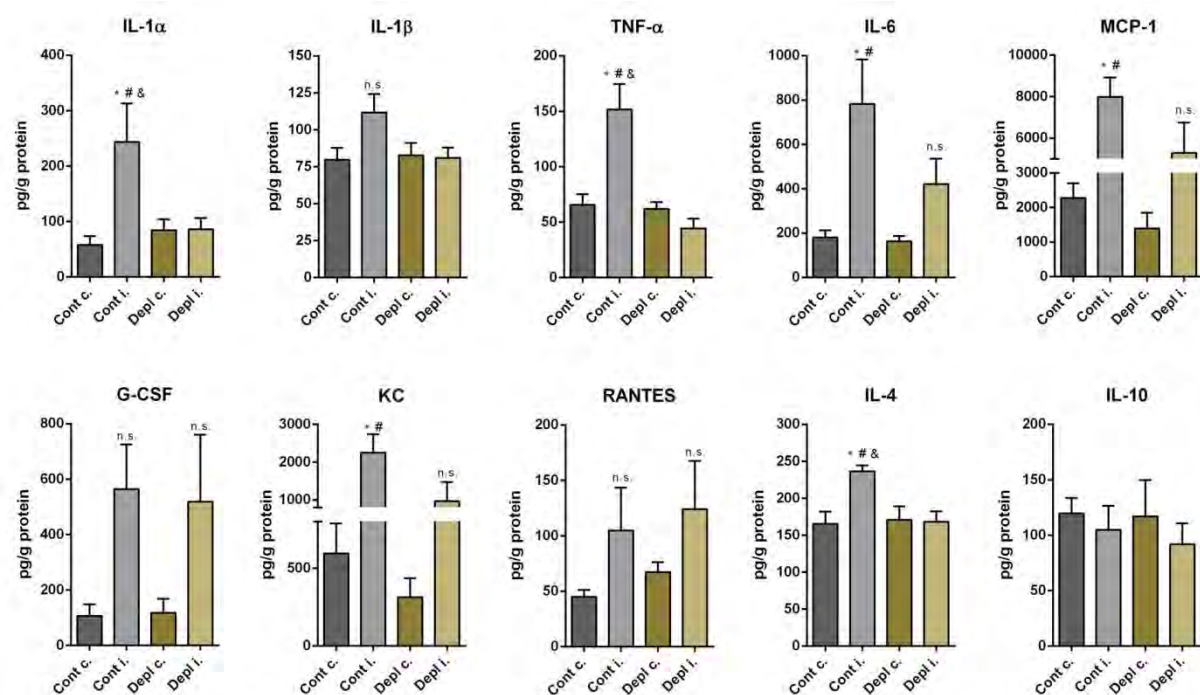
Supplementary Figure 10. Super-resolution microscopy reveals sites of microglia-neuron interactions in the brain. **A.** Confocal images showing a precise colocalisation between GFP signal in Cx3Cr1^{GFP/+} microglia reporter mice and P2Y12 receptors. **B.** STORM super-resolution microscopy identifies clusters of P2Y12 receptors (P2Y12 STORM, cyan) overlapping with confocal images of P2Y12 –positive microglial processes (P2Y12 conf., red). Microglial processes come to close contact with GCaMP6s-positive neurons. Images were captured in the cerebral cortex of a mouse subjected to sham surgery. Note the sparse microglial labelling around the neuronal cell bodies compared to that seen in mice after cerebral ischemia (Fig. 3I, J). Scale bar: A, 10 μ m; B, 5 μ m.



Supplementary Figure 11. Local field potential measurements correlate with GCaMP6s signal changes in the brain *in vivo*. Local field potential (LFP) was recorded with a borosilicate glass electrode (~ 0.1 M Ω) filled with ACSF. Neuronal calcium responses were recorded with resonant scanning using GCaMP6s labelling. Simultaneous LFP recordings were performed in IC mode at 0 mV holding potential. The distance between the pipette and the imaging area was approximately 100-150 μm . **A.** Spontaneous calcium responses and LFP recorded prior to KCl application. Calcium curves from 7 representative neurons (circled) are shown. **B.** Correlation between LFP (area under the curve, mV x ms) and calcium signals expressed as an average $\Delta F/F$ of 11 neurons (area under the curve) is shown for 26 spontaneous burst events. **C.** 100 mM KCl was applied topically to the surface of the brain and GCaMP6s signal recorded in parallel with LFP measurements.



Supplementary Figure 12. Microglia rapidly react to changes in blood brain barrier permeability after cerebral ischemia. A. Immunofluorescent characterization of microglia reveal an association between microglial processes (Iba1, red) and GCaMP6s expressing neurons (green, arrowheads) as well as between microglial processes and capillaries (blue, arrows). **B.** Pie chart showing percentage of microglia contacting different numbers of neurons based on *in vivo* two-photon imaging data (see Figure 2) and histological assessment. **C.** *In vivo* two-photon imaging in Cx3Cr1^{GFP/+} microglia reporter mice showing that microglia isolate sites of BBB injury (red, Dextran-Rhodamine, 70,000 MW) and transform to an amoeboid shape in close vicinity of injured blood vessels. Times indicate minutes after the induction of cerebral ischemia. Scale bars: A, 10 μ m; C, 20 μ m.



Supplementary Figure 13. Changes in cytokine production after cerebral ischemia in the brain. Cytokine levels in homogenates of the ipsilateral (i) and contralateral (c) hemispheres were measured by cytometric bead array in control (cont) and microglia depleted (depl) mice, 8h after the onset of cerebral ischemia. Mice were transcardially perfused with saline prior to the collection of brain samples. IFN γ was not detectable in the brain (detection limit of the assay was 5 pg/ml), hence values are not shown. ANOVA followed by Tukey's post hoc test, *P<0.05 vs Cont c., #P<0.05 vs Depl c., &P<0.05 vs Depl i., Data are expressed as mean \pm s.e.m., n=5 mice per group. n.s. – not significant.

RESEARCH ARTICLE

CELLULAR NEUROSCIENCE

Microglia monitor and protect neuronal function through specialized somatic purinergic junctions

Csaba Cserép^{1*}, Balázs Pósfa^{1,2*}, Nikolett Lénárt¹, Rebeka Fekete^{1,2}, Zsófia I. László^{2,3}, Zsolt Lele³, Barbara Orsolits¹, Gábor Molnár⁴, Steffanie Heindl⁵, Anett D. Schwarcz¹, Katinka Ujvári¹, Zsuzsanna Környei¹, Krisztina Tóth^{1,2}, Eszter Szabadits¹, Beáta Sperlách⁶, Mária Baranyi⁶, László Csiba⁷, Tibor Hortobágyi^{8,9,10}, Zsófia Maglóczky¹¹, Bernadett Martinecz¹, Gábor Szabó¹², Ferenc Erdélyi¹², Róbert Szipócs¹³, Michael M. Tamkun¹⁴, Benno Gesierich⁵, Marco Duering^{5,15}, István Katona³, Arthur Liesz^{5,15}, Gábor Tamás⁴, Ádám Dénes^{1†}

Microglia are the main immune cells in the brain and have roles in brain homeostasis and neurological diseases. Mechanisms underlying microglia–neuron communication remain elusive. Here, we identified an interaction site between neuronal cell bodies and microglial processes in mouse and human brain. Somatic microglia–neuron junctions have a specialized nanoarchitecture optimized for purinergic signaling. Activity of neuronal mitochondria was linked with microglial junction formation, which was induced rapidly in response to neuronal activation and blocked by inhibition of P2Y12 receptors. Brain injury–induced changes at somatic junctions triggered P2Y12 receptor–dependent microglial neuroprotection, regulating neuronal calcium load and functional connectivity. Thus, microglial processes at these junctions could potentially monitor and protect neuronal functions.

Microglia are the main immunocompetent cells of the nervous system and their role in brain development and maintenance of proper neuronal function throughout life is widely recognized (1, 2). Changes in microglial activity are linked with major human diseases, including different forms of neurodegeneration, stroke, epilepsy, and psychiatric disorders (3, 4).

Microglia perform dynamic surveillance of their microenvironment using motile microglial processes that constantly interact with neurons (5, 6). However, the molecular mechanisms of bidirectional microglia–neuron communication are unclear. To date, most studies have focused on the interactions between microglial processes and synaptic elements, including axonal boutons and dendritic spines, which have commonly been perceived as the main form of interaction between microglia and neurons (7, 8). However, neurons are extremely polarized cells with a high degree of functional independence concerning metabolism and signal integration in their dendritic and axonal compartments (9–11). The large-scale structure of neurons (i.e., their cell body and axonal or dendritic branches) in the brain is relatively

stable under most conditions. In comparison, small synaptic structures such as dendritic spines and axonal boutons are often distant from neuronal cell bodies and are highly dynamic. Therefore, the interactions between microglia and synapses may not fully explain how microglia are capable of monitoring and influencing the activity of neurons or how early events of cellular injury in the perisomatic compartment are detected. This may be particularly relevant for the migration and differentiation of neural precursors, cell survival and programmed cell death, adult neurogenesis, and the phagocytosis of damaged neuronal cell bodies (12–15). It is not understood how microglia could monitor neuronal status over years or even decades and discriminate salvageable neurons from irreversibly injured cells mainly on the basis of changes occurring at distant synaptic structures.

To understand the possible mechanisms of effective communication between microglia and neurons, we tested the hypothesis that specialized junctions on neuronal cell bodies may support the dynamic monitoring and assistance of neuronal function by microglia.

Microglial processes contact specialized areas of neuronal cell bodies in mouse and human brains

To visualize microglia together with cortical neurons and to study microglia–neuron interactions in the intact brain in real time, CX3CR1^{+/GFP} microglia reporter mice were electroporated in utero with *pCAG-IRES-tdTomato* plasmid (fig. S1A). In vivo two-photon (2P) imaging revealed microglial processes contacting the cell bodies of cortical layer 2 to 3 neurons in the adult brain (Fig. 1, A and B, and movie S1). Microglial processes preferentially returned to the same areas on the neuronal soma (observed in 23 neurons out of 28 from 3 mice). The average lifetime of somatic microglia–neuron contacts was 25 min; some contacts persisted for >1 hour (fig. S1B), whereas dendritic contacts had a significantly shorter lifetime of 7.5 min (Fig. 1C; $p = 0.00035$; $n = 26$ contacts from 3 mice), similar to that reported for synaptic contacts (16). Post hoc confocal laser scanning microscopy (CLSM) and electron microscopic analysis further validated the direct interaction between microglial processes and the cell bodies of cortical pyramidal neurons (Fig. 1D and fig. S1, C and D), which we named somatic microglial junction. Similar interactions were present on well-characterized interneuron populations, namely type 3 vesicular glutamate transporter–positive (vGluT3⁺) and parvalbumin-expressing (PV⁺) cells in the neocortex and the hippocampus (fig. S1E). Somatic microglia–neuron junctions were also observed in the human neocortex (Fig. 1E). Somatic microglial junctions were present on 93% of cortical pyramidal neurons, 95% of vGluT3⁺ neurons, and 89% of PV⁺ interneurons in mice ($n = 443$ cells from 4 mice). Despite the well-established microglial regulation of neuronal synapses, only 9% of glutamate-releasing and 11% of γ -aminobutyric acid (GABA)-releasing synapses were associated with microglial processes (Fig. 1F and fig. S1F; $n = 1183$ synapses from 4 mice). Eighty-seven percent of neurons in the human neocortex received microglial contact with their cell body (Fig. 1, E and F; $n = 170$ cells from 3 patients). We also tested the possible presence of somatic microglial junctions in subcortical areas. Ninety-eight percent of neurons in the caudate putamen, 91% of neurons in the nucleus reticularis gigantocellularis, and 96% of neurons in the medial septum were contacted by microglial processes

¹Momentum Laboratory of Neuroimmunology, Institute of Experimental Medicine, Budapest, Hungary. ²Szentágotai János Doctoral School of Neuroscience, Semmelweis University, Budapest, Hungary. ³Momentum Laboratory of Molecular Neurobiology, Institute of Experimental Medicine, Budapest, Hungary. ⁴MTA-SZTE Research Group for Cortical Microcircuits of the Hungarian Academy of Sciences, Department of Physiology, Anatomy and Neuroscience, University of Szeged, Szeged, Hungary. ⁵Institute for Stroke and Dementia Research, Ludwig-Maximilians-University, Munich, Germany. ⁶Laboratory of Molecular Pharmacology, Institute of Experimental Medicine, Budapest, Hungary. ⁷MTA-DE Cerebrovascular and Neurodegenerative Research Group, Department of Neurology, University of Debrecen, Debrecen, Hungary. ⁸Institute of Pathology, Faculty of Medicine, University of Szeged, Szeged, Hungary. ⁹Department of Old Age Psychiatry, Institute of Psychiatry, Psychology and Neuroscience, King's College London, London, UK. ¹⁰Centre for Age-Related Medicine, SESAM, Stavanger University Hospital, Stavanger, Norway. ¹¹Human Brain Research Laboratory, Institute of Experimental Medicine, Budapest, Hungary. ¹²Medical Gene Technology Unit, Institute of Experimental Medicine, Budapest, Hungary. ¹³Institute for Solid State Physics and Optics of Wigner RCP, Budapest, Hungary. ¹⁴Department of Biomedical Sciences, Colorado State University, Fort Collins, Colorado, USA. ¹⁵Munich Cluster for Systems Neurology (SyNergy), Munich, Germany.

*These authors contributed equally to this work.

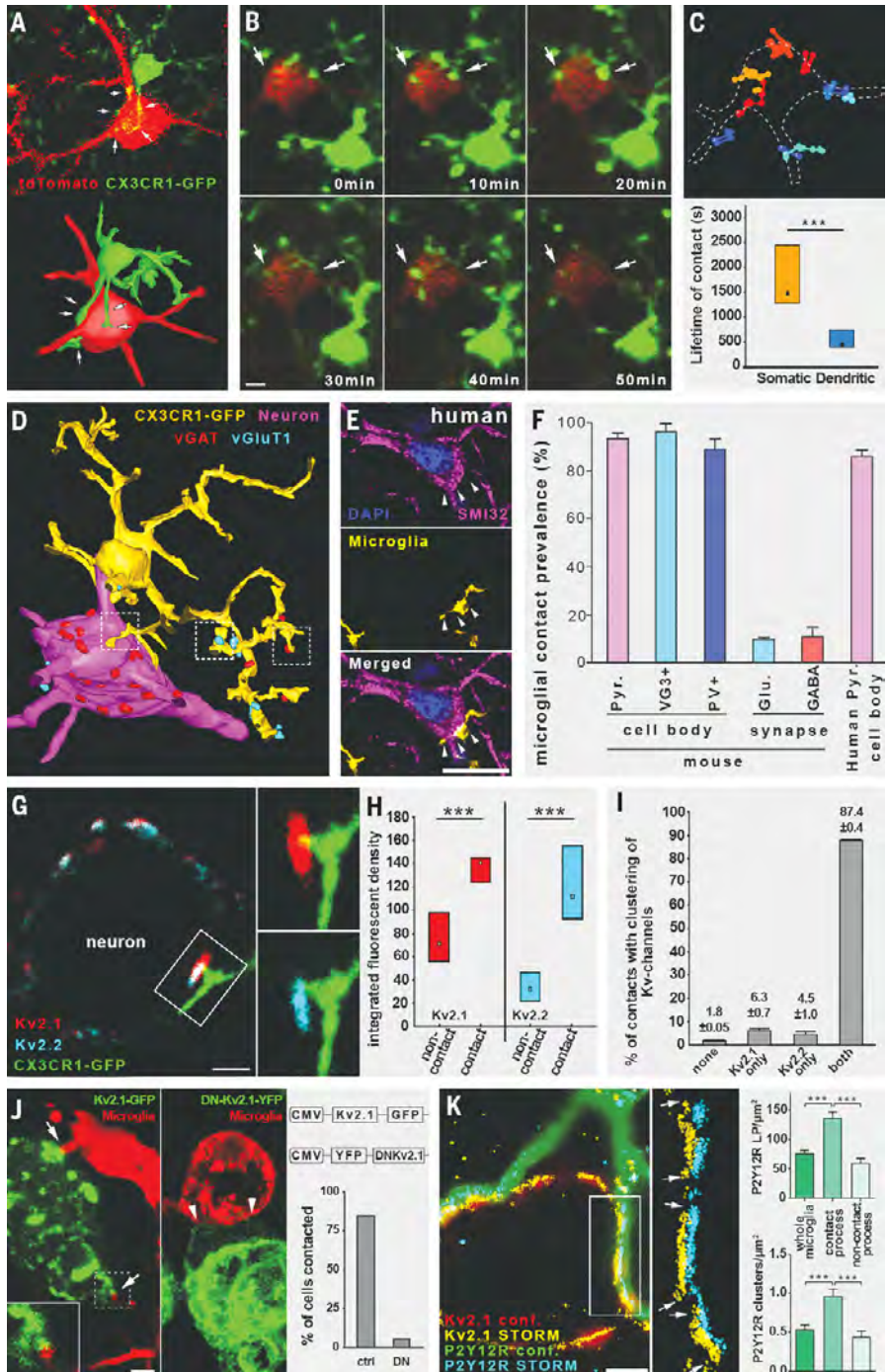
†Corresponding author. Email: denes.adam@koki.mta.hu

($n = 268$ cells from 2 mice). Thus, these contacts are evolutionary conserved and present in all main areas of the brain.

Microglia at somatic junctions may sense changes in neuronal state through signals released by exocytosis. In neurons, clustered Kv2.1 proteins are well known to provide exocytotic surfaces by anchoring vesicle fusion molecules to the neuronal membrane (17, 18). Furthermore, both Kv2.1 and Kv2.2 proteins are involved in forming endoplasmic reticulum (ER)–plasma membrane (PM) junctions (membrane-trafficking

hubs) and in anchoring intracellular organelles to the neuronal PM (19). Microglia contacted neuronal somatic membranes at sites of Kv2.1 and Kv2.2 clustering (Fig. 1G). The integrated density of Kv2.1 signal at these sites was 96% higher and the density of Kv2.2 signal was 254% higher compared with those without microglial contacts (Fig. 1H; $p < 0.0001$ in both cases; $n = 114$ and $n = 107$, respectively, from 3 mice). Eighty-seven percent of all microglia–neuron contacts expressed both types of clusters, 6.3% expressed only Kv2.1

clusters, 4.5% only Kv2.2 clusters, and only 1.8% of contacts were void of any Kv clusters (Fig. 1I; $n = 111$ contacts from 2 mice). Furthermore, 99% of neocortical and 94% of hippocampal CA1-region neurons expressed both Kv2.1 and Kv2.2 channels at the cellular level (fig. S2, A to C). The spatial association between Kv2.1 clusters and microglial processes was also observed on human cortical neurons (fig. S1, G and H; $n = 21$ cells). Because Kv2.1 clusters are implicated in a large number of cellular processes involved in cell-to-cell



communication, we focused on Kv2.1 in our further experiments. Kv2.1 hot spots appeared to define preformed neuronal microdomains because Kv2.1 clusters remained unaltered after selective elimination of microglia by PLX5622 (fig. S1, I and J; 4.71 clusters per cross-section in control versus 6.64 clusters per cross-section in depleted; $n = 59$ cells from 4 mice). To test the functional involvement of Kv2.1 clusters in the formation of somatic junctions, we developed a dominant-negative Kv2.1 mutant construct, DNKv2.1. This construct could not integrate into the PM and blocked the forward trafficking of any endogenous Kv2 proteins that may be expressed. We transfected human embryonic kidney (HEK) 293 cells, which naturally lack Kv2.1 protein (20), with fluorescent protein-coupled Kv2.1 or DNKv2.1 constructs and cocultured these with microglia. Microglial processes contacted Kv2.1-transfected HEK cells preferentially at Kv2.1 clusters and did not contact the DNKv2.1-transfected HEK cells (Fig. 1J and movie S2). Eighty-four percent of Kv2.1-transfected HEK cells received microglial process contacts (97% of these contacts arrived onto Kv2.1 clusters), whereas only 5.4% of DNKv2.1-transfected HEK cells received process contacts ($n = 75$ cells from 3 experiments). Thus, cell surface expression and clustering of Kv2.1 proteins is sufficient to induce contact formation by microglial processes.

Activity-dependent exocytotic adenosine 5'-triphosphate (ATP) or adenosine 5'-diphosphate (ADP) release takes place from neuronal cell bodies under physiological conditions (21, 22). ATP (ADP) is a major chemoattractant for microglial processes through the microglial purinoceptor P2Y₁₂ receptor (5, 23). We thus asked whether signaling through P2Y₁₂ receptor was also essential for microglia–neuron interactions at these somatic junctions. In fact, all microglia, but no other cells in the brain, including perivascular macrophages, were found to be P2Y₁₂ receptor positive (fig. S3), including their processes recruited to somatic junctions (fig. S3B). The restriction of P2Y₁₂ receptor expression to microglia within the brain agrees with results of earlier single-cell transcriptomics studies (24, 25).

To investigate the nanoscale architecture of P2Y₁₂ receptors at somatic microglia–neuron junctions, we used correlated CLSM and STORM superresolution microscopy, which enables the precise assessment of P2Y₁₂ receptor and Kv2.1 clusters at 20-nm lateral resolution (26). P2Y₁₂ receptors formed dense clusters on microglial processes at somatic junctions directly facing neuronal Kv2.1 clusters (Fig. 1K). Unbiased cluster analysis revealed that P2Y₁₂ receptor localization point density and cluster density were both significantly higher on microglial processes inside the junctions than on processes outside the junctions or on the whole microglial cell (Fig. 1K and fig. S2D; for detailed statistics

dc_2027_22

and numbers, see table S1). Furthermore, somatic contact-dependent clustering of P2Y₁₂ receptors occurred on both pyramidal cells and interneurons (fig. S2E; for detailed statistics and numbers, see table S1). Contact-dependent molecular clustering, however, could not be observed in the case of the microglial calcium-binding protein Iba1 (fig. S2F). Contact-dependent P2Y₁₂ receptor clustering was specific to somatic junctions, and immunogold density was 62% lower on microglial membranes contacting boutons than on those contacting somata (fig. S2G; $p = 0.0002$; $n = 26$ contacts from 3 mice). Thus, we suggest the existence of a functionally specialized yet ubiquitous communication site between P2Y₁₂ receptor-positive microglial processes and neuronal cell bodies.

Somatic microglia–neuron junctions have a specific nanoarchitecture and molecular fingerprints

To further investigate the ultrastructural features of somatic microglia–neuron junctions, we performed transmission electron microscopy and high-resolution electron tomography with three-dimensional (3D) reconstruction. P2Y₁₂ receptor immunogold labeling confirmed the formation of direct junctions between microglial processes and neuronal somata both in mice (Fig. 2A) and in postmortem human brain tissue (fig. S4A). Microglia–neuron junctions were composed of closely apposed mitochondria, reticular membrane structures, intracellular tethers, and associated vesicle-like membrane structures within the neuronal cell body (Fig. 2A). 3D electron tomography confirmed this nanoarchitecture in neurons (Fig. 2B and movies S3 and S4). These morphological features were not observed in perisomatic boutons contacted by microglia. Furthermore, automated 3D analysis of tomographic volumes showed that P2Y₁₂ receptor density negatively correlated with the distance between microglial and neuronal membranes within the junctions (Fig. 2, C and D, and fig. S4C; $p < 0.001$; $n = 13,055$ points from 3 contacts). We also compared P2Y₁₂ receptor density between microglial membrane surfaces establishing junctions with neuronal somata and adjacent surfaces (within a few micrometers) that contacted boutons or other neuronal elements. We detected a significantly higher P2Y₁₂ receptor density at microglial membranes directly contacting neuronal cell bodies (Fig. 2E and movie S5; $p = 0.00115$; $n = 24$ surfaces). This suggests an important role for purinergic signaling in the formation of somatic microglia–neuron junctions.

We also observed discrete intercellular structures resembling cell-adhesion molecules in the extracellular space that connected the membranes of microglia and neuronal cell bodies (average length 23.5 ± 3.1 nm; $n = 89$ from 3 mice; fig. S4B). This falls in the range of the size of integrins expressed by microglia

(27, 28) or the width of immunological synapses between peripheral immune cells (29). Mitochondria-associated membranes (MAMs, average distance: 19.5 nm; $n = 104$ from 3 mice; fig. S4B) were observed (30) and discrete tethers between mitochondria and MAMs were also visible (movie S4).

We hypothesized that mitochondrial ATP production and changes in neuronal activity could trigger microglial process recruitment. Thus, we investigated the possible enrichment of neuronal mitochondria at microglial junctions on a large sample size using an unbiased, semiautomatic analysis of the outer mitochondrial membrane protein TOM20. TOM20 immunofluorescent intensity was 420% higher at somatic junctions compared with adjacent areas (Fig. 2, F and G; $p < 0.001$; $n = 14$ contacts from 2 mice), confirming the strong accumulation of neuronal mitochondria at the somatic junctions.

TOM20-positive vesicles were observed between mitochondria and the neuronal membrane in addition to TOM20-negative vesicles (Fig. 2H and fig. S4, E and F). This may suggest trafficking and possible exocytosis of mitochondria-derived vesicles (31) at somatic microglial junctions. Mitochondria-derived vesicles (MDVs) often integrate into the endolysosomal pathway (31), and these vesicles are positive for the lysosomal marker LAMP1 (32). Indeed, LAMP1-positive puncta were closely associated with 83.3% of all Kv2.1 clusters at somatic junctions (fig. S4G; $n = 72$ contacts from 2 mice), suggesting the release of MDVs and lysosomal content at these junctions.

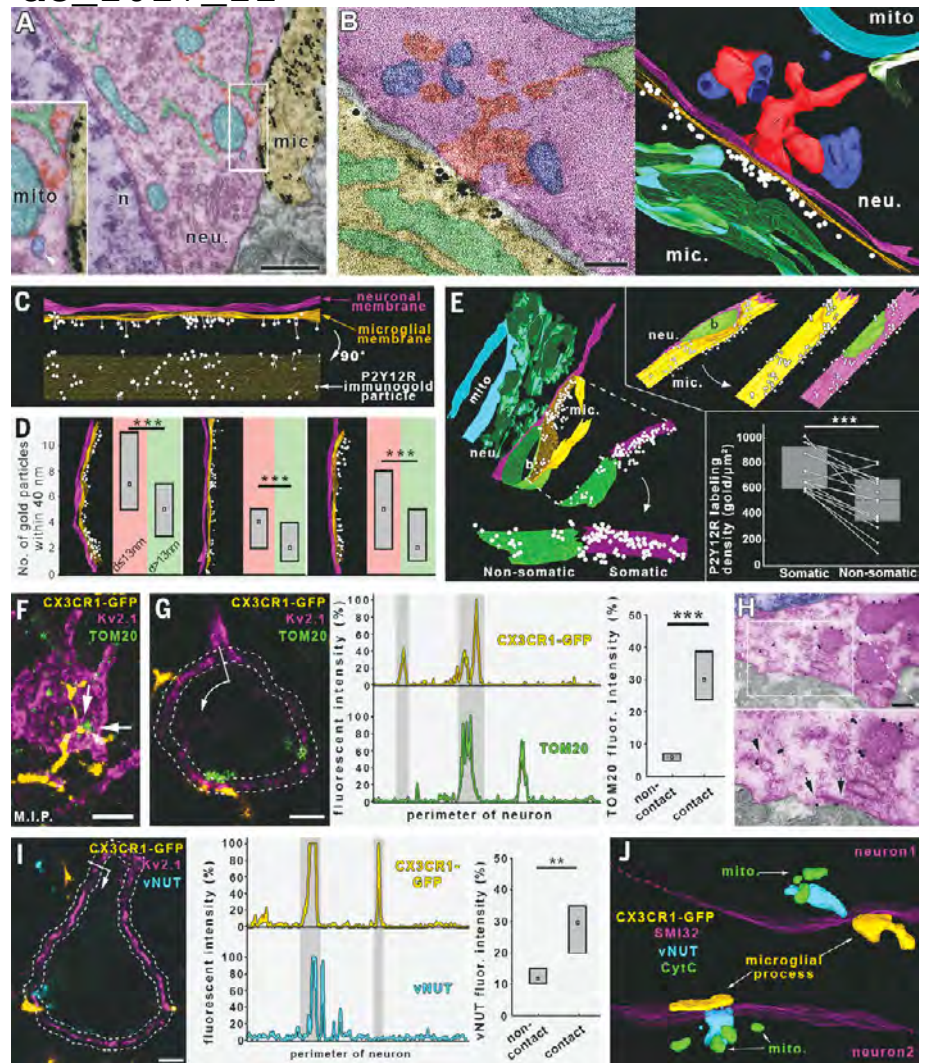
Kv2.1-immunogold clusters were tightly associated with the observed neuronal structures (i.e., closely apposed mitochondria, MAMs, ER, vesicle-like structures, cytoplasmic densities) within these junctions (fig. S4D). Similarly to our CLSM results (fig. S1I), Kv2.1 nanoclustering was not affected by the absence of microglia (fig. S4D). These structures may function as mitochondria-related signaling hubs in neurons that microglia can recognize. Vesicular release of mitochondria-derived ATP from neurons may occur in a vesicular nucleotide transporter (vNUT)-dependent manner (33, 34). Indeed, vNUT signal intensity was 2.5 times higher in the vicinity of the neuronal membranes at somatic microglia–neuron junctions compared with areas outside the junctions (Fig. 2I; $p = 0.002$; $n = 15$ contacts from 2 mice). Neuronal vNUT labeling was concentrated between mitochondria and the microglia-contacted neuronal membranes (Fig. 2J).

Kv2.1 or vNUT signal was not present in perisomatic axon terminals (GABA-releasing synaptic boutons), including those contacted by microglial processes (fig. S4, H and I; $n = 220$ boutons for Kv2.1 and $n = 194$ boutons for vNUT from 2 mice), confirming again that

dc_2027_22

Fig. 2. Microglia–neuron junctions have a specialized nanoarchitecture and molecular machinery optimized for purinergic cell-to-cell communication.

(A) Transmission electron micrograph showing the area of the neuronal cell body (neu.) contacted by a P2Y12 receptor–immunogold (black grains)–labeled microglial process (mic.). The junction has a specific ultrastructure with closely apposed mitochondria (mito., cyan), reticular membrane structures (green), and intracellular tethers (red). A mitochondria-associated vesicle (blue, marked by white arrowhead) is also visible. The nucleus (n) of the neuron is purple. (B) A 0.5-nm-thick virtual section of an electron tomographic volume (left) and 3D model (right) showing the special nanoarchitecture of a somatic microglia–neuron junction [colors represent the same structures as in (A)]. Note the specific enrichment of P2Y12 receptor labeling at the core of the junction. (C and D) P2Y12 receptor density negatively correlates with the distance between microglial and neuronal membranes within the junctions. (E) P2Y12 receptor density is highest at those surfaces of microglial processes that are in direct contact with the neuronal cell bodies (P2Y12 receptor labeling is white; b, bouton). (F) CLSM maximal intensity projection (M.I.P.) showing microglial processes (yellow) contacting neuronal somata (magenta) with adjacent mitochondria (green). (G) Neuronal mitochondria are enriched at microglial junction sites. (H) Transmission electron micrographs showing TOM20–immunogold labeling in neocortical neurons. Immunogold labeling (black grains) is specifically associated with outer mitochondrial membranes, whereas TOM20-positive vesicles can also be observed (arrowheads). Some immunogold particles can be found on the PM of the neurons (arrows), suggesting the exocytosis of mitochondria-derived vesicles. (I) vNUT-labeled vesicles are enriched at microglial junction sites. (J) 3D reconstruction of high-resolution confocal Z-stack showing parts of two neuronal cell bodies (magenta), both contacted by microglial processes (yellow). The vNUT signal (cyan) was concentrated between the junctions and closely positioned mitochondria (green). For statistical details, see the supplementary text for Fig. 2.



these molecular fingerprints were associated with somatic microglia–neuron junctions.

Physiological microglia–neuron communication at somatic junctions is P2Y12 receptor dependent and linked with neuronal mitochondrial activity

Next, we aimed to test whether microglial process recruitment to somatic junctions was functionally linked with the activity of mitochondria in neurons. To this end, CX3CR1^{+/GFP} mice were electroporated in utero with the mitochondria-targeted *CAG-Mito-R-Geco1* reporter construct (fig. S5A). Again, we observed the involvement of somatic mitochondria in microglial junctions (Fig. 3A). In vivo 2P imaging was performed to monitor microglial process recruitment to neuronal mitochondria in the cerebral cortex (Fig. 3B). As expected, recruited microglial processes came into close apposition with neuronal mitochondria. These

processes stayed in the vicinity of neuronal mitochondria for ~29 min in vivo (Fig. 3B and movie S6; *n* = 25 contacts on 19 neurons from 3 mice, median value), closely matching the value measured in tdTomato-electroporated mice (Fig. 1C). To study the functional relationship between microglial junction formation and activity of neuronal mitochondria, we assessed intracellular changes of the metabolic electron carrier nicotinamide adenine dinucleotide (NADH) (35) in coronal slices of visual and somatosensory cortices from CX3CR1^{+/GFP} mice. Intracellular NADH fluorescence showed a granular pattern, indicating a mitochondrial NADH source. Indeed, the NADH signal colocalized with the *Mito-R-Geco1* signal, confirming its mitochondrial origin (fig. S5C). To search for somatic junction formation, we performed 2P imaging, which allowed us to track the movement of microglial processes and monitor cytosolic NADH in viable layer 2/3 neurons

simultaneously (fig. S5D). We detected apparent increases in NADH intrinsic fluorescence (Fig. 3, C and E; *p* = 0.024; *n* = 10 cells) in parallel with the formation of somatic microglial junctions. By contrast, we found no changes in the mean intrinsic NADH fluorescence detected at neuronal somata contacted by microglial processes in P2Y12 receptor^{-/-} tissue (Fig. 3, D and E; *p* = 0.3; *n* = 11 cells). Thus, microglial process recruitment to somatic junctions is linked to the metabolic activity of neuronal mitochondria through a P2Y12 receptor–dependent mechanism.

The molecular machinery and intercellular interactions identified above suggested the involvement of purinergic signaling in these somatic junctions. To test whether neuronal somata could release ATP at these sites, we conducted a series of in vitro experiments. Quinacrine-labeled ATP-containing vesicles localized between neuronal mitochondria and

neuronal membranes were present at sites where microglial processes contacted neuronal Kv2.1 clusters in microglia–neuron cocultures (Fig. 3F). Quinacrine labeling also colocalized with vNUT signal (Fig. 3F), as previously demonstrated for neurons (33).

Next, we tested whether neuronal activity could release ATP-containing vesicles from neuronal cell bodies. KCl (40 mM) stimulation induced a rapid membrane depolarization and calcium influx in cultured neurons (fig. S5E; $n = 23$ cells for FluoVolt measurements, $n = 20$ cells for Rhod3 measurements). CLSM *in vitro*

dc_2027_22

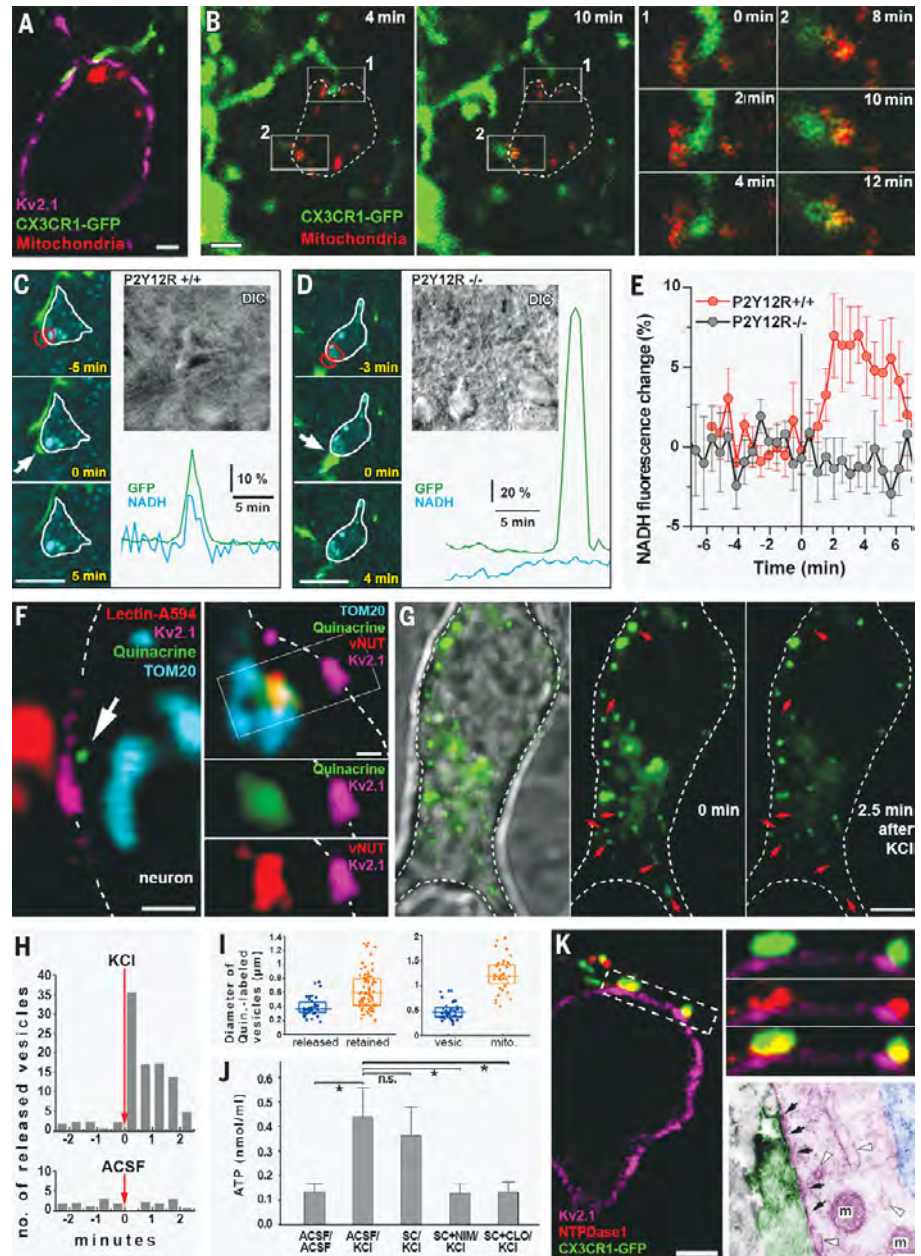
time-lapse imaging confirmed that quinacrine-labeled (ATP-containing) vesicles were released from neuronal cell bodies after KCl stimulation (Fig. 3, G and H; 880% increase in release events after KCl versus a 27% decrease after vehicle; $n = 13$ cells). Size analysis confirmed that the smaller vesicles were released [Fig. 3I; median diameter of released vesicles was 0.37 μm and that for retained vesicles was 0.59 μm ($n = 118$ puncta), similar to previous reports (33)]. The larger vesicles were identified as mitochondria by their uniform TOM20 labeling (Fig. 3I; median diameter of vesicle

labeling was 0.45 μm and that for mitochondrial labeling was 1.2 μm ; $n = 83$ puncta).

Next, we applied high-sensitivity high-performance liquid chromatography (HPLC) to detect the levels of released ATP in the medium (Fig. 3J). KCl induced a robust ATP release in cultured neurons ($p = 0.0218$; $n = 11$), which was not inhibited by a mixture of the synaptic calcium-channel blockers ω -agatoxin and ω -conotoxin ($p = 0.6532$; $n = 11$), but was almost completely inhibited by the L-type calcium-channel blocker nimodipine [known to be important for somatic vesicular release

Fig. 3. Neuronal mitochondrial activity and purinergic signaling are involved in microglia–neuron communication.

(A) CLSM image showing a microglial process (green) contacting Kv2.1 clusters (magenta) on a neuronal soma in the vicinity of a mitochondrion (Mito-R-Geco1, red) in a perfusion-fixed brain. (B) *In vivo* 2P imaging of CX3CR1^{+/GFP} mice *in utero* electroporated with CAG-Mito-R-Geco1 construct. Dashed line shows the outline of the neuron. Green microglial processes touch the neuronal cell body where somatic mitochondria are present. Regions of interest 1 and 2 are enlarged to show the development of somatic junctions. (C and D) Representative samples from time-lapse imaging of microglia showing processes extending and contacting neuronal soma in CX3CR1^{+/GFP}/P2Y12 receptor^{+/+} (C) and CX3CR1^{+/GFP}/P2Y12 receptor^{-/-} (D) mice. White arrow indicates the contact site of microglia. Differential interference contrast (DIC) images of the imaged neurons and the fluorescence signal of GFP (green) and NADH (dark cyan) of red outlined areas are shown. (E) Average (and standard deviation) of NADH intrinsic fluorescence of all neurons in P2Y12 receptor^{+/+} (red, $n = 10$) and P2Y12 receptor^{-/-} (black, $n = 11$) mice. (F) CLSM image showing microglial process contacting a neuronal Kv2.1 cluster with closely apposed quinacrine-labeled ATP-containing vesicle and closely localized neuronal mitochondria. Quinacrine labeling colocalizes with the vNUT signal. (G) Images from CLSM *in vitro* time-lapse imaging showing that quinacrine-labeled ATP-containing vesicles (green) are released (red arrows) from the neuronal cell body (white dashed outline) after KCl stimulation (M.I.P. of Z stack, 2.5 μm). (H) Number of released quinacrine-positive vesicles plotted as a function of time after KCl or vehicle treatment. (I) Size distribution of quinacrine-labeled puncta. The smaller ones (vesicles) tend to be released and the larger ones (mitochondria) are retained. (J) KCl induces a robust ATP release in cultured neurons, which could not be inhibited by a mixture of the synaptic calcium-channel blockers ω -agatoxin and ω -conotoxin (SC), but was almost completely inhibited by the L-type calcium-channel blocker nimodipine (NIM) or the vNUT inhibitor clodronate (CLO). (K) CLSM image showing robust NTPDase1 expression on microglial processes within the somatic junctions. Electron microscopic insert shows NTPDase1-labeled (dark precipitate) microglial process contacting the neuronal cell body. Neuronal mitochondria (m), vesicles, and membrane structures (white arrowheads) are closely apposed to the contact site (black arrows) where NTPDase1 is expressed on the microglial membrane. For statistical data, see the supplementary text for Fig. 3.



(36); $p = 0.0271$; $n = 10$] or the vNUT inhibitor clodronate ($p = 0.0284$; $n = 10$). These data confirmed the presence of an activity-dependent somatic ATP release from neurons. Because the main ligand for microglial P2Y12 receptors is ADP, we tested the possible presence of nucleosidase expression at microglia–neuron contacts. Using CLSM and electron microscopy, we found robust NTPDase1 expression on 99.6% of all microglial processes within the somatic junctions (Fig. 3K; $n = 275$ contacts from 2 mice). Thus, neuron-derived ATP can readily be converted into ADP and sensed by microglia right within the somatic junctions.

Because microglial processes are in a position at the somatic junctions to sense neuronal activity, we further explored the signaling mechanisms at these sites *in vivo* using 2P imaging in CX3CR1^{+/GFP} microglia reporter mice that were electroporated *in utero* with the neuronal reporter *pCAG-IRES-tdTomato* (Fig. 4, A and B). Intra-cisterna magna administration of the potent and selective P2Y12 receptor inhibitor PSB0739 (PSB) reduced somatic junction lifetime by 45% but did not affect the lifetime of dendritic microglia–neuron contacts (Fig. 4C, control somata versus PSB somata; $p = 0.0331$; $n = 40$). We also tested synapse density after acute intra-cisterna magna administration of vehicle (control) or PSB. PSB treatment did not alter neocortical synapse

numbers (fig. S6G; 0.353 synapses/ μm^2 in control somata and 0.352 synapses/ μm^2 in PSB-injected somata; $n = 423$ appositions from 4 animals). Because the maintenance of somatic microglia–neuron junctions depends on physiological P2Y12 receptor function, we tested whether microglia would react directly to changes in neuronal activity. We induced neuronal activation by using the chemogenetic DREADD (designer receptor exclusively activated by designer drug) approach. pAAV carrying the hSyn-hM3D(Gq)-mCherry construct was injected into the cerebral cortex of P2Y12 receptor^{+/+} and P2Y12 receptor^{-/-} mice that had been crossed with CX3CR1^{+/GFP} mice to visualize microglial responses in the presence or absence of P2Y12 receptor signaling (fig. S5, F and G). After intraperitoneal injection of clozapine-*N*-oxide (CNO) to induce hM3D(Gq)-DREADD activation, we observed a 234% increase in neuronal cFos signal compared with vehicle treatment (fig. S5H; $p < 0.001$; $n = 100$), confirming a specific and robust neuronal activation.

Chemogenetic neuronal activation resulted in an increased microglial process coverage of the soma of DREADD- and cFos-coexpressing neurons in P2Y12 receptor^{+/+} mice (Fig. 4D; 243% of control, $p = 0.0139$; $n = 101$ neurons from 8 mice), but not in P2Y12 receptor^{-/-} mice (Fig. 4E; 133% of control, $p = 0.7497$; $n =$

85 neurons from 6 mice). We also tested the effect of acute central pharmacological blockade of microglial P2Y12 receptors (Fig. 4F) and found that PSB injected intra-cisterna magna completely abolished the neuronal activity-induced increase in microglial process coverage (Fig. 4G; 72.34% lower process coverage in CNO+PSB than in CNO+vehicle, $p < 0.001$; $n = 124$ neurons from 6 mice). Thus, microglia dynamically react to changes in neuronal activity at somatic microglia–neuron junctions in a P2Y12 receptor-dependent manner, leading to a rapid increase of somatic coverage by microglial processes.

Microglia protect neurons after acute brain injury in a P2Y12 receptor-dependent manner through altered somatic junctions

Because somatic microglia–neuron junctions were abundant in the healthy brain, we next investigated whether these morphofunctional communication sites were altered in response to brain injury. Microglia are known to respond rapidly to changes in neuronal activity in the boundary zone of the infarct after stroke (37). Thus, we performed experimental stroke and delineated the evolving penumbra on the basis of the metabolic activity of the tissue as assessed by the redox indicator tetrazolium chloride coregistered with the immunofluorescent signal for MAP2 and microglia

Fig. 4. Physiological microglia–neuron communication at the somatic junction site is P2Y12 receptor dependent. (A) Outline of acute P2Y12 receptor–blockade experiments. i.c.m., intra-cisterna magna. (B) CLSM images showing examples of the recorded microglia–neuron contacts. Empty arrowheads point to dendritic contacts and full arrowheads mark somatic junctions. (C) Acute intra-cisterna magna administration of PSB significantly reduced somatic junction lifetime, but did not affect the lifetime of dendritic microglia–neuron contacts. n.s., not significant. (D) Neuronal activity induced a robust elevation of microglial process coverage of neuronal cell bodies in CNO-treated animals but not in DREADD⁺/cFos⁻ cells. (E) CNO-triggered neuronal activity could not induce an elevation of microglial process coverage of neuronal cell bodies in P2Y12 receptor^{-/-} mice. (F) Outline of combined chemogenetic and acute P2Y12 receptor–blockade experiments. (G) Acute inhibition of microglial P2Y12 receptors prevented neuronal activity–induced increase of microglial process coverage. For statistical data, see the supplementary text for Fig. 4.

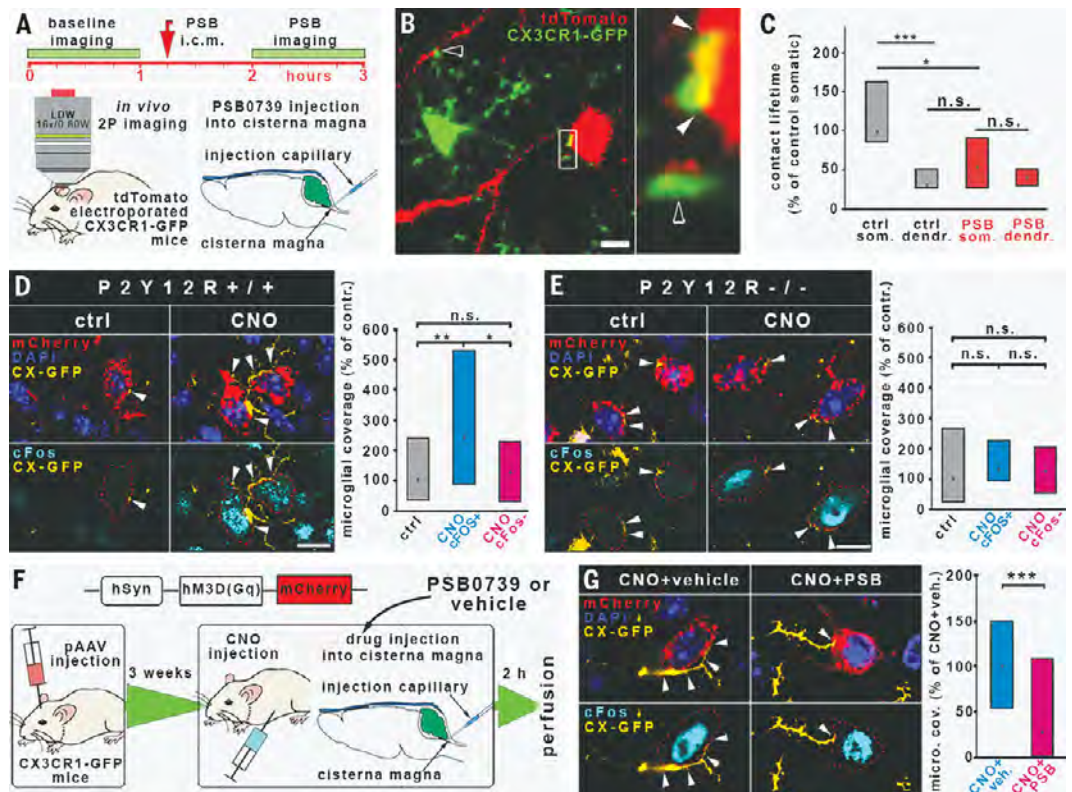


(fig. S6A). We observed the fragmentation of mitochondria (Fig. 5A, 74% decrease of individual mitochondrial area, 46% decrease of mitochondrial major axis; $p < 0.001$ for both; $n = 189$ mitochondria) and an almost complete declustering of Kv2.1 proteins in morphologically intact penumbral neurons (Fig. 5B and fig. S6E, from 4 to 0 median clusters/cross-section and from 0.0947 to 0 clusters/ μm in control and stroke, respectively, $p < 0.001$; $n = 58$ cells). These morphological changes were accompanied by a robust increase in the microglial process coverage of neuronal cell bodies originating from somatic microglia-neuron junctions in both mice and human postmortem brain tissues (Fig. 5, B to E; mouse: 3.8-fold increase, $p < 0.001$; $n = 30$ neurons; human: 1.5-fold increase, $p = 0.007$; $n = 249$ neurons). Acute intra-cisterna magna administration of the P2Y₁₂ receptor inhibitor PSB or preventing mitochondrial injury by using the mitochondrial ATP-sensitive potassium (KATP) channel opener diazoxide (38) completely abolished stroke-induced increases in microglial process coverage around somatic junctions (Fig. 5D, control versus stroke: $p < 0.001$, PSB control versus PSB stroke: $p =$

0.792, diazoxide control versus diazoxide stroke: $p = 0.053$; $n = 140$ neurons). The viability of the examined neurons with increased microglial process coverage was confirmed by normal chromatin structure and membrane integrity (fig. S6, B and C). Transmission electron tomography also confirmed increased microglial process coverage and mitochondrial fragmentation of neurons (Fig. 5C).

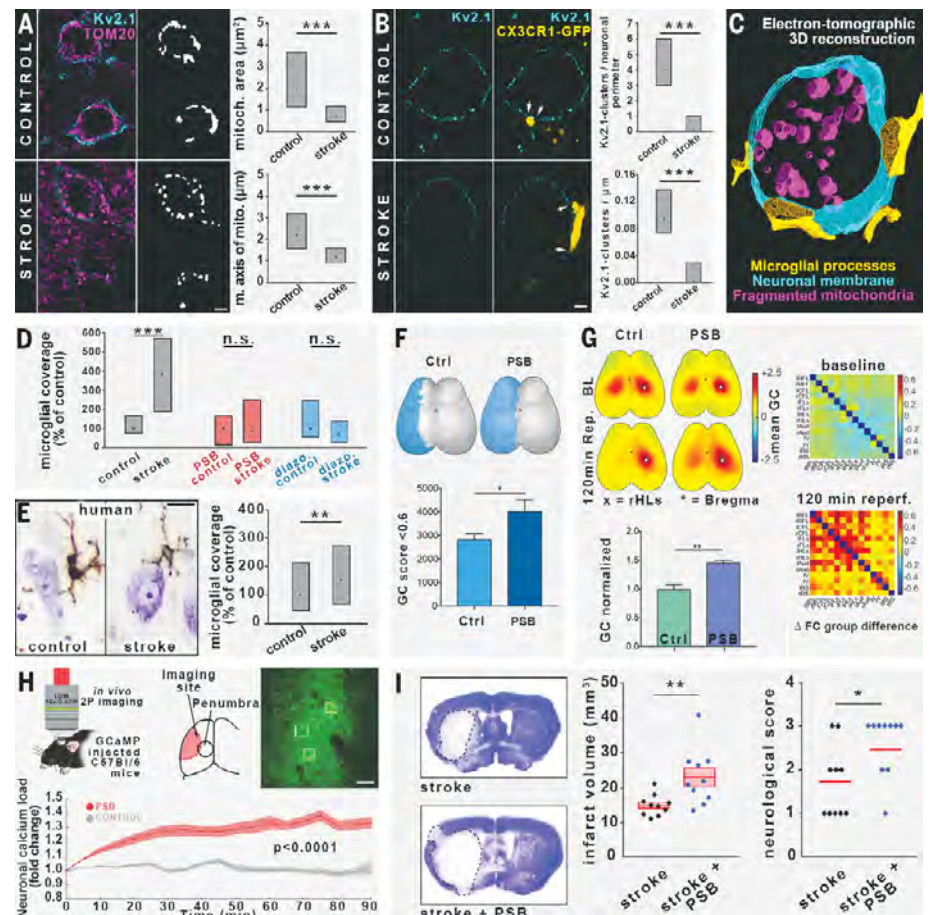
To test the impact of P2Y₁₂ receptor-dependent microglial functions on neuronal viability in vivo, we investigated pharmacological inhibition of P2Y₁₂ receptor by injection of PSB intra-cisterna magna before middle cerebral artery occlusion (MCAo). Inhibition of microglial P2Y₁₂ receptor prevented increases in microglial process coverage of neuronal cell bodies in the penumbra and altered functional connectivity in the brain as assessed by a widefield-imaging approach in Thy1-GCaMP6s mice (Fig. 5, F and G). An absence of P2Y₁₂ receptor signaling significantly increased the area of functional disconnection (global connectivity < 0.6) in the ipsilateral hemisphere during ischemia, accompanied by a trend toward elevated neuronal calcium load (Fig. 5F and fig. S6F; $p = 0.0439$; $n = 17$ mice). Seed-based

connectivity analysis revealed a significant increase in the contralateral sensory hindlimb area after reperfusion in PSB-treated animals. Moreover, connectivity analysis of 14 functional areas revealed a substantial and widespread increase in connectivity strength in the absence of microglial P2Y₁₂ receptor signaling (Fig. 5G; $p = 0.0077$; $n = 7$ mice).

To examine the effect of P2Y₁₂ receptor inhibition at the single-neuron level in the evolving ischemic penumbra in vivo, we investigated GCaMP6f-injected mice with 2P microscopy. In control mice, neuronal GCaMP6f signal remained unchanged for the first 90 min of reperfusion, whereas blockade of microglial P2Y₁₂ receptors with PSB resulted in a strong elevation in neuronal calcium load (Fig. 5H; $p < 0.0001$; $n = 96$ neurons from 3 mice). This corroborated the findings obtained from the widefield-imaging approach at the cellular level as well. Furthermore, P2Y₁₂ receptor inhibition significantly increased lesion volume at 24 hours reperfusion (Fig. 5I; 54% increase, $p = 0.008$; $n = 20$ mice) and resulted in worse neurological outcome (Fig. 5I; Bederson score, stroke: 1.7 ± 0.26 ; stroke+PSB: 2.5 ± 0.224 , $p = 0.033$; $n = 20$ mice).

Fig. 5. Microglia protect neurons after acute brain injury in a P2Y₁₂ receptor-dependent manner through altered somatic junctions.

(A) CLSM images showing that stroke induces the fragmentation of mitochondria (magenta) in neuronal cell bodies (Kv2.1 labeling, cyan) in the penumbra. Mitochondrial area and mitochondrial major axis are both significantly decreased. (B) CLSM images of cortical neurons showing that, in parallel with the declustering of Kv2.1-channels (cyan), microglial coverage (yellow) is significantly increased after stroke in the penumbra. (C) 3D reconstruction from electron tomographic volume showing elevated microglial coverage and fragmentation of neuronal mitochondria. (D) Microglial coverage of neuronal cell bodies is robustly increased after stroke, whereas acute central blockade of P2Y₁₂ receptors or activation of KATP channels completely abolishes the stroke-induced increase of coverage. (E) Stroke induces a 1.5-fold increase in somatic microglia coverage of human cortical neurons. (F) Topographical maps showing the area of pixels with a global connectivity (GC) score < 0.6 after ischemia. The sum of outlined pixels revealed higher dropdown of GC in PSB-treated animals after stroke. (G) Left panel: Topographical maps showing increased region of interest to GC of the contralateral HLs in PSB-treated mice 120 min after stroke. Right panel: Seed-to-seed connectivity is increased in PSB-treated animals after stroke. (H) In vivo 2P calcium imaging revealing a significant increase of neuronal calcium load during reperfusion after acute P2Y₁₂ receptor inhibition with PSB. (I) Infarct volume is increased after acute central P2Y₁₂ receptor inhibition, which is accompanied by a significantly worse neurological outcome. For statistical data, see the supplementary text for Fig. 5.



To investigate the duration of the PSB effect *in vivo*, 2-hour-long imaging sessions were performed with 2P microscopy 1 to 3 hours and 24 to 26 hours after intra-cisterna magna PSB injection ($n = 173$ contacts analyzed from 3 mice). The lifetime of somatic junctions was significantly reduced by up to 3 hours after PSB administration (56.3% of lifetime under baseline conditions, $p = 0.0139$), whereas there was no effect observed 1 day later (93.8% of lifetime under baseline conditions), suggesting an acute effect of intra-cisterna magna PSB (fig. S6, H and I). The acute effect of PSB was also confirmed by the histological measurements performed 4 hours after MCAo (Fig. 5D). To verify that PSB injected intra-cisterna magna only inhibited microglial P2Y₁₂ receptors, and not those expressed by circulating platelets, we measured ADP-induced platelet activation in plasma samples 1 hour after MCAo, when blood-brain barrier injury is apparent (37, 39, 40). ADP-induced increases in platelet CD62P were not altered in mice treated with intra-cisterna magna PSB compared with vehicle-treated animals (fig. S5J).

Disintegration of somatic microglia-neuron junctions after neuronal injury triggers increased microglial process coverage of the cell bodies of compromised but potentially viable neurons through P2Y₁₂ receptor and mitochondrial signaling. This could allow the initiation of protective microglial responses that limit brain injury.

Discussion

Here, we describe a form of interaction between microglia and neurons. Under physiological conditions, somatic microglia-neuron junctions were present on most of the neurons in both mice and humans. The junctions appeared to function as communication sites that are rapidly altered in response to brain injury. We propose that microglia constantly monitor neuronal status through these somatic junctions, allowing neuroprotective actions to take place in a targeted manner.

Sites of somatic junctions in neurons were preferentially and repeatedly contacted by microglia. Such interactions had much longer lifetimes compared with the microglial contacts targeting dendrites. In previous studies, the proximity between microglial cell bodies or processes with neuronal somata has been observed in zebrafish and mice (41, 42). However, the formation of direct membrane-to-membrane junctions, the molecular identity of neuronal membranes contacted, activity-dependent recruitment of microglial processes to neuronal cell bodies, the mechanisms of junction formation, and the function of somatic microglia-neuron interactions have not been addressed. Therefore, we took advantage of cutting-edge neuroanatomical approaches and discovered that somatic microglia-neuron junc-

dc_2027_22

tions are characterized by specific ultrastructural and molecular composition. These morphological and molecular features are absent in perisomatic boutons contacted by microglia, suggesting that the main form of neuronal quality control by microglial processes is not mediated by interactions between microglia and perisomatic axon terminals.

Mitochondria are the primary energy generators in cells, playing fundamental roles in calcium homeostasis, intracellular signaling (43, 44), and neuronal quality control (45), as well as in determining cellular fate (46). Although neuronal mitochondria are also considered “immunometabolic hubs” involved in antigen presentation and the regulation of innate immune responses (47, 48), changes in mitochondrial function caused by metabolic imbalance, oxidative stress, inflammation, cellular injury, or cell death occur in most neuropathological states (49). MAMs are also considered to be key integrators of metabolic and immunological signals, playing a central role in neurodegeneration and cell-fate decisions (30, 50, 51). Thus, somatic mitochondria and MAMs are ideally positioned to report neuronal status to microglia and to mediate neuronal quality control. Consistent with this, we show that the recruitment of microglial processes to somatic junctions in the vicinity of neuronal mitochondria is linked with mitochondrial activity. This may indicate rapid sensing of mitochondrial activity-associated changes of neurons by microglial processes through the release of ATP and other mediators or the impact of microglia-derived substances on neuronal activity and/or mitochondrial function at somatic junctions. Neurons can execute somatic ATP release through pannexin hemichannels, voltage-dependent anion channels, or activity-dependent vesicle exocytosis (21, 22, 36). vNUT is known to be responsible for somatic vesicular ATP release in neurons (34). In fact, we demonstrated the enrichment of vNUT between neuronal mitochondria and the somatic membranes contacted by microglia and, using time-lapse imaging and HPLC measurements, we confirmed the presence of activity-dependent somatic ATP release from neurons that was blocked by vNUT inhibition. TOM20-positive mitochondria-derived vesicles and other vesicles were also observed within the neuronal cytoplasm at somatic microglia-neuron junctions, together with the enrichment of LAMP1-positive lysosomes, which could, together with the released ATP, provide a constant readout of neuronal activity and mitochondrial function as seen in neurons and other cells (31, 52). The strong enrichment of vNUT in these contacts, the existence of an activity- and vNUT-dependent somatic ATP release, the presence of filamentous cytoplasmic structures connecting vesicles to the core of the junction, the presence of TOM20

immunogold-positive vesicles within the contacts attached to the neuronal PM, the close association of neuronal lysosomes, and the massive accumulation and nanoscale clustering of exocytosis-promoting Kv2.1 proteins within these contact sites collectively indicate the convergence of multiple parallel vesicular exocytotic pathways at somatic microglia-neuron junctions.

Kv2.1 channels are major regulators of neuronal potassium levels. However, they tend to assemble into discrete clusters on the surface of neurons, where they do not function as ion channels, but rather provide sites for intensive membrane trafficking as exocytotic and endocytotic hubs (17, 18, 53). Furthermore, Kv2.1 clusters are known to induce stable ER-PM junctions (53), anchoring MAMs and mitochondria into these morphofunctional units and providing an ideal site for the release of mitochondria-associated messenger molecules (31). The functional importance of these interactions is confirmed by our results showing that Kv2.1 clusters on transfected HEK cells readily induced the formation of microglial process contacts to these clusters, which could not be observed on HEK cells transfected with the dominant-negative mutant Kv2.1. Furthermore, microglial P2Y₁₂ receptor clusters were precisely aligned with neuronal Kv2.1 clusters at somatic junctions.

The activation of P2Y₁₂ receptors was mainly associated with injury or pathological states in previous studies and was considered negligible for physiological microglial surveillance on the basis of *ex vivo* studies (54). Compared with normal extracellular ATP levels in the brain, high levels of ATP (1 mM) were shown to induce P2Y₁₂ receptor-dependent microglial recruitment, similar to that seen during microglial phagocytosis or in models of synaptic plasticity, whereas microglial surveillance is considered to be P2Y₁₂ receptor independent (54, 55). Our *in vivo* results refine this view and highlight the importance of the compartment-dependent effects of P2Y₁₂ receptor on microglial process responses: PSB0739 significantly reduced somatic junction lifetime but did not affect the lifetime of dendritic microglia-neuron contacts, whereas it abolished microglial reactions to altered neuronal activity, confirming P2Y₁₂ receptor dependence of microglial actions under physiological conditions. Furthermore, neuronal mitochondrial activity was also linked with physiological microglial P2Y₁₂ receptor activity at these junctions. It is also possible that P2Y₁₂ receptor-mediated actions are more important for sustaining than for forming somatic junctions during the communication between neuronal somata and microglial processes. The contact-dependent clustering of P2Y₁₂ receptors further confirms their involvement in physiological microglia-neuron interactions at somatic

junctions. Blockade of microglial P2Y12 receptor left cortical synapse numbers completely unchanged and contact-dependent nanoclustering of microglial P2Y12 receptors was not seen when microglia contacted synaptic boutons. Thus, microglia–neuron interactions at these sites are not only P2Y12 receptor dependent, they are also fundamentally different from those seen at synapses.

The failure of most neuroprotection trials in stroke and other brain diseases strongly indicates the importance of understanding the complexity of pathophysiological processes, including microglial actions. Potentially salvageable neurons around the infarct core may show metabolic activity up to 6 to 17 hours after stroke in patients and experimental animals (56, 57). Here, Kv2.1 declustering was observed in compromised neurons of the penumbra as early as 4 hours after brain injury, which paralleled mitochondrial fragmentation in neurons and increased microglial process coverage around somatic microglia–neuron junctions. Thus, P2Y12 receptor-dependent microglial actions protect neurons, whereas blockade of microglial P2Y12 receptor signaling alone impaired cortical network function and increased calcium load and the area of ischemia-induced disconnection within 2 hours after stroke (a clinically relevant time window). This increase in brain injury was similar to that seen after the complete and selective elimination of microglia (37). These protective microglia- and P2Y12 receptor-mediated effects were linked with mitochondrial actions initiated upon neuronal injury because the diazoxide (a KATP channel opener)-abolished increases in microglial process coverage of neurons after stroke were similar to those seen after blockade of P2Y12 receptor signaling.

All of these results unequivocally indicate that microglia continuously monitor neuronal status through somatic junctions, rapidly responding to neuronal changes and initiating neuroprotective actions.

We propose that healthy neurons may constitutively release ATP and other signaling molecules at these junctions, communicating their “well-being” to microglia. In turn, disintegration of these specialized morphofunctional hubs caused by excitotoxicity, energy depletion, or other noxious stimuli may trigger rapid and inherently protective microglial responses, leading to the restoration of neuronal function or the isolation and phagocytosis of dying neurons in case terminal neuronal injury occurs (55). Along with P2Y12 receptor-mediated microglial process recruitment, it is likely that a broad range of signals is integrated at somatic microglial junctions and, through these, microglia may sense products of neuronal exocytosis and changes in the cell membrane (e.g. apoptotic signals) and alter the duration of physical contact or initiate phagocytosis. The most im-

portant open research areas include the clarification of additional signaling mechanisms (vesicular and nonvesicular) involved in neuron-to-microglia communication at these junctions and the mechanisms of microglial neuroprotection (e.g. regulation of neuronal ion fluxes, neuronal calcium dynamics, or the metabolism of neuronal mitochondria). Because the role of microglia–neuron somatic junctions in most brain diseases is completely unknown, microglia–neuron interactions through these sites may differ in different forms of acute and chronic neuropathologies.

REFERENCES AND NOTES

- M. S. Thion, F. Ginhoux, S. Garel, *Science* **362**, 185–189 (2018).
- K. Kierdorf, M. Prinz, *J. Clin. Invest.* **127**, 3201–3209 (2017).
- M. W. Salter, B. Stevens, *Nat. Med.* **23**, 1018–1027 (2017).
- W. M. Song, M. Colonna, *Nat. Immunol.* **19**, 1048–1058 (2018).
- D. Davalos et al., *Nat. Neurosci.* **8**, 752–758 (2005).
- A. Nimmerjahn, F. Kirchhoff, F. Helmchen, *Science* **308**, 1314–1318 (2005).
- Y. Wu, L. Dissing-Olesen, B. A. MacVicar, B. Stevens, *Trends Immunol.* **36**, 605–613 (2015).
- L. Weinhard et al., *Nat. Commun.* **9**, 1228 (2018).
- J.-M. Cioni, M. Koppers, C. E. Holt, *Curr. Opin. Neurobiol.* **51**, 86–94 (2018).
- T. Misgeld, T. L. Schwarz, *Neuron* **96**, 651–666 (2017).
- M. Terenzi, G. Schiavo, M. Fainzilber, *Neuron* **96**, 667–679 (2017).
- J. Aarum, K. Sandberg, S. L. B. Haeblerlein, M. A. A. Persson, *Proc. Natl. Acad. Sci. U.S.A.* **100**, 15983–15988 (2003).
- M. Ueno et al., *Nat. Neurosci.* **16**, 543–551 (2013).
- J. L. Marin-Teva, M. A. Cuadros, D. Martín-Oliva, J. Navascués, *Neuron Glia Biol.* **7**, 25–40 (2011).
- A. Sierra et al., *Neural Plast.* **2014**, 610343 (2014).
- H. Wake, A. J. Moorhouse, S. Jinno, S. Kohsaka, J. Nabekura, *J. Neurosci.* **29**, 3974–3980 (2009).
- E. Deutsch et al., *Mol. Biol. Cell* **23**, 2917–2929 (2012).
- L. Feinschreiber, D. Singer-Lahat, U. Ashery, I. Lotan, *Ann. N. Y. Acad. Sci.* **1152**, 87–92 (2009).
- M. Kirmiz, N. C. Vierra, S. Palacio, J. S. Trimmer, *J. Neurosci.* **38**, 7562–7584 (2018).
- B. Jiang, X. Sun, K. Cao, R. Wang, *Mol. Cell. Biochem.* **238**, 69–79 (2002).
- A. Menéndez-Méndez et al., *Front. Pharmacol.* **8**, 951 (2017).
- R. D. Fields, *Semin. Cell Dev. Biol.* **22**, 214–219 (2011).
- S. E. Haynes et al., *Nat. Neurosci.* **9**, 1512–1519 (2006).
- Y. Zhang et al., *J. Neurosci.* **34**, 11929–11947 (2014).
- O. Butovsky et al., *Nat. Neurosci.* **17**, 131–143 (2014).
- B. Dudok et al., *Nat. Neurosci.* **18**, 75–86 (2015).
- I. D. Campbell, M. J. Humphries, *Cold Spring Harb. Perspect. Biol.* **3**, a004994 (2011).
- H. Akiyama, P. L. McGeer, *J. Neuroimmunol.* **30**, 81–93 (1990).
- F. E. McCann et al., *J. Immunol.* **170**, 2862–2870 (2003).
- G. Csordás, D. Weaver, G. Hajnóczky, *Trends Cell Biol.* **28**, 523–540 (2018).
- A. Sugiyama, G.-L. McLelland, E. A. Fon, H. M. McBride, *EMBO J.* **33**, 2142–2156 (2014).
- V. Soubannier et al., *Curr. Biol.* **22**, 135–141 (2012).
- T. Ho et al., *Front. Cell. Neurosci.* **9**, 389 (2015).
- Y. Moriyama, M. Hiasa, S. Sakamoto, H. Omote, M. Nomura, *Purinergic Signal.* **13**, 387–404 (2017).
- A. M. Brennan, J. A. Connor, C. W. Shuttleworth, *J. Cereb. Blood Flow Metab.* **26**, 1389–1406 (2006).
- X. Zhang, Y. Chen, C. Wang, L.-Y. M. Huang, *Proc. Natl. Acad. Sci. U.S.A.* **104**, 9864–9869 (2007).
- G. Szalay et al., *Nat. Commun.* **7**, 11499 (2016).
- J. O. Onukwufo, D. Stevens, C. Kamunde, *J. Exp. Biol.* **219**, 2743–2751 (2016).
- F. Orsini et al., *Arterioscler. Thromb. Vasc. Biol.* **38**, 2678–2690 (2018).
- K. Bekó et al., *J. Thromb. Haemost.* **15**, 1223–1235 (2017).

- Y. Li, X.-F. Du, C.-S. Liu, Z.-L. Wen, J.-L. Du, *Dev. Cell* **23**, 1189–1202 (2012).
- R. D. Stowell et al., *Dev. Neurobiol.* **78**, 627–644 (2018).
- C. N. Hall, M. C. Klein-Flügge, C. Howarth, D. Attwell, *J. Neurosci.* **32**, 8940–8951 (2012).
- N. S. Chandel, *BMC Biol.* **12**, 34 (2014).
- E. I. Rugarli, T. Langer, *EMBO J.* **31**, 1336–1349 (2012).
- A. Kasahara, L. Scorrano, *Trends Cell Biol.* **24**, 761–770 (2014).
- D. Arnoult, F. Soares, I. Tattoli, S. E. Girardin, *EMBO Rep.* **12**, 901–910 (2011).
- G. R. Bantug et al., *Immunity* **48**, 542–555.e6 (2018).
- A. U. Joshi, D. Mochly-Rosen, *Pharmacol. Res.* **138**, 2–15 (2018).
- J. Rieusset, *Biochem. Biophys. Res. Commun.* **500**, 35–44 (2018).
- R. Bravo-Sagua et al., *Curr. Mol. Med.* **13**, 317–329 (2013).
- G.-L. McLelland, S. A. Lee, H. M. McBride, E. A. Fon, *J. Cell Biol.* **214**, 275–291 (2016).
- P. D. Fox et al., *J. Cell Sci.* **128**, 2096–2105 (2015).
- C. Madry et al., *Neuron* **97**, 299–312.e6 (2018).
- R. Fekete et al., *Acta Neuropathol.* **136**, 461–482 (2018).
- G. Marchal et al., *Stroke* **27**, 599–606 (1996).
- J. C. Baron, M. E. Moseley, *J. Stroke Cerebrovasc. Dis.* **9**, 15–20 (2000).

ACKNOWLEDGMENTS

We thank L. Barna and the Nikon Imaging Center at the Institute of Experimental Medicine (IEM) for kindly providing microscopy support, D. Mastronarde at MCDB for his continuous help with IMOD software, and S. Kovács from ETH Zurich for scripting analytic tools. We are also grateful to N. Hájós (IEM), Z. Nusser (IEM), and J. Trimmer (University of California, Davis) for their support and useful comments. We thank the Department of Pathology, St. Borbála Hospital, Tatabánya, and the Human Brain Research Lab at the IEM for providing human brain tissue and D. Gali-Györkei and R. Rácz for excellent technical assistance. We also thank Plexikon for providing PLX5622 and Deltagen for the donation of P2Y12 receptor^{-/-} mice. **Funding:** This work was supported by a Momentum Research Grant from the Hungarian Academy of Sciences (LP2016-4/2016 to A.D.) and ERC-CoG 724994 (A.D.), a János Bolyai Research Scholarship of the Hungarian Academy of Sciences (C.C., and N.L.), and grants UNKP-19-3-I (B.P.) and UNKP-19-4 (C.C.) from the New National Excellence Program of the Ministry for Innovation and Technology. Additionally, this work was funded by H2020-ITN-2018-813294-ENTRAIN (A.D.), the Hungarian Academy of Sciences (G.T.), the National Research, Development and Innovation Office of Hungary (GINOP-2.3.2-15-2016-00018, VKSZ-14-1-2015-0155, G.T.), the Ministry of Human Capacities, Hungary (20391-3/2018/FEKUSTRAT, G.T.), the German Research Foundation (FOR 2879), and ERC-StG 802305 to A.L. I.K. was supported by a Momentum Research Grant from the Hungarian Academy of Sciences (LP2013-54), the Hungarian Scientific Research Fund (OTKA, K 116915), and the National Research, Development and Innovation Office of Hungary (VKSZ-14-1-2015-0155). M.M.T. was supported by National Institutes of Health grant R01GM109888. B.S. and Z.M. were supported by the National Research, Development and Innovation Office of Hungary (K116654 to B.S. and K125436 to Z.M.) and by the National Brain Research Program (2017-1.2.1-NKP-2017-00002). T.H. was supported by the Hungarian Brain Research Program (1.2.1-NKP-2017-00002). G.M. was supported by Hungarian Scientific Research Fund (OTKA, K128863). L.C. was supported by the National Research, Development and Innovation Fund (GINOP-2.3.2-15-2016-00048-Stay Alive). R.S. was supported by Hungarian Scientific Research Fund (OTKA, K 129047). This work was also supported by EFOP-3.6.3-VEKOP-16-2017-00009 from Semmelweis University. **Author contributions:** The project was conceived by C.C., B.P., and A.D. Surgery was performed by N.L. and A.D. Two-photon imaging was performed by R.F. Immunohistochemistry and light microscopy were performed by C.C., B.P., A.D., B.O., A.D.S., and E.S. STORM microscopy was performed by B.O. Electron microscopy was performed by C.C., B.P., E.S., and A.D.S. Electron tomography was performed by C.C. and B.P. In vitro NADH imaging was performed by G.M. under the supervision of G.T. Plasmid engineering and in utero electroporation were performed by Z. L. and Z. I. L. In vitro cell culture transfection and experiments were performed by Z.K., K.T., and Z.I.L. Virus injection was performed by R.F. and B.M. Widefield calcium imaging was performed by S.H. under the supervision of A.L. HPLC measurements were performed by M.B. under the supervision of B.S. Data were analyzed by C.C., B.P., B.O., G.M., S.H., N.L., A.D.S., K.U., A.L., and A.D. Critically important clinical and neuropathological data and materials were contributed by L.C.,

T.H., Z.M. G.S., M.M.T., and F.E. The laser-optical setup for dual wavelength in vitro 2P measurements was optimized by R.S. Resources were provided and essential intellectual contributions were made by I.K., G.T., and A.L., who also revised the manuscript. Funding was obtained and the project supervised by A.D. The paper was written by C.C., B.P., and A.D. with input from all authors. **Competing interests:** The authors declare no competing interests. **Data and materials availability:** PLX5622

dc_2027_22

was obtained under a material transfer agreement with Plexikon (Berkeley, CA). All data are available in the main text or the supplementary materials.

SUPPLEMENTARY MATERIALS

science.sciencemag.org/content/367/6477/528/suppl/DC1
Materials and Methods
Figs. S1 to S6

Tables S1 to S3
Movies S1 to S7
References (58–67)

12 April 2019; resubmitted 14 October 2019
Accepted 3 December 2019
Published online 12 December 2019
10.1126/science.aax6752

Science

Microglia monitor and protect neuronal function through specialized somatic purinergic junctions

Csaba Cserép, Balázs Pósai, Nikolett Lénárt, Rebeka Fekete, Zsófia I. László, Zsolt Lele, Barbara Orsolits, Gábor Molnár, Steffanie Heindl, Anett D. Schwarcz, Katinka Ujvári, Zsuzsanna Környei, Krisztina Tóth, Eszter Szabadits, Beáta Sperlág, Mária Baranyi, László Csiba, Tibor Hortobágyi, Zsófia Maglóczky, Bernadett Martinecz, Gábor Szabó, Ferenc Erdélyi, Róbert Szipocs, Michael M. Tamkun, Benno Gesierich, Marco Duering, István Katona, Arthur Liesz, Gábor Tamás and Ádám Dénes

Science **367** (6477), 528-537.

DOI: 10.1126/science.aax6752 originally published online December 12, 2019

Microglia take control

Changes in the activity of microglia, the primary immune cells of the central nervous system, are linked with major human diseases, including stroke, epilepsy, psychiatric disorders, and neurodegeneration. Cserép *et al.* identified a specialized morphofunctional communication site between microglial processes and neuronal cell bodies in the mouse and the human brain (see the Perspective by Nimmerjahn). These junctions are formed at specific areas of the neuronal somatic membranes and possess a distinctive nanoarchitecture and specialized molecular composition linked to mitochondrial signaling. The junctions appear to provide a major site for microglia-neuron communication and may help to mediate the neuroprotective effects of microglia after acute brain injury.

Science, this issue p. 528; see also p. 510

ARTICLE TOOLS

<http://science.sciencemag.org/content/367/6477/528>

SUPPLEMENTARY MATERIALS

<http://science.sciencemag.org/content/suppl/2019/12/11/science.aax6752.DC1>

RELATED CONTENT

<http://science.sciencemag.org/content/sci/367/6477/510.full>

REFERENCES

This article cites 66 articles, 20 of which you can access for free
<http://science.sciencemag.org/content/367/6477/528#BIBL>

PERMISSIONS

<http://www.sciencemag.org/help/reprints-and-permissions>

Use of this article is subject to the [Terms of Service](#)

Science (print ISSN 0036-8075; online ISSN 1095-9203) is published by the American Association for the Advancement of Science, 1200 New York Avenue NW, Washington, DC 20005. The title *Science* is a registered trademark of AAAS.

Copyright © 2020 The Authors, some rights reserved; exclusive licensee American Association for the Advancement of Science. No claim to original U.S. Government Works



Supplementary Materials for

Microglia monitor and protect neuronal function via specialized somatic purinergic junctions

Csaba Cserép*, Balázs Pósfai*, Nikolett Lénárt, Rebeka Fekete, Zsófia I. László, Zsolt Lele, Barbara Orsolits, Gábor Molnár, Steffanie Heindl, Anett D. Schwarcz, Katinka Ujvári, Zsuzsanna Környei, Krisztina Tóth, Eszter Szabadits, Beáta Sperlág, Mária Baranyi, László Csiba, Tibor Hortobágyi, Zsófia Maglóczky, Bernadett Martinecz, Gábor Szabó, Ferenc Erdélyi, Róbert Szipócs, Michael M. Tamkun, Benno Gesierich, Marco Duering, István Katona, Arthur Liesz, Gábor Tamás, Ádám Dénes†

*These authors contributed equally to this work.

†Corresponding author. Email: denes.adam@koki.mta.hu

Published 12 December 2019 on *Science* First Release

DOI: [10.1126/science.aax6752](https://doi.org/10.1126/science.aax6752)

This PDF file includes:

Materials and Methods
Supplementary Text for Main Figs. 1 to 5
Figs. S1 to S6
Tables S1 to S3
Captions for Movies S1 to S7
References

Other Supplementary Material for this manuscript includes the following:

(available at science.sciencemag.org/cgi/content/full/science.aax6752/DC1)

Movies S1 to S7

Materials and Methods

Ethical considerations

All experiments were performed in accordance with the Institutional Ethical Codex and the Hungarian Act of Animal Care and Experimentation guidelines (40/2013, II.14), which are in concert with the European Communities Council Directive of September 22, 2010 (2010/63/EU). The Animal Care and Experimentation Committee of the Institute of Experimental Medicine and the Animal Health and Food Control Station, Budapest, have also approved the experiments under the number PE/EA/1021-7/2019, PE/EA/673-7/2019. Control human brain tissue was obtained from two female (59- and 60-years-old) and one male (73-years-old) subjects who died from causes not linked to brain diseases, and did not have a history of neurological disorders (ethical approval ETT TUKEB 31443/2011/EKU [518/PI11]). Tissues from patients who died after ischemic stroke affecting the MCA area were obtained from two female (77- and 78-years-old) and one male (66-years-old) subjects (ethical approval ETT-TUKEB 62031/2015/EKU, 34/2016 and 31443/2011/EKU (518/PI11)) See Supplementary Table 2. Informed consent was obtained for the use of brain tissue and for access to medical records for research purposes. Tissue was obtained and used in a manner compliant with the Declaration of Helsinki.

Post-mortem human brain tissues

Brains of patients who died in non-neurological diseases were removed 3-5 h after death. The internal carotid and the vertebral arteries were cannulated, and the brains were perfused first with physiological saline (using a volume of 1.5 l in 30 min) containing heparin (5 ml), followed by a fixative solution containing 4% paraformaldehyde, 0.05% glutaraldehyde and 0.2% picric acid (vol/vol) in 0.1 M PB, pH 7.4 (4–5 l in 1.5–2 h). The cortical and hippocampal samples were removed from the brains after perfusion, and were postfixed overnight in the same fixative solution, except for glutaraldehyde, which was excluded. Blocks were dissected, and 50 µm thick sections were prepared on a vibratome (VT1200S, Leica, Germany). Brains of stroke patients were removed after 10-15 h after death and immersion fixed in 4% paraformaldehyde. Small regions from the affected cerebral cortex were dissected, embedded into paraffin both from the ipsilateral and contralateral hemisphere and 6-8 µm thick sections were cut on a sledge microtome.

Animals

Experiments were carried out on 12-18 weeks old C57BL/6 (RRID:IMSR_JAX:000664), CAMK2 GFP, PVA GFP, GAD65 GFP, CX3CR1^{+/GFP} (IMSR_JAX:005582), CX3CR1^{+/GFP}/P2Y12^{-/-} and C57BL/6J-Tg(Thy1-GCaMP6s)GP4.12Dkim/J mice (23, 58–61). Mice were bred and genotyped at the SPF unit of the Animal Care Unit of the Institute of Experimental Medicine (IEM, Budapest, Hungary) as described earlier (37). Mice had free access to food and water and were housed under light-, humidity- and temperature-controlled conditions. All experimental procedures were in accordance with the guidelines set by the European Communities Council Directive (86/609 EEC) and the Hungarian Act of Animal Care and Experimentation (1998; XXVIII, section 243/1998), approved by the Animal Care and Use Committee of the IEM. All experiments were performed in accordance with ARRIVE guidelines.

In vivo pharmacological treatments and chemogenetics

To study the effect of P2Y₁₂ receptor (P2Y₁₂R) antagonists in healthy mice or after experimental stroke, either a single dose of PSB0739 (Tocris, R&D Systems, Minneapolis, USA, 15 µg dissolved in saline), or vehicle was administered to the cisterna magna in 5 µl final volume using a glass capillary. The diffusion of materials injected i.c.m. was controlled with i.c.m. dye injections (Fig. S5e). For experiments aiming to assess the effect of microglial P2Y₁₂R blockade on infarct size and neurological outcome, PSB0739 was administered at reperfusion after 30 min MCAo. For technical reasons, mice subjected to in vivo widefield calcium imaging and two-photon imaging received i.c.m. PSB0739 60 min prior to MCAo. Brains were harvested 24 hours later for histology. Diazoxide (#D9035, Sigma, Merck KGaA, Darmstadt, Germany) dissolved in 0.4% DMSO and 0.01 M NaOH was administered in a single dose of 10 mg/kg intraperitoneally, immediately before reperfusion of the MCAo took place during the stroke surgeries. Brains were prepared 4 hours later for histological assessment. For selective microglia elimination, C57BL/6J mice were fed a chow diet containing the CSF1 receptor antagonist, PLX5622 (Plexxikon Inc., 1200 mg PLX5622 in 1 kg chow) for 3 weeks to eliminate microglia from the brain (and another group of C57BL/6J mice were fed control chow diet). For the chemogenetic activation of neurons 0.1 µl of AVV8-pAAV-hSyn-HA-hM3D(Gq)-MCherry (RRID: Addgene_50474, Addgene, USA) was injected into the neocortex of CX3CR1^{+GFP} mice. After 3 weeks of incubation, mice received saline or clozapine-N-oxide (0.1 mg/ml) intraperitoneally to induce DREADD activation. Animals were perfused 1 hour after the injections, and processed for histology. For in vivo calcium imaging C57BL/6J mice were used. 200 nl concentrated AAV1.Syn.GCaMP6f.WPRE.SV40 (RRID: Addgene_100837, Penn Vector Core) was injected into the cortex 200-300 µm below the surface with glass capillary. The injection coordinates were 1.5 mm lateral from midline, 1.2 mm posterior from bregma. Cranial window surgery and two-photon (2P) resonant imaging were performed 2 weeks after injection.

Experimental stroke

MCAo was performed using the intraluminal filament technique as described earlier (37). In brief, animals were anaesthetized with isoflurane and a silicone-coated monofilament (210-230 µm tip diameter, Doccol, Sharon, US) was introduced into the left external carotid artery and advanced along the internal carotid artery to occlude the MCA for 30 or 45 min. Occlusion was confirmed by a laser Doppler (Moor Instruments, UK). During surgery, core temperature was maintained at 37±0.5 °C. The following exclusion criteria were set up: animals having less than 70% relative reduction in blood flow, either having haemorrhage or having shorter survival than 24 h were excluded from any further analysis pre hoc. In total 2 animals (one control and one PSB treated) were excluded post hoc due to intracerebral haemorrhage, 1 PSB treated animal died before 24 h. Altogether 3 out of 36 animals were excluded (8.33%) from the analysis, and total mortality was 2.77%.

Functional outcome of mice was assessed 24 h after MCAo using the corner test (62) and the 5-point Bederson's sensory-motor deficit scoring system (63). Briefly, the following scores were given: a 0, no motor deficit; 1, flexion of torso and contralateral forelimb when mouse was lifted by the tail; 2, circling to the contralateral side when mouse is held by the tail on a flat surface, but normal posture at rest; 3, leaning to the contralateral side at rest, 4, no spontaneous motor activity, 5, early death due to stroke.

Infarct size was calculated based on cresyl-violet stained coronal sections as described previously (37). In brief, lesion volume at 24 h reperfusion was calculated by integration of areas

of damage measured at eight neuro-anatomically defined coronal levels (between 2.9 mm rostral and 4.9 mm caudal to bregma) followed by correction for oedema.

To delineate the ischemic penumbra, unfixed 1 mm thick brain slices were incubated in 1% TTC (2,3,5-Triphenyltetrazolium chloride, Sigma) dissolved in PBS at 37 °C for 20 minutes. Slices were then postfixed with 4% PFA in PB for 24 hours at 4 °C, resectioned and processed for immunostaining.

Perfusion and tissue processing for histology

Adult mice were anesthetized by intraperitoneal injection of 0.15-0.25 ml of an anaesthetic mixture (containing 20 mg/ml ketamine, 4 mg/ml xylazine-hydrochloride). Animals were perfused transcardially with 0.9% NaCl solution for 1 minute, followed by 4% freshly depolymerized paraformaldehyde (PFA) in 0.1 M phosphate buffer (PB) pH 7.4 for 40 minutes, and finally with 0.1 M PB for 10 minutes to wash the fixative out. Blocks containing the primary somatosensory cortex and dorsal hippocampi were dissected and coronal sections were prepared on a vibratome (VT1200S, Leica, Germany) at 20 µm thickness for STORM experiments, 50 µm thickness for immunofluorescent experiments and electron microscopy/electron tomography.

Cloning

CAG-IRES-tD_{Tomato} (*pCAG-IRES-tD_{Tomato}*): The GFP-polyA part of the pCAGIG plasmid (a gift from Connie Cepko, Addgene plasmid #11159, RRID:Addgene_11159) was replaced with tD_{Tomato}-pA (a gift from Gyula Balla, IEM, Hungary) using blunt-end cloning (pCAGIG:PstI-BstXI, pcDNA3-tD_{Tomato}: HindIII-PvuII), fragments were blunted via Klenow chewback/fill-in respectively.

CAG-Mito-R-Geco: *CMV-Mito-R-Geco1* (a gift from Robert Campbell; Addgene plasmid #46021, RRID:Addgene_46021) was digested PmeI and the mito-R-Geco fragment then subcloned into EcoRV-digested pBSKII SK+ (Stratagene). Orientation was checked with restriction analysis. Then pBSKII-Mito-R-Geco was cut with Acc65I-NotI and cloned into pCAG-GFP (a gift from Connie Cepko (Addgene plasmid #11150, RRID:Addgene_11150) digested with Acc65I-NotI.

Kv2.1-EGFP: *CMV-hKv2.1-pEGFP-C1* was a gift from Federico Sesti (Addgene plasmid #111538; <http://n2t.net/addgene:111538> ; RRID:Addgene_111538)

Kv2.1-ruby: *CMV-Kv2.1-Ruby2* encoding plasmid was constructed by removing the NheI-GFP-EcoRI fragment in pEGFPC1-rKv2.1 (described earlier (53)) and replacing it with an in frame NheI-Ruby2-EcoRI fragment.

DNKv2.1-YFP (*CMV-DNKv2.1-YFP*): A YFP and myc epitope tagged Kv2.1 dominant negative construct was assembled using standard PCR-based cloning methods to insert the desired nucleotide sequences. Rat Kv2.1 cDNA fragment corresponding to amino acids 1-218 and encoding the N-terminus and first transmembrane domain was amplified and tagged with the myc epitope on the 3' end. This fragment was then inserted into the BamHI-XbaI sites of the pEYFP-C1 polylinker. The resulting construct expresses the Kv2.1 peptide with YFP on the N-terminus and the myc epitope on the C-terminus.

In utero electroporation:

Timed-pregnant C57BL/6J (Jackson) females bred with homozygous CX3CR1^{GFP/GFP} transgenic animals were anesthetized by isoflurane vaporization at embryonic day 14.5. Abdominal cavity was opened longitudinally and uterine horns were exposed. Approximately 1 µl of expression vector (1 µg/µl all of the constructs) in endotoxin-free water containing Fast

Green dye (Roth 1:10000 dilution) was injected into the embryonic lateral ventricles, using glass capillary and mouth pipette. Electroporation was performed with tweezer electrodes, 5x50 V pulses of 50 millisecond duration were applied with 950 millisecond intervals using the In Utero Electroporator SP-3c (Supertech). After the electroporation, uterine horns were returned into the abdominal cavity, the muscle wall and skin were sutured, and embryos were allowed to continue their normal development. All the littermates were CX3CR1^{+GFP} heterozygous and were born naturally.

Mito-R-Geco1 in vitro transfection into HEK-cells

HEK-293 cells were cultured in Dulbecco's Modified Eagle Medium (4.5 g/L glucose, L-glutamine & sodium pyruvate; Corning) with 10% heat-inactivated Fetal Bovine Serum (Biosera) and incubated at 37 °C in 5% CO₂ in air. On the day of transfection, cells were plated on poly-D-lysine (Sigma) coated 18 mm coverslips in 12-well cell culture plates. For transfection 2 µl Lipofectamine® 2000 Reagent (Thermo Fisher Sc.) were mixed with 2 µg Mito-R-Geco1 in Gibco® Opti-MEM™ Media (Thermo Fisher Sc.) and stored in the hood approximately half an hour. Transfection solution was mixed with the culturing media and cells were incubated overnight. Next day, cells were fixed with 4% PFA for 10 minutes, then washed with PBS. Permeabilization and blocking steps were performed by 0.1% TritonX and 5% NDS (Normal Donkey Serum; Sigma)/PBS solution for 30 mins. TOM20 antibody (1:1000) was applied in PBS for 90 mins. After several PBS washes cells were treated with secondary antibodies/PBS solution for an hour. Finally coverslips were washed in PBS and mounted with VECTASHIELD® HardSet™ mounting medium and sealed with nail polish. Confocal images were taken with 60X objective by Nikon AIR confocal system guide by NIS-Elements Microscope Imaging Software.

Isolation of microglial cells

Primary microglial cells were isolated from astroglia/microglia mixed cell cultures, as described earlier (55). In brief, meninges were removed and tissue pieces were subjected to enzymatic dissociation, using 0.05% w/v trypsin and 0.05% w/v DNase for 10 minutes at room temperature. The cells were plated onto poly-L-lysine coated plastic dishes and were grown in Minimal Essential Medium (MEM, ThermoFisher Sc. 21090-055) supplemented with 10% fetal bovine serum (FBS, Thermofisher 16000044), glutamine (4 mM; Sigma-Aldrich G3126), gentamycin (40 µg/ml; Gentamicin Sandoz, 80 mg/ml injection) and amphotericin B (2.5 µg/ml; Sigma-Aldrich A2411) in humidified air atmosphere containing 5% CO₂, at 37 °C. The culture medium was changed on the first two days and every third day afterwards. Microglial cells were isolated from 21-28 day old mixed cultures by mild trypsinization. In some experiments, microglia were isolated from P8 mice using anti-CD11b conjugated magnetic microbeads (Miltenyi Biotec 130-093-634) and magnetic-activated cell sorting (MACS), according to the manufacturer's protocol. The P8-derived cells were maintained in the presence of 10 nM Macrophage Colony-Stimulating Factor (M-CSF; Thermofisher PMC2044) until use.

HEK-microglia co-cultures and Kv2.1 construct transfections

In co-cultures used for transfection HEK293 cells were plated at 2.5×10^4 cell/cm² density and microglial cells were seeded on top of HEK293 cell cultures in 2.5×10^4 cell/cm² density a day prior to transfection. The cells were transfected with 1 µg Kv2.1-GFP, Kv2.1-Ruby2 or DNKv2.1-YFP plasmid DNA. Transfection was carried out using Lipofectamine™ 3000 Transfection Reagent (ThermoFisher Sc. L3000001) and Opti-MEM™ Media (ThermoFisher Sc.

31985-062), according to the manufacturer's instructions. In brief, 1.5 μ l LipofectamineTM 3000 reagent was mixed with 25 μ l Opti-MEMTM and 1 μ g DNA was mixed with 1 μ l P-3000 reagent and 25 μ l Opti-MEMTM. The two solutions were combined, incubated for 20 min at room temperature and the mix was added to the cells. Gene expression was evaluated the day after transfection. To label microglia, isolectin B4–Alexa 488 or 594 (Isolectin GS-IB4 From Griffonia simplicifolia, Alexa FluorTM 488 or 594 Conjugate, ThermoFisher Sc. I21411 and I21413) was applied in 5 μ g/ml during imaging sessions. Live imaging was performed in HEPES buffered ACSF (NaCl 124.5 mM, KCl 2.5 mM, glucose 10 mM, MgCl₂ 2 mM, CaCl₂ 2 mM, NaHCO₃ 8 mM, HEPES 20 mM) at room temperature on a Nikon A1R confocal microscope at 60 \times magnification (Plan Apo VC NA=1.2 WD=0.31-0.28 mm FOV=215.04 μ m). Images were analyzed using the NIS-Elements AR software.

Neuronal cultures

Primary cultures of embryonic hippocampal cells were prepared from C57BL/6J mice on embryonic day 18, as described earlier (55). Briefly, cells were seeded onto poly-L-lysine coated tissue culture plates or laminin coated glass coverslips at 1×10^5 cells/cm² density and grown in NeuroBasal medium (ThermoFisher Sc. 21103-049) supplemented with 5% FBS (ThermoFisher Sc. 16000044), B-27TM Supplement (50 \times) (ThermoFisher Sc. 17504-044), GlutaMaxTM Supplement (0.5 mM; ThermoFisher Sc. 35050061), gentamicin (40 μ g/ml; Gentamicin Sandoz, 80 mg/ml injection), amphotericin B (2.5 μ g/ml; Sigma-Aldrich A2411). Cytosine-arabinofuranoside (CAR, 10 μ M; Sigma-Aldrich C1768) was added to the cultures 24-120 h after plating to limit glia growth. 48 h after CAR treatment half of the culture medium was changed to BrainPhys-SM1 medium (BrainPhysTM Neuronal Medium and SM1 Kit, Stemcell Technologies 05792) without FBS. Medium change was repeated every 3-4 days thereafter. Media of cultures treated with CAR as early as DIV1 were supplemented with astroglial conditioned media (1:1) collected from 1-2 week old primary astrocytic cultures after 72 h incubation. Primary neuronal cultures were cultivated for 7-14 days at 37 °C in 5% CO₂, 95% air atmosphere.

In vitro quinacrine experiments

To monitor vesicular ATP release, neuronal cultures were incubated with 20 μ M quinacrine-dihydrochloride (Sigma-Aldrich Q3251) for 20 min at 37 °C. Live imaging was performed in HEPES buffered ACSF (NaCl 124.5 mM, KCl 2.5 mM, glucose 10 mM, MgCl₂ 2 mM, CaCl₂ 2 mM, NaHCO₃ 8 mM, HEPES 20 mM) at room temperature on a Nikon A1R confocal microscope at 60 \times magnification (Plan Apo VC NA=1.2 WD=0.31-0.28mm FOV=215.04 μ m). Images were analyzed using the NIS-Elements AR software. For neuron-microglia cocultures microglial cells were seeded on top of primary neuronal cultures in 2.5×10^4 cell/cm² density a day prior to quinacrine-loading and imaging.

Quantification of ATP

The levels of ATP was determined in culture media by using HPLC method. The primary cultures were highly enriched in neurons, as non-neuronal cell proliferation was blocked by CAR as early as DIV1, as described above. Cell culture supernatants were collected at DIV7, 5 min after 40 mM KCl treatment, preceded by a 20 min incubation period with combinations of the following drugs: Nimodipine (20 μ M; Alomone Labs N-150), Clodronate disodium (10 μ M; Sigma Aldrich D4434), Omega-Agatoxin IVA (100 nM; Alomone Labs STA-500), Omega-Conotoxin GVIA (1 μ M; Alomone Labs SNX-124). Media (400 μ l/well) were separated into a

cold Eppendorf tube which contained 50 μ l of homogenization solution (0.1 M perchloric acid containing theophylline as an internal standard at 10 μ M concentration). Perchloric anion from the supernatant was precipitated by 1 M potassium hydroxide, the precipitate was then removed by centrifugation. The extracted purines were kept at -20 °C until analysis. The adenine nucleotides and adenosine in culture media were determined by online column switching separation using Discovery HS C18 50 x 2 mm and 150 x 2 mm columns. The flow rate of the mobile phases ["A" 10 mM potassium phosphate, 0.25 mM EDTA "B" with 0.45 mM octane sulphonyl acid sodium salt, 8% acetonitrile (v/v), 2% methanol (v/v), pH 5.2] was 350 or 450 μ l/min, respectively, in a step gradient application. The enrichment and stripping flow rate of buffer [10 mM potassium phosphate, pH 5.2] was during 4 min and the total runtime was 55 min. The HPLC system used was a Shimadzu LC-20 AD Analytical & Measuring Instruments System, with an Agilent 1100 Series Variable Wavelength Detector set at 253 nm. Concentrations were calculated by a two-point calibration curve using internal standard method.

Platelet aggregation in response to P2Y₁₂ receptor inhibition after stroke

12-14 weeks old male C57BL/6J mice were subjected to 30 min MCA occlusion and immediately after the induction of reperfusion a specific P2Y₁₂ receptor inhibitor (PSB0739, #3983 Tocris, 15 μ g in 5 μ l volume) or vehicle (PBS) was administered to the cisterna magna. 1 h later mice were sacrificed and venipuncture was performed from the vena cava inferior. Platelet-rich plasma samples from anticoagulated (3.8% Sodium citrate) blood samples were isolated by centrifugation (100 x g, 10 min), were plated (30 μ l/ well in a 24-well plate) and incubated at 37 °C for 30 min before treatment with 0.5 mM ADP for 1 h at 37 °C. ADP-induced platelet activation was measured by FACS based on CD62-P and CD42d fluorescence intensity, as described earlier in (40, 64). After 10 min antibody staining (CD62-P-APC, 1:400, #17-0626-80 eBioScience, CD42d-PE, 1:400, #12-0421-80 eBioScience) samples were lysed to remove any red blood cell contamination (BD FACS Lysing Solution), acquired with a BD FACSVerser instrument, and analyzed with BD FACSSuite software (BD Biosciences). Changes in CD62P mean fluorescence intensity values were determined on CD42d-positive platelets.

In vivo two-photon imaging

Animals were anaesthetized using fentanyl (100-200 μ l). Cranial window (3 mm diameter) was opened on the left hemisphere above the primary somatosensory area and supplementary somatosensory area border (centered 3 mm lateral and 2 mm posterior to bregma) without hurting the dura mater. After removal of the skull bone a 3 mm and 5 mm double glass coverslip construct was fixed with 3M™ Vetbond™ tissue glue on top of the dura mater. Then a custom made metal headpiece (Femtonics Ltd., Budapest, Hungary) was fixed with dental cement on the surface of the skull. All experiments were performed on a Femto2D-DualScanhead microscope (Femtonics Ltd., Budapest, Hungary) coupled with a Chameleon Discovery laser (Coherent, Santa Clara, USA). For tdTomato electroporated animals the wavelength of the laser was set to 920 nm to measure the tdTomato and GFP signals simultaneously. For Mito-R-Gecol1 mitochondrial electroporated animals the wavelength was set to 1000 nm. Following excitation the fluorescent signal was collected using a Nikon 18X water immersion objective. Data acquisition was performed by MES software (Femtonics Ltd.). Since it has recently been shown that volatile anesthetics such as isoflurane may influence microglial process motility (54), we used fentanyl anaesthesia for these studies, which did not block microglial responses. (Fig. S5b; median process motility observed: isoflurane 0.6 μ m/min, 0.3-0.83 interquartile; fentanyl 0.6 μ m/min, 0.42-0.78; urethane 0.48 μ m/min, 0.36-0.84; n=153 processes from 9 animals).

To analyze contacts established by microglial processes on neuronal cell bodies and proximal dendrites, we used in utero tdTomato electroporated CX3CR1^{+/GFP} mice. To visualize microglial processes and neuronal mitochondria simultaneously, we used Mito-R-Geco1 electroporated CX3CR1^{+/GFP} mice. Galvano Z-stacks of 7 images (820x820 pixels, 5 μ m step size, range=200-225 μ m from pial surface) were made at every 2 or 2.5 minutes. Two-photon image sequences were exported from MES and analyzed using FIJI. Dual colour images were analyzed with the Manual Tracking plugin of FIJI. We applied a local maximum centering correction method with a search square of 5 pixels. Pixel size was 167 nm/px.

Microglial process velocity was measured on time-series images acquired with 2P microscopy. Following motion correction, monocolour images from the same region of CX3CR1^{+/GFP} mice taken 135 seconds apart were analyzed with the Manual Tracking plugin of FIJI. We applied a local maximum centering correction method with a search square of 5 pixels. Pixel size was 167 nm/px. Processes were included in the measurement, when they were clearly traceable for at least 10 minutes. The GCaMP6f signal was imaged with the laser wavelength set to 920 nm, using the resonant scanner at 32.75 Hz. Image size was 512x488 pixels.

Immunofluorescent labeling and confocal laser scanning microscopy (CLSM)

Before the immunofluorescent staining, the 50 μ m thick sections were washed in PB and Tris-buffered saline (TBS). This was followed by blocking for 1 hour in 1% human serum albumin (HSA; Sigma-Aldrich) and 0.1% Triton X-100 dissolved in TBS. After this, sections were incubated in mixtures of primary antibodies overnight at room temperature. After incubation, sections were washed in TBS and were incubated overnight at 4 °C in the mixture of secondary antibodies, all diluted in TBS. Secondary antibody incubation was followed by washes in TBS, PB, the sections were mounted on glass slides, and coverslipped with Aqua-Poly/Mount (Polysciences). Immunofluorescence was analyzed using a Nikon Eclipse Ti-E inverted microscope (Nikon Instruments Europe B.V., Amsterdam, The Netherlands), with a CFI Plan Apochromat VC 60X oil immersion objective (numerical aperture: 1.4) and an AIR laser confocal system. We used 405, 488, 561 and 647 nm lasers (CVI Melles Griot), and scanning was done in line serial mode, pixel size was 50x50 nm. Image stacks were obtained with NIS-Elements AR software and deconvolved using Huygens Professional software (www.svi.nl). For primary and secondary antibodies used in this study, please see Supplementary Table 3.

Quantitative analysis of CLSM data

Quantitative analysis of each dataset was performed by at least two observers, who were blinded to the origin of the samples, the experiments and did not know of each other's results. For the analysis of somatic junction prevalence, confocal stacks with double immunofluorescent labeling (cell type-marker and microglia) were acquired from at least three different regions of mouse cortex. All labeled and identified cells were counted, when the whole cell body was located within the Z-stack. Given somata were considered to be contacted by microglia, when a microglial process clearly touched it (i.e. there was no space between neuronal soma and microglial process) on at least 0.5 μ m long segment.

For the analysis of synaptic contact prevalence, confocal stacks with triple immunofluorescent labeling (pre- and postsynaptic markers and microglia) were analyzed using an unbiased, semi-automatic method. First, the two channels representing the pre- and postsynaptic markers were exported from a single image plane. The channels were thresholded automatically in FIJI, the „fill in holes” and „erode” binary processes applied. After automatic particle tracking, synapses were identified where presynaptic puncta touched postsynaptic ones.

From these identified points we selected 200/animal in a systematic random manner. After this, the corresponding synapses were found again in the original Z-stacks. A synapse was considered to be contacted by microglia, when a microglial process was closer than 200 nm (4 pixels on the images).

To measure the distribution of Kv2.1 and Kv2.1 labeling relative to microglial processes, confocal stacks were exported into single-channel TIFF-series. Identical measuring frames (1.32 μm^2) were placed randomly along the surface of pyramidal cells and integrated Kv2.1 fluorescent density was measured in each frame in FIJI. Afterwards, frames containing microglial contacts were identified (“contact” group) and compared with frames not containing microglial processes (“non-contact” group).

For the measurements of mitochondrial fragmentation, we used tissue from mice that were sacrificed 4 hours after a one hour-long unilateral MCAo. Confocal stacks with double immunofluorescent labeling (Kv2.1 and TOM20) were taken from the penumbra and the corresponding contralateral region. We used the Kv2.1 labeling to trace neuronal cell bodies as regions of interest (ROI). Every cell was counted once using the confocal plane containing its largest cross-section. Within the ROIs TOM20 labeling was investigated with FIJI: after automatic thresholding, we ran the ‘Analyze Particles’ command to obtain the area and the major axis of individual somatic mitochondria.

For the analysis of Kv2.1 clusters, individual cells were measured by using the confocal Z-plane containing the largest cross-section of the cell body. The intensity profile of Kv2.1 labeling was plotted using FIJI. A cluster was identified when at least three adjacent pixels’ intensity was more than 25 grayscale values (10% of an 8-bit image) larger than the average fluorescent intensity of that particular cells Kv2.1 labeling.

Microglial process coverage was measured on CLSM Z-stacks acquired with a step size of 300 nm. On single-channel images, Kv2.1-positive cells were selected randomly, the cell bodies of which were fully included in the captured volume. The surface of these cells was calculated by measuring the circumference of the soma on every section multiplied by section thickness. The length of microglial process contacts was measured likewise.

TOM20 and vesicular nucleotide transporter (vNUT) fluorescent intensity profiles were analyzed using a semi-automatic method. Confocal stacks with triple immunofluorescent labeling (microglia, Kv2.1 and TOM20/vNUT) were collected. The section containing the largest cross-section of a pyramidal cell was used to trace the cell membrane according to Kv2.1-labeling. This contour was then expanded and narrowed by 0.5 μm to get an extracellular and an intracellular line, respectively. The intensity of fluorescent labeling was analyzed along these lines. After normalizing and scaling, microglial contact was identified where microglial fluorescent intensity was over 20% of total, for at least 500 nm. Then the contact area was extended 500-500 nm on both sides, and TOM20/vNUT fluorescent intensity within these areas was measured for “contact” value. 3-dimensional reconstruction of CLSM and 2P imaging stacks was performed using the IMOD software package (65).

STORM super-resolution imaging

Free-floating brain sections were blocked with 2% normal donkey serum followed by immunostaining with rabbit anti-P2Y12R and mouse anti-Kv2.1 antibodies, followed by anti-rabbit Alexa 647 and anti-mouse Alexa 594 secondary antibodies. Sections were mounted onto #1.5 borosilicate coverslips and covered with imaging medium containing 5% glucose, 0.1 M mercaptoethylamine, 1 mg/ml glucose oxidase, and catalase (Sigma, 1500 U/ml) in Dulbecco’s PBS (Sigma), immediately before imaging. STORM imaging was performed for P2Y12R

(stimulated by a 647 nm laser) by using a Nikon N-STORM C2+ superresolution system that combines ‘Stochastic Optical Reconstruction Microscopy’ technology and Nikon’s Eclipse Ti research inverted microscope to reach a lateral resolution of 20 nm and axial resolution of 50 nm (26). Imaging was performed using the NIS-Elements AR 4.3 with N-STORM 3.4 software, and we used VividSTORM open-source software. Molecule lists were exported from NIS in txt format, and the three image planes of the ics-ids file pairs from the deconvolved confocal stacks matching the STORM volume were converted to the ome-tiff format using FIJI software. Confocal and corresponding STORM images were fitted in VividSTORM. Localization points exceeding a photon count of 2000 were counted as specific superresolution localization points. Local density filter (10 neighbours within 150 nm for P2Y12R and Iba1, and 5 neighbours within 150 nm for Kv2.1) and Z-filter (± 300 nm from focal plane) was applied to the localization points.

Pre-embedding immunoelectron microscopy

After extensive washes in PB and 0.05 M TBS sections were blocked in 1% HSA in TBS. Then, they were incubated in primary antibodies (Supplementary Table 3) diluted in TBS containing 0.05% sodium azide for 2-3 days. After repeated washes in TBS, the sections were incubated in blocking solution (Gel-BS) containing 0.2% cold water fish skin gelatine and 0.5% HSA in TBS for 1 h. Next, sections were incubated in gold-conjugated or biotinylated secondary antibodies (Supplementary Table 3) diluted in Gel-BS overnight. After extensive washes in TBS the sections were treated with 2% glutaraldehyde in 0.1 M PB for 15 min to fix the gold particles into the tissue. This was occasionally followed by incubation in avidin–biotinylated horseradish peroxidase complex (Elite ABC; 1:300; Vector Laboratories) diluted in TBS for 3 h at room temperature or overnight at 4 °C. The immunoperoxidase reaction was developed using 3,3-diaminobenzidine (DAB; Sigma-Aldrich) as chromogen. To enlarge immunogold particles, sections were incubated in silver enhancement solution (SE-EM; Aurion) for 40-60 min at room temperature. The sections were then treated with 1% (for electron tomography) or 0.5% OsO₄ in 0.1 M PB, at room temperature (for electron tomography) or on ice, dehydrated in ascending alcohol series and in acetonitrile and embedded in Durcupan (ACM; Fluka). During dehydration, the sections were treated with 1% uranyl acetate in 70% ethanol for 20 min. For electron microscopic analysis, tissue samples from the CA1 area of dorsal hippocampus/somatosensory cortex (S1) were glued onto Durcupan blocks. Consecutive 70 nm thick (for conventional electron microscopic analysis) or 150 nm thick (for electron tomography) sections were cut using an ultramicrotome (Leica EM UC6) and picked up on Formvar-coated single-slot grids. Ultrathin sections for conventional electron microscopic analysis were examined in a Hitachi 7100 electron microscope equipped with a Veleta CCD camera (Olympus Soft Imaging Solutions, Germany). 150 nm thick electron tomography sections were examined in FEI Tecnai Spirit G2 BioTwin TEM equipped with an Eagle 4k HS camera.

Electron tomography

For the electron tomographic investigation, we used 150 nm thick sections from the hippocampal CA1 region from the anti-P2Y12R immunogold stained material (see: “Pre-embedding immunoelectron-microscopy”). Before electron tomography, serial sections on single-slot copper grids were photographed with a Hitachi H-7100 electron microscope and a Veleta CCD camera. After this, grids were put on drops of 10% HSA in TBS for 10 minutes, dipped in distilled water (DW), put on drops of 10 nm gold conjugated Protein-A (Cytodiagnostics #AC-10-05) in DW (1:3), and washed in DW. Finally, we deposited 5 nm thick

layers of carbon on both sides of the grids. Electron tomography was performed using a Tecnai T12 BioTwin electron microscope equipped with a computer-controlled precision stage (CompuStage, FEI). Acquisition was controlled via the Xplore3D software (FEI). Regions of interest were pre-illuminated for 4-6 minutes to prevent further shrinkage. Dual-axis tilt series were collected at 2 degree increment steps between -65 and +65 degrees at 120 kV acceleration voltage and 23000x magnification with -1.6 – -2 μm objective lens defocus. Reconstruction was performed using the IMOD software package (65). Isotropic voxel size was 0.49 nm in the reconstructed volumes. After combining the reconstructed tomograms from the two axes, the nonlinear anisotropic diffusion filtering algorithm was applied to the volumes. Segmentation of different profiles has been performed on the virtual sections using the 3Dmod software, and measurements were done on the scaled 3D models.

Analysis of the connection between membrane distance and P2Y12R density was carried out by investigating all points of the microglial membrane facing neuronal soma, using reconstructed 3D models. Coordinates of the points of neuronal membrane, soma-facing microglial membrane and P2Y12R labeling gold particles were exported using IMOD. For every single point of microglial membrane, the lowest distance to the neuronal membrane and the number of P2Y12R labeling gold particles within 40 nm was calculated with a unique algorithm running in program R (The R Foundation). Since neuronal junctions established by microglial processes are dynamic, a strong linear correlation cannot be expected; therefore statistical analysis was carried out by dividing data into two groups. In the analyzed tomograms the average distance between neuronal somatic membranes and facing microglial membranes was 13.06 nm, which we used as demarcation point.

Analysis of P2Y12R density along different surfaces of microglial processes was done using reconstructed 3D models. We identified segments of microglial membranes facing (running parallel with) different neuronal membranes. These segments were grouped depending on opposing neuronal profiles (e.g. neuronal soma or other neuronal parts). Using IMOD, the surfaces of microglial profiles were measured and gold particles were assigned to the closest membrane part. Due to different labeling density and penetration differences, we only performed pairwise comparisons between ‘somatic’ and ‘non-somatic’ microglial membranes within the same microglial processes. Only those gold particles were counted that localized within 40 nm of the microglial membrane.

In vitro nicotinamide adenine dinucleotide (NADH) imaging

Mice were anaesthetized by inhalation of halothane, and following decapitation 200 μm thick coronal slices were prepared from the somatosensory and visual cortex with a vibrating blade microtome (Microm HM 650 V) immersed in slicing solution containing (in mM): 130 NaCl, 3.5 KCl, 1 NaH_2PO_4 , 24 NaHCO_3 , 1 CaCl_2 , 3 MgSO_4 , 10 D(+)-glucose, saturated with 95% O_2 and 5% CO_2 . The solution used during experiments was identical to the slicing solution, except it contained 3 mM CaCl_2 and 1.5 mM MgSO_4 . Experiments were carried out less than 4 hours after slicing. During image acquisition slices were kept at $\sim 36^\circ\text{C}$. Imaging with multiphoton excitation was performed using a Zeiss LSM 7MP scanning microscope (Carl Zeiss, Germany) through a 40X water-immersion objective (W-Plan, NA 1.0, Carl Zeiss). To acquire simultaneous excitation of GFP and NADH autofluorescence of acute brain slices we used two single wavelength mode-locked Ti:sapphire lasers the beams of which were coupled to each other by a dichroic beam splitter (t810lpxr, Chroma Technology Corp, USA). One of our lasers (MaiTai DeepSee, Spectra-Physics, Santa Clara, USA) exciting GFP operated at 885 nm, while our second laser (FemtoRose 100 TUN, R&D Ultrafast Lasers, Hungary) exciting NADH had an

operation wavelength of 750 nm. Both laser systems delivered ~100 fs pulses at ~80 MHz and ~76 MHz repetition rate, respectively. A total average laser power of 16-18 mW was measured after the objective during imaging. Time-lapse images (1024x1024 pixels) were collected continuously for up to 55 minutes with 30.98 seconds frame scan time. Emission filters were chosen to separate intrinsic NADH fluorescence (ET460/50m, Chroma Technology Corp, USA) from GFP fluorescence (ET525/50m, Chroma Technology Corp, USA). Time lapse images were processed and analyzed in FIJI (ImageJ, NIH) software. As a first step images were spatially filtered (mean filter smooth with 1 pixel diameter) and corrected for contrast. To remove jitter in image series stabilization was applied with a FIJI plugin (K. Li, "The image stabilizer plugin for ImageJ," http://www.cs.cmu.edu/~kangli/code/Image_Stabilizer.html, February, 2008). Analysis and quantification of NADH fluorescence was carried out in manually selected areas of compartments of cell bodies at microglial contact site.

In vivo widefield calcium imaging

In vivo widefield calcium imaging was performed as previously described in detail (66). In brief, as an optogenetic calcium-reporter mouse strain, C57BL/6J-Tg(Thy1-GCaMP6s)GP4.12Dkim/J (61) heterozygous mice were bred at the Institute for Stroke and Dementia Research, Munich. The skin covering the skull and the underlying connective tissue were removed in head-fixed mice and a layer of transparent dental cement was distributed on the window area and covered with a coverslip. Afterwards, the mice were allowed to recover from the surgery for more than 48 h before the first image acquisition. For image acquisition, mice were injected with 0.05 mg/kg bodyweight of medetomidine intraperitoneally 5 minutes prior to inducing inhalation anesthesia with a mixture of 5% isoflurane in 70% nitrous oxide and 30% oxygen. After 70 seconds, the animals were fixed in a stereotactic frame, the dose of isoflurane was decreased to 1.5% for 140 seconds and finally decreased to 0.75% for 4 minutes to maintain steady-state before data-acquisition. In vivo widefield calcium imaging was performed on a custom-built imaging setup described in (66). This setup allowed widefield imaging through the chronic window on top of the skull into the cortex of both forebrain hemispheres by covering a field-of-view of 12x12 mm, corresponding to an image matrix of 330x330 pixels. Image acquisition was conducted for 29 minutes (44 x 1000 frames, immediately after MCAo induction, starting 60 min after injection of PSB) or 4 minutes (6 x 1000 frames, baseline acquisition, starting 60 min after injection of PSB and after 120 min reperfusion, respectively). After the imaging session, anesthesia was terminated by intraperitoneally injecting the mice with 0.1 mg/kg bodyweight Atipamezole. During all anesthetized procedures body temperature was maintained using a feedback-controlled heating system. After end of surgeries animals were put in a heating chamber until they had recovered from anesthesia. Post-surgery analgesia and sedation protocols were conducted in accordance with approved protocols by the governmental committee.

Images of every acquisition were masked in a two-step procedure. First, a general mask was applied to exclude lateral cortical areas, which were out of focus due to the curvature of the cortical surface as described in (66). Second, an individual mask was computed to exclude all pixels, in which the calcium signal was saturated due to autofluorescence, as occurring in areas affected by the infarct (66). Both, the general and the individual masks were combined for every acquisition.

To characterize changes in the cortical network after stroke, functional connectivity was computed between pairs of ROIs, representing functional cortical areas, previously defined (66). Functional connectivity was calculated as the Fisher z-transformed Pearson-moment correlation

between the ROI signal time-courses. The average connectivity scores were calculated within each group (PSB-treated and control group), and the difference between groups was depicted for all ROI pairs in a heatmap.

For seed-based functional connectivity analysis, connectivity scores were calculated in the same way but between a selected ROI in the right hindlimb sensory area (rHLs) and the signal time series of all pixels on the cortical surface included in the combined general and individual masks. In order to quantify connectivity change of the rHLs after stroke, the connectivity scores were normalized by dividing through the connectivity scores resulting in the baseline condition. Results were visualized as topographical maps of all brain pixel.

Overall functional connectivity alterations due to treatment of the mice with PSB (naïve and stroke) were assessed by computing the global connectivity (GC) for each pixel inside the combined general and individual mask. For a given pixel, GC was calculated by calculating the functional connectivity with each other pixel inside the mask, followed by averaging across the resulting connectivity scores. In order to assess treatment effects, GC scores were averaged pixel-wise within group (PSB and control group). The difference between groups was then visualized as topographical map of all brain pixels.

To compare the extent of GC dropdown between PSB and control treated animals after stroke, the sum of all pixels with a moderate GC (i.e. global connectivity less than 0.6 according to (67)) was calculated for every mouse. The mean area of each group was contoured within the GC map and the area was assessed quantitatively per animal and compared between the groups.

To represent the non-functionality of cortical tissue during the occlusion of the middle cerebral artery, the number of saturated pixels during the occlusion was calculated. During the occlusion, cortical spreading depressions (CSDs) appeared. Given the high degree of neuronal activation within areas covered by these waves, the high amplitude of the Ca^{2+} derived signal caused saturation in these areas. Therefore, we quantified the spatial extent of CSDs by counting the saturated pixels during these waves. The start- and end-time of every cortical wave were defined as first appearance of saturated pixels and the full disappearance of saturated pixels. The absolute maximum spatial extent of every cortical wave was identified and used to align the individual cortical waves of all animals. The area of saturated pixels was then acquired for every CSD wave for every animal at the endpoint of the shortest wave (which ended 37 seconds after the aligned absolute maximum). The area of saturated pixels was groupwise depicted as overlay of the area of every CSD wave upon the general mask.

Statistical analysis

All quantitative assessment was performed in a blinded manner and based on power calculation wherever it was possible. Based on the type and distribution of data populations (examined with Shapiro-Wilks W test) we applied appropriate statistical tests: in case of two independent groups of data unpaired t-test or Mann Whitney U-test, for two dependent groups of data Wilcoxon signed-rank test, for multiple comparisons one-way ANOVA (with Tukey's test) or Kruskal-Wallis test was used. Statistical analysis was performed with the Statistica 13.4.0.14 package (TIBCO), differences with $p < 0.05$ were considered significant throughout this study.

Supplementary Text for Main Figures

Figure 1.

(C) somatic vs dendritic contact lifetimes: $p < 0.001$, $n = 26$ contacts from 3 mice.

(F) $n = 443$ neurons and 1183 synapses in 4 mice, and 170 neurons in 3 human patients.

(H) $p < 0.001$ in both cases, $n = 114$ and 107 ROIs from 4 mice.

(I) $n = 111$ junctions from 4 mice.

(J) $n = 50$ cells.

Scale bars: 5 μm on B, 20 μm on E, 2 μm on G, J and K. Median values and interquartile ranges are plotted on C and H, mean+SD on F and I, mean+SEM on K.

Figure 2

(C) Side- and face (90 degrees rotated) view of the 3D model of a contact site. Immunogold density is the highest where the intercellular distance is the smallest.

(D) Density versus distance analysis performed on 3D models of contact sites confirms that the density of P2Y₁₂R-immunogold particles within the junction is significantly higher where the distance between neuronal and microglial membrane is smaller than 13 nm ($p < 0.001$, MWU test, $n = 13055$ points from 3 neocortical contacts, 3 mice). Median values and interquartile ranges are shown.

(E) Different views of the 3D models of two junctions illustrate that P2Y₁₂R-immunogold density shows an uneven distribution along microglial membranes, being strongly and selectively enriched where the processes are in direct contact with neuronal somata (microglial membrane contacting neuronal cell body – „Somatic”, microglial membrane contacting profiles other than neuronal somata – „Non-somatic”). ($p < 0.001$, MWU test, $n = 24$ surfaces, neocortex, 3 mice).

(G) TOM20 immunofluorescent intensity is significantly higher along neuronal membrane parts where microglial processes contact the somata ($p < 0.001$, MWU test, $n = 14$, 2 mice).

(I) vNUT immunofluorescent intensity is significantly higher in neurons where microglial processes contact the somata. ($p = 0.002$, MWU test, $n = 15$, 2 mice).

Scale bars: 500 nm on A, 100 nm on B, 5 μm on F, 3 μm on G and I, 300 nm on H. Median values and interquartile ranges are plotted on D, E, G and I.

Figure 3

(B) Contact lifetime was 29 min (median, 10-41 interquartile, $n = 25$ contacts on 19 neurons from 3 mice).

(I) The measured diameter of the released puncta can correspond to sub-diffraction sized emitters because of the point-spread function size (~ 0.3 - 0.4 μm at 488 nm), meaning that the size of the released vesicles can be as small as 40 nm.

(J) ACSF/KCl vs ACSF/ACSF $p = 0.0218$, MWU test, $n = 11$ measurements; SC/KCl vs ACSF/KCl $p = 0.6532$, MWU test, $n = 11$; SC+NIM/KCl vs ACSF/KCl $p = 0.0271$, $n = 10$; SC+CLO/KCl vs ACSF/KCl $p = 0.0284$, $n = 10$.

Scale bars: 2 μm on A and K, 4 μm on B, 10 μm on C and D, 500 nm on F, 3 μm on G, and 200 nm on the EM insert on K. Median values and interquartile ranges are plotted on I, mean+SD on E, mean+SEM on J.

Figure 4

(A) Baseline in vivo 2P imaging of cortical microglia-neuron contacts of tdTomato electroporated CX3CR1^{+/GFP} mice was followed by administration of the P2Y12R-inhibitor PSB0739 (PSB) into the cisterna magna (i.c.m.) and a further imaging session.

(C) ctrl som. vs. PSB som. $p=0.0331$, MWU test, $n=12$ contacts for ctrl som., 14 ctrl dendr., 15 PSB som., 13 PSB dendr. from 2 mice.

(D) ctrl vs CNO+/cFos+ $p=0.0139$; ctrl vs CNO+/cFos- cells, $p=1$, Kruskal-Wallis test, $n=101$ cells from 8 mice.

(E) ctrl vs CNO+/cFos+ $p=0.7497$; ctrl vs CNO+/cFos- cells, $p=1$, Kruskal-Wallis test, $n=85$ cells from 6 mice.

(G) ($p<0.001$, MWU test, $n=124$ cells from 6 mice).

Scale bars: 5 μm on B and G, 8 μm on D and E. Median values and interquartile ranges are plotted on C, D, E and G.

Figure 5

(A) $p<0.001$, $n=189$ mitochondria.

(B) $p<0.001$, $n=30$ neurons.

(D) ctrl vs. stroke: $p<0.001$, PSB ctrl vs. PSB stroke: $p=0.792$, diazo. ctrl vs. diazo. stroke: $p=0.053$, MWU test, $n=140$ neurons

(E) $p=0.007$, MWU test, $n=113$ and 136 neurons from 3 control and 3 stroke patients, respectively

(F) $p=0.0439$, unpaired t-test, $n=9$ control and 8 PSB-treated mice

(G) left panel: Individual ROI-to-GC scores were normalized to baseline and quantified for group comparison ($p=0.0077$, unpaired t-test, $n=4$ control and 3 PSB-treated mice).

(H) $p<0.0001$, $n=96$ neurons from 3 mice

(I) Infarct volumes: stroke: $14.96\pm 0.95 \text{ mm}^3$; stroke+PSB: $23.06\pm 2.519 \text{ mm}^3$, $p=0.008$, MWU test, $n=10$ control and 10 stroke mice

Scale bars: 4 μm on A, 2 μm on B, 8 μm on E, 20 μm on H. Median values and interquartile ranges are plotted on A, B, D and E, mean+SEM on F, G, H and I.

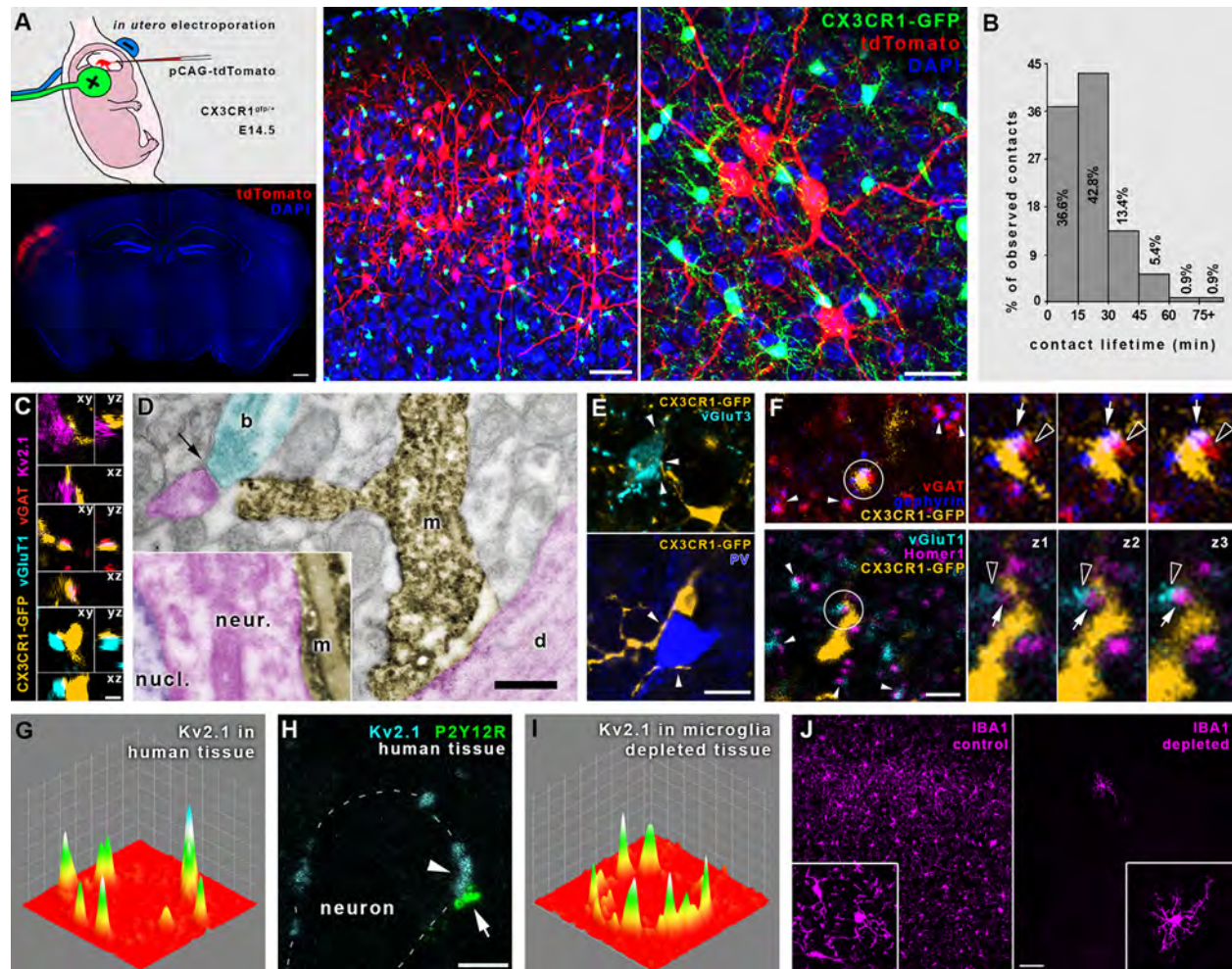


Fig. S1.

(A) Result of CX3CR1^{+/GFP} mouse *in utero* electroporation with pCAG-IRES-tdTomato. Lower left panel shows the spread of tdTomato-positive neurons in red. Middle and right panels show the non-overlapping staining of electroporated neurons (red) and microglia (green). Cell nuclei are visible in blue. (B) Distribution of microglial contact lifetimes observed with *in vivo* 2P imaging (n=112 contacts from 2 mice). (C) Orthogonal projections show microglial (yellow) contacts with neuronal cell body (magenta), GABAergic (red) and glutamatergic (cyan) synapses. Images represent contacts marked on Fig. 1D. (D) Electron microscopic images showing microglial processes (m) establishing direct contact with neuronal cell body (neur.), dendritic shaft (d) and presynaptic bouton (b) in mice. Microglia are visualized by immunoperoxidase reaction against Iba1. Pseudocoloring shows microglia in yellow, neuronal cell body and dendritic processes in magenta, presynaptic bouton in cyan and nucleus (nucl.) in purple. Arrow points at a dendritic spine receiving asymmetric synaptic contact. (E) CLSM image planes show microglial processes (yellow) touching cell bodies of hippocampal vGluT3+ (cyan) and PV+ (blue) interneurons. (F) Microglial processes contacting cortical inhibitory and excitatory synapses. Presynaptic terminals are visible by stainings against vesicular GABA transporter (vGAT, red) and type 1 vesicular glutamate transporter (vGluT1, cyan), while postsynaptic side is characterized by stainings against gephyrin (blue) and Homer1 (magenta).

dc_2027_22

White arrowheads point at colocalization of pre- and postsynaptic markers. Microglial contacts in white circles are enlarged in the panels right, with the previous and following Z-planes from the stack (Z-step = 250 nm). Empty arrowheads point at the presynaptic marker, white arrows point at the postsynaptic side. **(G)** Heatmap shows Kv2.1 clusters of a human cortical neuron. **(H)** CLSM image shows that a P2Y12R-labeled microglial process contacts a human cortical neuron exactly at the spot where a Kv2.1 cluster is located. **(I)** Heatmap shows that Kv2.1-clustering of mouse cortical neurons is not affected by microglia depletion. **(J)** CLSM images show that 3 week PLX5622-diet almost completely depleted microglia from the brain. Scale bars: 500 μm on left panel of A, 50 μm on middle panel of A and on J, 25 μm on right panel of A, 1 μm on C and D, 15 μm on E, 2 μm on F and H.

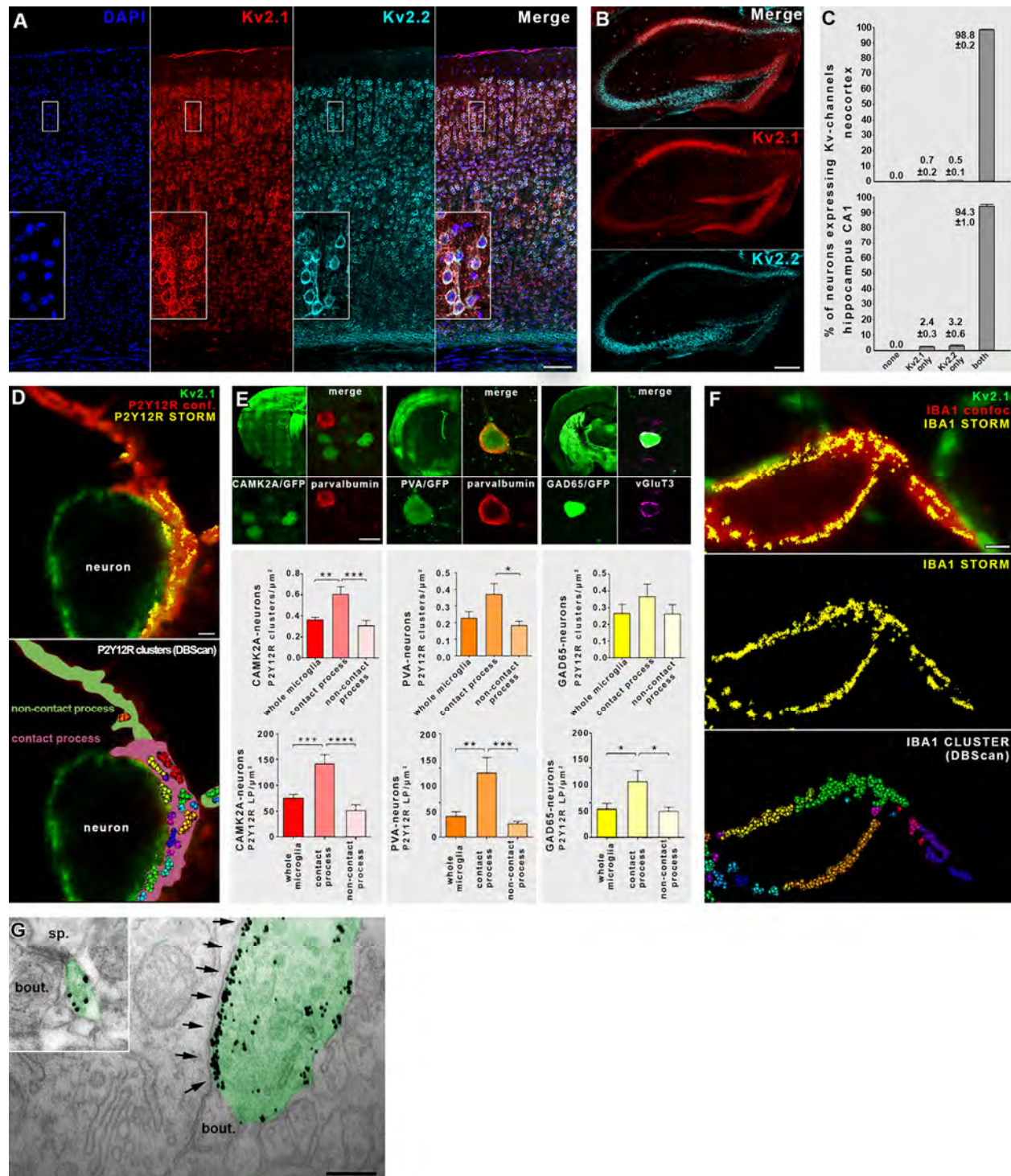


Fig. S2.

(A) CLSM images show labeling patterns of Kv2.1 and Kv2.2 in the neocortex. (B) CLSM images show labeling patterns of Kv2.1 and Kv2.2 in the hippocampus. (C) Percentages of neurons expressing Kv-channels in the neocortex and hippocampus. (D) P2Y12R clustering differs depending on location. Microglial processes were classified depending on neuronal contacts established: contact processes are pale magenta, non-contact processes are pale green on

bottom panel. **(E)** Analysis of P2Y₁₂R cluster and LP density on different microglial processes contacting distinct cell populations. Microglial contact processes on CamK2a (red) and PVA-positive cells (orange) possess significantly higher cluster density, than non-contact segments, while there is a similar trend observable in the case of GAD65-positive cells (yellow, for detailed results see Supplementary Table 1.). Contact processes had significantly higher number of P2Y₁₂R LPs in all populations. Anti-PV and vGluT3 labelings were used to confirm cell specificity. **(F)** Super-resolution imaging of microglial Iba1 shows no clustering at somatic junctions. CLSM images show neuronal Kv2.1 (green) and a contacting microglial process made visible by Iba1-labeling (red). Iba1 (yellow) STORM-signal is overlaid and shown individually in the middle panel. Lower panel shows a homogenous distribution of Iba1 LPs using DBScan analysis. **(G)** Contact dependent clustering of P2Y₁₂R is absent at synapses as confirmed by immunogold-electron microscopy. Scale bars: 100 μ m on A and B, 1 μ m on D and F, 10 μ m on E, 250 nm on G. Mean+range is plotted on C, Mean+SEM is plotted on E.

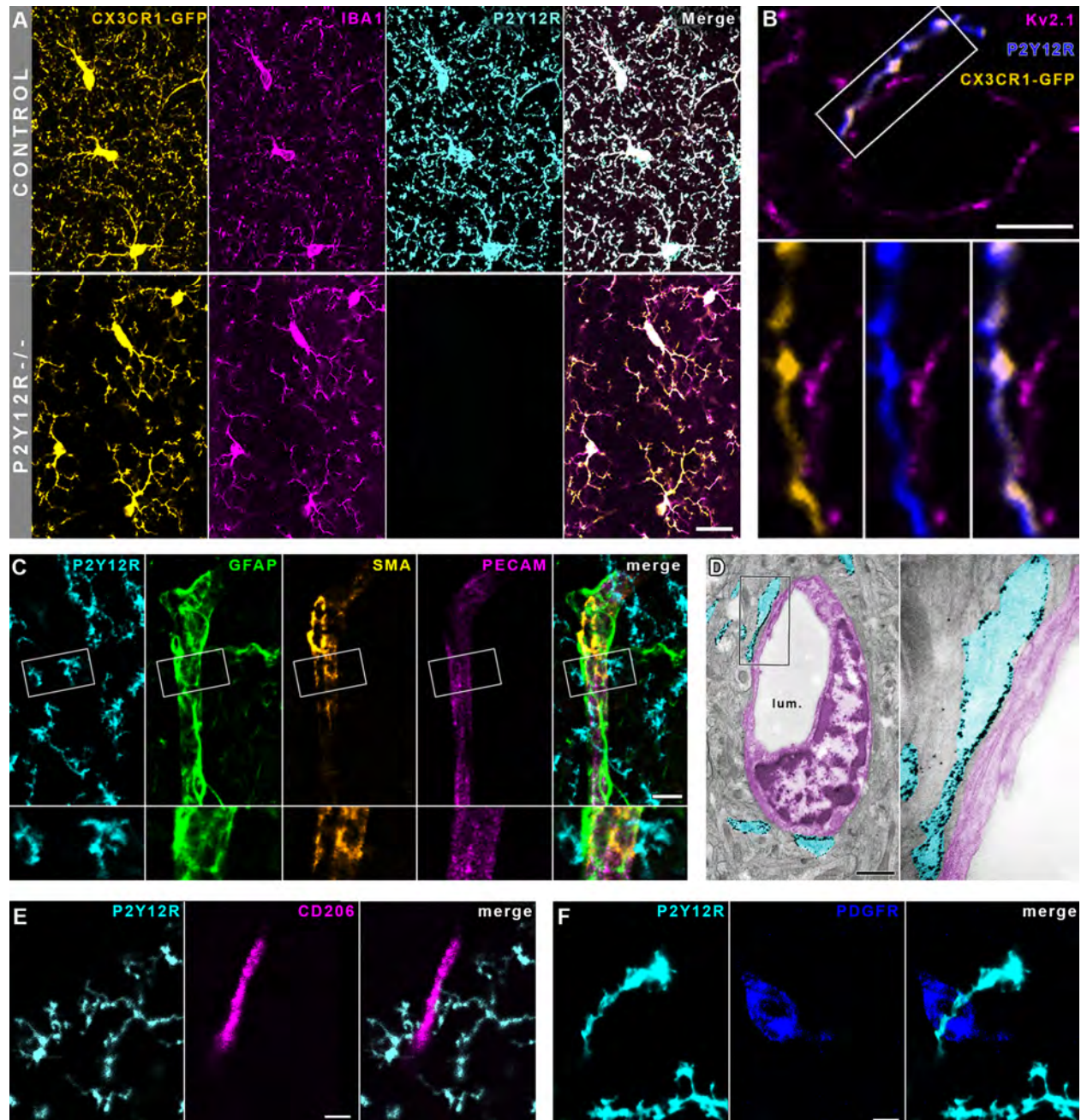


Fig. S3.

(A) CLSM images show triple immunolabeling for GFP, Iba1 and P2Y12R in CX3CR1^{+/GFP} and CX3CR1^{+/GFP} -P2Y12R^{-/-} animals. (B) CX3CR1-GFP and P2Y12R double positive microglial processes touch Kv2.1 clusters on neuronal somatic membrane. (C) P2Y12R-positive microglial processes contact cells of the neurovascular unit. (D) Transmission electron micrographs show P2Y12R-immunogold labeled microglial processes (cyan pseudocolour) touching vascular endothelial cell (magenta pseudocolour). P2Y12R expression is clearly restricted to microglia. (E) P2Y12R-labeled microglial processes are contacting CD206-positive perivascular macrophages (PVM). PVMs do not express P2Y12Rs. (F) P2Y12R-labeled microglial processes

dc_2027_22

are contacting PDGFR β -positive pericytes. Pericytes are not expressing P2Y₁₂Rs. Scale bars: 20 μ m on A, 4 μ m on B, 10 μ m on C, 1 μ m on D, 5 μ m on E, 3 μ m on F.

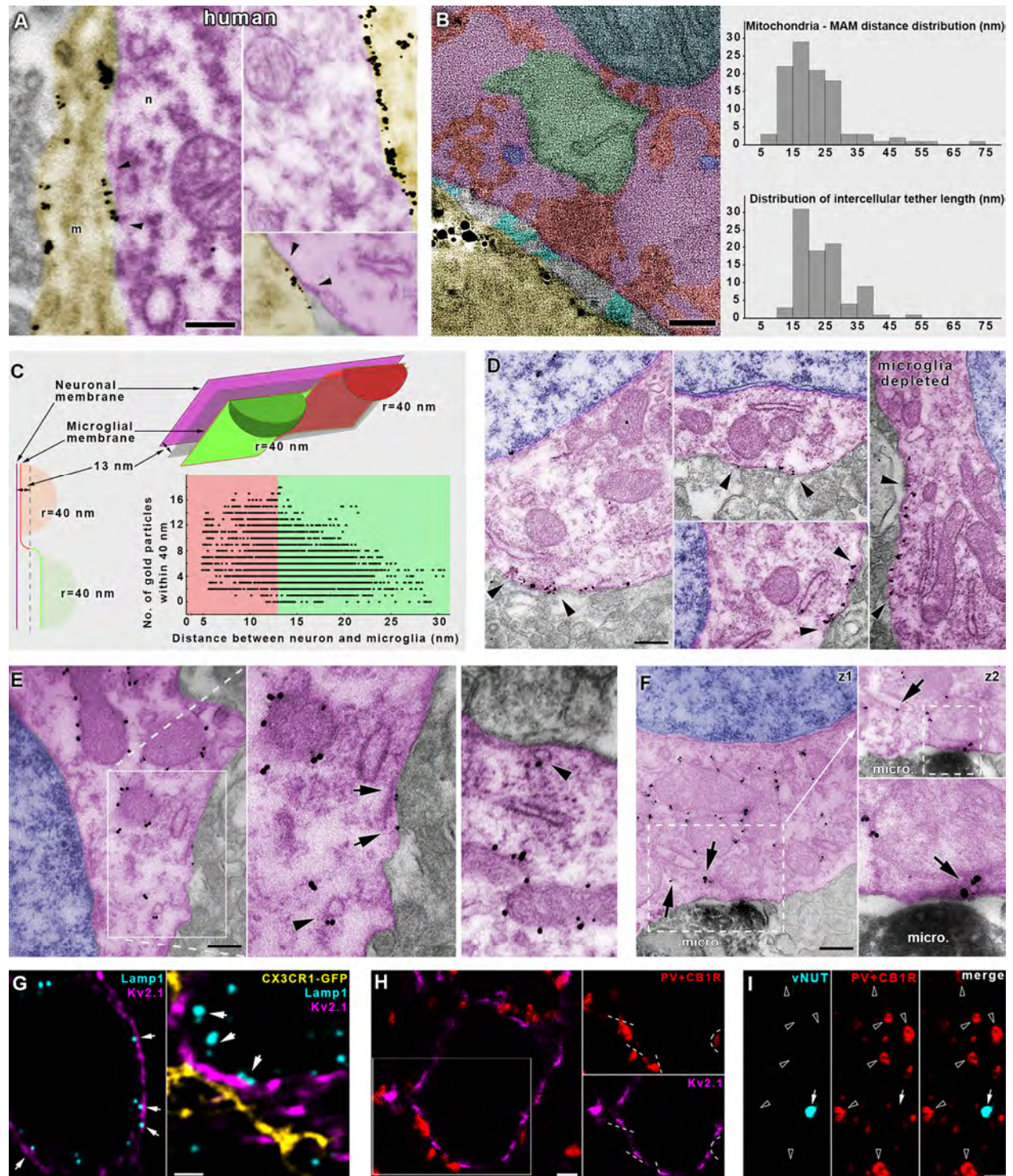


Fig. S4.

(A) Electron microscopic image shows a microglial process (m) establishing direct contact with neuronal cell body (n) in human tissue. Microglia is identified by immunogold-labeling against P2Y12R. Arrowheads point at accumulation of gold particles at contact sites. (B) Single virtual plane of an electron tomographic volume (thickness: 0.49 nm) showing a P2Y12R-positive

(black immunogold particles) microglial process (yellow) contacting a neuronal cell body (magenta). Mitochondria (blue), mitochondria-associated membranes (MAM, green), vesicles (purple) and intracellular densities (red) are commonly visible in the vicinity of these junctions. In some cases, intercellular linking structures (cyan) can be seen within the cleft. Right: distribution of measured distances between mitochondria and MAM (upper chart, n=105) and measured length of intercellular tethers (lower chart, n=89). (C) Schematic illustration showing the principles of P2Y₁₂R density and membrane distance measurements using electron tomography (Fig. 2C, D). Single points of the microglial membrane were divided into two groups based on their closest distance from the neuronal membrane: closer than the average distance of 13 nm (red) or farther (green). For every observed point, P2Y₁₂R labeling gold particles were counted within a radius of 40 nm. In the bottom right corner, the distribution of measured points is shown in the case of a representative junction. (D) Transmission electron micrographs show Kv2.1 clusters on cortical neuronal cell bodies (arrowheads). Kv2.1-clustering and the association of the cluster with neuronal organelles is not affected by microglia depletion (right panel). (E) Transmission electron micrographs show TOM20-immunogold labeling in neocortical neurons. Immunogold labeling (black grains) is specifically associated with outer mitochondrial membranes, while TOM20-positive vesicles can also be observed (arrowheads). Some immunogold particles can be found on the plasma membrane of the neurons (arrows), suggesting the exocytosis of mitochondria-derived vesicles. Nucleus is blue, neuronal cytoplasm is magenta. Left and middle panel is the same as on Fig. 2H. (F) Electron micrographs from TOM20-Iba1 combined immunogold-immunoperoxidase reaction. Right upper panel is taken from a consecutive serial section and corresponds to the dashed area on the left panel. Right lower panel is enlarged from the right upper. Iba1-positive (dark DAB precipitate) microglial process contacts the cell body of a cortical pyramidal cell. TOM20-immunogold signal decorates the outer mitochondrial membrane, while arrows point to smaller membrane structures (putative MDVs), also positive for TOM20. Note the presence of a TOM20 positive vesicle attached to the neuronal plasmamembrane within the somatic junction on the right lower panel. (G) CLSM images show Lamp1-positive neuronal lysosomes closely apposed to neuronal Kv2.1-clusters. Right panel shows a microglial process touching a neuronal Kv2.1-cluster with closely located/attached Lamp1-positive lysosomes. (H) Kv2.1 accumulation does not overlap with somatic inhibitory terminals. CLSM images show perisomatic terminals stained with antibodies against cannabinoid receptor type 1 (CB1R) and PV (red) and neuronal Kv2.1 (magenta). Panels on the right show the area in white rectangle on the first image. Dashed lines mark clear separation between perisomatic boutons and Kv2.1-signal, n=220 perisomatic boutons tested for Kv2.1 from two mice. (I) Neuronal vNUT signal (cyan) is not present in perisomatic inhibitory terminals (red), n=194 perisomatic boutons tested for vNUT from two mice. Scale bars: 300 nm on A (400 for right bottom panel), 50 nm on B, 300 nm on D, E and F, 1 μ m on G (2 μ m for left panel), 2 μ m on H and I.

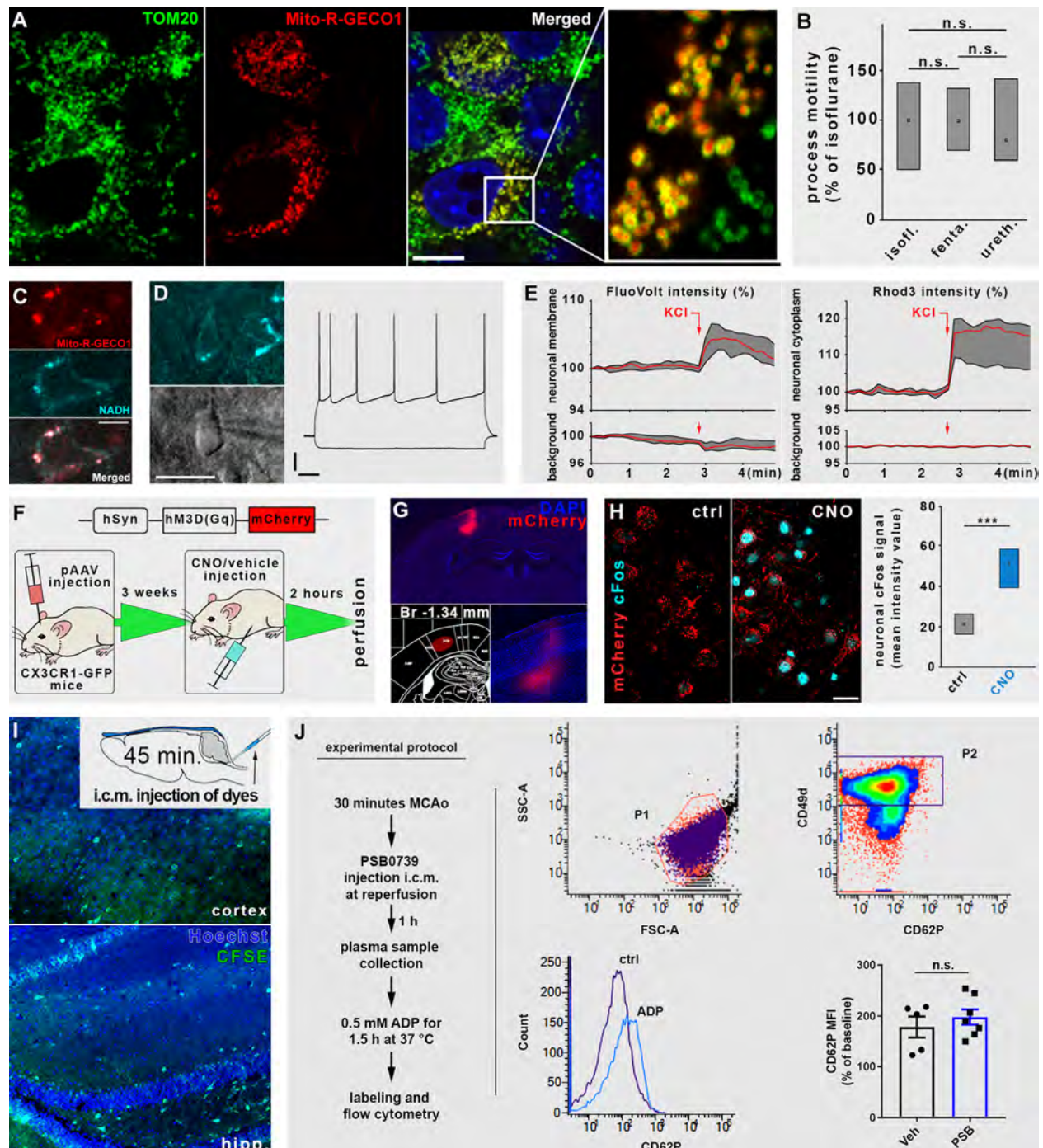


Fig. S5.

(A) Neuronal cell culture transfected with CMV-Mito-R-Geco1 and counterstained with TOM20 and DAPI. (B) Effects of different anaesthetics on microglial process motility. Median process motility observed: isoflurane 0.6 $\mu\text{m}/\text{min}$, 0.3-0.83 interquartile; fentanyl 0.6 $\mu\text{m}/\text{min}$, 0.42-0.78; urethane 0.48 $\mu\text{m}/\text{min}$, 0.36-0.84; $n=153$ processes from 9 animals. (C) Mito-R-Geco1 expression colocalizes with NADH intrinsic fluorescence. (D) Representative NADH intrinsic fluorescence image of a pyramidal cell. Left: Sample image of NADH fluorescence of neuronal somata. Middle: DIC image of the same region with whole cell patch clamp electrode. Right:

Electrophysiological recordings of membrane potential response to -100 and +160 pA current injections. Scales: 20 mV and 100 ms. **(E)** 40 mM KCl induces rapid membrane depolarization and calcium influx in cultured neurons in vitro. **(F)** Outline of chemogenetic experiments. **(G)** An example of an injection site. **(H)** CNO administration induced a 2.3-fold increase in cFos mean fluorescent intensity value in DREADD expressing neurons ($p < 0.001$, $n = 50$ -50 cells from 3 vehicle and 3 CNO-treated mice). **(I)** Mixture of carboxyfluorescein succinimidyl ester (CFSE) and Hoechst injected into the cisterna magna (i.c.m.) rapidly diffuses to all layers of neocortex and hippocampus. **(J)** Central blockade of microglial P2Y₁₂R with PSB does not alter ADP-induced platelet activation. Platelet rich plasma samples were collected from mice 1h after 30min MCAo and stimulated ex vivo with 0.5mM ADP for 1.5h at 37 °C. Platelets shown on SSC x FSC dot blots were labeled with anti-CD49d PE and anti-CD62P APC. ADP-induced increases in platelet CD62P were not altered in mice treated with i.c.m. PSB compared to vehicle-treated animals ($n = 5$ vehicle-treated and 7 PSB-treated samples). Unpaired t-test, n.s. – not significant. Scale bars: 10 μ m on A, 5 μ m on C, 25 μ m on D, 20 μ m on G. Median and interquartile ranges are plotted on B, E and H, mean+SEM is plotted on J.

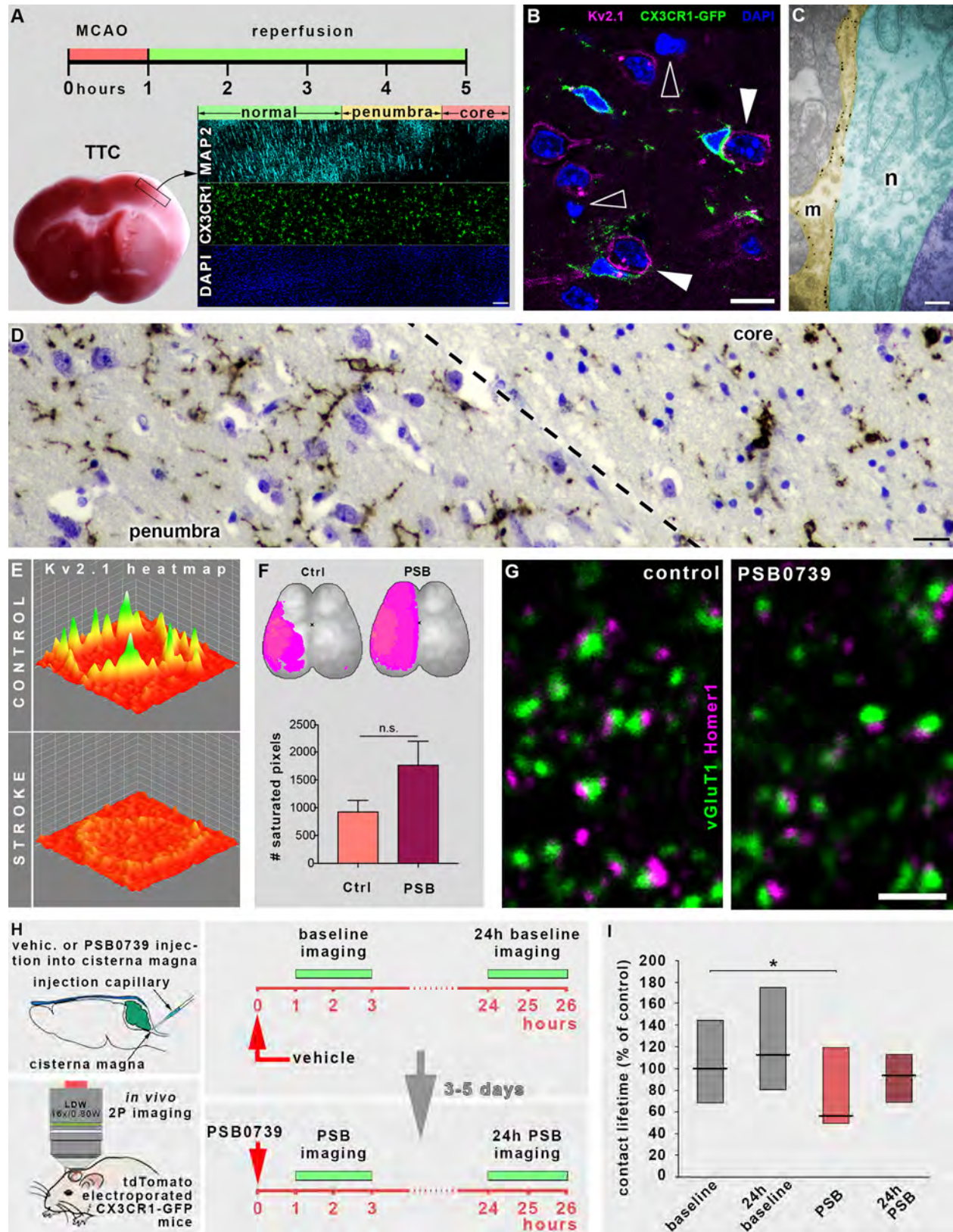


Fig. S6.

(A) Outline of middle cerebral artery occlusion (MCAo) experiment and delineation of core/penumbra regions of stroke affected brain. 1 hour MCAo was followed by 4 hours of reperfusion. Delineation was performed with the use of TTC staining and immunofluorescent labeling of MAP2 and microglia. (B) DAPI staining pattern reveals that neurons with increased microglial coverage (white arrowheads) in the penumbra region possess normal chromatin structure, confirming their viability. Empty arrowheads point to pycnotic nuclei. (C) Transmission electron micrograph shows a P2Y12R-immunogold particle labeled microglial process (yellow pseudocolour) covering a neuron in the penumbra region. Neuronal membrane integrity and chromatin structure are sustained. (D) Delineation of core/penumbra border in postmortem human cortical tissue. Neurons and nuclei are visualized by Nissl-staining (blue), microglia is labeled by anti-P2Y12R DAB-Ni immunoperoxidase reaction (dark brown precipitate). (E) Heatmaps of Kv2.1 immunostaining reveal that Kv2.1 clusters disappear after stroke in the penumbra. (F) The saturated calcium signal after experimental stroke (left MCAo in every experiment) corresponds to the dysfunctional tissue during the occlusion. The maps show an overlay of the area of saturated pixels (pink) of every animal in the two groups (n=9 control and 8 PSB-treated mice). (G) CLSM images show vGluT1 and Homer1 immunolabeling after acute i.c.m. administration of vehicle (control) or PSB. The closely apposed vGluT1 and Homer1 puncta represent glutamatergic synaptic contacts. PSB-treatment did not alter neocortical synapse numbers (0.353 synapse/ μm^2 in control, and 0.352 synapse/ μm^2 in PSB-injected, n=423 appositions from 4 animals). (H) Schematic outline of repeated 2P imaging of PSB effects. Vehicle was administered i.c.m., and baseline imaging performed between the 1st and 3rd hours after injection. The imaging session was repeated after 24h (24h baseline). After 3-5 days, PSB was injected i.c.m., and imaging performed between the 1st and 3rd hours after injection (PSB). The imaging session was repeated after 24h (24h PSB). (I) Acute central PSB administration decreased the contact lifetime to 56% of control, but this effect could not be observed after 24 hours (68.8-143.8% baseline interquartile range, 112.5% (81.3-175) 24h baseline, 56.3% (50-118.8) after PSB, 93.8 (68.8-112.5) 24h after PSB; p=0.0139, n=173 contacts from 3 mice). Scale bars: 100 μm on A, 10 μm on B, 300 nm on C, 12 μm on D, 2 μm on G. Mean+SEM is plotted on F, median and interquartile ranges on I.

Table S1.

Statistical data for analyses depicted on Figures 1K and S2E.

Localisation point density (LP/um2)						
animal	category	mean	S.E.M.	n	comparison (Tukey's multiple comparisons test)	p-value
GCamp6-injected	contact	136.8	10.02	12	contact vs. non-contact	<0,0001
	non-contact	60.42	7.719	12	contact vs. whole microglia	<0,0001
	whole microglia	76.8	5.128	12	whole microglia vs. non-contact	0.3179
camK2A/gfp/22	contact	142.6	17.17	18	contact vs. non-contact	<0,0001
	non-contact	52.2	10.08	17	contact vs. whole microglia	0.0008
	whole microglia	76.47	6.054	18	whole microglia vs. non-contact	0.3423
gad65_3e/gfp 5.5/30	contact	81.05	15.37	11	contact vs. non-contact	0.0116
	non-contact	38.62	4.892	13	contact vs. whole microglia	0.0197
	whole microglia	41.58	7.661	13	whole microglia vs. non-contact	0.973
BAC_pva/gfp/2	contact	93.75	21.59	10	contact vs. non-contact	0.0009
	non-contact	20.03	2.746	10	contact vs. whole microglia	0.003
	whole microglia	31.17	5.736	12	whole microglia vs. non-contact	0.7957
Cluster density (cluster/um2)						
animal	category	mean	S.E.M.	n	comparison (Tukey's multiple comparisons test)	p-value
GCamp6-injected	contact	0.9705	0.084	12	contact vs. non-contact	<0,0001
	non-contact	0.4451	0.071	12	contact vs. whole microglia	0.0004
	whole microglia	0.5401	0.055	12	whole microglia vs. non-contact	0.6164
camK2A/gfp/22	contact	0.6089	0.069	18	contact vs. non-contact	0.0002
	non-contact	0.3111	0.046	18	contact vs. whole microglia	0.0031
	whole microglia	0.3673	0.02	18	whole microglia vs. non-contact	0.7007
gad65_3e/gfp 5.5/30	contact	0.368	0.072	9	contact vs. non-contact	0.4608
	non-contact	0.2659	0.052	13	contact vs. whole microglia	0.4681
	whole microglia	0.2684	0.051	14	whole microglia vs. non-contact	0.9994
BAC_pva/gfp/2	contact	0.3726	0.062	10	contact vs. non-contact	0.0107
	non-contact	0.1839	0.024	11	contact vs. whole microglia	0.0553
	whole microglia	0.2293	0.036	12	whole microglia vs. non-contact	0.7145

Table S2.

Data of human patients.

Subject	Code	Gender	Age (years)	Health status	Survival after stroke (days)	Comorbidities	Cause of death	Tissue sample type
Stroke patient	2011/0092	female	77	normal	2	arterial hypertension, type II diabetes, hyperthyreosis	stroke	paraffin embedded sections
Stroke patient	2003/0029	male	66	preceding systemic inflammatory burden	1	arterial hypertension	stroke	paraffin embedded sections
Stroke patient	2014/0050	female	78	normal	1	unknown	stroke	paraffin embedded sections
Control subject	SKO3	female	59	normal	n.a.	ischemic cardiomyopathy	cardiogenic shock	free floating and paraffin sections
Control subject	SKO13	female	60	normal	n.a.	chronic bronchitis	respiratory arrest	free floating and paraffin sections
Control subject	SKO16	male	73	normal	n.a.	atherosclerosis, pneumonia	respiratory arrest	free floating and paraffin sections

Table S3.

List of antibodies used in the study.

Primary antibodies	host	source	catalog nr.	RRID
CB1	goat	MyBioSource	MBS422809	n.a.
CytC	mouse	BioLegend	612302	RRID:AB_315774
c-fos	guinea-pig	Synaptic Systems	226 004	RRID:AB_2619946
CD206	rat	BioRad	MCA2235	RRID:AB_324622
CD42d	armenian	eBioScience	12-0421-80	RRID:AB_10804037
CD62-P-APC	mouse	eBioScience	17-0626-80	RRID:AB_11218294
Gephyrin	mouse	Synaptic Systems	147 021	RRID:AB_2232546
GFAP	chicken	Synaptic Systems	173 006	RRID:AB_2619873
GFP	chicken	Invitrogen	A10262	RRID:AB_2534023
Homer1	chicken	Synaptic Systems	160 006	RRID:AB_2631222
Homer1	rabbit	Synaptic Systems	160 003	RRID:AB_887730
Iba1	goat	Novusbio	NB100-	RRID:AB_521594
Iba1	rabbit	Wako Chemicals	019-19741	RRID:AB_839504
Kv2.1	mouse	NeuroMab	75-014	RRID:AB_10673392
Kv2.1	rabbit	Synaptic Systems	231 002	RRID:AB_2131650
Kv2.2	rabbit	Synaptic Systems	231 103	RRID:AB_10805652
Lamp1	rabbit	Abcam	ab24170	RRID:AB_775978
MAP2	guniea-pig	Synaptic Systems	188 004	RRID:AB_2138181
NTPDase1	rabbit	Labome	rN1-6L	n.a.
P2Y12R	rabbit	Anaspec	AS-55042A	RRID:AB_2267540
P2Y12R	rabbit	Anaspec	AS-55043A	RRID:AB_2298886
Parvalbumin	goat	Swant	PVG 213	RRID:AB_2721207
PDGFRB	goat	R and D Systems	AF1042	RRID:AB_2162633
Pecam1	rat	BioLegend	102501	RRID:AB_312908
RFP	rat	ChromoTek	5f8-100	RRID:AB_2336064
SMA	mouse	Abcam	ab7817	RRID:AB_262054
SMI32	mouse	Covance	SMI-32P	RRID:AB_10719742
TOM20	rabbit	Santa Cruz	sc-11415	RRID:AB_2207533
vGAT	guinea pig	Synaptic Systems	131 004	RRID:AB_887873
vGluT1	guinea pig	Millipore	AB5905	RRID:AB_2301751
vGLuT3	guinea pig	Synaptic Systems	135 204	RRID:AB_2619825
vNUT	guinea pig	Millipore	ABN83	n.a.
Secondary antibodies				
biotinylated anti-rabbit	donkey	BioRad	644008	RRID:AB_619842
DyLight 405 anti-	donkey	Jackson	715-475-150	RRID:AB_2340839
Alexa 405 anti-rabbit	donkey	Jackson	711-475-152	RRID:AB_2340616
Alexa 488 anti-chicken	donkey	Jackson	703-546-155	RRID:AB_2340376
Alexa 488 anti-goat	donkey	Jackson	705-546-147	RRID:AB_2340430
Alexa 488 anti-rabbit	donkey	Jackson	711-546-152	RRID:AB_2340619
CF568 anti-mouse	donkey	Biotium	20802	RRID:AB_10853136

dc_2027_22

Alexa 594 anti-goat	donkey	LifeTech	A11058	RRID:AB_2534105
Alexa 594 anti-guinea	goat	LifeTech	A11076	RRID:AB_141930
Alexa 594 anti-mouse	donkey	LifeTech	A21203	RRID:AB_141633
Alexa 594 anti-rabbit	donkey	LifeTech	A21207	RRID:AB_141637
Alexa 594 anti-rat	donkey	Jackson	712-585-150	RRID:AB_2340688
Alexa 647 anti-goat	donkey	Jackson	705-606-147	RRID:AB_2340438
Alexa 647 anti-guinea	donkey	Jackson	706-606-148	RRID:AB_2340477
Alexa 647 anti-mouse	donkey	Jackson	715-605-150	RRID:AB_2340866
Alexa 647 anti-rabbit	donkey	Jackson	711-605-152	RRID:AB_2492288

Movie S1.

In vivo 2P time-lapse imaging shows temporal dynamics of microglia-neuron contacts. A tdTomato expressing neocortical neuron (red) is being contacted by processes of a microglial cell (green) in CX3CR1^{+/GFP} mouse electroporated in utero with pCAG-IRES-tdTomato. The analyzed trajectories of microglial processes contacting the neuron are shown on the right panel, warm colors label trajectories of somatic contacts, while cold colors label trajectories of microglial processes contacting neuronal dendrites. The middle panel shows the trajectories overlaid on the recording.

Movie S2.

In vitro CLSM time-lapse imaging of cocultured HEK293 and microglial cells. HEK cells were transfected with GFP-coupled control Kv2.1 construct on the left panel, and with YFP-coupled dominant-negative (DN) Kv2.1 construct on the right panel. Microglia is visualized by Alexa594-conjugated Lectin (red). Microglial processes contact Kv2.1-transfected HEK-cells at the clusters, but not those transfected with a dominant-negative mutant.

Movie S3.

Left: stack of electron tomographic 0.5 nm thick virtual sections shows the special nano-architecture of a somatic microglia-neuron junction with closely apposed mitochondria, mitochondria-associated membranes (MAMs) and cytoplasmic structures. The silver-intensified P2Y12R-immunogold grains are clearly visible at the cytoplasmic surface of microglial membrane. Note that large number of gold particles are clustered exactly where the neuronal cytoplasmic structure is anchored. Right: 3D model of the same tomographic volume, neuronal membrane is magenta, microglial membrane is green, immunogold particles white, mitochondria light blue, MAM light green, cytoplasmic densities red, vesicle-like structures blue and microglial reticular membrane structures darker green.

Movie S4.

Stack of electron tomographic virtual sections shows the special nano-architecture of the core of a somatic microglia-neuron junction. The silver-intensified P2Y12R-immunogold grains are clearly visible at the cytoplasmic surface of microglial membrane. The tethers between the anchored mitochondria and MAM are clearly visible. The neuronal cytoplasmic structure (mitochondria, MAM) is anchored to a membrane segment that is precisely facing the high density of P2Y12Rs on the microglial membrane. Note that distance between the neuronal and microglial membrane is the smallest exactly here, and intercellular tethers are also clearly visible.

Movie S5.

Left: stack of electron tomographic virtual sections shows the special nano-architecture of a somatic microglia-neuron junction with closely apposed mitochondria, MAMs and cytoplasmic structures. The silver-intensified P2Y12R-immunogold grains are clearly visible at the cytoplasmic surface of microglial membrane that touches the neuronal cell body, but are present only at a lower density at membrane segments, where the microglia touches a perisomatic bouton. Right: 3D model of the same tomographic volume, neuronal membrane is magenta, microglial membrane is ocker, immunogold particles white, mitochondria light blue, MAM light green, bouton membrane vivid green.

Movie S6.

In vivo 2P imaging of CX3CR1^{+/GFP} mice in utero electroporated with CAG-Mito-R-Geco1 construct. Dashed lines show the outline of a neuron, green microglial processes touch neuronal cell body where somatic mitochondria (red) are present. White arrows indicate the contact sites of microglia.

Movie S7.

In vitro CLSM time-lapse imaging of KCl-stimulation of quinacrine-loaded cultured neuron. Left panel shows transmitted channel and superimposed green channel (quinacrine-labeled ATP-containing vesicles), right panel shows the green channel and the outline of the neuron (white dashed line). White arrows point to vesicles that are released spontaneously, red arrows point to vesicles that are released after 40 mM KCl stimulation. MIP of z-stack (z-range: 2.5 μm), frame dimension: 12.3 x 22.2 μm .

References and Notes

1. M. S. Thion, F. Ginhoux, S. Garel, Microglia and early brain development: An intimate journey. *Science* **362**, 185–189 (2018). [doi:10.1126/science.aat0474](https://doi.org/10.1126/science.aat0474) [Medline](#)
2. K. Kierdorf, M. Prinz, Microglia in steady state. *J. Clin. Invest.* **127**, 3201–3209 (2017). [doi:10.1172/JCI90602](https://doi.org/10.1172/JCI90602) [Medline](#)
3. M. W. Salter, B. Stevens, Microglia emerge as central players in brain disease. *Nat. Med.* **23**, 1018–1027 (2017). [doi:10.1038/nm.4397](https://doi.org/10.1038/nm.4397) [Medline](#)
4. W. M. Song, M. Colonna, The identity and function of microglia in neurodegeneration. *Nat. Immunol.* **19**, 1048–1058 (2018). [doi:10.1038/s41590-018-0212-1](https://doi.org/10.1038/s41590-018-0212-1) [Medline](#)
5. D. Davalos, J. Grutzendler, G. Yang, J. V. Kim, Y. Zuo, S. Jung, D. R. Littman, M. L. Dustin, W.-B. Gan, ATP mediates rapid microglial response to local brain injury in vivo. *Nat. Neurosci.* **8**, 752–758 (2005). [doi:10.1038/nn1472](https://doi.org/10.1038/nn1472) [Medline](#)
6. A. Nimmerjahn, F. Kirchhoff, F. Helmchen, Resting microglial cells are highly dynamic surveillants of brain parenchyma in vivo. *Science* **308**, 1314–1318 (2005). [doi:10.1126/science.1110647](https://doi.org/10.1126/science.1110647) [Medline](#)
7. Y. Wu, L. Dissing-Olesen, B. A. MacVicar, B. Stevens, Microglia: Dynamic mediators of synapse development and plasticity. *Trends Immunol.* **36**, 605–613 (2015). [doi:10.1016/j.it.2015.08.008](https://doi.org/10.1016/j.it.2015.08.008) [Medline](#)
8. L. Weinhard, G. di Bartolomei, G. Bolasco, P. Machado, N. L. Schieber, U. Neniskyte, M. Exiga, A. Vadisiute, A. Raggioli, A. Schertel, Y. Schwab, C. T. Gross, Microglia remodel synapses by presynaptic trogocytosis and spine head filopodia induction. *Nat. Commun.* **9**, 1228 (2018). [doi:10.1038/s41467-018-03566-5](https://doi.org/10.1038/s41467-018-03566-5) [Medline](#)
9. J.-M. Cioni, M. Koppers, C. E. Holt, Molecular control of local translation in axon development and maintenance. *Curr. Opin. Neurobiol.* **51**, 86–94 (2018). [doi:10.1016/j.conb.2018.02.025](https://doi.org/10.1016/j.conb.2018.02.025) [Medline](#)
10. T. Misgeld, T. L. Schwarz, Mitostasis in neurons: Maintaining mitochondria in an extended cellular architecture. *Neuron* **96**, 651–666 (2017). [doi:10.1016/j.neuron.2017.09.055](https://doi.org/10.1016/j.neuron.2017.09.055) [Medline](#)
11. M. Terenzio, G. Schiavo, M. Fainzilber, Compartmentalized signaling in neurons: From cell biology to neuroscience. *Neuron* **96**, 667–679 (2017). [doi:10.1016/j.neuron.2017.10.015](https://doi.org/10.1016/j.neuron.2017.10.015) [Medline](#)
12. J. Aarum, K. Sandberg, S. L. B. Haeberlein, M. A. A. Persson, Migration and differentiation of neural precursor cells can be directed by microglia. *Proc. Natl. Acad. Sci. U.S.A.* **100**, 15983–15988 (2003). [doi:10.1073/pnas.2237050100](https://doi.org/10.1073/pnas.2237050100) [Medline](#)
13. M. Ueno, Y. Fujita, T. Tanaka, Y. Nakamura, J. Kikuta, M. Ishii, T. Yamashita, Layer V cortical neurons require microglial support for survival during postnatal development. *Nat. Neurosci.* **16**, 543–551 (2013). [doi:10.1038/nn.3358](https://doi.org/10.1038/nn.3358) [Medline](#)
14. J. L. Marín-Teva, M. A. Cuadros, D. Martín-Oliva, J. Navascués, Microglia and neuronal cell death. *Neuron Glia Biol.* **7**, 25–40 (2011). [doi:10.1017/S1740925X12000014](https://doi.org/10.1017/S1740925X12000014) [Medline](#)
15. A. Sierra, S. Beccari, I. Diaz-Aparicio, J. M. Encinas, S. Comeau, M.-È. Tremblay, Surveillance, phagocytosis, and inflammation: How never-resting microglia influence

- adult hippocampal neurogenesis. *Neural Plast.* **2014**, 610343 (2014).
[doi:10.1155/2014/610343](https://doi.org/10.1155/2014/610343) [Medline](#)
16. H. Wake, A. J. Moorhouse, S. Jinno, S. Kohsaka, J. Nabekura, Resting microglia directly monitor the functional state of synapses in vivo and determine the fate of ischemic terminals. *J. Neurosci.* **29**, 3974–3980 (2009). [doi:10.1523/JNEUROSCI.4363-08.2009](https://doi.org/10.1523/JNEUROSCI.4363-08.2009)
[Medline](#)
17. E. Deutsch, A. V. Weigel, E. J. Akin, P. Fox, G. Hansen, C. J. Haberkorn, R. Loftus, D. Krapf, M. M. Tamkun, Kv2.1 cell surface clusters are insertion platforms for ion channel delivery to the plasma membrane. *Mol. Biol. Cell* **23**, 2917–2929 (2012).
[doi:10.1091/mbc.e12-01-0047](https://doi.org/10.1091/mbc.e12-01-0047) [Medline](#)
18. L. Feinshreiber, D. Singer-Lahat, U. Ashery, I. Lotan, Voltage-gated potassium channel as a facilitator of exocytosis. *Ann. N. Y. Acad. Sci.* **1152**, 87–92 (2009). [doi:10.1111/j.1749-6632.2008.03997.x](https://doi.org/10.1111/j.1749-6632.2008.03997.x) [Medline](#)
19. M. Kirmiz, N. C. Vierra, S. Palacio, J. S. Trimmer, Identification of VAPA and VAPB as Kv2 channel-interacting proteins defining endoplasmic reticulum-plasma membrane junctions in mammalian brain neurons. *J. Neurosci.* **38**, 7562–7584 (2018).
[doi:10.1523/JNEUROSCI.0893-18.2018](https://doi.org/10.1523/JNEUROSCI.0893-18.2018) [Medline](#)
20. B. Jiang, X. Sun, K. Cao, R. Wang, Endogenous Kv channels in human embryonic kidney (HEK-293) cells. *Mol. Cell. Biochem.* **238**, 69–79 (2002). [doi:10.1023/A:1019907104763](https://doi.org/10.1023/A:1019907104763)
[Medline](#)
21. A. Menéndez-Méndez, J. I. Díaz-Hernández, F. Ortega, J. Gualix, R. Gómez-Villafuertes, M. T. Miras-Portugal, Specific temporal distribution and subcellular localization of a functional vesicular nucleotide transporter (VNUT) in cerebellar granule neurons. *Front. Pharmacol.* **8**, 951 (2017). [doi:10.3389/fphar.2017.00951](https://doi.org/10.3389/fphar.2017.00951) [Medline](#)
22. R. D. Fields, Nonsynaptic and nonvesicular ATP release from neurons and relevance to neuron-glia signaling. *Semin. Cell Dev. Biol.* **22**, 214–219 (2011).
[doi:10.1016/j.semcdb.2011.02.009](https://doi.org/10.1016/j.semcdb.2011.02.009) [Medline](#)
23. S. E. Haynes, G. Hollopeter, G. Yang, D. Kurpius, M. E. Dailey, W.-B. Gan, D. Julius, The P2Y₁₂ receptor regulates microglial activation by extracellular nucleotides. *Nat. Neurosci.* **9**, 1512–1519 (2006). [doi:10.1038/nn1805](https://doi.org/10.1038/nn1805) [Medline](#)
24. Y. Zhang, K. Chen, S. A. Sloan, M. L. Bennett, A. R. Scholze, S. O’Keeffe, H. P. Phatnani, P. Guarnieri, C. Caneda, N. Ruderisch, S. Deng, S. A. Liddelow, C. Zhang, R. Daneman, T. Maniatis, B. A. Barres, J. Q. Wu, An RNA-sequencing transcriptome and splicing database of glia, neurons, and vascular cells of the cerebral cortex. *J. Neurosci.* **34**, 11929–11947 (2014). [doi:10.1523/JNEUROSCI.1860-14.2014](https://doi.org/10.1523/JNEUROSCI.1860-14.2014) [Medline](#)
25. O. Butovsky, M. P. Jedrychowski, C. S. Moore, R. Cialic, A. J. Lanser, G. Gabriely, T. Koeglspenger, B. Dake, P. M. Wu, C. E. Doykan, Z. Fanek, L. Liu, Z. Chen, J. D. Rothstein, R. M. Ransohoff, S. P. Gygi, J. P. Antel, H. L. Weiner, Identification of a unique TGF- β -dependent molecular and functional signature in microglia. *Nat. Neurosci.* **17**, 131–143 (2014). [doi:10.1038/nn.3599](https://doi.org/10.1038/nn.3599) [Medline](#)
26. B. Dudok, L. Barna, M. Ledri, S. I. Szabó, E. Szabadits, B. Pintér, S. G. Woodhams, C. M. Henstridge, G. Y. Balla, R. Nyilas, C. Varga, S.-H. Lee, M. Matolcsi, J. Cervenak, I. Kacsokovics, M. Watanabe, C. Sagheddu, M. Melis, M. Pistis, I. Soltesz, I. Katona, Cell-

- specific STORM super-resolution imaging reveals nanoscale organization of cannabinoid signaling. *Nat. Neurosci.* **18**, 75–86 (2015). [doi:10.1038/nn.3892](https://doi.org/10.1038/nn.3892) [Medline](#)
27. I. D. Campbell, M. J. Humphries, Integrin structure, activation, and interactions. *Cold Spring Harb. Perspect. Biol.* **3**, a004994 (2011). [doi:10.1101/cshperspect.a004994](https://doi.org/10.1101/cshperspect.a004994) [Medline](#)
28. H. Akiyama, P. L. McGeer, Brain microglia constitutively express beta-2 integrins. *J. Neuroimmunol.* **30**, 81–93 (1990). [doi:10.1016/0165-5728\(90\)90055-R](https://doi.org/10.1016/0165-5728(90)90055-R) [Medline](#)
29. F. E. McCann, B. Vanherberghen, K. Eleme, L. M. Carlin, R. J. Newsam, D. Goulding, D. M. Davis, The size of the synaptic cleft and distinct distributions of filamentous actin, ezrin, CD43, and CD45 at activating and inhibitory human NK cell immune synapses. *J. Immunol.* **170**, 2862–2870 (2003). [doi:10.4049/jimmunol.170.6.2862](https://doi.org/10.4049/jimmunol.170.6.2862) [Medline](#)
30. G. Csordás, D. Weaver, G. Hajnóczky, Endoplasmic reticulum-mitochondrial contactology: Structure and signaling functions. *Trends Cell Biol.* **28**, 523–540 (2018). [doi:10.1016/j.tcb.2018.02.009](https://doi.org/10.1016/j.tcb.2018.02.009) [Medline](#)
31. A. Sugiura, G.-L. McLelland, E. A. Fon, H. M. McBride, A new pathway for mitochondrial quality control: Mitochondrial-derived vesicles. *EMBO J.* **33**, 2142–2156 (2014). [doi:10.15252/embj.201488104](https://doi.org/10.15252/embj.201488104) [Medline](#)
32. V. Soubannier, G.-L. McLelland, R. Zunino, E. Braschi, P. Rippstein, E. A. Fon, H. M. McBride, A vesicular transport pathway shuttles cargo from mitochondria to lysosomes. *Curr. Biol.* **22**, 135–141 (2012). [doi:10.1016/j.cub.2011.11.057](https://doi.org/10.1016/j.cub.2011.11.057) [Medline](#)
33. T. Ho, A. I. Jobling, U. Greferath, T. Chuang, A. Ramesh, E. L. Fletcher, K. A. Vessey, Vesicular expression and release of ATP from dopaminergic neurons of the mouse retina and midbrain. *Front. Cell. Neurosci.* **9**, 389 (2015). [doi:10.3389/fncel.2015.00389](https://doi.org/10.3389/fncel.2015.00389) [Medline](#)
34. Y. Moriyama, M. Hiasa, S. Sakamoto, H. Omote, M. Nomura, Vesicular nucleotide transporter (VNUT): Appearance of an actress on the stage of purinergic signaling. *Purinergic Signal.* **13**, 387–404 (2017). [doi:10.1007/s11302-017-9568-1](https://doi.org/10.1007/s11302-017-9568-1) [Medline](#)
35. A. M. Brennan, J. A. Connor, C. W. Shuttleworth, NAD(P)H fluorescence transients after synaptic activity in brain slices: Predominant role of mitochondrial function. *J. Cereb. Blood Flow Metab.* **26**, 1389–1406 (2006). [doi:10.1038/sj.jcbfm.9600292](https://doi.org/10.1038/sj.jcbfm.9600292) [Medline](#)
36. X. Zhang, Y. Chen, C. Wang, L.-Y. M. Huang, Neuronal somatic ATP release triggers neuron-satellite glial cell communication in dorsal root ganglia. *Proc. Natl. Acad. Sci. U.S.A.* **104**, 9864–9869 (2007). [doi:10.1073/pnas.0611048104](https://doi.org/10.1073/pnas.0611048104) [Medline](#)
37. G. Szalay, B. Martinecz, N. Lénárt, Z. Környei, B. Orsolits, L. Judák, E. Császár, R. Fekete, B. L. West, G. Katona, B. Rózsa, Á. Dénes, Microglia protect against brain injury and their selective elimination dysregulates neuronal network activity after stroke. *Nat. Commun.* **7**, 11499 (2016). [doi:10.1038/ncomms11499](https://doi.org/10.1038/ncomms11499) [Medline](#)
38. J. O. Onukwufor, D. Stevens, C. Kamunde, Bioenergetic and volume regulatory effects of mitoKATP channel modulators protect against hypoxia-reoxygenation-induced mitochondrial dysfunction. *J. Exp. Biol.* **219**, 2743–2751 (2016). [doi:10.1242/jeb.140186](https://doi.org/10.1242/jeb.140186) [Medline](#)
39. F. Orsini, S. Fumagalli, E. Császár, K. Tóth, D. De Blasio, R. Zangari, N. Lénárt, Á. Dénes, M.-G. De Simoni, Mannose-binding lectin drives platelet inflammatory phenotype and

- vascular damage after cerebral ischemia in mice via IL (interleukin)-1 α . *Arterioscler. Thromb. Vasc. Biol.* **38**, 2678–2690 (2018). [doi:10.1161/ATVBAHA.118.311058](https://doi.org/10.1161/ATVBAHA.118.311058) [Medline](#)
40. K. Bekő, B. Koványi, F. Göloncsér, G. Horváth, Á. Dénes, Z. Környei, B. Botz, Z. Helyes, C. E. Müller, B. Sperlágh, Contribution of platelet P2Y₁₂ receptors to chronic Complete Freund's adjuvant-induced inflammatory pain. *J. Thromb. Haemost.* **15**, 1223–1235 (2017). [doi:10.1111/jth.13684](https://doi.org/10.1111/jth.13684) [Medline](#)
41. Y. Li, X.-F. Du, C.-S. Liu, Z.-L. Wen, J.-L. Du, Reciprocal regulation between resting microglial dynamics and neuronal activity in vivo. *Dev. Cell* **23**, 1189–1202 (2012). [doi:10.1016/j.devcel.2012.10.027](https://doi.org/10.1016/j.devcel.2012.10.027) [Medline](#)
42. R. D. Stowell, E. L. Wong, H. N. Batchelor, M. S. Mendes, C. E. Lamantia, B. S. Whitelaw, A. K. Majewska, Cerebellar microglia are dynamically unique and survey Purkinje neurons in vivo. *Dev. Neurobiol.* **78**, 627–644 (2018). [doi:10.1002/dneu.22572](https://doi.org/10.1002/dneu.22572) [Medline](#)
43. C. N. Hall, M. C. Klein-Flügge, C. Howarth, D. Attwell, Oxidative phosphorylation, not glycolysis, powers presynaptic and postsynaptic mechanisms underlying brain information processing. *J. Neurosci.* **32**, 8940–8951 (2012). [doi:10.1523/JNEUROSCI.0026-12.2012](https://doi.org/10.1523/JNEUROSCI.0026-12.2012) [Medline](#)
44. N. S. Chandel, Mitochondria as signaling organelles. *BMC Biol.* **12**, 34 (2014). [doi:10.1186/1741-7007-12-34](https://doi.org/10.1186/1741-7007-12-34) [Medline](#)
45. E. I. Rugarli, T. Langer, Mitochondrial quality control: A matter of life and death for neurons. *EMBO J.* **31**, 1336–1349 (2012). [doi:10.1038/emboj.2012.38](https://doi.org/10.1038/emboj.2012.38) [Medline](#)
46. A. Kasahara, L. Scorrano, Mitochondria: From cell death executioners to regulators of cell differentiation. *Trends Cell Biol.* **24**, 761–770 (2014). [doi:10.1016/j.tcb.2014.08.005](https://doi.org/10.1016/j.tcb.2014.08.005) [Medline](#)
47. D. Arnoult, F. Soares, I. Tattoli, S. E. Girardin, Mitochondria in innate immunity. *EMBO Rep.* **12**, 901–910 (2011). [doi:10.1038/embor.2011.157](https://doi.org/10.1038/embor.2011.157) [Medline](#)
48. G. R. Bantug, M. Fischer, J. Grählert, M. L. Balmer, G. Unterstab, L. Develioglu, R. Steiner, L. Zhang, A. S. H. Costa, P. M. Gubser, A.-V. Burgener, U. Sauder, J. Löliger, R. Belle, S. Dimeloe, J. Lötscher, A. Jauch, M. Recher, G. Hönger, M. N. Hall, P. Romero, C. Frezza, C. Hess, Mitochondria-endoplasmic reticulum contact sites function as immunometabolic hubs that orchestrate the rapid recall response of memory CD8⁺ T cells. *Immunity* **48**, 542–555.e6 (2018). [doi:10.1016/j.immuni.2018.02.012](https://doi.org/10.1016/j.immuni.2018.02.012) [Medline](#)
49. A. U. Joshi, D. Mochly-Rosen, Mortal engines: Mitochondrial bioenergetics and dysfunction in neurodegenerative diseases. *Pharmacol. Res.* **138**, 2–15 (2018). [doi:10.1016/j.phrs.2018.08.010](https://doi.org/10.1016/j.phrs.2018.08.010) [Medline](#)
50. J. Rieusset, Mitochondria-associated membranes (MAMs): An emerging platform connecting energy and immune sensing to metabolic flexibility. *Biochem. Biophys. Res. Commun.* **500**, 35–44 (2018). [doi:10.1016/j.bbrc.2017.06.097](https://doi.org/10.1016/j.bbrc.2017.06.097) [Medline](#)
51. R. Bravo-Sagua, A. E. Rodriguez, J. Kuzmicic, T. Gutierrez, C. Lopez-Crisosto, C. Quiroga, J. Díaz-Elizondo, M. Chiong, T. G. Gillette, B. A. Rothermel, S. Lavandero, Cell death and survival through the endoplasmic reticulum-mitochondrial axis. *Curr. Mol. Med.* **13**, 317–329 (2013). [doi:10.2174/156652413804810781](https://doi.org/10.2174/156652413804810781) [Medline](#)

52. G.-L. McLelland, S. A. Lee, H. M. McBride, E. A. Fon, Syntaxin-17 delivers PINK1/parkin-dependent mitochondrial vesicles to the endolysosomal system. *J. Cell Biol.* **214**, 275–291 (2016). [doi:10.1083/jcb.201603105](https://doi.org/10.1083/jcb.201603105) [Medline](#)
53. P. D. Fox, C. J. Haberkorn, E. J. Akin, P. J. Seel, D. Krapf, M. M. Tamkun, Induction of stable ER-plasma-membrane junctions by Kv2.1 potassium channels. *J. Cell Sci.* **128**, 2096–2105 (2015). [doi:10.1242/jcs.166009](https://doi.org/10.1242/jcs.166009) [Medline](#)
54. C. Madry, V. Kyrargyri, I. L. Arancibia-Cárcamo, R. Jolivet, S. Kohsaka, R. M. Bryan, D. Attwell, Microglial ramification, surveillance, and interleukin-1 β release are regulated by the two-pore domain K⁺ channel THIK-1. *Neuron* **97**, 299–312.e6 (2018). [doi:10.1016/j.neuron.2017.12.002](https://doi.org/10.1016/j.neuron.2017.12.002) [Medline](#)
55. R. Fekete, C. Cserép, N. Lénárt, K. Tóth, B. Orsolits, B. Martinecz, E. Méhes, B. Szabó, V. Németh, B. Gönci, B. Sperlágh, Z. Boldogkői, Á. Kittel, M. Baranyi, S. Ferenczi, K. Kovács, G. Szalay, B. Rózsa, C. Webb, G. G. Kovacs, T. Hortobágyi, B. L. West, Z. Környei, Á. Dénes, Microglia control the spread of neurotropic virus infection via P2Y12 signalling and recruit monocytes through P2Y12-independent mechanisms. *Acta Neuropathol.* **136**, 461–482 (2018). [doi:10.1007/s00401-018-1885-0](https://doi.org/10.1007/s00401-018-1885-0) [Medline](#)
56. G. Marchal, V. Beaudouin, P. Rioux, V. de la Sayette, F. Le Doze, F. Viader, J. M. Derlon, J. C. Baron, Prolonged persistence of substantial volumes of potentially viable brain tissue after stroke: A correlative PET-CT study with voxel-based data analysis. *Stroke* **27**, 599–606 (1996). [doi:10.1161/01.STR.27.4.599](https://doi.org/10.1161/01.STR.27.4.599) [Medline](#)
57. J. C. Baron, M. E. Moseley, For how long is brain tissue salvageable? Imaging-based evidence. *J. Stroke Cerebrovasc. Dis.* **9**, 15–20 (2000). [doi:10.1053/jscd.2000.18910](https://doi.org/10.1053/jscd.2000.18910) [Medline](#)
58. X. Wang, C. Zhang, G. Szábo, Q.-Q. Sun, Distribution of CaMKII α expression in the brain in vivo, studied by CaMKII α -GFP mice. *Brain Res.* **1518**, 9–25 (2013). [doi:10.1016/j.brainres.2013.04.042](https://doi.org/10.1016/j.brainres.2013.04.042) [Medline](#)
59. A. H. Meyer, I. Katona, M. Blatow, A. Rozov, H. Monyer, In vivo labeling of parvalbumin-positive interneurons and analysis of electrical coupling in identified neurons. *J. Neurosci.* **22**, 7055–7064 (2002). [doi:10.1523/JNEUROSCI.22-16-07055.2002](https://doi.org/10.1523/JNEUROSCI.22-16-07055.2002) [Medline](#)
60. G. López-Bendito, K. Sturgess, F. Erdélyi, G. Szabó, Z. Molnár, O. Paulsen, Preferential origin and layer destination of GAD65-GFP cortical interneurons. *Cereb. Cortex* **14**, 1122–1133 (2004). [doi:10.1093/cercor/bhh072](https://doi.org/10.1093/cercor/bhh072) [Medline](#)
61. H. Dana, T.-W. Chen, A. Hu, B. C. Shields, C. Guo, L. L. Looger, D. S. Kim, K. Svoboda, Thy1-GCaMP6 transgenic mice for neuronal population imaging in vivo. *PLOS ONE* **9**, e108697 (2014). [doi:10.1371/journal.pone.0108697](https://doi.org/10.1371/journal.pone.0108697) [Medline](#)
62. K. L. Schaar, M. M. Brenneman, S. I. Savitz, Functional assessments in the rodent stroke model. *Exp. Transl. Stroke Med.* **2**, 13 (2010). [doi:10.1186/2040-7378-2-13](https://doi.org/10.1186/2040-7378-2-13) [Medline](#)
63. J. B. Bederson, L. H. Pitts, M. Tsuji, M. C. Nishimura, R. L. Davis, H. Bartkowski, Rat middle cerebral artery occlusion: Evaluation of the model and development of a neurologic examination. *Stroke* **17**, 472–476 (1986). [doi:10.1161/01.STR.17.3.472](https://doi.org/10.1161/01.STR.17.3.472) [Medline](#)
64. K. L. Singel, K. S. Grzankowski, A. N. M. N. H. Khan, M. J. Grimm, A. C. D’Auria, K. Morrell, K. H. Eng, B. Hylander, P. C. Mayor, T. R. Emmons, N. Lénárt, R. Fekete, Z.

- Környei, U. Muthukrishnan, J. D. Gilthorpe, C. F. Urban, K. Itagaki, C. J. Hauser, C. Leifer, K. B. Moysich, K. Odunsi, Á. Dénes, B. H. Segal, Mitochondrial DNA in the tumour microenvironment activates neutrophils and is associated with worse outcomes in patients with advanced epithelial ovarian cancer. *Br. J. Cancer* **120**, 207–217 (2019). [doi:10.1038/s41416-018-0339-8](https://doi.org/10.1038/s41416-018-0339-8) [Medline](#)
65. J. R. Kremer, D. N. Mastronarde, J. R. McIntosh, Computer visualization of three-dimensional image data using IMOD. *J. Struct. Biol.* **116**, 71–76 (1996). [doi:10.1006/jsbi.1996.0013](https://doi.org/10.1006/jsbi.1996.0013) [Medline](#)
66. J. V. Cramer, B. Gesierich, S. Roth, M. Dichgans, M. Düring, A. Liesz, In vivo widefield calcium imaging of the mouse cortex for analysis of network connectivity in health and brain disease. *Neuroimage* **199**, 570–584 (2019). [doi:10.1016/j.neuroimage.2019.06.014](https://doi.org/10.1016/j.neuroimage.2019.06.014) [Medline](#)
67. D. Hinkle, W. Wiersma, S. Jurs, *Applied Statistics for the Behavioral Sciences* (Houghton Mifflin, ed. 5, 2002).

Microglia alter the threshold of spreading depolarization and related potassium uptake in the mouse brain

Journal of Cerebral Blood Flow & Metabolism

0(0) 1–14

© The Author(s) 2020

Article reuse guidelines:

sagepub.com/journals-permissions

DOI: 10.1177/0271678X19900097

journals.sagepub.com/home/jcbfm



Dániel P Varga¹, Ákos Menyhárt¹, Balázs Pósfai^{2,3} ,
 Eszter Császár^{2,3}, Nikolett Lénárt², Csaba Cserép² ,
 Barbara Orsolits², Bernadett Martinecz², Tamás Szlepák^{2,3},
 Ferenc Bari¹, Eszter Farkas^{1,*} and Ádám Dénes^{2,*}

Abstract

Selective elimination of microglia from the brain was shown to dysregulate neuronal Ca^{2+} signaling and to reduce the incidence of spreading depolarization (SD) during cerebral ischemia. However, the mechanisms through which microglia interfere with SD remained unexplored. Here, we identify microglia as essential modulators of the induction and evolution of SD in the physiologically intact brain in vivo. Confocal- and super-resolution microscopy revealed that a series of SDs induced rapid morphological changes in microglia, facilitated microglial process recruitment to neurons and increased the density of P2Y12 receptors (P2Y12R) on recruited microglial processes. In line with this, depolarization and hyperpolarization during SD were microglia- and P2Y12R-dependent. An absence of microglia was associated with altered potassium uptake after SD and increased the number of c-fos-positive neurons, independently of P2Y12R. Thus, the presence of microglia is likely to be essential to maintain the electrical elicitation threshold and to support the full evolution of SD, conceivably by interfering with the extracellular potassium homeostasis of the brain through sustaining $[\text{K}^+]_e$ re-uptake mechanisms.

Keywords

Microglia, spreading depolarization, P2Y12 receptor, extracellular potassium clearance, inflammation

Received 27 June 2019; Revised 13 December 2019; Accepted 13 December 2019

Introduction

Microglia play many roles in the brain beyond their primary immune function, including the removal of terminally injured neurons and the support of tissue repair through their interactions with neurons or glial cells.^{1–3} In addition, microglia are critical for the consolidation of neuronal networks. Microglia monitor synaptic function, prune redundant boutons in a complement-mediated manner and assist synapse formation by secreting brain-derived neurotrophic factor.^{4,5} In the healthy adult brain, surveilling microglia are characterized by motile, ramified processes, which form contacts with different compartments of neurons and respond to increased neuronal depolarization. In turn, the spontaneous and evoked activity of the contacted neurons is suppressed.⁶ Microglia–neuron interactions may be partially independent of astrocytes, because blockade of astrocyte function by

fluoroacetate did not alter glutamate-induced microglial process recruitment to neurons.⁷

Microglia respond to a wide range of stimuli via purinergic signaling. For example, P2Y12R, which is

¹Department of Medical Physics and Informatics, University of Szeged, Szeged, Hungary

²Laboratory of Neuroimmunology, Institute of Experimental Medicine, Budapest, Hungary

³Szentágothai János Doctoral School of Neuroscience, Semmelweis University, Budapest, Hungary

*Co-senior authors.

Corresponding authors:

Ádám Dénes, Laboratory of Neuroimmunology, Institute of Experimental Medicine, Szigony u. 43. Budapest H-1038, Hungary.

Email: denes.adam@koki.mta.hu

Eszter Farkas, Department of Medical Physics and Informatics, University of Szeged, Szeged, H-6720, Hungary.

Email: eszter.farkas.szeged@gmail.com

specifically expressed by microglia in the brain,⁸ is essential for ATP-induced chemotaxis, process outgrowth to injury, and enhanced surveillance activity.^{9,10} In turn, microglia can release a wide range of signaling molecules including pro-inflammatory cytokines (IL-1b, IL-18, TNF- α) or K⁺, which can modulate neuronal excitability.^{9,11–14}

We have previously found that selective elimination of microglia with a colony-stimulating factor 1 receptor (CSF1R) kinase inhibitor¹⁵ triggered slow neuronal calcium oscillations (0.1 Hz) in the acute phase of focal cerebral ischemia in mice, while the spontaneous occurrence of cortical spreading depolarization (SD) was hampered.¹⁶ SD is a self-propagating wave of abrupt, transient, mass depolarization that reflects a near-complete breakdown of neuronal transmembrane ion gradients and travels slowly (3–5 mm/min) over the cerebrocortical gray matter.^{17,18} The hallmark of SD is a negative shift in the local field potential filtered in direct current (DC) mode, and an immense elevation of extracellular potassium ([K⁺]_e) and glutamate concentration, accompanied by cellular swelling and the initiation of inflammatory cascades.^{19–22} SD has been recognized as a potentially harmful event promoting secondary injury in the metabolically compromised ischemic brain, and has been recognized to be the cellular counterpart of migraine aura.²³

Microglia react to SD by increased IL-1 β release,^{24,25} and enhanced outward potassium conductivity.²⁶ They have also been shown to remain reactive for days after series of SDs triggered in rats²⁷ and to modulate SD initiation *ex vivo*.²⁸ However, the mechanisms through which microglia may tune the susceptibility of the nervous tissue to SD are yet to be explored *in vivo*. Neuronal hyperexcitability and impaired K⁺ clearance have long been accepted as key contributors to the evolution of SD.^{29,30} Thus, we hypothesized that surveilling or activated microglia may sustain SD susceptibility by interfering with either of these mechanisms. Accordingly, we investigated whether the presence of microglia is critical for the elicitation or the propagation of an SD triggered in the nervous tissue at resting state (i.e. no prior SDs occurred), and for recurrent SDs *in vivo*. To understand the mechanisms involved, we evaluated [K⁺]_e changes associated with SDs using ion-selective microelectrodes in microglia-depleted and P2Y12R knock out (P2Y12R KO) mice, and analyzed nanoscale changes in the expression of microglial P2Y12R using super-resolution microscopy.

Materials and methods

Mice

Experiments were carried out in 12–14-weeks-old adult male C57BL/6J ($n = 28$) and P2Y12R KO (#TF1881,

Taconic) ($n = 7$) mice (male, C57BL/6J background), bred in the SPF unit of the Institute of Experimental Medicine (Budapest, Hungary). The animals were housed under controlled temperature, humidity and lightning conditions (23°C, 12:12-h light/dark cycle, lights on at 7 a.m.), with *ad libitum* access to food and water.

Selective elimination of microglia was performed in C57BL/6J mice ($n = 12$) by feeding a chow diet containing CSF1R inhibitor, PLX5622 for three weeks.¹⁵ PLX5622 was provided by Plexikon Inc. and formulated in AIN-76A standard chow by Research Diets (1200 p.p.m.; 1200 mg PLX5622 in 1 kg chow). Body temperature was recorded for every mouse before surgery or electrophysiological recording. No mice were excluded from these studies due to fever, weight loss, infection or behavioral alterations as a result of PLX5622 treatment. P2Y12R KO mice ($n = 7$) and reference groups ($n = 14$) were on control diet (Supplementary Table 1).

Surgical procedures

All procedures were approved by the National Food Chain Safety and Animal Health Directorate of Csongrád County, Hungary, conforming to the guidelines of the Scientific Committee of Animal Experimentation of the Hungarian Academy of Sciences (updated Law and Regulations on Animal Protection: 40/2013. (II. 14.) Gov. of Hungary), following the EU Directive 2010/63/EU on the protection of animals used for scientific purposes, and reported in compliance with the ARRIVE guidelines.

Mice were anesthetized with 1.5–2% isoflurane in N₂O:O₂ (3:2) and were allowed to breathe spontaneously through a head mask. Atropine (0.1%, 0.01 ml) was injected intramuscularly to avoid the production of airway mucus. Body temperature was maintained at 37°C with a servo-controlled heating pad (507222 F, Harvard Apparatus, USA). The animal was fixed in a stereotaxic frame, and two craniotomies (3 mm lateral from sagittal suture, –1 and –3 caudal from bregma) were created with a dental drill (ProLab Basic, Bien Air, Switzerland) on the right parietal bone. The dura mater in each craniotomy was left intact. The rostral window was used for SD elicitation, while electrophysiological variables were monitored in the caudal window. To assess whether any focal inflammatory reaction developed at the site of electrode insertion, microglial activation, leukocyte recruitment and vascular activation were investigated by Iba1, CD45 and ICAM-1 immunofluorescence, respectively. Only minor changes in microglial morphology were noticed no deeper than 100 μ m below the meninges, while no increases in CD45 or ICAM-1 immunofluorescence

were found. Quantitative measurements took place remotely from the site of electrode insertion (Figure 1).

Experimental protocols

Two series of experiments were designed (Supplementary Table 1). In series 1, the electrical threshold of SD induction was determined, whereas in series 2, $[K^+]_e$ was assessed during SD induced with a topical application of 1 M KCl in the absence of microglia or P2Y12R.

Electrophysiology

In series 1, a glass capillary electrode (outer tip diameter = 20 μm) filled with physiological saline was inserted into the cortex. An Ag/AgCl reference electrode was implanted under the skin of the animal's neck. DC potential was recorded via a high input impedance pre-amplifier (NL100AK, Digitimer Ltd, UK), connected to a differential amplifier with associate filter and conditioner systems (NL107, NL125 and NL530, Digitimer Ltd, UK). Potential line frequency noise (50 Hz) was removed by a noise eliminator (HumBug, Quest Scientific Instruments, Canada). The resulting signal was then digitized and continuously acquired at a sampling frequency of 500 Hz with a dedicated analog-to-digital (A/D) converter (NI USB-6008/6009, National Instruments, USA) controlled through a custom-made software in Labview (National Instruments, USA).

In series 2, ion-sensitive microelectrodes were prepared according to Viitanen et al.³¹ Glass capillary microelectrode tips (outer tip diameter: 10–12 μm) were filled with a liquid K^+ -ion exchanger (Potassium ionophore I – cocktail A; Sigma-Aldrich, Germany),^{31,32} and the shank of the microelectrode was backfilled with 100 mM KCl. Each K^+ -selective microelectrode was calibrated in standard solutions of known K^+ concentrations (1, 3, 5, 10, 30, 50 and 100 mM) (Figure 3(a)).³³ In each experiment, a K^+ -sensitive microelectrode was lowered into the cortex, together with another microelectrode (outer tip diameter = 20 μm) filled with 150 mM NaCl and 1 mM HEPES to serve as reference and acquire DC potential (<1 Hz). An Ag/AgCl electrode implanted under the skin of the animal's neck was used as common ground. Microelectrodes were connected to a custom-made dual-channel high input impedance electrometer (including AD549LH, Analog Devices, USA) via Ag/AgCl leads. The voltage signal recorded by the reference electrode was subtracted from that of the K^+ -sensitive microelectrode by dedicated differential amplifiers and associated filter modules (NL106 and NL125, Digitimer Ltd, UK), which yielded potential variations related to changes in $[K^+]_e$. The recorded

signals were then forwarded to an A/D converter (MP 150, BIOPAC Systems, USA) and digitized by a sample rate of 1 kHz using the software AcqKnowledge 4.2.0 (BIOPAC Systems, USA). The completed preparations were enclosed in a Faraday cage. K^+ signals were displayed together with the DC potential essentially as described above.

Induction of SD

In each animal, four SDs were triggered at a 15-min of inter-SD interval. In series 1, SDs were triggered as reported earlier.³⁴ Briefly, a concentric bipolar needle electrode with a tip diameter of 40 μm (Neuronelektrod KFT, Hungary) was placed upon the dura. It was connected to an opto-coupled stimulus isolator with a constant current output (NL 800, Digitimer Ltd, UK), a pulse generator (NL301), a with-delay panel (NL405), and a pulse buffer (NL510), which enabled the adjustment of amplitude and duration of the stimuli at will. Stimulation was implemented with a single bipolar constant current stimulation. The charge delivered was quantified as $Q(\mu\text{C}) = I(\text{mA}) \times t(\text{ms})$, and it was raised stepwise with an interstimulus interval of 1 min until SD was observed. Whenever necessary, the position of the needle electrode was adjusted to optimize the contact between the electrode tip and the tissue. Successful elicitation of SD was confirmed by a negative DC-shift of an amplitude greater than 5 mV at the recording electrode.

In series 2, a cotton ball soaked in 1 M KCl was placed into the rostral cranial window. The cotton ball was removed, and the cranial window rinsed with artificial cerebrospinal fluid (aCSF; mM concentrations: 126.6 NaCl, 3 KCl, 1.5 CaCl_2 , 1.2 MgCl_2 , 24.5 NaHCO_3 , 6.7 urea, 3.7 glucose bubbled with 95% O_2 and 5% CO_2 to achieve a constant pH of 7.4) immediately after each successful elicitation.

Tissue processing and immunostaining

Following in vivo measurements, mice were deeply anesthetized with an overdose of chloral hydrate (i.p.). For immunohistochemistry, animals were transcardially perfused with ice-cold saline followed by 4% paraformaldehyde 1.5 h after the induction of the first SD. Subsequently, the brains were removed, post-fixed and cryoprotected overnight in 10% sucrose/4% PFA/PBS and were stored in 10% sucrose/PBS at 4°C until 25 μm thick coronal sections were prepared using a sliding microtome (Leica SM 2010 R).

Immunofluorescence

Thick free-floating brain sections (25 μm) were blocked with 5–10% normal donkey serum for 1 h and incubated with different primary antibodies at 4°C,

overnight: rabbit anti-Iba-1 (1:1000, #019-19741, Wako Chemicals), goat anti-Iba1 (1:500, NB100-1028, Novusbio), rabbit anti-P2Y12R (1:1000, #55043 A, AnaSpec), rabbit anti-c-fos (1:500, #sc-52, Santa Cruz Biotechnology), guinea pig anti-c-fos (1:500, #226 004, Synaptic Systems), chicken anti-GFAP (1:500, #173 006, Synaptic Systems), guinea pig anti-glutamine synthetase (1:500, #367 005, Synaptic Systems), rat anti-CD45 (1:250, #MCA1388, Bio-Rad), goat anti-ICAM-1 (1:250, #AF796, R&D Systems) and mouse anti-Kv2.1 (1:500, #75-014 NeuroMab). Sections were washed several times with TBS and incubated with the corresponding secondary antibody (Jackson ImmunoResearch, unless specified below) for 2 h: donkey anti-rabbit Alexa 488 (1:1000, #711-546-152), donkey anti-mouse Alexa 488 (1:1000, #715-006-151), donkey anti-chicken Alexa 488 (1:500, #703-546-155), donkey anti-goat Alexa488 (1:500, #705-546-147), donkey anti-rabbit CF568 (1:1000, #20098-1mg, Biotium), donkey anti-rabbit Alexa 594 (1:5000, #A21207, Invitrogen), donkey anti-mouse Alexa 594 (1:500, #715-586-151), donkey anti-rabbit Alexa 647 (1:1000, #711-605-152), donkey anti-mouse Alexa 647 (1:1000, #715-605-150), donkey anti-guinea pig Alexa647 (1:500, #706-606-148). After washing, sections were mounted on glass slides and coverslipped (Fluoromount-G, Southern Biotech).

STORM super-resolution microscopy

To examine the exact localization of P2Y12R, STORM imaging was performed. Immunolabeled (rabbit anti-P2Y12R, 1:1000, #55043 A, AnaSpec, mouse anti-Kv2.1 1:500, #75-014 NeuroMab) sections were covered with imaging medium³⁵ immediately before imaging. Correlated confocal and super-resolution imaging was performed with VividSTORM (donkey anti-rabbit Alexa 647, 1:1000, #711-605-152, Jackson ImmunoResearch, donkey anti-mouse Alexa 488, 1:1000, #715-006-151, Jackson ImmunoResearch, donkey anti-rabbit CF568, 1:1000, #20098-1mg, Biotium). Images were captured with a Nikon N-STORM C2+ super-resolution system based on the platform of a Nikon Ti-E inverted microscope, equipped with a Nikon C2 confocal scan head and an Andor iXon Ultra 897 EMCCD camera and a CFI Apo TIRF 100× objective. Image acquisition and processing were performed using Nikon NIS-Elements AR software with N-STORM module.

Quantitative analysis

In the PLX5622-treated groups, microglia depletion was validated based on P2Y12R immunofluorescence

(Figure 1(d)). Two mice were excluded from the analysis pre hoc due to insufficient microglia depletion (less than 85%).

All physiological variables (i.e. DC potential and $[K^+]_e$) were first downsampled to 1 Hz, then either analyzed with the inbuilt tools of AcqKnowledge 4.2.0 (BIOPAC System, USA) software, or were transferred into a MATLAB environment (MathWorks, USA). The transient negative DC shift indicative of SD was analyzed to assess amplitude of depolarization, duration of depolarization at half amplitude and area under the curve of post-SD hyperpolarization. Raw $[K^+]_e$ data expressed in mV were translated into mM concentration using polynomial cubic regression ($R^2=1$) on calibration solutions of data range (1, 3, 10, 30 mM).³⁶ Polynomial regression was used to determine subtle changes in the lower range of the $[K^+]_e$ concentration accurately. Baseline level of $[K^+]_e$ was determined by sampling a 1-min average before induction of each SD. Changes in $[K^+]_e$ during SD were analyzed to determine: peak $[K^+]_e$, and duration at half maximum and AUC of potassium elevation. The rate of $[K^+]_e$ release was determined by linear regression, while half-time recovery of $[K^+]_e$ to baseline ($[K^+]_e$ clearance) was calculated by exponential regression as described previously.³³

Immunofluorescent quantification

To assess the level of microglia depletion after PLX5622 treatment, images were captured with Zeiss Axiovert 200 M epi-fluorescent microscope and the number of P2Y12R-positive cells counted in three randomly selected ROIs at five different coronal sections from the cortex, hippocampus and striatum.

The number of activated neurons was counted based on c-fos immunostaining on three different coronal sections. Two ROIs (200 $\mu\text{m} \times 300 \mu\text{m}$) were placed near to, and one ROI was placed distant from the stimulating electrode and the number of c-fos positive cells was averaged in each ROI.

Astrocyte reaction to SD was investigated by staining of glial fibrillary acidic protein (GFAP) and glutamine synthetase (GS) on free floating coronal brain sections and images were taken with a 20× objective by Nikon A1R confocal system guided by NIS-Elements Microscope Imaging Software. Integrated density values were measured in three ipsilateral and three contralateral ROIs (250 $\mu\text{m} \times 80 \mu\text{m}$).

For precise microglial morphology analysis, sections were analyzed and only those included that had the best signal-to-noise ratio (crisp microglia-specific staining with low background). Confocal images were taken with a 60× objective by Nikon A1R confocal system

guided by NIS-Elements Microscope Imaging Software with a Z-step of 1 μm . Two-dimensional morphological analysis was performed on maximum intensity projection images of the confocal stacks. Data were analyzed using GraphPad Prism 8.0. software.

STORM super-resolution microscopy analysis

The 3D STORM localization points were filtered for photon number, z position (within -300 ; 300 nm axial distances from the center plane) and local density using VividSTORM software.³⁵ The clusters of selected localization points were determined by the density-based spatial clustering of applications with noise (DBSCAN) algorithm.

Statistical analysis

The statistical approach used has been specified in each figure legend. The software SPSS (SPSS Statistics, Version 22.0, IBM, USA) or the inbuilt statistical functions of MATLAB (MathWorks, USA) were used for statistical analysis. The distribution of the data was tested with Shapiro–Wilk normality test. Outliers were filtered with Grubbs test. Homogeneity of the variances was checked by Levene’s test. A Friedman analysis of variance (ANOVA) and Mann–Whitney U test were used to evaluate electrical threshold level differences of SD induction. A one-way ANOVA model followed by Tukey’s HSD or Games-Howell post hoc test was applied for the analysis of variables derived from the DC potential signature of SD, $[\text{K}^+]_e$ shift with SD, whereas data from series 1 were evaluated by independent t-test or Welch-t test, dependent on the type of data set. A repeated measures paradigm was used to evaluate baseline $[\text{K}^+]_e$ changes. Mann–Whitney U test was used to assess morphological changes (cell body area, number of branches) in microglia labelled with Iba1. Data from P2Y12R, P2Y12R/Kv2.1 immunofluorescence and combined P2Y12R confocal and STORM labeling were analyzed with unpaired-t test, while data from GFAP, GS, Kv2.1/c-fos immunofluorescence were analyzed using two-way ANOVA followed by Sidak’s multiple comparison. The level of significance was defined as $p < 0.05^*$ and $p < 0.01^{**}$.

Data and software availability

Supplementary material for this paper can be found at <http://jcbfm.sagepub.com/content/by/supplemental-data>. All reagents and protocols used in this study are available for sharing upon reasonable request to the authors.

Results

SD facilitates microglia-to-neuron interactions, while microglia depletion alters the electrical threshold of SD elicitation

SD travels across the cerebral cortex restricted to the ipsilateral hemisphere,³⁷ and microglia are supposed to detect changes in neuronal activity induced by SD.^{26,38} To test the possible effect of repeated SDs on microglia, we first performed 2D morphology analysis on representative microglial cells sampled randomly from the ipsi- and the corresponding contralateral insular cortex of mice (Figure 1(a) and (b)). We found a small, but significant decrease in the area of microglial cell bodies (ipsilateral: $36.14 \mu\text{m}^2$ (median, 32.2 – 42.2 interquartile range), $n = 66$ cells; contralateral: $38.84 \mu\text{m}^2$ (33.6 – 44.36), $n = 79$ cells from three mice), and the number of microglial processes originating from the soma was reduced by 17% ($n = 79$ cells from three mice). SD did not affect microglial numbers in the ipsilateral hemisphere (not shown). Next, we assessed the relationship between microglial processes and neurons in two representative areas in the cerebral cortex (Figure 1(c)). P2Y12R-positive microglial processes were recruited to the vicinity of neurons in the cerebral cortex after repeated SD induction leading to a 25% increase in microglial process density around the neuronal soma visualized by Kv2.1 immunostaining, which was most apparent in the ROI closer to SD induction (Figure 1(c)). This was in line with our earlier observation made under ischemic conditions by using in vivo two-photon imaging.¹⁶

To investigate the functional contribution of microglia to neuronal responses following a series of SDs, we selectively eliminated microglia from the brain (Figure 1(d)).⁸ The electric threshold of SD elicitation was expressed as the lowest electric charge sufficient to trigger SD (Figure 1(e) and (f)). The initiation of the first SD (SD1) required lower electric charge in the microglia depleted group (41 ± 30 vs. $88 \pm 28 \mu\text{C}$; depleted vs. control), whereas the electric threshold of elicitation for recurrent SDs (rSDs) increased considerably in the microglia depleted group (182 ± 120 vs. $85 \pm 30 \mu\text{C}$; microglia depleted vs. control) (Figure 1(f)). Statistical analysis confirmed that the elicitation of a series of subsequent rSDs at the absence of microglia required increasingly greater electric charge (from 41 ± 30 to $210 \pm 120 \mu\text{C}$, corresponding to SD1 and SD4 in the microglia-depleted group). In contrast, the charge necessary for SD elicitation did not change during a series of SDs in the control group (Figure 1(e)). Similarly, during the chemical elicitation (series 2), 1 M KCl proved to be sufficient to trigger SDs repeatedly in the control group, yet higher concentrations of

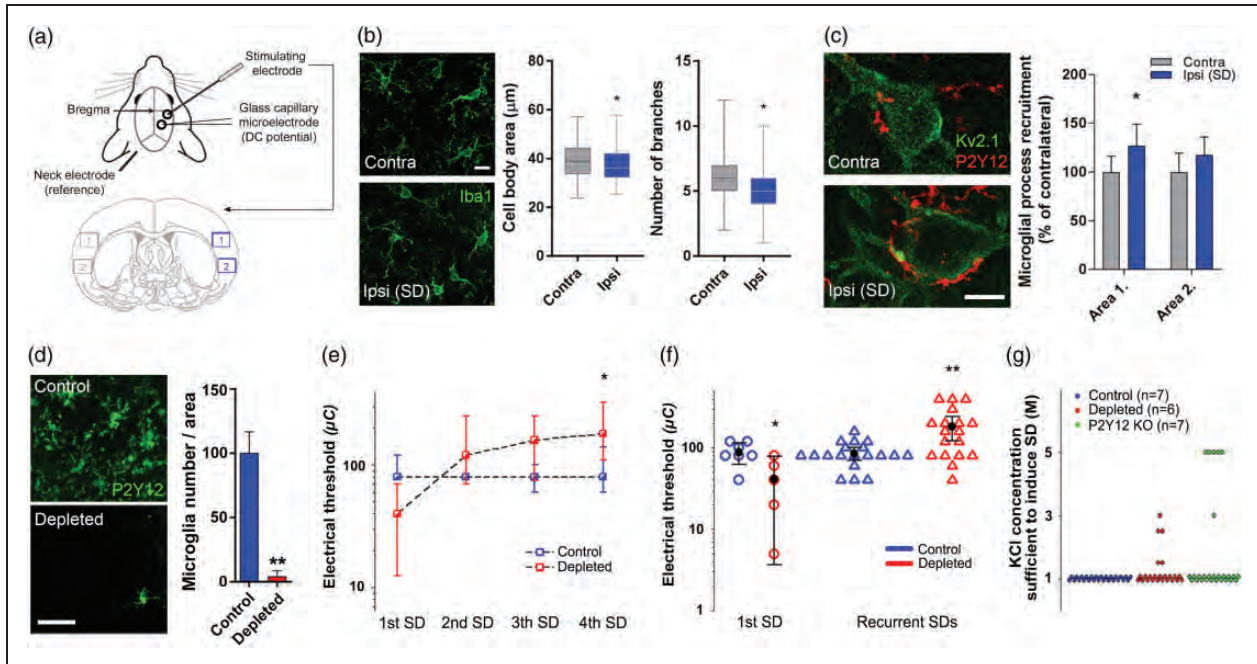


Figure 1. Spreading depolarization (SD) attracts microglial processes to neuronal somata and selective elimination of microglia alters the electrical threshold of SD elicitation. (a) Schematic illustration of the experimental setting in series 1, and areas of quantification for the immunofluorescent analysis shown in Panels (b) and (c). Area size ($420 \mu\text{m} \times 320 \mu\text{m}$). (b) Changes in microglial cell body area and the number of branches as obtained from 2D morphological analysis of Iba1-positive microglia in the cerebral cortex (the region used for analysis is identical to Area 1 shown in panel (a)). Mann–Whitney U test ($p < 0.05^*$). Scale bar, $10 \mu\text{m}$. (c) Representative images demonstrating microglial (P2Y12R, red) process recruitment to Kv2.1 labeled neuronal soma (green) in the neocortex, contralateral and ipsilateral to SD elicitation. Microglial process density is increased around neurons in the ipsilateral cortex relative to the contralateral cortex in Area 1 (near SD induction) depicted in Panel A. Data are expressed as mean \pm stdev. Control vs. ipsi $p < 0.01$, two-way ANOVA followed by Sidak’s multiple comparison test ($p < 0.05$ for Area 1). Scale bar, $10 \mu\text{m}$. (d) Representative images and quantitative analysis confirming elimination of microglia (P2Y12 receptors, green) after feeding mice a PLX5622 (1200 ppm)-containing diet for three weeks. Data are expressed as mean \pm stdev. Unpaired t-test ($p < 0.01^{**}$). Scale bar, $50 \mu\text{m}$. (e) Microglia depletion increased the electric threshold of SD elicitation for each consecutive SD in a train (Series 1). Data are shown as median and interquartile ranges. Friedman ANOVA for time ($p < 0.05^*$ vs. 1st SD, in the depleted group), and a Mann–Whitney U test for group comparison (no significant differences between groups). (f) Microglia depletion altered the electric threshold of SD elicitation (series 1). First SDs (circles) are shown apart from pooled, recurrent SDs (triangles). Black circle and error bars stand for mean \pm 95% CI. Mann–Whitney U test ($p < 0.05^*$ and $p < 0.01^{**}$ vs. respective Control). (g) The induction of SD required a KCl concentration higher than 1 M in some of the microglia-depleted and P2Y12R KO animals (series 2). Each colored sphere in the graph stands for the induction of an individual SD.

KCl were required to induce SDs in the microglia depleted and P2Y12R KO groups (1.25 ± 0.57 and 1.81 ± 1.6 vs. 1.0 M KCl; microglia depleted and P2Y12R KO vs. control, Figure 1(g)). Thus, microglia appear to be substantially involved in the induction of SDs in the otherwise healthy brain.

The DC potential signature of SD is altered by selective microglia elimination or in the absence of functional P2Y12R signaling

P2Y12R signaling is essential for microglial process chemotaxis towards sites of tissue damage or neuronal hyperactivity in response to the release of purinergic metabolites such as ATP, ADP or adenosine,³⁹ while

adenosine is released to the extracellular space upon the development of SD.⁴⁰ We found that a series of SDs resulted in increased P2Y12R immunopositivity (by 27%) in microglia in the ipsilateral side (Figure 2(a)). Next, we visualized P2Y12 receptors at 20 nm lateral resolution by using STORM super-resolution microscopy as established earlier,¹⁶ which are specific for microglia in the brain.⁸ We found that a series of SDs increased the density of P2Y12R on microglial processes in the vicinity of the neuronal soma (278 ± 29 and 404 ± 44 clustered NLP/cluster in the contralateral side vs. ipsilaterally after SD, Figure 2(b)), suggesting that recruited microglial processes upregulate and/or redistribute P2Y12R in response to SD. The absence of microglial P2Y12Rs also resulted in

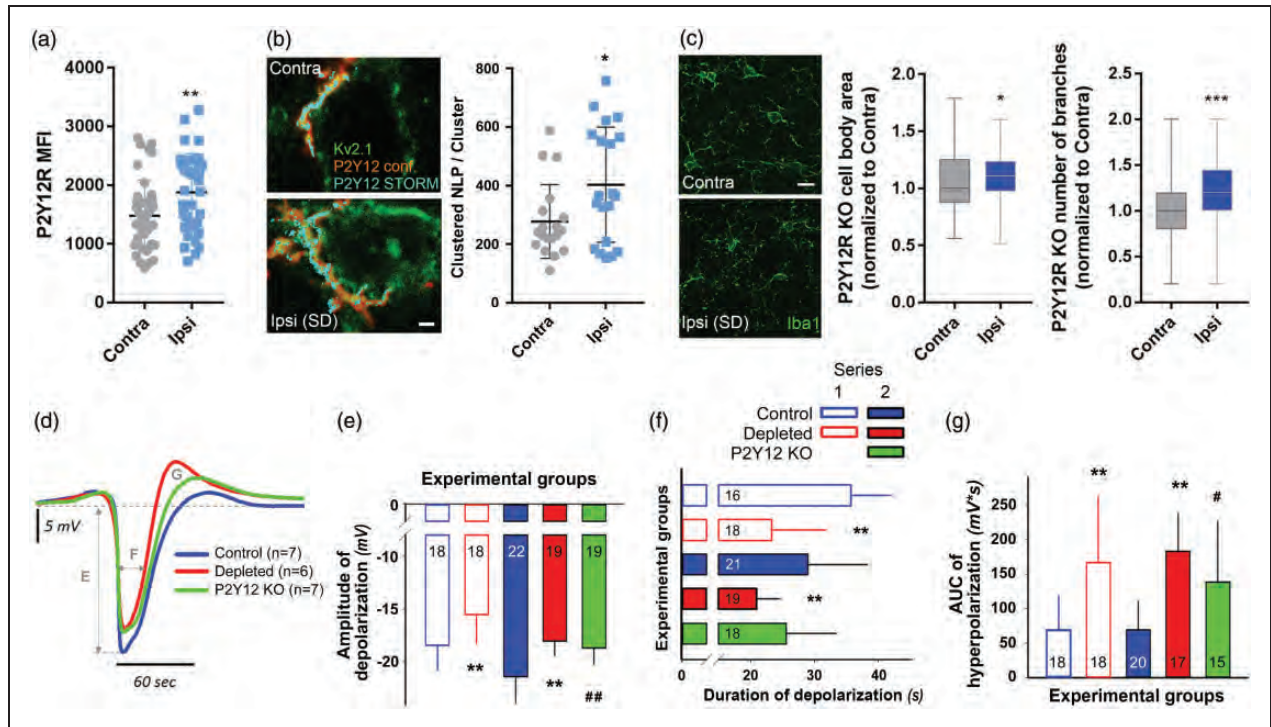


Figure 2. Selective elimination of microglia or absence of P2Y12R curbs SD and supports hyperpolarization after SD. (a) Confocal analysis revealed increased microglial P2Y12R mean fluorescence intensity (MFI) in response to a series of SDs (assessed in Area I according to Figure 1 (a)). Unpaired *t*-test, $n = 40$ randomly selected microglia from the contralateral hemisphere and $n = 38$ microglia from the ipsilateral hemisphere from seven mice per group. (b) Representative images depict the enrichment of P2Y12R (STORM, cyan) on microglial processes (P2Y12R, confocal, red) recruited to the Kv2.1 (green) labeled neurons in the neocortex, contralateral and ipsilateral to SD elicitation. Scale bar, 1000 nm. STORM super-resolution microscopy reveals increased P2Y12R densities on microglial processes recruited to neurons, in response to SD. Mean \pm stdev values of the number of localization points (NLP) are shown normalized to P2Y12R clusters determined by the density-based spatial clustering of applications with noise (DBSCAN) algorithm (Local density filter: 10 neighbours within 150 nm Z-filter: ± 300 nm from focal plane). Unpaired *t* test, $p < 0.05^*$, $n = 20$ neurons randomly selected from seven mice per group. (c) Changes in microglial cell body area and the number of branches in P2Y12R KO mice as obtained from 2D morphological analysis of Iba1-positive microglia in the cerebral cortex (the region used for analysis is identical to Area I shown on Figure 1 Panel (a)). Values normalized to the contralateral side are shown as median \pm interquartile range. Mann-Whitney U test, ($p < 0.05^*$). Scale bar, 10 μ m. (d) The direct current (DC) potential signature of recurrent SDs (rSDs) (each trace is the mean of rSDs in each experimental group, series 2). Capital letters indicate variables quantitated in the respective Panels. (e) Amplitude of the negative DC potential shift of rSDs (series 1 and 2). (f) Duration of the negative DC potential shift of rSDs (series 1 and 2). (g) Area under the curve of the hyperpolarization after rSDs (series 1 and 2). In Panels (d)–(f), data are given as mean \pm stdev. Sample size is indicated in each bar. Statistical analysis of data in series 1 relied on an independent *t*-test or a Welch-*t* test. Data in series 2 were evaluated by a one-way ANOVA paradigm followed by a multiple comparison of Tukey for equal variances, or Games-Howell for unequal variances ($p < 0.01^{**}$ depleted vs. respective control, $p < 0.05^{\#}$ and $p < 0.01^{\#\#}$ P2Y12R KO vs. respective control).

altered microglial response to repeated SDs: opposite to the decrease in cell body area and number of branches observed in wild type mice ipsilaterally to SDs, P2Y12R KO microglial cells showed an increase in these parameters after SDs (P2Y12R KO somatic area – ipsi: 1.11 of contralateral value (0.97–1.24), $n = 66$ cells; contra: 1 (0.88–1.25), $n = 86$ cells from three mice; P2Y12R KO number of branches – ipsi: 1.2 (1–1.4) of contralateral value; contra: 1 (0.8–1.2); Figure 2(c)).

Subsequently, we studied whether P2Y12R-mediated actions in microglia contribute to the

evolution of SD. In agreement with the results that microglia depletion elevates the elicitation threshold of rSDs, both microglia depletion and the absence of P2Y12R decreased the amplitude of rSDs consistent for both electrical (series 1) and chemical (i.e. 1M KCl, series 2) SD elicitation (-15.5 ± 2.8 vs. -18.4 ± 2.3 mV, microglia depleted vs. control, series 1; -18 ± 1.3 and -18.7 ± 1.5 vs. -21.4 ± 2.5 mV, microglia depleted and P2Y12R KO vs. control, series 2) (Figure 2(d) and (e)). However, the duration of depolarization was shorter only in the microglia-depleted groups, but not in P2Y12R KO mice, with respect to

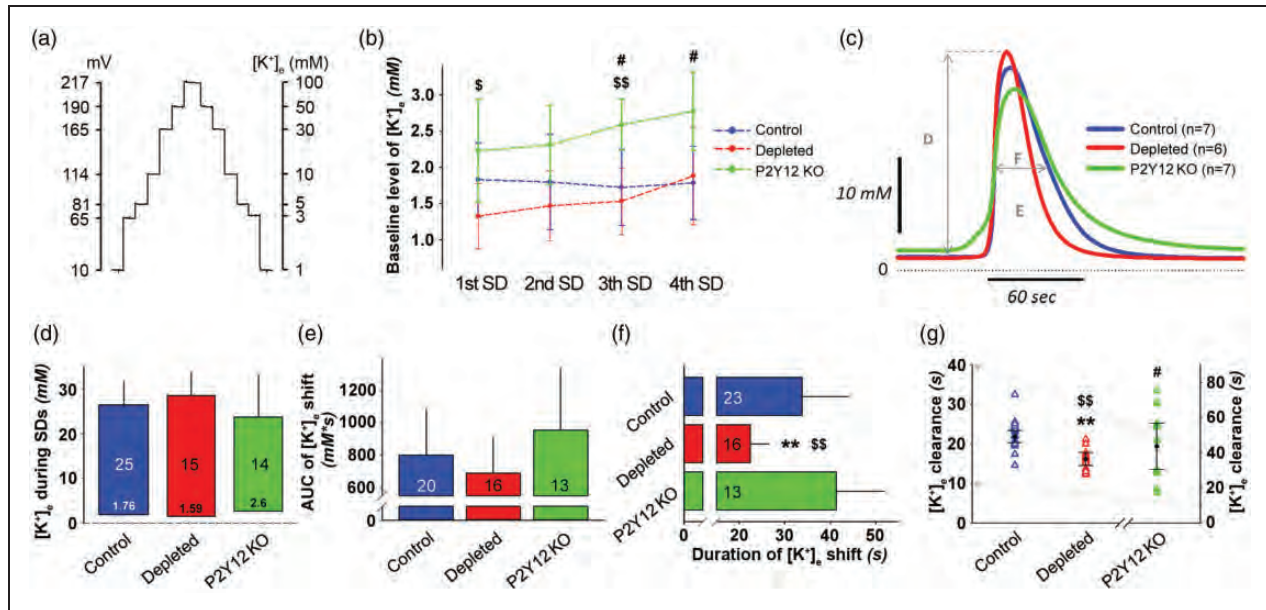


Figure 3. Selective elimination of microglia shortens the duration of spreading depolarization (SD)-related potassium elevation. (a) Calibration curve for the K⁺-selective microelectrodes using K⁺ solution standards (1, 3, 5, 10, 30, 50, and 100 mM KCl). Microelectrodes were calibrated before and after each in vivo measurement. (b) Baseline level of extracellular potassium concentration ([K⁺]_e) (mean of 60 s) immediately before the induction of each SD. Data are given as mean ± stdev. Repeated measures ANOVA for within group variation, and one-way ANOVA followed by Tukey's multiple comparison for group evaluation ($p < 0.05^{\$}$ and $p < 0.01^{\$\$}$ P2Y12R KO vs. depleted, $p < 0.05^{\#}$ P2Y12R KO vs. control). (c) The transient increase of [K⁺]_e with recurrent SDs (rSDs) (each trace is the mean of rSDs in each experimental group, series 2). Capital letters indicate variables quantitated in the respective Panels. (d) Peak elevation of the [K⁺]_e shift with rSDs. The base of each bar in the chart is set at [K⁺]_e immediately prior to rSDs. (e) Magnitude of the [K⁺]_e shift with rSDs, expressed as area under the curve (AUC). (f) Duration of the [K⁺]_e shift with rSDs, taken at half amplitude. (g) [K⁺]_e clearance, calculated by an exponential regression at half-time recovery of [K⁺]_e to baseline. In Panels (d)–(f), data are given as mean ± stdev. Sample size is indicated in each bar. In Panel (g), triangles denote individual values, while black circle and error bars stand for mean ± CI. Note, that the y-axis for control and depleted (left) is an expanded segment of the y-axis (right) for P2Y12R KO (grey arrows). One-way ANOVA followed by Tukey's multiple comparison for equal variances, or Games-Howell for unequal variances ($p < 0.01^{**}$ Depleted vs. control, $p < 0.05^{\$}$ and $p < 0.01^{\$\$}$ P2Y12R KO vs. depleted, $p < 0.05^{\#}$ P2Y12R KO vs. Control).

the control (23.3 ± 8.5 vs. 35.7 ± 6.2 s, microglia depleted vs. control, series 1; 20.9 ± 3.6 vs. 29 ± 9.3 and 25.6 ± 7.8 s, microglia depleted vs. control and P2Y12R KO, series 2) (Figure 2(f)). Finally, the AUC of post-SD hyperpolarization increased in both microglia-depleted and P2Y12R KO mice (166.8 ± 96 vs. 68.8 ± 49 mV × s, microglia depleted vs. control, series 1; 182.8 ± 54.3 vs. 138.6 ± 87.9 vs. 68.9 ± 41.1 mV × s, microglia depleted vs. P2Y12R KO vs. control, series 2) (Figure 2(g)). Thus, microglia appear to contribute to SD propagation – in part – via P2Y12R.

The absence of microglia but not of P2Y12R limits the duration of [K⁺]_e shift during SD

The quantitative assessment of [K⁺]_e variation by potassium-selective microelectrodes was conducted in series 2 (Figure 3(a), Supplementary Table 1). Baseline [K⁺]_e (i.e. the value taken prior to the elicitation of each SD in a train) proved to be consistently

higher in P2Y12R KO mice compared to controls or the microglia-depleted group (Figure 3(b)), although the higher concentration remained within the physiological range throughout (i.e. below 4–5 mM) and is, therefore, not expected to have significant pathophysiological consequences. In line with this, microglia depletion did not alter baseline [K⁺]_e or physiological interstitial potassium levels in the cortex (Figure 3(b)).

The analysis of the [K⁺]_e shift with rSDs did not reveal any notable difference in magnitude characterized by the peak amplitude or the AUC across different groups of mice (Figure 3(c) to (e)). However, the duration of [K⁺]_e shift was considerably shorter in the absence of microglia compared to the other two groups (22.4 ± 4 vs. 33.8 ± 10.2 and 41.3 ± 10.6 s, microglia depleted vs. control and P2Y12R KO) (Figure 3(f)), which is consistent with the shorter duration of the DC potential deflection in the same mice (Figure 2(f)). At last, a more rapid clearance of [K⁺]_e was revealed in microglia-depleted mice compared to

the other groups. At the same time, $[K^+]_e$ clearance in the P2Y12R KO mice was hindered with respect to both other groups (16.2 ± 3 vs. 21.8 ± 3.5 and 43.6 ± 21.1 s, microglia depleted vs. control and P2Y12R KO, Figure 3(g)). Taken together, activated microglia seem not only to elongate K^+ release but also to decelerate $[K^+]_e$ uptake, whereas P2Y12 receptor signaling seems not to be involved in these processes.

The absence of microglia alters neuronal activation in response to SD

Since the effects of microglia depletion and P2Y12R-deficiency on potassium uptake after SDs were different and astrocytes are known to contribute to K^+ clearance in the brain,⁴¹ we investigated whether SD induction resulted in changes in astrocyte GFAP and glutamine synthetase (GS) levels. No significant changes in the integrated density of GFAP and GS immunofluorescence were seen in response to SD (Figure 4(a)), and levels were not altered in P2Y12R KO or microglia-depleted mice (Figure 4(b)). We next investigated whether the absence of microglia or P2Y12R-deficiency resulted in any changes in neuronal activation in response to SD. The transcription of c-fos is controlled by an increase in the intracellular Ca^{2+} concentration,⁴² which occurs in neurons in response to SD.^{43,44} We found that recurrent SDs markedly increased neuronal c-fos expression in the ipsilateral hemisphere (by 54% in Area 1, 88% in Area 2 and 124% in Area 3), compared to the contralateral side (Figure 4(c)). Importantly, the number of c-fos-positive neurons markedly increased in the microglia-depleted group, which was most apparent in the insular cortex and less obvious in the cingulum, in line with the area of SD induction and propagation (Figure 4(c)). These differences were not seen in the insular cortex of P2Y12R KO mice (Figure 4(d)).

Discussion

Here, we identify microglia as essential modulators of the induction of SD in the physiologically intact brain, in vivo. Moreover, we show that SD alters microglial responses that include enhanced interaction between microglia and neurons, which is associated with sustained potassium uptake and altered neuronal activity after SD. Indeed, c-fos expression induced by SD is attenuated by the inhibition of NMDA receptors or voltage-gated calcium channels,^{44,45} both involved in physiological neuronal signaling,⁴⁶ SD evolution⁴⁷ and excitotoxic injury.⁴⁸ Our results also provide mechanistic insight into how microglial responses are altered by SD, in part via P2Y12R.

First, we sought to determine whether microglia react to SD in the physiologically intact mouse brain in vivo. Our histological findings that activated microglial processes are recruited to neurons in response to SD, while P2Y12Rs are upregulated and redistributed at this interface extrapolate that microglia sense SD and are ideally positioned to modulate neuronal activity in the non-ischemic brain. In line with our findings, the upregulation of P2Y12R on spinal cord microglia was found to promote hypersensitivity of the nociceptive network in the development of neuropathic pain after peripheral nerve injury.⁴⁹

Subsequently, we set out to investigate whether selective elimination of microglia alters SD induction in the mouse brain. With constant current stimulation 1 mm rostral to the implanted microelectrodes, we reliably induced SD with no interference with the acquired electrophysiological parameters,³⁴ while the sensibility of the nervous tissue for SD elicitation could be precisely determined. Our data indicate that microglia are essential to maintain the susceptibility of the cerebral cortex for SD. Interestingly, the absence of microglia may render the otherwise intact brain more sensitive to the initiation of an SD, whereupon subsequent SDs are impeded. Microglia have been shown to downregulate both spontaneous and evoked neuronal activities in the optic tectum of larval zebrafish, while injury-induced microglial recruitment augmented neuronal firing.⁶ The increased neuronal activity state may make it easier to simultaneously discharge a sufficient number of neurons in order to generate an SD via electrical stimulation.⁴⁷ This suggests that microglial actions may also shape SD induction or propagation differently in different forms of neuropathologies. For example, microglia activated by SD or other stimuli may induce a more proinflammatory milieu making the brain prone to recurrent SDs,^{26,28} while an absence of microglia was found to reduce SD incidence in the evolving penumbra after experimental stroke in mice.¹⁶ Thus, these observations provide evidence for the first time that microglia effectively modulate SD threshold in the non-injured brain in vivo, similar to that seen during brain ischemia,¹⁶ indicating that SD susceptibility seems to depend on the activity status of microglia (Figure 5).

Surveilling microglia may not only respond rapidly to SD elicitation, but are also expected to change their activity and produce inflammatory mediators to shape the excitability of the nervous tissue during recurrent SD events. This is in agreement with the in vitro observations that pro-inflammatory cytokines, especially TNF α released from activated microglia lowered SD threshold,²⁸ and reduced SD amplitude.⁵⁰ Besides, there is an existing continuous outward potassium current on surveilling microglia through a recently

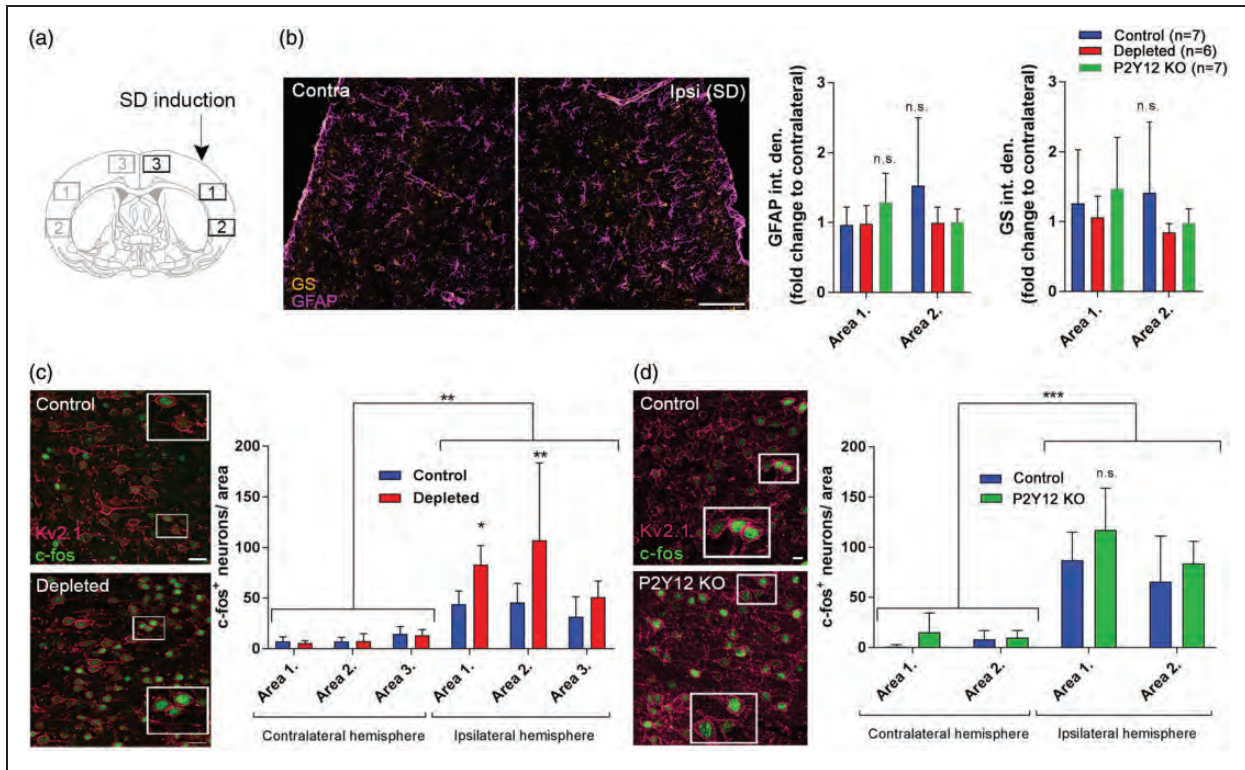


Figure 4. The absence of microglia is associated with augmented neuronal activation after spreading depolarization (SD). (a) Schematic showing the areas used for quantitative analysis relative to the site of SD induction. (b) Representative images showing glial fibrillary acidic protein (GFAP) and glutamine synthetase (GS) immunofluorescence in the ipsilateral hemisphere 1.5 h after SD induction (Area 1 is displayed). Graphs showing integrated density values of GFAP and GS signal normalized to the corresponding areas of the contralateral hemisphere as mean \pm stdev. Two-way ANOVA followed by Sidak's multiple comparison. (c) Representative images demonstrate activated, c-fos labeled (green) neurons (Kv2.1, a voltage-dependent K⁺ channel; magenta) in the cerebral cortex ipsilateral to SD elicitation (mean \pm stdev). Mice were sacrificed 1.5 h after the induction of the first SD in a train of four events, to allow the assessment of c-fos protein expression. Scale bar, 10 μ m. Quantification of c-fos protein expression was performed in areas indicated in the schematic coronal brain section in Panel (a) (ROI: 300 μ m \times 200 μ m). $p < 0.01^{**}$; control vs. depleted (ipsilaterally), two-way ANOVA followed by Sidak's multiple comparison. (d) Representative images demonstrate activated, c-fos labeled (green) neurons (Kv2.1, magenta) in the cerebral cortex ipsilateral to SD elicitation in control and P2Y12R KO mice (Area 1 on panel A is shown). Quantification of c-fos protein expression was performed in areas indicated in the schematic coronal brain section in Panel (a) (ROI: 300 μ m \times 200 μ m, only Area 1 and Area 2 assessed based on the results of microglia depletion studies). $n = 4-7$, data are expressed mean \pm stdev.

identified two-pore domain K⁺ channel,⁹ which can be potentiated by P2Y12R activation.¹⁰ Microglial slow outward potassium currents therefore could curtail the neuronal transmembrane potassium leakage, shifting neuronal membrane potential to more positive values and altering the excitability of neurons.⁵¹

We also found that the SD-related transient negative shift of DC potential was markedly attenuated by microglia depletion, and in mice lacking the P2Y12R. Although there is no ultimate consensus on the conditions that govern SD amplitude, a causal link has recently been established between the amplitude of the negative DC shift and the total number of synchronously discharged cortical neurons.⁵² Considering this association, the reduced SD amplitude observed in our studies may infer the involvement of a possibly smaller

cell mass locally depolarized, thus reduced neuronal excitability in the absence of activated microglia, in line with increased SD threshold for recurring SDs. Our results confirm that the excitability of the nervous tissue after SD occurrence is modulated by microglial responses implicating P2Y12R signaling in this process. The repolarization after SD is achieved by the ATP-consuming Na⁺/K⁺ pump and astrocytic buffering of K⁺ and glutamate,^{20,47,53,54} the efficacy of which is subject to the metabolic status of the tissue.⁵⁵ Our data indicate that the presence of activated microglia decelerates the uptake of the accumulated [K⁺]_e or glutamate. This process, however, may not require P2Y12R signaling, suggesting that additional microglia-dependent mechanisms also contribute to the restoration of extracellular ion homeostasis after

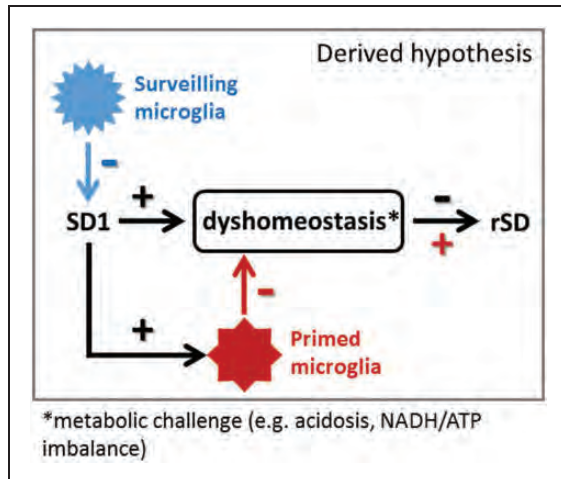


Figure 5. Surveilling microglia may favor lower tissue susceptibility to SD, while primed microglia could support SD occurrence. We propose that resting microglia balance out neuronal overactivation and make SD occurrence less likely. Once SD occurs, the homeostasis of the nervous tissue is challenged, microglia transform to a primed state, which together preserve or increase the susceptibility of the nervous tissue to sustain subsequent SDs.

SD. The hyperpolarization that follows an SD is thought to be a transient overshoot of extracellular Cl^- , which accompanies cationic changes due to an increased pumping activity of the Na^+/K^+ ATPase.²⁰ This seems to be consistent with the finding that the absence of activated microglia curbs the peak of depolarization. The smaller depolarization and the more enhanced hyperpolarization observed in the microglia-depleted mice all together signify that microglia shift the balance from hyperpolarization to depolarization, possibly by restraining Na^+/K^+ ATPase activity.

The evolution of SD is dependent on a massive efflux of potassium through tetraethylammonium-sensitive, ATP-sensitive or large-conductance Ca^{2+} -activated potassium channels,^{56,57} all of which are also expressed by microglia.^{58,59} Accordingly, we hypothesized that activated microglia may tune the susceptibility of the cortex to SD by modulating transmembrane potassium currents. Thus, we set out to evaluate $[\text{K}^+]_e$ dynamics with SD at the absence of microglia or P2Y12R. We observed shorter $[\text{K}^+]_e$ -related changes during SDs and facilitated K^+ uptake following SDs only in the microglia-depleted group. In contrast to microglia depletion, K^+ reuptake was found hindered in the P2Y12R KO animals. Even though the activation of P2Y12R enhances microglial outward potassium currents, which was shown to be countered by pharmacological blockade of the microglial P2Y12R,^{9–11} and thus P2Y12R appears to be

implicated in K^+ homeostasis, the mechanism behind the low rate of $[\text{K}^+]_e$ clearance in the absence of P2Y12R cannot be identified with certainty. In line with this, while astrocytes are known for their contribution to the uptake of extracellular potassium, levels of astrocyte markers did not differ between control, microglia-depleted and P2Y12R KO mice. However, astrocyte-microglia interactions may still be altered in microglia-depleted and P2Y12R KO mice, which are not reflected by the markers assessed within this time frame upon SD induction. Similarly, the potential interactions between microglial P2Y12R and neuronal potassium channels such as $\text{Kv}2.1$ will need to be investigated in future studies. Here, $\text{Kv}2.1$ was merely used to visualize neuronal membranes for microglia–neuron interactions and its functional contribution to SD propagation or microglial activity was not investigated. The duration of $[\text{K}^+]_e$ shift is determined by a competing force of opposing potassium currents. Activated microglia may contribute to the potassium outflow through inward rectifying, calcium-activated or ATP-sensitive K^+ channels,^{58–60} independent of P2Y12R signaling. Likewise, increased barium sensitive K^+ conductance of microglial cells was shown in response to SD in vitro.²⁶ As the recovery from SD is critically dependent on the activity of the Na^+/K^+ -ATPase, as well as the buffering capacity of the astrocyte network,⁵⁴ our results indicate that microglia modulate the sustenance or termination of SD by interacting with either of these mechanisms. Here we identified potassium homeostasis as a novel microglia-associated SD-regulatory pathway, in addition to the previously proposed cytokine signaling.²⁸ Furthermore, activated microglia have been known to alter glutamate homeostasis⁶¹ and are critical source of the pro-inflammatory $\text{IL-1}\beta$ in the brain,¹¹ both of which have been shown to modulate neuronal sensitivity^{12,14} and influence either the induction or the evolution of SD.^{21,47,62} Thus, it is conceivable that these additional, microglia-linked pathways are also implicated in the modulation of SD evolution.

To investigate how selective elimination of microglia affects neuronal activation in the cerebral cortex after SD, we turned to *c-fos* immunofluorescence. Spreading depolarization induces the expression of the early proto-oncogene *c-fos*, which is a widely used marker of neuronal activation.^{45,49} We observed elevated *c-fos* expression ipsilateral to the SD induction. Based on the known contribution of NMDA receptors and voltage-gated calcium channels to *c-fos* expression during SD,^{45,63} microglia are proposed to suppress calcium influx through these channels, and thus protect neurons against SD-related hyperactivity or potential injury. The lack of a major effect of P2Y12R-deficiency on potassium clearance and neuronal *c-fos* expression

collectively suggests that microglia shape neuronal activity via different mechanisms after SD, which is only partially dependent on microglial P2Y₁₂R.

In conclusion, the presence of microglia is likely to be essential to maintain the electrical elicitation threshold and to support the full evolution of SD, partly by sustaining the release or the cellular clearance of [K⁺]_e. While microglial P2Y₁₂R signaling is suggested to take part in sensitizing the tissue to SD, it appears that activated microglia decelerate the recovery from SD independent of their P2Y₁₂ receptors. Altogether, our findings suggest that surveilling microglia may favor SD suppression, while in turn, SD-induced microglial activation preserves the susceptibility of the nervous tissue to sustain subsequent, recurrent SDs.

Funding

The author(s) disclosed receipt of the following financial support for the research, authorship, and/or publication of this article: This work was supported by grants from National Research, Development and Innovation Office (NKFIH: K120358, K111923, PD128821), the Ministry for National Economy of Hungary (GINOP-2.3.2-15-2016-00048), the Ministry of Human Capacities of Hungary (EFOP-3.6.1-16-2016-00008) the Momentum Program of the Hungarian Academy of Sciences (LP2016-4/2016), by ERC-CoG 724994, by the János Bolyai Research Scholarship of the Hungarian Academy of Sciences, and by the Ministry for Innovation and Technology (ÚNKP-19-3-I and ÚNKP-19-4).

Acknowledgements

The authors are grateful for the technical assistance provided by Orsolya Ivánkovitsné Kiss. We thank Plexikon Inc. (Berkeley, USA) for the generous contribution of PLX5622 diet.

Declaration of conflicting interests



The author(s) declared no potential conflicts of interest with respect to the research, authorship, and/or publication of this article.

Authors' contributions

Dániel P. Varga, Conceptualization, Methodology, Investigation, Formal analysis, Visualization, Writing – original draft, Writing – review & editing; Akos Menyhárt, Methodology, Investigation, Formal analysis, Writing – review and editing; Eszter Császár, Investigation, Formal analysis, Visualization; Bernadett Martinecz, Investigation, Visualization; Tamás Szlepák, Investigation, Visualization; Balázs Pósfai, Methodology, Investigation, Formal analysis, Writing – review and editing; Nikolett Lénárt, Methodology, Investigation, Writing – review and editing; Barbara Orsolits, Methodology, Investigation; Csaba Cserép, Methodology, Investigation, Formal analysis, Writing – review and editing; Ferenc Bari, Writing – review and editing; Eszter Farkas,

Conceptualization, Supervision, Writing – original draft; Writing – review and editing, Funding acquisition; Ádám Dénes, Conceptualization, Supervision, Methodology, Writing – review and editing, Funding acquisition, Project administration.

ORCID iDs

Balázs Pósfai  <https://orcid.org/0000-0003-1035-565X>
Csaba Cserép  <https://orcid.org/0000-0001-5513-2471>

Supplemental material

Supplemental material for this article is available online.

References

- Shinozaki Y, Shibata K, Yoshida K, et al. Transformation of astrocytes to a neuroprotective phenotype by microglia via P2Y₁receptor downregulation. *Cell Rep* 2017; 19: 1151–1164.
- Lehnardt S. Innate immunity and neuroinflammation in the CNS: the role of microglia in toll-like receptor-mediated neuronal injury. *Glia* 2010; 58: 253–263.
- Neumann H, Kotter MR and Franklin RJM. Debris clearance by microglia: an essential link between degeneration and regeneration. *Brain* 2009; 132: 288–295.
- Paolicelli RC, Bolasco G, Pagani F, et al. Synaptic pruning by microglia is necessary for normal brain development. *Science* 2011; 333: 1456–1458.
- Parkhurst CN, Yang G, Ninan I, et al. Microglia promote learning-dependent synapse formation through brain-derived neurotrophic factor. *Cell* 2013; 155: 1596–609.
- Li Y, Du XF, Liu CS, et al. Reciprocal regulation between resting microglial dynamics and neuronal activity in vivo. *Dev Cell* 2012; 23: 1189–1202.
- Eyo UB, Peng J, Swiatkowski P, et al. Neuronal hyperactivity recruits microglial processes via neuronal NMDA receptors and microglial P2Y₁₂ receptors after status epilepticus. *J Neurosci* 2014; 34: 10528–10540.
- Fekete R, Cserép C, Lénárt N, et al. Microglia control the spread of neurotropic virus infection via P2Y₁₂ signalling and recruit monocytes through P2Y₁₂-independent mechanisms. *Acta Neuropathol* 2018; 136: 461–482.
- Madry C, Kyrargyri V, Arancibia-Cárcamo IL, et al. Microglial ramification, surveillance, and interleukin-1 β release are regulated by the two-pore domain K⁺ channel THIK-1. *Neuron* 2018; 97: 299–312.e6.
- Swiatkowski P, Murugan M, Eyo UB, et al. Activation of microglial P2Y₁₂ receptor is required for outward potassium currents in response to neuronal injury. *Neuroscience* 2016; 318: 22–33.
- Kettenmann H, Hanisch U-K, Noda M, et al. Physiology of microglia. *Physiol Rev* 2011; 91: 461–553.
- Takeuchi H, Jin S, Wang J, et al. Tumor necrosis factor- α induces neurotoxicity via glutamate release from hemichannels of activated microglia in an autocrine manner. *J Biol Chem* 2006; 281: 21362–21368.

13. Carmen J, Rothstein JD and Kerr DA. Tumor necrosis factor- α modulates glutamate transport in the CNS and is a critical determinant of outcome from viral encephalomyelitis. *Brain Res* 2009; 1263: 143–154.
14. Klapal L, Igelhorst BA and Dietzel-Meyer ID. Changes in neuronal excitability by activated microglia: differential Na⁺ current upregulation in pyramid-shaped and bipolar neurons by TNF- α and IL-18. *Front Neurol* 2016; 7: 1–13.
15. Elmore MRP, Najafi AR, Koike MA, et al. Colony-stimulating factor 1 receptor signaling is necessary for microglia viability, unmasking a microglia progenitor cell in the adult brain. *Neuron* 2014; 82: 380–397.
16. Szalay G, Martinecz B, Lénárt N, et al. Microglia protect against brain injury and their selective elimination dysregulates neuronal network activity after stroke. *Nat Commun* 2016; 7: 11499.
17. Pietrobon D and Moskowitz MA. Chaos and commotion in the wake of cortical spreading depression and spreading depolarizations. *Nat Rev Neurosci* 2014; 15: 379–393.
18. Dreier JP. The role of spreading depression, spreading depolarization and spreading ischemia in neurological disease. *Nat Med* 2011; 17: 439–447.
19. Chen S-P, Qin T, Seidel JL, et al. Inhibition of the P2X7–PANX1 complex suppresses spreading depolarization and neuroinflammation. *Brain* 2017; 140: 1643–1656.
20. Hansen AJ and Zeuthen T. Extracellular ion concentrations during spreading depression and ischemia in the rat brain cortex. *Acta Physiol Scand* 1981; 113: 437–45.
21. Zhou N, Rungta RL, Malik A, et al. Regenerative glutamate release by presynaptic NMDA receptors contributes to spreading depression. *J Cereb Blood Flow Metab* 2013; 33: 1582–94.
22. Steffensen AB, Sword J, Croom D, et al. Chloride cotransporters as a molecular mechanism underlying spreading depolarization-induced dendritic beading. *J Neurosci* 2015; 35: 12172–12187.
23. Dreier JP and Reiffurth C. The stroke-migraine depolarization continuum. *Neuron* 2015; 86: 902–922.
24. Jander S, Schroeter M, Peters O, et al. Cortical spreading depression induces proinflammatory cytokine gene expression in the rat brain. *J Cereb Blood Flow Metab* 2001; 21: 218–225.
25. Takizawa T, Qin T, Lopes de Moraes A, et al. Non-invasively triggered spreading depolarizations induce a rapid pro-inflammatory response in cerebral cortex. *J Cereb Blood Flow Metab*. Epub ahead of print 26 June 2019. DOI: 10.1177/0271678X19859381.
26. Wendt S, Wogram E, Korvers L, et al. Experimental cortical spreading depression induces NMDA receptor dependent potassium currents in microglia. *J Neurosci* 2016; 36: 6165–74.
27. Caggiano AO and Kraig RP. Eicosanoids and nitric oxide influence induction of reactive gliosis from spreading depression in microglia but not astrocytes. *J Comp Neurol* 1996; 369: 93–108.
28. Pusic KM, Pusic AD, Kemme J, et al. Spreading depression requires microglia and is decreased by their M2a polarization from environmental enrichment. *Glia* 2014; 62: 1176–1194.
29. Matsuura T and Bureš J. The minimum volume of depolarized neural tissue required for triggering cortical spreading depression in rat. *Exp Brain Res* 1971; 12: 238–249.
30. Grafstein B. Mechanism of spreading cortical depression. *J Neurophysiol* 1956; 19: 154–71.
31. Viitanen T, Ruusuvoori E, Kaila K, et al. The K⁺-Cl⁻ cotransporter KCC2 promotes GABAergic excitation in the mature rat hippocampus. *J Physiol* 2010; 588: 1527–1540.
32. Bazzigaluppi P, Dufour S and Carlen PL. Wide field fluorescent imaging of extracellular spatiotemporal potassium dynamics in vivo. *Neuroimage* 2015; 104: 110–116.
33. Yao X, Smith AJ, Jin BJ, et al. Aquaporin-4 regulates the velocity and frequency of cortical spreading depression in mice. *Glia* 2015; 63: 1860–1869.
34. Hertelendy P, Menyhart A, Makra P, et al. Advancing age and ischemia elevate the electric threshold to elicit spreading depolarization in the cerebral cortex of young adult rats. *J Cereb Blood Flow Metab* 2017; 37: 1763–1775.
35. Barna L, Dudok B, Miczán V, et al. Correlated confocal and super-resolution imaging by VividSTORM. *Nat Protoc* 2016; 11: 163–83.
36. Hansen AJ. Extracellular potassium concentration in juvenile and adult rat brain cortex during anoxia. *Acta Physiol Scand* 1977; 99: 412–420.
37. Ayata C and Lauritzen M. Spreading depression, spreading depolarizations, and the cerebral vasculature. *Physiol Rev* 2015; 95: 953–993.
38. Grinberg YY, Milton JG and Kraig RP. Spreading depression sends microglia on Lévy flights. *PLoS One* 2011; 6: e19294.
39. Haynes SE, Hollopeter G, Yang G, et al. The P2Y₁₂ receptor regulates microglial activation by extracellular nucleotides. *Nat Neurosci* 2006; 9: 1512–1519.
40. Kaku T, Hada J and Hayashi Y. Endogenous adenosine exerts inhibitory effects upon the development of spreading depression and glutamate release induced by microdialysis with high K⁺ in rat hippocampus. *Brain Res* 1994; 658: 39–48.
41. Kofuji P and Newman EA. Potassium buffering in the central nervous system. *Neuroscience* 2004; 129: 1045–1056.
42. Kaczmarek L. c-Fos in learning: beyond the mapping of neuronal activity. In: L Kaczmarek and HA Robertson (eds) *Handbook of chemical neuroanatomy*. Stockholm: Elsevier, 2002, pp.189–215.
43. Siesjo BK and Bengtsson F. Calcium fluxes, calcium antagonists, and calcium-related pathology in brain ischemia, hypoglycemia, and spreading depression: a unifying hypothesis. *J Cereb Blood Flow Metab* 1989; 9: 127–140.
44. Reinhart KM and Shuttleworth CW. Ketamine reduces deleterious consequences of spreading depolarizations. *Exp Neurol* 2018; 305: 121–128.

45. Herrera DG and Robertson HA. Application of potassium chloride to the brain surface induces the c-fos proto-oncogene: reversal by MK-801. *Brain Res* 1990; 510: 166–170.
46. Mayford M, Siegelbaum SA and Kandel ER. Synapses and memory storage. *Cold Spring Harb Perspect Biol* 2012; 4: 1–18.
47. Hertelendy P, Varga DP, Menyhárt Á, et al. Susceptibility of the cerebral cortex to spreading depolarization in neurological disease states: the impact of aging. *Neurochem Int* 2019;127: 125–136.
48. Brouns R and De Deyn PP. The complexity of neurobiological processes in acute ischemic stroke. *Clin Neurol Neurosurg* 2009; 111: 483–95.
49. Kobayashi K, Yamanaka H, Fukuoka T, et al. P2Y12 receptor upregulation in activated microglia is a gateway of p38 signaling and neuropathic pain. *J Neurosci* 2008; 28: 2892–2902.
50. Richter F, Lütz W, Eitner A, et al. Tumor necrosis factor reduces the amplitude of rat cortical spreading depression in vivo. *Ann Neurol* 2014; 76: 43–53.
51. Kato G, Inada H, Wake H, et al. Microglial contact prevents excess depolarization and rescues neurons from excitotoxicity. *eNeuro* 2016; 3: 1–9.
52. Speckmann E-J, Elger CE and Gorji A. Neurophysiologic basis of EEG and DC potentials. In: Schomer DL, da Silva LF (eds) *Niedermeyer's Electroencephalography: Basic Principles, Clinical Applications, and Related Fields*. 6th ed. Philadelphia: Lippincott Williams and Wilkins, 2011, pp.17–32.
53. Walz W. Role of astrocytes in the spreading depression signal between ischemic core and penumbra. *Neurosci Biobehav Rev* 1997; 21: 135–142.
54. Seidel JL, Escartin C, Ayata C, et al. Multifaceted roles for astrocytes in spreading depolarization: a target for limiting spreading depolarization in acute brain injury? *Glia* 2016; 64: 5–20.
55. Feuerstein D, Backes H, Gramer M, et al. Regulation of cerebral metabolism during cortical spreading depression. *J Cereb Blood Flow Metab* 2016; 36: 1965–1977.
56. Menyhárt Á, Farkas AE, Varga DP, et al. Large-conductance Ca²⁺-activated potassium channels are potently involved in the inverse neurovascular response to spreading depolarization. *Neurobiol Dis* 2018; 119: 41–52.
57. Somjen GG. Mechanisms of spreading depression and hypoxic spreading depression-like depolarization. *Physiol Rev* 2001; 81: 1065–1096.
58. Coccozza G, di Castro MA, Carbonari L, et al. Ca²⁺-activated K⁺ channels modulate microglia affecting motor neuron survival in hSOD1G93A mice. *Brain Behav Immun* 2018; 73: 584–595.
59. Du RH, Sun HB, Hu ZL, et al. Kir6.1/K-ATP channel modulates microglia phenotypes: implication in Parkinson's disease. *Cell Death Dis* 2018; 9: 404.
60. Di Lucente J, Nguyen HM, Wulff H, et al. The voltage-gated potassium channel Kv1.3 is required for microglial pro-inflammatory activation in vivo. *Glia* 2018; 66: 1881–1895.
61. Takaki J, Fujimori K, Miura M, et al. L-glutamate released from activated microglia downregulates astrocytic L-glutamate transporter expression in neuroinflammation: the 'collusion' hypothesis for increased extracellular L-glutamate concentration in neuroinflammation. *J Neuroinflammation* 2012; 9: 1.
62. Richter F, Eitner A, Leuchtweis J, et al. Effects of interleukin-1 β on cortical spreading depolarization and cerebral vasculature. *J Cereb Blood Flow Metab* 2017; 37: 1791–1802.
63. Shimazawa M, Hara H, Watano T, et al. Effects of Ca²⁺-channel blockers on cortical hypoperfusion and expression of c-Fos-like immunoreactivity after cortical spreading depression in rats. *Br J Pharmacol* 1995; 115: 1359–1368.

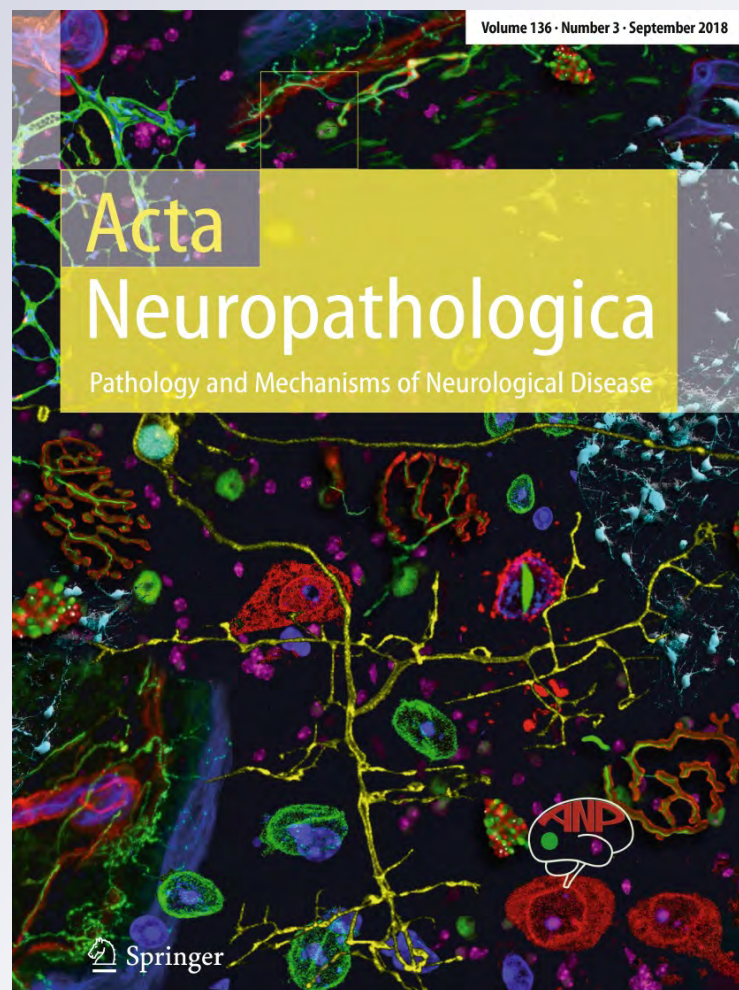
Microglia control the spread of neurotropic virus infection via P2Y12 signalling and recruit monocytes through P2Y12-independent mechanisms

Rebeka Fekete, Csaba Cserép, Nikolett Lénárt, Krisztina Tóth, Barbara Orsolits, Bernadett Martinecz, Előd Méhes, Bálint Szabó, et al.

Acta Neuropathologica
Pathology and Mechanisms of
Neurological Disease

ISSN 0001-6322
Volume 136
Number 3


Acta Neuropathol (2018) 136:461-482
DOI 10.1007/s00401-018-1885-0



Your article is published under the Creative Commons Attribution license which allows users to read, copy, distribute and make derivative works, as long as the author of the original work is cited. You may self-archive this article on your own website, an institutional repository or funder's repository and make it publicly available immediately.



Microglia control the spread of neurotropic virus infection via P2Y12 signalling and recruit monocytes through P2Y12-independent mechanisms

Rebeka Fekete¹ · Csaba Cserép¹ · Nikolett Lénárt¹ · Krisztina Tóth¹ · Barbara Orsolits¹ · Bernadett Martinecz¹ · Előd Méhes² · Bálint Szabó² · Valéria Németh² · Balázs Gönci² · Beáta Sperlách³ · Zsolt Boldogkői⁴ · Ágnes Kittel³ · Mária Baranyi³ · Szilamér Ferenczi⁵ · Krisztina Kovács⁵ · Gergely Szalay⁶ · Balázs Rózsa⁶ · Connor Webb¹ · Gabor G. Kovacs^{7,8} · Tibor Hortobágyi^{9,10,11} · Brian L. West¹² · Zsuzsanna Környei¹ · Ádám Dénes¹ 

Received: 16 February 2018 / Revised: 11 June 2018 / Accepted: 5 July 2018 / Published online: 19 July 2018
© The Author(s) 2018

Abstract

Neurotropic herpesviruses can establish lifelong infection in humans and contribute to severe diseases including encephalitis and neurodegeneration. However, the mechanisms through which the brain's immune system recognizes and controls viral infections propagating across synaptically linked neuronal circuits have remained unclear. Using a well-established model of alphaherpesvirus infection that reaches the brain exclusively via retrograde transsynaptic spread from the periphery, and in vivo two-photon imaging combined with high resolution microscopy, we show that microglia are recruited to and isolate infected neurons within hours. Selective elimination of microglia results in a marked increase in the spread of infection and egress of viral particles into the brain parenchyma, which are associated with diverse neurological symptoms. Microglia recruitment and clearance of infected cells require cell-autonomous P2Y12 signalling in microglia, triggered by nucleotides released from affected neurons. In turn, we identify microglia as key contributors to monocyte recruitment into the inflamed brain, which process is largely independent of P2Y12. P2Y12-positive microglia are also recruited to infected neurons in the human brain during viral encephalitis and both microglial responses and leukocyte numbers correlate with the severity of infection. Thus, our data identify a key role for microglial P2Y12 in defence against neurotropic viruses, whilst P2Y12-independent actions of microglia may contribute to neuroinflammation by facilitating monocyte recruitment to the sites of infection.

Keywords Microglia · P2Y12 · Neurotropic virus · Transsynaptic spread · Neuroinflammation

Introduction

Microglia are the main immunocompetent cell type of the brain that play a role in diverse physiological processes, including brain development, synaptic plasticity and memory. In turn, alterations in microglial function are linked with common brain diseases such as stroke, epilepsy, Alzheimer's or Parkinson's disease [3, 28, 47, 63]. But how

microglial actions determine the fate of individual neurons remained largely unclear to date. Microglia are capable of removing synapses via complement-mediated manner [26, 59] and eliminate injured neurons via recognising translocated phosphatidylserine on the cell membrane [7]. Numerous mediators including chemokines, metalloproteinases, growth factors, purinergic metabolites, alarmins or damage-associated molecular patterns such as HMGB1, histones and DNA have been revealed as indicators of neuronal injury and triggers for microglial activation [9, 29, 30, 57, 58]. Among these, microglial P2Y12 receptor-mediated actions have been shown to facilitate the movement of microglial processes to sites of injury or ATP administration [14, 25], whilst constant microglial surveillance of the brain was found to be largely P2Y12-independent [39, 53]. However, whether microglial P2Y12 is involved in early recognition

Electronic supplementary material The online version of this article (<https://doi.org/10.1007/s00401-018-1885-0>) contains supplementary material, which is available to authorized users.

✉ Ádám Dénes
denes.adam@koki.mta.hu

Extended author information available on the last page of the article

and clearance of injured neurons independently of mediating generic microglial actions to tissue injury remained unclear.

One of the major difficulties in studying microglial responses to mediators released from stressed neurons *in vivo* is the immediate response of surveilling microglia to any noxious stimuli [46], which is an inherent confounder of most experimental models that include manipulation in the brain parenchyma. To overcome these difficulties, we took advantage of the genetically modified strains of pseudorabies virus (PRV), a member of the subfamily Alphaherpesvirinae (similar to human herpes simplex virus type 1 or varicella-zoster virus), widely used for neuroanatomical tract-tracing and as a well-established model of neurotropic virus infection [6, 8]. When injected into peripheral organs, the “Bartha-Dup” strains of PRV display slow and highly specific retrograde transsynaptic spread in central autonomic circuits [6], allowing us to study directed microglial recruitment in parallel with the propagation of virus infection in the brain using *in vivo* imaging and advanced histological approaches. Since in this model microglia may only sense signals identifying affected neurons in their vicinity, but do not become infected with PRV even under *ex vivo* conditions unlike in the case of most viruses with potential or preferential neurotropism *in vivo* [6, 50], we could also investigate the functional role of microglia and microglial P2Y12 receptors in the control of infection together with the associated neuroinflammatory response.

Although some previous papers have implicated microglia in anti-viral immunity [11, 17, 40, 49, 50], most of them have not used selective microglia manipulation *in vivo*, and the potential mechanisms of early microglia recruitment including the role of microglial P2Y12 have not been investigated. We have shown earlier that microglia sense changes in neuronal activity and selective elimination of microglia by CSF1R-blockade leads to the dysregulation of neuronal network activity and augmented brain injury [56]. Since neurons infected with PRV-Bartha derivatives have normal electrophysiological characteristics but display increased activity [42], we hypothesised that microglia may detect detrimental changes in the case of individual cells before irreversible neuronal injury occurs. Using this model system, we demonstrate the rapid and targeted recruitment of microglia to compromised neurons using *in vivo* two-photon and *in vitro* time-lapse imaging and show that nucleotides released from infected neurons mediate this effect via microglial P2Y12 receptors. We show that through these actions, microglia are instrumental to prevent contact infection and control the transneuronal spread of neurotropic virus infection. Whilst demonstrating the role for P2Y12 in the elimination of infected cells by microglia in both the mouse and the human brain, we also show that microglia, but not microglial P2Y12 contribute to the recruitment of monocytes to transsynaptically infected neurons during viral encephalitis.

Since neurotropic herpesviruses are capable of causing both acute and chronic infection in humans and also contribute to diverse forms of neurodegeneration [38, 64], these results are likely to be relevant for a number of neuroinflammatory and neurodegenerative diseases.

Materials and methods

Mice

Experiments were carried out on 12–18 weeks old C57BL/6 J, P2Y12^{-/-}, P2RX7^{-/-}, Cx3Cr1^{GFP/+} and Cx3Cr1^{GFP/+} P2Y12^{-/-} mice. All experimental procedures were in accordance with the guidelines set by the European Communities Council Directive (86/609 EEC) and the Hungarian Act of Animal Care and Experimentation (1998; XXVIII, Sect. 243/1998), approved by the Animal Care and Use Committee of the IEM HAS.

Selective elimination of microglia from the brain

Mice were fed PLX5622 (Plexxikon Inc. Berkeley, USA; 1200 mg PLX5622 in 1 kg chow) for 3 weeks to eliminate microglia from the brain.

Neurotropic herpesvirus infection

Mice were randomly assigned to experimental groups and were injected either intraperitoneally or directly into the epididymal white adipose tissue with a genetically modified PRV-Bartha derivative, PRV-Bartha-Dup-Green (BDG) [5] to induce retrograde transsynaptic infection in the brain. In a set of studies, mice were infected with BDG on 16th day of PLX5622 diet to assess the effect of microglia depletion on central propagation of virus infection. For *in vivo* two-photon imaging, Cx3Cr1^{GFP/+} mice were infected with PRV-Bartha-DupDsRed (BDR) [4] enabling the co-detection of infected neurons with microglia. After virus injection, mice were let to survive for 5–7 days depending on study design and were regularly monitored for neurobehavioral symptoms.

Tissue processing and immunofluorescence

Brain tissues were fixed by transcardial perfusion (saline, followed by 4% PFA). Immunofluorescence was performed on 25 μm thick free-floating brain sections. Images were captured with a Nikon Ni-E C2 + confocal microscope.

Super-resolution (STORM) microscopy

Sections were mounted onto #1.5 thick borosilicate coverslips and covered with imaging medium [50] immediately before imaging. STORM imaging was performed for P2Y12 (stimulated by a 647 nm laser) using a Nikon N-STORM C2 + super-resolution system that combines ‘Stochastic Optical Reconstruction Microscopy’ technology and Nikon’s Eclipse Ti research inverted microscope to reach a lateral resolution of 20 nm and axial resolution of 50 nm [1, 18].

Immuno-electron microscopy

After the combined immunogold–immunoperoxidase stainings, sections were treated with osmium tetroxide, dehydrated in ascending ethanol series and acetonitrile, and embedded in epoxy resin. During dehydration, sections were treated with uranyl acetate. After polymerization, 70 nm thick sections were cut on an ultramicrotome, picked up on formvar-coated single-slot copper grids, and sections were examined using a Hitachi H-7100 electron microscope.

Correlated confocal laser-scanning microscopy, electron microscopy and electron tomography

Following multiple immunofluorescent staining, sections were analysed using a Nikon Eclipse Ti-E inverted microscope, and an AIR laser confocal system. After imaging, sections were recovered and the immunoperoxidase reaction was developed. Electron tomography was performed using a Tecnai T12 BioTwin electron microscope equipped with a computer-controlled precision stage and an Eagle™ 2 k CCD 4 megapixel TEM CCD camera. Reconstruction was performed using the IMOD software package.

Post-mortem human brain samples

To investigate microglia recruitment in response to neurotropic virus infection in the human brain, paraffin-embedded (FFPE) post-mortem brain tissues from five patients with known HSV-encephalitis aged 42–66 years were analysed (ethical approval ETT-TUKEB 62031/2015/EKU, 34/2016 and 31443/2011/EKU (518/PI/11)). Tissue samples from two additional patients with no known neurological disease were used as controls. After deparaffinisation, immunohistochemistry was performed, and representative pictures were captured using a Nikon Ni-E C2 + microscope.

Two-photon imaging

To assess microglia recruitment to infected neurons in the mouse brain in real-time, Cx3CR1^{GFP/+} mice were i.p. injected with 10 µl of the BDR virus. The survival time was

set to 7 days post-infection, when numerous infected cells were present in the cerebral cortex. After cranial window preparation, measurements were performed on a Femto2D-DualScanhead microscope (Femtonics Ltd., Hungary) coupled with a Chameleon Ultra II laser [10, 27]. Data acquisition was performed by MES softver (Femtonics Ltd.), two-photon image sequences were exported from MES and analysed using ImageJ.

Primary neuronal, astroglia and microglia cell cultures

Primary cultures of embryonic cortical cells were prepared from mice on embryonic day 15 [12] and astroglia/microglia mixed cell cultures were prepared from the whole brains of mouse pups, as described earlier [32]. Microglial cells were isolated from 21 to 28 days old mixed cultures either by shaking or by mild trypsinization. In cultures used for time-lapse recordings, microglial cells were seeded on top of astrocytic or neuronal cell cultures in 10000 cell/cm² density. Neuronal or astroglia cultures were infected with either PRV-Bartha-Dup-Green (BDG) virus or PRV-Bartha-DupLac (BDL) at a final titer of 2.5×10^5 PFU/ml, as described earlier [24]. The multiplicity of infection (MOI) was ~0,17 PFU/cell.

Time-lapse microscopy and cell motility data analysis

Time-lapse recordings were performed on a computer-controlled Leica DM IRB inverted fluorescent microscope. Phase contrast and epifluorescent images were collected consecutively every 10 min for up to 48 h post-infection. Images were edited using NIH ImageJ software. Cell tracking: images were analysed individually with the help of custom-made cell-tracking programs (G-track and Wintrack) enabling manual marking of individual cells and recording their position parameters into data files.

Cytokine measurement from media of primary cell cultures

Concentrations of IL-1 α , IL-1 β , TNF- α , IL-6, MCP-1, RANTES (CCL5), G-CSF and KC (CXCL1) were measured from conditioned media of primary neuronal, astroglial and microglial cell cultures using cytometric bead array (CBA) Flex Sets. Measurements were performed on a BD FACS-Verse machine and data were analysed using an FCAP Array software (BD Biosciences) as described earlier [16]. The cytokine levels of conditional media were corrected for total protein concentrations of the samples measured by Bradford Protein Assay Kit.

Total RNA isolation and quantitative RT-PCR

For total RNA isolation, cell culture samples were homogenized in 500 µl TRI Reagent and isolation was performed using Tissue Total RNA Mini Kit according to the manufacturer's instructions. The primers were used in real-time PCR reaction with Fast EvaGreen qPCR Master Mix on a StepOnePlus instrument. The gene expression was analysed using the StepOne 2.3 program. Amplicons were tested by Melt Curve Analysis on StepOnePlus instrument. Experiments were normalized to *gapdh* expression.

Quantification of nucleotides and adenosine

The adenine nucleotides (ATP, ADP, AMP) and adenosine (Ado) were determined in extracts from cells and culture media using HPLC method. The HPLC system used was a Shimadzu LC-20 AD Analytical & Measuring Instruments System, with an Agilent 1100 Series Variable Wavelength Detector set at 253 nm.

Immunohistochemical staining for NTPDase1

Coronal brain sections were incubated in the solution of the polyclonal NTPDase1 antibody. After secondary antibody incubation and chromogen development, sections were osmicated, dehydrated in ascending ethanol series, and embedded in Taab 812 resin. Ultrathin sections were examined using a Hitachi 7100 transmission electron microscope.

Enzyme histochemistry for detection of ecto-ATPase activity

A cerium precipitation method was used for electron microscopic investigation of ecto-ATPase activity [31]. The tissue blocks were then postfixed, dehydrated, treated and embedded into Taab 812 resin for ultrathin sectioning and microscopic examination.

Flow cytometric analysis of brain, spleen and blood samples

Cells were isolated from mouse brains by enzymatic digestion with the mixture of DNase I and Collagenase/Dispase. Spleen cells were isolated by mechanical homogenization of the spleen. Venous blood was collected from the heart before transcardial perfusion using 3.8% sodium citrate as an anticoagulant. Cells were acquired on a BD FACSVerser flow cytometer and data were analysed using FACSsuite software.

Total blood cell counts were calculated using 15 µm polystyrene microbeads.

Statistical assessment

All quantitative measurements and analysis were performed in a blinded manner in accordance with STAIR and ARRIVE guidelines. Data were analysed using the GraphPad Prism 7.0 software. For comparing two experimental groups Student's *t* test with Welch's correction or Mann–Whitney *U* test, for comparing three or more groups one-way or two-way ANOVA followed by Tukey's, Sidak's and Dunnett's post hoc comparison was used. $P < 0.05$ was considered statistically significant.

Please refer to the Supplementary Methods (Online Resource 1) for additional details.

Results

Microglia are instrumental for anti-viral immunity in the brain

To study whether microglia respond to local cues and are recruited to virus-infected neurons, we made use of the precisely controlled, retrograde transsynaptic spread of the PRV derivative, Bartha-DupGreen (BDG) to central autonomic nuclei [5, 6] from peripheral targets (Fig. 1a). In the hypothalamic paraventricular nucleus (PVN), microglial numbers increased threefold in response to infection and infected neurons were surrounded by numerous Iba1-positive cells (Fig. 1b, c), 6 days after intraperitoneal (i.p.) virus injection. To investigate whether microglia are involved in the control of neurotropic virus infection, we performed selective depletion of microglia, by feeding mice the CSF1R antagonist PLX5622, as demonstrated earlier [20, 56]. After 3 weeks of depletion, 96% of microglia were eliminated from the brain as evidenced by the lack of the microglial markers Iba1 and P2Y12 (Fig. 1d, e). Selective elimination of microglia resulted in a marked increase in the number of virus-infected neurons in the brain (Fig. 1f–g). This phenomenon was not dependent on the route of virus administration, since after i.p. virus injection or injection of the virus into the epididymal white adipose tissue (an organ receiving predominantly sympathetic innervation [2]), the number of virus-infected neurons was much higher in the brain in the absence of microglia [Fig. 1h; Suppl. Fig. 1 (Online Resource 1)]. In microglia-depleted mice, numerous infected cells were also present in the cerebral cortex already on day 5, and retrograde infection reaching the cortex was more widespread, affecting several areas normally not infected when microglia were present. In addition, more than a threefold increase in the number of disintegrated neurons containing viral proteins

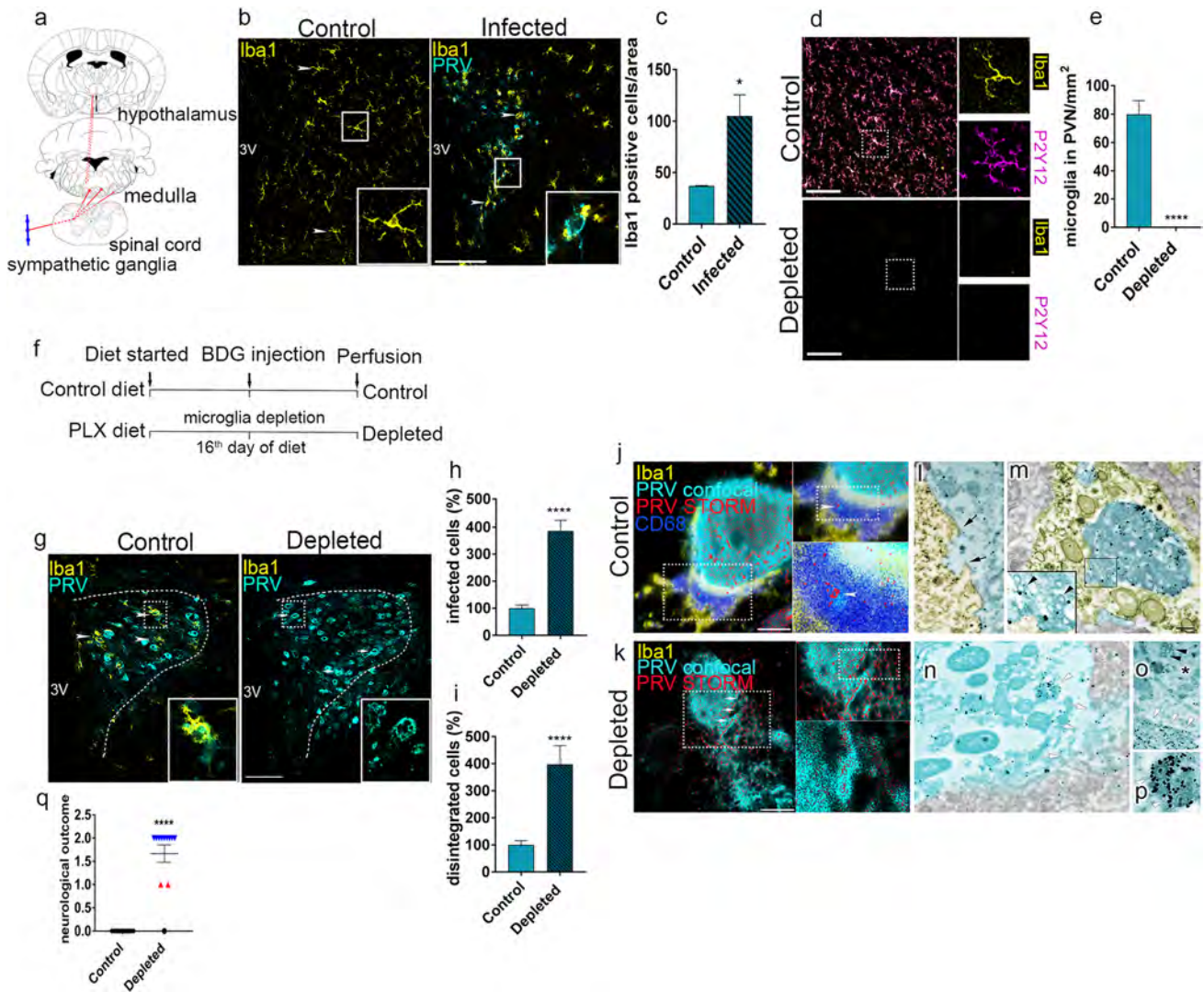
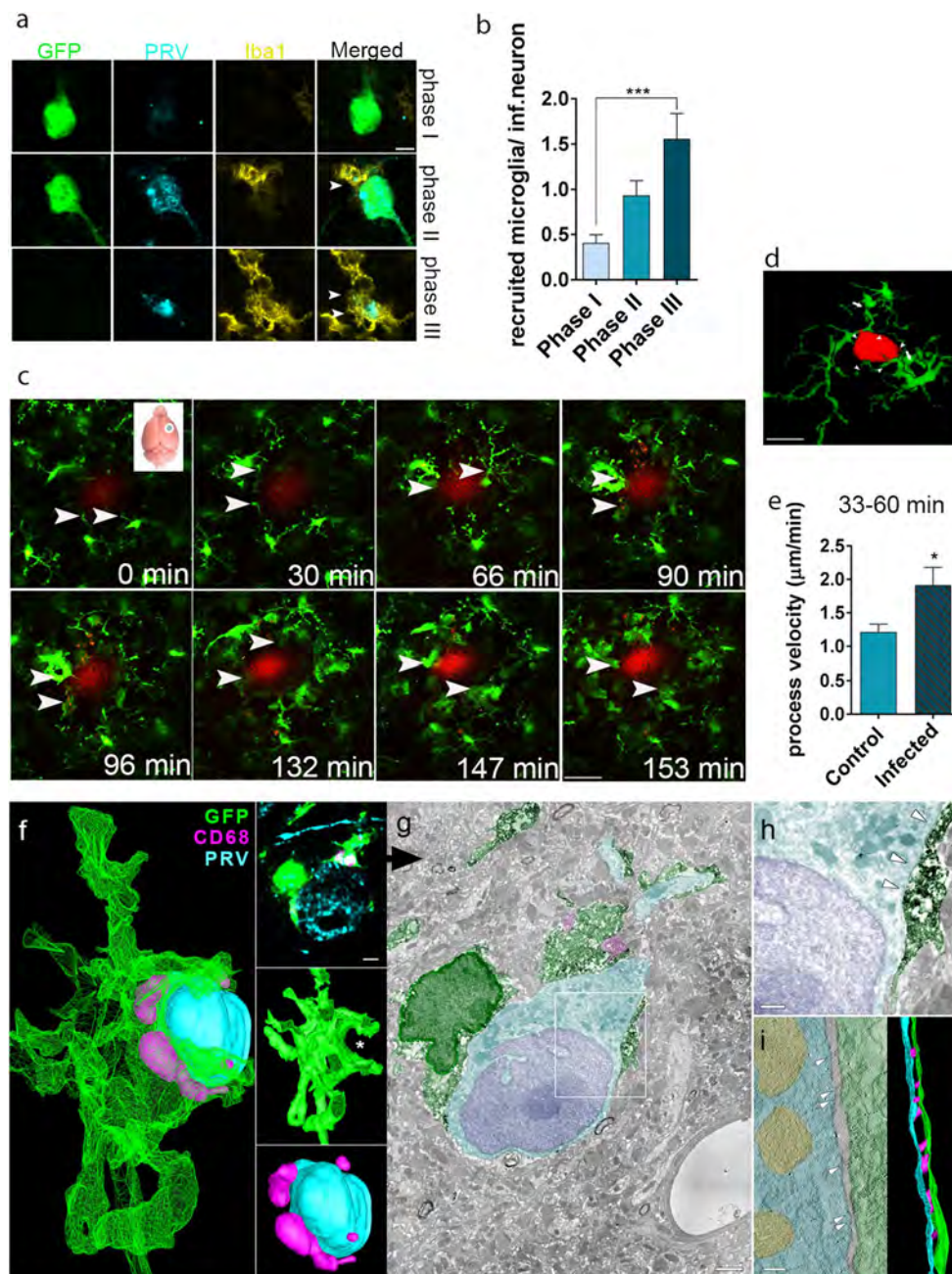


Fig. 1 Selective elimination of microglia results in uncontrolled viral spread and neurobehavioral pathologies. **a** Retrograde transneuronal spread of PRV-Bartha-DupGreen (BDG) to the hypothalamic paraventricular nucleus (PVN) 6 days after intraperitoneal injection. **b** Focal neuronal infection induces recruitment of microglia (Iba1: yellow) to infected neurons (PRV: cyan) in the PVN. **c** Microglial numbers increase significantly at sites of virus-infected neurons, area: 0.2 mm². **d** Selective depletion of microglia by PLX5622 for 3 weeks (yellow: Iba-1, magenta: P2Y12). **e** Depletion results in the elimination of 96% of microglia from the PVN. **f** An absence of microglia results in profound increases in virus-infected neurons in the brain. Control and microglia-depleted mice were injected intraperitoneally with BDG on the 16th day of the diet and allowed to survive for 5 days to induce transsynaptic spread of PRV to the hypothalamus. Note the numerous infected neurons outside the nucleus indicating increases in non-synaptic (contact) infection in the absence of microglia. **g** The number of infected neurons in the PVN increases over twofold in microglia depleted mice 5 days after virus injection. **h** An absence of microglia leads to profound increases in the number of infected neurons in the PVN. **i** An absence of microglia leads to increased number of infected, disintegrated neurons in the PVN. **j** Superresolution microscopic analysis (STORM) reveals the colocalization of the phagosome marker, CD68 (dark blue), with neuronal debris containing viral structural proteins (PRV) inside recruited microglia. **k** An absence of microglia leads to mas-

sive increases in extracellular virus proteins around infected, disintegrated neurons. **l–p** Transmission electron microscopic (TEM) images showing viruses in microglia competent (**l, m**) and depleted (**n–p**) animals. **l** Microglial processes (yellow pseudocolor) are found tightly attached to the cell membrane of infected neuron (cyan pseudocolor), as identified by anti-PRV immunogold labelling (black grains). Black arrows indicate a disrupted neuronal membrane segment isolated by a microglial process. **m** Infected neuronal cell debris is phagocytosed by microglia. Note the presence of viral capsids inside phagocytosed neuronal particles labelled with anti-PRV immunogold (insert). **n** In the absence of microglia disintegrated neuronal membranes with anti-PRV-immunogold labelled content invading the surrounding neuropil can be seen (white arrows). **o** Infected neuron contains viral capsids (black arrowheads), asterisk marks the nucleus, mature virions with strong PRV-immunogold labelling can be seen in the cytoplasm (white arrowheads). **p** PRV-virions are displayed at higher magnification. **q** Absence of microglia results in rapidly appearing neurological symptoms 5 days after PRV infection (0: no symptoms, 1: drooling and heavy breathing, 2: seizures and muscle spasms). Data expressed as mean ± s.e.m **c** **p* < 0.05 *n* = 4–5, Mann–Whitney test **e** *****p* < 0.0001 *n* = 6 unpaired *t* test, **h, i** *****p* < 0.0001 Mann–Whitney test *n* = 10–11 **i** ***p* < 0.001 unpaired *t* test *n* = 9–12, **q** *****p* < 0.0001 Mann–Whitney test *n* = 20–21 Scale bars: **b** 50 μm, **d** 50 μm, **g**, 100 μm, **j–k** 100 μm. Scale bar on **m** is 400 nm for **l–o**, 175 nm for **p**



was found in the brain parenchyma in microglia-depleted mice (Fig. 1i), indicating the lack of effective elimination of the infected neurons by microglia. To investigate this phenomenon further, we visualized viral proteins using super-resolution microscopy together with the microglial phagosome/lysosome marker CD68 (Fig. 1j, k). In control mice, microglial processes tightly surrounded the cell bodies of infected neurons with viral proteins appearing in microglial phagosomes (Fig. 1j). Importantly, the absence of microglia resulted in a massive increase in extracellular viral proteins and PRV-immunopositive cell debris (Fig. 1k). Confirming these observations, electron microscopy revealed a direct

contact between microglial processes and the cell membrane of the infected neurons as well as the uptake of infected neurons by microglia (Fig. 1l, m). In contrast, disintegrated neuronal membranes and extracellular immunogold-labelled viral proteins were observed in microglia-depleted animals (Fig. 1n–p). BDG products, including GFP signal [5, 6], viral capsids and PRV-immunopositive profiles were not observed in the nucleus or the cytoplasm of microglia [Suppl. Fig. 2 (Online Resource 1)], indicating that productive infection does not develop in these cells, in line with earlier reports [6, 50]. The absence of microglia was also associated with the development of diverse neurological symptoms in infected

Fig. 2 Microglia rapidly isolate virus-infected neurons in the brain. **a** Microglia (Iba1, yellow) are recruited to neurons infected with PRV expressing GFP with immediate-early kinetics (BDG) in the hypothalamic paraventricular nucleus (PVN). Note that microglia recruitment starts after the expression of the immediate-early marker GFP (phase I), when low levels of viral structural proteins become detectable (phase II). High levels of viral structural proteins indicate a late stage of viral infection (phase III), which is associated with higher number of microglia recruited to infected cells. **b** Microglial numbers increase significantly around virus-infected neurons in parallel with the propagation of infection **c** In vivo two-photon imaging reveals the recruitment of microglia (green) to virus-infected neurons (red) in real-time. Retrograde transsynaptic infection was induced by the virus BDR in Cx3Cr1^{+GFP} microglia reporter mice 7 days prior to imaging to visualize infected cells in the cerebral cortex based on the immediate-early DSRRed expression. **d** Merged Z-planes of microglial cells around a PRV-DSRed-positive neuron (arrows indicate recruited microglia, arrowheads indicate microglial processes contacting the infected cell). **e** Microglial process velocity increases significantly in response to viral infection compared to that seen in control mice. **f–i** Correlated CLSM, electron microscopy and electron tomography confirms direct microglia–neuron contact with intercellular molecular links in early phase of viral infection. **f**, 3D-reconstruction from deconvolved confocal stack of a recruited microglia (green) engulfing a PRV-positive neuronal cell body (cyan) with CD68-positive phagolysosomes (magenta) within the microglia, arranged around infected neuron. Upper insert: single image plane of the same confocal stack. Middle insert: 3D-reconstruction of the same microglial cell, rotated 180° around the vertical axis. Asterisk labels the bay engulfing the soma of the infected neuron. Lower insert: 3D-reconstruction of the infected neuronal cell body with surrounding phagolysosomes located within the microglia. **g** Transmission electron micrograph shows the same cells on an ultrathin section matching the confocal image plane in the upper insert in **f**. Note that microglial processes surround the apical dendrites of the infected neuron. **h** Part of **g** (in white box) enlarged. Note that the nucleus is void of viral capsids and the membrane of the neuron is intact (white arrowheads), confirming the early phase of infection. **i** 3 nm thick electron tomographic section and corresponding 3D-reconstruction shows the very close cell–cell contact between the same microglia (green pseudocolor) and infected neuron (cyan pseudocolor, mitochondria are in yellow). White arrows point to putative contact sites, where the distance between the membranes is the smallest, and several filament-like structures (magenta) can be observed connecting the two cells. **b** *** $p < 0.001$ one-way ANOVA, $n = 8$; **e** * $p < 0.05$, unpaired t test, $n = 10$. Scale bars: **a** 10 μm ; **c** 20 μm ; **d** 20 μm ; **f** 2 μm ; **g** 1 μm ; **h** 400 nm; **i** 100 nm

mice starting on the 5th day of infection, when infected neurons were numerous in the brain stem, the hypothalamus and the autonomic-associated nuclei in the limbic system. These symptoms included heavy breathing, muscle spasms and seizure-like episodes, which were absent in control mice (Fig. 1q).

Microglia recruitment is initiated rapidly to virus-infected neurons in the brain

Having confirmed the instrumental role of microglia in controlling neurotropic virus infection, we aimed to investigate whether the recruitment of microglia occurs early enough to allow the isolation of infected neurons prior to

the breakdown of neuronal cell membranes. To this end, we made use of the immediate-early marker, GFP, expressed in infected neurons several hours prior to the production of viral structural proteins, which allows time-mapping the different phases of infection at a single neuron level [5, 6, 15]. GFP-positive neurons expressing low levels of viral structural proteins (Phase II cells) already appeared more surrounded by microglia than the majority of neurons expressing GFP only (Phase I, Fig. 2a, b), suggesting that recruitment of microglia is induced within a few hours of infection, by the time viral structural proteins are produced [5, 6, 15]. The number of microglia increased further around neurons expressing high levels of viral proteins (Phase III), resulting in 1–3 microglial cells contacting the cell body of a single, infected neuron (Fig. 2a, b).

To investigate the processes of microglia recruitment in vivo in real-time, we used another virus strain, PRV-Bartha-DupDSRed (BDR), enabling early phases of infection to be identified based on the production of the red fluorescent protein, DSRRed [4]. Mice with functional microglia were allowed a longer, 7 days survival after virus injection, resulting in the spread of infection to the upper layers of the cerebral cortex (Fig. 2c). In vivo two-photon imaging in Cx3Cr1^{+GFP} (microglia reporter) mice revealed the recruitment of microglia within 3 h of the increases observed in neuronal DSRRed signal [Suppl. Video 1. (Online Resource 2)]. We used an optimized cranial window preparation for these studies as developed earlier, to avoid any disturbance of microglia [56]. 3D reconstruction from 2P Z-stack revealed that microglial processes formed a barrier-like structure, with several contact points around the cell body of the infected neuron (Fig. 2d). Microglia recruited to infected cells showed increased process velocity compared to microglia distant from sites of virus infection (Fig. 2e), indicating that microglia may respond to local signals induced by infected neurons. To further explore whether microglial contacts with the cell membranes of infected neurons can be formed in the early phases of virus infection, we visualized microglia–neuron contacts with confocal microscopy in Cx3Cr1^{+GFP} mice, followed by the investigation of selected neurons with correlated electron microscopy and electron tomography. 3D reconstruction from confocal Z-stack revealed the formation of microglial contacts around the cell body and the main dendrites of infected neurons [Fig. 2f; Suppl. Video 2. (Online Resource 3)] prior to the appearance of mature virions in the neuronal cytoplasm (Fig. 2g, h). At this stage of infection, neuronal cell membranes were intact with normal chromatin structure seen in the nucleus [Suppl. Fig. 2b (Online Resource 1)]. Microglial processes surrounding infected neurons showed CD68-immunopositivity, indicating the phagocytic activity of microglia (Fig. 2f, g). In addition, electron tomography revealed the formation of specific membrane interactions between infected neurons

and microglia suggesting the recognition and contact of the intact cell membranes by recruited microglial processes (Fig. 2i).

Virus-infected cells are recognised and engulfed by microglia in vitro

To study the mechanisms of microglia recruitment to sites of infection, we first established co-cultures of neurons and

GFP-positive microglia from $Cx3Cr1^{+/GFP}$ mice and performed time-lapse imaging over a 48 h period. Microglia contacted the cell body and the main processes of uninfected neurons without causing injury or showing phagocytic activity [Fig. 3a, upper and mid panel and Suppl. Videos 3, 4. (Online Resources 4, 5)]. In contrast, microglia added to virus-infected neurons were recruited to and phagocytosed infected cells [Fig. 3a, bottom panel and Suppl. Video 5. (Online Resource 6)]. Next, we aimed to study the behaviour

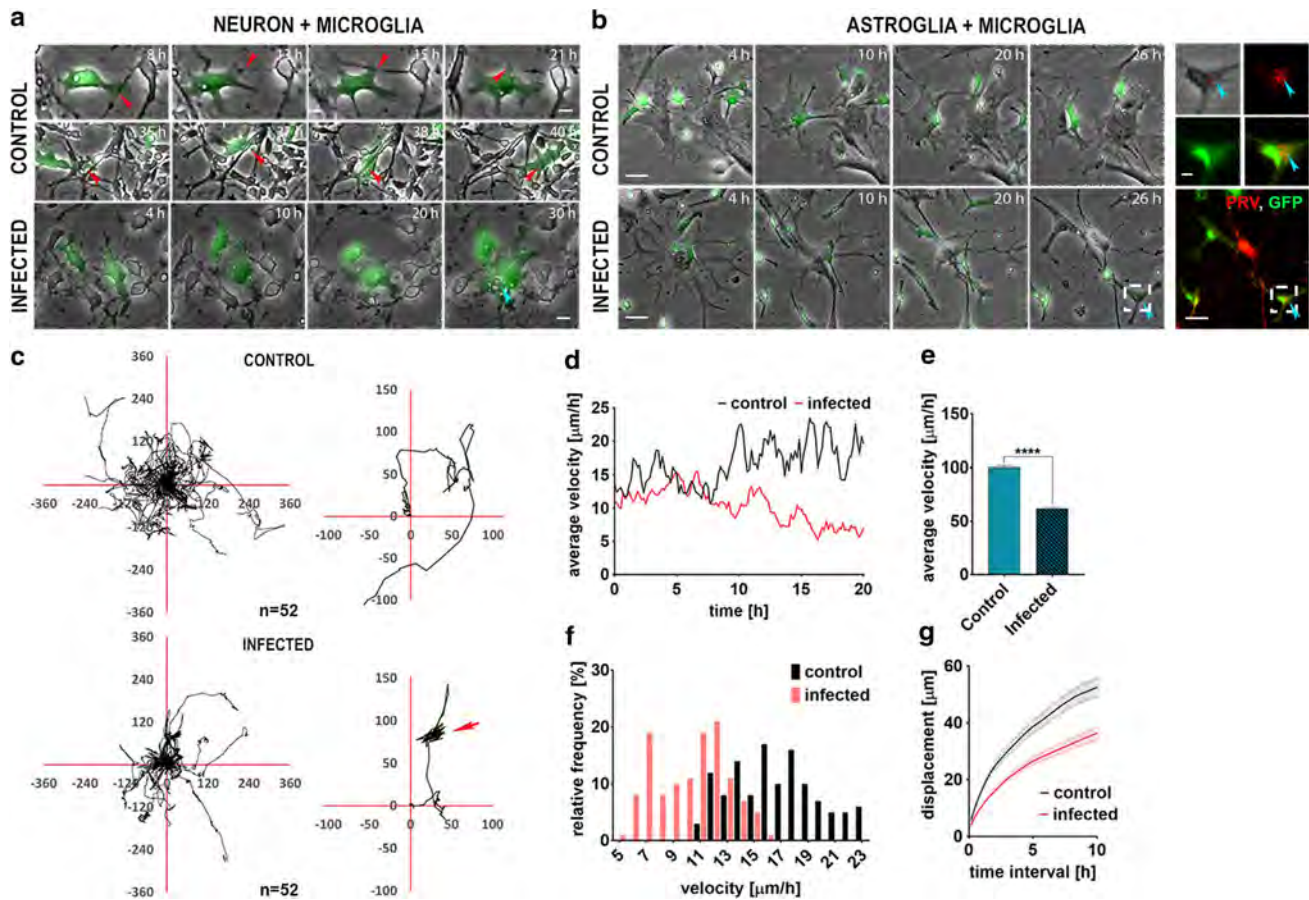


Fig. 3 Virus infection triggers the recruitment and phagocytic activity of microglia in vitro. **a** $Cx3Cr1^{+/GFP}$ microglial cells (green) repeatedly interact with non-infected neuronal processes and cell bodies without hindering process outgrowth or affecting network stability. Red arrows point to an uninterrupted growing neurite (upper panel and Supplementary Video 3.) or a microglia slipping under a dense neuronal network (mid panel and Supplementary Video 4.). Microglial cells contacting PRV-infected neurons flatten and phagocytose compromised cells (blue arrow, bottom panel), also see Supplementary Video 5. **b** $Cx3Cr1^{+/GFP}$ microglial cells (green) move freely in non-infected astroglial cultures making and releasing contacts with several astrocytes (upper panel and Supplementary Video 6.) while they are recruited to infected cells (bottom panel and Supplementary Video 7.) and after scanning they display phagocytic activity (blue arrow). Satellite images: PRV + particles (red), eaten up by a $Cx3Cr1^{+/GFP}$ microglial cell (green). **c** Trajectories of randomly chosen microglial cells ($n=52$) over 24 h in control or infected astroglial

cultures. Individual cell trajectories were centered to start from the origin and superimposed for better comparison of migration directionality. Insets show typical trajectories. Note the random walk behaviour in the trajectory in the upper inset (control), and the shorter trajectory with targeted directionality (arrow) characterizing the slower migrating and scanning microglial cells in infected cultures in the lower inset. **d** Time-dependent average velocities of microglial cell populations in control ($n=54$) or infected ($n=56$) astroglial cultures. **e** Average velocities of microglial cells over 24 h are significantly lower in infected astroglial cultures. **f** Frequency distribution of time-dependent average velocities of microglial populations in control or infected astroglial cultures. **g** Average displacement of microglial cells in various time intervals of migration in control or infected astroglial cultures. Error stripes correspond to s.e.m. Scale bars: **a** 10 μm ; **b** 25 and 10 μm , respectively. Data are expressed as mean \pm s.e.m. **e** $n=121$, unpaired t test, **** $p < 0.0001$

of microglia with more advanced statistical approaches [24, 43, 44], which required co-cultures of microglia with very sparsely distributed cells. Since this was not feasible with neuronal cultures, we took advantage that astrocytes are also infected with PRV under in vitro conditions [24]. In fact, in sparse astrocyte cultures microglial cells migrated much longer distances on average to reach infected cells. Statistical analysis of longer cell trajectories thus enabled us to more effectively separate random migration from targeted migration of microglial cells to infected cells, followed by localized scanning activity and phagocytosis [Fig. 3b, upper panel and Suppl. Video 6. (Online Resource 7)].

As seen in neuronal cultures, microglia recognised and phagocytosed infected astrocytes, which was confirmed by immunofluorescent detection of the engulfed cells after imaging [Fig. 3b, bottom panel and insert, Suppl. Video 7. (Online Resource 8)]. Statistical analysis revealed the recruitment of microglia to PRV-infected cells and the formation of prolonged cell-to-cell contacts. This was evidenced by microglia trajectories showing characteristic localized pattern as cells tend to remain at virus-infected cells once they met them (Fig. 3c), which is in sharp contrast with microglia trajectories in uninfected cultures showing a random walk behaviour pattern. This phenomenon was associated with a reduction of cell velocities in infected cultures ($16.6 \pm 3.2 \mu\text{m/h}$ in control and $10.3 \pm 2.6 \mu\text{m/h}$ in infected cultures, Fig. 3d–g) indicating that signals from infected cells direct microglial migration, scanning behaviour and subsequent phagocytic activity. Similar microglial responses were seen in neuronal/microglial co-cultures [Suppl. Fig. 3 (Online Resource 1)]. Importantly, the development of productive infection was never observed in microglia in vivo or in vitro even after the direct exposure of the cells to high viral titres or following extensive phagocytic activity, as evidenced by the absence of the immediate-early GFP signal and PRV proteins from microglia outside phagosomes [Suppl. Fig. 4 (Online Resource 1)].

Nucleotides released from infected cells trigger microglia recruitment and phagocytosis via microglial P2Y12

To investigate the production of inflammatory mediators induced by neurotropic virus infection, we measured several inflammatory cytokines and chemokines that are commonly upregulated in response to virus infection [37] in cultured neurons and astrocytes. Bacterial lipopolysaccharide (LPS), a widely used proinflammatory stimulus, induced a robust increase in TNF α , IL-6, CXCL1, CCL5 (RANTES), G-CSF and MCP-1 levels in astrocytes and CXCL1, CCL5 and MCP-1 levels in neurons. In contrast, virus infection increased only CCL5 levels in both cell types at mRNA and peptide levels 24 h after infection [Suppl. Fig. 5 (Online

Resource 1)], which did not explain the rapid recruitment of microglia to infected cells.

Since synthesis and release of chemokines could last for several hours and our in vivo data suggested rapid microglia recruitment to sites of virus infection, we checked whether purine nucleotides such as ATP that are chemotactic for microglia at a short time scale [14] could be released from compromised cells. We found that cultured neurons released ATP after virus infection, which was associated with reduced ATP, ADP, AMP and adenosine levels in cell lysates (Fig. 4a, b), within hours upon the expression of the immediate-early marker, GFP, which precedes the expression of viral structural proteins required for productive infection [5, 6, 15]. The changes in purinergic metabolites were associated with increased ecto-ATPase levels in infected cells (Fig. 4c), but were not due to apoptosis or necrosis, since at the early stages of infection neurons expressing high levels of GFP showed no annexin V binding or uptake of propidium iodide [Suppl. Fig. 6 (Online Resource 1)]. In addition, increased ecto-ATPase levels and NTDPase1 expression were found in microglia at sites of virus infection in the brain (Fig. 4d–f), indicating that microglia respond to changes in the levels of purine nucleotides [55]. To investigate the mechanisms mediating microglial responses to purine nucleotides released from infected cells, we assessed microglial responses in co-cultures of P2X7 $^{-/-}$ or P2Y12 $^{-/-}$ microglia and wild type astrocytes. Similarly to that seen in wild type microglia (Fig. 3c–g), motility of P2X7 $^{-/-}$ cells decreased when exposed to infected cells (Fig. 4g–j) and trajectories showed characteristic localized pattern due to frequent scanning activity [Fig. 4k, Suppl. Video 8. (Online Resource 9)], indicating that P2X7 deficiency does not prevent the recognition of virus-infected cells by microglia. In contrast, virus-exposed P2Y12-deficient microglia showed increased motility (Fig. 4l–o) with trajectories characteristic of random walk behaviour and lacking the localized pattern [Fig. 4p, Suppl. Video 9. (Online Resource 10)], suggesting that these cells are unable to display targeted recruitment in response to infection. Furthermore, wild type and P2X7 $^{-/-}$ microglia showed a markedly increased phagocytic activity in infected cultures, which was fully abolished in P2Y12-deficient microglia [Fig. 4q–s and Suppl. Videos 10–11 (Online Resources 11–12)]. Thus, P2Y12 is a key contributor to recognition of compromised cells by microglia and to microglial phagocytosis of virus-infected cells in vitro.

Recruitment of microglia and elimination of virus-infected neurons are mediated by microglial P2Y12 in vivo

Next, we investigated whether nucleotides released from compromised neurons are involved in the recruitment of microglia in vivo. We found that virtually all microglia

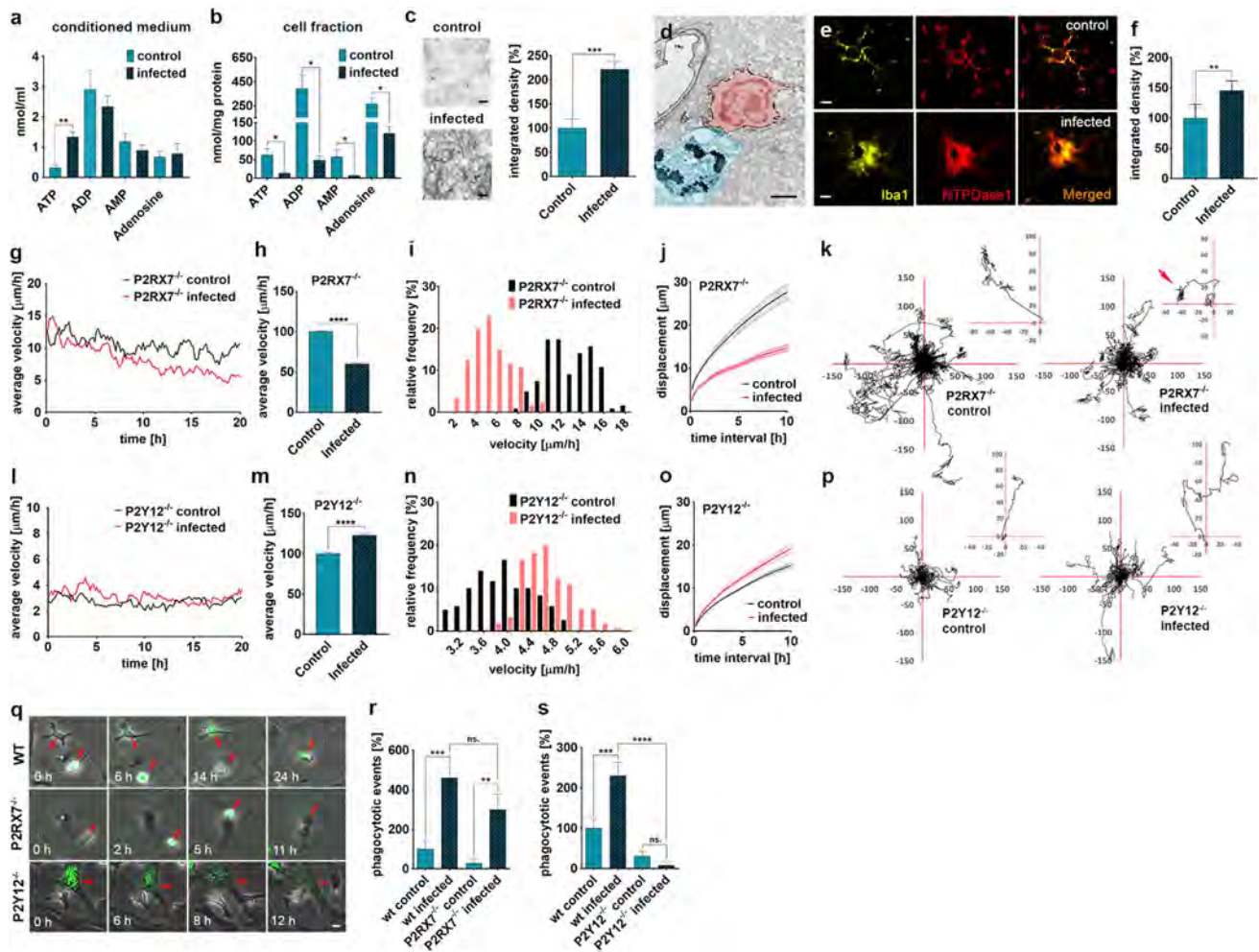


Fig. 4 Purinergic signaling mediates microglia recruitment and phagocytosis upon virus infection. **a** and **b**, HPLC analysis of ATP, ADP, AMP and adenosine levels in the supernatant (**a**) and in the cellular fraction (**b**) of control and virus-infected neuronal cultures. **c** Ecto-ATPase enzyme histochemistry and densitometric analysis. The ecto-ATPase activity is significantly enhanced upon infection. **d** NTPDase1 expression of a microglial cell (red) in the PRV-infected brain. Note that the NTPDase1⁺ microglia is in contact with an apparently disintegrating neuron (blue). **e** NTPDase1 expressing Iba1⁺ microglial cells in control and infected mouse brains. **f** Densitometric analysis of NTPDase1 expression in control and infected mouse brain slices. **g** and **l** Time-dependent average velocities of P2RX7^{-/-} ($n_c=67$, $n_i=74$) or P2Y12^{-/-} ($n_c=51$, $n_i=59$) microglial cell populations in control or infected astroglial cultures. Note the gradual decrease in population velocity of P2RX7^{-/-} microglia in infected culture and the lack of such decrease in P2Y12^{-/-} microglia in similar conditions. **h** and **m** Average velocities of P2RX7^{-/-} or P2Y12^{-/-} microglial cells over 24 h in control or infected astroglial cultures, **i** and **n** Frequency distribution of time-dependent average velocities of P2RX7^{-/-} or P2Y12^{-/-} microglial populations in control or infected astroglial cultures. **j** and **o** Average displacement of P2RX7^{-/-} or P2Y12^{-/-} microglial cells in various time intervals in control or infected astroglial cultures. Error stripes cor-

respond to s.e.m. **k** and **p** Trajectories of equal number ($n=50$) of randomly chosen P2RX7^{-/-} or P2Y12^{-/-} microglial cells over 24 h in control or infected astroglial cultures. Individual cell trajectories were centered to start from the origin and superimposed for better comparison of migration directionality. Insets show typical trajectories. Note the more localized migration pattern due to the scanning activity of P2RX7^{-/-} microglia in infected conditions (red arrow) as compared to random walk behaviour and the lack of such localization in the trajectories of P2Y12^{-/-} microglia in infected astroglial culture. **q** Phagocytosis activity of wild type (WT), P2RX7^{-/-} or P2Y12^{-/-} microglial cells in astroglial cultures infected with BDG virus. Green colour indicates the virus initiated expression of GFP in infected cells. Red arrows point to the phagocytosed cells. Note, that P2Y12^{-/-} microglia is unable to incorporate the infected cell. **r** and **s** Percentage of phagocytotic events by wild type vs. P2RX7^{-/-} (**r**) or P2Y12^{-/-} (**s**) microglial cells in control and infected cultures. **a**, **b** $n=4$ per group, unpaired t test, $*p<0.05$; $**p<0.001$ **c** $n=6$, unpaired t test, $***p<0.0001$ **f** $n=7$, unpaired t test, $**p<0.01$. **h** and **m** $n=121$, unpaired t test, $****p<0.0001$. **r** and **s**, $n=9$ per group, one-way ANOVA, $**p<0.001$; $***p<0.0005$, $****p<0.0001$, ns=not significant. Scale bars: **c** 25 μm ; **d** 5 μm ; **e** 10 μm ; **q** 10 μm data are expressed as mean \pm s.e.m

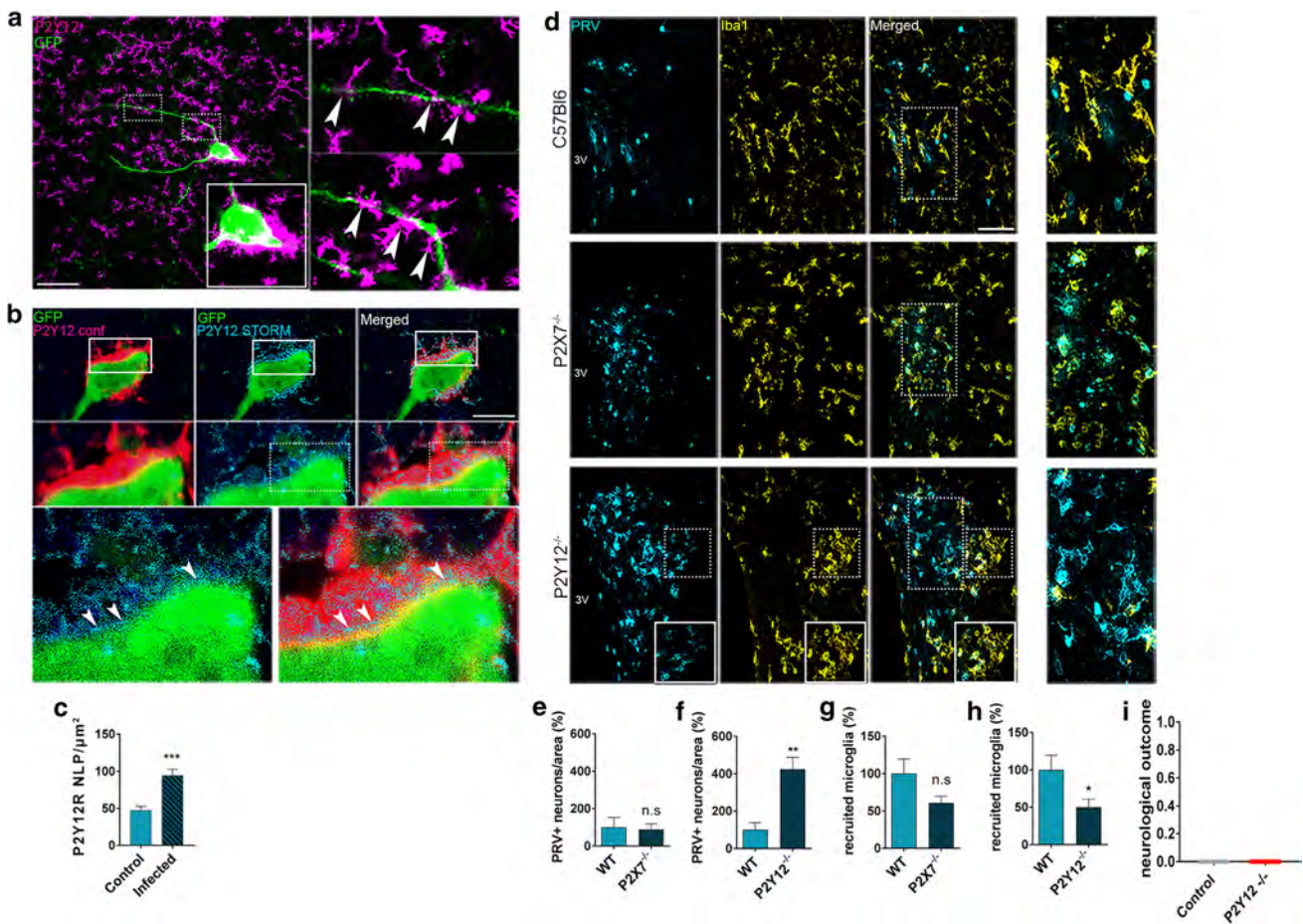


Fig. 5 P2Y12 receptor mediates recruitment of microglia in response to virus infection in vivo. **a** P2Y12-positive microglia are recruited to virus-infected neurons in the mouse brain (paraventricular hypothalamic nucleus is shown, maximum intensity projection from confocal Z stack of 30 steps, made with 0,50 µm step size). **b** STORM super-resolution microscopy reveals P2Y12 receptors clustering at microglial cell membranes contacting virus-infected neurons. Neurons are identified by GFP expression with immediate-early kinetics indicating early stages of PRV infection. **c** Based on STORM images, microglial P2Y12 localisation point numbers (NLP) are significantly increased at microglia–neuron contact sites, when microglia contacting infected neurons are compared with microglia contacting uninfected cells. **d** Fluorescent images showing the propagation of virus infection in the paraventricular nucleus of the hypothalamus in wild type, P2X7^{-/-} and P2Y12^{-/-} mice. Infected neurons in the late phase of PRV infection

are revealed by immunostaining against viral structural proteins (cyan blue), and microglia are labelled with Iba1 (yellow) (Maximum Intensity Projection from confocal Z stack of 16 steps, made with 0.88 µm step size). **e, f** In P2Y12^{-/-} mice ($n=7$) significantly less ($p<0.05$) microglia are recruited to infected neurons compared to that seen in wild type ($n=6$) and P2X7^{-/-} mice ($n=7$), area: 0.2 mm². **g, h** Correspondingly, significantly higher numbers of infected neurons are seen in P2Y12^{-/-} mice compared to wild-type animals, whilst no significant difference is observed between P2X7^{-/-} and wild-type mice. area: 0.2 mm². **i** Absence of P2Y12 receptor did not result in any neurological symptoms 6 days after virus infection. 3 V - 3rd ventricle. Scale bars: a, 50 µm; b, 100 µm; d, 50 µm. All data expressed as mean ± s.e.m **c** *** $p<0.0001$ unpaired t test $n=7-13$ cells **e, g** N.S. not significant **f** ** $p<0.01$ Mann–Whitney test, $n=7$ **h** * $p<0.05$ $n=7$ unpaired t test

surrounding the cell body and the processes of infected neurons in either C57BL/6 or Cx3Cr1^{+/-GFP} mice expressed P2Y12 receptors [Fig. 5a, Suppl. Fig. 7 (Online Resource 1)]. STORM super-resolution microscopy, which allowed visualization of P2Y12 receptors at 20 nm lateral resolution showed that microglial P2Y12 receptor numbers increased over twofold in response to infection and P2Y12 clusters in microglial processes contacting infected neurons were localized around the membrane of the infected cell (Fig. 5b, c). To investigate the contribution of purinergic signalling

to antiviral immunity in vivo, we induced virus infection in mice lacking P2X7 or P2Y12 receptors (Fig. 5d). Both receptors are abundant in microglia, whereas P2Y12 is a microglia-specific marker in the brain [55] [see also Suppl. Fig. 7 (Online Resource 1)]. We found that an absence of P2Y12 resulted in >50% reduction in the numbers of microglia recruited to infected neurons in the PVN (Fig. 5f, h; $p<0.05$), whereas a non-significant trend to reduction (by 35%) was seen in P2X7^{-/-} mice (Fig. 5e, g). Similarly to that seen after selective elimination of microglia (Fig. 1g),

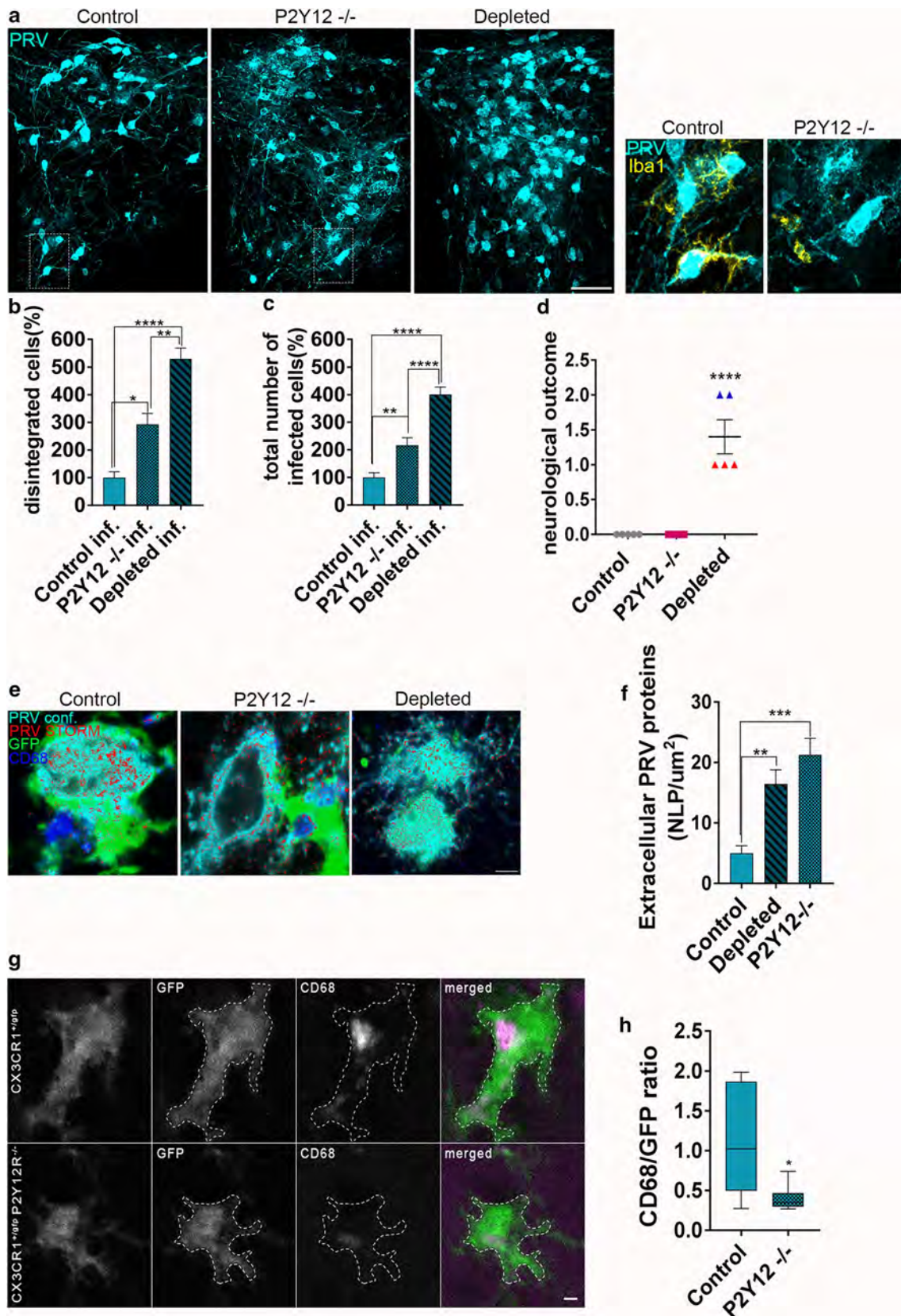


Fig. 6 The absence of P2Y12-positive microglia leads to increased neuronal infection, impaired phagocytosis and the accumulation of extracellular virus particles. **a** PRV immunofluorescence showing a marked increase in the number of infected (PRV-positive) neurons in P2Y12^{-/-} mice and after microglia depletion, compared to control animals. Note the lack of recruited Iba1 + microglia (yellow) to PRV-positive neurons in P2Y12^{-/-} mice (inserts). **b** Numbers of infected (PRV+), disintegrated neurons in control, P2Y12^{-/-} and microglia-depleted mice. **c** Total number of infected (PRV+) neurons is significantly higher in P2Y12^{-/-} and microglia-depleted mice. **d** An absence of microglia, but not P2Y12-deficiency results in rapidly deteriorating neurological symptoms 5 days after PRV infection (0: no symptoms, 1: drooling and heavy breathing, 2: seizures and muscle spasms). **e** STORM super-resolution microscopy reveals a marked increase in extracellular PRV proteins in both P2Y12^{-/-} and microglia-depleted mice compared to wild type mice. **f** Quantitative assessment of extracellular PRV proteins on STORM images. Number of extracellular PRV-positive localisation points (NLP) is shown in each group. **g** Images showing microglial phagolysosomes identified by CD68 immunofluorescence in control Cx3Cr1^{+/eGFP}, and P2Y12-deficient (Cx3Cr1^{+/eGFP} x P2Y12^{-/-}) mice. **h** P2Y12-deficient microglia show a significant reduction of CD68-positive phagolysosomes compared to wild-type microglia (CD68 immunofluorescent integrated density/GFP immunofluorescent integrated density within microglial cell bodies, $p=0.0322$, Mann–Whitney U test, $n=35$ cells/16 ROIs). Data on **d** expressed as median and interquartile range, otherwise as mean \pm s.e.m. **b, c, d** Mann–Whitney U test, $n=5-6$. Scale bars: **a** 100 μ m; **e** and **g** 2 μ m. All data expressed as mean \pm s.e.m. **b** Control vs P2Y12 $*p < 0.05$; Control vs Depleted $****p < 0.0001$; P2Y12 vs Depleted $**p < 0.001$, One-Way ANOVA **c** Control vs P2Y12 $**p < 0.001$; Control vs Depleted $****p < 0.0001$; P2Y12 vs Depleted $****p < 0.0001$ One-Way ANOVA **d** Control vs Depleted $****p < 0.0001$; P2Y12 vs Depleted $****p < 0.0001$ One-Way ANOVA **f** Control vs Depleted $**p < 0.001$; Control vs P2Y12 $****p < 0.0001$ One-Way ANOVA

the number of infected neurons containing viral structural proteins increased over threefold in P2Y12^{-/-} mice (Fig. 5f, h), but no changes were seen in P2X7^{-/-} mice (Fig. 5e, g). Interestingly, clusters of microglia observed in the brain at sites of virus infection in P2Y12^{-/-} mice were located in the close vicinity of degenerated, PRV-immunopositive neurons, suggesting that P2Y12 deficiency markedly impairs microglial responses to signals released from infected neurons and compromises phagocytic responses, but does not fully block microglial migration to already disintegrated cells.

Despite the markedly increased number of infected neurons in P2Y12^{-/-} mice, no neurological symptoms have been observed (Fig. 5i), suggesting that the absence of microglia (Fig. 1q), but not of microglial P2Y12 alone, can cause the adverse neurological outcome in this model. To confirm this and to test for possible mechanisms underlying this difference, a new study was performed enabling a direct comparison of control, P2Y12^{-/-} and microglia-depleted mice after infection. In P2Y12^{-/-} mice there was deficient recruitment of microglia to infected neurons. As earlier, both the absence of P2Y12 and microglia depletion caused marked elevations in the numbers of infected and disintegrated neurons, but both these measures were elevated significantly

more in the microglia-depleted animals (Fig. 6a–c). Histological analysis on cresyl violet-stained brain sections also demonstrated significantly increased neuronal injury/loss in both P2Y12^{-/-} and microglia-depleted animals with highest levels seen after microglia depletion [Suppl Fig. 8 (Online Resource 1)]. However, the neurological symptoms only emerged with microglia depletion (Fig. 6d). In contrast, levels of extracellular virus proteins were identical in P2Y12^{-/-} and microglia-depleted mice, while markedly increased compared to control mice (Fig. 6e, f). P2Y12^{-/-} microglia did show significantly lower levels of CD68-positive phagolysosomes compared to that seen in control animals (Fig. 6g, h), indicating the lack of normal phagocytic activity in the absence of P2Y12.

Microglia recruit leukocytes into the brain in response to virus infection independently of P2Y12-mediated signalling

Since previous studies have shown that blood-borne cells are recruited to the brain after virus infection [15, 48], we wondered whether microglia and P2Y12-mediated actions are involved in neuroinflammatory and neurobehavioral changes in this model. As expected, numerous round-shaped or elongated leukocytes with high CD45 immunopositivity were recruited to sites of virus infection (Fig. 7a). These were clearly discriminated from microglia based on their higher CD45 expression, morphology, the absence of the microglia/macrophage marker Iba1 from the majority of the cells and the complete absence of P2Y12, which is a microglia-specific marker in the brain [Fig. 7b, Suppl Fig. 7 (Online Resource 1)]. P2Y12 is known to be expressed at high levels by microglia compared to monocytes or monocyte-derived macrophages [45]. Surprisingly, selective elimination of microglia resulted in a profound reduction in CD45-positive leukocytes at sites of virus infection (Fig. 7a, c), despite the increased number of infected neurons compared to that seen in control mice (Fig. 1g). This was not due to changes in peripheral leukocyte populations in response to PLX5622, since elimination of microglia by PLX5622 did not cause a significant reduction in circulating or splenic myeloid cell populations including monocytes, granulocytes and macrophages, and did not affect numbers of T cells and B cells [Suppl. Figs. 9 and 10 (Online Resource 1)], confirming our earlier results obtained by another CSF1R antagonist, PLX3397 [56]. Infiltrating leukocyte populations have also been characterized by flow cytometry. The main population of CD45-positive cells recruited in response to virus infection were monocytes (CD45^{high}, Cx3Cr1⁺, CD11b⁺, Ly6C^{high}, Ly6G⁻ cells), which population was markedly reduced in the absence of functional microglia (Fig. 7d–g). A non-significant trend to increased

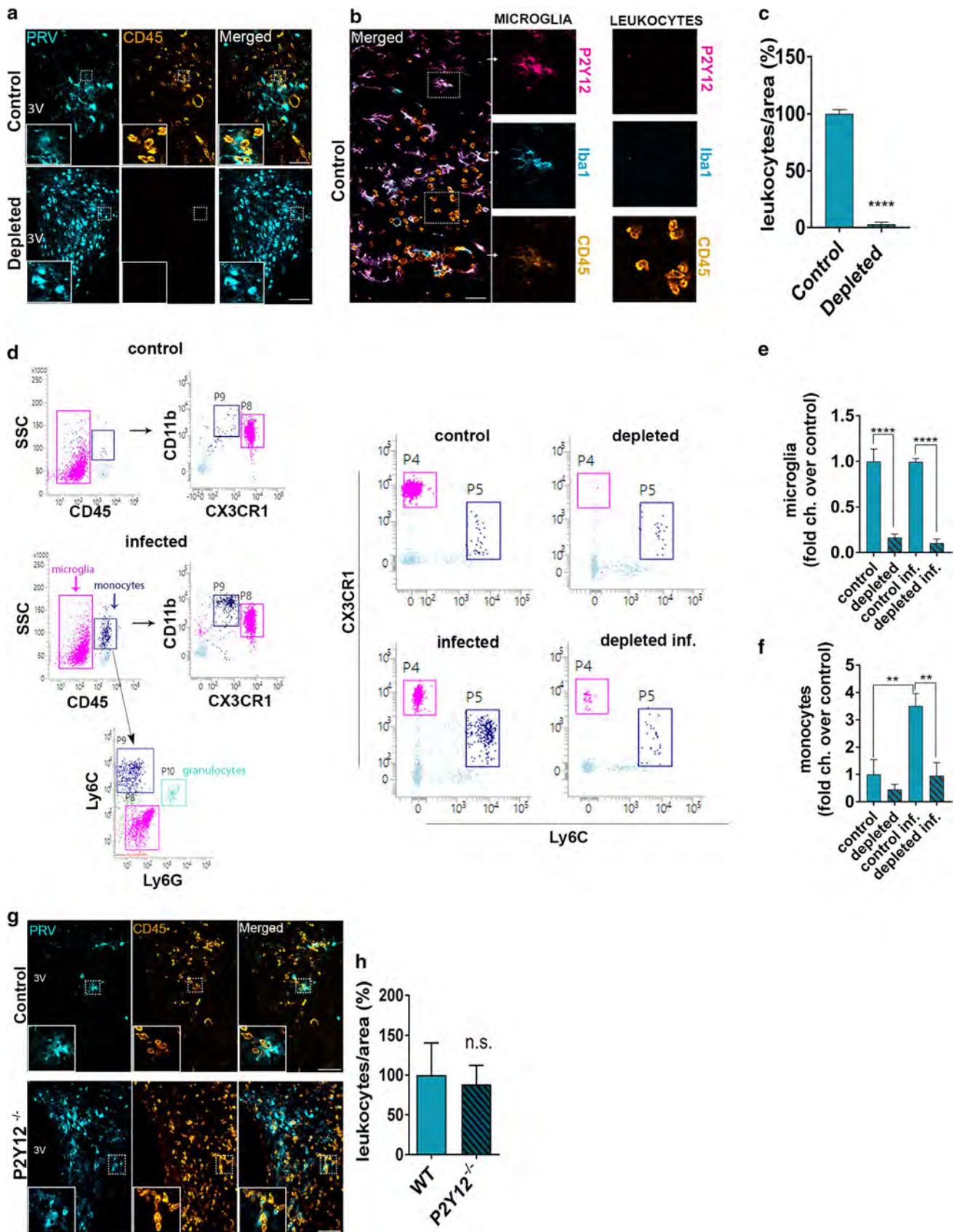


Fig. 7 Microglia are instrumental for leukocyte recruitment into the brain in response to virus infection, which is independent of P2Y12-mediated signaling. **a** Recruitment of CD45-positive leukocytes (orange) to the hypothalamic paraventricular nucleus (PVN) is seen around virus-infected neurons (cyan), which is markedly reduced by selective elimination of microglia **b** P2Y12 expression (magenta) discriminates microglia from blood-borne cells expressing high levels of CD45 (orange), most of which are negative for the microglia/macrophage marker Iba1 (cyan). **c** Leukocyte numbers are significantly lower in microglia depleted animals, area: 0.2 mm², **d** Flow cytometric dot plots showing that microglia (Cx3Cr1^{high}, CD45^{low} Lys6⁻ cells, P8) can be well characterized and separated from infiltrating monocytes (Cx3Cr1^{+/int}, CD45^{high}, Ly6C^{high}, Ly6G⁻ cells, P9), during viral infection in the brain. The almost complete absence of microglia is seen after selective microglia depletion (gates P4). In spite of the exaggerated virus infection in the absence of microglia, CD45^{high} blood-borne leukocytes (P9 gate), specifically monocytes (CD45^{high}, Cx3Cr1⁺, CD11b⁺, Lys6^{high} cells, P5 gate) are profoundly reduced in the microglia depleted brains. **e** Cx3Cr1^{+/gfp} microglia are profoundly reduced in the brain after feeding mice the CSF1R inhibitor PLX5622 for 3 weeks. **f** Monocyte numbers increase significantly in response to virus infection in the brain, which is markedly reduced in microglia depleted animals. **g** Immunofluorescence shows infiltrating CD45-positive leukocytes (orange) around virus-infected neurons (cyan) in the paraventricular nucleus. **h** Numbers of infiltrating leukocytes (orange) in P2Y12^{-/-} mice are not significantly different from control animals, area: 0.2 mm² All data expressed as mean ± s.e.m **c**, *****p* < 0.0001 unpaired *t* test *n* = 12; **e** control vs depleted *****p* < 0.0001, control inf. vs depleted inf. *****p* < 0.0001 One-Way ANOVA; **f** control vs control inf. ***p* < 0.001, control inf. vs depleted inf. ***p* < 0.001 One-Way ANOVA. **h** n.s. not significant Scale bar **a**, **b**, **g**, 50 μm

CD8 T cells in the brain in response to infection was also observed, which was not influenced by microglia depletion [Suppl. Fig. 11 (Online Resource 1)]. We also found that microglia exposed to PRV in vitro produced (CCL5) RANTES and MCP-1, whereas CCL5 and IL-1α were significantly reduced in hypothalamus homogenates of infected mice after microglia depletion [Suppl. Fig. 13 (Online Resource 1)]. Importantly, exaggerated virus infection in the brain was associated with an increase in circulating granulocytes in microglia depleted mice, suggesting that peripheral myeloid populations were capable of responding to virus infection, but their recruitment into the brain was inhibited by the absence of microglia [Suppl. Fig. 9 (Online Resource 1)]. Next, we investigated whether purinergic signalling through P2Y12 in microglia could contribute to leukocyte recruitment into the brain in response to virus infection. Importantly, no changes in the numbers of CD45-positive, blood-borne leukocytes were seen in P2Y12^{-/-} mice after infection and monocyte infiltration was not impaired [Fig. 7g, h; Suppl. Fig. 12a, c, (Online Resource 1)]. Thus, microglia appear to be key inducers of monocyte recruitment into the brain, but these processes are largely independent of microglial P2Y12-mediated mechanisms that play a key role in controlling the spread of virus infection.

Recruitment of P2Y12-positive microglia and leukocytes at sites of infection in the human brain during herpes simplex encephalitis

To investigate microglia recruitment and neuroinflammatory changes in the human brain, we analysed herpes simplex type 1 (HSV-1) encephalitis temporal lobe samples in which infection had been confirmed both by PCR and immunohistochemistry as reported earlier [13]. Processes of P2Y12-positive human microglial cells were extended to HSV-1-positive cells, and infected neurons were surrounded by activated microglial cells [Fig. 8a, Suppl. Table 1 (Online Resource 1)]. This has been confirmed with another specific microglial marker, Tmem119 (Fig. 8b). Infected cells were contacted by 1–3 microglia (on average 1.5 microglia/HSV1 + cell, Fig. 8c). Groups of recruited, amoeboid cells showing CD68-immunopositivity indicating phagocytic activity were also observed at sites of virus infection (Fig. 8d). Microglial cells were negative to HSV antigens suggesting that productive virus infection does not develop in these cells. Leukocytes identified by CD45-immunohistochemistry and Giemsa staining, whilst being P2Y12- and Tmem119-negative have been found at sites of virus infection in close vicinity of HSV-1-positive cells and microglia (Fig. 8e–g). A strong positive correlation between leukocyte numbers and HSV-1-positive cells was also observed (Fig. 8h). Populations of CD15-positive myeloid cells, and in lower amount, scattered CD3-positive lymphocytes and CD20-positive B cells were identified at areas of HSV1 infection (Fig. 8i). In the absence of HSV1 infection, the vast majority of Iba1-positive microglia was found to be P2Y12 positive (96%) and numbers of Tmem119-positive and P2Y12-positive microglia were similar in the brain parenchyma [Suppl. Fig. 14 (Online Resource 1)]. We found that moderate HSV1 infection (less than 50 HSV1-positive cells/mm²) was mostly associated with the activation of local microglia which were Tmem119- and P2Y12-positive. CD68-positive cells with either ramified or amoeboid morphology were also observed in these areas. At areas of advanced HSV1 infection (50–500 HSV1-positive cells/mm²), numerous CD45-positive cells were observed in the brain parenchyma, which was associated with markedly increased numbers of CD68-positive-macrophages (likely to be of both microglial and blood-borne origin). In line with this, the number of ramified microglia, and the total number of P2Y12-positive or Tmem119-positive cells was reduced [Fig. 8j, k and Suppl. Fig. 15. (Online Resource 1)]. Interestingly, similar reduction in microglial numbers was seen in mice at areas showing heavy virus load at the advanced stages of virus infection in the brain [Suppl. Fig. 16 (Online resource 1)].

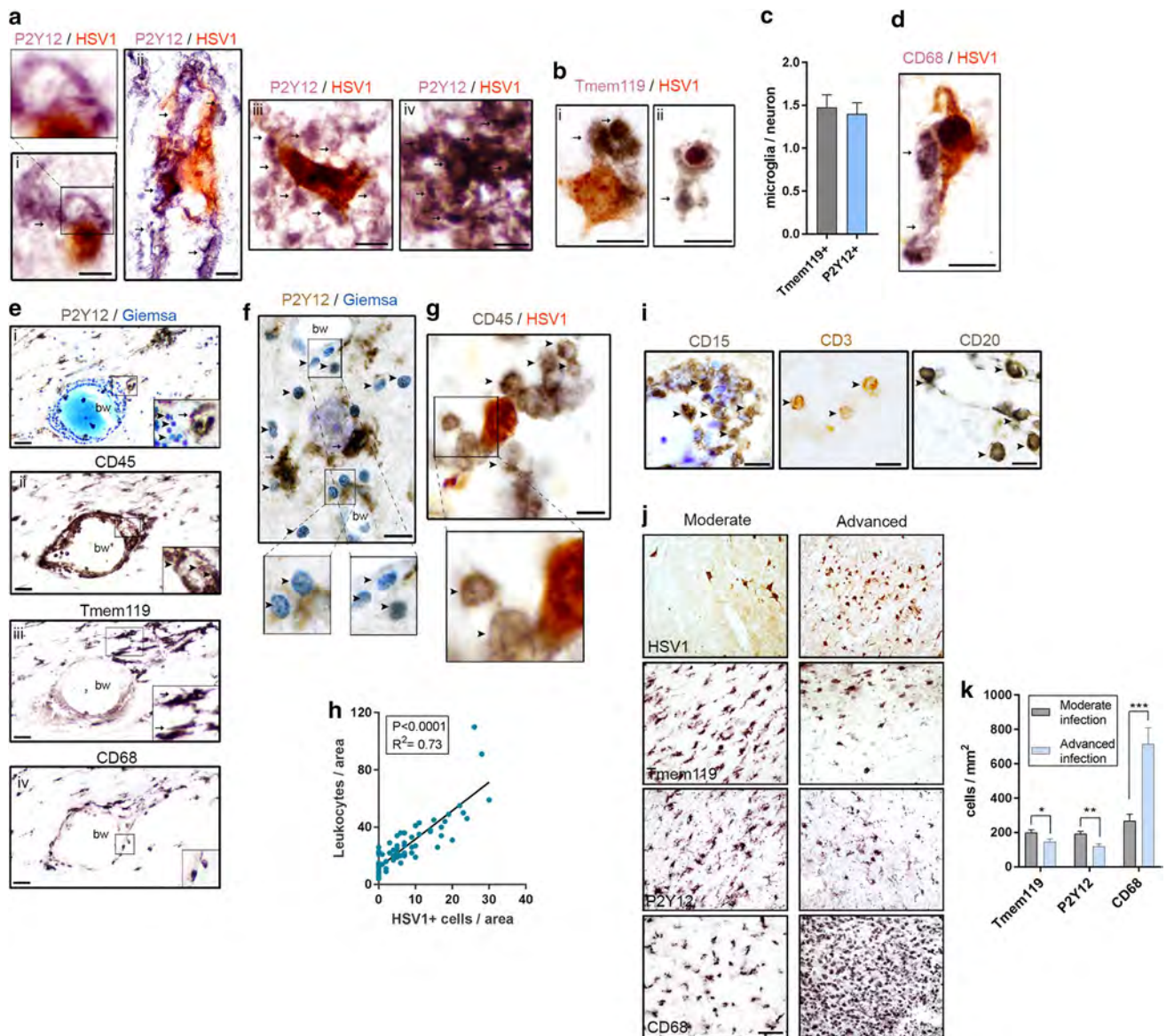


Fig. 8 Microglia and leukocytes are recruited to infected neurons in the human brain. **a** Different stages of recruitment of P2Y12+ microglia (arrows, visualized by DAB-Ni) are observed around herpes simplex-1 (HSV1)-infected cells (brown, visualized by NovaRED HRP substrate) in the human cerebral cortex. Processes of P2Y12-positive microglia contact HSV-positive neurons (i–ii) and assemblies of microglial cells are seen around infected cells (iii). Groups of P2Y12-positive microglia displaying amoeboid, phagocytic morphology in the absence of detectable HSV antigens are also found in infected areas (iv). **b** Microglia labelled with Tmem119 (arrows) are recruited to HSV1-positive neurons (i) and engulf HSV-positive cells (ii). **c** Quantification showing the average number of Tmem119-positive or P2Y12-positive microglia contacting HSV1-positive cells. **d** CD68-positive brain macrophages (DAB-Ni) surround infected neurons (NovaRED). **e** Viral infection is associated with the recruitment of leukocytes (arrowheads) visualized by Giemsa stain (i) and CD45 immunostaining (ii) in the vicinity of microglia (arrows) labelled with P2Y12 (i) or Tmem119 (iii). CD68-positive macrophages in close association with blood vessels and parenchymal CD68-positive cells with microglial morphology suggest a mixed (blood-borne and res-

ident) origin of brain phagocytes (iv). **f** In areas of virus infection, neurons surrounded by P2Y12-positive microglia are associated with leukocytes (Giemsa, arrowhead) and **g** CD45-positive leukocytes are recruited to HSV1-positive cells. **h** Leukocyte numbers in infected brain areas show correlation with the number of virus-infected cells. $p < 0.0001$, linear regression, $n = 64$ FOV, from 5 patients. **i** CD15-positive myeloid cells, and in lower amount, CD3-positive lymphocytes and CD20-positive B cells are observed at areas of HSV1 infection. **j** Moderate HSV1 infection (less than 50 HSV+ cells/mm²) is associated with the presence of numerous Tmem119-positive, P2Y12-positive microglia, and CD68-positive microglia/macrophages, whilst decreased numbers of Tmem119 and P2Y12-positive cells. In advanced HSV1 infection (50–500 HSV+ cells/mm²), markedly increased numbers of CD68-positive brain macrophages are observed in the brain parenchyma. **k** Quantification of parenchymal microglia and CD68-positive brain macrophages in the case of moderate and advanced HSV1 infection. bw—blood vessel. Scale bars: **a**, **b**, **d**, **f**, **g**, **h**, **i**—10 μ m; **e** and **j**—50 μ m. **k** * $p < 0.05$, ** $p < 0.001$, *** $p < 0.0001$

Discussion

Here, we show that microglial P2Y₁₂-mediated responses are essential for the recognition and effective elimination of compromised neurons after virus infection that reaches the brain exclusively via retrograde transsynaptic spread. Microglia recruitment occurs within a few hours *in vivo* and leads to the phagocytosis of infected cells. Marked increases in the number of disintegrated cells and leakage of viral antigens into the extracellular space are seen in the absence of functional microglia, which are associated with exaggerated infection and the development of neurological symptoms. We also show that P2Y₁₂ receptors are key drivers of microglial phagocytosis both *in vivo* and *in vitro* and that microglial P2Y₁₂ is essential for appropriate responses to nucleotides released by infected neurons in the brain. Furthermore, we identify microglia as key inducers of monocyte recruitment into the brain in response to neurotropic virus infection and also demonstrate the relevance of these findings in the human brain.

Signals mediating early recognition of injured cells and those inducing phagocytosis of synapses or neurons by microglia in the brain are poorly defined, and the mechanisms of microglial decision-making regarding the fate of injured neurons are presently unclear. Microglia may sense changes in neuronal activity via altered extracellular ion gradients, CX3CL1-CX3CR1 or CD200-CD200R interactions, purinergic signalling, pannexin-1 hemichannels and other mechanisms to shape synaptic connectivity and neuronal networks under both physiological or pathological conditions [3, 28, 36, 53]. In addition, we and others have shown that 'danger signals' from injured cells in the brain such as DNA, HMGB1, heat shock proteins or ATP act as potent activators of microglia and also contribute to the outcome in different brain pathologies [16, 21, 34, 35]. However, due to the complexity of these signalling pathways and the immediate response of microglia to any tissue disturbance, it is difficult to dissect the mechanisms through which microglia recognize stressed neurons in most experimental models of brain injury.

To establish a model of neuronal injury in which microglial responses to local signals can be studied within a realistic time frame and without *in situ* manipulation of the brain microenvironment, we have used genetically modified PRV-Bartha derivatives, which exhibit precisely controlled, retrograde transneuronal spread but do not infect microglia [6, 50]. In addition, these recombinant PRV strains allowed precise time-mapping of the spread of infection due to the expression of reporter proteins with different kinetics [4, 6]. At the same time, we could investigate the functional contribution of microglia to neurotropic herpesvirus infection, which has not been previously

investigated using selective elimination of microglia. Since immune surveillance by circulating immune cells is restricted in the brain parenchyma [52], early recognition of infection by microglia is likely to be critical to mount an appropriate immune response. The central inflammatory response induced by neurotropic herpesviruses including microglial activation and recruitment of blood-borne immune cells has been previously characterized by excellent earlier studies [19, 48, 50] and our former data has also shown that microglia surround infected neurons in the brain [15]. Recent reports highlighted the importance of central type I interferon responses against vesicular stomatitis virus and herpes simplex virus type 1 implicating microglia as a source of inflammatory mediators in anti-viral immunity in the brain [17, 49]. However, the kinetics and the mechanisms of microglia recruitment to infected cells have remained unexplored to date, similarly to the need for phagocytic activity by microglia to control the spread of infection. Our data obtained both *in vivo* and *in vitro* shows that the rapid and precisely controlled migration of functional microglia is critical not only to limit the spread of infection in the brain, but timely elimination of infected neurons is essential to prevent contact infection and to control the leakage of viral particles and antigens into the brain parenchyma. The rapidly worsening neurological symptoms of mice in the absence of microglia, but not in P2Y₁₂-deficient mice, may be due to both exaggerated infection and the lack of microglial factors that control neuronal activity in the injured brain [3, 38, 56], which should be investigated in further studies. Since the PRV Bartha-Dup strains show highly specific neurotropism *in vivo* [4–6] and we did not find any sign of hematogenous dissemination of infection or immunopositivity to viral antigens in the liver or the spleen even after PLX5622 treatment, a major role of peripheral immune mechanisms in the markedly increased spread of infection in microglia-depleted mice is unlikely.

Infected cells, including neurons and microglia were reported to sense HSV-1 via cytoplasmic DNA sensors, namely the adaptor protein stimulator of type I IFN genes (STING) [49]. However, the signals initiating microglia recruitment to infected neurons in the absence of microglial infection had remained unclear. Our *in vivo* and *in vitro* data suggest that soon after the development of productive infection, purinergic mediators released from neurons recruit the processes of uninfected microglia in their vicinity, followed by the displacement of the cells, leading to the formation of tight membrane–membrane interactions with the infected neurons. Since PRV infection alters neuronal activity [42], we hypothesised that the earliest signals from infected neurons to microglia are more likely to include mediators regulating rapid microglia–neuron interactions *in vivo* than *de novo* production of inflammatory chemokines. Specifically,

noxious stimuli in neurons can trigger a sustained increase of extracellular ATP, which results in microglial activation and recruitment within minutes to hours [14, 22]. In fact, our data shows that purine nucleotides released from affected neurons contribute to microglial process extension, cell migration to infected neurons and subsequent phagocytic activity via microglial P2Y12 receptors. ATP released from injured cells leads to the activation of P2-type and adenosine receptors upon extracellular ATP catabolism by ectonucleotidases [51]. In line with this, we observed increased ecto-ATPase levels and NTPDase1 activity in infected cells and microglia. ATP is a strong chemotactic signal for microglia in vivo [14] and hydrolysis of ATP to ADP, which is the main ligand for P2Y12 takes place by ecto-nucleotidases within minutes [51, 55]. In turn, increased P2Y12 receptor levels were found on microglial processes contacting infected neurons, as assessed by super-resolution microscopy. Since infected neurons at the stage of immediate-early reporter protein expression are viable and electrophysiologically active [42], these results also imply that microglia are well-equipped to identify injured neurons way earlier than the integrity of the cell membranes is compromised. Our ultrastructural analysis and in vitro data also confirm this, showing normal cell membrane integrity until late stages of virus infection. Thus, in spite that P2Y12 has been implicated earlier in the recruitment of microglia to sites of tissue injury in the brain [14, 25], the present in vivo and in vitro studies have identified the cell-autonomous effect of P2Y12 on microglia to rapidly recognize and eliminate infected neurons for the first time. We also show that P2X7, which plays a major role in microglial inflammatory responses and cytokine production [54] is dispensable for anti-viral immunity in this experimental model.

We also identify microglia as key contributors to monocyte recruitment to the brain during virus infection. Previous studies have implicated activated microglia in leukocyte recruitment into the brain upon virus infection, and showed that antibodies to CXCL10 and CCL2 (MCP-1) reduce the migration of murine splenocytes toward HSV-infected microglia in vitro [40, 41]. In our experimental model, elimination of microglia by CSF1R blockade was highly selective, as it did not have a significant impact on circulating and splenic leukocytes (including myeloid cell types), and infection-induced increases in circulating granulocytes was preserved in PLX5622-treated mice. In contrast, recruitment of monocytes to the brain was almost completely abolished in microglia depleted mice. In these studies, we made use of both CD45 and Cx3Cr1 as markers to reliably discriminate microglia (CD45^{low}, Cx3Cr1^{high}, Ly6c⁻ cells) from monocytes (CD45^{high}, Cx3Cr1⁺, Ly6c^{high} cells) without the need of complex BM chimeric studies that inherently include changes in BBB function and may cause microglia activation [62]. Importantly, microglial P2Y12 was essential to

mediate microglia recruitment and phagocytosis, but was dispensable for monocyte recruitment to the brain. These data suggest that other microglial chemotactic factors (such as MCP-1 or RANTES) could be responsible for driving leukocyte migration to sites of infection and injury in the brain, which should be investigated in further studies. Since monocyte recruitment in P2Y12^{-/-} mice was identical to that seen in control animals, but both an absence of microglia and P2Y12 deficiency resulted in markedly enhanced spread of infection, blood-borne monocytes may not significantly limit viral spread in the current experimental model. A similar conclusion was presented in a model of corona virus infection induced by direct injection of the virus into the brain, in spite that reduction of microglia numbers was associated with higher number of blood-borne macrophages in this study [61]. Histological characterization of post-mortem samples from human HSV-1 encephalitis cases also suggests that P2Y12-positive microglia isolate infected neurons, and a marked increase in leukocyte recruitment was also associated with severe infection.

Microglia depletion, but not P2Y12 deficiency leads to characteristic neurological symptoms in virus-infected mice. In line with this, microglia-depleted mice had higher numbers of infected/dying neurons than that seen in P2Y12^{-/-} mice, while the levels of extracellular virus proteins were not different, although significantly increased in both groups compared to control mice. Thus, the rapidly deteriorating neurological outcome seen in microglia-depleted animals may be partially due to the markedly increased neuronal infection and to the absence of potentially neuroprotective microglial mediators, such as interleukin-10 [23]. While our data show that P2Y12-dependent mechanisms are instrumental to limit neurotropic virus infection in the brain, additional microglial receptors could also contribute to this process. Since P2Y12^{-/-} mice showed comparable leukocyte infiltration to control animals, while microglia depletion markedly influenced leukocyte responses, a role for blood-borne cells in shaping neurobehavioral symptoms seen in this experimental model cannot be fully excluded.

The implications of these data for neurological diseases are far-reaching. The findings that microglia control neurotropic virus infection via P2Y12 in mice and the recruitment of P2Y12-positive microglia to HSV-1 cells was observed in the human brain suggest that microglial P2Y12 could play in general an important role in anti-viral immunity in the CNS (Fig. 9). Beyond infectious diseases caused by alphaherpesviruses such as PRV in swine or HSV-1 in humans, other viruses such as rabies, Zika virus, Alphaviruses, West-Nile virus, Epstein Barr virus, Influenza A viruses, and Enteroviruses can exhibit neurotropism and cause diverse neuropathologies in both humans and rodents [33, 38, 60]. In addition, the emerging role of neurotropic viruses in many forms of

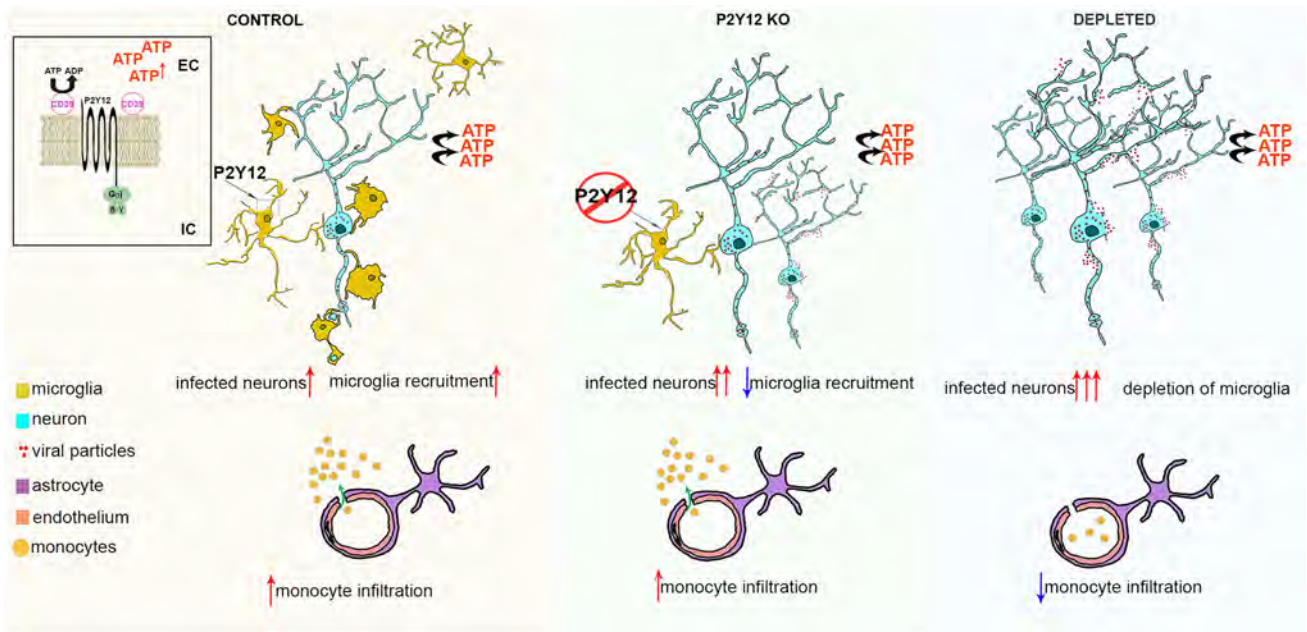


Fig. 9 Summary of neuroinflammatory changes after virus infection. In microglia-competent control mice, microglia recruitment around BDG-infected neurons is observed, which is associated with monocyte recruitment at sites of infection. ATP released by compromised neurons may be cleaved by CD39 to ADP leading to stimulation of P2Y12 receptors and act as a trigger for microglia recruitment and

phagocytosis. The lack of microglia leads to markedly increased numbers of viral infected neurons and an almost complete absence of monocyte recruitment. The lack of microglial P2Y12 leads to reduced microglial recruitment compared to control animals, suggesting the pivotal role of P2Y12 receptor in this process, whilst monocyte infiltration is comparable to that seen in control animals

neurodegeneration [33, 38, 64] and the common molecular fingerprints of cellular injury suggest that understanding the mechanisms through which microglia control the elimination of injured neurons in the brain could facilitate the development of targeted therapies in several common brain diseases.

Acknowledgements Funding was provided by the “Momentum” Program of the Hungarian Academy of Sciences LP2016-4/2016 (AD), ERC-CoG 724994 (AD), OTKA K109743, K116654, the Hungarian Brain Research Program KTIA_13_NAP-A-I, and 2017-1.2.1-NKP-2017-00002. We thank the Cell Biology Center (Flow Cytometry Core Facility) at the Institute of Experimental Medicine of the Hungarian Academy of Sciences, Budapest, Hungary for their assistance. We are grateful for the Department of Pathology, Saint Borbála Hospital, Tatabánya, Hungary, and the Human Brain Research Laboratory, Institute of Experimental Medicine, Budapest, Hungary for providing post-mortem human brain tissue samples from patients with no known neurological disease. We also thank Tamás Vicsek at Department of Biological Physics, Eötvös University, Budapest, for his contribution to in vitro cell motility studies. We thank László Barna, Csaba Pongor and the NMC Imaging Center at the Institute of Experimental Medicine for providing experimental and technical support.

Author contributions AD and ZK designed research; RF, CS, CS, BO, NL, BM, KT, CW, VN, EM, MB, ÁK, SF and AD performed research. TH and GK provided human post mortem brain materials and served as clinical and neuropathological experts for the study. ZB generated and provided recombinant PRV strains. BG, BSz and EM measured/analysed in vitro data. BLW contributed new reagents. BR and GSZ

contributed to in vivo two-photon imaging studies. AD and ZK supervised the study. AD wrote the paper with input from all authors.

Compliance with ethical standards

Conflict of interest BLW is an employee of Plexxikon. BR is the founder of Femtonics Kft. and a member of its scientific advisory board.

Open Access This article is distributed under the terms of the Creative Commons Attribution 4.0 International License (<http://creativecommons.org/licenses/by/4.0/>), which permits unrestricted use, distribution, and reproduction in any medium, provided you give appropriate credit to the original author(s) and the source, provide a link to the Creative Commons license, and indicate if changes were made.


References

1. Barna L, Dudok B, Miczan V, Horvath A, Laszlo ZI, Katona I (2016) Correlated confocal and super-resolution imaging by VividSTORM. *Nat Protoc* 11:163–183. <https://doi.org/10.1038/nprot.2016.002>
2. Bartness TJ, Liu Y, Shrestha YB, Ryu V (2014) Neural innervation of white adipose tissue and the control of lipolysis. *Front Neuroendocrinol* 35:473–493. <https://doi.org/10.1016/j.yfrne.2014.04.001>

3. Bechade C, Cantaut-Belarif Y, Bessis A (2013) Microglial control of neuronal activity. *Front Cell Neurosci* 7:32. <https://doi.org/10.3389/fncel.2013.00032>
4. Boldogkoi Z, Balint K, Awatramani GB, Balya D, Buskamp V, Viney TJ, Lagali PS, Duebel J, Pasti E, Tombacz D et al (2009) Genetically timed, activity-sensor and rainbow transsynaptic viral tools. *Nat Methods* 6:127–130. <https://doi.org/10.1038/nmeth.1292>
5. Boldogkoi Z, Reichart A, Toth IE, Sik A, Erdelyi F, Medveczky I, Llorens-Cortes C, Palkovits M, Lenkei Z (2002) Construction of recombinant pseudorabies viruses optimized for labeling and neurochemical characterization of neural circuitry. *Brain Res Mol Brain Res* 109:105–118
6. Boldogkoi Z, Sik A, Denes A, Reichart A, Toldi J, Gerendai I, Kovacs KJ, Palkovits M (2004) Novel tracing paradigms—genetically engineered herpesviruses as tools for mapping functional circuits within the CNS: present status and future prospects. *Prog Neurobiol* 72:417–445. <https://doi.org/10.1016/j.pneurobio.2004.03.010>
7. Brown GC, Neher JJ (2014) Microglial phagocytosis of live neurons. *Nat Rev Neurosci* 15:209–216. <https://doi.org/10.1038/nrn3710>
8. Card JP, Enquist LW (2014) Transneuronal circuit analysis with pseudorabies viruses. *Curr Protoc Neurosci* 68:151–239. <https://doi.org/10.1002/0471142301.ns0105s68>
9. Chen R, Kang R, Fan XG, Tang D (2014) Release and activity of histone in diseases. *Cell Death Dis* 5:e1370. <https://doi.org/10.1038/cddis.2014.337>
10. Chiovini B, Turi GF, Katona G, Kaszas A, Palfi D, Maak P, Szalay G, Szabo MF, Szabo G, Szadai Z et al (2014) Dendritic spikes induce ripples in parvalbumin interneurons during hippocampal sharp waves. *Neuron* 82:908–924. <https://doi.org/10.1016/j.neuron.2014.04.004>
11. Conrady CD, Zheng M, van Rooijen N, Drevets DA, Royer D, Alleman A, Carr DJ (2013) Microglia and a functional type I IFN pathway are required to counter HSV-1-driven brain lateral ventricle enlargement and encephalitis. *J Immunol* 190:2807–2817. <https://doi.org/10.4049/jimmunol.1203265>
12. Czondor K, Ellwanger K, Fuchs YF, Lutz S, Gulyas M, Mansuy IM, Haussler A, Pfizenmaier K, Schlett K (2009) Protein kinase D controls the integrity of Golgi apparatus and the maintenance of dendritic arborization in hippocampal neurons. *Mol Biol Cell* 20:2108–2120. <https://doi.org/10.1091/mbc.E08-09-0957>
13. Csonka T, Szepesi R, Bidiga L, Peter M, Klekner A, Hutoczkzy G, Csiba L, Mehes G, Hortobagyi T (2013) The diagnosis of herpes encephalitis—a case-based update. *Ideggyogy Sz* 66:337–342
14. Davalos D, Grutzendler J, Yang G, Kim JV, Zuo Y, Jung S, Littman DR, Dustin ML, Gan WB (2005) ATP mediates rapid microglial response to local brain injury in vivo. *Nat Neurosci* 8:752–758. <https://doi.org/10.1038/nn1472>
15. Denes A, Boldogkoi Z, Hornyak A, Palkovits M, Kovacs KJ (2006) Attenuated pseudorabies virus-evoked rapid innate immune response in the rat brain. *J Neuroimmunol* 180:88–103. <https://doi.org/10.1016/j.jneuroim.2006.07.008>
16. Denes A, Coutts G, Lenart N, Cruickshank SM, Pelegrin P, Skinner J, Rothwell N, Allan SM, Brough D (2015) AIM2 and NLRC4 inflammasomes contribute with ASC to acute brain injury independently of NLRP3. *Proc Natl Acad Sci U S A* 112:4050–4055. <https://doi.org/10.1073/pnas.1419090112>
17. Drokhyansky E, Goz Ayurk D, Soh TK, Chrenek R, O’Loughlin E, Madore C, Butovsky O, Cepko CL (2017) The brain parenchyma has a type I interferon response that can limit virus spread. *Proc Natl Acad Sci U S A* 114:E95–E104. <https://doi.org/10.1073/pnas.1618157114>
18. Dudok B, Barna L, Ledri M, Szabo SI, Szabadits E, Pinter B, Woodhams SG, Henstridge CM, Balla GY, Nyilas R et al (2015) Cell-specific STORM super-resolution imaging reveals nanoscale organization of cannabinoid signaling. *Nat Neurosci* 18:75–86. <https://doi.org/10.1038/nn.3892>
19. Egan KP, Wu S, Wigdahl B, Jennings SR (2013) Immunological control of herpes simplex virus infections. *J Neurovirol* 19:328–345. <https://doi.org/10.1007/s13365-013-0189-3>
20. Elmore MR, Najafi AR, Koike MA, Dagher NN, Spangenberg EE, Rice RA, Kitazawa M, Matusow B, Nguyen H, West BL et al (2014) Colony-stimulating factor 1 receptor signaling is necessary for microglia viability, unmasking a microglia progenitor cell in the adult brain. *Neuron* 82:380–397. <https://doi.org/10.1016/j.neuron.2014.02.040>
21. Faraco G, Fossati S, Bianchi ME, Patrone M, Pedrazzi M, Sparatore B, Moroni F, Chiarugi A (2007) High mobility group box 1 protein is released by neural cells upon different stresses and worsens ischemic neurodegeneration in vitro and in vivo. *J Neurochem* 103:590–603. <https://doi.org/10.1111/j.1471-4159.2007.04788.x>
22. Fields RD, Burnstock G (2006) Purinergic signalling in neuron-glia interactions. *Nat Rev Neurosci* 7:423–436. <https://doi.org/10.1038/nrn1928>
23. Garcia JM, Stillings SA, Leclerc JL, Phillips H, Edwards NJ, Robicsek SA, Hoh BL, Blackburn S, Dore S (2017) Role of interleukin-10 in acute brain injuries. *Front Neurol* 8:244. <https://doi.org/10.3389/fneur.2017.00244>
24. Gonci B, Nemeth V, Balogh E, Szabo B, Denes A, Kornyei Z, Vicsek T (2010) Viral epidemics in a cell culture: novel high resolution data and their interpretation by a percolation theory based model. *PLoS ONE* 5:e15571. <https://doi.org/10.1371/journal.pone.0015571>
25. Haynes SE, Hollopeter G, Yang G, Kurpius D, Dailey ME, Gan WB, Julius D (2006) The P2Y₁₂ receptor regulates microglial activation by extracellular nucleotides. *Nat Neurosci* 9:1512–1519. <https://doi.org/10.1038/nn1805>
26. Hong S, Beja-Glasser VF, Nfonoyim BM, Frouin A, Li S, Ramakrishnan S, Merry KM, Shi Q, Rosenthal A, Barres BA et al (2016) Complement and microglia mediate early synapse loss in Alzheimer mouse models. *Science* 352:712–716. <https://doi.org/10.1126/science.aad8373>
27. Katona G, Szalay G, Maak P, Kaszas A, Veress M, Hillier D, Chiovini B, Vizi ES, Roska B, Rozsa B (2012) Fast two-photon in vivo imaging with three-dimensional random-access scanning in large tissue volumes. *Nat Methods* 9:201–208. <https://doi.org/10.1038/nmeth.1851>
28. Kettenmann H, Kirchhoff F, Verkhratsky A (2013) Microglia: new roles for the synaptic stripper. *Neuron* 77:10–18. <https://doi.org/10.1016/j.neuron.2012.12.023>
29. Kiernan EA, Smith SM, Mitchell GS, Watters JJ (2016) Mechanisms of microglial activation in models of inflammation and hypoxia: implications for chronic intermittent hypoxia. *J Physiol* 594:1563–1577. <https://doi.org/10.1113/JP271502>
30. Kim JB, Sig Choi J, Yu YM, Nam K, Piao CS, Kim SW, Lee MH, Han PL, Park JS, Lee JK (2006) HMGB1, a novel cytokine-like mediator linking acute neuronal death and delayed neuroinflammation in the posts ischemic brain. *J Neurosci* 26:6413–6421. <https://doi.org/10.1523/JNEUROSCI.3815-05.2006>
31. Kittel A (1999) Lipopolysaccharide treatment modifies pH- and cation-dependent ecto-ATPase activity of endothelial cells. *J Histochem Cytochem* 47:393–400. <https://doi.org/10.1177/002215549904700313>
32. Kornyei Z, Szlavik V, Szabo B, Gocza E, Czirok A, Madarasz E (2005) Humoral and contact interactions in astroglia/stem cell co-cultures in the course of glia-induced neurogenesis. *Glia* 49:430–444. <https://doi.org/10.1002/glia.20123>

33. Koyuncu OO, Hogue IB, Enquist LW (2013) Virus infections in the nervous system. *Cell Host Microbe* 13:379–393. <https://doi.org/10.1016/j.chom.2013.03.010>
34. Leak RK (2014) Heat shock proteins in neurodegenerative disorders and aging. *J Cell Commun Signal* 8:293–310. <https://doi.org/10.1007/s12079-014-0243-9>
35. Lenart N, Brough D, Denes A (2016) Inflammasomes link vascular disease with neuroinflammation and brain disorders. *J Cereb Blood Flow Metab* 36:1668–1685. <https://doi.org/10.1177/0271678X16662043>
36. Li Y, Du XF, Liu CS, Wen ZL, Du JL (2012) Reciprocal regulation between resting microglial dynamics and neuronal activity in vivo. *Dev Cell* 23:1189–1202. <https://doi.org/10.1016/j.devce.12012.10.027>
37. Lokensgard JR, Cheeran MC, Hu S, Gekker G, Peterson PK (2002) Glial cell responses to herpesvirus infections: role in defense and immunopathogenesis. *J Infect Dis* 186(Suppl 2):S171–179. <https://doi.org/10.1086/344272>
38. Ludlow M, Kortekaas J, Herden C, Hoffmann B, Tappe D, Trebst C, Griffin DE, Brindle HE, Solomon T, Brown AS et al (2016) Neurotropic virus infections as the cause of immediate and delayed neuropathology. *Acta Neuropathol* 131:159–184. <https://doi.org/10.1007/s00401-015-1511-3>
39. Madry C, Kyrargyri V, Arancibia-Carcamo IL, Jolivet R, Kohsaka S, Bryan RM, Attwell D (2018) Microglial ramification, surveillance, and interleukin-1beta release are regulated by the two-pore domain K(+) channel THIK-1. *Neuron* 97(299–312):e296. <https://doi.org/10.1016/j.neuron.2017.12.002>
40. Marques CP, Cheeran MC, Palmquist JM, Hu S, Urban SL, Lokensgard JR (2008) Prolonged microglial cell activation and lymphocyte infiltration following experimental herpes encephalitis. *J Immunol* 181:6417–6426
41. Marques CP, Hu S, Sheng W, Lokensgard JR (2006) Microglial cells initiate vigorous yet non-protective immune responses during HSV-1 brain infection. *Virus Res* 121:1–10. <https://doi.org/10.1016/j.virusres.2006.03.009>
42. McCarthy KM, Tank DW, Enquist LW (2009) Pseudorabies virus infection alters neuronal activity and connectivity in vitro. *PLoS Pathog* 5:e1000640. <https://doi.org/10.1371/journal.ppat.1000640>
43. Mehes E, Czirik A, Hegedus B, Szabo B, Vicsek T, Satz J, Campbell K, Jancsik V (2005) Dystroglycan is involved in laminin-1-stimulated motility of Muller glial cells: combined velocity and directionality analysis. *Glia* 49:492–500. <https://doi.org/10.1002/glia.20135>
44. Mehes E, Czirik A, Hegedus B, Vicsek T, Jancsik V (2002) Laminin-1 increases motility, path-searching, and process dynamism of rat and mouse Muller glial cells in vitro: implication of relationship between cell behavior and formation of retinal morphology. *Cell Motil Cytoskeleton* 53:203–213. <https://doi.org/10.1002/cm.10062>
45. Moore CS, Ase AR, Kinsara A, Rao VT, Michell-Robinson M, Leong SY, Butovsky O, Ludwin SK, Seguela P, Bar-Or A et al (2015) P2Y12 expression and function in alternatively activated human microglia. *Neurol Neuroimmunol Neuroinflamm* 2:e80. <https://doi.org/10.1212/NXI.0000000000000080>
46. Ousman SS, Kubes P (2012) Immune surveillance in the central nervous system. *Nat Neurosci* 15:1096–1101. <https://doi.org/10.1038/nn.3161>
47. Prinz M, Priller J (2014) Microglia and brain macrophages in the molecular age: from origin to neuropsychiatric disease. *Nat Rev Neurosci* 15:300–312. <https://doi.org/10.1038/nrn3722>
48. Rassnick S, Enquist LW, Sved AF, Card JP (1998) Pseudorabies virus-induced leukocyte trafficking into the rat central nervous system. *J Virol* 72:9181–9191
49. Reinert LS, Lopusna K, Winther H, Sun C, Thomsen MK, Nandakumar R, Mogensen TH, Meyer M, Vaegter C, Nyengaard JR et al (2016) Sensing of HSV-1 by the cGAS-STING pathway in microglia orchestrates antiviral defence in the CNS. *Nat Commun* 7:13348. <https://doi.org/10.1038/ncomms13348>
50. Rinaman L, Card JP, Enquist LW (1993) Spatiotemporal responses of astrocytes, ramified microglia, and brain macrophages to central neuronal infection with pseudorabies virus. *J Neurosci* 13:685–702
51. Rodrigues RJ, Tome AR, Cunha RA (2015) ATP as a multi-target danger signal in the brain. *Front Neurosci* 9:148. <https://doi.org/10.3389/fnins.2015.00148>
52. Russo MV, McGavern DB (2015) Immune surveillance of the CNS following infection and injury. *Trends Immunol* 36:637–650. <https://doi.org/10.1016/j.it.2015.08.002>
53. Sipe GO, Lowery RL, Tremblay ME, Kelly EA, Lamantia CE, Majewska AK (2016) Microglial P2Y12 is necessary for synaptic plasticity in mouse visual cortex. *Nat Commun* 7:10905. <https://doi.org/10.1038/ncomms10905>
54. Sperlagh B, Illes P (2014) P2X7 receptor: an emerging target in central nervous system diseases. *Trends Pharmacol Sci* 35:537–547. <https://doi.org/10.1016/j.tips.2014.08.002>
55. Sperlagh B, Illes P (2007) Purinergic modulation of microglial cell activation. *Purinergic Signal* 3:117–127. <https://doi.org/10.1007/s11302-006-9043-x>
56. Szalay G, Martinecz B, Lenart N, Kornyei Z, Orsolits B, Judak L, Csaszar E, Fekete R, West BL, Katona G et al (2016) Microglia protect against brain injury and their selective elimination dysregulates neuronal network activity after stroke. *Nat Commun* 7:11499. <https://doi.org/10.1038/ncomms11499>
57. Tsuda M (2016) Microglia in the spinal cord and neuropathic pain. *J Diabetes Investig* 7:17–26. <https://doi.org/10.1111/jdi.12379>
58. Tsuda M, Inoue K (2016) Neuron-microglia interaction by purinergic signaling in neuropathic pain following neurodegeneration. *Neuropharmacology* 104:76–81. <https://doi.org/10.1016/j.neuropharm.2015.08.042>
59. Vasek MJ, Garber C, Dorsey D, Durrant DM, Bollman B, Soung A, Yu J, Perez-Torres C, Frouin A, Wilton DK et al (2016) A complement-microglial axis drives synapse loss during virus-induced memory impairment. *Nature* 534:538–543. <https://doi.org/10.1038/nature18283>
60. Vermillion MS, Lei J, Shabi Y, Baxter VK, Crilly NP, McLane M, Griffin DE, Pekosz A, Klein SL, Burd I (2017) Intrauterine Zika virus infection of pregnant immunocompetent mice models transplacental transmission and adverse perinatal outcomes. *Nat Commun* 8:14575. <https://doi.org/10.1038/ncomms14575>
61. Wheeler DL, Sariol A, Meyerholz DK, Perlman S (2018) Microglia are required for protection against lethal coronavirus encephalitis in mice. *J Clin Invest*. <https://doi.org/10.1172/jci97229>
62. Wilkinson FL, Sergijenko A, Langford-Smith KJ, Malinowska M, Wynn RF, Bigger BW (2013) Busulfan conditioning enhances engraftment of hematopoietic donor-derived cells in the brain compared with irradiation. *Mol Ther* 21:868–876. <https://doi.org/10.1038/mt.2013.29>
63. Wu Y, Dissing-Olesen L, MacVicar BA, Stevens B (2015) Microglia: dynamic mediators of synapse development and plasticity. *Trends Immunol* 36:605–613. <https://doi.org/10.1016/j.it.2015.08.008>
64. Zhou L, Miranda-Saksena M, Saksena NK (2013) Viruses and neurodegeneration. *Virology* 453:172. <https://doi.org/10.1186/1743-422X-10-172>

Affiliations

Rebeka Fekete¹ · Csaba Cserép¹ · Nikolett Lénárt¹ · Krisztina Tóth¹ · Barbara Orsolits¹ · Bernadett Martinecz¹ · Előd Méhes² · Bálint Szabó² · Valéria Németh² · Balázs Gönci² · Beáta Sperlágh³ · Zsolt Boldogkői⁴ · Ágnes Kittel³ · Mária Baranyi³ · Szilámér Ferenczi⁵ · Krisztina Kovács⁵ · Gergely Szalay⁶ · Balázs Rózsa⁶ · Connor Webb¹ · Gabor G. Kovacs^{7,8} · Tibor Hortobágyi^{9,10,11} · Brian L. West¹² · Zsuzsanna Környei¹ · Ádám Dénes¹ 

¹ “Momentum” Laboratory of Neuroimmunology, Institute of Experimental Medicine, Hungarian Academy of Sciences, Szigony u. 43, 1083 Budapest, Hungary

² Department of Biological Physics, Eötvös University, Budapest, Hungary

³ Laboratory of Molecular Pharmacology, Institute of Experimental Medicine, Hungarian Academy of Sciences, Budapest, Hungary

⁴ Department of Medical Biology, Faculty of Medicine, University of Szeged, Szeged, Hungary

⁵ Laboratory of Molecular Neuroendocrinology, Institute of Experimental Medicine, Hungarian Academy of Sciences, Budapest, Hungary

⁶ Laboratory of 3D Functional Network and Dendritic Imaging, Institute of Experimental Medicine, Hungarian Academy of Sciences, Szigony u. 43, 1083 Budapest, Hungary

⁷ Institute of Neurology, Medical University of Vienna, Vienna, Austria

⁸ Neuropathology and Prion Disease Reference Center, Semmelweis University, Budapest, Hungary

⁹ MTA-DE Cerebrovascular and Neurodegenerative Research Group, University of Debrecen, Debrecen, Hungary

¹⁰ Institute of Psychiatry Psychology and Neuroscience, King’s College London, London, UK

¹¹ Institute of Pathology, Faculty of Medicine, University of Szeged, Szeged, Hungary

¹² Plexxikon Inc, Berkeley, CA 94710, USA

Online Resource Supplemental Material 1

Acta Neuropathologica

Microglia control the spread of neurotropic virus infection via P2Y12 signalling and recruit monocytes through P2Y12-independent mechanisms

Rebeka Fekete¹, Csaba Cserép¹, Nikolett Lénárt¹, Krisztina Tóth¹, Barbara Orsolits¹, Bernadett Martinecz¹, Előd Méhes², Bálint Szabó², Valéria Németh², Balázs Gönci², Beáta Sperlág³, Zsolt Boldogkői⁴, Ágnes Kittel³, Mária Baranyi³, Szilamér Ferenczi⁵, Krisztina Kovács⁵, Gergely Szalay⁶, Balázs Rózsa⁶, Connor Webb¹, Gabor G. Kovacs⁷, Tibor Hortobágyi⁸, Brian L. West⁹, Zsuzsanna Környei¹ and Ádám Dénes^{1,*}

1. "Momentum" Laboratory of Neuroimmunology, Institute of Experimental Medicine, Hungarian Academy of Sciences, Budapest, Hungary
2. Department of Biological Physics, Eötvös University, Budapest, Hungary
3. Laboratory of Molecular Pharmacology, Institute of Experimental Medicine, Hungarian Academy of Sciences, Budapest, Hungary
4. Department of Medical Biology, Faculty of Medicine, University of Szeged, Szeged, Hungary
5. Laboratory of Molecular Neuroendocrinology, Institute of Experimental Medicine, Hungarian Academy of Sciences, Budapest, Hungary
6. Laboratory of 3D Functional Network and Dendritic Imaging, Institute of Experimental Medicine, Hungarian Academy of Sciences, Szigony u. 43., 1083 Budapest, Hungary
7. Institute of Neurology, Medical University of Vienna, Vienna, Austria and Neuropathology and Prion Disease Reference Center, Semmelweis University, Budapest, Hungary
8. MTA-DE Cerebrovascular and Neurodegenerative Research Group, University of Debrecen, Debrecen, Hungary & Institute of Psychiatry Psychology and Neuroscience, King's College London, London, UK
9. Plexikon Inc., Berkeley, CA 94710, USA

***Correspondence:** Dr. Ádám Dénes, Institute of Experimental Medicine, Szigony u. 43, 1083 Budapest, Hungary. Email: denes.adam@koki.mta.hu; Phone: +36 209549149

This PDF file includes:

Supplementary Figures 1-16

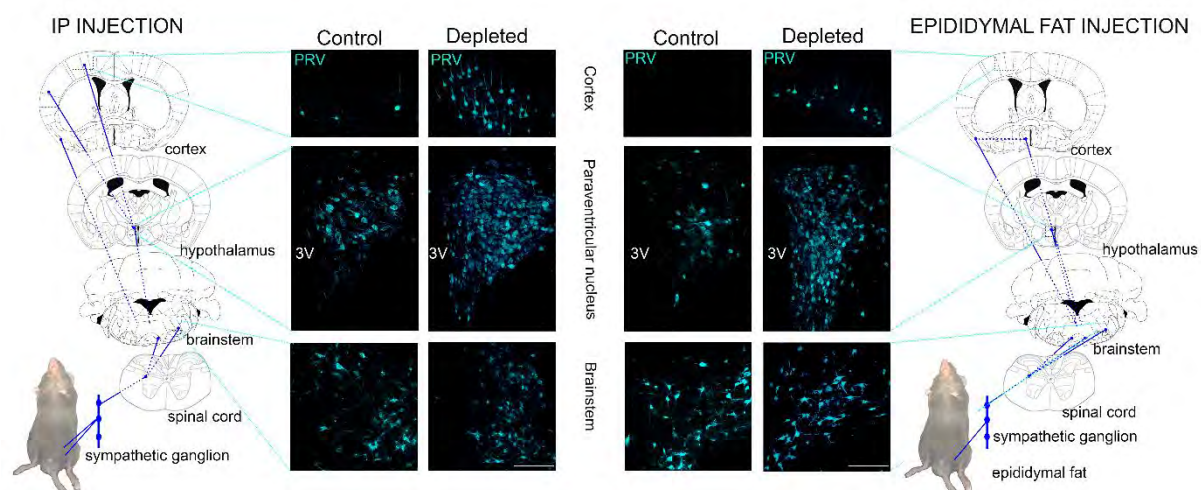
Supplementary Table 1

Legends for Supplementary Videos 1-11

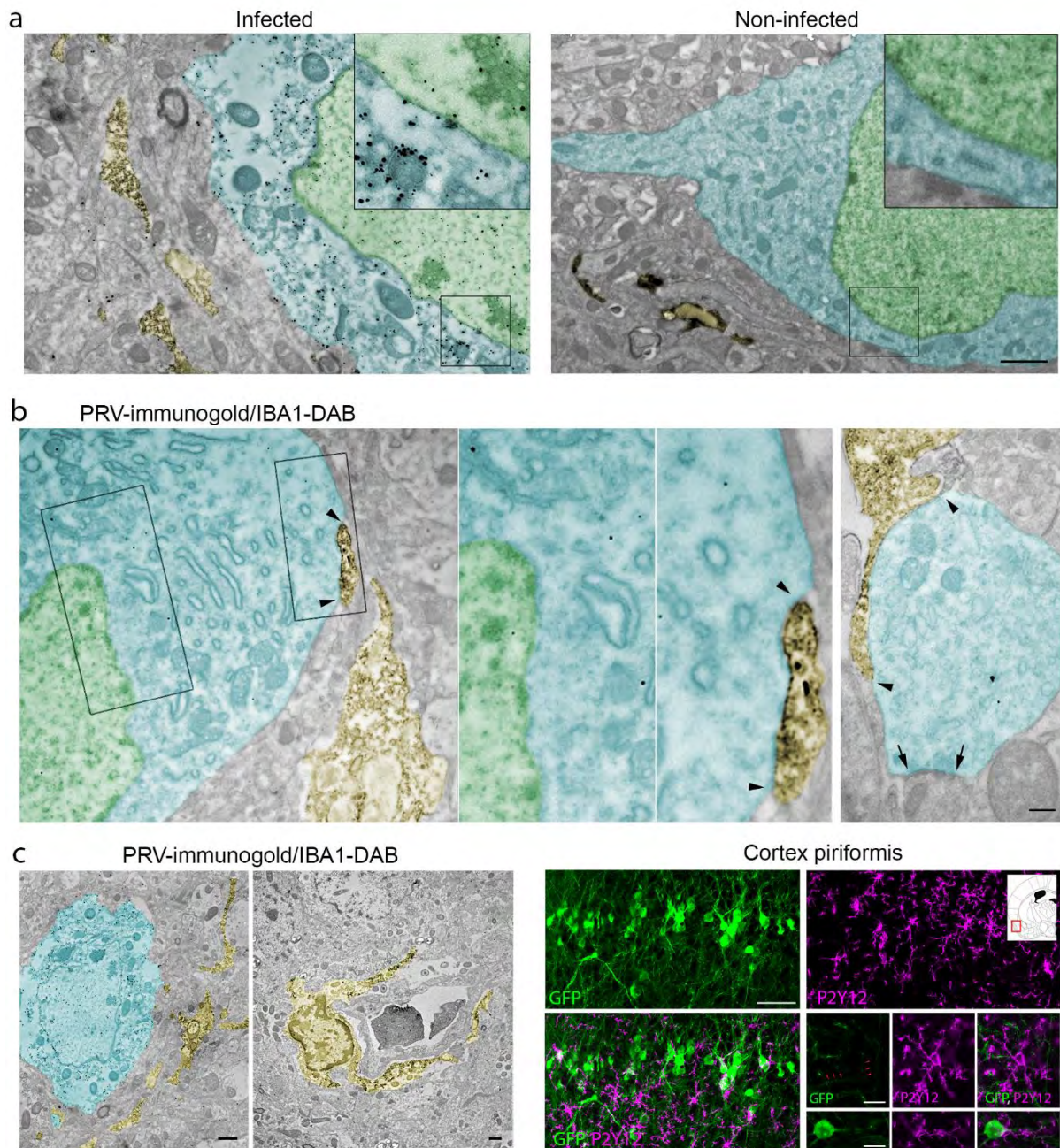
Supplementary Methods

Other Supplementary Materials for this manuscript includes the following:

Supplementary Videos 1-11



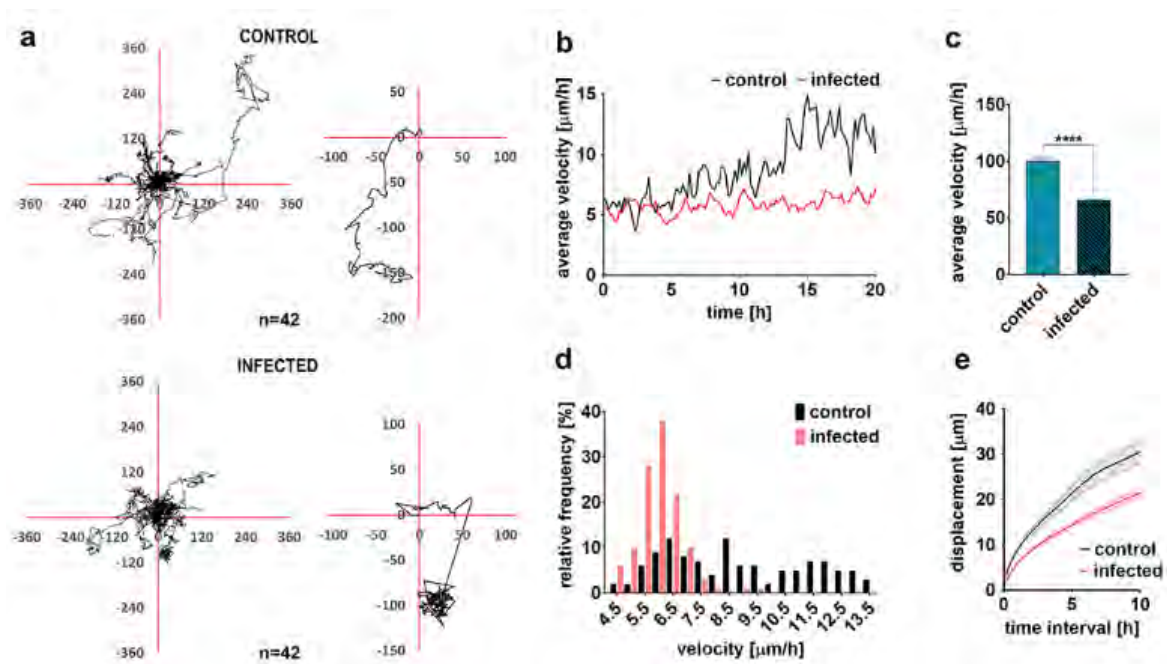
Supplementary Figure 1. The impact of microglia depletion on the spread of virus infection in the brain. Bartha-DupGreen (BDG) was injected intraperitoneally or into the epididymal white adipose tissue (left side) to initiate retrograde transsynaptic spread of infection into the CNS, with or without the selective depletion of microglia with PLX5622. The propagation of infection in the brain was assessed 5 days after infection. Note the marked increase of PRV-immunopositive neurons (cyan) in the brain in the absence of microglia. This includes the spread of infection to higher cortical areas, including the piriform cortex, the insular cortex and the primary motor cortex after intraperitoneal injection. Due to the primarily sympathetic autonomic innervation of the white adipose tissue, the infection affects mostly the piriform cortex in microglia depleted animals, whereas the virus does not reach the cerebral cortex in control mice. 3V – third ventricle. Maximum Intensity Projection from confocal Z stack of 5 steps were made with 3,38 μm (cortex), 0,83 μm (PVN), 4,05 μm (brainstem) step size. Scale bars: 50 μm .



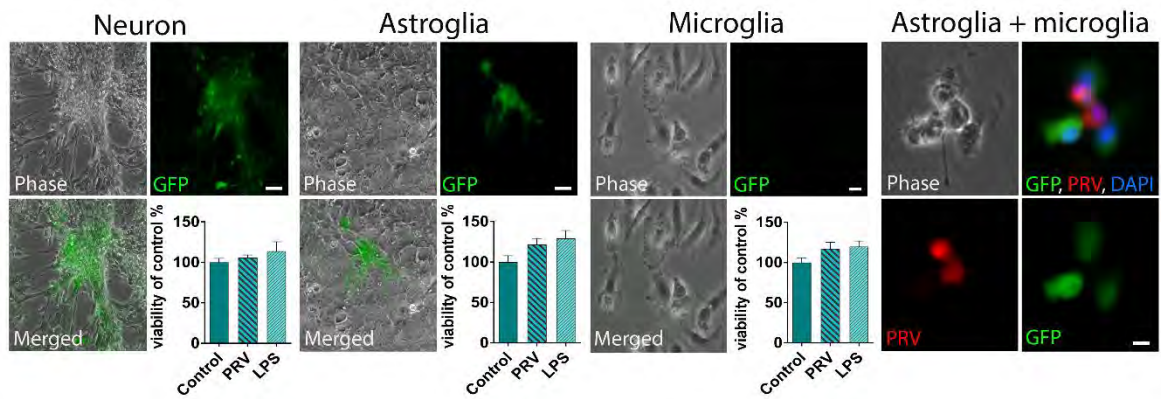
Supplementary Figure 2. Pseudorabies virus infects neurons but does not induce productive infection in microglial cells *in vivo*. a) PRV-immunolabeling is completely absent in virus-free animals. Transmission electron microscopic (TEM) images showing the presence of anti-PRV immunogold labeling in infected, and its complete absence in non-infected animals. Microglial processes (dark DAB-precipitate, yellow pseudocolor) are found in the vicinity of neurons (cytoplasm: cyan pseudocolor, nucleus: green pseudocolor). The infected neuron contains a high level of anti-PRV immunogold particles (black grains), viral capsids and mature virions (insert). The non-infected animal is void of viral particles and PRV-immunogold particles, confirming the specificity of the antibody. Scale bar: 1 μ m. b) TEM images show that microglial processes (dark DAB-precipitate, yellow pseudocolor) find and contact PRV-infected neurons even at the early phases of infection, when only low levels of anti-PRV immunogold labeling is present (cytoplasm: cyan pseudocolor, nucleus: green pseudocolor). Arrowheads mark sites of microglial contacts, arrows point to a synapse on the

dc_2027_22

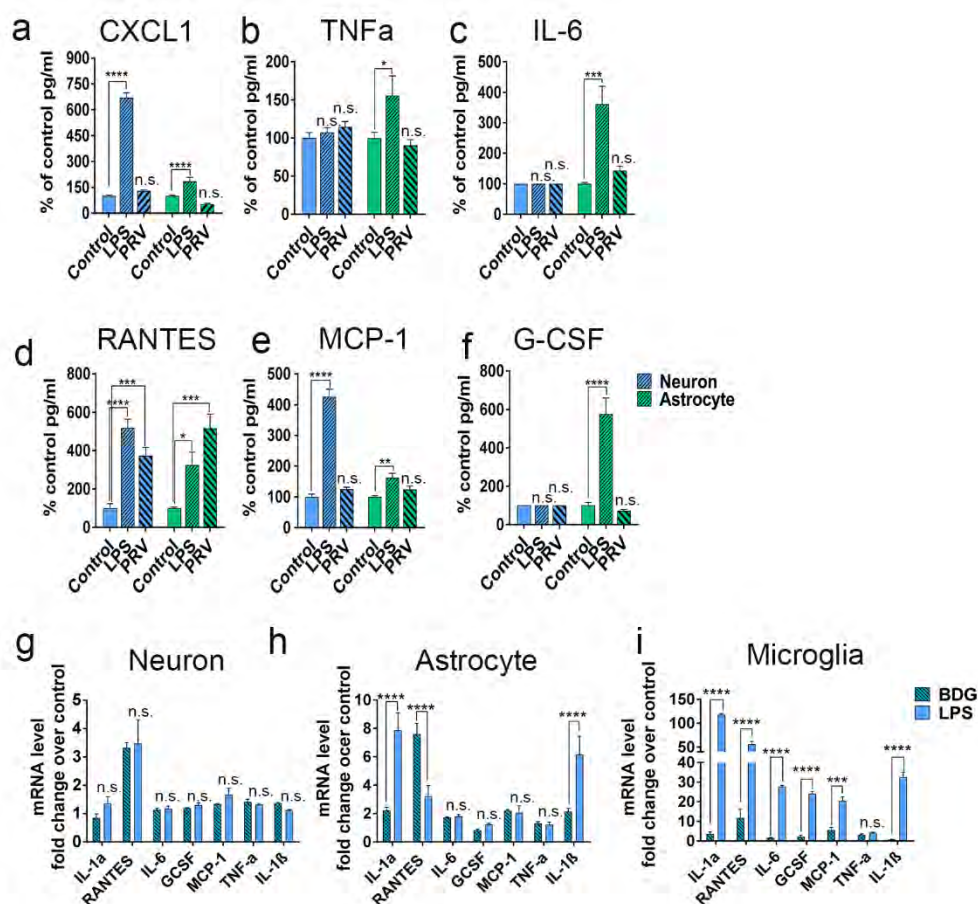
dendrite of an infected neuron. Scale bar: 300 nm on left panel, 200 nm on right panel. c) TEM pictures (first panel) show that DAB-positive microglia (yellow pseudocolor) completely lack viral capsids and anti-PRV immunogold particles, in contrary to PRV-infected neurons (cyan pseudocolor). Confocal pictures (second panel) showing that microglia do not express the immediate early GFP marker, in contrast to neurons, where a strong GFP expression can be seen in both the cell bodies and neurites. Scale bars: 1 μm on TEM images, 50 μm , 10 μm on the confocal panels.



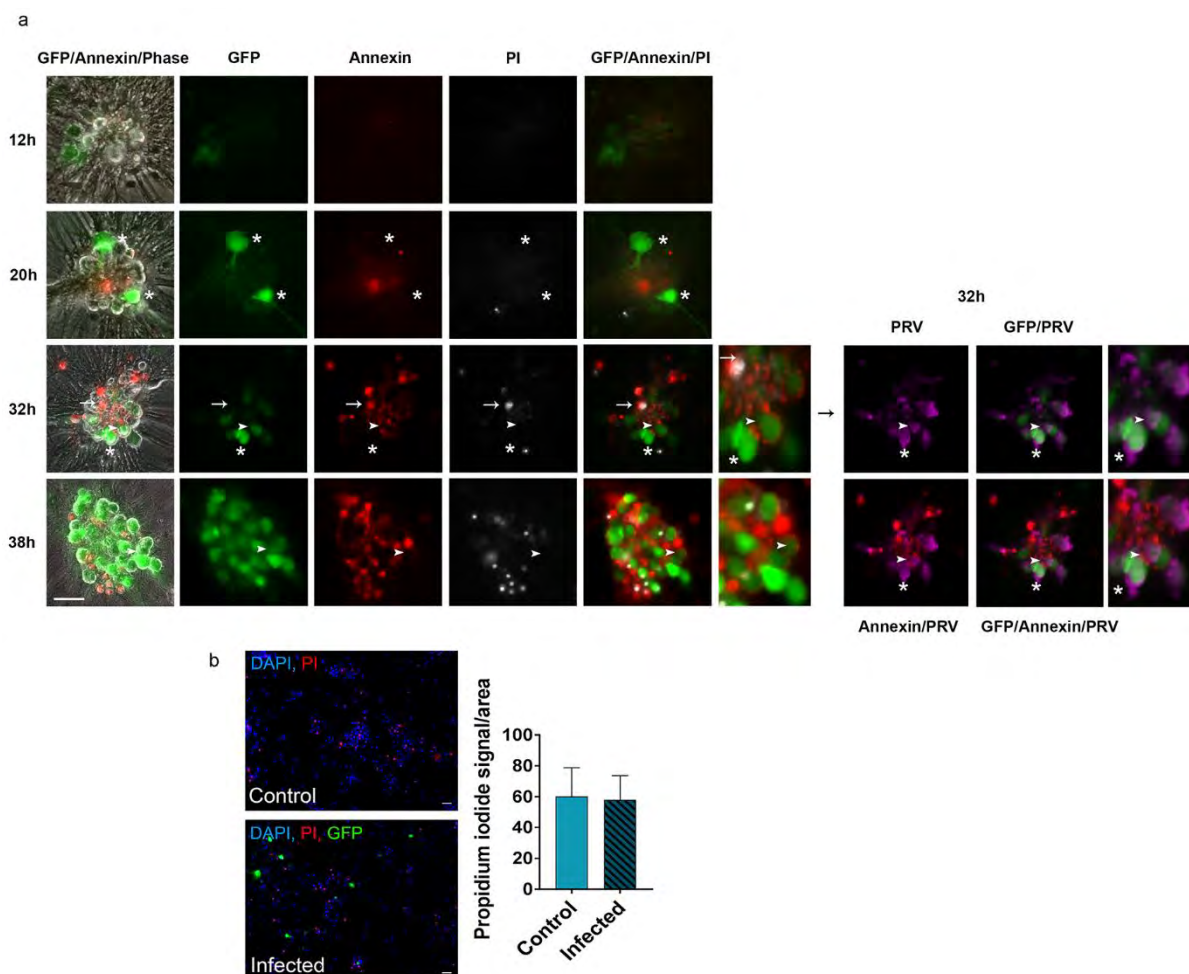
Supplementary Figure 3. Virus infection triggers the recruitment and phagocytic activity of microglia in primary neuronal cell cultures. a) Trajectories of microglial cells over a 24-hour imaging period in control and infected primary neuronal cultures. Individual cell trajectories were centered at the origin. Insets show typical trajectories of individual cells. b) Time-dependent average velocities of microglial cell populations in control (n=43) or infected (n=155) neuronal cultures. c) Average velocities of microglial cells over 24 hours are significantly lower in infected neuronal cultures ($p < 0.0005$, error bars correspond to s.e.m). d) Frequency distribution of time-dependent average velocities of microglial populations in control or infected neuronal cultures. e) Average displacement of microglial cells in various time intervals of migration in control or infected neuronal cultures. Error stripes correspond to s.e.m.



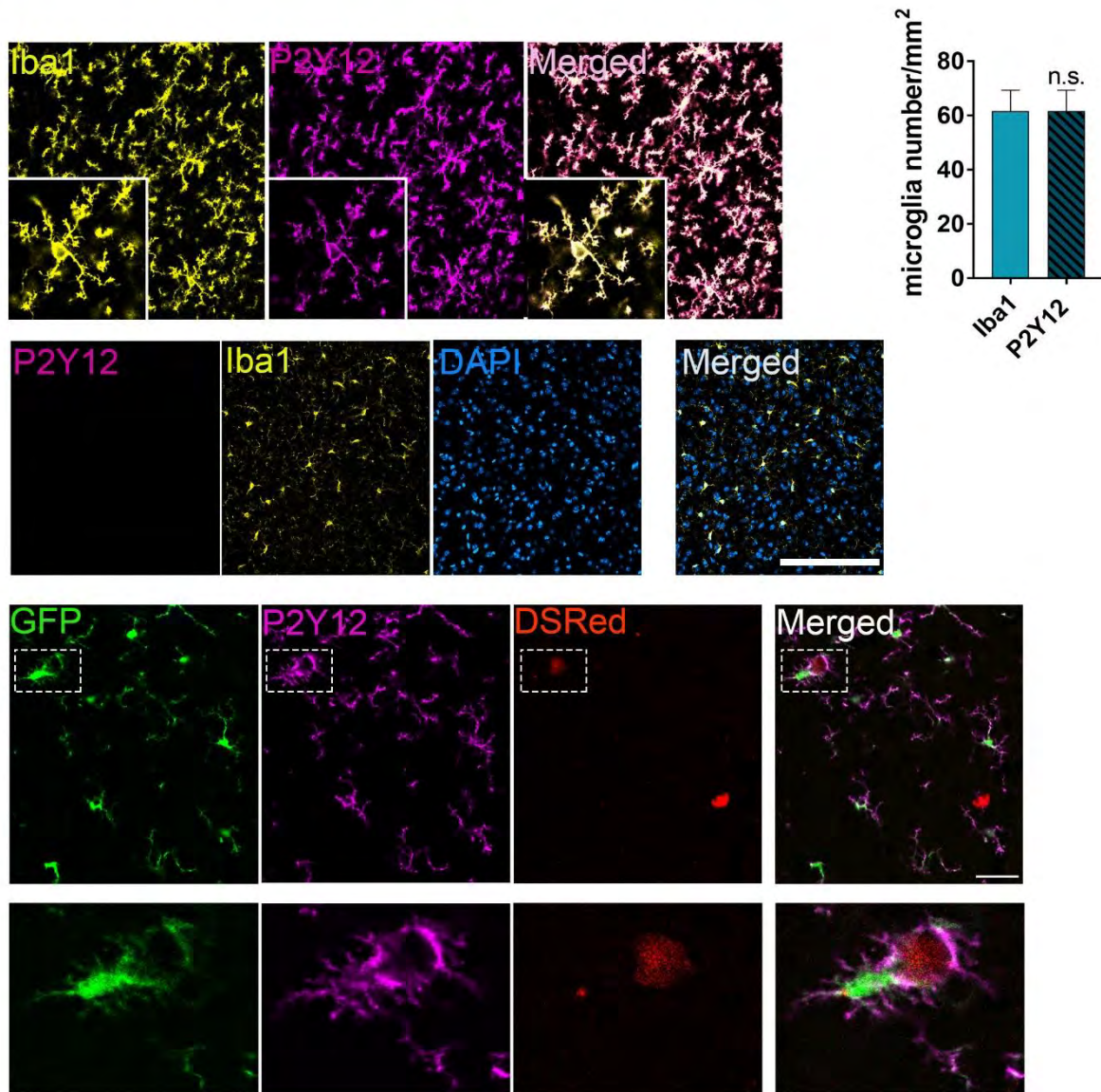
Supplementary Figure 4. Pseudorabies virus does not induce productive infection in microglial cells *in vitro*. In primary neuronal, astroglial or microglial cell cultures (bottom panels) infection with Bartha-DupGreen (BDG) was induced 24 hours prior to the assessment of infection-induced GFP expression or the cell viability (MTT) assay. Note that productive infection does not develop in microglia while it can be seen both in neurons and astrocytes. Viability of neurons, astrocytes and microglia is not reduced upon PRV infection or treatment with bacterial lipopolysaccharide (LPS). Data are expressed as mean \pm s.e.m.. Scale bars: 50 μ m, 15 μ m.



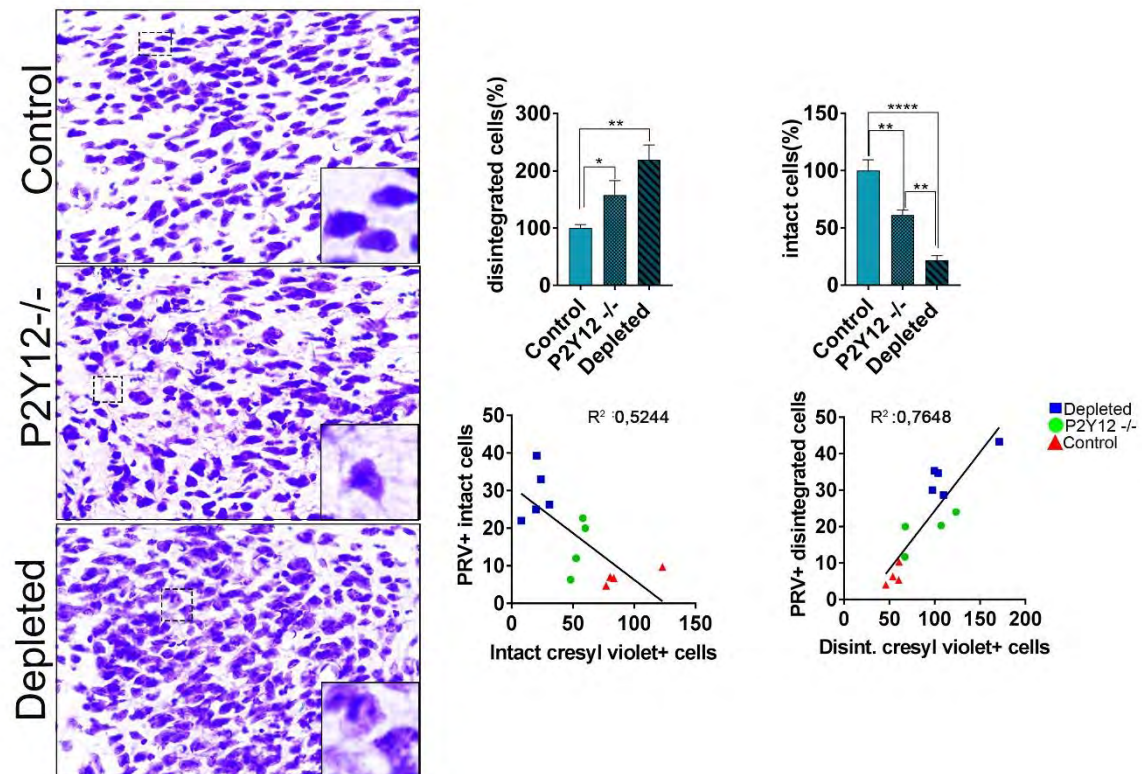
Supplementary Figure 5. Changes in peptide and mRNA levels of inflammatory cytokines and chemokines in response to virus infection in astroglial, neuronal and microglia cell cultures. Cytokine levels were measured in the conditioned medium of astroglial and neuronal cell cultures by cytometric bead array after LPS treatment or PRV infection. Samples were collected 24 hours after infection. Cell homogenates were collected for qPCR measurement. a-f, one-way ANOVA, followed by Tukey's post hoc test, a, **** $P < 0.0001$ Cont vs LPS, b, * $P < 0.05$ Cont vs LPS, c, *** $P < 0.0001$ Cont vs LPS, d, **** $P < 0.0001$ Cont vs LPS, **** $P < 0.0001$ Cont vs PRV, * $P < 0.05$ Cont vs LPS, e, **** $P < 0.0001$ Cont vs LPS, ** $P < 0.01$ Cont vs LPS, f, **** $P < 0.0001$ Cont vs LPS, g-i, 2way ANOVA followed by Sidak's multiple comparisons test. h, **** $P < 0.0001$ BDG vs LPS, i, **** $P < 0.0001$ BDG vs LPS, *** $P < 0.0001$ BDG vs LPS.



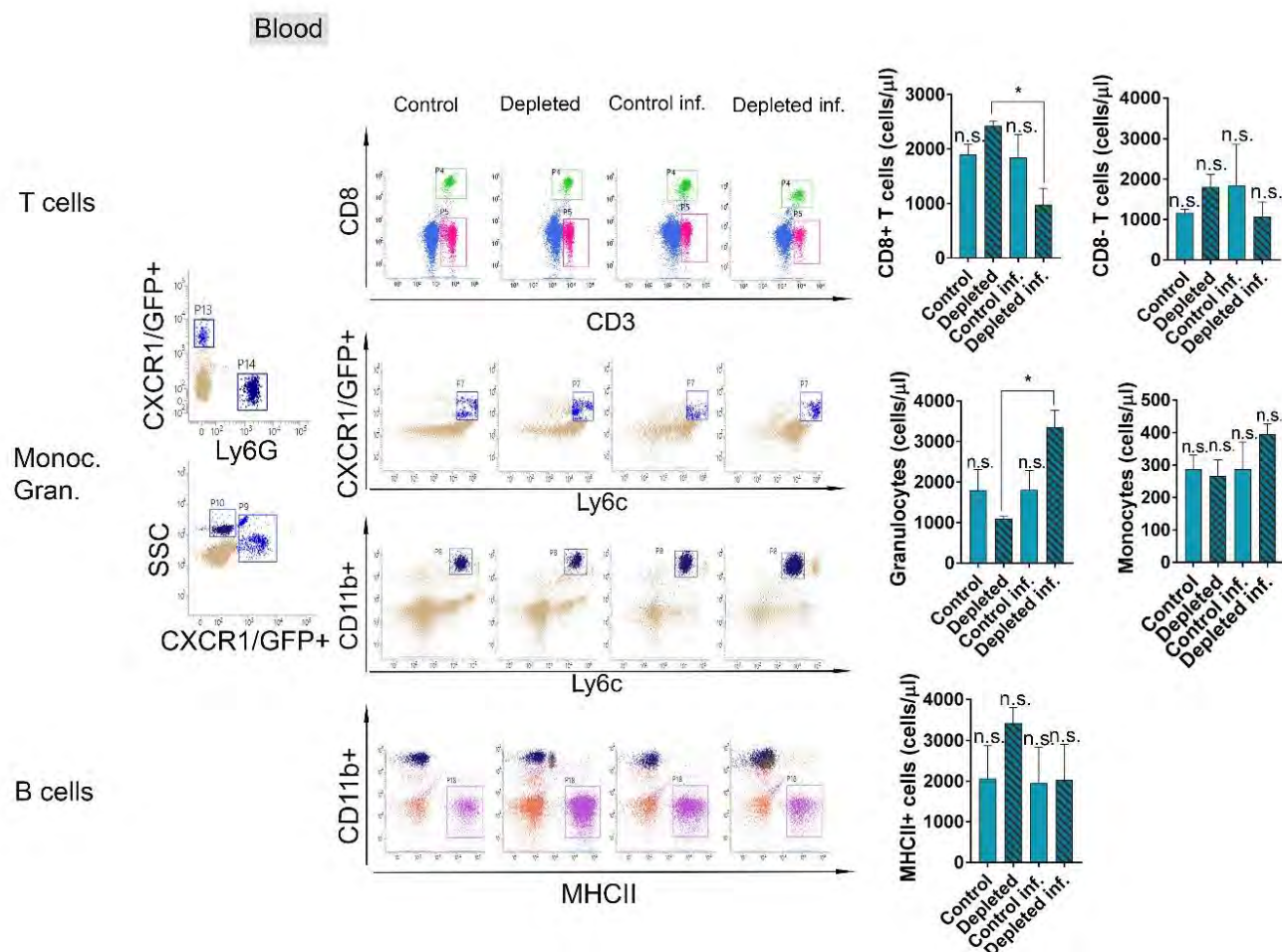
Supplementary Figure 6. Infected neurons remain morphologically intact until late stages of virus infection *in vitro*. a) Time course of BDG infection in primary neuronal cell cultures. Neuronal cultures were infected with a low titre of BDG to induce slow propagation of infection enabling the investigation of apoptotic and dead cells by using neuron-specific live annexin V staining and Propidium iodide (PI), respectively. Infected neurons show neither annexin V binding nor PI uptake until several hours following the appearance of the immediate early reporter protein, GFP. Neuron-specific live annexin V staining was first detected in neurons with decaying GFP expression. Note GFP^{high}/annexin⁻ (asteriks) and GFP^{low}/annexin⁺ (arrowheads) cells. PI entered cells only with intense annexin V labelling and little or no detectable GFP expression (arrow) indicating advanced infection. Immunostaining of the same cell culture after 32h post-infection revealed viral structural proteins (PRV) both in the GFP^{high} and GFP^{low} cells, indicating that both immediate-early reporter protein expression and viral protein expression precede the onset of infection-induced neuronal apoptosis. The images were captured with a Zeiss Axiovert epifluorescent microscope. Scale bar: 50 μ m. b) Propidium iodide (PI, red) uptake was not altered in infected neurons 16 hours after infection. This particular PI uptake experiment was performed in parallel cultures to those used for HPLC analysis (Fig4.a,b). Scale bar: 50 μ m.



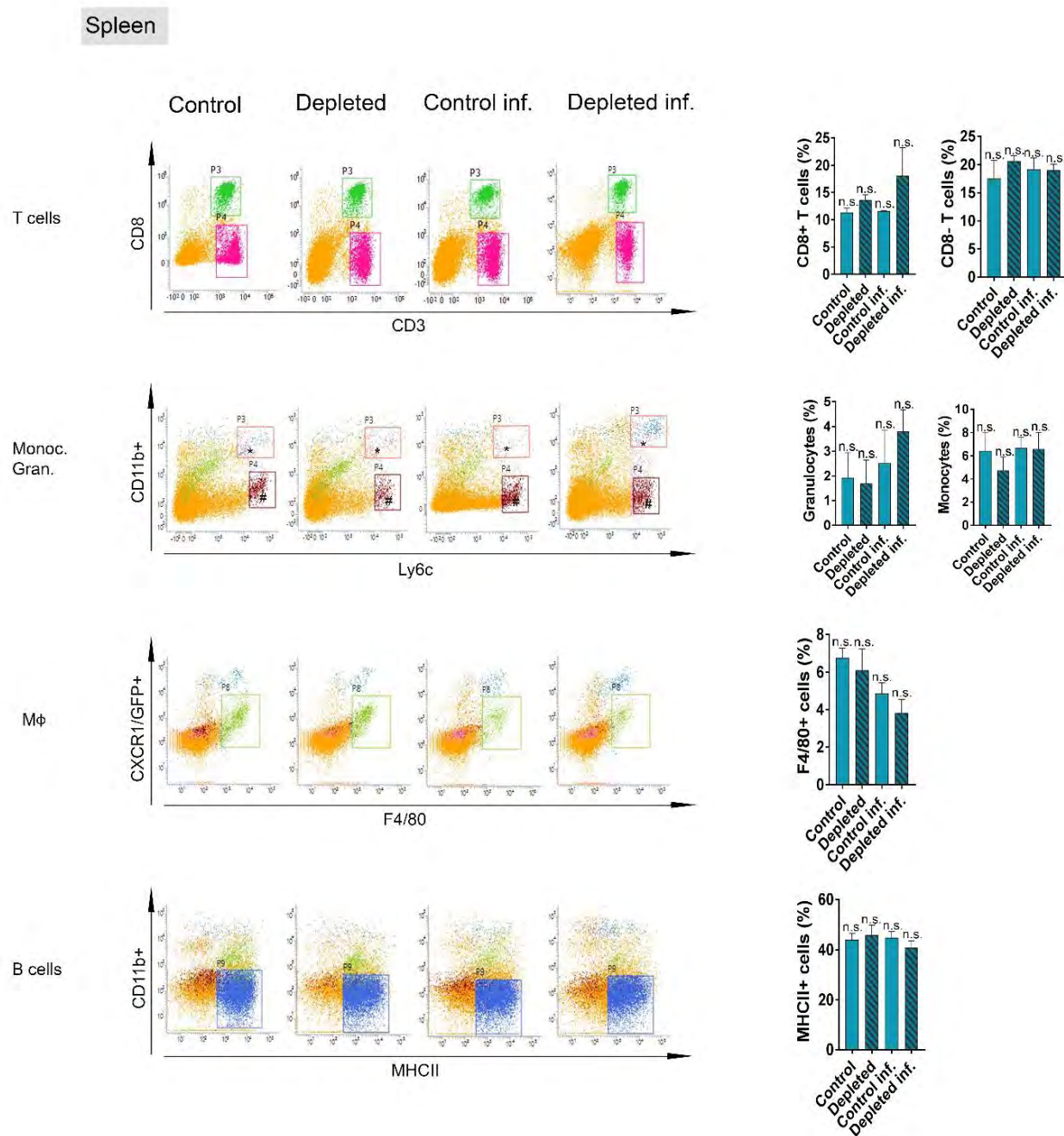
Supplementary Figure 7. P2Y12 is expressed by Iba1-positive microglia in the brain. P2Y12 immunofluorescence precisely identifies microglia in the brain that are co-expressing the microglia/macrophage marker Iba1. Note that virtually all microglia are P2Y12-positive. P2Y12 immunostaining is absent in P2Y12^{-/-} mice. P2Y12 immunofluorescence co-localises with Iba1 and GFP in Cx3Cr1^{+gfp} microglia recruited to infected neurons expressing the immediate early marker, DSRRed. Data are expressed as mean \pm s.e.m. n.s.- not significant, Scale bar: 100 μ m (top), 50 μ m (bottom).



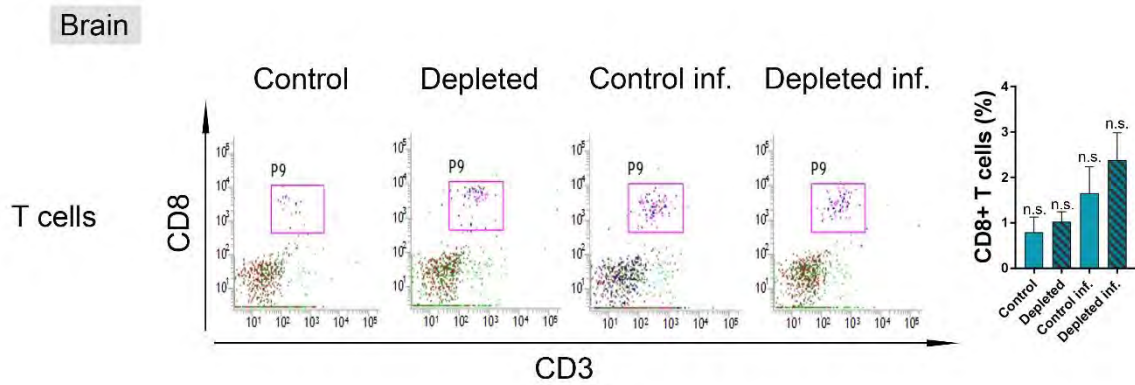
Supplementary Figure 8. The amount of disintegrated and dead cells is markedly increased in the brain in microglia-depleted and P2Y12^{-/-} mice. a) Cresyl violet staining was performed on brain sections derived from control, P2Y12^{-/-} and microglia-depleted mice 6 days after BDG infection. The number of disintegrated cells were increased (b), while the number of intact cells were markedly decreased (c) in the hypothalamus (PVN) of P2Y12^{-/-} and microglia-depleted mice compared to control animals. d) The number of morphologically intact cells (based on cresyl violet staining) show negative correlation with the number of intact, PRV-immunopositive cells (as presented in Fig.2a). e) The number of disintegrated, PRV-positive cells in Fig.2a correlates with morphologically damaged cells based on cresyl violet staining. b,c, one-way ANOVA, followed by Tukey's post hoc test, b, *P<0.05 Control vs P2Y12^{-/-}, **P<0.01 Control vs Depleted. c, one-way ANOVA, followed by tukey's post hoc test, **P<0.01 Control vs P2Y12^{-/-}; P2Y12^{-/-} vs Depleted, ****P<0.0001 Control vs Depleted. Scale bar: 10 μ m.



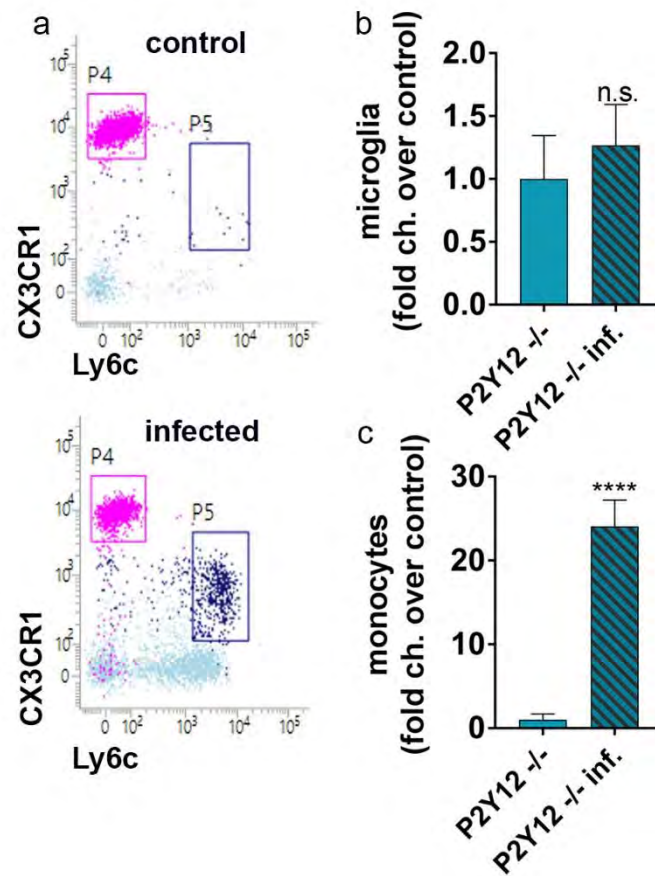
Supplementary Figure 9. Selective depletion of microglia does interfere with main blood cell populations. *Cx3Cr1^{+gfp}* mice were fed a PLX5622 chow diet for 21 days to deplete microglia. On the 16th day of the diet, a group of mice were injected with Bartha-DupGreen (BDG). Blood samples were collected from control mice and from mice 5 days after virus infection with or without microglia depletion, and labelled with mixtures of specific antibodies against leukocyte markers followed by flow cytometric analysis. Total blood cell counts were calculated by using 15 μm polystyrene microbeads (Polybead Microspheres, 18328-5). The number of CD8⁺ (P5 gate) T lymphocytes, CD11b⁺ Ly6c⁺ SSC^{high} Ly6G⁺ granulocytes (P8 gate), CD11b⁺ Ly6c^{high} *Cx3Cr1⁺* (Ly6G⁻) monocytes (P7 gate) and MHCII⁺ CD11b⁻ B cells (P18 gate) were no different between control, depleted, control infected and depleted infected animals. In association with the profoundly increased CNS infection in microglia depleted mice, numbers of CD3⁺ CD8⁺ T lymphocytes (P4 gate) and CD11b⁺ Ly6c⁺ SSC^{high} Ly6G⁺ granulocytes (P8 gate) showed significant difference between depleted and depleted virus infected animals. Data are expressed as mean ± s.e.m. one-way ANOVA, n=4. n.s. - not significant.



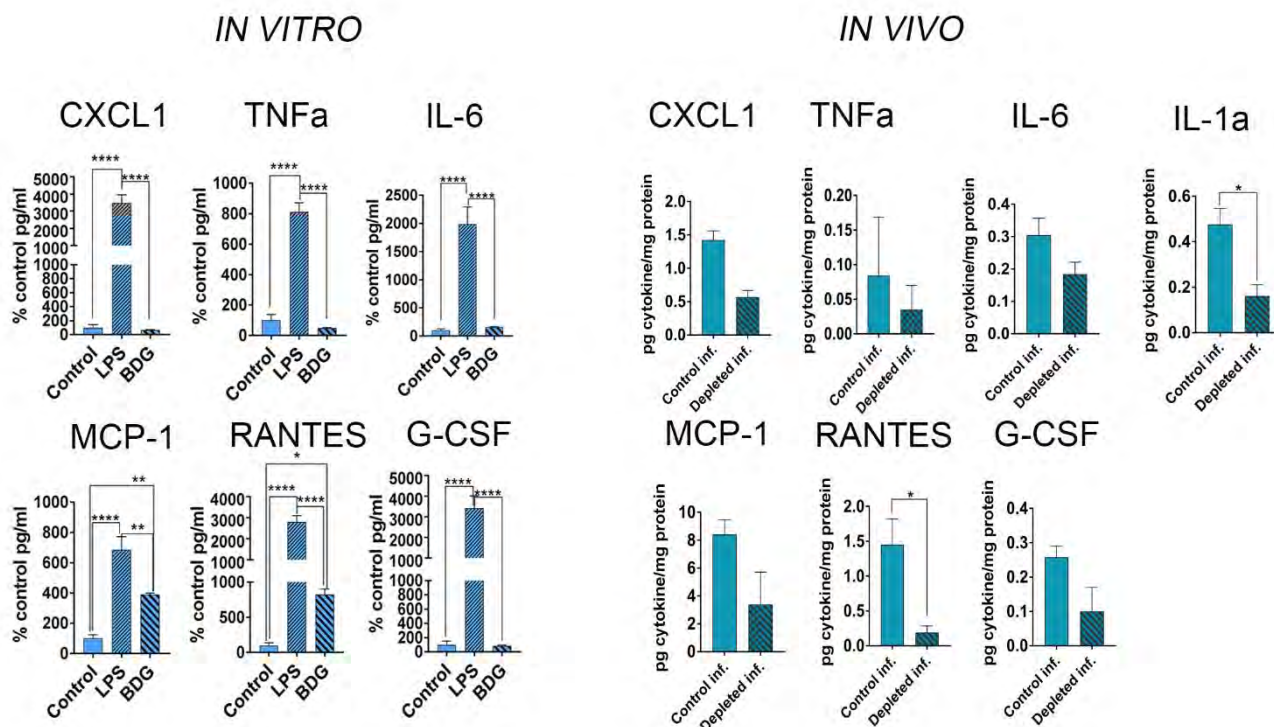
Supplementary Figure 10. Selective depletion of microglia does interfere with leukocyte numbers in the spleen. *Cx3Cr1^{+/gfp}* mice were fed a PLX5622 chow diet for 21 days to deplete microglia. On the 16th day of the diet mice were injected with Bartha-DupGreen (BDG). Blood samples were collected from control mice and from mice 5 days after PRV infection, and labelled with mixtures of specific antibodies against leukocyte markers followed by flow cytometric analysis. Numbers of CD8⁺ T cells (P3 gate), CD8⁻ T cells (P4 gate) and MHCII⁺ B cells (P9 gate) were not different between control, depleted, control infected and depleted infected animals. Spleen macrophages (Cx3Cr1-gfp⁺ F4/80⁺ cells, P8 gate), granulocytes (P3* gate, CD11b⁺, Ly6c⁺, SSC^{high} cells) and monocytes (P4# gate, CD11b^{low} Ly6c^{high} cells) were not different between control, depleted, control infected and depleted infected mice. Data are expressed as mean ± s.e.m. One-way ANOVA, n=4.



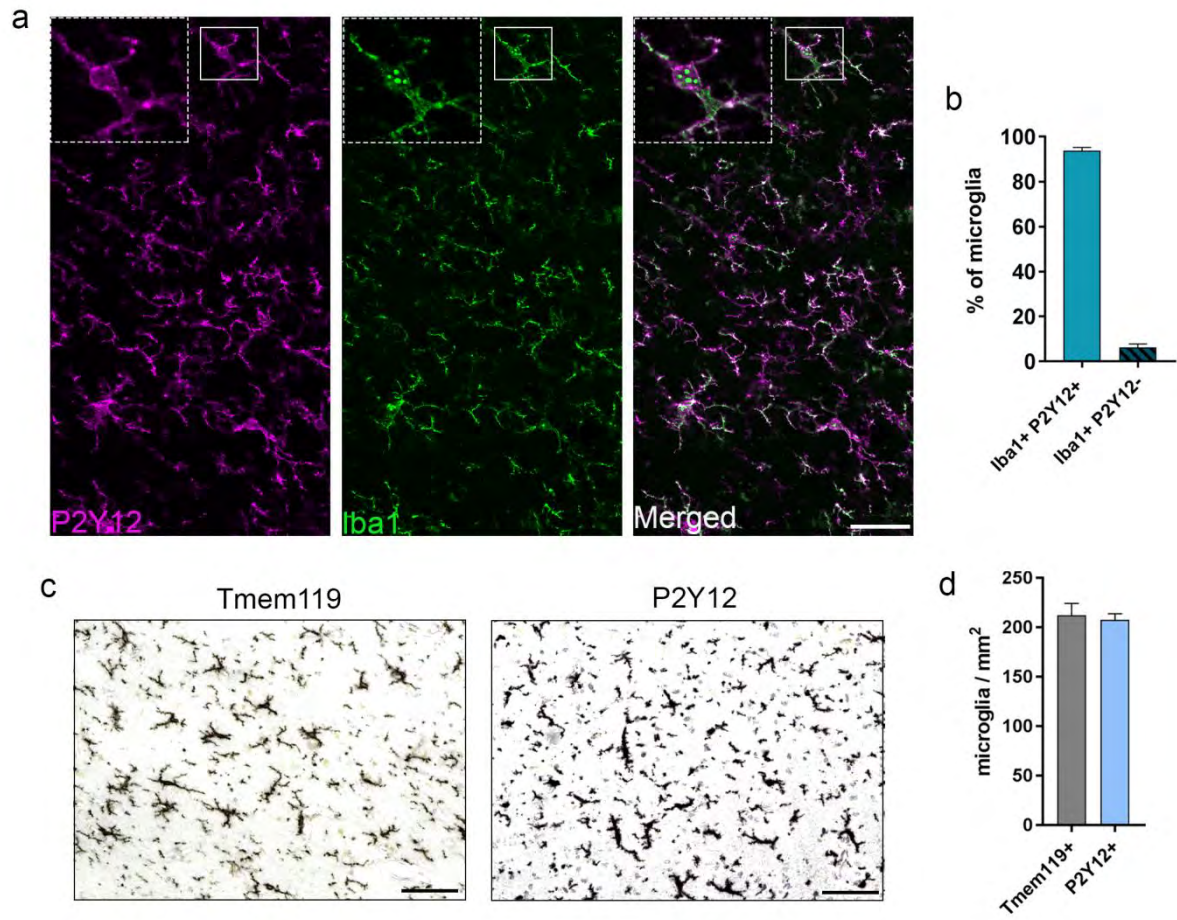
Supplementary Figure 11. Virus infection and selective manipulation of microglia do not alter the numbers of T lymphocytes in the brain. *Cx3Cr1^{+/-gfp}* mice were fed a PLX5622 chow diet for 21 days to deplete microglia. On the 16th day of the diet mice were injected with Bartha-DupGreen (BDG), to assess the role of microglia in inflammatory cell recruitment into the brain. Brain cells were isolated and T lymphocytes labelled with CD8, CD3 antibodies followed by flow cytometric analysis. Numbers of CD8+ T cells (P9 gate) were not different between control, depleted, control infected and microglia depleted infected animals. Data are expressed as mean \pm s.e.m. One-way ANOVA, n=4.



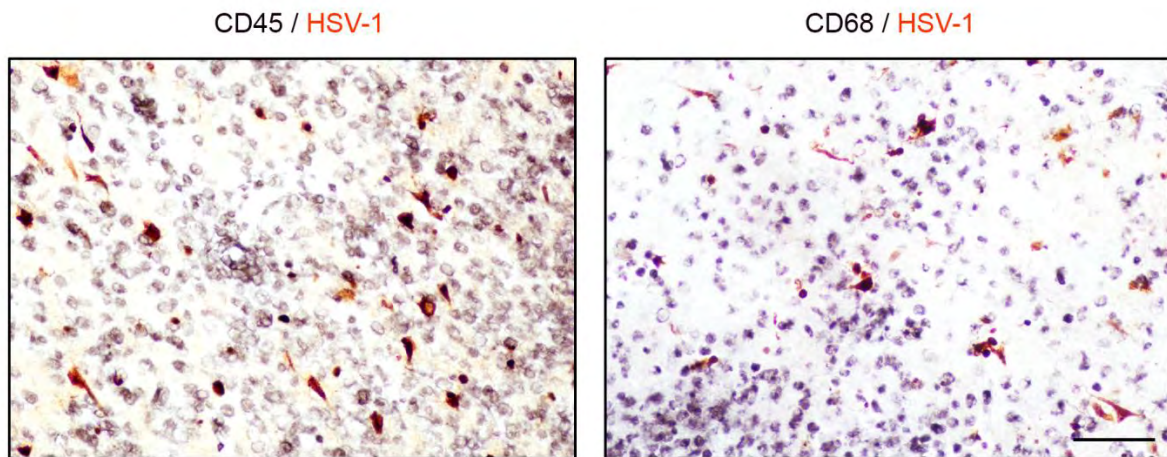
Supplementary Figure 12. Deficiency for P2Y12 does not influence infiltration of leukocytes into the brain upon virus infection. a, Flow cytometric dot plots showing infiltrating monocytes (P5) in the brain. **b,** Microglial numbers do not change in response to viral infection compared to control conditions. **c,** In response to viral infection monocytes infiltrate into the brain in P2Y12^{-/-} mice. Data expressed as mean \pm s.e.m. **b,c,** n.s. not significant **c,** **** $p < 0.0001$ $n = 10$ unpaired t-test.



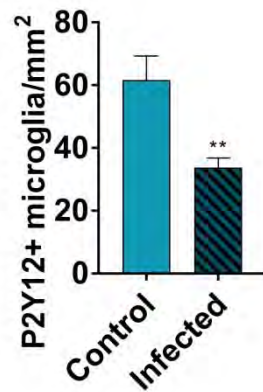
Supplementary figure 13. Changes in inflammatory cytokines and chemokines in response to virus infection and selective elimination of microglia. Left, *in vitro* data: Cytokine and chemokine levels were measured in the conditioned medium of microglial cell cultures by cytometric bead array after LPS treatment or exposure to PRV. Samples were collected 24 hours after infection. Right, *in vivo* data: Cytokine and chemokine levels were measured from homogenates of hypothalamic brain tissues of control and microglia-depleted mice infected with PRV in a retrograde transneuronal manner, 5 days prior to sample collection. All measurements were performed by cytometric bead array. One-way ANOVA, followed by Tukey's post-hoc test (left) or unpaired t test (right). n=5-6. Data are expressed as mean \pm s.e.m.



Supplementary figure 14. Microglia express P2Y12 in the human brain. a) Co-localization of microglial P2Y12 and Iba1 on perfusion-fixed, free-floating brain sections (frontal cortex). b) Proportion of P2Y12-positive microglia among Iba1+ cells. c) Immunohistochemistry showing Tmem119-positive and P2Y12-positive microglia in paraffin-embedded brain sections (frontal cortex). d) Quantification of Tmem119-positive and P2Y12-positive microglia in the brain. All samples are derived from patients with no known neurological disease.



Supplementary figure 15. Advanced HSV-1 infection is associated with marked neuroinflammatory responses in the human brain. Recruitment of numerous CD45-positive cells and CD68-positive brain macrophages is seen at sites of advanced virus infection characterized by large number of HSV-1-positive cells. Scale bar: 50 μ m.



Supplementary Figure 16. Numbers of Cx3Cr1^{+gfp} microglia are reduced in areas of advanced PRV infection (heavy virus load) compared to that seen in uninfected (control) mice. Unpaired t test, n=5-6. Data are expressed as mean ± s.e.m.

	Nr.	Age (y)	Sex	HSVE survival	Assessed region	Co-pathology	Cause of death	Post-mortem delay	Fixation time
cases	1	35	female	21 years	temporal lobe	none	bronchopneumonia	<24 h	8 weeks
	2	66	female	16 days	temporal lobe	none	acute encephalitis / brain edema / herniation	<24 h	8 weeks
	3	65	female	9 days	temporal lobe	none	acute encephalitis / brain edema / herniation	<24 h	3 weeks
	4	41	female	24 months	temporal lobe	none	bronchopneumonia	<24 h	4 weeks
	5	24	male	10 days	temporal lobe	none	acute encephalitis / brain edema/herniation	62h	3 weeks
controls	Sko 13	60	female	N.A.	temporal lobe	chronic bronchitis	respiratory arrest	<24 h	2-3h perfusion and overnight post-fixation
	Sko 16	72	male	N.A.	temporal lobe	acute bronchitis	respiratory arrest	<24 h	2-3h perfusion and overnight post-fixation

Supplementary Table 1. Patient characteristics and tissue processing information for post-mortem human brain tissues

Supplementary Video legends

Supplementary Video 1. *In vivo* two-photon imaging shows PRV-Bartha-DupDSRed (BDR) positive neuron contacted by CX3CR1^{+gfp} microglia. Note that the recruitment of microglia, including the displacement of the cell bodies takes place within 3 hours. The video corresponds to Figure 2 c, panel.

Supplementary Video 2. 3D-reconstruction from deconvolved confocal stack showing a recruited microglia (green) engulfing a PRV-positive neuronal cell body (cyan) with CD68-positive phagolysosomes (magenta) within the microglia, arranged around the infected neuron. The thickness of the reconstructed volume is 50 μm , for details, see Figure 2.

Supplementary Video 3. Time-lapse recording of a neuron-microglia co-culture in the absence of infection. Note that the CX3CR1^{+gfp} microglia cell (green) neither perturbs neuronal process outgrowth nor disrupts an existing process. The time-lapse covers a 12h period. Phase-contrast and fluorescent images were recorded simultaneously every 10 min. The video corresponds to Figure 3 a, upper panel.

Supplementary Video 4. Time-lapse recording of a neuron-microglia co-culture in the absence of infection. Note that the CX3CR1^{+gfp} microglia cell (green) slipping under neurons does not harm the dense network above. The time-lapse covers a 7h period. Phase-contrast and fluorescent images were recorded simultaneously every 10 min. The video corresponds to Figure 3 a, mid panel.

Supplementary Video 5. Time-lapse recording of a neuron-microglia co-culture after neurotrophic virus infection. Neurons were infected with BDL virus 2 hours prior the start of imaging. Note that GFP-expressing, microglial cells (green) flatten (become activated) and phagocytose compromised cells. The time-lapse covers a 40h period. Phase-contrast and fluorescent images were recorded simultaneously every 10 min. The video corresponds to Figure 3 a, bottom panel.

Supplementary Video 6. Time-lapse recording of an astroglia-microglia co-culture in the absence of infection. Note, that some of the CX3CR1^{+gfp} microglial cells (green) interact with multiple astrocytes. The time-lapse covers a 24h period. Phase-contrast and fluorescent images were recorded simultaneously every 10 min. Trajectory of a typical microglial cell is shown with spectral color codes changing from red to blue as time elapses. The video corresponds to Figure 3 b, upper panel.

Supplementary Video 7. Time-lapse recording of an astroglia-microglia co-culture after neurotrophic virus infection. Cells were infected with BDL virus 2 hours prior the the start of imaging. CX3CR1^{+gfp} microglial cells (green) intensely scan the compromised cells and phagocytose them. Trajectories of microglial cells are shown with spectral color codes changing from red to blue as time elapses. The time-lapse covers a 28h period. Phase-contrast and fluorescent images were recorded simultaneously every 10 min. The video corresponds to Figure 3 b, bottom panel.

Supplementary Video 8. Trajectories of P2RX7⁻ microglial cells migrating for a 20 h period in untreated (left) or BDG virus infected (right) astroglial cultures. For better visibility 20 randomly selected individual trajectories were centered to start from the origin on each side and superimposed with color codes changing from red to blue as time elapses. Note the more localized migration pattern of microglial cells in virus-infected culture on the right.

Supplementary Video 9. Trajectories of P2RY12^{-/-} microglial cells migrating for a 20 h period in untreated (left) or BDG virus infected (right) astroglial cultures. For better visibility 20 randomly selected individual trajectories were centered to start from the origin on each side and superimposed with color codes changing from red to blue as time elapses.

Supplementary Video 10. Phagocytic activity of wild type microglia. The flattened microglial cell phagocytoses two BDG virus infected (GFP-expressing) cells (green) within 24 hours. Phase-contrast and fluorescent images were recorded simultaneously every 10 min. The video corresponds to Figure 4 q.

Supplementary Video 11. Phagocytic activity of microglia with deficient purinergic signaling. Note that P2RX7^{-/-} microglia (left panel) readily phagocytose a BDG virus infected (GFP-expressing) cell (green) while the phagocytic activity of P2RY12^{-/-} microglia (right panel) is abolished. The time-lapse covers a 12h period. Phase-contrast and fluorescent images were recorded simultaneously every 10 min. The video corresponds to Figure 4 q.

Supplementary Methods

Mice

Mice were bred and genotyped at the SPF unit of the Animal Care Unit of the Institute of Experimental Medicine (IEM HAS, Budapest, Hungary) as described earlier[12, 17]. Mice had free access to food and water and were housed under light-, humidity- and temperature-controlled conditions.

Selective elimination of microglia from the brain

PLX5622 was provided by Plexxikon Inc. (Berkeley, USA) and formulated by Research Diets (New Brunswick, USA) into an AIN-76A standard chow in 1200 p.p.m. (1200mg PLX 5622 in 1kg chow) concentration. Mice were fed PLX5622 for 3 weeks, to eliminate microglia from the brain. We could not observe any sign of physiological illness (alterations in food intake, weight, physical appearance) or behavioural changes (social interactions, exploration) during the diet period, in accordance with other studies[10, 17].

Neurotropic herpesvirus infection

Mice were randomly assigned to experimental groups and were injected either intraperitoneally or directly into the epididymal white adipose tissue with a genetically modified PRV-Bartha derivative, PRV-Bartha-Dup-Green (BDG)[3] to induce retrograde transsynaptic infection in the brain. To enable a defined, exclusively retrograde transsynaptic spread of infection *in vivo*, the neuroinvasiveness of BDG was modified by insertion of a GFP gene expression cassette to the putative antisense promoter (ASP) located at the repeated invert region of the virus. This construct also allows time-mapping the spread of infection in individual cells[3, 4, 7]. The activity of the strong immediate-early promoter/enhancer of the human cytomegalovirus is independent from the viral protein, enabling very early stages of infection to be detected by GFP expression. PRV genes encoding structural proteins are driven by late promoters, resulting in the appearance of the virus proteins in the late stage of the infection. In a set of studies, mice were infected with BDG on 16th day of PLX5622 diet to assess the effect of microglia depletion on central propagation of virus infection. For *in vivo* two-photon imaging, Cx3Cr1^{GFP/+} mice were infected with PRV-Bartha-DupDsRed (BDR)[2] enabling the co-detection of infected neurons with microglia. The virus was grown in porcine kidney (PK)-15 cells to a titer of 6×10^8 plaque-forming units (PFU)/ml. After virus injection (10 μ l intraperitoneally or into the epididymal white adipose tissue), mice were let to survive for 6 or 7 days and were regularly monitored for neurobehavioral symptoms.

Tissue processing and immunostaining

Mice were transcardially perfused with saline followed by an ice-cold 4% PFA solution. Brains were post-fixed, cryoprotected and 25 μ m thick sections were cut. Fluorescent immunohistochemistry was performed on free-floating brain sections using a combination of goat anti-mouse Iba1 (1:500, # NB100-1028, Novus Biologicals), chicken anti-GFP tag (1:1000, #A10262, Invitrogen), rabbit anti-PRV (1:500, generous gift of Lynn Enquist), rabbit anti-mouse P2Y12 (1:500, # 55043A, AnaSpec), rat anti-mouse CD45 (1:250, #MCA1388, AbD Serotec), and rat anti-mouse CD68 antibodies (1:250 dilution, #MCA1957GA, AbD Serotec). Brain sections were blocked with 2% normal donkey serum and incubated with a mixture of primary antibodies overnight at 4C° which was followed by the cocktail of

dc_2027_22

appropriate secondary antibodies: donkey-anti-goat Alexa 594 (1:500, #A11058, Invitrogen), donkey anti-chicken Alexa 488 (1:500, #703-546-155, Jackson ImmunoResearch), or donkey-anti-rabbit Alexa 647 antibodies (1:400, #711-605-152, Jackson ImmunoResearch). Biotinylated tomato lectin (1:100, #L0651-1 mg, Sigma-Aldrich) was visualized by streptavidin Marina Blue or Alexa 594 conjugates (1:250, #S-11221, Invitrogen). Images were captured with a Nikon Ni-E C2+ confocal microscope, and image processing was done using the NIS Elements Viewer 4.20 software. Quantitative analysis was performed on 3 randomly selected fields within the region of interest for each brain section, on 3-3 serial coronal sections for given brain areas.

Super-resolution (STORM) microscopy

Free-floating brain sections were blocked with 2% normal donkey serum followed by immunostaining with rabbit anti-mouse P2Y12 antibody (1:500, #AS-55043A, AnaSpec) and donkey anti-rabbit Alexa 647 secondary antibody (1:400, #711-605-152, Jackson ImmunoResearch), chicken anti-GFP tag (1:1000, #A10262, Invitrogen) and donkey anti-chicken Alexa 488 (1:500, #703-546-155, Jackson ImmunoResearch), rabbit anti-PRV (1:500, gift of Lynn Enquist,) and donkey anti-rabbit Alexa 647 (1:400, #711-605-152, Jackson ImmunoResearch). Sections were mounted onto #1.5 thick borosilicate coverslips and covered with imaging medium⁵⁰ immediately before imaging. The imaging medium contained: 5% glucose, 0.1 M mercaptoethylamine, 1 mg ml⁻¹ glucose oxidase, and catalase (1500 U ml⁻¹, Sigma-Aldrich) in Dulbecco's PBS (Sigma-Aldrich). STORM imaging was performed for P2Y12 (stimulated by a 647 nm laser) by using a Nikon N-STORM C2+ super-resolution system that combines 'Stochastic Optical Reconstruction Microscopy' technology and Nikon's Eclipse Ti research inverted microscope to reach a lateral resolution of 20 nm and axial resolution of 50 nm[1, 9].

Immuno-electron microscopy

For combined immunogold-immunoperoxidase stainings, animals were perfused with 4% paraformaldehyde (PFA) and 0.1% glutaraldehyde in 0.1 M phosphate buffer (PB) pH 7.4 for 40 minutes and 50 µm thick sections were cut. Sections were washed in PB, treated with 0.5% sodium-borohydride for 5 minutes, and further washed in PB and TBS. This was followed by incubation in 1% human serum albumin (HSA, #A1653-5G, Sigma-Aldrich), diluted in TBS. Then the sections were incubated for 48 hours in the following solutions of primary antibodies diluted in TBS: either guinea-pig anti-Iba1 (1:500, #234 004, Synaptic Systems) or chicken anti-eGFP (in case of the Cx3CR1^{GFP/+} mice, 1:1000, #A10262, ThermoFisher Scientific) was mixed with rabbit anti-PRV (1:500, from Lynn Enquist). To eliminate non-specific binding, the anti-PRV antibody solution was incubated with control brain sections for one day before use. After repeated washes in TBS, sections were treated with blocking solution (Gel-BS) containing 0.5% cold water fish skin gelatin (#900.033, Aurion, The Netherlands) and 0.5% HSA in TBS for 1 h. This was followed by 24 h incubation in the following solutions of secondary antibodies diluted in Gel-BS: 1.4 nm gold conjugated goat anti-rabbit Fab-fragment (1:200, #2004, NanoProbes) combined either with biotinylated donkey anti-guinea pig (1:500, #706-065-148, Jackson ImmunoResearch) or biotinylated goat anti-chicken (1:500, #BA-9010, Vector Laboratories). After intensive washes in TBS and 0.1 M PB sections were treated with 2% glutaraldehyde in 0.1 M PB for 15 minutes. This was followed by further washes in 0.1 M PB, TBS and incubation in ABC (1:300, Vectastain Elite ABC HRP Kit, #PK-6100, Vector Laboratories) diluted in TBS. Sections were washed in TBS, and tris-buffer (TB) pH 7.6, and the immunoperoxidase

dc_2027_22

reaction was developed using 3,3-diaminobenzidine as chromogen (DAB, #32750-25G-F, Sigma-Aldrich). After repeated washes in TBS and enhancement conditioning solution (ECS, #500.055, Aurion), gold particles were intensified using the silver enhancement solution (SE-EM, #500.044, Aurion) for 60 minutes at room temperature. After subsequent washes, sections were treated with 0.5 % osmiumtetroxide in PB for 20 minutes. Then sections were dehydrated in ascending ethanol series and acetonitrile, and embedded in epoxy resin (Durcupan, #44610-1EA, Sigma-Aldrich). During dehydration sections were treated with 1% uranylacetate in 70% ethanol for 20 minutes. After polymerization, 70 nm thick sections were cut on a Leica EM UC6 ultramicrotome (Nussloch, Germany), and picked up on formvar-coated single-slot copper grids. The sections were examined using a Hitachi H-7100 electron microscope (Tokyo, Japan) and a side-mounted Veleta CCD camera (Olympus Soft Imaging Solutions).

Correlated confocal laser-scanning microscopy, electron microscopy and electron tomography

Before the immunofluorescent staining, the 50 μm thick brain sections from BDG-injected Cx3CR1^{GFP/+} mice were washed in PB, treated with 0.5% sodiumborohydride for 5 minutes, and further washed in PB and TBS. This was followed by blocking for 1 hour in 1% human serum albumin (HSA). After this, sections were incubated in mixtures of primary antibodies: chicken anti-eGFP (1:4000, #A10262, ThermoFisher Scientific), rat-anti-mouse CD68 (1:250, #MCA1957GA, AbD Serotec) and rabbit anti-PRV (1:500, gift of Lynn Enquist). To eliminate non-specific binding, the anti-PRV antibody solution was incubated with control brain sections for one day before use. After repeated washes in TBS, sections were treated with blocking solution containing 0.5% cold water fish skin gelatin and 0.5% HSA in TBS for 1 h. After incubation, sections were washed in TBS, and incubated overnight at 4 °C in the mixture of biotinylated goat-anti-chicken (1:500, #103-065-155, Jackson ImmunoResearch), Alexa 594 conjugated donkey-anti-rat (1:500, #A21209, Invitrogen) and Alexa 647 conjugated donkey-anti-rabbit (1:500, #711-605-152, Jackson ImmunoResearch) diluted in GelBS. Secondary antibody incubation was followed by washes in TBS and PB. Sections were mounted in PB, coverslipped, sealed with nail-polish. Immunofluorescence was analysed using a Nikon Eclipse Ti-E inverted microscope (Nikon Instruments Europe B.V., Amsterdam, The Netherlands), with a CFI Plan Apochromat VC 60X water immersion objective (NA: 1.2) and an A1R laser confocal system. We used 488, 561 and 642 nm lasers, and scanning was done in line serial mode. Image stacks were obtained with NIS-Elements AR software with a pixel size of 50x50 nm in X-Y, and 150 nm Z-steps. Stacks were deconvolved using Huygens Professional software (www.svi.nl), and 3D-reconstruction was performed using the IMOD software package[16]. After imaging, sections were washed 0.1 M PB, TBS and incubated in ABC (1:300, Vectastain Elite ABC HRP Kit, #PK-6100, Vector Laboratories) diluted in TBS. Sections were washed in TBS, and tris-buffer (TB) pH 7.6, and the immunoperoxidase reaction was developed using 3,3-diaminobenzidine as chromogen. After subsequent washes, sections were treated with 0.5 % osmiumtetroxide in PB for 20 minutes. Then sections were dehydrated in ascending ethanol series and acetonitrile, and embedded in epoxy resin. During dehydration sections were treated with 1% uranylacetate in 70% ethanol for 20 minutes. After polymerization, 70 or 150 nm thick sections were cut on an ultramicrotome, and picked up on formvar-coated single-slot copper grids. The sections were examined using a Hitachi H-7100 electron microscope and a side-mounted Veleta CCD camera. For the electron tomographic investigation, we used the 150 nm thick sections. Grids were put on drops of 10% HSA in TBS for 10 minutes, dipped in distilled water (DW), put on drops of 10 nm gold conjugated Protein-A (#AC-10-05-05, Cytodiagnosics) in DW (1:3), and washed in DW. Finally, we deposited 5-5 nm thick layers of carbon on both sides of the grids. Electron tomography was performed using a Tecnai T12 BioTwin electron microscope equipped with a computer-controlled precision stage and an Eagle™ 2k CCD 4

megapixel TEM CCD camera. Acquisition was controlled via the Xplore3D software (FEI). Regions of interest were pre-illuminated for 4-6 minutes to prevent further shrinkage. Tilt series were collected at 2 degree increment steps between -65 and +65 degrees at 120 kV acceleration voltage and 23000x magnification with -1.6 – -2 μm objective lens defocus. Reconstruction was performed using the IMOD software package. Isotropic voxel size was 0.49 nm in the reconstructed volumes. Segmentation has been performed on the virtual sections using the 3Dmod software.

Immunohistochemistry and immunofluorescence on post-mortem human brain samples

To investigate microglia recruitment in response to neurotropic virus infection in the human brain, formalin-fixed paraffin-embedded (FFPE) post-mortem brain tissues from five patients aged 42-66 years were analyzed (ethical approval ETT-TUKEB 62031/2015/EKU and TUKEB 34/2016) with Herpes simplex type 1 encephalitis (HSVE1) confirmed by PCR and immunohistochemistry. Tissue samples from two additional patients with no known neurological disease have been used as controls. Control samples were perfuse-fixed with Zamboni fixative (4% PFA, 15 % PIC) and postfixed overnight in the same solution. 4-6 μm thick brain sections were cut and samples were mounted on gelatin-coated slides. After deparaffinisation, HIER (Novocastra Epitope Retrieval Solution pH9, Leica Biosystems) and peroxidase blocking (in 1% H₂O₂ solution) was carried out. Sections were blocked with 2.5% Normal Horse serum (#S-2012, Vector Laboratories) and were incubated with rabbit anti-HSV I (#361A-14, Cell Marque), rabbit anti-P2Y12 (#AS-55043A, AnaSpec, Inc.), rabbit-anti-Tmem119, mouse anti-CD68, mouse anti-CD45, mouse anti-CD3, mouse anti-CD20 and mouse anti-CD15 antibodies. For signal amplification ImmPRESS anti-rabbit HRP Kit (#MP-7401, Vector Laboratories) and for visualisation either ImmPACT NovaRED HRP substrate (for detection of HSV I) or DAB-Ni HRP substrate (for detection of other markers, #SK-4805, Vector Laboratories) was used. Representative pictures were taken on 20x magnification using a Nikon Ni-E C2+ microscope. To assess the proportion of P2Y12-positive microglia, P2Y12 and Iba1 double immunofluorescence has been performed on 50 μm thick free-floating brain sections. Images were captured using a Nikon Eclipse Ti-E inverted microscope (Nikon Instruments Europe B.V., Amsterdam, The Netherlands), with a CFI Plan Apochromat VC 60X water immersion objective (NA: 1.2) and an A1R laser confocal system.

Two-photon imaging

To assess microglia recruitment to infected neurons in the mouse brain in real-time, Cx3CR1^{GFP/+} mice were i.p. injected with 10 μl of the BDR virus. 7 days after virus injection, cranial window surgery was performed on anaesthetized (using 3% isoflurane for induction, 1.5-2% during surgery) mice and a circular craniotomy (3 mm diameter) was made above motor cortex (Bregma – 0,82); on the right hemisphere. A custom made aluminium head plate was fixed to the skull using Cyanoacrylate glue. During skull opening the place of craniotomy was washed continuously with cold Ringer solution. The craniotomy was covered with a circular cover glass and dura mater remained intact under the glass to ensure that microglial activation is not induced[17]. The cover glass was fixed with Paladur mixed Cyanoacrylate.

Measurements were performed on a Femto2D-DualScanhead microscope (Femtonics Ltd., Hungary) coupled with a Chameleon Ultra II laser (Coherent, Santa Clara, USA) [5, 13]. The wavelength of the laser was set to 980nm to measure DsRed and GFP signal simultaneously. Excitation was delivered to the sample, and the fluorescent signal was

collected using a CFI75 LWD 16XW/0.8 lens (Nikon, 16x, NA 0.8) and then separated using a dichroic mirror (700dcxru) before the two channel detector unit, which was sitting on the objective arm (travelling detector system) as described in detail earlier[5, 13]. The dichroic mirror and emission filters (490-550 nm for the green and 570-640 nm for the red channel) was purchased from Chroma Technology Corp. (Vermont, USA). Data acquisition was performed by MES softver (Femtonics Ltd.) A Z-stack from of 32 images (800x800 pixel, field-of-view=210x210 μ , Z stack contained 12 image planes with 4.6 μ m step size (range= 80-135 μ m from pial surface) was made at every 3 minutes. Two-photon image sequences were exported from MES and analysed using ImageJ.

Primary neuronal cultures

Primary cultures of embryonic cortical cells were prepared from CD1 mice on embryonic day 15[6]. Cells were seeded onto poly-L-lysine-coated (#P1524, Sigma-Aldrich) 24-well tissue culture plates at 3×10^5 cells/well density and grown in NeuroBasal medium (#21103-049, ThermoFisher Scientific) supplemented with 5% fetal bovine serum (FBS, #F7524, Sigma), B27 (#17504-044, ThermoFisher Scientific), Glutamax (#35050061, ThermoFisher Scientific), gentamicin (40 μ g/ml, Sandoz), amphotericin B (2.5 μ g/ml, #A2411, Sigma-Aldrich). Cytosine-arabino-furanoside (CAR, 5 μ M, #C6645, Sigma-Aldrich) was added to the cultures 48-72 h after plating to limit glia growth, and then one third of the culture medium was changed to NeuroBasal medium supplemented with B27 without FBS every 3–4 day thereafter. Cells were cultivated for 6-8 days at 37°C in 5% CO₂, 95% air atmosphere until further measurements.

Astroglia and microglia cell cultures

Astroglia/microglia mixed cell cultures were prepared from the whole brains of CD1, C57BL/6J, CX3CR1^{GFP/+}, P2X7^{-/-} or P2Y12^{-/-} newborn (P0-P1) mouse pups, as described earlier[15]. In brief, meninges were removed and the tissue pieces were subjected to enzymatic dissociation, using 0.05% w/v trypsin (#T4549, Sigma Aldrich) and 0.05% w/v DNase (#DN-25, Sigma-Aldrich) for 10 minutes at room temperature. The cells were plated onto poly-L-lysine (#P1524, Sigma-Aldrich) coated plastic surfaces and were grown in Minimal Essential Medium (#M2279, Sigma-Aldrich) supplemented with 10% FBS (#10500, Gibco), 4 mM glutamine (#G3126, Sigma-Aldrich), 40 μ g/ml gentamycin (Sandoz) and amphotericin B (2.5 μ g/ml, #A2411, Sigma-Aldrich) in humidified air atmosphere containing 5% CO₂, at 37°C. The culture medium was changed on the first two days and every third day afterwards. Cultures reaching confluency at ~DIV7 were harvested by trypsinization and re-plated onto pLL coated glass coverslips or into petri dishes, according to the actual experimental design. Secondary astrocytic cultures reaching confluency and displaying mosaic-like pattern were infected with PRV strains, as it follows. Microglial cells were isolated from 21-28 day old mixed cultures either by shaking or by mild trypsinization.

Neurotropic herpesvirus infection of primary neuronal and glial cultures

The neuronal or astroglia cultures were infected with either PRV-Bartha-Dup-Green (BDG) virus or PRV-Bartha-DupLac (BDL) at a final titer of 2.5×10^5 PFU/ml, as described earlier[11]. The multiplicity of infection (MOI) was ~0,17 PFU/cell. The cells were incubated with the virus containing medium for 1h, at room temperature. In order to remove infective virus particles from the culture medium we washed the cultures at least three times after the 1h viral exposure. For quantification of ATP derivatives released by or retained in control vs. infected cells, embryonic (E16) primary cortical neuronal cultures were used. The cells were infected at DIV9. 16 hours post-infection GFP expression was initiated in most cells, while the cell membrane integrity was not compromised and the overall viability was not reduced based on

MTT cell viability tests. The cell culture media and the cell fractions were collected 15 min after media change, as it is described below. For determination of cytokine production as well as quantitative RT-PCR the following cultures and conditions were used.

Establishment of neuron/microglia and astroglia/microglia co-cultures

In cultures used for time-lapse recordings microglial cells isolated from mixed glial cultures were seeded on top of astrocytic or neuronal cell cultures in 10 000 cell/cm² density, immediately after the infection and the subsequent washing steps. If not CX3CR1^{GFP/+} microglia were used, the cells were subjected to staining with the orange or red vital CellTracker dyes CMTMR/CMPX (#C2927, #C34552, ThermoFisher Scientific) prior co-culture establishment (30min, 37°C).

Time-lapse microscopy

Time-lapse recordings were performed on a computer-controlled Leica DM IRB inverted fluorescent microscope equipped with a Marzhauser SCAN-IM powered stage and a 10x N-PLAN objective with 0.25 numerical aperture and 5.8 mm working distance. The microscope was coupled to an Olympus DP70 color CCD camera and a Zeiss Colibri LED epifluorescent illumination system. Cell cultures were kept at 37°C in humidified 5% CO₂ atmosphere in tissue culture grade Petri dishes in a stage-top incubator mounted on the powered stage of the microscope. Stage positioning, focusing, illumination and image collection were controlled by a custom-made experiment manager software on a PC. Phase contrast and epifluorescent images were collected consecutively every 10 minutes from several microscopic fields for durations up to 48 hours. Images were edited using NIH ImageJ software.

Cell motility data analysis

Cell tracking: Images were analyzed individually with the help of custom-made cell-tracking programs (G-track and Wintrack) enabling manual marking of individual cells and recording their position parameters into data files. At the magnification applied, the precision of this tracking procedure is estimated to be 10 μm, comparable to the average cell diameter (10-50 μm). In the following, the position of the i^{th} cell at time t is denoted by $x_i(t)$.

Trajectories: Cell positions, $x_i(t)$, from several microscopic fields were recorded over 24 hours and each cell's trajectory was plotted. Subsequently, the starting positions of trajectories were aligned to the origin ($x=0$, $y=0$) and consecutive relative cell positions were plotted and superposed yielding groups of centered trajectories enabling the comparison of cell migration directionality. Trajectories in the monolayer cell cultures studied indicate a persistent random walk behavior with different velocity and directional persistence.

Displacement: The motion of individual cells is often evaluated in terms of average cell displacement, d , over a time period t as:

$$d^2(t) = \left\langle (X_i(t+t_0) - X_i(t_0))^2 \right\rangle_i$$

where $X_i(t)$ denoting the center of cell i at time t , $\langle \cdot \rangle_i$ is an average over all possible cells, and t_0 is an arbitrary reference frame of the image sequence analyzed. The empirical $d(t)$ curves indicate a persistent random walk behavior in monolayer cell cultures studied.

dc_2027_22

Average velocity: Average cell velocity was calculated directly from cell displacements in consecutive steps of cell tracking. The velocity, $v_i(t)$, of a given cell i at time t was calculated as

$$v_i(t) = |x_i(t + Dt) - x_i(t)| / Dt$$

where Dt is the difference of two consecutive steps of cell tracking and thus the time resolution data acquisition. To characterize the motility of an ensemble of cells, time-dependent average velocity $v(t)$ was calculated as

$$v(t) = \frac{1}{N(t)} \sum_{i=1}^{N(t)} v_i(t)$$

where the summation goes over each $N(t)$ cell being in the cell population. Average velocity, v , was calculated by averaging $v(t)$ over all time steps of cell tracking as

$$v = \frac{1}{K} \sum_{t=\Delta t}^{K \cdot \Delta t} v(t)$$

where K is the number of time steps of tracking.

Cytokine measurement from media of primary cell cultures

Concentrations of IL-1 α , IL-1 β , TNF- α , IL-6, MCP-1, RANTES (CCL5), G-CSF and KC (CXCL1) were measured from conditioned media of primary neuronal, astroglial and microglial cell cultures by using cytometric bead array (CBA) Flex Sets (all from BD Biosciences, #560157, #560232, #558299, #558301, #558342, #558345, #560152, #558340, respectively). Measurements were performed on a BD FACSVerse machine and data were analysed using an FCAP Array software (BD Biosciences) as described earlier[8]. The cytokine levels of conditional media were corrected for total protein concentrations of the samples measured by Bradford Protein Assay Kit (#50000201, Bio-Rad Laboratories).

Total RNA isolation and quantitative RT-PCR

For total RNA isolation, cell culture samples were homogenized in 500 μ l TRI Reagent and isolation was performed using Tissue Total RNA Mini Kit according to the manufacturer's instructions. To eliminate genomic DNA contamination, DNase I treatment was introduced (1 U/reaction, reaction volume: 50 μ l). Sample quality control and the quantitative analysis were carried out by NanoDrop. cDNA synthesis was performed with the High Capacity cDNA Reverse Transcription Kit according to the manufacturer's instructions. The chosen primer sequences used for the comparative C_T experiments were verified with the Primer Express 3.0 and Primer-BLAST software. The sequences were as follows:

GAPDH	fw TGA CGT GCC GCC TGG AGA AA, rev AGT GTA GCC CAA GAT GCC CTT CAG
IL-1α	fw CCA TAA CCC ATG ATC TGG AAG AG, rev GCT TCA TCA GTT TGT ATC TCA AAT CAC
TNF-α	fw CAG CCG ATG GGT TGT ACC TT, rev GGC AGC CTT GTG CCT TGA
MCP-1	fw CCAGCACCAGCACCAGCCAA, rev TGGATGCTCCAGCCGGCAAC
RANTES	fw CAGCAGCAAGTGCTCCAATCTT, rev TTCTTGAACCCACTTCTTCTCTGG
IL-6	fw CTCTGCAAGAGACTTCCATCC, rev AGTCTCCTCTCCGGACTTGT
G-CSF	fw TGCCCAGAGGCGCATGAAGC, rev GGGGAACGGCCTCTCGTCCT

The primers (purchased from Invitrogen) were used in real-time PCR reaction with Fast EvaGreen qPCR Master Mix (Biotium, USA) on a StepOnePlus (Applied Biosystems) instrument. The gene expression was analyzed using the StepOne 2.3 program (Applied Biosystems). Amplicons were tested by Melt Curve Analysis on StepOnePlus instrument. Experiments were normalized to *gapdh* expression.

Quantification of nucleotides and adenosine

The adenine nucleotides (ATP, ADP, AMP) and adenosine (Ado) were determined in extracts from cells and culture media by using HPLC method. The medium (400 μ l) was separated into a cold Eppendorf tube which contained 50 μ l of homogenization solution. The cell layer was frozen with liquid nitrogen and extracted in 100 μ l volume of ice-cold homogenization solution. The homogenization solution was 0.1 M perchloric acid that contained theophylline (as an internal standard) at 10 μ M concentration. The cell extract was centrifuged at 3510 g for 10 min at 0-4°C and the pellet was saved for protein measurement. Perchloric anion from the supernatant was precipitated by 1 M potassium hydroxide, the precipitate was then removed by centrifugation. The culture media after the acid extraction was centrifuged as described above. The extracted purines were kept at -20°C until analysis. The adenine nucleotides and adenosine in extracts from cells and culture media were determined by online column switching separation using Discovery HS C18 50 x 2-mm and 150 x 2-mm columns. The flow rate of the mobile phases ["A" 10 mM potassium phosphate, 0.25 mM EDTA "B" with 0.45 mM octane sulphonyl acid sodium salt, 8 % acetonitrile (v/v), 2 % methanol (v/v), pH 5.2] was 350 or 450 μ l/min, respectively in a step gradient application. The enrichment and stripping flow rate of buffer [10 mM potassium phosphate, pH 5.2] was during 4 min and the total runtime was 55 min. The HPLC system used was a Shimadzu LC-20 AD Analytical & Measuring Instruments System, with an Agilent 1100 Series Variable Wavelength Detector set at 253nm. Concentrations were calculated by a two-point calibration curve using internal standard method. The data are expressed as pmol per mg protein or pmol per mL.

Immunohistochemical staining for NTPDase1

After the fixative was washed out, the coronal brain sections were incubated in blocking solution (5% normal goat serum and 1 mg/ml BSA) for 1 h at 22 °C. Incubation in the solution of the polyclonal NTPDase1 antibody (1:500, #rN1-6L, I4), was performed overnight at 4 °C. Following three, 10 min washes in PBS, the sections were incubated with biotinylated secondary antibody for 2 h. The staining was performed with Vectastain ABC Elite kit using DAB as the chromogen. After washing thoroughly with distilled water, sections were postfixated in 1% OsO₄, dehydrated in ethanol, stained with 1% uranyl acetate in 50% ethanol for 30 min, and embedded in Taab 812. Negative control experiments were performed using the same protocol but substituting pre-immune serum for the primary antibody. Ultrathin sections were cut using a Leica UCT ultramicrotome (Leica Microsystems, Milton Keynes, UK) and examined using a Hitachi 7100 transmission electron microscope (Hitachi; Tokyo, Japan).

Enzyme histochemistry for detection of ecto-ATPase activity

A cerium precipitation method was used for electron microscopic investigation of ecto-ATPase activity[14]. Briefly, thoroughly washed sections were incubated in a medium containing 1 mM ATP as substrate, 3 mM CeCl₃ (precipitating agent for the liberated phosphate), 1 mM levamisole (inhibitor of alkaline phosphatases, Amersham, Poole, UK), 1

dc_2027_22

mM ouabain (Na⁺, K⁺-ATPase inhibitor; Merck, Darmstadt, Germany), 50 mM $\alpha\beta$ -methylene ADP (5'-nucleotidase inhibitor) and 5 mM KCl in 70 mM Tris–maleate buffer (pH 7.4) for 30 min at room temperature. Incubation was followed by three rinses in Tris–maleate buffer and washing with distilled water. The tissue blocks were then postfixed, dehydrated and treated and embedded into Taab 812 resin for ultrathin sectioning and microscopic examination as described above. Control reactions were performed without adding the ATP substrate.

Flow cytometric analysis of brain, spleen and blood samples

Cells were isolated from mouse brains by enzymatic digestion with the mixture of DNase I (10 μ g/ml, #11284932001, Roche) and Collagenase/Dispase (0,5mg/ml, #11088866001, Roche) in 10% FCS/DMEM, followed by several centrifugation steps with Percoll (40% and 70%) and washing in 10% FCS/DMEM. Spleen cells were isolated by mechanical homogenization of the spleen and red blood cells were removed by centrifugation. Brain and spleen cells were diluted with FACS buffer (PBS containing 0.1% Tween 20) before acquisition. Venous blood was collected from the heart before transcardial perfusion using 3.8% sodiumcitrate as an anticoagulant. For flow cytometric analysis, Fc receptor blockade was performed (anti-mouse CD16/CD32, 1:100, #16-0161-85, eBioScience), followed by labelling blood cells, splenic leukocytes or brain cells with cocktails of selected antibodies: anti-mouse CD8a-PE (1:400, #12-0081-82 eBioScience); anti-mouse CD3e-APC (1:200, #17-0032-80, eBioScience), anti-mouse CD11b-PE (1:200, #101207, BioLegend); anti-mouse Ly-6C-PE-Cy7 (1:400, #25-5932-80, eBioScience); anti-mouse CD115-APC (1:100, #17-1152-80, eBioScience), anti-mouse F4/80-like receptor-BV421 (1:200, #563900, BD Biosciences), anti-mouse CD39-PE (1:100, #143803, BioLegend), CD45-PercyP5.5 (1:200, #103131, BioLegend) and for viability Zombie Violet (1:200, #423113, BioLegend). Cells were acquired on a BD FACSVerse flow cytometer and data were analysed using FACSuite software (BD Biosciences). Total blood cell counts were calculated by using 15 μ m polystyrene microbeads (#18328-5, Polysciences).

References:

- 1 Barna L, Dudok B, Miczan V, Horvath A, Laszlo ZI, Katona I (2016) Correlated confocal and super-resolution imaging by VividSTORM. *Nat Protoc* 11: 163-183 Doi 10.1038/nprot.2016.002
- 2 Boldogkoi Z, Balint K, Awatramani GB, Balya D, Busskamp V, Viney TJ, Lagali PS, Duebel J, Pasti E, Tombacz Det al (2009) Genetically timed, activity-sensor and rainbow transsynaptic viral tools. *Nat Methods* 6: 127-130 Doi 10.1038/nmeth.1292
- 3 Boldogkoi Z, Reichart A, Toth IE, Sik A, Erdelyi F, Medveczky I, Llorens-Cortes C, Palkovits M, Lenkei Z (2002) Construction of recombinant pseudorabies viruses optimized for labeling and neurochemical characterization of neural circuitry. *Brain Res Mol Brain Res* 109: 105-118
- 4 Boldogkoi Z, Sik A, Denes A, Reichart A, Toldi J, Gerendai I, Kovacs KJ, Palkovits M (2004) Novel tracing paradigms--genetically engineered herpesviruses as tools for mapping functional circuits within the CNS: present status and future prospects. *Prog Neurobiol* 72: 417-445 Doi 10.1016/j.pneurobio.2004.03.010
- 5 Chiovini B, Turi GF, Katona G, Kaszas A, Palfi D, Maak P, Szalay G, Szabo MF, Szabo G, Szadai Z et al (2014) Dendritic spikes induce ripples in parvalbumin interneurons during hippocampal sharp waves. *Neuron* 82: 908-924 Doi 10.1016/j.neuron.2014.04.004
- 6 Czondor K, Ellwanger K, Fuchs YF, Lutz S, Gulyas M, Mansuy IM, Hausser A, Pfizenmaier K, Schlett K (2009) Protein kinase D controls the integrity of Golgi apparatus and the maintenance of dendritic arborization in hippocampal neurons. *Mol Biol Cell* 20: 2108-2120 Doi 10.1091/mbc.E08-09-0957
- 7 Denes A, Boldogkoi Z, Hornyak A, Palkovits M, Kovacs KJ (2006) Attenuated pseudorabies virus-evoked rapid innate immune response in the rat brain. *J Neuroimmunol* 180: 88-103 Doi 10.1016/j.jneuroim.2006.07.008
- 8 Denes A, Coutts G, Lenart N, Cruickshank SM, Pelegrin P, Skinner J, Rothwell N, Allan SM, Brough D (2015) AIM2 and NLRC4 inflammasomes contribute with ASC to acute brain injury independently of NLRP3. *Proc Natl Acad Sci U S A* 112: 4050-4055 Doi 10.1073/pnas.1419090112
- 9 Dudok B, Barna L, Ledri M, Szabo SI, Szabadits E, Pinter B, Woodhams SG, Henstridge CM, Balla GY, Nyilas Ret et al (2015) Cell-specific STORM super-resolution imaging reveals nanoscale organization of cannabinoid signaling. *Nat Neurosci* 18: 75-86 Doi 10.1038/nn.3892
- 10 Elmore MR, Najafi AR, Koike MA, Dagher NN, Spangenberg EE, Rice RA, Kitazawa M, Matusow B, Nguyen H, West BL et al (2014) Colony-stimulating factor 1 receptor signaling is necessary for microglia viability, unmasking a microglia progenitor cell in the adult brain. *Neuron* 82: 380-397 Doi 10.1016/j.neuron.2014.02.040
- 11 Gonci B, Nemeth V, Balogh E, Szabo B, Denes A, Kornyei Z, Vicsek T (2010) Viral epidemics in a cell culture: novel high resolution data and their interpretation by a percolation theory based model. *PLoS One* 5: e15571 Doi 10.1371/journal.pone.0015571
- 12 Horvath G, Goloncser F, Csolle C, Kiraly K, Ando RD, Baranyi M, Kovanyi B, Mate Z, Hoffmann K, Algaier let al (2014) Central P2Y12 receptor blockade alleviates inflammatory and neuropathic pain and cytokine production in rodents. *Neurobiol Dis* 70: 162-178 Doi 10.1016/j.nbd.2014.06.011
- 13 Katona G, Szalay G, Maak P, Kaszas A, Veress M, Hillier D, Chiovini B, Vizi ES, Roska B, Rozsa B (2012) Fast two-photon in vivo imaging with three-dimensional random-access scanning in large tissue volumes. *Nat Methods* 9: 201-208 Doi 10.1038/nmeth.1851
- 14 Kittel A (1999) Lipopolysaccharide treatment modifies pH- and cation-dependent ecto-ATPase activity of endothelial cells. *J Histochem Cytochem* 47: 393-400 Doi 10.1177/002215549904700313
- 15 Kornyei Z, Szlavik V, Szabo B, Gocza E, Czirok A, Madarasz E (2005) Humoral and contact interactions in astroglia/stem cell co-cultures in the course of glia-induced neurogenesis. *Glia* 49: 430-444 Doi 10.1002/glia.20123
- 16 Kremer JR, Mastronarde DN, McIntosh JR (1996) Computer visualization of three-dimensional image data using IMOD. *J Struct Biol* 116: 71-76 Doi 10.1006/jsbi.1996.0013
- 17 Szalay G, Martinecz B, Lenart N, Kornyei Z, Orsolits B, Judak L, Csaszar E, Fekete R, West BL, Katona G et al (2016) Microglia protect against brain injury and their selective elimination dysregulates neuronal network activity after stroke. *Nat Commun* 7: 11499 Doi 10.1038/ncomms11499

ARTICLE

Microglia modulate blood flow, neurovascular coupling, and hypoperfusion via purinergic actions

Eszter Császár^{1,2*}, Nikolett Lénárt^{1*}, Csaba Cserép¹, Zsuzsanna Környei¹, Rebeka Fekete¹, Balázs Pósfai^{1,2}, Diána Balázsfői³, Balázs Hangya³, Anett D. Schwarcz¹, Eszter Szabadits¹, Dávid Szöllősi⁴, Krisztián Szigeti⁴, Domokos Máthé⁵, Brian L. West⁶, Katalin Sviatkó³, Ana Rita Brás^{1,2}, Jean-Charles Mariani⁷, Andrea Kliewer⁷, Zsolt Lenkei⁷, László Hricisák⁸, Zoltán Benyó⁸, Mária Baranyi⁹, Beáta Sperlág⁹, Ákos Menyhárt^{10,11}, Eszter Farkas^{10,12}, and Ádám Dénes¹

Microglia, the main immunocompetent cells of the brain, regulate neuronal function, but their contribution to cerebral blood flow (CBF) regulation has remained elusive. Here, we identify microglia as important modulators of CBF both under physiological conditions and during hypoperfusion. Microglia establish direct, dynamic purinergic contacts with cells in the neurovascular unit that shape CBF in both mice and humans. Surprisingly, the absence of microglia or blockade of microglial P2Y12 receptor (P2Y12R) substantially impairs neurovascular coupling in mice, which is reiterated by chemogenetically induced microglial dysfunction associated with impaired ATP sensitivity. Hypercapnia induces rapid microglial calcium changes, P2Y12R-mediated formation of perivascular phallopodia, and microglial adenosine production, while depletion of microglia reduces brain pH and impairs hypercapnia-induced vasodilation. Microglial actions modulate vascular cyclic GMP levels but are partially independent of nitric oxide. Finally, microglial dysfunction markedly impairs P2Y12R-mediated cerebrovascular adaptation to common carotid artery occlusion resulting in hypoperfusion. Thus, our data reveal a previously unrecognized role for microglia in CBF regulation, with broad implications for common neurological diseases.

Introduction

Microglia are key regulators of inflammatory processes in the brain and altered microglial activity is linked to the development of common brain diseases (Colonna and Butovsky, 2017; Prinz and Priller, 2014). The contribution of microglia to diverse physiological processes, including brain development, synaptic plasticity, learning, or memory is also emerging (Thion et al., 2018; Wolf et al., 2017). Communication between microglia and other cell types is mediated by motile microglial processes, through which microglia perform dynamic surveillance of their environment (Davalos et al., 2005; Haynes et al., 2006; Nimmerjahn et al., 2005). In addition to the well-documented microglia–neuron interactions, microglial processes are recruited to blood vessels and cells of the neurovascular unit (NVU), although the function of these interactions has remained vaguely defined (Benyo et al., 2016; Dudvarski Stankovic et al., 2016; Zhao et al., 2018). Microglia–vascular interactions are

present in the brain from early development into adulthood, through which microglia regulate blood–brain barrier (BBB) permeability, leukocyte extravasation, and angiogenesis (Dudvarski Stankovic et al., 2016; Jolivel et al., 2015; Lou et al., 2016). In fact, microglia and microglial processes are closely associated with developing blood vessels in the neuroepithelium or in the ventricular zone, while $\text{Pu.1}^{-/-}$ mice or $\text{Csf1}^{\text{op/op}}$ mice that lack microglia and macrophages display impaired angiogenesis in the retina (Arnold and Betsholtz, 2013; Dixon et al., 2021; Dudvarski Stankovic et al., 2016; Penna et al., 2021). In the adult brain, CD206-positive perivascular macrophages (PVMs) remain closely associated with blood vessels, while CD206-negative microglial cell bodies occupy the brain parenchyma isolated by the glia limitans (Goldmann et al., 2016; Kida et al., 1993; Ransohoff and Engelhardt, 2012). PVMs have recently been shown to play an important role in neurovascular dysfunction

¹“Momentum” Laboratory of Neuroimmunology, Institute of Experimental Medicine, Budapest, Hungary; ²János Szentágotthai Doctoral School of Neurosciences, Schools of PhD Studies, Semmelweis University, Budapest, Hungary; ³Lendület Laboratory of Systems Neuroscience, Institute of Experimental Medicine, Budapest, Hungary; ⁴Department of Biophysics and Radiation Biology, Semmelweis University, Budapest, Hungary; ⁵Hungarian Centre of Excellence for Molecular Medicine, Szeged, Hungary; ⁶Plexikon Inc., Berkeley, CA; ⁷Institute of Psychiatry and Neurosciences of Paris, INSERM U1266, Université de Paris, Paris, France; ⁸Institute of Translational Medicine, Semmelweis University, Budapest, Hungary; ⁹Laboratory of Molecular Pharmacology, Institute of Experimental Medicine, Budapest, Hungary; ¹⁰Hungarian Centre of Excellence for Molecular Medicine, University of Szeged, Cerebral Blood Flow and Metabolism Research Group, Szeged, Hungary; ¹¹Department of Medical Physics and Informatics, Albert Szent-Györgyi Medical School, University of Szeged, Szeged, Hungary; ¹²Department of Cell Biology and Molecular Medicine, Albert Szent-Györgyi Medical School, Faculty of Science and Informatics, University of Szeged, Szeged, Hungary.

*E. Császár and N. Lénárt are joint first authors; Correspondence to Ádám Dénes: denes.adam@koki.hu.

© 2022 Császár et al. This article is available under a Creative Commons License (Attribution 4.0 International, as described at <https://creativecommons.org/licenses/by/4.0/>).

associated with hypertension, via promoting BBB permeability (Faraco et al., 2016). However, little is known about the possible contribution of microglia to cerebral blood flow (CBF) or perfusion deficits in the adult brain.

Microglia respond to vascular injury, as seen in experimental models of stroke, Alzheimer's disease, or multiple sclerosis (Dudvarski Stankovic et al., 2016; Zhao et al., 2018), and microglial processes are recruited to sites of BBB leakage within minutes (Davalos et al., 2012; Jolivel et al., 2015; Lou et al., 2016). However, we could not detect major differences in the extent of BBB injury after experimental stroke in the absence of microglia (Szalay et al., 2016). Interestingly, changes in microglial process dynamics around capillaries are proportional to the level of CBF reduction during transient ischemia (Masuda et al., 2011), suggesting a possible role for microglia-vascular interactions beyond vascular injury.

We have recently identified specific sites on neuronal cell bodies through which microglia shape neuronal responses via purinergic mechanisms (Cserep et al., 2019). Because microglia interact with both neurons and blood vessels (Szalay et al., 2016) and neuronal activity-dependent changes in CBF are precisely controlled via multicellular interactions in the NVU (Iadecola, 2017), we argued that microglia are ideally positioned to sense and influence neurovascular responses under normal conditions or when the balance between oxygen/nutrient demand and blood supply is disturbed. Supporting this, inflammatory changes and altered microglial activity together with impaired CBF and neurovascular coupling often precede symptom onset in common neurological disorders (Iadecola, 2017; Kisler et al., 2017). Here, by using microglia depletion, transgenic mice, and pharmacological interventions, we identify microglia as important modulators of CBF during neurovascular coupling, hypercapnia-induced vasodilation, and adaptation to hypoperfusion in the cerebral cortex.

Results

Microglia form dynamic purinergic contacts with cells in the NVU that regulate CBF

We first investigated the formation and dynamics of microglia-vascular interactions using *in vivo* two-photon imaging. Intravenous FITC-dextran administration in CX3CR1^{tdTomato} microglia reporter mice allowed three-dimensional (3D) reconstruction of penetrating arterioles in the cerebral cortex down to 600 μm below the dura mater (Fig. 1 a). *In vivo* imaging revealed microglia ensheathing arterial bifurcations at the level of first-, second-, and third-order vessels and identified contacting microglial processes at all levels of the vascular tree (Fig. 1, a and b; and Video 1). The average lifetime of contacts ranged from 5 to 15 min, and microglial processes frequently recontacted the same sites at both arterioles and microvessels, suggesting that specific sites for microglia-vascular interactions may exist in the brain. Next, we studied the formation of physical contact between microglia and other cells in the NVU, using the microglial marker P2Y12 receptor (P2Y12R), which is not expressed by any other cells in the brain (Butovsky et al., 2014). Surprisingly, we found that processes of

parenchymal microglial cells were extended beyond glial fibrillary acidic protein (GFAP)-positive perivascular glial endfeet at the level of penetrating arterioles, directly contacting smooth muscle actin (SMA)-positive smooth muscle cells (Fig. 1 c) and endothelial cells in both large vessels and microvessels as evidenced by both confocal laser scanning microscopy (CLSM) and immuno-electron microscopy (immuno-EM; Fig. 1, d and e). 3D analysis of Z-stacks recorded by CLSM revealed that 85% of blood vessel segments are contacted by microglial processes and 15% of the endothelial cell surface is covered by microglial processes (Fig. 1 f). The vast majority of pericytes (83%) also received direct microglial contact (Fig. 1, g and h). ATP (and ADP) is a major chemotactic factor for microglia via P2Y12R (Haynes et al., 2006), and purinergic signaling in endothelial cells and pericytes markedly influences CBF (Lohman et al., 2012). We have recently shown that clustering of microglial P2Y12R occurs at sites of somatic ATP release in neurons, through which microglia sense and influence neuronal activity and mitochondrial function (Cserep et al., 2019). To study whether ATP released at the perivascular compartment could also act as a chemotactic signal for microglial processes, we turned to 3D electron tomography. Importantly, we found contacting P2Y12R-positive microglial processes in close apposition with endothelial mitochondria, while immunogold particles were enriched at the interface (Fig. 1 i). Unbiased immunofluorescent analysis revealed 214% higher TOM20 immunofluorescence (a mitochondrial marker) in endothelial cells at microglial contact sites (Figs. 1 j and S1 d). Importantly, immuno-EM also confirmed the direct contact between P2Y12R-positive microglial processes and endothelial cells in the human brain (Fig. 1 k). The perivascular endfeet of GFAP expressing astrocytes contribute to CBF regulation (Howarth et al., 2017). We found that 93% of astrocytes were contacted by P2Y12R-positive microglial processes, while microglial cell bodies were found directly attached to 18% of astrocytes (Fig. 1 l; and Fig. S1, a and b). To visualize perivascular astrocyte endfeet, aquaporin-4 (AQP4) immunostaining was used, showing that microglial processes directly contact endothelial cells at sites void of the AQP4 signal (Fig. S1 c) or by extending through the astrocytic endfeet layer (Fig. S1 e). Combined immunogold-immunoperoxidase labeling and EM confirmed the direct contact between microglial processes and parenchymal astrocytes or perivascular astrocytic endfeet (Fig. 1 m). Similar observations were made in the human cerebral cortex from both aged and middle-aged patients who died in nonneurological conditions: P2Y12R-positive microglial processes established contact with both perivascular astrocyte endfeet and the endothelial monolayer of small arterioles and capillaries (Fig. 1, n and o; and Fig. S1 f). Furthermore, we found that individual microglial cells contact multiple microvessels and nearby neurons simultaneously in the brain (Fig. 1 p). Thus, not only do microglial processes directly contact cells in the NVU along the vascular tree (Fig. S1 g), which are known to shape CBF (Attwell et al., 2010; Hall et al., 2014; Iadecola, 2017; Kisler et al., 2017; Takano et al., 2006), but simultaneous contacts with neurons and vascular structures may provide an ideal platform for microglia to influence neurovascular responses.

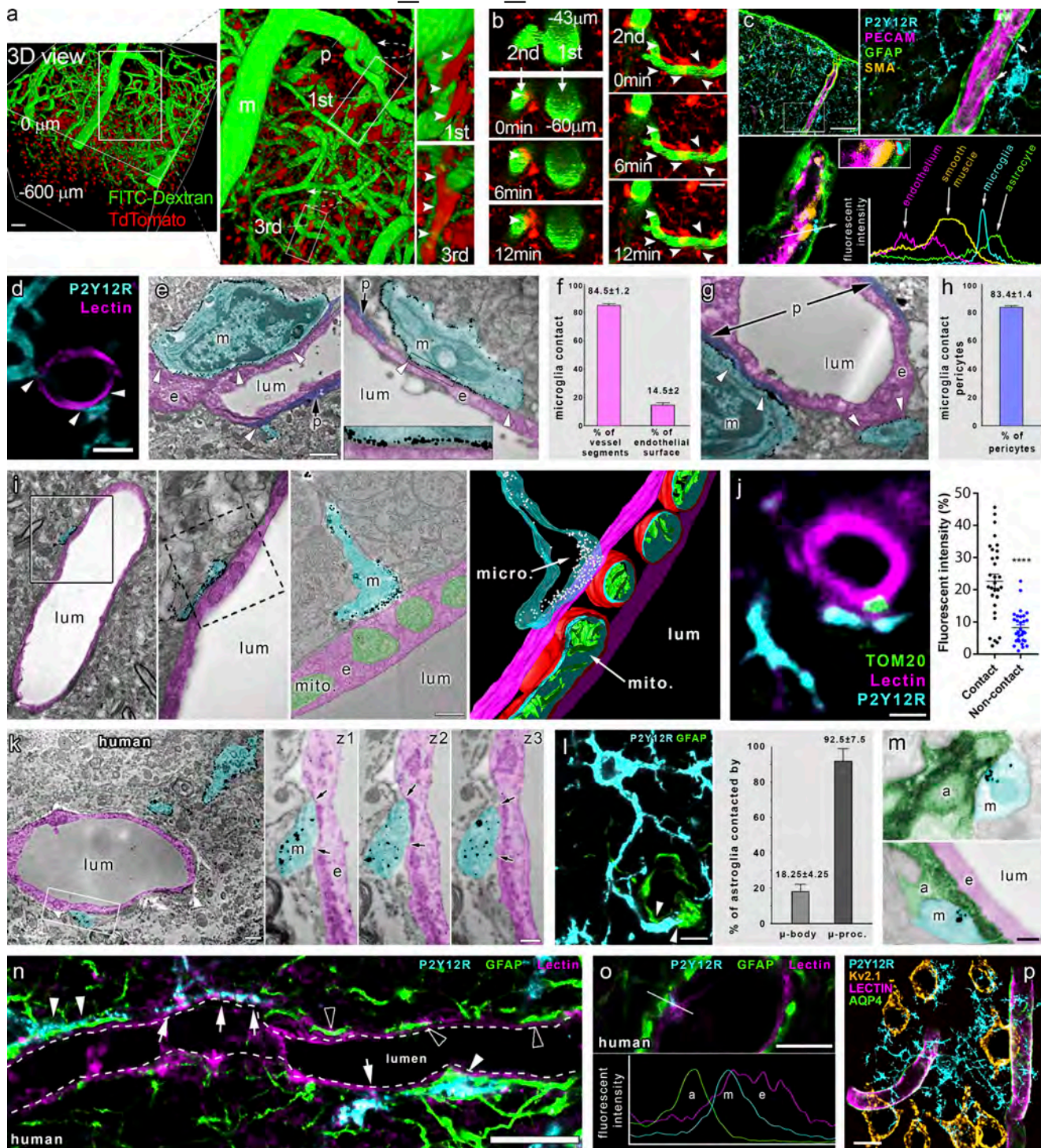


Figure 1. Microglia form direct purinergic contact with cells in the NVU that regulate CBF. (a) 3D reconstruction of in vivo two-photon Z-stacks down to 600 μm below the dura mater in the cerebral cortex of CX3CR1^{tdTomato} mice. Note contacting microglia (arrowheads) at meningeal (m), penetrating (p), and first- to third-order capillaries. Scale bar, 50 μm . (b) Microglial processes (arrowheads) dynamically contact different segments of the vascular tree (visualized by i.v. FITC-dextran). Scale bar, 50 μm . (c) Microglial processes are extended beyond the perivascular glial endfeet and form direct contact with smooth muscle cells (arrows) at the level of penetrating arteries. (d) CLSM images show microglia (P2Y12R, cyan) contacting endothelial cells (tomato lectin, magenta) in the cerebral cortex. (e) EM images show microglia (m, P2Y12R-immunogold labeling, cyan) directly contacting endothelial cells (e, magenta) and pericytes (p, purple). (f) Frequency of vessels receiving microglial contact, and microglial process coverage of endothelial cell surface. (g) EM images show microglia (m, P2Y12R-immunogold labeling, cyan) directly contacting pericytes (p, purple). (h) 83.4 \pm 1.4% of pericytic cell bodies are contacted by microglial processes. (i) 3D reconstruction of electron tomogram shows clustering of anti-P2Y12R-immunogold on microglial processes (m) directly contacting the endothelium (e) of an arteriole/postcapillary venule. The left two panels are conventional EM images of the same area on the adjacent ultrathin section. The right panels show a tomographic virtual section and 3D reconstruction of the direct contact. (j) Unbiased anatomic analysis reveals enrichment of endothelial mitochondria (TOM20⁺, green), at sites of microglial contacts (P2Y12R⁺, cyan). ********, $P < 0.0001$, Mann–Whitney U test. See analysis details in Fig. S1 d. (k) EM images show

microglia (m, P2Y12R-immunogold, cyan) directly contacting endothelial cells (e, magenta) in human neocortex. z1–z3 panels show the contact on three consecutive ultrathin sections; arrows mark the edges of direct membrane contact. **(l)** CLSM image shows microglia (P2Y12R, cyan) contacting the cell body of an astrocyte (GFAP labeling, green) and astrocytic endfeet (arrowheads). **(m)** EM images show direct contact between microglial (m, cyan) and astrocytic (a, green) processes. e, endothelial cell, magenta; lum, lumen. **(n)** CLSM images in human neocortex reveal P2Y12R⁺ microglial processes (cyan) contacting perivascular astrocytes (GFAP, green) on astrocyte endfeet (white arrowheads) and endothelial cells (tomato-lectin, magenta, white arrows), with astrocytic endfeet directly touching the endothelial monolayer (empty arrowheads). **(o)** CLSM image and fluorescent intensity plots show microglial process (m) contacting the endothelial layer (e) within the astrocytic layer (a). **(p)** To reveal 3D connections of individual microglial cells, a CLSM maximum-intensity plot was generated. Microglia (cyan) contact several microvessels (lectin, magenta; AQP4, green) and neurons (Kv2.1, ochre) simultaneously. For appropriate visualization of neuronal cell bodies, Kv2.1 is shown in yellow pseudocolor only with the maximal diameter planes included. Scale bars: (c) 50 μ m; (d) 3 μ m; (e) 2 μ m; (i) 200 nm; (j) 2 μ m; (k) left, 1 μ m, and z3, 400 nm; (l) 10 μ m; (m) 200 nm; (n) 10 μ m; (o) 5 μ m; (p) 10 μ m.

Microglia contribute to neurovascular coupling via P2Y12R-mediated actions

In our previous studies, we could not detect major alterations in the number or morphology of endothelial cells, astrocytes, or pericytes after elimination of microglia by CSF1R blockade (Szalay et al., 2016). To investigate whether prolonged absence of microglia could compromise overall vascular architecture or metabolism, we performed HMPAO-SPECT and FDG-PET measurements (Apostolova et al., 2012; Tai and Piccini, 2004) after microglia depletion by PLX5622 (Elmore et al., 2014). No significant changes in HMPAO or FDG uptake were observed in any brain areas after microglia depletion (Fig. S1, i–k). To investigate the role of microglia in CBF responses to physiological stimuli, we turned to the whisker-stimulation model, which is widely used to study the mechanisms of neurovascular coupling in mice (Tarantini et al., 2018) and performed laser speckle contrast imaging (LSCI), optimized to assess changes in the microcirculation through the intact skull bone in real time (Dunn, 2012). Whiskers on the left side were stimulated under mild ketamine-medetomidine sedation, allowing stable and reproducible CBF responses to be observed (Fig. 2, a and b). Surprisingly, the absence of microglia resulted in impaired functional hyperemia, as evidenced by a significant 15.3% reduction in CBF response in the right barrel cortex compared with that seen in control mice after a series of stimulation (six series of stimulations for 30 s each; Fig. 2, b and c; and Video 2). In addition, a 17% smaller CBF response to whisker stimulation was seen after acute microglial P2Y12R blockade by a specific P2Y12R inhibitor, PSB0739, injected into the cisterna magna 40 min before LSCI measurements (Cserep et al., 2019). Because only microglia express P2Y12R in the brain (Cserep et al., 2019; Fekete et al., 2018), this way we could also validate the specificity of microglial actions on CBF responses.

To extend these observations with genetic P2Y12R blockade, another series of measurements were performed, using manual whisker stimulation followed by a set of electromechanically controlled stimulations. We found reduced CBF responses to whisker stimulation in both microglia-depleted and P2Y12R knockout (KO) mice, irrespective of the type of stimulation used (Fig. 2, d–f). Given the pivotal roles of NO in vasodilation, and specifically in neurovascular coupling (Attwell et al., 2010; Iadecola, 2017), we investigated the relationship between microglia depletion and nitric oxide synthase (NOS) blockade by L-NAME. Interestingly, we found that both L-NAME and microglia depletion significantly decreased the CBF response to whisker stimulation compared with control mice, while

L-NAME combined with depletion had an additive effect (Fig. 2 g). These results suggest that in addition to microglial modulation of vasodilation in response to somatosensory stimulation, a microglia-independent NO-based component is also involved.

Finally, to confirm the role of microglia in neurovascular coupling with an alternative approach, we turned to functional ultrasound (fUS) imaging, which detects hemodynamic changes in the brain based on cerebral blood volume (CBV; Mace et al., 2011). We found that the absence of microglia resulted in significantly smaller (by 28%) CBV increases in the contralateral barrel cortex in response to whisker stimulation compared with that seen in control mice (Fig. 2, h–j). Thus, microglia-mediated and microglial P2Y12R-mediated actions are important to maintain normal blood flow responses to somatosensory stimulation in the cortical microcirculation, which is partially independent of NO.

Changes in whisker stimulation-evoked neuronal responses do not explain altered CBF responses after microglia manipulation

To test whether substantial shifts in neuronal responses to whisker stimulation could explain the effect of microglia manipulation on functional hyperemia, we repeated these experiments while recording neuronal activity from the contralateral barrel cortex, using either chronically implanted tetrode electrodes or in vivo two-photon calcium imaging. We isolated $n = 42$, $n = 41$, and $n = 61$ putative single units from two electrophysiological recordings each of control, microglia-depleted, and P2Y12R KO mice, respectively ($n = 5$). This allowed us to test baseline firing rates in the stimulus-free periods as well as stimulus-induced firing responses of individual neurons. We found significantly increased baseline firing rates of barrel cortex neurons in both microglia-depleted and P2Y12R KO mice compared with controls (Fig. 3, a and d). However, using either electromechanically controlled automated whisker stimulation or manual stimulation, we did not detect differences in the extent of stimulus-evoked neuronal responses (Fig. 3 e).

Then, we turned to in vivo two-photon measurements, using electromechanical whisker stimulation, which was repeated two times with 40-s intervals (Fig. 3 f). Only neurons in the contralateral barrel cortex that specifically responded to both stimuli were selected for analysis. We found that somatosensory stimulus-induced increases in the neuronal GCaMP6s signal in Thy1-GCaMP6s mice did not reveal significant differences between control and microglia-depleted mice

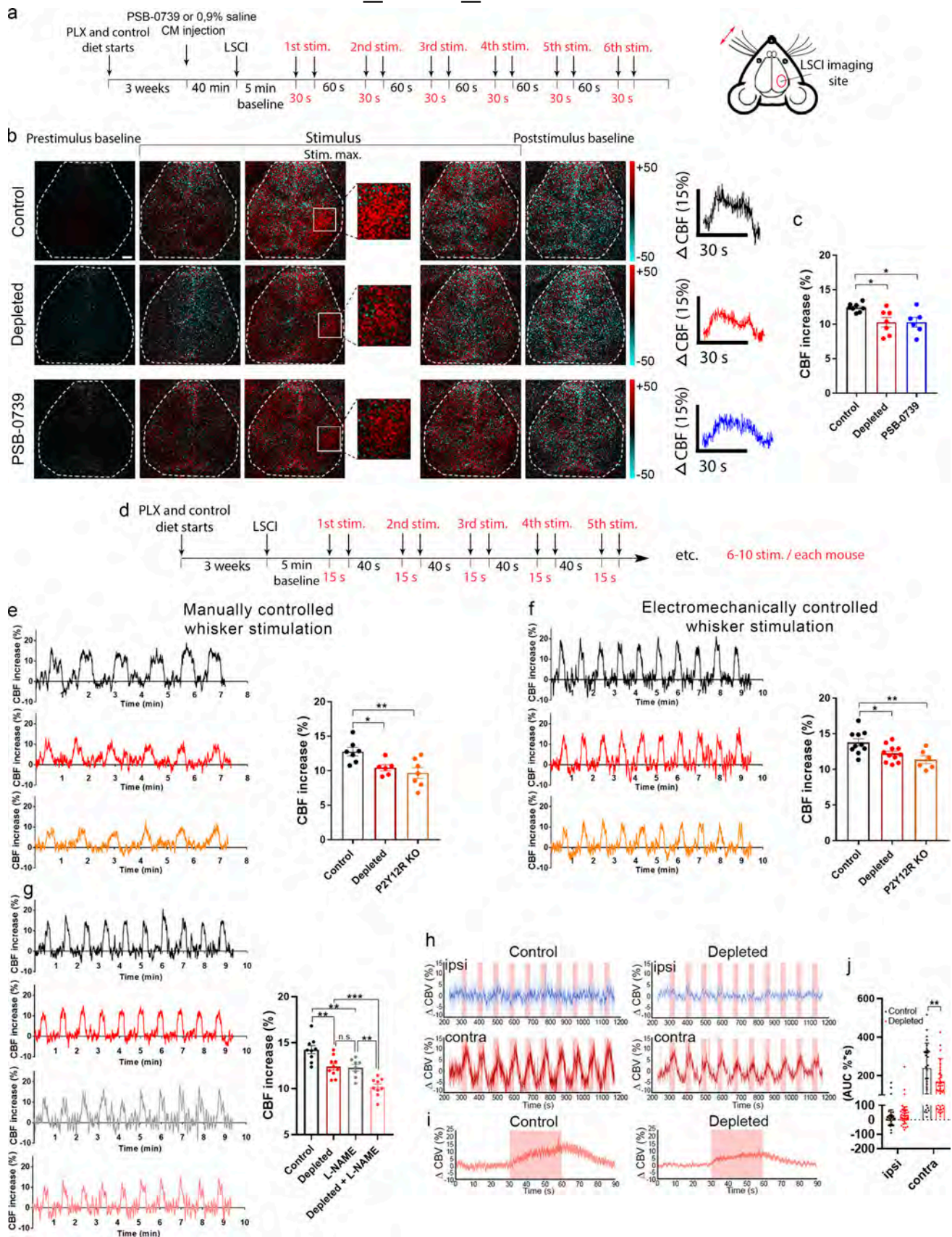


Figure 2. **Microglia contribute to neurovascular coupling in a P2Y12R-mediated manner.** (a) Schematic showing the outline of the experiment. (b) Difference images show CBF changes in the right barrel cortex relative to baseline in response to contralateral whisker stimulation before, during, and after

stimulus (stim.; white rectangle indicates the barrel field). Time course of stimulus-evoked CBF responses is shown in the right of b. Scale bar, 1 mm. **(c)** Absence of microglia or acute blockade of P2Y₁₂R reduces the maximum of evoked CBF responses compared with controls. $n = 7$ control, $n = 7$ depleted, and $n = 6$ PSB-0739 injected mice; *, $P < 0.05$, one-way ANOVA followed by Dunnett's multiple comparison test (control versus depleted, $P = 0.0191$; control versus PSB-0739, $P = 0.0243$). **(d)** Protocol of manually and electromechanically controlled whisker stimulation. **(e and f)** Representative CBF traces and quantification show impaired neurovascular coupling response in the absence of microglia and in P2Y₁₂R KO mice. $n = 7$ control, $n = 6$ depleted, and $n = 7$ P2Y₁₂R KO mice (e and f); $n = 10$ control, $n = 11$ depleted, and $n = 6$ P2Y₁₂R KO mice; **, $P = 0.0075$ (e); **, $P = 0.0058$ (f), one-way ANOVA followed by Dunnett's multiple comparison test (e: *, $P = 0.0378$, control versus depleted; **, $P = 0.0052$ control versus P2Y₁₂R KO; f: *, $P = 0.0311$ control versus depleted; **, $P = 0.0047$ control versus P2Y₁₂R KO). **(g)** Representative CBF traces and graph show changes in neurovascular coupling response in L-NAME-treated mice in both the presence and the absence of microglia. $n = 9$ control, $n = 10$ depleted, $n = 8$ L-NAME-treated, $n = 9$ L-NAME-treated depleted; $P < 0.0001$, one-way ANOVA followed by Tukey's multiple comparison test (**, $P = 0.005$, control versus depleted; **, $P = 0.0049$, control versus L-NAME; **, $P = 0.0026$, L-NAME versus depleted + L-NAME; ***, $P = 0.0008$, depleted versus depleted + L-NAME). **(h)** fUS imaging reveals reduced CBV responses compared with controls in the ipsilateral (ipsi) and contralateral (contra) barrel cortex. Representative traces of 10 subsequent stimulations (30 s each) are shown for control and microglia-depleted mice. **(i)** Peak trace averages of the contralateral side in control and depleted mice, with 95% confidence intervals. **(j)** Averaged AUC distribution for each group, as shown in pink window in i. Data are presented as mean \pm SEM; $n = 30$ and $n = 40$ stimulations from three control and four depleted mice, respectively (j); **, $P = 0.0093$, two-way ANOVA followed by Sidak's multiple comparisons test. Data are presented as mean \pm SEM. LSCI data have been pooled from two to three independent experiments.

(Fig. 3 g and Video 3). Thus, while the absence (PLX5622 depleted) or dysfunction (P2Y₁₂R KO) of microglia may shift baseline neuronal activity as expected (Badimon et al., 2020; Cserep et al., 2019), stimulus-evoked neuronal responses do not explain the marked differences in CBF changes observed after microglia manipulation.

Real-time chemogenetic modulation of microglial activity results in impaired functional hyperemia

To explore the effect of real-time chemogenetic microglia manipulation on CBF changes, we generated a novel mouse line by crossing Cre-dependent hM3Dq DREADD mice with CX3CR1-CreERT2 mice (Ginhoux et al., 2010), named MicroDREADD^{Dq} mice. Tamoxifen (TMX) administration resulted in specific recombination in 95.3% of microglia (Fig. 4 a). Recombination based on the weak mCitrine signal is still likely to be underestimated, because using the identical CX3CR1-CreERT2 driver line, virtually 100% of Iba1/P2Y₁₂R double-positive microglia were found to express tdTomato in the cerebral cortex of CX3CR1^{tdTomato} reporter mice (see Materials and methods and Fig. S1 h). HM3Dq DREADD agonists 1 μ M clozapine-*N*-oxide (CNO) or 1 μ M Compound 21 (C21; Thompson et al., 2018) induced rapid increases in intracellular calcium levels in microglia derived from MicroDREADD^{Dq} mice, which was completely absent in TMX-untreated cells (Fig. 4 b; and Fig. S2, a–e). Single chemogenetic activation led to the blockade of microglial process motility within a few minutes, while microglia showed reduced calcium responses to repeated C21 stimulations (Fig. 4, c and d; Fig. S2, a–e; and Videos 4 and Video 5). Chemogenetic stimulation also resulted in altered microglial morphology and branch structure in vivo (Fig. S2 f). Importantly, C21 stimulation markedly impaired responses of MicroDREADD^{Dq} microglia to 10 μ M ATP (Fig. 4, e and f), suggesting that chemogenetic priming disables the recruitment of microglial processes to ambient ATP released in the NVU during functional hyperemia (Pelligrino et al., 2011).

To investigate microglial calcium dynamics and the effect of chemogenetic activation in vivo, we crossed MicroDREADD^{Dq} mice with Cre-dependent CGaMP5g-tdTomato mice (i.e., both constructs could be induced by TMX using the same CX3CR1-CreERT2 driver line). Interestingly, we found that microglial

processes interacting with arterioles and microvessels in the cerebral cortex showed dynamic calcium fluctuations, as assessed by in vivo two-photon imaging (Fig. 4 g). Chemogenetic activation in MicroDREADD^{Dq} \times CGaMP5g-tdTomato mice resulted in an average of 18% increase in microglial somatic CGaMP5g signal within 15–30 min, leading to the temporary detachment and withdrawal of a population of perivascular microglial processes, which was most apparent around arterioles. As a likely compensatory response, 1 h after chemogenetic activation, microglial process coverage increased around endothelial cells ($P = 0.001$) and smooth muscle cells ($P = 0.026$), whereas a nonsignificant trend was observed in process coverage of pericytes (Fig. 4 h). Importantly, we found that chemogenetic modulation of microglia 30 min before LSCI measurements resulted in a similar degree of CBF reduction to both manual and electromechanical whisker stimulation (Fig. 4, i–k), as seen after microglia depletion (Fig. 2, e and f).

Microglia modulate hypercapnia-induced vasodilation in a P2Y₁₂R-dependent manner

To further investigate the mechanisms through which microglia modulate CBF, we turned to hypercapnic challenge to induce vasodilation independently of direct neuronal stimulation. Hypercapnia is considered to induce primarily endothelium-driven vasodilation, including actions of astrocytes and other cells (Faraci et al., 2019; Hamilton et al., 2010; Howarth et al., 2017; Meng and Gelb, 2015; Yoon et al., 2012). In vivo two-photon imaging revealed a population of dynamic microglial processes that readily changed their morphology at both arterioles and microvessels in response to vasodilation induced by 2-min inhalation of 10% CO₂ under normoxic conditions (Figs. 5 a; and S3 a). Around arterioles, SR101-labeled perivascular astrocyte endfeet were also dynamically contacted by microglia (Fig. 5 b), and the number of contacting filopodia at the end of microglial processes increased in response to hypercapnia (Fig. 5 b). Confirming the rapid effect of hypercapnia on microglial process dynamics, we also found that perivascular microglia responded rapidly (within 1–2 min) to hypercapnia with calcium pulses as assessed in CX3CR1^{CGaMP5g-tdTomato} mice with in vivo two-photon imaging. Calcium pulses were apparent in both filopodia and large processes (Fig. 5 c and Video 7). Importantly,

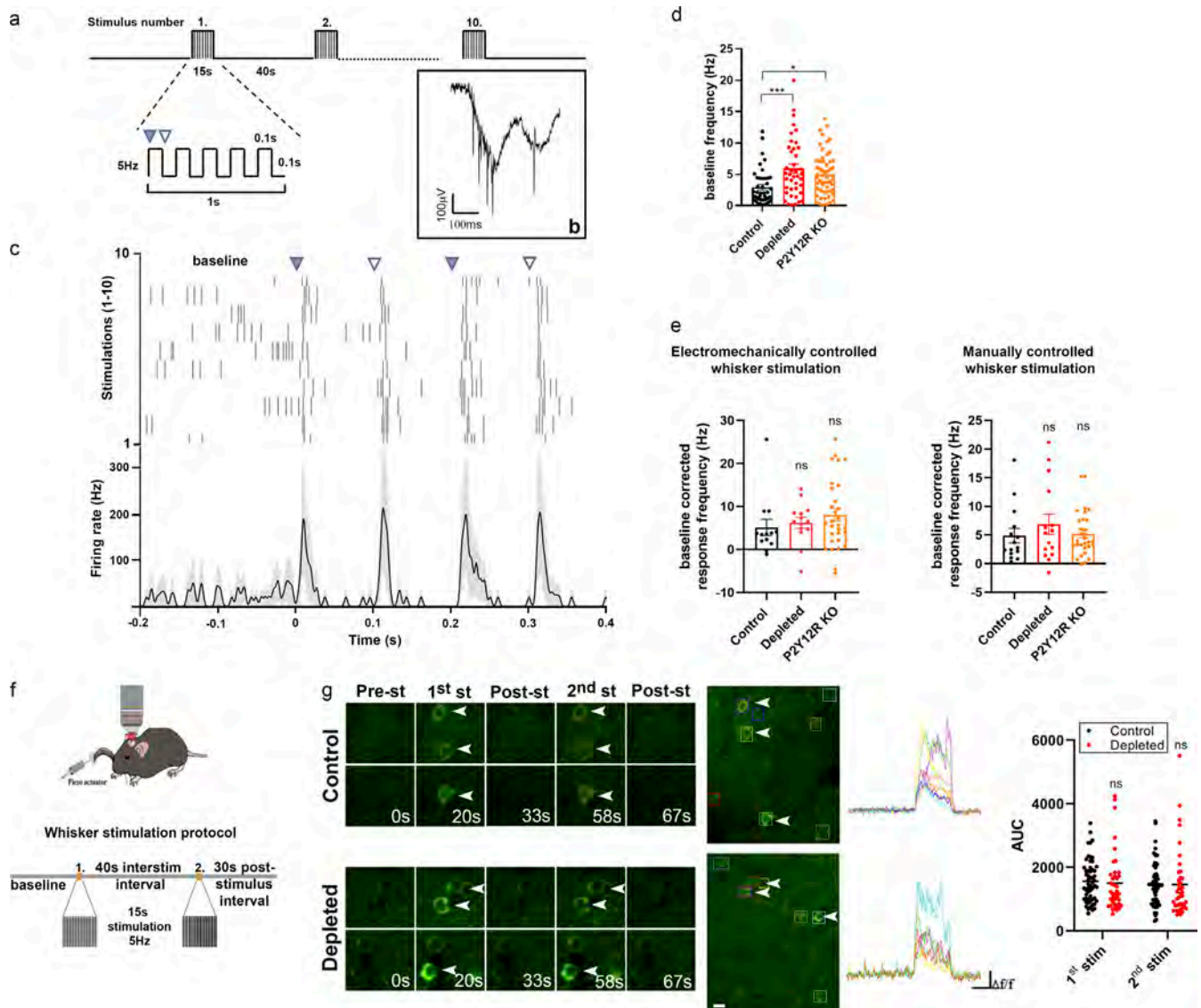


Figure 3. Whisker stimulation–evoked neuronal responses in the barrel cortex do not explain altered CBF responses after microglia manipulation. **(a)** Schematics of the whisker stimulation protocol. Whiskers were stimulated electromechanically with 5 Hz, causing alternating passive deflections of the vibrissae in the anterior and posterior directions (filled and empty arrowheads, respectively) for 15 s, followed by a 40-s pause, repeated 10 times. **(b)** Raw tetrode data showing extracellular spikes recorded from the barrel cortex. **(c)** Example of a single neuron activated by passive whisker deflections. Top, raster plot aligned to whisker stimulation onset (black ticks, individual action potentials). Bottom, peristimulus time histogram showing mean firing responses of the same neuron (shading, SEM). **(d)** Baseline firing rates were significantly higher in depleted and P2Y12R KO mice compared with controls. $n = 4$ control, $n = 3$ depleted, and $n = 5$ P2Y12R KO mice; $P = 0.001$, one-way ANOVA with Dunnett's multiple comparisons test (***, $P < 0.006$, control versus depleted; *, $P = 0.0109$, control versus P2Y12R KO). **(e)** Stimulus-induced firing rate changes were comparable across controls and microglia-depleted mice using either electromechanically or manually controlled whisker stimulation. Data are presented as baseline corrected response frequency (for corresponding baseline frequencies, mean \pm SEM); $n = 4$ control, $n = 3$ depleted, and $n = 5$ P2Y12R KO mice; $P = 0.2087$ and $P = 0.6391$, Kruskal–Wallis test with Dunn's multiple comparisons test. **(f)** Schematic outlines of the whisker stimulation protocol used for in vivo two-photon $[Ca^{2+}]_i$ imaging in the barrel cortex of Thy1-GCaMP6s mice. interstim, interstimulation. **(g)** Representative images show stimulus-evoked neuronal $[Ca^{2+}]_i$ responses with individual traces of neurons labeled with rectangles during baseline imaging and 15-s stimulation and after stimulation. AUC values of neuronal GCaMP6s signal changes in response to the first and second electromechanically controlled whisker stimulation in control and microglia-depleted mice. $n = 4$ mice per group, $n = 56$ neurons from control and $n = 40$ neurons from depleted mice from two trials; $P = 0.765$, two-way ANOVA with Sidak's multiple comparisons test. Scale bar, 20 μ m. st and stim, stimulation. Data are presented as mean \pm SEM.

in vivo two-photon imaging revealed significantly impaired hypercapnia-induced vasodilation in meningeal and penetrating arteries (Fig. 5 d), which paralleled smaller CBF responses in microglia-depleted mice as assessed by LSCI (Fig. 5, e–g). To exclude the potential effect of α_2 adrenergic blockade via the

cardiovascular system during ketamine-medetomidine anesthesia (Janssen et al., 2004), we repeated hypercapnic challenge after the administration of atipamezole, an α_2 receptor antagonist (Pal et al., 2020). Hypercapnia-induced CBF response was similarly reduced in microglia-depleted mice compared with

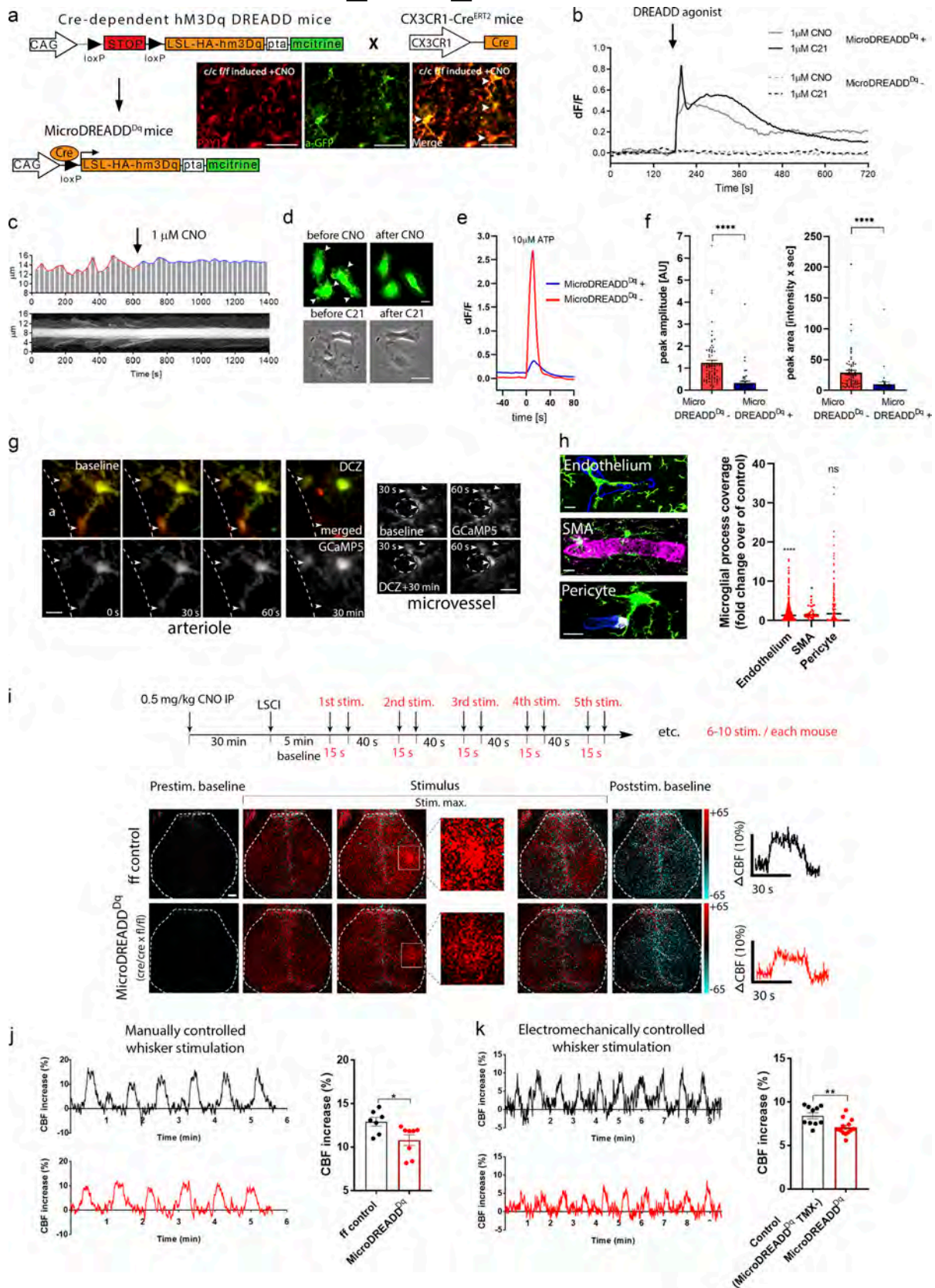


Figure 4. Chemogenetic modulation of microglial activity leads to decreased process motility and impaired neurovascular coupling response to whisker stimulation. (a) Generation of a novel chemogenetic mouse model. TMX-induced recombination was confirmed by anti-P2Y12R and anti-GFP (mCitrine) double staining (white arrowheads), allowing chemogenetic activation of microglia by CNO. Scale bar, 50 μ m. (b) Representative $\Delta F/F$ calcium traces of MicroDREADD^{Dq} microglia cells responding to DREADD agonists CNO or C21. (c and d) The kymogram (c) and fluorescent/phase contrast images (d)

taken from time-lapse sequences show that cell membrane ruffling is ceased upon treatment with DREADD agonists, and the cells acquire a flattened morphology. Scale bars, 5 μm , upper panel; 10 μm , lower panel. See also [Video 4](#) and [Video 5](#). **(e and f)** Analyses of calcium curves reveal an attenuated responsiveness to ATP in MicroDREADD^{Dq+} cells previously responding to C21. See details in [Fig. S2](#). $n = 64$ for MicroDREADD^{Dq+}, $n = 73$ for MicroDREADD^{Dq-}; ****, $P < 0.0001$, Mann-Whitney U test (f). **(g)** Microglial processes interacting with blood vessels show dynamic $[\text{Ca}^{2+}]_i$ fluctuations (arrowheads) in the cerebral cortex of MicroDREADD^{Dq} \times CGaMP5g-tdTomato mice in vivo. Microglial responses have been investigated before (baseline) and 30 min after administration of the DREADD agonist deschloroclozapine (DCZ) around arterioles (a, lumen of the arteriole is shown) and microvessels ($n = 4$ mice). Scale bar, 10 μm . **(h)** 1 h after chemogenetic activation, microglial process coverage (Iba1, green) of endothelial cells (lectin, blue), smooth muscle cells (SMA, magenta), and pericytes (PDGFR β , white) was assessed on perfusion fixed brain sections. Scale bar, 10 μm . $n = 263$ blood vessels, $n = 66$ SMA-positive vessels, and $n = 291$ pericytes were measured from $n = 3$ mice; ****, $P = 0.0001$ endothelium versus control and *, $P = 0.026$ SMA versus control, Mann-Whitney U test. **(i)** 6 wk after TMX, CBF was measured by LSCI during whisker stimulations in MicroDREADD^{Dq} and control mice 30 min after a single i.p. (IP) CNO administration. Representative difference images show CBF changes relative to baseline in control and MicroDREADD^{Dq} mice (white rectangle indicates the area of barrel cortex). Representative stimulus-evoked response curves are shown in the right of i. Scale bar, 1 mm. **(j and k)** Representative CBF curves of manually and electromechanically controlled whisker stimulation measured by LSCI. The maximum of evoked responses show a marked reduction in MicroDREADD^{Dq} mice compared with controls. $n = 7$ control and $n = 8$ MicroDREADD^{Dq} mice; *, $P = 0.0401$, Mann-Whitney U test (j); $n = 10$ control and $n = 13$ MicroDREADD^{Dq} mice; **, $P = 0.0045$, unpaired t test (k). Data are presented as mean \pm SEM. LSCI data have been pooled from two to three independent experiments.

controls in the presence of atipamezole ([Fig. 5 h](#)). Importantly, baseline and hypercapnia-induced pCO_2 and pO_2 levels and pH in blood samples taken from the femoral artery were not altered by microglia depletion ([Fig. S3 b](#)). Similar to that seen after microglia depletion, decreased CBF response to hypercapnia was also apparent in P2Y12R KO mice compared with controls as measured by LSCI ([Fig. 5 i](#)). In vivo two-photon imaging also revealed 37% smaller hypercapnia-induced vasodilation in the absence of microglial P2Y12R (using CX3CR1^{GFP/+} \times P2Y12R KO mice), compared with control (CX3CR1^{GFP/+}) mice ([Fig. 5 j](#) and [Video 6](#)). Supporting the important role of microglial process interactions with the vasculature, formation of perivascular phylopodia was also significantly reduced after hypercapnia in P2Y12R KO mice ([Fig. 5 k](#)). In contrast, neuronal activity did not differ between control, microglia-depleted, and P2Y12R KO mice during hypercapnic challenge ([Fig. 5 l](#)).

Finally, we investigated the possible links between microglial P2Y12R and NO in hypercapnia-induced vasodilation. NO functions, including vasodilation, are mediated by cGMP, which is directly activated by NO ([Toda et al., 2009](#)). To achieve precise timing of hypercapnia, we prepared neocortical acute slices from mice and induced hypercapnia by bubbling 14.6% CO_2 under normoxic conditions for 15 min before measuring cGMP immunoreactivity on rapidly fixed brain slices. Hypercapnia induced a robust increase of cGMP levels (to 311% of control values) in CD13-positive cells, a marker known to homogeneously label both smooth muscle ensheathing and thin-strand/mesh pericytes from large vessels to capillaries ([Smyth et al., 2018](#)). Importantly, increases in cGMP levels were markedly inhibited by the blockade of microglial P2Y12R with PSB0739 ([Fig. 5 m](#)). Confirming that indeed the NO-sGC-cGMP pathway caused the large increase of cGMP levels, the NO donor sodium nitroprusside (SNP) resulted in marked increases in identical anatomic structures, which was not affected by P2Y12R blockade ([Fig. S3 f](#)). Hypercapnia also increased cGMP in CD13-positive profiles in vivo ([Fig. S3 g](#)).

Stimulus-specific release of purinergic metabolites by NVU cells parallels microglial modulation of brain pH and hypercapnia-induced adenosine production

Hypercapnia drives vasodilation in the brain mainly through reducing brain pH ([Yoon et al., 2012](#)). To further investigate the

mechanisms through which microglia shape CBF, cortical blood flow (by laser Doppler) and tissue pH (by pH-selective electrode) were simultaneously assessed during hypercapnia. Surprisingly, baseline brain pH was significantly lower in depleted mice, while the relative amplitude of the hypercapnia-induced negative pH shift was not different in control versus depleted animals ([Fig. 6, a and b](#)), suggesting that microglia contribute to modulation of brain pH. As seen previously with LSCI ([Fig. 5, e-g](#)), laser Doppler flowmetry confirmed significantly smaller hypercapnia-induced CBF elevation in the absence of microglia ([Fig. 6 c](#)).

We next asked whether hypercapnia-induced negative pH shift leads to the production of specific purinergic metabolites (e.g., ATP or ADP) in astrocytes and endothelial cells that may drive microglial process recruitment, as suggested by clustering of microglial P2Y12R at endothelial contact sites near mitochondria ([Fig. 1, i and j](#)) and by MicroDREADD^{Dq} experiments ([Fig. 4, e and f](#)). Hypercapnic challenge reduced both extracellular and intracellular pH ([Fig. S3, c and d](#)) and triggered rapid ATP and adenosine production by cultured astrocytes, while ATP and ADP were produced by endothelial cells ([Fig. 6 d](#)), as assessed by HPLC. In contrast, hypoxic challenge resulted in endothelial ATP, but not ADP, production, while astrocytes released mainly ADP ([Figs. 6 f and S3 e](#)). Importantly, hypercapnia, but not hypoxia, triggered a robust, 10-fold increase in microglial adenosine production ([Fig. 6 d](#)), and hypercapnia-induced adenosine levels were attenuated by microglia depletion in vivo ([Fig. 6 e](#)). Collectively, these experiments suggest that hypercapnia and hypoxia lead to rapid production of different purinergic metabolites, with high levels of adenosine, a potent vasodilator, produced by microglia in response to hypercapnic challenge.

Selective elimination of microglia augments hypoperfusion after common carotid artery occlusion (CCAo)

Stimulus-specific release of purinergic mediators by different NVU cells suggested that microglial effects on CBF are likely to be important for the maintenance of sufficient cerebral blood perfusion, which is compromised in diverse vascular diseases including stroke, chronic hypoperfusion, or vascular dementia, among others ([Iadecola, 2017](#); [Kisler et al., 2017](#); [Wolters et al., 2017](#)). To study the actions of hypoperfusion-primed microglia

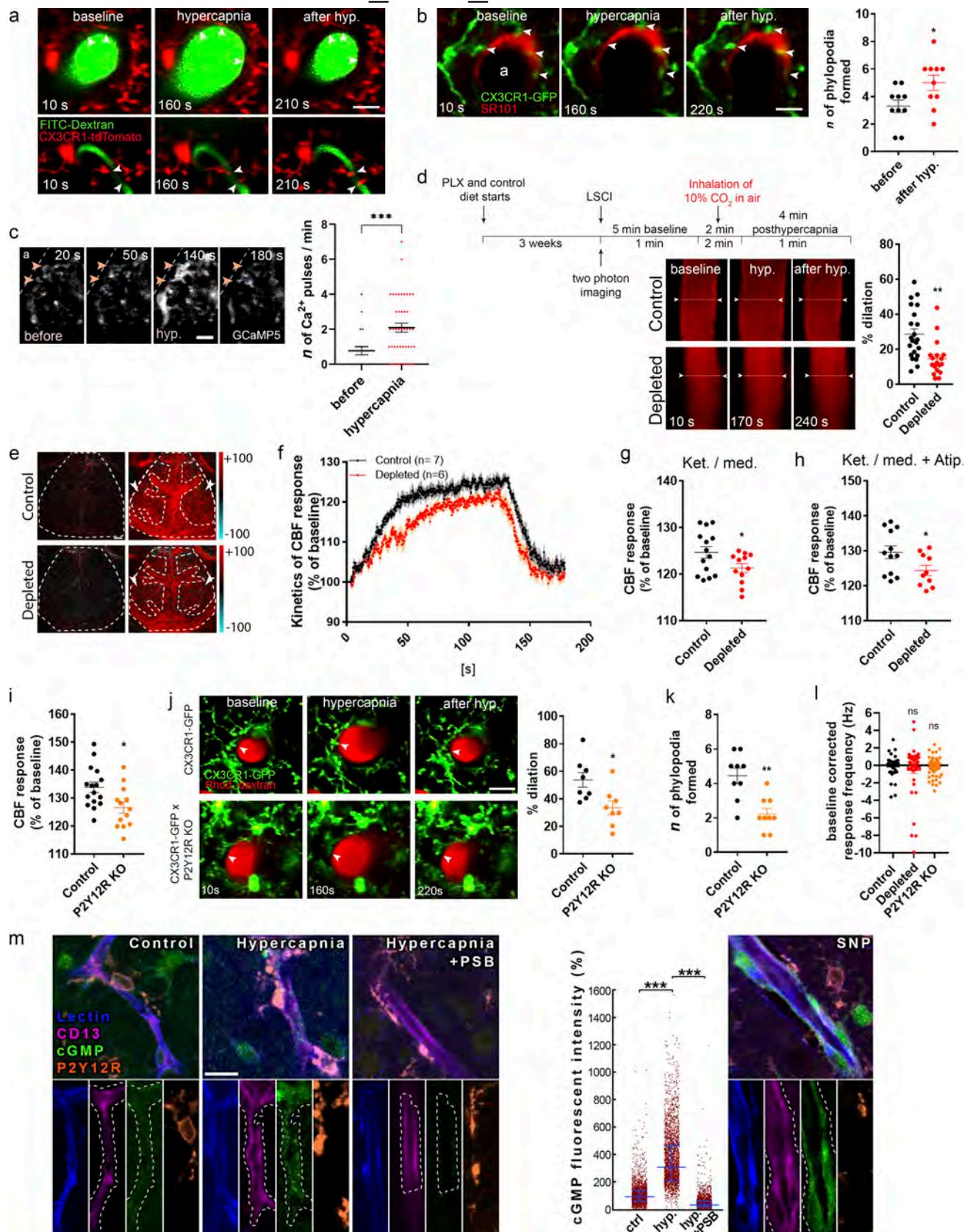


Figure 5. Microglia contribute to hypercapnia-induced vasodilation. (a) In vivo two-photon resonant (32-Hz) imaging was performed in the somatosensory cortex of CX3CR1^ΔTomato mice during hypercapnia (by inhalation of 10% CO₂ under normoxic conditions). The middle panel shows the maximal vasodilation provoked by hypercapnia. Scale bar, 20 μm. (b) Identical hypercapnic challenge and imaging protocol was performed in CX3CR1^{GFP/+} mice after

intracortical injection of SR101 to visualize astrocytes. The number of filopodia formed at the end of contacting microglial processes (arrowheads) increased in response to hypercapnia. $n = 5$ mice; *, $P = 0.0316$, Mann–Whitney U test. Scale bar, 20 μm . **(c)** Perivascular microglia respond rapidly to hypercapnia with $[\text{Ca}^{2+}]_i$ pulses in small (arrowheads) and large processes as assessed in $\text{CX3CR1}^{\text{CGaMP5g-tDTomato}}$ mice. Individual processes were followed with in vivo two-photon resonant (31-Hz) imaging; see also [Video 7](#). Scale bar, 10 μm . $n = 4$ mice; ***, $P = 0.001$, Mann–Whitney U test. **(d)** In vivo two-photon imaging reveals impaired vasodilation at the level of penetrating arteries in the absence of microglia. $n = 22$ and $n = 18$ vessels from eight control and six depleted mice; **, $P = 0.0013$, unpaired t test. The experimental protocol shown for hypercapnic (hyp.) challenge was identical for in vivo two-photon imaging (a–d and j–l) and LSCI (e–i). **(e)** Difference images show reduced CBF response in microglia-depleted mice to hypercapnic challenge (ROIs are labeled with arrowheads). Scale bar, 1 mm. **(f)** The average kinetics of hypercapnic responses show difference in depleted mice compared with controls. $n = 14$ –12 ROIs from seven control and six depleted mice, two ROIs/mouse (f and g); ***, $P < 0.0001$, Mann–Whitney U test (f); *, $P = 0.0472$, unpaired t test (g). **(g and h)** Hypercapnia-evoked CBF response is markedly decreased in the absence of microglia under ketamine-medetomidine (Ket./med.; g) or Ket./med. (h) anesthesia after administration of atipamezole (Atip.). $n = 12$ –10 ROIs from six control and five depleted mice, two ROIs/mouse; *, $P = 0.0436$, unpaired t test. **(i)** Hypercapnia-evoked CBF response is markedly decreased in P2Y12R KO mice as assessed by LSCI. $n = 16$ control, $n = 13$ P2Y12R KO; *, $P = 0.0131$, unpaired t test. **(j)** In vivo two-photon imaging reveals that elimination of P2Y12R impairs hypercapnia-induced vasodilation in double transgenic ($\text{CX3CR1}^{\text{GFP/+}} \times \text{P2Y12R KO}$) mice compared with P2Y12R-competent $\text{CX3CR1}^{\text{GFP/+}}$ mice. $n = 8$ and 8 vessels from $n = 5$ control and $n = 5$ P2Y12R KO mice; *, $P = 0.0104$, Mann–Whitney U test. Scale bar, 20 μm . **(k)** The number of filopodia formed at the end of perivascular microglial processes in response to hypercapnia is significantly reduced in P2Y12R KO mice. $n = 5$ control and $n = 5$ P2Y12R KO mice; **, $P = 0.003$, Mann–Whitney U test. **(l)** During hypercapnic challenge, neuronal activity did not differ between control, microglia-depleted, and P2Y12R KO mice. $n = 49$ single units in control, $n = 44$ in depleted, and $n = 61$ in P2Y12R KO group; $P = 0.4852$, Kruskal–Wallis test with Dunn's multiple comparison. **(m)** Single image planes for CLSM imaging show small blood vessel segments from the second to third layer of the neocortex in acute brain slices. Lectin (blue) outlines the vessels, CD13 labels contractile elements (pericytes and smooth muscle cells), microglial P2Y12R is orange, and cGMP signal can be seen in green. cGMP levels were measured within areas (outlined by white dashed line) masked based on CD13 staining. A low level of basal cGMP levels can be seen under control conditions, while hypercapnia induced a robust increase in vascular cGMP levels. Preincubation with the P2Y12R inhibitor PSB0739 abolished hypercapnia-induced cGMP elevation. As a control, application of the NO donor SNP also induced robust cGMP production. Scale bar is uniformly 15 μm . $n = 3$ mice; ***, $P < 0.0001$, Kruskal–Wallis test. Data are expressed as mean \pm SEM (b–d and f–l) and median \pm IQR (m). LSCI data have been pooled from two to three independent experiments.

(Masuda et al., 2011) on subsequent CBF changes, we developed a model by performing repeated transient unilateral CCAo and reperfusion three times ([Fig. S4, a and b](#)). Redistribution of blood flow to the ipsilateral cortical circulation requires vasodilation (Polycarpou et al., 2016), and unilateral CCAo does not cause cerebral ischemia (Nishijima et al., 2016; Polycarpou et al., 2016), making this model ideal to study vascular adaptation responses during hypoperfusion in the absence of neuronal injury, which is influenced by microglia manipulation (Szalay et al., 2016). In vivo two-photon imaging revealed rapid microglial process response to CBF reduction, as shown by increased process motility of blood vessel-associated microglia immediately after CCAo ([Fig. 7 a](#)). High-resolution automated analysis demonstrated that alterations in microglial process morphology are maintained up to 24 h after CCAo ([Fig. 7 b](#)). Importantly, LSCI measurements showed markedly impaired adaptation to reduced cortical perfusion after CCAo in the absence of microglia. This was evidenced by lower baseline-corrected CBF values after 5 min CCAo and subsequent reperfusion for 5 min, which effect gradually increased as CCAo and reperfusion were repeated two more times ($P < 0.0001$, two-way ANOVA; [Fig. 7, c and d](#); and [Fig. S4, a and b](#)). In fact, average CBF values by the third occlusion reached only 79% of baseline in microglia-depleted mice, as opposed to 89% in control mice in the ipsilateral hemisphere ([Fig. 7 d and Video 8](#)).

Interestingly, the absence of microglia also markedly impaired CBF recovery after repeated CCAo in the contralateral hemisphere ($P < 0.0001$, two-way ANOVA, [Fig. 7 d](#), and [Video 8](#)), indicating that microglial actions are involved in normalizing CBF responses during reperfusion. Impaired CBF recovery was also evident in both hemispheres between the second and the third reperfusion in microglia-depleted mice (2.8-fold larger reduction compared with control mice both ipsilaterally and

contralaterally, $P = 0.042$ and $P = 0.048$, respectively, unpaired t test). Selective elimination of PVMs by intracerebroventricular (ICV) administration of clodronate without an effect on resident microglia ([Fig. 7, e and f](#)) did not influence blood flow responses after repeated CCAo ([Fig. 7, g and h](#)), suggesting that microglia sense and influence CBF changes differently in this model of hypoperfusion than other brain macrophages.

The effect of microglial actions on CBF is mediated via P2Y12R signaling during hypoperfusion

Our HPLC studies demonstrated that both ADP and ATP are released rapidly by NVU cells in response to hypercapnia and hypoxia. ADP, which can rapidly form upon ATP hydrolysis by ectoATPases, is the main ligand for microglial P2Y12R expressed by microglial processes (Cserep et al., 2019), among other cells. To this end, we tested whether an inhibition of microglial P2Y12R using either genetic deletion of P2Y12R or acute pharmacological blockade by PSB0739 injected into the cisterna magna (Cserep et al., 2019) alters CBF responses after repeated CCAo. Importantly, we found that blood flow recovery was markedly impaired after both genetic and pharmacological P2Y12R blockade in the ipsilateral and contralateral hemispheres ([Fig. 8, a–c](#)), similar to that seen in microglia depletion studies ([Fig. 7](#)). Thus, these results collectively suggest that both microglia and microglial P2Y12R are essential for normalizing CBF responses during adaptation to reduced cortical perfusion after CCAo.

Discussion

Here, we identify microglia as a novel cell type modulating blood flow in the brain. Using three different experimental models, we show that the presence of functional microglia is essential to

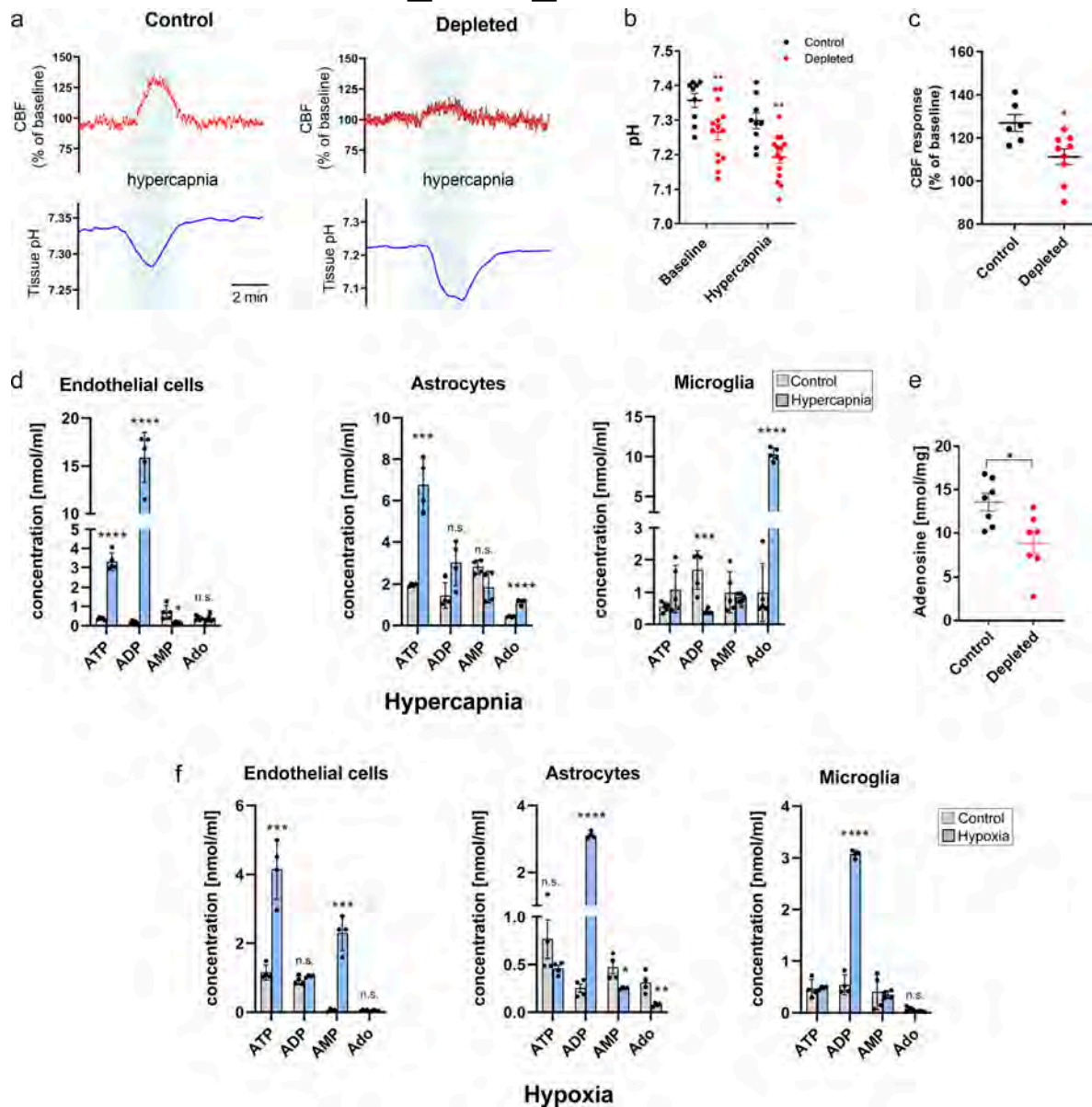


Figure 6. Stimulus-specific release of purinergic metabolites by NVU cells parallels microglial modulation of brain pH and hypercapnia-induced adenosine production. (a) CBF by laser Doppler flowmetry and tissue pH by pH-selective electrode were simultaneously assessed during hypercapnic challenge for 2 min. (b) Depleted mice show reduced extracellular brain pH. $n = 10$ and $n = 16$ measurements from six control and nine depleted mice; $P < 0.0001$, two-way ANOVA followed by Sidak's multiple comparison (**, $P = 0.0093$, control versus depleted baseline; **, $P = 0.0028$, control versus depleted hypercapnia). (c) CBF response to hypercapnia is reduced in microglia-depleted mice. $n = 6$ control and 9 depleted mice; *, $P = 0.012$, Mann-Whitney test. (d) Effect of hypercapnia on levels of purinergic metabolites (ATP, ADP, AMP, and Ado [adenosine]) in primary endothelial, astrocyte, and microglia cultures as measured by HPLC. Endothelial cells: ATP: ****, $P < 0.0001$; ADP: ****, $P < 0.0001$; AMP: *, $P = 0.01226$, control versus hypercapnia; astrocytes: ATP: ***, $P = 0.00029$; Ado: ****, $P = 0.000057$, control versus hypercapnia; microglia: ADP: ***, $P = 0.00134$; Ado: ****, $P < 0.0001$, control versus hypercapnia; multiple t test. (e) Adenosine levels are significantly reduced in the cerebral cortex in the absence of microglia upon hypercapnic challenge. Adenosine was measured by HPLC in cortical brain tissue homogenates. $n = 7$ control and $n = 7$ depleted mice; *, $P = 0.0142$, unpaired t test. (f) Effect of hypoxia on levels of purinergic metabolites (ATP, ADP, AMP, and Ado) in primary endothelial, astrocyte, and microglia cultures as measured by HPLC. Endothelial cells: ATP: ***, $P = 0.00054$; AMP: ***, $P = 0.00011$, control versus hypercapnia; astrocytes: ADP: ****, $P < 0.0001$; AMP: *, $P = 0.0148$; Ado: **, $P = 0.0059$, control versus hypercapnia; microglia: ADP: ****, $P < 0.0001$, control versus hypercapnia; multiple t test. Data are expressed as mean \pm SEM.

maintain optimal CBF responses to physiological neuronal activity and hypercapnia and during cerebrovascular adaptation to reduced cortical perfusion after CCAo. These actions are dependent on microglial P2Y₁₂R signaling, clearly discriminating microglial responses from those mediated by PVMs or other brain macrophages (Prinz et al., 2017).

While microglia produce several vasoactive or inflammatory mediators, including IL-1 β , TNF- α , NO, PGE₂, or ROS (Wolf et al., 2017), that may modulate cerebral perfusion (Iadecola, 2017; Zhao et al., 2018), the potential contribution of microglia to CBF has been largely neglected to date. Instead, research has focused on their role in BBB function, extravasation of

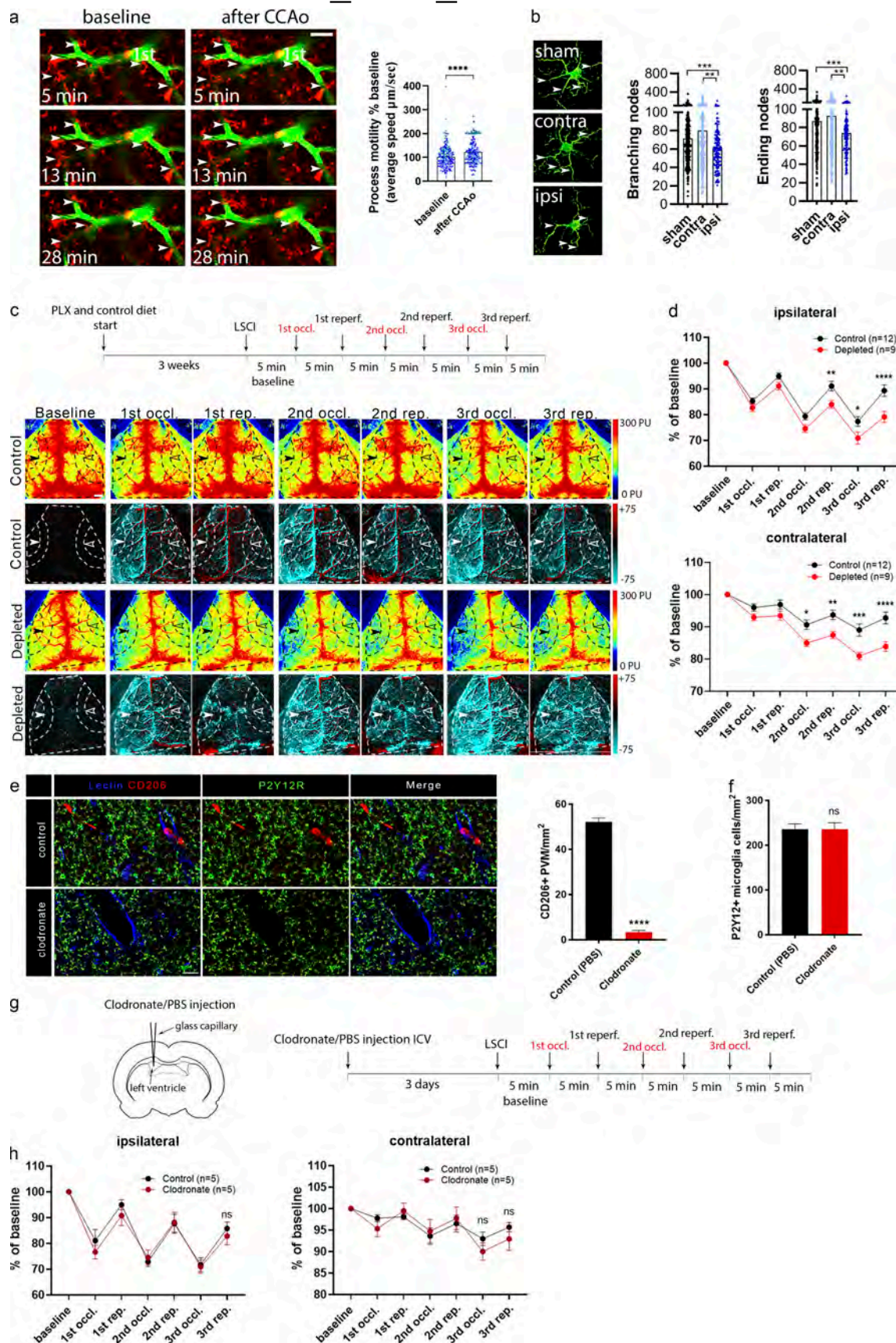


Figure 7. **Adaptation to cortical hypoperfusion is impaired in the absence of microglia.** (a) In vivo two-photon imaging reveals increased microglial process motility (arrowheads) to repeated (3 \times) CCAo in CX3CR1^{tdTomato} mice (1st, first-order capillary). $n = 6$ mice; ****, $P < 0.0001$, Mann-Whitney U test.

Scale bar, 20 μm . **(b)** Automated morphological analysis demonstrates reduced number of branching and ending nodes of microglial processes ipsilaterally in CX3CR1^{GFP/+} mice 24 h after 3 \times CCAo compared with the contralateral side (contra) and sham animals in the cerebral cortex. Branching/ending nodes of $n = 386$ –388 sham, $n = 197$ contralateral (contra), and $n = 134$ ipsilateral (ipsi) cells from $n = 3$ sham and $n = 3$ CCAo mice; ***, $P = 0.0008$, Kruskal–Wallis test followed by Dunn’s multiple comparisons test (branching nodes: ***, $P = 0.0008$, sham versus ipsi; **, $P = 0.005$, contra versus ipsi; ending nodes: ***, $P = 0.0007$, sham versus ipsi; **, $P = 0.0083$, contra versus ipsi). **(c)** Representative perfusion (first and third rows), and difference LSCI images (second and fourth rows) showing cortical perfusion changes in response to 3 \times CCAo (occl.) in control and microglia-depleted mice. Dashed lines indicate the area of quantification in both the ipsilateral (white arrowheads) and contralateral (empty arrowheads) hemisphere as shown in d. Venous sinuses were excluded from the analysis. Scale bar, 1 mm. reper., reperfusion. **(d)** CBF responses to 3 \times CCAo are shown as the percentage of baseline. A significant CBF reduction is seen in the absence of microglia in both hemispheres. $n = 9$ control and $n = 12$ depleted mice; ****, $P < 0.0001$, two-way ANOVA followed by Sidak’s multiple comparison test (ipsilateral second reperfusion [rep.], **, $P = 0.0099$; third occl., *, $P = 0.0270$; third rep., ****, $P < 0.0001$ control versus depleted; contralateral second occl., *, $P = 0.0233$; second rep., **, $P = 0.0052$; third occl., ***, $P = 0.0001$; third rep., ****, $P < 0.0001$ control versus depleted). **(e)** ICV clodronate administration resulted in the depletion of CD206-positive PVMs but did not affect microglial cells (P2Y12R labeling, green). Blood vessels were visualized using the endothelial marker, tomato lectin (blue). Scale bar, 20 μm . Quantification of the number of PVMs after ICV clodronate liposomes or PBS injection. $n = 5$ –5 mice control versus clodronate injected; ****, $P < 0.0001$, unpaired t test with Welch’s correction. **(f)** Quantification of the number of P2Y12-positive microglia cells after ICV clodronate liposomes or PBS injection. $n = 5$ –5 mice control versus clodronate injected, unpaired t test with Welch’s correction. **(g)** PVMs were eliminated from the brain by ICV liposomal clodronate injection before LSCI measurements. **(h)** No difference in CBF is seen between clodronate-treated and control mice after 3 \times CCAo. $n = 5$ and 5 mice control versus clodronate injected, two-way ANOVA followed by Sidak’s multiple comparison test. Data are expressed as mean \pm SEM. LSCI data have been pooled from two to three independent experiments.

leukocytes, and angiogenesis from embryonic stages into adulthood (Dudvarski Stankovic et al., 2016). Because microglial cell bodies are located in the brain parenchyma, while the endothelial basal lamina is surrounded by a second, glial basement membrane (Engelhardt and Sorokin, 2009), we first asked whether a direct contact between microglia and endothelial cells

exists in the adult neocortex. We found that microglia dynamically contact different levels of the vascular tree in vivo and establish direct, purinergic contacts with endothelial cells, per-arterial smooth muscle cells, pericytes, and astrocytes in both the mouse and the human brain, which regulate blood flow. These observations suggested that purinergic mediators, such as

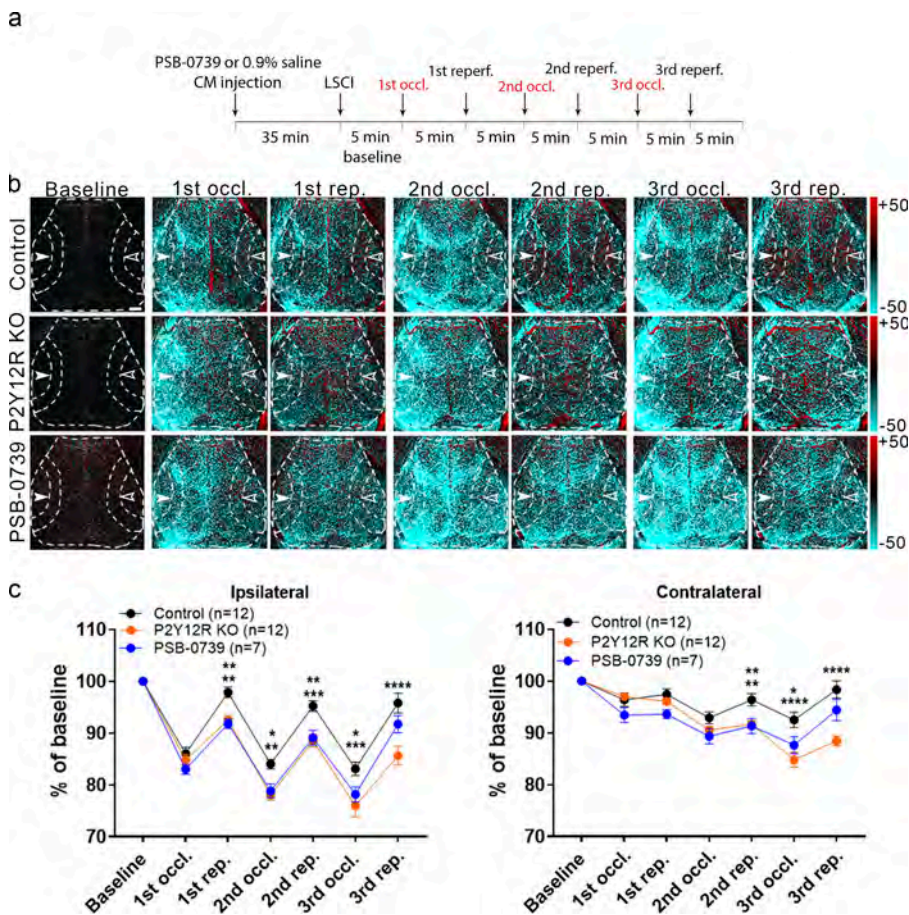


Figure 8. Microglial actions on CBF require P2Y12R signaling. **(a)** Outline of the experimental 3 \times CCAo protocol (occl., occlusion; reper., reperfusion). **(b)** Representative difference images show altered perfusion in both hemispheres in response to 3 \times CCAo in P2Y12R KO and PSB0739-injected mice compared with controls. Dashed lines show the MCA2 area both in the ipsilateral (white arrowheads) and in the contralateral hemisphere (empty arrowheads) corresponding to the quantitative analysis shown in c. Scale bar, 1 mm. reper., reperfusion. **(c)** A significant impairment in adaptation to hypoperfusion is seen both in the ipsilateral and contralateral hemispheres of P2Y12R KO mice and PSB0739-injected mice compared with controls. $n = 12$ control, $n = 12$ P2Y12R KO, $n = 7$ PSB0739-injected mice; ****, $P < 0.0001$, two-way ANOVA followed by Tukey’s multiple comparison test (ipsilateral first rep., **, $P = 0.0042$ control versus P2Y12R KO; **, $P = 0.0057$ control versus PSB-0739; second occl., **, $P = 0.0013$ control versus P2Y12R KO; *, $P = 0.0214$ control versus PSB-0739; second rep., ***, $P = 0.0002$ control versus P2Y12R KO; **, $P = 0.0049$ control versus PSB-0739; third occl., ***, $P = 0.0001$ control versus P2Y12R KO; *, $P = 0.0302$ control versus PSB-0739; third rep., ****, $P < 0.0001$ control versus P2Y12R KO; contralateral second rep., **, $P = 0.004$ control versus P2Y12R KO; **, $P = 0.0096$ control versus PSB-0739; third occl., ****, $P < 0.0001$ control versus P2Y12R KO; *, $P = 0.0133$ control versus PSB-0739; third rep., ****, $P < 0.0001$ control versus P2Y12R KO). Data are expressed as mean \pm SEM. LSCI data have been pooled from two to three independent experiments.

ATP or ADP may be released from NVU cells to recruit P2Y₁₂R-positive microglial processes during vascular adaptation responses or perfusion changes, even under physiological conditions.

To investigate whether microglia could influence CBF responses to physiological neuronal activity, we turned to the widely used whisker stimulation model. Neurovascular coupling is a dynamic functional change in CBF in response to local neuronal activity, which involves different cell types within the NVU, including astrocytes, vascular smooth muscle cells, pericytes, and endothelial cells (Iadecola, 2017; Kisler et al., 2017). However, a role for microglia has not been previously established. During functional hyperemia, dilation of arterioles propagates at high speed in a retrograde direction to upstream arteries, including branches of pial arteries, with both arteriolar and capillary dilation playing a role in increased O₂ delivery (Kisler et al., 2017). Our LSCI and fUS studies revealed significantly smaller CBF response to whisker stimulation in the barrel cortex in the absence of microglia, or microglial P2Y₁₂R, which was not explained by altered neuronal responses in the barrel cortex as assessed by *in vivo* electrophysiology or two-photon calcium imaging. While neuronal activity during hypercapnia was not different between control, P2Y₁₂R KO, and microglia-depleted mice either, it remains to be investigated whether microglia-dependent effects may also influence CBF through changing baseline activity of neurons that control blood flow in the brain (Badimon et al., 2020; Cserep et al., 2019; Kisler et al., 2017). To test the specificity of the microglial actions observed, we developed a mouse model allowing selective chemogenetic targeting of microglia in real time *in vivo*, which disrupts normal microglial process dynamics and renders depolarized cells less responsive to ambient ATP. Smaller CBF responses to whisker stimulation upon chemogenetically induced microglial dysfunction suggest that sustained microglial sensing of purine metabolites and directed process recruitment are required to modulate functional hyperemia in the cerebral microcirculation. These experiments also indicate that even temporary impairment in the dynamic communication between microglial processes and the vasculature could have marked impact on CBF and tentatively on other vascular responses, which has broad implications to any pathological conditions that are associated with altered microglial phenotypes.

We next tested whether microglia-mediated mechanisms influence vascular responses to hypercapnia. Hypercapnia induces vasodilation via complex actions that involve NO release from the endothelium, relaxation of smooth muscle cells and pericytes, release of astrocytic prostaglandin E₂, and other processes (Faraci et al., 2019; Hamilton et al., 2010; Howarth et al., 2017; Meng and Gelb, 2015; Yoon et al., 2012). Importantly, while perivascular microglial processes rapidly responded to hypercapnia with calcium pulses and generation of new filopodia, the absence of microglia markedly inhibited increases of CBF (as demonstrated independently by both LSCI and laser Doppler flowmetry) and vasodilation (as shown by *in vivo* two-photon imaging). This was independent of arterial blood pH, pO₂, and pCO₂ levels, which were not different in microglia-depleted mice. Surprisingly, we found that absence of

microglia reduced brain pH, while microglia rapidly produced adenosine in response to hypercapnia. Supporting this, recent findings showed that microglia represent a key source of adenosine in the brain, which modulates neuronal responses at synapses (Badimon et al., 2020). Hypercapnia drives vasodilation mainly via reduced extracellular pH, which is a major regulator of cerebrovascular reactivity and acts directly on cerebrovascular smooth muscle cells to cause relaxation, mediating the effects of increased CO₂ levels (Yoon et al., 2012). Microglial P2Y₁₂R-mediated Ca²⁺ signaling, migration, and cytokine production are also pH dependent (Jin et al., 2014; Langfelder et al., 2015). Because adenosine is a potent vasodilator in the cerebral circulation (Pelligrino et al., 2011), we suggest that lower brain pH in the absence of microglia may partially compensate for the loss of microglial vasoactive mediators, with a net effect of reduced vasodilation during different vascular adaptation responses. It should be investigated in future studies whether microglial loss or dysfunction could induce compensatory actions in other NVU cells, such as promoting adenosine production by astrocytes (MacVicar and Newman, 2015).

To further investigate the mechanisms through which microglial P2Y₁₂R may modulate vascular responses, we investigated the possible links with NO, a key mediator of vasodilation (Attwell et al., 2010; Iadecola, 2017; Toda et al., 2009). The observation that the absence of microglia and NO blockade by L-NAME had an additive effect to reduce the coupling response upon somatosensory stimulation, strongly suggests that P2Y₁₂R-positive microglia regulate the CBF response to somatosensory stimulation through signaling mechanisms that are, at least in part, additional to NO-mediated vasodilation. This may have broad physiological and pathological consequences given the complexity of CBF regulation in health and disease (Attwell et al., 2010; Iadecola, 2017; Kisler et al., 2017; Toda et al., 2009).

These conclusions are extended further by our hypercapnia studies. NO functions, including vasodilation, are mediated by cGMP synthesized through soluble guanylyl cyclase, a heme-containing enzyme, which is directly activated by NO (Toda et al., 2009). Rapid response of microglia to hypercapnia as demonstrated by calcium fluctuations and generation of perivascular filopodia, which was P2Y₁₂R dependent *in vivo*, together with inhibition of hypercapnia-induced cGMP by P2Y₁₂R blockade in CD13-positive, contractile elements (smooth muscle cells and pericytes) *ex vivo*, suggest that contacting microglial processes may interfere with vasodilation via tentatively different cell types and mediators, which may include NO and adenosine. It should be noted that hypercapnia also increased cGMP in CD13-positive profiles *in vivo*, but the extent of this response was heterogeneous, most likely due to the difficulties with precise timing of tissue collection and the rapid hydrolysis of cGMP by phosphodiesterases, which we were able to block effectively in acute brain slices (Szabadits et al., 2011). It will also need to be investigated further in future studies how microglial modulation of NO actions could interact with the production of adenosine or other vasoactive mediators by microglia and other cells in the NVU.

We finally asked whether microglia sense and respond to cerebral hypoperfusion. CBF is controlled by feed-forward and

feedback mechanisms that maintain or re-establish optimal oxygen and nutrient supply of neurons in case disturbances of the cardiovascular system occur (Colonna and Butovsky, 2017). Adaptation to reduced cerebral perfusion requires vasodilation (Zaharchuk et al., 1999). Unilateral CCAo is an established model of cerebrovascular adaptation to the reduction of perfusion, which is mediated primarily by the activation of feedback pathways through the collateral circulation (Polycarpou et al., 2016), while it does not induce neuronal death or BBB injury in rodents (Nishijima et al., 2016; Polycarpou et al., 2016). Since the cell types in the NVU contacted by microglia regulate CBF (Attwell et al., 2010; Iadecola, 2017; Kisler et al., 2017), we argued that microglia primed by hypoperfusion during the first occlusion would interfere with subsequent vascular adaptation responses, and hence elimination of microglia may alter CBF after repeated CCAo. As supported by previous results showing that microglial process responses around microvessels change proportionally to the level of CBF reduction (Masuda et al., 2011), we found that microglial processes rapidly respond to CCAo. Importantly, absence of microglia and both genetic and pharmacological blockade of microglial P2Y₁₂R resulted in impaired adaptation to reduced cortical perfusion during repeated CCAo, which strengthens their different roles compared with P2Y₁₂R-negative PVMs (Cserep et al., 2019; Fekete et al., 2018), as also confirmed by the lack of an effect of PVM depletion.

The importance of ATP signaling in the vasculature has been demonstrated under both homeostatic and pathological conditions (Lohman et al., 2012). Microglial processes are recruited to sites of ATP release via P2Y₁₂R, which primarily sense ADP produced by ATP hydrolysis or cleavage by NTPDase1 expressed on the microglial membrane, among other cells (Cserep et al., 2019; Davalos et al., 2005; Haynes et al., 2006). Our electron tomography studies revealed an accumulation of P2Y₁₂R on microglial processes contacting endothelial cells in the vicinity of endothelial mitochondria, where ATP release may recruit microglial processes to the vasculature in response to CBF changes (Lohman et al., 2012). Similar interactions are seen at somatic purinergic junctions (Cserep et al., 2019), through which microglia sense neuronal mitochondrial activity and modulate neuronal responses via purinergic signaling. ATP derived from astrocytes is also known to constrict vascular smooth muscle cells and regulate blood flow (Kisler et al., 2017). Importantly, our HPLC studies demonstrated that endothelial cells and astrocytes release different purinergic metabolites in response to hypoxia and hypercapnia, both of which occur during hypoperfusion. While we found rapid alterations in microglia-endothelium and microglia-astrocyte interactions after CCAo and hypercapnia, hypoxia and hypercapnia also triggered different purinergic responses in microglia. Although the mechanisms through which different purinergic mediators are released in the NVU remain to be explored, pannexin-1 (PANX1) channels are likely to be involved, which is also suggested by reduced hypercapnia-induced CBF responses in PANX1 KO mice (Bisht et al., 2021). Thus, cell- and stimulus-specific production of vasoactive metabolites may provide means for different vascular adaptation responses, during which microglia may alter CBF via actions on different cell types in the NVU or protect

against mild hypoxia-induced vascular leakage (Halder and Milner, 2019). Our in vivo two-photon imaging data also indicate that individual microglial processes may perform functionally distinct tasks to influence vascular (and other) responses in given microdomains, which is largely supported by the high level of functional autonomy of calcium signaling in microglial processes (Umpierre et al., 2020).

Because all experimental models have their limitations, we made efforts to use alternative approaches wherever possible during these complex studies. For example, prolonged (7-wk-long) treatment with PLX5622 has been found to affect the choroidal vasculature and alter angiogenic growth (Yang et al., 2020). However, the structural/cellular integrity of blood vessels was not found to be disturbed in the neocortex after 3 wk of depletion in the present study, as also seen earlier (Elmore et al., 2014; Szalay et al., 2016). This is also confirmed by our [^{99m}Tc]-HMPAO SPECT and [¹⁸F]-FDG PET measurements, which are widely used noninvasive methods to assess regional perfusion and glucose metabolism changes, respectively (Apostolova et al., 2012; Tai and Piccini, 2004). Another possible confounder could be that CX3CR1 (used as a promoter in the CX3CR1^{CreERT2} driver line to generate MicroDREADD^{Dq} mice) may also be expressed by other brain macrophages apart from microglia (Kim et al., 2021). It is theoretically possible that in addition to microglia, other brain myeloid cells such as meningeal macrophages or PVMs could have contributed to shaping vascular responses in the present study. However, in line with the very high specific recombination rate of microglia in CX3CR1tdTomato microglia reporter mice and MicroDREADD^{Dq} mice, we demonstrated that all parenchymal CX3CR1-positive cells were P2Y₁₂R-positive microglia. Importantly, the contribution of microglia to CBF regulation has been confirmed with a number of independent strategies in all three experimental models, including pharmacological and genetic blockade of P2Y₁₂R, which is specific for microglia in the central nervous system (Cserep et al., 2019). Effective blockade of microglial P2Y₁₂R by PSB0739 injected into the cisterna magna has also been characterized in detail in our previous study (Cserep et al., 2019).

Clinical significance

We believe that the implication of these data is far-reaching. Altered microglial activity and impaired CBF or neurovascular coupling precede symptom onset in common brain pathologies such as Alzheimer's disease, Lewy body dementia, idiopathic Parkinson's disease, chronic hypoperfusion, and amyloid angiopathy (Attwell et al., 2010; Iadecola, 2017; Kisler et al., 2017; Wolf et al., 2017). Thus, dysfunction of microglia could contribute to disease pathophysiology by modulating CBF via endothelial cells or other cells in the NVU. Interestingly, homozygous missense mutations of TREM2 (a microglial receptor) are linked with increased risk of dementia, while Trem2 p.T66M knock-in mice display an age-dependent reduction in microglial activity, CBF, and brain glucose metabolism (Kleinberger et al., 2017). In patients with risk factors for stroke, carotid stenosis, aneurysm, hypertension, chronic vascular inflammation, or transient ischemic attack, altered microglial activity may impact clinical outcome merely via modulating

cerebral perfusion or adaptation to reduced perfusion. As such, microglia could also contribute to ischemic preconditioning, vasospasm after subarachnoid hemorrhage, or the “no reflow phenomenon” after cerebral ischemia (Kloner et al., 2018), while microglial surveillance is likely to be disturbed during hypoxia or ischemia, as evidenced in the developing brain (Eyo and Dailey, 2012; Masuda et al., 2011).

In conclusion, our data demonstrate that microglia should be considered an important modulatory cell type involved in physiological and pathological alterations of CBF. Understanding their actions may facilitate the discovery of novel treatment opportunities in common neurological disorders.

Materials and methods

Mice

Experiments were carried out on 11–17-wk-old C57BL/6J (RRID:IMSR_JAX:000664); P2Y12R^{-/-} (B6;129-P2ry12^{tm1Dgen}/H P2Y12R KO); CX3CR1^{GFP/+} (RRID:IMSR_JAX:005582), CX3CR1^{GFP/+}/P2Y12^{-/-}, CX3CR1^{GFP/GFP}, CX3CR1^{tdTomato}, and Thy1-GCaMP6s (C57BL/6J-Tg[Thy1-GCaMP6s]GP4.12Dkim/J, RRID:IMSR_JAX:025776; Dana et al., 2014); MicroDREADD^{Dq}, CX3CR1^{CGaMP5g-tdTomato} (RRID:IMSR_JAX:024477); and MicroDREADD^{Dq} × CGaMP5g-tdTomato mice (all on C57BL/6J background). Mice were kept in a 12-h dark/light cycle environment, under controlled temperature and humidity, with food and water ad libitum. All experimental procedures were in accordance with the guidelines set by the European Communities Council Directive (86/609 EEC) and the Hungarian Act of Animal Care and Experimentation (1998; XXVIII, Sect. 243/1998), approved by the Animal Care and Experimentation Committee of the Institute of Experimental Medicine and the Government Office of Pest County Department of Food Chain Safety, Veterinary Office, Plant Protection and Soil Conservation Budapest, Hungary, under the numbers PE/EA/1021-7/2019 and PE/EA/673-7/2019, and the Department of Food Chain Safety and Animal Health Directorate of Csongrád County, Hungary. Experiments were performed according to EU Directive 2010/63/EU on the protection of animals used for scientific purposes and are reported in compliance with the ARRIVE guidelines.

Generation of CX3CR1^{tdTomato}, MicroDREADD^{Dq}, MicroDREADD^{Dq} × CGaMP5g-tdTomato, and CX3CR1^{CGaMP5g-tdTomato} mice

CX3CR1^{tdTomato}, MicroDREADD^{Dq}, CX3CR1^{CGaMP5g-tdTomato}, and MicroDREADD^{Dq} × CGaMP5g-tdTomato mice were generated by crossing TMX-inducible CX3CR1^{CreERT2} mice (B6.129P2[C]-CX3CR1^{tm2.1[cre/ERT2]}ung/J, RRID:IMSR_JAX:020940; Yona et al., 2013) with a mouse line expressing Cre-dependent tdTomato (B6;129S6-Gt[ROSA]26Sortm9[CAG-tdTomato]Hze/J, RRID:IMSR_JAX:007905), hM3Dq DREADD (B6N;129-Tg[CAG-CHRM3^{*}-mCitrine]1Ute/J (Zhu et al., 2016), RRID:IMSR_JAX:026220), or CGaMP5g-tdTomato (B6;129S6-Polr2a^{Tn[tp-CAG-GCaMP5g,-tdTomato]}Tvrđ/J; Gee et al., 2014; RRID:IMSR_JAX:024477). To induce tdTomato, hM3Dq DREADD, or CGaMP5g-tdTomato expression in microglia, Cre recombinase activity was induced by two i.p. injections of TMX (2 mg/100 μl, dissolved in corn oil; #T5648; Sigma-Aldrich), 48 h apart in 3–4-wk-old male mice, shortly after weaning. 4 wk after TMX induction, 95.3% of microglia

expressed hM3Dq receptors, as confirmed by anti-GFP (goat anti-GFP antibody, 1:300; #600-101-215; Rockland) and anti-P2Y12R immunostaining, to detect mCitrine and microglia, respectively (Zhu et al., 2016). Using CX3CR1^{CreERT2} mice, microglia show constant Cre-dependent expression, while most peripheral macrophages/monocytes expressing CX3CR1 are replaced by the end of the fourth week after TMX induction, owing to their rapid turnover (Yona et al., 2013). Therefore, all experiments were carried out at 11 and 12 wk of age. Microglial responses were modulated in real time either by i.p. CNO (0.5 mg/kg; #4936; Bio-Techne Corp.) or i.p. deschloroclozapine (1 μg/kg; #HB9126; HelloBio) administration, via the activation of hM3Dq DREADD (Alexander et al., 2009).

Characterization of CX3CR1^{tdTomato} microglia reporter mice

4 wk after TMX induction, virtually 100% of microglia in the cerebral cortex expressed tdTomato, as assessed by P2Y12 and Iba1 immunostaining. In the whole population, 94% of Tomato-positive cells coexpressed both P2Y12 and Iba1, 2.4% of the cells were only Iba1-positive, and 3.6% of tdTomato cells did not express either Iba1 or P2Y12. tdTomato-positive cell bodies and processes were analyzed in the somatosensory cortex on high-resolution CLSM stacks (CFI Plan Apochromat VC 60XH oil-immersion objective, 0.1 μm/pixel, Z-step: 2 μm) with homogeneous sampling (Fig. S1 h). Cell nuclei were identified by DAPI.

In vivo two-photon imaging

Cranial window preparation in CX3CR1^{GFP/+}, CX3CR1^{tdTomato}, CX3CR1^{GFP/+} × P2Y12^{-/-}, Thy1-GCaMP6s CX3CR1^{CGaMP5g-tdTomato}, and MicroDREADD^{Dq} × CGaMP5g-tdTomato mice was performed above the primary somatosensory or the barrel cortex. Blood vessels were labeled with either Rhodamine B-dextran or FITC-dextran (70,000 mol wt). 3 wk after cranial window surgery, microglia-vascular interactions in response to 3× CCAo or hypercapnia (ketamine-medetomidine anesthesia, i.p. 30–0.1 mg/kg) and neuronal intracellular Ca²⁺ ([Ca²⁺]_i) in response to whisker stimulations (in ketamine-medetomidine anesthesia) were imaged in body temperature-controlled animals. For microglia process motility measurements in response to 3× CCAo, the galvo-scanning light path with 16× water-immersion objective (Nikon CFI75 LWD 16× W, NA 0.8) was used to acquire four-image Z-stacks with 8.5-μm step size, 150–200 μm below the dura, at 500 × 500-pixel resolution. For measuring vascular responses to hypercapnia, after obtaining 1 min at baseline, a 2-min hypercapnic episode (inhaling a 10% CO₂-containing air mixture) and 1-min posthypercapnic period were imaged with the resonant light path at 32.7521 Hz. For in vivo [Ca²⁺]_i imaging in control and microglia-depleted Thy1-GCaMP6s mice, the right whiskers were stimulated, and neuronal [Ca²⁺]_i transients were imaged in the left barrel cortex at 920-nm wavelength using the resonant scanner at 180–250-μm depth below the dura, under ketamine-medetomidine sedation. The stimulation protocol consisted of 5-Hz square pulses for 15 s, repeated 6 times with 40-s intervals. Measurements were performed at 32.48 Hz using a Nikon 16× water-immersion objective. Imaging was performed by a Femto2D-DualScanhead

microscope (Femtonics) coupled with a Chameleon Discovery laser (Coherent). Data acquisition was performed with MESc software (v.3.5.6.9395SLE; Femtonics), and data were analyzed in MES software (v.5.3560; Femtonics).

Tissue processing and immunostaining

Under terminal (ketamine-xylazine) anesthesia, mice were transcardially perfused with 4% paraformaldehyde, and brains were dissected. Brain samples were postfixed and cryoprotected for 24 h, and 25- μ m-thick coronal sections were cut using a sledge microtome (Leica). Immunostaining was performed on free-floating brain sections, blocked with 5% normal donkey serum (Jackson ImmunoResearch). The following primary antibodies were used: rabbit anti-P2Y12R (1:500; #55043AS; AnaSpec), chicken anti-GFP-tag (1:500; #A10262; Invitrogen), goat anti-GFP (1:300; #600-101-215; Rockland), rat anti-CD206 (1:200; #MCA2235; AbD Serotec), and biotinylated tomato lectin (1:100; #B-1175; Vectorlabs). After washing, sections were incubated with the corresponding secondary antibodies (from Jackson ImmunoResearch): donkey anti-rabbit A647 (1:500; #711-605-152), donkey anti-chicken A488 (1:500; #703-546-155), donkey anti-goat A488 (1:500; #705-546-147), donkey anti-rat A594 (1:500; #712-586-153), and streptavidin DyL405 (1:500; #016-470-084). Slices were mounted with Fluoromount-G (SouthernBiotech) or Aqua-Poly/Mount (Polysciences). For high-resolution CLSM and EM assessments, 50- μ m-thick vibratome sections were washed in PB and TBS, followed by blocking with 1% human serum albumin (HSA). Sections were then incubated in different mixtures of primary antibodies: rabbit anti-P2Y12R (1:500; #55043AS; AnaSpec), chicken anti-GFAP (1:500; #173 006; Synaptic Systems), goat anti-PDGFR- β (1:500; #AF1042; R&D Systems), rat anti-CD206 (1:200; #MCA2235; AbD Serotec), rat anti-PECAM-1 (1:500; #102 501; BioLegend), mouse anti- α SMA (1:250; #ab7817; Abcam), guinea pig anti-AQP4 (1:500; #429 004; Synaptic Systems), mouse anti-TOM20 (1:500; #H00009804-M01; Abnova), guinea pig anti-Iba1 (1:500; #234 004; Synaptic Systems), mouse anti-Kv2.1 (1:500; #75-014; NeuroMab), and biotinylated tomato lectin (1:100; #B-1175; Vectorlabs). After washing in TBS, sections were incubated in the corresponding mixtures of secondary antibodies (from Jackson ImmunoResearch): donkey anti-chicken DyLight405 (1:500; #703-474-155), donkey anti-chicken A488 (1:500; #703-546-155), donkey anti-chicken A647 (1:500; #703-606-155), donkey anti-rabbit A647 (1:500; #711-605-152), donkey anti-rabbit A488 (1:500; #A21206; Invitrogen), donkey anti-rat A594 (1:500; #A21209; Invitrogen), donkey anti-rat A647 (1:500; #712-606-153), donkey anti-mouse A594 (1:500; #A21203; Invitrogen), donkey anti-mouse A647 (1:500; #715-605-150), donkey anti-guinea pig DyLight405 (1:500; #706-476-148), donkey anti-guinea pig A594 (1:500; #706-586-148), donkey anti-guinea pig A647 (1:500; #706-606-148), streptavidin DyL405 (1:500; #016-470-084), and streptavidin A594 (1:500; #S11227; Invitrogen). Incubation was followed by washing in TBS and PB, then sections were mounted on glass slides with Aqua-Poly/Mount (Polysciences). Immunofluorescence was analyzed using a Nikon Eclipse Ti-E inverted microscope (Nikon Instruments), with a CFI Plan Apochromat VC 60 \times oil-immersion objective (NA 1.4) or a Plan Apochromat

VC 20 \times objective (NA 0.75) and an A1R laser confocal system. The following lasers were used: 405, 488, 561, and 647 nm (CVI Melles Griot). Scanning was done in line serial mode. Image stacks were obtained with NIS-Elements AR 5.00.00 software.

Pre-embedding immuno-EM

After extensive washes in PB and TBS (pH 7.4), vibratome sections were blocked in 1% HSA. Then, they were incubated with rabbit anti-P2Y12R (1:500; #55043AS; AnaSpec) alone or mixed with mouse anti-GFAP (1:1,000; #G3893; Sigma-Aldrich) in TBS for 2–3 days. After several washes, sections were incubated in blocking solution (Gel-BS) containing 0.2% cold water fish skin gelatin and 0.5% HSA for 1 h. Next, sections were incubated with 1.4 nm gold-conjugated goat anti-rabbit Fab-fragment (1:200; #2004; Nanoprobes) alone or mixed with biotinylated donkey anti-mouse (1:500; #715-065-150; Jackson ImmunoResearch) antibodies diluted in Gel-BS overnight. After extensive washes, sections were treated with 2% glutaraldehyde for 15 min to fix the gold particles into the tissue. For the combined immunogold-immunoperoxidase reactions, this was followed by an incubation in avidin-biotinylated HRP complex (Vectastain Elite ABC kit; 1:300; Vector Laboratories) for 3 h at room temperature (RT) or overnight at 4°C. The immunoperoxidase reaction was developed using 3,3-diaminobenzidine (Sigma-Aldrich) as chromogen. To develop the immunogold reaction, sections were incubated in silver enhancement solution (SE-EM; Aurion) for 40–60 min at RT. The sections were then treated with 0.5% OsO₄ in PB, at RT, dehydrated in ascending alcohol series and in acetonitrile, and embedded in Durcupan (ACM; Fluka). During dehydration, sections were treated with 1% uranyl acetate in 70% ethanol for 20 min. For EM analysis, tissue samples from the somatosensory cortex (S1) were glued onto Durcupan blocks. Consecutive 70-nm-thick (for conventional EM analysis) or 150-nm-thick (for electron tomography) sections were cut using an ultramicrotome (Leica EM UC6) and picked up on Formvar-coated single-slot grids. Ultrathin sections for conventional EM analysis were examined in a Hitachi H-7100 electron microscope equipped with a Veleta charge-coupled device (CCD) camera (Olympus Soft Imaging Solutions). 150-nm-thick electron tomography sections were examined in FEI Tecnai Spirit G2 BioTwin TEM equipped with an Eagle 4k camera.

Electron tomography and analysis

Before electron tomography, serial sections on single-slot copper grids were photographed with a Hitachi H-7100 electron microscope and a Veleta CCD camera. Serial sections were examined at lower magnification, and P2Y12R-positive microglial processes contacting the vasculature were selected. After this, grids were put on drops of 10% HSA in TBS for 10 min, dipped in distilled water (DW), put on drops of 10-nm gold-conjugated Protein-A (#AC-10-05; CytoDiagnostics) in DW (1:3), and washed in DW. Electron tomography was performed using a Tecnai T12 BioTwin electron microscope equipped with a computer-controlled precision stage (FEI; CompuStage). Acquisition was controlled via Xplore3D software (FEI). Regions of interest (ROIs) were pre-illuminated for 4–6 min to prevent further

shrinkage. Dual-axis tilt series were collected at 2°-increment steps between -65 and +65° at 120 kV acceleration voltage and 23,000× magnification with -1.6 to -2 μm objective lens defocus. Reconstruction was performed using the IMOD software package (Kremer et al., 1996). Isotropic voxel size was 0.49 nm in the reconstructed volumes. After combining the reconstructed tomograms from the two axes, the nonlinear anisotropic diffusion filtering algorithm was applied to the volumes. Segmentation of different profiles was performed on the virtual sections using 3Dmod software.

Postmortem human brain samples

Postmortem human brain tissue was obtained from one 60-yr-old female, one 73-yr-old male, and one 27-yr-old male, without any known neurological disease as also confirmed by neuropathological examination (ETT TUKEB 31443/2011/EKU [518/PI/11]). Informed consent was obtained for the use of brain tissue and for access to medical records for research purposes. Tissue was obtained and used in a manner compliant with the Declaration of Helsinki. Brains of patients who died of non-neurological diseases were removed 4–5 h after death (Table S1). The internal carotid and the vertebral arteries were cannulated, and the brain was perfused first with heparin containing physiological saline, followed by a fixative solution containing 4% paraformaldehyde, 0.05% glutaraldehyde, and 0.2% picric acid (vol/vol) in PB. The hippocampus was removed from the brain after perfusion and was postfixed overnight in the same fixative solution, except that glutaraldehyde was excluded. Blocks were dissected, and 50-μm-thick sections were prepared on a vibratome (VT1200S; Leica).

LSCI

CBF was measured by a PeriCam PSI High Resolution LSCI system (Perimed AB) at 21 frames/s frequency in a 10 × 10-mm field of view. Perfusion responses were expressed as a percentage of baseline CBF. Uniformly, a 1-min-long baseline was set in all experiments, registered at the beginning of the measurements. Three adjacent ROIs were placed (denoted as MCA1-3) over the middle cerebral artery (MCA) territory both to the ipsilateral and to the contralateral hemispheres to assess microglia-mediated effects on gradual perfusion changes ranging from the MCA core region to the midline. During whisker stimulation, ROIs were placed over the contralateral barrel cortex, while during hypercapnic challenge, ROIs were placed over the left and right hemispheres excluding venous sinuses. CCA occlusion experiments were performed under ketamine-xylazine (i.p. 100 to 10 mg/kg) anesthesia, while the whisker stimulation protocol and hypercapnic challenge was performed under mild ketamine-medetomidine (i.p. 30 to 0.1 mg/kg) sedation (Lecrux et al., 2017).

Cisterna magna injection for drug delivery into the brain and i.p. drug administration

To block P2Y₁₂R-mediated microglial actions, a P2Y₁₂R antagonist, PSB-0739 (dissolved in 0.9% saline, 40 mg/kg in 5 μl volume; #3983; Bio-Techne Corp.) was injected into the cisterna magna 35 min before imaging, while vehicle (0.9% saline) injection was used as control. Cisterna magna injections were done

under 1–1.5% isoflurane anesthesia. L-NAME, a nonselective NOS inhibitor (#0665; Tocris) was injected i.p. (30 mg/kg dissolved in 0.9% saline) 5 min before imaging.

SPECT and PET imaging

SPECT and PET studies were carried out on mice anesthetized with 2% isoflurane (Apostolova et al., 2012). SPECT measurements were performed using the [^{99m}Tc]-HMPAO ligand (hexamethylpropylene amine oxime; Medi-Radiopharma). The acquisition started 3 min after the i.v. injection of the radiotracer via the tail vein (injected activity: 99.22 ± 9.33 MBq). The measurements were performed on a NanoSPECT/CT PLUS device (Mediso) equipped with multipinhole mouse collimators. Measurements were reconstructed with 0.25-mm isovoxels, and the results were quantified as units of radioactivity (MBq/ml). After SPECT acquisition, [¹⁸F]-FDG PET measurements were performed. PET acquisition started 20 min after i.v. [¹⁸F]-FDG injection (2-deoxy-2-(¹⁸F)fluoro-D-glucose, injected activity: 12.05 ± 1.93 MBq; Pozitron-Diagnosztika) with an acquisition time of 10 min using a microPET P4 (Concorde Microsystems). A maximum a posteriori algorithm was used to reconstruct the data with 0.3-mm isovoxels. After reconstruction, manual coregistration and atlas-based ROI measurements were done using VivoQuant software (InviCRO) in the cerebellum, cerebral cortex, and whole brain. For microglia-depleted and control groups, mean [¹⁸F]-FDG and [^{99m}Tc]-HMPAO standardized uptake values were analyzed by using two-way ANOVA followed by Sidak's post hoc test (GraphPad Prism 7.0) and a permutation *t* test in R 3.5.1 (R Foundation for Statistical Computing).

Whisker stimulation protocol

Whisker stimulation was performed manually and electromechanically (with a bending actuator, #PL112-PL140; PICMA; bender connected to a piezo amplifier, #E-650 Amplifier, Physik Instrumente). For manual stimulation, an earpick was used (at 4–5 Hz frequency) according to the following protocol: left whiskers were stimulated for 30 s, repeated 6 times, 60 s apart. During electromechanically controlled stimulation (5 Hz), whiskers were stimulated for 15 s, repeated 10 times with 40-s intervals. Stimulation-evoked CBF responses in the contralateral barrel cortex were recorded. CBF measurements were carried out under ketamine-medetomidine sedation (30 to 0.1 mg/kg dissolved in 0.9% saline, i.p.). All coupling experiments performed were time-matched from the time of anesthetic injection to ensure comparable results across different experiments.

fUS

fUS acquisition was done with a 15-MHz probe of 128 elements (Vermon SA) connected to a prototype ultrafast research ultrasound scanner (hardware and software functionally analogous to the Iconeus One system; Iconeus). Recordings were performed through the skull while the animal was anesthetized with ketamine-medetomidine (i.p. 30 to 0.1 mg/kg). The head of the animal was shaved and fixed into a stereotactic frame. The probe was positioned using a built-in software based registration to the 3D Allen Brain Atlas (2015 Allen Institute for Brain Science, Allen Brain Atlas API, available from brain-map.org/

[api/index.html](#)). Doppler images were obtained as described earlier (Tiran et al., 2017). 11 tilted planes were insonifying the medium at 5,500-Hz pulse repetition frequency to compute one compounded image every 2 ms. Of a block of 200 images, a Power Doppler image was obtained by removing the 60 first modes of SVD decomposition to extract the blood signal (Demene et al., 2015) from tissue clutter at a 2.5-Hz sampling rate. Acquisition started and ended with a 5-min baseline followed by 10 phases of 30-s manual stimulation of the whiskers (Ferrier et al., 2020) with 1 min of resting in between. A fourth-order polynomial detrending of the data was applied to remove drifts of baseline (Rabut et al., 2020).

In vivo electrophysiology

Surgical procedures, microdrive construction, and implantation have been described previously (Kvitsiani et al., 2013). Briefly, custom-built microdrives with eight nichrome tetrodes (diameter, 12.7 μm ; Sandvik) and a 50- μm core optic fiber (outer diameter, $65 \pm 2 \mu\text{m}$; Laser Components) were implanted into the right barrel cortex: anteroposterior, -1.4; mediolateral, 3.0; and dorsoventral, 0.75–2.0 mm. Although photostimulation was not applied here, the optic fiber is part of our typical drive design as it also provides mechanical support for the tetrodes. The microdrive contained a moveable shuttle, allowing more precise targeting. The custom-built microdrives were implanted under deep anesthesia. The stereotaxic surgery was followed by a 3-d-long resting period. Tetrodes were lowered (40–120 μm based on the estimated electrode positions and the presence of single units) between recording sessions to collect neuronal activity from different dorsoventral positions. The experiment was repeated two or three times, with a 2-d gap between sessions. Every session started with a 5-min recording without stimulation, defined as basal activity. Automated whisker stimulation epochs lasted for 15 s with 5-Hz frequency, followed by a 40-s-long interstimulus period. Stimulation was repeated 10 times. The entire protocol was repeated with the stimulator positioned close to the whiskers without touching them, to provide a sham stimulation condition that allowed us to exclude possible contaminations from electric noise from the stimulator circuit in our recordings. Next, manual whisker stimulation was applied (15-s stimulation with 40-s interstimulus period, repeated two times). Finally, changes in neuronal firing were measured during a 2-min-long hypercapnic challenge, by inhalation of a 10% CO_2 containing air mixture (21.1% O_2 and 68.9% N_2) under normoxic conditions. Data acquisition was conducted with an Open Ephys (open source data acquisition system, hiv4) board, synchronized with the electromechanical whisker stimulator through a pulse generator (PulsePal 1102; Sanworks; Siegle et al., 2017). Data analysis was performed in Matlab R2016a (MathWorks). Spike sorting was carried out using MClust 3.5 (A.D. Redish). Only neurons with isolation distance >20 and L-ratio <0.15 (a cluster quality measure based on Mahalanobis-distance; Schmitzer-Torbert et al., 2005) were included.

Primary microglial cell cultures

Primary cultures of astroglial cells were prepared from neonatal mouse brains, as described earlier (Kornyei et al., 2005). In

brief, meninges were removed from postnatal day 0–2 whole brains and tissues were chopped. The tissue pieces were digested with 0.05% wt/vol trypsin and 0.5 mg/ml DNase I (#T4549, #DN25; Sigma-Aldrich) in PBS for 10 min at RT. Cells were then plated onto plastic surfaces coated with poly-L-lysine (#P1524; Sigma-Aldrich) at a cell density of $3\text{--}4 \times 10^5$ cell/ cm^2 . The cultures were grown in minimal essential medium (#21090022; Thermo Fisher Scientific) supplemented with 10% FBS (#FB-1090; BioSera), 4 mM glutamine (#G3126; Sigma-Aldrich), and 40 $\mu\text{g}/\text{ml}$ gentamycin (Sandoz). The culture medium was changed twice a week. For the hypoxia/hypercapnia experiments, the primary cultures were passaged and plated at 1.5×10^5 cell/ cm^2 density into poly-L-lysine-coated 48-well plates and used within 96 h. Astrocytes no older than 6–8 days in vitro were used. Primary microglia cells were isolated from astroglia/microglia mixed cultures derived from the whole brains of C57BL/6J newborn mouse pups. Microglia isolation was performed between days 21 and 28 of culture maintenance, by mild trypsinization (Saura et al., 2003). For the in vitro hypoxia and hypercapnia experiments, the isolated cells were seeded at 1.5×10^5 cell/ cm^2 density into poly-L-lysine-coated 48-well plates and used within 48 h.

Primary microglia cell cultures and calcium imaging

Primary microglia cells were isolated from astroglia/microglia mixed cultures (described above) derived from the whole brains of MicroDREADD^{Dq} newborn mouse pups. Half of the mixed cultures were treated repeatedly with 2 μM 4-hydroxy TMX (#H6278; Sigma-Aldrich) for 1 wk before microglia isolation, which was performed between days 21 and 28 of culture maintenance, by mild trypsinization (Saura et al., 2003). The cells were seeded onto poly-L-lysine-coated glass coverslips at cell density of 40,000 cell/ cm^2 and used for imaging within 2–3 days. Phase-contrast time-lapse images to assess microglia process motility were captured on a Zeiss Axiovert 200M microscope at 20 \times magnification (20 \times Plan-Neofluar Ph2 objective), with a frame rate of 0.2 fps. For calcium imaging, the cells were loaded with 1 μM Oregon Green 488 BAPTA-1 AM (#O6807; Invitrogen) or 5 μM Calbryte 590 AM (#20701; AAT Bioquest) dyes in the presence of 2,000 \times Pluronic F-127 (#P6866; Invitrogen) or 100 \times PowerLoad Concentrate (#P10020; Invitrogen) for 30 min at RT. During imaging, the cells were perfused with ACSF (125 mM NaCl, 2.5 mM KCl, 8 mM NaHCO_3 , 1 mM MgCl_2 , 2 mM CaCl_2 , 20 mM Hepes acid, and 10 mM glucose) with a flow rate of 1 ml/min at RT. In some experiments, no perfusion was used. The cells were treated by DREADD agonists CNO (1 μM or 100 nM; #6329; Bio-Techne Corp) or C21 (1 μM ; #HB6124; HelloBio). In experiments related to Fig. S2, the cultures were repeatedly treated with 1 μM C21 for 1 min, 10 min apart, followed by a single application of 10 μM ATP. Calcium imaging was performed either on a Nikon AIR confocal laser-scanning system built on a Ti-E inverted microscope, at 60 \times magnification (60 \times Plan Apo VC WI objective, NA = 1.2), with a frame rate of 20 fps, or on a Nikon Ti2 microscope equipped with a CoolLed pE-4000 illumination system and a Hamamatsu ORCA-Flash 4.0 camera, at 40 \times magnification (40 \times Apo WI λS objective, NA = 1.25), with a frame rate of 2 fps. Signal extraction

from the time-lapse series was computed in Fiji (ImageJ; National Institutes of Health [NIH]), and the data were analyzed on Clampfit (pClamp10 suite; Molecular Devices). Statistics were calculated with GraphPad Prism 8.4.3.

Induction of hypercapnia in vivo

Hypercapnia was induced by inhalation of a 10% CO₂-containing air mixture (21.1% O₂ and 68.9% N₂) for 2 min under normoxic conditions under mild ketamine-medetomidine (i.p. 30 to 0.1 mg/kg) sedation, followed by a 2-min-long posthypercapnic imaging period. In a group of control and microglia-depleted mice, before the hypercapnic challenge, 0.01 μg/g atipamezole (Revertor, 5 mg/ml; CP-Pharma) was administered i.p. to withdraw α-2-agonistic effects of medetomidine. 3–5 min were allowed to get the effect of atipamezole established, before recording baseline CBF and induction of hypercapnia.

Acute slice hypercapnia experiment and cGMP immunolabeling

Mice were deeply anesthetized with isoflurane ($n = 3$) and decapitated, brains were removed, and 300-μm-thick horizontal hippocampal slices were cut on vibratome (VT1200S; Leica). Slices were placed into an interface-type incubation chamber that contained standard ACSF at 35°C that gradually cooled down to RT. Slices were preincubated for 20 min with 1 ml of modified ACSF (mACSF) containing 1 mM 3-isobutyl-1-methylxanthine, 10 μM BAY 73-6691 phosphodiesterase inhibitors (to avoid cGMP hydrolysis), and 0.2 mM L-arginine (the substrate of NOS). L-arginine (0.2 mM) alone had no effect on NOS activity and cGMP levels (Garthwaite et al., 1989). For selective blockade of the microglial P2Y₁₂R, 2 μM PSB 0739 (in mACSF) was used. After preincubation in mACSF or mACSF + PSB, slices were gradually subjected to hypercapnia by elevating the CO₂ level from 5% to 14.6% with bubbling. 200 μM SNP (NO donor) was used as a positive control. After 15-min hypercapnia, the slices were immediately fixed with ice-cold 4% paraformaldehyde for 48 h at 4°C. After washing with 0.1 M PB, slices were embedded to 4% agar and 50-μm-thick vibratome (VT1200S; Leica) sections were cut followed by an immunofluorescent labeling. Sections were incubated in the following primary antibody mixture: sheep anti-cGMP (1:4,000; (de Vente and Steinbusch, 1997), rat anti-CD13 (1:500; MCA2183EL; Bio-Rad), biotinylated tomato Lectin (1:500; B-1175; Vectorlabs), and rabbit anti-P2Y₁₂R (1:2,000, 55043A; AnaSpec) diluted in PBS for 48 h at 4°C. After subsequent washes in PBS, sections were incubated in a mixture of corresponding secondary antibodies (all from Jackson ImmunoResearch): donkey anti-sheep Alexa Fluor 488 (1:500; 713-546-147), donkey anti-rat Alexa Fluor 647 (1:500; 712-606-153), streptavidin Dylight405 (1:500; 016-470-084), and donkey anti-rabbit Alexa Fluor 594 (1:500; 711-586-152) diluted in PBS. Sections were mounted onto glass slides, coverslipped with Slowfade Diamond antifade mountant (S36972; RI: 1.52; Invitrogen) and Menzel-Glaser coverslip (#1). All steps were performed below 4°C. Fluorescent images were acquired using a Nikon Eclipse Ti-E inverted microscope (Nikon Instruments Europe B.V.), with a Plan Apochromat VC 20× objective (NA 0.75) and an AIR laser confocal system; scanning was done in line serial

mode, and pixel size was 0.31 μm. Image stacks were obtained with NIS-Elements AR. 3-Isobutyl-1-methylxanthine, BAY 73-6691 (1-(2-chlorophenyl)-6-[(2R)-3,3,3-trifluoro-2-methylpropyl]-1,5-dihydro-4H-pyrazolo[3,4-d]pyrimidine-4-one), L-arginine, and SNP were purchased from Sigma-Aldrich and PSB0739 from Tocris.

Simultaneous measurement of CBF and brain pH during hypercapnia

Electrophysiological variables (DC potential, brain pH) and local CBF (by laser Doppler) were simultaneously monitored after craniotomy using ion-sensitive microelectrodes connected to a custom-made dual-channel high-input impedance electrometer (including AD549LH; Analog Devices) via Ag/AgCl leads and associated filter modules (NL106 and NL125; NeuroLog System; Digitimer). Ion-sensitive microelectrodes were prepared according to Voipio and Kaila (1993). In each experiment, a pH-sensitive microelectrode was lowered into the cortex with a micromanipulator, together with another glass capillary microelectrode (tip diameter, 20 μm) filled with saline to serve as reference. The tips of the two electrodes were positioned as near as possible. The reference electrode acquired slow cortical or DC potential. An Ag/AgCl electrode was implanted under the skin of the animal's neck to be used as common ground. The voltage signal recorded by the reference electrode was subtracted from that of the pH-sensitive microelectrode by dedicated differential amplifiers and associated filter modules (NL106 and NL125; NeuroLog System; Digitimer), which yielded potential variations related to changes in H⁺ ion concentration. The recorded signals were then forwarded to an analogue-to-digital converter (MP 150; Biopac Systems). Electric signals were continuously acquired at a sampling frequency of 1 kHz using the software AcqKnowledge 4.2.0 (Biopac Systems). Extracellular pH changes were expressed in millivolts to be translated into pH units off-line, using least squares linear regression. The laser-Doppler flow signal was digitized and displayed together with the DC potential and pH signals (MP 150 and AcqKnowledge 4.2.0; Biopac Systems). Surgical preparations were done under 1.5–2% isoflurane, and pH and laser-Doppler flow measurements were performed under medetomidine anesthesia (initiation: i.p. 0.5 mg/kg, repeated 5 min later for maintenance) in a Faraday cage. After 15-min baseline acquisition, 2 min hypercapnia was imposed by CO₂-enriched gas inhalation (9.7% CO₂, 21% O₂ in N₂; Messer) at spontaneous respiration, which was repeated after a 5-min resting period.

Primary endothelial cells

Primary endothelial cultures were prepared from 6–8-wk-old C57BL/6J mouse brains as described earlier (Deli et al., 2003), now performed with modifications (Lenart et al., 2015). In brief, mouse forebrains were collected to PBS, and the meninges were removed using sterile chromatography paper. The tissue was cut into small pieces by scalpels and was enzymatically digested in a mixture of Collagenase II (CLS2, 1 mg/ml; #C6885; Sigma-Aldrich) and DNase I (0.025 mg/ml; ~50 U, #D4513; Sigma-Aldrich) in DMEM-F12 (#10-103-CV; Corning) for 55 min at 37°C. Using a 20% BSA (#A7906; Sigma-Aldrich, in DMEM-F12)

gradient (1,000 *g*, 20 min; three times), microvessels were separated from the myelin. The collected microvessels were further digested using a mixture of Collagenase/Dispase (1 mg/ml; #11097113001; Sigma-Aldrich) and DNase I (0.038 mg/ml; ~75 U; #D4513; Sigma-Aldrich) for 35 min at 37°C. Digested cerebral microvessels were washed three times with DMEM-F12, then seeded to plates coated with Collagen type I (#354236; Corning). During the first 4 d, puromycin (Perriere et al., 2005; Perriere et al., 2007; 4 µg/ml, #P7255; Sigma-Aldrich) selection was applied in the primary medium (15% PDS [#60-00-850; First Link] for seeding, 10% for cultivation, 1 ng/ml bFGF [#F0291; Sigma-Aldrich], 100 µg/ml heparin [#H3149; Sigma-Aldrich], 100× ITS [#41400045; Gibco], and 4 µg/ml puromycin in DMEM-F12) to selectively eliminate non-P-gp-expressing cells. After reaching confluency in 5–6 d, the cells were passaged to 48-well plates coated with Collagen type IV (100 µg/ml; #C5533; Sigma-Aldrich) and fibronectin (25 µg/ml; #F1141; Sigma-Aldrich) at a cell density of 15,000 cells/well and used for *in vitro* hypoxia or hypercapnia experiments in Passage 1.

In vitro hypoxia and hypercapnia

Cytation 5 Cell Imaging Multi-Mode Reader (BioTek) equipped with O₂/CO₂ gas controllers was used to maintain 1% O₂/5% CO₂/94% N₂ (hypoxia) or 15% CO₂/85% air (hypercapnia) levels at 37°C. Endothelial or astroglial cells grown in 48-well plates to confluency or microglia were placed into the reading chamber of the instrument for 5 min (hypercapnia) or 10 min (hypoxia), after taking the lids off. To avoid medium change-induced release events, cell culture medium was replaced with 400 µl complete fresh medium 16 h before the onset of the experiments. To follow the build-up of hypoxia at the cellular level, some cultures were loaded with 5 µM Image-iT Green Hypoxia Reagent (#I14834; Invitrogen) for 30 min at 37°C. The Hypoxia Reagent begins to fluoresce when atmospheric oxygen levels drop below 5%. Fluorescent images taken with Cytation5 (10× magnification) at 0/10 min were analyzed with Fiji software (v1.53; NIH), measuring mean gray values in 10 × 10-pixel ROIs of *n* = 50 individual cells from three independent experiments. Changes in medium pH during hypercapnia were measured by Phenol Red absorbance at 415 and 560 nm using the Cytation 5 Multi-Mode Reader (BioTek; Michl et al., 2019). Measurements were taken from 400 µl complete cell culture media in 48-well plates at 37°C (*n* = 10). The ratios of the 415- and 560-nm peaks were analyzed against a calibration curve obtained from 10 mg/liter phenol red and 10% FBS containing PBS formulations at different pH, in the range of pH 5.5–8. Changes in the intracellular pH during hypercapnia were determined by fluorescence intensity readings of glial cells labeled with pHrodo Green AM (#P35373; Invitrogen) on a Cytation 5 Multi-Mode Reader (*n* = 4). Intracellular pH calibration was performed by incubating the pHrodo Green AM-labeled cells in ACSF set to different pH values of pH 5.5–7.5 and supplemented with 10 µM nigericin and 10 µM valinomycin (#431; #3373; Bio-Techne Corp.) for 5 min.

Quantification of nucleotides and nucleoside

Released concentrations of adenine nucleotides (ATP, ADP, and AMP) and adenosine (Ado) from culture media and tissue

homogenates were determined using HPLC by Shimadzu LC-20 AD Analytical System using UV detection (Agilent 1100 VW set at 253 nm). Concentrations were calculated by a two-point calibration curve using internal standard method. The data (*n* = 4 or 5 in each group) are expressed as nanomoles per milliliter. Briefly, the medium (400 µl) was transferred into a cold Eppendorf tube that contained 50 µl of 0.1 M perchloric acid with 10 µM theophylline (as an internal standard) solution, then samples were centrifuged (at 3,510 *g* for 10 min at 0–4°C) and the supernatants were kept at –20°C until analysis. The weighed frozen tissue was homogenized in the same solution as the media, and the precipitated protein content was removed by centrifugation at 3,510 *g* for 10 min at 4°C. The pellet was saved for protein measurement according to Lowry et al. (1951). A 4-M K₂HPO₄ solution was used to neutralize the supernatant, and the centrifugation step was repeated. The extracted purines were kept at –20°C until analysis. Online solid phase extraction coupled to the column-switching technique was applied to quantification of the nucleotide content of samples. HPLC separation was performed by Shimadzu LC-20 AD Analytical System using UV (Agilent 1100 VW set at 253 nm) detection. The phenyl-hexyl packed (7.5 × 2.1-mm) column was used for online sample enrichment and the separation was completed by coupling the analytical C-18 (150 × 2.1-mm) column. The flow rate of the mobile phases (phase A, 10 mM potassium phosphate buffer with 0.25 mM EDTA; phase B contained additional components such as 0.45 mM octane sulphonyl acid sodium salt, 8% acetonitrile [vol/vol], and 2% methanol [vol/vol], pH 5.55) was 350 or 450 µl/min, respectively, in a step gradient application (Baranyi et al., 2006). The sample enrichment flow rate of buffer A was 300 µl/min during 4 min, and the total runtime was 55 min. Concentrations of the homogenates were calculated by a two-point calibration curve using internal standard method. The data (*n* = 4 or 5 in each group) are expressed as picomoles per milligram protein or nanomoles per milligram.

Blood gas analysis

Arterial blood from the femoral artery under ketamine-medetomidine anesthesia (30 to 0.1 mg/kg ± 0.1 µg/g atipamezole) was sampled to glass capillaries and measured with a blood gas analyzer (ABL90 FLEX PLUS; Radiometer Medical) to determine arterial blood gas tensions (pO₂, pCO₂) and pH.

Repeated, transient CCAo

Transient, repeated unilateral CCAo was performed to induce hypoperfusion without causing ischemia or cellular injury to the brain. The CCA was temporarily pulled away with a silk suture for 5 min, followed by a 5-min-long reperfusion period. The protocol consisted of repeating these steps three times (3× CCAo) on anesthetized (ketamine-xylazine, i.p. 100 to 10 mg/kg dissolved in 0.9% saline) mice. During CBF measurements, the core temperature of mice was maintained at 37 ± 0.5°C using a homeothermic blanket.

Elimination of microglia or PVMs

C57BL/6J mice were fed a chow diet containing the CSF1R inhibitor, PLX5622 (1,200 mg PLX5622 in 1 kg chow; Plexxikon) to

eliminate microglia from the brain (Szalay et al., 2016), or with control diet for 3 wk. PVMs were depleted by a single dose of clodronate-containing liposomes (70 $\mu\text{g}/\text{mouse}$ in 10- μl volume; #F70101C-N-2; FormuMax Scientific) injected into the left ventricle (ICV) as described earlier (Faraco et al., 2016). 3 d later, at maximal efficacy of depletion, LSCI was carried out.

Quantitative analysis

All quantitative analyses were done in a blinded manner. For the measurements of microglial process coverage of endothelial surface or pericytes, microglial process coverage was measured on confocal Z-stacks acquired with a step size of 300 nm. On single-channel images, lectin-positive vessels were selected randomly. The surface of these vessels was calculated by measuring their circumference on every section multiplied by section thickness. The length of microglial process contacts was measured likewise. Continuous capillary segments ($<6 \mu\text{m}$) were also randomly chosen, and the presence of microglial process contacts was examined. All labeled and identified pericytes (PDGFR β -positive) were counted when the whole cell body was located within the Z-stack. 3D reconstruction of CLSM and two-photon imaging stacks was performed using the IMOD software package (Kremer et al., 1996). TOM20 fluorescent intensity profiles were analyzed using a semiautomatic method (Fig. S1 d). Confocal stacks with triple immunofluorescent labeling (P2Y12R, TOM20, and Lectin) were collected. The image planes containing the largest diameter of longitudinal or cross-cut vessels were used to trace the outer membrane of endothelial cells based on the Lectin labeling. This contour was then expanded and narrowed by 0.5 μm to get an extracellular and an intracellular line, respectively. The intensity of fluorescent labeling was analyzed along these lines (TOM20 intensity along the intracellular, P2Y12R labeling along the extracellular line). After normalizing and scaling, microglial contacts were identified along the membrane of the endothelial cell, where microglial fluorescent intensity was over 20% of the maximal value, for at least along a 500-nm-long continuous segment. Then the contact area was extended 500 nm on both sides, and TOM20 fluorescent intensity within these areas was measured for contact value. TOM20 fluorescent intensity outside these identified contacts was considered noncontact.

For the analysis of GFAP⁺ astroglial cell body contact frequency, CLSM stacks with double immunofluorescent labeling (GFAP and P2Y12R) were acquired from mouse cerebral cortex. All labeled and identified astrocytes were counted when the whole cell body was located within the Z-stack. To assess microglia process motility, baseline (28 min) and after 3 \times CCAo (49 min) two-photon image sequences were exported from MES software v.5.3560 (Femtonics) and analyzed using Fiji (version 2.0.0; NIH). The acquired hyperstacks were motion corrected using the StackReg plugin, then individual perivascular microglia processes (30 processes/image/plane) were tracked using the Manual Tracking plugin of Fiji. Based on the obtained XYZ coordinates, process motility speed was calculated. To study the effects of 3 \times CCAo on microglial morphology, 3-3 C57BL/6J mice were randomized into two groups: CCAo or sham surgery. 24 h after 3 \times CCAo, mice were transcardially perfused

and processed for automated microglial morphology analysis. In both cases, 100- μm -thick sections with microglia (Iba1) and cell nuclei (DAPI) labeling were imaged with CLSM (0.2 $\mu\text{m}/\text{pixel}$, Z-step of 0.4 μm). Obtained confocal stacks were processed with the Microglia Morphology Quantification Tool (Heindl et al., 2018). For LSCI recordings, venous sinuses were excluded from the analysis. LSCI generates relative perfusion values (arbitrary units); therefore, CBF was expressed as percentage change over baseline values in the 3 \times CCAo experiments. For the CCAo occlusion experiments, a 1-min long period (typically 250 datapoints), recorded at the beginning of the imaging session, was averaged and considered as baseline. Then, every occlusion and reperfusion event was normalized to baseline. To assess the plasticity of the cerebrovasculature in response to repeated hypoperfusion, normalized occlusion or reperfusion events were averaged and compared between experimental groups. To demonstrate the CBF kinetics of individual animals, every 20th image was extracted, and CBF values were presented on a scatter plot (Fig. S4 b). Quantification of P2Y12R immunostaining in control and microglia-depleted tissues or P2Y12R and CD206 immunostaining in control and clodronate-treated mice were performed in at least three randomly selected fields of view within the cortex on three different coronal planes in each mouse. Data obtained from every mouse brain were averaged and compared between experimental groups.

To investigate microglial actions on hypercapnic vasodilation, two-photon image sequences were exported from the MESc software v.3.5.6.9395 (Femtonics). After motion correction using the StackReg plugin of Fiji, the extent of vasodilation was measured and expressed as percentage of baseline at maximal vasodilation using Fiji. Obtained data were averaged and compared between control and microglia-depleted or between CX3CR1^{GFP/+} and CX3CR1^{GFP/+} \times P2Y12R KO mice. The hypercapnia-evoked CBF responses (2 min long) were normalized to the baseline, then maximum values of individual responses were averaged per animal and compared between control and microglia-depleted groups. For the analysis of cGMP fluorescence, a systematic random sampling of parenchymal vessels based on Lectin staining was performed. These vessel segments were numbered, and their lumen diameter was measured. This was followed by masking the CD13⁺ profiles of these vessels, and automated cGMP intensity measurement was performed within these masks. Measurements were done using ImageJ software. Concentrations of released cellular purine nucleotides in response to hypoxia or hypercapnia were calculated by a two-point calibration curve, using internal standard method. The obtained values were averaged and compared with baseline ones.

For neurovascular coupling experiments (manual and electromechanical whisker stimulations) the stimulus-evoked responses were normalized to baseline and were expressed as CBF increase (% change). The evoked CBF responses were averaged per mouse. The magnitude of evoked CBF responses was compared between experimental groups. Before and after L-NAME injection, whiskers were stimulated, and the difference between the two sets of stimulations was analyzed and compared between the experimental groups. GCaMP6s signals of individual

neurons were collected with MESC software v.3.5.6.9395 (Femtonics) and imported into the MES software v.5.3560 (Femtonics) curve analysis module. The individual cellular $[Ca^{2+}]_i$ traces were normalized to the baseline GCaMP6s signal, and data were expressed as relative fluorescence intensity change ($\Delta F/F$). Then area under the curve (AUC) was calculated for each response, and AUC values were compared between experimental groups. During electrophysiological assessment, the baseline frequency of individual units was determined by averaging a 5-min-long period at the beginning of registration, when whisker stimulation was not applied. Only those units were selected for further analysis, which responded to electromechanical stimulations. Then the stimulus-evoked responses were corrected to baseline frequencies (called as baseline-corrected response frequency), and the magnitude of responses was compared between experimental groups. Signal extraction from the microglial $[Ca^{2+}]_i$ time-lapse series in response to ATP treatment was computed in Fiji. In brief, the mean fluorescence intensity values were determined in $10 \times 10\text{-}\mu\text{m}$ ROIs (each representing an individual cell) and were used to calculate dF/F values ($dF/F = [F - F_0]/F_0$, where F_0 is the average baseline fluorescence in a 300-s time window before drug application and F is the background-corrected fluorescence intensity value at a given time point). The data were further analyzed with Clampfit software (pClamp10 suite; Molecular Devices), manually determining the peak time and amplitude parameters and using the built-in functions to calculate peak amplitude, half width, and peak area.

Statistical analysis

Animals were randomized for in vivo experiments using GraphPad Random Number Generator. Sample size was determined by a priori power calculation using G^* , Power 3.1.9.2 with mean differences and 20–25% SDs based on pilot studies (power 80%, $\alpha = 0.05$). Data were analyzed by GraphPad Prism 7.0 software, unless stated otherwise. Data were assessed for normal distribution using the D'Agostino–Pearson normality test or the Shapiro–Wilk W test to determine parametric or nonparametric analysis. For comparing two or more groups with normal distribution, unpaired t test with Welch's correction and either one-way ANOVA with Dunnett's multiple comparison test or two-way ANOVA with Tukey's or Sidak's multiple comparison test was used. For unevenly distributed data, the Mann–Whitney U test and either one-way ANOVA with Dunnett's multiple comparison test or two-way ANOVA with Tukey's or Sidak's multiple comparison test was used. Refer to the figure legends and the results section concerning the actual study design. All data needed to evaluate the conclusions in the paper are presented in the paper and in the supplementary material. Additional data related to this paper may be requested from the authors.

Online supplemental material

Fig. S1 presents further details on cellular anatomic interactions of microglia with astrocytes, pericytes, endothelial cells, and immunohistochemical characterization of microglia in CX3CR1^{tdTomato} mice, supporting findings in **Fig. 1**; confirmation for the efficacy of microglia depletion; and associated HMPAO-SPECT and FDG-PET measurements in relation to **Fig. 2**. **Fig. S2**

shows characteristics of in vitro-recorded microglial $[Ca^{2+}]_i$ responses and in vivo morphology changes in response to chemogenetic activation by C21 in connection with data presented in **Fig. 4**. **Fig. S3** depicts in vivo two-photon imaging examples of microglial process dynamics around small capillaries in response to hypercapnia. For characterization of the hypercapnic challenge both in vivo and in vitro, measured blood gas parameters, extra- and intracellular pH values are provided, complementing results in **Figs. 5** and **6**. **Fig. S4** shows the characteristic blood flow changes during CCAo as measured with LSCI in selected ROIs placed over the territory of MCA in line with results of **Figs. 7** and **8**. Effects of hypercapnia or microglial P2Y12R blockade on cGMP fluorescent intensity changes are also presented. Fluorescent intensity changes of Hypoxia Green have also been validated during in vitro hypoxic conditions. **Video 1** demonstrates microglial process dynamics in CX3CR1^{tdTomato} mice corresponding to **Fig. 1 b**. While **Video 8** represents perfusion changes during CCAo, **Video 2** demonstrates the neurovascular coupling response in control and microglia-depleted mice recorded with LSCI. **Video 3** provides in vivo two-photon imaging examples of neuronal $[Ca^{2+}]_i$ responses during whisker stimulation recorded in control and microglia-depleted Thy1-GCaMP6s mice related to **Fig. 3, f and g**. **Videos 4** and **5** display in vitro microglial $[Ca^{2+}]_i$ dynamics and process motility changes in response to treatment with the C21 DREADD agonist corresponding to the results in **Fig. 4**. **Video 6** recorded in CX3CR1^{GFP/+} \times P2Y12R KO and CX3CR1^{GFP/+} mice show vasodilation during hypercapnia depicted in **Fig. 5 j**. **Video 7** displays microglial $[Ca^{2+}]_i$ changes during hypercapnia-induced vasodilation as measured in CX3CR1^{GCaMP5g-tdTomato} mice using in vivo two-photon imaging depicted in **Fig. 5c**. **Video 8** shows the third occlusion-reperfusion period in microglia-depleted and control mice. Table S1 provides information on patient data and the processing of postmortem human brain tissues shown in **Fig. 1**.

Acknowledgments

The authors thank László Barna, Csaba Pongor, and Pál Vági of the Nikon Microscopy Center at the Institute of Experimental Medicine, Hungary, and Auro-Science Consulting, Ltd., for kindly providing microscopy support. We also thank the Medical Gene Technology Unit and the Cell Biology Center at the Institute of Experimental Medicine for their support. fUS imaging was carried out at the ElfUS core facility, part of the IPNP, INSERM 1266 unit, and Université de Paris. The authors are grateful to Plexxikon for providing PLX5622 for these studies. The authors also thank the Department of Pathology, St. Borbála Hospital, Tatabánya, and the Human Brain Research Lab at the Institute of Experimental Medicine (Zsófia Maglóczky) for providing human brain tissue. The authors acknowledge Dóra Gali-Györkei for her excellent technical assistance.

This work was supported with funding from the ERC-CoG 724994 (Á. Dénes), ERC-StG 715043 (B. Hangya), the “Momentum” Program of the Hungarian Academy of Sciences (LP2016-4/2016 to A. Dénes and B. Hangya), “PurinesDx” (B. Sperlágh), and the Hungarian Brain Research Program KTIA_13_NAP-A-I/2 (A. Dénes) and NKFIH KH125294 (B. Hangya). This project has

also received funding from the European Union's Horizon 2020 research and innovation programme under the Marie Skłodowska-Curie grant "ENTRAIN" agreement no. 813294 (A.R. Brás and A. Dénes). K. Szigeti and D. Máthé received support from the European Union's Seventh Framework Programme (FP7/2007–2013) under grant agreements HEALTH-F2-2011-278850 (INMiND) and FP7 HEALTH-305311 (INSERT), the Thematic Excellence Programme of the Ministry of Innovation and Technology of Hungary, the COST Action CA16122 and under grant agreement no. 739593. N. Lénárt, C. Cserép, and K. Szigeti were supported by the János Bolyai Research Scholarship of the Hungarian Academy of Sciences. C. Cserép (UNKP-20-5) and B. Pósfai (UNKP-20-3-II) were supported by the New National Excellence Program of the Ministry for Innovation and Technology. N. Lénárt was supported by the ÚNKP-21-5 New National Excellence Program of the Ministry for Innovation and Technology from the source of the National Research, Development and Innovation Fund. B. Hangya was a member of the FENS-Kavli Network.

Author contributions: E. Császár and N. Lénárt designed and conducted the experiments; E. Császár, N. Lénárt, C. Cserép, Z. Környei, R. Fekete, B. Pósfai, E. Szabadits, A.D. Schwarcz, J.C. Mariani, A. Kliewer, L. Hricisák, M. Baranyi, and Á. Menyhárt performed imaging, light microscopy, histology, and data analysis; C. Cserép designed anatomic experiments and performed electron microscopy; D. Szöllösi and K. Szigeti contributed to SPECT and PET imaging; N. Lénárt, Z. Környei, and A.R. Brás conducted cell culture studies; Á. Menyhárt and E. Farkas designed and performed the CCAo study with brain pH measurements; Z. Lenkei, A. Kliewer, and J.C. Mariani designed and performed fUS measurements; D. Balázsfi, K. Sviatkó, and B. Hangya performed electrophysiology and data analysis and provided intellectual support; B.L. West, Z. Lenkei, Z. Benyó, and E. Farkas contributed reagents and provided intellectual support; M. Baranyi and B. Sperlág performed HPLC analyses and provided intellectual support; A. Dénes devised the study, designed the experiments, provided overall supervision for the project, obtained funding, and wrote the manuscript with input from all authors.

Disclosures: D. Máthé reported grants from European Union H2020 HCEMM-739593 and from NRDIO, Hungary, TKP-BIO-Imaging-2020-4.1.1-TKP2020 during the conduct of the study. D. Máthé is CEO and stakeholder of CROmed Ltd. Z. Lenkei reported personal fees from Iconeus outside the submitted work. No other disclosures were reported.

Submitted: 17 May 2021

Revised: 28 October 2021

Accepted: 3 January 2022

References

Alexander, G.M., S.C. Rogan, A.I. Abbas, B.N. Armbruster, Y. Pei, J.A. Allen, R.J. Nonneman, J. Hartmann, S.S. Moy, M.A. Nicoletis, et al. 2009. Remote control of neuronal activity in transgenic mice expressing evolved G protein-coupled receptors. *Neuron*. 63:27–39. <https://doi.org/10.1016/j.neuron.2009.06.014>.

Apostolova, I., A. Wunder, U. Dirnagl, R. Michel, N. Stemmer, M. Lukas, T. Derlin, B. Gregor-Mamoudou, J. Goldschmidt, W. Brenner, et al. 2012.

Brain perfusion SPECT in the mouse: Normal pattern according to gender and age. *Neuroimage*. 63:1807–1817. <https://doi.org/10.1016/j.neuroimage.2012.08.038>.

Arnold, T., and C. Betsholtz. 2013. The importance of microglia in the development of the vasculature in the central nervous system. *Vasc. Cell*. 5:4. <https://doi.org/10.1186/2045-824x-5-4>.

Attwell, D., A.M. Buchan, S. Charpak, M. Lauritzen, B.A. Macvicar, and E.A. Newman. 2010. Glial and neuronal control of brain blood flow. *Nature*. 468:232–243. <https://doi.org/10.1038/nature09613>.

Badimon, A., H.J. Strasburger, P. Ayata, X. Chen, A. Nair, A. Ikegami, P. Hwang, A.T. Chan, S.M. Graves, J.O. Uweru, et al. 2020. Negative feedback control of neuronal activity by microglia. *Nature*. 586:417–423. <https://doi.org/10.1038/s41586-020-2777-8>.

Baranyi, M., E. Milusheva, E.S. Vizi, and B. Sperlág. 2006. Chromatographic analysis of dopamine metabolism in a Parkinsonian model. *J. Chromatography. A*. 1120:13–20. <https://doi.org/10.1016/j.chroma.2006.03.018>.

Benyo, Z., E. Ruisanchez, M. Leszl-Ishiguro, P. Sandor, and P. Pacher. 2016. Endocannabinoids in cerebrovascular regulation. *Am. J. Physiol. Heart Circ. Physiol.* 310:H785–H801. <https://doi.org/10.1152/ajpheart.00571.2015>.

Bisht, K., K.A. Okojie, K. Sharma, D.H. Lentferink, Y.Y. Sun, H.R. Chen, J.O. Uweru, S. Amancherla, Z. Calcuttawala, A.B. Campos-Salazar, et al. 2021. Capillary-associated microglia regulate vascular structure and function through PANX1-P2RY12 coupling in mice. *Nat. Commun.* 12: 5289. <https://doi.org/10.1038/s41467-021-25590-8>.

Butovsky, O., M.P. Jedrychowski, C.S. Moore, R. Cialic, A.J. Lanser, G. Gabriely, T. Koeglspenger, B. Dake, P.M. Wu, C.E. Doykan, et al. 2014. Identification of a unique TGF-beta-dependent molecular and functional signature in microglia. *Nat. Neurosci.* 17:131–143. <https://doi.org/10.1038/nn.3599>.

Colonna, M., and O. Butovsky. 2017. Microglia function in the central nervous system during health and neurodegeneration. *Annu. Rev. Immunol.* 35: 441–468. <https://doi.org/10.1146/annurev-immunol-051116-052358>.

Cserép, C., B. Pósfai, N. Lenart, R. Fekete, Z.I. Laszlo, Z. Lele, B. Orsolits, G. Molnar, S. Heindl, A.D. Schwarcz, et al. 2019. Microglia monitor and protect neuronal function via specialized somatic purinergic junctions. *Science*. 367:528–537.

Dana, H., T.W. Chen, A. Hu, B.C. Shields, C. Guo, L.L. Looger, D.S. Kim, and K. Svoboda. 2014. Thyl-GCaMP6 transgenic mice for neuronal population imaging in vivo. *PLoS One*. 9:e108697. <https://doi.org/10.1371/journal.pone.0108697>.

Davalos, D., J. Grutzendler, G. Yang, J.V. Kim, Y. Zuo, S. Jung, D.R. Littman, M.L. Dustin, and W.B. Gan. 2005. ATP mediates rapid microglial response to local brain injury in vivo. *Nat. Neurosci.* 8:752–758. <https://doi.org/10.1038/nn1472>.

Davalos, D., J.K. Ryu, M. Merlini, K.M. Baeten, N. Le Moan, M.A. Petersen, T.J. Deerinck, D.S. Smirnov, C. Bedard, H. Hakozaki, et al. 2012. Fibrinogen-induced perivascular microglial clustering is required for the development of axonal damage in neuroinflammation. *Nat. Commun.* 3:1227. <https://doi.org/10.1038/ncomms2230>.

Deli, M.A., C.S. Abraham, M. Niwa, and A. Falus. 2003. N,N-diethyl-2-[4-(phenylmethyl)phenoxy]ethanamine increases the permeability of primary mouse cerebral endothelial cell monolayers. *Inflamm. Res.* 52 Suppl 1:S39–S40. <https://doi.org/10.1007/s000110300045>.

Demene, C., T. Deffieux, M. Pernot, B.F. Osmanski, V. Biran, J.L. Gennisson, L.A. Sieu, A. Bergel, S. Franqui, J.M. Correas, et al. 2015. Spatiotemporal clutter filtering of ultrafast ultrasound data highly increases Doppler and fUltrasound sensitivity. *IEEE Trans. Med. Imag.* 34:2271–2285. <https://doi.org/10.1109/TMI.2015.2428634>.

Dixon, M.A., U. Greferath, E.L. Fletcher, and A.I. Jobling. 2021. The contribution of microglia to the development and maturation of the visual system. *Front Cell Neurosci.* 15:659843. <https://doi.org/10.3389/fncel.2021.659843>.

Dudvarski Stankovic, N., M. Teodorczyk, R. Ploen, F. Zipp, and M.H.H. Schmidt. 2016. Microglia-blood vessel interactions: A double-edged sword in brain pathologies. *Acta Neuropathol.* 131:347–363. <https://doi.org/10.1007/s00401-015-1524-y>.

Dunn, A.K. 2012. Laser speckle contrast imaging of cerebral blood flow. *Ann. Biomed. Eng.* 40:367–377. <https://doi.org/10.1007/s10439-011-0469-0>.

Elmore, M.R., A.R. Najafi, M.A. Koike, N.N. Dagher, E.E. Spangenberg, R.A. Rice, M. Kitazawa, B. Matusow, H. Nguyen, B.L. West, and K.N. Green. 2014. Colony-stimulating factor 1 receptor signaling is necessary for microglia viability, unmasking a microglia progenitor cell in the adult brain. *Neuron*. 82:380–397. <https://doi.org/10.1016/j.neuron.2014.02.040>.

- Engelhardt, B., and L. Sorokin. 2009. The blood-brain and the blood-cerebrospinal fluid barriers: Function and dysfunction. *Semin. Immunopathol.* 31:497–511. <https://doi.org/10.1007/s00281-009-0177-0>.
- Eyo, U., and M.E. Dailey. 2012. Effects of oxygen-glucose deprivation on microglial mobility and viability in developing mouse hippocampal tissues. *Glia.* 60:1747–1760. <https://doi.org/10.1002/glia.22394>.
- Faraci, F.M., R.J. Taugher, C. Lynch, R. Fan, S. Gupta, and J.A. Wemmie. 2019. Acid-sensing ion channels: Novel mediators of cerebral vascular responses. *Circ. Res.* 125:907–920. <https://doi.org/10.1161/CIRCRESAHA.119.315024>.
- Faraco, G., Y. Sugiyama, D. Lane, L. Garcia-Bonilla, H. Chang, M.M. Santisteban, G. Racchumi, M. Murphy, N. Van Rooijen, J. Anrather, and C. Iadecola. 2016. Perivascular macrophages mediate the neurovascular and cognitive dysfunction associated with hypertension. *J. Clin. Invest.* 126:4674–4689. <https://doi.org/10.1172/JCI86950>.
- Fekete, R., C. Cserep, N. Lenart, K. Toth, B. Orsolits, B. Martinecz, E. Mehes, B. Szabo, V. Nemeth, B. Gonci, et al. 2018. Microglia control the spread of neurotropic virus infection via P2Y12 signalling and recruit monocytes through P2Y12-independent mechanisms. *Acta Neuropathol.* 136:461–482. <https://doi.org/10.1007/s00401-018-1885-0>.
- Ferrier, J., E. Tiran, T. Deffieux, M. Tanter, and Z. Lenkei. 2020. Functional imaging evidence for task-induced deactivation and disconnection of a major default mode network hub in the mouse brain. *Proc. Natl. Acad. Sci. USA.* 117:15270–15280. <https://doi.org/10.1073/pnas.1920475117>.
- Garthwaite, J., G. Garthwaite, R.M.J. Palmer, and S. Moncada. 1989. NMDA receptor activation induces nitric oxide synthesis from arginine in rat brain slices. *Eur. J. Pharmacol.* 172:413–416. [10.1016/0922-4106\(89\)90023-0](https://doi.org/10.1016/0922-4106(89)90023-0).
- Gee, J.M., N.A. Smith, F.R. Fernandez, M.N. Economo, D. Brunert, M. Rothermel, S.C. Morris, A. Talbot, S. Palumbos, J.M. Ichida, et al. 2014. Imaging activity in neurons and glia with a Polr2a-based and cre-dependent GCaMP5G-IRES-tdTomato reporter mouse. *Neuron.* 83:1058–1072. <https://doi.org/10.1016/j.neuron.2014.07.024>.
- Ginhoux, F., M. Greter, M. Leboeuf, S. Nandi, P. See, S. Gokhan, M.F. Mehler, S.J. Conway, L.G. Ng, E.R. Stanley, et al. 2010. Fate mapping analysis reveals that adult microglia derive from primitive macrophages. *Science.* 330:841–845. <https://doi.org/10.1126/science.1194637>.
- Goldmann, T., P. Wieghofer, M.J.C. Jordao, F. Prutek, N. Hagemeyer, K. Frenzel, L. Amann, O. Staszewski, K. Kierdorf, M. Krueger, et al. 2016. Origin, fate and dynamics of macrophages at central nervous system interfaces. *Nat. Immunol.* 17:797–805. <https://doi.org/10.1038/ni.3423>.
- Halder, S.K., and R. Milner. 2019. A critical role for microglia in maintaining vascular integrity in the hypoxic spinal cord. *Proc. Natl. Acad. Sci. USA.* 116:26029–26037. <https://doi.org/10.1073/pnas.1912178116>.
- Hall, C.N., C. Reynell, B. Gesslein, N.B. Hamilton, A. Mishra, B.A. Sutherland, F.M. O'Farrell, A.M. Buchan, M. Lauritzen, and D. Attwell. 2014. Capillary pericytes regulate cerebral blood flow in health and disease. *Nature.* 508:55–60. <https://doi.org/10.1038/nature13165>.
- Hamilton, N.B., D. Attwell, and C.N. Hall. 2010. Pericyte-mediated regulation of capillary diameter: A component of neurovascular coupling in health and disease. *Front. Neuroenergetics.* 2:5. <https://doi.org/10.3389/fnene.2010.00005>.
- Haynes, S.E., G. Hoppel, G. Yang, D. Kurpius, M.E. Dailey, W.B. Gan, and D. Julius. 2006. The P2Y12 receptor regulates microglial activation by extracellular nucleotides. *Nat. Neurosci.* 9:1512–1519. <https://doi.org/10.1038/nn1805>.
- Heindl, S., B. Gesierich, C. Benakis, G. Llovera, M. Duering, and A. Liesz. 2018. Automated morphological analysis of microglia after stroke. *Front. Cell. Neurosci.* 12:106. <https://doi.org/10.3389/fncel.2018.00106>.
- Howarth, C., B. Sutherland, H.B. Choi, C. Martin, B.L. Lind, L. Khennouf, J.M. LeDuc, J.M. Pakan, R.W. Ko, G. Ellis-Davies, et al. 2017. A critical role for astrocytes in hypercapnic vasodilation in brain. *J. Neurosci.* 37:2403–2414. <https://doi.org/10.1523/jneurosci.0005-16.2016>.
- Iadecola, C. 2017. The neurovascular unit coming of age: A journey through neurovascular coupling in health and disease. *Neuron.* 96:17–42. <https://doi.org/10.1016/j.neuron.2017.07.030>.
- Janssen, B.J., T. De Celle, J.J. Debets, A.E. Brouns, M.F. Callahan, and T.L. Smith. 2004. Effects of anesthetics on systemic hemodynamics in mice. *Am. J. Physiol. Heart Circ. Physiol.* 287:H1618–H1624. <https://doi.org/10.1152/ajpheart.01192.2003>.
- Jin, Y., K. Sato, A. Tobo, C. Mogi, M. Tobo, N. Murata, S. Ishii, D.S. Im, and F. Okajima. 2014. Inhibition of interleukin-1 β production by extracellular acidification through the TDAG8/cAMP pathway in mouse microglia. *J. Neurochem.* 129:683–695. <https://doi.org/10.1111/jnc.12661>.
- Jolivel, V., F. Bicker, F. Biname, R. Ploen, S. Keller, R. Gollan, B. Jurek, J. Birkenstock, L. Poisa-Beiro, J. Bruttger, et al. 2015. Perivascular microglia promote blood vessel disintegration in the ischemic penumbra. *Acta Neuropathol.* 129:279–295. <https://doi.org/10.1007/s00401-014-1372-1>.
- Kida, S.Y., P.V. Steart, E.T. Zhang, and R.O. Weller. 1993. Perivascular cells act as scavengers in the cerebral perivascular spaces and remain distinct from pericytes, microglia and macrophages. *Acta Neuropathologica.* 85:646–652. <https://doi.org/10.1007/BF00334675>.
- Kim, J.S., M. Kolesnikov, S. Peled-Hajaj, I. Scheyltjens, Y. Xia, S. Trzebanski, Z. Haimon, A. Shemer, A. Lubart, H. Van Hove, et al. 2021. A binary cre transgenic approach dissects microglia and CNS border-associated macrophages. *Immunity.* 54:176–190.e7. <https://doi.org/10.1016/j.immuni.2020.11.007>.
- Kisler, K., A.R. Nelson, A. Montagne, and B.V. Zlokovic. 2017. Cerebral blood flow regulation and neurovascular dysfunction in Alzheimer disease. *Nat. Rev. Neurosci.* 18:419–434. <https://doi.org/10.1038/nrn.2017.48>.
- Kleinberger, G., M. Brendel, E. Mracsok, B. Wefers, L. Groeneweg, X. Xiang, C. Focke, M. Deussing, M. Suarez-Calvet, F. Mazaheri, et al. 2017. The FTD-like syndrome causing TREM2 T66M mutation impairs microglia function, brain perfusion, and glucose metabolism. *EMBO J.* 36:1837–1853. <https://doi.org/10.15252/embj.201796516>.
- Kloner, R.A., K.S. King, and M.G. Harrington. 2018. No-reflow phenomenon in the heart and brain. *Am. J. Physiol. Heart Circ. Physiol.* 315:H550–H562. <https://doi.org/10.1152/ajpheart.00183.2018>.
- Kornyei, Z., V. Szlavik, B. Szabo, E. Gocza, A. Czirok, and E. Madarasz. 2005. Humoral and contact interactions in astroglia/stem cell co-cultures in the course of glia-induced neurogenesis. *Glia.* 49:430–444. <https://doi.org/10.1002/glia.20123>.
- Kremer, J.R., D.N. Mastronarde, and J.R. McIntosh. 1996. Computer visualization of three-dimensional image data using IMOD. *J. Struct. Biol.* 116:71–76. <https://doi.org/10.1006/jsbi.1996.0013>.
- Kremer, J.R., D.N. Mastronarde, and J.R. McIntosh. 1996. Computer visualization of three-dimensional image data using IMOD. *J. Struct. Biol.* 116:71–76. <https://doi.org/10.1006/jsbi.1996.0013>.
- Kvitsiani, D., S. Ranade, B. Hangya, H. Taniguchi, J.Z. Huang, and A. Kepecs. 2013. Distinct behavioural and network correlates of two interneuron types in prefrontal cortex. *Nature.* 498:363–366. <https://doi.org/10.1038/nature12176>.
- Langfelder, A., E. Okonji, D. Deca, W.C. Wei, and M.D. Glitsch. 2015. Extracellular acidosis impairs P2Y receptor-mediated Ca²⁺ signalling and migration of microglia. *Cell Calcium.* 57:247–256. <https://doi.org/10.1016/j.ceca.2015.01.004>.
- Lecrux, C., C.H. Sandoe, S. Neupane, P. Kropf, X. Toussay, X.K. Tong, M. Lacalle-Aurilio, A. Shmuel, and E. Hamel. 2017. Impact of altered cholinergic tones on the neurovascular coupling response to whisker stimulation. *J. Neurosci.* 37:1518–1531. <https://doi.org/10.1523/JNEUROSCI.1784-16.2016>.
- Lenart, N., F.R. Walter, A. Bocsik, P. Santha, M.E. Toth, A. Harazin, A.E. Toth, C. Vizler, Z. Torok, A.M. Pilbat, et al. 2015. Cultured cells of the blood-brain barrier from apolipoprotein B-100 transgenic mice: Effects of oxidized low-density lipoprotein treatment. *Fluids Barriers CNS.* 12:17. <https://doi.org/10.1186/s12987-015-0013-y>.
- Lohman, A.W., M. Billaud, and B.E. Isakson. 2012. Mechanisms of ATP release and signalling in the blood vessel wall. *Cardiovasc. Res.* 95:269–280. <https://doi.org/10.1093/cvr/cvs187>.
- Lou, N., T. Takano, Y. Pei, A.L. Xavier, S.A. Goldman, and M. Nedergaard. 2016. Purinergic receptor P2RY12-dependent microglial closure of the injured blood-brain barrier. *Proc. Natl. Acad. Sci. USA.* 113:1074–1079. <https://doi.org/10.1073/pnas.1520398113>.
- Lowry, O.H., N.J. Rosebrough, A.L. Farr, and R.J. Randall. 1951. Protein measurement with the Folin phenol reagent. *J. Biol. Chem.* 193:265–275.
- Mace, E., G. Montaldo, I. Cohen, M. Baulac, M. Fink, and M. Tanter. 2011. Functional ultrasound imaging of the brain. *Nat. Methods.* 8:662–664. <https://doi.org/10.1038/nmeth.1641>.
- MacVicar, B.A., and E.A. Newman. 2015. Astrocyte regulation of blood flow in the brain. *Cold Spring Harbor Perspect. Biol.* 7:a020388. <https://doi.org/10.1101/cshperspect.a020388>.
- Masuda, T., D. Croom, H. Hida, and S.A. Kirov. 2011. Capillary blood flow around microglial somata determines dynamics of microglial processes in ischemic conditions. *Glia.* 59:1744–1753. <https://doi.org/10.1002/glia.21220>.
- Meng, L., and A.W. Gelb. 2015. Regulation of cerebral autoregulation by carbon dioxide. *Anesthesiology.* 122:196–205. <https://doi.org/10.1097/ALN.0000000000000506>.
- Michl, J., K.C. Park, and P. Swietach. 2019. Evidence-based guidelines for controlling pH in mammalian live-cell culture systems. *Commun. Biol.* 2:144. <https://doi.org/10.1038/s42003-019-0393-7>.

- Nimmerjahn, A., F. Kirchhoff, and F. Helmchen. 2005. Resting microglial cells are highly dynamic surveillants of brain parenchyma in vivo. *Science*. 308:1314–1318. <https://doi.org/10.1126/science.1110647>.
- Nishijima, Y., Y. Akamatsu, S.Y. Yang, C.C. Lee, U. Baran, S. Song, R.K. Wang, T. Tominaga, and J. Liu. 2016. Impaired collateral flow compensation during chronic cerebral hypoperfusion in the type 2 diabetic mice. *Stroke*. 47:3014–3021. <https://doi.org/10.1161/STROKEAHA.116.014882>.
- Pal, E., L. Hricisak, A. Lekai, D. Nagy, A. Fulop, R.G. Erben, S. Varbiro, P. Sandor, and Z. Benyo. 2020. Ablation of vitamin D signaling compromises cerebrovascular adaptation to carotid artery occlusion in mice. *Cells*. 9. <https://doi.org/10.3390/cells9061457>.
- Pelligrino, D.A., F. Vetri, and H.L. Xu. 2011. Purinergic mechanisms in gliovascular coupling. *Semin. Cell Dev. Biol.* 22:229–236. <https://doi.org/10.1016/j.semcdb.2011.02.010>.
- Penna, E., J.M. Mangum, H. Shepherd, V. Martinez-Cerdeno, and S.C. Noctor. 2021. Development of the neuro-immune-vascular plexus in the ventricular zone of the prenatal rat neocortex. *Cereb. Cortex*. 31:2139–2155. <https://doi.org/10.1093/cercor/bhaa351>.
- Perriere, N., P. Demeuse, E. Garcia, A. Regina, M. Debray, J.P. Andreux, P. Couvreur, J.M. Scherrmann, J. Temsamani, P.O. Couraud, et al. 2005. Puromycin-based purification of rat brain capillary endothelial cell cultures. Effect on the expression of blood-brain barrier-specific properties. *J. Neurochem.* 93:279–289. <https://doi.org/10.1111/j.1471-4159.2004.03020.x>.
- Perriere, N., S. Yousif, S. Cazaubon, N. Chaverot, F. Bourasset, S. Cisternino, X. Declèves, S. Hori, T. Terasaki, M. Deli, et al. 2007. A functional in vitro model of rat blood-brain barrier for molecular analysis of efflux transporters. *Brain Res.* 1150:1–13. <https://doi.org/10.1016/j.brainres.2007.02.091>.
- Polycarpou, A., L. Hricisak, A. Iring, D. Safar, E. Ruisanchez, B. Horvath, P. Sandor, and Z. Benyo. 2016. Adaptation of the cerebrocortical circulation to carotid artery occlusion involves blood flow redistribution between cortical regions and is independent of eNOS. *Am. J. Physiol. Heart Circ. Physiol.* 311:H972–H980. <https://doi.org/10.1152/ajpheart.00197.2016>.
- Prinz, M., D. Erny, and N. Hagemeyer. 2017. Ontogeny and homeostasis of CNS myeloid cells. *Nat. Immunol.* 18:385–392. <https://doi.org/10.1038/ni.3703>.
- Prinz, M., and J. Priller. 2014. Microglia and brain macrophages in the molecular age: From origin to neuropsychiatric disease. *Nat. Rev. Neurosci.* 15:300–312. <https://doi.org/10.1038/nrn3722>.
- Rabut, C., J. Ferrier, A. Bertolo, B. Osmanski, X. Mousset, S. Pezet, T. Deffieux, Z. Lenkei, and M. Tanter. 2020. PharmacofUS: Quantification of pharmacologically-induced dynamic changes in brain perfusion and connectivity by functional ultrasound imaging in awake mice. *Neuroimage*. 222:117231. <https://doi.org/10.1016/j.neuroimage.2020.117231>.
- Ransohoff, R.M., and B. Engelhardt. 2012. The anatomical and cellular basis of immune surveillance in the central nervous system. *Nat. Rev. Immunol.* 12:623–635. <https://doi.org/10.1038/nri3265>.
- Saura, J., J.M. Tusell, and J. Serratos. 2003. High-yield isolation of murine microglia by mild trypsinization. *Glia*. 44:183–189. <https://doi.org/10.1002/glia.10274>.
- Schmitzer-Torbert, N., J. Jackson, D. Henze, K. Harris, and A.D. Redish. 2005. Quantitative measures of cluster quality for use in extracellular recordings. *Neuroscience*. 131:1–11. <https://doi.org/10.1016/j.neuroscience.2004.09.066>.
- Siegle, J.H., A.C. Lopez, Y.A. Patel, K. Abramov, S. Ohayon, and J. Voigts. 2017. Open Ephys: An open-source, plugin-based platform for multichannel electrophysiology. *J. Neural. Eng.* 14:045003. <https://doi.org/10.1088/1741-2552/aa5eea>.
- Smyth, L.C.D., J. Rustenhoven, E.L. Scotter, P. Schweder, R.L.M. Faull, T.I.H. Park, and M. Dragunow. 2018. Markers for human brain pericytes and smooth muscle cells. *J. Chem. Neuroanat.* 92:48–60. <https://doi.org/10.1016/j.jchemneu.2018.06.001>.
- Szabadits, E., C. Cserep, A. Szonyi, Y. Fukazawa, R. Shigemoto, M. Watanabe, S. Itohara, T.F. Freund, and G. Nyiri. 2011. NMDA receptors in hippocampal GABAergic synapses and their role in nitric oxide signaling. *J. Neurosci.* 31:5893–5904. <https://doi.org/10.1523/JNEUROSCI.5938-10.2011>.
- Szalay, G., B. Martincz, N. Lenart, Z. Kornyei, B. Orsolits, L. Judak, E. Csaszar, R. Fekete, B.L. West, G. Katona, et al. 2016. Microglia protect against brain injury and their selective elimination dysregulates neuronal network activity after stroke. *Nat. Commun.* 7:11499. <https://doi.org/10.1038/ncomms11499>.
- Tai, Y.F., and P. Piccini. 2004. Applications of positron emission tomography (PET) in neurology. *J. Neurol. Neurosurg. Psychiatr.* 75:669–676. <https://doi.org/10.1136/jnnp.2003.028175>.
- Takano, T., G.F. Tian, W. Peng, N. Lou, W. Libionka, X. Han, and M. Nedergaard. 2006. Astrocyte-mediated control of cerebral blood flow. *Nat. Neurosci.* 9:260–267. <https://doi.org/10.1038/nn1623>.
- Tarantini, S., N.M. Valcarcel-Ares, A. Yabluchanskiy, G.A. Fulop, P. Herteledy, T. Gautam, E. Farkas, A. Perz, P.S. Rabinovitch, W.E. Sonntag, et al. 2018. Treatment with the mitochondrial-targeted antioxidant peptide SS-31 rescues neurovascular coupling responses and cerebrovascular endothelial function and improves cognition in aged mice. *Aging Cell*. 17:e12731. <https://doi.org/10.1111/acer.12731>.
- Thion, M.S., F. Ginhoux, and S. Garel. 2018. Microglia and early brain development: An intimate journey. *Science*. 362:185–189. <https://doi.org/10.1126/science.aat0474>.
- Thompson, K.J., E. Khajehali, S.J. Bradley, J.S. Navarrete, X.P. Huang, S. Slocum, J. Jin, J. Liu, Y. Xiong, R.H.J. Olsen, et al. 2018. DREADD agonist 21 is an effective agonist for muscarinic-based DREADDs in vitro and in vivo. *ACS Pharmacol. Transl. Sci.* 1:61–72. <https://doi.org/10.1021/acspsci.8b00012>.
- Tiran, E., J. Ferrier, T. Deffieux, J.L. Gennisson, S. Pezet, Z. Lenkei, and M. Tanter. 2017. Transcranial functional ultrasound imaging in freely moving awake mice and anesthetized young rats without contrast agent. *Ultrasound Med. Biol.* 43:1679–1689. <https://doi.org/10.1016/j.ultrasmedbio.2017.03.011>.
- Toda, N., K. Ayajiki, and T. Okamura. 2009. Cerebral blood flow regulation by nitric oxide: Recent advances. *Pharmacol. Rev.* 61:62–97. <https://doi.org/10.1124/pr.108.000547>.
- Umpierre, A.D., L.L. Bystrom, Y. Ying, Y.U. Liu, G. Worrell, and L.J. Wu. 2020. Microglial calcium signaling is attuned to neuronal activity in awake mice. *eLife*. 9:e56502. <https://doi.org/10.7554/eLife.56502>.
- de Vente, J., and H.W.M. Steinbusch. 1997. cGMP-Lmmunocytochemistry. In *Neurotransmitter Methods*. Humana Press, New Jersey. pp. 125–144.
- Voipio, J., and K. Kaila. 1993. Interstitial PCO₂ and pH in rat hippocampal slices measured by means of a novel fast CO₂/H⁺-sensitive microelectrode based on a PVC-gelled membrane. *Pflugers Arch.* 423:193–201. <https://doi.org/10.1007/bf00374394>.
- Wolf, S.A., H.W.G.M. Boddeke, and H. Kettenmann. 2017. Microglia in physiology and disease. *Annu. Rev. Physiol.* 79:619–643. <https://doi.org/10.1146/annurev-physiol-022516-034406>.
- Wolters, F.J., H.I. Zonneveld, A. Hofman, A. van der Lugt, P.J. Koudstaal, M.W. Vernooij, and M.A. Ikram. 2017. Cerebral perfusion and the risk of dementia: A population-based study. *Circulation*. 136:719–728. <https://doi.org/10.1161/CIRCULATIONAHA.117.027448>.
- Yang, X., L. Zhao, M.M. Campos, M. Abu-Asab, D. Ortolan, N. Hotaling, K. Bharti, and W.T. Wong. 2020. CSFIR blockade induces macrophage ablation and results in mouse choroidal vascular atrophy and RPE disorganization. *eLife*. 9:e55564. <https://doi.org/10.7554/eLife.55564>.
- Yona, S., K.W. Kim, Y. Wolf, A. Mildner, D. Varol, M. Breker, D. Strauss-Ayali, S. Viukov, M. Guillemins, A. Misharin, et al. 2013. Fate mapping reveals origins and dynamics of monocytes and tissue macrophages under homeostasis. *Immunity*. 38:79–91. <https://doi.org/10.1016/j.immuni.2012.12.001>.
- Yoon, S., M. Zuccarello, and R.M. Rapoport. 2012. pCO₂ and pH regulation of cerebral blood flow. *Front. Physiol.* 3:365. <https://doi.org/10.3389/fphys.2012.00365>.
- Zaharchuk, G., J.B. Mandeville, A.A. Bogdanov Jr., R. Weissleder, B.R. Rosen, and J.J. Marota. 1999. Cerebrovascular dynamics of autoregulation and hypoperfusion. An MRI study of CBF and changes in total and microvascular cerebral blood volume during hemorrhagic hypotension. *Stroke*. 30:2197–2204. discussion 2204–2195. <https://doi.org/10.1161/01.str.30.10.2197>.
- Zhao, X., U.B. Eyo, M. Murugan, and L.J. Wu. 2018. Microglial interactions with the neurovascular system in physiology and pathology. *Dev. Neurobiol.* 78:604–617. <https://doi.org/10.1002/dvne.22576>.
- Zhu, H., D.K. Aryal, R.H. Olsen, D.J. Urban, A. Swearingen, S. Forbes, B.L. Roth, and U. Hochgeschwender. 2016. Cre-dependent DREADD (designer receptors exclusively activated by designer drugs) mice. *Genesis*. 54:439–446. <https://doi.org/10.1002/dvg.22949>.

Supplemental material

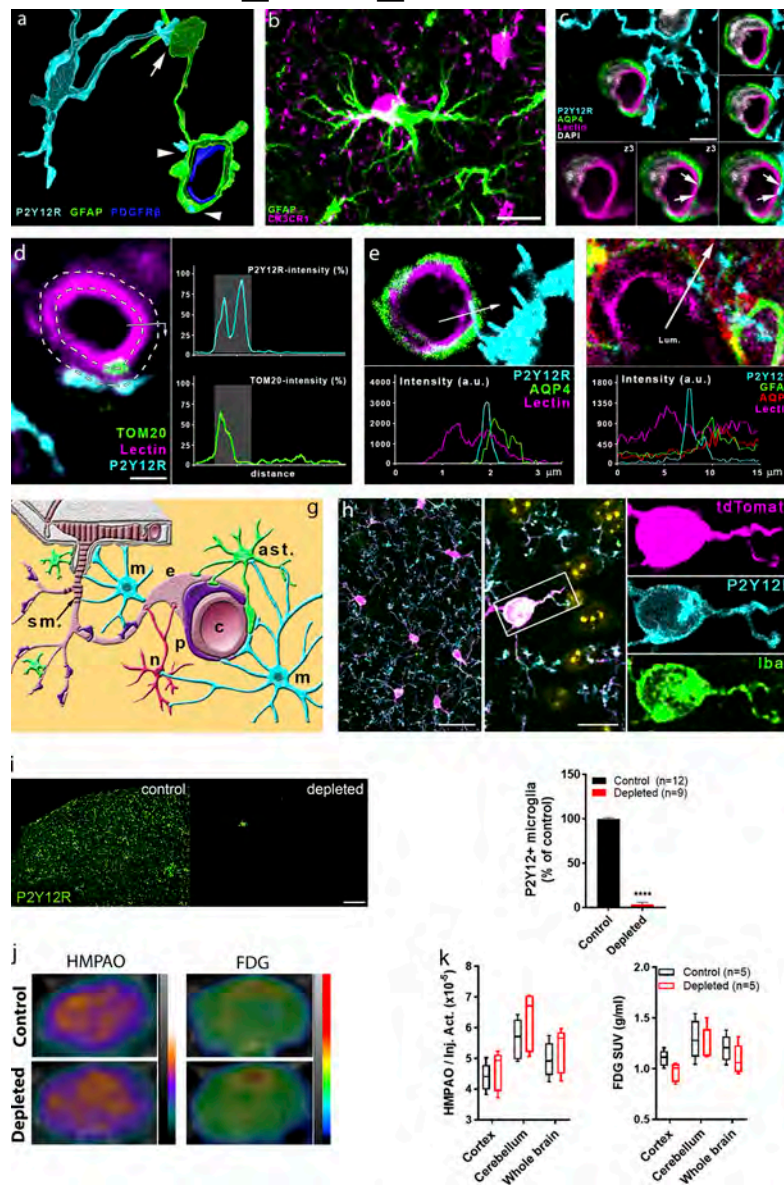


Figure S1. Microglia form direct contacts with cells in the NVU, but microglia depletion does not disrupt cerebral perfusion or metabolism. (a) 3D reconstruction of a high-resolution CLSM Z-stack shows microglia (P2Y12R, cyan) contacting both the cell body of an astrocyte (GFAP labeling, green, arrow) and astrocytic endfeet (arrowheads) ensheathing a capillary. Pericytes are visualized by anti-PDGFR β labeling (blue). (b) Microglia (CX3CR1, magenta) are able to form direct contact by their cell body with astrocytes (GFAP labeling, green) in the cerebral cortex. Scale bar, 10 μ m. (c) CLSM image shows P2Y12R-positive microglial process (cyan) contacting perivascular AQP4-positive astrocyte endfeet (green) and also extends to the endothelial layer (lectin, magenta) where astrocytic coverage is not present (arrows). z1–z3 panels show the contact area on three consecutive confocal sections. Scale bar, 3 μ m. (d) The process of semiautomated unbiased analysis of fluorescent intensity area for the graph presented in Fig. 1 j is depicted. White dashed lines represent the outer and the inner profiles, based on the outline of the endothelial cell. P2Y12R intensity was measured along the outer profile and TOM20 intensity along the inner profile, starting from the arrow. The intensity values are plotted (right) along the perimeter of the vessel. Contact site (marked by the gray column in the plots) was defined automatically. Scale bar, 2 μ m. (e) CLSM image and fluorescent intensity plots show microglial process extending beyond perivascular astrocytic endfeet to interact with the endothelium. The fluorescent intensity profile plot (measured along the 3.5- μ m long white arrow) clearly shows the presence of the microglial process under the astrocytic endfeet. (f) CLSM image and fluorescent intensity plots show microglial processes interacting with GFAP- and AQP4-positive astrocytes in the human brain. The fluorescent intensity profile plot (measured along the 15- μ m-long white arrow) clearly shows the presence of the microglial process between the endothelium and the endfeet of perivascular astrocytes. (g) Schematic summary of contacts formed between microglia (m; cyan) and different cell types of the NVU. Neurons (n; red), astrocytes (ast.; green), pericytes (p; purple), endothelial cells (e; pale crimson), and vascular smooth muscle cells (s.m.; dark crimson) are shown. (h) Characterisation of CX3CR1^{tdTomato} mice. Parenchymal tdTomato-positive cells coexpress Iba1 and P2Y12R in the cerebral cortex. Cell nuclei stained with DAPI appear in yellow pseudocolor in the merged middle image. Scale bars, 25 μ m (left), 10 μ m (middle). (i) Feeding C57BL/6J mice with a diet containing PLX5622 results in an almost complete (97%) elimination of resident microglia as evidenced by the numbers of P2Y12R-positive cells in the cerebral cortex. Scale bar, 100 μ m. $n = 12$ control and $n = 9$ depleted mice per group; ****, $P < 0.0001$ control versus depleted, unpaired t test with Welch's correction. (j and k) HMPAO-SPECT and FDG-PET images of control and microglia-depleted mice. Proportion of measured and injected HMPAO activity (Inj. Act.) and standard uptake values (SUVs) of FDG are shown. Atlas-based ROI analysis (j) shows no significant differences between the normalized regional uptake values (k) of the two groups. $n = 5$ and 5 mice. Data are expressed as mean \pm SEM.

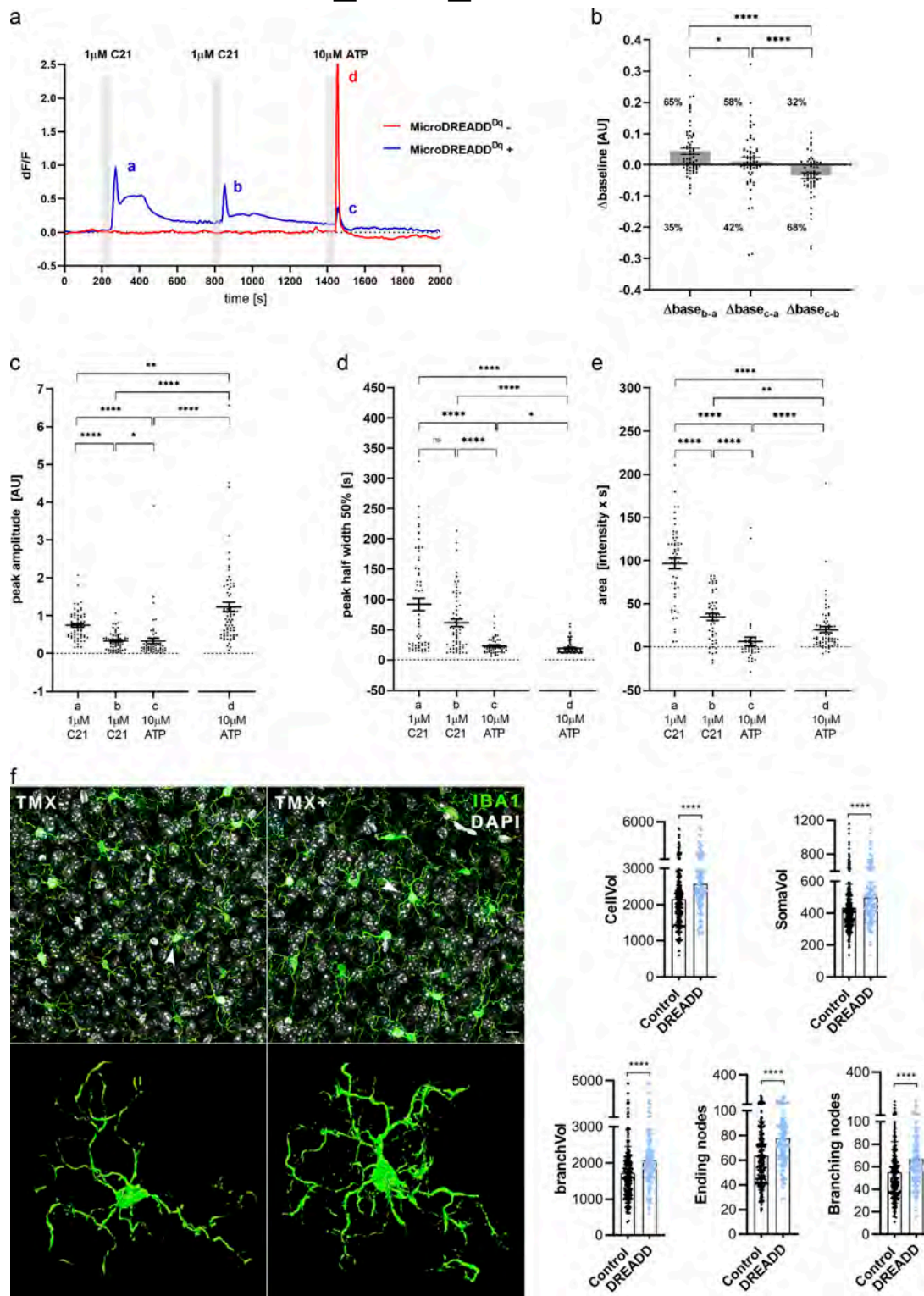


Figure S2. **Microglial cells expressing DREADD (hm3Dq) respond to DREADD agonist C21 with a biphasic $[Ca^{2+}]_i$ response and reduced ATP responsiveness.** (a) Representative calcium signals of cultured MicroDREADD^{Dq+} and MicroDREADD^{Dq-} microglia cells repeatedly exposed to 1 μ M C21 and 10 μ M ATP for 1 min. (b) Differences of average baseline values determined within 50 s before the onset of the responses. Mann-Whitney *U* test; *, *P* < 0.05; ****, *P* < 0.0001. (c–e) Peak amplitudes (c), half-width values (d), and peak areas (e) of a, b, c and d peaks denoted in the line graph (a). *n* = 64 for MicroDREADD^{Dq+}, *n* = 73 for MicroDREADD^{Dq-}; Mann-Whitney *U* test; ****, *P* < 0.0001; **, *P* < 0.01; *, *P* < 0.05 (c–e). (f) Automated analysis shows marked morphological changes in MicroDREADD^{Dq+} microglia in TMX-treated mice 1 h after i.p. CNO administration, compared with littermates in which hm3Dq DREADD expression was not induced with TMX (control). *n* = 275 control (MicroDREADD^{Dq-}) and *n* = 122 DREADD (MicroDREADD^{Dq+}) microglia from *n* = 3 mice from each group were analysed. Mann-Whitney *U* test; ****, *P* < 0.0001 for cell volume (CellVol), soma volume (SomaVol), branch volume (branchVol), ending nodes, and branching nodes. Scale bar, 20 μ m. Data are expressed as mean \pm SEM.

dc_2027_22

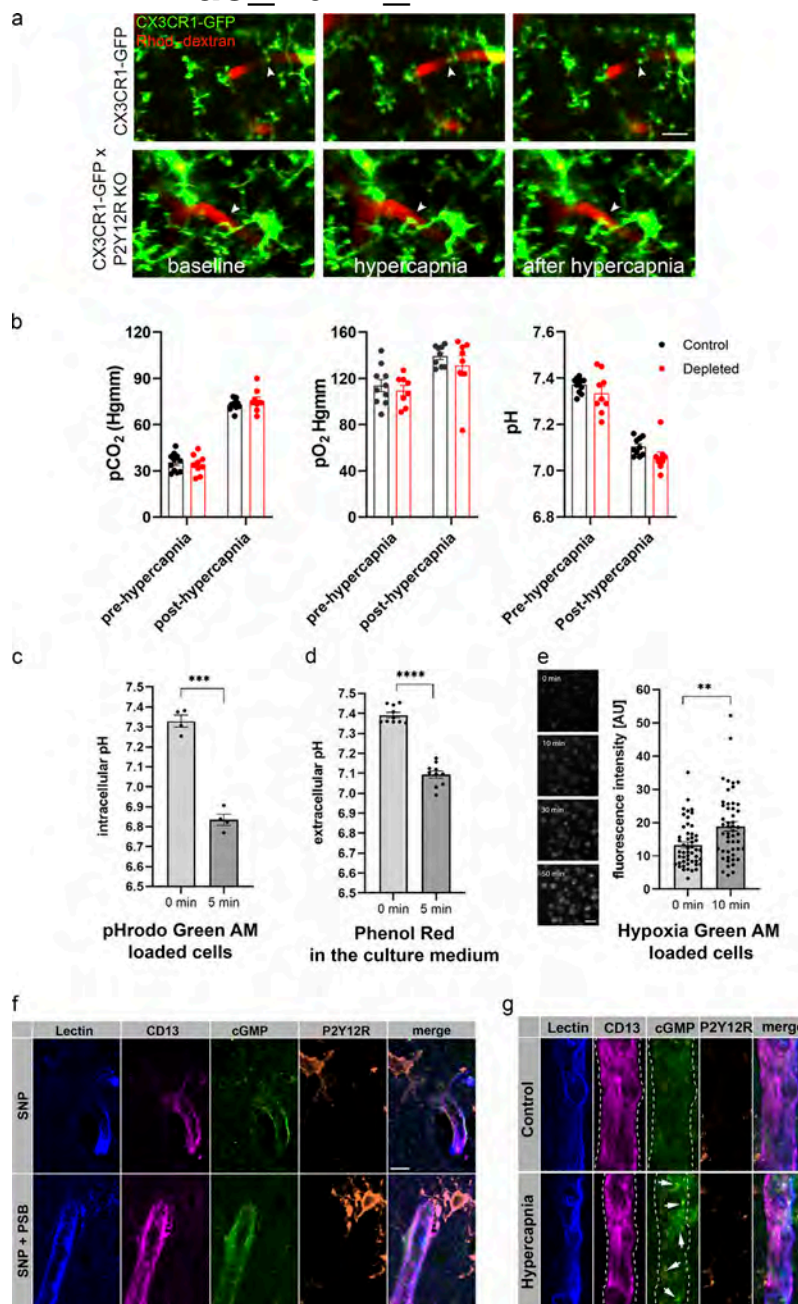


Figure S3. Microglia modulation does not change blood gases but impacts on cGMP levels in the cerebral vasculature. (a) In vivo two-photon imaging was performed with resonant scanning (32 Hz) in the somatosensory cortex of CX3CR1^{GFP/+} x P2Y12R KO and CX3CR1^{GFP/+} (P2Y12R-competent) mice following intravenous Rhodamine B-Dextran (Rhod.-dextran) administration to visualize blood vessels. After recording 60 s of baseline, vasodilation was induced by inhalation of 10% CO₂ in air for 120 s (61–180 s) under normoxic conditions, followed by 60 s of posthypercapnia recording, using a protocol identical to that shown in Fig. 5 d. Scale bar, 10 μ m. (b) Arterial pCO₂, pO₂, and pH measurements under ketamine-medetomidine anesthesia after the administration of atipamezole performed before and after hypercapnic challenge. Blood samples were taken from the femoral artery. No significant difference was observed between control and microglia-depleted mice. $n = 10$ control and $n = 8$ depleted mice, two-way ANOVA followed by Sidak's multiple comparison test. (c and d) Both intracellular (c) and extracellular (d) pH markedly decreases within a few minutes after exposing cells to 15% CO₂/85% air gas mixture, as a model of hypercapnia. Extracellular pH was determined by Phenol Red absorbance measurements, and intracellular pH was measured as changes in pHrodo Green AM dye fluorescence in glial cells. $n = 4$ parallels per group; ***, $P = 0.0001$, 0 min versus 5 min, paired t test (c); $n = 10$ parallels per group; ****, $P < 0.0001$, 0 min versus 5 min, paired t test (d). (e) Hypoxia Green AM loaded cells exhibit significant increase in fluorescent intensity within 10 min after placing microglia cultures to hypoxic environment (1% O₂/5% CO₂/94% N₂). The reagent begins to fluoresce when oxygen levels drop below 5%. $n = 50$ parallels per group; **, $P = 0.0019$ 0 min versus 10 min, Mann-Whitney U test. Scale bar, 30 μ m. Data are shown as mean \pm SEM (b–e). (f) Single image planes for CLSM imaging show small blood vessel segments from second and third layer of the neocortex in acute brain slices. Lectin (blue) outlines the vessels, CD13 labels contractile elements (pericytes and smooth muscle cells), microglial P2Y12R is orange, and cGMP signal can be seen in green (arrows). Note that PSB0739 treatment has no effect on SNP-induced cGMP. (g) CLSM imaging shows small blood vessel segments from the second and third layer of the neocortex in perfusion-fixed brain sections. Hypercapnia was induced in vivo and maintained in anesthetized mice until sacrifice. Lectin (blue) outlines the vessels, CD13 labels contractile elements (pericytes and smooth muscle cells), microglial P2Y12R is orange, and cGMP signal can be seen in green (arrows).

dc_2027_22

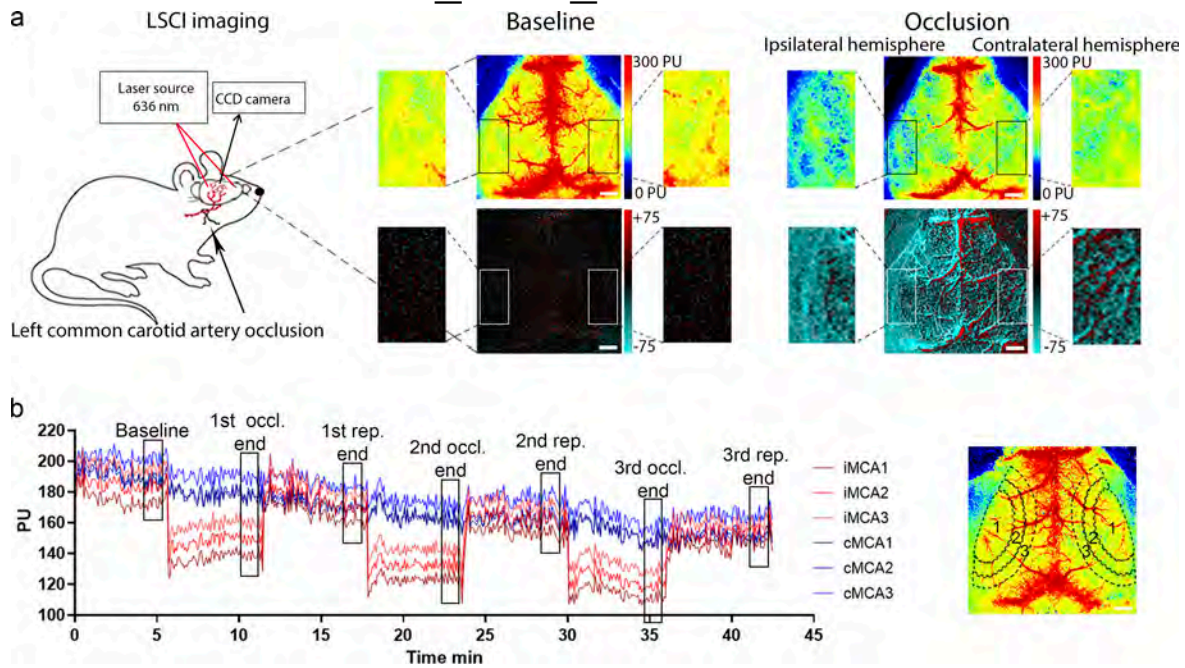


Figure S4. **CBF was measured during transient left CCAo through the intact skull bone by LSCI. (a)** Representative perfusion (0–300 PU, on the top of a, and difference images (–75 to +75) on the bottom of a show baseline CBF and perfusion changes during CCA occlusion. Scale bar, 1 mm. **(b)** Representative graph showing the typical kinetics of repeated (3× CCA) occlusions on the areas (MCA1–3 areas) investigated on both hemispheres. ROIs are shown on a representative perfusion image on the right. Black rectangles on the kinetic graph display the sections of curves, which were used for detailed analysis. Scale bar, 1 mm.

Video 1. **Cerebral blood vessels were visualized by i.v. FITC-Dextran administration in CX3CR1^{tdTomato} mice, and microglial process dynamics was investigated by in vivo two-photon microscopy along the vascular tree.** Refer to Fig. 1, a and b for further details. Fig. 1b depicts blood vessels identical to those shown in the video file, with arrowheads indicating the contact surfaces between microglial processes and first- or second-order capillaries.

Video 2. **Representative LSCI videos showing the whisker stimulation–evoked reduced neurovascular coupling response in microglia-depleted mice compared with controls.** Difference images are shown, which display the stimulus-evoked CBF increase over baseline. White rectangles indicate the area of the barrel cortex.

Video 3. **Representative resonant in vivo two-photon imaging videos showing individual neuronal $[Ca^{2+}]_i$ responses to electromechanically controlled whisker stimulation in control and microglia-depleted Thy1-GCaMP6s mice.** Red dot indicates the onset of the individual stimuli (15 s long) repeated twice with 40-s intervals.

Video 4. **Fluorescent time-lapse recording of cultured MicroDREADD^q microglia cells responding to 1 μ M C21 DREADD agonist.** The cells were loaded with Cal590 AM fluorogenic calcium sensitive dye (red) and the cell membrane was stained with the FluoVolt membrane labeling dye (green). The video was recorded at 0.25 frame/s in a 150 × 107- μ m field of view. Scale bar, 10 μ m. Note decreased process motility already after the first C21 treatment and markedly decreased calcium responses to repeated C21 stimulations.

Video 5. **Phase-contrast video of MicroDREADD^q microglia cells responding to 1 μ M C21 DREADD agonist.** The video was recorded at 2 frame/min for 60 min on a Zeiss Axiovert 200M microscope in a 150 × 107- μ m field of view. Scale bar, 10 μ m. Note decreased process dynamics after C21 treatment.

Video 6. **Representative in vivo two-photon imaging videos recorded by the resonant scanner showing reduced hypercapnia-induced vasodilation in P2Y12R KO (CX3CR1^{GFP/+} × P2Y12R KO) mice compared with control (CX3CR1^{GFP/+}) mice.** Blood vessels were visualized by administration of Rhodamine B-dextran. Hypercapnia was induced at 60 s and maintained until 180 s with a 60-s-long posthypercapnic period. Identical fields of view are shown in Fig. 5 j.

Video 7. **Representative in vivo two-photon resonant imaging video recorded in the cerebral cortex of CX3CR1^{CGaMP5g-tdTomato} mice during hypercapnic challenge (shown in Fig. 5 c).** Perivascular microglial processes show dynamic $[Ca^{2+}]_i$ activity changes in response to hypercapnia. The arterial segment on the left is labeled with "a."

Video 8. **Representative LSCI video showing the third occlusion-reperfusion period in microglia-depleted and control mice.** Difference images display the marked CBF reduction caused by the third occlusion over the second reperfusion period. White ellipses show the area of the cerebral cortex (MCA territory) with significant CBF reduction after CCA occlusion. Note: to reduce the size of the video, a 2-min-long section from the third occlusion and a 3-min-long section from the second reperfusion have been removed. No significant CBF changes were seen during these periods.

Provided online is Table S1. Table S1 lists patient data and processing of postmortem human brain tissues.

Table S1. Patient data and processing of post-mortem human brain tissues.

Subject	Code	Gender	Age (years)	Health status	Comorbidities	Cause of death	Tissue sample type
Control subject	SKO13	female	60	normal	chronic bronchitis	respiratory arrest	free floating and paraffin sections
Control subject	SKO16	male	73	normal	Unspec. atherosclerosis, pneumonia	respiratory arrest	free floating and paraffin sections
Control subject	SKO20	male	27	normal	unspec. jaundice, malignant pancreatic neoplasm.	pulmonary embolism	free floating sections